International Tables for Crystallography (2019). Vol. H, Chapter 1.1, pp. 2–23.

1.1. Overview and principles of powder diffraction

R. E. Dinnebier and S. J. L. Billinge

1.1.1. Information content of a powder pattern

The structures of real materials comprise not only the crystal structure – the time- and space-averaged periodic configuration of atoms on an idealized periodic lattice – but also the microstructure, which is caused by imperfections, dislocations and all kinds of disorder. The microstructure is often responsible for interesting properties of the material. A powder diffraction pattern contains a wealth of information about this microstructure in addition to the average crystal structure, as shown schematically in Fig. 1.1.1.

At each stage of a powder diffraction study, great effort and ingenuity are needed to find the optimal experimental conditions and to understand and analyse the resulting line shapes and signals. As experimental equipment, theoretical understanding and computational tools have improved, it has become possible to tap into the rich information content of the line peak shapes and diffuse background of a typical powder diffraction pattern, yielding unprecedented information about real materials for materials scientists, chemists, physicists, earth scientists and engineers. For example, in the modern practice of whole-pattern modelling, the line profile is calculated from first principles, taking into account all aspects of the state of the sample, such as particle-size distributions, inhomogeneous strains and texture, as well as the experimental setup and aberrations. There is a useful feedback effect in that better profile descriptions result in more accurate determinations of the intensities of the Bragg peaks, which is important to extract accurate structural information (Bragg peaks are introduced in detail in the next section). Similarly, great progress has been made in the extraction of information from the diffuse signal that used to be called the 'background'. Rather than fitting the background using arbitrary fitting parameters, as is done in a traditional Rietveld refinement, careful corrections can be made for experimental effects such as Compton scattering, fluorescence, multiple scattering and scattering from sample environments. The resulting 'background' beneath and between the Bragg peaks of the corrected data is information-rich diffuse scattering from the sample, which contains information about the local structure and how it deviates from the average crystal structure in the form of defects and correlated lattice dynamics (phonons). Total-scattering methods that include both the Bragg and diffuse scattering are only now being fully appreciated, with quantitative analyses being carried out in real space using the atomic pair distribution function (PDF) method, and in reciprocal space with Monte Carlo simulated-annealing-type modelling based on the Debye equation.

In this introductory chapter, the basic physics behind the observation of a powder diffraction pattern is described. In accordance with the scheme in Fig. 1.1.1, the information in a powder diffraction pattern can be described by the Bragg-peak positions, the peak profile, the Bragg-peak intensities and the non-Bragg-scattering contributions to the background. After describing the fundamentals of scattering by a crystalline powder, the chapter is organized such that each of the paths illustrated in Fig. 1.1.1 is followed and described in an introductory way. Detailed descriptions of the state of the art in the kinds of studies covered in Fig. 1.1.1 can be found in following chapters, but here we discuss each aspect of powder diffraction in turn, giving a high-level overview of what information is available from powder diffraction as well as explaining the fundamental origin of the features containing that information. We do not attempt to review applications of the different kinds of studies, leaving that to the following chapters.

In this chapter we have drawn heavily on information within three textbooks (Dinnebier & Billinge, 2008; Mittemeijer & Welzel, 2012; Egami & Billinge, 2013) and references therein.

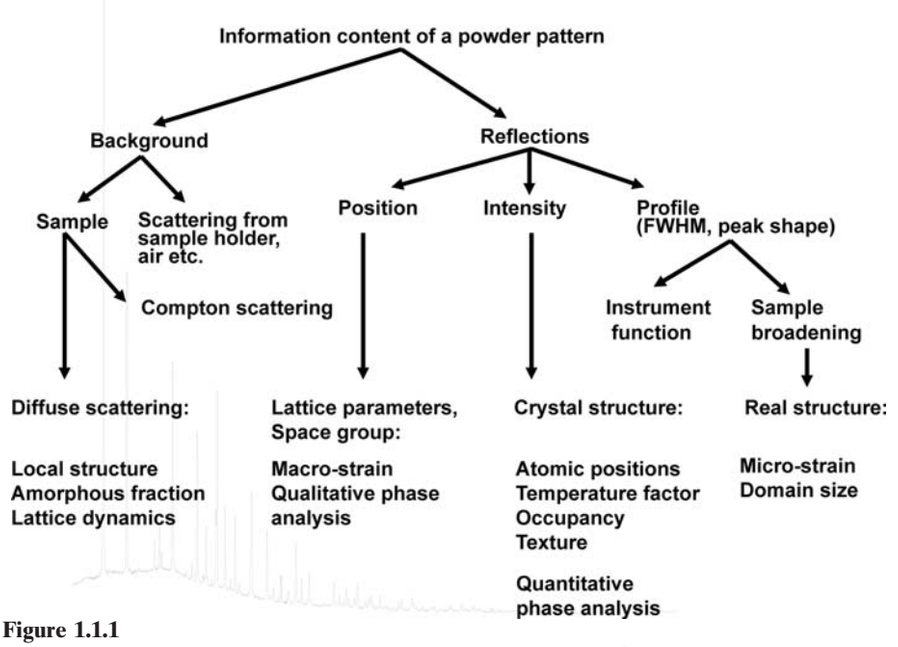

Figure 1.1.1
Schematic picture of the information content of a powder pattern. [Reproduced from Dinnebier & Billinge (2008) with permission from the Royal Society of Chemistry.]

1.1.2. The peak position

1.1.2.1. *The Bragg equation derived*

The easiest way to understand the structural information contained in powder diffraction, and historically one of the first ways in which diffraction was described, is *via* the well known Bragg equation (Bragg, 1913), which describes the principle of X-ray diffraction in terms of the reflection of X-rays by sets of lattice planes.

To understand the concept of a lattice plane, first imagine a three-dimensional periodic lattice of points, for example the corners of an array of cubes stacked in three dimensions. We can imagine a particular plane through the lattice by placing each layer of the stack of cubes on a tray: the tray then defines a lattice plane. Now imagine making the tray thinner and thinner until it

is infinitely thin, but still goes through the same set of points (the cube corners). What we see is that there is not just a single plane, but a series of equivalent planes: for example, between the top and second layers, the second and third layers, and so on. Each plane is parallel to the others and subsequent planes are separated by the same distance (the height of the cube). This is a set of lattice planes. We can also envisage inserting the trays in other ways. For example, we could place the trays vertically rather than horizontally and running from the left side to the right side of the stack of cubes, or alternatively running from the front of the stack to the back of the stack. Each of these is a different set of lattice planes (Fig. 1.1.2), although in this case they have the same layer spacing, or periodicity. If we were able to insert the tray at different angles to the cubes, for example at 45°, we could find other sets of parallel planes that, when we force them to go through some well defined subset of the points defining the lattice, will have well defined layer spacings or periodicities. Bragg's law showed that the diffraction pattern could be understood in terms of X-rays reflecting specularly off subsequent planes in each of these sets of planes and emerging in phase. (In reality, the actual effect is not specular reflection of light from an abstract plane, but a diffraction effect. However, the combination of diffraction and periodicity results in a selection rule that intense scattering only occurs when this particular specular-reflection condition holds.)

There are actually an infinite number of lattice planes in an infinite lattice, and it is important to have a way of labelling them, which is commonly done using the triplet of indices *hkl*, called Miller indices, where h, k and l are integers, and the separation of the planes is denoted by the distance d_{hkl}. When h, k and l have small values the planes are said to be 'low-order' planes. Low-order planes have the largest interplanar separations, and for a particular symmetry of the lattice there is a direct relationship between the Miller indices and d_{hkl}.

The Bragg equation gives the condition that must hold for specular reflection from subsequent planes in a set to be perfectly in phase, as illustrated in Fig. 1.1.3. It is evident in Fig. 1.1.3 that the wave reflecting off the lower plane travels a longer distance (by PN before and NQ after reflection occurs) than the wave reflecting off the upper plane. The two waves are in phase, resulting in constructive interference, only when $\Delta = |\mathrm{PN}| + |\mathrm{NQ}|$ is a multiple $n = 0, 1, 2, \ldots$ of the wavelength λ,

$$\Delta = n\lambda. \tag{1.1.1}$$

In all other cases, destructive interference results, since it is always possible to find a deeper plane, p, for which the relation

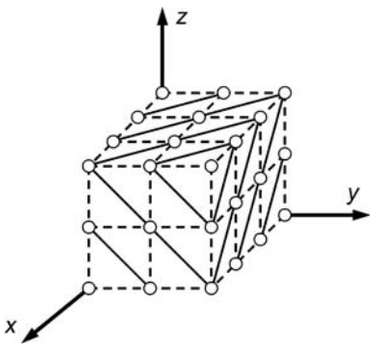

Figure 1.1.2
Schematic drawing of a set of parallel lattice planes (111) passing through all points of the cubic lattice.

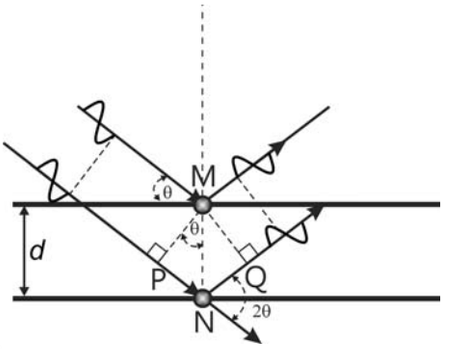

Figure 1.1.3
Illustration of the geometry used for the simplified derivation of Bragg's law. [Reproduced from Dinnebier & Billinge (2008) with permission from the Royal Society of Chemistry.]

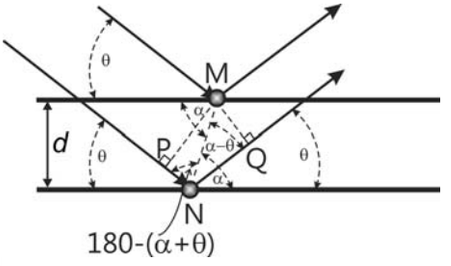

Figure 1.1.4
Illustration of the geometry in the general case where scattering takes place at the position of atoms in consecutive planes. [Reproduced from Dinnebier & Billinge (2008) with permission from the Royal Society of Chemistry.]

$p\Delta = n\lambda + 1/2$ exactly holds, giving rise to perfect destructive interference. Thus, when a narrow beam of X-rays impinges on a crystalline sample, sharp peaks in the intensity of the scattered X-rays are seen only at the angles for which equation (1.1.1) holds, with no intensity observed at other angles. As can easily be seen from Fig. 1.1.3, geometrically,

$$\Delta = 2d\sin\theta, \tag{1.1.2}$$

where d is the interplanar spacing of the parallel lattice planes and 2θ is the diffraction (or 'scattering') angle, the angle between the incoming and outgoing X-ray beams. The angle $\theta = 2\theta/2$ is often called the Bragg angle. Combining equations (1.1.1) and (1.1.2) we get

$$n\lambda = 2d\sin\theta, \tag{1.1.3}$$

which is the Bragg equation (Bragg, 1913).

This simplified derivation of the Bragg equation is often reproduced in textbooks. Although it leads to the correct solution, it has a serious drawback. In reality the X-rays are not reflected by planes, but are scattered by electrons bound to the atoms in the sample. The planes within a crystal are not like shiny optical mirrors, but contain discrete atoms separated by regions of much lower electron density and, in general, the atoms in one plane will not lie exactly above atoms in the plane below as implied by Fig. 1.1.3. How is it then that the simplified picture shown in Fig. 1.1.3 gives the correct result? A more general description shows that equation (1.1.3) is also valid if the atom in the lower lattice plane in Fig. 1.1.3 is shifted by an arbitrary amount within the plane (Fig. 1.1.4).

The phase shift can immediately be deduced from Fig. 1.1.4 as

$$\begin{aligned} n\lambda &= \mathrm{MN}\cos[180^\circ - (\alpha+\theta)] + \mathrm{MN}\cos(\alpha-\theta) \\ &= \mathrm{MN}[-\cos(\alpha+\theta) + \cos(\alpha-\theta)]. \end{aligned} \tag{1.1.4}$$

Using the standard trigonometric results

$$\cos(\alpha+\theta)=\cos\alpha\cos\theta-\sin\alpha\sin\theta,$$
$$\cos(\alpha-\theta)=\cos\alpha\cos\theta+\sin\alpha\sin\theta, \quad (1.1.5)$$

equation (1.1.4) becomes

$$n\lambda=\mathrm{MN}(2\sin\alpha\sin\theta) \quad (1.1.6)$$

with

$$d=\mathrm{MN}\sin\alpha, \quad (1.1.7)$$

which may be substituted to yield the Bragg equation:

$$n\lambda=2d\sin\theta. \quad (1.1.8)$$

The Bragg equation holds for any radiation or particle that is used to probe the structure of the sample: X-rays, neutrons or electrons. Another equivalent, and highly useful, form of the Bragg equation for the particular case of X-rays is

$$Ed=\frac{6.199}{\sin\theta}\ \text{with}\ \lambda=\frac{12.398}{E}, \quad (1.1.9)$$

where the energy E of the X-rays is in keV and λ is in ångströms.

The Bragg law results in narrow beams of high intensity that emerge from the crystal in specific directions given by the Bragg equation, resulting in sharp spots on the detector, and there is a one-to-one correspondence between these Bragg spots (often referred to as Bragg reflections) and each set of crystallographic planes. Each Bragg spot is therefore labelled with the same set of Miller indices, *hkl*, as the set of planes that gave rise to it.

It is possible to construct a 'reciprocal space' where the axes of the space are in units of inverse length. The reference coordinate frame of the reciprocal space is defined by a set of basis vectors whose directions are perpendicular to the plane normals of the (100), (010) and (100) planes of the crystal. Thus, a *point* in this reciprocal space corresponds to a *direction* in direct space and every allowed reflection according to the Bragg law is represented by a point in reciprocal space. The set of points arising from the Bragg law forms a lattice in reciprocal space, which is called the 'reciprocal lattice', and each single crystal has its own reciprocal lattice. [See *International Tables for Crystallography* Volume B (Shmueli, 2008) for more details.]

To derive the Bragg equation, we used an assumption of specular reflection, which is borne out by experiment: for a crystalline material, destructive interference eliminates scattered intensity in all directions except where equation (1.1.3) holds. Strictly this holds only for crystals that are infinite in extent and which the incident X-ray beam can penetrate without loss of intensity. This does not sound like a particularly good approximation, but in practice it holds rather well. Even a fairly low energy X-ray beam that only penetrates, say, a micrometre into the material will still probe ~10 000 atomic layers. The condition is not strictly obeyed in the presence of defects and disorder in the material. In such materials the Bragg peaks are modified in their position, their width and their shape, and there is also an additional component of the diffracted intensity that may be observed in all directions, away from reciprocal-lattice points, known as diffuse scattering.

1.1.2.2. *The Bragg equation from the reciprocal lattice*

Here we develop in more detail the mathematics of the reciprocal lattice. The reciprocal lattice has been adopted by crystallographers as a simple and convenient representation of the physics of diffraction by a crystal. It is an extremely useful tool for describing all kinds of diffraction phenomena occurring in powder diffraction.

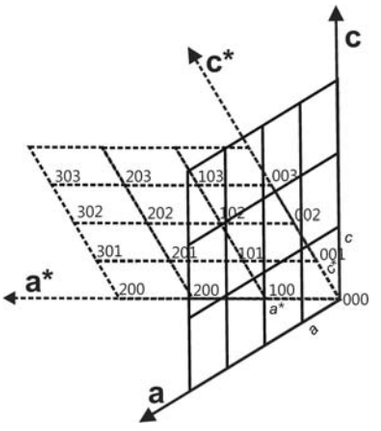

Figure 1.1.5
A two-dimensional monoclinic lattice and its corresponding reciprocal lattice. [Adapted from Dinnebier & Billinge (2008) with permission from the Royal Society of Chemistry.]

Consider a 'normal' crystal lattice with lattice vectors **a**, **b** and **c**, which have lengths a, b and c, respectively, and angles α between **b** and **c**, β between **a** and **c** and γ between **a** and **b**. The unit-cell volume is given by V. A second lattice with lattice parameters a^*, b^*, c^*, α^*, β^*, γ^* and unit-cell volume V^* with the same origin exists such that

$$\mathbf{a}\cdot\mathbf{b}^*=\mathbf{a}\cdot\mathbf{c}^*=\mathbf{b}\cdot\mathbf{c}^*=\mathbf{a}^*\cdot\mathbf{b}=\mathbf{a}^*\cdot\mathbf{c}=\mathbf{b}^*\cdot\mathbf{c}=0,$$
$$\mathbf{a}\cdot\mathbf{a}^*=\mathbf{b}\cdot\mathbf{b}^*=\mathbf{c}\cdot\mathbf{c}^*=1. \quad (1.1.10)$$

This is known as the reciprocal lattice[1] (Fig. 1.1.5), which exists in so-called reciprocal space. As mentioned above, we will see that it turns out that the points in the reciprocal lattice are related to the vectors defining the crystallographic plane normals. There is one point in the reciprocal lattice for each set of crystallographic planes, (*hkl*), separated by distance d_{hkl}, as discussed below. For now, just consider h, k and l to be integers that index a point in the reciprocal lattice. A reciprocal-lattice vector $\mathbf{h}_{hkl}$ is the vector from the origin of reciprocal space to the reciprocal-lattice point for the plane (*hkl*),

$$\mathbf{h}_{hkl}=h\mathbf{a}^*+k\mathbf{b}^*+l\mathbf{c}^*,\quad h,k,l\in\mathbb{Z}. \quad (1.1.11)$$

where $\mathbb{Z}$ is the set of all integers.

The length of the reciprocal basis vector $\mathbf{a}^*$ is defined according to

$$\mathbf{a}^*=x(\mathbf{b}\times\mathbf{c}), \quad (1.1.12)$$

where the scale factor x can easily be deduced, using equations (1.1.12) and (1.1.10), as

$$\mathbf{a}^*\cdot\mathbf{a}=x(\mathbf{b}\times\mathbf{c}\cdot\mathbf{a})=xV\Rightarrow x=\frac{1}{V}, \quad (1.1.13)$$

leading to

$$\mathbf{a}^*=\frac{1}{V}(\mathbf{b}\times\mathbf{c}),\quad \mathbf{b}^*=\frac{1}{V}(\mathbf{c}\times\mathbf{a}),\quad \mathbf{c}^*=\frac{1}{V}(\mathbf{a}\times\mathbf{b}) \quad (1.1.14)$$

and, *vice versa*,

[1] The reciprocal lattice is a commonly used construct in solid-state physics, but with a different normalization: $\mathbf{a}\cdot\mathbf{a}^*=2\pi$.

$$\mathbf{a} = \frac{1}{V^*}(\mathbf{b}^* \times \mathbf{c}^*), \quad \mathbf{b} = \frac{1}{V^*}(\mathbf{c}^* \times \mathbf{a}^*), \quad \mathbf{c} = \frac{1}{V^*}(\mathbf{a}^* \times \mathbf{b}^*). \tag{1.1.15}$$

The relationship between the reciprocal and the real lattice parameters expressed geometrically rather than in the vector formalism used above is

$$\begin{aligned} a^* &= \frac{bc\sin\alpha}{V}, \\ b^* &= \frac{ac\sin\beta}{V}, \\ c^* &= \frac{ab\sin\gamma}{V}, \\ \cos\alpha^* &= \frac{\cos\beta\cos\gamma - \cos\alpha}{\sin\beta\sin\gamma}, \\ \cos\beta^* &= \frac{\cos\alpha\cos\gamma - \cos\beta}{\sin\alpha\sin\gamma}, \\ \cos\gamma^* &= \frac{\cos\alpha\cos\beta - \cos\gamma}{\sin\alpha\sin\beta}, \\ V &= abc\sqrt{1 + 2\cos\alpha\cos\beta\cos\gamma - \cos^2\alpha - \cos^2\beta - \cos^2\gamma}. \end{aligned} \tag{1.1.16}$$

Equation (1.1.16) is the most general expression for non-orthogonal lattices. The expressions simplify considerably for higher-symmetry crystal systems.

We now re-derive Bragg's law using the vector notation introduced above (Fig. 1.1.6). The wave vectors of the incoming and outgoing beams are given by $\mathbf{s}_0$ and $\mathbf{s}$, respectively. They point in the direction of propagation of the wave and their length depends on λ. For elastic scattering (for which there is no change in wavelength on scattering), $\mathbf{s}_0$ and $\mathbf{s}$ have the same length.

We define the scattering vector as

$$\mathbf{h} = (\mathbf{s} - \mathbf{s}_0), \tag{1.1.17}$$

which for a specular reflection is always perpendicular to the scattering plane. The length of $\mathbf{h}$ is given by

$$\frac{h}{s} = 2\sin\theta. \tag{1.1.18}$$

Comparison with the formula for the Bragg equation (1.1.3),

$$\frac{n\lambda}{d} = 2\sin\theta, \tag{1.1.19}$$

gives

$$\frac{n\lambda}{d} = \frac{h}{s}. \tag{1.1.20}$$

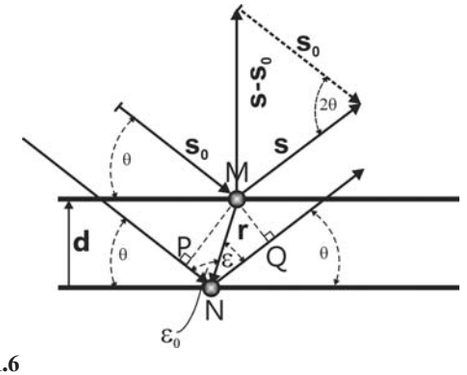

Figure 1.1.6
Illustration of the important wave and scattering vectors in the case of elastic Bragg scattering. [Reproduced from Dinnebier & Billinge (2008) with permission from the Royal Society of Chemistry.]

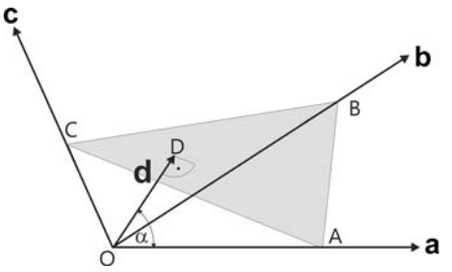

Figure 1.1.7
Geometrical description of a lattice plane in terms of real-space basis vectors. The arc and dot below the letter D indicate a right angle. [Reproduced from Dinnebier & Billinge (2008) with permission from the Royal Society of Chemistry.]

Setting the magnitude of $\mathbf{s}$ to $1/\lambda$, we get the Bragg equation in terms of the magnitude h of the scattering vector,

$$h = \frac{n}{d}. \tag{1.1.21}$$

This shows that diffraction occurs when the magnitude of the scattering vector is an integral number of reciprocal-lattice spacings $1/d$. We define a vector $\mathbf{d}^*$ perpendicular to the lattice planes with length $1/d$. Since $\mathbf{h}$ is perpendicular to the scattering plane, this leads to

$$\mathbf{h} = n\mathbf{d}^*. \tag{1.1.22}$$

Diffraction can occur at different scattering angles 2θ for the same crystallographic plane, giving the different orders n of diffraction. For simplicity, the number n will be incorporated in the indexing of the lattice planes, where

$$d^*_{nh,nk,nl} = nd^*_{hkl}, \tag{1.1.23}$$

e.g., $d^*_{222} = 2d^*_{111}$, and we get an alternative expression for Bragg's equation:

$$\mathbf{h} = \mathbf{d}^*_{hkl}. \tag{1.1.24}$$

The vector $\mathbf{d}^*_{hkl}$ points in a direction perpendicular to a real-space lattice plane. We would like to express this vector in terms of the reciprocal-space basis vectors $\mathbf{a}^*$, $\mathbf{b}^*$, $\mathbf{c}^*$.

First we define $\mathbf{d}_{hkl}$ in terms of the real-space basis vectors $\mathbf{a}$, $\mathbf{b}$, $\mathbf{c}$. Referring to Fig. 1.1.7, we can define

$$\mathbf{OA} = \frac{1}{h}\mathbf{a}, \quad \mathbf{OB} = \frac{1}{k}\mathbf{b}, \quad \mathbf{OC} = \frac{1}{l}\mathbf{c} \tag{1.1.25}$$

with h, k and l being integers, as required by the periodicity of the lattice.

The plane-normal vector $\mathbf{d}_{hkl}$ originates on one plane and terminates on the next parallel plane. Therefore, $\mathbf{OA} \cdot \mathbf{d} = (\mathrm{OA})d\cos\alpha$. From Fig. 1.1.7 we see that, geometrically, $(\mathrm{OA})\cos\alpha = d$. Substituting, we get $\mathbf{OA} \cdot \mathbf{d} = d^2$. Combining this with equation (1.1.25) leads to

$$\frac{1}{h}\mathbf{a} \cdot \mathbf{d} = d^2 \tag{1.1.26}$$

and consequently

$$h = \mathbf{a} \cdot \frac{\mathbf{d}}{d^2}, \quad k = \mathbf{b} \cdot \frac{\mathbf{d}}{d^2}, \quad l = \mathbf{c} \cdot \frac{\mathbf{d}}{d^2}. \tag{1.1.27}$$

By definition, h, k and l are divided by their largest common integer to be Miller indices. The vector $\mathbf{d}^*_{hkl}$, from Bragg's equation (1.1.24), points in the plane-normal direction parallel to $\mathbf{d}$ but with length $1/d$. We can now write $\mathbf{d}^*_{hkl}$ in terms of the

vector **d**:

$$\mathbf{d}^*_{hkl} = \frac{\mathbf{d}}{d^2}, \tag{1.1.28}$$

which gives

$$\mathbf{d}^*_{hkl} = \frac{\mathbf{d}_{hkl}}{d^2} = h\mathbf{a} + k\mathbf{b} + l\mathbf{c}, \tag{1.1.29}$$

or written in terms of the reciprocal basis

$$\mathbf{d}^*_{hkl} = h\mathbf{a}^* + k\mathbf{b}^* + l\mathbf{c}^*, \tag{1.1.30}$$

which was obtained using

$$\begin{aligned}
\mathbf{d}^*_{hkl} \cdot \mathbf{a}^* &= h\mathbf{a} \cdot \mathbf{a}^* + k\mathbf{b} \cdot \mathbf{a}^* + l\mathbf{c} \cdot \mathbf{a}^* = h, \\
\mathbf{d}^*_{hkl} \cdot \mathbf{b}^* &= h\mathbf{a} \cdot \mathbf{b}^* + k\mathbf{b} \cdot \mathbf{b}^* + l\mathbf{c} \cdot \mathbf{b}^* = k, \\
\mathbf{d}^*_{hkl} \cdot \mathbf{c}^* &= h\mathbf{a} \cdot \mathbf{c}^* + k\mathbf{b} \cdot \mathbf{c}^* + l\mathbf{c} \cdot \mathbf{c}^* = l.
\end{aligned} \tag{1.1.31}$$

Comparing equation (1.1.30) with equation (1.1.11) proves the identity of $\mathbf{d}^*_{hkl}$ and the reciprocal-lattice vector $\mathbf{h}_{hkl}$. Bragg's equation, (1.1.24), can be re-stated as

$$\mathbf{h} = \mathbf{h}_{hkl}. \tag{1.1.32}$$

In other words, diffraction occurs whenever the scattering vector **h** equals a reciprocal-lattice vector $\mathbf{h}_{hkl}$. This powerful result is visualized in the useful Ewald construction, which is described in Section 1.1.2.4.

Useful equivalent variations of the Bragg equation are

$$|\mathbf{h}| = \left|\mathbf{s} - \mathbf{s}_0\right| = \frac{2\sin\theta}{\lambda} = \frac{1}{d} \tag{1.1.33}$$

and

$$|\mathbf{Q}| = \frac{4\pi\sin\theta}{\lambda} = \frac{2\pi}{d}. \tag{1.1.34}$$

The vector **Q** is the physicist's equivalent of the crystallographer's **h**. The physical meaning of **Q** is the momentum transfer on scattering and it differs from the scattering vector **h** by a factor of 2π.

1.1.2.3. *The Bragg equation from the Laue equation*

Another approach for describing scattering from a material was first described by Laue (von Laue, 1912). The Laue equation can be derived by evaluating the phase relation between two wavefronts after hitting two scatterers that are separated by the vector **r**. The path-length difference $\Delta = |\mathrm{CD}| - |\mathrm{BA}|$ between the two scattered waves introduces a phase shift between the two outgoing waves (Fig. 1.1.8). From Fig. 1.1.8 one immediately sees that the path-length difference is given by

$$\Delta = r\cos\varepsilon - r\cos\varepsilon_0. \tag{1.1.35}$$

This path-length difference gives rise to a phase shift

$$\varphi = 2\pi\frac{\Delta}{\lambda} = 2\pi\left(\frac{r}{\lambda}\cos\varepsilon - \frac{r}{\lambda}\cos\varepsilon_0\right). \tag{1.1.36}$$

The term in parentheses is

$$\mathbf{s}\cdot\mathbf{r} - \mathbf{s_0}\cdot\mathbf{r} = (\mathbf{s} - \mathbf{s_0})\cdot\mathbf{r} = \mathbf{h}\cdot\mathbf{r}. \tag{1.1.37}$$

The amplitude of the scattered wave at a large distance away in the direction of the vector **s** is

$$A(\mathbf{h}) = \exp(2\pi i 0) + \exp(2\pi i\mathbf{h}\cdot\mathbf{r}) \tag{1.1.38}$$

When we generalize the idea laid out above to *n* scatterers, we get

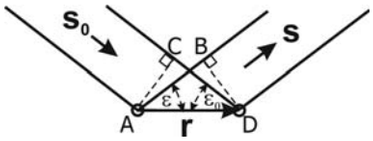

Figure 1.1.8
Scattering from an object consisting of two scatterers separated by **r**.

$$A(\mathbf{h}) = \sum_{j=1}^{n} \exp\left(2\pi i\mathbf{h}\cdot\mathbf{r}_j\right). \tag{1.1.39}$$

For simplicity, consider the case of an infinite one-dimensional crystal of scatterers that are equally spaced by distance a_i. In this case, $r_j = aj$ and

$$A(h) = \sum_{j=-\infty}^{\infty} \exp(2\pi i h a j). \tag{1.1.40}$$

Using the definition for a periodic delta function,

$$\lim_{n\to\infty} \sum_{j=-n}^{n} \exp(2\pi i h a j) = \sum_{k=-\infty}^{\infty} \delta(k - ha) \tag{1.1.41}$$

and

$$A(h) = \sum_{k=-\infty}^{\infty} \delta(k - ha), \tag{1.1.42}$$

which is a periodic array of delta functions at positions $h = k/a$. This means that sharp peaks of intensity will only appear when this expression holds, which are the reciprocal-lattice points. This is the same result as given by the Bragg equation (1.1.3) in one dimension. Extending to three dimensions, equations (1.1.40) and (1.1.42) become

$$\begin{aligned}
A(\mathbf{h}) = &\sum_{j=-\infty}^{\infty} \exp\left(2\pi i(\mathbf{h}\cdot\hat{\mathbf{a}})aj\right) \sum_{k=-\infty}^{\infty} \exp\left(2\pi i(\mathbf{h}\cdot\hat{\mathbf{b}})bk\right) \\
&\times \sum_{l=-\infty}^{\infty} \exp\left(2\pi i(\mathbf{h}\cdot\hat{\mathbf{c}})cl\right),
\end{aligned} \tag{1.1.43}$$

where $\hat{\mathbf{a}} = \mathbf{a}/a$, and

$$A(\mathbf{h}) = \sum_{\mu,\nu,\eta=-\infty}^{\infty} \delta[\mu - (\mathbf{h}\cdot\hat{\mathbf{a}})a]\delta[\nu - (\mathbf{h}\cdot\hat{\mathbf{b}})b]\delta[\eta - (\mathbf{h}\cdot\hat{\mathbf{c}})c]. \tag{1.1.44}$$

Equation (1.1.44) has the same meaning in three dimensions, where intensity appears only when all three delta functions are non-zero. This occurs for the conditions

$$\mathbf{h}\cdot\hat{\mathbf{a}} = \frac{\mu}{a},\ \ \mathbf{h}\cdot\hat{\mathbf{b}} = \frac{\nu}{b} \text{ and } \mathbf{h}\cdot\hat{\mathbf{c}} = \frac{\eta}{c}, \tag{1.1.45}$$

where μ, ν and η are integers. From this follows

$$\mathbf{h}\cdot\mathbf{a} = \mu,\ \ \mathbf{h}\cdot\mathbf{b} = \nu \text{ and } \mathbf{h}\cdot\mathbf{c} = \eta. \tag{1.1.46}$$

These conditions are met when

$$\mathbf{h} = \mu\mathbf{a}^* + \nu\mathbf{b}^* + \eta\mathbf{c}^* = \mathbf{d}^*_{\mu\nu\eta}. \tag{1.1.47}$$

This is exactly Bragg's equation in the form given in equation (1.1.30).

For practical purposes including the indexing of powder patterns and refinement of a structural model, given a set of lattice parameters *a*, *b*, *c*, α, β, γ, the positions for all possible reflections *hkl* can be calculated according to

$$\frac{1}{d_{hkl}} = \frac{1}{V}\left\{\left[h^2b^2c^2\sin^2\alpha + k^2a^2c^2\sin^2\beta + l^2a^2b^2\sin^2\gamma + 2hkabc^2(\cos\alpha\cos\beta - \cos\gamma) + 2kla^2bc(\cos\beta\cos\gamma - \cos\alpha) + 2hlab^2c(\cos\alpha\cos\gamma - \cos\beta)\right]\right\}^{1/2}, \quad (1.1.48)$$

for the triclinic case. Equation (1.1.48) simplifies considerably with symmetry to, for example,

$$\frac{1}{d_{hkl}} = \frac{\sqrt{h^2 + k^2 + l^2}}{a} \quad (1.1.49)$$

for the cubic case.

1.1.2.4. *The Ewald construction and Debye–Scherrer cones*

The Bragg equation shows that diffraction occurs when the scattering vector equals a reciprocal-lattice vector. The scattering vector depends on the geometry of the experiment, whereas the reciprocal-lattice vectors are determined by the orientation and the lattice parameters of the crystalline sample. Bragg's law shows the relationship between these vectors in a scattering experiment. Ewald developed a powerful geometric construction that combines these two concepts in an intuitive way (Ewald, 1921). A sphere of radius $1/\lambda$ is drawn following the recipe below. The Bragg equation is satisfied and diffraction occurs whenever a reciprocal-lattice point coincides with the surface of the sphere.

The recipe for constructing Ewald's sphere[2] is as follows (Fig. 1.1.9):

(1) Draw the incident wave vector $\mathbf{s}_0$. This points in the direction of the incident beam and has length $1/\lambda$.
(2) Draw a sphere centred on the tail of this vector with radius $1/\lambda$. The incident wave vector $\mathbf{s}_0$ defines the radius of the sphere. The scattered wave vector $\mathbf{s}$, also of length $1/\lambda$, points in the direction from the sample to the detector. This vector is also drawn starting from the centre of the sphere and also terminates at a point on the surface of the sphere. The scattering vector $\mathbf{h} = \mathbf{s} - \mathbf{s}_0$ completes the triangle from the tip of $\mathbf{s}$ to the tip of $\mathbf{s}_0$, both of which lie on the surface of the sphere. Thus the surface of the sphere defines the locus of points in reciprocal space where the scattering vector in our experiment may possibly lie.
(3) Draw the reciprocal lattice with the origin lying at the tip of $\mathbf{s}_0$.
(4) Find all the places on the surface of the sphere where reciprocal-lattice points lie. This gives the set of points in reciprocal space where the expression $\mathbf{h} = \mathbf{h}_{hkl}$ may possibly be satisfied in our experiment.

This construction places a reciprocal-lattice point at one end of $\mathbf{h}$. The other end of $\mathbf{h}$ lies on the surface of the sphere by definition. Thus, Bragg's law is only satisfied when another reciprocal-lattice point coincides with the surface of the sphere. Diffraction can be envisaged as beams of X-rays emanating from the sample in these directions. In order to detect the intensity of these diffracted beams, one simply moves the detector to the right position. Any vector between two reciprocal-lattice points has the potential to produce a Bragg peak. The Ewald-sphere construction indicates which of these possible reflections are experimentally accessible.

[2] For practical reasons, plots of the Ewald 'sphere' are circular cuts through the sphere and the corresponding slice of reciprocal space.

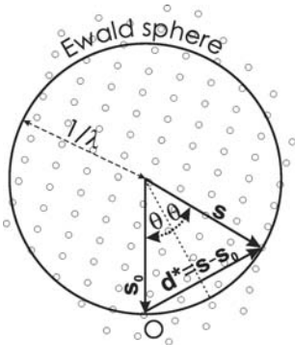

Figure 1.1.9
Simplified representation of the Ewald-sphere construction as a circle in two dimensions. O marks the origin of reciprocal space. The vectors are defined in the text. [Reproduced from Dinnebier & Billinge (2008) with permission from the Royal Society of Chemistry.]

Changing the orientation of the crystal reorients the reciprocal lattice, bringing different reciprocal-lattice points onto the surface of the Ewald sphere. In a single-crystal experiment it is necessary to repeatedly reorient the crystal to bring new reciprocal-lattice points onto the surface of the Ewald sphere, and then to reorient the detector in such a way as to measure the scattering from each particular reflection on the surface. This is done in a highly automated fashion these days. Once a diffraction pattern has been indexed so that the lattice vectors and the orientation matrix (the relation of the lattice vectors to the laboratory coordinate frame) are found, then all of the diffractometer settings that are required to collect all the Bragg peaks are fully determined and this process can be accomplished automatically.

In this chapter we are considering scattering from powders. An ideal powder contains individual crystallites in all possible orientations with equal probability. The powder experiment is equivalent to placing a detector at a fixed position and rotating a single crystal through every orientation, spending an equal amount of time in each orientation. The first powder experiment was reported by Debye & Scherrer in 1916, and independently by Hull in 1917. In the Ewald construction, this is the same as

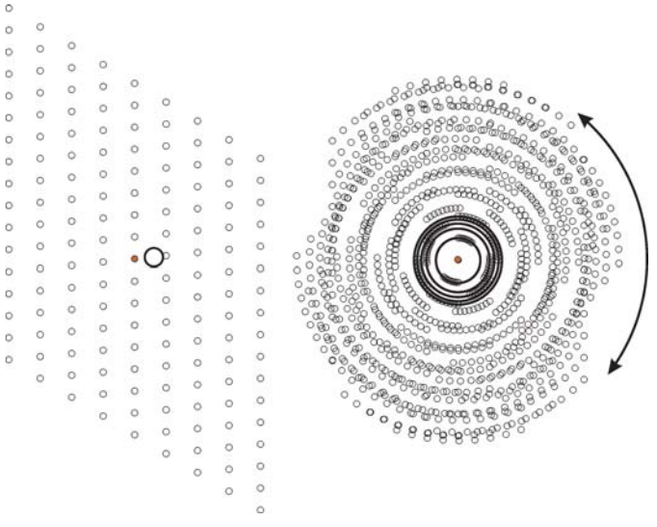

Figure 1.1.10
Illustration of the reciprocal lattice associated with a single-crystal lattice (left) and a large number of randomly oriented crystallites (right). A real powder consists of so many grains that the dots of the reciprocal lattice form into continuous lines. [Reproduced from Dinnebier & Billinge (2008) with permission from the Royal Society of Chemistry.]

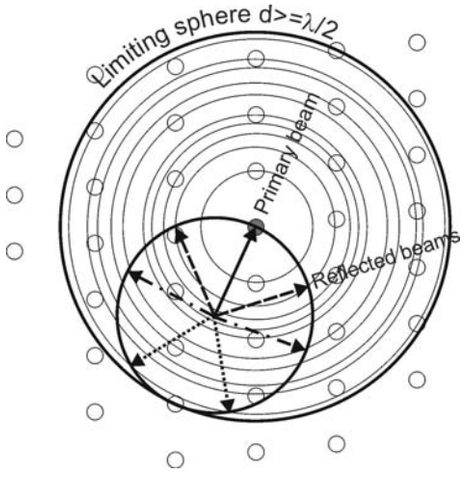

Figure 1.1.11
Simplified representation of the Ewald-sphere construction as a circle in two dimensions. Illustration of the region of reciprocal space that is accessible in a powder diffraction experiment. The smaller circle represents the Ewald sphere. As shown in Fig. 1.1.10, a powder sample has crystallites in all possible orientations, which is modelled by rotating the reciprocal lattice to sample all orientations. An equivalent operation is to rotate the Ewald sphere in all possible orientations around the origin of reciprocal space. The volume swept out is the region of reciprocal space accessible in the experiment. [Reproduced from Dinnebier & Billinge (2008) with permission from the Royal Society of Chemistry.]

smearing out every reciprocal-lattice point over the surface of a sphere centred on the origin of reciprocal space. This is illustrated in Fig. 1.1.10. The orientation of the $\mathbf{d}^*_{hkl}$ vector is lost and the three-dimensional vector space is reduced to one dimension with the independent variable being the modulus of the vector $\left|\mathbf{d}^*_{hkl}\right| = 1/d$.

These spherical shells intersect the surface of the Ewald sphere in circles. A two-dimensional projection is shown in Fig. 1.1.11. Diffracted beams can be envisaged as emanating from the sample in, and only in, the directions where the thin circles from the smeared reciprocal lattice intersect the thick circle of the Ewald sphere. A few representative diffraction beams are indicated by the dashed, dotted and dash-dotted arrows.

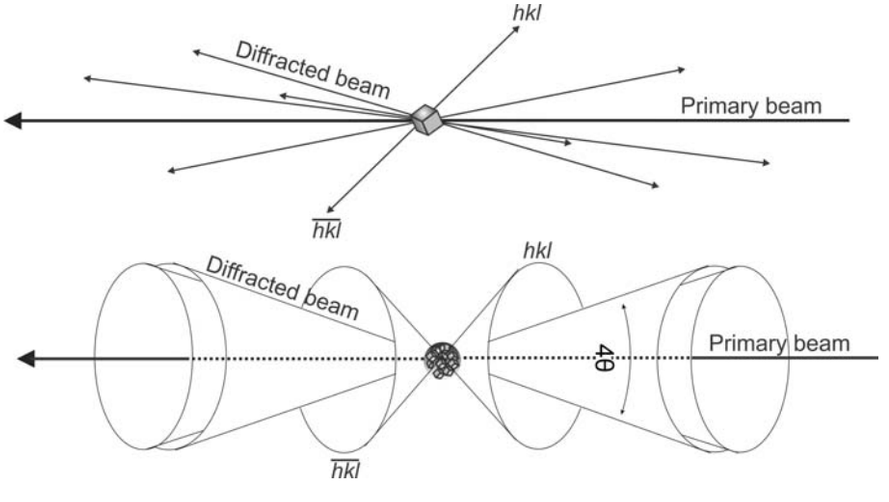

Figure 1.1.12
Comparison between the scattered beams originating from a single crystal (top) and a powder (bottom). For the latter, some Debye–Scherrer cones are drawn in reciprocal space. [Reproduced from Dinnebier & Billinge (2008) with permission from the Royal Society of Chemistry.]

The reflections from planes with the smallest d-spacing that are accessible in the experiment are determined by the diameter of the Ewald sphere, which is $2/\lambda$. In order to increase the number of reflections that can be detected, one must decrease the incident wavelength. In the case of an energy-dispersive experiment such as a time-of-flight neutron powder diffraction experiment, which makes use of a continuous distribution of wavelengths from λ_{min} to λ_{max} at fixed angle, all reflections that lie in the cone-shaped region of reciprocal space between the two limiting Ewald spheres at $2/\lambda_{min}$ and $2/\lambda_{max}$ will be detected.

As mentioned above, in a powder the reciprocal-lattice points get smeared into a spherical surface, which intersects the Ewald sphere as a circle. This means that, in three dimensions, the resulting diffracted radiation associated with the reflection hkl forms a cone emanating from the sample on an axis given by the direct beam, the so-called Debye–Scherrer cone. Different reciprocal-lattice points, at different values of $1/d_{hkl}$, give rise to coaxial cones of scattering. This is illustrated in Fig. 1.1.12.

The smearing of reciprocal space in a powder experiment makes the measurement of a powder diffraction pattern easier than the measurement of a set of single-crystal data, because the sample does not have to be repeatedly re-oriented, but this comes at the cost of a loss of information. At first sight the loss of information seems to be the directional information about the points in the reciprocal lattice. However, once the lattice is indexed (*i.e.* its basis vectors are known) the directional information in the pattern can be recovered without difficulty, which is why three-dimensional structures can be determined from the one-dimensional diffraction information in a powder pattern. The loss of information comes from the fact that reflections from lattice planes whose vectors lie in different directions but which have the same d-spacing overlap. These reflections cannot be resolved by the measurement and so the intensity in each of the peaks is not known. The peak-overlap problem becomes increasingly worse with increasing scattering angle as the number of diffraction planes in a particular d-spacing range increases and their separation decreases.

Some of these overlaps are dictated by symmetry (systematic overlaps) and others are accidental. Systematic overlaps are less problematic because the number of equivalent reflections (the multiplicity) is known from the symmetry, and, by symmetry, each of the overlapping peaks has the same intensity. For highly crystalline samples, the number of accidental overlaps can be reduced by making measurements with higher resolution, since this allows similar but not identical d-spacings to be separated.

To obtain the maximum amount of information, a spherical-shell detector would be desirable, although this is currently impractical. Often, a flat two-dimensional detector, either film, an image plate or a charge-coupled device (CCD), is placed perpendicular to the direct beam, or offset to one side to increase the angular range of the data collected. In this case, the Debye–Scherrer cones appear as circles, as shown in Fig. 1.1.13, or as ellipses if the detector is at an angle to the direct beam.

For an ideal powder, the intensity distribution around the rings is uniform. In a traditional powder diffraction experiment using a point detector, for example a scin-

tillator detector behind a receiving slit that defines the angular resolution of the measurement, at each position the detector samples a point on the two-dimensional diffraction pattern shown in Fig. 1.1.13. As the detector is moved to higher 2θ angles the locus of the points that are sampled is a horizontal or vertical (depending on whether the detector is moving in the horizontal or the vertical plane) line across the two-dimensional image. The intensity that is detected is low except where the detector crosses the circles of high intensity. This type of measurement is preferred for obtaining the highest resolution, especially if a highly perfect analyser crystal is used instead of a slit for defining the angle of the scattered beam. However, if the full rings, or fractions of them, are detected with two-dimensional detectors, the counting statistics can be improved enormously by integrating azimuthally around the rings at constant $|\mathbf{h}|$. This mode is becoming very popular for time-resolved, *in situ* and parametric studies where rapid throughput is more important than high resolution. It is also useful for samples that are weakly scattering and for nanometre-sized crystals or defective crystals, which may not show sharper peaks even when measured at higher resolution.

If the powder is non-ideal, the intensity distribution around the ring is no longer uniform, as illustrated in the right part of Fig. 1.1.13, and a one-dimensional scan will give arbitrary intensities for the reflections. To check for this in a conventional measurement it is possible to measure a rocking curve by keeping the detector positioned so that the Bragg condition for a reflection is satisfied and then taking measurements while the sample is rotated. If the powder is ideal, *i.e.* it is uniform and fine-grained enough to sample every orientation uniformly, this will result in a constant intensity as a function of sample angle, while large fluctuations in intensity will suggest a poor powder average. To improve powder statistics, powder samples may be rotated during a single measurement exposure, both for conventional point measurements and for measurements with two-dimensional detectors. Additional averaging of the signal also occurs during the azimuthal integration in the case of two-dimensional detectors. Outlier intensities can be identified and excluded from the integration. On the other hand, the intensity variation around the rings can give important information about the sample, such as preferred orientation of the crystallites or texture.

The d-spacings that are calculated from a powder diffraction pattern will include measurement errors, and it is important to minimize these as much as possible. These can come from uncertainty in the position of the sample, the zero point of 2θ, the angle of the detector or the angle of a pixel on a two-dimensional detector, uncertainties in the wavelength and so on. These effects will be dealt with in detail in later chapters. These aberrations often have a well defined angular dependence which can be included in fits to the data so that the correct underlying Bragg-peak positions can be determined with high accuracy.

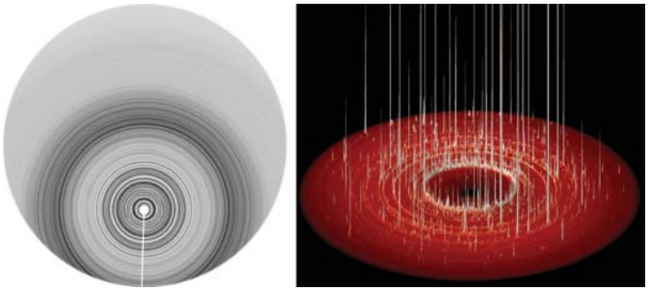

Figure 1.1.13
Left: Debye–Scherrer rings from an ideal fine-grained powder sample of a protein (courtesy Bob Von Dreele). Right: perspective view of Debye–Scherrer rings from a grainy powder sample of $BiBO_3$ at high pressure in a diamond anvil cell.

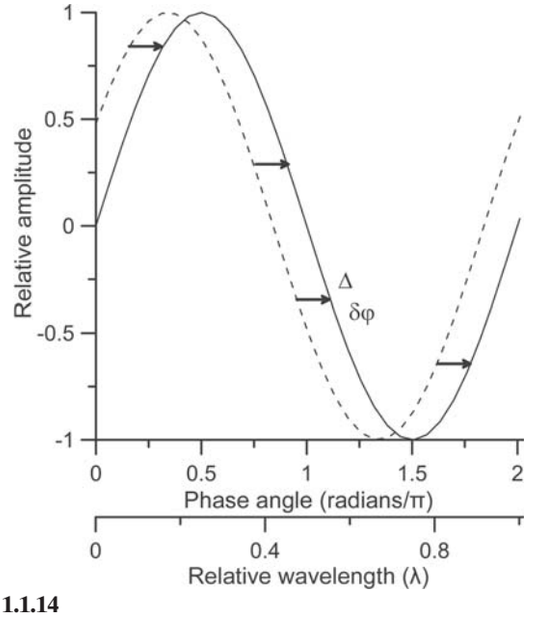

Figure 1.1.14
Graphical illustration of the phase shift between two sine waves of equal amplitude. [Reproduced from Dinnebier & Billinge (2008) with permission from the Royal Society of Chemistry.]

1.1.3. The peak intensity

1.1.3.1. *Adding phase-shifted amplitudes*

Bragg's law gives the *positions* at which diffraction by a crystal will lead to sharp peaks (known as Bragg peaks) in diffracted intensity. We now want to investigate the factors that determine the intensities of these peaks.

X-rays are electromagnetic (EM) waves with a much shorter wavelength than visible light, typically of the order of 1 Å (= 10^{-10} m). The physics of EM waves is well understood and excellent introductions to the subject are found in every textbook on optics. Here we briefly review the results that are most important in understanding the intensities of Bragg peaks.

Classical EM waves can be described by a sine wave of wavelength λ that repeats every 2π radians. If two identical waves are not coincident, they are said to have a phase shift, which is either measured as a shift, Δ, on a length scale in units of the wavelength, or equivalently as a shift in the phase, $\delta\varphi$, on an angular scale, such that

$$\frac{\Delta}{\lambda} = \frac{\delta\varphi}{2\pi} \Rightarrow \delta\varphi = \frac{2\pi}{\lambda}\Delta. \tag{1.1.50}$$

This is shown in Fig. 1.1.14.

The detected intensity, I, is proportional to the square of the amplitude, A, of the sine wave. With two waves present that are coherent and can interfere, the amplitude of the resultant wave is not just the sum of the individual amplitudes, but depends on the phase shift $\delta\varphi$. The two extremes occur when $\delta\varphi = 0$ (constructive interference), where $I \simeq (A_1 + A_2)^2$, and $\delta\varphi = \pi$ (destructive interference), where $I \simeq (A_1 - A_2)^2$. In general, $I \simeq \left[A_1 + A_2 \exp(i\delta\varphi)\right]^2$. When more than two waves are present, this equation becomes

$$I \simeq \left[\sum_j A_j \exp\left(i\varphi_j\right)\right]^2, \tag{1.1.51}$$

where the sum is over all the sine waves present and the phases, φ_j, are measured with respect to some origin.

Measuring X-ray diffraction involves the measurement of the intensity of X-rays scattered from electrons bound to atoms. Waves scattered by atoms at different positions arrive at the detector with a relative phase shift. Therefore, the measured intensities yield information about the relative atomic positions.

In the case of X-ray diffraction, the Fraunhofer approximation is valid. This is a far-field approximation, where the distances L_1 from the source to the place where scattering occurs (the sample) and L_2 from the sample to the detector are much larger than the separation, D, of the scatterers. This is an excellent approximation, since in this case $D/L_1 \simeq D/L_2 \simeq 10^{-10}$. The Fraunhofer approximation greatly simplifies the mathematics. The incident X-rays come from a distant source and form a wavefront of constant phase that is a plane wave. X-rays scattered by single electrons are outgoing spherical waves, which again appear as plane waves in the far field. This allows us to express the intensity of the diffracted X-rays using equations (1.1.51) and (1.1.39).

This is the origin of equation (1.1.39), which gives the amplitude of the scattered radiation in terms of the scattering vector, $\mathbf{h} = \mathbf{s}_0 - \mathbf{s}$, and the atomic positions, $\mathbf{r}_j$. In fact, the amplitude of the scattered radiation is only proportional to this expression. The actual intensity depends on the amplitude of the incident wave and also on the absolute scattering power of the scatterers. If we neglect for now the incident intensity and assume that our measured intensities are normalized to the incident beam intensity, we get

$$A(\mathbf{h}) = \sum_{j=1}^{n} f_j(h) \exp\left(2\pi i \mathbf{h} \cdot \mathbf{r}_j\right), \tag{1.1.52}$$

where $f_j(h)$ is the atomic form factor and $h = |\mathbf{h}|$ is the magnitude of the scattering vector, and is described in more detail in *International Tables for Crystallography*, Volume C, Part 6. This is a measure of the strength of scattering from the jth atom. At $h = 0$, scattering is in the forward direction with all electrons scattering in phase. As a result, $f_j(0)$ equals the number of electrons bound to the atom (in units of the Thomson scattering cross section for an electron), usually taken to be the atomic number of the atomic species at the jth site. An additional h-dependent reduction of the amplitude comes from positional disorder of the atoms. A Gaussian blurring is used with a width that is often falsely called the 'temperature factor', but is more correctly known as the atomic displacement parameter (ADP). The Gaussian is known as the Debye–Waller factor, which is discussed below. More information can be found in Chapter 4.7.

The crystal structure consists of periodic arrangements of atoms. The simplest structures have one atom in a periodically repeated unit cell. However, in general, there is a well defined group of atoms that forms a structural motif that is periodically repeated. This motif can range from one atom to thousands of atoms in complex protein structures. Solving the crystal structure consists of finding the unit-cell parameters and determining the positions in the unit cell of the atoms in the structural motif. In this sense, the structure of the infinite crystal can be thought of mathematically as a convolution of the periodic lattice that we discussed above with the structural motif. This results in a perfect, orientationally ordered copy of the structural motif in every unit cell translated in three-dimensional space.

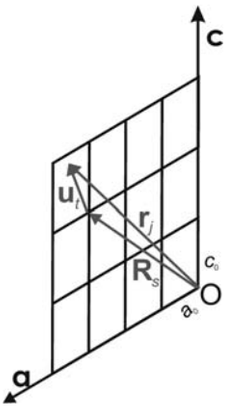

Figure 1.1.15
The position vector of the jth atom $\mathbf{r}_j$ can be decomposed into a vector $\mathbf{R}_s$ from the origin of the crystal to the origin of the unit cell containing the jth atom, and the vector $\mathbf{u}_t$ from the unit cell origin to the jth atom.

As we discussed above, the direct-space lattice has a reciprocal lattice associated with it which determines the positions of the Bragg peaks, or allowed delta functions of scattered intensity. The reciprocal lattice is actually a Fourier transform of the periodic lattice in direct space. The convolution theorem of Fourier transforms tells us that a convolution of two functions in direct space will result in a product of the Fourier transforms of those functions in the Fourier space. Since the structure is a convolution of the direct-space lattice with the structural motif, the reciprocal lattice will be *multiplied* by the Fourier transform of the structural motif. This Fourier transform of the structural motif is called the crystallographic structure factor, F_{hkl}.

This result can be readily derived from equation (1.1.52). In this equation $\mathbf{r}_j$ is the vector from the (arbitrary but fixed) origin to the jth atom in the material. If we now think of the crystal as consisting of n identical cells, each containing an identical structural motif consisting of m atoms, we can write $\mathbf{r}_j$ as a sum of two vectors: a vector that goes from the origin to the corner of the sth unit cell that contains the jth atom, and a second vector that goes from the corner of the sth cell to the position of the jth atom. This is illustrated in Fig. 1.1.15.

Equation (1.1.52) can then be written as

$$A(\mathbf{h}) = \sum_{s=1}^{n}\sum_{t=1}^{m} f_t(h) \exp\left(2\pi i \mathbf{h} \cdot (\mathbf{R}_s + \mathbf{u}_t)\right), \tag{1.1.53}$$

where it is readily seen that the first sum is taken over all the cells in the crystal and the second sum is taken over the m atoms in the structural motif. The equation is readily factored as follows:

$$A(\mathbf{h}) = \sum_{s=1}^{n} \exp(2\pi i \mathbf{h} \cdot \mathbf{R}_s) \sum_{t=1}^{m} f_t(h) \exp(2\pi i \mathbf{h} \cdot \mathbf{u}_t). \tag{1.1.54}$$

Taking n to infinity, we immediately recognise the first sum as the lattice sum of equation (1.1.43), and we can therefore rewrite equation (1.1.54) as

$$\begin{aligned} A(\mathbf{h}) &= \sum_{t=1}^{m} f_t(h) \exp(2\pi i \mathbf{h} \cdot \mathbf{u}_t) \\ &\quad \times \sum_{\mu,\nu,\eta=-\infty}^{\infty} \delta\left[\mu - (\mathbf{h} \cdot \hat{\mathbf{a}})a\right]\delta\left[\nu - (\mathbf{h} \cdot \hat{\mathbf{b}})b\right]\delta\left[\eta - (\mathbf{h} \cdot \hat{\mathbf{c}})c\right], \\ A(\mathbf{h}) &= F_{hkl} \sum_{\mu,\nu,\eta=-\infty}^{\infty} \delta\left[\mu - (\mathbf{h} \cdot \hat{\mathbf{a}})a\right]\delta\left[\nu - (\mathbf{h} \cdot \hat{\mathbf{b}})b\right]\delta\left[\eta - (\mathbf{h} \cdot \hat{\mathbf{c}})c\right]. \end{aligned} \tag{1.1.55}$$

The delta functions determine the positions of the reciprocal-

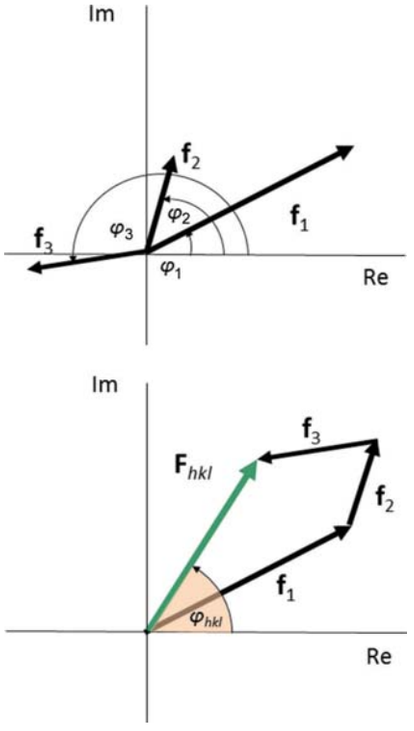

Figure 1.1.16
Graphical illustration of the summation of scattered wave amplitudes $\mathbf{f}_t$ in the complex plane, accounting for the phase shifts coming from the different positions of the atoms in the unit cell.

lattice points (directions of the Bragg peaks), and their intensities are multiplied by a factor, the crystallographic structure factor,

$$F_{hkl} = \sum_{t=1}^{m} f_t(h) \exp(2\pi i \mathbf{h} \cdot \mathbf{u}_t). \qquad (1.1.56)$$

If we write each term as a complex number denoted $\mathbf{f}_t$, we can represent this complex sum as a vector sum in the complex plane, as illustrated in Fig. 1.1.16, where the $\varphi_t = 2\pi \mathbf{h} \cdot \mathbf{u}_t$. The intensity of the Bragg peak depends only on the length of the $\mathbf{F}_{hkl}$, not its direction. However, its length depends on both the lengths *and the phases* of each contribution, which in turn depend on the positions of the atoms within the unit cell. This is the phase information that is 'lost' in a diffraction experiment. Given a structure, we can directly calculate all the Bragg-peak intensities (the 'forward problem'). However, given all the Bragg-peak intensities, we cannot directly calculate the structure (the 'inverse problem'). Structure determination uses the measured intensities and reconstructs the lost phase information using various iterative methods and algorithms.

In fact, the intensity of a Bragg reflection *hkl* is given by the squared absolute value of the structure-factor amplitude F_{hkl},

$$\left|F_{hkl}\right|^2 = \sum_{t,t'=1}^{m} f_t(h) f_{t'}^*(h) \exp\left(2\pi i \mathbf{h} \cdot (\mathbf{u}_t - \mathbf{u}_{t'})\right), \qquad (1.1.57)$$

where * indicates the complex conjugate. This analysis shows that the *positions* of the Bragg peaks determine the geometry of the periodic lattice (the size and shape of the unit cell, for example), but the *intensities* of the Bragg peaks are determined by the relative positions of atoms within the unit cell, scaled by their respective scattering power. To solve the internal structure of the structural motif within the unit cell, it is necessary to measure quantitatively the intensities of many Bragg peaks and use some kind of iterative procedure to move the atoms within the cell until the calculated structure factors self-consistently reproduce the intensities of all the measured Bragg peaks.

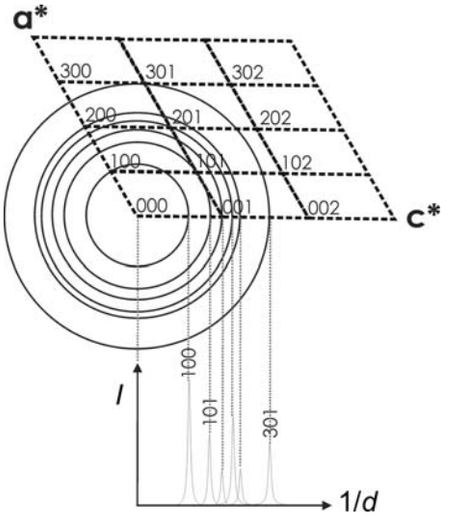

Figure 1.1.17
Schematic illustration of the projection of the reciprocal **a***/**c*** plane (representing the three-dimensional reciprocal-lattice space) into the one-dimensional powder pattern.

The situation is not fundamentally different in a powder diffraction experiment from the single-crystal case, except that the Bragg peaks in three-dimensional reciprocal space are projected into one dimension, as shown in Fig. 1.1.17.

'Indexing' is the term used for deriving the lattice parameters from the positions of the Bragg peaks (see Chapter 3.4). Once the size and shape of the reciprocal lattice is determined, Miller indices can be assigned to each of the Bragg peaks in a one-dimensional powder pattern. If it is possible to extract the intensities of those peaks from the pattern, diffraction data from a powder can be used to reconstruct the three-dimensional structure in exactly the same way as is done with data from a single crystal. This process is known as structure solution from powder diffraction, and is often successful, although it is less well automated than structure solution from data from single crystals. As mentioned above, the main problem with powder data is a loss of information due to systematic and accidental peak overlap, but this can often be overcome.

There are various methods for extracting quantitative peak intensities from indexed powder patterns by computer fitting of profiles to the Bragg peaks at their known positions. Two of the most common are Pawley refinement (Pawley, 1981) and Le Bail refinement (Le Bail *et al.*, 1988), as discussed in Chapter 3.5.

In general, the intensities of the Bragg reflections must be corrected by the product K_{hkl} of various correction factors. Some common correction factors are given by

$$K_{hkl} = M_{hkl} \mathrm{Abs}_{hkl} \mathrm{Ext}_{hkl} \mathrm{LP}_{hkl} \mathrm{PO}_{hkl} \ldots, \qquad (1.1.58)$$

where M_{hkl} is the multiplicity, Abs_{hkl} is an absorption correction, Ext_{hkl} is an extinction correction, LP_{hkl} is the geometrical Lorentz–polarization correction and PO_{hkl} is a correction for preferred orientation (see Chapter 4.7).

If there is more than one crystalline phase present in the sample, and the structures of all the crystalline phases are known, then we can find a scale factor for each phase in the mixture which reproduces the data. This is then a way of determining the proportion of each phase in the sample. This is called quantitative phase analysis (see Chapter 3.9).

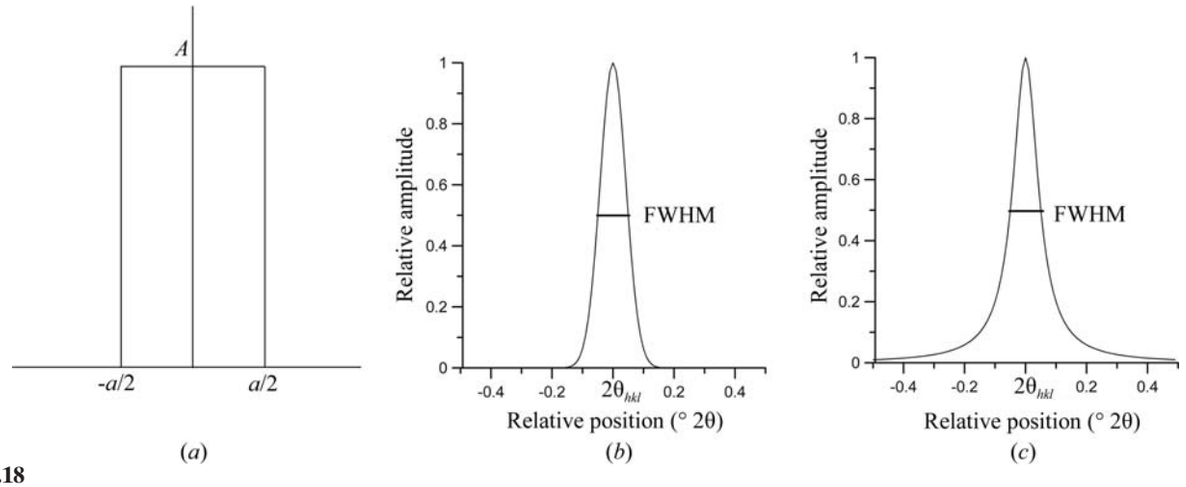

Figure 1.1.18
Normalized peak-shape functions. (*a*) The hat function, (*b*) the Gaussian function and (*c*) the Lorentzian function.

1.1.4. The peak profile

The peak profile refers to the shape of the measured Bragg peak. In the treatment above, the Bragg peaks from a perfect infinite crystal were delta functions and therefore infinitely narrow. In reality, the finite size of the crystal, the finite resolution of the measurement and defects in the material that result in inhomogeneous strains all broaden the delta function, giving it a finite width and some characteristic shape. When fitting a model to the measured diffraction pattern we should correctly account for these effects in order to obtain correct values for the Bragg-peak intensities. On the other hand, a careful study of the peak shapes yields important information about the size of the crystallites in the sample and defects that they contain. With recent improvements in instrumentation and computational data-analysis methods, this latter type of study has become more important and is having considerable scientific and technological impact.

The convolution theorem of the Fourier transform that was introduced in the derivation of the crystallographic structure factor above is also very useful in understanding the peak profile. In this case, the measured Bragg peak can be thought of as a delta function convoluted with a profile (Klug & Alexander, 1974). The profile of the Bragg reflection *hkl*, Φ_{hkl}, can be written as

$$\Phi_{hkl}(2\theta_i - 2\theta_{hkl}) = \mathrm{EP}(2\theta_i) \otimes \mathrm{IP}(2\theta_i) \otimes \mathrm{MS}(2\theta_i - 2\theta_{hkl}), \tag{1.1.59}$$

where $\mathrm{EP}(2\theta_i)$ is the emission profile of the X-ray source (tube or synchrotron), $\mathrm{IP}(2\theta_i)$ contains additional contributions to the profile from the instrument and $\mathrm{MS}(2\theta_i - 2\theta_{hkl})$ is the contribution from the microstructure of the sample. The symbol $\otimes$ denotes convolution.

The convolution of two functions $f(t)$ and $g(t)$ in real space is defined as

$$(f \otimes g)(t) = \int_{\tau=-\infty}^{\infty} f(\tau) g(t-\tau)\, \mathrm{d}\tau. \tag{1.1.60}$$

The convolution theorem tells us that the Fourier transform (FT) of two convoluted functions is the product of the Fourier transforms of those functions:

$$\mathrm{FT}(f \otimes g)(t) = \big(\mathrm{FT}(f)\big)\big(\mathrm{FT}(g)\big). \tag{1.1.61}$$

Normalization of the transform leads to scaling factors like 2π which have been omitted here for simplicity.

In practice, numerical integrations are almost always required, as many of the instrument aberration functions cannot be convoluted analytically. This convolution approach is the basis of the so-called fundamental-parameter (FP) approach (Cheary & Coelho, 1992) and has proven to be superior to other more empirical or phenomenological methods. The idea behind the FP approach is to build up the profile from first principles, exclusively using measurable physical quantities like slit widths, slit lengths, Soller-slit opening angles *etc*. The process of convolution from a fundamental-parameters perspective is an approximation whereby second- and higher-order effects are typically neglected for computational speed and simplicity. The instrumental profile is usually fully characterized by measuring a line-profile standard such as NIST SRM 660c LaB_6, which is expected to contain only small microstructural contributions, and comparing the calculated diffraction pattern to the measured one. Once the instrumental part of the profile is sufficiently well determined, it can be assumed that the remaining contributions to the 'real' profile are purely sample dependent (*e.g.* domain size, strain).

In general, it is desirable to keep the number of functions that are used to describe the peak profile to a minimum. Typical examples of mathematical functions which are convoluted to form the profile of a Bragg reflection include:

(*a*) the hat function H (*e.g.* for all kinds of rectangular slits),

$$H(2\theta - 2\theta_{hkl}) = \begin{cases} A \text{ for } -a/2 < (2\theta - 2\theta_{hkl}) < a/2, \\ 0 \text{ for } (2\theta - 2\theta_{hkl}) \le -a/2 \\ \quad \text{and } (2\theta - 2\theta_{hkl}) \ge -a/2 \end{cases} \tag{1.1.62}$$

(Fig. 1.1.18*a*);

(*b*) the normalized Gaussian G (*e.g.* for microstrain broadening),

$$G(2\theta - 2\theta_{hkl}) = \left(\frac{2\sqrt{\ln(2)/\pi}}{\mathrm{FWHM}}\right) \exp\left(\frac{-4\ln(2)(2\theta - 2\theta_{hkl})^2}{\mathrm{FWHM}^2}\right), \tag{1.1.63}$$

(Fig. 1.1.18*b*), where FWHM denotes the full width at half maximum of the Gaussian function in ° 2θ; and

(*c*) the Lorentzian function L (*e.g.* for the emission profile),

$$L(2\theta - 2\theta_{hkl}) = \frac{1}{2\pi}\left(\frac{\mathrm{FWHM}}{(2\theta - 2\theta_{hkl}) + \mathrm{FWHM}^2/4}\right), \tag{1.1.64}$$

(Fig. 1.1.18*c*).

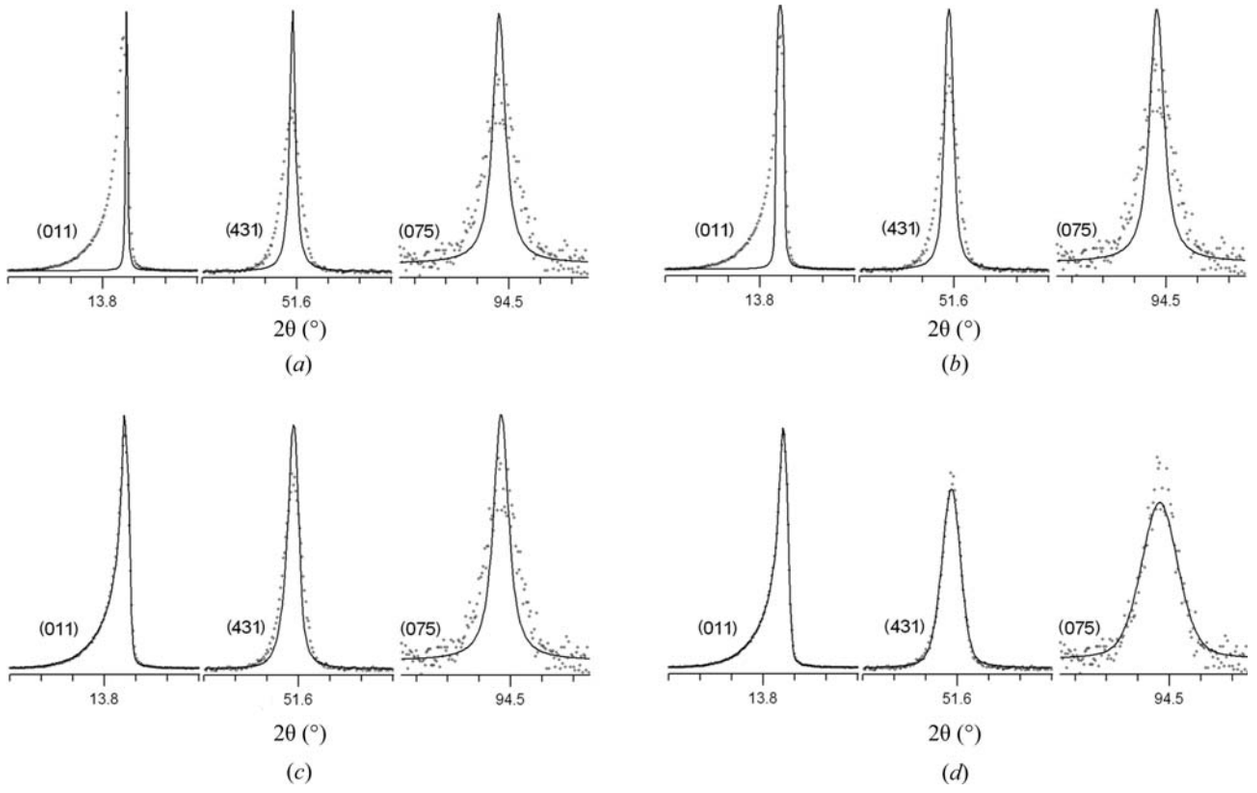

Figure 1.1.19
Peak fits of three selected reflections for an LaB_6 standard measured with Mo $K\alpha_1$ radiation ($\lambda = 0.7093$ Å) from a Ge(220) monochromator in Debye–Scherrer geometry using the fundamental-parameter approach. (*a*) A pure Lorentzian emission profile with a half width of 0.2695 mÅ is applied, refining the peak position and intensity only; (*b*) additionally, a hat shape function of the receiving slit in the equatorial plane with a width of 0.1 mm has been convoluted into the profile; (*c*) additionally, an axial convolution with filament-, sample- and receiving-slit lengths of 8 mm each and a secondary Soller slit with an opening angle of 2.5° has been convoluted into the profile; (*d*) additionally a small contribution of Gaussian broadening coming from the position-sensitive detector is convoluted into the profile. [From Mittemeijer & Welzel (2012). Copyright Wiley-VCH Verlag GmbH & Co. KGaA. Reproduced with permission.]

These functions can be convoluted sequentially as needed, first with the delta-function Bragg peak, and subsequently with the existing profile from the previous convolutions, each time resulting in a new profile that can become quite complex (Fig. 1.1.19). It is often the case that for a particular resolution effect the angular dependence of the profile function is known from the geometry of the measurement, and the convolution function for each peak is determined with only a very small number of parameters.

1.1.4.1. *Sample contributions to the peak profile*

Features of the sample that affect the peak profile include crystallite domain size and shape, dislocations, disclinations, twin and stacking faults, antiphase domains, microstrains, grain surface relaxations, and compositional fluctuations. Here we reproduce some basic results as examples; they also illustrate some fundamental aspects of diffraction from real crystals.

1.1.4.1.1. *Crystallite size*

The starting point for the analysis of finite size effects is the Laue equation, equation (1.1.39), which is reproduced here for a one-dimensional crystal:

$$A(h) = \sum_{j=0}^{n} \exp(2\pi i a j h). \tag{1.1.65}$$

When we were deriving the Bragg equation from the Laue equation we assumed an infinite crystal, and the sum taken to infinity resulted in delta functions at the reciprocal-lattice points. Now we want to consider a finite crystal with n unit cells. There is an analytic form for this sum which, using Euler's identity, is given by

$$\begin{aligned} A(h) &= \frac{\exp\left(2\pi i(n+1)ah\right) - 1}{\exp(2\pi i a h) - 1} \\ &= \frac{\exp\left(i\pi(n+1)ah\right)}{\exp(i\pi a h)} \frac{\exp\left(i\pi(n+1)ah\right) - \exp\left(-i\pi(n+1)ah\right)}{\exp(i\pi a h) - \exp(-i\pi a h)} \\ &= \exp(i\pi n a h) \frac{\sin\left(\pi(n+1)ah\right)}{\sin(\pi a h)}. \end{aligned} \tag{1.1.66}$$

The intensity is obtained by taking the modulus squared of this complex function, resulting in

$$I(h) = \frac{\sin^2\left(\pi(n+1)ah\right)}{\sin^2(\pi a h)}. \tag{1.1.67}$$

This function has sharp maxima when $h = \nu(1/a)$, where ν is an integer. This large central maximum falls off with a width proportional to $1/n^2$ with oscillating tails of intensity where the frequency of the oscillations increases with increasing n. This is illustrated in Fig. 1.1.20 for two different values of n but the same value of a.

In general, the Fourier transforms of periodic patterns become sharper with increasing number of unit cells. The expression $\sin(\pi(n+1)ah)/\sin(\pi a h)$ is also called the geometric factor of the structure amplitude.

This size broadening is often modelled in practice by using an equation due to Scherrer. We now reproduce the simple deri-

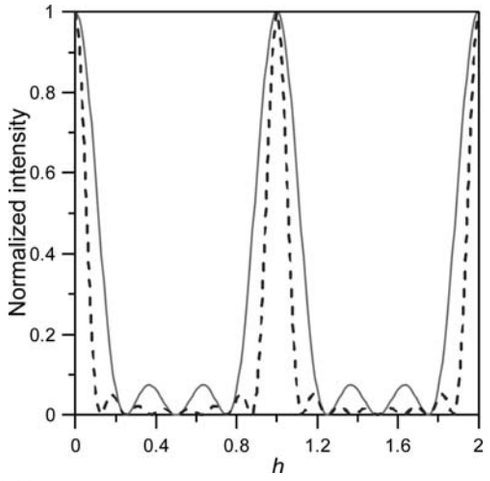

Figure 1.1.20
Normalized intensity from a finite lattice with $n = 3$ (solid curve) and $n = 8$ (dashed line), demonstrating the sharpening of peaks with increasing number of unit cells n. The normalization was done such that the peaks have the same peak maximum rather than the same integrated intensity for a clearer comparison of the relative peak widths.

vation of the Scherrer equation following Klug & Alexander (1974).

Fig. 1.1.21 shows the path-length difference *versus* the depth of the lattice plane. When the angle between the incoming beam and the lattice plane θ is different by an amount ε from the Bragg condition, it is always possible to find a lattice plane inside an infinite crystal where the extra path is $\Delta = \lambda(n + \frac{1}{2})$ for n integer, producing destructive interference. For a thick crystal this is true for arbitrarily small ε, which explains the sharp Bragg reflections. In the case of a crystal with finite dimensions, for small ε the plane for which $\Delta = \lambda(n + \frac{1}{2})$ holds will not be reached, thus leading to an intensity distribution over some small angular range. We can use this idea to estimate the broadening of a Bragg reflection due to size effects.

The thickness of a crystallite in the direction perpendicular to p planes of separation d_{hkl} (Fig. 1.1.21) is

$$L_{hkl} = pd_{hkl}. \tag{1.1.68}$$

The additional beam path between consecutive lattice planes at the angle $\theta + \varepsilon$ is

$$\begin{aligned}\Delta &= 2d\sin(\theta + \varepsilon)\\ &= 2d(\sin\theta\cos\varepsilon + \cos\theta\sin\varepsilon)\\ &= n\lambda\cos\varepsilon + 2d\sin\varepsilon\cos\theta\\ &\simeq n\lambda + 2d\sin\varepsilon\cos\theta.\end{aligned} \tag{1.1.69}$$

The corresponding phase difference is then

$$\delta\varphi = 2\pi\frac{\Delta}{\lambda} = 2\pi n + \frac{4\pi}{\lambda}\varepsilon d\cos\theta = \frac{4\pi\varepsilon d\cos\theta}{\lambda} \tag{1.1.70}$$

and the phase difference between the top and the bottom layer (layer p) is then

$$p\delta\varphi = p\frac{4\pi\varepsilon d\cos\theta}{\lambda} = \frac{4\pi L_{hkl}\varepsilon\cos\theta}{\lambda}. \tag{1.1.71}$$

Rearranging equation (1.1.71) leads to

$$\varepsilon = \frac{\lambda\delta\varphi}{4\pi L_{hkl}\cos\theta}, \tag{1.1.72}$$

which gives an expression for the misalignment angle in terms of the crystallite size L_{hkl} and the phase difference $\delta\varphi$ between the reflections originating from the top plane and the bottom plane. Clearly, the scattered intensity is at a maximum for $\delta\varphi = 0$ ($\varepsilon = 0$). With increasing ε the intensity decreases, giving rise to a peak of finite width. Perfect cancellation of the waves from the top and bottom planes occurs for a phase difference of $\delta\varphi = \pm\pi$, at which point $\varepsilon = \pm\lambda/(4L_{hkl}\cos\theta)$. On a 2θ scale, the measured angular width between these points is

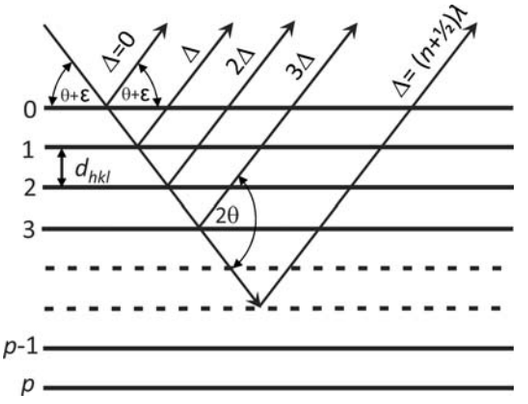

Figure 1.1.21
Path-length difference of the scattered ray *versus* the depth of the lattice plane in the crystal. [Reproduced from Dinnebier & Billinge (2008) with permission from the Royal Society of Chemistry.]

$$\beta_{hkl} = 4\varepsilon = \frac{\lambda}{L_{hkl}\cos\theta}, \tag{1.1.73}$$

giving us some measure of the peak width in radians that results from the finite particle size. A full treatment taking into account the correct form for the intensity distribution gives

$$\beta_{hkl} = \frac{K\lambda}{L_{hkl}\cos\theta}, \tag{1.1.74}$$

with a scale factor of $K = 0.89$ for perfect spheres. In general K depends on the shape of the grains (*e.g.* K is 0.94 for cube-shaped grains), but it is always close to unity. This equation is not valid for crystallites[3] that are too large or too small. In the case of large crystallites the peak width is governed by the coherence of the incident beam and not by particle size. For nanometre-sized crystallites, Bragg's law fails and the Debye equation needs to be used instead. The Debye equation (see Section 1.1.5.3) gives the scattering from an isotropically scattering sample such as a glass, liquid or powder, and does not presume that the sample is periodic.

1.1.4.1.2. *Microstrain*

Several important relationships in crystallography, including the effect of strain and microstrain on Bragg peaks, follow directly from a derivative of the Bragg equation (1.1.3). First we rewrite Bragg's law making the d-spacing the subject of the equation:

$$d = \frac{n\lambda}{2\sin\theta}. \tag{1.1.75}$$

The uncertainty of the measured lattice spacing is given by the total derivative dd,

$$\mathrm{d}d = \frac{\partial d}{\partial\theta}\mathrm{d}\theta + \frac{\partial d}{\partial\lambda}\mathrm{d}\lambda, \tag{1.1.76}$$

[3] Strictly speaking, the term crystallite size here refers to the dimension of a coherently scattering domain. Only in a perfect crystal is this the grain size.

Table 1.1.1
Types of scattering from a sample

Type of scattering	Coherent	Incoherent
Elastic	Bragg scattering Magnetic Bragg scattering Bragg scattering from ferroelectric/magnetic order Diffuse scattering from static defects Diffuse signal from small nanoparticles (<10 nm) Scattering from amorphous material (except excitations) Multiple scattering (coherent)	Laue monotonic diffuse scattering Neutron incoherent scattering Multiple scattering (incoherent)
Inelastic	Thermal diffuse scattering Spin-wave scattering Paraelectric/paramagnetic scattering Scattering from liquids	Compton scattering Fluorescence Incoherent scattering from hydrogen

leading to

$$\mathrm{d}d = -\frac{n\lambda}{2\sin\theta}\frac{\cos\theta}{\sin\theta}\mathrm{d}\theta + \frac{n}{2\sin\theta}\mathrm{d}\lambda \qquad (1.1.77)$$

and finally

$$\frac{\mathrm{d}d}{d} = -\frac{\mathrm{d}\theta}{\tan\theta} + \frac{\mathrm{d}\lambda}{\lambda}. \qquad (1.1.78)$$

When a crystal is strained, the d-spacings vary. A *macroscopic* strain changes the interplanar spacing by Δd_{hkl}, giving rise to a shift of $\Delta\theta$ in the *average* position of the diffraction peak. On the other hand, *microscopic* strains result in a distribution of d-spacings of width δd_{hkl}, which has the effect of *broadening* the diffraction peak by $\delta\theta$. Equation (1.1.78) gives an expression for the amount of Bragg-peak broadening that occurs for a given δd_{hkl}.

1.1.5. The background

1.1.5.1. *Information content in the background*

As discussed above, the elastic scattering from a crystalline powder consists of sharp rings, or peaks, of scattering at the 2θ angles where the Bragg or von Laue laws are satisfied. In general these sharp peaks sit on top of a 'background' which is broad and somewhat featureless. There are two components to this background, illustrated in Fig. 1.1.1: extraneous counts in the detector from things other than the sample, and non-Bragg scattering from the sample itself. The former are rarely of interest scientifically and the objective of a good experimental design is to minimize them as far as possible, or explicitly measure and subtract them, and then account well in any model or data interpretation for the part that cannot be eliminated from the measurement. Historically, the diffuse-scattering signals from the sample itself were also considered to be an inconvenience to be minimized and removed, and indeed in many cases this is still the best course of action (for example, sample fluorescence can be eliminated by choosing to work at an X-ray energy that lies below the absorption edge of a constituent atom). However, the diffuse 'background' from the sample can contain crucial information about defects, disorder and nanoscale order in the sample, and increasingly we are interested in studying it in order to understand the properties of the material that is under investigation. In some cases, such as glasses, liquids and samples of small nanoparticles, there is no Bragg scattering at all and only a diffuse scattering signal (see Chapter 5.6).

All the intensity scattered by the sample can be categorized as either coherent or incoherent and as elastic or inelastic, which are defined as follows. The coherency of the signal derives from whether or not the scattered waves interfere with each other constructively, and the resulting intensities are different in each case. For coherent scattering, the waves contributing to the signal are all summed first, before the wave amplitude is squared, to find the intensity distribution, which is the modulus squared of the resulting wave. For incoherent waves, one simply squares the amplitude of each wave to get its intensity and sums these together to get the total intensity. Switching to a consideration of the elasticity of the scattering, we define the scattering as elastic if the incident and scattered waves have the same energy, in which case no energy was exchanged during the scattering process between the incident wave and the sample, and inelastic scattering as the opposite. Inelastic scattering may result in a gain or a loss of energy of the scattered particle depending on the nature of the scattering, which results in a change in the wavelength of the scattered particle. There are also some non-scattering processes that can take place, such as absorption and fluorescence, but emissions resulting from these processes can also be categorized by whether or not they are coherent and elastic. It should be noted that the total energy of the system must be conserved during the scattering process, and so when a scattered wave gains or loses energy it exchanges it with the sample. This is used as a way of probing excitations in a material. Table 1.1.1 summarizes many of the types of diffuse scattering coming from a sample and categorizes them by their coherency and elasticity.

1.1.5.2. *Background from extraneous sources*

The most commonly observed extraneous, or parasitic, scattering is from the sample container (such as a capillary) that holds the sample during the measurement. Another large contribution may come from air scattering, which originates principally from scattering of the direct beam by molecules in the air in the beam path, both before and after the sample. Air-scattering effects can be minimized by enclosing as much of the beam path as possible in a tube which may be evacuated or where the air is replaced by a weakly scattering gas (such as He in the case of X-rays). Air scattering that is detected by the detector can also be reduced by careful collimation of the beams and then shielding the detector from detecting radiation that does not originate from the sample position. Collimating the incident beam is straightforward and results in a big reduction in air scattering. For point detectors it is also straightforward to collimate the scattered beam, but the modern trend towards using linear and area detectors makes this more difficult. There is sometimes a trade-off between collimating the scattered beam to reduce background and having uniform backgrounds that do not vary with angle because of

incomplete angle-dependent collimation. Incomplete angle-dependent collimation can be very difficult to correct when trying to measure diffuse scattering quantitatively and the current trend is to have minimal secondary collimation.

There is increasing interest in carrying out *in situ* experiments under extreme conditions of pressure, temperature, magnetic field and so on (see Chapters 2.6 to 2.8). These experiments inevitably introduce additional scattering from the environment. Again, there is a balance between finding creative ways to reduce these backgrounds, and simply making them less problematic in the data analysis. For example, in a diamond-anvil cell, where the beam accesses the sample through the diamond, one can drill a hole part way through the diamond to accommodate the direct beam and make the direct beam small enough to fit in the hole. This increases the complexity of the measurement as alignment becomes harder, but it is usually worth it. Shielding structural parts of the environment cell with an absorbing material, such as lead for X-rays or a borated material for neutrons, can help to reduce unwanted background intensity a lot, as can making thin, transparent windows for the incident and scattered beams.

An additional source of background in the signal does not come from scattering at all, but from electrical noise in the detector electronics. For some types of detectors it may be important to measure 'dark' exposures with the X-rays turned off and subtract these carefully from the experimental data. It is also possible to detect signals from cosmic rays, which can leave tracks in two-dimensional detector signals.

1.1.5.3. *Sources of background from the sample*

1.1.5.3.1. *Elastic coherent diffuse scattering*

As discussed in Section 1.1.4.1.1, decreasing the size of a crystal leads to an increase in the width of the Bragg peaks. When the size of the crystallite becomes very small, as a rule of thumb below 10 nm in diameter for typical unit cells, the widths of the Bragg peaks become so large that they merge and overlap, and it does not make sense to use delta-function Bragg peaks as the starting point for the analysis. At this point the coherent diffraction is completely diffuse in nature. Nonetheless, it still contains structural information. To see this we begin again with the Laue equation before we assumed periodicity [equation (1.1.39)]. For the simple case of a diatomic gas such as N_2, the sum would be taken only over two atoms, since scattering from a single molecule will be coherent but that from different molecules will be incoherent. In that case we have

$$A(\mathbf{h}) = \sum_{j=1}^{2} f_j(h) \exp(2\pi i \mathbf{h}\cdot\mathbf{r}_j),$$
$$A(\mathbf{h}) = f_1 \exp(2\pi i \mathbf{h}\cdot\mathbf{r}_1) + f_2 \exp(2\pi i \mathbf{h}\cdot\mathbf{r}_2), \quad (1.1.79)$$

and the intensity is proportional to

$$I(\mathbf{h}) = (f_1 f_1^* + f_2 f_2^*) + f_1 f_2^* \exp\left(2\pi i \mathbf{h}\cdot\mathbf{r}_{12}\right) + f_2 f_1^* \exp\left(-2\pi i \mathbf{h}\cdot\mathbf{r}_{12}\right), \quad (1.1.80)$$

where $\mathbf{r}_{12} = \mathbf{r}_1 - \mathbf{r}_2$. For a diatomic molecule where both atoms are the same $f_1 = f_2$ and

$$I(\mathbf{h}) = f^* f \cos^2(\pi \mathbf{h}\cdot\mathbf{r}_{12}). \quad (1.1.81)$$

The scattering from a diatomic molecule of an element is simply a single-component cosine wave with a wavelength that depends on the separation of the atoms in the molecule. In an actual experiment there will be scattering from all the molecules that have every orientation with equal probability, so it is necessary to take an orientational average of the scattering. How this is done is shown in Chapter 5.7 on PDF analysis, but the result is the Debye equation (Debye, 1915),

$$I(h) = \frac{1}{N\langle f\rangle^2} \sum_{i,j} f_j^* f_i \left[\frac{\sin(Qr_{ij})}{Qr_{ij}}\right], \quad (1.1.82)$$

where N is the total number of atoms. For our diatomic molecule this becomes

$$I(h) = \frac{1}{N}\left[\frac{\sin(Qr_{ij})}{Qr_{ij}}\right]. \quad (1.1.83)$$

For clusters of atoms such as larger molecules or small nanoparticles that are intermediate in size between a diatomic molecule and a small chunk of crystal, the Debye equation is exact and may be used to calculate the intensity of the scattering. As the clusters get larger and the structure more periodic, such as small chunks of crystal, the scattering calculated from the Debye equation crosses smoothly to that obtained from the periodic Laue equation. The finite size broadened crystallographic model works well as a starting point for calculating scattering from well ordered crystals down to nanoparticle sizes of 10 nm, but loses accuracy rapidly below this particle size. The Debye equation is accurate for all particle sizes, but becomes computationally intractable for larger clusters much above 10 nm.

1.1.5.3.2. *Total-scattering and atomic pair distribution function analysis*

An alternative approach to the analysis of diffuse scattering from nanostructures is to Fourier transform the data to obtain the atomic pair distribution function, or PDF. In fact, the Fourier transform does not depend on whether the structure is periodic or not, and it is also possible to Fourier transform the Bragg scattering from crystals. If there is no nanoscale disorder in the crystal there are few real benefits in doing this rather than using the powerful crystallographic methods described elsewhere in this chapter. However, the PDF approach utilizes both the Bragg *and* diffuse components, and yields additional information about the structure that is particularly valuable when the crystal contains some kind of nanoscale domains. The presence of such domains was rarely considered in the past, but we now know that they are often found in materials. In the sense that both Bragg and diffuse scattering data are used without prejudice, and also that the data are measured over a wide range of the scattering vector so that, as far as possible, the coherent scattering in all of the reciprocal space is measured, this method is known as 'total-scattering analysis', and as 'PDF analysis' when the data are Fourier transformed and studied in real space.

The powder diffraction data for total-scattering studies are measured in much the same way as in a regular powder diffraction experiment. However, explicit corrections are made for extrinsic contributions to the background intensity from such effects as Compton scattering, fluorescence, scattering from the sample holder and so on. The resulting coherent scattering function $I(Q)$ is a continuous function of $Q = |\mathbf{Q}| = 2h = 4\pi \sin\theta/\lambda$, with sharp peaks where there are Bragg reflections and broad features in between. In general it is usual to work with a normalized version of this scattering intensity, $S(Q)$. This is the intensity normalized by the incident flux per atom in the sample. $S(Q)$ is called the total-scattering structure function. It is a dimensionless quantity and the normalization is such that the average value $\langle S(Q)\rangle = 1$. In short, $S(Q)$ is nothing other than the powder diffraction pattern that

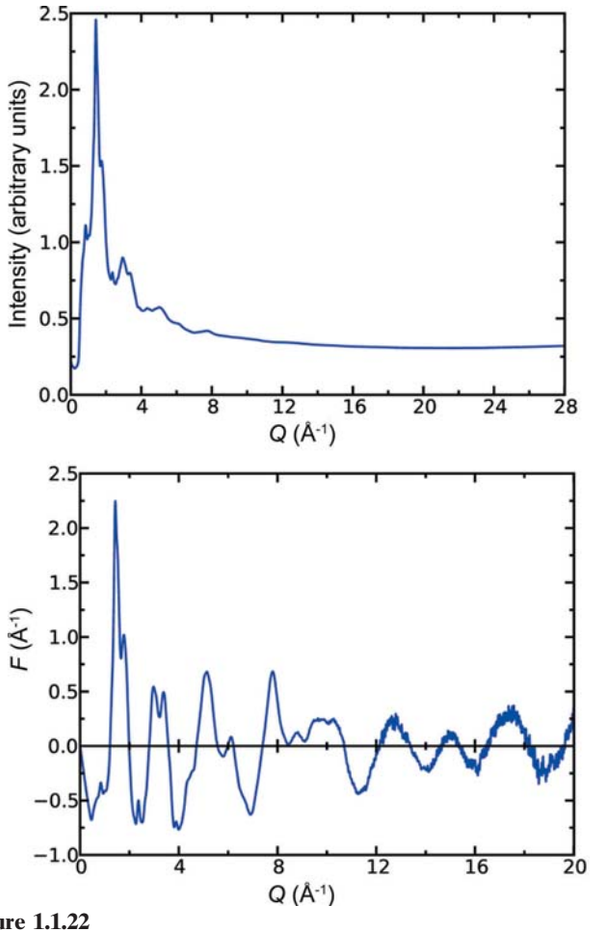

Figure 1.1.22
Comparison of raw data and the normalized reduced total-scattering structure function $F(Q) = Q[S(Q) - 1]$. The sample is a powder of 2 nm diameter CdSe nanoparticles and the data are X-ray data from beamline 6ID-D at the Advanced Photon Source at Argonne National Laboratory. The raw data are shown in the top panel. The high-Q data in the region $Q > 9$ Å^{-1} appear smooth and featureless. However, after normalizing and dividing by the square of the atomic form factor, important diffuse scattering is evident in this region of the diffraction pattern (bottom panel).

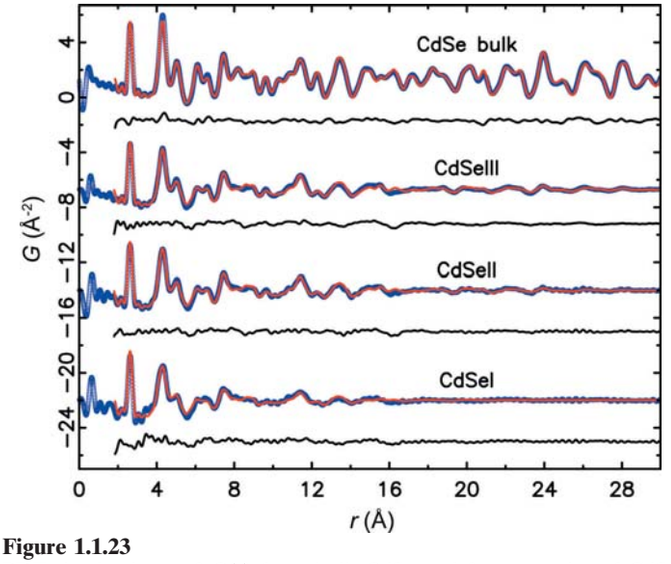

Figure 1.1.23
PDFs in the form of $G(r)$ from bulk CdSe and from a series of CdSe nanoparticles. The blue curve at the bottom is the PDF obtained from the data shown in Figure 1.1.22. The blue symbols are from the data and the thin red lines on top are from models of the local structure in these nanoparticles. Offset below are difference curves between the model and the data. [Reprinted with permission from Masadeh *et al.* (2007). Copyright (2007) by the American Physical Society.]

has been corrected for experimental artifacts and suitably normalized (Egami & Billinge, 2013).

Measuring over a wide range of Q values yields better resolution in real space, as well as yielding more information, and is desirable. The coherent intensity (the features) in $S(Q)$ dies out with increasing Q because of the Debye–Waller factor (which comes from thermal and quantum zero-point motion of the atoms), as well as any static displacive disorder in the material and, for X-ray measuerments, because of the X-ray form factor. In a neutron measurement, the atomic displacement effects are still present, but the neutron has no form factor and the scattering length is constant in Q. By a Q value of 30–50 Å^{-1} (depending on the temperature and the stiffness of the bonding in the sample) there are no more features in $S(Q)$ and there is no need to measure data to higher Q. Still, this is a much higher maximum value of Q than is measured in conventional powder diffraction experiments using laboratory X-rays or reactor neutrons. The maximum value of Q attainable in back scattering from a Cu $K\alpha$ tube is around 8 Å^{-1} and from an Mo $K\alpha$ tube it is around 16 Å^{-1}. Routine total-scattering measurements can be made using laboratory sources with Mo or Ag tubes; however, for the highest real-space resolution, and the smallest statistical uncertainties, synchrotron data are preferred. In the case of neutron scattering, spallation neutron sources are ideal for total-scattering experiments.

The total-scattering function $S(Q)$ appears to be different from the function measured in a standard powder diffraction experiment because of the Q range studied, and also because of an important aspect of the normalization: the measured intensity is divided by the total scattering cross section of the sample. In the case of X-ray scattering, the sample scattering cross section is the square of the atomic form factor, $\langle f(Q)\rangle^2$, which becomes very small at high Q. Thus, during the normalization process the data at high Q are amplified (by being divided by a small number), which has the effect that even rather weak intensities at high Q, which are totally neglected in a conventional analysis of the data, become rather important in a total-scattering experiment. Because the signal at high Q is weak it is important to collect the data in that region with good statistics. This is illustrated in Fig. 1.1.22.

The Fourier transform of the total-scattering data is the reduced pair distribution function, $G(r)$, which is related to $S(Q)$ through a sine Fourier transform according to

$$G(r) = \frac{2}{\pi}\int_{Q_{\min}}^{Q_{\max}} Q[S(Q) - 1]\sin(Qr)\,\mathrm{d}Q. \qquad (1.1.84)$$

Examples of $G(r)$ functions from small nanoparticles of CdSe are shown in Fig. 1.1.23.

$G(r)$ has peaks at positions, r, that separate pairs of atoms in the solid with high probability. For example, there are no physically meaningful peaks below the nearest-neighbour peak at ~2.5 Å, which is the Cd–Se separation in CdSe. However, in addition to the nearest-neighbour information, valuable structural information is contained in the pair correlations that extend to much higher values of r. In fact, with data to a high resolution in Q, PDFs can be measured out to hundreds of nanometres (*i.e.*, thousands of ångströms) and the structural information that can be obtained from the data remains quantitatively reliable (Levashov *et al.*, 2005).

The function $G(r)$ is related to the atomic density. However, it is not the atomic density itself, but its autocorrelation. This is

obtained by taking the atomic density of the molecule or cluster (which are the atoms at their respective positions) and convoluting it with a replica of the same thing. This object is then orientationally averaged to obtain the PDF. It is not a particularly intuitive object, but it is straightforward to calculate it from a given structural model. The inverse problem, calculating the structure from a PDF, is not possible directly, although in favourable cases, as with structure solution from powder diffraction, it is possible to obtain a unique structure solution from a PDF (Juhás *et al.*, 2006).

We described above how to obtain $G(r)$ from powder data. Here we briefly describe how to calculate a PDF from a structural model. To do this we have to introduce a related function to the PDF, the radial distribution function (RDF), $R(r)$, which is related to $G(r)$ by

$$G(r) = \frac{R(r)}{r} - 4\pi r\rho_0, \tag{1.1.85}$$

where ρ_0 is the atomic number density (Egami & Billinge, 2013).

The function $R(r)$ is important because it is more closely related to the physical structure than $G(r)$, since $R(r)\,\mathrm{d}r$ gives the number of atoms in an annulus of thickness $\mathrm{d}r$ at distance r from another atom. For example, the coordination number (or the number of neighbours) of an atom, N_C, is given by

$$N_\mathrm{C} = \int_{r_1}^{r_2} R(r)\,\mathrm{d}r, \tag{1.1.86}$$

where r_1 and r_2 define the start and end positions of the RDF peak corresponding to the coordination shell in question. This suggests a scheme for calculating PDFs from atomic models. Consider a model consisting of a large number of atoms situated at positions $\mathbf{r}_\nu$ with respect to some origin. Expressed mathematically, this amounts to a series of delta functions, $\delta(\mathbf{r} - \mathbf{r}_\nu)$. The RDF is then given as

$$R(r) = \frac{1}{N}\sum_\nu \sum_\mu \delta(r - r_{\nu\mu}), \tag{1.1.87}$$

where $r_{\nu\mu} = |\mathbf{r}_\nu - \mathbf{r}_\mu|$ is the magnitude of the separation of the νth and μth ions, and the double sum runs twice over all atoms in the sample. In Chapter 5.7 on PDF analysis we address explicitly samples with more than one type of atom, but for completeness we give here the expression for $R(r)$ in this case:

$$R(r) = \frac{1}{N}\sum_\nu \sum_\mu \frac{f_\nu f_\mu}{\langle f\rangle^2}\delta(r - r_{\nu\mu}), \tag{1.1.88}$$

where f_ν and f_μ are the form factors, evaluated at $Q = h = 0$, for the νth and μth atoms, respectively, and $\langle f\rangle$ is the sample-average form factor.

1.1.5.3.3. *Inelastic coherent diffuse scattering*

Scattering events must conserve energy and momentum. When a wave is scattered it changes direction and therefore changes its momentum. To satisfy conservation, this momentum, $\mathbf{Q} = 2\pi\mathbf{h} = 2\pi(\mathbf{s} - \mathbf{s}_0)$, must be transferred to the material. When radiation is scattered by a crystal, the mass of the crystal is so large that this produces a negligible acceleration and the scattering is elastic. However, scattering from free atoms or fluids will produce a recoil, which results from a transfer of energy to the atom and the scattering is strictly inelastic. Even within a bulk crystal, there are lattice excitation modes (phonons) which may be created during a particular scattering event and the resulting scattering is inelastic. In an X-ray experiment, the energy resolution of the measurement usually is much too poor to separate this from the elastic scattering and it all appears mixed together (and is often simply referred to as 'elastic scattering'). As the excitation energies of internal modes of the system have energies of the order of meV (10^{-3} eV) and the X-ray energy is of the order of keV (10^3 eV), resolving the inelastic modes would require an energy resolution of $\Delta E/E = 10^{-6}$, which is often unachievable. Nonetheless, such experiments are now carried out at synchrotron sources and provide important scientific insights, although the experiments are very slow and very specialized (Burkel, 1991).

These experiments are rarely carried out on powders. If the inelastic scattering is not resolved during the measurement, as is usually the case, it appears as a diffuse-scattering component in the signal from the powder or single crystal and it can be interpreted and modelled to extract information. In powder diffraction, when the scattering occurs from lattice vibrations, or phonons, the diffuse signal is called 'thermal diffuse scattering' or TDS (Warren, 1990). Over the last 50–60 years, a number of attempts have been made to extract information about phonon energies and phonon dispersions from TDS with varying amounts of success (Warren, 1990; Jeong *et al.*, 1999; Graf *et al.*, 2003; Goodwin *et al.*, 2005). In the case of PDF analysis, the information in the TDS manifests itself in real space as correlated motion, and it is observed that the low-r peaks are sharper than the high-r peaks. This is because closely bonded atoms tend to move together: if an atom moves to the right it tends to push its neighbour also over to the right, so the motion is correlated. There is useful information in the TDS and the r dependence of the PDF peak broadening, but this is at best a very indirect way of measuring lattice-dynamical effects.

When the energy transfer is not resolved it is hard to separate the cases of scattering arising from phonons (which are dynamic atomic displacements) and scattering arising from static atomic displacements. To some extent these can be disentangled by studying the temperature dependence of the atomic displacement parameters (ADPs) obtained from modelling the data either in reciprocal space or real space (Billinge *et al.*, 1991). This is often done by using a Debye model (Debye, 1912), where the temperature dependence of the mean-square ADP is given by

$$\overline{u^2} = \left(\frac{3h^2T}{4\pi^2 M k_B \theta_D^2}\right)\left[\varphi\left(\frac{\theta_D}{T}\right) + \frac{1}{4}\frac{\theta_D}{T}\right] + A_\mathrm{offset}, \tag{1.1.89}$$

where

$$\varphi\left(\frac{\theta_D}{T}\right) = \frac{T}{\theta_D}\int_0^{\theta_D/T}\left[\frac{x}{\exp(x) - 1}\right]\mathrm{d}x, \tag{1.1.90}$$

is the Debye integral. Here, θ_D is the Debye temperature, which is a measure of the stiffness of the bonding, h and k_B are Planck's and Boltzmann's constants, respectively, and M is the mass of the oscillating atom. The constant A_offset is a temperature-independent offset that is generally needed in the model to account for static distortions. The Debye model is rather crude but surprisingly useful and works well in many cases.

As in the case of phonons, if the scatterer couples to something else in the solid that has an excitation spectrum, this can be studied too. The case of neutrons scattered by magnetic moments is the best known example. Inelastic scattering gives direct information about the magnon dispersion curves. Information about magnetic excitations may also be obtained indirectly from

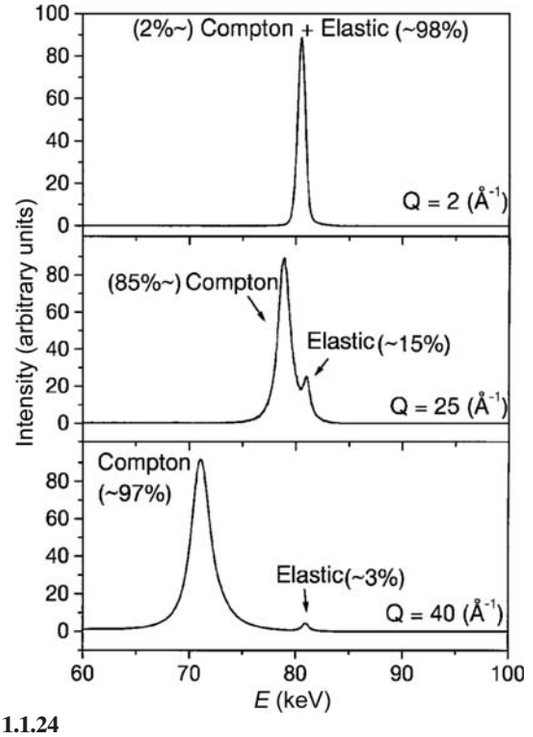

Figure 1.1.24
Spectrum from an energy-resolving detector that shows the elastic and Compton signals as a function of scattering vector **Q**. [Reprinted with permission from Petkov *et al.* (2000). Copyright (2007) by the American Physical Society.]

the non-energy-resolved magnetic diffuse scattering signal. Magnetic PDF is now possible (Frandsen & Billinge, 2015) as described in Chapter 5.7, as well as reciprocal-space studies of magnetic diffuse scattering (Paddison & Goodwin, 2012).

1.1.5.3.4. *Incoherent scattering*

Incoherent scattering does not contain any structural information, and cannot be used to study structure in a diffraction experiment since the intensities of the scattered waves do not depend on the position of the scatterers. This does not mean that all incoherent scattering intensity is useless. The fluorescence intensity is incoherent, but may be used in EXAFS experiments to yield structural information. This is because coherent scattering of the photoexcited electron during an absorption event modulates the absorption cross section and therefore the incoherent fluorescence intensity, so a coherent scattering process leaves a measurable response in an incoherent intensity. Incoherent scattering can also be used to measure excitations, although all momentum-transfer information is lost so it is not possible to measure, for example, dispersions of excitations such as phonons and magnons. Even if the scattering process is incoherent, the energy exchanged between the probe and the sample can be measured by the change in wavelength of the scattered wave, and the amplitude of the scattering at each energy transfer is proportional to the density of states of the excitation being probed. In the case of neutrons, the very large incoherent cross section for scattering by hydrogen ($\sim$100$\times$ the scattering cross section of most atoms) provides a strong signal for studying low-probability inelastic scattering events. Measuring inelastic scattering from powders can be a rapid way of determining the density of states of phonons, magnons and so on, which is very useful for determining the thermodynamic properties of materials, even though it is less precise than measurement of the full set of dispersion curves.

Another type of incoherent scattering that can be observed in X-ray experiments is Compton scattering (Compton, 1923; Cooper *et al.*, 2004), which is an inelastic incoherent process where the scattering atom recoils during the scattering event. An example of Compton scattering measured in the spectrum from an energy-resolving detector is shown in Fig. 1.1.24.

The Compton scattering is strong in this experiment because the incident X-ray energy is high (80 keV) and the sample is a low-atomic-number alumina-silicate glass. Both the high X-ray energy and the low atomic numbers of the atoms in the sample increase the Compton cross section with respect to the coherent elastic scattering. As the magnitude of the scattering vector, Q, is increased the Compton scattering moves to lower energy and increases in intensity, but the elastic line stays fixed in energy and its intensity decreases because of form-factor and Debye–Waller effects. Momentum as well as energy is conserved in this process and the Compton scattering can be used to measure the momentum distribution of electrons in a material, although this kind of experiment is not widespread these days.

Elastic incoherent scattering provides no information about the sample, and simply degrades the signal-to-noise ratio of the measurement. As such, it is just inconvenient and cannot be easily removed. Monotonic Laue diffuse scattering originates from different chemical species with different scattering powers residing on different sites in the crystal, and when a destructive interference condition is satisfied the resulting intensity does not go to zero but is proportional to $[f_i(h) - f_j(h)]^2$ (Warren, 1990). In pure elements in an X-ray experiment, the atoms on every site are the same and there is no Laue diffuse scattering. This is not true in neutron experiments where different nuclei have different scattering powers and most elements contain a range of isotopes in their natural form (the 'natural abundance'; Squires, 1996). This results in Laue diffuse scattering even in an element, although it is normally not referred to in these terms but is encompassed by a so-called 'incoherent neutron cross section' that is defined and tabulated (see Table 4.4.4.1 in *International Tables for Crystallography*, Volume C) for each element. This is not the only source of incoherent scattering in neutron diffraction, since the scattering power also depends on the relative orientation of the neutron and nuclear spins. In general these spins are all orientationally disordered (and fluctuating) and the result is an additional scattering-event-dependent contribution to the incoherent scattering from the sample, again encompassed by the 'incoherent neutron cross section' of the element. Where necessary, it may be possible to make isotopically enriched samples for neutron experiments so that the proportion of isotopes with large incoherent scattering cross sections is minimized (or the isotopes are removed altogether), and the range of isotopes can also be reduced, which further reduces the incoherent component of the signal. However, the cost and difficulty of doing this means that it is rarely done.

1.1.6. Local and global optimization of crystal structures from powder diffraction data

1.1.6.1. *Rietveld refinement*

More than 40 years have passed since the publication of the pioneering papers by Hugo Rietveld (Rietveld, 1967, 1969), in which he described a method for the refinement of crystal structures from neutron powder diffraction data. Neutron data sets from reactor sources were more amenable than X-ray data sets to this method because the line profiles are quite Gaussian.

However, it was not long before the method was extended to X-ray powder diffraction. The quality of the data and the computation power available these days have allowed the technique to develop enormously, to the point that even the (successful) Rietveld refinement of small protein structures from synchrotron powder diffraction data is now possible (see Chapter 7.1). Another development is the extension of the Rietveld method towards parametric refinement on large numbers of complimentary data sets with various as-yet unexplored new applications. Rietveld refinement is so important it is described in detail in Chapter 4.7, but we describe a number of important fundamentals of the method here by way of introduction.

The basic idea behind the Rietveld method is simple: Instead of extracting the integrated intensities of Bragg peaks and fitting models to these, as would be done in single-crystal and early powder diffraction studies, the full powder pattern, for example available as step-scanned intensity data, is fitted using a model whose parameters are refined using a least-squares procedure. The model parameters are varied in such a way as to minimize the sum of the squares of the difference between the n observed $Y\mathrm{obs}_i$ and n calculated $Y\mathrm{calc}_i(\{p\})$ step-scan intensities in the powder pattern, where the latter are calculated from a model containing a set of parameters $\{p\}$. The function that is minimized is usually the profile-weighted residual function, or R factor, given by

$$R_w = \sum_{i=1}^{n} w_i \big(Y\mathrm{obs}_i(2\theta) - Y\mathrm{calc}_i(2\theta; \{p\})\big)^2. \qquad (1.1.91)$$

The weight w_i is derived from the variance of the values of $Y\mathrm{obs}_i$, while all covariances between different $Y\mathrm{obs}_i$ values are assumed to be zero.

The calculated intensity $Y\mathrm{calc}_i$ is expressed by combinations of mostly nonlinear and analytic or non-analytic functions as

$$Y\mathrm{calc}_i = \sum_{ph=1}^{\text{phases}} \left(S_{ph} \sum_{hkl(ph)} \left(K_{hkl(ph)} \left|F_{hkl(ph)}\right|^2 \Phi_{hkl(ph)}\left(2\theta_i - 2\theta_{hkl(ph)}\right)\right)\right) + b_i(\mathrm{obs}). \qquad (1.1.92)$$

The outer sum runs over all phases ph present in the powder pattern, while the inner sum runs over all reflections hkl of a phase ph that contribute to the intensity at the position i in the powder pattern. A scaling factor S_{ph} is assigned to the reflection intensities for each phase; the scaling factor is proportional to the weight fraction of the phase. $K_{hkl(ph)}$ represents the product of various correction factors to the square of the structure-factor amplitudes, $\left|F_{hkl(ph)}\right|^2$, which may depend on the diffraction geometry and/or individual reflections. The value of the profile function $\Phi_{hkl}(2\theta_i - 2\theta_{hkl})$ is given for the profile point $(2\theta_i - 2\theta_{hkl})$ relative to the position of the Bragg reflection hkl. The observed background at position i in the powder pattern is denoted as $b_i(\mathrm{obs})$. Parameters in the model such as atomic positions, lattice parameters and experimental factors that affect peak shape and background are varied, using a least-squares approach, until the agreement between the calculated and measured diffraction profiles is optimized. In a least-squares approach, optimization consists of minimizing a cost function that is the weighted sum of the squared differences. This is a refinement method: a good initial guess at, or knowledge of, the structure is required and this model is refined by small adjustments.

This approach requires the modelling of the *entire* powder pattern. To simplify this complex task, the information content of the powder pattern can be divided into several parts (Fig. 1.1.1), allowing the separation of groups of parameters with respect to their origin:

(*a*) the peak intensity $\left|F_{hkl(ph)}\right|^2$ – the time- and space-averaged crystal structure and geometrical contributions;
(*b*) the peak position – crystallographic lattice and symmetry, and instrumental contributions;
(*c*) the peak shape $\Phi_{hkl}(2\theta_i - 2\theta_{hkl})$ – microstructural parameters and instrument profile;
(*d*) the background $b_i(\mathrm{obs})$ – local structure and instrumental conditions.

Each part contains contributions from the sample and the instrument.

Rietveld refinement is a nonlinear least-squares process and requires starting values for all parameters. It is generally implemented with a local, rather than a global, optimizer and it is important for the starting parameters to be close to those of the actual solution to ensure that it is in the valley in parameter space that contains the global minimum. It is usual to guide the refinement into the (relatively narrow) range of convergence by hand by adding the parameters to the refinement sequentially. In this sense, Rietveld refinement takes some time to learn, but with care it can provide robust quantitative structures and a wealth of information can be extracted from the data.

Of course, there is no reason (other than computational efficiency) why the minimization algorithm could not be a more robust global optimizer, and this is now starting to be implemented in modern Rietveld codes. The most common and most easily implemented global optimizer, though one of the least efficient, is the Metropolis or simulated-annealing (SA) algo-

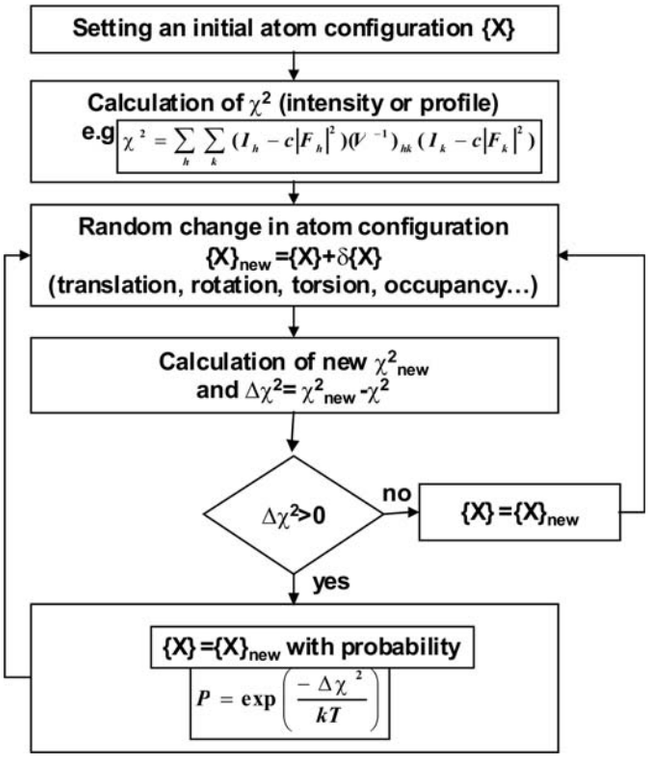

Figure 1.1.25
Flow diagram of a simulated-annealing procedure used for structure determination from powder diffraction data (from Mittemeijer & Welzel, 2012). F in the double sum is the structure factor from the structural model at each step of the optimization. Each sum runs over all reflections. h and k are summation indices representing hkl and $h'k'l'$, respectively.

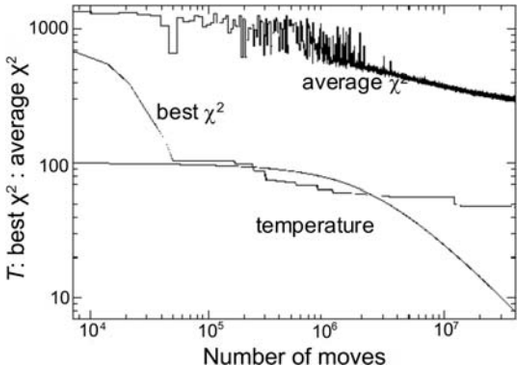

Figure 1.1.26
χ^2 (cost function) and 'temperature' dependence of the number of moves during a simulated-annealing run. [From Mittemeijer & Welzel (2012). Copyright Wiley-VCH Verlag GmbH & Co. KGaA. Reproduced with permission.]

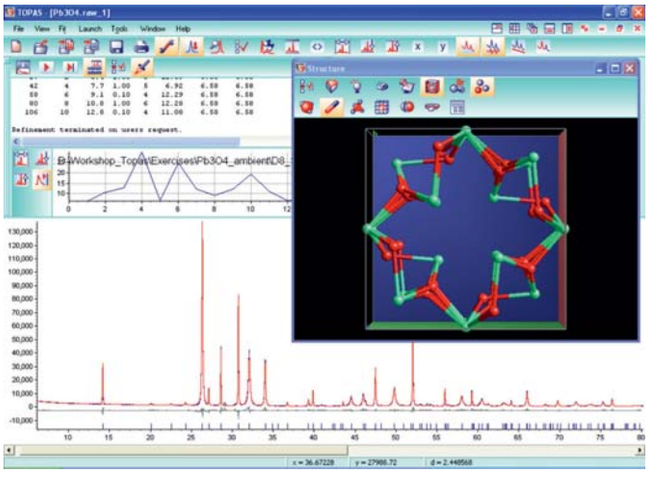

Figure 1.1.27
Screen shot (*TOPAS* 4.1; Bruker-AXS, 2007) of a simulated-annealing run on Pb_3O_4 measured with a D8 advance diffractometer in Bragg–Brentano geometry. [From Mittemeijer & Welzel (2012). Copyright Wiley-VCH Verlag GmbH & Co. KGaA. Reproduced with permission.]

rithm. The most usual implementation is actually as a 'regional' optimizer where the updates to parameters such as atomic position are constrained to be not too far from the previous values in such a way that the algorithm makes a random walk through the parameter space. This algorithm can avoid being trapped in a local minimum by 'walking uphill', since changes to the parameters that produce a worse agreement may be accepted with a probability based on the Boltzmann criterion, $\exp(-\Delta R/kT)$. The temperature in this expression is fictitious (*i.e.*, it does not refer to any real temperature) and ΔR is the change in the agreement produced by the trial update. The temperature plays the role of tuning the probability of accepting a bad move. It is initially chosen to have a high value, giving a high probability of escaping a minimum and allowing the algorithm to explore more of the parameter space. Later in the run the temperature is lowered, trapping the solution into successively finer valleys in the parameter space until it settles into (hopefully) the global minimum (Fig. 1.1.26). The calculation of R can be based on the entire profile, or on integrated intensities. For the latter, the correlation between partially or fully overlapping reflections must be taken into account (as shown schematically in Fig. 1.1.25).

A flow diagram of a typical SA algorithm as used for structure determination from powder diffraction data is shown in Fig. 1.1.25. Parameters that can be varied during the SA runs include internal and external degrees of freedom like translations (fractional coordinates or rigid-body locations), rotations (Cartesian angles, Eulerian angles or quaternions, describing the orientation of molecular entities), torsion angles, fractional occupancies, displacement parameters *etc*. Fig. 1.1.26 shows the results of a typical simulated-annealing run in which the cost function, χ^2, falls dramatically in the first few thousand moves, indicating that the scattering is dominated by the positioning of heavier atoms or globular molecules. Several million trial structures are usually generated before a minimum can be reached. At the end of the simulated-annealing run, Rietveld refinement is used to find the bottom of the global minimum valley.

Special algorithms are not usually used to prevent close contact of atoms or molecules during the global-optimization procedure, as in general these have not been found to be necessary, as the fit to the intensities alone quickly moves the molecules to regions of the unit cell where they do not grossly overlap with neighbouring molecules. A subsequent Rietveld refinement in which only the scale and overall displacement parameters are refined will immediately show whether further refinement of bond lengths and bond angles is necessary. Since unconstrained refinement often results in severe distortions from the ideal molecular geometry, either rigid bodies or soft constraints on bond lengths, the planarity of flat groups and bond angles can be used to stabilize the refinement. Another advantage of the simulated-annealing technique is that hydrogen atoms can often be included at calculated positions from the beginning if their relative position with respect to other atoms can be anticipated, which is often the case for molecular structures.

For inorganic crystal structures in particular, the identification of special positions or the merging of defined rigid bodies is useful during the final stages of structure solution. This can be accomplished by a so-called 'occupancy-merge' procedure as proposed by Favre-Nicolin & Černý (2004; see also Chapter 4.5). Here, the occupancies of the sites are modified as a function of the fractional coordinates, *i.e.* they are changed when the atoms get 'too close' to a special position. The sites are thought of as spheres with a radius r. In this way any number of sites can be merged when their distances are less than $2r$. As an example, the crystal structure solution of minium (Pb_3O_4) is shown in Fig. 1.1.27. In this example, special positions are identified when two oxygen or lead atoms approach within a distance less than the sum of their respective merging radii, which is estimated as 0.7 Å. The occupancies of the sites then become: 1/(1 + intersection fractional volumes).

The power of the Rietveld approach lies in its ability to extract the maximum information from the region of the data where peaks overlap. Since peak overlap is a significant problem even at moderate d-spacings, this method revolutionized powder diffraction to the point where the quantitative results are often trusted more than those coming from refinements of single-crystal data, since they are less sensitive to factors such as extinction that can affect single-crystal structure refinements. Single-crystal data are still preferred for structure solution, but Rietveld refinement is often the method of choice for obtaining the fine quantitative details of the structure after a solution has been found. However, the Rietveld method has also opened the door to using powder data for structure solution. In structure-solution methods, the structure factors are calculated from the intensities of all the available peaks, and algorithms are used to find the missing phases for each of these peaks and therefore the positions of the atoms in the unit cell. As mentioned above, full

profile fitting following the Rietveld method can be carried out without a model, where the 'parameters' are the Bragg-peak intensities themselves; this is known as Pawley or Le Bail refinement, depending on details of the approach used (see Chapter 3.5). This allows more accurate determination of the structure factors from Bragg peaks in regions where there is significant peak overlap.

These days, with high-quality data from synchrotron X-ray sources and excellent algorithms (either direct methods or global-optimization methods in direct space), determination of even quite complex crystal structures from powder diffraction data is becoming a routine method in almost all branches of natural sciences and engineering. The success rate mainly depends on three parameters: the choice of measurement device, how well the pattern profile is described and how good the structure-solving algorithm is. It is becoming increasingly evident that the use of highly monochromatic parallel-beam synchrotron radiation is a huge advantage for obtaining accuracy in the atomic parameters, which allows for the interpretation of bonding and reaction mechanisms. In some cases, even details like rotational disorder can be extracted from powder diffraction data if maximum-entropy methods are combined with high-resolution synchrotron data.

1.1.6.2. *Local structure refinement*

As described in Section 1.1.5.3.2, similar full-profile-fitting strategies are now also carried out on total-scattering data that include diffuse-scattering intensity residing in what used to be considered as the 'background'. This is either done by taking a structural model, which may be similar to the crystal model used in the Rietveld method (but the crystallographic symmetry of the model could also be reduced) or be a discrete cluster or molecule. As with the Rietveld method, structural parameters are varied in such as way as to obtain a good fit of the calculated function to the measured one. These methods go beyond the average structure and yield information about the local structure in the material, which may be different from the long-range ordered (LRO) crystal structure (or indeed there may be no LRO structure, as is the case in liquids and glasses). They are becoming more popular as data quality and computational power increase.

Solving the structures of nanoparticles from PDF data is less well developed, although it has been demonstrated for some simple structures such as C_{60} and simple inorganic crystalline compounds. We expect that this will grow in importance in the coming years, following the trend of the Rietveld method and structure solution from powders.

1.1.6.3. *Parametric Rietveld refinement*

The conventional approach to analysing a set of powder patterns is to treat each powder pattern independently, thus refining the entire set of all relevant parameters for each pattern separately. Further analysis of the values of these parameters, for example fitting with empirical or physics-based functions such as fitting the temperature dependence of the ADPs with a Debye model, is then performed after the Rietveld refinements. Alternatively, all powder patterns can be subjected to refinement simultaneously, which allows the refinement of the functional dependence of external variables instead of deriving the parameters of the function from the individual Rietveld refinements afterwards. This so-called parametric or surface Rietveld refinement was first introduced by Stinton & Evans (2007). Parametric refinement offers several advantages over the traditional sequential refinement approach because the correlation between parameters and the final standard uncertainty can be reduced by introducing simple and physically meaningful constraints and restraints. Furthermore, it is possible to refine noncrystallographic parameters such as rate constants or temperatures directly from Rietveld refinement (Stinton & Evans, 2007). Of course, introducing external constraints in this way may introduce bias into the refinement if the constraint is not valid. For example, if there is anharmonicity in the motion and the temperature dependence of the ADPs does not follow the Debye law, carrying out a parametric refinement where the Debye law is presumed will result in biased refinements. However, with careful application, this is a potentially powerful approach to maximizing the quantitative information available from powder data in complex systems. In the following, the basic concept of parametric refinement is illustrated with several examples.

If we assume a set of $p_{\max}$ powder patterns from a single sample that have been measured as a function of the value of an external variable, *e.g.* time, temperature or pressure, equation (1.1.92) can be formally written for each powder pattern separately:

$$\begin{aligned}
&Y\mathrm{calc}_{i,\mathrm{pattern}(1)} = \mathrm{function}(p_{1,\mathrm{pattern}(1)}, p_{2,\mathrm{pattern}(1)}, \ldots, p_{m,\mathrm{pattern}(1)})\\
&Y\mathrm{calc}_{i,\mathrm{pattern}(2)} = \mathrm{function}(p_{1,\mathrm{pattern}(2)}, p_{2,\mathrm{pattern}(2)}, \ldots, p_{m,\mathrm{pattern}(2)})\\
&Y\mathrm{calc}_{i,\mathrm{pattern}(p_{\max})}\\
&\quad = \mathrm{function}(p_{1,\mathrm{pattern}(p_{\max})}, p_{2,\mathrm{pattern}(p_{\max})}, \ldots, p_{m,\mathrm{pattern}(p_{\max})}).
\end{aligned} \tag{1.1.93}$$

If a functional dependency of some of the parameters p on external variables T exists, these parameters may be expressed as functions of these variables, for example T. This functional relationship can be used to constrain together the p parameters for individual patterns measured at different temperatures, drastically reducing the number of global parameters. Equation (1.1.93) can thus be written as

$$\begin{aligned}
&Y\mathrm{calc}_{i,\mathrm{pattern}(1)}\\
&= \mathrm{function}\big(p_{1,\mathrm{pattern}(1)}, p_{2,\mathrm{pattern}(1)} = f(T_1, T_2, \ldots, T_t), \ldots, p_{m,\mathrm{pattern}(1)}\big)\\
&Y\mathrm{calc}_{i,\mathrm{pattern}(2)}\\
&= \mathrm{function}\big(p_{1,\mathrm{pattern}(2)}, p_{2,\mathrm{pattern}(2)} = f(T_1, T_2, \ldots, T_t), \ldots, p_{m,\mathrm{pattern}(2)}\big)\\
&\vdots\\
&Y\mathrm{calc}_{i,\mathrm{pattern}(p_{\max})}\\
&= \mathrm{function}\big(p_{1,\mathrm{pattern}(p_{\max})}, p_{2,\mathrm{pattern}(p_{\max})} = f(T_1, T_2, \ldots, T_t),\\
&\qquad \ldots, p_{m,\mathrm{pattern}(p_{\max})}\big).
\end{aligned} \tag{1.1.94}$$

The cost function (1.1.91) to be minimized changes accordingly:

$$R_w = \sum_{\mathrm{pattern}=1}^{p_{\max}} \left(\sum_{i=0}^{n-1} \left(w_{i,\mathrm{pattern}} \big(Y\mathrm{obs}_{i,\mathrm{pattern}} - Y\mathrm{calc}_{i,\mathrm{pattern}} \big)^2 \right) \right). \tag{1.1.95}$$

1.1.7. Outlook

As is evident from the above, the information content in a powder diffraction pattern is enormous. This chapter gives only an overview of the types of information about materials that can be obtained from powder diffraction data, and the various approaches mentioned here are described in greater detail in the rest of this volume. The powder community is growing, as is the number of applications of powder diffraction in all the materials

sciences as instrumentation and computer modelling become ever more powerful. Although intense modern X-ray and electron sources can measure data from tiny single crystals (of a size approaching that of a single powder grain), this does not diminish the usefulness and impact of powder diffraction, as powder diffraction is much more than just crystal structure solution. It probes real materials in real environments, yielding information about defects, texture, nanostructure, strain, phase composition, kinetics, phase transformations, size and shape distributions, and heterogeneity. In short, crystallography gives us the structure, but powder diffraction allows us to study the 'materials science', of materials.

References

Billinge, S. J. L., Davies, P. K., Egami, T. & Catlow, C. R. A. (1991). *Deviations from planarity of copper-oxygen sheet in $Ca_{0.85}Sr_{0.15}CuO_2$. Phys. Rev. B*, **43**, 10340–10352.

Bragg, W. L. (1913). *The diffraction of short electromagnetic waves by a crystal. Proc. Camb. Philos. Soc.* **17**, 43–57.

Bruker-AXS (2007). *TOPAS* version 4.1. Bruker-AXS, Karlsruhe, Germany.

Burkel, E. (1991). *Inelastic Scattering of X-rays With Very High Energy Resolution*. Springer Tracts in Modern Physics. Amsterdam: Springer-Verlag.

Cheary, R. W. & Coelho, A. (1992). *A fundamental parameters approach to X-ray line-profile fitting. J. Appl. Cryst.* **25**, 109–121.

Compton, A. H. (1923). *A quantum theory of the scattering of X-rays by light elements. Phys. Rev. Lett.* **21**, 483.

Cooper, M. J., Mijnarends, P. E., Shiotani, N., Sakai, N. & Bansil, A. (2004). *X-ray Compton Scattering*. Oxford University Press.

Debye, P. (1912). *Zur Theorie der spezifischen Wärmen. Ann. Phys.* **344**, 789–839.

Debye, P. (1915). *Dispersion of Röntgen rays. Ann. Phys.* **46**, 809–823.

Debye, P. & Scherrer, P. (1916). *Interferenzen an regellos orientierten Teilchen im Röntgenlicht. Nachr. Ges. Wiss. Göttingen*. **29**, 1–15.

Dinnebier, R. E. & Billinge, S. J. L. (2008). Editors. *Powder Diffraction: Theory and Practice*, 1st ed. London: Royal Society of Chemistry.

Egami, T. & Billinge, S. J. L. (2013). *Underneath the Bragg Peaks: Structural Analysis of Complex Materials*, 2nd ed. Amsterdam: Elsevier.

Ewald, P. P. (1921). *Das reziproke Gitter in der Strukturtheorie. Z. Kristallogr.* **56**, 129–156.

Favre-Nicolin, V. & Černý, R. (2004). *Fox: Modular approach to crystal structure determination from powder diffraction. Mater. Sci. Forum*, **443–444**, 35–38.

Frandsen, B. A. & Billinge, S. J. L. (2015). *Magnetic structure determination from the magnetic pair distribution function (mPDF): ground state of MnO. Acta Cryst.* A**71**, 325–334.

Goodwin, A. L., Tucker, M. G., Cope, E. R., Dove, M. T. & Keen, D. A. (2005). *Model-independent extraction of dynamical information from powder diffraction data. Phys. Rev. B*, **72**, 214304.

Graf, M. J., Jeong, I. K., Starr, D. L. & Heffner, R. H. (2003). *Limits on phonon information extracted from neutron pair-density functions. Phys. Rev. B*, **68**, 064305.

Hull, A. W. (1917). *A new method of X-ray crystal analysis. Phys. Rev.* **10**, 661–696.

Jeong, I.-K., Proffen, T., Mohiuddin-Jacobs, F. & Billinge, S. J. L. (1999). *Measuring correlated atomic motion using X-ray diffraction. J. Phys. Chem. A*, **103**, 921–924.

Juhás, P., Cherba, D. M., Duxbury, P. M., Punch, W. F. & Billinge, S. J. L. (2006). *Ab initio determination of solid-state nanostructure. Nature*, **440**, 655–658.

Klug, H. P. & Alexander, L. E. (1974). *X-ray Diffraction Procedures*, 2nd ed. New York: John Wiley.

Laue, M. von (1912). *Eine quantitative Prüfung der Theorie für die Interferenz-Erscheinungen bei Röntgenstrahlen. Sitzungsber. K. Bayer. Akad. Wiss.* pp. 363–373. [Reprinted in *Ann. Phys.* (1913), **41**, 989–1002.]

Le Bail, A., Duroy, H. & Fourquet, J. L. (1988). *Ab-initio structure determination of $LiSbWO_6$ by X-ray powder diffraction. Mater. Res. Bull.* **23**, 447–452.

Levashov, V. A., Billinge, S. J. L. & Thorpe, M. F. (2005). *Density fluctuations and the pair distribution function. Phys. Rev. B*, **72**, 024111.

Masadeh, A. S., Božin, E. S., Farrow, C. L., Paglia, G., Juhás, P., Billinge, S. J. L., Karkamkar, A. & Kanatzidis, M. G. (2007). *Quantitative size-dependent structure and strain determination of CdSe nanoparticles using atomic pair distribution function analysis. Phys. Rev. B*, **76**, 115413.

Mittemeijer, E. J. & Welzel, U. (2012). Editors. *Modern Diffraction Methods*. Weinheim: Wiley-VCH Verlag GmbH.

Paddison, J. A. M. & Goodwin, A. L. (2012). *Empirical magnetic structure solution of frustrated spin systems. Phys. Rev. Lett.* **108**, 017204.

Pawley, G. S. (1981). *Unit-cell refinement from powder diffraction scans. J. Appl. Cryst.* **14**, 357–361.

Petkov, V., Billinge, S. J. L., Shastri, S. D. & Himmel, B. (2000). *Polyhedral units and network connectivity in calcium aluminosilicate glasses from high-energy X-ray diffraction. Phys. Rev. Lett.* **85**, 3436–3439.

Rietveld, H. M. (1967). *Line profiles of neutron powder-diffraction peaks for structure refinement. Acta Cryst.* **22**, 151–152.

Rietveld, H. M. (1969). *A profile refinement method for nuclear and magnetic structures. J. Appl. Cryst.* **2**, 65–71.

Shmueli, U. (2008). Editor. *International Tables for Crystallography*, Vol. B, *Reciprocal Space*, 3rd ed. Chichester: Wiley.

Squires, G. L. (1996). *Introduction to the Theory of Thermal Neutron Scattering*. New York: Dover Publications.

Stinton, G. W. & Evans, J. S. O. (2007). *Parametric Rietveld refinement. J. Appl. Cryst.* **40**, 87–95.

Warren, B. E. (1990). *X-ray Diffraction*. New York: Dover Publications.

International Tables for Crystallography (2019). Vol. H, Chapter 2.1, pp. 26–50.

2.1. Instrumentation for laboratory X-ray scattering techniques

A. Kern

2.1.1. Introduction

X-ray scattering techniques are among the most essential means of characterizing materials, as they are the most direct analytical methods for providing structural information for a material. In particular, X-ray powder diffraction has become one of the most important techniques in materials science, since many materials are first formed or are only available or used as powders or other polycrystalline forms.

The ever-increasing need for materials characterization, from basic research to industrial quality control, has led to a multitude of evolutionary and revolutionary instrument and application developments. In the past two decades, the capabilities and thus the range of application of laboratory X-ray diffractometers have increased exponentially.

The present chapter covers the full range of commonly used instrumentation for home-laboratory X-ray scattering analyses as detailed in Section 2.1.2, with the focus on powder diffraction. The scope is limited to recent and commercial designs, available off-the-shelf from the major manufacturers. Neither technologically obsolete nor niche instrumentation will be discussed. A short description of the history of X-ray instrumentation is given in Section 2.1.3, illustrating the significant technological advances made since 1985. Sections 2.1.4 to 2.1.7 describe the components of the diverse range of currently available home-laboratory X-ray powder diffractometers. The most important concepts are discussed here; for technological details the reader is referred to the original literature or to textbooks.

In order to maintain neutrality as well as timeliness, the use of brand names and photos of real equipment has been avoided.

2.1.2. Scope and terminology

An X-ray (powder) diffractometer is by definition an instrument for measuring X-ray diffraction phenomena (from powders), where 'diffraction' is defined as elastic, coherent scattering of X-rays from a crystal lattice (in the crystallographic literature, the terms 'diffraction', 'X-ray diffraction' and 'Bragg diffraction' are frequently used synonymously). In recent texts, a 'powder' is frequently defined as a 'solid containing small crystallites or particles that will flow when agitated' in accordance to the usual sense of the word in colloquial speech.

Such definitions for 'X-ray diffractometer' and 'powder' are problematic, as their scope is too narrow and arbitrarily limited. They are probably the result of the historical development of the methodology and the lack of interaction between groups representing different application areas, such as X-ray scattering, emission or absorption techniques. The application range and thus capabilities of today's instrumentation are neither comprehensively nor even appropriately described by their implicit limitation to measuring X-ray diffraction phenomena of crystalline solids in powdered form.

It is well known that scattering and thus interference phenomena will occur with any type of waves and obstacles, and are by no means restricted to X-rays or perfectly regular arrays of atoms exhibiting long-range order (X-ray diffraction). In general, X-ray scattering can provide information on the arrangement of atoms or particles in materials with short-range order or no order at all, like gases, liquids and amorphous solids. For this reason it is obvious that X-ray diffractometers are intrinsically suited (and are actually used) for a wide range of X-ray techniques beyond X-ray diffraction as defined above. These techniques not only comprise X-ray scattering from any solids or liquids with any degree of order, but also X-ray absorption (radiography) or X-ray emission (XRF) techniques, see also Section 2.1.4.3. Consequently, the following terminology will be used throughout the remainder of this chapter:

A *sample* is the object or quantity of material to be investigated, while the *specimen* is the representative portion of the sample that is actually prepared and analysed. Specimen properties such as microstructure and packing density may differ from the properties of the sample as a result of specimen preparation. This must be taken into account for selection of the appropriate instrument configuration, data acquisition and evaluation.

A *powder* is defined in EN-1330-11 (2007) as a 'large number of crystallites and/or particles (*i.e.* grains, agglomerates or aggregates; crystalline or non-crystalline) irrespective of any adhesion between them' and thus can be a loose powder (in the sense of common language), a solid block, a thin film or even a liquid. An *ideal powder* is represented by a virtually unlimited number of sufficiently sized, randomly oriented and spherical crystallites.

The term *X-ray diffractometer* will refer to an instrument that, in principle, is capable of doing any of the X-ray techniques mentioned above, further detailed in Section 2.1.4.3. Instrument components will be described independently of applications, as they are not exclusive to any application area. Note that the term X-ray diffractometer also explicitly includes 'film cameras'. This is worth mentioning, as even recent texts still differentiate between (i) cameras, originally characterized by the use of X-ray films, and (ii) diffractometers, originally defined as an instrument derived from a camera in which the film had been replaced by a point detector. In principle, any so-called cameras and any diffractometers can be equipped with any type of today's point, linear and area detectors, so the former distinction between cameras and diffractometers, which arose from the historical development of X-ray instrumentation, is completely obsolete.

2.1.3. Historical overview

2.1.3.1. *From film cameras to diffractometers*

2.1.3.1.1. *Film cameras*

Powder diffraction analysis started with the development of simple film cameras, right after von Laue formulated his basic diffraction theory and the Braggs, father and son, laid down the foundations of crystal structure analysis, in the years 1912–1914. The first and simplest cameras were developed independently by Debye & Scherrer (1916) and Hull (1917), using a film to detect the scattered X-rays, with the instrument geometry termed 'Debye–Scherrer geometry'. The basic drawback of Debye–Scherrer cameras was their lack of resolution. Consequently,

since standard X-ray tubes readily produce divergent beams, the next evolutionary step was to employ self-focusing geometries, as first proposed independently by Seemann (1919) and Bohlin (1920), termed 'Seemann–Bohlin geometry'. In addition to significantly improved resolution, the intensity was also greatly increased by using a para-focusing arrangement using an X-ray source and specimen with finite width (line focus). Guinier (1937) extended the Seemann–Bohlin geometry using an incident-beam monochromator. Although the monochromator significantly reduced the intensity, this disadvantage was overcompensated for by improved beam conditioning, leading to unparalleled resolution at that time and elimination of the $K\alpha_2$ component of the radiation. This made the Guinier camera the best-performing film camera at that time and it therefore enjoyed high popularity.

The idea of using powder diffraction for phase identification of substances in pure form or in mixtures, originally suggested by Hull (1919) and then formalized by Hanawalt *et al.* (1938), attracted enormous interest, and developed into the powder diffraction method, making it a fundamental tool for material scientists. However, while classic film cameras laid down the historical foundation for the success of polycrystalline diffraction, their use was mostly limited to phase identification, semi-quantitative phase analysis and macroscopic stress measurements. Inherent difficulties included, but were not limited to, obtaining reliable intensities (because of film grain size and nonlinearity of the film response), very limited flexibility in terms of hardware extensions such as non-ambient specimen stages, and lack of diffracted-beam conditioning (*e.g.* the use of diffracted-beam monochromators).

Detailed descriptions of the many camera types as well as their use are given in a large number of texts. The interested reader is specifically referred to the textbook of Klug & Alexander (1974), which also contains an extensive bibliography.

2.1.3.1.2. *Diffractometers*

Photographic films have two important weaknesses: the detection efficiency is low and quantification of the diffracted intensities, including the line-profile shapes, is indirect and cumbersome. These shortcomings led to the idea of replacing the film with a photon counter (most commonly utilizing the Geiger–Müller counter at that time) and thus to the development of a device called a 'diffractometer'. The design resembled that of the Bragg ionization spectrometer, but dispersed monochromatic radiation from lattice planes rather than a spectrum of X-ray wavelengths. The first diffractometer developed by Le Galley (1935) was a non-focusing arrangement using a point-focus X-ray tube, making use of the cylindrical geometry of a normal film camera. In subsequent instrument designs focusing geometries were adopted, mostly the 'Bragg–Brentano geometry' (Brentano, 1924), a modification of the Seemann–Bohlin geometry, first introduced by Lindemann & Trost (1940) and Friedmann (1945).

The introduction of the first commercial focusing diffractometer in the early 1950s resulted in another major advance of the polycrystalline diffraction method, and may be largely credited to Parrish and co-workers (*e.g.* Parrish, 1949). This instrument consisted of a fixed-anode X-ray tube and a mechanical goniometer, operating in Bragg–Brentano geometry. The initial replacement of photographic film by the Geiger–Müller counter, and soon after by scintillation and lithium-drifted silicon detectors, allowed accurate intensities and line-profile shapes with high resolution to be recorded. The large space around the specimen permitted the design of various interchangeable stages for specimen rotation and translation, automatic specimen changing and non-ambient analyses. As a consequence, powder diffraction found many new applications beyond phase identification, including, but not limited to, quantitative analysis of crystalline and amorphous phases, microstructure analysis, and texture and strain analysis, at ambient and non-ambient conditions.

In the following decades, diffractometers were fully automated, fully digitized, and electronically and mechanically stabilized. The data quality they delivered became generally superior to that of film cameras, including in terms of resolution, eventually even facilitating structure determination and refinement from powders. Attempts to improve Guinier or Seemann–Bohlin cameras by replacing the film with image plates or any other stationary or scanning detectors did not produce competitive instrumentation in terms of instrument flexibility and mechanical simplicity. As a result, film cameras were steadily replaced by automated diffractometers using the Bragg–Brentano geometry. Since the 1990s, classic film cameras as well as other Guinier- or Seemann–Bohlin-based instruments are no longer used in practical polycrystalline diffraction analysis and thus lost any commercial relevance, apart from for a few niche applications. The Bragg–Brentano geometry, as developed in the 1940s, became the dominating instrument geometry and accounted for more than 90% of all instruments sold. The remainder almost exclusively used Debye–Scherrer-type arrangements, either employing focusing incident-beam monochromators for flat-plate or capillary transmission setups, or parallel-beam setups based on (pinhole) slits and/or Soller collimators and/or channel-cut monochromators for micro-diffraction, small-angle X-ray scattering and the characterization of thin films.

While powder diffractometers have changed little in their construction and geometry since the 1940s, considerable advances have made in X-ray detection and X-ray beam conditioning (X-ray optics).

Significant detector developments include one- and two-dimensional position-sensitive detectors (PSDs) based on gas proportional counter technology, and especially that of the scanning one-dimensional PSD (Göbel, 1980). The replacement of a point detector by a scanning one-dimensional PSD allowed the measurement time required to record a full pattern to be reduced down to minutes without significant compromise on resolution. This enabled time-critical applications (such as non-ambient and high-throughput analyses), or compensation of the intensity loss when employing incident-beam monochromators.

The introduction of laterally graded multilayers on figured reflectors, so-called 'Göbel mirrors' (Schuster & Göbel, 1996), allowed the conversion of a convergent beam into a parallel beam, and thus added a new dimension to laboratory beam conditioning – at a time when X-ray techniques were expanding into the now very rapidly growing area of thin-film characterization, sparking a renaissance of the Debye–Scherrer geometry.

Until the late 1980s and early 1990s, traditional powder diffraction and thin-film characterization were seen as two different techniques with diverse requirements. As a consequence, thin-film techniques formed a different X-ray diffraction application sector, served by different and specialized instrumentation, in addition to the already existing distinction between single-crystal and powder diffraction applications and instrumentation. The X-ray powder diffraction market was characterized by dedicated (and separately marketed) instruments for traditional powder diffraction, usually based on the Bragg–

Brentano geometry, and for thin-film analysis, usually based on the Debye–Scherrer geometry.

2.1.3.2. *Recent years*

In the 1990s, more and more laboratories started to deal with a full range of materials and related applications - from powders through polycrystalline thin films to epitaxial thin films. Dedicated and inflexible instruments were no longer economic for serving the increasing range of applications and also their increasing data-quality requirements.

The growing need for multipurpose instrumentation led to a new generation of X-ray diffractometers in the late 1990s, from all of the major manufacturers, based on a platform concept covering all relevant beam-path components including X-ray sources, optics, specimen stages and detectors. This concept, described in Section 2.1.4, allowed for a faster development of more and more differentiated instrumentation to optimally meet the requirements of all possible applications and sample types. Particularly successful were design improvements that allow the user to transform an instrument on-site by changing beam-path components, often without any need for alignment or even tools, to cover a larger range of applications and sample types using a single instrument.

A major contribution to the platform concept came from the continued development of beam conditioners based on multilayers, resulting in a wealth of X-ray beam optics for different applications. Advanced sputtering techniques allow the fabrication of multilayer optics with virtually arbitrary beam divergence, which can be used to generate focusing, parallel and divergent beams for both point- and line-focus applications.

The introduction of a series of new detector technologies in the early 2000s represented another technological quantum leap, which completely changed the X-ray detection landscape for laboratory diffraction. Within only a few years, detectors based on silicon micro-strip, silicon pixel and micro-gap technologies reached a market share of more than 90% in newly sold systems. Proportional and scintillation point detectors will probably become obsolete in only a few years from now, but can still be found, usually in lower-budget systems.

Today's instruments, with their different possible configurations of beam-path components, are now capable of performing a wider range of X-ray scattering applications than ever (see Section 2.1.4.3). Not surprisingly, the platform concept has become so successful that all modern X-ray diffractometers are now, at least to some extent, equipped with interchange capabilities for beam-path components. However, the fundamental principles remain the same and date back to the first film cameras and diffractometers, no matter how advanced today's instrumentation is.

2.1.4. The platform concept – fitting the instrument to the need

Modern X-ray diffractometers are highly modular assembly systems based on a platform concept, with a shared set of major components over a number of distinct diffractometer models, serving different X-ray scattering application areas. Such a platform concept has two important advantages. Firstly, a common design allows differentiated instruments to be developed faster, and eases the integration of new or improved beam-path components, potentially over the whole model range. Secondly, it enables the design of an X-ray optical bench with on-site interchange capabilities, allowing the mounting of selected beam-path components to meet specific application and specimen-property requirements.

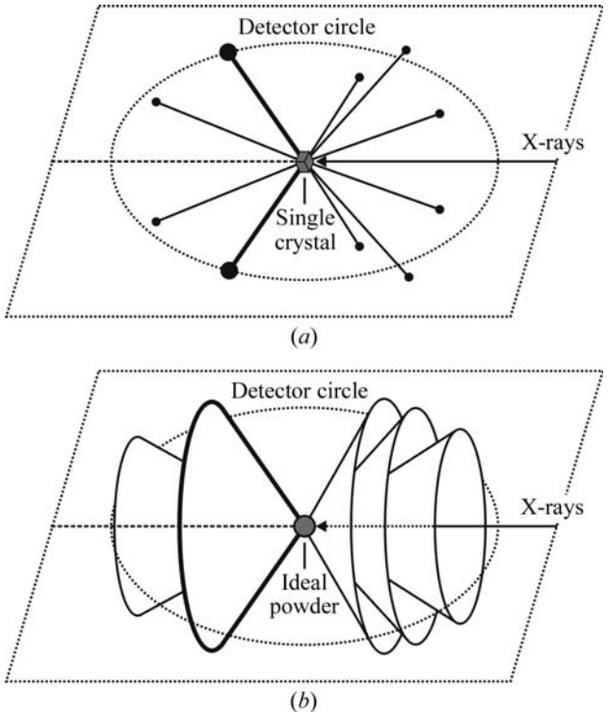

Figure 2.1.1
Diffraction of X-rays by (*a*) a rotating single crystal and (*b*) an ideal powder. The scattered intensity may be measured by a detector placed on the detector circle.

2.1.4.1. *Basic design principles and instrument geometry considerations*

X-ray scattering data are generally recorded in what is virtually the simplest possible manner, where the scattered intensity is measured by a detector mounted at some distance from the specimen. This is illustrated in Fig. 2.1.1, where a narrow, essentially monochromatic beam illuminates a small spherical specimen. For a rotating single crystal, the diffracted beams point in discrete directions in space as given by Bragg's law for each lattice vector d_{hkl} (Fig. 2.1.1*a*). For an ideal powder consisting of a virtually unlimited number of randomly oriented crystallites, the diffracted beams will form concentric cones ('Debye cones') with a semi-apex angle of 2θ, representing all randomly oriented identical lattice vectors d_{hkl} (Fig. 2.1.1*b*). Note that in contrast to a single crystal, an ideal powder does not need to be rotated to obtain a complete powder diffraction pattern.

Most instruments are built around a central specimen and consist of the following beam-path components, the numbering of which is consistent with the mounting positions shown in Fig. 2.1.2:

(1) X-ray source;
(2) incident-beam optics;
(3) goniometer base or specimen stage;
(4) diffracted-beam optics;
(5) detector.

The directions of the *incident* and *diffracted beams* (also called 'primary' and 'secondary' beams) form the *diffraction plane* (also called the 'equatorial plane' or 'scattering plane'). The goniometer base can be mounted horizontally (horizontal diffraction plane) or vertically (vertical diffraction plane). The direction perpendicular to the equatorial plane is known as the *axial*

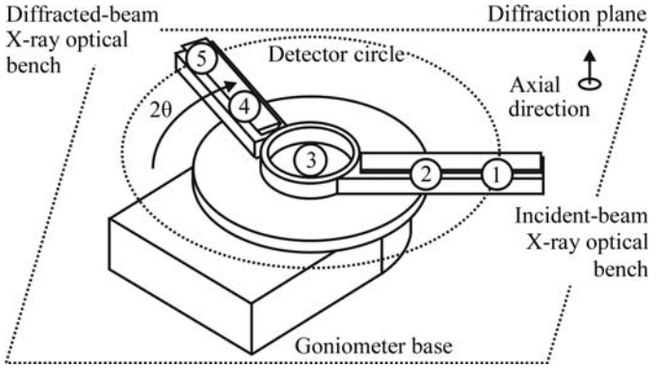

Figure 2.1.2
The basic design principle of modern diffractometers. Currently available instruments are built around a centrally mounted specimen and represent an X-ray optical bench with mounting positions for any (1) X-ray sources, (2) incident-beam optics, (3) specimen stages, (4) diffracted-beam optics and (5) detectors. The 2θ position of the scattered-X-ray optical bench refers to the 2θ angle of the Debye cone shown in bold in Fig. 2.1.1(*b*).

direction. The *detector circle* (also called the 'goniometer circle' or 'diffractometer circle') is defined either by the centre of the active window of a stationary detector, or, in most cases, by a detector moving around the specimen, and is coplanar to the diffraction plane. The 2θ angle of both the diffracted beam in Fig. 2.1.1(*a*) and the Debye cone in Fig. 2.1.1(*b*) (shown in bold) refers to the 2θ position of the diffracted-beam X-ray optical bench in Fig. 2.1.2. It is obvious from Figs. 2.1.1 and 2.1.2 that, in principle, diffraction from single crystals and (ideal) powders can be measured using the same instrument.

An instrument design with a centrally mounted specimen has the important advantage that it implicitly allows the operation of one and the same instrument in both Bragg–Brentano and Debye–Scherrer geometry, depending on the beam divergence chosen. The actual instrument geometry is thus a function of the actual beam propagation angle (divergent, parallel or convergent), making the X-ray optics the most important part of any instrument-geometry conversion. The relationship between the two geometries and their implementation in a single instrument using an incident-beam X-ray optical bench is illustrated in Fig. 2.1.3.

As laboratory X-ray sources invariably produce divergent beams, the 'natural' instrument geometry is self-focusing, 'automatically' leading to the Bragg–Brentano geometry as shown in Fig. 2.1.3(*a*). In this geometry the angle of both the incident and the diffracted beam is θ with respect to the specimen surface. The X-ray-source-to-specimen and the specimen-to-detector distances are equal. The diffraction pattern is collected by varying the incidence angle of the incident beam by θ and the diffracted-beam angle by 2θ. The focusing circle is defined as positioned tangentially to the specimen surface. The focusing condition is fulfilled at the points where the goniometer circle intersects the focusing circle, and thus requires measurements in reflection mode.

The Bragg–Brentano geometry may be extended by an incident- or a diffracted-beam monochromator. In the case of an incident-beam monochromator as shown in Fig. 2.1.3(*b*), the focus of the X-ray source is replaced by the focus of the monochromator crystal. This involves mounting the monochromator crystal (and the X-ray source) a certain distance away along the incident-beam X-ray optical bench, as given by the focusing length of the monochromator crystal (the dotted line in Fig. 2.1.3*b*). For a diffracted-beam monochromator or mirror, the geometry shown in Fig. 2.1.3(*b*) can be thought of as reversed (simply consider the X-ray source and detector switching their positions).

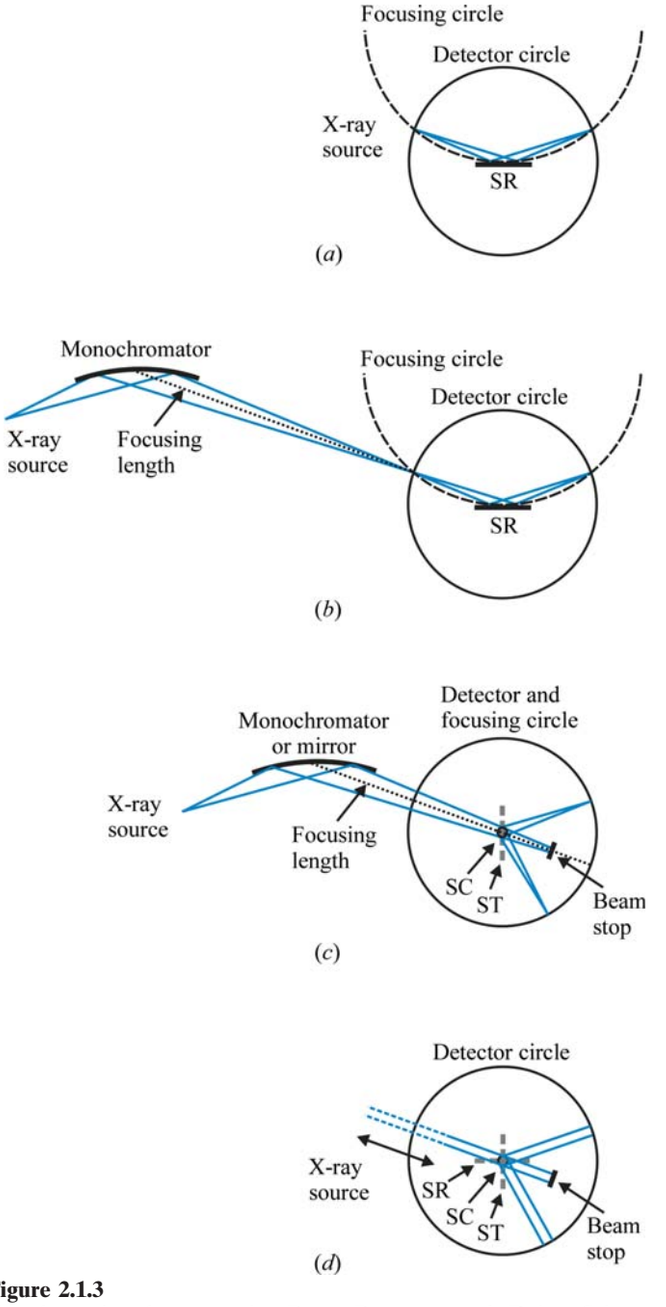

Figure 2.1.3
Transformation between the Bragg–Brentano and Debye–Scherrer geometries using a incident-beam X-ray optical bench. SR: flat specimen, reflection mode; SC: capillary specimen, transmission mode; ST: flat specimen, transmission mode. The actual instrument geometry is a function of the actual beam-propagation angle, making the X-ray optics the most important part of any instrument-geometry conversion. (*a*) Divergent beam: Bragg–Brentano geometry, (*b*) divergent beam: Bragg–Brentano geometry extended by an incident-beam monochromator. (*c*) Convergent beam: focusing Debye–Scherrer geometry, (*d*) parallel beam: Debye–Scherrer geometry. Transformation is achieved by mounting the X-ray tube and pre-aligned optical components at predefined positions of the optical bench. None of the figures are to scale.

The conversion from Bragg–Brentano to Debye–Scherrer geometry involves the mounting of some kind of optics designed to convert the divergent beam coming from the X-ray source into a focusing or parallel beam; this is shown in Figs. 2.1.3(*c*) and (*d*), respectively.

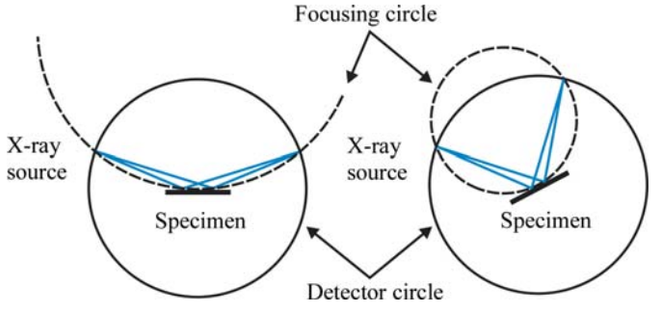

Figure 2.1.4
Bragg–Brentano geometry. The focusing circle, given for two different angles 2θ, is tangential to the specimen surface. Its diameter is given by the intersections between the detector and the focusing circles and is thus 2θ dependent.

In a focusing Debye–Scherrer geometry setup, as shown in Fig. 2.1.3(*c*), the divergent beam coming from the X-ray source is normally focused on the detector circle (for highest resolution) by means of an incident-beam monochromator or a focusing mirror. The focusing circle is identical to the detector circle and the focusing condition requires measurements in transmission mode. When employing an incident-beam monochromator with sufficient focusing length, then conversion between the Bragg–Brentano geometry and the focusing Debye–Scherrer geometry involves a shift of the monochromator crystal (and the X-ray source) along the incident-beam X-ray optical bench (note the identical focusing length of the monochromator shown in Figs. 2.1.3*b* and *c*).

For a parallel-beam setup, as shown in Fig. 2.1.3(*d*), parallelization of the divergent beam coming from the X-ray source may be achieved by different means, such as collimators (classic Debye–Scherrer geometry) or reflective optics such as mirrors or capillaries. In principle, the X-ray source and the detector may be placed at any distance from the specimen, as there are no focusing requirements. As a consequence, measurements can be performed in both reflection and transmission mode.

In a simplified scheme, conversion between the geometries discussed above involves repositioning of the X-ray source, together with mounting of X-ray optics with suitable beam divergence. To make this possible, the incident-beam optical X-ray bench offers the necessary predefined mounting positions including relevant translationary and rotationary degrees of freedom.

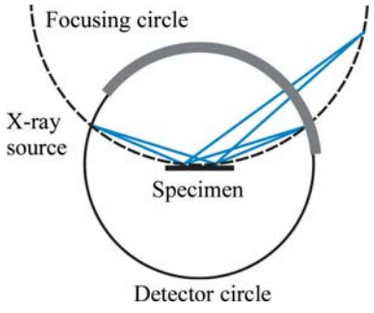

Figure 2.1.5
Bragg–Brentano geometry. While all diffracted beams focus on the (variable-diameter) focusing circle (here shown for two beams), focusing on the detector circle is only achieved at the X-ray source and detector positions (located at the intersections between the detector and the focusing circles). This prevents the use of larger position-sensitive detectors because of defocusing, as indicated by the hypothetical large position-sensitive detector represented by the bold grey line.

An important aspect directly related to the choice of the instrument geometry is the geometric compatibility with position-sensitive detectors. In contrast to Debye–Scherrer geometry, large line and area detectors may not be used in Bragg–Brentano geometry. This is an important limitation of the latter, as the focusing circle does not coincide with the detector circle and has a 2θ-dependent diameter, as illustrated in Fig. 2.1.4. As a consequence, the diffracted beam is only focused on a single point of the goniometer circle, as shown in Fig. 2.1.5. However, small position-sensitive detectors with an angular coverage of not more than about 10° 2θ are used with great success, as defocusing can be ignored at diffraction angles larger than about 20° 2θ if high angular accuracy and resolution are not required. For measurements at smaller 2θ angles, or for highest angular accuracy and resolution, the active window size of a position-sensitive detector may be reduced by means of slits and/or electronically down to a point, allowing the use of this detector as a point detector.

2.1.4.2. *Range of hardware*

An X-ray diffractometer is generally characterized by the relationship between a conditioned beam, the specimen orientation and the subsequent interception of the diffracted beams by a detector of given geometry and imaging properties. There are only a very few instrument configurations that will be ideal for any two application areas, or every conceivable sample within a single application area. It is the user's responsibility to match the instrument to the specimen properties, which can be challenging, particularly in multi-user environments with a large variety of sample types. The platform and the X-ray optical-bench concepts allow the user to choose and mount the most appropriate beam-path components in order to optimize an instrument with respect to a specific application and specimen-property requirements. Table 2.1.1 provides an overview of the currently available types of beam-path components from the X-ray source through to the detector.

The length of available X-ray optical benches varies, and is typically in the range of about 15 cm up to 100 cm. Larger benches allow mounting of bulky components (*e.g.* moving-target X-ray sources or large detectors) as well as mounting of several X-ray optics in a row (*e.g.* combinations of mirrors and channel-cut monochromators). Some diffractometer models allow mounting of two incident- and/or diffracted-beam X-ray optical benches to mount different beam-path components in parallel, *e.g.* X-ray sources with different wavelengths or beam shapes (very popular in single-crystal diffraction), X-ray optics with different beam divergence (*e.g.* to switch between Bragg–Brentano and Debye–Scherrer geometry), and different detector types.

While Table 2.1.1 and the above may imply an enormous combinatorial diversity, in practice this is not entirely the case. In general, beam-path components have to be compatible with the selected instrument geometry, which is dictated by the choice of the X-ray source (point or line), the beam characteristics (wavelength distribution, divergence) and the detector (point, linear or area). This automatically narrows down the range of combinations. As an obvious example, many crystal monochromators and X-ray mirrors are only compatible with a particular wavelength. Also, the size and weight of bulky components, such as moving-target X-ray sources, large specimen stages and large two-dimensional detectors, may impose practical constraints that require consideration. For example, the acces-

Table 2.1.1
Types of beam-path components available in laboratory X-ray powder diffraction

The column numbering corresponds to the positions indicated in Fig. 2.1.2 at which individual components can be mounted.

Position 1	Positions 2 and 4	Position 3		Position 5
X-ray sources	X-ray optics	Goniometer base	Specimen stages	Detectors
Fixed target Moving target (rotating anodes, liquid-metal jets)	Absorptive (apertures, metal filters) Diffractive (monochromators, analysers) Reflective (multilayer mirrors, capillary optics)	Vertical [ω–θ (θ–θ), ω–2θ (θ–2θ)] Horizontal [ω–θ (θ–θ), ω–2θ (θ–2θ)]	Fixed, rotating Specimen changer Eulerian cradles Kappa stages Tilt/fixed χ stages *XYZ* stages Flow-through cells Non-ambient (low temperature, high temperature, humidity, high pressure)	Scintillation Gas ionization (metal wire, micro-gap) Semiconductor (SiLi, strip/pixel, CCD/CMOS)

sible angular range may be limited for large components owing to collision issues, while heavy loads on vertical goniometers may impede alignment and lead to early wear and tear. Restrictions will be discussed in Sections 2.1.5 to 2.1.7 for the individual components.

These days, the exchange of lighter components, such as most X-ray optics, specimen stages and detectors, does not require any tools at all (such as when a snap-lock mechanism is employed) or more than a few screws for fixing. Alignment is normally not required when components are factory pre-aligned and handled with care, and when mounts are manufactured with good quality. Intrinsic changes of the beam direction (*e.g.* focusing crystal monochromators or X-ray mirrors) or beam offsets (*e.g.* two-bounce channel-cut monochromators) need compensating translation and/or rotation of the components involved.

The exchange of large, heavy components, or complicated rebuildings such as the conversion of a goniometer (vertical $\leftrightarrow$ horizontal, θ–$\theta \leftrightarrow \theta$–2$\theta$ *etc.*), may be still possible for technically skilled users. However, special tools may be necessary, requiring shipment of the component(s), or even the instrument, back into the factory. In addition, X-ray, machine and electrical safety directives by the local authorities have to be obeyed, and conversions may require updating approval to use the instrument. In such cases it may be more economic to operate two dedicated instruments instead.

The instrument control software plays a particularly important role in the context of instrument configuration and automated instrument conversion. In modern instruments, each beam-path component is equipped with an identification chip or hole masks read out by light barriers, which uniquely identify the respective component and link it with all its individual stored or coded properties. This information may range from part numbers, usage history or alignment information such as beam offsets, through to a virtually unlimited wealth of any physical data required to configure and operate that particular component. This 'component recognition' feature provides for completely new and important capabilities of laboratory powder diffractometers, the most important of which are:

(*a*) Any beam-path components, and each change of status, can be automatically detected, validated and configured, allowing true 'plug & play' operation.

(*b*) Real-time conflict detection: detection of incompatible, incorrectly mounted or missing instrument components. This feature can also help the user in choosing compatible instrument components, as already discussed above.

(*c*) Automatic, motorized adjustments of beam direction or beam-offset changes, based on the information stored in the related components' ID chips, as individually determined at the factory *via* pre-alignment.

(*d*) Every instrument detail can be saved together with the measurement data, providing for a complete and accurate documentation of the experiment. In principle, every measurement can be exactly reproduced even years later.

(*e*) Measurement instructions can include instrument information. For example, manufacturers or users can configure the measurement software to propose instrument configurations deemed best for particular applications. A user with appropriate rights can choose to enforce a certain instrument configuration so that measurements will not start unless the instrument has detected the required configuration.

Both the platform concept and the huge advances in instrumentation and instrument control software have dramatically changed the laboratory X-ray instrumentation landscape in the past few years. The ease with which an instrument configuration can be changed is not only useful for less-skilled users. Probably even more importantly, it allows the use of the same instrument, in different configurations, for different X-ray application areas. It can generally be said that laboratory X-ray instrumentation has overcome the (mostly historical) dividing lines between different applications, which were mostly between single-crystal diffraction, powder diffraction and thin-film analysis. As far as differences still remain, these are usually solely the consequence of dedicated instrument components for meeting specific application requirements, resulting in specialized measurement and data-evaluation software, which is rarely included with each instrument.

2.1.4.3. *Range of applications*

It is the flexibility of today's X-ray diffractometers that leads to their usefulness for a wide range of X-ray scattering techniques beyond traditional X-ray powder 'Bragg diffraction'. Table 2.1.2 provides an overview.

X-ray scattering techniques represent the vast majority of techniques that X-ray diffractometers are used for. Properly configured, however, the same instrument can also be used to collect X-ray absorption (X-ray radiography) or X-ray emission (X-ray fluorescence) data, even if the achievable data quality cannot compete with dedicated instruments.

For X-ray radiography, an instrument will be configured in transmission geometry with the X-rays projected towards a

Table 2.1.2
X-ray applications for with modern X-ray diffractometers

X-ray scattering
Powder diffraction
Qualitative (phase identification) and quantitative phase analysis
Indexing, structure determination and structure refinement from powder data
Microstructure analysis (texture, size, strain, microstrain, disorder and other defects)
Pair distribution function analysis ('total scattering')
Thin-film analysis
Grazing incidence X-ray diffraction (GIXRD)
X-ray reflectometry
Stress and texture
High-resolution X-ray diffraction
Reciprocal-space mapping
In-plane GIXRD
Single-crystal diffraction
Chemical crystallography
Protein crystallography
Small-angle X-ray scattering
X-ray topography
X-ray absorption
X-ray radiography (X-ray-absorption-based imaging)
X-ray emission
X-ray fluorescence

specimen. X-rays that pass through the specimen can be detected to give a two-dimensional representation of the absorption contrast within the specimen. For tomography, the X-ray source and detector will be moved to blur out structures not in the focal plane. Multiple images can be used to generate a three-dimensional representation of the specimen by means of computed tomography. Obvious disadvantages are the large effective focal spot size of the X-ray sources and the relatively low resolution of the detectors that are typically used for powder diffraction, which, in combination with a limited adjustability of both the X-ray-source-to-specimen and specimen-to-detector distances, lead to substantial unsharpness issues and poor resolution. High-quality images can be achieved when using micro-focus X-ray sources and charge-coupled device (CCD) detectors with focus and pixel sizes smaller than 10 μm, respectively, but such an instrument configuration is not suitable for applications requiring ideal powders (see also Sections 2.1.6 and 2.1.7).

Collecting X-ray fluorescence data is comparatively straightforward. Data can be collected simultaneously to X-ray scattering data when employing a suitable detector, such as an energy-dispersive detector (Section 2.1.7.2.3). There are a couple of disadvantages to be considered, such as absorption issues (the specimen will be normally measured in air rather than in vacuum, hampering the analysis of light elements) and the inefficiency of excitation by the characteristic line energies of the X-ray source anode materials typically used for diffraction (hampering the analysis of elements with higher atomic numbers than that of the anode material).

2.1.5. Goniometer designs

A goniometer, by definition, is an instrument that either measures an angle or allows an object to be rotated to a precise angular position. In an X-ray diffractometer the purpose of the goniometer is to move the X-ray source, specimen and detector in relation to each other. Goniometers are usually categorized by the number of axes available for X-ray source, specimen and detector rotation, and are thus called one-, two-, three-, ..., n-axis (or -circle) goniometers.

Because of practical reasons, most goniometers consist of two distinct components, a goniometer base and a specimen stage, with the specimen stage mounted on the goniometer base.

The goniometer base typically offers two axes, one axis to rotate the X-ray source or the specimen stage, the other axis to rotate the detector. In some designs goniometer bases are omitted, specifically if there is no need to move the X-ray source and the detector, such as in Debye–Scherrer-type diffractometers with large detectors. Such machines are usually dedicated to a particular application without the need for high flexibility.

Depending on the requirements of the application, additional rotational and translational degrees of freedom may be needed to rotate and translate a specimen in space; these are usually implemented in the specimen stage. More rotational degrees of freedom may include the rotation of the X-ray source line focus or a rotation of the detector out of the diffraction plane to measure diffraction by lattice planes (nearly) perpendicular to the specimen surface, so-called non-coplanar diffraction.

2.1.5.1. *Geometrical conventions and scan modes*

In the literature there is some inconsistency related to the naming of axes and the choice of signs for angles (left- *versus* right-handed). A comprehensive treatment of geometrical conventions has recently been given by He (2009); in the following these conventions will be adhered to.

In many texts the notations θ–2θ and θ–θ rather than ω–2θ and ω–θ are used, mostly because of historical reasons. The first diffractometers operated in Bragg–Brentano geometry (see Section 2.1.3.1.2) and were equipped with single-axis goniometers. In such a goniometer the single axis drives two shafts which are mechanically coupled 1:2 or 1:1; thus the notations θ–2θ and θ–θ were coined. Today, the majority of all goniometer bases allow coupled as well as uncoupled rotation of the ω and θ axes. Therefore the ω–2θ and ω–θ notations should be generally preferred, as they represent the more general notations.

2.1.5.1.1. *Goniometer base*

A typical goniometer base provides two coaxial and independently driven axes, ω and 2θ, mounted perpendicular to the diffraction plane. These two axes are the main axes of a goniometer, since they have the most effect on the accuracy and precision of measured Bragg angles. The diffraction plane and the axes are generally described by a right-handed Cartesian coordinate system, as illustrated in Fig. 2.1.6, where the direct X-ray beam propagates along the X_L axis. Z_L is up and coincident with the ω and 2θ axes, and X_L–Y_L define the diffraction plane with the detector circle coplanar to it. Since X_L is coincident with the incident X-ray beam, it is also the axis of the Debye cones. The semi-apex angles of the cones are determined by the 2θ values given by the Bragg equation. The angles 2θ and γ describe the direction of scattering vectors in space (compare Fig. 2.1.1), where γ is defined as the azimuthal angle from the origin at $-Z_L$ with a right-hand rotation axis along the opposite direction of the incident beam ($-X_L$ direction).

The ω and 2θ axes are mechanically arranged as the inner circle and outer circle, respectively. The inner circle usually carries either the specimen stage or the X-ray source, while the detector is mounted on the outer circle. As a consequence, there are two common base goniometer configurations in use: In the ω–2θ (or θ–2θ with $\omega = \theta$) configuration, the incident-beam direction is

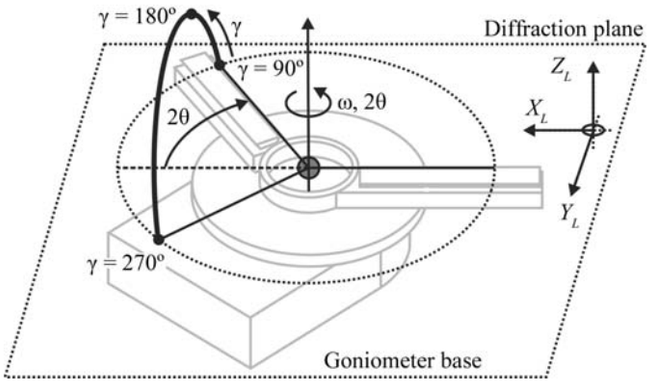

Figure 2.1.6
Laboratory coordinates and geometric definition of the coaxial goniometer axes ω and 2θ. If the azimuthal angle γ takes all values from 0 to 360° at a given Bragg angle 2θ, the trace of the diffracted beams forms a Debye cone (compare with Fig. 2.1.1).

mechanically fixed. The ω axis rotates the specimen stage, while the 2θ axis rotates the detector. In the ω–θ (or θ–θ with $\omega = \theta$) configuration, the ω axis defines the incident-beam angle by rotating the X-ray source, while the other axis scans the detector. In this configuration the specimen stage is mechanically fixed. Both configurations allow identical positioning of the X-ray source, specimen and detector relative to each other.

The goniometer base orientation is defined by the diffraction plane, which can be either horizontal or vertical. Vertical-base goniometers in ω–θ configuration are particularly popular, as the specimen is always kept horizontal, effectively preventing it from falling off. However, heavy specimens and beam-path components require particular attention in both the goniometer base design and choice of orientation, as they have a strong impact on goniometer accuracy, precision and early wear and tear (see also Section 2.1.5.2). Where loads exceed the maximum specifications for a vertically mounted goniometer base, and whenever horizontal specimen positioning is not imperative, either a vertical goniometer base in ω–2θ configuration or a horizontal goniometer should be chosen.

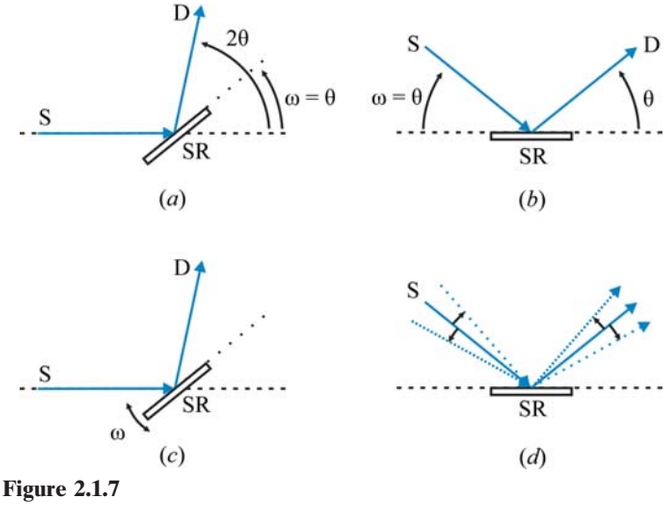

Figure 2.1.7
Goniometer base configurations and scan modes suitable for both Bragg–Brentano or Debye–Scherrer geometry. Symmetric beam path setup in (*a*) ω–2θ and (*b*) ω–θ configuration. Rocking curve setup in (*c*) ω–2θ and (*d*) ω–θ configuration. Only the central beams are shown for clarity, rotations are indicated by arrows. S: X-ray source, D: detector, SR: flat specimen, reflection mode.

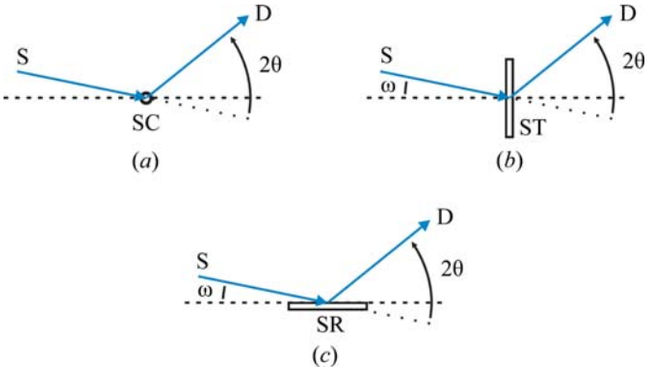

Figure 2.1.8
Goniometer base configurations and scan modes suitable for the Debye–Scherrer geometry only. Only the central beams are shown for clarity. (*a*) Capillary specimen in transmission mode, (*b*) flat specimen in transmission mode, (*c*) flat specimen in reflection mode, grazing incidence with fixed ω. S: X-ray source, D: detector, SR: flat specimen, reflection mode; SC: capillary specimen, transmission mode; ST: flat specimen, transmission mode.

In Figs. 2.1.7 and 2.1.8 a range of typical goniometer base configurations and scan modes are illustrated.

A symmetric beam-path setup in reflection mode, where both the incident and diffracted beam form an angle of θ with respect to the specimen surface, is mandatory for instruments operating in Bragg–Brentano geometry to maintain the focusing condition (see Section 2.1.4.1), but is also commonly used in Debye–Scherrer geometry. Scanning involves coupling of the ω (with $\omega = \theta$) and 2θ axes in a ratio of 1:2 for the ω–2θ configuration (Fig. 2.1.7*a*) and 1:1 for the ω–θ configuration (Fig. 2.1.7*b*), but only allows probing of lattice planes essentially parallel to the specimen surface. Where determination of a texture parameter is sought, a so-called 'rocking-curve' measurement can be performed by rocking either the specimen or the X-ray source and detector around the position of a Bragg peak. Two scenarios need to be considered and are illustrated in Fig. 2.1.7(*c*) and Fig. 2.1.7(*d*). In the ω–2θ configuration with fixed X-ray source (Fig. 2.1.7*c*), the detector will be fixed at the 2θ position of a selected Bragg peak, while the specimen is rotated ('rocked') independently, to perform a so-called 'ω-scan'. To achieve the same in an ω–θ configuration with fixed specimen, the X-ray source and the detector will be coupled 1:−1 or −1:1 to perform a clockwise or anticlockwise scan while maintaining the selected 2θ position, respectively, as illustrated in Fig. 2.1.7(*d*).

In Debye–Scherrer geometry there is no geometrical restraint requiring coupled scans to maintain 2θ-dependent focusing conditions, as is the case in the Bragg–Brentano geometry, providing high flexibility. Specimens can be measured in both reflection as well as transmission mode. In principle, the incident-beam direction may be any relative to the specimen surface, and can be fixed or variable, while the detector performs a 'detector scan'. The ω and 2θ axes may be coupled or not. Choices solely depend on the specimen properties and the requirements of the application. This is demonstrated in Fig. 2.1.8 for a few representative examples. The classic Debye–Scherrer geometry using a capillary specimen is shown in Fig. 2.1.8(*a*). The capillary specimen can be readily exchanged for a flat-plate specimen as shown in Fig. 2.1.8(*b*) and Fig. 2.1.8(*c*) for flat-plate transmission and reflection, respectively. ω can be set to different angles or perform a coupled scan to allow access to higher 2θ angles (Fig. 2.1.8*b*) or can be set to a different angle for grazing-incidence measurements (Fig. 2.1.8*c*). In some applications it may be beneficial to perform a (usually coupled) scan of both ω and 2θ to

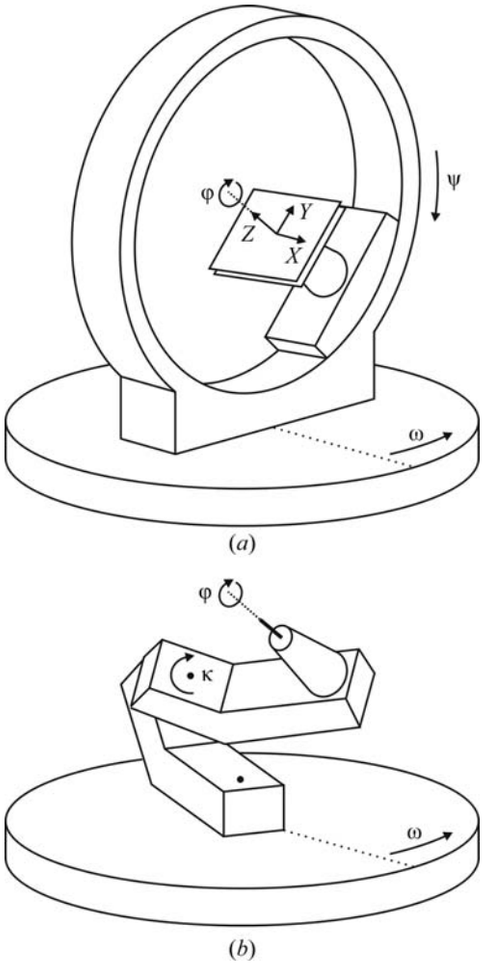

Figure 2.1.9
Geometric definition of the Eulerian and kappa geometries with identical specimen orientation in space. (*a*) Specimen rotation and translation in a Eulerian cradle equipped with an *XYZ* stage, (*b*) specimen rotation on a kappa stage.

improve particle statistics ('wobbling'). Obviously, all the setups shown in Fig. 2.1.8 will work for the full range of X-ray scattering and absorption techniques as discussed in Section 2.1.4.3, leading to the renaissance of the Debye–Scherrer geometry within the past 20 years.

2.1.5.1.2. *Specimen stage*

Depending on the requirements of the application, the specimen stage may offer additional degrees of freedom for specimen rotation as well as X, Y, Z translation. The goniometer base may be configured as ω–2θ as well as ω–θ, and may be oriented vertically as well as horizontally.

To orient a specimen in all possible orientations in space, the specimen stage will offer two more rotational degrees of freedom in addition to the ω and 2θ axes provided by the goniometer base. Such goniometers are known as four-axis diffractometers, with two basic geometries in common use for specimen orientation: Eulerian geometry and kappa geometry.

In the Eulerian geometry the specimen is oriented through the three Euler angles ω (defined by the ω axis of the goniometer base), ψ (psi), and φ (phi). The relationship between the laboratory and rotation axes is shown in Fig. 2.1.9(*a*) for a typical Eulerian cradle. The ω angle is defined as a right-handed rotation about the ω (or Z_L) axis. The ψ angle is a right-hand rotation about the ψ axis, which lies in the diffraction plane and runs parallel to the bisectrix between the incident and diffracted beams. The φ angle defines a left-handed rotation about an axis on the specimen, typically the normal to a flat specimen surface. In some texts the angle χ (chi) is used instead of ψ, with the relationship between the two angles defined as $\psi = 90 - \chi$. Eulerian cradles have the advantage of high mechanical stability and are often integrated with *XYZ* stages to handle bulky specimens. The geometrical definitions of specimen X, Y, Z translations are also shown in Fig. 2.1.9(*a*).

The kappa (κ) geometry shown in Fig. 2.1.9(*b*) represents an alternative way to orient a specimen in space. The ψ axis of the Eulerian geometry is replaced by the κ axis, which is tilted at 50° relative to the diffraction plane. It supports an arm carrying the specimen, with the φ axis tilted at 50° to κ. The role of the Eulerian ψ rotation is fulfilled by means of combined rotation along κ and φ, which allows Eulerian ψ angles in the range −100 to +100° to be obtained. The absence of the (bulky) ψ circle of Eulerian cradles allows an unobstructed view of the specimen and unhindered access from 'above', for example to mount a cooling device without risk of collision. These two advantages made the kappa geometry popular in single-crystal work. On the other hand, it is not possible to move the specimen to an 'upside-down' position, *i.e.* equivalent to Eulerian ψ angles less than −100° or greater than 100°.

Most goniometers do not offer all six rotational and translational degrees of freedom. The majority of these are actually three-axis goniometers, where the specimen stage offers one additional axis for specimen rotation.

A comprehensive overview of commercially available specimen stages is beyond the scope of this chapter owing to the huge number of dedicated specimen stages available for different kinds of specimen types, levels of automation and non-ambient analyses. The most complete and most current information will be found in manufacturers' product information.

2.1.5.2. *Accuracy and precision*

Particularly high demands are made on goniometer accuracy and precision in Bragg-angle positioning (goniometer base) and specimen orientation (specimen stage). These are usually expressed by the angular accuracy and precision of the goniometer-base axes (ω, 2θ) and the sphere of confusion of specimen positioning in space. A detailed discussion is given by He (2009).

Depending on the application and the actual instrument configuration, additional requirements may be imposed on goniometers, and may limit the maximum accuracy and precision that are achievable. Typical requirements, often not compatible with each other, are:

(*a*) mounting of heavy and bulky beam-path components and specimens;
(*b*) variable goniometer radii, typically ranging from about 15 to 60 cm; and
(*c*) vertical goniometer operation to prevent specimens from falling off the holder.

Each of these requirements may have an impact on goniometer accuracy and precision, and potential early wear and tear. Typical loads range from several kg for fixed-target X-ray sources up to 50 kg and more for moving-target X-ray sources. Small detectors such as point and one-dimensional detectors range from less than 1 kg up to a few kg, while large two-dimensional detectors may weigh up to 50 kg and sometimes even more.

For vertical goniometers, the loads on the main axis bearings can be effectively reduced by counterbalances, as shown in Fig.

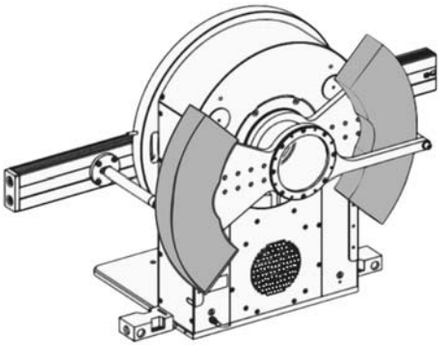

Figure 2.1.10
Example of counterbalancing of a vertical θ–θ goniometer. The counterweights (grey parts) are located at positions matching the weights and locations of the X-ray source and detector. Mounting of different beam-path components with significantly different weight or moving of, for example, the X-ray source and/or the detector to change the respective radii may require repositioning of the counterweights to maintain goniometer accuracy and instrument alignment.

2.1.10 for a goniometer in the ω–θ configuration. Heavy specimen stages may also be supported from below or mounted directly on the bench, disconnected from the goniometer base. However, for heavy beam-path components and larger goniometer radii there is the additional issue of high torques on the incident- and/or the diffracted-beam X-ray optical benches, leading to torsions along the benches. These may significantly deteriorate both the angular accuracy of a goniometer and instrument alignment. For heavy incident-beam-path components such as moving-target X-ray sources, a vertical goniometer base in the ω–2θ configuration is commonly used, as the incident-beam optical X-ray bench is mechanically fixed. For heavy incident- and diffracted-beam-path components a horizontal goniometer base is preferred.

Modern goniometers are equipped with stepping motors and optical encoders, and feature life-span lubrication for maintenance-free operation. The typical accuracy of the two goniometer base axes (ω, 2θ) is of the order of a few thousandths of a degree, with a precision of the order of a few tens of thousandths of a degree. The ψ and φ axes of the specimen stage are mostly used for specimen orientation; the typical angular accuracy and precision are in the range of about 0.01°.

The sphere of confusion of a goniometer is the result of a superposition of all axes and represents the minimum spherical volume covering all possible locations of an infinitely small specimen at all possible orientations. The size of the sphere of confusion depends on issues such as individual axis accuracy and precision, mechanical tolerances, thermal-expansion mismatches, and the weights of the specimen and beam-path components. The sphere of confusion for a two-axis goniometer or a four-axis goniometer with a kappa stage is typically less than 10 μm, and for a four-axis goniometer with a Eulerian cradle less than 50 μm; both values are without a specimen loaded.

Note that the final accuracy of the Bragg angles of the measurement data is mostly determined by instrument alignment, and not by the accuracy specifically of the two goniometer base axes. Optical encoders can measure and control axis positions, but they cannot detect any misaligned or even loose beam-path components. The final data accuracy is determined by the adjustability of an X-ray diffractometer with all its beam-path components. A modern X-ray diffractometer can be aligned to an angular accuracy of equal or better than 0.01° 2θ, which can be checked using suitable standard reference materials (see Chapter 3.1).

2.1.5.3. *Hybrid beam-path systems*

The trend towards multipurpose instrumentation as well as specific application requirements has led to a few specialized goniometer designs. Two major representatives of such designs are (1) multiple-beam-path systems and (2) systems with additional rotational degrees of freedom of beam-path components, such as is required for non-coplanar grazing-incidence diffraction (GID).

2.1.5.3.1. *Multiple-beam-path systems*

Multiple-beam-path systems are usually characterized by integrating more than one beam path on a single goniometer, employing different, complementary beam-path components to meet different application and specimen-property requirements. Mounting two different fixed-target X-ray sources (usually microsources) with different wavelengths (Cu, Mo) is very popular in single-crystal crystallography. Double detector arms are used to mount different types of detectors, most frequently one-dimensional detectors in combination with point detectors. Different X-ray optics can be used to implement different instrument geometries.

A significant driving force behind such multipurpose instrumentation is convenience, *i.e.* to serve a maximum range of applications and specimen types, ideally without the need to manually change the instrument configuration. Indeed, switching between different, preconfigured beam paths may often only require the push of a single software button. However, parallel mounting of different beam-path components raises issues related to the goniometer load and to limitations of angular scan ranges owing to collision issues.

In more recent designs, different X-ray optics have been combined into single motorized modules, allowing switching between different beam paths. Such 'combi-optics' are described in Section 2.1.6.3.4.

2.1.5.3.2. *Non-coplanar beam-path systems*

Non-coplanar (or 'in-plane') grazing-incidence diffraction is a technique for investigating the near-surface region of specimens (ten or fewer nanometres beneath the air–specimen interface). It exploits the high intensity of the total external reflection condition while simultaneously involving Bragg diffraction from planes that are nearly perpendicular to the specimen surface.

As illustrated in Fig. 2.1.11, the incident beam is set at an angle α_I, enabling total external reflection in the coplanar direction (that is coplanar to the diffraction plane); related applications include reflectometry and grazing-incidence small-angle X-ray scattering (GISAXS). 'In-plane' grazing-incidence diffraction

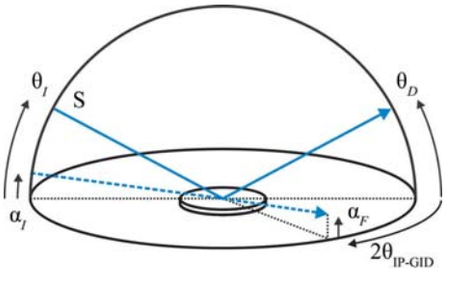

Figure 2.1.11
Illustration of coplanar and in-plane diffraction. S: X-ray source. θ_I, θ_D: incident and diffracted beams for coplanar diffraction. α_I, α_F, $2\theta_{\text{IP-GID}}$: incident-beam angle, exit angle and diffracted-beam angle, respectively, for in-plane grazing-incidence diffraction.

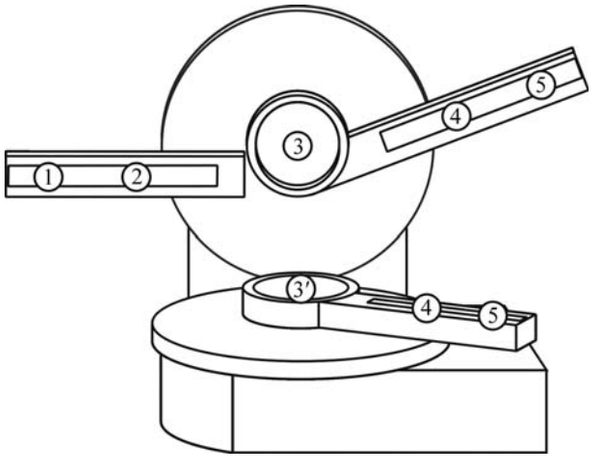

Figure 2.1.12
Sophisticated IP-GID implementation by placing two goniometers vertically with respect to each other, allowing simultaneous coplanar and in-plane measurements using two independent scattered-beam optical X-ray benches (compare with Fig. 2.1.2). The sample stage may be mounted at position 3 or 3′.

(IP-GID) may be measured at angles $2\theta_{\text{IP-GID}}$ in the non-coplanar direction at an exit angle α_F.

There are two principal instrument designs implementing coplanar and in-plane data collection. Firstly, as is obvious from Fig. 2.1.11, a dual-goniometer system may be employed. The most sophisticated implementation has two goniometers placed vertically one above the other, allowing simultaneous coplanar and in-plane measurements using two independent scattered-beam optical X-ray benches as shown in Fig. 2.1.12. Alternatively, the second goniometer may be integrated into the scattered-beam optical X-ray bench, allowing sequential coplanar and in-plane measurements. As a further alternative, a single goniometer may be used, with a Eulerian cradle mounted at the detector position, allowing the detector to be moved around the specimen to perform in-plane measurements. Secondly, a single goniometer equipped with a Eulerian cradle may be used, where the specimen is simply turned by 90° in ψ. As line focus is usually employed for IP-GID measurements, the X-ray source is also turned by 90° to increase the flux.

For all systems, the diffracted-beam optical X-ray benches may be equipped as for multiple beam-path systems, as described in Section 2.1.5.3.1, providing extremely high flexibility. The choice of the most appropriate design depends on issues such as specimen size and weight, the weight of any components in the diffracted-beam path, related spheres of confusion, and the potential need to measure the specimen in a horizontal position.

2.1.6. X-ray sources and optics

This section covers both the generation as well as the conditioning of X-ray beams. All types of X-ray sources, whether laboratory or synchrotron sources, emit a wide range of wavelengths with a characteristic beam divergence and with an intensity related to the power load applied. The function of the incident- and diffracted-beam X-ray optics is to condition the emitted beam in terms of desired wavelength spread, divergence, cross-section size, and shape, and to conserve as much intensity as possible. To achieve maximum performance in terms of intensity and angular resolution, it is essential to design the X-ray optics so that their properties match the characteristics of the X-ray source. Important parameters are the X-ray source beam size and shape, as well as the acceptance angle of the optics given by their design and the distance to the X-ray source.

The optimum choice of an X-ray source and the X-ray optics always depends on the properties of the specimen and the requirements of the applications. Applications requiring high spatial resolution (*e.g.* small single crystals or microdiffraction) or low-angle scattering (*e.g.* thin-film analysis or SAXS) usually require parallel and narrow beams, while diffraction by ideal powders usually works best with larger and slightly divergent beams. As X-ray sources are hardly ever used without X-ray optics, all the components should be seen as one unit determining the beam characteristics at the specimen and eventually at the detector position.

2.1.6.1. *X-ray beam quality measures*

An X-ray beam is characterized by its intensity, wavelength spread, divergence, cross-section size, homogeneity and shape. Simple means for quantifying the quality of an X-ray beam are often useful, and can be used to design an optimal measurement setup by appropriate choice of a combination of X-ray source and X-ray optics. The quantities that are typically used are flux, flux density, brightness and brilliance, all within a 0.1% bandwidth represented by a wavelength range, $\Delta\lambda$, centred around a specific wavelength λ, *i.e.* $\Delta\lambda$ is equal to 1/1000 of λ. While flux, flux density, brightness and brilliance are inter-related, they are distinct and one thus has to consider all of these when comparing X-ray beam characteristics.

Flux represents the integrated intensity of an X-ray beam and is defined as the number of X-ray photons emitted per unit time. The unit for flux is photons per second (p.p.s.).

Flux density is defined as the flux passing through a unit area. The unit is p.p.s. mm^{-2}. Flux density is an appropriate parameter for measuring local counting rates and is synonymous to the term 'intensity' as used in colloquial speech.

Brightness takes the beam divergence into account, and is defined as the flux per unit of solid angle of the radiation cone. The unit is p.p.s. mrad^{-2}. Brightness is an appropriate parameter to use when comparing two X-ray sources with identical focal spot size, as the definition does not contain a unit area.

Brilliance additionally takes the beam dimensions into account and is defined as brightness per mm^2. The unit is p.p.s. mm^{-2} mrad^{-2}. Brilliance is maximized by making the beam size and divergence as small as possible, and the photon flux as large as possible. Two X-ray beams may have the same flux density but different brilliance if the two beams have different beam divergence. Brilliance is thus an appropriate parameter to use when comparing two X-ray sources with different focal spot sizes.

Note that the X-ray source brilliance is an invariant quantity, *i.e.* the brilliance at the specimen position cannot be improved by any optical techniques, but only by increasing the brilliance of the X-ray source. This is a consequence of Liouville's theorem, which states that phase space is conserved. Accordingly, focusing the beam to a smaller size by means of any diffractive or reflective optics will necessarily increase the flux density and the divergence of the X-ray beam, and *vice versa*. Additionally, any diffractive or reflective optics lose flux owing to their reflectivity, which usually is $\leq$90%. Apertures such as slits can help to reduce beam size and divergence, but only at the expense of flux.

Brilliance is more important than flux for experiments with small specimens (*e.g.* single crystals) or small regions of interest (*e.g.* microdiffraction), where it is generally desirable to work

Table 2.1.3
Characteristic wavelengths and absorption edges of metal filters in common use

These data are taken from *International Tables for Crystallography* Vol. C (2004). Metal filters are discussed in Section 2.1.6.3.1.2.

Anode material	$K\alpha_2$	$K\alpha_1$	$K\beta_3$	$K\beta_1$	Metal filter	K absorption edge (Å)
Cr	2.2936510 (30)	2.2897260 (30)	2.0848810 (40)	2.0848810 (40)	V	2.269211 (21)
Co	1.7928350 (10)	1.7889960 (10)	1.6208260 (30)	1.6208260 (30)	Fe	1.7436170 (49)
Cu	1.54442740 (50)	1.54059290 (50)	1.3922340 (60)	1.3922340 (60)	Ni	1.4881401 (36)
Ga†	1.3440260 (40)	1.3401270 (96)	1.208390 (75)	1.207930 (34)		
Mo	0.713607 (12)	0.70931715 (41)	0.632887 (13)	0.632303 (13)	Zr Nb	0.6889591 (31) 0.6531341 (14)
Ag	0.5638131 (26)	0.55942178 (76)	0.4976977 (60)	0.4970817 (60)	Rh Pd	0.5339086 (69) 0.5091212 (42)

† Currently used with dedicated Montel optics only.

with a beam of low divergence and to match the incident beam size to the size of the specimen or the region of interest.

The illumination of larger specimen areas is particularly important for any applications involving polycrystalline specimens, where focusing of the diffracted beam has an advantage over parallel-beam optics in terms of higher beam flux and divergence in that the angular resolution in the diffraction pattern increases. Using an X-ray beam with too small a cross section and/or divergence will result in a smaller or even too small number of diffracting crystallites. This will generally lead to a loss in the diffracted intensity, and may additionally lead to an inhomogeneous intensity distribution in space, leading to random and uncorrectable intensity errors (known as 'particle statistics error', 'spottiness error' or 'granularity error'), and needs to be avoided by all means.

The combination of an appropriate X-ray source with appropriate X-ray optics thus depends on the properties of the specimen and the requirements of the application, and contributes most to the attainable data quality. This is in full agreement with the statement made earlier that there are only a few instrument configurations that will be ideal for any two application areas, or every conceivable sample within a single application area. While changes of most X-ray optics are extremely easy these days, changing between different types of X-ray sources may require significant effort. The choice of the most appropriate X-ray source therefore requires, at the time of instrument acquisition, careful consideration of the types of specimen in relation to the analyses to be conducted.

2.1.6.2. *X-ray sources*

In this section the general concepts of the commonest types of X-ray sources will be described. The physics of X-ray generation and the properties of X-rays have been extensively covered in the literature. More detailed information can be found in, for example, *International Tables for Crystallography* Vol. C (2004) as well as in the textbooks by Pecharsky & Zavalij (2009), Clearfield *et al.* (2008), Jenkins & Snyder (1996), and Klug & Alexander (1974).

2.1.6.2.1. *Generation of X-rays and the X-ray spectrum*

In laboratory X-ray sources, X-rays are produced by a multi-keV electron beam impinging on a metallic target. The X-ray spectrum that is obtained is characterized by a broad band of continuous radiation, accompanied by a number of discrete spectral lines characteristic of the target material. The continuous part of the spectrum ('*Bremsstrahlung*') is generated by the rapid deceleration of the electrons within the target, ranging from lowest energies as a result of gradual deceleration through to a cutoff wavelength whose energy corresponds to the initial kinetic energy of the electron, as a result of instantaneous deceleration. The discrete spectral lines ('characteristic radiation') are the result of electrons knocking out core electrons from the target material. This results in emission of 'fluorescent' X-rays when the perturbed atom relaxes to its ground state by filling up the energy levels of the electrons that have been knocked-out by means of electron transitions from higher electron shells. The energy of the fluorescent radiation is characteristic of the atomic energy levels of the target material. The most commonly used characteristic radiation is that of $K\alpha$, representing the transition of a $2p$ electron (L shell) filling a hole in a $1s$ (K) shell.

The target materials that are commonly in use strongly depend on the application and the type of X-ray source used. The most commonly used target materials range from Cr through to Co, Cu, Mo and Ag. With the recent introduction of liquid-metal targets, see Section 2.1.6.2.2.2(*b*), Ga will find increasing use in applications requiring the smallest spot sizes and highest brilliance. A list of characteristic wavelengths and absorption edges of commonly used metal ($K\beta$) filters is given in Table 2.1.3.

Today's laboratory X-ray sources can be classified as shown in Table 2.1.1, and are described in Section 2.1.6.2.2. For performance considerations see Section 2.1.6.2.3.

2.1.6.2.2. *Types of X-ray sources*

The performance of X-ray sources is usually characterized *via* brilliance as a measure for the quality of the emitted X-rays. The brilliance of an X-ray source is determined by several factors such as electron power density and the take-off angle.

The electron power density is the most important factor. Only a small fraction of <1% of the applied electron energy is converted into X-rays, so most of the incident energy is dissipated within the target as heat. The maximum power density and thus brightness of the X-ray source is limited by the melting or evaporation temperature of solid or liquid metal targets, respectively, and the efficiency with which the heat is removed from the area on which the electrons impact.

The take-off angle describes the angle under which the focal spot is viewed, and typically ranges from 3° to 7°, but may be up to 45°, depending on the type of X-ray source. The actual take-off angle that is chosen represents a compromise. On the one hand, it should be as small as possible to minimize the effectively seen

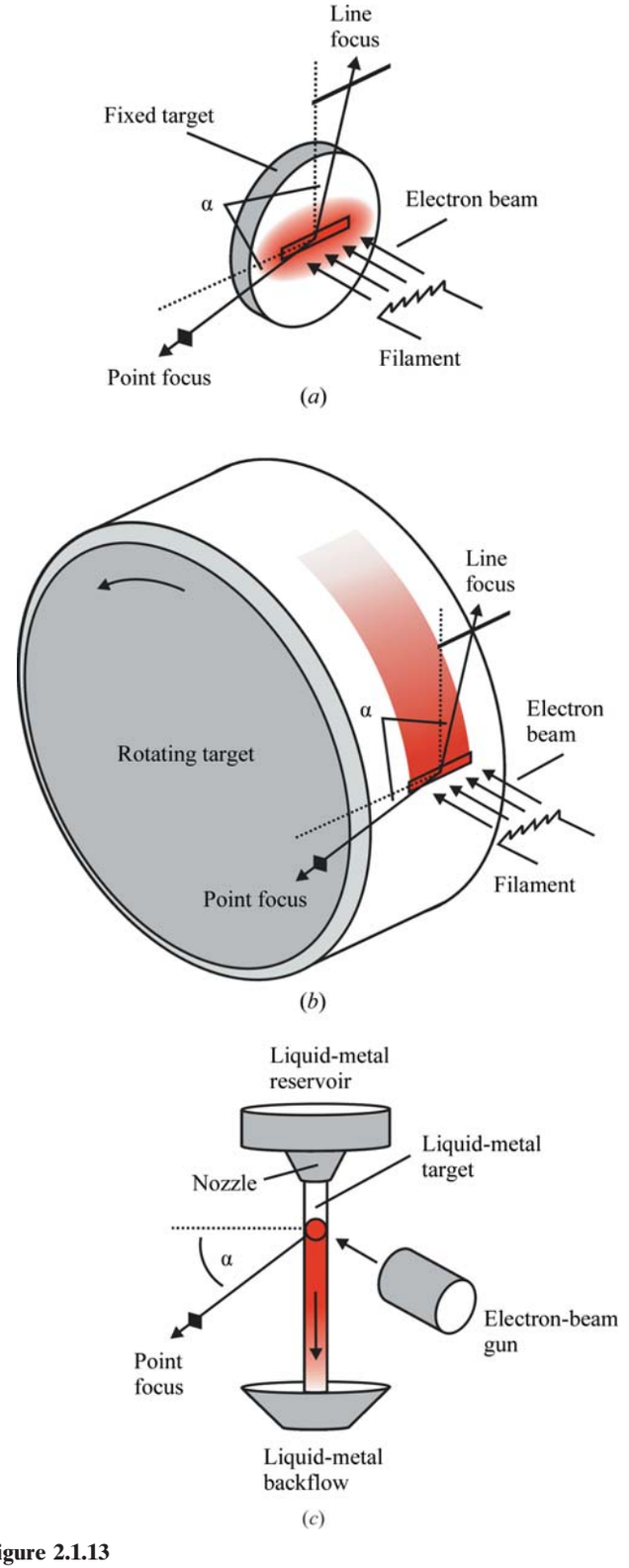

Figure 2.1.13
Illustration of the working principle of laboratory X-ray sources: (*a*) fixed target, (*b*) rotating target, (*c*) liquid-metal jet. α: take-off angle. For fixed targets (*a*) the heat mainly flows towards the cooled back end of the target. For moving targets (*b*, *c*) cold parts of the target are moved into the electron beam continously, providing an extremely large effective cooling efficiency.

width of the focal spot to increase resolution. On the other hand, it cannot be made arbitrarily small to avoid self-absorption by the metal target due to the finite depth in which the X-ray radiation is produced. The higher the tube voltage the larger the take-off angle should be to avoid intensity losses by self-absorption.

In the history of laboratory X-ray source development, most effort has probably been concentrated on techniques for removing the heat from the metal target as efficiently as possible, as illustrated in Fig. 2.1.13, leading to two different categories of X-ray sources for laboratory use: fixed- and moving-target X-ray sources.

2.1.6.2.2.1. Fixed-target X-ray sources

Fixed-target X-ray sources are used in more than 90% of all X-ray diffractometer installations (Fig. 2.1.13*a*). Electrons are generated by heating a filament (cathode) and accelerated towards the metal target (anode) by means of a high potential, typically of the order of 30–60 kV.

In conventional X-ray sources the electrons are focused by an electrostatic lens onto the anode to form the focal spot. Typical power ratings range from several hundred watts up to about 3 kW. The anode is water-cooled from the back. Focal spots are of rectangular shape, and can be viewed at the two long and the two short faces, giving two line and two point foci, respectively. This allows up to four instruments to be operated with a single X-ray source. However, the vast majority of all today's X-ray diffractometers are equipped with an individual X-ray source (and sometimes two, see Section 2.1.5.3.1). This significantly eases alignment as there is no need to align the instrument with respect to the X-ray source, and allows instrument configurations with moving X-ray sources. Modern X-ray-source stage designs allow switching between point and line focus by rotating the X-ray source 90° without alignment and even without the need to disconnect the powder cables and water supply.

Conventional X-ray sources have long and wide electron beams so that a large area of the target is heated (Fig. 2.1.13*a*). The heat generated in the middle of this area can mainly flow in just one direction: towards the water-cooled back of the anode. Heat flow parallel to the surface is minimal, thus limiting the cooling efficiency. It is for this reason that conventional X-ray sources achieve the lowest brilliance of any laboratory X-ray source. Conventional X-ray sources are usually coupled with relatively simple optics and are cheap compared to moving-target systems. In addition they are maintenance-free, apart from periodic changes of the X-ray source owing to ageing.

'Micro-focus' X-ray sources represent another category of X-ray source and are characterized by very small focal spot sizes ranging from a few μm up to about 50 μm. In this type of X-ray source, the improved focusing of the electron beam is achieved by very fine electrostatic or magnetic lenses. Power requirements are significantly less than conventional X-ray sources, ranging from a few watts up to some hundred watts, depending on focal spot size; water cooling is frequently not required. Again, there is no maintenance required beyond periodic tube changes.

As the focal spot area is very small, heat can also flow sideways, improving the thermal cooling efficiency and thus allowing this type of X-ray-source tube to achieve significantly higher brilliance than conventional X-ray sources. To benefit from this increased performance, relatively large optics of the reflective type (see Section 2.1.6.3.3) are required, making micro-focus X-ray source systems significantly more expensive than conventional systems.

The lifetime of a fixed-target X-ray source depends on many factors, of which operation of the source within specifications (such as specific loading and cooling) is particularly important. The 'useful' lifetime may be significantly shorter, even though the X-ray source still operates. Deposition of tungsten from the

filament on the anode and on the inner beryllium window surfaces leads to spectral contamination and substantial loss of intensity with time. Increasing deterioration of the filament may change its position relative to the electrostatic lens used for focusing and result in beam inhomogeneity and additional intensity losses. Further intensity losses and beam inhomogeneity may arise from pitting of the anode surface as a result of the intense electron flux on the anode surface.

2.1.6.2.2.2. *Moving-target X-ray sources*

(*a*) *Rotating-target X-ray sources*. Rotating-target X-ray sources are able to remove heat more efficiently than fixed-target sources, and can thereby sustain higher fluxes of X-ray photons (Fig. 2.1.13*b*). This is achieved by rotating a cooled anode, with a typical diameter ranging from about 10 to 30 cm, at about 6000–12 000 revolutions per minute. The maximum power loads depend on the focal spot size, and can range up to 18 kW for conventional rotating-target X-ray sources, and 3 kW for micro-focus rotating-target X-ray sources. Rotating-target X-ray sources are thus inherently more brilliant, and gain up to an order of magnitude in brilliance compared to their respective fixed-target counterparts.

Rotating-target systems do require routine maintenance such as periodic anode refurbishment and changes of the filament, bearings and seals. The maintenance requirements of micro-focus systems are significantly lower than those of conventional rotating-target systems because of the lower total power loading.

(*b*) *Liquid-metal-jet X-ray sources*. A very recent development is that of liquid-metal-jet micro-focus X-ray sources (Fig. 2.1.13*c*), where a jet of liquid metal acts as the electron-beam target (Hemberg *et al.*, 2003). A thin (<100–225 μm) high-speed (>50 m s^{-1}) liquid-metal jet is injected into vacuum by applying a backing pressure of about 200 bar and is targeted by a focused electron beam with a beam power of up to 200 W and a focal spot size of down to 6 μm. The focal spot is viewed at a take-off angle of about 45° to obtain a symmetric beam usually coupled into Montel optics. (Montel optics are described in Section 2.1.6.3.3.1.)

Ideal materials for use in liquid-jet anodes are electrically conductive to avoid charging and have low vapour pressure to simplify vacuum operation. Among a few materials currently being evaluated, Galinstan (a eutectic mixture of 68.5% Ga, 21.5% In and 10% Sn by weight) is particularly suited for laboratory X-ray analyses, as it is liquid at room temperature (melting point 254 K), with the most intense Ga $K\alpha$ line at 9.25 keV, and less intense In $K\alpha$ and Sn $K\alpha$ lines at 24 and 25.3 keV, respectively.

The obvious advantage of a metal-jet anode is that the maximum electron-beam power density can be significantly increased compared to solid-metal anodes and thus the brilliance can be increased by up to an order of magnitude.

2.1.6.2.3. *Performance of X-ray sources*

The single most important property of an X-ray source is its brilliance, which is proportional to the maximum target loading per unit area of the focal spot, also referred to as the specific loading.

In Table 2.1.4 the maximum target loading and specific loading (relative brilliance) for some typical sealed tubes and some rotating-anode sources with a Cu target are compared. Also listed are data for the liquid-metal jet with Ga as a target. Micro-focus fixed-target X-ray sources have up to two orders of magnitude higher specific loadings compared to conventional fixed target tubes, and even 2 to 5 times higher specific loadings compared to conventional rotating-anode systems. In contrast to fixed-target micro-focus X-ray sources, where the specific loading can only be increased by reducing the source size, moving-target X-ray sources are also made brighter by increasing the speed of the target relative to the electron beam. Moving-target X-ray sources are thus inherently brighter than stationary targets. The liquid-gallium jet has a higher (by a further order of magnitude) specific loading than the most brilliant rotating-anode systems, and now rivals the intensity of second-generation synchrotron beamlines.

Table 2.1.4
Maximum target loading and specific loading for some selected fixed- and moving-target X-ray sources

X-ray source	Focal spot (mm^2)	Maximum load (kW)	Specific loading (kW mm^{-2})
Fixed target			
Broad focus (Cu)	2 × 10	3	0.15
Normal focus (Cu)	1 × 10	2.5	0.25
Long fine focus (Cu)	0.4 × 12	2.2	0.5
Micro-focus (Cu)	0.01–0.05	<0.05	5–50
Moving target			
Rotating anode (Cu)	0.5 × 10 0.3 × 3 0.2 × 2 0.1 × 1	18 5.4 3 1.2	3.6 6 7.5 12
Micro-focus rotating anode (Cu)	0.1	2.7	27
Liquid-metal jet (Ga)	0.02 × 0.02	0.2	>500

2.1.6.3. *X-ray optics*

The purpose of X-ray optical elements is to condition the beam emitted by an X-ray source in terms of desired wavelength spread, divergence, cross-section size and shape, and to conserve as much intensity as possible. X-ray optics currently employed in laboratory X-ray diffractometers may be classified as absorptive, diffractive and reflective, as shown in Table 2.1.1.

Absorptive and diffractive X-ray optics represent selective beam-conditioning techniques, where parts of the beam are eliminated to achieve a particular wavelength distribution and divergence. In contrast to this, reflective optics modify the beam divergence to direct the full beam to the specimen or to the detector. The extremely large number of X-ray optical elements available allows for an enormous range of incident and diffracted beam-path configurations. Choosing the most appropriate X-ray optics and X-ray optics combination for a particular experiment is a challenge for the user. The general rule to be obeyed in order to obtain the best data quality is that the beam dimension, wavelength distribution and divergence should compare to the specimen dimension and angular spread of the structural features to be resolved.

In this section the most common features of X-ray optics in current use will be discussed. A comprehensive survey cannot be given, since there exists an incredible multitude of variants of the basic X-ray optic types listed in Table 2.1.1. X-ray optics have been extensively covered in the literature, for example in *International Tables for Crystallography* Vol. C (2004) and in the textbooks by He (2009), Pecharsky & Zavalij (2009), Paganin

(2006), Fewster (2003), Bowen & Tanner (1998), Jenkins & Snyder (1996), Klug & Alexander (1974), and Peiser *et al.* (1955). An extensive discussion of the principles of combining X-ray optics to optimally suit a wide range of different powder diffraction as well as thin-film applications has been given in the textbook by Fewster (2003).

2.1.6.3.1. *Absorptive X-ray optics*

2.1.6.3.1.1. Apertures

The simplest way of beam conditioning is to place apertures such as slits (line focus) or pinholes (point focus) into the incident and/or diffracted beam to control beam divergence and shape, and to reduce unwanted scattering from air or any beam-path components. Apertures are 'shadow-casting' optics and thus cannot increase flux density. Reducing beam divergence and beam dimensions by means of apertures invariably results in a loss of intensity that is inversely proportional to the slit aperture.

The principles are shown in Fig. 2.1.14. The divergence of a beam is established by the dimensions of the focal spot as well as the aperture and the distance of the aperture from the source (Fig. 2.1.14*a*). The divergence in the diffraction plane is usually called 'equatorial divergence' and the divergence in the axial direction 'axial divergence'. Apertures can be of the plug-in type requiring manual changes of the aperture to obtain different divergence angles, or – usually only for equatorial divergence slits – motorized. Motorized slits are mostly used in the Bragg–Brentano geometry to limit equatorial divergence, which can be arbitrarily chosen and either be kept constant to keep the diffracting specimen volume constant (as is invariably the case with plug-in slits), or varied as a function of 2θ to keep the illuminated specimen length constant. Typical aperture angles range from 0.1–1°.

To provide additional collimation, a second aperture may be placed at some distance away from the first (Fig. 2.1.14*b*). When using the same aperture, an almost-parallel beam may be obtained from a divergent beam at the cost of high intensity losses. A third aperture is often used to reduce scattering by the second slit. In laboratory X-ray diffractometers dedicated for SAXS analysis such collimation systems may reach lengths of more than 1 m.

Another way to parallelize radiation is to use a parallel-plate collimator (PPC), which is manufactured from sets of parallel, equally spaced thin metal plates, as shown in Fig. 2.1.14(*c*). Each pair of neighbouring plates works like a double-aperture arrangement as shown in Fig. 2.1.14(*b*). In contrast to simple slits and pinholes, PPCs do not change the shape of the beam. PPCs arranged parallel to the diffraction plane are usually called 'Soller slits' and are used to control axial divergence. Such devices can be used for focusing as well as parallel-beam geometries with typical aperture angles ranging from 1–5°. Soller slits are usually mounted on both the incident- and diffracted-beam sides of the specimen. PPCs arranged parallel to the diffraction plane are specifically used in parallel-beam geometries to minimize equatorial beam divergence, with typical aperture angles ranging from 0.1–0.5°.

The ways in which the diffracted beam can be conditioned are limited when employing one- or two-dimensional detectors. A particular issue related to these types of detectors is unwanted scattering from air or any beam-path components. Ideally, a closed, evacuated or He-flushed beam path will be used, but this is often not feasible owing to collision issues. For smaller detectors it is possible to place the anti-scatter aperture closer to the specimen surface. Alternatively, a knife edge may be placed on top of the specimen. As knife edges may interfere with divergent beams at higher 2θ angles, it is necessary to move them away from the specimen at higher 2θ angles. Another possibility, limited to one-dimensional detectors, is to use radial Soller slits as shown in Fig. 2.1.14(*d*).

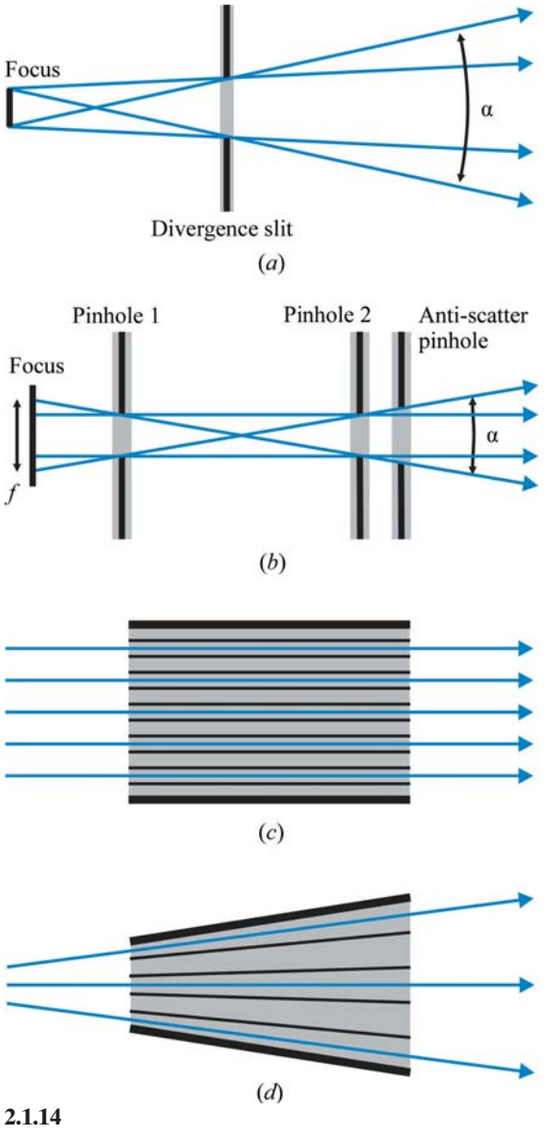

Figure 2.1.14
Apertures used for beam collimation. α: divergence angle, f: virtual focus. (*a*) Single slit or pinhole, (*b*) parallelization through double slits or pinholes, (*c*) parallelization through a parallel-plate collimator, (*d*) a radial plate collimator.

2.1.6.3.1.2. Metal filters

Metal filters are the most frequently used devices for monochromatization of X-rays in laboratory diffractometers. Metal filters represent single-band bandpass devices where monochromatization is based on the K absorption edge of the filter material to selectively allow transmission of the $K\alpha$ characteristic lines while filtering white radiation, $K\beta$ radiation (hence they are frequently known as '$K\beta$ filters'), and other characteristic lines.

A properly selected metal filter has its K absorption edge right between the energies of the $K\alpha$ and $K\beta$ characteristic lines of the source. As a rule of thumb, this is achieved by choosing an element just one atomic number less than the X-ray source target material in the periodic table. For heavy target materials such as

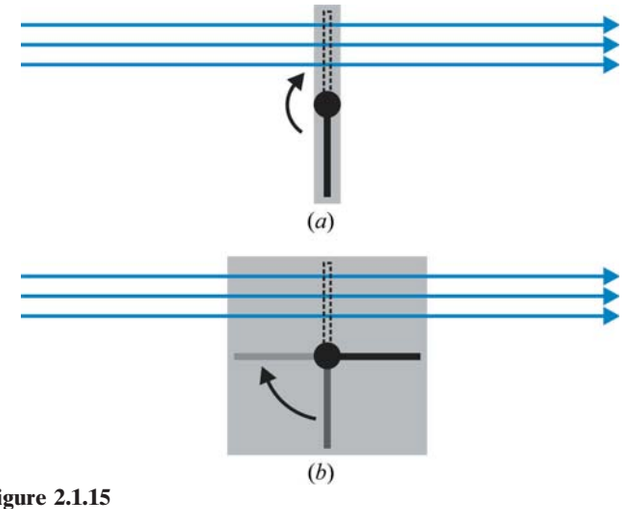

Figure 2.1.15
Motorized switchable (*a*) and rotating (*b*) absorbers.

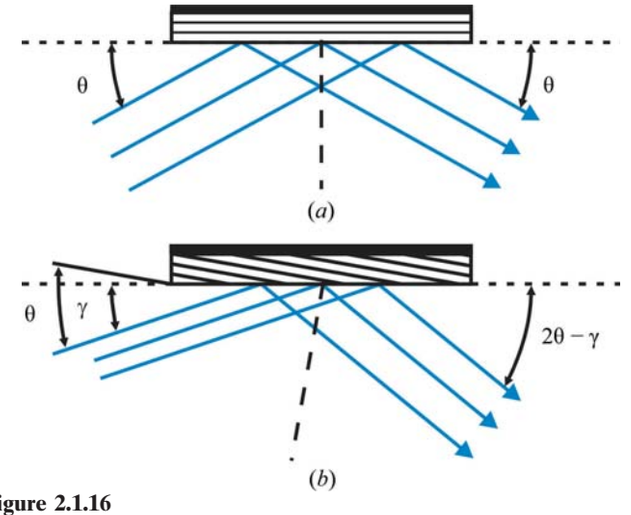

Figure 2.1.16
Illustration of flat single-reflection monochromators. (*a*) Symmetrically cut crystal, (*b*) asymmetrically cut crystal with an angle γ between the reflecting lattice planes and the crystal surface.

Mo or Ag, this rule can be extended to two atomic numbers. A list of metal filters suitable for the most commonly used target materials is given in Table 2.1.3.

A major disadvantage of metal filters is that they cannot completely eliminate $K\beta$ radiation at bearable intensity losses. In addition, they introduce absorption edges at the high-energy (low-angle) side of diffraction peaks, the magnitudes of these being dependent on the wavelength as well as on the filter material and its thickness. While for point detectors absorption edges are usually obscured by counting statistics, they are much more readily visible to position-sensitive detectors owing to the high number of counts that are typically collected.

Positioning of the metal filter does not make a difference in terms of filtering of $K\beta$ or white radiation, but can in the case of specimen fluorescence. Placing the metal filter in the diffracted beam can filter some fluorescence radiation, unless the specimen contains the same element as the metal filter. Taking Cu radiation as an example, most fluorescence radiation excited by Ni in the specimen will pass through a diffracted-beam Ni filter. In this instance, the $K\beta$ filter should be mounted in the incident beam to suppress Cu $K\beta$ radiation, which is very efficient at exciting Ni fluorescence. Balanced-filter techniques, employing two (or more) filters that have absorption edges just above and below $K\alpha$, are no longer in use as the resulting bandpass is still much wider than that of crystal monochromators at even higher intensity losses.

Metal filters are generally supplemented by some energy discrimination by the detector to remove the high-energy white radiation from the X-ray source. The effectiveness of this white-radiation removal depends upon the energy resolution of the detector, and is discussed in Section 2.1.7 for the different detector technologies currently in use. Recent improvements in the energy-discrimination capabilities for silicon strip detectors now even allow filtering of $K\beta$ radiation, completely eliminating the need for metal filters (see Section 2.1.7.2.3.2). As a consequence, the use of metal filters is likely to decline.

Another type of metal filter is represented by absorbers, *e.g.* Cu foils, which are used at high intensities to avoid detector saturation or even damage. Absorbers can be motorized and switched in and out automatically depending on the actual count rates that are detected (Fig. 2.1.15*a*). Several absorbers with different thickness may be combined in the form of motorized rotating absorbers (Fig. 2.1.15*b*).

2.1.6.3.2. *Diffractive X-ray optics*

Single crystals or highly textured polycrystals (mosaic crystals) represent effective beam conditioners by allowing the spectral bandwidth as well as the X-ray beam divergence to be modified. When they are placed at a specific angle with respect to the incident and diffracted beams, according to Bragg's law, only a small spectral bandwidth will be transmitted depending on the divergence of the incident beam and the rocking angle (mosaic spread) of the crystal. Higher harmonics ($\lambda/2$, $\lambda/3, \ldots$) are diffracted as well, but can be successfully suppressed by using materials with small higher-order structure factors and *via* energy discrimination by the detector. Depending on the application, a crystal monochromator can be either used as a spectral filter ('monochromator'), typically used in the incident beam, or as an angular filter ('analyser'), typically used in the diffracted beam to restrict the angular acceptance of the detector.

It is likely that all monochromators currently employed in laboratory X-ray diffractometers are of the reflective type ('Bragg geometry'). Transmission-type monochromators ('Laue geometry') play no role in laboratory powder diffraction. Two designs are in common use and are described below: (*a*) single-reflection monochromators and (*b*) multiple-reflection monochromators.

2.1.6.3.2.1. Single-reflection monochromators

The most common types of single-reflection monochromators are illustrated in Figs. 2.1.16 and 2.1.17. Flat crystals (Fig. 2.1.16) are used in parallel-beam geometry and curved crystals in focusing geometries (Fig. 2.1.17). A beam reflected from a flat crystal with the reflecting lattice planes parallel to its surface (symmetric cut) is nearly parallel (Fig. 2.1.16*a*). If the crystal is cut at an angle to the reflecting lattice planes (asymmetric cut), then the beam will be expanded (Fig. 2.1.16*b*), or compressed if reversed (Fankuchen, 1937). Monochromators can be curved (Johann, 1931) or curved and ground (Johannson, 1933), and may be cut symmetrically (Fig. 2.1.17*a*) or asymmetrically (Fig. 2.1.17*b*). The latter has the particular advantage of providing different focal lengths for the incident and diffracted beam. A shortened incident beam allows the monochromator to be mounted closer to the X-ray source to capture a larger solid angle of the emitted beam. If the diffracted-beam focusing length is

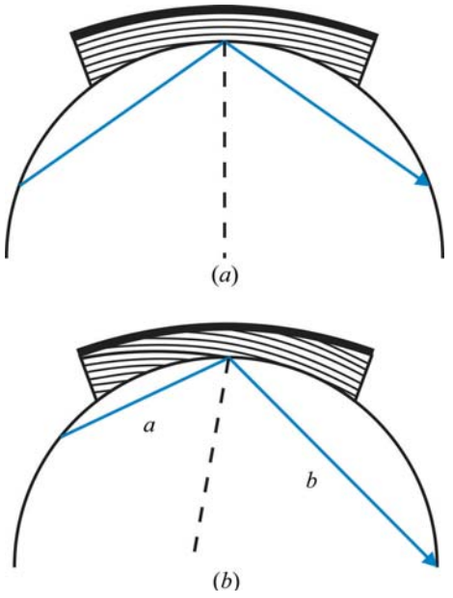

Figure 2.1.17
Illustration of curved and ground single-reflection monochromators. Only the central beam is shown for clarity. (*a*) Symmetrically cut crystal, (*b*) asymmetrically cut crystal with two different focal lengths *a* and *b*.

sufficiently large, then the instrument geometry can be converted between the Bragg–Brentano and the focusing Debye–Scherrer geometries by shifting the monochromator crystal and the X-ray source along the incident-beam X-ray optical bench (see Section 2.1.4.1 and Fig. 2.1.3).

The most commonly used monochromator crystal materials are germanium and quartz, which have very small mosaic spreads and are able to separate the $K\alpha_1/K\alpha_2$ doublet. In contrast to germanium and quartz crystals, graphite and lithium fluoride have large mosaic spreads and thus high reflectivity, but cannot suppress $K\alpha_2$. In principle, any of these monochromators can be mounted in the incident as well as the diffracted beam; the choice mostly depends on the purpose of the monochromator. Germanium and quartz monochromators are typically used as incident-beam monochromators to produce pure $K\alpha_1$ radiation. Graphite (focusing geometries) and lithium fluoride (parallel-beam geometry) are often used as diffracted-beam monochromators to suppress fluorescence radiation. Germanium and quartz can also be used as diffracted-beam monochromators, but are usually not because of their lower reflectivity. Where mounting of diffracted-beam monochromators is difficult or impossible, which is specifically true for one- and two-dimensional detector applications, curved graphite monochromators are frequently used as incident-beam monochromators.

The use of diffracted-beam monochromators – at least in powder X-ray diffraction – is declining steeply because of the geometric incompatibility issues with one- and two-dimensional detector systems (which, since 2010, have been sold with more than 90% of all diffractometers; see Section 2.1.3.2). With the recent improvements of energy-discrimination capabilities for silicon micro-strip detectors, the need for diffracted-beam monochromators will further diminish (see Section 2.1.7.2.3).

2.1.6.3.2.2. Multiple-reflection monochromators

Multiple-reflection monochromators can reduce the wavelength dispersion $\Delta\lambda/\lambda$ significantly more than single-reflection monochromators. Multiple-reflection monochromators are often made of monolithically grooved single crystals and are also known as channel-cut monochromators (Bonse & Hart, 1965). In Fig. 2.1.18 an overview is given of the most common channel-cut monochromator types; for a detailed discussion see *e.g.* Hart (1971) and Bowen & Tanner (1998). Successive reflection of the X-ray beam at the channel walls by the same lattice planes causes a strong reduction of the X-ray intensity contained in the tails of the beam. Depending on the number of reflections, multiple-reflection monochromators are denoted as two-bounce, three-bounce *etc*. channel-cut monochromators. The Bartels monochromator (Bartels, 1983) comprises two two-bounce channel-cut crystals. For Cu radiation, such a monochromator results in a wavelength spread which is less than the natural line width of the Cu $K\alpha_1$ line. The most commonly used crystal material is germanium, which delivers higher intensity than silicon, using the 400, 220, or 440 reflections. Crystals may be cut symmetrically or asymmetrically. In Table 2.1.5 several types of

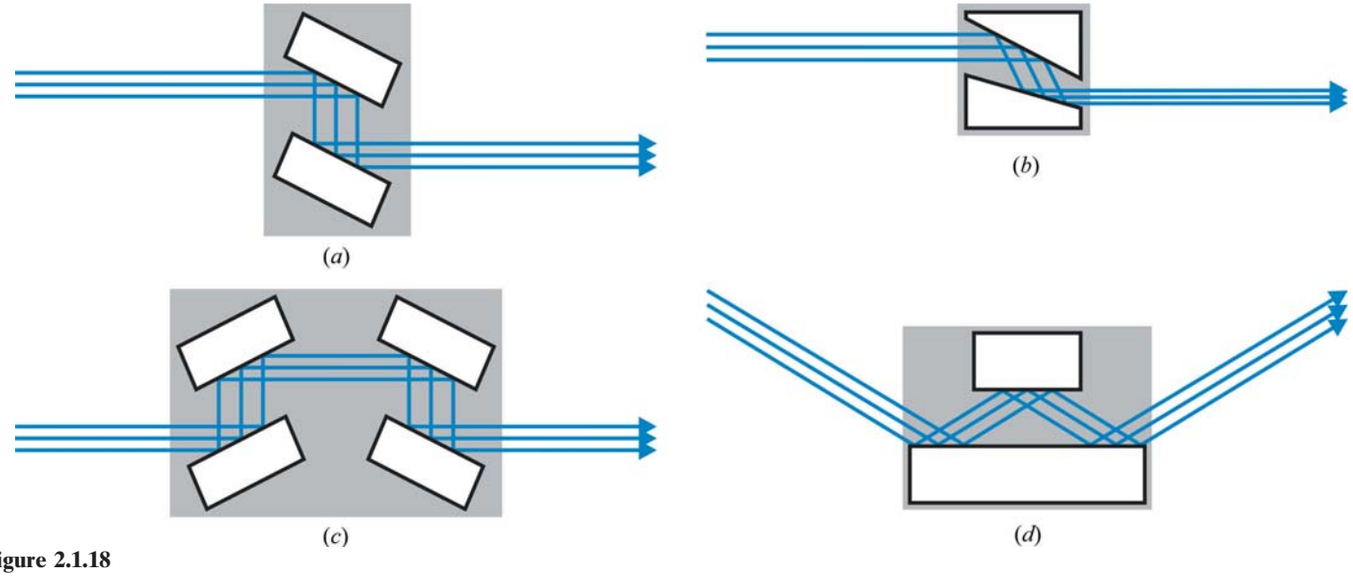

Figure 2.1.18
Illustration of multiple-reflection monochromators. (*a*) Symmetrically cut two-bounce channel-cut monochromator, (*b*) asymmetrically cut two-bounce channel-cut monochromator for beam compression, or, if reversed, for beam expansion, (*c*) symmetrically or asymmetrically cut four-bounce channel-cut monochromator, (*d*) symmetrically cut three-bounce channel-cut monochromator.

Table 2.1.5
Comparison of divergence and intensity for several types of germanium channel-cut monochromators

In each case, the monochromator is coupled with a graded multilayer providing 3×10^9 counts per second at <0.028° beam divergence. The values in parentheses denote the percentage of intensity diffracted by the respective monochromator crystals.

Type	(*hkl*)	Divergence (°)	Intensity
Two-bounce	220, symmetric	<0.0052	5.0×10^7 (∼1.5%)
Two-bounce	220, asymmetric	<0.0085	3.3×10^8 (∼10%)
Two-bounce	400, asymmetric	<0.0045	4.8×10^7 (∼1.5%)
Four-bounce	220, symmetric	<0.0035	6.5×10^6 (∼0.2%)
Four-bounce	220, asymmetric	<0.0080	2.7×10^7 (∼1%)
Four-bounce	440, symmetric	<0.0015	2.2×10^5 (∼0.075%)

germanium channel-cut monochromators are compared in terms of divergence and intensity.

Switching between different channel-cut monochromators is extremely easy these days and can be accomplished without the need for any tools and without realignment. This is also true for cases where a beam offset is introduced, *e.g.* by switching between two- and four-bounce channel-cut monochromators. In sophisticated instruments such an offset can be compensated fully automatically by a software-controlled motor.

The combination of different types of channel-cut monochromators in both the incident and diffracted beam allows the construction of advanced diffractometer configurations with extremely high resolution capabilities. It should be emphasized that laboratory X-ray diffractometers can have identical optical configurations to diffractometers operated at synchrotron beamlines. The important and obvious difference, however, is the extremely low flux coming from laboratory X-ray sources, which is further diminished by each reflection in a channel-cut monochromator (Table 2.1.5). While such configurations work perfectly for strongly scattering single-crystal layers in thin films, for example, analysis of ideal powders is normally not possible.

2.1.6.3.3. *Reflective X-ray optics*

2.1.6.3.3.1. Multilayer mirrors

Multilayer mirrors used in laboratory X-ray diffractometers are efficient beam conditioners, using total reflection as well as Bragg reflection on inner interfaces of a multilayer structure to modify beam divergence, cross-section size, shape and – to some extent – spectral bandwidth. A comprehensive description of current mirror designs and important mirror properties is found in the VDI/VDE Guideline 5575 Part 4 (2011).

Multilayer mirrors consist of a multilayer coating deposited on a flat or curved substrate. The *imaging* characteristics are mostly determined by the contour of the mirror surface as defined by the substrate surface. The most common contours include planes, ellipsoids, paraboloids, elliptic cylinders or parabolic cylinders. The *spectral reflection* properties are determined by the coating, which may consist of some 10 up to 1000 alternating layers of amorphous low-density ('spacer') and high-density ('reflector') materials, with a period of a few nanometres. The first curved mirrors were produced by depositing the multilayers on a flat substrate that was subsequently bent to the desired contour, yielding typical r.m.s. slope errors of about 15 arcsec. By using prefigured substrates with r.m.s. slope errors below 1.7 arcsec, significantly improved reflectivity and lower beam divergence are obtained. Laterally graded multilayer mirrors (so-called 'Göbel mirrors') have a layer thickness gradient parallel to the surface

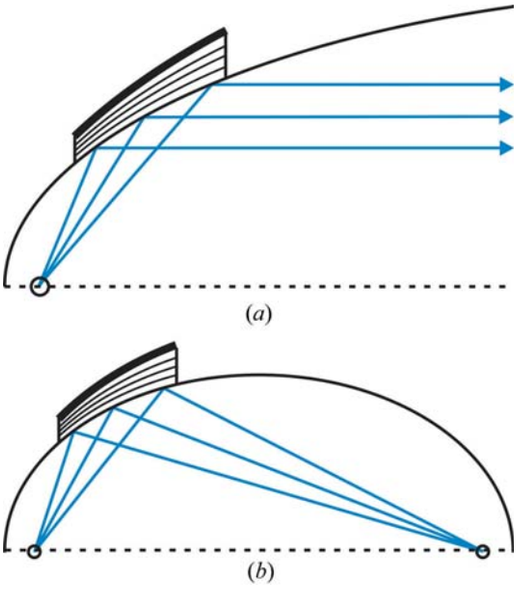

Figure 2.1.19
Schematic of graded multilayer mirrors. (*a*) Parabolic mirror for parallelization of a divergent beam, or, if reversed, focusing of a parallel beam. In the latter case the mirror will also filter some specimen fluorescence. (*b*) Elliptical mirror for focusing of a divergent beam.

(Schuster & Göbel, 1996), which, when combined with a planar, parabolic or elliptic substrate contour, produce a divergent, parallel or focusing beam. Fig. 2.1.19 illustrates graded multilayer mirrors for parallelization and focusing in the plane of diffraction.

For beam conditioning in two perpendicular directions, two perpendicularly oriented curved mirrors may be used, as illustrated in Fig. 2.1.20. In the Kirkpatrick–Baez scheme (Kirkpatrick & Baez, 1948), two mirrors are cross-coupled as shown in Fig. 2.1.20(*a*). This setup has some issues related to the inherently different capture angles and magnification of both mirrors, resulting in less flux from smaller sources and in different divergences in both directions for elliptical mirrors. The Montel optics (Montel, 1957) shown in Fig. 2.1.20(*b*) overcome these issues by arranging both mirrors in a 'side-by-side' configuration.

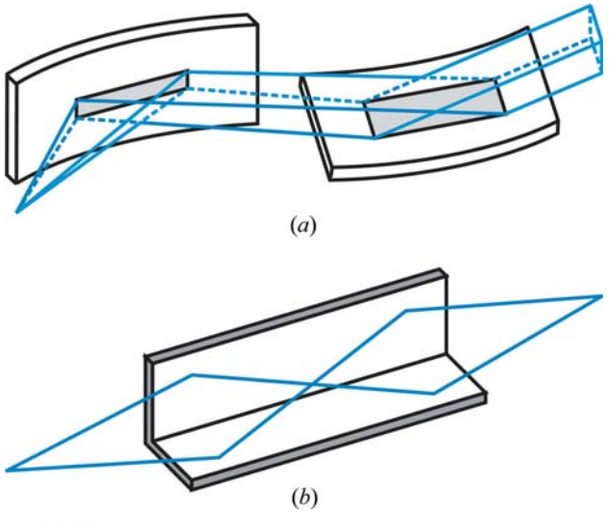

Figure 2.1.20
Examples for orthogonally positioned curved mirrors for beam conditioning. (*a*) Kirkpatrick–Baez scheme employing two parabolic mirrors to create a parallel beam, (*b*) Montel optics employing two elliptical mirrors side-by-side to create a focusing beam.

Mirrors are available for all characteristic wavelengths used in laboratory X-ray powder diffractometers. A wealth of different materials are being used as double layers (reflector/spacer), including but not limited to W/Si, W/B_4C, Ni/C, Ru/B_4C, Ti/B_4C, V/B_4C, Cr/B_4C and Mo/B_4C. The double-layer materials may be selected according to the energies of their absorption edges to make the mirror act as a filter as well. While none of these mirrors is strictly speaking a monochromator, appropriate selection of the double-layer materials, depending on the wavelength used, will allow monochromatization of the radiation to $K\alpha$ while $K\beta$ and *Bremsstrahlung* are suppressed.

Within the past two decades mirror systems have become invaluable for all applications requiring a small and/or highly parallel beam. In particular, coupling of a parallel-beam mirror with multiple-reflection channel-cut monochromators allows the use of a wider solid-angle range of the X-ray source and a gain of nearly two orders of magnitude in intensity (Schuster & Göbel, 1995). For applications requiring ideal powders, however, too-small as well as too-parallel beams may result in too small a number of diffracting crystallites, which will generally reduce the diffracted intensity, and may additionally lead to particle statistics errors (see also Section 2.1.6.1).

Today, advanced sputtering techniques allow the fabrication of a wealth of different multilayer optics with virtually arbitrary beam divergences to generate focusing, parallel and divergent beams, for both point- and line-focus applications. The most comprehensive overview of currently available mirrors and up-to-date specifications will be found in manufacturers' brochures.

2.1.6.3.3.2. Capillaries

X-ray capillary optics are finding increasing use in applications where a small focused beam with high intensity is required. Their design, important properties and applications are discussed by *e.g.* Bilderback (2003), He (2009), and the VDI/VDE Guideline 5575 Part 3 (2011).

X-ray capillary optics employ total external reflection by the inner surface of hollow glass tubes to guide and shape X-ray radiation. For incidence angles lower than the critical angle of total reflection the X-ray radiation is guided through the optics at very low losses. The transmission efficiency depends upon the X-ray energy, the capillary materials, reflection surface smoothness, the number of reflections, the capillary inner diameter and the incident beam divergence, and is thus determined by the particular design of the given optics. Generally, the transmission efficiency decreases with increasing X-ray energy owing to the decreasing critical angle of total reflection. The role of X-ray capillary optics as energy filters is insignificant, therefore capillaries are usually used in combination with monochromatization

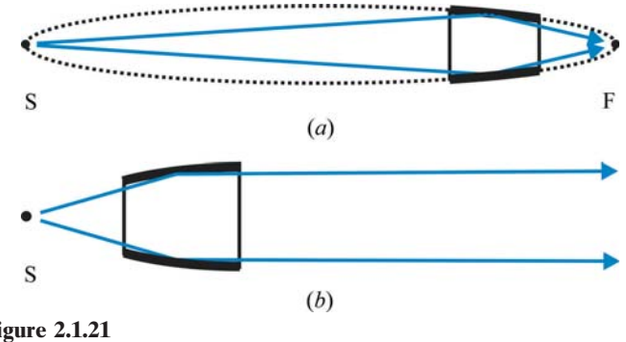

Figure 2.1.21
Schematic of monocapillary optics. (*a*) Elliptical and (*b*) parabolic monocapillary. S = source; F = focal point.

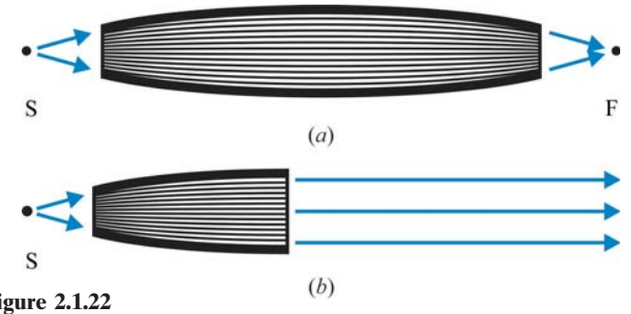

Figure 2.1.22
Schematic of polycapillary optics. (*a*) Focusing and (*b*) parallel-beam polycapillary. S = source; F = focal point.

devices such as metal filters, incident-beam graphite monochromators or graded multilayers. Gains in flux density of more than two orders of magnitude compared to pinhole systems have been reported. The most common X-ray capillary optics currently used in laboratory X-ray powder diffractometers can be categorized as either monocapillaries or polycapillaries.

Monocapillaries consist of ellipsoidal or paraboloidal capillaries for focusing or parallelizing X-rays by means of single or multiple total reflections, as illustrated in Fig. 2.1.21. The exit-beam divergence is controlled by the capillary diameter and length as well as the critical angle of total reflection; typical spot sizes range from some 20 mm down to less than 1 µm. Single-reflection monocapillaries are achromatic and almost 100% efficient. Their most important limitations are figure slope errors limiting the spot size. Multi-reflection monocapillaries can have the smallest spot sizes, which do not depend on the source size. An important drawback is that the beam is smallest at the capillary tip. In order to obtain the smallest possible spot size the sample has to be positioned to within 10–100 times the diameter of the tip exit size, *e.g.* 10–100 µm for a capillary with a 1 µm tip exit size.

Polycapillaries (*e.g.* Kumakhov & Komarov, 1990) are monolithic systems of micro-structured glass consisting of thousands up to several millions of channels, which are tapered at one or both ends to form desired beam profiles as illustrated in Fig. 2.1.22. A single channel can efficiently turn an 8 keV beam by up to 30° by multiple total reflections. Polycapillaries can collect a very large solid angle up to 20°, resulting in very high intensity gains. Typical spot sizes range from some 20 mm down to about 10 µm and are energy dependent, getting larger at lower energies.

2.1.6.3.4. *Combi-optics*

The steadily growing trend towards multipurpose instrumentation has led to a multitude of X-ray optics combined in single modules to eliminate reassembling and realignment. Such 'combi-optics' are usually motorized and allow a fully automatic, software-controlled switch between different beam paths to switch between different instrument geometries or to optimize beam conditioning (*e.g.* high flux *versus* high resolution).

A frequent requirement is the ability to switch between the divergent-beam Bragg–Brentano and parallel-beam Debye–Scherrer geometries, which can be achieved by two combi-optics as illustrated in Fig. 2.1.23. In this example, the incident-beam combi-optics consist of a variable slit and a Göbel mirror. When operating as a variable slit (Fig. 2.1.23*a*), the parallel-beam path is blocked by the variable slit. Turning the variable slit parallel to the divergent beam (Fig. 2.1.23*b*) enables the parallel beam and blocks the divergent beam. The diffracted-beam combi-optics consist of a set of two parallel-plate collimators, which are

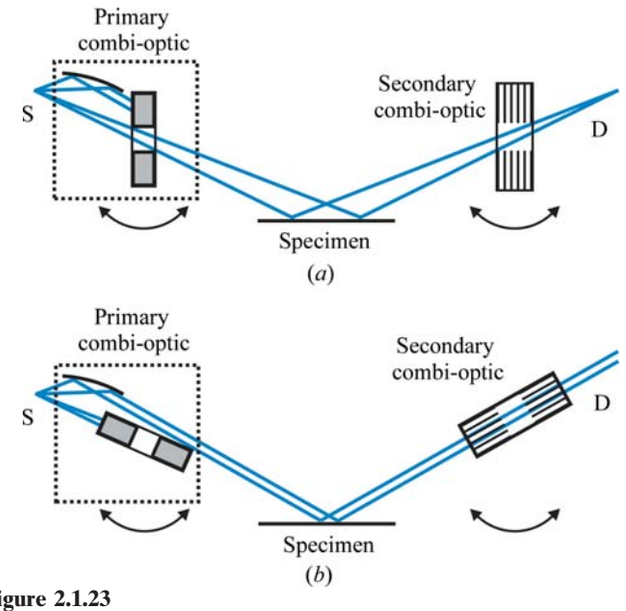

Figure 2.1.23
Incident and diffracted beam combi-optics for switching between (*a*) the Bragg–Brentano geometry and (*b*) the parallel-beam geometry. S: X-ray source; D: detector.

separated by a small gap. When turning the two parallel-plate collimators into the beam direction, only those diffracted rays running parallel to the collimator plates will reach the detector (Fig. 2.1.23*b*). When turning the collimators by approximately 90°, the gap between the two collimators acts as a variable slit enabling a divergent beam (Fig. 2.1.23*a*).

Significantly more sophisticated combi-optics are used in X-ray diffractometers that are mostly used for thin-film analysis. In Fig. 2.1.24 an example for two different incident-beam and four different diffracted-beam paths is shown, providing the choice between eight different beam paths depending on the properties of the specimen and the application requirements. The incident beam path is characterized by a fixed-target X-ray source equipped with a Göbel mirror, attached on a motorized mount. By rotating this arrangement by about 5°, the beam travels either through a rotary absorber followed by a two-bounce channel-cut monochromator and a slit (upper beam path, high-resolution setting), or just through a single slit (lower beam path, high-flux setting). The diffracted beam path represents a double-detector setup, typically consisting of a point detector (D1) and a position-sensitive detector (D2). For the point detector three different beam paths can be chosen by means of a switchable slit, which either sends the beam through a three-bounce channel-cut analyser, or through the same two-parallel-plate-collimator arrangement already discussed in Fig. 2.1.23, either acting as a parallel-plate collimator or a variable slit. A fourth beam path without any diffracted-beam X-ray optics allows use of the position-sensitive detector.

2.1.7. X-ray detectors

The general concepts of X-ray detectors are described here with the focus on practical aspects. The physics of X-ray detection and the individual detector technologies are extensively covered in the literature. He (2009) gives a comprehensive discussion that also includes the most recent detector technologies. Additional detailed descriptions are found in *International Tables for Crystallography* Vol. C (2004), as well as in the textbooks by Pecharsky & Zavalij (2009), Clearfield *et al.* (2008), Paganin (2006), Jenkins & Snyder (1996), and Klug & Alexander (1974).

2.1.7.1. *Detector parameters*

There are many ways to characterize the properties and performance of an X-ray detector.

Ideally, in a given detector operated under appropriate conditions, (1) each photon will produce a detectable signal and (2) the signal recorded is proportional to the number of photons detected. If both conditions are fulfilled then the detector has unit *quantum efficiency*. The *detective quantum efficiency* (DQE) may be defined as the squared ratio of the output signal-to-noise ratio to the input signal-to-noise ratio, expressed as a percentage. A detector's DQE is generally less than 100% because there is always detector noise and not every photon is detected. The DQE thus depends on the characteristics of the detector (*e.g.* transmission of the detector window, count rates and dead time, *etc*.) and varies with the X-ray energy for the same detector.

The *detector linearity* determines the accuracy of intensity measurements and depends on the ratio between the photon

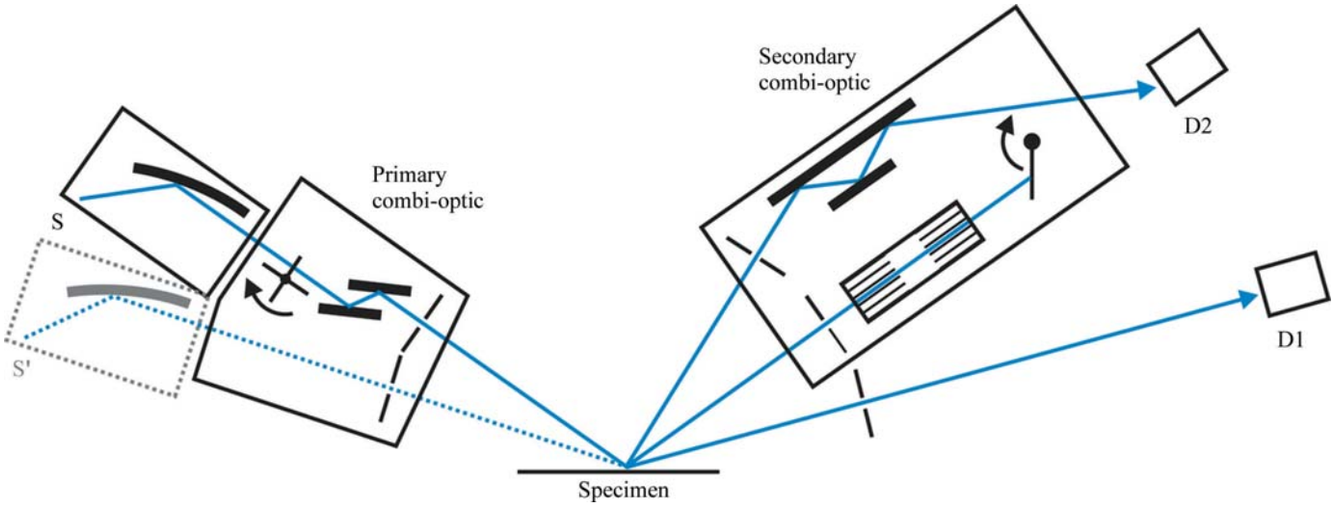

Figure 2.1.24
Example of the use of highly sophisticated incident- and diffracted-beam combi-optics in combination with a rotatable X-ray source and a double detector arm. This setup enables two different incident-beam and four different diffracted-beam paths, and thus provides a choice between eight different beam paths, depending on the properties of the specimen and the requirements of the application. S: X-ray source, S′: X-ray source rotated by about 5°, D1, D2: detectors.

count rate and the rate of signals generated and registered by the detector. In any detector it takes some time to process the conversion of an individual photon to a voltage pulse, which is related to the detector *dead time*: photons arriving while the detector is still processing the previous photon conversion may be lost. The detector dead time is related to the physical characteristics of the detector, *e.g.* the drift time in a gas-ionization detector, or the read-out time of the counting electronics, *e.g.* the shaping time of the amplifier. The effect of dead time becomes a substantial issue at high photon count rates, when the dead time becomes a significant part of the average time separation between two arriving photons, leading to increasing intensity losses at higher count rates. Detectors can be categorized as being non-paralysable or paralysable with respect to dead time. A non-paralysable detector is dead for a fixed time after each count, but not influenced by photons arriving during the dead time. Counting losses increase with increasing count rates, but the true count rate of a nonparalysable detector can be corrected unless the maximum observed count rate is equal to the inverse of the dead time. In a paralysable detector, a second photon arriving within the dead time can not be counted but will extend the dead time up to a point where the detector will be incapable of collecting any counts at all (saturation point). Modern detectors can stand the count rates obtained in powder diffraction experiments using fixed-target X-ray sources. At very high count rates, *e.g.* those obtained in thin-film experiments such as reflectometry, it may be necessary to attenuate the beam. Sophisticated instruments are equipped with an electronic feedback system and automatic absorbers (see Section 2.1.6.3.1.2) to ensure that detector saturation is avoided.

The *dynamic range* of a detector may be defined as the range between the smallest detectable photon count rates (determined by inherent detector noise such as readout and dark noise) to the largest acceptable photon count rates (determined by the dead time).

Energy resolution is the ability of a detector to resolve two photons that have different energies. Energy resolution is typically characterized by the size of the detector energy window, ΔE, in electron volts, as determined by the full width at half maximum (FWHM) of the detector-efficiency curve as a function of energy, with the detector and counting electronics set to a specific wavelength. Another frequently used expression for energy resolution is the ratio of the detector energy window size to the energy of the monochromatic X-ray beam, E, expressed as $\Delta E/E$.

The *proportionality* of the detector determines how the size of the generated voltage pulse is related to the energy of the absorbed X-ray photons, and electronic methods (pulse-height selection) can be used to discriminate between different energies. An accurate proportionality thus allows the use of *energy discrimination* as a form of monochromatization, where the energy is filtered by the detector rather than by an optical element such as a metal filter, crystal or mirror; see Section 2.1.6.3. Signals corresponding to photons with too high or too low energies are discarded.

The size and weight of detectors may impose several practical constraints, see also Section 2.1.4.2. For large detectors the accessible angular range may be limited owing to collision issues. For heavy detectors a horizontal goniometer may be preferred over a vertical goniometer (unless horizontal specimen positioning is imperative) in order to minimize the goniometer load.

X-ray detectors may be broadly classified as *counting detectors* or *integrating detectors*. Counting (digital) detectors are able to detect and count individual photons. The number of pulses counted per unit time is proportional to the incident X-ray flux. Integrating (or analogue) detectors accumulate photon-induced signals for a given period of time, prior to the integrated signal being read out and converted into an (analogue) electrical signal. The signal size is proportional to the flux density of the incident X-rays.

Counting and integrating detectors each have their clear advantages and disadvantages. Counting detectors normally have a greater dynamic range than integrating detectors, while integrating detectors normally have better spatial resolution (Section 2.1.7.3). Energy resolution is only possible for counting detectors. Readout and dark noise are usually higher for integrating detectors. Integrating detectors are not limited by the photon count rate as there is no dead time; nevertheless, the measurement time has to be kept sufficiently small to avoid saturation.

2.1.7.2. *Detector types*

Counting and integrating detectors can be further distinguished by their working principle, and are represented by scintillation, gas-ionization and semiconductor detectors. The most commonly used detector types and their properties are listed in Tables 2.1.1 and 2.1.6, respectively.

At the end of the 1990s the types of detectors in use were scintillation, gas-ionization, Si(Li) and image-plate detectors, with the scintillation counter being the most common by far. Usage of photographic film had already greatly diminished by that time. With the introduction of a series of new one- and two-dimensional detector technologies since the late 1990s, the X-ray detection landscape changed completely. New semiconductor-based detectors (silicon micro-strip, silicon pixel) as well as gas-ionization-based detectors (micro-gap) reached a market share of >90% in newly sold X-ray powder diffractometers within only a few years. As a consequence, classical metal-wire-based proportional counters and scintillation counters will probably become obsolete before 2020. The same is expected for CCD-based detectors, which will be replaced by the very recently introduced complementary metal–oxide–semiconductor (CMOS) active pixel sensor technology.

In the following the working principles of currently available detector types will be briefly described. Matters that are specific to zero- (0D), one- (1D) and two-dimensional (2D) detection are discussed in Section 2.1.7.3. While image plates are still in use, their market share in newly sold systems has become insignificant. Photographic film techniques are totally obsolete. For these reasons, these two detector types will not be taken into further consideration.

2.1.7.2.1. *Scintillation counters*

Scintillation counters are constructed from a scintillator crystal optically coupled to a photomultiplier tube. The crystal is typically made of sodium iodide (NaI) doped with about 1% thallium, frequently denoted as NaI(Tl). When irradiated by X-ray radiation, blue light (∼415 nm) is emitted and converted to electrons in a photomultiplier and amplified; the resulting pulses are registered as photon counts.

The height of the outgoing pulses is proportional to the energy of the incoming X-ray photons. This permits the use of pulse-height selection but only allows for poor energy resolution. The relatively high count rate and a moderate noise level result in a moderate dynamic range. These characteristics are the reason for the formerly wide-ranging acceptance of the scintillation counter

Table 2.1.6
Important detector properties at 8 keV as reported by various vendors

Only typical values are given to allow approximate comparisons. Detector properties strongly depend on individual detector designs and are subject to high development rates.

		Gas ionization (Xe/CO_2 gas filling)		
	Scintillation	Wire based (0D)	Wire based (1D/2D)	Micro-gap (1D/2D)
DQE	∼95%	∼95%	∼80%	∼80%
Dynamic range	$>6 \times 10^6$	$>10^6$	$>10^4$ (1D) $>10^6$ (2D)	$>8 \times 10^7$ (1D) $>10^9$ (2D)
Maximum global count rate	$>2 \times 10^6$ c.p.s.	$>7.5 \times 10^5$	$>10^5$ (1D) $>4 \times 10^4$ c.p.s. (2D)	$>8 \times 10^5$ (1D) $>1.6 \times 10^6$ c.p.s. (2D)
Maximum local count rate	n/a	n/a	$>10^4$ (1D) $>10^4$ c.p.s. mm^{-2} (2D)	$>9 \times 10^5$ c.p.s. mm^{-2} (1D, 2D)
Noise	∼0.3 c.p.s.	∼1 c.p.s.	∼1 c.p.s. (1D) $<5 \times 10^{-4}$ c.p.s. mm^{-2} (2D)	<0.01 c.p.s. (1D) $<5 \times 10^{-4}$ c.p.s. mm^{-2} (2D)
Energy resolution	∼3500 eV (∼45%)	∼1600 eV (∼20%)	∼1600 eV (∼20%)	∼1600 eV (∼20%)
Detection mode	Photon counting	Photon counting	Photon counting	Photon counting

	Semiconductor				
	Si(Li)	Strip	Pixel	CCD	CMOS
DQE	>98%	>98%	>98%	∼20–60%	∼75%
Dynamic range	$>10^6$	$>7 \times 10^6$ per strip	$>10^9$	$>5 \times 10^4$	$>1.6 \times 10^4$
Maximum global count rate	$>10^5$ c.p.s.	$>10^8$ c.p.s	$>10^7$ c.p.s. mm^{-2}	n/a	n/a
Maximum local count rate	n/a	$>7 \times 10^5$ c.p.s. per strip	$>10^4$ per pixel	n/a	n/a
Noise	∼0.1 c.p.s.	∼0.1 c.p.s. per strip	$\sim 2.5 \times 10^{-3}$ c.p.s. mm^{-2}	<0.1 c.p.s. per pixel	<0.05 c.p.s. per pixel
Energy resolution	∼200 eV (∼4%)	∼1600 eV (∼20%)†	>1000 eV (∼12.5%)	n/a‡	n/a
Detection mode	Photon counting	Photon counting	Photon counting	Integrating§	Integrating

† ∼380 eV/∼5%; Wiacek *et al.* (2015). ‡ >300 eV/>6% in photon-counting mode, see text. § Photon-counting mode possible, see text.

as the detector of choice. An important disadvantage these days is the limitation to 0D detection.

2.1.7.2.2. *Gas-ionization detectors*

The gas-ionization detectors in current use are proportional counters and can be of the 0D, 1D or 2D detection type. Common to all proportional counters is a gas-filled chamber permeated by a non-uniform electric field between positive and negative electrodes, held at a constant potential difference relative to each other. Typically the noble gases Ar or Xe are used as gas fill, mixed with a small amount of quenching gas such as CH_4 or CO_2 to limit discharges. When an X-ray photon travels through the gas-filled volume, it may be absorbed by a noble-gas atom, resulting in the ejection of an electron (photoelectric and Compton recoil). This electron, accelerated by the electric field towards the anode, will cause an avalanche by subsequent ionization along its path (gas amplification), generating an electric pulse which can be registered. The height of the generated pulse is proportional to the energy of the incoming X-ray photon and permits the use of pulse-height selection to achieve moderate energy resolution.

2.1.7.2.2.1. Wire-based proportional counters

In a point proportional detector (0D detection), the pulses generated are measured at one end of a wire (or a knife edge). Position-sensitive (1D and 2D detection) proportional detectors have the added capability of detecting the location of an X-ray photon absorption event. In a 1D proportional detector, pulses are detected at both ends of the wire. Thus the time difference between the measurements of a given pulse can be used to determine the location of the discharge. 2D proportional counters consist of three arrays of wires (multiwire proportional counter, MWPC; Sauli, 1977; Charpak *et al.*, 1968), where one array forming the anode plane is placed between two cathode arrays with their wires oriented parallel and orthogonal to the anode-plane wires, respectively.

Low count rates and low-to-moderate detector noise result in low-to-moderate dynamic ranges. Wire-based proportional counters are not competitive with micro-gap and semiconductor detectors, as can be seen in Table 2.1.6, and are therefore being driven out of the market.

2.1.7.2.2.2. Micro-gap detectors

The maximum count rates in 'classical' metal-wire-based proportional counters are severely limited by the long ion-drift times in the chamber (which typically have a cathode to anode spacing of ∼10 mm). This issue has been successfully addressed by so-called micro-gap technology using parallel-plate avalanche chambers with a readout electrode separated from a resistive anode. The key feature is the resistive anode, which allows a very small amplification gap (1–2 mm cathode to anode spacing) at an increased average electric field intensity, while preventing discharges (Durst *et al.*, 2003; Khazins *et al.*, 2004). As a result, micro-gap detectors can achieve count rates several orders of magnitude higher than classical proportional counters at higher position sensitivity. Micro-gap detectors of the 1D and 2D detection type are available. Moderate count rates and very small

noise levels result in very high dynamic ranges. Notably, in contrast to wire detectors, micro-gap detectors are not likely to be damaged by accidental exposure to a high-intensity direct beam, as a patterned anode plane is used rather than wires.

2.1.7.2.3. *Semiconductor detectors*

Semiconductor (or solid-state) detectors are solid-state ionization devices in which electron–hole pairs instead of electron–ion pairs are generated by incoming photons, and they are sensitive to the entire electromagnetic spectrum from visible light to X-rays. The energy required for production of an electron–hole pair is very low compared to the energy required for production of paired ions in a noble-gas-filled detector. As a consequence, a larger number of charge pairs with a smaller statistical variation are generated in semiconductor detectors, resulting in intrinsically higher energy-resolution capabilities. The efficiency of semiconductor detectors is very high due to the high absorption of the semiconductor materials, usually reaching 100%, but may decline at higher photon energies if the photons are not fully absorbed in the semiconductor *e.g.* because of insufficient thickness.

2.1.7.2.3.1. The Si(Li) detector

The Si(Li) detector sensor consists of a lithium-drifted silicon crystal which must be cooled to prevent lithium diffusion and to reduce dark noise. An important advantage of this detector is its excellent energy resolution of even better than 200 eV (4%) at 8 keV (Cu radiation), allowing very effective filtering of Kβ and fluorescence radiation and thus operation without a metal filter or a diffracted-beam monochromator. As Peltier cooling is sufficient, the Si(Li) detector type has found wide interest for applications benefitting from high energy resolution, unlike energy-dispersive detectors requiring operation under cryogenic conditions [*e.g.* Ge(Li)]. In particular, the Si(Li) detector significantly extends the application range of today's X-ray diffractometers by allowing energy-dispersive X-ray powder diffraction (EDXRD) as well as – to some extent – XRF (see Section 2.1.4.3).

An important disadvantage of Si(Li) detectors is their large dead time, which prohibits the handling of higher count rates. Moderate noise levels result in low-to-moderate dynamic ranges. An additional important disadvantage is the limitation to 0D detection.

2.1.7.2.3.2. Silicon micro-strip and silicon pixel detectors

Silicon micro-strip and silicon pixel detectors employ silicon sensors, which are one- or two-dimensional arrays of p–n diodes in the form of strips or pixels, respectively, individually connected to an array of readout channels. The development of this type of detector technology has obviously been driven by the idea of massive parallelism: each strip or pixel actually represents an individual detector. Accordingly, the silicon micro-strip and silicon pixel detectors are therefore of the 1D and 2D detection type, respectively.

Count rates recorded by silicon micro-strip and silicon pixel detectors are very high with very low noise levels, resulting in very large dynamic ranges. The energy resolution of most silicon micro-strip and silicon pixel detectors is of the order of 1600 eV (20%) at 8 keV (Cu radiation). Recently, a silicon micro-strip detector with an energy resolution of better than 380 eV at 8 keV has been introduced (Wiacek *et al.*, 2015). At such high energy resolution Cu Kβ is filtered out to below the detection limit while Mn, Fe and Co fluorescence is filtered completely, allowing this detector to be operated without a metal filter or a diffracted-beam monochromator for most applications.

2.1.7.2.3.3. CCD and CMOS detectors

Charge-coupled device (CCD) detectors are represented by one- or two-dimensional arrays of square or rectangular pixels consisting of metal–oxide–semiconductor (MOS) capacitors, and can detect X-ray photons directly or indirectly. The pixel size may be less than 10 µm. The majority of detectors use indirect detection, where the incoming X-ray photons are first converted to visible-light photons by a phosphor layer. CCD detectors employ the 'bucket brigade' readout method, in which charge is shifted one pixel at a time by phasing the bias on the gate electrodes that overlay each pixel until it reaches the output, resulting in relatively large readout times ranging from a few tenths of a second up to several seconds per frame. Cooling (Peltier-type) is required to reduce the dark-current noise representing the dominant noise source for long exposures. In some detector designs fibre-optic demagnification is used to increase the effective active detector area, resulting in an imaging area larger than the active area of the CCD chip at the cost of detector sensitivity and spatial resolution.

CCD detectors are usually operated as integrating detectors. As such, they have no dead time and therefore provide excellent linearity over a moderate dynamic range, but cannot have energy resolution. CCD detectors are the detectors of choice for single-crystal diffraction and imaging, but are not favourable for applications with weak diffraction signals, such as powder X-ray diffraction, owing to the relatively large dark-current noise.

CCD detectors may also function as counting detectors by making the exposure time sufficiently short. In single-event mode the energy of each photon can be determined, providing an energy resolution down to about 300 eV at 8 keV (Cu radiation) and allowing a spectrum at each pixel of the CCD array to be built up by a series of consecutive measurements. Such a detector can record energy-dispersive X-ray powder diffraction (EDXRD) as well as – to some extent – XRF (see Section 2.1.4.3); however, owing to the readout time, count rates are extremely low with high statistical noise.

Unlike the bucket-brigade readout of a CCD, the complementary metal–oxide–semiconductor (CMOS) active-pixel sensor (He *et al.*, 2011) uses a completely different architecture in which each pixel incorporates a readout preamplifier and is then read out through a bus, as in random-access memory (He *et al.*, 2011). Cooling is not required. CMOS detectors are immune to the blooming effect (in which a light source overloads the sensitivity of the sensor, causing the signal to bleed vertically into surrounding pixels forming vertical streaks). Additionally, they offer the very significant advantage of shutter-free operation, that is dead-time-free continuous scans which improve the efficiency of data collection and also improve data quality by eliminating shutter-timing jitter.

As a consequence of these characteristics, CMOS-detector active-pixel sensors are now replacing CCD chips in a number of high-end applications (*e.g.* professional digital photography and high-definition television), and have reached a level of performance where they are also starting to displace CCD chips in the most demanding scientific applications.

2.1.7.3. *Position sensitivity and associated scanning modes*

2.1.7.3.1. *Pixel size, spatial resolution and angular resolution*

Detectors of the line (1D) or area (2D) type have the important property of position sensitivity, which is characterized by the two parameters pixel size and spatial resolution.

The pixel size of a position-sensitive detector (PSD) can be represented either by the intrinsic size of the smallest addressable sensitive component of a detector (*e.g.* the actual size of the diodes), which can be binned to form larger pixels, or is set by the readout electronics (*e.g.* for wire-based detectors such as proportional counters). The spatial resolution is determined by the actual pixel size, the point-spread function (PSF) and parallax. The PSF represents the spread of a signal produced by a single photon over several pixels by mapping the probability density that a photon is recorded by a pixel in the vicinity of the point that the photon hit. Parallax will lead to an additional smearing if the photon travels at an angle to the detector normal. The final angular resolution of a detector system is given by the spatial detector resolution and the specimen-to-detector distance.

Point (0D) detectors do not provide position sensitivity, regardless of the actual size of the active window (representing a single pixel). Simply speaking, in analogy to PSDs, the spatial resolution of a point detector is determined by the goniometer step size representing the actual pixel size, and the size of the detector slit representing the PSF. As for PSDs, the angular resolution is given by the spatial resolution and the specimen-to-detector distance.

Detectors can be operated in fixed as well as in (2θ) scanning mode, where the step size is usually determined by the detector pixel size. Subsampling, that is scanning using an angular step size smaller than the angular pixel resolution, may be used to improve observed line profile shapes if the pixel resolution is too small. As a rule of thumb some 5–8 data points need be collected over the FWHM of a diffraction peak to allow for an appropriate description of the line-profile shape.

2.1.7.3.2. *Dimensionality*

Area detectors can be operated as line or point detectors. Electronic binning of the pixels into columns will form a line detector, while binning all pixels together will form a point detector, each associated with improvements of count rates and thus dynamic ranges. Alternatively, 1D or 0D 'regions of interest' can be defined electronically and/or by mounting suitable diffracted-beam-path X-ray optics. Area detectors – when operated as such – require point-focus operation.

Line detectors can be used as point detectors, which may be formed in several ways. One way is to only use one or more central pixels by either electronically switching off outer pixels and/or by mounting suitable X-ray optics. Another way is to turn the detector by 90° and to bin all pixels, leading to an improved count rate and thus dynamic range.

Obviously, when turning a line detector by 90°, it will function as an area detector if it is scanned over an angular range; the trace of the scan will form a cylindrical surface that is a two-dimensional diffraction image (He, 2009). This scan mode may be associated with a few advantages, in addition to lower costs. For example, the elimination of parallax and the possibility of using diffracted-beam-path optics improve the angular resolution in the 2θ direction and allow air scattering to be reduced.

2.1.7.3.3. *Size and shape*

PSDs are available in different sizes with flat (1D, 2D), curved (1D), cylindrical (2D) and spherical (2D) detection surfaces. Curved, cylindrical and spherical detectors are designed for focusing or parallel-beam geometries with a fixed specimen-to-detector distance, and cannot normally be used with the Bragg–Brentano geometry because of its 2θ-dependent focusing circle (Section 2.1.4.1). Flat detectors can be used at different specimen-to-detector distances, with either high angular resolution at a large distance or large angular coverage at a short distance. For large flat detectors, parallax errors must be addressed. Small flat detectors are perfectly suited for operation in Bragg–Brentano geometry but the angular coverage should not exceed about 10° 2θ (Section 2.1.4.1) to minimize defocusing, particularly at small 2θ angles.

References

Bartels, W. J. (1983). *Characterization of thin layers on perfect crystals with a multipurpose high resolution X-ray diffractometer*. *J. Vac. Sci. Technol. B*, **1**, 338–345.

Bilderback, D. H. (2003). *Review of capillary X-ray optics from the 2nd International Capillary Optics Meeting*. *X-ray Spectrom.* **32**, 195–207.

Bohlin, H. (1920). *Eine neue Anordnung für röntgenkristallographische Untersuchungen von Kristallpulver*. *Ann. Phys.* **366**, 421–439.

Bonse, U. & Hart, M. (1965). *Tailless X-ray single crystal reflection curves obtained by multiple reflection*. *Appl. Phys. Lett.* **7**, 238–240.

Bowen, D. K. & Tanner, B. K. (1998). *High Resolution X-ray Diffractometry and Topography*. London: Taylor & Francis.

Brentano, J. C. M. (1924). *Focussing method of crystal powder analysis by X-rays*. *Proc. Phys. Soc.* **37**, 184–193.

Charpak, G., Bouclier, R., Bressani, T., Favier, J. & Zupančič, Č. (1968). *The use of multiwire proportional counters to select and localize charged particles*. *Nucl. Instrum. Methods*, **62**, 262–268.

Clearfield, A., Reibenspiess, J. & Bhuvanesh, N. (2008). *Principles and Applications of Powder Diffraction*. New York: Wiley.

Debye, P. & Scherrer, P. (1916). *Interference of X-rays, employing amorphous substances*. *Phys. Z.* **17**, 277–283.

Durst, R. D., Diawara, Y., Khazins, D. M., Medved, S., Becker, B. L. & Thorson, T. A. (2003). *Novel, photon counting X-ray detectors*. *Powder Diffr.* **18**, 103–105.

EN 1330–11 (2007). *Non-Destructive Testing*. Part 11. *Terms used in X-ray Diffraction from Polycrystalline and Amorphous Materials*. Brussels: European Committee for Standardization (CEN).

Fankuchen, I. (1937). *A condensing monochromator for X-rays*. *Nature (London)*, **139**, 193–194.

Fewster, P. F. (2003). *X-ray Scattering from Semiconductors*. London: Imperial College Press.

Friedmann, H. (1945). *Geiger counter spectrometer for industrial research*. *Electronics*, **18**, 132–137.

Göbel, H. E. (1980). *The use and accuracy of continuously scanning position-sensitive detector data in X-ray powder diffraction*. *Adv. X-ray Anal.* **24**, 123–138.

Guinier, A. (1937). *Arrangement for obtaining intense diffraction diagrams of crystalline powders with monochromatic radiation*. *C. R. Acad. Sci. Paris*, **204**, 1115–1116.

Hanawalt, J. D., Rinn, H. W. & Frevel, L. K. (1938). *Chemical analysis by X-ray diffraction*. *Ind. Eng. Chem. Anal.* **10**, 457–512.

Hart, M. (1971). *Bragg-reflection X-ray optics*. *Rep. Prog. Phys.* **34**, 435–490.

He, B. B. (2009). *Two-Dimensional X-ray Diffraction*. New York: Wiley.

He, T., Durst, R. D., Becker, B. L., Kaercher, J. & Wachter, G. (2011). *A large area X-ray imager with online linearization and noise suppression*. *Proc. SPIE*, **8142**, 81421Q.

Hemberg, O. E., Otendal, M. & Hertz, H. M. (2003). *Liquid-metal-jet anode electron-impact X-ray source*. *Appl. Phys. Lett.* **83**, 1483–1485.

Hull, A. W. (1917). *A new method of X-ray crystal analysis*. *Phys. Rev.* **10**, 661–696.

Hull, A. W. (1919). *A new method of chemical analysis*. *J. Am. Chem. Soc.* **41**, 1168–1175.

International Tables for Crystallography (2004). Volume C, 3rd ed., edited by E. Prince. Dordrecht: Kluwer Academic Publishers.

Jenkins, R. & Snyder, B. (1996). *Introduction to X-ray Powder Diffractometry*. New York: Wiley.
Johann, H. H. (1931). *Die Erzeugung lichtstarker Röntgenspektren mit Hilfe von Konkavkristallen*. *Z. Phys.* **69**, 185–206.
Johannson, T. (1933). *Über ein neuartiges, genau fokussierendes Röntgenspektrometer*. *Z. Phys.* **82**, 507–528.
Khazins, D. M., Becker, B. L., Diawara, Y., Durst, R. D., He, B. B., Medved, S. A., Sedov, V. & Thorson, T. A. (2004). *A parallel-plate resistive-anode gaseous detector for X-ray imaging*. *IEEE Trans. Nucl. Sci.* **51**, 943–947.
Kirkpatrick, P. & Baez, A. V. (1948). *Formation of optical images by X-rays*. *J. Opt. Soc. Am.* **38**, 766–774.
Klug, H. P. & Alexander, L. E. (1974). *X-ray Diffraction Procedures for Polycrystalline and Amorphous Materials*, 2nd ed. New York: Wiley.
Kumakhov, M. A. & Komarov, F. F. (1990). *Multiple reflection from surface X-ray optics*. *Phys. Rep.* **191**, 289–350.
Le Galley, D. P. (1935). *A type of Geiger–Müller counter suitable for the measurement of diffracted X-rays*. *Rev. Sci. Instrum.* **6**, 279–283.
Lindemann, R. & Trost, A. (1940). *Das Interferenz-Zählrohr als Hilfsmittel der Feinstrukturforschung mit Röntgenstrahlen*. *Z. Phys.* **115**, 456–468.
Montel, M. (1957). *X-ray microscopy with catamegonic roof-shaped objective*. In *X-ray Microscopy and Microradiography*, pp. 177–185. New York: Academic Press.
Paganin, D. M. (2006). *Coherent X-ray Optics*. Oxford University Press.
Parrish, W. (1949). *X-ray powder diffraction analysis: film and Geiger counter techniques*. *Science*, **110**, 368–371.
Pecharsky, V. K. & Zavalij, P. Y. (2009). *Fundamentals of Powder Diffraction and Structural Characterisation of Materials*, 2nd ed. New York: Springer.
Peiser, M. A., Rooksby, H. P. & Wilson, A. J. C. (1955). *X-ray Diffraction by Polycrystalline Materials*. London: Institute of Physics.
Sauli, F. (1977). *Principle of operation of multi-wire proportional and drift chambers*. CERN 77–09, May 1977.
Schuster, M. & Göbel, H. (1995). *Parallel-beam coupling into channel-cut monochromators using curved graded multilayers*. *J. Phys. D Appl. Phys.* **28**, A270–A275.
Schuster, M. & Göbel, H. (1996). *Application of graded multilayer optics in X-ray diffraction*. *Adv. X-ray Anal.* **39**, 57–72.
Seemann, H. (1919). *Eine fokussierende röntgenspektroskopische Anordnung für Kristallpulver*. *Ann. Phys.* **364**, 455–464.
VDI/VDE Guideline 5575 Part 3 (2011). *X-ray Optical Systems: Capillary X-ray Lenses*. Berlin: Beuth.
VDI/VDE Guideline 5575 Part 4 (2011). *X-ray Optical Systems: X-ray Mirrors. Total Reflection Mirrors and Multilayer Mirrors*. Berlin: Beuth.
Wiacek, P., Dabrowski, W., Fink, J., Fiutowski, T., Krane, H.-G., Loyer, F., Schwamberger, A., Świentek, K. & Venanzi, C. (2015). *Position sensitive and energy dispersive X-ray detector based on silicon strip detector technology*. *J. Instrumen.* **10**, P04002.

International Tables for Crystallography (2018). Vol. H, Chapter 2.2, pp. 51–65.

2.2. Synchrotron radiation and powder diffraction

A. Fitch

2.2.1. Introduction

X-rays produced at a synchrotron source are exploited in a wide range of applications in crystallography and structural science, and this includes studies by powder diffraction. Many synchrotron-radiation facilities have one or more dedicated powder-diffraction beamlines or end stations in regular user service. The high intensity, collimation and wavelength tunability of the radiation allow instruments to be designed whose performance and flexibility surpass what is possible with conventional laboratory apparatus. The majority of instruments operate with monochromatic radiation and an angle-dispersive diffractometer, but the polychromatic nature of synchrotron radiation means that an energy-dispersive setup is also possible. The general properties of synchrotron radiation include:

(*a*) High brightness, *i.e.* a highly collimated, intense X-ray beam and small source size.
(*b*) High flux of photons delivered to the sample.
(*c*) A range of wavelengths is available, possibly extending from the soft to the hard X-ray regimes, depending on the facility.
(*d*) Polarized source: synchrotron radiation is linearly polarized with the electric vector lying in the plane of the synchrotron orbit, but becomes progressively less polarized out of the plane.
(*e*) Pulsed source: the distribution of the bunches of electrons circulating in the storage ring allows the time structure to be exploited for specialized experiments.

Further information about the nature of synchrotron radiation can be found in texts by, for example, Margaritondo (1988), Als-Nielsen & McMorrow (2001) and Kim (2001).

Synchrotrons are usually user facilities, where scientists from external laboratories visit to perform experiments that have been approved by a peer-review or other procedure, and are supported by the scientific and technical staff for the beamlines. Most facilities have regular rounds in which users submit proposals for beam time, with special arrangements for access to carry out proprietary research. Arrangements can also usually be made for urgent access to the facility (when justified), and some beamlines run a routine mail-in service, allowing samples to be measured under defined conditions without the user needing to attend.

For any powder X-ray diffraction experiment, the wavelength of the radiation to be used is of high importance. The wavelength, λ, is a measure of the photon energy, ε, and the terms 'photon energy' and 'wavelength' tend to be used interchangeably at synchrotron beamlines. They can readily be converted by

$$\varepsilon = h\nu = hc/\lambda,$$

where h is the Planck constant, ν is the frequency of the radiation and c is the speed of light. If expressed in convenient units with λ in Å and ε in keV then

$$\varepsilon\ [\text{keV}] = hc/e\lambda \times 10^7\ [\text{Å}] \simeq 12.3984/\lambda\ [\text{Å}] \simeq 12.4/\lambda\ [\text{Å}],$$

where e is the elementary charge.

2.2.2. Production of synchrotron radiation

Synchrotron radiation is emitted by charged particles travelling at relativistic speeds when they are accelerated to move in a curved trajectory. In a modern synchrotron facility dedicated to the production of X-ray beams for scientific experiments, electrons are circulated in a closed horizontal orbit in a storage ring at an energy of several GeV, steered by magnetic fields from bending magnets. The overall circumference of the orbit can be several hundred metres depending on the design and specifications of an individual ring. The synchrotron ring is built up of cells (Fig. 2.2.1) comprising a straight section and a bending magnet by which the electrons are guided into the following straight section. Beamlines emerge tangentially from the bending magnets where synchrotron radiation is emitted by the electrons as they curve from one straight section into the next. Beamlines are also constructed on the straight sections where insertion devices, arrays of magnets providing an alternating magnetic field, are placed to cause the path of the electrons to oscillate and so also emit synchrotron radiation. By choosing the period of the magnetic array and by varying the strength of the magnetic field, the wavelength distribution and divergence of the X-rays emitted from an insertion device can be controlled. A straight section may accommodate more than one insertion device in series, allowing greater intensity or flexibility in the emitted radiation for the associated beamline. In the storage ring, the energy that the electrons lose by emitting synchrotron radiation is replaced by coupling the electrons to radio-frequency radiation supplied from klystrons or solid-state devices. Thus the synchrotron facility converts electrical energy, *via* radio waves and relativistic electrons, into powerful beams of electromagnetic radiation.

One key parameter of a storage ring is the energy of the circulating electrons. The energy of an electron moving with

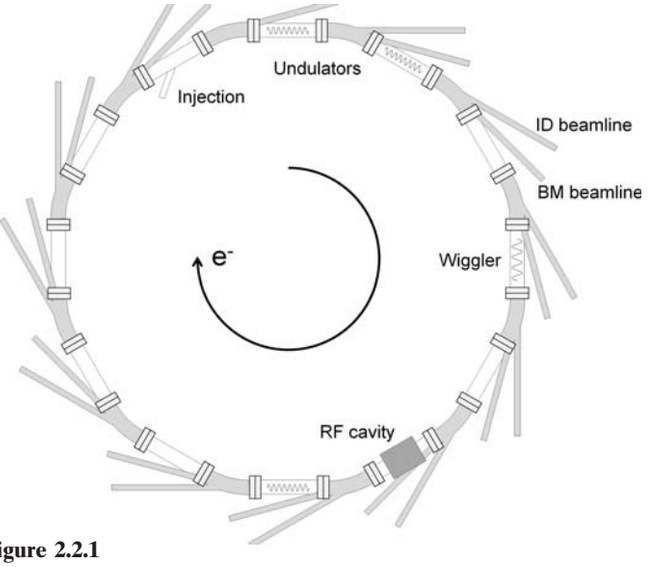

Figure 2.2.1
Schematic representation of a synchrotron storage ring with beamlines radiating tangentially from the bending magnets and in line with the straight sections. ID = insertion device, BM = bending magnet; RF = radio-frequency.

speed v is

$$E_e = \frac{m_e c^2}{(1 - v^2/c^2)^{1/2}} = \gamma m_e c^2,$$

where m_e is the rest mass of the electron, $9.10938356\,(11) \times 10^{-31}$ kg. The term $1/(1 - v^2/c^2)^{1/2}$ is referred to as γ and is the factor by which the mass of the electron increases from its rest mass because of its relativistic speed. Expressed in eV (the conversion factor from kg to eV is c^2/e), the electron rest mass is $5.109989461\,(31) \times 10^5$ eV, so that

$$\gamma \simeq 1957 E_e \text{ [GeV]}$$

when E_e is given in the customary units of GeV. Thus for a 3-GeV machine, a common energy for a synchrotron-radiation source, γ has the value of 5871. The mass of an electron with energy 3 GeV is therefore 3.22 atomic mass units, so around 7% more massive than a stationary atom of ^{3}H or ^{3}He.

Electrons do not circulate individually in the storage ring but in a series of bunches that are in phase with the accelerating radio frequency. Radiation is therefore emitted in pulses as each bunch passes through a bending magnet or insertion device. Thus the number and distribution of the electron bunches around the orbit determine the time structure of the emitted radiation. For most powder-diffraction applications using synchrotron radiation, the pulsed nature of the source can be neglected and the radiation can be regarded as continuous, although attention should also be paid to the performance of detectors that are more susceptible to pulse pile-up problems when the radiation arrives at very high average rates or in concentrated bursts (Cousins, 1994; Laundy & Collins, 2003; Honkimäki & Suortti, 2007), which can happen with certain bunch-filling modes. Certain specialized experiments requiring very fast time resolution can exploit the time structure of the source. In such experiments the longitudinal dimension of the bunches controls the pulse duration, which is usually a few tens of picoseconds.

In discussing the performance of different beamlines, the spectral brightness (Mills *et al.*, 2005) is often quoted for the source and is defined as

spectral brightness =

photons per second per 0.1% bandwidth per mrad^2 per mm^2,

where '0.1% bandwidth' represents $\delta\lambda/\lambda = 0.001$, the mrad^2 term expresses the solid-angle of the emission of the X-rays from the source and the mm^2 term relates to the cross-sectional area of the source. Thus a source of high spectral brightness emits many photons per second of the specified energy, into a narrow solid angle, with a small source size. The source size, which may well differ in the horizontal and vertical directions, is an important consideration as source size and beam divergence ultimately limit the performance of the beamline optical system in terms of collimation, energy resolution and focal spot size.

2.2.2.1. *Bending magnets*

A bending magnet provides a vertical magnetic field to deflect the electrons laterally in the horizontal plane from a straight-line trajectory, and thereby causes the emission of synchrotron radiation (see Fig. 2.2.2). The lateral Lorentz force, F, acting on an electron travelling at velocity v in a magnetic field B is mutually perpendicular to both the magnetic field and the direction of travel of the electron, and is given by

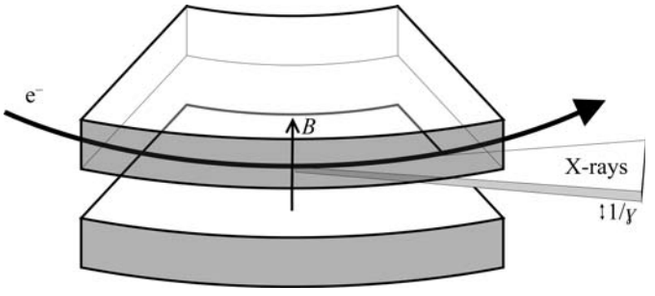

Figure 2.2.2
Emission of a fan of radiation by the electron beam as it curves in a bending magnet from one straight section of the ring to the next.

$$F = evB.$$

In a bending magnet the magnetic field is applied over an extended distance leading to a curved path of radius ρ. The centripetal acceleration is $F/\gamma m_e$, which for circular motion is equal to v^2/ρ. Since $v \simeq c$,

$$\rho = \frac{\gamma m_e c}{eB},$$

so the radius of curvature decreases with magnetic field strength and increases with machine energy *via* increased γ. With the electron energy expressed in GeV, this can be approximated to $\rho \simeq 3.34 E_e$ [GeV]$/B$ (where $10^9/c \simeq 3.34$).

Synchrotron radiation is emitted in a forward cone tangential to the direction of the electrons' motion (Fig. 2.2.3) with a nominal Gaussian distribution and an opening angle of the order of $1/\gamma$. Thus the radiation is highly collimated in the vertical plane. In the horizontal plane, synchrotron radiation is emitted in a broad fan, tangential to the curved trajectory of the electrons as they sweep through the bending magnet. Only a fraction of the radiation emitted by a bending magnet enters the associated beamline *via* a cooled aperture defining a horizontal acceptance angle of a few mrad. The radiation is polarized in the plane of the synchrotron orbit. Sometimes, more than one beamline can be built on a bending magnet with a suitable angular separation between them.

Photons are emitted over a broad spectral range. The critical photon energy, ε_c, divides the emitted power into equal halves and is given by

$$\varepsilon_c = \frac{3\hbar c\gamma^3}{2\rho} = \frac{3\hbar\gamma^2 eB}{2m_e} = \frac{3\hbar e E_e^2 B}{2m_e^3 c^4} = 4.151 E_e^2 B,$$

or, with photon and electron energies in keV and GeV, respectively,

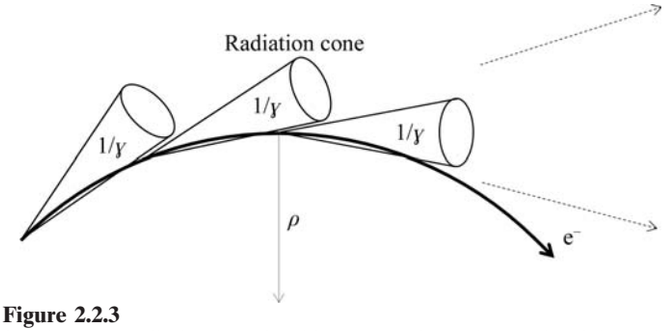

Figure 2.2.3
Synchrotron radiation is emitted in a cone of opening angle of the order of $1/\gamma$ tangential to the electrons as they follow a curved trajectory through the bending magnet.

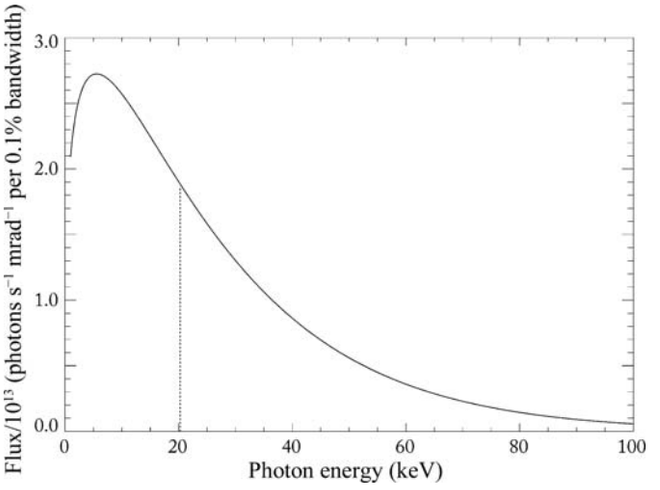

Figure 2.2.4
Spectrum of a bending magnet (B = 0.85 T) at the ESRF with an electron energy of 6 GeV (γ = 11 742), shown as flux per horizontal mrad for a 0.1% energy bandwidth at a storage-ring current of 200 mA. The critical energy of 20.3 keV divides the emitted power into equal halves.

$$\varepsilon\ [\mathrm{keV}] = 0.665 E_e^2\ [\mathrm{GeV}] B.$$

The higher the critical energy, the greater the number of photons produced with short X-ray wavelengths. As an example, consider a bending magnet at the ESRF in Grenoble, France, which has a 6-GeV storage ring and bending magnets with a field of 0.85 T. The bending radius is 23.5 m and the critical photon energy is 20.3 keV (equivalent to a wavelength of 0.61 Å). The spectrum of such a device is shown in Fig. 2.2.4.

The vertical collimation of the radiation varies with photon energy in a nonlinear manner (Kim, 2001). Nevertheless, the divergence decreases with increased photon energy, so beams with the shortest wavelengths are the most vertically collimated. Various approximations can be written to describe the variation, such as for a single electron (Margaritondo, 1988),

$$\sigma_v(\varepsilon) \simeq \frac{0.565}{\gamma}\left(\frac{\varepsilon_c}{\varepsilon}\right)^{0.425},$$

where $\sigma_v(\varepsilon)$ is the standard deviation of the vertical-divergence distribution of photons of energy ε. For a population of electrons circulating in a storage ring, the distribution of the trajectories with respect to the plane of the orbit (of the order μrad) must also be considered, as these add to the vertical emission distribution. An approximation such as

$$\Psi_v(\varepsilon) = 2\sigma_v(\varepsilon) \simeq \frac{1.2}{\gamma}\left(\frac{\varepsilon_c}{\varepsilon}\right)^{1/2}$$

will often be adequate to estimate the vertical divergence Ψ_v in the vicinity of ε_c. Thus for the bending magnet illustrated in Fig. 2.2.4, photons at the critical energy of 20.3 keV will have a vertical divergence of ∼100 μrad. A beamline would probably accept less than this, *e.g.* a 1.5-mm-high slit at 25 m from the source defining the beam onto a monochromator crystal defines an angle of ∼60 μrad.

2.2.2.2. *Insertion devices*

Insertion devices can be classified into two main types, termed 'wigglers' and 'undulators', illustrated in Fig. 2.2.5. A wiggler has a relatively long magnetic period and the radiation from each oscillation is emitted like a series of powerful bending magnets, summing together to provide increased intensity. An undulator has a relatively short magnetic period and the radiation from sequential oscillations interferes coherently to give modified beam characteristics.

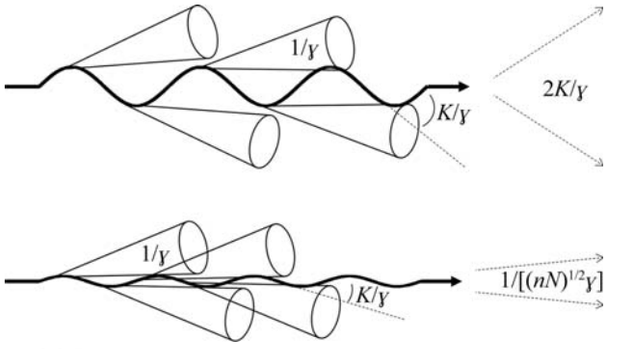

Figure 2.2.5
Schematic illustration of a wiggler (upper) and an undulator (lower).

For insertion devices the magnetic field acting on the electrons varies sinusoidally along the device,

$$B(z) = B_0 \sin(2\pi z/\lambda_u),$$

where B_0 is the peak magnetic field, z is the distance along the insertion-device axis and λ_u is the magnetic period. With a vertical field, the alternating magnetic field causes the electron path to oscillate in the horizontal plane. Note that the radiation is emitted mainly towards the outsides of the oscillations where the electrons change transverse direction, and where the magnetic field and beam-path curvature are highest. The maximum angular deflection of an electron from the axis of the insertion device is K/γ, where the deflection parameter K is given by

$$K = \frac{eB_0\lambda_u}{2\pi m_e c},$$

which simplifies to $K = 0.0934 B_0 \lambda_u$ [mm] with λ_u expressed in mm. K is a crucial parameter that determines the behaviour of the insertion device.

2.2.2.2.1. *Wigglers*

If K is large (10 or above), the insertion device is a wiggler and the electrons oscillate with an amplitude significantly greater than the emitted radiation's natural opening angle $1/\gamma$. Every oscillation along the device produces a burst of synchrotron radiation and these add together incoherently so increasing the flux in proportion to the number of magnetic periods. The radiation emerges from the wiggler in a horizontal fan with a horizontal opening angle $\sim 2K/\gamma$. The intensity of a wiggler-based beamline can be very high because each oscillation produces synchrotron radiation, and this radiation is directed close to the axis of the device. Like a bending magnet, wigglers produce a continuous spectrum but with the critical energy shifted to harder energies because the magnetic field is (usually) greater. Thus for a wiggler at a 6-GeV source, with a magnetic field of 1.2 T and a magnetic period of 125 mm, K is 14, the maximum deflection of the electrons from the straight-line path is 1.2 mrad and the critical photon energy is 28.7 keV. Magnetic fields of several tesla can be exploited using superconducting magnets to obtain even higher critical photon energies.

2.2.2.2.2. *Undulators*

If the value of K is 2 or less, the insertion device is an undulator. The deflection of the electrons is comparable to the natural opening angle of the emitted radiation $1/\gamma$. Radiation emitted from sequential oscillations interferes coherently, and the beam

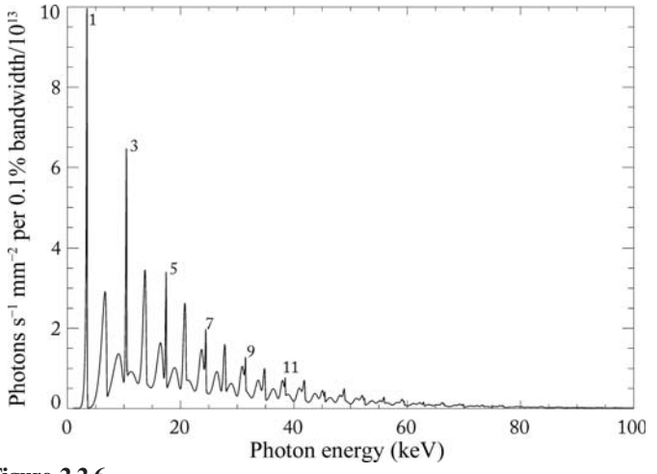

Figure 2.2.6
Photon flux *versus* energy through a 1-mm^2 aperture 30 m from the source, 0.1% bandwidth, for an ESRF u35 undulator (magnetic periodicity 35 mm, 1.6 m long, magnetic gap of 11 mm, peak magnetic field B_0 = 0.71 T, electron energy 6 GeV, K = 2.31, storage-ring current 200 mA). Odd-numbered harmonics are labelled, which are those usually employed for powder-diffraction experiments as they have maximum intensity on axis.

becomes highly collimated in the horizontal and vertical directions. Thus, the radiation from an undulator is concentrated into a central on-axis cone (fundamental and odd harmonics), surrounded by rings from higher-order even harmonics. The flux density arriving on a small sample from this central cone is therefore very high. With high on-axis intensity, it is therefore the undulators that provide the beams with the highest spectral brightness at any synchrotron-radiation source. The interference also modifies the spectrum of the device, which has a series of harmonics derived from a fundamental energy. At a horizontal angle θ to the axis of the insertion device, the wavelength of harmonic n is given by

$$\lambda_n = \frac{1 + (K^2/2) + \gamma^2\theta^2}{2n\gamma^2}\lambda_u,$$

which can be simplified on axis ($\theta = 0$) to

$$\lambda_n\ [\text{Å}] = 1.3056\frac{1 + K^2/2}{nE_e^2\ [\text{GeV}]}\lambda_u\ [\text{mm}]$$

or

$$\varepsilon_n\ [\text{keV}] = 9.50\frac{nE_e^2\ [\text{GeV}]}{\lambda_u\ [\text{mm}](1 + K^2/2)}.$$

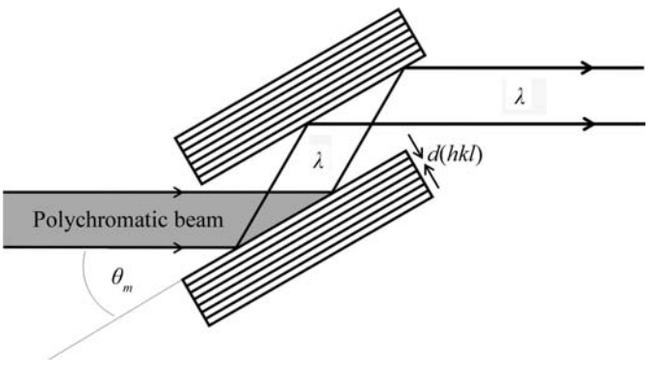

Figure 2.2.7
Double-crystal monochromator arrangement.

On axis, only odd-numbered harmonics are emitted and it is these that are usually employed in a powder-diffraction experiment. The horizontal and vertical divergence of the radiation emerging from an undulator is of the order of $1/[(nN)^{1/2}\gamma]$, where N is the number of magnetic periods making up the device. The spectrum of an undulator at a 6-GeV source with a 35-mm magnetic period is shown in Fig. 2.2.6. By carefully shimming the magnetic lattice so that it is highly regular, the higher-order harmonics persist, allowing the undulator to be a powerful source of high-energy X-rays. Any imperfections in the magnetic periodicity cause the higher-order harmonics to broaden and fade away, reducing the utility of the device at higher energies.

2.2.2.2.3. *Tuning*

For insertion devices the magnetic field can be modified by changing the vertical distance between the magnetic poles. By opening the gap, the magnetic field and K decrease following

$$B_0 \simeq B_r \exp(-\pi G/\lambda_u),$$

where B_r is proportional to the remanent magnetic field, which depends upon the nature of the magnets used in the insertion device, and G is the magnetic gap. Decreasing K for an undulator means that the energy of the fundamental harmonic increases; however, this is at the expense of the intensities of the higher harmonics. Thus the insertion device can be tuned to produce high intensity at the wavelength most suitable for a particular measurement. The smallest gap possible for a device depends on the design of the storage-ring vacuum vessel in which the electrons circulate. It is difficult to have a vessel smaller than about 10 mm high, and hence for an externally applied field a minimum magnetic gap of about 11 mm is to be expected. For smaller gaps, the magnets must be taken into the vacuum of the storage ring, a so-called 'in-vacuum' insertion device.

2.2.3. Optics

The intense polychromatic beam from the source needs to be conditioned before hitting the sample and diffracting. In the simplest experimental configuration, the white beam is used in an energy-dispersive experiment, and conditioning may involve no more than using slits to define the horizontal and vertical beam sizes and suppress background scattering. More usually, monochromatic radiation is employed, and the desired wavelength is chosen from the source by a monochromator. A monochromator consists of a perfect crystal, or a pair of crystals, set to select the chosen wavelength by Bragg diffraction. Additional optical elements can also be incorporated into the beamline for focusing, collimation, or for filtering out unwanted photons to reduce heat loads or remove higher-order wavelengths transmitted by the monochromator.

2.2.3.1. *Monochromator*

The monochromator is a crucial optical component in any angle-dispersive powder-diffraction beamline, and consists of one or a pair of perfect crystals (*e.g.* Beaumont & Hart, 1974), Fig. 2.2.7, set to a particular angle to the incident beam, θ_m, that transmits by diffraction wavelengths that satisfy the Bragg equation, $n\lambda = 2d(hkl)\sin\theta_m$, where $d(hkl)$ is the lattice spacing of the chosen reflection. Note that photons from higher-order reflections can also be transmitted, corresponding to wavelengths λ/n, depending on the structure factor of the nth-order reflection and its Darwin width, but these can be eliminated by use of a

mirror (see Section 2.2.3.2), or by adjusting the electronic acceptance windows of the detector system, if possible. They can also be suppressed to some extent by slightly detuning the second crystal from the first, because the Darwin width of a higher-order reflection is narrower than that of a lower-order reflection, and is thus more seriously affected by the mismatch between Bragg angles.

For a given reflection, a crystal does not transmit a unique single wavelength but a narrow distribution. The width of the distribution, $\delta\lambda$, is determined by the effective divergence of the incident beam Ψ (which corresponds to a range of values for θ_m) and the Darwin width of the reflection, ω, at the chosen wavelength. The energy resolution of a monochromator crystal can be estimated *via*

$$\delta\varepsilon/\varepsilon = \delta\lambda/\lambda = \cot\theta_m(\Psi^2 + \omega^2)^{1/2}.$$

With a highly collimated beam incident on a crystal and with a narrow Darwin width, high energy resolution is achieved. The Darwin width of a reflection can be calculated from dynamical theory [Zachariasen (1945); Chapter 5.1 of *International Tables for Crystallography*, Volume B (Authier, 2006)] *via*

$$\omega = \frac{2r_e\lambda^2}{\pi V}|F(\mathbf{h})|\frac{K}{\sin 2\theta_m},$$

where r_e is the classical electron radius ($\sim$2.818 fm), V is the volume of the unit cell, $F(\mathbf{h})$ is the structure factor and K the polarization factor (1 for reflection in the vertical plane, $\cos 2\theta_m$ for the horizontal plane). Thus for Si(111), with $d(111)$ = 3.1356 Å and $F(\mathbf{h}) \simeq 59$, a Darwin width of about 8.3 µrad is obtained at 31 keV (λ = 0.4 Å). With an effective beam divergence of say 25 µrad (delivering a beam 1.1 mm high at 44 m from the source), an energy resolution of 4.8×10^{-4} is obtained. Even better energy resolution can be obtained by increasing the collimation of the beam before the monochromator, *e.g.* with a curved mirror.

Energy resolution is an important quantity to control. Its value needs to be known when modelling powder-diffraction peak shapes *via* a fundamental-parameters approach, and it affects the angular resolution of the powder-diffraction pattern, broadening the peaks as 2θ increases, as can be seen by differentiating the Bragg equation to yield

$$\frac{\delta\lambda}{\lambda} = \cot\theta\,\delta\theta \quad \text{or} \quad \delta\theta = \frac{\delta\lambda}{\lambda}\tan\theta. \tag{2.2.1}$$

Thus powder-diffraction peaks broaden towards higher 2θ angles because of this effect.

Silicon is a common choice for a monochromator; it forms large, perfect single crystals, with dimensions of cm if required, has appropriate mechanical, diffraction and thermal properties, and can resist prolonged exposure to an intense radiation source. A monochromator crystal absorbs a large fraction of the energy incident upon it, and hence must be cooled. Even when cooled, the high power density (tens or even more than a hundred W mm^{-2} at normal incidence) can cause local heating of the surface, which leads to distortion of the lattice planes *via* thermal expansion. This degrades the performance, as a heat bump increases the range of θ_m values, broadening the energy band transmitted by the crystal. With a double-crystal arrangement, this bump cannot be matched by the second crystal, which has a much lower heat load so is flat, with the result that photons from the first crystal are not transmitted by the second, thus losing intensity from the monochromatic beam. By cooling to cryogenic temperatures, the thermal expansion of Si can be reduced to a very small value, going through zero at around 120 K (Bilderback, 1986; Glazov & Pashinkin, 2001) and thereby alleviating the heat-bump problem. Thus cryogenically cooled monochromators can be found at high-performance synchrotron beamlines. Other crystals employed as monochromators are germanium and diamond, the latter in transmission because of the small size of available diamond crystals.

Although a monochromator assembly can employ only one crystal, for example deflecting the beam horizontally into a side branch of a beamline, a double-crystal arrangement (Fig. 2.2.7) is more usually used to conserve the direction of the beam from the storage ring. This can exploit either a channel-cut crystal or two crystals, with a number of adjustments in the position and orientation of the second crystal to allow it to be aligned optimally to transmit the wavelength envelope defined by the first crystal. In some cases, the second crystal can be bent sagittally to focus X-rays horizontally onto the sample. Although this increases the divergence of the beam arriving at the sample and so affects the 2θ resolution of the powder pattern, it can lead to a significant increase in intensity, and is useful to capture more radiation from a horizontally divergent source such as a bending magnet or wiggler.

2.2.3.2. *Mirror*

Some powder-diffraction beamlines are equipped with X-ray mirrors, which can be used to focus or to improve the collimation of the already highly collimated beam, and to act as a high-energy filter for photons with energies above a certain value, *e.g.* to remove higher-order wavelengths transmitted by the monochromator. Usually reflecting in the vertical plane, a mirror consists of a highly polished substrate (*e.g.* Si) with a thin metal coating, such as Pt or Rh, set at grazing incidence. The nature of the coating and the graze angle determine the energy cutoff, where the reflectivity falls to very low values following

$$\theta_c\ [\text{mrad}] = 2.324(\rho Z/A)^{1/2}\lambda\ [\text{Å}],$$

where θ_c is the critical graze angle for X-rays of wavelength λ, ρ is the density, Z is the atomic number and A is the atomic weight of the metal coating. As an example, an Rh-coated mirror set at a grazing incidence of 2 mrad will only reflect X-rays with a wavelength longer than around 0.37 Å. A Pt-coated mirror set at the same graze angle will transmit shorter wavelengths, down to 0.30 Å. The wavelength cutoff for a particular mirror can be adjusted by changing the angle of grazing incidence. However, this then entails realignment of the beamline downstream of the mirror. To avoid this, some beamlines have mirrors with stripes of different metals, allowing adjustment of the cutoff by simply translating the mirror sideways to change the coating while keeping the graze angle constant.

Curving a mirror concavely as shown in Fig. 2.2.8 allows focusing or collimation, following

$$R = \frac{2L_1L_2}{(L_1 + L_2)\sin\alpha},$$

where R is the radius of curvature, L_1 is the source-to-mirror distance, L_2 is the mirror-to-focus distance and α is the angle of grazing incidence. For collimation ($L_2 = \infty$), this reduces to $R = 2L_1/\sin\alpha$. Thus a mirror 25 m from the source set at a graze angle of 2 mrad must be curved to a radius of 25 km to collimate the beam. As noted above, silicon is frequently chosen as a substrate for a mirror as it is sufficiently stiff to help minimize the intrinsic

Figure 2.2.8
Curved mirror set to collimate the beam.

curvature of the mirror caused by its own weight. Even then, very careful mounting and precise mechanics are required to achieve this level of accuracy. If placed in the polychromatic beam directly from the source, cooling of the mirror will be necessary.

Other mirror arrangements can be employed, such as a horizontal and vertical pair of focusing mirrors in a Kirkpatrick–Baez (Kirkpatrick & Baez, 1948) arrangement. Such a device might be used to produce a small focal spot for powder-diffraction measurements from a sample in a diamond anvil cell. Multilayer mirrors can also be found in service on certain beamlines.

2.2.3.3. *Compound refractive lens*

The refractive index n of a material for X-rays is given (Gullikson, 2001; Spiller, 2000) by

$$n = 1 - \delta - i\beta = 1 - \frac{r_e}{2\pi}\lambda^2 \sum_n N_n f_n,$$

where $f_n = f_1 + if_2$ is the complex scattering factor for forward scattering for atom n and N_n is the number of atoms of type n per unit volume. δ and β are known as the refractive index decrement and the absorption index, respectively, and vary with photon energy depending on the proximity of an absorption edge. The real part of the refractive index is therefore slightly less than 1, with δ typically of the order 10^{-6}–10^{-9} depending on the energy. Thus a hole drilled in a piece of metal can act like a conventional convex lens, as the hole has a higher refractive index than the surrounding metal. With such a small difference in n between hole and metal, the focusing power is very slight; however, a series of holes (Fig. 2.2.9) can be used to focus the X-ray beam over a reasonable distance (Snigirev *et al.*, 1997, 1998). For a series of cylindrical lenses, the focal length, f, is given by $f = r/2N\delta$, where r is the radius of the hole and N is the number of holes.

Note that further away from the axis of the device the X-ray beam must pass through increasing amounts of material which absorb the radiation. Hence, only relatively small holes and apertures are possible (a maximum of a few mm in diameter) and weakly absorbing metals such as Be and Al are preferred. With hard-energy photons, Ni lenses are possible, and indeed the construction of such a device is a compromise between refractive power, absorption, aperture and the desired focal length. Such devices can be placed in the monochromatic beam or in a polychromatic beam with cooling.

Many variants of the basic scheme exist, with lenses pressed from foil with a parabolic form to eliminate spherical aberrations, with axial symmetry to focus in both the horizontal and vertical simultaneously (Lengeler *et al.*, 1999), etched *via* lithography from plastic or other material, or with a more complex profile to minimize the amount of redundant material attenuating the transmitted beam by absorption and so allowing a larger aperture. A 'transfocator' can be constructed whereby series of lenses can be accurately inserted or removed from the beam path, thus allowing the focusing power to be adjusted depending on the desired focal distance and the wavelength of the experiment (Vaughan *et al.*, 2011).

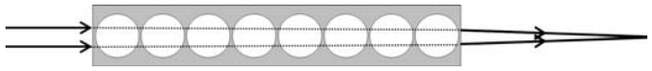

Figure 2.2.9
Schematic diagram of a set of refractive lenses.

2.2.4. Diffractometers

Most powder-diffraction beamlines are angle dispersive, operating with monochromatic radiation. When scanning a detector arm or employing a curved position-sensitive detector (PSD), detection is normally in the vertical plane because the polarization of the radiation in the plane of the synchrotron orbit means there is very little effect on the intensities due to polarization. By contrast, if diffracting in the horizontal plane, the projection of the electric vector onto the direction of the diffracted beam means that the intensity is reduced by a factor of $\cos^2 2\theta$, going to zero at $2\theta = 90°$, and so horizontal detection is less useful unless working at hard energies when 2θ angles are correspondingly small. In addition, for the highest angular resolution, the natural beam divergence in the vertical plane is usually lower than in the horizontal plane, particularly if the instrument has a bending magnet or wiggler as its source.

In general, diffractometers are heavy-duty pieces of equipment and are designed to have excellent angular accuracy while working with substantial loads. A high degree of mechanical accuracy is required to match the high optical accuracy inherent in the techniques employed. The calibration of the incident wavelength and any 2θ zero-point error is best done by measuring the diffraction pattern from a sample such as NIST standard Si (640 series), each of which has a certified lattice parameter (see Chapter 3.1). It is also good practice to measure the diffraction pattern of a standard sample regularly and whenever the instrument is realigned or the wavelength changed, to be sure that everything is working as expected.

Monochromatic instruments can have an analyser crystal or long parallel-foil collimators in the diffracted beam (a so-called parallel-beam arrangement), or can scan a receiving slit, or possess a one- or two-dimensional PSD, similar to Debye–Scherrer or Laue front-reflection geometry. Instruments equipped with a PSD can collect data much faster than those with a scanning diffractometer, so are exploited especially for time-resolved measurements. They may also have advantages for rapid data collection if the sample is sensitive to radiation, or be helpful if the sample is prone to granularity or texture to assess the extent of the problem.

Instruments can also be equipped with a sample changer, allowing measurements on a series of specimens, perhaps prepared by systematically changing the conditions of synthesis or the composition in a combinatorial approach. The use of beam time can be optimized with minimal downtime due to interventions around the instrument, and with the possibility to control the data acquisition remotely if desired.

2.2.4.1. *Parallel-beam instruments*

Cox *et al.* (1983, 1986), Hastings *et al.* (1984) and Thompson *et al.* (1987) described the basic ideas behind these instruments *via* their pioneering work at CHESS (Cornell, USA) and NSLS (Brookhaven, USA). The highly collimated monochromatic

incident beam is diffracted by the sample and passes *via* a perfect analyser crystal [such as Si or Ge(111)] to the detector. The analyser crystal defines a very narrow angular acceptance for the diffracted radiation, determined by its Darwin width. The combination of the collimation of the incident radiation, its highly monochromatic nature and the stringent angular acceptance defines the instrument's excellent angular resolution. The detector arm supporting the analyser is scanned through the desired range of 2θ angles either in a step-scan mode or continuously, reading out at very short intervals the electronic modules that accumulate the detector counts.

To be transmitted by the analyser crystal, a photon must be incident on the crystal at the correct angle θ_a that satisfies the Bragg condition. The analyser crystal defines therefore a true direction (2θ angle) for the diffracted beam irrespective of where in the sample it originates from. This removes a number of aberrations that affect diffractometers with a scanning slit or PSD where the 2θ angle is inferred from the position of the slit or detecting pixel. Thus, with a capillary specimen, peak widths are independent of the capillary diameter, so a fat capillary of non-absorbing sample can be used to optimize diffracted intensity, and any modest misalignment of the sample from the diffractometer axis, or specimen transparency or surface roughness for flat-plate samples, does not lead to shifts in the peak positions. Modest movement of the sample with temperature changes in a furnace *etc*. does not cause shifts in peak positions. These instruments are therefore highly accurate, and are ideal for obtaining peak positions for indexing a diffraction pattern of a material of unknown unit cell (the first step in the solution of a structure from powder data), or following the evolution of lattice parameter with temperature *etc*. For flat samples, the $\theta/2\theta$ parafocusing condition does not need to be satisfied to have high resolution. The peak width does not therefore depend on sample orientation, which is useful for measurements of residual strain by the $\sin^2\psi$ technique or for studying surfaces and surface layers by grazing-incidence diffraction. Interchange between capillary and flat-plate samples can easily be done as required without major realignment of the instrument. The stringent acceptance conditions also help to suppress parasitic scattering originating from sample-environment windows *etc*. and inelastic scattering such as fluorescence and Compton scattering.

On the other hand, at any 2θ angle only a tiny fraction of the diffracted photons can be transmitted by an analyser crystal, so this is a technique that consumes a lot of photons, and the high incident flux is essential to keep scan times to reasonable values. To overcome this, at least to some extent, Hodeau *et al.* (1998) devised a system of multiple analyser crystals, with nine channels mounted in parallel, each separated from the next by 2° (Fig. 2.2.10). In effect, as the detector arm is scanned, nine high-resolution powder-diffraction patterns are measured in parallel, each offset from the next by 2°. If the data from the channels are to be combined, which is the usual procedure, the detectors must be calibrated with respect to each other, in terms of counting efficiency and exact angular offset, by comparing regions of the diffraction pattern scanned by several detectors (Wright *et al.*, 2003). A multianalyser system speeds up data collection significantly and can be found in various modified forms at a number of powder-diffraction beamlines (*e.g.* Lee, Shu *et al.*, 2008).

The multianalyser approach is best suited to capillary samples because of the axial symmetry of the arrangement. With flat plates in reflection, only one detector can be in the $\theta/2\theta$ condition where the effect of specimen absorption (for a sufficiently thick sample) is isotropic. Corrections must therefore be made to the intensities from the other channels (Lipson, 1967; Koopmans & Rieck, 1968). For a capillary, choosing the wavelength and the diameter allows absorption to be kept to an acceptable value. Maximum diffracted intensity is expected at $\mu r = 1$ (where μ is the linear absorption coefficient and r the radius of the capillary), and below this value simple absorption corrections can be applied (Hewat, 1979; Sabine *et al.*, 1998). A value of μr greater than 1.5 begins to degrade the quality of the pattern significantly. If a sample with high absorption is unavoidable, such as when working close to an absorption edge of an element, *e.g.* the *K* edge of Mn at 6.539 keV (1.896 Å), then it can be preferable to stick a thin layer of sample on the outside of a 1-mm-diameter capillary. The shell-like nature of the sample has no effect on the peak shape or resolution because of the use of analyser crystals.

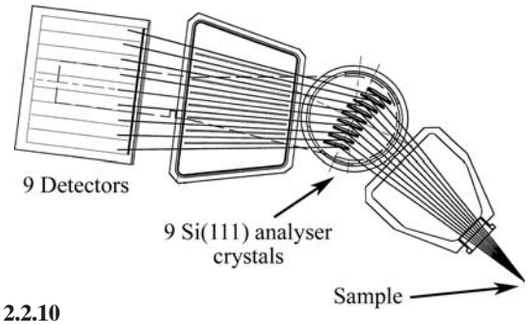

Figure 2.2.10
Multianalyser stage, nine channels separated by 2°, devised by Hodeau *et al.* (1998), originally installed on the BM16 bending-magnet beamline at the ESRF with Ge(111) analyser crystals. With an undulator source, the greatly increased flux allows use of Si(111), which has a narrower Darwin width (by a factor of ∼2.4) and thus improved 2θ resolution, but with a lower fraction of the diffracted radiation accepted.

Capillaries also have the advantage that preferred orientation can be significantly less as compared to a flat sample, where there is a tendency for crystallites to align in the surface layers, especially if compressed to hold the powder in place. Spinning or otherwise moving the sample is necessary, whether capillary or flat plate, to increase the number of crystallites appropriately oriented to fulfil the Bragg condition and avoid a spotty diffraction pattern, the likelihood of which is exacerbated by the highly collimated nature of the incident radiation.

2.2.4.1.1. *Angular resolution*

Various authors (*e.g.* Sabine, 1987*a*,*b*; Wroblewski, 1991; Masson *et al.*, 2003; Gozzo *et al.*, 2006) have discussed the resolution of a synchrotron-based diffractometer equipped with a double-crystal monochromator and an analyser crystal. The most usual setting of the diffracting crystals, ignoring any mirrors or other optical devices, is non-dispersive, alternatively described as parallel or (1, −1, 1, −1).

The approach developed by Sabine (1987*a*,*b*) involves modelling the vertical divergence of the source and the angular acceptance of the monochromator and analyser crystals as Gaussian distributions with the same full width at half-maximum (FWHM) as the real distributions, and considering a powder as a crystal with an infinite mosaic spread. The rocking curve of the analyser crystal (equivalent to rocking 2θ) is given by

$$I(\beta) = \int\int \mathrm{d}\alpha\,\mathrm{d}\delta \exp\left\{-\left[\left(\frac{\alpha}{\alpha'_m}\right)^2 + 2\left(\frac{\delta-\alpha}{\Delta'_m}\right)^2 + \left(\frac{b\delta+\alpha-\beta}{\Delta'_a}\right)^2\right]\right\},$$

where

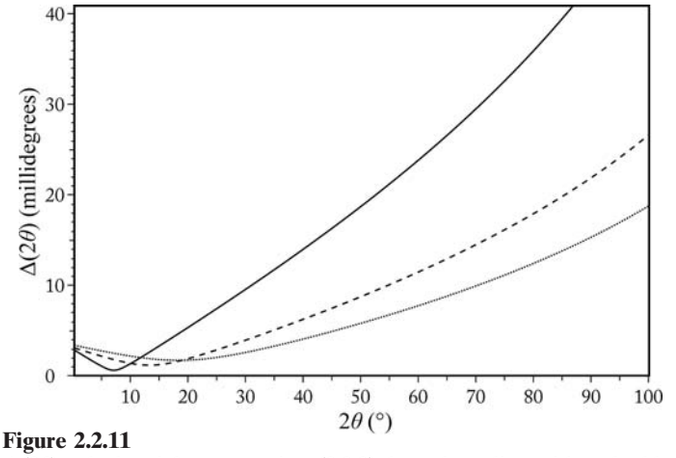

Figure 2.2.11
$\Delta(2\theta)$ calculated from equation (2.2.2) for a beamline with a double-crystal Si(111) monochromator, an Si(111) analyser ($\Delta_m = \Delta_a$ and $\theta_m = \theta_a$) and an FWHM vertical divergence of 25 μrad at $\lambda = 0.4$ Å (solid line: $\Delta_m \simeq 8.3$ μrad, $\theta_m = 3.6571°$), $\lambda = 0.8$ Å (dashed line: $\Delta_m \simeq 16.6$ μrad, $\theta_m = 7.3292°$) and $\lambda = 1.2$ Å (dotted line: $\Delta_m \simeq 25.2$ μrad, $\theta_m = 11.0319°$).

$$b = \tan\theta_a/\tan\theta_m - 2\tan\theta/\tan\theta_m.$$

Here α represents the vertical divergence from the source, δ is the difference between the Bragg angles of a central ray reflected from the monochromator at the angle θ_m and of another ray at angle θ'_m such that $\delta = \theta'_m - \theta_m$, and θ_a is the Bragg angle of the analyser crystal. The terms α'_m, Δ'_m and Δ'_a are related to the FWHM of the Gaussians representing the vertical divergence distribution or the Darwin widths of the monochromator and analyser crystals, α_m, Δ_m and Δ_a, respectively, with

$$\alpha'_m = \alpha_m/2(\ln 2)^{1/2}, \quad \Delta'_m = \Delta_m/2(\ln 2)^{1/2}, \quad \Delta'_a = \Delta_a/2(\ln 2)^{1/2}.$$

From the above equation, the intrinsic FWHM of the Gaussian-approximated peaks of the powder-diffraction pattern can be obtained as

$$\Delta^2(2\theta) = \alpha_m^2\left(\frac{\tan\theta_a}{\tan\theta_m} - 2\frac{\tan\theta}{\tan\theta_m} + 1\right)^2 + \tfrac{1}{2}\Delta_m^2\left(\frac{\tan\theta_a}{\tan\theta_m} - 2\frac{\tan\theta}{\tan\theta_m}\right) + \Delta_a^2. \quad (2.2.2)$$

Note that the true peak shape is not Gaussian, and a pseudo-Voigt (*e.g.* as described by Thompson *et al.*, 1987), Voigt (*e.g.* Langford, 1978; David & Matthewman, 1985; Balzar & Ledbetter, 1993) or other function modelled from first principles (*e.g.* Cheary & Coelho, 1992; Ida *et al.*, 2001, 2003) is usually better. Examples of FWHM curves calculated from equation (2.2.2) are plotted in Fig. 2.2.11 at three wavelengths. Differentiating the Bragg equation gives $\Delta d/d = -\cot\theta\,\Delta(\theta)$, where θ is in radians.

Gozzo *et al.* (2006) have extended the formulation of Sabine to include the effects of collimating and focusing mirrors in the overall scheme. Axial (horizontal) divergence of the beam between the sample and the detector causes shifts and broadening of the peaks, as well as the well known low-angle peak asymmetry due to the curvature of the Debye–Scherrer cones. Sabine (1987*b*), based on the work of Hewat (1975) and Hastings *et al.* (1984), suggests the magnitude of the broadening, $B(2\theta)$, due to horizontal divergence Φ can be estimated *via*

$$B(2\theta) = (\tfrac{1}{4}\Phi)^2(\cot 2\theta + \tan\theta_a),$$

where B and Φ are in radians. This value is added to $\Delta(2\theta)$.

2.2.4.1.2. *Hart–Parrish design*

A variant of the parallel-beam scheme replaces the analyser crystal with a set of long, fine Soller collimators (Parrish *et al.*, 1986; Parrish & Hart, 1987; Parrish, 1988; Cernik *et al.*, 1990; Collins *et al.*, 1992) (Fig. 2.2.12). The collimators define a true angle of diffraction, but with lower 2θ resolution than an analyser crystal because their acceptance angle is necessarily much larger and so the transmitted intensity is greater. They are not particularly suitable for fine capillary specimens, as the separation between foils may be similar to the capillary diameter, resulting in problems of shadowing of the diffracted beam. However, they are achromatic, and so do not need to be reoriented at each change of wavelength, which may have advantages when performing anomalous-scattering studies around an element's absorption edge. Unlike an analyser crystal, however, they do not suppress fluorescence. Peak shapes and resolution can be influenced by reflection of X-rays from the surface of the foils, or any imperfections in their manufacture, *e.g.* if the blades are not straight and flat. The theoretical resolution curve of such an instrument can be obtained from equation (2.2.2) by setting $\tan\theta_a$ to zero and replacing the angular acceptance of the analyser crystal Δ_a with the angular acceptance of the collimator Δ_c.

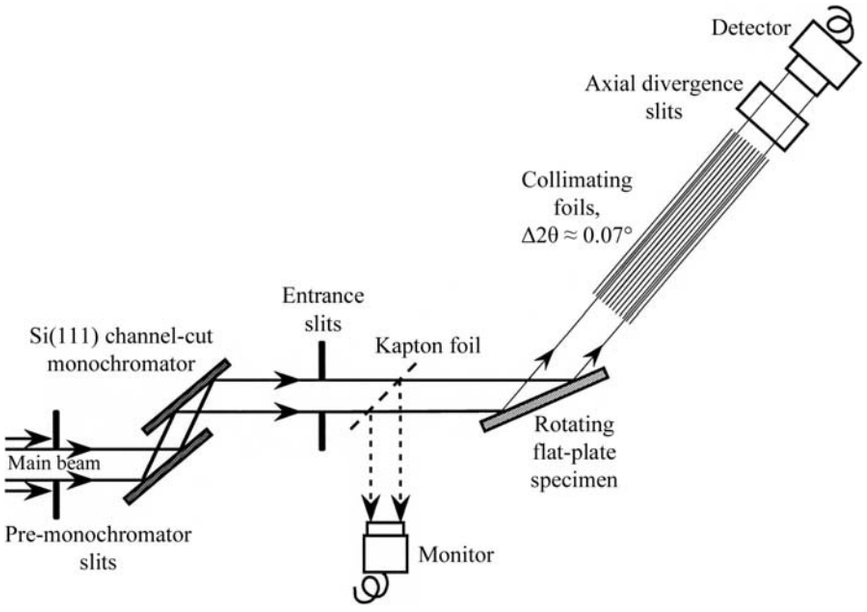

Figure 2.2.12
Schematic representation of a parallel-beam diffractometer of the Hart–Parrish design. The collimators installed on Stations 8.3 and 2.3 at the SRS Daresbury (Cernik *et al.*, 1990; Collins *et al.*, 1992) had steel blades 50 μm thick, 355 mm long, separated by 0.2 mm spacers, defining a theoretical opening angle (FWHM Δ_c) of 0.032° and a transmission of 80%.

2.2.4.2. *Debye–Scherrer instruments*

The simplest diffractometer has a receiving slit at a convenient distance from the sample in front of a point detector such as a scintillation counter. The height of the slit should match the capillary diameter, or incident beam height for flat plates. A slightly larger antiscatter slit near the sample should also be employed to reduce

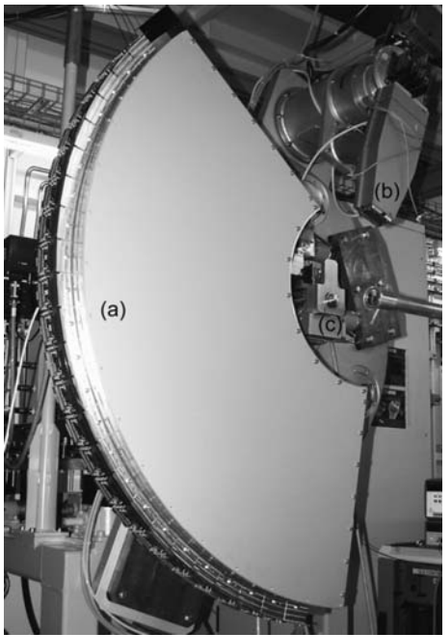

Figure 2.2.13
(*a*) 120° Mythen detector box, containing helium, mounted on the powder diffractometer of the materials science beamline at the Swiss Light Source. (*b*) Multianalyser detector stage. (*c*) Capillary spinner. (Bergamaschi *et al.*, 2009, 2010.)

background. The detector arm is scanned and a powder pattern recorded. This arrangement can be used for narrow capillary samples on lower-flux sources, avoiding the loss of intensity that use of an analyser crystal entails. The resolution is largely determined by the opening angle defined by the capillary and the receiving slit. Despite the simplicity of such an instrument, high-quality high-resolution data can be obtained.

For much faster data acquisition, a one-dimensional (1D) PSD or an area detector can be employed. Any sort of 1D detector with an appropriate number of channels, channel separation, efficiency, count rate (in an individual channel and overall) and speed of read out can be employed. Technology evolves and detectors make continual progress in performance. At the time of writing the most advanced 1D detector is the Mythen module developed by the Swiss Light Source (SLS). Mythen modules are based on semiconducting silicon technology and have 1280 8-mm-wide strips with a 50 μm pitch (64 × 8 mm^2). They can be combined to form very large curved detectors such as that on the powder diffractometer of the materials science beamline at the SLS (Fig. 2.2.13). This detector consists of 24 modules, 30 720 channels, set on a radius of 760 mm, covering 120° 2θ. Detector elements are therefore separated by ∼0.004°. The whole detector can be read out in 250 μs. Being Si based, its efficiency falls off above 20–25 keV, where the absorbing power of Si falls to very small values. Nevertheless, at intermediate and low energies a full powder-diffraction pattern for structural analysis can be measured in just seconds, or even faster if the intention is to follow a dynamic process.

Two-dimensional (2D) detectors are generally flat, so cannot extend to the same 2θ values as a curved multistrip detector unless scanned on a detector arm. This is possible, but usually a short wavelength is used with a fixed detector. This allows an adequate data range to be recorded, particularly if the detector is positioned with the direct beam ($2\theta = 0$) near an edge. A 2D detector records complete or partial Debye–Scherrer rings, which increases the counting efficiency with respect to scanning an analyser crystal by several orders of magnitude. In addition, if the rings do not appear smooth and homogeneous, this indicates problems with the sample, such as preferred orientation or granularity, both of which can seriously affect diffraction intensities when measuring just a thin vertical strip. Detectors that have been used are diverse and include image plates, though these have slow read out, charge-coupled devices (CCDs) or Si-based photon-counting pixel detectors used for single-crystal diffraction or protein crystallography (*e.g.* Broennimann *et al.*, 2006), and medical-imaging detectors, which are designed for hard-energy operation. Examples include the CCD-based Frelon camera, developed at the ESRF (Labiche *et al.*, 2007), and commercially available large flat-panel medical-imaging detectors up to 41 × 41 cm^2, based on scintillator-coated amorphous silicon, which have been exploited at speeds of up to 60 Hz for selected read-out areas (Chupas, Chapman & Lee, 2007; Lee, Aydiner *et al.*, 2008; Daniels & Drakopoulos, 2009).

Note that a 2D detector can be used as a 1D detector by applying a mask and reading out only a narrow strip, which can enhance the rate of data acquisition. For CCD chips, the electronic image can be rapidly transferred to pixels behind the masked part of the detector from where it can be read out while the active area is re-exposed. Translating an image plate behind a mask is a simple way of acquiring a series of diffraction patterns for following a process with modest time resolution.

These instruments are vulnerable to aberrations that cause systematic shifts in peak positions, such as misalignment of the capillary or surface of the sample from the diffractometer axis, and specimen transparency, which also affects the peak width and shape. The peak width also depends on whether a flat sample is in the $\theta/2\theta$ condition, or on the diameter of a capillary sample, *etc*. Focusing the incident beam onto the detector decreases the peak width, as fewer pixels are illuminated compared to using a highly collimated incident beam. PSDs are much more open detectors than those behind an analyser crystal or set of slits, so are more susceptible to background and parasitic scatter from sample environments *etc*. However, the speed and efficiency of data acquisition usually outweigh such concerns.

2.2.4.3. *Energy-dispersive instruments*

The broad, continuous spectrum from a wiggler or bending magnet is suitable for energy-dispersive diffraction (EDD). Here, the detector is fixed at an angle 2θ and the detector determines the energy, ε, of each arriving photon scattered by the sample (Fig. 2.2.14). The energy [keV] can be converted to d-spacing [Å] *via*

$$d \simeq 12.3984/2\varepsilon \sin\theta.$$

The detector usually consists of a cryogenically cooled semiconducting Ge diode. An absorbed X-ray photon promotes electrons to the conduction band in proportion to its energy. By

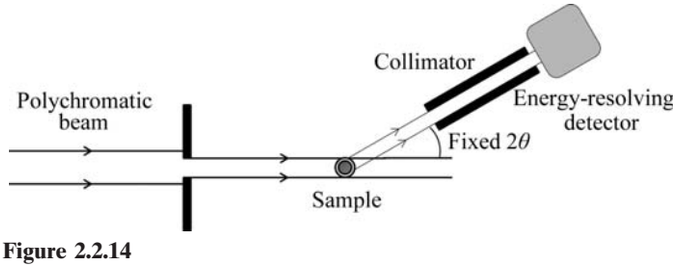

Figure 2.2.14
Schematic representation of an energy-dispersive diffraction arrangement.

analysing the size of the charge pulse produced, the energy of the photon is determined. The powder-diffraction pattern is recorded as a function of energy (typically somewhere within the range 10–150 keV, depending on the source) *via* a multichannel analyser (MCA). Instruments may have multiple detectors, at different 2θ angles covering different ranges in d-spacing (Barnes *et al.*, 1998), or arranged around a Debye–Scherrer ring, as in the 23-element semi-annular detector at beamline I12 at Diamond Light Source (Korsunsky *et al.*, 2010; Rowles *et al.*, 2012).

Prior to performing the EDD experiment, the detector and MCA system must be calibrated, *e.g.* by measuring signals from sources of known energy, such as ^{241}Am (59.5412 keV) or ^{57}Co (122.06014 and 136.4743 keV) at hard energies, and/or from the fluorescence lines of elements such as Mo, Ag, Ba *etc*. The 2θ angle also needs to be calibrated if accurate d-spacings are desired. This should be done by measuring the diffraction pattern of a standard sample with known d values.

The detector angle is typically chosen in the range 2–6° 2θ and influences the range of d-spacings accessible *via* the term $1/\sin\theta$, *i.e.* the lower the angle, the higher the energy needed to access any particular d. Normally, the range of most interest should be matched to the incident spectrum, taking account also of sample absorption and fluorescence, to produce peaks with high intensity. More than one detector at different angles can also be employed. Energy-sensitive Ge detectors do not count particularly fast, up to 50 kHz being a typical value compared to possibly 1–2 MHz with a scintillation detector. Hence they are relatively sensitive to pulse pile-up and other effects of high count rates (Cousins, 1994; Laundy & Collins, 2003; Honkimäki & Suortti, 2007), particularly if the synchrotron is operating in a mode with a few large electron bunches giving very intense pulses of X-rays on the sample.

The energy resolution of the detector is of the order of 2%, which dominates the overall resolution of the technique. Its main uses are where a fixed geometry with penetrating X-rays is required, *e.g.* in high-pressure cells, for *in situ* studies (Häusermann & Barnes, 1992), *e.g.* of chemical reactions under hydrothermal conditions (Walton & O'Hare, 2000; Evans *et al.*, 1995), electrochemistry (*e.g.* Scarlett *et al.*, 2009; Rijssenbeek *et al.*, 2011; Rowles *et al.*, 2012), or measurements of residual strain (Korsunsky *et al.*, 2010). Owing to the use of polychromatic radiation, the technique has very high flux on the sample and can be used for high-speed data collection, following rapid processes *in situ*. However, accurate modelling of the intensities of the powder-diffraction pattern for structural or phase analysis is difficult because of the need to take several energy-dependent effects into account, *e.g.* absorption and scattering factors, the incident X-ray spectrum, and the detector response. Nevertheless, examples where this has been successfully carried out have been published (*e.g.* Yamanaka & Ogata, 1991; Scarlett *et al.*, 2009).

A higher-resolution variant of the energy-dispersive technique can be performed by using a standard detector behind a collimator at fixed 2θ scanning the incident energy *via* the monochromator. The Hart–Parrish design with long parallel foils is suitable. Such an approach has been demonstrated in principle (Parrish, 1988), but is rarely used in practice. The advantage is to be able to measure data of improved d-spacing resolution, as compared to using an energy-dispersive detector, from sample environments with highly restricted access. In principle, as a further variant, white incident radiation could be used with scanning of θ_a, the angle of the analyser crystal, and associated detector at $2\theta_a$, all at fixed 2θ.

2.2.5. Considerations for powder-diffraction experiments

Synchrotron radiation allows considerable flexibility for a powder-diffraction experiment, offering choice and optimization of a number of quantities such as the wavelength, with high energy resolution, range in d-spacing, angular resolution, angular accuracy, and spatial or time resolution (but not all of these can necessarily be optimized at the same time). Increasingly, powder-diffraction experiments at synchrotrons are combined with complementary measurements, simultaneously applying techniques such as Raman spectroscopy (Boccaleri *et al.*, 2007; Newton & van Beek, 2010), particularly when carrying out *in situ* studies of an evolving system. In this respect, the open nature of a synchrotron instrument, with space around the sample to position auxiliary equipment, is an advantage.

2.2.5.1. *Polarization*

Assuming the beam is 100% polarized in the horizontal plane of the synchrotron orbit and with detection in the vertical plane, there is no need for any polarization correction to the diffracted intensities. However, if a small amount of vertical polarization of the beam does need to be taken into account (possibly up to a few per cent depending on the source), the polarization factor that describes its effect on the intensity of the diffracted beam can be derived, following the approach of Azároff (1955) and Yao & Jinno (1982), as

$$P = \frac{1 - dp + dp\cos^2 2\theta\cos^2 2\theta_a}{1 - dp + dp\cos^2 2\theta_a} = \frac{1 - dp + dp\cos^2 2\theta\cos^2 2\theta_a}{1 - dp\sin^2 2\theta_a}, \tag{2.2.3}$$

where dp is the depolarization fraction (*i.e.* the fraction of the total intensity incident on the sample that is vertically polarized), $2\theta_a$ is the Bragg angle of the analyser crystal (if any), and the denominator scales P to unity at 2θ equal to zero (Dwiggins, 1983) and is a constant for any particular experimental setup. If there is no analyser crystal, or we ignore the effect it would have (*i.e.* by putting $2\theta_a = 0$), then

$$P = 1 - dp\sin^2 2\theta.$$

Beamline staff can usually advise on the appropriate values to use. These expressions reduce to the usual polarization factor for unpolarized (dp = 0.5) laboratory X-rays without a monochromator or analyser crystal, $\frac{1}{2}(1 + \cos^2 2\theta)$.

An alternative formulation of equation (2.2.3) considers the ratio of the vertical to horizontal polarization,

$$rp = \frac{dp}{1 - dp} \quad \text{and} \quad dp = \frac{rp}{1 + rp},$$

so that

$$P = \frac{1 + rp\cos^2 2\theta\cos^2 2\theta_a}{1 + rp\cos^2\theta_a}. \tag{2.2.4}$$

Note that rp = 1.0 for unpolarized (laboratory) X-rays. In reality, because the synchrotron beam is near 100% plane polarized, dp and rp have similar values. The same expressions can be used if diffracting and analysing in the horizontal plane, except that now the value of dp or rp is replaced with the value of $(1 - dp)$ or $1/rp$, respectively.

For Debye–Scherrer rings detected on a 2D detector, the azimuthal angle around the ring needs to be taken into account, yielding

$$P = (1 - dp)(\cos^2 2\theta \sin^2 \kappa + \cos^2 \kappa) + dp(\cos^2 2\theta \cos^2 \kappa + \sin^2 \kappa)$$

or

$$P = \frac{(\cos^2 2\theta \sin^2 \kappa + \cos^2 \kappa) + rp(\cos^2 2\theta \cos^2 \kappa + \sin^2 \kappa)}{1 + rp},$$

where κ is the azimuthal angle (zero in the vertical direction) (Rowles *et al.*, 2012).

2.2.5.2. *Radiation damage*

The intensity of the incident beam can be so high that radiation damage becomes a real concern, particularly for samples containing organic molecules, such as pharmaceuticals, or organometallic materials. Radiation damage manifests itself by progressive shifts (often anisotropic) in the peak positions, a general reduction in peak intensities and peak broadening as the sample's crystallinity degrades. With high-resolution data, the effects are easily seen and can appear after only a few seconds in the worst cases. In such circumstances it may be better to use a 1D or 2D PSD to collect data of sufficient statistical quality before the damage is too severe. However, if the highest-resolution data are required, *via* scanning an analyser crystal, then the problem can be alleviated by filling a long capillary with sample and translating it between scans to expose fresh sample to the beam, thus acquiring multiple data sets which can be summed together. Such an approach necessarily requires a sufficient amount of disposable sample. If attempting to study the evolution of a particular part of the sample, *e.g.* undergoing heat treatment in the beam, then substituting fresh sample is not necessarily an option, and radiation damage can be a frustrating hindrance.

2.2.5.3. *Beam heating*

With a photon intensity of the order 10^{12} photons $\text{mm}^{-2}\,\text{s}^{-1}$ incident on the sample – a possible value for the unfocused beam on a beamline based on an insertion device at a modern third-generation source – the power in the beam corresponds to a few mW mm^{-2}. If a small fraction is absorbed by the sample this can represent a significant heat load that becomes troublesome when trying to work with samples at cryogenic temperatures, where heat capacities are relatively low.

As an example, consider a sample of microcrystalline silicon, composed of cubic 1 μm^3 grains irradiated by a 31 keV beam (0.4 Å wavelength) with 10^{12} photons $\text{mm}^{-2}\,\text{s}^{-1}$. The power of the beam is 5 mW mm^{-2} ($31 \times 10^3\ e \times 10^{12}$ W mm^{-2}). The mass absorption coefficient of Si at 0.4 Å wavelength $\mu/\rho \simeq 1.32\ \text{cm}^2\ \text{g}^{-1}$ (Milledge, 1968) leading to a linear absorption coefficient of $3.1\ \text{cm}^{-1}$ (density of Si = $2.33\ \text{g cm}^{-3}$). Any problems with absorption by such a sample might usually be discounted; for a 1-mm-diameter capillary the value of μr is 0.1, assuming the powder density is 2/3 of the theoretical density.

A single 1-μm^3 grain of cross section 1 μm^2 is hit by 10^6 photons s^{-1}, of which a small fraction are absorbed,

$$\begin{aligned}\text{photons absorbed} &= 10^6[1 - \exp(-3.1 \times 10^{-4})] \\ &= 310\ \text{photons s}^{-1},\end{aligned}$$

corresponding to an absorbed power of 1.54×10^{-12} W. Not all this energy is retained; significant amounts are lost as fluorescence, Compton scatter *etc*. Consultation of tables of mass attenuation coefficients and mass energy-absorption coefficients (Hubbell, 1982; Seltzer, 1993) indicates that for Si at 31 keV about 80% of the energy is retained, thus a net heating power of 1.2×10^{-12} W. The mass of the Si grain is 2.33×10^{-15} kg. At ambient temperature, where the specific heat capacity of Si is $704.6\ \text{J kg}^{-1}\,\text{K}^{-1}$, this leads to an instantaneous tendency to increase the temperature by $\sim 0.7\ \text{K s}^{-1}$. At cryogenic temperatures, *e.g.* 10 K, the specific heat capacity is over three orders of magnitude lower, $0.28\ \text{J kg}^{-1}\,\text{K}^{-1}$ (Desai, 1986), leading to a very strong tendency for the temperature to rise ($1840\ \text{K s}^{-1}$). The extent of the potential problem varies depending on the real net absorption of energy of the sample at the wavelength being used. However, it is clear that to prevent local beam-heating effects, the absorbed energy must be removed from the sample as efficiently as possible, *i.e.* by having excellent thermal contact between the grains of the sample and the external medium. At cryogenic temperatures this can be accomplished *via* the He exchange gas in the cryostat. Thus, if using a capillary sample, the capillary must either be left unsealed, to allow the He to permeate between the grains of sample, or it must be sealed under He, allowing transport of the heat to the walls of the capillary. Sealing under air, nitrogen, argon or other atmosphere leads to a loss of heat-transport capability when the gas solidifies, with consequent unpredictable behaviour for the sample caused by the beam-heating effects. This can involve significant shifts in peak positions and peak broadening depending on the instantaneous local temperature gradients. The problems tend to be worse at softer energies, where X-ray absorption is generally higher. Notwithstanding the potential problems, good-quality low-temperature data can be measured with appropriate care.

2.2.5.4. *Choice of wavelength*

The tunability of synchrotron radiation allows the wavelength best suited to the measurements to be selected. The collimation of the beam from the source combined with a perfect crystal monochromator lead automatically to high energy resolution, with a narrow wavelength distribution about a mean value. Consequently there are no issues to contend with such as α_1, α_2 doublets or other effects due to a composite incident spectrum, contributing to a relatively simple instrumental peak-shape function. High energy resolution is essential for high 2θ resolution, because, as shown in equation (2.2.1), the effect of the energy envelope is to broaden the diffraction peaks as 2θ increases.

In choosing the wavelength for an experiment, factors to consider include:

(*a*) The optimum operational range for the beamline to be used, which will principally depend on the characteristics of the source.

(*b*) Absorption: choosing a sufficiently hard energy generally reduces absorption and allows the use of a capillary specimen in transmission for a wide range of compounds, *e.g.* those containing transition metals or heavier elements, thus minimizing preferred orientation. Selecting the energy a little way below (in energy) the K or L_{III} absorption edge of an element in the sample may help minimize sample absorption. For any sample or series of samples, it is good practice in the planning of the experiment to calculate the linear absorption coefficient to assess the optimum capillary diameter, the wavelength to use and those to avoid.

(*c*) The use of hard energies can be advantageous for penetration through sample environments, although these should normally, as much as possible, be designed with appropriate X-ray windows *etc*. However, when absorbing environments are unavoidable, such as containing a sample in a spinning Pt

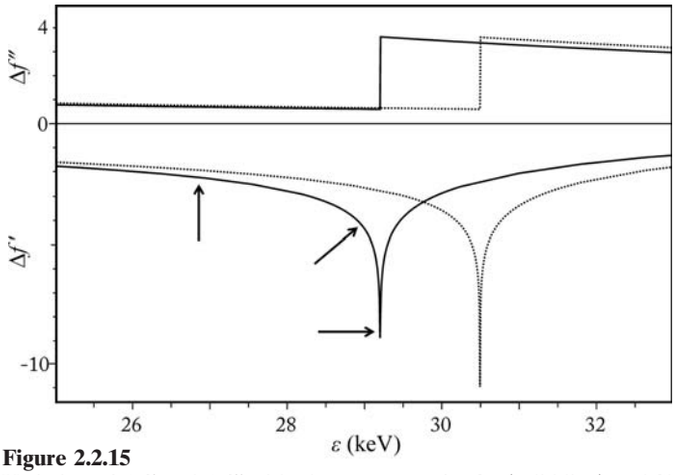

Figure 2.2.15
Variation of $\Delta f'$ and $\Delta f''$ with photon energy for Sn (solid line) and Sb (dotted line) in the vicinity of their K absorption edges (from the tables of Sasaki, 1989). An anomalous-scattering experiment seeking to distinguish the arrangement of the two elements could make measurements at the Sn edge (29.2001 keV), at a few eV below the edge and at an energy significantly removed from the edge (arrows). Equivalent measurements could be made at the Sb edge (30.4912 keV), but as this is above the energy of the Sn edge careful attention must be paid to the increase in the sample's absorption (reflected in the values of $\Delta f''$).

capillary for heating to very high temperatures, then high energy can be a major benefit.

(*d*) Hard energies are essential to measure to high Q values, where $Q = 4\pi \sin\theta/\lambda = 2\pi/d$. For pair distribution function (PDF) analysis, data to $Q > 25$ Å^{-1} ($d < 0.25$ Å) or more are required, with patterns of good statistical quality. Such Q values are not possible with Mo or Ag radiation (Ag $K\alpha$, λ = 0.56 Å, $Q \simeq 22$ Å^{-1} at $2\theta = 160°$), but are easily accessible at λ = 0.4 Å (31 keV) by scanning to 2θ = 106°. At 80.7 keV (0.154 Å, ten times shorter than Cu $K\alpha$) patterns to $Q \simeq$ 35 Å^{-1} can be obtained in minutes (even seconds) with a large stationary medical-imaging flat-panel detector (Lee, Aydiner *et al.*, 2008). Even for more classical powder-diffraction experiments, access to data for high Q values can be advantageous for Rietveld refinement of crystal structures, or for measuring several orders of reflections for peak-shape analysis in the investigation of microstructure.

(*e*) Anomalous scattering: performing measurements near the absorption edge of an element in a sample and away from that edge gives element-specific changes in the diffraction intensities, enhancing the experiment's sensitivity to that element (Fig. 2.2.15). The approach can be complimentary to isotopic substitution in a neutron-diffraction experiment or may be the only option when no suitable isotope is available. Good energy resolution is important for these experiments. The values of $\Delta f'$ and $\Delta f''$ vary sharply over only a few eV at the edge, so poor energy resolution would average the abruptly changing values over too broad a range to the detriment of elemental sensitivity and sample absorption if part of the wavelength envelope strays above the edge. Moreover, it is necessary to know accurately where on the edge the measurement is being made to allow the correct values of $\Delta f'$ and $\Delta f''$ to be used in the data analysis. Tables of values have been calculated (*e.g.* Sasaki, 1989), but these do not take account of shifts in an edge due to the oxidation state(s) and chemical environment(s) of the elements. It is advisable to measure the fluorescence of the sample as the energy is scanned through the edge (by varying the monochromator angle θ_m) and then use the Kramers–Kronig relation to calculate the variation of $\Delta f'$ and $\Delta f''$ with energy. A program such as *CHOOCH* (Evans & Pettifer, 2001) allows this to be done.

(*f*) A wavelength greater than 1 Å may be best when working with large unit cells, such as found for proteins, organic molecules or organometallic compounds. Using a long wavelength helps by moving the diffraction pattern to higher 2θ values, away from the zone most affected by background air scatter or masked by the beam stop, and to where the peak asymmetry due to axial beam divergence is less severe. Longer wavelengths are also useful when working in reflection with plate samples to minimize beam penetration and thus enhance sensitivity to the surface regions, *e.g.* in the study of surfaces or coatings.

(*g*) The broad continuous spectrum available from a bending magnet or wiggler allows powder-diffraction measurements *via* the energy-dispersive approach, which is exploited when geometric considerations of the sample or environment mean that a restricted range of 2θ values is accessible or when attempting to obtain the maximum time resolution from a source, as a larger fraction of the photons from the source can be exploited.

2.2.5.5. *Angular resolution*

The highest angular resolution is obtained from a diffractometer equipped with an analyser crystal such as Si(111) or Ge(111). This also gives the robust parallel-beam optical configuration so that peak positions are accurately determined. For well crystallized high-quality samples, peak FWHMs of a few millidegrees are possible, thus maximizing the resolution of reflections with similar d-spacings. For less ideal samples, which represent the majority, microstructural effects broaden the peaks, and indeed high-resolution synchrotron data are exploited for detailed investigation of peak shapes and characterization of a range of properties such as crystallite size, microstrain (Chapter 5.2), defects, chemical homogeneity *etc*. Accurate high-resolution data are particularly useful for solving crystal structures from powders (Chapter 4.1), increasing the possibilities for indexing the powder diffraction pattern (Chapter 3.4), assessing the choice of possible space groups, and providing high-quality data for the structural solution and refinement steps. With a high-resolution pattern, the maximum amount of information is stored in the complex profile composed from the overlapping peaks.

2.2.5.6. *Spatial resolution*

Focusing the X-ray beam gives improved spatial resolution, *e.g.* for studying a small sample contained in a diamond anvil cell at high pressure. A beam with dimensions of a few μm can be obtained, though at the expense of the divergence of the beam arriving at the sample. In such cases the use of a 2D detector to record the entire Debye–Scherrer rings will be required to accumulate the diffraction pattern in a reasonable time and to reveal any problems with preferred orientation or granularity in the sample. With a very small sample only a few grains may be correctly oriented to provide each powder reflection. Alternatively, provided the intensity of the beam is high enough, simply cutting down the beam size with slits may be appropriate, *e.g.* to map residual strain in a weld or mechanical component where a spatial resolution on the 50–100 μm scale may be required. Smaller beam sizes may not be useful if they are comparable to the intrinsic grain size of the material, thus leading

to a poor statistical average of grain orientations and a spotty diffraction pattern.

2.2.5.7. *Time resolution*

The high flux allows powder-diffraction patterns to be measured quickly, opening up the possibilities for time-resolved studies, following the evolution of samples on a timescale, if appropriate, down to milliseconds, *e.g.* to investigate the kinetics and the mechanism of a phase transition caused by a change of the temperature, pressure or other external condition, or a chemical reaction taking place in the sample, such as self-propagating combustion synthesis (Labiche *et al.*, 2007). Many instruments allow great flexibility in the design of experiments to study systems *in situ*, helped by the availability of hard radiation to penetrate through sample environments and reduce the angular range that must be accessed to measure enough diffraction peaks to yield the desired information.

2.2.5.7.1. *Using fast detectors*

Scanning a detector through the d-spacing range of interest necessarily takes a few seconds, so is too slow to measure the fastest processes. Thus, for speed, a multichannel detector system is required that acquires the full diffraction pattern synchronously and that can be read out rapidly, such as *via* a fast PSD or using the energy-dispersive approach. Many different types of detector systems have been exploited for fast powder-diffraction studies using the monochromatic Debye–Scherrer configuration (Section 2.2.4.2), including 1D photodiode arrays (Pennartz *et al.*, 1992; Wong *et al.*, 2006; Palmer *et al.*, 2004), the Mythen curved 1D PSD (Fadenberger *et al.*, 2010), pixel detectors (Yonemura *et al.*, 2006; Terasaki & Komizo, 2011), CCD-based detectors (Malard *et al.*, 2011; Elmer *et al.*, 2007), and medical-imaging detectors (Chupas, Chapman, Jennings *et al.*, 2007; Newton *et al.*, 2010). The former of these last two studies shows that these large detectors working at hard X-ray energies above 60 keV register a wide enough Q range in a single cycle to allow PDF analysis to be made, thus allowing the conduct of time-resolved PDF analysis of, for example, catalytic systems composed of evolving nanoparticles. For the latter study, the diffraction measurements were combined with simultaneous monitoring of the reacting system with the acquisition of complementary mass and diffuse reflectance infrared Fourier transform spectra (DRIFTS).

2.2.5.7.2. *Using the pulse structure*

For investigating very fast, reversible processes, use can be made of the bunch structure of the synchrotron source and the stroboscopic measurement approach. The time for an orbit of an electron circulating in a synchrotron is (circumference/c) s. For a synchrotron such as at the ESRF (with a circumference of 844.4 m), this corresponds to 2.82 µs (*i.e.* a frequency of 355036 Hz). Thus when operating with 16 electron bunches distributed evenly around the ring, there is a burst of X-rays delivered to a beamline every 176 ns, and because of the longitudinal dimension of the electron bunch (∼20 mm), each burst lasts ∼70 ps. Such a pulsed source can be used in pump–probe powder-diffraction experiments, whereby a sample is excited by a short laser pulse (∼100 fs duration) then probed by the X-ray beam a chosen delay time later. The scattered X-rays are recorded with a suitable (probably 2D) detector and the process is repeated, with the statistical quality of the diffraction pattern building up over a number of cycles, after which the detector is read out. A high-speed chopper in the X-ray beam can be used to select the pulse frequency desired for any particular set of measurements. By varying the delay time the evolution of the sample as a function of time after the initial excitation can be investigated. The whole experiment needs fast, accurate electronics to correlate the timing of the firing of the laser, the arrival of the X-ray pulse and the phasing of the chopper.

Examples include the study of 4-(dimethylamino)benzonitrile and 4-(diisopropylamino)benzonitrile (Davaasambuu *et al.*, 2004; Techert & Zachariasse, 2004), whose fluorescence properties indicate that photoexcitation leads to the formation of an intramolecular charge-transfer state. Powder-diffraction patterns were collected over 10-minute periods at a frequency of 897 Hz at delay times ranging from −150 ps (as a reference before the laser excitation) to +2500 ps after excitation. Only about 5% of the molecules are excited by the laser, so the powder-diffraction pattern is from a sample containing both excited and ground-state molecules. Rietveld refinement of the structures from the diffraction patterns gave the fraction of excited molecules as a function of delay time, and the nature of the structural change induced by the photoexcitation. For the isopropyl analogue, an exponential relaxation time of 6.3 (±2.8) ns was observed for the excited molecules (compared to 3.28 ns seen spectroscopically). The main distortion to the molecules was a change in the torsion angle between the diisopropylamino group and the benzene ring, from 13–14° determined from the pre-excitation patterns (14.3° *via* single-crystal analysis) to 10 (±1–2)°.

2.2.5.8. *Beamline evolution*

A beamline at a synchrotron source will certainly evolve in its specifications and capabilities. Users and prospective users should follow updates on a facility's website, or contact the beamline staff, for information concerning possibilities for experiments.

References

Als-Nielsen, J. & McMorrow, D. (2001). *Elements of Modern X-ray Physics*. New York: Wiley.

Authier, A. (2006). *Dynamical theory of X-ray diffraction. International Tables for Crystallography*, Vol. B, *Reciprocal Space*, 1st online ed., ch. 5.1. Chester: International Union of Crystallography.

Azároff, L. V. (1955). *Polarization correction for crystal-monochromatized X-radiation*. *Acta Cryst.* **8**, 701–704.

Balzar, D. & Ledbetter, H. (1993). *Voigt-function modeling in Fourier analysis of size- and strain-broadened X-ray diffraction peaks*. *J. Appl. Cryst.* **26**, 97–103.

Barnes, P., Jupe, A. C., Colston, S. L., Jacques, S. D., Grant, A., Rathbone, T., Miller, M., Clark, S. M. & Cernik, R. J. (1998). *A new three-angle energy-dispersive diffractometer*. *Nucl. Instrum. Methods Phys. Res. B*, **134**, 310–313.

Beaumont, J. H. & Hart, M. (1974). *Multiple Bragg reflection monochromators for synchrotron X radiation*. *J. Phys. E Sci. Instrum.* **7**, 823–829.

Bergamaschi, A., Cervellino, A., Dinapoli, R., Gozzo, F., Henrich, B., Johnson, I., Kraft, P., Mozzanica, A., Schmitt, B. & Shi, X. (2009). *Photon counting microstrip detector for time resolved powder diffraction experiments*. *Nucl. Instrum. Methods Phys. Res. A*, **604**, 136–139.

Bergamaschi, A., Cervellino, A., Dinapoli, R., Gozzo, F., Henrich, B., Johnson, I., Kraft, P., Mozzanica, A., Schmitt, B. & Shi, X. (2010). *The MYTHEN detector for X-ray powder diffraction experiments at the Swiss Light Source*. *J. Synchrotron Rad.* **17**, 653–668.

Bilderback, D. H. (1986). *The potential of cryogenic silicon and germanium X-ray monochromators for use with large synchrotron heat loads*. *Nucl. Instrum. Methods Phys. Res. A*, **246**, 434–436.

Boccaleri, E., Carniato, F., Croce, G., Viterbo, D., van Beek, W., Emerich, H. & Milanesio, M. (2007). *In situ simultaneous Raman/high-resolution X-ray powder diffraction study of transformations occurring in materials at non-ambient conditions*. *J. Appl. Cryst.* **40**, 684–693.

Broennimann, Ch., Eikenberry, E. F., Henrich, B., Horisberger, R., Huelsen, G., Pohl, E., Schmitt, B., Schulze-Briese, C., Suzuki, M., Tomizaki, T., Toyokawa, H. & Wagner, A. (2006). *The PILATUS 1m detector*. *J. Synchrotron Rad.* **13**, 120–130.

Cernik, R. J., Murray, P. K., Pattison, P. & Fitch, A. N. (1990). *A two-circle powder diffractometer for synchrotron radiation with a closed loop encoder feedback system*. *J. Appl. Cryst.* **23**, 292–296.

Cheary, R. W. & Coelho, A. (1992). *A fundamental parameters approach to X-ray line-profile fitting*. *J. Appl. Cryst.* **25**, 109–121.

Chupas, P. J., Chapman, K. W., Jennings, G., Lee, P. L. & Grey, C. P. (2007). *Watching nanoparticles grow: the mechanism and kinetics for the formation of TiO_2-supported platinum nanoparticles*. *J. Am. Chem. Soc.* **129**, 13822–13824.

Chupas, P. J., Chapman, K. W. & Lee, P. L. (2007). *Applications of an amorphous silicon-based area detector for high-resolution, high-sensitivity and fast time-resolved pair distribution function measurements*. *J. Appl. Cryst.* **40**, 463–470.

Collins, S. P., Cernik, R. J., Pattison, P., Bell, A. M. T. & Fitch, A. N. (1992). *A two-circle powder diffractometer for synchrotron radiation on Station 2.3 at the SRS*. *Rev. Sci. Instrum.* **63**, 1013–1014.

Cousins, C. S. G. (1994). *High-resolution diffraction at synchrotron sources: correction for counting losses*. *J. Appl. Cryst.* **27**, 159–163.

Cox, D. E., Hastings, J. B., Cardoso, L. P. & Finger, L. W. (1986). *Synchrotron X-ray powder diffraction at X13A: a dedicated powder diffractometer at the National Synchrotron Light Source*. *Mater. Sci. Forum*, **9**, 1–20.

Cox, D. E., Hastings, J. B., Thomlinson, W. & Prewitt, C. T. (1983). *Application of synchrotron radiation to high resolution powder diffraction and Rietveld refinement*. *Nucl. Instrum. Methods*, **208**, 573–578.

Daniels, J. E. & Drakopoulos, M. (2009). *High-energy X-ray diffraction using the Pixium 4700 flat-panel detector*. *J. Synchrotron Rad.* **16**, 463–468.

Davaasambuu, J., Durand, P. & Techert, S. (2004). *Experimental requirements for light-induced reactions in powders investigated by time-resolved X-ray diffraction*. *J. Synchrotron Rad*. **11**, 483–489.

David, W. I. F. & Matthewman, J. C. (1985). *Profile refinement of powder diffraction patterns using the Voigt function*. *J. Appl. Cryst.* **18**, 461–466.

Desai, P. D. (1986). *Thermodynamic properties of iron and silicon. J. Phys. Chem. Ref. Data*, **15**, 967–983.

Dwiggins, C. W. Jr (1983). *General calculation of the polarization factor for multiple coherent scattering of unpolarized and plane-polarized X-rays*. *Acta Cryst.* A**39**, 773–777.

Elmer, J. W., Palmer, T. A. & Specht, E. D. (2007). *In situ observations of sigma phase dissolution in 2205 duplex stainless steel using synchrotron X-ray diffraction*. *Mat. Sci. Eng. A*, **459**, 151–155.

Evans, G. & Pettifer, R. F. (2001). *CHOOCH: a program for deriving anomalous-scattering factors from X-ray fluorescence spectra*. *J. Appl. Cryst.* **34**, 82–86.

Evans, J. S. O., Francis, R. J., O'Hare, D., Price, S. J., Clark, S. M., Flaherty, J., Gordon, J., Nield, A. & Tang, C. C. (1995). *An apparatus for the study of the kinetics and mechanism of hydrothermal reactions by in situ energy dispersive x-ray diffraction*. *Rev. Sci. Instrum.* **66**, 2442–2445.

Fadenberger, K., Gunduz, I. E., Tsotsos, C., Kokonou, M., Gravani, S., Brandstetter, S., Bergamaschi, A., Schmitt, B., Mayrhofer, P. H., Doumanidis, C. C. & Rebholz, C. (2010). *In situ observation of rapid reactions in nanoscale Ni–Al multilayer foils using synchrotron radiation*. *Appl. Phys. Lett.* **97**, 144101.

Glazov, V. M. & Pashinkin, A. S. (2001). *The thermophysical properties (heat capacity and thermal expansion) of single-crystal silicon*. *High Temp.* **39**, 413–419.

Gozzo, F., De Caro, L., Giannini, C., Guagliardi, A., Schmitt, B. & Prodi, A. (2006). *The instrumental resolution function of synchrotron radiation powder diffractometers in the presence of focusing optics*. *J. Appl. Cryst.* **39**, 347–357.

Gullikson, E. M. (2001). *Atomic scattering factors*. *X-ray Data Booklet*, edited by A. C. Thompson & D. Vaughan. Lawrence Berkeley National Laboratory, USA. http://xdb.lbl.gov/Section1/Sec_1-7.pdf.

Hastings, J. B., Thomlinson, W. & Cox, D. E. (1984). *Synchrotron X-ray powder diffraction*. *J. Appl. Cryst.* **17**, 85–95.

Häusermann, D. & Barnes, P. (1992). *Energy-dispersive diffraction with synchrotron radiation: optimization of the technique for dynamic studies of transformations*. *Phase Transit.* **39**, 99–115.

Hewat, A. W. (1975). *Design for a conventional high-resolution neutron powder diffractometer*. *Nucl. Instrum. Methods*, **127**, 361–370.

Hewat, A. W. (1979). *Absorption corrections for neutron diffraction*. *Acta Cryst.* A**35**, 248.

Hodeau, J.-L., Bordet, P., Anne, M., Prat, A., Fitch, A. N., Dooryhée, E., Vaughan, G. & Freund, A. (1998). *Nine-crystal multianalyzer stage for high-resolution powder diffraction between 6 keV and 40 keV*. *Proc. SPIE*, **3448**, 353–361.

Honkimäki, V. & Suortti, P. (2007). *Energy-dispersive diffraction with synchrotron radiation and a germanium detector*. *J. Synchrotron Rad.* **14**, 331–338.

Hubbell, J. H. (1982). *Photon mass attenuation and energy-absorption coefficients*. *Int. J. Appl. Radiat. Isot.* **33**, 1269–1290.

Ida, T., Hibino, H. & Toraya, H. (2001). *Peak profile function for synchrotron X-ray diffractometry*. *J. Appl. Cryst.* **34**, 144–151.

Ida, T., Hibino, H. & Toraya, H. (2003). *Deconvolution of instrumental aberrations for synchrotron powder X-ray diffractometry*. *J. Appl. Cryst.* **36**, 181–187.

Kim, K.-J. (2001). *Characteristics of synchrotron radiation*. *X-ray Data Booklet*, edited by A. C. Thompson & D. Vaughan. Lawrence Berkeley National Laboratory, USA. http://xdb.lbl.gov/Section2/Sec_2-1.html.

Kirkpatrick, P. & Baez, A. V. (1948). *Formation of optical images by X-rays*. *J. Opt. Soc. Am.* **38**, 766–774.

Koopmans, K. & Rieck, G. D. (1968). *International Tables for X-ray Crystallography*, Vol. III, edited by C. H. MacGillavry & G. D. Rieck, pp. 194–195. Birmingham: Kynoch Press.

Korsunsky, A. M., Song, X., Hofmann, F., Abbey, B., Xie, M., Connolley, T., Reinhard, C. R. C., Atwood, R. C., Connor, L. & Drakopoulos, M. (2010). *Polycrystal deformation analysis by high energy synchrotron X-ray diffraction on the I12 JEEP beamline at Diamond Light Source*. *Mater. Lett.* **64**, 1724–1727.

Labiche, J.-C., Mathon, O., Pascarelli, S., Newton, M. A., Ferre, G. G., Curfs, C., Vaughan, G., Homs, A. & Carreiras, D. F. (2007). *The fast readout low noise camera as a versatile X-ray detector for time resolved dispersive extended X-ray absorption fine structure and diffraction studies of dynamic problems in materials science, chemistry, and catalysis*. *Rev. Sci. Instrum.* **78**, 091301–1–11.

Langford, J. I. (1978). *A rapid method for analysing the breadths of diffraction and spectral lines using the Voigt function*. *J. Appl. Cryst.* **11**, 10–14.

Laundy, D. & Collins, S. (2003). *Counting statistics of X-ray detectors at high counting rates*. *J. Synchrotron Rad.* **10**, 214–218.

Lee, J. H., Aydiner, C. C., Almer, J., Bernier, J., Chapman, K. W., Chupas, P. J., Haeffner, D., Kump, K., Lee, P. L., Lienert, U., Miceli, A. & Vera, G. (2008). *Synchrotron applications of an amorphous silicon flat-panel detector*. *J. Synchrotron Rad.* **15**, 477–488.

Lee, P. L., Shu, D., Ramanathan, M., Preissner, C., Wang, J., Beno, M. A., Von Dreele, R. B., Ribaud, L., Kurtz, C., Antao, S. M., Jiao, X. & Toby, B. H. (2008). *A twelve-analyzer detector system for high-resolution powder diffraction*. *J. Synchrotron Rad.* **15**, 427–432.

Lengeler, B., Schroer, C., Tümmler, J., Benner, B., Richwin, M., Snigirev, A., Snigireva, I. & Drakopoulos, M. (1999). *Imaging by parabolic refractive lenses in the hard X-ray range*. *J. Synchrotron Rad.* **6**, 1153–1167.

Lipson, H. (1967). *International Tables for X-ray Crystallography*, Vol. II, edited by J. S. Kasper & K. Lonsdale, pp. 291–292. Birmingham: Kynoch Press.

Malard, B., Pilch, J., Sittner, P., Delville, R. & Curfs, C. (2011). *In situ investigation of the fast microstructure evolution during electropulse treatment of cold drawn NiTi wires*. *Acta Mater.* **59**, 1542–1556.

Margaritondo, G. (1988). *Introduction to Synchrotron Radiation.* Oxford University Press.

Masson, O., Dooryhée, E. & Fitch, A. N. (2003). *Instrument line-profile synthesis in high-resolution synchrotron powder diffraction*. *J. Appl. Cryst.* **36**, 286–294.

Milledge, H. J. (1968). *International Tables for X-ray Crystallography*, Volume III, *Physical and Chemical Tables*, edited by C. H. MacGillavry, G. D. Rieck & K. Lonsdale, pp. 175–192. Birmingham: Kynoch Press.

Mills, D. M., Helliwell, J. R., Kvick, Å., Ohta, T., Robinson, I. A. & Authier, A. (2005). *Report of the Working Group on Synchrotron Radiation Nomenclature - brightness, spectral brightness or brilliance?* *J. Synchrotron Rad.* **12**, 385.

Newton, M. A., Di Michiel, M., Kubacka, A. & Fernández-García, M. (2010). *Combining time-resolved hard X-ray diffraction and diffuse*

reflectance infrared spectroscopy to illuminate CO dissociation and transient carbon storage by supported Pd nanoparticles during CO/NO cycling. *J. Am. Chem. Soc.* **132**, 4540–4541.

Newton, M. A. & van Beek, W. (2010). *Combining synchrotron-based X-ray techniques with vibrational spectroscopies for the in situ study of heterogeneous catalysts: a view from a bridge*. *Chem. Soc. Rev.* **39**, 4845–4863.

Palmer, T. A., Elmer, J. W. & Babu, S. S. (2004). *Observation of ferrite/austenite transformations in the heat affected zone of 2205 duplex stainless steel spot welds using time resolved X-ray diffraction*. *Mater. Sci. Eng. A*, **374**, 307–321.

Parrish, W. (1988). *Advances in synchrotron X-ray polycrystalline diffraction*. *Aust. J. Phys.* **41**, 101–112.

Parrish, W. & Hart, M. (1987). *Advantages of synchrotron radiation for polycrystalline diffractometry*. *Z. Kristallogr.* **179**, 161–173.

Parrish, W., Hart, M., Erickson, C. G., Masciocchi, N. & Huang, T. C. (1986). *Instrumentation for synchrotron X-ray powder diffractometry*. *Adv. X-ray Anal.* **29**, 243–250.

Pennartz, P. U., Löchner, U., Fuess, H. & Wroblewski, T. (1992). *Powder diffraction in the range of milliseconds*. *J. Appl. Cryst.* **25**, 571–577.

Rijssenbeek, J., Gao, Y., Zhong, Z., Croft, M., Jisrawi, N., Ignatov, A. & Tsakalakos, T. (2011). *In situ X-ray diffraction of prototype sodium metal halide cells: time and space electrochemical profiling*. *J. Power Sources*, **196**, 2332–2339.

Rowles, M. R., Styles, M. J., Madsen, I. C., Scarlett, N. V. Y., McGregor, K., Riley, D. P., Snook, G. A., Urban, A. J., Connolley, T. & Reinhard, C. (2012). *Quantification of passivation layer growth in inert anodes for molten salt electrochemistry by in situ energy-dispersive diffraction*. *J. Appl. Cryst.* **45**, 28–37.

Sabine, T. M. (1987*a*). *The N-crystal spectrometer*. *J. Appl. Cryst.* **20**, 23–27.

Sabine, T. M. (1987*b*). *A powder diffractometer for a synchrotron source*. *J. Appl. Cryst.* **20**, 173–178.

Sabine, T. M., Hunter, B. A., Sabine, W. R. & Ball, C. J. (1998). *Analytical expressions for the transmission factor and peak shift in absorbing cylindrical specimens*. *J. Appl. Cryst.* **31**, 47–51.

Sasaki, S. (1989). *Numerical Tables of Anomalous Scattering Factors Calculated by the Cromer and Liberman Method*. KEK Report, 88–14, 1–136.

Scarlett, N. V. Y., Madsen, I. C., Evans, J. S. O., Coelho, A. A., McGregor, K., Rowles, M., Lanyon, M. R. & Urban, A. J. (2009). *Energy-dispersive diffraction studies of inert anodes*. *J. Appl. Cryst.* **42**, 502–512.

Seltzer, S. M. (1993). *Calculation of photon mass energy-transfer and mass energy-absorption coefficients*. *Radiat. Res.* **136**, 147–170.

Snigirev, A. A., Filseth, B., Elleaume, P., Klocke, Th., Kohn, V., Lengeler, B., Snigireva, I., Souvorov, A. & Tuemmler, J. (1997). *Refractive lenses for high-energy X-ray focusing*. *Proc. SPIE*, **3151**, 164–170.

Snigirev, A., Kohn, V., Snigireva, I., Souvorov, A. & Lengeler, B. (1998). *Focusing high-energy X rays by compound refractive lenses*. *Appl. Opt.* **37**, 653–662.

Spiller, E. (2000). *X-ray optics*. *Adv. X-ray Anal.* **42**, 297–307.

Techert, S. & Zachariasse, K. A. (2004). *Structure determination of the intramolecular charge transfer state in crystalline 4-(diisopropylamino) benzonitrile from picosecond X-ray diffraction*. *J. Am. Chem. Soc.* **126**, 5593–5600.

Terasaki, H. & Komizo, Y. (2011). *Diffusional and displacive transformation behaviour in low carbon-low alloy steels studied by a hybrid in situ observation system*. *Scr. Mater.* **64**, 29–32.

Thompson, P., Cox, D. E. & Hastings, J. B. (1987). *Rietveld refinement of Debye–Scherrer synchrotron X-ray data from Al_2O_3*. *J. Appl. Cryst.* **20**, 79–83.

Vaughan, G. B. M., Wright, J. P., Bytchkov, A., Rossat, M., Gleyzolle, H., Snigireva, I. & Snigirev, A. (2011). *X-ray transfocators: focusing devices based on compound refractive lenses*. *J. Synchrotron Rad.* **18**, 125–133.

Walton, R. I. & O'Hare, D. (2000). *Watching solids crystallise using in situ powder diffraction*. *Chem. Commun.* pp. 2283–2291.

Wong, J., Larson, E. M., Waide, P. A. & Frahm, R. (2006). *Combustion front dynamics in the combustion synthesis of refractory metal carbides and di-borides using time-resolved X-ray diffraction*. *J. Synchrotron Rad.* **13**, 326–335.

Wright, J., Vaughan, G. & Fitch, A. (2003). *Merging data from a multi-detector continuous scanning powder diffraction system*. *International Union of Crystallography Commission on Crystallographic Computing Newsletter*, **1**, 92–96.

Wroblewski, T. (1991). *Resolution functions of powder diffractometers at a synchrotron-radiation source*. *Acta Cryst.* A**47**, 571–577.

Yamanaka, T. & Ogata, K. (1991). *Structure refinement of GeO_2 polymorphs at high pressures and temperatures by energy-dispersive spectra of powder diffraction*. *J. Appl. Cryst.* **24**, 111–118.

Yao, T. & Jinno, H. (1982). *Polarization factor for the X-ray powder diffraction method with a single-crystal monochromator*. *Acta Cryst.* A**38**, 287–288.

Yonemura, M., Osuki, T., Terasaki, H., Komizo, Y., Sato, M. & Toyokawa, H. (2006). *Two-dimensional time-resolved X-ray diffraction study of directional solidification in steels*. *Mater. Trans.* **47**, 2292–2298.

Zachariasen, W. H. (1945). *Theory of X-ray Diffraction in Crystals*. Dover Publications Inc.

2.3. Neutron powder diffraction

C. J. Howard and E. H. Kisi

2.3.1. Introduction to the diffraction of thermal neutrons

Diffraction of neutrons occurs by virtue of their wave character, the de Broglie wavelength λ being

$$\lambda = \frac{h}{mv} = \frac{h}{(2mE)^{1/2}}, \tag{2.3.1}$$

where m, v and E are the mass, speed and energy of the neutron, respectively, and h is Planck's constant. It may be convenient to express the neutron energy in meV, in which case the wavelength in ångströms is given by

$$\lambda\ (\text{Å}) = 9.045/(E)^{1/2}\ (\text{meV}). \tag{2.3.2}$$

Thermal neutrons produced by a fission reactor have a representative energy of 25 meV, and accordingly a wavelength of 1.809 Å, which is well suited to the study of condensed matter since it is of the order of the interatomic spacings therein.

Neutrons have a number of distinctive properties making neutron diffraction uniquely powerful in several applications. They may be scattered by nuclei or by magnetic entities in the sample under study.

(*a*) *Scattering by nuclei*: The atomic nucleus is tiny compared with the atomic electron cloud, which is the entity that scatters X-rays and electrons. The scattering cross section for a particular nucleus is written as

$$\sigma = 4\pi b^2, \tag{2.3.3}$$

where σ is typically of the order of 10^{-28} m^2 (1×10^{-28} m^2 = 1 barn) and b, which is termed the *scattering length*, is of the order of femtometres. The small size of the nucleus relative to the wavelength of interest means that the scattering is isotropic – there is no angle-dependent form factor, as occurs in the X-ray case (*cf.* Section 1.1.3.1). This confers advantages in studies aimed at determining atomic displacement parameters (ADPs),[1] and indeed for the total-scattering studies requiring data over a large Q range ($Q = 4\pi \sin\theta/\lambda$) that are described in Chapter 5.7. Importantly, scattering lengths vary somewhat erratically with atomic number Z; this is in marked contrast to the X-ray case in which the form factor increases monotonically with Z (see Figs. 2.3.1 and 2.3.2). This can make it much easier to detect the scattering from light (low-Z) elements in the presence of much heavier ones; it also makes it easier to distinguish scattering from elements adjacent in the periodic table, *e.g.* Cu with Z = 29, b = 7.718 fm and Zn with Z = 30, b = 5.680 fm. The scattering length is also different for different isotopes of the same element,[2] *e.g.* for ^{1}H b = −3.741 fm, whereas for ^{2}H b = 6.671 fm, so that sometimes isotopic substitution can be employed to obtain contrast as desired.

(*b*) *Scattering by magnetic entities*: The neutron carries a magnetic moment of $-1.913\ \mu_N$ (where μ_N is the nuclear magneton) and accordingly it interacts with magnetic entities in the sample. These may be nuclei, with magnetic moments of the order of the nuclear magneton, or atoms with much larger magnetic moments, of the order of the Bohr magneton (μ_B). If the magnetic entities are disordered, then the result is magnetic diffuse scattering, but if they are in some way ordered then the magnetic structure can be studied *via* the magnetic Bragg reflections that arise. (These may not be so obvious if they coincide with the nuclear Bragg reflections.) The magnetic moment of the neutron interacts with atomic magnetic moments, attributable to unpaired electrons in the atoms. These electrons tend to be the outer electrons, spread over dimensions comparable with atomic spacings and hence with the wavelengths used for diffraction; a consequence is that magnetic scattering is characterized by a magnetic form factor which falls off with Q more rapidly than does the form factor for the X-ray case (Fig. 2.3.3). The confirmation of the antiferromagnetic ordering in MnO below its ordering (Néel) temperature of 120 K (Fig. 2.3.4; Shull *et al.*, 1951) was the first of numerous studies of magnetic structure by neutron powder diffraction that have continued to the present day (Izyumov & Ozerov, 1970; Chatterji, 2006; Chapter 7 in Kisi & Howard, 2008). Investigations of nuclear moments are more challenging largely because the smaller moments mean extremely low ordering temperatures; nevertheless neutron diffraction has been used, for example, to study the ordering

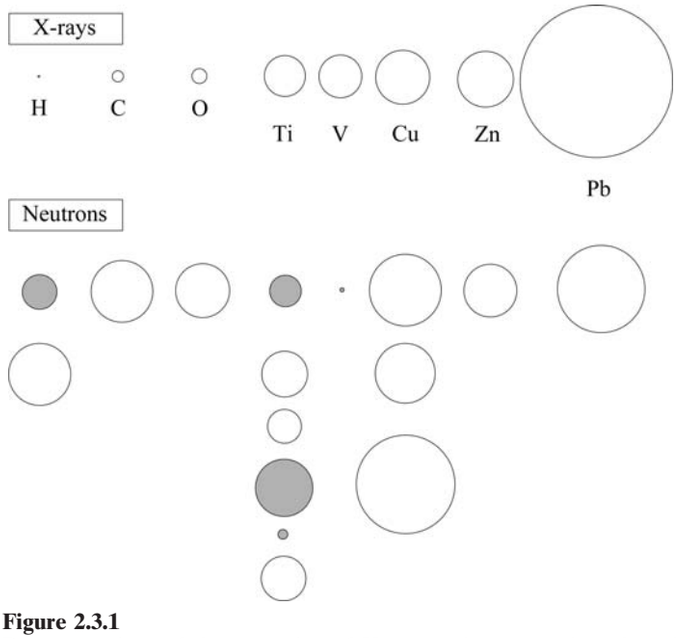

Figure 2.3.1
Representations of the scattering of X-rays and neutrons by selected elements. The scattering cross sections are proportional to the areas of the circles shown. For the neutron case, separate entries appear for the different isotopes and negative scattering lengths are indicated by shading. The figure is not intended to imply a relationship between the X-ray and neutron cross sections.

[1] The atomic displacements (*e.g.* thermal vibrations) smear the scattering sites to an extent that is likely to be considerably smaller than the atom itself, but very much larger than the nucleus.

[2] If the nucleus in question carries spin, the scattering length also depends on the relative orientation of the neutron and nuclear spins.

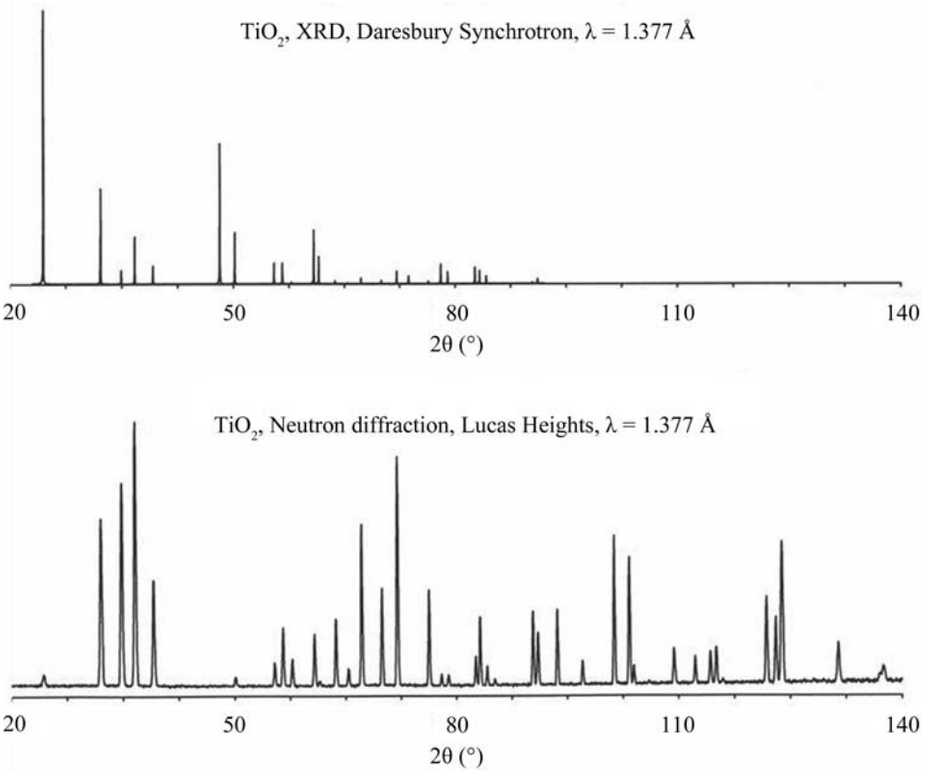

Figure 2.3.2
Comparison of X-ray and neutron powder-diffraction patterns from rutile, TiO_2. The patterns were recorded at the same wavelength, 1.377 Å. The differences between form factors and scattering lengths give rise to large differences in the relative intensities of the different peaks; note also that the fall off in the form factor evident in the X-ray case does not occur for neutrons.

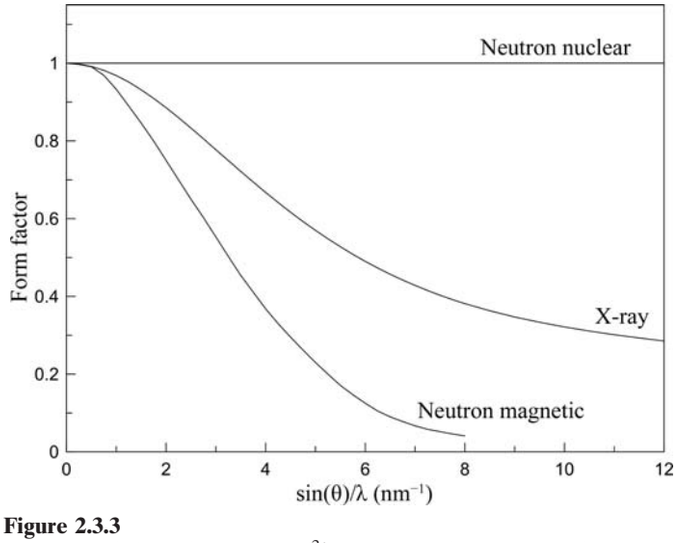

Figure 2.3.3
The magnetic form factor for Mn^{2+} compared with the normalized X-ray form factor and the normalized neutron nuclear scattering length.

of nuclear moments in metallic copper (^{65}Cu) at temperatures below 60 nK (Hakonen *et al.*, 1991).[3]

(*c*) *Low attenuation*: The combination of the small scattering cross sections and generally low cross sections for absorption (notable exceptions are B, Cd and Gd) gives thermal neutrons the ability to penetrate quite deeply into most materials. Indeed, the linear attenuation coefficient for thermal (25 meV) neutrons in Fe is 110 m^{-1}, and for neutrons in Al it is only about 9.8 m^{-1}; the implication is that it takes about 10 cm of Al to reduce the intensity by a factor 1/*e*. The fact that neutrons are so little attenuated by these materials makes it easier to design large and complex sample-environment chambers which may be used for *in situ* studies at high temperature, under pressure or stress, in magnetic fields, and in reaction cells (Chapters 2.6–2.9; Chapter 3 in Kisi & Howard, 2008). Neutron powder diffraction is well suited to quantitative phase analysis (QPA, see Chapter 3.9 and Chapter 8 in Kisi & Howard, 2008); as pointed out in Chapter 8, Section 8 of Kisi & Howard (2008), neutron QPA provides a better sampling ability and is less prone to micro-absorption errors than the X-ray technique; indeed, neutron diffraction was the method employed in one of the earliest and most convincing demonstrations of the Rietveld method in QPA (Hill & Howard, 1987). Another advantage conferred by the deep penetration of neutrons is the ability to probe below the surface of samples to measure such aspects as structure, phase composition and stress; a particular example is the application to the analysis of zirconia ceramics (Kisi *et al.*, 1989) where the surface composition (as would be measured by X-rays) is unrepresentative of the bulk. A downside of the small scattering cross sections (along with neutron sources of limited 'brightness') is that relatively large samples may be required.

(*d*) *Low energy*: We note from equation (2.3.1) that, for a specified wavelength, the energy of the neutron is much less than that for lighter probes, such as electrons or photons. This is critically important for studying inelastic processes (*e.g.* measurement of phonon dispersion curves), but is usually not a factor in neutron powder diffraction.[4]

Neutron sources, in common with synchrotrons, are large national or international facilities, set up to cater for scientists from external laboratories. There are usually well defined access procedures, involving the submission and peer review of research proposals. Visiting users are usually assisted in their experiments by in-house staff. In some cases external users can mail in their samples for collection of diffraction data by the resident staff.

2.3.2. Neutrons and neutron diffraction – pertinent details

2.3.2.1. *Properties of the neutron*

The basic properties of the neutron are summarized in Table 2.3.1.

[3] This study depends on the spin-dependent scattering lengths rather than magnetic scattering *per se*.

[4] However, if the incident beam is monochromatic, a crystal monochromator placed in the diffracted beam can be used to exclude inelastic scattering from the 'background'.

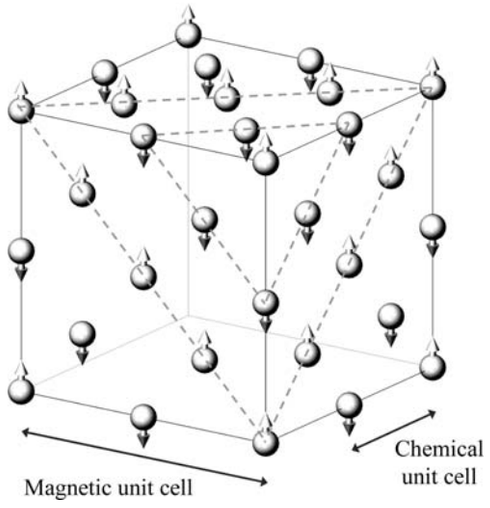

Figure 2.3.4
Magnetic structure for MnO proposed by Shull *et al.* (1951). The figure shows only the Mn atoms, and indeed only those Mn atoms located on the visible faces of the cubic cell. [From Shull *et al.* (1951), redrawn using *ATOMS* (Dowty, 1999).]

2.3.2.2. *Neutron scattering lengths*

The scattering lengths of most interest in neutron powder diffraction are those for coherent elastic scattering, $b_{\rm coh}$, often abbreviated to b. As already mentioned, there is no angle (Q) dependence, since the scattering from the nucleus is isotropic. A selection of scattering lengths for different isotopes and different elements is given in Table 2.3.2.

The first thing to note is the variation in scattering length from element to element and indeed from isotope to isotope. The scattering lengths are in most cases positive real numbers, in which case there is a phase reversal of the neutron on scattering, but for some isotopes the scattering lengths are negative, so there is no change in phase on scattering. The scattering lengths are determined by the details of the neutron–nucleus interaction (Squires, 1978).[5] In the event that the neutron–nucleus system is close to a resonance, such as it is for ^{10}B, ^{155}Gd and ^{157}Gd, scattering lengths will be complex quantities and the scattered neutron will have some different phase relationship with the incident one. The imaginary components imply absorption, which is reflected in the very high absorption cross sections, σ_a, for these isotopes.

The total scattering cross section, σ_s, is given by $\sigma_s = 4\pi b_{\rm coh}^2$ when only coherent scattering from a single isotope is involved, which is very nearly the case for oxygen since 99.76% of naturally occurring oxygen is zero-spin ^{16}O. In most cases there is a more substantial contribution from incoherent scattering, which may be either spin or isotope incoherent scattering. Spin incoherent scattering arises because the scattering length depends on the relative orientation of the neutron and nuclear spins, parallel and antiparallel arrangements giving rise to scattering lengths b_+ and b_-, respectively. Isotope incoherent scattering arises because of the different scattering of neutrons from different isotopes of the same element. In almost all circumstances (except, for example, at the extraordinarily low temperatures mentioned in Section 2.3.1) the distributions of spins and isotopes are truly random, which means that there is no angle dependence in this scattering: this is sometimes described as Laue monotonic scattering.

[5] It is evident from Fig. 2.3 in this reference that even for an attractive interaction between neutron and nucleus positive scattering lengths will predominate.

Table 2.3.1
Properties of the neutron (adapted from Kisi & Howard, 2008)

Mass (m)	1.675×10^{-27} kg
Charge	0
Spin	$\frac{1}{2}$
Magnetic moment (μ_n)	$-1.913\ \mu_N$
Wavelength (λ)	h/mv
Wavevector (**k**)	Magnitude $2\pi/\lambda$
Momentum (**p**)	$\hbar\mathbf{k}$
Energy (E)	$(1/2)mv^2 = h^2/2m\lambda^2$

When b varies from nucleus to nucleus (even considering just a single element), the coherent scattering is determined by the average value of b, that is $b_{\rm coh} = \overline{b}$, $\sigma_{\rm coh} = 4\pi(\overline{b})^2$, and the average incoherent cross section is given by $\sigma_{\rm inc} = 4\pi[\overline{b^2} - (\overline{b})^2]$. The total scattering cross section σ_s is the sum of the two cross sections (Squires, 1978; see also Section 2.3.2 in Kisi & Howard, 2008). For the particular case of a nucleus with spin I, the states $I + 1/2$ and $I - 1/2$ give scattering determined by b_+ and b_-, respectively, and have multiplicities $2I + 2$ and $2I$, respectively, from which it follows that

$$b_{\rm coh} = \overline{b} = \frac{I+1}{2I+1}b_+ + \frac{I}{2I+1}b_-,$$
$$b_{\rm inc}^2 = \left[\overline{b^2} - (\overline{b})^2\right] = \frac{I(I+1)}{(2I+1)^2}(b_+ - b_-)^2.$$

More information, including a comprehensive listing of scattering lengths, can be found in Section 4.4.4 of *International Tables for Crystallography* Volume C (Sears, 2006). This listing presents the spin-dependent scattering lengths *via* $b_{\rm coh}$ and $b_{\rm inc}$ as just defined. Other compilations can be found in the *Neutron Data Booklet* (Rauch & Waschkowski, 2003), and online through the Atominstitut der Österreichischen Universitäten, Vienna, at http://www.ati.ac.at/~neutropt/scattering/table.html. In addition, the majority of computer programs used for the analysis of data from neutron diffraction incorporate, for convenience, a list of $b_{\rm coh}$ values for the elements.

2.3.2.3. *Refractive index for neutrons*

The coherent scattering lengths of the nuclei determine the refractive index for neutrons through the relationship (Squires, 1978)

$$n = 1 - \frac{1}{2\pi}\lambda^2 N b_{\rm coh}, \tag{2.3.4}$$

where N is the number of nuclei per unit volume. For elements with positive values of the coherent scattering length the refractive index is slightly less than one, and that leads to the possibility of total external reflection of the neutrons by the element in question. In fact, when the coherent scattering length is positive, neutrons will undergo total external reflection for glancing angles less than a critical angle γ_c given by

$$\cos\gamma_c = n = 1 - \frac{1}{2\pi}\lambda^2 N b_{\rm coh}, \tag{2.3.5}$$

which, since γ_c is small, reduces to

$$\gamma_c = \lambda\left(\frac{N b_{\rm coh}}{\pi}\right)^{1/2}. \tag{2.3.6}$$

It can be seen that the pertinent material quantity is $Nb_{\rm coh}$, the 'coherent scattering length density'; for materials comprising more than one element this is the quantity that would be

Table 2.3.2
Coherent scattering lengths and absorption cross sections (for 25 meV neutrons) for selected isotopes

Data are taken from Section 4.4.4 of Volume C (Sears, 2006). Where not stated, the values are for the natural isotopic mix. The X-ray atomic form factors, f, evaluated at $Q = 1.2\pi$ Å^{-1}, are included for comparison.

Element	Isotope	b_{coh} (fm)	$\sigma_{s(tot)}$ (10^{-24}cm^2)	σ_a (10^{-24}cm^2)	f	Isotopic abundance (%)
H		−3.7390 (11)	82.02 (6)	0.3326 (7)	0.25	
	1	−3.7406 (11)	82.03 (6)	0.3326 (7)		99.985
	2	6.671 (4)	7.64 (3)	0.000519 (7)		0.015
	3	4.792 (27)	3.03 (5)	0		—
B		5.30 (4) − 0.213 (2)*i*	5.24 (11)	767 (8)	1.99	
	10	−0.1 (3) − 1.066 (3)*i*	3.1 (4)	3835 (9)		20.0
	11	6.65 (4)	5.78 (9)	0.0055 (33)		80.0
C		6.6460 (12)	5.551 (3)	0.00350 (7)	2.50	
	12	6.6511 (16)	5.559 (3)	0.00353 (7)		98.90
	13	6.19 (9)	4.84 (14)	0.00137 (4)		1.10
O		5.803 (4)	4.232 (6)	0.00019 (2)	4.09	
Ti		−3.370 (13)	4.06 (3)	6.43 (6)	13.2	
	46	4.725 (5)	2.80 (6)	0.59 (18)		8.2
	47	3.53 (7)	3.1 (2)	1.7 (2)		7.4
	48	−5.86 (2)	4.32 (3)	8.30 (9)		73.8
	49	0.98 (5)	3.4 (3)	2.2 (3)		5.4
	50	5.88 (10)	4.34 (15)	0.179 (3)		5.2
V		−0.3824 (12)	5.10 (6)	5.08 (2)	14.0	
Ni		10.3 (1)	18.5 (3)	4.49 (16)	18.7	
	58	14.4 (1)	26.1 (4)	4.6 (3)		68.27
	60	2.8 (1)	0.99 (7)	2.9 (2)		26.10
	61	7.60 (6)	9.2 (3)	2.5 (8)		1.13
	62	−8.7 (2)	9.5 (4)	14.5 (3)		3.59
	64	−0.37 (7)	0.017 (7)	1.52 (3)		0.91
Cu		7.718 (4)	8.03 (3)	3.78 (2)	19.9	
	63	6.43 (15)	5.2 (2)	4.50 (2)		69.17
	65	10.61 (19)	14.5 (5)	2.17 (3)		30.83
Zn		5.680 (5)	4.131 (10)	1.11 (2)	20.8	
Zr		7.16 (3)	6.46 (14)	0.185 (3)	27.0	
Gd		6.5 (5)	180 (2)	49700 (125)	45.9	
	155	6.0 (1) − 17.0 (1)*i*	66 (6)	61100 (400)		14.8
	157	−1.14 (2) − 71.9 (2)*i*	1044 (8)	259000 (700)		15.7
Pb		9.405 (3)	11.118 (7)	0.171 (2)	60.9	

computed. Since the critical angle for total external reflection is proportional to the neutron wavelength, it is convenient to express this as degrees per ångstrom of neutron wavelength. These are important considerations in the design and development of neutron guides (Section 2.3.3.4).

2.3.2.4. *Neutron attenuation*

Neutron beams are attenuated by coherent scattering, incoherent scattering and true absorption. The cross sections for all these processes are included in the tables cited above. For powder diffraction, the coherent scattering is usually small because it takes place only in that small fraction of crystallites correctly oriented for Bragg reflection; the other processes, however, take place throughout the sample.

If a particular scattering entity i with scattering cross sections $(\sigma_i)_{inc}$ and $(\sigma_i)_{abs}$ is present at a number density N_i, then the contribution it makes to the linear attenuation coefficient μ is $\mu_i = N_i[(\sigma_i)_{inc} + (\sigma_i)_{abs}]$. If the mass is M_i, then the density is simply $\rho_i = N_i M_i$, so we have the means to evaluate the mass absorption coefficient $(\mu/\rho)_i$. The calculation of absorption for elements, compounds and mixtures commonly proceeds by the manipulation of mass absorption coefficients, in the same manner as is employed for X-rays (see Section 2.4.2 in Kisi & Howard, 2008).

2.3.2.5. *Magnetic form factors and magnetic scattering lengths*

For a complete treatment of the magnetic interaction between the neutron and an atom carrying a magnetic moment, and the resulting scattering, the reader is referred elsewhere [Marshall & Lovesey, 1971; Squires, 1978; Section 6.1.2 of Volume C (Brown, 2006*a*)]. The magnetic moment of an atom is associated with unpaired electrons, but may comprise both spin and orbital contributions. The magnetic interaction between the neutron and the atom depends on the directions of the scattering vector and the magnetic moment vector according to a triple vector product. The direction of polarization of the neutron must also be taken

into account. For an unpolarized incident beam, the usual case in neutron powder diffraction, it is a useful consequence of the triple vector product that the magnetic scattering depends on the sine of the angle that the scattering vector makes with the magnetic moment on the scattering atom (see Section 2.3.4 and Chapter 7 in Kisi & Howard, 2008). The extent of the unpaired electron distribution (usually outer electrons) implies that the scattering diminishes as a function of Q, an effect that can be described by a magnetic form factor. For a well defined direction for the magnetic moment $\mathbf{M}$, and with a distribution of moment that can be described by a normalized scalar $m(\mathbf{r})$, the form factor as a function of the scattering vector $\mathbf{h}$ [defined in equation (1.1.17) in Chapter 1.1][6] is the Fourier transform of $m(\mathbf{r})$,

$$f(\mathbf{h}) = \int m(\mathbf{r}) \exp(2\pi i \mathbf{h} \cdot \mathbf{r})\, \mathrm{d}\mathbf{r},$$

where $m(\mathbf{r})$ can comprise both spin and orbital contributions [Section 6.1.2 of Volume C (Brown, 2006*a*)]. The tabulated form factors are based on the assumption that the electron distributions are spherically symmetric, so that $m(\mathbf{r}) = m(r) = U^2(r)$, where $U(r)$ is the radial part of the wave function for the unpaired electron. In the expansion of the plane-wave function $\exp(2\pi i \mathbf{h} \cdot \mathbf{r})$ in terms of spherical Bessel functions, we find that the leading term is just the zeroth-order spherical Bessel function $j_0(2\pi hr)$ with a Fourier transform

$$\langle j_0(h) \rangle = 4\pi \int_0^\infty U^2(r) j_0(2\pi hr) r^2\, \mathrm{d}r.$$

This quantity is inherently normalized to unity at $h = 0$, and may suffice to describe the form factor for spherical spin-only cases. In other cases it may be necessary to include additional terms in the expansion, and these have Fourier transforms of the form

$$\langle j_l(h) \rangle = 4\pi \int_0^\infty U^2(r) j_l(2\pi hr) r^2\, \mathrm{d}r$$

with l even; these terms are zero at $h = 0$ (Brown, 2006*a*). In practice these quantities are evaluated using theoretical calculations of the radial distribution functions for the unpaired electrons [Section 4.4.5 of Volume C (Brown, 2006*b*)].

Form factors can be obtained from data tabulated in Section 4.4.5 of Volume C (Brown, 2006*b*). Data are available for elements and ions in the 3*d*- and 4*d*-block transition series, for rare-earth ions and for actinide ions. These data are provided by way of the coefficients of analytical approximations to $\langle j_l(h) \rangle$, the analytical approximations being

$$\langle j_0(s) \rangle = A \exp\left(-as^2\right) + B \exp\left(-bs^2\right) + C \exp\left(-cs^2\right) + D$$

and for $l \neq 0$

$$\langle j_l(s) \rangle = s^2 \left[A \exp\left(-as^2\right) + B \exp\left(-bs^2\right) + C \exp\left(-cs^2\right) + D\right],$$

where $s = h/2$ in Å^{-1}. These approximations, with the appropriate coefficients, are expected to be coded in to any computer program purporting to analyse magnetic structures. Although the tabulated form factors are based on theoretical wave functions, it is worth noting that the incoherent scattering from an ideally disordered (*i.e.*, paramagnetic) magnetic system will display the magnetic form factor directly.

It is often convenient to define a (Q-dependent) magnetic scattering length

$$p = \left(\frac{e^2\gamma}{2m_e c^2}\right) gJf,$$

where m_e and e are the mass and charge of the electron, γ ($= \mu_n$) is the magnetic moment of the neutron, c is the speed of light, J is the total angular momentum quantum number, and g is the Landé splitting factor given in terms of the spin S, orbital angular momentum L, and total angular momentum quantum numbers by

$$g = 1 + \frac{J(J+1) + S(S+1) - L(L+1)}{2J(J+1)}.$$

For the spin-only case, $L = 0$, $J = S$, so $g = 2$. The differential magnetic scattering cross section per atom is then given by q^2p^2 where $|q| = \sin\alpha$, α being the angle between the scattering vector and the direction of the magnetic moment. This geometrical factor is very important, since it can help in the determination of the orientation of the moment of interest; there is no signal, for example, when the moment is parallel to the scattering vector. Further discussion appears in Chapters 2 (Section 2.3.4) and 7 in Kisi & Howard (2008).

2.3.2.6. *Structure factors*

The locations of the Bragg peaks for neutrons are calculated as they are for X-rays[7] (Section 1.1.2), and the intensities of these peaks are determined by a structure factor, which in the nuclear case is [*cf.* Chapter 1.1, equation (1.1.56)]

$$F_{hkl}^{\text{nuc}} = \sum_{i=1}^{m} b_i T_i \exp(2\pi i \mathbf{h} \cdot \mathbf{u}_i), \tag{2.3.7}$$

where b_i here denotes the coherent scattering length, T_i has been introduced to represent the effect of atomic displacements (thermal or otherwise, see Section 2.4.1 in Kisi & Howard, 2008), $\mathbf{h}$ is the scattering vector for the hkl reflection, and the vectors $\mathbf{u}_i$ represent the positions of the m atoms in the unit cell.

For coherent magnetic scattering, the structure factor reads

$$F_{hkl}^{\text{mag}} = \sum_{i=1}^{m} p_i \mathbf{q}_i T_i \exp(2\pi i \mathbf{h} \cdot \mathbf{u}_i), \tag{2.3.8}$$

where p_i is the magnetic scattering length. The vector $\mathbf{q}_i$ is the 'magnetic interaction vector' and is defined by a triple vector product (Section 2.3.4 in Kisi & Howard, 2008), and has modulus $\sin\alpha$ as already mentioned. In this case the sum needs to be taken over the magnetic atoms only.

As expected by analogy with the X-ray case, the intensity of purely nuclear scattering is proportional to the square of the modulus of the structure factor $|F_{hkl}^{\text{nuc}}|^2$. In the simplest case of a collinear magnetic structure and an unpolarized incident neutron beam, the intensity contributed by the magnetic scattering is proportional to $|F_{hkl}^{\text{mag}}|^2$, and the nuclear and magnetic contributions are additive.

2.3.3. Neutron sources

2.3.3.1. *The earliest neutron sources*

The earliest neutron source appears to have been beryllium irradiated with α-particles (helium nuclei), as emitted for example by polonium or radon. First described as 'beryllium radiation', the radiation from a Po/Be source was identified by

[6] To reiterate, $\mathbf{h} = \mathbf{s} - \mathbf{s}_0$, where $\mathbf{s}_0$ and $\mathbf{s}$ are vectors, each of magnitude $1/\lambda$, defining the incident and scattered beams. Note that $\mathbf{Q} = 2\pi\mathbf{h}$.

[7] The nuclear unit cell is expected to coincide with the X-ray unit cell, but the magnetic unit cell may be larger. So, although the methods of calculation are the same, the larger magnetic cell may give rise to additional (magnetic) Bragg peaks.

Chadwick (1932) as comprising neutrons:

$$^{4}_{2}\mathrm{He} + ^{9}_{4}\mathrm{Be} \rightarrow ^{12}_{6}\mathrm{C} + ^{1}_{0}\mathrm{n}.$$

It was soon found (Szilard & Chalmers, 1934) that the disintegration of beryllium under irradiation by the γ-rays from radium also led to the release of neutrons; this represented an alternative neutron source. The first demonstrations of the diffraction of neutrons (Mitchell & Powers, 1936; von Halban & Preiswerk, 1936) made use of Rn/Be sources, analogous to Chadwick's Po/Be source. These were now surrounded by paraffin to reduce the energy ('moderate') and hence increase the de Broglie wavelength of the neutrons, and so provide a reasonable match to the atomic spacings in the crystalline samples; in the Mitchell & Powers' demonstration the reflection of neutrons of estimated wavelength 1.6 Å from (100) planes in large single crystals of MgO, the separation of these planes being 4.2 Å, showed a dependence on crystal orientation that was indicative of Bragg reflection. The intensities available from these sources, however, were not sufficient to allow the observation of diffraction from polycrystalline (powder) samples.

A source based on the bombardment of Be by cyclotron-accelerated MeV deuterons (nuclei of deuterium)

$$^{2}_{1}\mathrm{H} + ^{9}_{4}\mathrm{Be} \rightarrow ^{10}_{5}\mathrm{B} + ^{1}_{0}\mathrm{n}$$

was also employed in early work, notably by Alvarez & Bloch (1940) in their determination of the neutron magnetic moment.

The further development of neutron diffraction, and indeed the first observation of neutron powder diffraction, awaited the development of much more intense neutron sources; the first suitably intense neutron sources were nuclear reactors. The neutron-induced fission of uranium isotope $^{235}_{92}\mathrm{U}$ was observed in 1938 and reported early in 1939 (Hahn & Strassmann, 1939; Meitner & Frisch, 1939; Anderson *et al.*, 1939). By this time Fermi and his co-workers (Fermi, Amaldi, D'Agostino *et al.*, 1934; Fermi, Amaldi, Pontecorvo *et al.*, 1934) had already carried out studies on neutron activation, in the course of which they found that neutrons could be moderated by hydrogenous materials, providing 'slow' neutrons for which the activation cross sections were enhanced. Once it was established that the neutron-induced fission of a $^{235}_{92}\mathrm{U}$ nucleus also led to the release of ~2–3 'fast' neutrons plus energy (von Halban *et al.*, 1939; Zinn & Szilard, 1939), then a self-sustaining 'chain reaction' based on the fission of $^{235}_{92}\mathrm{U}$ by a slow neutron, the slowing in a moderator of the several fast neutrons released, followed by the slow-neutron-induced fission of additional $^{235}_{92}\mathrm{U}$ nuclei, became a realistic possibility. The translation of this possibility into reality was given great impetus by the military potential of the chain reaction; the reader is referred to Mason *et al.* (2013) for the history of this development. The first self-sustaining chain reaction took place in Chicago Pile 1 (CP-1) on 2 December 1942. CP-1 made use of uranium oxide mixed with some metallic uranium as fuel, high-purity graphite as the neutron moderator and rods of neutron-absorbing cadmium for control. CP-1 was located on a squash court under the spectator stand at a sports field at the University of Chicago; remarkably, its construction took less than a month. In November 1943, an essentially scaled up version of this reactor, the X-10 pile (also known as the Oak Ridge Graphite Reactor) achieved criticality. The fuel was now metallic uranium, and the greater power (1 MW as compared with the 200 W of CP-1) necessitated an air cooling system; the neutron flux[8] was a creditable 10^{12} n cm^{-2} s^{-1} and the main purpose was the production of plutonium. May 1944 saw the completion of yet another reactor, Chicago Pile 3 (CP-3), outside Chicago at the site of the present Argonne laboratories. This was a 300 kW reactor, using natural uranium fuel, with heavy water serving as both moderator and coolant; this also provided a flux of 10^{12} n cm^{-2} s^{-1}.

Early diffraction experiments using reactor neutrons were carried out 'in the wings of the Manhattan project' (Mason *et al.*, 2013). Evidently, Wollan & Borst (1945) obtained rocking curves when collimated thermal neutrons from X-10 were beamed onto single crystals of gypsum and rocksalt, while Zinn was able to reflect neutrons from a calcite crystal [see, for example, the post-war publication by Zinn (1947)]; much of the wartime interest was in using these crystals for neutron spectrometry. However, the potential use of these copious sources of neutrons was recognized, so by the early months of 1946 (according to Shull, 1995) the first neutron powder-diffraction patterns, from polycrystalline NaCl and from light and heavy water, had been recorded. Wollan and co-workers (Wollan & Shull, 1948; Shull *et al.*, 1948) published a number of these early diffraction patterns, along with a schematic of the diffractometer employed.

Although accelerator-based neutron sources had been around as early as 1940 (see above), the development of such sources, at least for diffraction applications, proceeded at a relatively slower pace. Indeed, it was not until 1968 that the first reports of neutron powder diffraction using accelerator-based sources appeared in the literature (Moore *et al.*, 1968; Kimura *et al.*, 1969; Day & Sinclair, 1969). All this work involved the use of linear electron accelerators (LINACs) delivering pulses of ~150 MeV electrons onto a heavy-metal target; the deceleration results in *Bremsstrahlung* radiation (photons) of sufficient energy to bring about the release of neutrons from the target. These fast neutrons were moderated, and the result was a pulsed source of thermal neutrons. Diffraction patterns were recorded by time-of-flight methods which had already been developed on reactor sources (Buras & Leciejewicz, 1964).

It may be helpful to describe one of these experiments in more detail (Kimura *et al.*, 1969). A tungsten target immersed in water was bombarded by 2.5 μs pulses of 250 MeV electrons from the Tohoku LINAC; the water, which served as a moderator, was also 'poisoned' by the addition of neutron-absorbing boric acid. The thermal neutron pulses were of 30–50 μs duration. It is a fundamental problem that the time taken to moderate the fast neutrons produced at an accelerator-based source degrades the time structure, and the addition of boron here was one method to counteract this effect. Kimura *et al.* presented a selection of time-of-flight diffraction patterns, from Al at different temperatures, as well as from Si, Ni, ZnO, $CaFe_2O_4$ and α-Fe_2O_3.

The next generation of accelerator-based sources were spallation sources, based on the breaking up of heavy target elements by bombardment with 10–1000 MeV protons; up to ~30 neutrons are ejected in each spallation event; such sources can be operated in either a pulsed mode or continuously. The first spallation sources were ZING-P (100 nA of 300 MeV protons, pulsed at 30 Hz, target Pb, moderator polyethylene) and ZING-P′ (3 μA of 500 MeV protons, 30 Hz, target W/natural U, moderator polyethylene/liquid hydrogen), both at the Argonne National Laboratory (Carpenter, 1977), and at the TRIUMF laboratory (400 μA of 500 MeV protons, steady, target liquid Pb/Bi, moderator light/heavy water) in Vancouver. The KENS facility (operational from 1980 to 2005, 9 μA of 500 MeV protons, 20 Hz, target W, moderator solid methane/ice) in Tsukuba, Japan, and

[8] The powers and fluxes given here are taken from a presentation by T. E. Mason at the Bragg Symposium, Adelaide, 6 December 2012.

the Intense Pulsed Neutron Source (IPNS) at the Argonne National Laboratory (operational from 1981 to 2008, 15 μA of 450 MeV protons, 30 Hz, target depleted U, moderator solid/liquid methane) are both worthy of mention for their work on techniques and applications at pulsed neutron sources; notable are contributions from IPNS on the subjects of high-temperature superconductors (Jorgensen *et al.*, 1987) and colossal magnetoresistance (Radaelli *et al.*, 1997).

The specifications and performance of modern currently operating spallation neutron sources will be presented in Section 2.3.3.3.

2.3.3.2. *Fission reactors for neutron-beam research*

Reactors used for neutron-beam research all rely on the fissile uranium isotope[9] $^{235}_{92}$U. This constitutes only about 0.7% of natural uranium; however, enrichment in this isotope is possible. A representative fission event would be

$$^{1}_{0}\mathrm{n} + {}^{235}_{92}\mathrm{U} \rightarrow {}^{236}_{92}\mathrm{U} \rightarrow {}^{141}_{56}\mathrm{Ba} + {}^{92}_{36}\mathrm{Kr} + 3{}^{1}_{0}\mathrm{n} + 170\ \mathrm{MeV}.$$

This equation indicates that a neutron of thermal energy is captured by ^{235}U to form ^{236}U in an unstable state, and in the majority of cases (88%) this breaks up almost instantly to yield fission products of intermediate mass, fast neutrons and energy. The unstable ^{236}U can break up in many different ways – there are usually products of intermediate but unequal masses, with masses distributed around 95 and 135 (Burcham, 1979), with the release of usually 2 or 3 neutrons (average 2.5; one of these neutrons is needed to initiate the next fission event), and of different amounts of energy (average around 200 MeV). As explained in Section 2.3.3.1, a chain reaction becomes possible if the fast neutrons released in the fission process are moderated to thermal energies so that they can be captured by another ^{235}U nucleus. Neutrons will lose energy most rapidly through collisions with nuclei of mass equal to the neutron mass, namely nuclei of hydrogen atoms, but collisions with other light nuclei are also quite effective. Hydrogenous substances are evidently useful, and water would seem ideal; however, there is some absorption of neutrons in water, so in some reactors, heavy water (D_2O, where D is $^{2}_{1}$H) is used since, as can be seen from the absorption cross sections (Table 2.3.2), thermal neutron capture in D is orders of magnitude less than for H. It has not been possible to achieve a self-sustaining chain reaction using natural uranium and light water as a moderator – for this reason uranium fuel enriched in ^{235}U and/or heavy-water moderators are in use. Adjacent to the reactor core is a so-called reflector, which is simply in place to moderate neutrons and prevent their premature escape. The energy released in the fission process ends up as heat, which must be dissipated (or used), so cooling is required – where light or heavy water is used as the moderator it can also serve as the coolant. Control rods are also essential – these are rods containing highly neutron absorbing materials, such as boron, cadmium or hafnium, which can be inserted into or withdrawn from the reactor to increase, maintain or reduce the thermal neutron flux as required. These control rods provide the means for reactor shutdown.

The neutrons in a reactor core range from the fast neutrons (~1 MeV) released in the fission process, through epithermal neutrons (in the range eV to keV), which are neutrons in the process of slowing down, to thermal neutrons (~25 meV), which are neutrons in equilibrium with the moderator (see Carlile, 2003). Evidently, for sustaining the chain reaction and for providing neutrons for diffraction instruments, the thermal neutrons are of the greatest interest. Neutrons in thermal equilibrium with the moderator have a Maxwellian distribution of energies, such that the number of neutrons with energies between E and $E + \mathrm{d}E$ is given by $N(E)\,\mathrm{d}E$, where

$$N(E) = \frac{2\pi N_0}{(\pi k_B T)^{3/2}} (E)^{1/2} \exp(-E/k_B T). \qquad (2.3.9)$$

Here N_0 is the total number of neutrons, T is the temperature (in kelvin) of the moderator, and k_B is Boltzmann's constant. The neutron flux is the product of the neutron density with the neutron speed, so the energy dependence of the flux distribution takes the form

$$\varphi(E) = \varphi_0 \frac{E}{(k_B T)^{3/2}} \exp(-E/k_B T). \qquad (2.3.10)$$

This distribution takes its peak value at $E = k_B T$; for a temperature of 293 K, this leads to a peak in the flux distribution at 25.2 meV (*cf.* Section 2.3.1). In the diffraction context the wavelength dependence of the flux is of more interest. Making use of the relationships $E = h^2/2m\lambda^2$ and $\mathrm{d}E/\mathrm{d}\lambda = -h^2/m\lambda^3$, we find that the variation of flux with wavelength can be described by $\varphi(\lambda)\,\mathrm{d}\lambda$, where

$$\varphi(\lambda) \propto \lambda^{-5} \exp(-h^2/2m\lambda^2 k_B T). \qquad (2.3.11)$$

This distribution peaks at $\lambda = h/(5mk_B T)^{1/2}$; at 293 K the peak in this wavelength distribution is at 1.15 Å. For some applications of neutron diffraction it may be desirable to have a greater neutron flux at shorter or longer wavelengths; as indicated in Fig. 2.3.5 this can be achieved by cooling or heating strategically placed special moderators.

As one specific example of a research reactor, we consider the NBSR located at the National Institute of Standards and Technology, Gaithersburg, USA. This reactor uses highly enriched (93% ^{235}U) uranium in U_3O_8-Al as fuel, and heavy water as moderator and coolant. The thermal neutron flux in this reactor is 4×10^{14} n cm^{-2} s^{-1}. It uses four cadmium control blades. An early plan view of this reactor and a cutaway view of the core assembly

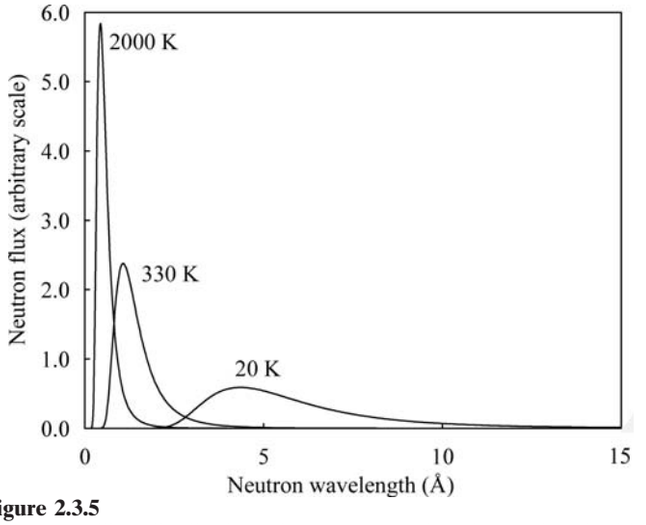

Figure 2.3.5
The Maxwellian distribution of neutron wavelengths produced within moderators at different temperatures. Reproduced from Kisi & Howard (2008) by permission of Oxford University Press.

[9] Bombardment with >1 MeV neutrons can cause the fission of the predominant uranium isotope ^{238}U; however, there are too few neutrons at these energies to support a chain reaction based on this isotope.

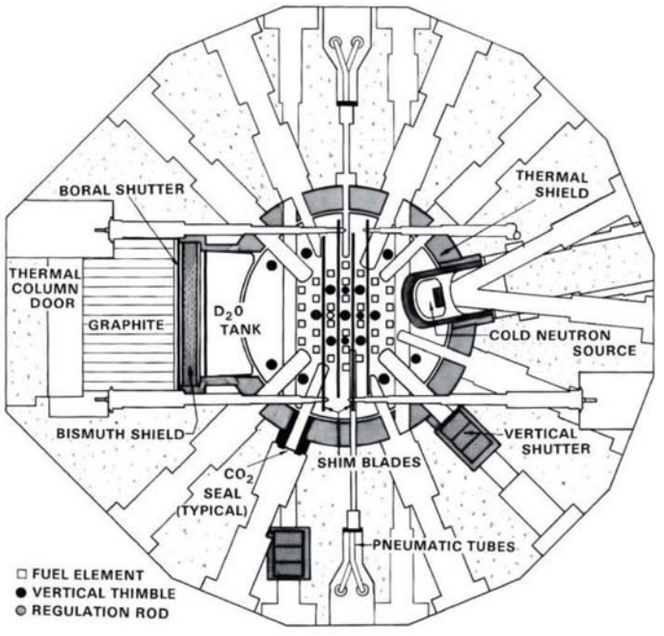

Figure 2.3.6
The NBSR at the National Institute of Standards and Technology Center for Neutron Research. Part (*a*) is a plan view (reproduced from Rush & Cappelletti, 2011) while (*b*) is a recent cutaway view of the reactor core showing the liquid-hydrogen cold source on the right-hand side.

are shown in Fig. 2.3.6. Note the presence of numerous beam tubes that allow neutrons to be taken out from the vicinity of the reactor core. This view of the NBSR (Fig. 2.3.6*a*) shows provision for a cold neutron source, and for beam tubes to transport cold neutrons to experiments, but it was years before any cold neutron source was installed. The first cold source, installed in 1987, was frozen heavy water; this was replaced in 1995 by a liquid-hydrogen cold source, and that was upgraded in turn in 2003. The NBSR first went critical in December 1967; the history of its subsequent development and use in neutron-beam research has been recounted by Rush & Cappelletti (2011).

The HFR at the Institut Laue–Langevin (ILL), considered to be the premier source for reactor-based neutron-beam research, serves as our second example. It too uses highly enriched uranium, here in a single centrally located U_3Al_x-Al fuel element, and it relies on heavy water for moderator and coolant. It operates at 58 MW and the thermal neutron flux is 1.5 $\times$

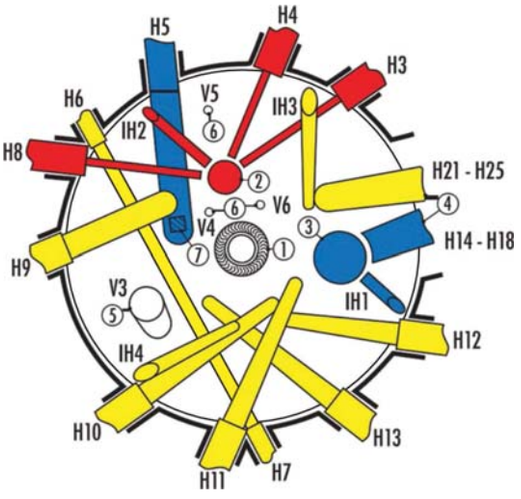

Figure 2.3.7
Schematic diagram of the HFR operated by the Institut Laue–Langevin in Grenoble, France. It has a compact core – the beam tubes avoid viewing the central core in favour of the surrounding moderator. This reactor also features hot (red) and cold (blue) sources. (Diagram reproduced with permission from the ILL from The Yellow Book 2008, https://www.ill.eu/fileadmin/users_files/Other_Sites/Yellow-Book2008CDRom/index.htm.)

10^{15} n cm^{-2} s^{-1}. The reactor incorporates two liquid-deuterium cold sources, operating at 20 K, and a graphite hot source operating at 2000 K. In the HFR, being of modern design and purpose-built for neutron-beam research, the beam tubes do not view the core directly, but are 'tangential' to it (Fig. 2.3.7); this reduces the unwelcome fast-neutron component of the emerging beams. The HFR achieved criticality in July 1971. More details on this reactor can be found in the 'Yellow Book' which is maintained on the ILL web site, https://www.ill.eu.

From the opening paragraph of this section, it might be concluded that the more heavy water deployed, and the more highly is the uranium enriched in the fissile isotope ^{235}U, the greater the neutron fluxes that can be obtained. This conclusion would be correct, but concerns about nuclear proliferation have brought a shift to the use of low-enrichment uranium (LEU) in which the ^{235}U is enriched to less than 20%; however, in some reactors highly enriched uranium (HEU) with enrichment levels greater than 90% remains in use. Table 2.3.3 gives pertinent details on a number of research reactors important for neutron diffraction. Additional reactors are listed by Kisi & Howard (2008) in their Table 3.1, and a complete listing is available from the International Atomic Energy Agency Research Reactor Database (IAEA RRDB, https://nucleus.iaea.org/RRDB/RR/ReactorSearch.aspx).

2.3.3.3. *Spallation neutron sources*

The bombardment of heavy-element nuclei by high-energy protons, *i.e.* protons in the energy range 100 MeV to GeV, causes the nuclei to break up with the release of large numbers of neutrons. The word 'spallation' might suggest that neutrons are simply being chipped off the target nucleus, and indeed neutrons can be ejected by protons in a direct collision process with transfer of the full proton energy, but such simple events are relatively rare. In most cases there is a sequence involving incorporation of the bombarding proton into the nucleus, intra- and internuclear cascades accompanied by the ejection of assorted high-energy particles, including neutrons, and then an 'evaporation' process releasing neutrons from excited nuclei with

Table 2.3.3
Details on selected research reactors

The primary source of data is the IAEA Research Reactor Database (RRDB). The publicly accessible RRDB does not include information on fuel: limited information on this has been found from other internet sources.

Reactor (type)	Power (MW)	Location	Fuel (see text)	Moderator/ coolant	Reflector	Thermal flux (n cm^{-2} s^{-1})	Cold/hot neutron sources
CARR (tank in pool)	60	CIAE, Beijing, China	U_3Si_2-Al, LEU 19.75%	Light water	Heavy water	8×10^{14}	1 cold
FRM-II (pool)	20	TUM, Garching, Germany	U_3Si_2-Al, HEU	Light water	Heavy water	8×10^{14}	1 cold, 1 hot
HANARO (pool)	30	KAERI, Daejeon, Korea	U_3Si, LEU 19.75%	Light water	Heavy water	4.5×10^{14}	1 cold
HFIR (tank)	85	ORNL, Oak Ridge, USA	U_3O_8-Al, HEU 93%	Light water	Beryllium	2.5×10^{15}	1 cold
HFR (heavy water)	58.3	ILL, Grenoble, France	U_3Al_x-Al, HEU	Heavy water	Heavy water	1.5×10^{15}	2 cold, 1 hot
JRR-3M† (pool)	20	JAEA, Tokai, Japan	U_3O_8-Al, U_3Si_2-Al, LEU	Light water	Light water, heavy water, beryllium	2.7×10^{14}	1 cold
NBSR (heavy water)	20	NIST, Gaithersburg, USA	U_3O_8-Al HEU 93%	Heavy water	Heavy water	4×10^{14}	1 cold
OPAL (pool)	20	ANSTO, Sydney, Australia	U_3Si_2-Al, LEU 19.75%	Light water	Heavy water	2×10^{14}	1 cold

† This reactor has been temporarily shut down.

energies comparable to those released in the fission process (Carpenter, 1977; Carlile, 2003; Arai & Crawford, 2009). The numbers of neutrons released in these various processes depend on the proton energies and the target materials employed; for 1 GeV protons on a Pb target, around 25 neutrons are released per bombarding proton (Arai & Crawford, 2009). Target materials in use include Hg, Pb, W, Ta and ^{238}U (depleted uranium). The yield of neutrons per proton for non-fissionable target materials is approximated by $0.1(E - 0.12)(A + 20)$ where E is the proton energy in GeV and A is the atomic number of the target nucleus; for a target such as ^{238}U that is fissionable under bombardment by high-energy neutrons the yield is almost double that. Generally, the energy to be dissipated as heat in the spallation process will be no more than the energy of the bombarding proton, so for the example of 1 GeV protons on Pb it should not exceed 40 MeV per neutron produced. Nevertheless, cooling requires attention. The use of liquid targets such as Hg, and Pb either in pure form or in a Pb-Bi eutectic alloy, facilitates the dissipation of heat. Solid targets are usually water cooled. The fast neutrons from spallation need to be moderated, not in this case for sustaining the process, but simply to make them useful for diffraction and other applications. Moderators in common use include water, heavy water, liquid or solid methane (CH_4), and liquid hydrogen (H_2). The volumes of moderator are usually small, for reasons that will be explained below.

Most spallation neutron sources, though by no means all, operate in 'short-pulse mode', then employ time-of-flight methods in their instrumentation. The duration of the neutron pulse is critical in determining the time-of-flight resolution. Short-pulse operation depends first of all on a short-pulse structure of the bombarding protons. This is inherent in proton-accelerating systems that incorporate synchrotron accelerators or accumulator rings, since the protons become bunched[10] while travelling around these rings, and pulses of duration <1 μs are delivered. The frequency of these pulses is modest, say 50 Hz, in part to reduce power requirements, but also to avoid the situation in which the desired thermal (or cold) neutrons from one pulse are overtaken by fast neutrons from the next. For short-pulse operation, the proton pulse must be translated into a still-short pulse of moderated neutrons; this has significant implications for moderator design (Tamura *et al.*, 2003; Arai, 2008; Arai & Crawford, 2009; Batkov *et al.*, 2013; Zhao *et al.*, 2013; Thomsen, 2014). The normal processes of moderation – neutrons giving up energy in collisions with nuclei in the moderator until thermal equilibrium is achieved – need to be to some extent curtailed. One means to curtail these processes is to use only a small volume of moderator, so neutrons escape before spending excessive time in it. Another is to place neutron absorbers – cadmium or gadolinium – around the moderator, or indeed incorporate these absorbing materials into it, so that the slow neutrons remaining in the moderator are absorbed before the pulse length becomes excessive; in this case the moderator is said to be 'decoupled' from the target. For cold-neutron moderators on short-pulse spallation sources the use of an ambient-temperature 'pre-moderator' may be advantageous. Whatever the means to limit the dwell time in the moderator, the emerging neutrons will be under-moderated, hence their spectrum will contain more epithermal neutrons (*i.e.* neutrons with energies of the order of eV to keV) than fully moderated neutrons from a continuous source. Fig. 2.3.8 shows the results for energy spectra and pulse length, from Monte Carlo calculations, for different cryogenic moderators for the J-PARC spallation neutron source, Tokai, Japan. The neutron dwell time and therefore the pulse length are calculated to be smaller in the decoupled moderators (Fig. 2.3.8*b*), but comparison with the coupled moderator (Fig. 2.3.8*a*) shows that intensity is sacrificed. The pulse length in the high-energy region, and at lower energies for the poisoned moderators, varies as roughly $1/(E)^{1/2}$; from equation (2.3.1) this makes the pulse length Δt proportional to the wavelength λ. In a time-of-flight analysis we measure the flight time t over a length L; noting that $v = L/t$ and using that same equation we find that t is also proportional to λ, *viz.* $t = (mL/h)\lambda$. The result is that the time resolution $\Delta t/t$

[10] At the ISIS spallation neutron source, for example, the protons are injected into the synchrotron in 200 μs bursts, where they form two bunches each only 100 ns wide (detail from https://www.isis.stfc.ac.uk/Pages/How-ISIS-works–in-depth.aspx).

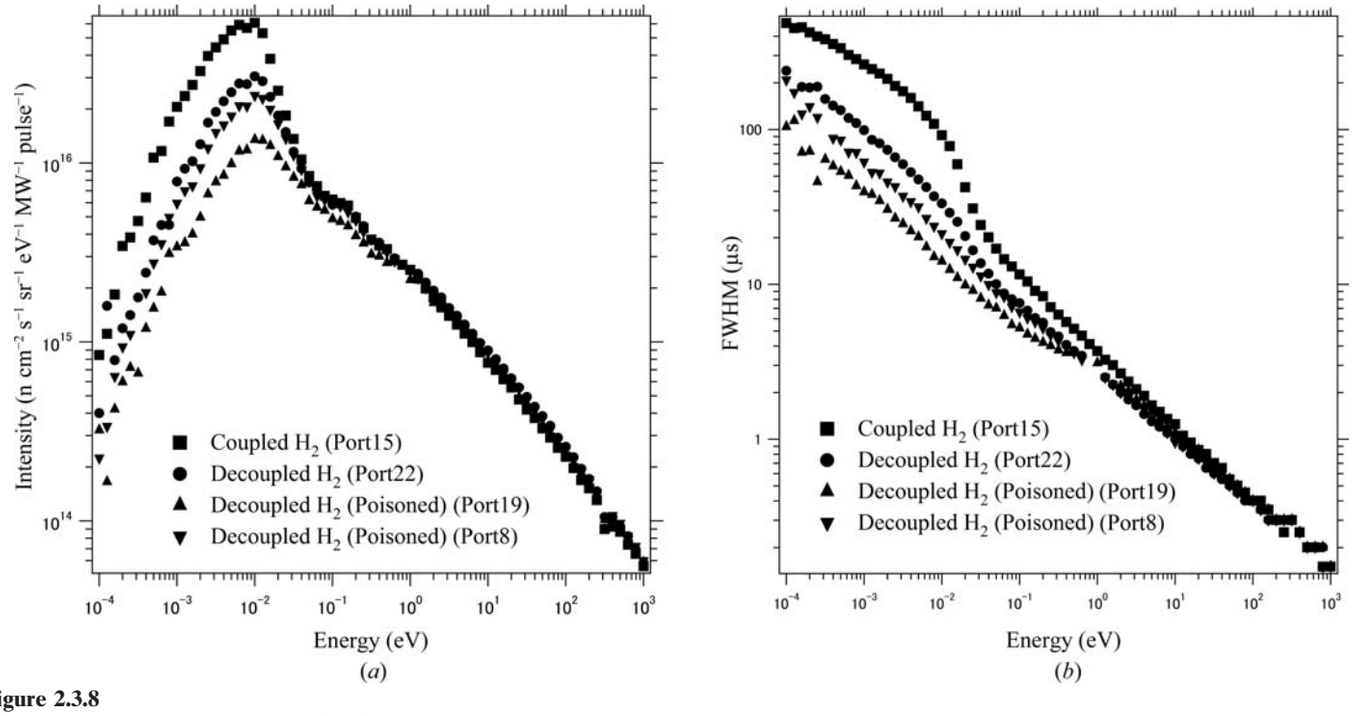

Figure 2.3.8
(*a*) The neutron energy distribution (flux) of the J-PARC neutron source for coupled, decoupled and poisoned decoupled moderators. The flux consists of a Maxwell distribution at low energies and a $1/E$ region at higher energies. (*b*) Pulse duration as a function of energy calculated for the same moderators. For the decoupled moderators, the peak widths vary approximately as $1/E^{1/2}$. Reproduced from Tamura *et al.* (2003).

is independent of flight time (or wavelength), which is a very satisfactory state of affairs (see Section 2.3.4.2.1).

As mentioned earlier, there is the problem for time-of-flight analysis that the slower neutrons from one pulse might be overtaken by the first arrivals from the next – a problem known as 'frame overlap'. Taking the example of 25 meV thermal neutrons, at a speed of 2190 m s^{-1} and a 50 Hz pulse repetition frequency, the neutrons from one pulse will have travelled 44 m when the next pulse occurs. If instrument flight paths are longer than this, or indeed if slower neutrons are involved, then the frame-overlap problem is encountered. A conceptually simple approach is to reduce the pulse frequency, and this has been implemented at the UK's ISIS neutron facility where Target Station 2 takes just one pulse in five from the proton-acceleration system, reducing the effective pulse frequency to 10 Hz; the other four pulses are directed to Target Station 1. Neutron choppers provide an alternative means to address this problem. The simplest kind of chopper is a disc (Fig. 2.3.9), usually of aluminium, nickel alloy or carbon fibre, coated in part with neutron-absorbing material such as boron, cadmium or gadolinium, rotating in a synchronous relationship with the source. A chopper located near to the source can be adjusted to block the fast neutrons and γ-rays that emerge immediately, but allow through neutrons in a restricted time window, from T_0 to $T_0 + \Delta T$, measured from the time of the pulse. Evidently, time $T_0 + \Delta T$ cannot exceed the time for a single rotation of the disc; when the disc is rotating at the pulse-repetition frequency this is the time between pulses. If the disc-rotation frequency is a submultiple of the pulse frequency, *i.e.* the rotation frequency is the pulse frequency divided by n, then the time window ΔT can be set to select only every nth pulse from the source. A two-chopper arrangement is used, for example, in the 96 m flight path of the High Resolution Powder Diffractometer (HRPD) at the ISIS facility; the first chopper at 6 m from the source runs at the pulse frequency and the second at 9 m from the source runs at one-fifth or one-tenth of that frequency, so that only every fifth or tenth pulse is used (HRPD user manual, http://www.isis.stfc.ac.uk/Pages/hrpd-manual.pdf).

Figure 2.3.9
One of the disc choppers in use at the ISIS neutron facility. This is an aluminium (2014A) alloy disc, and the neutron-absorbing coating (the darker region) is boron carbide in a resin. The cut-out on the right-hand side provides the aperture for neutrons. (Credit: STFC.)

Although we have introduced neutron choppers in the context of spallation sources, we should acknowledge that mechanical choppers and velocity selectors have a long history, dating back long before the advent of spallation sources. In fact, the first report on a velocity selector (Dunning *et al.*, 1935) pre-dates even the earliest demonstrations of neutron diffraction. Mechanical systems have long been used at continuous neutron sources to act as velocity (wavelength) selectors, and/or to tailor pulses of neutrons suitable for time-of-flight studies. Two disc choppers can be arranged to serve both purposes – the first chopper has a limited aperture transmitting a short pulse of neutrons, and the second chopper, with a similar aperture and located at some distance from the first, is phased so as to allow through only those neutrons with a particular velocity. This arrangement can provide short pulses of more-or-less monochromatic neutrons to an experiment. The helical velocity selector (Friedrich *et al.*, 1989) is conceptually somewhat similar. This takes the form of a cylinder,

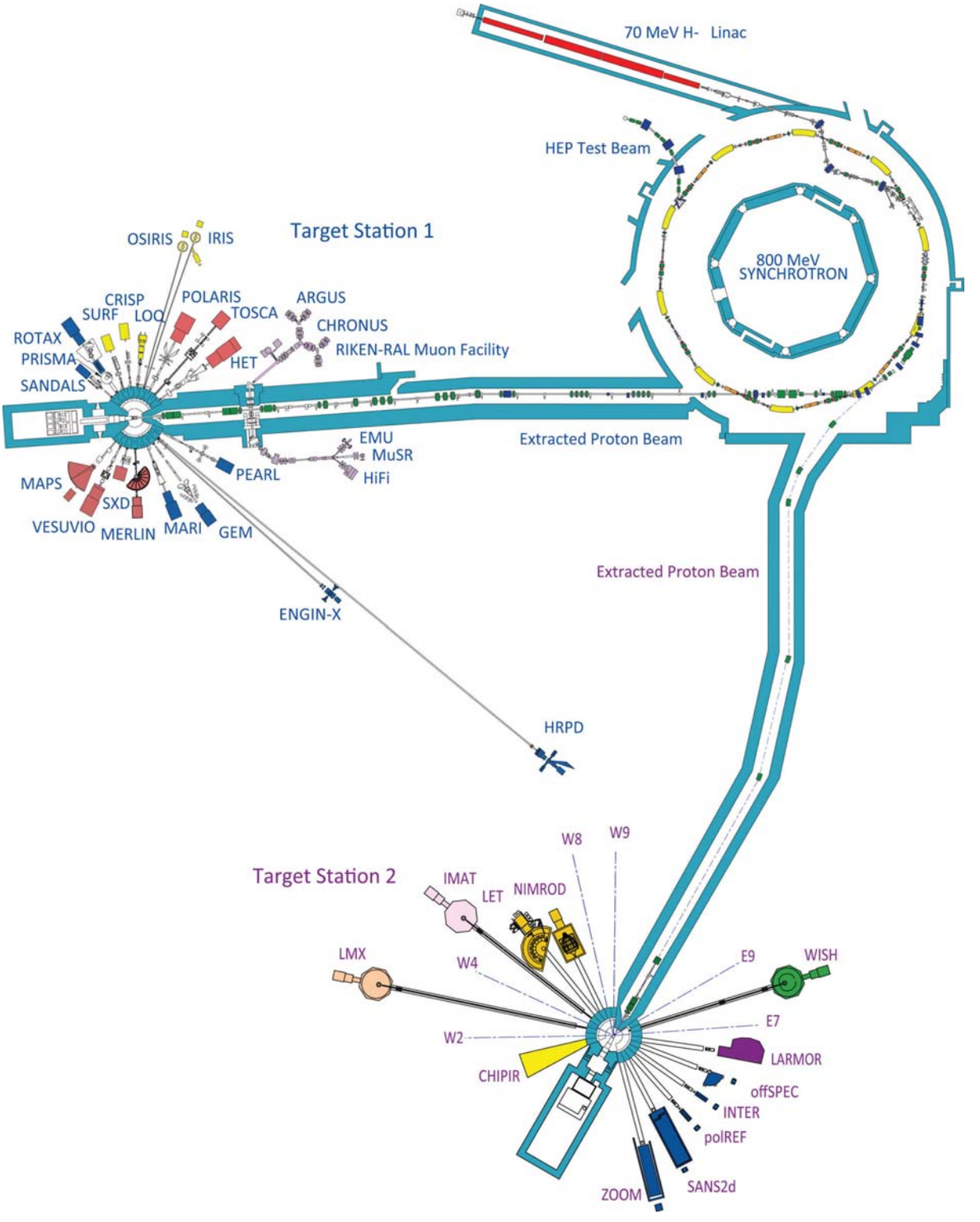

Figure 2.3.10
Layout of the ISIS spallation neutron source. (Credit: STFC.)

or indeed a stack of discs, rotating around an axis parallel to the neutron beam, with helical slits such that exits are offset from the entrance apertures in much the same manner as described above; the difference from the two-chopper arrangement is that there are apertures located all around the cylinder, giving closely spaced pulses unsuitable for time-of-flight studies. The purpose of mechanical wavelength selection at a continuous source is to select longer wavelengths and a broader range of wavelengths than a crystal monochromator (Section 2.3.4.1.2) could provide. Also worthy of mention is the Fermi chopper (Fermi *et al.*, 1947), comprising a package of neutron-transmitting slits set into a cylinder that rotates at rates of some hundreds of hertz around an axis in the plane of the slits, coincident with the cylinder axis, and perpendicular to the neutron beam. Neutrons above a threshold velocity are transmitted for the brief periods in which the slits are suitably aligned, so short (μs) but frequent pulses of neutrons are delivered. In a variation of the Fermi chopper (Marseguerra & Pauli, 1959), the transmitting slits are curved, providing for the transmission of rather slower neutrons while preventing the transmission of faster ones; in this variant the chopper not only delivers short pulses of neutrons but acts as a velocity selector as well. Neutron choppers are used in various combinations at both continuous and pulsed neutron sources; the Fermi chopper in particular can be used for 'shaping'

the pulses at long-pulse spallation neutron sources (Peters *et al.*, 2006).

As an initial case study, we consider the ISIS neutron facility, located in Oxfordshire, England, at the Rutherford Appleton Laboratory. This is a well established neutron spallation source supporting a strong programme of research using neutron beams. Of particular note are the excellent facilities for powder diffraction. First neutrons were delivered in 1984, but there have been upgrades since then, including the commissioning of a second target station in 2009. Fig. 2.3.10 is a schematic showing the layout of this facility. Some details about its operation are available on the ISIS web site, at https://www.isis.stfc.ac.uk/Pages/How-ISIS-works.aspx. Briefly, an ion source and radio-frequency quadrupole accelerator (not shown) inject bunches of negative hydrogen ions, H^-, into the linear accelerator where they are accelerated to 70 MeV. These are passed through aluminium foil, which strips them of their electrons, so they become protons, H^+, which are then accelerated to 800 MeV in the proton synchrotron. The protons, then travelling in two 100 ns bunches 230 ns apart, are kicked out of their synchrotron orbits and directed toward the targets. The whole process is repeated at a frequency of 50 Hz; the kickers are arranged to send one pulse in five to Target Station 2 (so that the pulse frequency there is just 10 Hz), and the remainder to Target Station 1. Both targets are made of tantalum-coated tungsten, as a stack of water-cooled plates in Target Station 1 and as a heavy-water surface-cooled cylinder in Target Station 2. As explained earlier, the fast neutrons produced in the spallation process must be moderated, and for this purpose moderators are located adjacent to the targets: two water moderators at 300 K, one liquid-methane moderator at 100 K and one liquid-hydrogen moderator at 20 K at Target Station 1; and one decoupled solid-methane moderator at 26 K and one coupled liquid-hydrogen/methane moderator at 26 K at Target Station 2. The widths of the pulses of the moderated neutrons are typically 30–50 μs, but 300 μs for the coupled moderator at Target Station 2. The target/moderator assemblies are surrounded, apart from beam exit ports, by beryllium reflectors. The schematic of Fig. 2.3.10 indicates the placement of the various neutron-beam instruments around the target stations.

The Swiss neutron spallation source, SINQ, located at the Paul Scherrer Institute in Villigen, is the only spallation source operating in continuous mode. SINQ reached full power in 1997. Since there is no time structure to be preserved, more generous quantities of moderator can be used; in fact the target, which becomes the source of neutrons, is located centrally in a moderator tank. The situation here is not very different from that in a medium-flux research reactor. The target comprises lead rods in Zircaloy tubes, the moderator is heavy water and there is a light-water reflector outside the moderator tank. Protons accelerated first by a Cockroft–Walton accelerator, then to 72 MeV by an injector cyclotron, and finally to 590 MeV in a proton ring cyclotron are directed onto the target from below (Fig. 2.3.11). The proton current is initially 2.4 mA, but this is reduced in muon production, so that only about 1.65 mA reaches the spallation target. The power is thus close to 1.0 MW. A horizontal insert in the moderator tank houses a liquid-deuterium cold source at 25 K.

As a final example we describe the 5 MW long-pulse European Spallation Source, now under construction in Lund, Sweden (see Fig. 2.3.12). A more detailed description is available at the ESS web site, https://europeanspallationsource.se/technology. The proton-acceleration system, although comprising a number of different components, will be linear. The protons from the ion source will be accelerated through a radio-frequency quadrupole and drift tube LINAC up to 90 MeV, then through a series of superconducting cavities up to the final energy of 2 GeV. This system will deliver proton pulses of 2.86 ms duration at a 14 Hz repetition rate; the average current will be 6.26 mA and hence the total power 5 MW. The target material will be helium-cooled tungsten encased in stainless steel, in the form of a 2.5 m-diameter rotating wheel. Such an arrangement assists in dissipation of the heat deposited in the target. Coupled liquid-hydrogen moderators will be located above and below the rotating wheel, and this assembly will be partially surrounded by a water pre-moderator and beryllium reflector. Neutron choppers will be used to shape the neutron pulses as required, and neutron optical systems will deliver neutrons to the experiments. First beam on target is expected in 2019.

Characteristics of these and other neutron spallation sources are recorded in Table 2.3.4. The information included there has been taken from the respective facility web sites.

2.3.3.4. *Neutron beam tubes and guides*

Ideally, neutron diffractometers should be designed following a holistic approach, designing the source of moderated neutrons, through the delivery system, to the instrument itself. This is not often possible in practice; for example the source must often be taken as a given, and in some cases the delivery of the neutrons as well. The holistic approach is commonly a very large Monte Carlo simulation, not suitable for purposes of description; in this chapter, therefore, we provide separate descriptions of these different components.

The simplest delivery system is a neutron beam tube or collimator. A collimator could comprise just two pinholes of diameters a_1 and a_2 cut into neutron-absorbing material, and placed at a distance L apart; this limits the divergence of the beam to (full angle) $2\alpha = (a_1 + a_2)/L$. It is of course possible to use apertures of different cross section, for example rectangular slits, if the divergence must be smaller in one direction than another.

Neutron guides are now widely used at both reactor and spallation neutron sources. These are able to transport neutrons over distances ranging to 100 m or more. They are evacuated tubes, normally of rectangular cross section, and transmission depends on the reflection of glancing-angle neutrons from the walls of the guide. The guides are constructed from glass plates with a reflective coating deposited on the internal surfaces.

Initially, total external reflection (Section 2.3.2.3) provided the basis for reflection; the coating was nickel, or preferably ^{58}Ni. Given that nickel has a face-centred cubic structure (4 atoms per unit cell) with lattice parameter 3.524 Å, and taking the scattering lengths from Table 2.3.2, we find from equation (2.3.6) that the critical glancing angles per unit wavelength for total external reflection are 0.10° Å^{-1} and 0.12° Å^{-1} for nickel and ^{58}Ni, respectively. Taking wavelengths of 0.4, 1.2 and 5 Å as representative of hot, thermal and cold neutrons, respectively (*cf.* Fig. 2.3.5), these angles for a nickel mirror are just 0.04, 0.12 and 0.5°. Consequently, these guides are most useful for transmitting cold neutrons and are moderately useful for thermal neutrons, but are not used for hot neutrons. The small glancing angles are demanding, not only on the precision of manufacture, but also because it is highly desirable to use a curved guide tube so there is no direct line of sight to the source (as in Fig. 2.3.13); this is a way of preventing fast neutrons and γ-radiation from impacting on the experiment. The guide tube still transmits a range of wave-

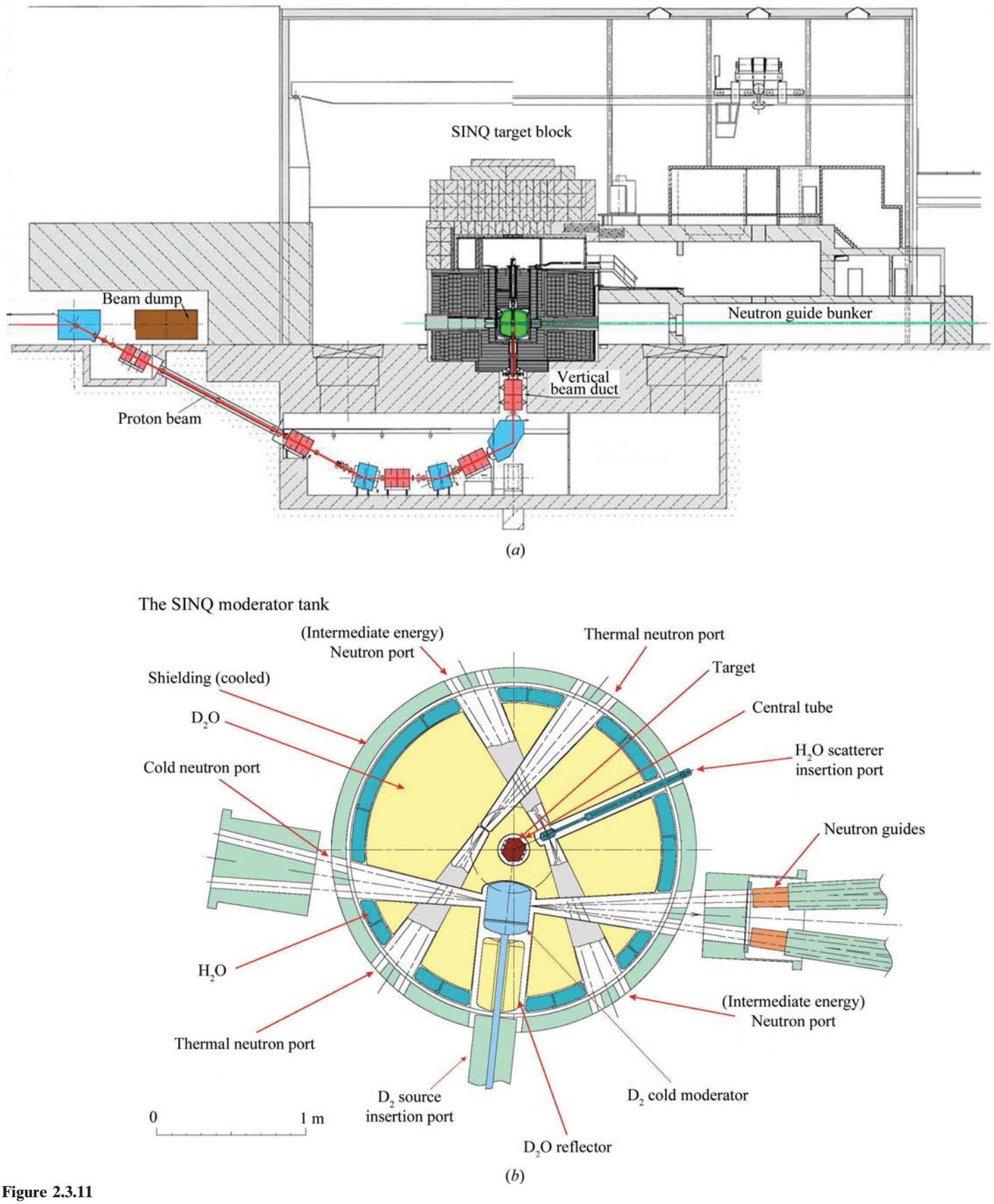

Figure 2.3.11
Layout at the SINQ neutron source. (*a*) Elevation: the target is located in the moderator tank, the high-energy protons being delivered from below. (*b*) Plan: showing the location of guide tubes relative to this central target. (Courtesy: Dr Bertrand Blau, Paul Scherrer Insitut.)

lengths, although only the longest wavelengths can travel by the zig-zag path indicated in Fig. 2.3.13. If the guide width is a, and its radius of curvature ρ (see Fig. 2.3.13), then the minimum length to avoid direct transmission is $(8a\rho)^{1/2}$. Critical to the transmission of a guide tube is the angle θ^*, which is the minimum glancing angle of incidence onto the outer surface that permits subsequent reflection from the inner surface, and is given by $\theta^* = (2a/\rho)^{1/2}$. The shortest wavelength, then, that can be transmitted involving reflection from the inner surface is given by [*cf.* equation (2.3.6)]

Table 2.3.4
Details of selected spallation neutron sources

Source	Type	Location	Proton energy	Current	Average power	Target(s)	Repetition rate (Hz)	Moderator(s)
CSNS†	Short pulse	Institute of High Energy Physics, Guangdong, China	1.6 GeV	62.5 μA	100 kW	Tungsten	25	Water, 2 × liquid hydrogen
ESS†	Long pulse	European Spallation Source, Lund, Sweden	2 GeV	2.5 mA	5 MW	Tungsten wheel (helium cooled)	14	2 × Liquid hydrogen (pancake geometry)
ISIS	Short pulse	Rutherford Appleton Laboratory, Oxfordshire, UK	800 MeV	200 μA	160 kW	2 × Tungsten	50	2 × Water, liquid methane, liquid hydrogen
							10	Hydrogen/methane, solid methane at 26 K
JSNS‡	Short pulse	J-Parc Centre, Tokai-mura, Japan	3 GeV	333 μA	1 MW	Liquid mercury	25	Supercritical hydrogen
LANSCE	Long pulse	Los Alamos National Laboratory, Los Alamos, USA	800 MeV	125 μA	100 kW	Tungsten	20	Water, 2 × liquid hydrogen
SINQ	Continuous	Paul Scherrer Institute, Villigen, Switzerland	590 MeV	1.64 mA§	0.97 MW	Lead	—	Heavy water; cold source: liquid deuterium at 20 K
SNS	Short pulse	Oak Ridge National Laboratory, Oak Ridge, USA	1 GeV	1.4 mA	1.4 MW	Liquid mercury	60	2 × Water, 2 × liquid hydrogen

† Under construction. ‡ Currently operating at <0.5 MW. § Current reaching spallation target after attenuation in muon source.

Figure 2.3.12
Schematic diagram of the ESS facility. The proton beam enters at the right, strikes the target and liberates neutrons for instruments in the three neutron experiment halls. (Image courtesy of the ESS.)

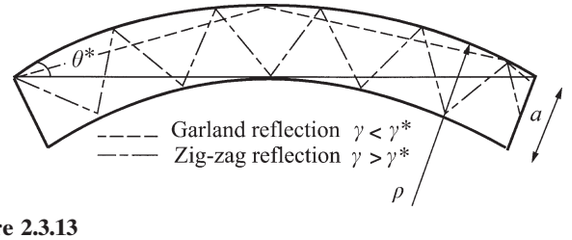

Figure 2.3.13
Plan of a curved neutron guide, indicating different possible neutron paths, labelled 'garland' and 'zig-zag'. Only the longer-wavelength neutrons can travel the zig-zag path because the glancing angles on this path (which must be less than the critical angle) are greater. In this schematic, the glancing angles, the width and the curvature have all been exaggerated. [From Section 4.4.2 of Volume C (Anderson & Schärpf, 2006).]

$$\lambda^* = \theta^* \left(\frac{\pi}{N b_{\rm coh}} \right)^{1/2}. \qquad (2.3.12)$$

This is known as the 'characteristic' wavelength of the guide [see Section 4.4.2 of Volume C by Anderson & Schärpf (2006)]; the majority of transmitted neutrons will have longer wavelengths than this.

The desire to use guides for shorter (*e.g.* thermal-neutron) wavelengths, and for retaining more neutrons at a given wavelength, has motivated the development of mirrors capable of reflecting neutrons incident at greater glancing angle. The earliest such mirrors were in fact monochromating mirrors obtained by laying down alternate layers of metals with contrasting coherent-scattering-length densities (Fig. 2.3.14). For a bilayer thickness d and angle of incidence θ these would select wavelengths according to Bragg's law [equation (1.1.3)],

$$\lambda = 2d \sin(\theta).$$

In an early implementation (Schoenborn *et al.*, 1974), the metals were Ge and Mn (which have coherent scattering lengths opposite in sign) and the bilayer thickness was of the order of 100 Å; this is a larger d-spacing giving access to longer wave-

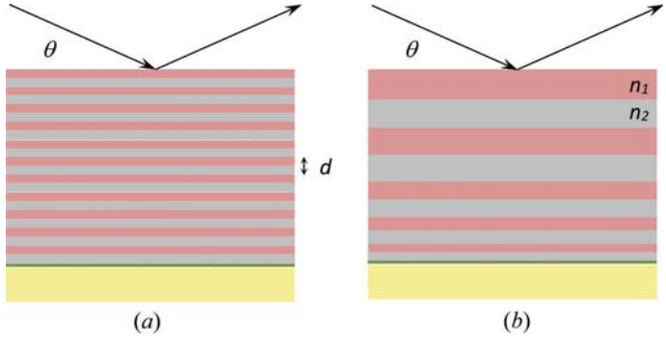

Figure 2.3.14
Schematic diagrams of (*a*) a multilayer monochromator and (*b*) a neutron supermirror.

lengths than would be accessible with the usual crystal monochromator (Section 2.3.4.1.2). The idea of supermirrors, comprising bilayers of graduated thickness, and in effect increasing the critical angle, was suggested by Turchin (1967) and Mezei (1976). For a perhaps simplistic explanation, we note first that since the bilayer dimension d is large compared with the neutron wavelength, we can approximate the above equation for reflection as

$$\theta \simeq \lambda \frac{1}{2d},$$

in which form it is reminiscent of equation (2.3.6). If we take $d_{\min}$ to be the thickness of the thinnest bilayer, then we can propose that the critical angle for reflection by the supermirror should be

$$\theta_c^{\rm SM} \simeq \lambda \frac{1}{2d_{\min}}. \qquad (2.3.13)$$

In order to ensure that all neutrons incident at angles less than this critical angle should be reflected, we need to incorporate a more-or-less continuous range of thicker bilayers into the supermirror (Fig. 2.3.14*b*). A more rigorous treatment (Hayter & Mook, 1989; Masalovich, 2013) takes account of the transmission and reflection at each interface, and lays down a prescription as to how the thicknesses should be varied. The most common pairing for the bilayer is now Ni with Ti; the coherent scattering cross sections are of opposite sign (see Table 2.3.2). The performance of a supermirror is normally quoted as the ratio m of the critical angle for the supermirror, $\theta_c^{\rm SM}$, to that for natural nickel, $\theta_c^{\rm Ni}$; a high value for reflectivity is also important. Supermirrors to m of 2 or 3 are in quite common use, while now Ni/Ti supermirrors with m up to 7 are offered for purchase (Swiss Neutronics AG; see also Maruyama *et al.*, 2007).

Consideration is currently being given to the variation of the cross section of the guide along its length. There is some loss on reflection by supermirrors, so these studies aim to reduce the number of reflections involved in transmission along the guide. One suggestion (also attributable to Mezei, 1997) is to use a 'ballistic guide', in which neutrons from the source travel through a taper of widening cross section into a length of larger guide, then through a taper of narrowing cross section to restore the original cross section at the exit. This is said to reduce the number of reflections suffered by the neutron by a factor of $(w_0/w)^2$, where w_0 is the width at entrance and exit and w the larger width along the main part of the guide (Häse *et al.*, 2002). Such a guide has been installed and is operating successfully on the vertical cold source at the Institut Laue–Langevin (Abele *et al.*, 2006). An extension of this idea is based on the well known property of ellipses that a ray emanating from one focus is reflected (just one bounce) to pass through the other; so if the guide cross section could be varied to give a very long ellipse, a source of neutrons placed at one focus, and the target point at the other, then perhaps the neutrons could be transmitted along the guide with just a single reflection (Schanzer *et al.*, 2004; Rodriguez *et al.*, 2011). Accordingly a number of neutron facilities have installed elliptical guides, and indeed a number of neutron powder diffractometers now are located on elliptical guides; these include diffractometer POWTEX at FRM-II, the high-resolution diffractometers HRPD and WISH at ISIS, and Super-HRPD at JSNS. Computer simulation by Cussen *et al.* (2013), however, questions whether, given the practicalities of finite source sizes and the approximation of elliptical variation by a number of linear segments, the theoretical improvement is fully realized.

2.3.4. Diffractometers

Put simply, the diffracted neutron beams associated with the different d-spacings in the sample under study satisfy Bragg's law,

$$\lambda = 2d \sin(\theta). \qquad (2.3.14)$$

As always, λ is the wavelength of the incident neutrons, and these neutrons are scattered through an angle 2θ.

There are basically two ways of exploiting this relationship. The first is to use a single wavelength for the investigation, in which case diffracted neutrons are observed at different angles 2θ corresponding to different d-spacings in the sample. A neutron powder diffractometer designed to carry out an investigation by this means we choose to call a 'constant wavelength' (CW) diffractometer. The other means is to fix the angle 2θ, illuminate the specimen with a range of wavelengths, and note the different wavelengths that are diffracted. In this case, we determine the wavelengths of the diffracted neutrons *via* their speed $\lambda = h/(mv)$ [equation (2.3.1)], and that in turn is measured by their flight time t over a path of length L, $v = L/t$; this leads to

$$\lambda = \frac{ht}{mL}. \qquad (2.3.15)$$

A diffractometer designed to carry out such an analysis of wavelengths we call a 'time-of-flight (TOF) diffractometer'.

The distinction between these two modes of operation can also be indicated *via* the Ewald construction in reciprocal space (Section 1.1.2.4). In this, the ideal powder is represented by concentric spheres in reciprocal space. In the constant-wavelength situation, the primary beam is fixed in direction and the Ewald sphere has a fixed radius; diffracted (reflected) beams are observed at any angle at which the surface of the Ewald sphere intersects one of the concentric spheres mentioned just above. In the wavelength-analysis (time-of-flight) situation, the directions of the primary and diffracted beams are fixed, but the radius of the Ewald sphere ($1/\lambda$) is variable through a range; diffracted beams are observed whenever the wavelength is such that the tip of the vector representing the reflected beam lies on one of the concentric spheres.

2.3.4.1. *Constant-wavelength neutron diffractometers*

The salient features of a constant-wavelength diffractometer are perhaps most easily explained by reference to a particular example; for this purpose we consider the High Resolution Powder diffractometer for Thermal neutrons (HRPT) installed at the SINQ continuous spallation source (Fischer *et al.*, 2000). Neutrons from the source travel through a guide tube to the crystal monochromator, which directs neutrons of a selected wavelength toward the sample. The diffracted neutrons are registered in a detector or detectors that cover a range of angles of scattering from the sample. Collimation is used to better define the directions of the neutron beams; in this instance a primary collimator is included in the guide tube and additional collimation is included between the sample and the position-sensitive detector. The various components will be described in more detail below.

2.3.4.1.1. *Collimation*

There need to be restrictions on the angular divergences of the neutron beams. The divergence of the beam impinging upon the crystal monochromator must be limited to better define the wavelength of the neutrons directed to the sample, whereas the divergences of the beams incident upon and diffracted from

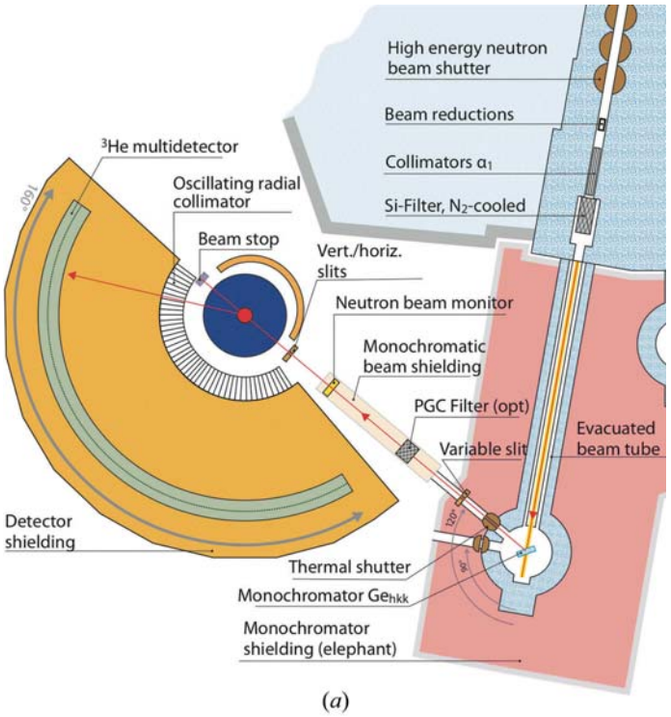

Figure 2.3.15
A constant-wavelength neutron powder diffractometer. This figure shows (*a*) a layout diagram and (*b*) the physical appearance (dominated by the monochromator and detector shieldings) for the HRPT diffractometer installed at the SINQ continuous spallation source. (Figures from https://www.psi.ch/sinq/hrpt/.)

the sample will control the precision with which the scattering angle 2θ can be determined. For a diffractometer detecting neutrons and measuring scattering angles in the horizontal plane (as shown in Fig. 2.3.15) the horizontal divergences are critical, the vertical divergences less so.[11] Indeed, the horizontal divergences are key parameters in the determination of resolution and intensity (Section 2.3.4.1.4); for this reason we denote by α_1, α_2 and α_3 the (half-angle) angular divergences of the primary beam (*i.e.* the beam onto the monochromator), the monochromatic beam (from monochromator to sample) and the diffracted beam (from sample to detector), respectively.

[11] For this reason large vertical divergences are employed to increase intensity; they do however have second-order impacts on the shapes (asymmetry) and positions of diffraction peaks (Howard, 1982; Finger *et al.*, 1994; see also Section 4.2 in Kisi & Howard, 2008).

The divergences are limited by various forms of collimation. The divergence of the primary beam will be limited in the first instance by the delivery system. For delivery through a simple beam tube of length L, with entrance and exit apertures of dimensions a_1 and a_2, respectively, the angular divergence (half-angle) is given by (as already noted in Section 2.3.3.4)

$$\alpha_1 = \frac{a_1 + a_2}{2L}. \tag{2.3.16}$$

Neutrons emerging from a guide tube would have divergence equal to the critical angle of the guide, $\alpha_1 = \theta_c$. Soller collimators (see below) can be used if there is a need to further reduce the horizontal divergence of the primary beam. The divergence of the monochromatic beam may be limited by slits, or a beam tube. The divergence of the diffracted beam, α_3, is often defined using another Soller collimator. Sometimes this divergence is limited just by the dimensions of the sample and the detecting elements; equation (2.3.16) gives α_3 if it now references the sample and detector element dimensions and the distance between them. Even in this circumstance (as in HRPT), Soller collimators may be used in front of the detector to reduce scattering from ancillary equipment and other background contributions.

Soller collimators (Soller, 1924) are used to transmit beams of large cross section while limiting (for example) horizontal divergence. They are in effect narrow but tall rectangular collimators stacked side by side; in practice they comprise thin neutron-absorbing blades equally spaced in a mounting box. It should be evident from equation (2.3.16) that if the length of the collimator is L and the separation between the blades is a, then the (half-angle) horizontal divergence is a/L. The transmission function for a Soller collimator is ideally triangular. It is technologically challenging to make compact Soller collimators, since, for a given collimation, a shorter collimator needs a smaller blade spacing. One very successful approach, due to Carlile *et al.* (1977), has been to make the neutron-absorbing blades from Mylar, stretched on thin steel or aluminium alloy frames, and subsequently coated with gadolinium oxide paint; these blades are stacked and connected *via* the frames which become the spacers in the final product. The collimators made by Carlile *et al.* were 34 cm long, and the blade spacing was 1 mm, giving a horizontal divergence of 0.17°. Compact Soller collimators of this type (Fig. 2.3.16) are now commercially available, with blade spacings down to 0.5 mm.

Even more compact collimators can be produced by eliminating the gaps in favour of solid layers of neutron-transmitting material; for example, a collimator only 2.75 cm long made by stacking 0.16 mm thick gadolinium-coated silicon wafers gave a divergence of 0.33° (Cussen *et al.*, 2001). Microchannel plates (Wilkins *et al.*, 1989) may offer additional possibilities for collimation and focusing.

2.3.4.1.2. *Monochromators*

The wavelength in a constant-wavelength powder diffractometer is almost invariably selected by a single-crystal monochromator. If the primary beam is incident onto the monochromator in such a way as to make an angle θ_M with a chosen set of planes in the crystal, then the wavelength that will be reflected from these planes is given by Bragg's law,

$$\lambda = 2d \sin(\theta_M),$$

where d is the spacing of the chosen planes. A spread of angles of incidence represented by $\Delta\theta_M$ will result in the selection of a

Figure 2.3.16
Commercially available compact Soller collimators. (Reproduced with permission from Eurocollimators Ltd, UK.)

band of wavelengths $\Delta\lambda$ given by

$$\frac{\Delta\lambda}{\lambda} = \cot\theta_M \Delta\theta_M. \qquad (2.3.17)$$

For high-resolution performance we need a rather precisely defined wavelength, so $\Delta\lambda$ should be small; if, on the other hand, intensity is an issue then a wider band of wavelengths needs to be accepted. It should be evident from equation (2.3.17) that a high-resolution diffractometer will operate with a take-off angle from the monochromator, $2\theta_M$, as high (*i.e.* as close to 180°) as practicable, and with tight primary collimation α_1.

It might be noticed that the integer n appearing on the right-hand side of equation (1.1.3) has been omitted from our formulation of Bragg's law. If the Miller indices of the chosen planes are hkl, if the spacing of these planes is d_{hkl}, and if we introduce $d_{nh,nk,nl} = d_{hkl}/n$ [*cf.* equation (1.1.23)], then the factor n is effectively restored. This means that, as well as reflecting the selected wavelength through the hkl reflection, the monochromator has the potential to reflect unwanted harmonics λ/n of the desired wavelength through the nh,nk,nl reflections. This problem can be largely overcome using the hkl planes with h, k, l all odd in crystals with the diamond structure, such as silicon and germanium; for this structure the structure factors [equation (2.3.7)] for the $2h,2k,2l$ reflections are zero so that there is no contamination by $\lambda/2$, and at the shorter wavelengths, $\lambda/3$ and so on, there are very few neutrons in the thermal neutron spectrum (Fig. 2.3.5).

Since 'perfect' crystals (of silicon and germanium, for example) have low reflectivity, for monochromator applications imperfect or 'mosaic' crystals are usually preferred. A mosaic crystal can be pictured as comprising small blocks of crystal with slightly differing orientations, the distribution in angle of these blocks being characterized by a full-width at half-maximum angle, β, known as the 'mosaic spread'. In addition to improving the intensity markedly,[12] this 'mosaic spread' will also increase the range of wavelengths obtained. Crystals intended for use as monochromators are very often deliberately deformed to achieve the desired mosaic structure. Further gains in intensity are sought by using vertically focusing monochromators, since the vertical divergence can be increased without serious detriment to the diffraction patterns. Vertically focusing monochromators usually comprise a number of separate monochromator crystals either individually adjustable (Fig. 2.3.17) or in fixed mountings on a bendable plate.

It is not common to find polarized neutrons being used in neutron powder diffractometers. Nevertheless, we think it appropriate to mention here that one means to obtain a polarized neutron beam is to use an appropriate polarizing crystal monochromator.[13] The 111 reflection from the ferromagnetic Heusler alloy Cu_2MnAl is commonly used for this purpose; the nuclear and magnetic structure factors [equations (2.3.7) and (2.3.8)] are of similar magnitude and they add or subtract depending on whether the neutron spin is antiparallel or parallel to the magnetization of the alloy. The beam reflected from such a monochromator can be polarized to better than 99%.

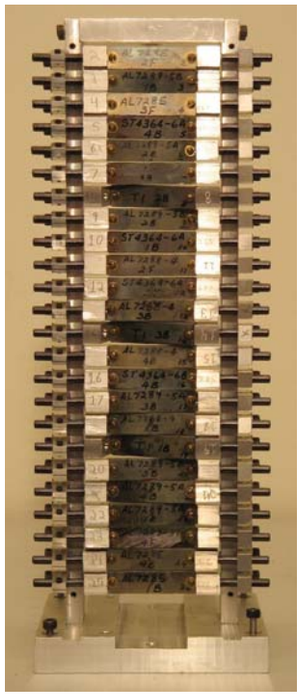

Figure 2.3.17
The vertically focusing monochromator constructed at the Brookhaven National Laboratory (Vogt *et al.*, 1994) and now used by the high-resolution powder diffractometer ECHIDNA at OPAL. The 24 monochromating elements are individually adjustable, and each of these is a 30-high stack of 0.3 mm thick Ge wafers, deformed to yield a suitable mosaic structure and then brazed together. (Reproduced with permission from ANSTO.)

The reader is referred to Section 4.4.2 of Volume C (Anderson & Schärpf, 2006) and to Kisi & Howard (2008) Sections 3.2.1 and 12.3 for further details.

2.3.4.1.3. *Neutron detectors*

Neutrons, being electrically neutral, do not themselves cause ionization and so cannot be detected directly; their detection and counting therefore depend on their capture by specific nuclei and the production of readily detectable ionizing radiation in the ensuing nuclear reaction. Only a limited number of neutron-capture reactions are useful for neutron detection [see Chapter 7.3 of Volume C (Convert & Chieux, 2006)]; they include

$$\begin{aligned}
{}^1_0\mathrm{n} + {}^3_2\mathrm{He} &\rightarrow {}^1_1\mathrm{H} + {}^3_1\mathrm{H} + 0.76\ \mathrm{MeV}\\
{}^1_0\mathrm{n} + {}^6_3\mathrm{Li} &\rightarrow {}^3_1\mathrm{H} + {}^4_2\mathrm{He} + 4.79\ \mathrm{MeV}\\
{}^1_0\mathrm{n} + {}^{10}_5\mathrm{B} &\rightarrow {}^7_3\mathrm{Li} + {}^4_2\mathrm{He} + 2.8\ \mathrm{MeV}\\
{}^1_0\mathrm{n} + {}^{157}_{64}\mathrm{Gd} &\rightarrow {}^{158}_{64}\mathrm{Gd} + \gamma\text{-rays} + \text{conversion electrons}\\
&\quad + \leq 0.18\ \mathrm{MeV}\\
{}^1_0\mathrm{n} + {}^{235}_{92}\mathrm{U} &\rightarrow \text{fission fragments} + \sim 200\,\mathrm{MeV}
\end{aligned}$$

(*cf.* Section 2.3.3.2).

[12] Most of the improvement is due to a change from a 'dynamical' to a 'kinematic' scattering regime.

[13] Polarized beams can also be produced using suitable mirrors or filters [see Section 4.4.2 of Volume C by Anderson & Schärpf (2006)].

The attenuation of neutrons in these materials (Section 2.3.2.4) will be dominated by the high absorption (by capture) cross sections (Table 2.3.2), so the linear attenuation coefficient will be given by $\mu = N\sigma_{\rm abs}$ where N is the number of absorbing nuclei per unit volume. We remark that absorption cross sections, with the exception of Gd, increase linearly with wavelength. The factor by which the neutron beam is diminished in a detector of thickness x is $\exp(-\mu x) = \exp(-N\sigma_{\rm abs}x)$. The detector efficiency, then, given by the fraction of neutrons absorbed (captured) in the detector, is $1 - \exp(-N\sigma_{\rm abs}x)$. In most cases the aim is to have high detector efficiency; however, in some circumstances it is desirable to monitor an incident neutron beam, in which case attenuation should be kept to a minimum. The account of neutron detection given here will be kept relatively brief since much has been written on this subject elsewhere [Oed, 2003; Chapter 7.3 of Volume C (Convert & Chieux, 2006)].

The task, following the neutron-capture reaction, is to detect the various charged particles or ionizing radiations that are produced. These are registered by the electrical signals they generate in a gas-filled proportional counter or ionization chamber, or in a semiconductor detector, recorded on film, or detected from the flashes of light they produce in a scintillator, for example ZnS. It is well worth noting that the secondary radiation carries no record of the energy of the detected neutrons; so whatever the means of detection, detectors can count neutrons but can provide no information on their energy distribution.

The gas-filled radiation detectors are essentially Geiger counters, comprising a gas-filled tube with a fine anode wire running along its centre. The anode collects the electrons released by ionization of the gas; if the anode voltage is high enough, there is a cascade of ionization providing amplification of the signal.[14] Detectors filled with boron trifluoride, $^{10}BF_3$, and helium-3, ^{3}He, have high efficiencies and are in common use; in these the nucleus designated to capture neutrons is incorporated in the filling gas. Such detectors operate with pulse-height discrimination, not in any attempt to determine neutron energy, but to discriminate against lower-voltage signals from γ-rays and other unwanted background. Another approach is to have a thin solid layer[15] of neutron-absorbing material, ^{235}U for example, releasing secondary radiation, in this case fission products, into a gas proportional counter filled with a standard argon/methane mixture; this would represent a low-efficiency neutron detector suitable for use as an incident-beam neutron monitor. Neutron detection based on semiconductor particle detectors is still in the developmental stage. The main problem is that the semiconductors used for charged-particle detection do not contain neutron-absorbing isotopes. Semiconductor particle detectors could be used to register the secondary radiation from an abutting layer of neutron-absorbing solid, but that layer would need to be thin, and another low-efficiency neutron detector would result. Scintillation detectors involve the placement of neutron-absorbing materials, such as ^{6}LiF, adjacent to a scintillator such as a ZnS screen, or perhaps the use of a Ce-doped lithium silicate glass, and counting the flashes of light that are produced. These light flashes can be recorded by photomultiplier tubes or on film. Scintillation detectors are, however, not used in constant-wavelength diffractometers because of their sensitivity to γ-radiation. They are used in time-of-flight diffractometers at spallation sources by exploiting the fact that the unwanted fast neutrons and γ-rays, and the thermal neutrons of interest, are separated in time (Section 2.3.4.2.2).

Much of the preceding description refers to single neutron counters, although it should be noted that there is a position-sensitive capability inherent in a film or scintillator screen. The earliest CW diffractometers employed just a single detector set on an arm that scanned through the scattering angle 2θ; the deployment of a Soller collimator just in front of the detector was advantageous. Conceptually the simplest but not necessarily the cheapest means for improvement was to mount a number of collimator/detector pairs on the detector arms. Such an improvement was made to diffractometer D1A at the Institut Laue–Langevin (Hewat & Bailey, 1976) by mounting ten sets of 10′ divergence Soller collimators/^{3}He detectors at intervals of 6°. The BT-1 diffractometer at NBSR operates with 32 ^{3}He detectors set at 5° intervals, so a scan through 5° covers a total angular range of 160°. The ultimate level for this kind of development was reached when D2B at the Institut Laue–Langevin operated in its former mode, with 64 detectors set at 2.5° intervals, each with its own 5′ Mylar Soller collimator; this required a scan through only 2.5° to record 160° of diffraction.

The alternative to using large numbers of individual detectors is to make use of position-sensitive neutron detectors (PSDs), and these have been in use for quite some time. The technology is that of the position-sensitive detection of charged particles, the important issue for neutrons being that the charged-particle detection should be located close to the neutron-capture event so that positional information is retained. A gas-filled ^{3}He detector with a single anode wire can serve as a linear PSD, for example by comparing the charges collected, after the capture event, at the opposite ends of the wire. The D2B diffractometer at the Institut Laue–Langevin has now been upgraded to 'SuperD2B', which uses 128 linear PSDs with their axes (anode wires) vertical, at 2θ intervals of 1.25°; this operates as a quasi-two-dimensional PSD. Diffractometers SPODI at FRM-II (80 detectors) and ECHIDNA at OPAL (128 detectors) are fitted with similar detector arrays. A single gas-filled chamber containing a number of separate parallel vertically aligned anodes, termed a multi-wire proportional counter (MWPC), provides another approach; the electronics needs to register at which of the wires the capture event occurred. This technology has extended from the first multi-wire PSD with 400 wires at 5 mm (0.2°) separation, used on the D1B diffractometer at the Institut Laue–Langevin in the 1970s, to a PSD with 1600 wires at 0.1° separation now in use on HRPT at SINQ (Fig. 2.3.15). A further advance is the development of the micro-strip gas chamber (MSGC) detector (Oed, 1988). In this detector the anodes and the cathodes are printed circuits on glass substrates, which are then mounted into the chamber. With this arrangement, an anode separation of 1 mm is achievable and the stability is excellent. The high-intensity diffractometer D20 at the Institut Laue–Langevin has a detector assembled from plates of micro-strip detectors and achieves 1600 anodes at 0.1° angle separation.

As pointed out above, the detection systems on SuperD2B, SPODI and ECHIDNA achieve a quasi-two-dimensional position capability by using banks of linear PSDs located side by side. An MWPC detector can achieve two-dimensional capability in a very similar manner, using the anode position to locate in the horizontal direction and charge division measurements at the ends of each anode wire to find the vertical position. An MWPC detector can also be fitted with segmented cathodes, either side of the anodes, one returning positional information in the horizontal

[14] Strictly speaking, the term 'Geiger counter' should be reserved for detectors operating in this amplification regime.
[15] The layer must be thin so that the secondary radiation, which has a short range in solids, can escape into the charged-particle detector.

direction and the other giving the vertical position. A detector of this kind is used on the WOMBAT diffractometer at the OPAL reactor. MSGC detectors can also be adapted to provide two-dimensional positional information after printing a set of cathodes orthogonal to the primary set on the back surface of the glass.

A few general comments about detecting systems are in order. The time for a detector to recover after registering a neutron count is known as the dead time, and this may be significant when count rates are high, in which case corrections are needed [Chapter 7.3 of Volume C (Convert & Chieux, 2006)]. For banks of detectors, and also for position-sensitive detectors, calibration for position and sensitivity becomes a critical issue. In the case of a smaller bank of detectors, it may be possible to scan the detector bank so the same diffraction pattern is recorded in the different detectors, in which case the relative positions and efficiencies of the different detectors can be determined quite well (see Section 4.1 of Kisi & Howard, 2008). For more extensive banks or large position-sensitive detectors, detector sensitivity calibration is performed by examining the very nearly isotropic incoherent scattering from vanadium. In this case checking for angular accuracy can be more difficult. The time taken to register a neutron count cannot be said to be a fundamental issue in CW powder diffraction, since in some applications it is scarcely relevant, although in other applications, such in the study of very fast reaction kinetics (Riley *et al.*, 2002), the constraints on time are very demanding.

2.3.4.1.4. *Resolution and intensity*

The resolution and intensity of a CW powder diffractometer are strongly influenced by the divergences α_1, α_2 and α_3 of the primary, monochromatic and diffracted beams, respectively, along with the mosaic spread β of the crystal monochromator. The situation was analysed by Caglioti *et al.* (1958) on the basis that the triangular transmission factor of each collimator, total width 2α, could be approximated by a Gaussian with full-width at half-maximum (FWHM) α, that the mosaic distribution of the monochromator could also be described by a Gaussian with FWHM β, but that there was no sample contribution to the peak widths. On this basis the diffraction peaks were found to be Gaussian, with the FWHM of the diffraction peak occurring at scattering angle 2θ given by (Hewat, 1975)

$$\mathrm{FWHM}^2 = U\tan^2\theta + V\tan\theta + W, \tag{2.3.18}$$

where

$$U = \frac{4(\alpha_1^2\alpha_2^2 + \alpha_1^2\beta^2 + \alpha_2^2\beta^2)}{\tan^2\theta_M(\alpha_1^2 + \alpha_2^2 + 4\beta^2)}, \tag{2.3.18a}$$

$$V = \frac{-4\alpha_2^2(\alpha_1^2 + 2\beta^2)}{\tan\theta_M(\alpha_1^2 + \alpha_2^2 + 4\beta^2)}, \tag{2.3.18b}$$

$$W = \frac{\alpha_1^2\alpha_2^2 + \alpha_1^2\alpha_3^2 + \alpha_2^2\alpha_3^2 + 4\beta^2(\alpha_2^2 + \alpha_3^2)}{\alpha_1^2 + \alpha_2^2 + 4\beta^2} \tag{2.3.18c}$$

and θ_M is the Bragg angle ($2\theta_M$ is the take-off angle) at the monochromator. Under these conditions the total (integrated) intensity in the diffraction peak is given by

$$L \propto \frac{\alpha_1\alpha_2\alpha_3\beta}{(\alpha_1^2 + \alpha_2^2 + 4\beta^2)^{1/2}}. \tag{2.3.19}$$

These equations have important implications and accordingly have received a good deal of attention. They return at once the well known resolution advantage in setting up the diffractometer in the parallel configuration (that seen in Fig. 2.3.15, in this configuration θ_M taken to be positive). Caglioti *et al.* (1958) deduced that for the simple case of $\alpha_1 = \alpha_2 = \alpha_3 = \beta = \alpha$ equations (2.3.18) and (2.3.19) reduce to

$$\mathrm{FWHM} = \alpha\left(\frac{11 - 12a + 12a^2}{6}\right)^{1/2} \text{ and } L \propto \alpha^3/(6)^{1/2},$$

where $a = \tan\theta/\tan\theta_M$; they went on to record results for a number of other combinations. In his design for a high-resolution diffractometer, Hewat (1975) considered the case $\alpha_2 = 2\beta > \alpha_1 \simeq \alpha_3$. Under these conditions, the peak widths are close to their minimum around the parallel focusing condition $\theta = \theta_M$, their widths there are given by

$$\mathrm{FWHM}^2 = \left(\alpha_1^2 + \alpha_3^2\right) - \frac{\alpha_1^4}{\alpha_1^2 + \alpha_2^2 + 4\beta^2} \simeq \alpha_1^2 + \alpha_3^2,$$

and the total intensity is approximately

$$L \propto \alpha_1\alpha_3\beta/(2)^{1/2}.$$

Hewat's conclusions, put briefly, were that good resolution could be obtained by keeping divergences α_1 and α_3 small, while intensity could be somewhat recovered by adopting relatively large values for the monochromator mosaic spread β and divergence α_2 of the monochromatic beam. Hewat also argued for a high monochromator take-off angle $2\theta_M$, not only to reduce peak widths [through the term $\cot\theta_M$ appearing in equation (2.3.17) and reappearing in equations (2.3.18)], but also to match the region of best resolution to that of the most closely spaced peaks in the diffraction pattern. Hewat's design was implemented in the D1A diffractometer at the Institut Laue–Langevin (Hewat & Bailey, 1976), subsequently in the D2B diffractometer at the same establishment, and elsewhere. In a version installed at the (now retired) HIFAR reactor in Sydney, Howard *et al.* (1983), using an Al_2O_3 (corundum) ceramic sample, reported a peak-width variation in close agreement with that calculated from equation (2.3.18). Although more sophisticated analyses are available in the literature (Cussen, 2000), this result would suggest that equations (2.3.18) still provide a good starting point.

The usual trade-off between intensity and resolution applies, and since neutron sources are rather less intense than X-ray sources, this is an important consideration. Intensity is sacrificed by using high monochromator take-off angles to limit the wavelength spread [equation (2.3.17)], and by using tight collimation [equation (2.3.19)]. Evidently intensities could be increased by relaxing these constraints. These days it is more common to build diffractometers of good-to-high resolution, and then to seek other means to improve data-collection rates. Focusing monochromators, such as described in Section 2.3.4.1.2, serve to increase the neutron intensity at the sample position without seriously degrading the resolution. In addition, the use of multi-detector banks and the development and deployment of position-sensitive detectors, as described in Section 2.3.4.1.3, has been very much driven by the desire to increase the speed of data collection. As mentioned earlier, the design and analysis of neutron powder diffractometers should be treated in a holistic fashion, and although some advanced analytical methods have been applied (Cussen, 2016 and references therein), Monte Carlo analyses using programs such as *McStas* (Willendrup *et al.*, 2014) and *VITESS* (Zendler *et al.*, 2014) to track large numbers of neutrons from the source right through to the neutron detectors are now widely employed.

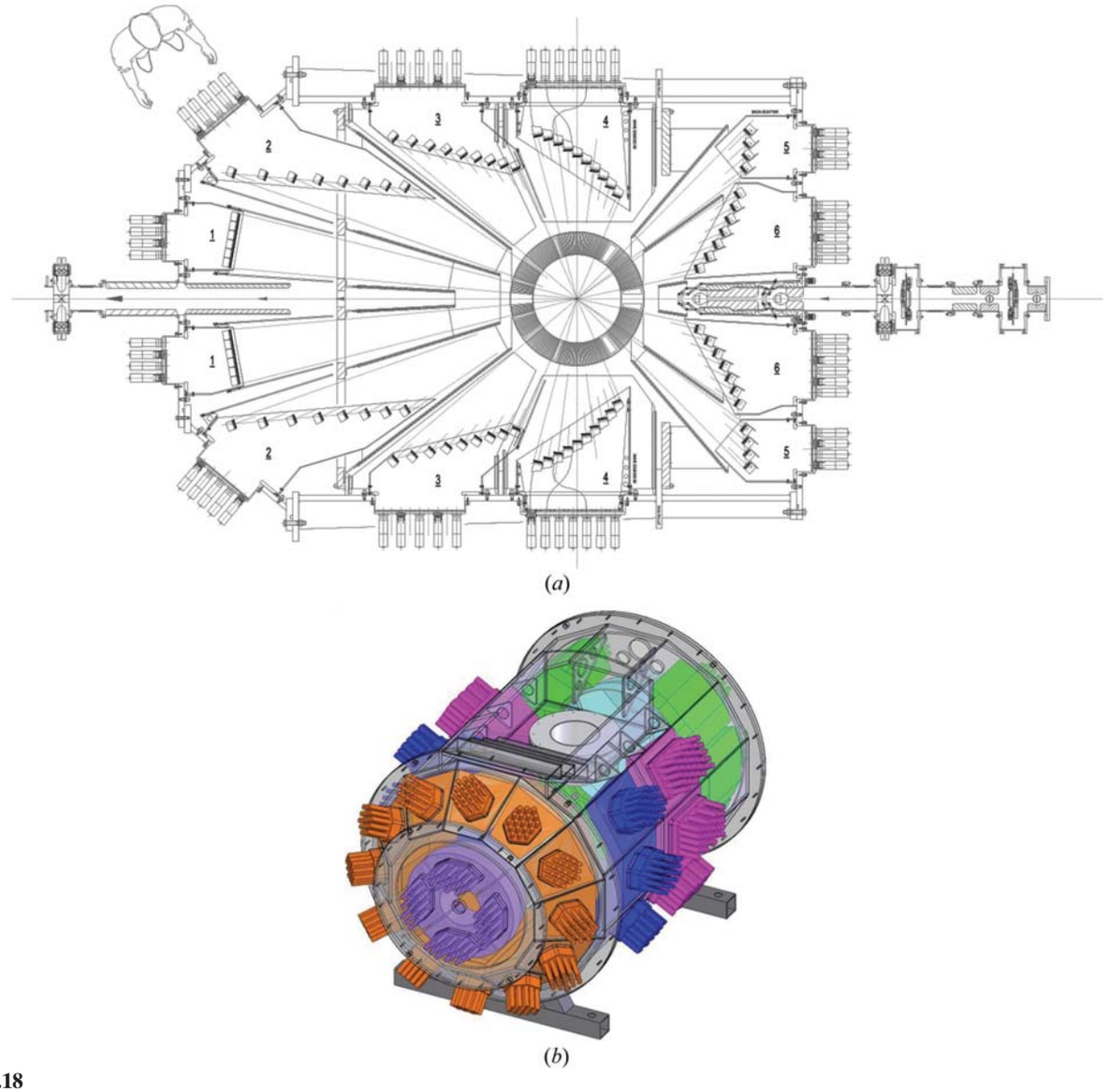

Figure 2.3.18
(*a*) Schematic cross section of the POLARIS diffractometer at the ISIS facility, UK, and (*b*) a three-dimensional solid model of the detector chamber. (Credit: STFC.)

2.3.4.2. *Time-of-flight (TOF) diffractometers*

Time-of-flight (TOF) diffractometers differ substantially from CW diffractometers. Neutrons delivered to the instrument are already partially collimated and TOF instruments have no monochromator and consequently no moving parts. The full incident neutron spectrum is utilized and needs to be well characterized in order to extract meaningful intensities; in addition the wavelength dependence of detector efficiencies needs to be taken into account. In principle, measurements from an incoherently (therefore isotropic and wavelength-independent) scattering sample such as V or H_2O provide the required characterization.[16] In practice, however, incident spectra are usually recorded using a low-efficiency detector (beam monitor) in the incident beam. Data from V are still required to correct for the relative efficiency of individual detectors or detector elements and their wavelength dependence (Soper *et al.*, 2000).

The basic components of a TOF powder diffractometer are the flight tube from the neutron source or a neutron guide, a precisely located sample position, banks of detectors at various positions around the sample position and a neutron-absorbing beam stop. In early TOF diffractometers, detector banks were relatively localized typically in forward scattering, close to $2\theta = 90^\circ$ and backscattering locations. More modern diffractometers have very extensive detector arrays such as the newly upgraded POLARIS instrument at the ISIS facility, which is illustrated in Fig. 2.3.18. Neutrons enter the diffractometer at the right of Fig. 2.3.18(*a*) through a number of adjustable neutron-absorbing jaws which trim the beam size to match the sample size. The beam is then incident on the sample, which is located within the chamber where the detectors, arranged in numbered banks, are housed. The entire sample/detector chamber (and flight tube) is evacuated during data collection in order to reduce absorption and scattering of the incident neutron beam by air, effects which both decrease the intensity of the neutrons incident on the sample and increase the background scattering. A human figure in Fig. 2.3.18(*a*) indicates the large scale of the device and it should be

[16] The much larger incoherent scattering cross section of H allows normalization data to be recorded much more quickly using H_2O; however, the small amount of additional moderation of the beam that occurs is usually considered undesirable.

noted that the substantial neutron shielding surrounding the detector chamber (known as the blockhouse) is not shown.

2.3.4.2.1. *Instrument resolution and design*

In a TOF instrument, all of the incident spectrum of neutron wavelengths is utilized, appropriately trimmed by the chopper system as previously described. The different wavelengths (λ) are identified through their time-of-flight (t) according to equation (2.3.15). Substituting that equation into Bragg's law, we obtain

$$d_{hkl} = \frac{ht}{2mL\sin\theta} = \frac{t}{505.554L\sin\theta} \quad (2.3.20)$$

for t in microseconds, d in ångstroms and L in metres.

The resolution of a TOF diffractometer is defined by the uncertainty in the d-spacing (Δd) relative to its absolute value d. Apparent as the width of the diffraction peaks, the resolution is given primarily by (Buras & Holas, 1968; Worlton *et al.*, 1976)

$$\frac{\Delta d}{d} = \left[\Delta\theta^2\cot^2\theta + \left(\frac{\Delta t}{t}\right)^2 + \left(\frac{\Delta L}{L}\right)^2\right]^{1/2}. \quad (2.3.21)$$

There are a number of important things to note concerning this equation:

(i) The terms $\Delta\theta\cot\theta$ and $\Delta L/L$ are fixed and independent of flight time once the diffractometer is constructed; in addition, as we have already noted (Section 2.3.3.3), for a spallation source with a suitably poisoned moderator the time resolution $\Delta t/t$ is practically constant. Thus the resolution of a TOF diffraction pattern is virtually constant across the entire range of d-spacing explored in a given detector bank.[17]

(ii) Uncertainties in the neutron path length, ΔL, can arise due to measurement uncertainty in determining L; however, these are usually overshadowed by the uncertainty that arises because neutrons can emerge into the neutron guide from any position within the finite-sized moderator and this uncertainty constitutes the major contribution to ΔL.

(iii) As ΔL is a constant, a linear improvement in resolution can be achieved merely by making the instrument longer, such as HRPD at ISIS and S-HRPD at J-PARC, which are almost 100 m long.

(iv) The contribution of the diffraction angle 2θ to resolution is considerable. For a fixed angular uncertainty (detector positioning and finite width) the $\cot\theta$ term varies from infinite at $2\theta = 0$ to zero at $2\theta = 180^\circ$. Therefore, the higher the detector angle, the better the resolution.

With these matters considered, we can return to our example of a modern TOF diffractometer in Fig. 2.3.18 and in particular the arrangement of the detectors. The strategy employed is to group multiple individual detector elements into a number of discrete banks. It may be seen from equation (2.3.21) that decreasing 2θ and increasing L have opposing effects on resolution. By appropriate manipulation of the equation and by expressing the overall neutron flight path as $L = L_1 + L_2$ where L_1 is the moderator-to-sample distance and L_2 is that from the sample to the detector, it is straightforward to obtain

$$L_2 = \Delta L\left[\left(\frac{\Delta d}{d}\right)^2 - \left(\frac{\Delta\theta}{\tan\theta}\right)^2 - \left(\frac{\Delta t}{t}\right)^2\right]^{-1/2} - L_1. \quad (2.3.22)$$

Therefore by adjusting 2θ and L_2 correctly, it is possible to construct banks of detectors covering a range of 2θ, for which the resolution is identical. This allows neutrons recorded in the entire detector bank to be 'focused' into a single diffraction pattern. The resulting curved detector arrangement is obvious in the high-resolution detector bank labelled 5 and 6 in Fig. 2.3.18(*a*). For a fixed (small) value of $\Delta d/d$, eventually space limitations impose restrictions on L_2 and a new, lower-resolution detector bank (4) commences. As the benefits of a curved arrangement become insignificant, the appropriate curve is approximated by a straight arrangement in the lower-angle banks and dispensed with altogether in the very low angle bank. In Fig. 2.3.18 the back-scattering (5, 6), 90° (4), two separate low-angle (2 & 3) and the very low angle (1) detector banks of POLARIS are identified. These have average 2θ angles of 146.72, 92.59, 52.21, 25.99 and 10.40°, respectively.

Raw diffraction patterns recorded in the various detector banks are compared in Fig. 2.3.19. Note that the curved background due to the incident spectrum is flattened when the patterns are normalized. A logarithmic scale is necessary to display the very wide range of d-spacings accessible across the whole instrument and this scale emphasises the near-constant resolution across each pattern. In keeping with equations (2.3.21) and (2.3.20), the effects of changing the detector angle are obviously greater resolution and access to shorter d-spacings as 2θ increases. Each detector bank can provide data for a different purpose according to its resolution and d-spacing coverage. For example, the combination of good resolution (4×10^{-3}) and a wide range of d-spacing (0.2–2.7 Å) makes data from the back-scattering bank (Fig. 2.3.19*e*) ideal for the refinement of medium- to large-scale crystal structures. The 90° bank (Fig. 2.3.19*d*) is optimized for use with complex sample environments such as high-pressure cells or reaction vessels, as this geometry combined with appropriate collimation of the incident and scattered neutron beams enables diffraction patterns to be collected that only contain Bragg reflections from the sample being studied. It can be used to obtain good-resolution data (7×10^{-3}) during a variety of *in situ* studies. The low-angle and very low angle banks with their access to very large d-spacings up to 20 Å are invaluable in determining unknown crystal structures and complex magnetic structures by allowing the indexing of low-index reflections and determining reflection conditions.

In order to reduce unwanted background counts and give better localization of the diffraction pattern from the sample, *i.e.* to better exclude sample environments such as cryostats or furnaces, the instrument is fitted with a radial collimator surrounding the sample position.[18] For more common sample environments, *e.g.* furnaces, this collimation allows all detector banks to view the sample unimpeded. The detector banks are contained within the large vacuum vessel shown in Fig. 2.3.18(*b*). This reduces attenuation and background due to scattering by air. The detector coverage on such an instrument is very large, in the case of POLARIS up to 45% of the available solid angle is covered. A full description of this instrument may be found in Smith *et al.* (2018).

[17] A small effect due to a time-dependent component of $\Delta t/t$ might be observed depending on the source and instrument configuration.

[18] Although typically constructed from planar vanes which are oscillated to average their shadow across all the detectors, the POLARIS collimator vanes are stationary, and are conical to follow the Debye–Scherrer cones of the diffracted neutrons.

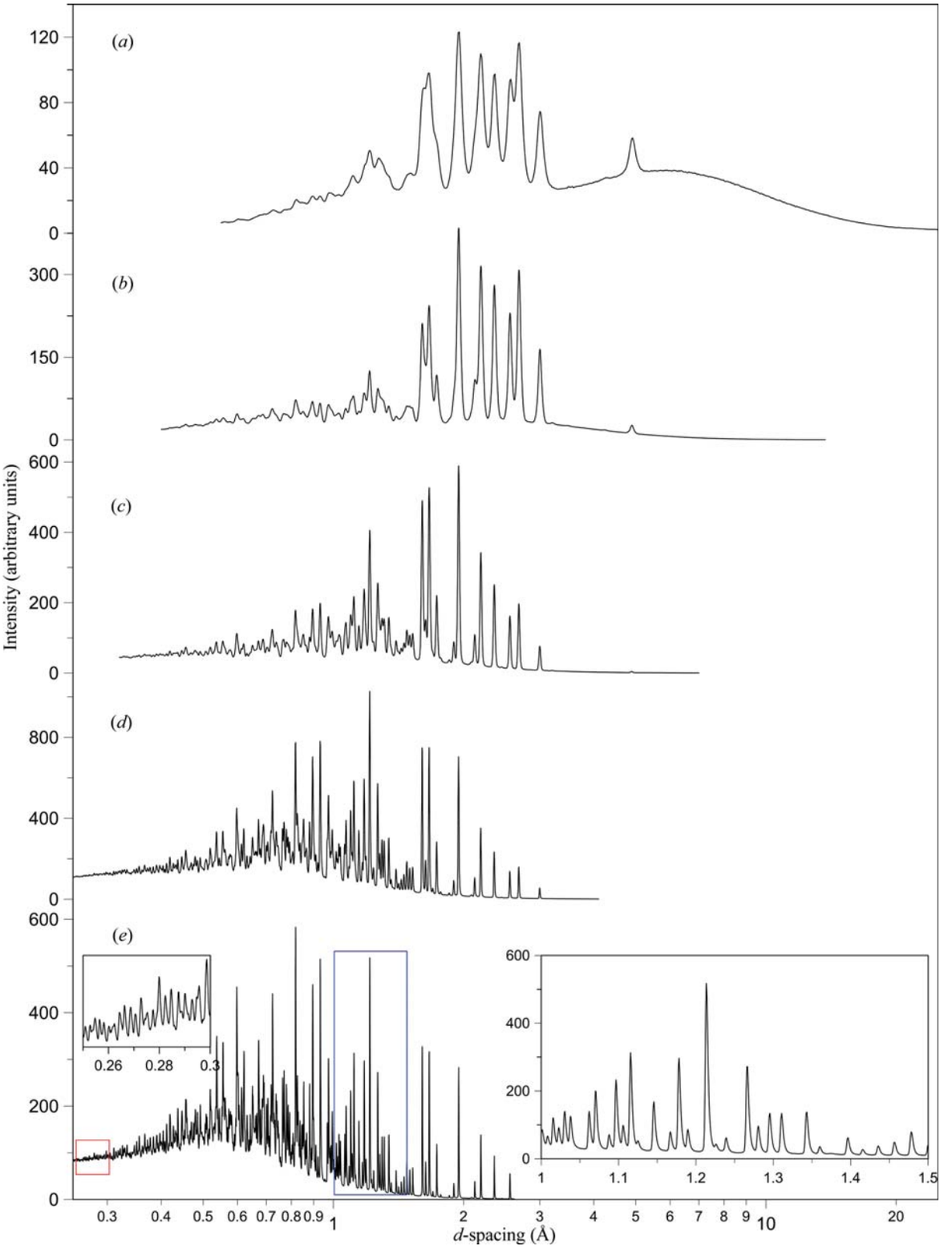

Figure 2.3.19
Raw neutron diffraction patterns from $Y_3Al_5O_{12}$ (YAG). Patterns from the five POLARIS detector banks, (*a*) very low angle, (*b*) low angle 1, (*c*) low angle 2, (*d*) 90° and (*e*) backscattering, are shown separately. Note that the very wide range of *d*-spacings accessible (~0.2–25 Å) necessitates the use of a $\log_{10}$ scale. Insets for the backscattering bank illustrate that useful data are obtained even at very small *d*-spacing (red) and that the resolution is very good (blue). Note the asymmetric peak shape that results from a rapid rise, followed by a slower exponential decay, in the number of neutrons emerging from the moderator after each incident proton pulse.

2.3.4.2.2. *Detection*

All the neutron detector types discussed in Section 2.3.4.1.3 are capable of detecting the scattered neutrons in a TOF pattern. Gas-filled proportional counters such as BF_3 and ^{3}He detectors have efficiencies governed by the neutron energy (or wavelength). Detectors on CW diffractometers are optimized for the narrow band of wavelengths available when using a crystal monochromator, say 1–2.4 Å. The wavelength range in TOF diffraction is generally much wider; as much as 0.2–6 Å or more,

and proportional detectors need to be specifically optimized. There is of course the added complexity of tracking the arrival time of each neutron and this has worked against the use of multi-wire proportional detectors and microstrip detectors as described in Section 2.3.4.1.3. Instead, there is extensive use of scintillation detectors, which are usually based on the ^{6}Li(n;t,α) reaction (Section 2.3.4.1.3). When doped into the ZnS film of a scintillator, the ^{6}Li provides excellent detection sensitivity and energy range. Discrimination against fast neutrons and γ-ray contamination in the incident beam is easily accommodated as these have different velocities to the thermal and epithermal neutrons used for TOF diffraction and are therefore readily excluded by the chopper system and detector electronics.

The detector electronics on older instruments recorded the diffraction pattern in a fixed set of time channels or bins; typically 1024 to begin with and progressively more as electronic and computational advances occurred. More recently, the technique has shifted to recording the data to memory in a continuous stream known as event mode, where the arrival time of each neutron is recorded. The user may then bin (and re-bin) the data into time channels to suit the resolution of the diffraction pattern, which may differ significantly from the instrument resolution because of microstructural features of the sample. Such features are discussed at length in Chapters 5.1 and 5.2.

In a new development, a neutron-sensitive microchannel plate detector has been developed (Tremsin, McPhate, Vallerga, Siegmund, Feller *et al.*, 2011). Microchannel plate detectors (MCPs) are divided into discrete pixels and record the arrival time of each neutron in each pixel. Initially used for high-resolution radiography at pulsed neutron sources, it was quickly realized that MCP detectors can be used for diffraction *via* the Bragg-edge phenomenon (Tremsin, McPhate, Vallerga, Siegmund, Kockelmann *et al.*, 2011). The resolution is typically 55 μm due to the data-acquisition electronics but can be sharpened to less than 15 μm using centroiding techniques. This type of detector opens the door to spatially resolved neutron powder diffraction in materials as well as strain-imaging applications on TOF neutron diffractometers.

2.3.4.3. *Variations on a theme*

The diffractometers HRPT (Fig. 2.3.15) and POLARIS (Fig. 2.3.18) are general-purpose instruments suitable for solving and studying medium-sized crystal structures under a range of non-ambient conditions and in some cases the study of non-crystalline or poorly crystalline materials. There are several such diffractometers at reactors [HB-2A at Oak Ridge (https://neutrons.ornl.gov/powder), D1B at ILL (https://www.ill.eu/instruments-support/instruments-groups/instruments/d1b/description/instrument-layout/), HRPD at KAERI (http://www.kaeri.re.kr:8080/english/sub/sub03_04_01_01.jsp), C2 at CINS (http://cins.ca/get-beam-time/beamline-specs/c2/)] and spallation sources around the world [POWGEN and NOMAD at SNS (https://neutrons.ornl.gov/powgen; https://neutrons.ornl.gov/nomad), GEM at ISIS (http://www.isis.stfc.ac.uk/instruments/gem/gem2467.html), iMATERIA at J-PARC (https://j-parc.jp/researcher/MatLife/en/instrumentation/images/BL20.gif) *etc*].

A more specialized type of TOF powder diffractometer is the High Resolution Powder Diffractometer (HRPD) at ISIS (https://www.isis.stfc.ac.uk/Pages/Hrpd.aspx) and a similar instrument, Super-HRPD at J-PARC (https://j-parc.jp/researcher/MatLife/en/instrumentation/images/BL08.jpg). Although both of these instruments have 90° and low-angle detector banks, their overall design has strongly centred on extremes of resolution, attaining $\Delta d/d$ values of 4×10^{-4} and 3×10^{-4}, respectively. Such extremes of resolution are attained primarily through making the flight path of both instruments nearly 100 m long and placing detectors at very high Bragg angles (150–176°). Data from these can supply individual peak positions to a precision of approximately 5 parts per million and whole pattern fitting can give correspondingly precise lattice parameters. Recalling that in TOF powder diffraction the resolution is constant across the whole pattern, this makes the instruments ideal for the solution of large crystal structures in which a great many diffraction peaks need to be resolved, for tracking phase transitions, and for solving structures involving pseudo-symmetry, which even in relatively small structures (*e.g.* perovskites) can be a challenge for lower-resolution instruments. Example diffraction patterns are shown in Fig. 2.3.20 for the structural transitions in $SrZrO_3$ (Howard *et al.*, 2000).

At the other extreme of instrument design are the very high intensity diffractometers exemplified by the CW instruments D20 at ILL (https://www.ill.eu/instruments-support/instruments-groups/instruments/d20/) and WOMBAT at ANSTO (http://www.ansto.gov.au/ResearchHub/Bragg/Facilities/Instruments/Wombat/). These diffractometers use a large degree of vertical focusing to greatly increase the incident flux on the sample and are fitted with large position-sensitive detectors from which the data can be stored at 1 MHz or faster. If there is a periodic time structure to the phenomenon under study due to some driving stimulus (*e.g.* a periodic laser, electric or magnetic field pulse), then the data can be analysed stroboscopically by synchronizing with the driving stimulus, giving an effective time resolution in the MHz range. Even in the absence of a periodic stimulus, useful diffraction patterns on these diffractometers can in favourable circumstances be stored at rates of 2, 10 or with a large enough sample even 50 Hz (Fig. 2.3.21).

It should be noted that for TOF diffractometers, the time structure imposed by the pulsed neutron source and chopper system places absolute limitations on the most rapid diffraction pattern that can be recorded. This is typically ~0.1 s at sources such as ISIS, J-PARC or SNS. An additional time penalty is often paid due to the time taken to save such large amounts of data (typically between 10 and 30 s). There is therefore no TOF equivalent of the very rapid stroboscopic mode of operation.

Other forms of specialized neutron powder diffractometer have also been developed. Among these are the engineering or residual stress diffractometers, exemplified by the TOF diffractometers ENGIN-X at ISIS (https://www.isis.stfc.ac.uk/Pages/Engin-X.aspx), VULCAN at SNS (https://neutrons.ornl.gov/vulcan), TAKUMI at J-PARC (https://j-parc.jp/researcher/MatLife/en/instrumentation/ns.html) and the CW diffractometers SALSA at ILL (https://www.ill.eu/instruments-support/instruments-groups/instruments/salsa/description/instrument-layout) and KOWARI at ANSTO (http://www.ansto.gov.au/ResearchHub/Bragg/Facilities/Instruments/Kowari/). The purpose of these diffractometers is to measure accurate interplanar spacing (d) within a small gauge volume defined by the intersection of incident and diffracted beams inside a larger sample, as illustrated for constant wavelength in Fig. 2.3.22.

Variations in the d-spacing relative to a strain-free reference value (d_o) represent the average strain in the gauge volume parallel to the scattering vector (*i.e.* perpendicular to the diffracting planes) as is also illustrated in Fig. 2.3.22. By determining strains in several directions, it is possible to reconstruct the full strain tensor within each gauge volume, and

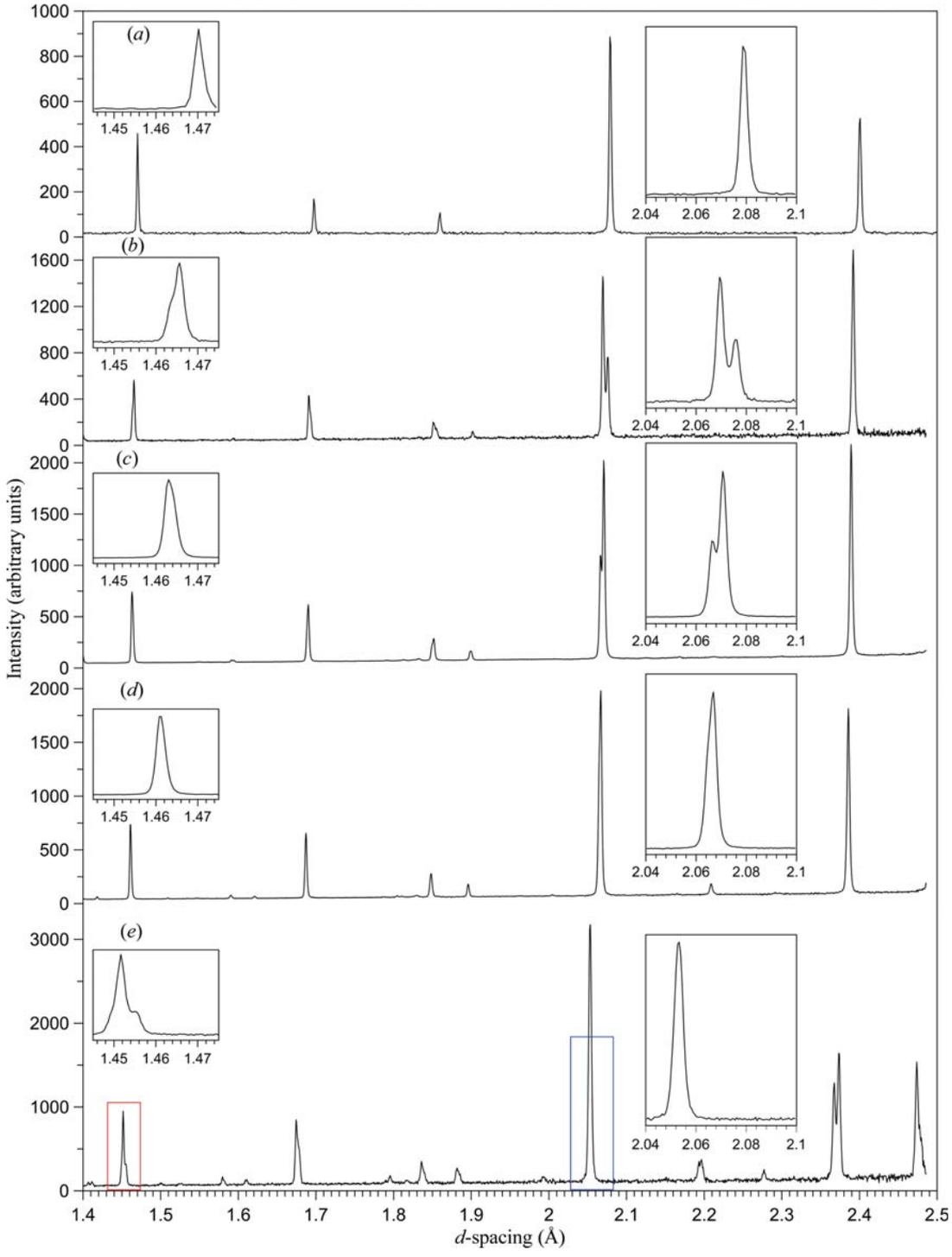

Figure 2.3.20
Parts of the very high resolution neutron powder-diffraction patterns recorded by the backscattering detector bank on the instrument HRPD at ISIS from $SrZrO_3$ at (*a*) 1403, (*b*) 1153, (*c*) 1053, (*d*) 933 and (*e*) 293 K. Insets to the left and right show subtle changes to the reflection shapes and splitting of reflections due to phase transitions from the cubic (*Pm*3*m*) in pattern (*a*), to the tetragonal phase (*I*4/*mcm*) in (*b*), an orthorhombic phase (*Imma*) in (*c*) and a second orthorhombic phase (*Pnma*) in (*d*) and (*e*). Note the intensity reversal in the 002 reflection (right insets), which was pivotal in finding and solving the orthorhombic phase in *Imma* (Howard *et al.*, 2000).

this may be converted into the stress tensor, the desired outcome for engineering purposes (Noyan & Cohen, 1987; Fitzpatrick & Lodini, 2003; Kisi & Howard, 2008). This procedure is widely used in residual stress analysis to study stress distributions in fabricated or welded components and also to observe the internal stress distribution due to an externally imposed load. An example is illustrated in Fig. 2.3.23 in relation to *in situ* experiments and the stress distribution in granular materials.

The required localization of the gauge volume is achieved by shaping the incident and diffracted beams with slits/collimators and is greatly assisted by fixing the diffraction angle 2θ at $\pm 90^\circ$. In CW instruments, the need for high resolution and good intensity is met by using a focusing (bent Si) monochromator and a small area detector to record the data. This generally limits the investigation to a single Bragg peak (reflection), the position of which is carefully mapped over the sampled area for each strain component under investigation.

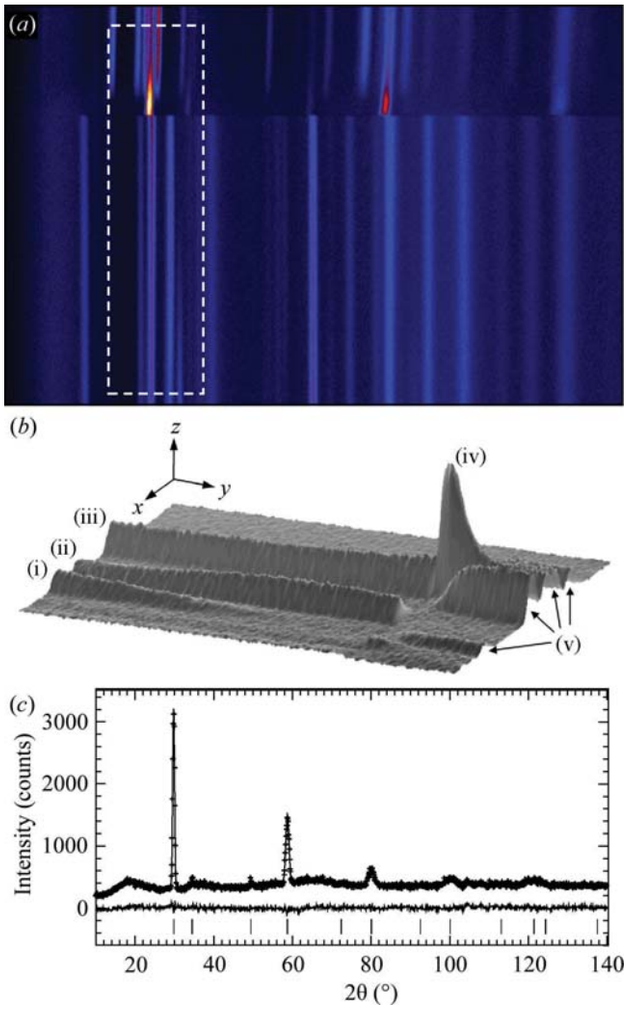

Figure 2.3.21
Neutron powder-diffraction patterns during combustion synthesis of Ti_3SiC_2 recorded in 400 ms each on the diffractometer D20 at ILL (Riley *et al.*, 2002). Panel (*a*) shows an overview of the reaction process with time vertical, diffraction angle horizontal and intensity as colour/brightness. Panel (*b*) is a three-dimensional view of the portion enclosed by dashed lines in (*a*), representing 140 s of reaction, wherein the numbered reflections show (i), (ii) a phase change in Ti, (iii) SiC, (iv) formation of an intermediate phase Ti(Si,C) and (v) growth of the Ti_3SiC_2 product. Panel (*c*) illustrates *via* Rietveld refinement the high quality of diffraction patterns even on this short timescale.

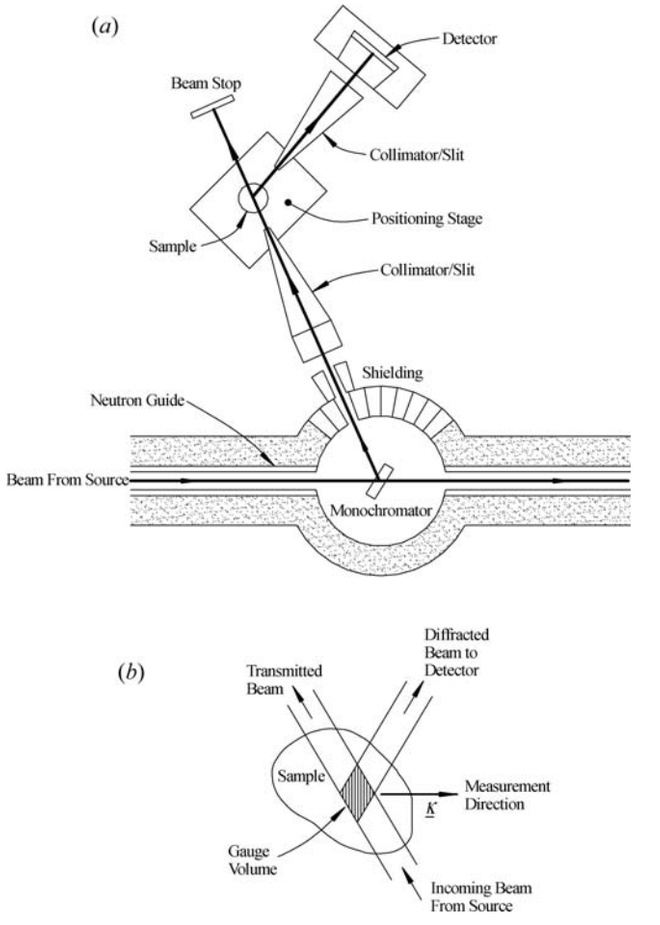

Figure 2.3.22
Illustrating (*a*) a CW engineering diffractometer and (*b*) the formation of a gauge volume at the intersection of the incident and diffracted beams.

TOF engineering diffractometers record a full diffraction pattern at each position. Localization of the gauge volume is achieved using symmetric detector banks and radial collimators on either side of the sample position (Fig. 2.3.24). All other instrument-design criteria are generally secondary to this, as a parallelepiped-shaped gauge volume allows a seamless strain (stress) map to be obtained. These instruments are usually 40–50 m long and have moderately high resolution, which allows peak positions and hence strains to be measured to a precision of 5×10^{-5} in favourable circumstances. In common engineering materials (steels, aluminium alloys *etc*.) this equates to an absolute minimum stress uncertainty of 4–10 MPa. The extreme resolution that would be available using very high resolution designs like HRPD and Super-HRPD (above) is sacrificed in order to obtain data on a reasonable timescale given the generally small gauge volume (0.5–30 mm^3) and the need to map the strain field piecewise over an extended region of the sample.

Although it is not usual for instruments to be specifically designed for the purpose, neutron diffraction is also particularly useful for studying crystallographic texture in materials, as the neutron-diffraction pattern is not distorted by surface coatings or preparation methods. In principle, any diffractometer can be used for measuring texture simply by recording a large number of diffraction patterns with the sample rastered in small angular intervals (5° is common) about two mutually perpendicular axes to form a grid over all orientations. This is extremely time consuming on a conventional CW diffractometer, although the whole pattern is captured each time, as the intensity recorded for the different reflections is subject to different corrections. This can be greatly sped up by using a CW engineering diffractometer (SALSA, KOWARI) with an intense, well collimated incident beam and fitted with an area detector. For example, on KOWARI, the detector spans 15° in both horizontal and vertical directions and so the sample needs to be re-positioned far fewer times. An added advantage is that the diffraction geometry is identical for each sample position and almost so for each reflection studied, and so a pure (*i.e.* model-independent) texture measurement is obtained. Texture measurements on modern TOF diffractometers (*e.g.* GEM, POLARIS, POWGEN, NOMAD and iMATERIA) are in principle quite straightforward. Because there are detectors in many positions all around the sample, the scattering vector and hence orientation of diffracting planes (crystal orientation) is sampled in many orientations all in one data collection. If data from the individual detectors are not 'focused' into composite diffraction patterns as for crystal-structure studies, then very few re-orientations are required to record data representing the full texture. However, since each reflection in each detector bank is sampled using

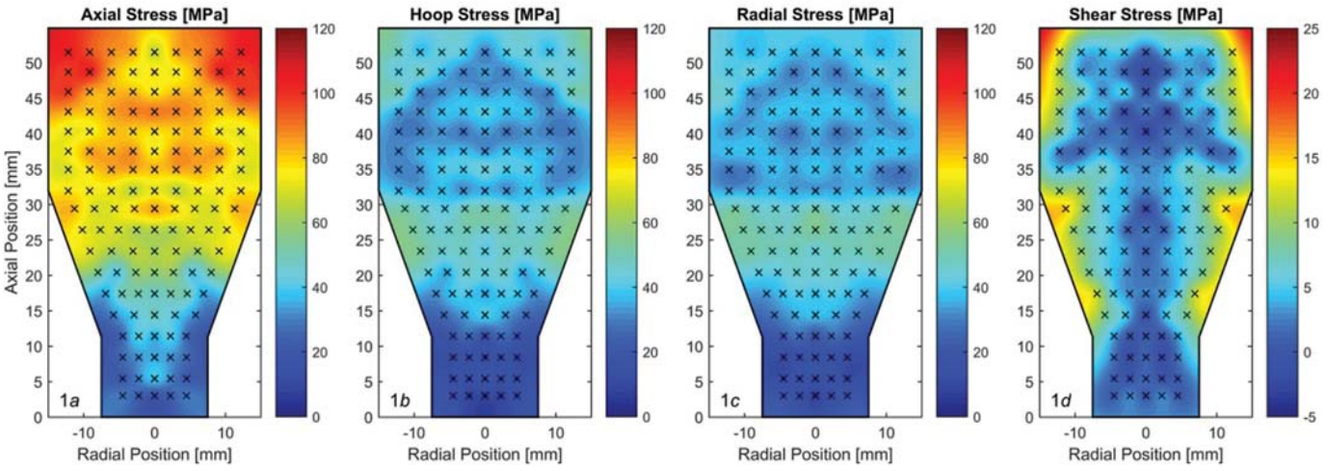

Figure 2.3.23
Stress distribution for four stress components in an iron powder compacted within a convergent die (see also Zhang *et al.*, 2016).

neutrons of different wavelength, each is recorded under different conditions for attenuation and extinction. In addition, to make full use of all the data, whole pattern or Rietveld analysis using a preferred-orientation (texture) model has to be conducted for each of the multitude of diffraction patterns recorded. As well as being time consuming, the reliability of the resultant pole figures and orientation density function is governed by the quality of all the individual models (for background, peak shape, peak width, sample centring, attenuation *etc*.) within the Rietveld refinement as well as the ability of the preferred-orientation model in the Rietveld program to accurately fit the real texture. A pure model-independent texture measurement can only be obtained using CW or TOF single-peak methods.

The instrument WISH at ISIS represents a departure from the normal TOF diffractometer design in that it receives *long wavelength* neutrons (1.5–15 Å) from a cold neutron source at Target Station 2. Ballistic supermirror neutron guides and three choppers deliver neutrons in an active bandwidth of 8 Å for a given chopper setting (https://www.isis.stfc.ac.uk/Pages/Wish.aspx). The pixelated ^{3}He detectors cover Bragg angles in the very wide range 10–170°. WISH is designed for the study of complex magnetic structures and large-unit-cell structures in chemistry and biology. Polarization analysis is available to assist the former.

The concept of long-wavelength neutron powder diffraction will be taken a step further in the DREAM instrument planned for the European Spallation Source (ESS, https://europeanspallationsource.se/realizing-dream-versatile-powder-diffractometer). This instrument will receive neutrons simultaneously from *thermal* and *cold* neutron moderators. It will have a complex array of choppers to shape the incident pulse prior to arrival at the sample. Modelling has indicated that intensity gains of a factor of 10–30 are to be expected and that the instrument may be able to deliver $\Delta d/d$ as low as 4×10^{-5}, albeit at very long wavelengths. More typically the projection is that $\Delta d/d$ as low as 1×10^{-4} could be achieved with more conventional wavelengths. Perhaps the major advantage of the instrument will not be its absolute resolution but the ability to change resolution over the full range during the experiment by simply altering the chopper settings. Therefore unexpected phenomena (phase transitions *etc*.) can be tracked during the initial experiment with no time lost by having to prepare a proposal for a different higher-resolution instrument.

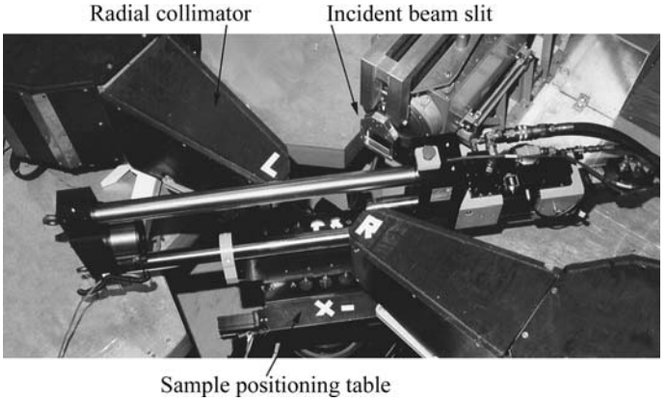

Figure 2.3.24
The engineering diffractometer ENGIN-X at ISIS. The incident beam enters through the flight tube at the top and the left (L) and right (R) 90° detector banks simultaneously record patterns with the scattering vector perpendicular and parallel to the sample axis, respectively. A mechanical testing machine used for *in situ* application of loads is also shown (https://www.isis.stfc.ac.uk). (Credit: STFC.)

2.3.4.4. *Comparison of CW and TOF diffractometers*

The preceding discussion has demonstrated that, although not necessarily the case for other types of neutron scattering, powder diffraction can be very successfully conducted on either CW or TOF instruments. Their relative advantages for the various types of powder-diffraction experiment are embedded in the discussion above and summarized in Table 2.3.5.

Plotting and summarizing the approximate intensity and resolution of different types of neutron diffractometer may be of assistance in assessing the options (Fig. 2.3.25). In the figure, resolution is shown as the inverse of the FWHM ($\Delta d/d$) and intensity is shown as the inverse of the time in seconds taken to record a single diffraction pattern, so that improvements follow the positive x and y axes.

There are two particular cases where the distinction between CW and TOF instruments can determine the success or failure of a neutron powder-diffraction experiment. The first is where crystal structures or phase transitions involving extreme pseudosymmetry are being studied. In this case, the very high resolution available over the entire Q-range (d-spacing range) using high-resolution TOF instruments such as HRPD at the ISIS

Table 2.3.5
Advantages of CW and TOF instruments (modified from Kisi & Howard, 2008)

CW	TOF
(1) Incident beam may be essentially monochromatic, in which case the spectrum is well characterized	(1) The whole incident spectrum is utilized, but it needs to be carefully characterized if intensity data are to be used
(2) Large d-spacings are easily accessible for study of complex magnetic and large-unit-cell structures	(2) Data are collected to very large Q values (small d-spacings)
	(3) Few cold neutron instruments are available for study of complex magnetic and large-unit-cell structures
(3) Can fine tune the resolution during an experiment	(4) Resolution is constant across the whole pattern
	(5) Very high resolution is readily attained by using long flight paths
(4) More common	(6) Complex sample environments are very readily used if 90° detector banks are available
(5) Peak shapes are simpler to model	
(6) Absorption and extinction corrections are relatively straightforward	(7) Simpler to intersect a large proportion of the Debye–Scherrer cones with large detector banks
(7) Data storage and reduction is simpler	
(8) Extremely rapid data collection and stroboscopic measurements are feasible	(8) Very fast data collection is feasible
(9) Engineering diffractometers are very well suited for strain scanning in complex objects	(9) Engineering diffractometers use an extended diffraction pattern, ideal for *in situ* loading and/or heating
(10) Texture is straightforward to measure on engineering diffractometers	(10) Texture can be measured on universal instruments

facility (UK) or SuperHRPD at J-PARC confers a particular advantage. The CW equivalent high-resolution powder diffractometers such as D2B at ILL and ECHIDNA at ANSTO can almost match the absolute resolution of the TOF instruments, D2B achieving $\Delta d/d$ of 5.6 $\times$ 10^{-4}; however, the resolution function for a CW diffractometer [equation (2.3.18)] has a strong minimum and so this resolution can only be achieved over a restricted range of d-spacing. The reflections appearing in the highest-resolution zone can be shifted by wavelength changes, which of necessity require re-recording of the pattern.

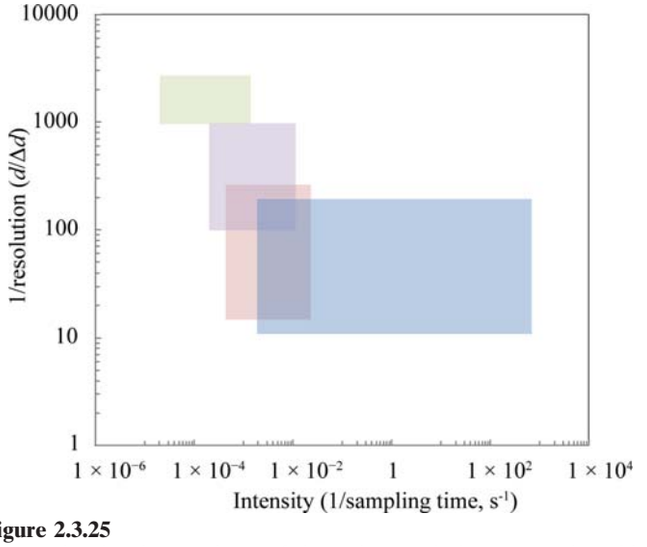

Figure 2.3.25
Schematic showing regions of intensity–resolution space in which different diffractometer types typically operate. High-resolution TOF diffractometers operate in the green area, engineering diffractometers (TOF or CW) in the purple area, multi-purpose TOF diffractometers such as POLARIS in the orange area and very high intensity CW diffractometers in the blue area.

The second extreme case is when rapid kinetic behaviours are to be studied. In this case, a small number of CW diffractometers (*e.g.* D20 at the Institut Laue–Langevin or WOMBAT at ANSTO) have a distinct advantage. Therefore at this time, processes that occur reproducibly and uniformly over a large sample on sub-1 s timescales are best suited to stroboscopic studies using one of the very rapid CW diffractometers available. There are nonetheless a great number of processes that can be studied on the timescales accessible using TOF, where near-constant resolution across the entire diffraction pattern lends considerable advantage.

If unaffected by extremes of resolution, intensity or highly specialized data types (stress, texture *etc.*), the choice between a CW or TOF instrument can be made based more casually on proximity to neutron sources and the access arrangements for national or regional neutron users.

2.3.5. Experimental considerations

2.3.5.1. *Preliminary considerations*

Neutron-diffraction studies are motivated by a desire to exploit the unique properties of neutrons as listed in Sections 2.3.1 and 2.3.2. As access to neutron diffraction is carefully regulated through an experiment proposal system, considerable planning is required in order to write a successful proposal. Owing to the expense of operating a neutron source and pressure on instrument time, there is an onus on the experimental team to make the best use of neutron beam time. Consideration should be given to the type of instrument required, the resolution that is needed, the d-spacing range of interest, how long each pattern will take to record, the requirement (or not) for standard samples and whether a special sample environment is needed.

Table 2.3.6
Suitability of problems to high-resolution or high-intensity diffractometers

Reproduced from Kisi & Howard (2008) by permission of Oxford University Press.

Problem	High resolution	High intensity (medium resolution)
Solve a complex crystal or magnetic structure	Essential, especially in the presence of pseudo-symmetry	Not usually suitable†‡
Refine a complex crystal or magnetic structure	Essential. Will benefit from a high Q-range if available	Not usually suitable†‡
Solve or refine small inorganic structures	Beneficial, but not usually essential unless pseudosymmetry is present	Usually adequate
Quantitative phase analysis	Only required when peaks from the different phases are heavily overlapped	Usually adequate. Allows phase quantities to be tracked in fine environmental variable steps (T, P, E, H *etc*.) during *in situ* experiments
Phase transitions	Depends on the nature of the transition and complexity of the structures. Essential for transitions involving subtle unit-cell distortions and pseudosymmetry	Often adequate for small inorganic structure transitions and order–disorder transitions. Allows fine steps in an environmental variable (T, P, E, H *etc*.)
Line-broadening analysis	Essential for complex line broadening such as from a combination of strain and particle size, dislocations, stacking faults *etc*.	Adequate for tracking changes in severe line broadening as a function of an environmental variable (T, P *etc*.) especially if the pure instrumental peak shape is well characterized
Rapid kinetic studies	Not appropriate	Essential

† In some cases the symmetry and lattice parameters are such that the diffraction peaks are well spaced and not severely overlapped even at modest resolution. ‡ May be necessary to supplement high-resolution data to observe weak superlattice reflections in the presence of very subtle or incomplete order–disorder transitions.

Table 2.3.7
Guidance on choice of wavelength/detector bank

Reproduced from Kisi & Howard (2008) by permission of Oxford University Press.

Problem	Choice	Reasons
Solve complex or low-symmetry structures	Longer wavelength	Increase d-spacing resolution to allow correct symmetry and space group to be assigned
Refine a large or complex crystal structure	Shorter wavelength	Ensure that the number of peaks greatly exceeds the number of parameters. Improve determination of site occupancies and displacement parameters
Solve or refine magnetic structures	Longer wavelength	Ensure that large d-spacing peaks are observed. Spread the magnetic form factor over the entire diffraction pattern
Quantitative phase analysis	Usually shorter wavelength	Improve the accuracy of the determination. Longer wavelengths only required if peak overlap is severe
Phase transitions	Shorter wavelength	Ensures adequate data for order–disorder or other unit-cell-enlarging transitions
	Longer wavelength	Subtle unit-cell distortion or pseudosymmetric structures

In the general case, there is competition between the resolution and the intensity of diffractometers, although some of the modern TOF diffractometers (*e.g.* POLARIS, GEM, POWGEN, NOMAD and iMATERIA) simultaneously record patterns of moderate resolution and intensity, and high-intensity patterns at low resolution, in different detector banks. For the purposes of this chapter, high resolution is defined as a minimum diffraction peak width at half maximum height corresponding to $\Delta d/d \leq 10^{-3}$. This is the resolution typically required to observe lattice-parameter differences [*e.g.* $(a - b)/a$] of as little as 4×10^{-5} or so in the absence of sample-related peak broadening. Such a diffractometer is typically of the order of 10 to 1000 times slower than corresponding high-intensity diffractometers at the same neutron source. The decision to opt for a high-resolution diffractometer or a high-intensity diffractometer will depend critically on the nature of the problem under study. This situation was considered in Kisi & Howard (2008) and their conclusions are reproduced in Table 2.3.6.

It might be expected that the total information content in a diffraction pattern correlates with the d-spacing range covered and therefore this should be maximized. However, this expectation overlooks the different purposes for which powder-diffraction patterns are used. A greater density of diffraction peaks (*e.g.* in a CW pattern recorded using a short neutron wavelength) makes the detailed refinement of complex crystal structures more precise; however, it makes the determination of unit cell and systematic absences *more* difficult as well as reducing access to information contained within the peak shapes concerning the sample microstructure. Table 2.3.7 summarizes these effects. It should be noted that in this context parallels exist between a short-wavelength CW diffraction pattern and a low-angle-detector-bank TOF pattern; and between a longer-

wavelength CW pattern and a high-angle-detector-bank TOF pattern, subject to limitations imposed by the wavelength distribution in the incident spectrum.

A decision must be made on how long to spend recording each diffraction pattern, such that the greatest number of patterns (samples) may be studied without compromising the information content of each pattern. Since counting is governed by Poisson statistics, the statistical precision of N counts in a radiation detector (X-ray, electron or neutron) is represented by the standard deviation σ:

$$\sigma = N^{1/2}. \tag{2.3.23}$$

This is true regardless of whether a single count is made or multiple counts are summed to give an integrated intensity or a total count from several detectors. For a relatively constant arrival rate of neutrons, the precision of each data point will increase with counting time t in proportion to $t^{1/2}$, and this will be reflected in the agreement indices (*e.g.* R_{wp}; Chapter 4.7) between the observed and calculated neutron intensities during structure refinements (*e.g.* Rietveld refinement) as well as in the estimated standard deviation (e.s.d.) of the refined crystal structure and other parameters. It has been shown by Hill & Madsen (1984) using CW X-ray powder-diffraction patterns that this is the case for small counting time; however, the agreement and e.s.d.'s quickly attain a plateau for counting times where 2000–5000 counts are recorded at the top of the largest diffraction peak. Beyond this, systematic errors in the models used for peak shapes, background *etc.* begin to dominate the fitting procedure. An important consequence is that since the expected values of the parameter e.s.d.'s fall in proportion to $t^{-0.5}$ whereas their actual values plateau, the statistical χ^2 increases for patterns recorded beyond the limit suggested by Hill & Madsen. A number of recommendations may be derived from these results:

(i) It is of no benefit for routine crystal structure refinements to record data beyond the point where the strongest peak has 5000 or so counts at its apex and to do so may render parameter e.s.d.'s invalid.

(ii) Counting for longer times *is* however recommended for problems that hinge upon weak superlattice or magnetic peaks. Similarly, it may be of benefit when minor phases are of interest, such as in complex engineering materials, in samples undergoing phase transitions or in multi-component geological materials.

(iii) An equally important result from Hill & Madsen is that respectable refined parameter estimates could be obtained using powder-diffraction patterns with only 200–500 counts at the apex of the strongest peak. This is extremely useful when assessing counting times in rapid kinetic studies where the shortest acceptable counting time is preferred. Modern data-acquisition electronics are often configured to allow very short acquisition times or 'event-mode operation' (Section 2.3.4.2.2) with patterns subsequently added together to obtain the required statistical and/or time resolution. In this case, the shortest time step available should be used provided sufficient data storage capacity is at hand.

In CW measurements with a detector bank scanned in small angular steps, similar arguments to those above apply to the sampling interval. This too has been investigated by Hill & Madsen (1986) and again, improvements to the agreement between the calculated and observed patterns and indeed improvements to refined parameter e.s.d.'s were only observed until systematic errors begin to dominate the fit. As a general rule of thumb, once the applicable counting *time* has been established, the counting interval should be adjusted to give at least 2 (but typically around 5) sampling points in the top half of the diffraction peak for routine crystal structure refinements. Finer sampling intervals are however beneficial in the case of:

(i) subtle symmetry changes that manifest in the peak shape well before peak splitting is observable,

(ii) following the evolution of a minor phase during an *in situ* experiment, or

(iii) peak-shape analyses to explore the sample microstructure (crystallite size, strain distribution, dislocation density, stacking-fault probability *etc.*).

CW measurements using instruments with a fixed position-sensitive detector and TOF measurements both have their raw sampling interval fixed by the instrument architecture, which cannot be varied. The recorded patterns can be subsequently re-binned to a larger sampling interval, although this would usually only be considered to reduce serial correlations during profile refinement (Hill & Madsen, 1986).

2.3.5.2. *Sample-related factors*

Recording a neutron powder-diffraction pattern is in itself a simple operation. There are, however, a number of sample-related variables that can affect the accuracy or the precision of the resulting patterns, or the ability to analyse them. It is worth mentioning here that neutron-diffraction samples are often large, in the range 1–40 g, to compensate for the lower incident fluxes and scattering cross sections as compared with the X-ray case. Large sample size has a strong mitigating effect on many of the sample-induced problems to be discussed in Chapter 2.10 and below.

The absolute *accuracy* of the position, intensity and shape of neutron powder-diffraction peaks is primarily determined by:

(i) *How representative the whole sample is of the whole system.* Known as disproportionation, this problem results from any non-random factor during sampling. For example, within rocks there is spatial variability in the mineral content (where to sample), hardness differences (different mineral particle sizes) and differing density (settling effects). Similar considerations apply to multiphase ceramic materials and metal alloys. With highly penetrating neutrons, this can be greatly reduced by using the polycrystalline solid sample provided that the crystallite size is relatively small [see (iii) below]. Disproportionation primarily influences quantitative phase analysis studies. Crystal-structure results are unaffected provided there is enough of each phase of interest to give a high-quality diffraction pattern.

(ii) *How representative the irradiated part of the sample is of the whole system.* Although ideally the entire sample is bathed in the incident beam, for highly focused neutron beams on high-intensity and/or strain-scanning diffractometers, the beam–sample interaction volume is smaller than the whole sample. In such cases, if a gradient in an experimental variable such as temperature, pressure or composition is present, then the irradiated portion of the sample can be quite unrepresentative and this needs to be addressed in the overall experiment plan.

(iii) *How representative the diffracting part of the sample is of the whole sample.* There are two circumstances in which the observed diffraction pattern may be unrepresentative of the irradiated portion of the sample. First, very large crystallite

size leads to the phenomenon of *granularity*, which is dealt with in detail in Section 2.10.1.1. Crystallites diffract only when the Bragg condition is met, so if the crystallite size is a sizable fraction of the irradiated part of the sample, only a small number of crystallites are aligned for diffraction. With only relatively few crystals diffracting, the peak shapes, intensities and apparent *d*-spacings are strongly distorted. Second, when there is amorphous material present, it is visible in the diffraction pattern only as structure in the background signal and is not analysed using standard crystallographic techniques.

(iv) *How representative the recorded pattern is of the sample.* There are two other factors that can affect accuracy of the diffraction pattern.

The first is that the crystallites may have preferred (rather than random) orientations, so that some sets of atomic planes are overrepresented and others underrepresented in the diffraction pattern. This effect and the means to overcome it in X-ray diffraction measurements are covered in Section 2.10.1.2. Neutron powder diffraction, by using large samples on a rotating sample holder in transmission geometry, is generally far less susceptible to preferred orientation than X-ray diffraction. In cases where preferred orientation is unavoidable, it is generally of a simple axial form due to the sample rotation. Quite good analytical means for modelling preferred orientation of this type are available in the various refinement programs described in Chapter 4.7.

The second effect is attenuation. For most materials, thermal neutrons are attenuated comparably by true absorption and scattering, the overall effect being very minor. For a small number of elements (*e.g.* B, Cd, Gd – see Table 2.3.2) the absorption is high, and in an even smaller number of isotopes (*e.g.* H) the incoherent scattering is high enough to give significant attenuation. Details of these processes are dealt with in Section 2.10.2.4 as well as in Sections 2.4.2 and 3.5.3 of Kisi & Howard (2008). In summary, when using transmission geometry and absorbing samples, diffraction peaks at low angle (CW) are attenuated more than those at higher angles. An additional linear dependence on neutron wavelength occurs in TOF patterns. Therefore the relative intensities are incorrect and during structure refinements unreasonable (often negative) displacement parameters will result. When strongly attenuating elements or isotopes are present three approaches are available; the data can be recorded in reflection geometry, the capillary-coating method can be adapted from X-ray diffraction, or the sample can be diluted with a large amount of a weakly absorbing material. The latter two methods are explained in Section 2.10.1.4.2.2.

Sample-related factors that interact with the precision of various crystallographic and microstructural parameters determined from a given diffraction pattern are:

(i) *The crystallite size within the sample.* As discussed at length in Chapter 2.10, the ideal size for crystallites in a powder-diffraction measurement is 2–5 μm. The upper limit is determined by onset of granularity [see (iii) above]. The lower limit is set by the onset of detectable crystallite size broadening (Chapter 5.1). To first order, the broadening of diffraction peaks due to small crystallite size is well understood. It has negligible effect on the measured intensity of diffraction peaks and does not affect the numerical value of the peak positions (hence *d*-spacings); however, the precision or standard error of such measured positions is strongly affected. In addition, the precision (standard error) of measurements of other microstructural features such as strain distributions, dislocation density or stacking-fault probability are strongly affected. Powdered samples should be sized to lie within the range 2–5 μm with the lower limit being the more important in this case. The crystallite size within solid polycrystalline samples is an inherent part of the system. Forming a material with a fine grain size is a universal method for strengthening metals and ceramics alike. In systems undergoing phase transitions the crystallites typically subdivide into small portions during the transition. Consequently, crystallite size broadening is often an inevitable part of a powder-diffraction experiment.

(ii) *How ideal the crystal structure is within the crystallites.* The preparation of powder samples can induce several types of lattice defects (dislocations, stacking faults, twin faults *etc*.) into the material under study. Each of these leads to changes to the peak positions, shapes and breadths. Likewise, in solid polycrystalline samples, thermal-expansion anisotropy and mismatch between different phases cause intergranular strains which manifest themselves in broadened peaks. Each new source of broadening strongly affects the precision with which other microstructural features of the sample can be determined from peak-shape analysis. In ground powders, it is sometimes possible to relieve stresses and repair defects by annealing, but only if it is certain that no detrimental changes to the material occur under the annealing conditions.

A common prerequisite for the detailed analysis of diffraction patterns is a good understanding of the instrument's characteristic peak shapes and widths, *i.e.* the resolution function (Sections 2.3.4.1.4 and 2.3.4.2.1). The parameters of the resolution function are needed to enable Rietveld (Chapter 4.7) or whole-pattern (Chapter 3.6) analysis of the diffraction patterns. A good description for the instrument resolution function is important in the study of sample microstructure (*e.g.* crystallite size, strain distribution or dislocation studies) and may be established using standard samples. Early versions of the NIST LaB_6 lattice-parameter and peak-shape standards (SRM 660) were unsuitable because of the high neutron absorption of natural boron. More recently, NIST has developed LaB_6 standards SRM 660b and 660c made with ^{11}B that can be used for neutron diffraction (see Section 3.1.4). Suitable air- and moisture-stable alternatives with a closely regulated crystallite size and a moderate density of diffraction peaks include Al_2O_3, CeO_2, Y_2O_3 and some intermetallic compounds such as Cu_9Al_4 and Cu_5Zn_8.

One's ability to successfully analyse a diffraction pattern is then strongly affected by:

(i) *Smooth and locally monotonic peak shapes.* The two primary causes of failing to meet this requirement are granularity (crystallites significantly above the preferred 2–5 μm size) and unusual sample shapes such as hollow samples. Examples of the former may be seen in Figs. 2.10.2 and 2.10.3, where large single crystals in the sample each give a discrete diffraction peak, the composite of which looks nothing like the true powder peak shape. The case of hollow samples is rarely seen unless the 'capillary-coating' technique (see Section 2.10.1.4.2.2) is adopted for a highly absorbing sample or diffraction peaks from a hollow sample container are also to be analysed. In this case, the peak shape will have a depression in the centre due to the non-uniform distribution of diffracting matter across the specimen.

(ii) *Crystallite perfection.* For crystal-structure studies, it is preferred that the crystallites in the sample be as near perfect[19] as possible. However, materials of interest are often far from perfect, containing stacking faults, domain walls, antiphase boundaries, compositional gradients, strain gradients *etc*. Fig. 9.22 in Kisi & Howard (2008) illustrates this for a ferroelectric material. Here the individual crystallites are subdivided into ferroelectric domains with different orientations defined by the symmetry relationship between the parent (cubic) and daughter (tetragonal) structures. Where differently oriented domains abut, there is a strain gradient over a finite portion of crystal. This is visible in the diffraction pattern as a plateau between twin-related pairs of peaks such as the 200/002 pair shown, because in the strain gradient all d-spacings between d_{200} and d_{002} are present.

(iii) *Sample perfection.* The major types of imperfection in sampling are described under *accuracy* in the preceding discussion. Our main interest here is in the preferred orientation of crystallites, which means some diffraction peaks are exaggerated and others underrepresented in the diffraction pattern. Methods for avoiding or reducing preferred orientation are dealt with in Section 2.10.1.2. In addition, whole-pattern fitting and reasonably robust mathematical models for preferred orientation, principally the March–Dollase model (Dollase, 1986) and models based on spherical harmonics (Ahtee *et al.*, 1989), have reduced the effect of preferred orientation on crystal-structure parameters and quantitative phase analyses derived from powder-diffraction patterns. In a small number of cases of severe and/or multi-axis preferred orientation, these models can fail and efforts to reduce the effect within the sample need to be revisited.

2.3.5.3. *Sample environment and in situ experiments*

It is more often the case with neutron diffraction than with X-ray or electron diffraction that the purpose is an experimental study involving rather more than a simple room-temperature data collection.[20] As such, there are a great variety and complexity of sample environments available, relating to studies: at room temperature, cryogenic temperatures, high temperature and high pressure; under magnetic fields, electric fields or applied stress; during gas–solid, liquid–solid, solid–solid or electrochemical reactions; and almost any combination of these. There are several other chapters in this volume that include descriptions of sample environments for neutron powder-diffraction experiments under high (hydrostatic) pressure (Chapter 2.7), electric and magnetic fields (Chapter 2.8) and chemical and electrochemical reactions (Chapter 2.9). Some general guidance on the mounting of samples is also given in Chapter 2.10. Additional information concerning sample containers for non-ambient studies, as well as sample environments not expressly covered in these chapters, will be presented briefly below.

2.3.5.3.1. *Sample containers*

Solid polycrystalline samples can be directly mounted on the diffractometer; however, powder samples require careful containment. Powder spillage must be avoided because samples may become activated in the neutron beam and spilled powders present a radiological hazard. Owing to the low neutron attenuation by most materials, neutron diffraction patterns are generally recorded in transmission (Debye–Scherrer) geometry. Therefore sample containers that do not contribute significantly to the diffraction pattern are required. Fortunately there are several materials that have essentially zero coherent neutron scattering length, *i.e.* they give no discernible diffraction peaks and minimal contribution to the background. Most versatile is elemental vanadium, which has a scattering length of just −0.3824 fm (Table 2.3.2), making its diffraction pattern 100–750 times weaker than most other metals. Coupled with excellent room-temperature resistance to atmospheric corrosion, it is not surprising that it is the material that is used most often for neutron powder diffraction sample holders. Typical designs are discussed in Section 2.10.2.3. Another useful material for room-temperature containment is Al, which has very low attenuation and few diffraction peaks of its own. This is especially useful in cases where only the large d-spacing peaks are of interest, for example with magnetic materials or large-scale structures, or where a fine radial collimator is able to exclude diffraction from the sample container.

Sample containers for specialized sample environments vary greatly. Low-temperature studies routinely use V or Al cans, as for room-temperature studies. High-temperature studies of powders can use V cans up to approximately 1073 K provided that an inert gas or vacuum environment is present. At higher temperatures, thin-walled fused silica (silica glass) can be used as it has several advantages: it is amorphous and therefore gives no sharp diffraction peaks; it is vacuum tight and relatively easy to seal to vacuum fittings *via* O-rings outside or graded glass–metal seals within the hot zone of the furnace; it is transparent, so the state of the sample can be viewed during loading and after the experiment; and it is immune to thermal shock. Silica can survive at temperatures up to 1473 K and for short periods can resist temperatures up to 1673 K, although some devitrification may occur. Care should be exercised since although fused silica has no sharp diffraction peaks, its short-range order does give a structured background which has to be carefully treated in subsequent analyses. Containers for still higher temperatures can be made from other ceramics such as alumina or from refractory metals such as Nb, Ta or W in increasing order of temperature resistance. Noble metals such as Pt may seem to have some advantages; however, they are extremely weak and fragile after high-temperature annealing. All high-temperature sample-container materials are able to chemically react with *some* samples at high temperature and great care must be taken when selecting them. If possible, a trial heating should be conducted off-line prior to the experiment.

2.3.5.3.2. *Non-ambient temperature*

As neutron powder diffraction is routinely conducted in transmission geometry, non-ambient sample environments have many common features. They are typically cylindrical in shape, with the sample can loaded centrally from above on a ‘sample stick’, which goes by various names in different fields.

An example is the liquid-helium cryostat developed at the Institut Laue–Langevin, shown in Fig. 2.3.26. The internal space is evacuated and heat is removed from the sample *via* conduction through the sample stick to cold reservoirs in contact with the liquid-helium tank. The sample protrudes below the helium and nitrogen tanks into the ‘tails’, which are thin-walled Al or V

[19] If the crystallites are too perfect, then diffracted intensities might be affected by ‘extinction’ (Sabine, 1985), so an ‘ideally imperfect’ crystallite is to be preferred.
[20] For example, more than 90% of recent neutron powder-diffraction proposals to Oak Ridge have requested non-ambient conditions (Kaduk, personal communication).

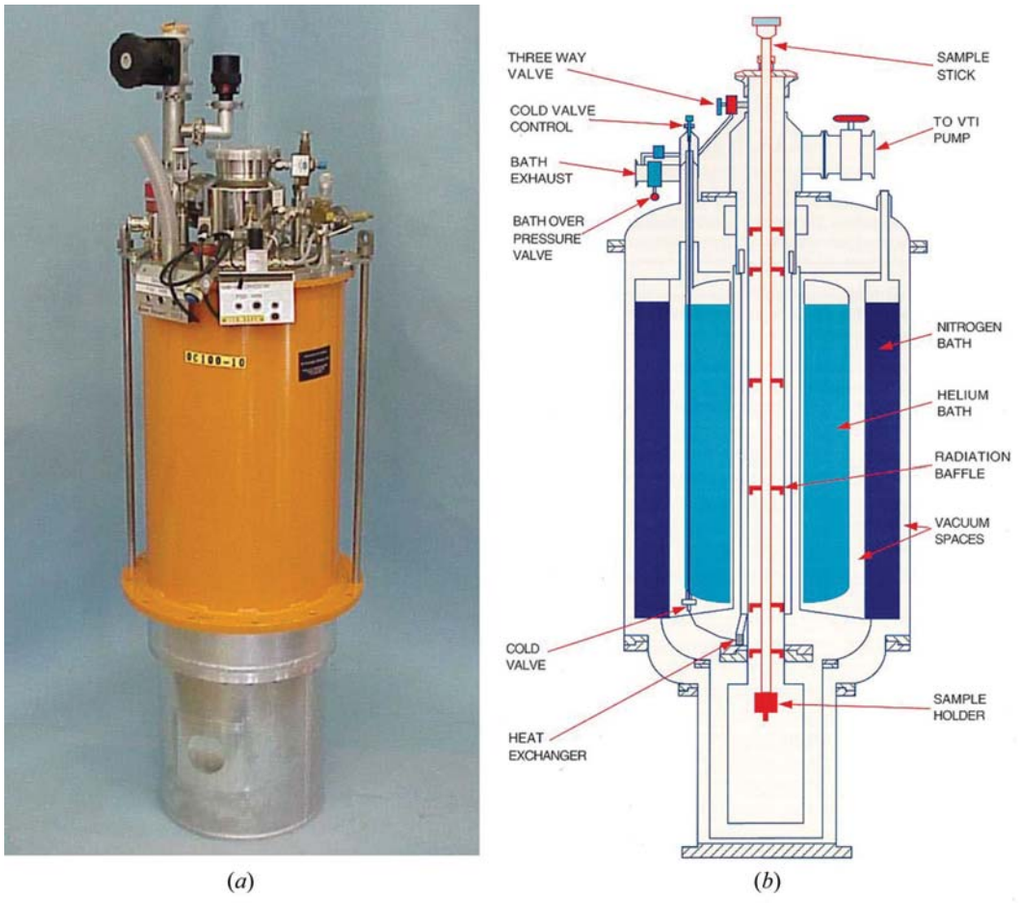

Figure 2.3.26
(*a*) Exterior and (*b*) interior of the standard ILL liquid-helium cryostat for cooling samples in the range 1.8–295 K. An internal heater allows samples to be studied without interruption from 1.8–430 K. Reproduced with permission from the ILL.

cylindrical sections that allow ready transmission of neutrons but preserve the vacuum and exclude radiant heat from the outside world. Liquid-helium cryostats can generally attain base temperatures of 4.2 K (He alone) or 1.9 K if pumped. Liquid-nitrogen cryostats are limited to 77 K. A second type of low-temperature device is the closed-cycle He refrigerator, commonly referred to by the trade name Displex. These are more compact than a liquid-helium cryostat and do not require refilling. Depending on the number of stages and internal design, refrigerators with base temperatures as low as 4 K are available.

Samples are typically first cooled to base temperature and then studied at the chosen sequence of increasing temperatures. This is achieved through a small electric resistance heater and control system. As heat transfer to and from the sample is deliberately poor in these devices, sufficient time should be allowed for the (often large) sample to reach thermal equilibrium before recording its neutron-diffraction pattern. It is worth noting that the attainment of thermal equilibrium does not guarantee that the sample has attained thermodynamic equilibrium. Some phase transitions are notoriously slow, for example the ordering of hydrogen (or deuterium) in Pd metal at 55 K and 75 K, which can take up to a month (Kennedy *et al.*, 1995; Wu *et al.*, 1996), or the ordering of C in TiC_x ($0.6 < x < 0.9$) around 973 K, which can take a week to complete (Moisy-Maurice *et al.*, 1982; Tashmetov *et al.*, 2002).

Raising samples to above ambient temperature is, for X-ray diffraction, the subject of a separate chapter (Chapter 2.6); however, neutron-diffraction high-temperature devices are somewhat different. Most commonly used and most versatile is the foil element resistance furnace, in which Cu bus bars transfer electric current to a cylindrical metal foil which heats up as a result of its electrical resistance. Foil elements are typically 30–60 mm in diameter and up to 200 or 250 mm long so as to provide a long hot zone of uniform temperature within the furnace. The sample is located, *via* a sample stick from above or occasionally *via* a pedestal support from below, in the centre of the foil heating element, ensuring that it is uniformly bathed in radiant heat. Concentric metal-foil heat shields greatly reduce heat loss to the exterior by radiation, while convective losses are avoided by evacuating the interior of the furnace to $\sim 10^{-5}$ mbar. Metals for manufacture of the foil elements include V, which has almost no coherent diffraction pattern and can operate continuously up to 1173 K or intermittently to 1273 K. For temperatures above this, progressively more refractory metals are chosen such as Nb (<1773 K), Ta (<2473 K) or W (2773 K). These materials will contribute some small diffraction peaks to the observed patterns, which requires the recording of reference patterns from the empty furnace before commencing. Owing to the internal vacuum, some types of sample are at risk of subliming, decomposing or disproportioning during the experiment. In such cases, sample cans that extend outside the hot zone, where they can be coupled to a gas-handling system and filled with an internal atmosphere of air, an inert gas or a reactive gas of interest as required, are used.

Alternatives to foil furnaces include variations of the wire-wound laboratory furnace with a split winding and reduced insulating material in the neutron beam path, Peltier devices, hot-air blowers and induction heaters. The first three of these are discussed by Kisi & Howard (2008).

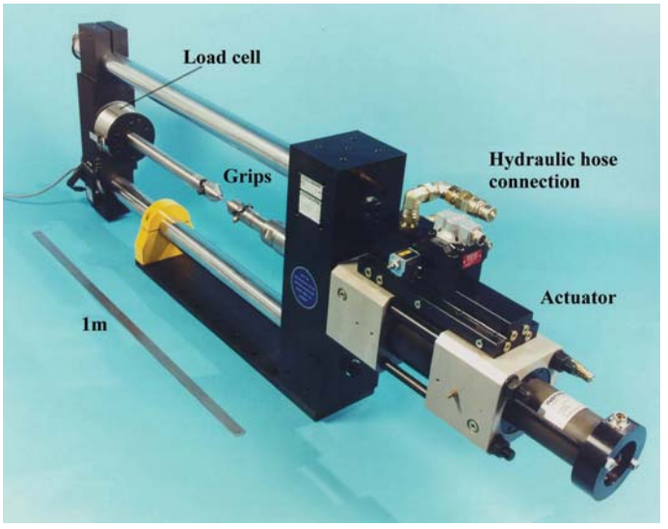

Figure 2.3.27
Elements of a typical mechanical testing machine used for applying uniaxial stress (pressure) to samples on an engineering neutron diffractometer. This example of a 100 kN device is from the instrument ENGIN-X at the ISIS facility, UK. (Credit: STFC.)

Non-ambient temperature devices are usually designed for operation either below or above ambient temperature. However, there are a large number of phase transitions and other phenomena that span from below to above ambient temperature. In order to avoid transferring samples from one sample environment to another mid-experiment, a useful hybrid device is the cryo-furnace. Cryo-furnaces are based around the liquid-helium cryostat and are equipped with more powerful heaters, allowing temperatures typically in the range 4–600 K to be covered.

2.3.5.3.3. *Uniaxial stress*

There are two major applications of *in situ* uniaxial loading. In the first, stress-induced phase transitions, ferroelasticity or simply mechanical response are studied throughout the whole sample as a function of applied stress. This may be undertaken on any powder diffractometer with a reasonable data-collection rate, depending on the resolution required. Parameters typically monitored are the relative phase proportions of parent and daughter structures, lattice parameters, individual peak shifts, which can yield the single-crystal elastic constants (Howard & Kisi, 1999), peak widths, which can indicate the breadth of strain distributions, and preferred-orientation parameters, which can indicate the degree of ferroelasticity (Kisi *et al.*, 1997; Ma *et al.*, 2001; Forrester & Kisi, 2004; Forrester *et al.*, 2005). The second application involves strain scanning using an engineering diffractometer as described in Section 2.3.4.3; however, in this instance an external load is applied to the object under study. This technique can be used to validate finite element analysis simulations of complex components with or without internal residual stresses.

Devices for the *in situ* application of uniaxial stress include adaptations of laboratory universal testing machines such as the 100 kN hydraulic load frame shown in Fig. 2.3.27. Devices such as this may be used in tension, compression, fatigue or even creep conditions depending on the sample and the problem under study.

For more specialized applications, it is sometimes possible to create a more compact device. A recent adaptation of strain scanning is to study the stress distribution within granular materials subjected to a variety of load cases as either the average stresses shown in Fig. 2.3.23 (Wensrich *et al.*, 2012; Kisi *et al.*, 2014), or the stress tensor in individual particles throughout a granular material bed. The latter provides insight into inhomogeneous stress distributions such as force chains (Wensrich *et al.*, 2014). The device that was used in these studies (Fig. 2.3.28) is a self-loading die within which a granular material is compacted while diffraction studies are conducted.

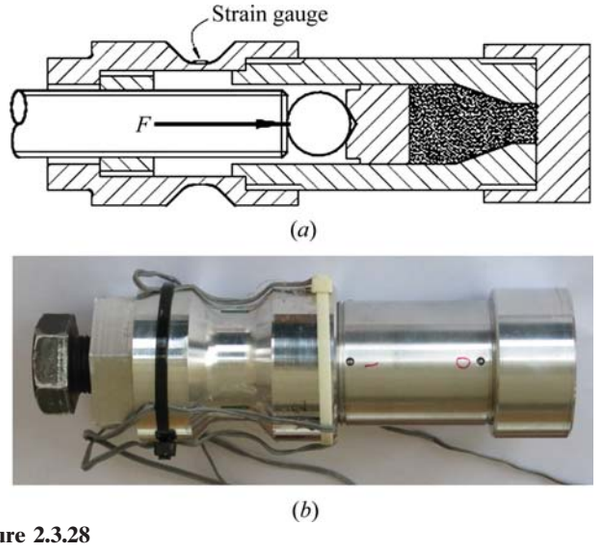

Figure 2.3.28
(*a*) Cross section and (*b*) exterior of a self-loading die for the study of stresses in granular materials.

2.3.6. Concluding remarks

Neutron powder diffraction is just one of many neutron-scattering techniques available; however, it is one that is very commonly used. In fact, the demand for this particular neutron technique is rivalled only by that for small-angle neutron scattering. The close analogy with X-ray powder diffraction makes the technique very familiar to many practitioners of that technique. The differences from X-rays are also critical (Sections 2.3.1 and 2.3.2), since these are the means by which neutron diffraction can obtain information not otherwise accessible. In this chapter we have included descriptions of the various types of neutron source, the neutron powder diffractometers installed at these sources, and a selection of routine and more specialized applications. Demand for the technique is expected to continue, buoyed by further developments in instrumentation and the exploration of new applications.

The authors thank Judith Stalick (NIST), Masatoshi Arai (ESS), Peter Galsworthy (ISIS), Philip King (STFC), Bertrand Blau (PSI), Oliver Kirstein (ESS), Vladimir Pomjakushin (PSI) and Ron Smith (ISIS) for their assistance in organizing Figs. 2.3.6, 2.3.8, 2.3.9, 2.3.10, 2.3.11, 2.3.12, 2.3.15 and 2.3.18, respectively. Ron Smith also provided the data for Fig. 2.3.19. The authors are also grateful for selected proof reading and specialized advice from Greg Storr (ANSTO) as well as Bertrand Blau, Oliver Kirstein and Ron Smith. The authors are particularly appreciative of the efforts of Mark Senn (Oxford) in reading the entire chapter and offering useful constructive comment.

References

Abele, H., Dubbers, D., Häse, H., Klein, M., Knöpfler, A., Kreuz, M., Lauer, T., Märkisch, B., Mund, D., Nesvizhevsky, V., Petoukhov, A., Schmidt, C., Schumann, M. & Soldner, T. (2006). *Characterization of a ballistic supermirror neutron guide*. *Nucl. Instrum. Methods Phys. Res. A*, **562**, 407–417.

Ahtee, M., Nurmela, M., Suortti, P. & Järvinen, M. (1989). *Correction for preferred orientation in Rietveld refinement*. *J. Appl. Cryst.* **22**, 261–268.

Alvarez, L. W. & Bloch, F. (1940). *A quantitative determination of the neutron moment in absolute nuclear magnetons*. *Phys. Rev.* **57**, 111–122.

Anderson, H. L., Booth, E. T., Dunning, J. R., Fermi, E., Glasoe, G. N. & Slack, F. G. (1939). *The fission of uranium*. *Phys. Rev.* **55**, 511–512.

Anderson, I. S. & Schärpf, O. (2006). *International Tables for Crystallography*, Volume C, *Mathematical, Physical and Chemical Tables*, 1st online ed., edited by E. Prince, pp. 431–432. Chester: International Union of Crystallography.

Arai, M. (2008). *J-Parc and the prospective neutron sciences. Pramana J. Phys.* **71**, 629–638.

Arai, M. & Crawford, K. (2009). *Neutron sources and facilties*. *Neutron Imaging and Applications: a Reference for the Imaging Community*, ch. 2. Springer.

Batkov, K., Takibayev, A., Zanini, L. & Mezei, F. (2013). *Unperturbed moderator brightness in pulsed neutron sources*. *Nucl. Instrum. Methods Phys. Res. A*, **729**, 500–505.

Brown, P. J. (2006*a*). *Magnetic scattering of neutrons*. *International Tables for Crystallography*, Volume C, *Mathematical, Physical and Chemical Tables*, 1st online ed., edited by E. Prince, pp. 590–593. Chester: International Union of Crystallography.

Brown, P. J. (2006*b*). *Magnetic form factors*. *International Tables for Crystallography*, Volume C, *Mathematical, Physical and Chemical Tables*, 1st online ed., edited by E. Prince, pp. 454–461. Chester: International Union of Crystallography.

Buras, B. & Holas, A. (1968). *Intensity and resolution in neutron time-of-flight powder diffractometry*. *Nukleonika*, **13**, 591–619.

Buras, B. & Leciejewicz, J. (1964). *A new method for neutron diffraction crystal structure investigations*. *Phys. Status Solidi B*, **4**, 349–355.

Burcham, W. E. (1979). *Elements of Nuclear Physics*, in particular §11.7.2 and p. 353. New York: Longman.

Caglioti, G., Paoletti, A. & Ricci, F. P. (1958). *Choice of collimators for a crystal spectrometer for neutron diffraction*. *Nucl. Instrum.* **3**, 223–228.

Carlile, C. J. (2003). *The production of neutrons*. *Neutron Data Booklet*, 2nd ed., edited by A. J. Dianoux & G. Lander, §3.1. Grenoble: Institut Laue–Langevin.

Carlile, C. J., Hey, P. D. & Mack, B. (1977). *High-efficiency Soller slit collimators for thermal neutrons*. *J. Phys. E Sci. Instrum.* **10**, 543–546.

Carpenter, J. M. (1977). *Pulsed spallation neutron sources for slow neutron scattering*. *Nucl. Instrum. Methods*, **145**, 91–113.

Chadwick, J. (1932). *The existence of a neutron*. *Proc. R. Soc. London Ser. A*, **136**, 692–708.

Chatterji, T. (2006). Editor. *Neutron Scattering from Magnetic Materials.* Amsterdam: Elsevier BV.

Convert, P. & Chieux, P. (2006). *Thermal neutron detection*. *International Tables for Crystallography*, Volume C, *Mathematical, Physical and Chemical Tables*, 1st online ed., edited by E. Prince, pp. 644–652. Chester: International Union of Crystallography.

Cussen, L. D. (2000). *Resolution calculations for novel neutron beam elements*. *J. Appl. Cryst.* **33**, 1393–1398.

Cussen, L. D. (2016). *Optimizing constant wavelength neutron powder diffractometers*. *Nucl. Instrum. Methods Phys. Res. A*, **821**, 122–135.

Cussen, L. D., Nekrassov, D., Zendler, C. & Lieutenant, K. (2013). *Multiple reflections in elliptic neutron guide tubes*. *Nucl. Instrum. Methods Phys. Res. A*, **705**, 121–131.

Cussen, L. D., Vale, C. J., Anderson, I. S. & Høghoj, P. (2001). *Tests of a silicon wafer based neutron collimator*. *Nucl. Instrum. Methods Phys. Res. A*, **471**, 392–397.

Day, D. H. & Sinclair, R. N. (1969). *A pulsed neutron diffraction measurement of preferred orientation in pressed powder compacts of bismuth seleno-telluride*. *J. Phys. C Solid State Phys.* **2**, 870–873.

Dollase, W. A. (1986). *Correction of intensities for preferred orientation in powder diffractometry: application of the March model*. *J. Appl. Cryst.* **19**, 267–272.

Dowty, E. (1999). *ATOMS*. Version 5.0.7. Shape Software, Kingsport, Tennessee, USA.

Dunning, J. R., Pegram, G. B., Fink, G. A., Mitchell, D. P. & Segrè, E. (1935). *Velocity of slow neutrons by mechanical velocity selector*. *Phys. Rev.* **48**, 704.

Fermi, E., Amaldi, E., D'Agostino, O., Rasetti, F. & Segrè, E. (1934). *Artificial radioactivity produced by neutron bombardment*. *Proc. R. Soc. London Ser. A*, **146**, 483–500.

Fermi, E., Amaldi, E., D'Agostino, O., Pontecorvo, B., Rasetti, F. & Segrè, E. (1934). *Azione di sostanze idrogenate sulla radioattivita provocata da neutroni. I. Ric. Sci.* **5**, 282–283.

Fermi, E., Marshall, J. & Marshall, L. (1947). *A thermal neutron velocity selector and its application to the measurement of the cross section of boron*. *Phys. Rev.* **72**, 193–196.

Finger, L. W., Cox, D. E. & Jephcoat, A. P. (1994). *A correction for powder diffraction peak asymmetry due to axial divergence*. *J. Appl. Cryst.* **27**, 892–900.

Fischer, P., Frey, G., Koch, M., Könnecke, M., Pomjakushin, V., Schefer, J., Thut, R., Schlumpf, N., Bürge, R., Greuter, U., Bondt, S. & Berruyer, E. (2000). *High-resolution powder diffractometer HRPT for thermal neutrons at SINQ Physica B*, **276–278**, 146–147.

Fitzpatrick, M. E. & Lodini, A. (2003). *Analysis of Residual Stress by Diffraction Using Neutron and Synchrotron Radiation*. Boca Raton: CRC Press.

Forrester, J. S. & Kisi, E. H. (2004). *Ferroelastic switching in a soft lead zirconate titanate*. *J. Eur. Ceram. Soc.* **24**, 595–602.

Forrester, J. S., Kisi, E. H. & Studer, A. J. (2005). *Direct observation of ferroelastic domain switching in polycrystalline $BaTiO_3$ using in situ neutron diffraction*. *J. Eur. Ceram. Soc.* **25**, 447–454.

Friedrich, H., Wagner, V. & Wille, P. (1989). *A high-performance neutron velocity selector*. *Physica B*, **156–157**, 547–549.

Hahn, O. & Strassmann, F. (1939). *Über den Nachweis und das Verhalten der bei der Bestrahlung des Urans mittels Neutronen entstehenden Erdalkalimetalle*. *Naturwissenschaften*, **27**, 11–15.

Hakonen, P., Lounasmaa, O. V. & Oja, A. (1991). *Spontaneous nuclear magnetic ordering in copper and silver at nano- and picokelvin temperatures*. *J. Magn. Magn. Mater.* **100**, 394–412.

Halban, H. von, Joliot, F. & Kowarski, L. (1939). *Number of neutrons liberated in the nuclear fission of uranium*. *Nature*, **143**, 680.

Halban, H. von & Preiswerk, P. (1936). *Preuve expérimentale de la diffraction des neutrons. C. R. Acad. Sci. Paris*, **203**, 73.

Häse, H., Knöpfler, A., Fiederer, K., Schmidt, U., Dubbers, D. & Kaiser, W. (2002). *A long ballistic supermirror guide for cold neutrons at ILL*. *Nucl. Instrum. Methods Phys. Res. A*, **485**, 453–457.

Hayter, J. B. & Mook, H. A. (1989). *Discrete thin-film multilayer design for X-ray and neutron supermirrors*. *J. Appl. Cryst.* **22**, 35–41.

Hewat, A. W. (1975). *Design for a conventional high-resolution neutron powder diffractometer*. *Nucl. Instrum. Methods*, **127**, 361–370.

Hewat, A. W. & Bailey, I. (1976). *D1A, a high resolution neutron powder diffractometer with a bank of Mylar collimators*. *Nucl. Instrum. Methods*, **137**, 463–471.

Hill, R. J. & Howard, C. J. (1987). *Quantitative phase analysis from neutron powder diffraction data using the Rietveld method*. *J. Appl. Cryst.* **20**, 467–474.

Hill, R. J. & Madsen, I. C. (1984). *The effect of profile-step counting time on the determination of crystal structure parameters by X-ray Rietveld analysis*. *J. Appl. Cryst.* **17**, 297–306.

Hill, R. J. & Madsen, I. C. (1986). *The effect of profile step width on the determination of crystal structure parameters and estimated standard deviations by X-ray Rietveld analysis*. *J. Appl. Cryst.* **19**, 10–18.

Howard, C. J. (1982). *The approximation of asymmetric neutron powder diffraction peaks by sums of Gaussians*. *J. Appl. Cryst.* **15**, 615–620.

Howard, C. J., Ball, C. J., Davis, R. L. & Elcombe, M. M. (1983). *The Australian high resolution neutron powder diffractometer*. *Aust. J. Phys.* **36**, 507–518.

Howard, C. J. & Kisi, E. H. (1999). *Measurement of single-crystal elastic constants by neutron diffraction from polycrystals*. *J. Appl. Cryst.* **32**, 624–633.

Howard, C. J., Knight, K. S., Kennedy, B. J. & Kisi, E. H. (2000). *The structural phase transitions in strontium zirconate revisited*. *J. Phys. Condens. Matter*, **12**, L677–L683.

Izyumov, Y. A. & Ozerov, R. P. (1970). *Magnetic Neutron Diffraction*. New York: Plenum Press.

Jorgensen, J. D., Beno, M. A., Hinks, D. G., Soderholm, L., Volin, K. J., Hitterman, R. L., Grace, J. D., Schuller, I. K., Segre, C. U., Zhang, K. & Kleefisch, M. S. (1987). *Oxygen ordering and the orthorhombic-to-*

tetragonal phase transition in $YBa_2Cu_3O_{7-x}$. Phys. Rev. B, **36**, 3608–3616.

Kennedy, S. J., Wu, E., Kisi, E. H., Gray, E. M. & Kennedy, B. J. (1995). *Ordering of deuterium in $PdD_{0.65}$ at 54 K. J. Phys. Condens. Matter*, **7**, L33–L40.

Kimura, M., Sugawara, M., Oyamada, M., Yamada, Y., Tomiyoshi, S., Suzuki, T., Watanabe, N. & Takeda, S. (1969). *Neutron Debye–Scherrer diffraction works using a linear electron accelerator*. *Nucl. Instrum. Methods*, **71**, 102–110.

Kisi, E. H. & Howard, C. J. (2008). *Applications of Neutron Powder Diffraction*. Oxford University Press.

Kisi, E. H., Howard, C. J. & Hill, R. J. (1989). *Crystal structure of orthorhombic zirconia in partially stabilized zirconia*. *J. Am. Ceram. Soc.* **72**, 1757–1760.

Kisi, E. H., Kennedy, S. J. & Howard, C. J. (1997). *Neutron diffraction observations of ferroelastic domain switching and tetragonal-to-monoclinic transformation in Ce-TZP*. *J. Am. Ceram. Soc.* **80**, 621–628.

Kisi, E. H., Wensrich, C. M., Luzin, V. & Kirstein, O. (2014). *Stress distribution in iron powder during die compaction*. *Mater. Sci. Forum*, **777**, 243–248.

Ma, Y., Kisi, E. H. & Kennedy, S. J. (2001). *Neutron diffraction study of ferroelasticity in a 3 mol% Y_2O_3-ZrO_2. J. Am. Ceram. Soc.* **84**, 399–405.

Marseguerra, M. & Pauli, G. (1959). *Neutron transmission probability through a curved revolving slit*. *Nucl. Instrum. Methods*, **4**, 140–150.

Marshall, W. & Lovesey, S. W. (1971). *Theory of Thermal Neutron Scattering: The Use of Neutrons for the Investigation of Condensed Matter*. Oxford: Clarendon Press.

Maruyama, R., Yamazaki, D., Ebisawa, T., Hino, M. & Soyama, K. (2007). *Development of neutron supermirrors with large critical angle*. *Thin Solid Films*, **515**, 5704–5706.

Masalovich, S. (2013). *Analysis and design of multilayer structures for neutron monochromators and supermirrors*. *Nucl. Instrum. Methods Phys. Res. A*, **722**, 71–81.

Mason, T. E., Gawne, T. J., Nagler, S. E., Nestor, M. B. & Carpenter, J. M. (2013). *The early development of neutron diffraction: science in the wings of the Manhattan Project*. *Acta Cryst.* A**69**, 37–44.

Meitner, L. & Frisch, O. R. (1939). *Disintegration of uranium by neutrons: a new type of nuclear reaction*. *Nature*, **143**, 239–240.

Mezei, F. (1976). *Novel polarized neutron devices: supermirror and spin component amplifier*. *Commun. Phys.* **1**, 81–85.

Mezei, F. (1997). *The raison d'être of long pulse spallation sources. J. Neutron Res.* **6**, 3–32.

Mitchell, D. P. & Powers, P. N. (1936). *Bragg reflection of slow neutrons*. *Phys. Rev.* **50**, 486–487.

Moisy-Maurice, V. N., Lorenzelli, N., De Novion, C. H. & Convert, P. (1982). *High temperature neutron diffraction study of the order–disorder transition in TiC_{1-x}. Acta Metall.* **30**, 1769–1779.

Moore, M. J., Kasper, J. S. & Menzel, J. H. (1968). *Pulsed LINAC neutron diffraction*. *Nature*, **219**, 848–849.

Noyan, I. C. & Cohen, J. B. (1987). *Residual Stress: Measurement by Diffraction and Interpretation*. New York: Springer.

Oed, A. (1988). *Position-sensitive detector with microstrip anode for electron multiplication with gases*. *Nucl. Instrum. Methods Phys. Res. A*, **263**, 351–359.

Oed, A. (2003). *Detectors for thermal neutrons*. *Neutron Data Booklet*, 2nd ed., edited by A. J. Dianoux & G. Lander, §3.3. Grenoble: Institut Laue–Langevin.

Peters, J., Champion, J. D. M., Zsigmond, G., Bordallo, H. N. & Mezei, F. (2006). *Using Fermi choppers to shape the neutron pulse*. *Nucl. Instrum. Methods Phys. Res. A*, **557**, 580–584.

Radaelli, P. G., Iannone, G., Marezio, M., Hwang, H. Y., Cheong, S. W., Jorgensen, J. D. & Argyriou, D. N. (1997). *Structural effects on the magnetic and transport properties of perovskite $A_{(1-x)}A_{(x)}'MnO_3$ (x = 0.25, 0.30)*. *Phys. Rev. B*, **56**, 8265–8276.

Rauch, H. & Waschkowski, W. (2003). *Neutron scattering lengths*. *Neutron Data Booklet*, 2nd ed., edited by A. J. Dianoux & G. Lander, §1.1. Grenoble: Institut Laue–Langevin.

Riley, D. P., Kisi, E. H., Hansen, T. C. & Hewat, A. W. (2002). *Self-propagating high-temperature synthesis of Ti_3SiC_2: I, ultra-high-speed neutron diffraction study of the reaction mechanism*. *J. Am. Ceram. Soc.* **85**, 2417–2424.

Rodriguez, D. M., Kennedy, S. J. & Bentley, P. M. (2011). *Properties of elliptical guides for neutron beam transport and applications for new instrumentation concepts*. *J. Appl. Cryst.* **44**, 727–737.

Rush, J. J. & Cappelletti, R. L. (2011). *The NIST Center for Neutron Research: Over 40 Years Serving NIST/NBS and the Nation*. National Institute of Standards Special Publication (NIST SP) 1120. National Institute of Standards, Gaithersburg, Maryland, USA.

Sabine, T. M. (1985). *Extinction in polycrystalline materials*. *Aust. J. Phys.* **38**, 507–518.

Schanzer, C., Böni, P., Filges, U. & Hils, T. (2004). *Advanced geometries for ballistic neutron guides*. *Nucl. Instrum. Methods Phys. Res. A*, **529**, 63–68.

Schoenborn, B. P., Caspar, D. L. D. & Kammerer, O. F. (1974). *A novel neutron monochromator*. *J. Appl. Cryst.* **7**, 508–510.

Sears, V. F. (2006). *Scattering lengths for neutrons*. *International Tables for Crystallography*, Volume C, *Mathematical, Physical and Chemical Tables*, 1st online ed., edited by E. Prince, pp. 444–454. Chester: International Union of Crystallography.

Shull, C. G. (1995). *Early development of neutron scattering*. *Rev. Mod. Phys.* **67**, 753–757.

Shull, C. G., Strauser, W. A. & Wollan, E. O. (1951). *Neutron diffraction by paramagnetic and antiferromagnetic substances. Phys. Rev.* **83**, 333–345.

Shull, C. G., Wollan, E. O., Morton, G. A. & Davidson, W. L. (1948). *Neutron diffraction studies of NaH and NaD*. *Phys. Rev.* **73**, 842–847.

Smith, R. I. *et al.* (2018). In preparation.

Soller, W. (1924). *A new precision X-ray spectrometer*. *Phys. Rev.* **24**, 158–167.

Soper, A. K., Howells, W. S., Hannon, A. C., Turner, J. Z. & Bowron, D. T. (2000). *ATLAS – analysis of time-of-flight diffractometer data from liquid and amorphous samples*. http://wwwisis2.isis.rl.ac.uk/Disordered/Manuals/ATLAS%20manual%20and%20SSG.pdf.

Squires, G. L. (1978). *Introduction to the Theory of Thermal Neutron Scattering.* Cambridge University Press.

Szilard, L. & Chalmers, T. A. (1934). *Detection of neutrons liberated from beryllium by gamma rays: a new technique for inducing radioactivity*. *Nature*, **134**, 494–495.

Tamura, I., Aizawa, K., Harada, M., Shibata, K., Maekawa, F., Soyama, K. & Arai, M. (2003). *Simulation for developing new pulse neutron spectrometers: creation of new McStas components of moderators of JSNS*. JAERI Research Report 2003-008. JAERI, Japan.

Tashmetov, M. Y., Em, V. T. E., Lee, C. H., Shim, H. S., Choi, Y. N. & Lee, J. S. (2002). *Neutron diffraction study of the ordered structures of nonstoichiometric titanium carbide*. *Physica B*, **311**, 318–325.

Thomsen, K. (2014). *Conceptual proposal for compound moderators with preferential emission directions*. *Phys. Procedia*, **60**, 278–293.

Tremsin, A. S., McPhate, J. B., Vallerga, J. V., Siegmund, O. H. W., Feller, W. B., Lehmann, E., Butler, L. G. & Dawson, M. (2011). *High-resolution neutron microtomography with noiseless neutron counting detector*. *Nucl. Instrum. Methods Phys. Res. A*, **652**, 400–403.

Tremsin, A. S., McPhate, J. B., Vallerga, J. V., Siegmund, O. H. W., Kockelmann, A., Steuwer, A. & Feller, W. B. (2011). *High-resolution neutron counting sensor in strain mapping through transmission Bragg edge diffraction*. *IEEE Sens. J.* **11**, 3433–3436.

Turchin, V. F. (1967). Deposited Paper, USSR Atomic Energy, 1967, p. 22.

Vogt, T., Passell, L., Cheung, S. & Axe, J. D. (1994). *Using wafer stacks as neutron monochromators*. *Nucl. Instrum. Methods Phys. Res. A*, **338**, 71–77.

Wensrich, C. M., Kisi, E. H., Luzin, V., Garbe, U., Kirstein, O., Smith, A. L. & Zhang, J. F. (2014). *Force chains in monodisperse spherical particle assemblies: three-dimensional measurements using neutrons*. *Phys. Rev. E*, **90**, 042203.

Wensrich, C. M., Kisi, E. H., Zhang, J. F. & Kirstein, O. (2012). *Measurement and analysis of the stress distribution during die compaction using neutron diffraction*. *Granular Matter*, **14**, 67–680.

Wilkins, S. W., Stevenson, A. W., Nugent, K. A., Chapman, H. & Steenstrup, S. (1989). *On the concentration, focusing, and collimation of x-rays and neutrons using microchannel plates and configurations of holes*. *Rev. Sci. Instrum.* **60**, 1026–1036.

Willendrup, P., Farhi, E., Knudsen, E., Filges, U. & Lefmann, K. (2014). *McStas: Past, present and future. J. Neutron Res.* **17**, 35–43.

Wollan, E. O. & Borst, L. B. (1945). *Physics Section III Monthly Report for the Period Ending December 31, 1944*, p. 37. Metallurgical Project Report No. M-CP-2222. Clinton Laboratories, Oak Ridge, Tennessee, USA.

Wollan, E. O. & Shull, C. G. (1948). *The diffraction of neutrons by crystalline powders*. *Phys. Rev.* **73**, 830–841.
Worlton, T. G., Jorgensen, J. D., Beyerlein, R. A. & Decker, D. L. (1976). *Multicomponent profile refinement of time-of-flight neutron powder diffraction data*. *Nucl. Instrum. Methods*, **137**, 331–337.
Wu, E., Kennedy, S. J., Gray, E. M. & Kisi, E. H. (1996). *The ordered structure of $PdD_{0.78}$ at 70–75K*. *J. Phys. Condens. Matter*, **8**, 2807–2813.
Zendler, C., Lieutenant, K., Nekrassov, D. & Fromme, M. (2014). *VITESS 3 – virtual instrumentation tool for the European Spallation Source*. *J. Phys. Conf. Ser.* **528**, 012036.
Zhang, J. F., Wensrich, C. M., Kisi, E. H., Luzin, V., Kirstein, O. & Smith, A. L. (2016). *Stress distributions in compacted powders in convergent and stepped dies*. *Powder Technol.* **292**, 23–30.
Zhao, J. K., Robertson, J. L., Herwig, K. W., Gallmeier, F. X. & Riemer, B. W. (2013). *Optimizing moderator dimensions for neutron scattering at the spallation neutron source*. *Rev. Sci. Instrum.* **84**, 125104.
Zinn, W. H. (1947). *Diffraction of neutrons by a single crystal*. *Phys. Rev.* **71**, 752–757.
Zinn, W. H. & Szilard, L. (1939). *Emission of neutrons by uranium*. *Phys. Rev.* **56**, 619–624.

International Tables for Crystallography (2018). Vol. H, Chapter 2.4, pp. 102–117.

2.4. Electron powder diffraction

J.-M. Zuo, J. L. Lábár, J. Zhang, T. E. Gorelik and U. Kolb

2.4.1. Introduction

Electron powder diffraction is commonly performed in transmission geometry inside a transmission electron microscope using ~80–300 kV high-energy electrons with wavelengths from 0.0418 to 0.0197 Å (Cowley, 1992; Peng *et al.*, 2004). The incident electron beam can be as small as a few nm or as large as tens of μm in diameter. Transmission electron powder diffraction can be obtained from randomly oriented nanocrystalline or amorphous materials. The short electron wavelengths allow the observation of powder diffraction rings over a large range of S (= $\sin\theta/\lambda$). Electron powder diffraction can also be performed using the Bragg reflection geometry in reflection high-energy electron diffraction (RHEED) with 10–30 kV electrons (Ichimiya & Cohen, 2004). RHEED has a limited penetration depth and therefore is mostly used for the study of supported nanoparticles.

Because the electron beam can be formed into a small probe using electromagnetic lenses in a transmission electron microscope, electron diffraction has the advantage of being able to address individual particles in a powder as single crystals. Single-crystal electron diffraction data are often used for the determination of unit-cell parameters (Zuo, 1993; Zuo *et al.*, 1998; Gramm *et al.*, 2006; Sun *et al.*, 2009; Kolb *et al.*, 2006; Zhuang *et al.*, 2011), phase identification (Gramm *et al.*, 2006) or quantitative structural analysis (Vincent & Exelby, 1991; Jansen *et al.*, 1998; Tsuda & Tanaka, 1999; Hovmoller *et al.*, 2002; Sun *et al.*, 2009; Gorelik *et al.*, 2010; Mugnaioli *et al.*, 2012), or in combination with X-ray and neutron powder diffraction for structure determination (Wu *et al.*, 2006; Baerlocher *et al.*, 2007; McCusker & Baerlocher, 2009).

The principle of electron diffraction is similar to that of X-ray diffraction. Both use atomic scattering and interference of the scattered waves to probe the atomic structure. The difference is that electrons are charged particles and interact with both the electrons and nucleus of the atom with a large elastic scattering cross section (several orders of magnitude larger than that of X-rays). The combination of short wavelength, the large scattering cross section and the small electron beam makes electron powder diffraction a powerful technique for the analysis of amorphous or nanocrystalline thin films, nanoparticles and 'small' crystals in general (see Fig. 2.4.1 for an example).

A drawback of the strong interaction of electrons with matter is the presence of multiple-scattering effects. In X-ray diffraction, the measured integrated intensity is often less than predicted by the theory for an ideally imperfect crystal (because of extinction) but larger than predicted by the theory for an ideal perfect crystal. There are two types of extinction: primary and secondary. Primary extinction describes the multiple scattering within a single mosaic block. Primary extinction diminishes the intensity when the mosaic blocks are so large that they behave as fragments of perfect crystals. The effect of electron multiple scattering is similar to primary extinction in X-ray diffraction, except the electron extinction length is short and comparable with the sample thickness. Strong extinction can be an issue when analysis based on kinematical diffraction (single-scattering) theory, as in X-ray powder diffraction, is used for electron diffraction intensities; thus dynamic theory, which takes into account multiple scattering of the incident and diffracted waves inside a crystal, is necessary. Secondary extinction also occurs in electron powder diffraction. However, so far there is no satisfactory treatment of this effect in electron diffraction. For small nanoparticles or nanocrystalline thin films the electron multiple-scattering effects are typically reduced, so quantitative structural information can be extracted from electron powder diffraction using the kinematical approximation (Cockayne & McKenzie, 1988; Ishimaru *et al.*, 2002; Chen & Zuo, 2007; Cockayne, 2007). Recent studies have demonstrated that multiple-scattering effects can be significantly reduced by averaging over a range of crystal orientations using precession electron diffraction (Vincent & Midgley, 1994; Gjonnes *et al.*, 1998; Gemmi *et al.*, 2003; Own *et al.*, 2006; Oleynikov & Hovmoller, 2007). The same benefit is expected in electron powder diffraction with 360° orientation averaging.

The quality of electron powder diffraction work has also benefited from the development of TEM (transmission electron microscopy) technologies. The adoption of field emission guns (FEGs) in conventional transmission electron microscopes led to the development of electron sources with high brightness, small probe size and improved coherence. Electron energy filters, such as the in-column Ω energy filter, allow a reduction of the inelastic background due to plasmon scattering, or higher electron energy losses, with an energy resolution of a few eV (Rose & Krahl, 1995). The development of array detectors, such as charge-coupled device (CCD) cameras or image plates, enables the recording of entire powder diffraction patterns and direct quantification of diffraction intensities over a large dynamic range that was not possible earlier (Zuo, 2000). The latest

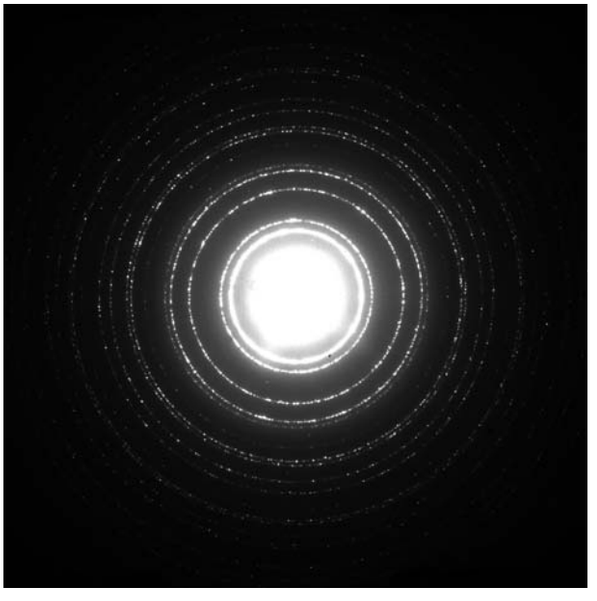

Figure 2.4.1
An electron powder diffraction pattern recorded on an imaging plate from a polycrystalline Al thin film using selected-area electron diffraction geometry with 200 kV electrons.

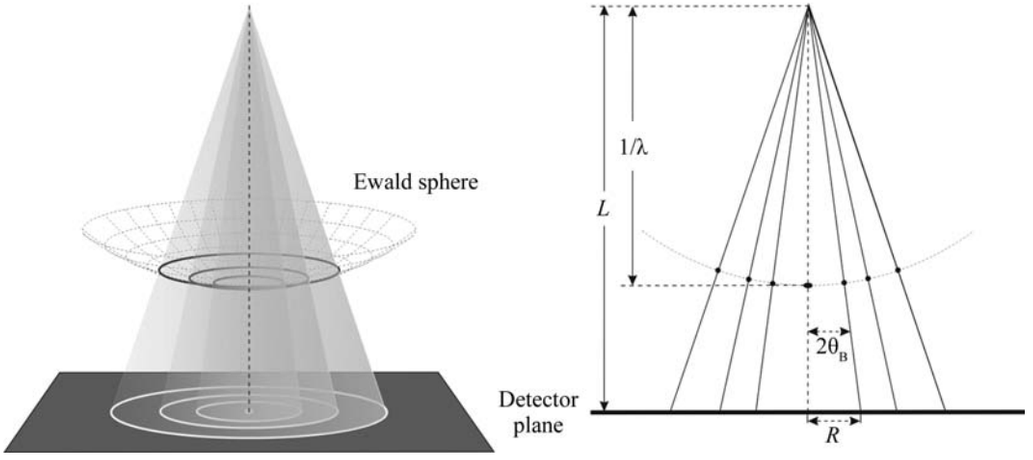

Figure 2.4.2
Schematic diagram of the Ewald sphere construction and the geometry for recording electron diffraction patterns.

development in time-resolved electron diffraction at a time resolution approaching femtoseconds (Elsayedali & Herman, 1990; Siwick *et al.*, 2003) will significantly improve the ability to interrogate structures at high spatial and time resolution.

Irradiation of both organic and inorganic materials with an electron beam can cause severe modification of the structure. The amount of energy deposited into the material can be estimated through the ratio of the elastic and inelastic scattering cross sections. For carbon the ratio for electrons (300 keV) and X-rays (with a wavelength of less than 1 Å) is comparable, meaning that the radiation damage caused by these sources is on the same scale (Henderson, 1995). Electron radiation damage is caused by all kinds of ionization processes, including bond breakdown and subsequent recombination of radicals and active molecular species. Inorganic materials can show knock-on damage (atomic displacement) or sputtering effects (loss of atoms). This damage may lead to a total structural collapse. The collective damage due to electron radiation is quantified using the electron dose and electron dose rates. In many cases the damage can be reduced by minimizing the electron dose received by the sample, cryo-protection, or deposition of a protective conductive layer (Reimer & Kohl, 2008).

This chapter covers the practical issues and theory of electron powder diffraction as well as applications for material analysis. A fundamental description of electron diffraction can be found in *International Tables for Crystallography*, Vol. C (2004) and the book by Zuo & Spence (2017). The present chapter is subdivided into seven sections. Sections 2.4.2 and 2.4.3 cover the theory and the experimental setup of an electron powder diffraction experiment using transmission electron microscopes, respectively. Sections 2.4.4 and 2.4.5 discuss the application of electron powder diffraction data to phase and texture analysis and related techniques. Rietveld refinement with electron powder diffraction data is a relatively new field; this is discussed in Section 2.4.6. The last section reviews pair distribution function (PDF) analysis using electron diffraction data.

2.4.2. Electron powder diffraction pattern geometry and intensity

By J.-M. Zuo and J. L. Lábár

The powder diffraction rings in transmission geometry appear where the cone of diffracted electron beams intersects the Ewald sphere. The intersection creates a ring of diffracted beams, which is then projected onto the planar detector (see Fig. 2.4.2) with a radius (R) according to

$$R = L \tan 2\theta_{\rm B}. \tag{2.4.1}$$

Here $\theta_{\rm B}$ is the Bragg diffraction angle and L is the camera length.

The d-spacing can be obtained by measuring the length of R in an experimental diffraction pattern using

$$d = \frac{\lambda}{2 \sin \theta_{\rm B}}. \tag{2.4.2}$$

The electron wavelength is determined by the electron accelerating voltage (Φ), in volts:

$$\lambda = \frac{h}{(2m_e\Phi)^{1/2}} \simeq \frac{1.226}{[\Phi(1 + 0.97845 \times 10^{-6}\Phi)]^{1/2}}. \tag{2.4.3}$$

The wavelength of high-energy electrons is relatively short. For 200 kV electrons, the wavelength is 0.025 Å and the Bragg angle is very small. For example, for d = 2.5 Å the electron scattering angle θ is 5 mrad. For a small Bragg angle one can use the approximation $\sin\theta \simeq \tan\theta \simeq \theta$. This gives the relationship

$$d \simeq \frac{L\lambda}{Rd}. \tag{2.4.4}$$

At large scattering angles with $\sin\theta/\lambda$ 2 Å^{-1} or greater, a better approximation is given by (Cowley & Hewat, 2004)

$$d \simeq \frac{L\lambda}{R}\left(1 + \frac{3R^2}{8L^2}\right). \tag{2.4.5}$$

The camera length L can be determined using a sample with known d-spacings, while the electron wavelength or acceleration voltage can be calibrated using high-order Laue zone (HOLZ) lines in convergent-beam electron diffraction (CBED) patterns (Zuo, 1993).

For a small parallelepiped crystal fully illuminated by a coherent electron beam of intensity I_0, the kinematic diffraction intensity is given by

$$I_{\rm SC} = I_0 \frac{\left|F_{hkl}\right|^2}{L^2}\left\{\frac{\sin[\pi\mathbf{S}_{hkl}\cdot N_1\mathbf{a}]}{\sin[\pi\mathbf{S}_{hkl}\cdot\mathbf{a}]}\frac{\sin[\pi\mathbf{S}_{hkl}\cdot N_2\mathbf{b}]}{\sin[\pi\mathbf{S}_{hkl}\cdot\mathbf{b}]}\frac{\sin[\pi\mathbf{S}_{hkl}\cdot N_3\mathbf{c}]}{\sin[\pi\mathbf{S}_{hkl}\cdot\mathbf{c}]}\right\}^2, \tag{2.4.6}$$

where N_1, N_2 and N_3 are the number of unit cells along the three axis directions, and F_{hkl} is the electron structure factor of the hkl reflection:

$$F_{hkl} = \sum_{i=1}^{n} f_i^e T_i \exp[2\pi i(hx_i + ky_i + lz_i)]. \qquad (2.4.7)$$

Here T is the atomic displacement factor, which accounts for atomic thermal vibrations, and the electron atomic scattering factor f_i^e is defined by equation (4.3.1.13) in *International Tables for Crystallography*, Vol. C (2004). For a reflection with the scattering vector $\mathbf{g}_{hkl}$ the deviation from the Bragg condition of the *hkl* reflection is expressed by the excitation error $\mathbf{S}_{hkl}$:

$$\mathbf{k} - \mathbf{k}_0 = \mathbf{g}_{hkl} + \mathbf{S}_{hkl}. \qquad (2.4.8)$$

The diffraction intensity recorded in a powder diffraction pattern is the integrated intensity over the crystal orientation and the detector area. A change in crystal orientation leads to a change in the excitation error normal to the diffracted beam in the plane of Bragg reflection. The integration in these three directions is equivalent to integration over the reciprocal-space volume around the Bragg peak. The result gives the diffraction power of a sample with a large number of crystallites for the *hkl* reflection as (Warren, 1990)

$$P_{hkl} = I_0 \frac{\lambda^2 m_{hkl} V_{\text{sample}} d_{hkl}}{2V_c^2} \left|F_{hkl}\right|^2, \qquad (2.4.9)$$

where V_{sample} is the sample volume, m_{hkl} is the multiplicity of the reflection based on the symmetry-equivalent number of *hkl* reflections, and V_c is the volume of the unit cell. For randomly oriented powder samples, the diffraction power is uniformly distributed over the bottom edge of a cone of half apex angle $2\theta_{hkl}$ and height L, and the peak intensity is more appropriately described by the power per unit length of the diffraction circle (Vainshtein, 1964):

$$I_k = \frac{P_{hkl}}{2\pi L \sin 2\theta_{hkl}} = \frac{I_0}{4\pi L} \frac{\lambda d_{hkl}^2 m_{hkl} V_{\text{sample}}}{V_c^2 \cos\theta_{hkl}} \left|F_{hkl}\right|^2. \qquad (2.4.10)$$

Here $\cos\theta_{hkl} \simeq 1$ is a good approximation for electron diffraction and this formula is presented in equation (2.4.1.3) in *International Tables for Crystallography*, Vol. C (2004).

The kinematic approximation in electron diffraction is valid only for very small crystals. Defining the validity of the kinematic approximation for different crystals has been difficult and the subject of extensive debate (Blackman, 1939; Vainshtein, 1964; Turner & Cowley, 1969; Cowley, 1995). For single-crystal electron diffraction, numerous studies using CBED have demonstrated an almost perfect fit to experimental diffraction intensities using dynamic theory. Using this fitting approach, experimental structure-factor amplitudes and phases can be measured through a refinement process with high accuracy (Saunders *et al.*, 1995; Tsuda *et al.*, 2002; Zuo, 2004). However, this approach requires knowledge of the approximate crystal structure and can rarely be used for powder electron diffraction, where unknown crystal structures are often studied. In developing a theory for the integrated intensity for powder electron diffraction, the magnitude of the dynamic effect and its dependence on crystal orientations, defects, thickness variations and crystal shape must be considered. In X-ray and neutron diffraction, the combination of these factors led to the highly successful kinematical theory of ideal imperfect crystals with randomly distributed mosaic blocks. For electron diffraction, an all-encompassing theory of integrated intensity has been elusive because of the small electron coherence length, which is much less than the size of typical mosaic blocks detected by X-ray and neutron diffraction, and strong scattering. An approximation has been developed to take account of dynamical scattering using the two-beam theory (Blackman, 1939). Under this approximation, the integrated dynamic intensity I_d over a large range of excitation is given by the expression

$$I_d \propto \left|F_{hkl}\right| \int_0^{A_{hkl}} J_0(2x)\,\mathrm{d}x. \qquad (2.4.11)$$

Here

$$A_{hkl} = \frac{\lambda\gamma\left|F_{hkl}\right|t}{V_c \cos\theta_{hkl}} \simeq \frac{\lambda\gamma\left|F_{hkl}\right|t}{V_c}, \qquad (2.4.12)$$

where t is the thickness of the crystallite along the electron-beam direction, γ is the relativistic constant of electrons and $J_0(2x)$ is the zero-order Bessel function. For a very small value of A_{hkl} the Bessel function $J_0(2x)$ is nearly constant with a value of 1 and the diffraction intensity approaches that of the kinematical limit. From this, the following formula can be derived for the dynamical intensity:

$$I_d = \frac{I_0}{4\pi L} \frac{d_{hkl}^2 m_{hkl} V_{\text{sample}}}{V_c \gamma t} \left|F_{hkl}\right| \int_0^{A_{hkl}} J_0(2x)\,\mathrm{d}x. \qquad (2.4.13)$$

For very large A_{hkl}, the integral over the Bessel function approaches the value of 1/2 and in this case the diffraction intensity is proportional to the structure-factor amplitude instead of its square as predicted by kinematical theory.

The extent of dynamic effects that can be reduced by averaging over crystal orientations has been demonstrated by precession electron diffraction (PED). This technique was originally developed by Vincent & Midgley (1994) to improve the single-crystal electron diffraction intensities for structural analysis. In PED, the incident electron beam is tilted and precessed along a conical surface that is centred on the electron optical axis. Below the crystal, the diffraction pattern is tilted back with the position of the direct beam remaining approximately constant during precession. The diffraction pattern then generally appears similar to a conventional electron diffraction pattern. The measured diffraction intensity, however, is a double integration over the two-dimensional detector and the incident-beam angles defined by the precession cone surface. Experimental and theoretical studies of PED integrated intensities have shown an overall 'more kinematical' behaviour with less sensitivity to crystal thickness and exact orientation than for conventional electron diffraction patterns. Simulations also showed that the dynamical effects are still present in the PED integrated intensities, but the extent of the dynamic effect as measured by the correlation between the integrated intensity and the squared amplitude of the structure factor follows the empirical rules:

(i) The correlation increases with the precession angle.
(ii) The correlation is more pronounced for higher-order reflections than lower-order ones, for which the integration over the different excitation error is less complete.
(iii) The correlation also improves as the crystal thickness decreases.

In the electron powder diffraction of randomly oriented crystals, the angular integration is performed over the entire solid angle. Zone-axis patterns with enhanced dynamical interaction between the diffracted beams are also included in this solid angle. However, the overall probability for a crystal to be in exact zone-axis orientation is very small, even if the zone axis is defined

within a wedge of tens of milliradians. Thus, powder electron data generally tend to be more kinematical than single-crystal data.

2.4.3. Electron powder diffraction techniques

By J.-M. Zuo and J. Zhang

The basic setup for electron powder diffraction uses a transmission electron microscope equipped with an area electron detector (photographic film, CCD camera *etc.*). Thin films, such as amorphous carbon or holey carbon films supported on metal grids, are typically used to support powder samples, which are then mounted and inserted into the transmission electron microscope inside a TEM sample holder. Solid free-standing thin films can be placed directly on top of a metal grid.

The electron beam used for a powder electron diffraction experiment is shaped using electromagnetic lenses. A modern transmission electron microscope uses at least three sets of magnetic lenses for the illumination system: condensers I and II, and the objective prefield. The prefield is part of the objective lens system before the sample acting as a lens. Some transmission electron microscopes come with an additional condenser lens (condenser III, or condenser mini-lens), which can be used for nanodiffraction. These lenses are used in various combinations to set up electron illumination for selected-area electron diffraction (SAED) or nano-area electron diffraction (NAED) (Zuo, 2004). The major difference between these two is the area of illumination, which is controlled by the strength (or focal length) of the condensers II and III.

An issue to be considered during setup of the electron beam for powder diffraction is the electron lateral coherence length. In a transmission electron microscope, the electron coherence is defined by the coherence length seen at the condenser aperture. According to the Zernike–Van Cittert theorem, the degree of coherence between electron wavefunctions at two different points far away from a monochromatic electron source is given by the Fourier transform of the source intensity distribution (Cowley, 1999). If we assume that the source has a uniform intensity within a circular disc, the coherence function is then given by $\lambda J_1(\pi\beta r/\lambda)/\beta r$ with J_1 being the first-order Bessel function, r the radial distance at the aperture and β the angle sustained by the electron source. The lateral coherence length L, which is often referred to in the literature, is defined by r at the first zero of J_1, which has the value of $L = 1.2\lambda/\beta$. The source seen by the condenser aperture inside a transmission electron microscope is the source image formed after the condenser-I lens. For a Schottky emission source, the emission diameter is between 20 and 30 nm according to Botton (2007). For a condenser aperture placed 10 cm away from the electron source image, a factor of 10 source demagnification provides a coherence length from 100 to 150 µm. When a smaller condenser aperture is used, such as in NAED, the electron beam can be considered as approximately coherent and the lateral coherence length on the same is limited by the beam convergence angle α with $L_{\text{sample}} = 1.2\lambda/\alpha$.

2.4.3.1. *Selected-area electron diffraction (SAED)*

SAED is formed using the transmission electron microscope illumination, which is spread out over a large area of the specimen to minimize the beam convergence angle. The diffraction pattern is first formed at the back focal plane of the objective lens and then magnified by the intermediate and projector lenses

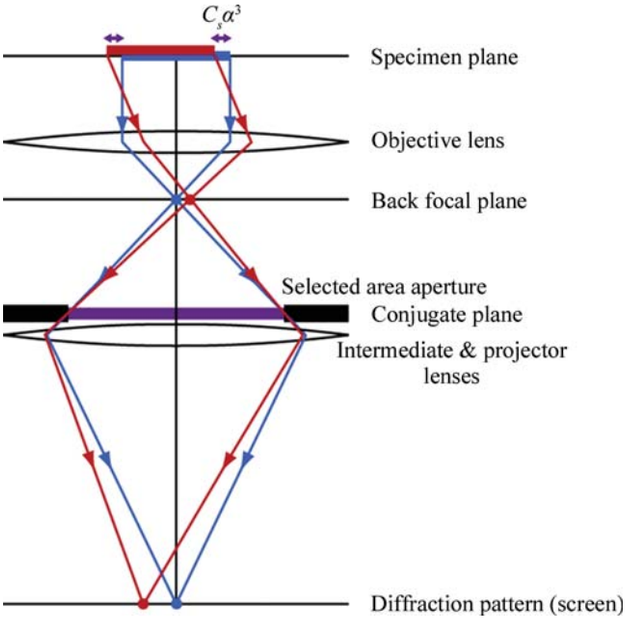

Figure 2.4.3
Schematic illustration of selected-area electron diffraction in conventional TEM. (Provided by Jun Yamasaki of Nagoya University, Japan.)

(only one is shown) onto the screen or electron detector (Fig. 2.4.3). The recorded diffraction pattern is from an area of interest selected by placing an aperture in the conjugate (imaging) plane of the objective lens. Only electron beams passing through this aperture contribute to the diffraction pattern. For a perfect lens without aberrations, electron beams recorded in the diffraction pattern come from an area that is defined by the image of the selected-area aperture at the specimen plane. The aperture image is demagnified by the objective lens. In a conventional electron microscope, rays at an angle to the optic axis are displaced away from the centre because of the spherical aberration of the objective lens (C_s) as shown in Fig. 2.4.3. The displacement is proportional to $C_s\alpha^3$, where α is twice the Bragg angle. The smallest area that can be selected in SAED is thus limited by the objective lens aberrations. This limitation is removed by using an electron microscope equipped with a transmission electron microscope aberration corrector placed after the objective lens (Haider *et al.*, 1998).

The major feature of SAED is that it provides a large illumination area, which is beneficial for recording diffraction patterns from polycrystalline samples as it leads to averaging over a large volume (for example, a large number of nanoparticles). SAED can also be used for low-dose electron diffraction, which is required for studying radiation-sensitive materials such as organic thin films.

2.4.3.2. *Nano-area electron diffraction (NAED)*

NAED uses a small (nanometre-sized) parallel illumination with the condenser/objective setup shown in Fig. 2.4.4 (Zuo *et al.*, 2004). The small beam is achieved by reducing the convergence angle of the condenser-II crossover and placing it at the focal plane of the objective prefield, which then forms a parallel-beam illumination on the sample for an ideal lens. A third condenser lens, or a mini-lens, is required for the formation of a nanometre-sized parallel beam. For a condenser aperture of 10 µm in diameter, the probe diameter is ~50 nm with an overall magnification factor of 1/200 in the JEOL 2010 electron microscopes (JEOL, USA). The smallest beam convergence angle in NAED is

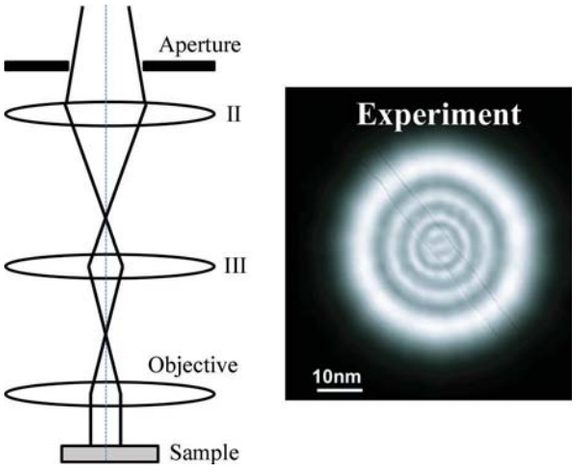

Figure 2.4.4
Schematic illustration of electron nanoprobe formation using a combination of condenser lenses (II and III) and the objective lens. The beam divergence angle is kept at a minimum by forming a crossover at the front focal plane of the objective lens. An image of an experimental electron nanoprobe is shown on the right with a carbon nanotube contained inside the probe.

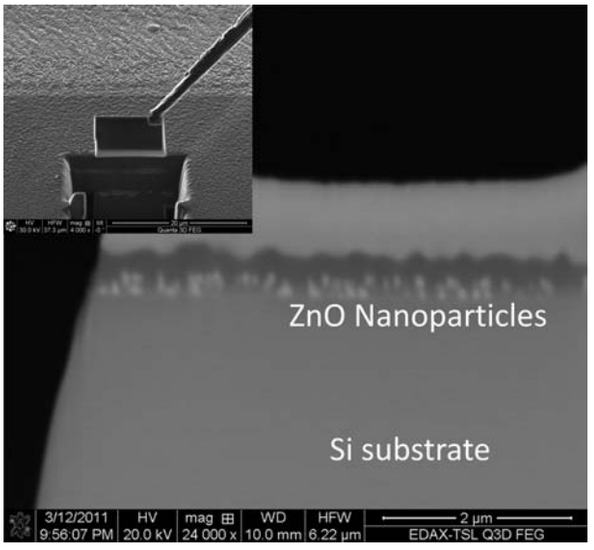

Figure 2.4.5
Sample preparation and lift-out using a focused ion beam (FIB). A thin section of the sample is cut out using the FIB and attached to a mechanical probe for lift-out (inset). The image shows the lift-out section containing ZnO nanoparticles in bright dot-like contrast supported on an Si substrate.

limited by the aberrations of the illumination lenses. A beam convergence angle as small as ∼0.05 mrad has been reported (Zuo *et al.*, 2004). A diffraction pattern recorded using NAED is similar to one recorded by SAED. The major difference is that the diffraction volume is defined directly by the electron probe in NAED. Since all electrons illuminating the sample are recorded in the diffraction pattern, NAED in an FEG microscope also provides higher beam intensity than SAED (the probe current intensity using a 10 µm condenser-II aperture in a JEOL 2010F is $\sim 10^5$ e s^{-1} nm^{-2}) (Zuo *et al.*, 2004).

The small probe size is most useful for studying a small section of thin films or for selection of nanoparticles for powder diffraction. The small beam size reduces the background in the electron diffraction pattern from the surrounding materials.

2.4.3.3. *Sample preparation*

The success of an electron powder diffraction experiment to a large extent depends on sample preparation. The powder sample has to be suitable for electron-beam observation, and the sample also needs to be compatible with the vacuum environment of the microscope. *In situ* experiments can be carried out using special holders for cooling, heating and cryogenic or environmental transfer. Special microscopes are also available to provide a gaseous or ultra high vacuum environment for the investigation of structures under a gas or at ultra low pressure, or *in situ* sample preparation.

The observed area of the sample must be electron transparent, *i.e.* have a thickness of less than or comparable to the inelastic mean free path of electrons. The inelastic mean free path increases with the electron voltage (Egerton, 2011). The typical sample thickness ranges from a few tens to hundreds of nanometres for 200 kV high-energy electrons (see Table F.1 in Zuo & Spence, 2017).

The sample-preparation techniques can be divided into three categories: (i) bulk-based for bulky materials and supported thin films, (ii) powder-based techniques and (iii) free-standing thin films over a supporting grid prepared by vacuum evaporation or sputtering.

The bulk-based techniques involve mechanical cutting, thinning/polishing and perforation. An ion beam is typically used in the last step of perforation to create a thin area around the edge of a hole for electron-beam observation. Chemical and electrolytic methods are also often used for preparing electron-transparent samples. While these methods have been applied to a broad range of materials, they are mostly used for metals or semiconductors to create smooth sample surfaces free from defects or sample heating caused by ion-beam irradiation. Mechanical thinning and polishing are sometimes done with a wedge angle with the help of a tripod. The thin region next to the edge only requires a brief ion-beam bombardment to make it electron transparent. A detailed description of traditional sample-preparation techniques for TEM can be found in Barna & Pécz (1997). The above techniques are applicable to both thin films and bulk nanocrystalline materials. The powder-based techniques use dispersion of powders on thin supporting films placed on metal grids specially made for TEM observations. This technique is most suitable for nanoparticles. For micron or larger-sized powders, additional grinding is used to produce smaller particles. The most commonly used supporting films are continuous amorphous carbon films, holey carbon films, networked carbon fibres (lacey carbon), amorphous silicon nitride and SiO_x. For amorphous carbon films, an ultra thin version is available which is especially useful for nanoparticle samples.

A recent development in TEM sample preparation is the use of a focused ion beam of Ga^+ ions for cross-sectioning a sample. The focused ion beam can drill a precise hole in the sample. The same ion beam can also be scanned over a sample surface to form an image by collecting the secondary electrons or ions generated by the beam. The ion column can be integrated into an electron column in a scanning electron microscope in the so-called dual-beam configuration. An image can be formed using either electrons or ions. Most often the electron beam is used for sample inspection, while the ion beam is used for patterning and milling. This allows precise control over the position and thickness of the cross section, which is very practical for characterization of

semiconductor devices or failure analysis in general (Fig. 2.4.5). Further details about ion-beam techniques can be found in Lábár & Egerton (1999) and Orloff *et al.* (2002). For a comprehensive review of sample-preparation techniques for TEM, see Őzdöl *et al.* (2012).

2.4.3.4. *Diffraction data collection, processing and calibration*

Experimental electron powder diffraction data are collected using two-dimensional area electron detectors. Experimental issues involved in the diffraction-pattern recording procedure are electron optical alignment, diffraction-pattern collection and calibration, with particular care taken in adjusting the specimen height position (eucentric position), selection of a suitable illumination-beam convergence angle and diffraction-camera length, and finally projector-lens focusing. The diffraction-camera length is determined by the setting of intermediate and projector lenses in combination with the objective lens. To calibrate the diffraction-camera length, a standard sample is placed in the eucentric position of the objective lens at the standard focus. At this setting, the specimen plane is conjugate to the selected-area aperture (Fig. 2.4.3) and the sample image appears in focus. To obtain a sharp diffraction pattern, the detector plane must be conjugate to the back focal plane of the objective lens. This can be achieved by setting up a parallel-beam illumination and adjusting the intermediate-lens focus length to bring the direct beam into a sharp focus.

Currently available area electron detectors are CCD and CMOS cameras, imaging plates (IPs) and photographic film. While photographic film has a long history of use in electron microscopy, its limited dynamic range makes it less useful for electron diffraction data collection. Both CCD cameras and IPs are digital recorders capable of collecting electron intensity over a large dynamic range. The crucial characteristics of digital recording systems are the gain (g), linearity, resolution, detector quantum efficiency (DQE) and the dynamic range. The gain of a CCD or CMOS camera can be normalized using a flat-field illumination; the gain in IPs is assumed to be constant. The detector resolution is characterized by the point-spread function (PSF), which is roughly the detector's response to a point-like illumination. These characteristics for CCDs and IPs have been compared by Zuo (2000). The intensity of an electron diffraction pattern recorded with a digital detector is given by

$$I^{\text{recorded}}(i,j) = g(i,j)H(i,j) \otimes I^{\text{original}}(i,j) + n(i,j), \qquad (2.4.14)$$

where $g(i, j)$ is the detector gain image, H is the PSF of the detector, n is the detector noise and I^{original} is the intensity of scattered electron beams originally received by the detector. The i and j are the pixel coordinates of the detector. The PSF is experimentally characterized and measured by the amplitude of its Fourier transform, or the so-called modulated transfer function (MTF). The effects of the PSF can be removed by deconvolution. The Richardson–Lucy method is specifically targeted for Poisson processes, which can be applied to CCD images (Zuo, 2000). The alternative to the removal of the PSF is to treat it as part of the peak broadening that can be used to fit the powder pattern.

The noise in the experimental data is characterized by the DQE:

$$\text{var}(I) = \frac{m\bar{g}I}{\text{DQE}(I)}. \qquad (2.4.15)$$

Here I is the experimentally measured intensity, var stands for the variance, m is the area under the MTF and $\bar{g}$ is the average gain of the detector. Once the DQE is known, this expression allows an estimation of the variance in measured intensity, which is essential for quantitative intensity analysis where the variance is often used as the weight for comparing experimental and fitted data.

The performances of CCDs and IPs for electron diffraction pattern recording are different at different electron dose rates. At low dose rates, the DQE of the CCD camera is limited by the readout noise and the dark current of the CCD. IPs have better performance in the low dose range due to the low dark current and low readout noise of the photomultipliers used in IP readers. At medium and high dose rates, the IP signal is affected mostly by the linear noise due to the granular variation in the phosphor and instability in the readout system, while for CCDs the noise is mostly linear noise in the gain image.

Electromagnetic lenses are not perfect and have aberrations affecting the collected data. In most transmission electron microscopes, electron diffraction patterns are produced using the post-specimen magnetic lenses. For electron diffraction, the most important aberration is the distortion of the projector lens, causing a shift of an image point. There is no blurring in diffraction patterns associated with the lens distortion. However, the distortion affects the overall shape of diffraction patterns. The distortion is most obvious at low camera lengths, where the pattern may seem stretched or twisted at high scattering angles. There are three types of distortion of the same order as the spherical aberration of the lens. They are called pin-cushion, barrel and spiral distortions (Reimer, 1984). A distortion can also arise from the use of an electron energy filter, where a lower order of distortion can be introduced with the use of non-spherical lenses (Rose & Krahl, 1995).

For quantitative analysis an electron powder diffraction pattern recorded on an area detector needs to be integrated into one-dimensional powder diffraction data (Fig. 2.4.6). The integration involves four separate steps: (i) identifying areas of the diffraction pattern for integration, (ii) centring the diffraction pattern, (iii) applying a diffraction pattern distortion correction, if there is any, and (iv) integrating intensities for a constant diffraction angle. Electron powder diffraction patterns can be recorded on a crystalline support film, which gives sharp diffraction spots distinct from the powder diffraction rings. The sharp diffraction patterns from the support film can be excluded from the powder diffraction intensity integration in step (i) by using a mask. The same approach can be used to eliminate any alien features from a diffraction pattern caused, for instance, by the aperture or the energy filter. The diffraction pattern centring is based on the analysis of the transmitted beam in the centre of the pattern. As the transmitted beam is usually very strong and is often overexposed, finding its centre may be a non-trivial task. In order to prevent detector damage in the area of the transmitted beam a beam stop is often used. In this case, the central area in the pattern may have an irregular shape not suitable for the centring procedure. Non-distorted diffraction patterns can be centred by finding the centre of the concentric diffraction rings either by locating the position of the maximum diffraction peak intensity along the ring and using these positions to determine the centre of the ring, or by searching for the centre that gives the maximum correlation between $I(g)$ and $I(-g)$. For distorted diffraction patterns, the centring and the distortion correction must be carried out simultaneously.

The distortion correction requires a powder sample with known d-spacings. The amount of distortion can be obtained by

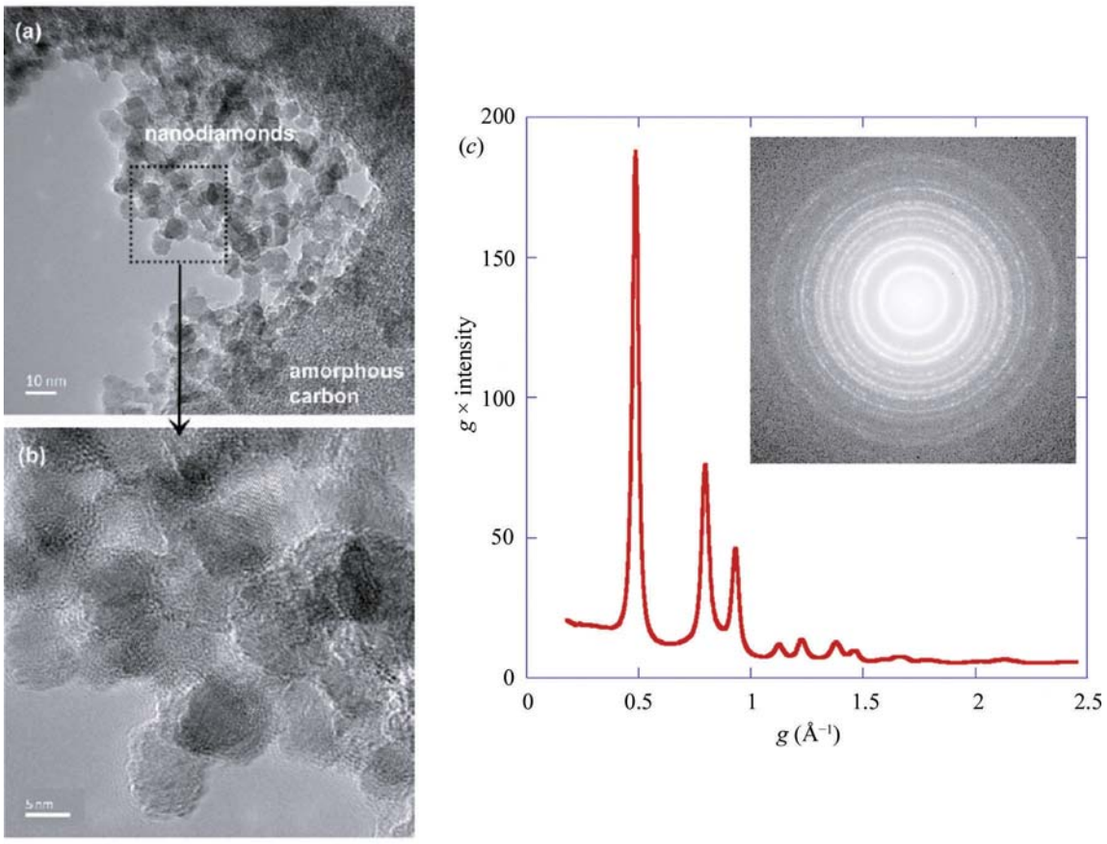

Figure 2.4.6
An example of electron powder diffraction recording for nanodiamonds. (*a*) A TEM image showing nanodiamond particles supported on amorphous carbon, (*b*) the magnified image from the boxed region of (*a*), and (*c*) the recorded electron powder diffraction pattern from nanodiamond particles and the obtained radial intensity profile.

fitting the diffraction ring position $R_d(\varphi)$ using a cosine expansion with

$$R_d(\varphi) = R + \sum_{n=1}^{N} \Delta R_n \cos n(\varphi - \varphi_n), \tag{2.4.16}$$

where R is the average radius (zero order) of the diffraction ring, ΔR represents the amplitude of distortion of order n and φ is the azimuthal angle. Once the distortion is calibrated and excluded from the data, the diffraction intensity integration can be simply carried out by summing the recorded diffraction intensity according to the radius using

$$I_n = \frac{1}{N} \sum I[i, j], \tag{2.4.17}$$

where the sum is taken over $R(i, j, i_0, j_0, \Delta R) \in \{n\delta, (n + 1)\delta\}$. Here the powder diffraction intensity is integrated in fine discrete steps along the radius of a diffraction pattern (corresponding to increasing scattering angle) with an interval of δ, the summation is done over all diffraction pixels that fall between the radius of $n\delta$ and $(n + 1)\delta$ and N is the number of these pixels.

Filtering the inelastic background is an option for electron microscopes equipped with an electron energy filter. A major contribution to the inelastic background in electron diffraction patterns comes from bulk plasmon excitation (Egerton, 2011). This can be filtered out by dispersing the electrons according to their energies using magnetic or electrostatic fields inside an electron energy filter and using a slit of a few eV in width around the elastic (zero-loss) electron beam. For use with an area electron detector for electron diffraction, the filter must also have a double focusing capability to function as an imaging lens. There are two types of electron imaging energy filters that are currently employed: one is the in-column Ω energy filter and the other is the post-column Gatan imaging filter (GIF). The in-column Ω filter is placed between the transmission electron microscope's intermediate and projector lenses and can be used in combination with IPs, as well as with a CCD or CMOS camera. The GIF is placed after the projector lens and the use of a GIF for electron diffraction typically requires the transmission electron microscope to be switched to a special low-camera-length setting. For electron diffraction, geometric distortions, isochromaticity and the angular acceptance are important characteristics of the imaging filter (Rose & Krahl, 1995). Geometrical distortions arise from the use of non-cylindrical lenses inside the energy filter. The distortion can be caused by optical misalignment, which is an issue with the GIF with its low camera-length setting. The amount of distortion can be measured using a standard calibration sample and corrected using numerical methods. Isochromaticity defines the range of electron energies for each detector position. Ideally, this should be the same across the whole detector area. The angular acceptance defines the maximum range of diffraction angles that can be recorded on the detector without a significant loss of isochromaticity (Rose & Krahl, 1995).

2.4.4. Phase identification and phase analysis

By J. L. Lábár

For known structures, powder diffraction patterns can be used for identification of the crystalline phases and quantification of their

volume fraction for samples containing multiple phases. These procedures are usually performed in two steps. First, the candidate phases must be selected to produce a shortlist of the structures that may be present in the sample. Preparation of the shortlist generally relies on *a priori* chemical information [obtained *e.g.* from energy-dispersive X-ray spectroscopy (EDS) or electron energy-loss spectrometry (EELS)] to reduce the number of candidate phases (crystalline structures) that are searched for (Lábár & Adamik, 2001; Lábár, 2006) in a comprehensive database such as the Powder Diffraction File (Faber & Fawcett, 2002). The identification of the crystalline phases in the experimental data is done through pattern fingerprinting. Final confirmation of phase identification is provided by the success of quantitative or semi-quantitative phase analysis, which determines the phase fractions and amount of texture.

In principle, the Le Bail structure-factor extraction (decomposition) method (see Chapter 3.5) could also be used for electron diffraction ring patterns from nanocrystals that are small enough to scatter kinematically or quasi-kinematically (Moeck & Fraundorf, 2007). The main advantage of this approach would be that no assumptions about the structure have to be made. However, none of the methods available for electron diffraction data follow this approach and identification of crystalline phases generally follows a different route [qualitative phase analysis (Lábár & Adamik, 2001) or traditional structural fingerprinting (Moeck & Rouvimov, 2010)].

After a two-dimensional ring pattern is integrated into a one-dimensional intensity distribution, the positions and intensities of peaks are extracted. The positions of the diffraction peaks are used as minimum information for fingerprinting. For successful phase identification the largest d values (at the smallest scattering angles) are crucial. Unfortunately, they are not always listed in the X-ray diffraction databases (Moeck & Fraundorf, 2007). Use of diffraction-peak intensities for fingerprinting has limited validity due to the deviation of electron diffraction intensities from the kinematic scattering formalism and the possible presence of texture in the sample. Phase analysis (fingerprinting) is complete when only one (set of) model structure(s) remains (out of several candidates listed in the previous step) on the basis of best fit between the model and the measured diffraction patterns. The addition of features to the Powder Diffraction File to make it more useful for phase identification using electron diffraction data is an active area of development.

Once a structural model is selected, the quantitative fit of diffraction intensities is performed. The quantitative modelling requires knowledge of the atomic positions within the unit cell. Atomic coordinates are not listed in the older PDF-2 database, but are given for many phases in the PDF-4+ database that combines five collections provided by different institutions. There are also open databases, like COD (http://www.crystallography.net/cod/), NIMS_MatNavi (http://crystdb.nims.go.jp/index_en.html) or AMCDS (http://rruff.geo.arizona.edu/AMS/periodictable.php). They also list atomic coordinates and can export structure data as CIF files.

For calculation of the electron structure factors, the electron atomic scattering factors are given in *International Tables for Crystallography*, Vol. C (2004). In the case of kinematical scattering, the intensity is proportional to the square of the electron structure factor F_{hkl}. If necessary, an absorption correction can be performed using the Weickenmeier & Kohl (1991) formalism.

Application of the quasi-kinematic formalism paves the way to giving an estimate of grain size in the beam direction (Lábár *et al.*, 2012). However, there is no straightforward correlation of this value with the actual crystal size or the thickness of the TEM sample. The grain size coming from the quasi-kinematic formula is also different from the size of the coherently scattering domains that could be determined from the broadening of the diffraction peaks (Ungár *et al.*, 2001), which is related to the lateral size of the crystallites (grains, particles) in the TEM sample.

In addition to peak positions and intensities, the peak shape and the background intensity have to be fitted. The pseudo-Voigt peak shape is most frequently used in electron diffraction phase analysis. The background intensity distribution in powder electron diffraction patterns is modelled empirically. The width of the diffraction peaks is an empirical parameter in the present implementation of phase analysis (Lábár, 2009). A Williamson–Hall type analysis of the variation of the experimentally observed peak width with the diffraction vector is also possible for simple profiles with well separated peaks (Gammer *et al.*, 2010); however, so far it has only been done for single-phase diffraction profiles with a known material without an attempt to combine it with phase analysis. Making the peak width dependent on grain size and defect structure (Ungár *et al.*, 2001) would in principle also be possible for phase analysis from powder electron diffraction data, but has not been implemented so far.

Selection of the appropriate structure model is done based on the value of the goodness-of-fit (GOF) criterion. For a one-dimensional electron diffraction profile recorded for n pixels, the GOF is given by

$$\mathrm{GOF} = \frac{1}{n-p}\sum_{k=n_0}^{n}\frac{1}{w_k}\left(I_k^{\mathrm{exp}} - I_k^{\mathrm{calc}}\right)^2, \tag{2.4.18}$$

where p is the number of parameters used in fitting, w_k is a relative weight of the intensity value at the kth pixel, and I_k^{exp} and I_k^{calc} are the experimentally measured and calculated intensity values for the kth pixel, respectively.

Structure models are described in parametric form (including experimental parameters, peak-shape parameters together with volume fractions of the phases and their fibre-textured components: p parameters altogether) and the p-dimensional parameter space is explored to calculate the GOF. The model with the smallest GOF is accepted. In phase analysis the best match is searched for by using the downhill simplex algorithm (Nelder & Mead, 1965). The semi-global simplex was found to be robust and allowed easy escape from local minima (Zuo & Spence, 1991) when used for fitting CBED patterns.

For polyphasic diffraction profiles, the volume fraction of phases is calculated at the end of the fitting procedure. It is assumed that the net diffraction intensity in each pixel is a linear combination of contributions of the individual phases (random and textured fractions are treated as independent model components). The over-determined set of equations is solved using least-squares minimization. The number of equations is reduced, while keeping the information content of all equations, by forming matrix **A** as

$$a_{i,j} = \sum_k \mathrm{Model}_k(i)\mathrm{Model}_k(j), \tag{2.4.19}$$

where summation is performed for all pixels k for the model functions of the ith and jth phases, and vector **b** as

$$b_i = \sum_k (\mathrm{Measured}_k - \mathrm{Background}_k)\mathrm{Model}_k(i). \tag{2.4.20}$$

The coefficients of the linear combination are obtained by solving for vector **x** the matrix equation **Ax** = **b** using matrix inversion.

The coefficients of this linear combination $[x(i)]$ put the intensities of the peaks in phase i on the absolute scale. $I_{max}(i)$, the intensity calculated on the absolute scale for the strongest (100%) diffraction peak of phase i, gives the intensity diffracted by one unit cell (structure factors are calculated for the atoms of one unit cell). Then $x(i)/I_{max}(i)$ is the number of unit cells of phase i in the analysed volume. Consequently, the volume extended by phase i in the analysed volume is $V(i)x(i)/I_{max}(i)$, where $V(i)$ is the volume of the unit cell of phase i. The volume fraction of phase f_i is then given by

$$f_i = \frac{V(i)x(i)}{I_{max}(i)} \Big/ \sum_i \frac{V(i)x(i)}{I_{max}(i)}. \qquad (2.4.21)$$

In addition to volume fractions of phases and their fibre-textured components, the same method can determine the variation (contraction, dilation, distortions) of the unit cell, provided experimental parameters specific to electron diffraction (*e.g.* the camera length and pattern distortion) are properly calibrated. The reliability of the camera-length calibration (systematic error) is usually around 2% (Williams & Carter, 2009); in the best cases accuracy of better than 0.3% has been reported (Lábár *et al.*, 2012). Consequently, only large variations in the lattice parameter can be determined reliably from powder electron diffraction data and the typical accuracy of powder X-ray diffraction cannot be attained.

There are two main advantages of phase analysis from powders by electron diffraction compared with X-ray diffraction. First, much smaller volumes can be studied. Diffraction information can be collected from thin layers of a few tens of nanometres thickness, enabling precise identification of the inspected volume. If needed, different lateral sections from different depths of a bulk sample can be studied by TEM, thus providing three-dimensional information about the sample. In a non-homogeneous sample, electron diffraction data can be collected from different areas, allowing detection of different phases or texture components at a spatial resolution and sensitivity superior to X-ray diffraction methods (Lábár *et al.*, 2012).

The accuracy of the phase-content identification in a mixture for the major components is around 10–15% (Lábár *et al.*, 2012). The detection limit depends on the scattering power of the component. A weakly scattering phase of Cr in a strongly scattering matrix of Ag could only be detected at the content of 2%, while the presence of 5% Ag in a relatively weakly scattering Ni matrix allowed full quantification of the two phases (Lábár *et al.*, 2012). Thus, generally 5% (by volume) is accepted as the detection limit for powder electron diffraction experiments.

2.4.5. Texture analysis

By J. L. Lábár

The orientation distribution in a polycrystalline (nanocrystalline) TEM sample (used for powder electron diffraction) can either be random or a large fraction of grains can favour a special direction, *i.e.* the sample is textured. The texture can originate from the non-spherical shape of the particles (as in sedimentation geology or drop-drying of a suspension of nanoparticles on a TEM grid) or from energetic and/or kinetic conditions during nucleation and growth of grains in the formation of polycrystalline thin films on a substrate or, alternatively, the texture can be a result of mechanical deformation (as in drawing wires or rolling sheets of metals). Although the distribution of the preferred orientations can be very different, a few general types are frequently observed.

In the simplest case only one preferred-orientation vector characterizes the sample and the orientations of the grains are distributed arbitrarily around that direction. This situation is called *fibre texture* (single-axis texture). The most typical representatives of this texture class are sedimentation platy particles on a flat surface where the preferred-orientation vector is normal to the flat face of the particles, or a drawn metal wire where the preferred-orientation vector is directed along the wire axis. Another texture type frequently observed in the sedimentation of rod-shaped particles is described by the preferred-orientation vector being confined within a plane, but being arbitrarily oriented within this plane. Rolling of metal sheets results in other, more complex, but well characterized texture types: 'copper-type', 'brass-type' and 'S-type' (Mecking, 1985).

There are different ways to handle texture with electron diffraction. One approach is to collect the orientation information from individual nanograins in an automated area scan and reconstruct pole figures and inverse pole figures on a medium-sized population of grains (Rauch *et al.*, 2008). In principle, this is a single-crystal method analysing the information from an assembly of crystals. The Russian crystallography group developed the theory of arcs in oblique texture and used such textured patterns in structure analysis (Vainshtein, 1964; Vainshtein & Zvyagin, 1992). The *TexPat* software (Oleynikov & Hovmoller, 2004) was designed and effectively applied to determining unit-cell parameters and refining structure from oblique textured electron diffraction patterns. Tang *et al.* (1996) developed a method to determine the axis of texture and distribution of directions around that axis. The March–Dollase model (Dollase, 1986) for the description of pole densities was adapted for electron diffraction and used for the simulation of ring patterns (Li, 2010); however, no attempt was made to determine the phase fractions or textured fractions automatically.

A simplified automatic treatment of texture was implemented in the *ProcessDiffraction* software (Lábár, 2008, 2009). Partial texture is approximated by a linear combination of an ideally sharp fibre texture and a random distribution of components. Both the textured and the random components are treated as separately determined volume fractions during quantitative phase analysis (see Section 2.4.4). The advantage of the method is that the determination of the textured fraction is combined with simultaneous handling of a quasi-kinematic scattering by the Blackman approximation, and these two effects, which both modify the relative intensities, are treated simultaneously on a unified platform.

The application of the most general method for determining texture from powder electron diffraction patterns is restricted to the thinnest samples where kinematic scattering holds (Gemmi, Voltolini *et al.*, 2011). The method consists of recording a set of powder electron diffraction patterns at defined tilt steps of the two-axis goniometer, covering a considerable part of the solid-angle range usually used for recording pole figures. Azimuthal sections are integrated separately in 10° steps. The resulting large three-dimensional data set is fed into a variant of the Rietveld method called *MAUD* (Lutterotti *et al.*, 1997), which has built-in scattering factors for electrons. The orientation density function (ODF) is determined from the measured data by discretization of the orientation space. For texture fitting the *EWIMV* algorithm is used (Lutterotti *et al.*, 2004), which can be applied with irregular pole figure coverage and includes smoothing methods based on a concept of the tube projection. Pole figures from the smoothed

ODF were obtained for both sediment aggregates and evaporated thin films (Gemmi, Voltolini *et al.*, 2011).

2.4.6. Rietveld refinement with electron diffraction data

By T. E. Gorelik and U. Kolb

The Rietveld refinement method was initially developed for neutron diffraction data (Rietveld, 1967, 1969). It has now become a standard technique which is extensively used with neutron, laboratory X-ray and synchrotron diffraction data. A detailed description of the method can be found in Chapter 4.7.

Compared with the popularity of Rietveld refinement in X-ray and neutron powder diffraction, its application to powder electron diffraction data is very limited. So far, Rietveld refinement with electron diffraction data has only been done for nanocrystalline Al, α-MnS (Gemmi, Fischer *et al.*, 2011), hydroxyapatite (Song *et al.*, 2012), intermetallic AuFe (Luo *et al.*, 2011), TiO_2 (Weirich *et al.*, 2000; Tonejc *et al.*, 2002; Djerdj & Tonejc, 2005, 2006) and $MnFe_2O_4$ (Kim *et al.*, 2009). An example of a fit with powder electron diffraction data obtained by Rietveld refinement for hydroxyapatite is shown in Fig. 2.4.7.

Two major factors limit the application of Rietveld refinement to electron powder diffraction. First, electron powder diffraction data are collected from a sample volume far smaller than that used in an X-ray experiment. Therefore, the average statistics are poor compared with those of X-ray data. Nevertheless, electron powder diffraction data from a small sample area or thin films can give specific information which is difficult to obtain using other methods. Second, the presence of dynamical effects in the electron diffraction data hinders quantitative assessment of reflection intensities. Dynamical effects are strongest in zone-axis electron diffraction geometry, when many beams belonging to the same systematic rows are excited simultaneously. In powder electron diffraction crystals are randomly oriented towards the electron beam, thus making the fraction of zonal patterns low, thereby reducing the dynamical scattering in the data (see Section 2.4.2 for a more detailed discussion).

Within the limit of kinematical diffraction, the principle of Rietveld refinement is the same for electrons and X-rays, except the electron atomic scattering factors are different. The refinement procedure can thus be performed using existing programs if it is possible to input the scattering factors for electrons. Most of the reported Rietveld refinements on electron powder diffraction data have been performed using *FullProf* (Rodríguez-Carvajal, 1993); a refinement in *MAUD* (Lutterotti *et al.*, 1999) has also been reported (Gemmi, Voltolini *et al.*, 2011).

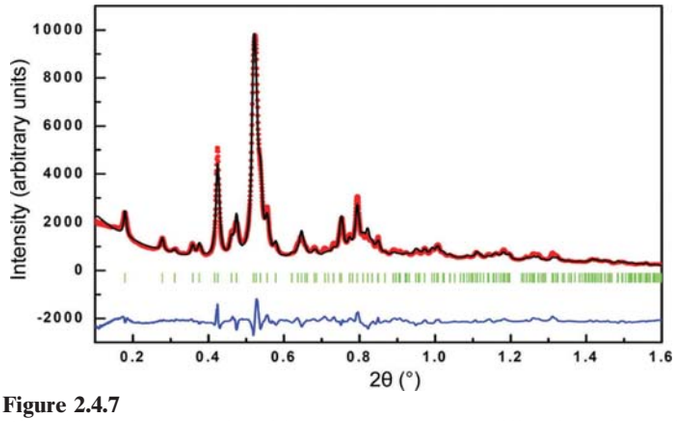

Figure 2.4.7
Rietveld analysis result with powder electron diffraction data of hydroxyapatite. Reproduced from Song *et al.* (2012) with permission from Oxford University Press.

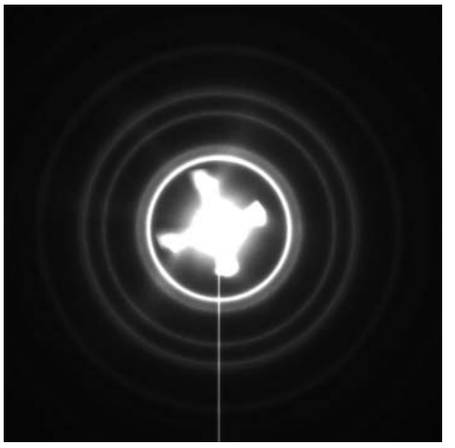

Figure 2.4.8
Powder electron diffraction pattern of nanocrystalline gold demonstrating non-symmetrical background features.

Electron powder diffraction patterns are recorded on an area detector. For a Rietveld refinement the two-dimensional diffraction patterns have to be integrated into one-dimensional profiles. The zero shift is treated as for the X-ray data integrated from a two-dimensional position-sensitive detector. Details about electron diffraction data processing and calibration are given in Section 2.4.3.4.

The background in electron powder patterns is a complex combination of inelastic scattering, scattering from the supporting film (when it is present) and other factors. For the Rietveld refinement procedure the background of a one-dimensional integrated profile is fitted by a polynomial function. If a supporting thin amorphous carbon film is used, the background can include broad rings, which after the one-dimensional integration can produce pronounced broad peaks. These peaks are difficult to subtract using a model based on a polynomial function; therefore, these intensities may hamper the powder diffraction profile matching (Kim *et al.*, 2009). In some cases, the background can even include radially non-symmetric features originating from the shape of the tip within the electron source (see Fig. 2.4.8); it can have blooming due to oversaturated CCD pixels, or streak shadows due to the fast transmission electron microscope beam-shutter movement. In these cases, a diffraction pattern from the adjacent 'empty' area of the sample can be acquired and subtracted from the diffraction pattern of the material prior to the integration into one dimension. This procedure allows elimination of some of the artifacts discussed above, which otherwise after the one-dimensional integration may be falsely interpreted as diffraction peaks, and are generally more difficult to fit.

Unit-cell parameters are mostly subject to the error due to the accuracy of the electron diffraction camera-length calibration. Although examples have been published showing 0.3% accuracy of the camera-length calibration, in most cases accuracy of about 2% can be achieved (Williams & Carter, 2009). The effective camera length depends on many instrumental parameters such as the convergence of the electron beam, the diffraction lens focus, the mechanical position of the sample within the objective lens, or the hysteresis of the electromagnetic lenses. Thus, while the ratio of the lattice parameters within one aligned diffraction pattern can be very precise, the absolute values might not be.

Atomic displacement parameters can be refined from electron powder diffraction data; however, the interpretation of the results can be manifold. For nanocrystalline materials, which have a relatively high surface-to-volume ratio, the surface effect can be enhanced compared with that of the bulk. Thus, the average atomic displacement factors can increase because of the high fraction of near-surface relaxed atoms. Consequently, the isotropic displacement parameter B resulting from the Rietveld refinement can be relatively high. Local heating (Reimer, 1984) during the electron illumination may also contribute to higher average displacement parameters. Finally, if the electron beam exceeds a material-dependent threshold acceleration voltage, it can cause knock-on damage (Williams & Carter, 2009) in both organic and inorganic materials. This is a dynamical process which can cause both material loss and rearrangement of atoms. The presence of defects resulting from the rearrangement of atoms may lead to an increase in the average displacement factors. Nevertheless, the refinement using polycrystalline anatase data showed the expected displacement parameters of 1.4 (1) Å^2 for Ti and 1.9 (2) Å^2 for oxygen (Weirich *et al.*, 2000). Of all the parameters used during Rietveld refinement, the displacement parameters and atomic coordinates are probably the most sensitive to a possible dynamical-scattering contribution in the data. It is noticeable that after the refinement of the anatase structure the atomic coordinates converged to reasonable positions: [0, $\frac{1}{4}$, 0.1656 (5)] for oxygen (Weirich *et al.*, 2000) compared with the previous range obtained in neutron diffraction studies of [0, $\frac{1}{4}$, 0.16686 (5)] (Burdett *et al.*, 1987) to [0, $\frac{1}{4}$, 0.20806 (5)] (Howard *et al.*, 1991).

The relative ratio of two components in a mixture can be determined using the Hill–Howard approach (Hill & Howard, 1987): the relative weight of a phase in a mixture of phases is proportional to the scaling factor of the phase given by the Rietveld refinement combined with the mass and the volume of the unit cell of the component. The relative content of a mixture of anatase and brookite was successfully determined from electron powder diffraction data (Djerdj & Tonejc, 2005, 2006).

For the modelling of the Bragg reflection shape the Pearson VII function can be used (Weirich *et al.*, 2000; Kim *et al.*, 2009), although recently the more popular pseudo-Voigt peak shape function has been used (Tonejc *et al.*, 2002; Djerdj & Tonejc, 2005, 2006) and provides a satisfactory fit between the experimental and calculated data.

The average crystalline domain size can be determined using line-broadening analysis. The measured intensity profile is a convolution of the physical line profile given by the sample with the instrumental profile broadening. When expressed in terms of the scattering angle θ, the width of the electron diffraction peaks is much smaller than that for X-rays. On the other hand, electrons generally have a smaller coherence length than X-rays. As a result, for the same material, the effective peak width for electron diffraction is larger than that for powder X-ray data (Song *et al.*, 2012). Because of this, it is sometimes difficult to separate the domain size and the instrumental contributions to the peak broadening. Therefore, the average domain size obtained after the refinement procedure should be cross-checked with the domain size determined from TEM images obtained, for instance, using the dark-field technique (Williams & Carter, 2009).

In electron diffraction various instrumental parameters can affect the peak width. The energy spread of the electrons causes additional broadening of diffracted spots. This effect can be partially reduced by energy filtering of the diffraction patterns (Kim *et al.*, 2009; Egerton, 2011). Finally, the electron diffraction camera length must be large enough that the detector broadening is much smaller than the peak width, as demonstrated in Fig. 2.4.9: large values of the camera length ('zoomed in' diffraction patterns) result in thinner, better separated peaks.

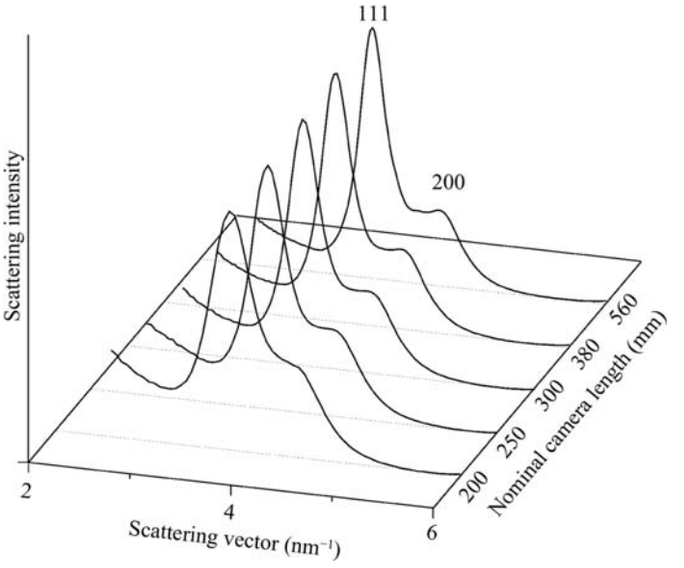

Figure 2.4.9
Electron powder diffraction profiles of gold nanoparticles (range 2–6 nm^{-1}) recorded at different electron diffraction camera lengths.

Preferred orientation can be an issue for electron powder diffraction: when the powder material is supported on a thin film, the crystals tend to orient themselves with their most developed facet facing the support. As a result, the relative intensities of the diffracted peaks are modified (Kim *et al.*, 2009). Texture within nanocrystalline powders introduced by the sample preparation on a support for TEM can be analysed using electron powder diffraction patterns recorded at different tilt positions of the sample. Refinement of the preferred orientation of two different materials – nanocrystalline aluminium and α-MnS powders – showed that the aluminium particles tend to have strong preferred orientation due to their facet morphology, while α-MnS particles are randomly oriented (Gemmi, Fischer *et al.*, 2011).

Although dynamical effects are believed to be reduced for nanocrystalline materials and additionally reduced by data collection from non-oriented crystals, the dynamical component of the scattering cannot be neglected. For the dynamical correction using the two-beam approximation formalism of equation (2.4.12), the reader is referred to Section 2.4.2. For a range of electron-beam energies from 20 to 50 kV it has been shown that polycrystalline electron diffraction patterns of aluminium crystals smaller than 9 nm have a dynamical scattering component below 10% (Horstmann & Meyer, 1962). For polycrystalline $MnFe_2O_4$ with an average crystal size of 11 nm measured using a 120 kV electron beam, the ratio of the kinematical to dynamical contributions in the structure factor was about 1:1.5 (Kim *et al.*, 2009). The application of the small (less than 3%) correction for the dynamical component during Rietveld refinement of nanocrystalline intermetallic Au_3Fe_{1-x} improved the refined long-range order parameter of the alloy (Luo *et al.*, 2011).

In summary, the Rietveld refinement technique applied to electron powder diffraction data is a new area of research. It can be successfully carried out for small volumes of nanocrystalline materials, for which the small electron beam is an advantage. Results obtained from Rietveld analysis of electron powder

diffraction data of nanocrystalline materials are encouraging. The refinement for powders containing large crystal grains is problematic because of dynamical scattering present in the data. There are also uncertainties caused by instrumental effects. The dynamical effects can be accounted for using the Blackman formalism, while the influence of diverse instrumental parameters needs further systematic study.

2.4.7. The pair distribution function from electron diffraction data

By T. E. Gorelik and U. Kolb

An extensive description of pair distribution function (PDF) analysis covering data acquisition, reduction and interpretation can be found in Chapter 5.7. Here, only a short outline is presented, concentrating on aspects that are specific to PDFs obtained by electron diffraction.

Poorly crystalline and amorphous materials exhibit no long-range order and therefore show no pronounced Bragg peaks in diffraction patterns. Nevertheless, owing to defined bonding geometry, these materials do have a specific local arrangement of atoms, denoted as short-range order. The short-range order can be analysed using the PDF obtained from the total scattering profile. The PDF can provide general information about the degree of order, the character of local atomic packing and the size of the correlation domains. The total scattering function is collected over a wide range of reciprocal space and includes not only the Bragg reflections (if present), but also the diffuse scattering information between them (Egami & Billinge, 2003).

The PDF $G(r)$ represents the probability of finding a pair of atoms with an interatomic distance r, weighted by the scattering power of the individual atoms. After normalization and suitable corrections, the reduced scattering function $F(Q)$ is derived. [In the PDF analysis, the scattering vector Q, which is related to the scattering angle θ as $Q = (4\pi \sin\theta)/\lambda$ is used, instead of $S = \sin\theta/\lambda$.] The PDF can be calculated by the Fourier transformation of $F(Q)$ into direct space (Warren, 1990; Egami & Billinge, 2003; Farrow & Billinge, 2009).

Powder diffraction data for PDF analysis should be measured over a sufficiently large range of the scattering angle θ; therefore, neutron or synchrotron sources or laboratory X-ray data with a short-wavelength source (Mo or Ag anode) are used. Powder electron diffraction data, with their flexibility in electron diffraction camera length, short wavelength and nuclear scattering at large scattering angles, can also cover the desired large range of scattering angles and are therefore highly suitable for PDF analysis. In addition, atoms have a much larger scattering cross section for electrons than for X-rays or neutrons, allowing sufficient signal collection from very small volumes. Finally, electrons can be focused with lenses down to a few nanometres. All these reasons make electron diffraction analysis attractive for the study of the structure of nanovolumes. The electron PDF is therefore a powerful tool for the investigation of the structures of amorphous or poorly crystalline thin films, or for small sample volumes of inhomogeneous samples.

There are several practical issues to consider when collecting electron diffraction data for PDF analysis:

Energy filtering. Traditionally, electron diffraction data for PDF analysis are collected using energy filtering in order to exclude the inelastic scattering contribution. However, quantitative or semi-quantitative electron PDFs can be obtained without filtering (Abeykoon *et al.*, 2012).

Multiple scattering/dynamical effects. In order to keep the contribution of non-kinematic scattering low, the sample thickness and the nanoparticle size should be as small as possible. Generally, particles 10 nm and smaller should scatter kinematically, and this is the size range that benefits most from PDF analysis (Abeykoon *et al.*, 2012).

Powder average. Proper statistics are important for PDF analysis. In order to decrease measurement errors one can increase the illumination area on the sample (or the selected-area aperture in the case of SAED), collect several diffraction patterns from different areas and average them.

Scattering angle range. A large θ range is essential for PDF analysis. An electron diffraction experiment offers significant flexibility in selecting the scattering range through the adjustment of the electron diffraction camera length and illumination wavelengths. Additionally, in order to enhance the data quality, merging of different scattering ranges recorded in a set of diffraction patterns is possible (Petersen *et al.*, 2005).

An electron diffraction pattern is a combination of signals produced by *elastically* and *inelastically* scattered electrons. The inelastic component is a result of electron energy loss due to plasmon or inner-shell excitation, electron Compton or thermal diffuse scattering (Egerton, 2011). For crystalline materials with distinct Bragg peaks the inelastic scattering is not particularly critical, as it mainly contributes to the background in diffraction patterns and can be neglected when only the intensities of the Bragg peaks are analysed. For PDF analysis the total scattering profile is used; thus, the inelastic scattering, which can significantly modify the scattering profile, needs to be considered (Ishimaru, 2006). Two strategies are followed in this respect: (i) energy filtering of diffraction patterns, which is the more accurate approach but demands specific instrumentation, and (ii) subtraction of the background scattering taken from an area adjacent to the sample (*i.e.* from the supporting film), which assumes that the main inelastic scattering component originates from the support, and the contribution from the sample can be neglected (Cockayne, 2007). The validity of this approximation depends on the level of quantification intended in the particular study.

The PDF formalism presented above is based on the single-scattering approximation. Multiple scattering, which is much stronger in electron diffraction than for X-rays and neutrons, significantly affects the total scattering profile and therefore the PDF. The multiple-scattering effects can modify the peak positions in the PDF as well as the relative intensities of the peaks, the latter being more sensitive to multiple scattering (Anstis *et al.*, 1988). It has been shown that for amorphous materials, owing to the contribution of the multiple scattering, the total scattering profile depends on the thickness of the foil (Childs & Misell, 1972; Rez, 1983). Knowledge of the film thickness allows extraction of the single-scattering distribution. An improved agreement with the expected PDF was shown for hydrogenated amorphous silicon (Anstis *et al.*, 1988) and amorphous germanium (Ankele *et al.*, 2005) using the single-scattering profile.

Experimentally, it is difficult to determine the sample thickness along the incident-electron-beam direction. In this case, the thickness parameter employed in calculations can be varied, adjusting the amplitudes of the PDF. An estimate for the sample thickness is found when the optimal fit is obtained. Different input values of the thickness result in different principal gradients of the oscillations. Once a reasonable fit is found, the correct thickness is determined and the contribution of multiple scattering can be eliminated (Ankele *et al.*, 2005). This method was

applied to amorphous NiNb alloy, allowing an estimate of the foil thickness, and thereafter improved the fit to the PDF obtained from Ag-anode X-ray scattering experiments (Ankele *et al.*, 2005).

Alternatively, the wavelength dependence of the multiple-scattering term can be used. A set of diffraction patterns of a glassy carbon film was collected from the same sample (apparently having the same thickness) using different wavelengths (Petersen *et al.*, 2005). These patterns were then processed in order to retrieve the single-scattering profile of tetrahedral amorphous carbon, which showed an improved fit to the reduced scattering function obtained with neutrons (Petersen *et al.*, 2005). This method can be applied to materials for which significant multiple scattering is expected and the thickness of the foil cannot be determined *a priori*. For very thin films the contribution of the multiple scattering is very low and, therefore, often neglected.

The PDF of elemental materials arising from only one contributing atomic scattering function can be directly interpreted in terms of coordination numbers and allows conclusions to be drawn about the local structure. PDF analysis of amorphous silicon prepared by deposition showed the existence of voids in the structure (Moss & Graczyk, 1969) which anneal on progressive heating. PDF investigation of amorphous carbon films prepared by arc plasma deposition showed that the material mainly consists of tetrahedrally coordinated carbon rather than having a graphitic structure (McKenzie *et al.*, 1991).

For ZrNi and ZrCu metallic glasses, partial PDFs were obtained by reverse Monte Carlo simulation (McGreevy & Pusztai, 1988) and fitted to the experimentally obtained electron scattering data. The analysis of the polyhedral statistics showed that the average coordination number of Cu was 11, while for Ni it was less than 10 (Hirata *et al.*, 2007). Study of amorphous FeB alloys (Hirata *et al.*, 2006) and $Fe_{90}Zr_7B_3$ (Hirotsu *et al.*, 2003) by PDF analysis allowed detection of nanoscale phase separation resulting in the formation of a mixture of different clusters.

Nanocrystals can be efficiently analysed by electron PDF analysis, giving information complementary to TEM imaging. The electron PDF of detonation nanodiamonds (DND) was used to estimate the average domain size (Zhang, 2011). Studies of phase separation in AgCu alloys showed the complex behaviour of the material with variation of temperature (Chen & Zuo, 2007). In the first stage, the nanodomains of the two terminal phases (Ag- and Cu-rich) are built; in the second stage, dewetting of the thin film and formation of large Ag and Cu grains occur. A comparison of electron PDFs from nanocrystalline, partially ordered and amorphous parts of silica glasses (Kovács Kis *et al.*, 2006) allowed the estimation of the degree of order developed by changing the connectivity and orientation of the undistorted SiO_4 tetrahedra. Indirect detection of hydrogen atoms was performed from a modified distribution of atomic distances in soot samples using electron PDF analysis (Kis *et al.*, 2006).

With an increase in the particle size the deviations from the kinematical scattering become severe. Nevertheless, the electron PDF calculated for 100 nm Au crystals reproduced the simulated data quite well: the peak positions and relative amplitudes were not significantly modified (Abeykoon *et al.*, 2012).

2.4.8. Summary

Powder electron diffraction can be used for materials structural characterization, just as is routinely done using X-rays and neutrons. The specific characteristics of electron scattering result in both benefits and drawbacks to using electron diffraction data. Strong scattering of electrons allows collection of a sufficient signal from nanovolumes of material, thus offering the possibility of studying small amounts of material and thin films. The opportunity to couple the diffraction information with imaging gives the unique possibility of performing a structural study on the nanoscale in a controlled way. The strong interaction of electrons with matter leads to dynamical-scattering effects that result in deviation of the electron diffraction intensities from the kinematical model. Since the amount of the dynamical-scattering component in a powder sample is difficult to quantify, the quantitative use of electron diffraction intensity data is limited. For large crystals, the dynamical treatment of electron diffraction data is efficiently done in CBED analysis, providing exclusive information about the structure. For nanocrystalline or amorphous materials, an increasing number of sets of experimental data show that quantitative structure information can be obtained using electron powder diffraction. This encourages further applications of different kinds of electron diffraction data, giving new perspectives for the quantitative use of electron diffraction in general.

APPENDIX A2.4.1
Computer programs for electron powder diffraction

CHECKCELL is a graphical powder-pattern indexing helper and space-group-assignment program that links into the *CRYSFIRE* powder indexing suite. More information and the program are available at http://www.ccp14.ac.uk/tutorial/lmgp/achekcelld.htm.

CRYSFIRE is a powder-pattern indexing system for DOS/Windows for unit-cell parameter determination from powder data (free for academic use). More information and the program are available at http://www.ccp14.ac.uk/tutorial/crys/.

ELD is a commercial program for calibrating and integrating two-dimensional electron diffraction patterns. The program is commercially available from Calidris, Sweden. More information is available from http://www.calidris-em.com/eld.php.

Electron diffraction pattern atlas. The website of Professor Jean-Paul Morniroli (http://electron-diffraction.fr/) provides an atlas of electron diffraction patterns that can be used to identify the space group of a crystal from observation of a few typical PED and CBED zone-axis patterns.

FIT2D is a general-purpose image and diffraction processing program, designed for use with synchrotron data, that integrates pre-selected sections of either one-dimensional or two-dimensional data. Corrections for geometrical distortion and for nonlinearity of intensity are included. It is available both for the Windows operating system (and DOS window) and for Macintosh OSX. The program is freely available for academic users. More information and the program are available at http://www.esrf.eu/computing/scientific/FIT2D/.

JEMS is a popular suite of simulation routines for a variety of platforms, mainly used for simulating high-resolution TEM (HRTEM), CBED, PED and SAED patterns. Simulation of powder diffraction rings is also included. The student version is free of charge. A licence is available from the author: http://www.jems-saas.ch/.

PCED is a program for the simulation of polycrystalline electron diffraction patterns (Li, 2010). A licence file is needed to unlock the program for loading input data files. More information is available at http://www.unl.edu/ncmn-cfem/xzli/.

PDFgui and *PDFfit2* are programs for full-profile fitting of the atomic PDF derived from X-ray or neutron diffraction data. *PDFgui* is a graphical front end for the *PDFfit2* refinement program, with built-in graphical and structure-visualization capabilities. *PDFgui* is currently in beta release and it is distributed as part of the DiffPy library. More information and the program are available at http://www.diffpy.org.

Process Diffraction is designed for processing of SAED and NAED patterns. It includes quantitative determination of phase fractions and texture from ring patterns recorded from nanocrystalline thin films in TEM. More information and the program are available at http://www.energia.mta.hu/~labar/ProcDif.htm.

QPCED and *PCED* are Java-based software for digitization, processing, quantification and simulation of powder electron diffraction patterns. For information contact Dr X. Z. Li (xzli@unl.edu) or visit http://www.unl.edu/ncmn-cfem/xzli.

TexPat is a program for quantification of texture (preferred orientation) from a tilt series of ring patterns recorded from nanocrystalline thin films in TEM (Oleynikov & Hovmoller, 2004).

WebEMAPS is a suite of computer programs that can be obtained at http://cbed.matse.illinois.edu/software_emaps.html. The programs include functions for visualization of crystal structures, simulation of single-crystal diffraction patterns, dynamic electron diffraction simulation, and calculations of electron structure factors and lattice *d*-spacings.

WinPLOTR is a peak-search program for plotting powder diffraction patterns and can be used as a graphical user interface for several programs used frequently in powder diffraction data analysis (*e.g. FullProf*, *DicVOL*, *SuperCELL*). *WinPLOTR* has been developed to run on PCs with a 32-bit Microsoft Windows operating system. More information and the program are available at http://www.cdifx.univ-rennes1.fr/winplotr/readme.htm.

References

Abeykoon, M. C. D., Malliakas, C. D., Juhás, P., Bozin, E. S., Kanatzidis, M. G. & Billinge, S. J. L. (2012). *Quantitative nanostructure characterization using atomic pair distribution functions obtained from laboratory electron microscopes. Z. Kristallogr.* **227**, 248–256.

Ankele, J., Mayer, J., Lamparter, P. & Steeb, S. (2005). *Quantitative electron diffraction data of amorphous materials. Z. Naturforsch. A*, **60**, 459–468.

Anstis, G. R. Z., Liu, Z. & Lake, M. (1988). *Investigation of amorphous materials by electron diffraction – the effects of multiple scattering. Ultramicroscopy*, **26**, 65–69.

Baerlocher, C., Gramm, F., Massüger, L., McCusker, L. B., He, Z., Hovmöller, S. & Zou, X. (2007). *Structure of the polycrystalline zeolite catalyst IM-5 solved by enhanced charge flipping. Science*, **315**, 1113–1116.

Barna, Á. & Pécz, B. (1997). *Preparation techniques for transmission electron microscopy.* In *Handbook of Microscopy*, edited by S. Amelinckx, D. van Dyck, J. van Landuyt & G. van Tendeloo, Vol. 3, pp. 751–801. Weinheim: Wiley-VCH Verlag GmbH.

Blackman, M. (1939). *On the intensities of electron diffraction rings. Proc. R. Soc. London Ser. A*, **173**, 68–82.

Botton, G. (2007). *Analytical electron microscopy*. In *Science of Microscopy*, edited by P. Hawkes & J. C. H. Spence, pp. 273–405. New York: Springer.

Burdett, J. K. T., Hughbanks, T., Miller, G. J., Richardson, J. W. & Smith, J. V. (1987). *Structural–electronic relationships in inorganic solids: powder neutron diffraction studies of the rutile and anatase polymorphs of titanium dioxide at 15 and 295 K. J. Am. Chem. Soc.* **109**, 3639–3646.

Chen, H. & Zuo, J. M. (2007). *Structure and phase separation of Ag–Cu alloy thin films. Acta Mater.* **55**, 1617–1628.

Childs, P. A. & Misell, D. L. (1972). *Some aspects of elastic plural scattering of electrons by atoms. J. Phys. D Appl. Phys.* **5**, 2095.

Cockayne, D. J. H. (2007). *The study of nanovolumes of amorphous materials using electron scattering. Annu. Rev. Mater. Res.* **37**, 159–187.

Cockayne, D. J. H. & McKenzie, D. R. (1988). *Electron diffraction analysis of polycrystalline and amorphous thin films. Acta Cryst.* A**44**, 870–878.

Cowley, J. M. (1992). *Electron Diffraction Techniques*. International Union of Crystallography Monographs on Crystallography. Oxford: IUCr/Oxford University Press.

Cowley, J. M. (1995). *Diffraction Physics*. Amsterdam: Elsevier Science BV.

Cowley, J. M. (1999). *Electron nanodiffraction. Microsc. Res. Tech.* **46**, 75–97.

Cowley, J. M. & Hewat, A. W. (2004). *Powder and related techniques: electron and neutron techniques*. *International Tables for Crystallography* Vol. C, pp. 80–83. Dordrecht: Kluwer Academic Publishers.

Djerdj, I. & Tonejc, A. M. (2005). *Transmission electron microscopy studies of nanostructured TiO_2 films on various substrates. Vacuum*, **80**, 371–378.

Djerdj, I. & Tonejc, A. M. (2006). *Structural investigations of nanocrystalline TiO_2 samples. J. Alloys Compd.* **413**, 159–174.

Dollase, W. A. (1986). *Correction of intensities for preferred orientation in powder diffractometry: application of the March model. J. Appl. Cryst.* **19**, 267–272.

Egami, T. & Billinge, S. J. L. (2003). *Underneath the Bragg Peaks: Structural Analysis of Complex Materials*. Oxford: Pergamon.

Egerton, R. F. (2011). *Electron Energy-Loss Spectroscopy in the Electron Microscope*. New York: Plenum Press.

Elsayedali, H. E. & Herman, J. W. (1990). *Ultrahigh vacuum picosecond laser-driven electron diffraction system. Rev. Sci. Instrum.* **61**, 1636–1647.

Faber, J. & Fawcett, T. (2002). *The Powder Diffraction File: present and future. Acta Cryst.* B**58**, 325–332.

Farrow, C. L. & Billinge, S. J. L. (2009). *Relationship between the atomic pair distribution function and small-angle scattering: implications for modeling of nanoparticles. Acta Cryst.* A**65**, 232–239.

Gammer, C. C., Mangler, C., Rentenberger, C. & Karnthaler, H. P. (2010). *Quantitative local profile analysis of nanomaterials by electron diffraction. Scr. Mater.* **63**, 312–315.

Gemmi, M. J., Fischer, J., Merlini, M., Poli, S., Fumagalli, P., Mugnaioli, E. & Kolb, U. (2011). *A new hydrous Al-bearing pyroxene as a water carrier in subduction zones. Earth Planet. Sci. Lett.* **310**, 422–428.

Gemmi, M., Voltolini, M., Ferretti, A. M. & Ponti, A. (2011). *Quantitative texture analysis from powder-like electron diffraction data. J. Appl. Cryst.* **44**, 454–461.

Gemmi, M., Zou, X. D., Hovmöller, S., Migliori, A., Vennström, M. & Andersson, Y. (2003). *Structure of Ti_2P solved by three-dimensional electron diffraction data collected with the precession technique and high-resolution electron microscopy. Acta Cryst.* A**59**, 117–126.

Gjonnes, K., Cheng, Y., Berg, B. S. & Hansen, V. (1998). *Corrections for multiple scattering in integrated electron diffraction intensities. Application to determination of structure factors in the [001] projection of Al_mFe. Acta Cryst.* A**54**, 102–119.

Gorelik, T., Matveeva, G., Kolb, U., Schleuss, T., Kilbinger, A. F. M., van de Streek, J., Bohled, A. & Brunklaus, G. (2010). *H-bonding schemes of di- and tri-p-benzamides assessed by a combination of electron diffraction, X-ray powder diffraction and solid-state NMR. CrystEngComm*, **12**, 1824–1832.

Gramm, F. C., Baerlocher, C., McCusker, L. B., Warrender, S. J., Wright, P. A., Han, B., Hong, S. B., Liu, Z., Ohsuna, T. & Terasaki, O. (2006). *Complex zeolite structure solved by combining powder diffraction and electron microscopy. Nature*, **444**, 79–81.

Haider, M. H., Rose, H., Uhlemann, S., Schwan, E., Kabius, B. & Urban, K. (1998). *A spherical-aberration-corrected 200 kV transmission electron microscope. Ultramicroscopy*, **75**, 53–60.

Henderson, R. (1995). *The potential and limitations of neutrons, electrons and X-rays for atomic resolution microscopy of unstained biological molecules. Q. Rev. Biophys.* **28**, 171–193.

Hill, R. J. & Howard, C. J. (1987). *Quantitative phase analysis from neutron powder diffraction data using the Rietveld method. J. Appl. Cryst.* **20**, 467–474.

Hirata, A., Hirotsu, Y., Ohkubo, T., Hanada, T. & Bengus, V. Z. (2006). *Compositional dependence of local atomic structures in amorphous $Fe_{100-x}B_x$ (x = 14, 17, 20) alloys studied by electron diffraction and high-resolution electron microscopy. Phys. Rev. B*, **74**, 214206.

Hirata, A. T., Morino, T., Hirotsu, Y., Itoh, K. & Fukunaga, T. (2007). *Local atomic structure analysis of Zr-Ni and Zr-Cu metallic glasses using electron diffraction. Mater. Trans.* **48**, 1299–1303.

Hirotsu, Y. T., Ohkubo, T., Bae, I.-T. & Ishimaru, M. (2003). *Electron diffraction structure analysis for amorphous materials. Mater. Chem. Phys.* **81**, 360–363.

Horstmann, M. & Meyer, G. (1962). *Messung der elastischen Elektronenbeugungsintensitäten polykristalliner Aluminium-Schichten. Acta Cryst.* **15**, 271–281.

Hovmoller, S., Zou, X. & Weirich, T. E. (2002). *Crystal structure determination from EM images and electron diffraction patterns. Adv. Imaging Electron Phys.* **123**, 257–289.

Howard, C. J., Sabine, T. M. & Dickson, F. (1991). *Structural and thermal parameters for rutile and anatase. Acta Cryst.* B**47**, 462–468.

Ichimiya, A. & Cohen, P. I. (2004). *Reflection High-Energy Electron Diffraction*. Cambridge University Press.

International Tables for Crystallography (2004). Volume C, *Mathematical, Physical and Chemical Tables*, edited by E. Prince. Dordrecht: Kluwer Academic Publishers.

Ishimaru, M. (2006). *Electron-beam radial distribution analysis of irradiation-induced amorphous SiC. Nucl. Instrum. Methods Phys. Res. Sect. B*, **250**, 309–314.

Ishimaru, M., Bae, I.-T., Hirotsu, Y., Matsumura, S. & Sickafus, K. E. (2002). *Structural relaxation of amorphous silicon carbide. Phys. Rev. Lett.* **89**, 055502.

Jansen, J., Tang, D., Zandbergen, H. W. & Schenk, H. (1998). *MSLS, a least-squares procedure for accurate crystal structure refinement from dynamical electron diffraction patterns. Acta Cryst.* A**54**, 91–101.

Kim, J. G., Seo, J. W., Cheon, J. & Kim, Y. J. (2009). *Rietveld analysis of nano-crystalline $MnFe_2O_4$ with electron powder diffraction. Bull. Korean Chem. Soc.* **30**, 183–187.

Kis, V. K. M., Posfai, M. & Labar, J. (2006). *Nanostructure of atmospheric soot particles. Atmos. Environ.* **40**, 5533–5542.

Kolb, U. K., Büscher, K., Helm, C. A., Lindner, A., Thünemann, A. F., Menzel, M., Higuchi, M. & Kurth, D. G. (2006). *The solid-state architecture of a metallosupramolecular polyelectrolyte. Proc. Natl Acad. Sci. USA*, **103**, 10202–10206.

Kovács Kis, V., Dódony, I. & Lábár, J. L. (2006). *Amorphous and partly ordered structures in SiO_2 rich volcanic glasses. An ED study. Eur. J. Mineral.* **18**, 745–752.

Lábár, J. L. (2006). *Phase identification by combining local composition from EDX with information from diffraction database.* In *Electron Crystallography*, edited by T. E. Weirich, J. L. Lábár & X. Zou, Nato Science Series II, Vol. 211, pp. 207–218. Dordrecht: Springer.

Lábár, J. L. (2008). *Electron diffraction based analysis of phase fractions and texture in nanocrystalline thin films, part I: principles. Microsc. Microanal.* **14**, 287–295.

Lábár, J. L. (2009). *Electron diffraction based analysis of phase fractions and texture in nanocrystalline thin films, part II: implementation. Microsc. Microanal.* **15**, 20–29.

Lábár, J. L. & Adamik, M. (2001). *ProcessDiffraction V1.2: new possibilities in manipulating electron diffraction ring patterns. Microsc. Microanal.* **7** (Suppl. 2), 372–373.

Lábár, J. L. M., Adamik, M., Barna, B. P., Czigány, Z., Fogarassy, Z., Horváth, Z. E., Geszti, O., Misják, F., Morgiel, J., Radnóczi, G., Sáfrán, G., Székely, L. & Szüts, T. (2012). *Electron diffraction based analysis of phase fractions and texture in nanocrystalline thin films, part III: application examples. Microsc. Microanal.* **18**, 406–420.

Lábár, J. L. & Egerton, R. (1999). *Special issue on ion beam techniques. Micron*, **30**, 195–196.

Li, X. Z. (2010). *PCED2.0 – a computer program for the simulation of polycrystalline electron diffraction pattern. Ultramicroscopy*, **110**, 297–304.

Luo, Z., Vasquez, Y., Bondi, J. F. & Schaak, R. E. (2011). *Pawley and Rietveld refinements using electron diffraction from $L1_2$-type intermetallic Au_3Fe_{1-x} nanocrystals during their in-situ order–disorder transition. Ultramicroscopy*, **111**, 1295–1304.

Lutterotti, L. D., Chateigner, D., Ferrari, S. & Ricote, J. (2004). *Texture, residual stress and structural analysis of thin films using a combined X-ray analysis. Thin Solid Films*, **450**, 34–41.

Lutterotti, L., Matthies, S. & Wenk, H. R. (1999). *MAUD: a friendly Java program for Material Analysis Using Diffraction. IUCr CPD Newsletters*, **21**, May 1999. http://www.mx.iucr.org/iucr-top/comm/cpd/Newsletters/no21may1999/art17/art17.htm.

Lutterotti, L. S., Matthies, S., Wenk, H.-R., Schultz, A. S. & Richardson, J. W. Jr (1997). *Combined texture and structure analysis of deformed limestone from time-of-flight neutron diffraction spectra. J. Appl. Phys.* **81**, 594–600.

McCusker, L. B. & Baerlocher, C. (2009). *Using electron microscopy to complement X-ray powder diffraction data to solve complex crystal structures. Chem. Commun.* pp. 1439–1451.

McGreevy, R. L. & Pusztai, L. (1988). *Reverse Monte Carlo simulation: a new technique for the determination of disordered structures. Mol. Simul.* **1**, 359–367.

McKenzie, D. R., Muller, D., Pailthorpe, B. A., Wang, Z. H., Kravtchinskaia, E., Segal, D., Lukins, P. B., Swift, P. D., Martin, P. J., Amaratunga, G., Gaskell, P. H. & Saeed, A. (1991). *Properties of tetrahedral amorphous carbon prepared by vacuum arc deposition. Diamond Relat. Mater.* **1**, 51–59.

Mecking, H. (1985). *Textures of metals*. In *Preferred Orientation in Deformed Metals and Rocks: An Introduction to Modern Texture Analysis*, edited by H.-R. Wenk, pp. 267–306. Orlando/London: Academic Press Inc.

Moeck, P. & Fraundorf, P. (2007). *Structural fingerprinting in the transmission electron microscope: overview and opportunities to implement enhanced strategies for nanocrystal identification. Z. Kristallogr.* **222**, 634–645.

Moeck, P. & Rouvimov, S. (2010). *Precession electron diffraction and its advantages for structural fingerprinting in the transmission electron microscope. Z. Kristallogr.* **225**, 110–124.

Moss, S. C. & Graczyk, J. F. (1969). *Evidence of voids within the as-deposited structure of glassy silicon. Phys. Rev. Lett.* **23**, 1167–1171.

Mugnaioli, E., Andrusenko, I., Schüler, T., Loges, N., Dinnebier, R. E., Panthöfer, M., Tremel, W. & Kolb, U. (2012). *Ab initio structure determination of vaterite by automated electron diffraction. Angew. Chem.* **51**, 7041–7045.

Nelder, J. A. & Mead, R. (1965). *A simplex method for function minimization. Comput. J.* **7**, 308–313.

Oleynikov, P. & Hovmoller, S. (2004). *TexPat – a program for quantitative analysis of oblique texture electron diffraction patterns. Z. Kristallogr.* **219**, 12–19.

Oleynikov, P. & Hovmoller, S. (2007). *Precession electron diffraction: observed and calculated intensities. Ultramicroscopy*, **107**, 523–533.

Orloff, J., Swanson, L. & Utlaut, M. (2002). *High Resolution Focused Ion Beams: FIB and Applications*. New York: Springer.

Own, C. S., Marks, L. D. & Sinkler, W. (2006). *Precession electron diffraction 1: multislice simulation. Acta Cryst.* A**62**, 434–443.

Őzdöl, V. B., Srot, V. & van Aken, P. A. (2012). *Sample preparation for transmission electron microscopy.* In *Handbook of Nanoscopy*, edited by G. Van Tendeloo, D. Van Dyck & S. J. Pennycook. Weinheim: Wiley.

Peng, L. M., Dudarev, S. L. & Whelan, M. J. (2004). *High-Energy Electron Diffraction and Microscopy*. USA: Oxford University Press.

Petersen, T. C., McBride, W., McCulloch, D. G., Snook, I. K. & Yarovsky, I. (2005). *Refinements in the collection of energy filtered diffraction patterns from disordered materials. Ultramicroscopy*, **103**, 275–283.

Rauch, E. F., Váron, M., Portillo, J., Bultreys, D., Maniette, Y. & Nicolopoulos, S. (2008). *Automatic crystal orientation and phase mapping in TEM by precession diffraction. Microsc. Anal.* **22**, S5–S8.

Reimer, L. (1984). *Transmission Electron Microscopy – Physics of Image Formation and Microanalysis*. Heidelberg: Springer-Verlag.

Reimer, L. & Kohl, H. (2008). *Transmission Electron Microscopy: Physics of Image Formation*. New York: Springer.

Rez, P. (1983). *A transport-equation theory of beam spreading in the electron microscope. Ultramicroscopy*, **12**, 29–38.

Rietveld, H. M. (1967). *Line profiles of neutron powder-diffraction peaks for structure refinement. Acta Cryst.* **22**, 151–152.

Rietveld, H. M. (1969). *A profile refinement method for nuclear and magnetic structures. J. Appl. Cryst.* **2**, 65–71.

Rodríguez-Carvajal, J. (1993). *Recent advances in magnetic structure determination by neutron powder diffraction. Physica B*, **192**, 55–69.

Rose, H. & Krahl, D. (1995). *Electron optics of imaging energy filters.* In *Energy-Filtering Transmission Electron Microscopy*, edited by L. Reimer, pp. 43–149. Berlin: Springer.

Saunders, M., Bird, D. M., Zaluzec, N. J., Burgess, W. G., Preston, A. R. & Humphreys, C. J. (1995). *Measurement of low-order structure factors for silicon from zone-axis CBED patterns. Ultramicroscopy*, **60**, 311–323.

Siwick, B. J., Dwyer, J. R., Jordan, R. E. & Miller, R. J. D. (2003). *An atomic-level view of melting using femtosecond electron diffraction. Science*, **302**, 1382–1385.

Song, K. Y. J., Kim, Y.-J., Kim, Y.-I. & Kim, J.-G. (2012). *Application of theta-scan precession electron diffraction to structure analysis of hydroxyapatite nanopowder. J. Electron Microsc.* **61**, 9–15.

Sun, J., Bonneau, C., Cantín, A., Corma, A., Díaz-Cabañas, M. J., Moliner, M., Zhang, D., Li, M. & Zou, X. (2009). *The ITQ-37 mesoporous chiral zeolite. Nature*, **458**, 1154–1157.

Tang, L., Feng, Y. C., Lee, L.-L. & Laughlin, D. E. (1996). *Electron diffraction patterns of fibrous and lamellar textured polycrystalline thin films. II. Applications. J. Appl. Cryst.* **29**, 419–426.

Tonejc, A. M., Djerdj, I. & Tonejc, A. (2002). *An analysis of evolution of grain size-lattice parameters dependence in nanocrystalline TiO_2 anatase. Mater. Sci. Eng. C*, **19**, 85–89.

Tsuda, K., Ogata, Y., Takagi, K., Hashimoto, T. & Tanaka, M. (2002). *Refinement of crystal structural parameters and charge density using convergent-beam electron diffraction – the rhombohedral phase of $LaCrO_3$. Acta Cryst.* A**58**, 514–525.

Tsuda, K. & Tanaka, M. (1999). *Refinement of crystal structural parameters using two-dimensional energy-filtered CBED patterns. Acta Cryst.* A**55**, 939–954.

Turner, P. S. & Cowley, J. M. (1969). *The effects of N-beam dynamical diffraction on electron diffraction intensities from polycrystalline materials. Acta Cryst.* A**25**, 475–481.

Ungár, T., Gubicza, J., Ribárik, G. & Borbély, A. (2001). *Crystallite size distribution and dislocation structure determined by diffraction profile analysis: principles and practical application to cubic and hexagonal crystals. J. Appl. Cryst.* **34**, 298–310.

Vainshtein, B. K. (1964). *Structure Analysis by Electron Diffraction*. Oxford: Pergamon Press.

Vainshtein, B. K., Zvyagin, B. B. & Avilov, A. S. (1992). *Electron diffraction structure analysis.* In *Electron Diffraction Techniques*, Vol. 1, edited by J. M. Cowley, pp. 216–312. Oxford University Press.

Vincent, R. & Exelby, D. R. (1991). *Structure of metastable Al–Ge phases determined from HOLZ Patterson transforms. Philos. Mag. Lett.* **63**, 31–38.

Vincent, R. & Midgley, P. A. (1994). *Double conical beam-rocking system for measurement of integrated electron diffraction intensities. Ultramicroscopy*, **53**, 271–282.

Warren, B. E. (1990). *X-ray Diffraction*. New York: Dover Publications.

Weickenmeier, A. & Kohl, H. (1991). *Computation of absorptive form factors for high-energy electron diffraction. Acta Cryst.* A**47**, 590–597.

Weirich, T. E. M., Winterer, M., Seifried, S., Hahn, H. & Fuess, H. (2000). *Rietveld analysis of electron powder diffraction data from nanocrystalline anatase, TiO_2. Ultramicroscopy*, **81**, 263–270.

Williams, D. B. & Carter, C. B. (2009). *Transmission Electron Microscopy: a Textbook for Materials Science*. New York: Springer.

Wu, J. S. K., Leinenweber, K., Spence, J. C. H. & O'Keeffe, M. (2006). *Ab initio phasing of X-ray powder diffraction patterns by charge flipping. Nat. Mater.* **5**, 647–652.

Zhang, J. (2011). *Atomic structures of carbon nanomaterials studied by coherent electron diffraction.* PhD thesis, University of Illinois, USA.

Zhuang, J. L. K., Lommel, K., Ceglarek, D., Andrusenko, I., Kolb, U., Maracke, S., Sazama, U., Fröba, M. & Terfort, A. (2011). *Synthesis of a new copper-azobenzene dicarboxylate framework in the form of hierarchical bulk solids and thin films without and with patterning. Chem. Mater.* **23**, 5366–5374.

Zuo, J. M. (1993). *New method of Bravais lattice determination. Ultramicroscopy*, **52**, 459–464.

Zuo, J. M. (2000). *Electron detection characteristics of a slow-scan CCD camera, imaging plates and film, and electron image restoration. Microsc. Res. Tech.* **49**, 245–268.

Zuo, J. M. (2004). *Measurements of electron densities in solids: a real-space view of electronic structure and bonding in inorganic crystals. Rep. Prog. Phys.* **67**, 2053–2103.

Zuo, J. M., Gao, M., Tao, J., Li, B. Q., Twesten, R. & Petrov, I. (2004). *Coherent nano-area electron diffraction. Microsc. Res. Tech.* **64**, 347–355.

Zuo, J. M., Kim, M. & Holmestad, R. (1998). *A new approach to lattice parameter measurements using dynamic electron diffraction and pattern matching. J. Electron Microsc.* **47**, 121–127.

Zuo, J. M. & Spence, J. C. H. (1991). *Automated structure factor refinement from convergent-beam patterns. Ultramicroscopy*, **35**, 185–196.

Zuo, J. M. & Spence, J. C. H. (2017). *Advanced Transmission Electron Microscopy: Imaging and Diffraction in Nanoscience*. New York: Springer.

International Tables for Crystallography (2019). Vol. H, Chapter 2.5, pp. 118–149.

2.5. Two-dimensional powder diffraction

B. B. He

2.5.1. Introduction

2.5.1.1. *The diffraction pattern measured by an area detector*

The diffracted X-rays from a polycrystalline or powder sample form a series of cones in three-dimensional space, since large numbers of crystals oriented randomly in the space are covered by the incident X-ray beam. Each diffraction cone corresponds to the diffraction from the same family of crystal planes in all the participating grains. The apex angles of cones are given by Bragg's law for the corresponding crystal interplanar *d*-spacing. A conventional X-ray powder-diffraction pattern is collected by scanning a point or linear detector along the 2θ angle. The diffraction pattern is displayed as scattering intensity *versus* 2θ angle (Klug & Alexander, 1974; Cullity, 1978; Warren, 1990; Jenkins & Snyder, 1996; Pecharsky & Zavalij, 2003). In recent years, use of two-dimensional (2D) detectors for powder diffraction has dramatically increased in academic and industrial research (Sulyanov *et al.*, 1994; Rudolf & Landes, 1994; He, 2003, 2009). When a 2D detector is used for X-ray powder diffraction, the diffraction cones are intercepted by the area detector and the X-ray intensity distribution on the sensing area is converted to an image-like diffraction pattern, also referred to as a frame. Since the diffraction pattern collected with a 2D detector is typically given as an intensity distribution over a two-dimensional region, so X-ray diffraction with a 2D detector is also referred to as two-dimensional X-ray diffraction (2D-XRD) or 2D powder diffraction. A 2D diffraction pattern contains far more information than a conventional diffraction pattern, and therefore demands a special data-collection strategy and data-evaluation algorithms. This chapter covers the basic concepts and recent progress in 2D-XRD theory and technologies, including geometry conventions, X-ray source and optics, 2D detectors, diffraction-data interpretation, and various applications, such as phase identification and texture, stress, crystallinity and crystallite-size analysis. The concepts and algorithms of this chapter apply to both laboratory and synchrotron diffractometers equipped with 2D detectors.

2.5.1.2. *Comparison between 2D-XRD and conventional XRD*

Fig. 2.5.1 is a schematic of X-ray diffraction from a powder (polycrystalline) sample. For simplicity, it shows only two diffraction cones; one represents forward diffraction ($2\theta \leq 90^\circ$) and one represents backward diffraction ($2\theta > 90^\circ$). The diffraction measurement in a conventional diffractometer is confined within a plane, here referred to as the diffractometer plane. A point (0D) detector makes a 2θ scan along a detection circle. If a line (1D) detector is used in the diffractometer, it will be mounted on the detection circle. Since the variations in the diffraction pattern in the direction (**Z**) perpendicular to the diffractometer plane are not considered in a conventional diffractometer, the X-ray beam is normally extended in the *Z* direction (line focus). Since the diffraction data out of the diffractometer plane are not detected, the structures in the material that are represented by the missing diffraction data will either be ignored, or extra sample rotation and time are needed to complete the measurement.

With a 2D detector, the diffraction measurement is no longer limited to the diffractometer plane. Depending on the detector size, the distance to the sample and the detector position, the whole or a large portion of the diffraction rings can be measured simultaneously. Diffraction patterns out of the diffractometer plane have for a long time been recorded using Debye–Scherrer cameras, so the diffraction rings are referred to as Debye rings. However, when a Debye–Scherrer camera is used, only the position of the arches in the 2θ direction and their relative intensities are measured for powder-diffraction analysis. The diffraction rings collected with a large 2D detector extend further in the 'vertical' direction and the intensity variation in the vertical direction is also used for data evaluation. Therefore, the terms 'diffraction cone' and 'diffraction ring' will be often be used in this chapter as alternatives to 'Debye cone' and 'Debye ring'.

2.5.1.3. *Advantages of two-dimensional X-ray diffraction*

A 2D diffraction frame contains far more information than a diffraction pattern measured using a conventional diffraction system with a point detector or a linear position-sensitive detector. In addition to the significantly higher data-collection speed, the intensity and 2θ variation along the diffraction rings can reveal abundant structural information typically not available from a conventional diffraction pattern. Fig. 2.5.2 shows a 2D pattern collected from a battery component containing multiple layers of different phases. Some diffraction rings have strong intensity variation due to preferred orientation, and the spotty diffraction rings are from a phase that contains large crystal grains. It is apparent that different diffraction-ring patterns are from different phases. 2D-XRD analyses commonly performed on polycrystalline materials include phase identification, quantitative phase analysis, preferred-orientation quantification and characterization of residual stresses.

Phase identification (phase ID) can be done by integration in a selected 2θ range along the diffraction rings (Hammersley *et al.*,

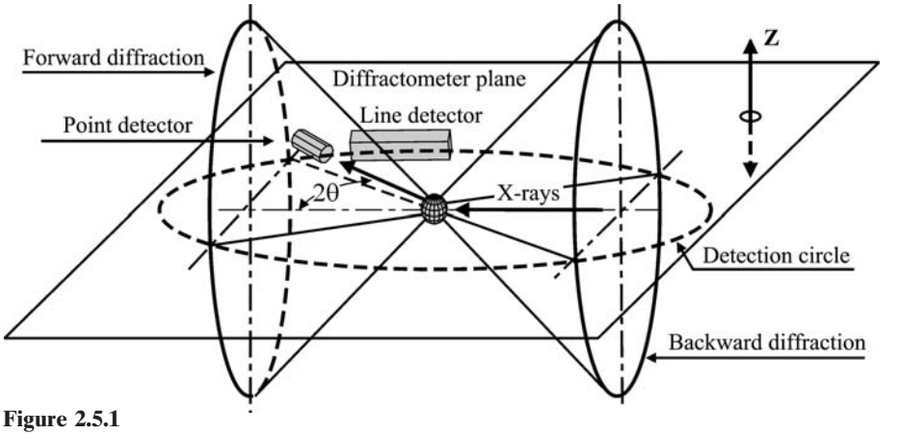

Figure 2.5.1
Diffraction patterns in 3D space from a powder sample and the diffractometer plane.

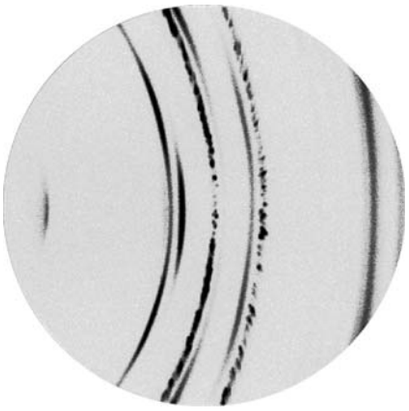

Figure 2.5.2
Diffraction pattern from a battery component containing multiple layers.

1996; Rodriguez-Navarro, 2006). The integrated data give better intensity and statistics for phase ID and quantitative analysis, especially for those samples with texture or large grain sizes, or where the sample is small. Then the integrated diffraction profiles can be analysed with existing algorithms and methods: profile fitting with conventional peak shapes and fundamental parameters, quantification of phases, and lattice-parameter indexing and refinement. The results can be used to search and match to entries in a powder-diffraction database, typically the Powder Diffraction File.

Texture measurement with 2D-XRD is extremely fast compared to measurement using a point or linear detector. The area detector collects texture data and background values simultaneously for multiple poles and multiple directions. Owing to the high measurement speed, pole figures can be measured at very fine steps, allowing detection of very sharp textures (Smith & Ortega, 1993; Bunge & Klein, 1996; He, 2009).

Stress measurement with 2D-XRD is based on a direct relationship between the stress tensor and distortion of the diffraction cones. Since the whole or a part of the diffraction ring is used for stress calculation, 2D-XRD can measure stress with high sensitivity, high speed and high accuracy (He & Smith, 1997; He, 2000). It is highly suitable for samples containing large crystals and textures. Simultaneous measurement of stress and texture is also possible, since 2D data contain both stress and texture information.

Concentrations of crystalline phases can be measured faster and more accurately with data analysis over 2D frames, especially for samples with an anisotropic distribution of crystallite orientations and/or amorphous content. The amorphous region can be defined by the user to consist of regions with no Bragg peaks, or the amorphous region can be defined with the crystalline region included when the crystalline region and the amorphous region overlap.

Microdiffraction data are collected with speed and accuracy. Collection of X-ray diffraction data from small sample amounts or small sample areas has always been a slow process because of limited beam intensity. The 2D detector captures whole or a large portion of the diffraction rings, so spotty, textured or weak diffraction data can be integrated over the selected diffraction rings (Winter & Squires, 1995; Bergese *et al.*, 2001; Tissot, 2003; Bhuvanesh & Reibenspies, 2003; He, 2004). The point beam used for microdiffraction allows diffraction mapping with fine space resolution, even on a curved surface (Allahkarami & Hanan, 2011).

Data can be collected from thin-film samples containing a mixture of single-crystal and polycrystalline layers with random orientation distributions, and highly textured layers, with all the features appearing simultaneously in diffraction frames (Dickerson *et al.*, 2002; He, 2006). The pole figures from different layers and the substrate can be overlapped to reveal the orientation relationships. The use of a 2D detector can dramatically speed up the data collection for reciprocal-space mapping on an in-plane reciprocal-lattice point (Schmidbauer *et al.*, 2008).

Because of the penetrating power of the X-ray beam, fast nondestructive data collection and the abundant information about atomic structure, two-dimensional X-ray diffraction can be used to screen a library of materials with high speed and high accuracy. Two-dimensional X-ray diffraction systems dedicated for combinatorial screening are widely used in the pharmaceutical industry for drug discovery and process analysis (Klein *et al.*, 1998; He *et al.*, 2001).

Forensic science and archaeology have benefited from using two-dimensional X-ray diffraction for identifying materials and structures from small specimens (Kugler, 2003; Bontempi *et al.*, 2008). It is nondestructive and does not require special sample treatment, so the original evidence or sample can be preserved. Two-dimensional diffraction patterns contain abundant information and are easy to observe and explain in the courtroom.

2.5.2. Fundamentals

A conventional powder-diffraction pattern is displayed as the scattering intensity *versus* scattering angle 2θ or d-spacing. A 2D-XRD pattern contains the scattering-intensity distribution as a function of two orthogonal dimensions. One dimension can be expressed in 2θ, which can be interpreted by Bragg's law. The distribution in the dimension orthogonal to 2θ contains additional information, such as the orientation distribution, strain states, and crystallite-size and -shape distribution. In order to understand and analyse 2D diffraction data, new geometry conventions and algorithms are introduced. The geometry conventions and algorithms used for 2D-XRD should also be consistent with conventional XRD, so that many existing concepts and algorithms are still valid when 2D diffraction data are used.

The geometry of a 2D-XRD system can be explained using three distinguishable and interrelated geometry spaces, each defined by a set of parameters (He, 2003). The three geometry spaces are the diffraction space, detector space and sample space. The laboratory coordinate system $\mathbf{X}_L$, $\mathbf{Y}_L$, $\mathbf{Z}_L$ is the basis of all three spaces. Although the three spaces are interrelated, the definitions and corresponding parameters should not be confused. Except for a few parameters introduced specifically for 2D-XRD, many of these parameters are used in conventional X-ray diffraction systems. Therefore, the same definitions are maintained for consistency. The three-circle goniometer in Eulerian geometry is the most commonly used, and all the algorithms for data interpretation and analysis in this chapter are based on Eulerian geometry. The algorithms can be developed for the geometries of other types (such as kappa) by following the same strategies.

2.5.2.1. *Diffraction space and laboratory coordinates*

2.5.2.1.1. *Diffraction cones in laboratory coordinates*

Fig. 2.5.3(a) describes the geometric definition of diffraction cones in the laboratory coordinate system $\mathbf{X}_L$, $\mathbf{Y}_L$, $\mathbf{Z}_L$. The laboratory coordinate system is a Cartesian coordinate system.

The plane given by X_L and Y_L is the diffractometer plane. The axis Z_L is perpendicular to the diffractometer plane. The axes X_L, Y_L and Z_L form a right-handed rectangular coordinate system with the origin at the instrument centre. The incident X-ray beam propagates along the X_L axis, which is also the rotation axis of all diffraction cones. The apex angles of the cones are determined by the 2θ values given by the Bragg equation. The apex angles are twice the 2θ values for forward reflection ($2\theta \leq 90^\circ$) and twice the value of $180^\circ - 2\theta$ for backward reflection ($2\theta > 90^\circ$). For clarity, only one diffraction cone of forward reflection is displayed. The γ angle is the azimuthal angle from the origin at the six o'clock direction with a right-handed rotation axis along the opposite direction of incident beam ($-X_L$ direction). A given γ value defines a half plane with the X_L axis as the edge; this will be referred to as the γ plane hereafter. The diffractometer plane consists of two γ planes at γ = 90° and γ = 270°. Therefore many equations developed for 2D-XRD should also apply to conventional XRD if the γ angle is given as a constant of 90° or 270°. A pair of γ and 2θ values represents the direction of a diffracted beam. The γ angle takes a value of 0 to 360° for a complete diffraction ring with a constant 2θ value. The γ and 2θ angles form a spherical coordinate system which covers all the directions from the origin of sample (instrument centre). The γ–2θ system is fixed in the laboratory system $\mathbf{X}_L$, $\mathbf{Y}_L$, $\mathbf{Z}_L$, which is independent of the sample orientation and detector position in the goniometer. 2θ and γ are referred to as the diffraction-space parameters. In the laboratory coordinate system $\mathbf{X}_L$, $\mathbf{Y}_L$, $\mathbf{Z}_L$, the surface of a diffraction cone can be mathematically expressed as

$$y_L^2 + z_L^2 = x_L^2 \tan^2 2\theta, \qquad (2.5.1)$$

with $x_L \geq 0$ or $2\theta \leq 90^\circ$ for forward-diffraction cones and $x_L < 0$ or $2\theta > 90^\circ$ for backward-diffraction cones.

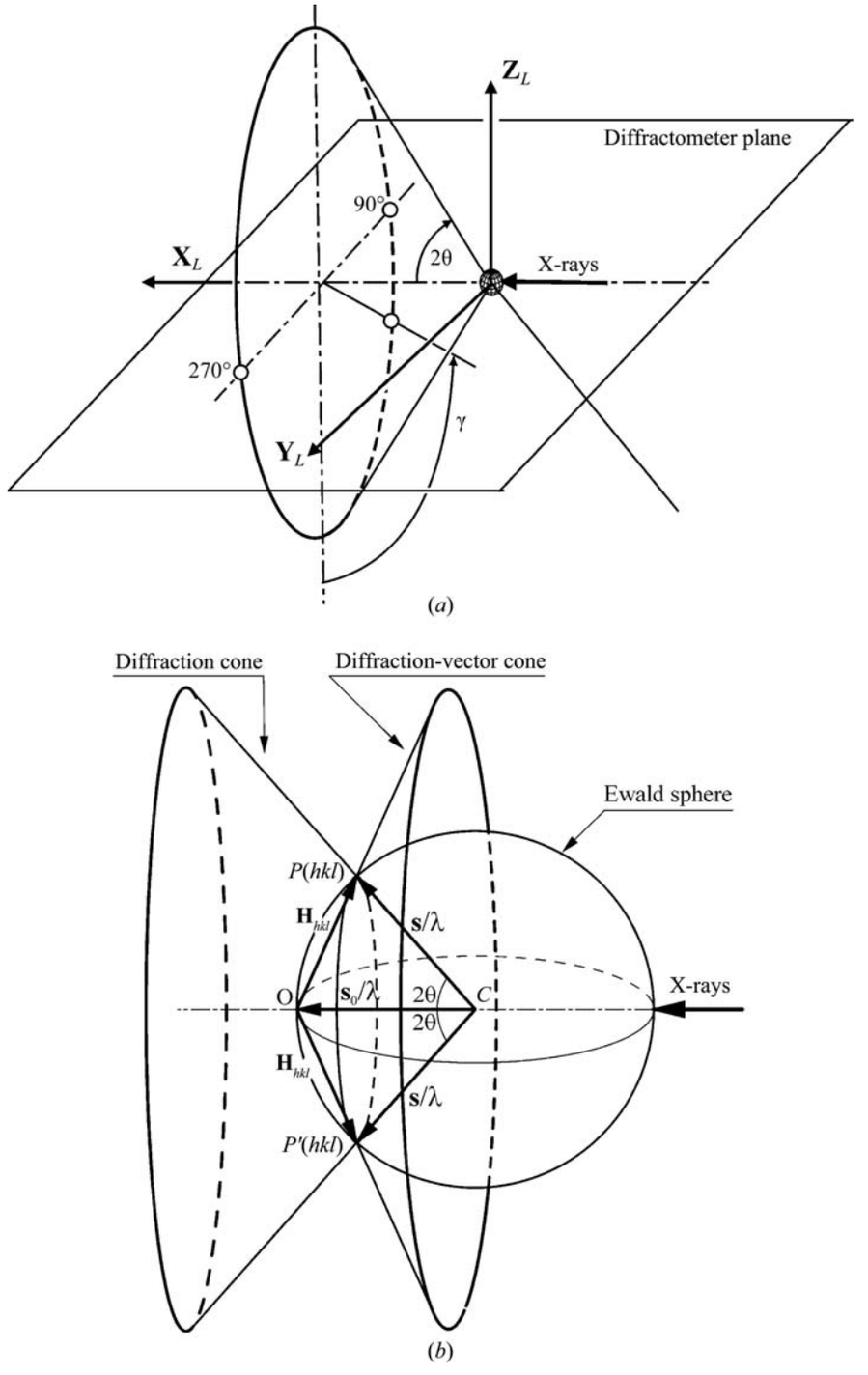

Figure 2.5.3
The diffraction cone and the corresponding diffraction-vector cone.

2.5.2.1.2. *Diffraction-vector cones in laboratory coordinates*

Fig. 2.5.3(*b*) shows the diffraction-vector cone corresponding to the diffraction cone in the laboratory coordinate system. *C* is the centre of the Ewald sphere. The diffraction condition can be given by the Laue equation as

$$\frac{\mathbf{s} - \mathbf{s}_0}{\lambda} = \mathbf{H}_{hkl}, \qquad (2.5.2)$$

where $\mathbf{s}_0$ is the unit vector representing the incident beam, $\mathbf{s}$ is the unit vector representing the diffracted beam and $\mathbf{H}_{hkl}$ is the reciprocal-lattice vector. Its magnitude is given as

$$\left|\frac{\mathbf{s} - \mathbf{s}_0}{\lambda}\right| = \frac{2\sin\theta}{\lambda} = \left|\mathbf{H}_{hkl}\right| = \frac{1}{d_{hkl}}, \qquad (2.5.3)$$

in which d_{hkl} is the d-spacing of the crystal planes (hkl). It can be easily seen that it is the Bragg law in a different form. Therefore, equation (2.5.2) is the Bragg law in vector form. In the Bragg condition, the vectors $\mathbf{s}_0/\lambda$ and $\mathbf{s}/\lambda$ make angles θ with the diffracting planes (hkl) and $\mathbf{H}_{hkl}$ is normal to the (hkl) crystal plane. In order to analyse all the X-rays measured by a 2D detector, we extend the concept to all scattered X-rays from a sample regardless of the Bragg condition. Therefore, the index (hkl) can be removed from the above expression. $\mathbf{H}$ is then a vector which takes the direction bisecting the incident beam and the scattered beam, and has dimensions of inverse length given by $2\sin\theta/\lambda$. Here 2θ is the scattering angle from the incident beam. The vector $\mathbf{H}$ is referred to as the scattering vector or, alternatively, the diffraction vector. When the Bragg condition is

satisfied, the diffraction vector is normal to the diffracting lattice planes and its magnitude is reciprocal to the d-spacing of the lattice planes. In this case, the diffraction vector is equivalent to the reciprocal-lattice vector. Each pixel in a 2D detector measures scattered X-rays in a given direction with respect to the incident beam. We can calculate a diffraction vector for any pixel, even if the pixel is not measuring Bragg scattering. Use of the term 'diffracted beam' hereafter in this chapter does not necessarily imply that it arises from Bragg scattering.

For two-dimensional diffraction, the incident beam can be expressed by the vector $\mathbf{s}_0/\lambda$, but the diffracted beam is no longer in a single direction, but follows the diffraction cone. Since the direction of a diffraction vector is a bisector of the angle between the incident and diffracted beams corresponding to each diffraction cone, the trace of the diffraction vectors forms a cone. This cone is referred to as the diffraction-vector cone. The angle between the diffraction vector and the incident X-ray beam is $90^\circ + \theta$ and the apex angle of a vector cone is $90^\circ - \theta$. It is apparent that diffraction-vector cones can only exists on the $-X_L$ side of the diffraction space.

For two-dimensional diffraction, the diffraction vector is a function of both the γ and 2θ angles, and is given in laboratory coordinates as

$$\mathbf{H} = \frac{\mathbf{s} - \mathbf{s}_0}{\lambda} = \frac{1}{\lambda}\begin{bmatrix} \cos 2\theta - 1 \\ -\sin 2\theta \sin\gamma \\ -\sin 2\theta \cos\gamma \end{bmatrix}. \qquad (2.5.4)$$

The direction of the diffraction vector can be represented by its unit vector, given by

$$\mathbf{h}_L = \frac{\mathbf{H}}{|\mathbf{H}|} = \begin{bmatrix} h_x \\ h_y \\ h_z \end{bmatrix} = \begin{bmatrix} -\sin\theta \\ -\cos\theta \sin\gamma \\ -\cos\theta \cos\gamma \end{bmatrix}, \qquad (2.5.5)$$

where $\mathbf{h}_L$ is a unit vector expressed in laboratory coordinates and the three components in the square brackets are the projections of the unit vector on the three axes of the laboratory coordinates, respectively. If γ takes all values from 0 to 360° at a given Bragg angle 2θ, the trace of the diffraction vector forms a diffraction-vector cone. Since the possible values of θ lie within the range 0 to 90°, h_x takes only negative values.

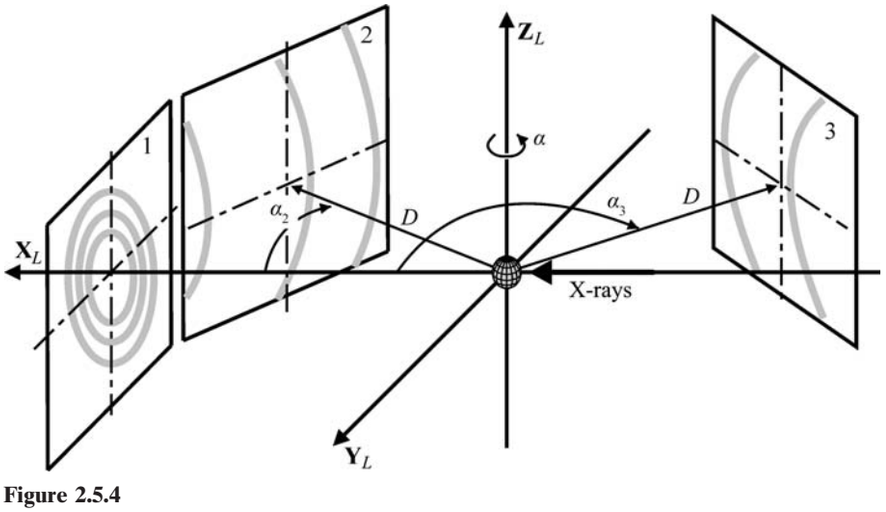

Figure 2.5.4
Detector positions in the laboratory-system coordinates.

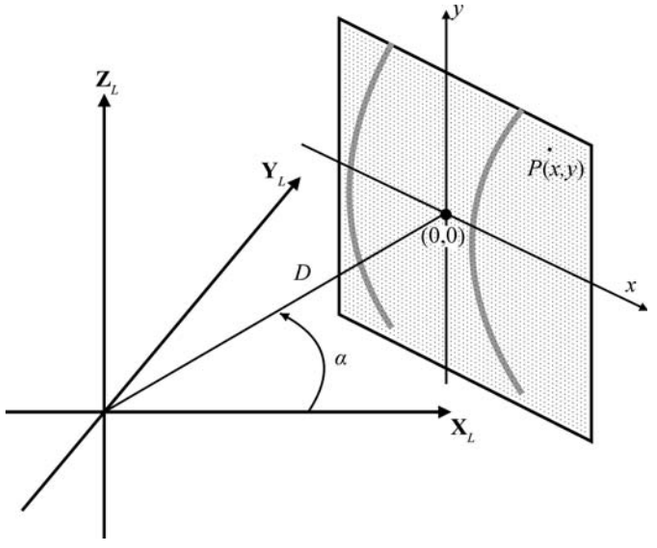

Figure 2.5.5
Relationship between a pixel P and detector position in the laboratory coordinates.

2.5.2.2. *Detector space and pixel position*

A typical 2D detector has a limited detection surface, and the detection surface can be spherical, cylindrical or flat. Spherical or cylindrical detectors are normally designed for a fixed sample-to-detector distance, while a flat detector has the flexibility to be used at different sample-to-detector distances so as to choose either high resolution at a large distance or large angular coverage at a short distance.

2.5.2.2.1. *Detector position in the laboratory system*

The position of a flat detector is defined by the sample-to-detector distance D and the detector swing angle α. D and α are referred to as the detector-space parameters. D is the perpendicular distance from the goniometer centre to the detection plane and α is a right-handed rotation angle about the Z_L axis. Detectors at different positions in the laboratory coordinates X_L, Y_L, Z_L are shown in Fig. 2.5.4. The centre of detector 1 is right on the positive side of the X_L axis (on-axis), $\alpha = 0$. Both detectors 2 and 3 are rotated away from the X_L axis with negative swing angles ($\alpha_2 < 0$ and $\alpha_3 < 0$). The detection surface of a flat 2D detector can be considered as a plane, which intersects the diffraction cone to form a conic section. Depending on the swing angle α and the 2θ angle, the conic section can appear as a circle, an ellipse, a parabola or a hyperbola.

2.5.2.2.2. *Pixel position in diffraction space for a flat detector*

The values of 2θ and γ can be calculated for each pixel in the frame. The calculation is based on the detector-space parameters and the pixel position in the detector. Fig. 2.5.5 shows the relationship of a pixel $P(x, y)$ to the laboratory coordinates X_L, Y_L, Z_L. The position of a pixel in the detector is defined by the (x, y) coordinates, where the detector centre is defined as $x = y = 0$. The diffraction-space coordinates $(2\theta, \gamma)$ for a pixel at $P(x, y)$ are given by

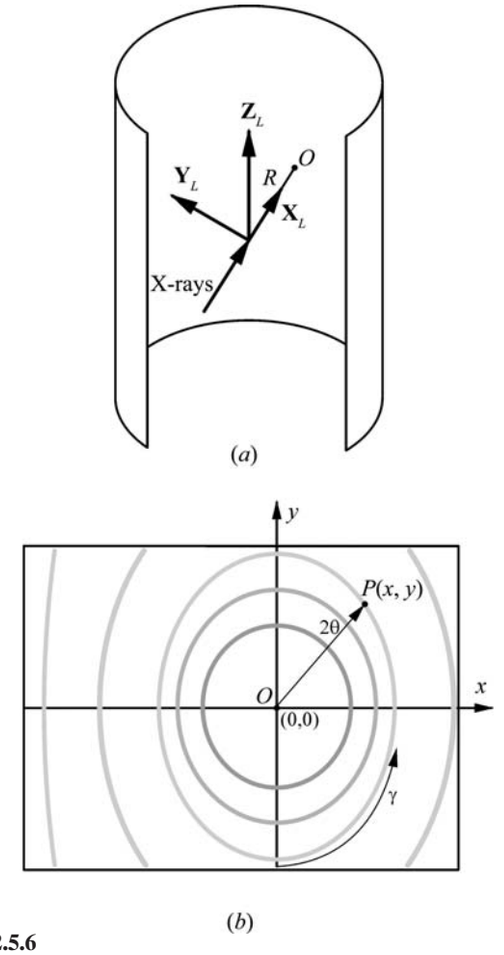

Figure 2.5.6
Cylinder-shaped detector in vertical direction: (*a*) detector position in the laboratory coordinates; (*b*) pixel position in the flattened image.

$$2\theta = \arccos\frac{x\sin\alpha + D\cos\alpha}{(D^2 + x^2 + y^2)^{1/2}} \quad (0 < 2\theta < \pi), \tag{2.5.6}$$

$$\gamma = \frac{x\cos\alpha - D\sin\alpha}{|x\cos\alpha - D\sin\alpha|}\arccos\frac{-y}{[y^2 + (x\cos\alpha - D\sin\alpha)^2)]^{1/2}} \quad (-\pi < \gamma \leq \pi). \tag{2.5.7}$$

2.5.2.2.3. *Pixel position in diffraction space for a curved detector*

The conic sections of the diffraction cones with a curved detector depend on the shape of the detector. The most common curved detectors are cylinder-shaped detectors. The diffraction frame measured by a cylindrical detector can be displayed as a flat frame, typically a rectangle. Fig. 2.5.6(*a*) shows a cylindrical detector in the vertical direction and the corresponding laboratory coordinates X_L, Y_L, Z_L. The sample is located at the origin of the laboratory coordinates inside the cylinder. The incident X-rays strike the detector at a point O if there is no sample or beam stop to block the direct beam. The radius of the cylinder is R. Fig. 2.5.6(*b*) illustrates the 2D diffraction image collected with the cylindrical detector. We take the point O as the origin of the pixel position (0, 0). The diffraction-space coordinates $(2\theta, \gamma)$ for a pixel at $P(x, y)$ are given by

$$2\theta = \arccos\left[R\cos\left(\frac{x}{R}\right)\Big/(R^2 + y^2)^{1/2}\right], \tag{2.5.8}$$

$$\gamma = \frac{x}{|x|}\arccos\left\{-y\Big/\left[y^2 + R^2\sin^2\left(\frac{x}{R}\right)\right]^{1/2}\right\} \quad (-\pi < \gamma \leq \pi). \tag{2.5.9}$$

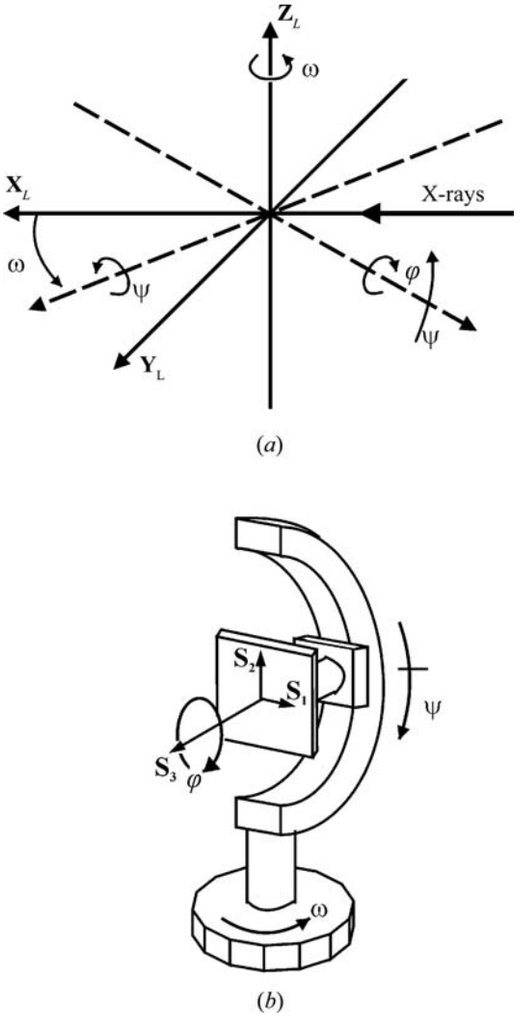

Figure 2.5.7
Sample rotation and translation. (*a*) Three rotation axes in laboratory coordinates; (*b*) rotation axes (ω, ψ, φ) and sample coordinates.

The pixel-position-to-$(2\theta, \gamma)$ conversion for detectors of other shapes can also be derived. Once the diffraction-space coordinates $(2\theta, \gamma)$ of each pixel in the curved 2D detector are determined, most data-analysis algorithms developed for flat detectors are applicable to a curved detector as well.

2.5.2.3. *Sample space and goniometer geometry*

2.5.2.3.1. *Sample rotations and translations in Eulerian geometry*

In a 2D-XRD system, three rotation angles are necessary to define the orientation of a sample in the diffractometer. These three rotation angles can be achieved either by a Eulerian geometry, a kappa (κ) geometry or another kind of geometry. The three angles in Eulerian geometry are ω (omega), ψ (psi) and φ (phi). Fig. 2.5.7(*a*) shows the relationship between rotation axes (ω, ψ, φ) in the laboratory system $\mathbf{X}_L$, $\mathbf{Y}_L$, $\mathbf{Z}_L$. The ω angle is defined as a right-handed rotation about the Z_L axis. The ω axis is fixed in the laboratory coordinates. The ψ angle is a right-handed rotation about a horizontal axis. The angle between the ψ axis and the X_L axis is given by ω. The ψ axis lies on X_L when ω is set at zero. The φ angle defines a left-handed rotation about an axis on the sample, typically the normal of a flat sample. The φ axis lies on the Y_L axis when $\omega = \psi = 0$. In an aligned diffraction system, all three rotation axes and the primary X-ray beam cross at the

origin of the X_L, Y_L, Z_L coordinates. This cross point is also known as the goniometer centre or instrument centre.

Fig. 2.5.7(*b*) shows the relationship and stacking sequence among all rotation axes (ω, ψ, φ) and the sample coordinates S_1, S_2, S_3. ω is the base rotation; all other rotations and translations are on top of this rotation. The next rotation above ω is the ψ rotation. The next rotation above ω and ψ is the φ rotation. The sample coordinates S_1, S_2, S_3 are fixed to the sample regardless of the particular sample orientation given by the rotation angles (ω, ψ, φ). The φ rotation in the goniometer is intentionally chosen as a left-handed rotation so that the diffraction vectors will make a right-hand rotation observed in the sample coordinates S_1, S_2, S_3.

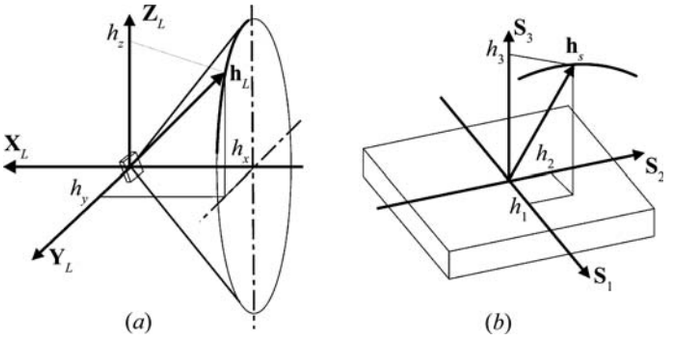

Figure 2.5.8
Unit diffraction vector in (*a*) the laboratory coordinates and (*b*) the sample coordinates.

2.5.2.4. *Diffraction-vector transformation*

2.5.2.4.1. *Diffraction unit vector in diffraction space and sample space*

In 2D-XRD data analysis, it is crucial to know the diffraction-vector distribution in terms of the sample coordinates S_1, S_2, S_3. However, the diffraction-vector distribution corresponding to the measured 2D data is always given in terms of the laboratory coordinates X_L, Y_L, Z_L because the diffraction space is fixed to the laboratory coordinates. Fig. 2.5.8 shows the unit vector of a diffraction vector in both (*a*) the laboratory coordinates X_L, Y_L, Z_L and (*b*) the sample coordinates S_1, S_2, S_3. In Fig. 2.5.8(*a*) the unit vector $\mathbf{h}_L$ is projected to the X_L, Y_L and Z_L axes as h_x, h_y and h_z, respectively. The three components are given by equation (2.5.5). In order to analyse the diffraction results relative to the sample orientation, it is necessary to transform the unit vector to the sample coordinates S_1, S_2, S_3. Fig. 2.5.8(*b*) shows the same unit vector, denoted by $\mathbf{h}_s$ projected to S_1, S_2 and S_3 as h_1, h_2 and h_3, respectively.

2.5.2.4.2. *Transformation from diffraction space to sample space*

The transformation of the unit diffraction vector from the laboratory coordinates X_L, Y_L, Z_L to the sample coordinates S_1, S_2, S_3 is given by

$$\mathbf{h}_s = \boldsymbol{A}\mathbf{h}_L, \tag{2.5.10}$$

where $\boldsymbol{A}$ is the transformation matrix. For Eulerian geometry in matrix form, we have

$$\begin{bmatrix} h_1 \\ h_2 \\ h_3 \end{bmatrix} = \begin{bmatrix} a_{11} & a_{12} & a_{13} \\ a_{21} & a_{22} & a_{23} \\ a_{31} & a_{32} & a_{33} \end{bmatrix} \begin{bmatrix} h_x \\ h_y \\ h_z \end{bmatrix}$$

$$= \begin{bmatrix} -\sin\omega\sin\psi\sin\varphi & \cos\omega\sin\psi\sin\varphi & -\cos\psi\sin\varphi \\ \quad -\cos\omega\cos\varphi & \quad -\sin\omega\cos\varphi & \\ \sin\omega\sin\psi\cos\varphi & -\cos\omega\sin\psi\cos\varphi & \cos\psi\cos\varphi \\ \quad -\cos\omega\sin\varphi & \quad -\sin\omega\sin\varphi & \\ -\sin\omega\cos\psi & \cos\omega\cos\psi & \sin\psi \end{bmatrix}$$

$$\times \begin{bmatrix} -\sin\theta \\ -\cos\theta\sin\gamma \\ -\cos\theta\cos\gamma \end{bmatrix}. \tag{2.5.11}$$

In expanded form:

$$\begin{aligned} h_1 &= \sin\theta(\sin\varphi\sin\psi\sin\omega + \cos\varphi\cos\omega) + \cos\theta\cos\gamma\sin\varphi\cos\psi \\ &\quad - \cos\theta\sin\gamma(\sin\varphi\sin\psi\cos\omega - \cos\varphi\sin\omega) \\ h_2 &= -\sin\theta(\cos\varphi\sin\psi\sin\omega - \sin\varphi\cos\omega) \\ &\quad - \cos\theta\cos\gamma\cos\varphi\cos\psi \\ &\quad + \cos\theta\sin\gamma(\cos\varphi\sin\psi\cos\omega + \sin\varphi\sin\omega) \\ h_3 &= \sin\theta\cos\psi\sin\omega - \cos\theta\sin\gamma\cos\psi\cos\omega - \cos\theta\cos\gamma\sin\psi \end{aligned} \tag{2.5.12}$$

In addition to the diffraction intensity and Bragg angle corresponding to each data point on the diffraction ring, the unit vector $\mathbf{h}_s\{h_1, h_2, h_3\}$ provides orientation information in the sample space. The transformation matrix of any other goniometer geometry, such as kappa geometry (Paciorek *et al.*, 1999), can be introduced into equation (2.5.10) so that the unit vector $\mathbf{h}_s\{h_1, h_2, h_3\}$ can be expressed in terms of the specified geometry. All equations using the unit vector $\mathbf{h}_s\{h_1, h_2, h_3\}$ in this chapter, such as in data treatment, texture analysis and stress measurement, are applicable to all goniometer geometries provided that the unit-vector components are generated from the corresponding transformation matrix from diffraction space to the sample space.

2.5.2.4.3. *Transformation from detector space to reciprocal space*

Reciprocal-space mapping is commonly used to analyse the diffraction patterns from highly oriented structures, diffuse scattering from crystal defects, and thin films (Hanna & Windle, 1995; Mudie *et al.*, 2004; Smilgies & Blasini, 2007; Schmidbauer *et al.*, 2008). The equations of the unit-vector calculation given above can also be used to transform the diffraction intensity from the diffraction space to the reciprocal space with respect to the sample coordinates. The direction of the scattering vector is given by the unit vector $\mathbf{h}_s\{h_1, h_2, h_3\}$ and the magnitude of the scattering vector is given by $2\sin\theta/\lambda$, so that the scattering vector corresponding to a pixel is given by

$$\mathbf{H} = \frac{2\sin\theta}{\lambda}\mathbf{h}_s. \tag{2.5.13}$$

The three-dimensional reciprocal-space mapping can be obtained by applying the normalized pixel intensities to the corresponding reciprocal points. With various sample orientations, all pixels on the detector can be mapped into a 3D reciprocal space.

2.5.3. Instrumentation

2.5.3.1. *X-ray source and optics*

2.5.3.1.1. *Beam path in a diffractometer equipped with a 2D detector*

The Bragg–Brentano (B-B) parafocusing geometry is most commonly used in conventional X-ray diffractometers with a point detector (Cullity, 1978; Jenkins & Snyder, 1996). In the Bragg–Brentano geometry, the sample surface normal is always a bisector between the incident beam and the diffracted beam. A divergent incident beam hits the sample surface with an incident angle θ. The area of the irradiated region depends on the incident angle θ and the size of the divergence slit. The diffracted rays leave the sample at an angle 2θ, pass through the anti-scatter slit and receiving slit, and reach the point detector. Soller slits are used on both the primary side and secondary side to minimize the effects of axial divergence due to the line-focus beam. The primary line-focus beam sliced by the Soller slits can also be considered as an array of point beams parallel to the diffractometer planes. Each of these point beams will produce a diffraction cone from the sample. The overlap of all the diffraction cones will create a smeared diffraction peak. The Soller slits on the receiving side allow only those diffracted beams nearly parallel to the diffractometer plane to pass through, so the smearing effect is minimized. In another words, the so-called 'line-focus geometry' in conventional diffractometry is actually a superposition of many layers of 'spot-focus geometry'.

The beam path in a diffractometer equipped with a 2D detector is different from that in a conventional diffractometer in many respects (He & Preckwinkel, 2002). In a 2D-XRD system the whole or a large portion of the diffraction rings are measured simultaneously, and neither slits nor monochromator can be used between the sample and detector. Therefore, the X-ray source and optics for 2D-XRD systems have different requirements in terms of the beam spectral purity, divergence and beam cross-section profile. Fig. 2.5.9 shows the beam path in a 2D-XRD system with the θ–θ configuration. The geometry for the θ–2θ configuration is equivalent. The X-ray tube, monochromator and collimator assembly are all mounted on the primary side. The incident-beam assembly rotates about the instrument centre and makes an incident angle θ_1 to the sample surface. The first main axis is also called the θ_1 axis. The diffracted beams travel in all directions and some are intercepted by a 2D detector. The detector is mounted on the other main axis, θ_2. The detector position is determined by the sample-to-detector distance D and the detector swing angle α ($= \theta_1 + \theta_2$).

All the components and space between the focal spot of the X-ray tube and sample are collectively referred to as the primary beam path. The primary beam path in a 2D-XRD system is typically sheltered by optical components except between the exit of the collimator and the sample. The X-rays travelling through this open incident-beam path are scattered by the air with two adverse effects. One is the attenuation of the primary beam intensity. The more harmful effect is that the scattered X-rays travel in all directions and some reach the detector, as is shown by the dashed lines with arrows in Fig. 2.5.9. This air scatter introduces a background over the diffraction pattern. Weak diffraction patterns may be buried under the background. Obviously, the air scatter from the incident beam is significantly stronger than that from diffracted X-rays. The intensity of the air scatter from the incident beam is proportional to the length of the open incident-beam path. The effect of air scatter also depends on the wavelength of the X-rays. The longer the wavelength is, the more severe is the air scatter. The secondary beam path is the space between the sample and the 2D detector. The diffracted X-rays are also scattered by air and the diffraction pattern is both attenuated and blurred by the air scattering. In a conventional diffractometer, one can use an anti-scatter slit, diffracted-beam monochromator or detector Soller slits to remove most of the air scatter that is not travelling in the diffracted-beam direction. These measures cannot be used for a 2D-XRD system, which requires an open space between the sample and the 2D detector. Therefore, the open incident-beam path should be kept as small as possible. In order to reduce the air attenuation and air scatter of the incident beam, a helium-purged beam path or a vacuum beam path are sometimes used in a diffractometer. The air scatter from the diffracted X-rays is relatively weak and the effect depends on sample-to-detector distance. It is typically not necessary to take measures to remove air scatter from the diffracted X-rays between the sample and 2D detector if the sample-to-detector distance is 30 cm or less with Cu $K\alpha$ radiation. However, if the sample-to-detector distance is larger than 30 cm or longer-wavelength radiation, such as Co $K\alpha$ or Cr $K\alpha$, is used, it is then necessary to use an He beam path or vacuum beam path to reduce the air scatter.

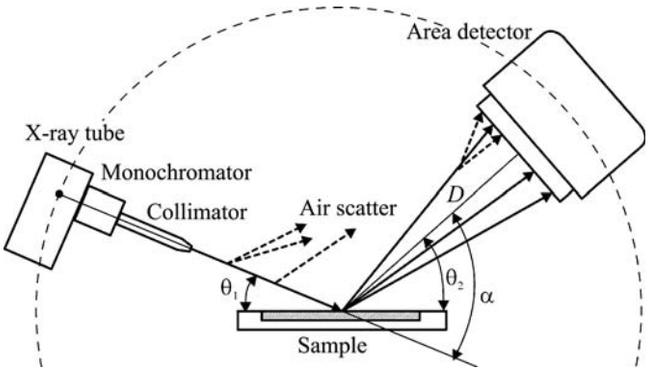

Figure 2.5.9
X-ray beam path in a two-dimensional X-ray diffraction system.

2.5.3.1.2. *Liouville's theorem*

Liouville's theorem can be used to describe the nature of the X-ray source, the X-ray optics and the coupling of the source and optics (Arndt, 1990). Liouville's theorem can be stated in a variety of ways, but for X-ray optics the best known form is

$$S_1\alpha = S_2\beta, \tag{2.5.14}$$

where S_1 is the effective size of the X-ray source and α is the capture angle determined by the effective size of the X-ray optics and the distance between the source and optics. S_2 is the size of the image focus. β is the convergence angle of the X-ray beam from the optics, which is also determined by the effective size of the X-ray optics and the distance between the optics and the image focus. The β angle is also called the crossfire of the X-ray beam. S_2 and β are typically determined by experimental requirements such as beam size and divergence. Therefore, the product $S_1\alpha$ is also determined by experimental conditions. In another expression of Liouville's theorem, the space volume containing the X-ray photons cannot be reduced with time along the trajectories of the system. Therefore, the brilliance of an X-ray source cannot be increased by optics, but may be reduced because of the loss of X-ray photons passing through the optics. In practice, no optics can have 100% reflectivity or transmission.

Considering this, Liouville's theorem given in equation (2.5.14) should be expressed as

$$S_1\alpha \leq S_2\beta. \tag{2.5.15}$$

This states that the product of the divergence and image size can be equal to or greater than the product of the capture angle and source size. If the X-ray source is a point with zero area, the focus image from focusing optics or the cross section of a parallel beam can be any chosen size. For focusing optics, the source size must be considerably smaller than the output beam size in order to achieve a gain in flux. In this case, the flux gain is from the increased capture angle. For parallel optics, the divergence angle β is infinitely small by definition, so it is necessary to use an X-ray source as small as possible to achieve a parallel beam. Focusing optics have an advantage over parallel optics in terms of beam flux. Using an X-ray beam with a divergence much smaller than the mosaicity of the specimen crystal does not improve the resolution, but does sacrifice diffraction intensity. For many X-ray diffraction applications with polycrystalline materials, a large crossfire is acceptable as long as the diffraction peaks concerned can be resolved. The improved peak profile and counting statistics can most often compensate for the peak broadening due to large crossfire.

2.5.3.1.3. *X-ray source*

A variety of X-ray sources, from sealed X-ray tubes and rotating-anode generators to synchrotron radiation, can be used for 2D powder diffraction. The history and principles of X-ray generation can be found in many references (Klug & Alexander, 1974; Cullity, 1978). The X-ray beam intensity depends on the X-ray optics, the focal-spot brightness and the focal-spot profile. The focal-spot brightness is determined by the maximum target loading per unit area of the focal spot, also referred to as the specific loading. A microfocus sealed tube (Bloomer & Arndt, 1999; Wiesmann *et al.*, 2007), which has a very small focal spot size (10–50 µm), can deliver a brilliance as much as one to two orders of magnitude higher than a conventional fine-focus sealed tube. The tube, which is also called a 'microsource', is typically air cooled because the X-ray generator power is less than 50 W. The X-ray optics for a microsource, either a multilayer mirror or a polycapillary, are typically mounted very close to the focal spot so as to maximize the gain on the capture angle. A microsource is highly suitable for 2D-XRD because of its spot focus and high brilliance.

If the X-rays used for diffraction have a wavelength slightly shorter than the *K* absorption edge of the sample material, a significant amount of fluorescent radiation is produced, which spreads over the diffraction pattern as a high background. In a conventional diffractometer with a point detector, the fluorescent background can be mostly removed by either a receiving monochromator mounted in front of the detector or by using a point detector with sufficient energy resolution. However, it is impossible to add a monochromator in front of a 2D detector and most area detectors have insufficient energy resolution. In order to avoid intense fluorescence, the wavelength of the X-ray-tube $K\alpha$ line should either be longer than the *K* absorption edge of the sample or far away from the *K* absorption edge. For example, Cu $K\alpha$ should not be used for samples containing significant amounts of the elements iron or cobalt. Since the $K\alpha$ line of an element cannot excite fluorescence of the same element, it is safe to use an anode of the same metallic element as the sample if the X-ray tube is available, for instance Co $K\alpha$ for Co samples. In general, intense fluorescence is produced when the atomic number of the anode material is 2, 3, or 4 larger than that of an element in the sample. When the sample contains Co, Fe or Mn (or Ni or Cu), the use of Cu $K\alpha$ radiation should be avoided; similarly, one should avoid using Co $K\alpha$ radiation if the sample contains Mn, Cr or V, and avoid using Cr $K\alpha$ radiation if the sample contains Ti, Sc or Ca. The effect is reduced when the atomic-number difference increases.

2.5.3.1.4. *X-ray optics*

The function of the X-ray optics is to condition the primary X-ray beam into the required wavelength, beam focus size, beam profile and divergence. Since the secondary beam path in a 2D-XRD system is an open space, almost all X-ray optics components are on the primary side. The X-ray optics components commonly used for 2D-XRD systems include a β-filter, a crystal monochromator, a pinhole collimator, cross-coupled multilayer mirrors, a Montel mirror, a polycapillary and a monocapillary. Detailed descriptions of these optic devices can be found in Chapter 2.1. In principle, the cross-sectional shape of the X-ray beam used in a 2D diffraction system should be small and round. In data-analysis algorithms, the beam size is typically considered to be a point. In practice, the beam cross section can be either round, square or another shape with a limited size. Such an X-ray beam is typically collimated or conditioned by the X-ray optics in two perpendicular directions, so that the X-ray optics used for the point beam are often called 'two-dimensional X-ray optics'.

A pinhole collimator is normally used to control the beam size and divergence in addition to other optic devices. The choice of beam size is often a trade-off between intensity and the ability to illuminate small regions or resolve closely spaced sample features. Smaller beam sizes, such as 50 µm and 100 µm, are preferred for microdiffraction and large beam sizes, such as 0.5 mm or 1 mm, are typically used for quantitative analysis, or texture or crystallinity measurements. In the case of quantitative analysis and texture measurements, using too small a collimator can actually be a detriment, causing poor grain-sampling statistics. The smaller the collimator, the longer the data-collection time. The beam divergence is typically determined by both the collimator and the coupling optic device. Lower divergence is typically associated with a long beam path. At the same time, the beam flux is inversely proportional to the square of the distance between the source and the sample. There are two main factors determining the length of the primary beam path: the first is the required distance for collimating the beam into the required divergence, the second is the space required for the primary X-ray optics, the sample stage and the detector. On the condition that the above two factors are satisfied, the primary X-ray beam path should be kept as short as possible.

2.5.3.2. *2D detector*

Two-dimensional (2D) detectors, also referred to as area detectors, are the core of 2D-XRD. The advances in area-detector technologies have inspired applications both in X-ray imaging and X-ray diffraction. A 2D detector contains a two-dimensional array of detection elements which typically have identical shape, size and characteristics. A 2D detector can simultaneously measure both dimensions of the two-dimensional distribution of the diffracted X-rays. Therefore, a 2D detector may also be referred to as an X-ray camera or imager. There are many technologies for area detectors (Arndt, 1986; Krause & Phillips, 1992; Eatough *et al.*, 1997; Giomatartis, 1998; Westbrook,

1999; Durst *et al.*, 2002; Blanton, 2003; Khazins *et al.*, 2004). X-ray photographic plates and films were the first generation of two-dimensional X-ray detectors. Now, multiwire proportional counters (MWPCs), image plates (IPs), charge-coupled devices (CCDs) and microgap detectors are the most commonly used large area detectors. Recent developments in area detectors include X-ray pixel array detectors (PADs), silicon drift diodes (SDDs) and complementary metal-oxide semiconductor (CMOS) detectors (Ercan *et al.*, 2006; Lutz, 2006; Yagi & Inoue, 2007; He *et al.*, 2011). Each detector type has its advantages over the other types. In order to make the right choice of area detector for a 2D-XRD system and applications, it is necessary to characterize area detectors with consistent and comparable parameters. Chapter 2.1 has more comprehensive coverage on X-ray detectors, including area detectors. This section will cover the characteristics specifically relevant to area detectors.

2.5.3.2.1. *Active area and pixel size*

A 2D detector has a limited detection surface and the detection surface can be spherical, cylindrical or flat. The detection-surface shape is also determined by the detector technology. For example, a CCD detector is made from a large semiconductor wafer, so that only a flat CCD is available, while an image plate is flexible so that it is easily bent to a cylindrical shape. The area of the detection surface, also referred to as the active area, is one of the most important parameters of a 2D detector. The larger the active area of a detector, the larger the solid angle that can be covered at the same sample-to-detector distance. This is especially important when the instrumentation or sample size forbid a short sample-to-detector distance. The active area is also limited by the detector technology. For instance, the active area of a CCD detector is limited by the semiconductor wafer size and fabrication facility. A large active area can be achieved by using a large demagnification optical lens or fibre-optical lens. Stacking several CCD chips side-by-side to build a so-called mosaic CCD detector is another way to achieve a large active area.

In addition to the active area, the overall weight and dimensions are also very important factors in the performance of a 2D detector. The weight of the detector has to be supported by the goniometer, so a heavy detector means high demands on the size and power of the goniometer. In a vertical configuration, a heavy detector also requires a heavy counterweight to balance the driving gear. The overall dimensions of a 2D detector include the height, width and depth. These dimensions determine the manoeuvrability of the detector within a diffractometer, especially when a diffractometer is loaded with many accessories, such as a video microscope and sample-loading mechanism. Another important parameter of a 2D detector that tends to be ignored by most users is the blank margin surrounding the active area of the detector. Fig. 2.5.10 shows the relationship between the maximum measurable 2θ angle and the detector blank margin. For high 2θ angle measurements, the detector swing angle is set so that the incident X-ray optics are set as closely as possible to the detector. The unmeasurable blank angle is the sum of the detector margin m and the dimension from the incident X-ray beam to the outer surface of the optic device h. The maximum measurable angle is given by

$$2\theta_{\max} = \pi - \frac{m+h}{D}. \qquad (2.5.16)$$

It can be seen that either reducing the detector blank margin or optics blank margin can increase the maximum measurable angle.

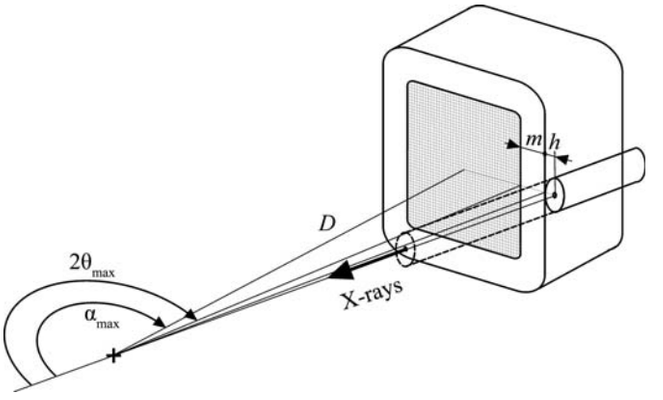

Figure 2.5.10
Detector dimensions and maximum measurable 2θ.

The solid angle covered by a pixel in a flat detector is dependent on the sample-to-detector distance and the location of the pixel in the detector. Fig. 2.5.11 illustrates the relationship between the solid angle covered by a pixel and its location in a flat area detector. The symbol S may represent a sample or a calibration source at the instrument centre. The distance between the sample S and the detector is D. The distance between any arbitrary pixel $P(x, y)$ and the detector centre pixel $P(0, 0)$ is r. The pixel size is Δx and Δy (assuming $\Delta x = \Delta y$). The distance between the sample S and the pixel is R. The angular ranges covered by this pixel are $\Delta\alpha$ and $\Delta\beta$ in the x and y directions, respectively. The solid angle covered by this pixel, $\Delta\Omega$, is then given as

$$\Delta\Omega = \Delta\alpha\Delta\beta = \frac{D}{R^3}\Delta y\Delta x = \frac{D}{R^3}\Delta A, \qquad (2.5.17)$$

where $\Delta A = \Delta x\Delta y$ is the area of the pixel and R is given by

$$R = (D^2 + x^2 + y^2)^{1/2} = (D^2 + r^2)^{1/2}. \qquad (2.5.18)$$

When a homogeneous calibration source is used, the flux to a pixel at $P(x, y)$ is given as

$$F(x, y) = \Delta\Omega B = \frac{\Delta ADB}{R^3} = \frac{\Delta ADB}{(D^2 + x^2 + y^2)^{3/2}}, \qquad (2.5.19)$$

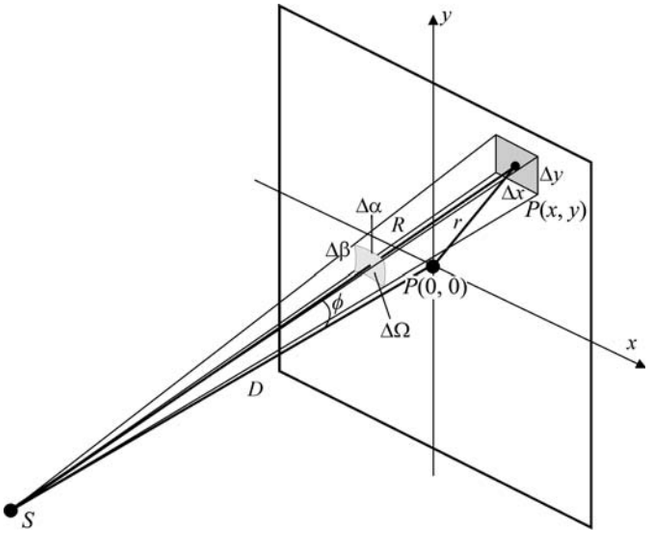

Figure 2.5.11
Solid angle covered by each pixel and its location on the detector.

where $F(x, y)$ is the flux (in photons s^{-1}) intercepted by the pixel and B is the brightness of the source (in photons s^{-1} $mrad^{-2}$) or scattering from the sample. The ratio of the flux in pixel $P(x, y)$ to that in the centre pixel $P(0, 0)$ is then given as

$$\frac{F(x, y)}{F(0, 0)} = \frac{D^3}{R^3} = \frac{D^3}{(D^2 + x^2 + y^2)^{3/2}} = \cos^3\phi, \qquad (2.5.20)$$

where ϕ is the angle between the X-rays to the pixel $P(x, y)$ and the line from S to the detector in perpendicular direction. It can be seen that the greater the sample-to-detector distance, the smaller the difference between the centre pixel and the edge pixel in terms of the flux from the homogeneous source. This is the main reason why a data frame collected at a short sample-to-detector distance has a higher contrast between the edge and centre than one collected at a long sample-to-detector distance.

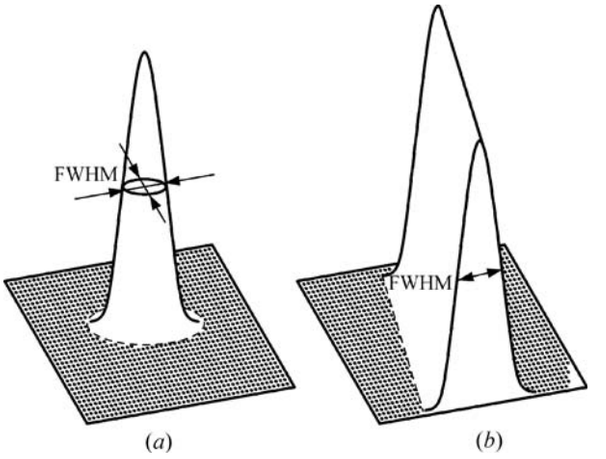

Figure 2.5.12
(*a*) Point-spread function (PSF) from a parallel point beam; (*b*) line-spread function (LSF) from a sharp line beam.

2.5.3.2.2. *Spatial resolution of area detectors*

In a 2D diffraction frame, each pixel contains the X-ray intensity collected by the detector corresponding to the pixel element. The pixel size of a 2D detector can be determined by or related to the actual feature sizes of the detector structure, or artificially determined by the readout electronics or data-acquisition software. Many detector techniques allow multiple settings for variable pixel size, for instance a frame of 2048 × 2048 pixels or 512 × 512 pixels. Then the pixel size in 512 mode is 16 (4 × 4) times that of a pixel in 2048 mode. The pixel size of a 2D detector determines the space between two adjacent pixels and also the minimum angular steps in the diffraction data, therefore the pixel size is also referred to as pixel resolution.

The pixel size does not necessarily represent the true spatial resolution or the angular resolution of the detector. The resolving power of a 2D detector is also limited by its point-spread function (PSF) (Bourgeois *et al.*, 1994). The PSF is the two-dimensional response of a 2D detector to a parallel point beam smaller than one pixel. When the sharp parallel point beam strikes the detector, not only does the pixel directly hit by the beam record counts, but the surrounding pixels may also record some counts. The phenomenon is observed as if the point beam has spread over a certain region adjacent to the pixel. In other words, the PSF gives a mapping of the probability density that an X-ray photon is recorded by a pixel in the vicinity of the point where the X-ray beam hits the detector. Therefore, the PSF is also referred to as the spatial redistribution function. Fig. 2.5.12(*a*) shows the PSF produced from a parallel point beam. A plane at half the maximum intensity defines a cross-sectional region within the PSF. The FWHM can be measured at any direction crossing the centroid of the cross section. Generally, the PSF is isotropic, so the FWHMs measured in any direction should be the same.

Measuring the PSF directly by using a small parallel point beam is difficult because the small PSF spot covers a few pixels and it is hard to establish the distribution profile. Instead, the line-spread function (LSF) can be measured with a sharp line beam from a narrow slit (Ponchut, 2006). Fig. 2.5.12(*b*) is the intensity profile of the image from a sharp line beam. The LSF can be obtained by integrating the image from the line beam along the direction of the line. The FWHM of the integrated profile can be used to describe the LSF. Theoretically, LSF and PSF profiles are not equivalent, but in practice they are not distinguished and may be referenced by the detector specification interchangeably. For accurate LSF measurement, the line beam is intentionally positioned with a tilt angle from the orthogonal direction of the pixel array so that the LSF can have smaller steps in the integrated profile (Fujita *et al.*, 1992).

The RMS (root-mean-square) of the distribution of counts is another parameter often used to describe the PSF. The normal distribution, also called the Gaussian distribution, is the most common shape of a PSF. The RMS of a Gaussian distribution is its standard deviation, σ. Therefore, the FWHM and RMS have the following relation, assuming that the PSF has a Gaussian distribution:

$$\text{FWHM} = 2[-2\ln(1/2)]^{1/2}\text{RMS} = 2.3548 \times \text{RMS}. \qquad (2.5.21)$$

The values of the FWHM and RMS are significantly different, so it is important to be precise about which parameter is used when the value is given for a PSF.

For most area detectors, the pixel size is smaller than the FWHM of the PSF. The pixel size should be small enough that at least a 50% drop in counts from the centre of the PSF can be observed by the pixel adjacent to the centre pixel. In practice, an FWHM of 3 to 6 times the pixel size is a reasonable choice if use of a smaller pixel does not have other detrimental effects. A further reduction in pixel size does not necessarily improve the resolution. Some 2D detectors, such as pixel-array detectors, can achieve a single-pixel PSF. In this case, the spatial resolution is determined by the pixel size.

2.5.3.2.3. *Detective quantum efficiency and energy range*

The detective quantum efficiency (DQE), also referred to as the detector quantum efficiency or quantum counting efficiency, is measured by the percentage of incident photons that are converted by the detector into electrons that constitute a measurable signal. For an ideal detector, in which every X-ray photon is converted to a detectable signal without additional noise added, the DQE is 100%. The DQE of a real detector is less than 100% because not every incident X-ray photon is detected, and because there is always some detector noise. The DQE is a parameter defined as the square of the ratio of the output and input signal-to-noise ratios (SNRs) (Stanton *et al.*, 1992):

$$\text{DQE} = \left(\frac{(S/N)_{\text{out}}}{(S/N)_{\text{in}}}\right)^2. \qquad (2.5.22)$$

The DQE of a detector is affected by many variables, for example the X-ray photon energy and the counting rate. The dependence of the DQE on the X-ray photon energy defines the

energy range of a detector. The DQE drops significantly if a detector is used out of its energy range. For instance, the energy range of MWPC and microgap detectors is about 3 to 15 keV. The DQE with Cu $K\alpha$ radiation (8.06 keV) is about 80%, but drops gradually when approaching the lower or higher energy limits. The energy range of imaging plates is much wider (4–48 keV). The energy range of a CCD, depending on the phosphor, covers from 5 keV up to the hard X-ray region.

2.5.3.2.4. *Detection limit and dynamic range*

The detection limit is the lowest number of counts that can be distinguished from the absence of true counts within a specified confidence level. The detection limit is estimated from the mean of the noise, the standard deviation of the noise and some confidence factor. In order to have the incoming X-ray photons counted with a reasonable statistical certainty, the counts produced by the X-ray photons should be above the detector background-noise counts.

The dynamic range is defined as the range extending from the detection limit to the maximum count measured in the same length of counting time. The linear dynamic range is the dynamic range within which the maximum counts are collected within the specified linearity. For X-ray detectors, the dynamic range most often refers to linear dynamic range, since only a diffraction pattern collected within the linear dynamic range can be correctly interpreted and analysed. When the detection limit in count rate approaches the noise rate at extended counting time, the dynamic range can be approximated by the ratio of the maximum count rate to the noise rate.

Dynamic range is very often confused with the maximum count rate, but must be distinguished. With a low noise rate, a detector can achieve a dynamic range much higher than its count rate. For example, if a detector has a maximum linear count rate of 10^5 s^{-1} with a noise rate of 10^{-3} s^{-1}, the dynamic range can approach 10^8 for an extended measurement time. The dynamic range for a 2D detector has the same definition as for a point detector, except that with a 2D detector the whole dynamic range extending from the detection limit to the maximum count can be observed from different pixels simultaneously. In order to record the entire two-dimensional diffraction pattern, it is necessary for the dynamic range of the detector to be at least the dynamic range of the diffraction pattern, which is typically in the range 10^2 to 10^6 for most applications. If the range of reflection intensities exceeds the dynamic range of the detector, then the detector will either saturate or have low-intensity patterns truncated. Therefore, it is desirable that the detector has as large a dynamic range as possible.

2.5.3.2.5. *Types of 2D detectors*

2D detectors can be classified into two broad categories: photon-counting detectors and integrating detectors (Lewis, 1994). Photon-counting area detectors can detect a single X-ray photon entering the active area. In a photon-counting detector, each X-ray photon is absorbed and converted to an electrical pulse. The number of pulses counted per unit time is proportional to the incident X-ray flux. Photon-counting detectors typically have high counting efficiency, approaching 100% at low count rate. The most commonly used photon-counting 2D detectors include MWPCs, Si-pixel arrays and microgap detectors. Integrating area detectors, also referred to as analogue X-ray imagers, record the X-ray intensity by measuring the analogue electrical signals converted from the incoming X-ray flux. The signal size of each pixel is proportional to the fluence of incident X-rays. The most commonly used integrating 2D detectors include image plates (IPs) and charge-coupled devices (CCDs).

The selection of an appropriate 2D detector depends on the X-ray diffraction application, the sample condition and the X-ray beam intensity. In addition to geometry features, such as the active area and pixel format, the most important performance characteristics of a detector are its sensitivity, dynamic range, spatial resolution and background noise. The detector type, either photon-counting or integrating, also leads to important differences in performance. Photon-counting 2D detectors typically have high counting efficiency at low count rate, while integrating 2D detectors are not so efficient at low count rate because of the relatively high noise background. An MWPC has a high DQE of about 0.8 when exposed to incoming local fluence from single photons up to about 10^3 photons s^{-1} mm^{-2}. The diffracted X-ray intensities from a polycrystalline or powder sample with a typical laboratory X-ray source fall into this fluence range. This is especially true with microdiffraction, where high sensitivity and low noise are crucial to reveal the weak diffraction pattern. Owing to the counting losses at a high count rate, the DQE of an MWPC decreases with increasing count rate and quickly saturates above 10^3 photons s^{-1} mm^{-2}. Therefore, an MWPC is not suitable for collecting strong diffraction patterns or for use with high intensity sources, such as synchrotron X-ray sources. An IP can be used in a large fluence range from 10 photons s^{-1} mm^{-2} and up with a DQE of 0.2 or lower. An IP is suitable for strong diffraction from single crystals with high-intensity X-ray sources, such as a rotating-anode generator or synchrotron X-ray source. With weak diffraction signals, the image plate cannot resolve the diffraction data near the noise floor. A CCD detector can also be used over a large X-ray fluence range from 10 photons s^{-1} mm^{-2} to very high fluence with a much higher DQE of 0.7 or higher. It is suitable for collecting diffraction of medium to strong intensity from single-crystal or polycrystalline samples. Owing to the relatively high sensitivity and high local count rate, CCDs can be used in systems with either sealed-tube X-ray sources, rotating-anode generators or synchrotron X-ray sources. With a low DQE at low fluence and the presence of dark-current noise, a CCD is not a good choice for applications with weak diffraction signals. A microgap detector has the best combination of high DQE, low noise and high count rate. It has a DQE of about 0.8 at an X-ray fluence from single photons up to about 10^5 photons s^{-1} mm^2. It is suitable for microdiffraction when high sensitivity and low noise are crucial to reveal weak diffraction patterns. It can also handle high X-ray fluence from strong diffraction patterns or be used with high-intensity sources, such as rotating-anode generators or synchrotron X-ray sources.

2.5.3.3. *Data corrections and integration*

2D diffraction patterns contain abundant information. In order to interpret and analyse 2D patterns accurately it is necessary to apply some data-treatment processes (Sulyanov *et al.*, 1994; Scheidegger *et al.*, 2000; Cervellino *et al.*, 2006; Boesecke, 2007; Rowe, 2009). Most data-treatment processes can be categorized as having one of the following four purposes: to eliminate or reduce errors caused by detector defects; to remove undesirable effects of instrument and sample geometry; to transfer a 2D frame into a format such that the data can be presented or further analysed by conventional means and software; and cosmetic treatment, such as smoothing a frame for reports and publications.

2.5.3.3.1. *Nonuniform response correction*

A 2D detector can be considered as an array of point detectors. Each pixel may have its own response, and thus a 2D detector may exhibit some nonuniformity in intensity measurement when exposed to an isotropic source. The nonuniform response can be caused by manufacturing defects, inadequate design or limitations of the detector technology. For instance, a nonuniform phosphor screen or coupling fibre optic for a CCD detector may cause nonuniformity in quantum efficiency (Tate *et al.*, 1995). A gas-filled detector may have a different intensity response between the detector edge and centre due to the variation in the electric field from the centre to the edge. A thorough correction to the nonuniformity of the intensity response can be performed if the detector counting curves of all pixels are given. In practice, this is extremely difficult or impossible, because the behaviour of a pixel may be affected by the condition of the adjacent pixels and the whole detector. The practical way to correct the nonuniformity of the intensity response is to collect an X-ray image from an isotropic point source at the instrument centre and use the image data frame to generate a correction table for the future diffraction frames. The frame collected with the isotropic source is commonly referred to as a 'flood-field' frame or a flat-field image, and the correction is also called a flood-field correction or flat-field correction (Stanton *et al.*, 1992). Another type of correction for a nonuniform response is background correction. Background correction is done by subtracting a background frame from the data frame. The background frame is collected without X-ray exposure. Integrating detectors, such as image plates or CCDs, have a strong background which must be considered in nonuniform response correction. Photon-counting detectors, such as MWPC and microgap detectors, have negligible background, so background correction is not necessary.

The X-ray source for calibration for flood-field correction should be a uniform, spherically radiating point source. Identical brightness should be observed at any pixel on the detector. The radiation strength of the source should match the intensity of the diffraction data to be collected. The photon energy of the source should be the same as or close to the X-ray beam used for diffraction-data collection so that the detector behaves the same way during calibration and data collection.

There are many choices of calibration sources, including X-ray tubes, radioactive sources, diffuse scattering or X-ray fluorescence. The radioactive source Fe-55 (^{55}Fe) is the most commonly used calibration source for a diffraction system because of its major photon energy level of 5.9 keV. X-ray fluorescence is an alternative to a radioactive source. Fluorescence emission is generated by placing a fluorescent material into the X-ray beam. Fluorescence radiation is an isotopic point source if the irradiated area is a small point-like area. For example, Cu $K\alpha$ can produce intense fluorescence from materials containing significant amounts of iron or cobalt and Mo $K\alpha$ can produce intense fluorescence from materials containing yttrium. In order to avoid a high localized intensity contribution from X-ray diffraction, the fluorescent material should be amorphous, such as a glassy iron foil. An alternative to a glassy alloy foil is amorphous lithium borate glass doped with the selected fluorescent element up to a 10% concentration (Moy *et al.*, 1996).

There are many algorithms available for flood-field correction depending on the nature of the 2D detector. The correction is based on the flood-field frame collected from the calibration source. The simplest flood-field correction is to normalize the counts of all pixels to the same level assuming that all pixels have the same response curve. The corrected frame from an isotropic source is not flat, but maintains the $\cos^3 \phi$ falloff effect, which will be considered in the frame integration. For gas-filled detectors, such as MWPC and microgap detectors, the pixel intensity response is not independent, but is affected by X-ray exposure to surrounding pixels and the whole detector. Flood-field correction is carried out by applying a normalization factor to each pixel in which a 'rubber-sheet' kind of stretching and shrinking in regions along the x and y detector axes slightly alters the size of each pixel (He, 2009). The total number of counts remains the same after the correction but is redistributed throughout the pixels so that the image from an isotropic source is uniformly distributed across the detector. The flood-field calibration must be done with the same sample-to-detector distance as for the diffraction-data collection.<

2.5.3.3.2. *Spatial correction*

In an ideal flat 2D detector, not only does each pixel have the same intensity response, but also an accurate position. The pixels are aligned in the x and y directions with equal spacing. In most cases we assume that the detective area is completely filled by pixels, so the distance between two neighbouring pixels is equivalent to the pixel size. The deviation from this perfect pixel array is called spatial distortion. The extent of spatial distortion is dependent on the nature and limitation of the detector technology. A CCD detector with 1:1 demagnification may have a negligible spatial distortion, but the barrel distortion in the coupling fibre-optic taper can introduce substantial spatial distortion. An image-plate system may have spatial distortion caused by imperfections in the scanning system (Campbell *et al.*, 1995). MWPC detectors typically exhibit more severe spatial distortion due to the window curvature and imperfections in the wire anode (Derewenda & Helliwell, 1989).

The spatial distortion is measured from X-ray images collected with a uniformly radiating point source positioned at the instrument centre and a fiducial plate fastened to the front surface of the detector. The source for spatial correction should have a very accurate position, point-like shape and small size. The fiducial plate is a metal plate with accurately distributed pinholes in the x and y directions. The X-ray image collected with this setup contains sharp peaks corresponding to the pinhole pattern of the fiducial plate. Since accurate positions of the peaks are given by the fiducial plate, the spatially corrected image is a projection of the collected image to this plane. Therefore, the detector plane is defined as the contacting plane between the fiducial plate and detector front face.

Spatial correction restores the spatially distorted diffraction frame into a frame with correct pixel positions. Many algorithms have been suggested for spatial correction (Sulyanov *et al.*, 1994; Tate *et al.*, 1995; Stanton *et al.*, 1992; Campbell *et al.*, 1995). In the spatially corrected frame each pixel is generated by computing the pixel count from the corresponding pixels based on a spatial-correction look-up table. In a typical spatial-correction process, an image containing the spots from the calibration source passing through the fiducial plate is collected. The distortion of the image is revealed by the fiducial spots. Based on the known positions of the corresponding pinholes in the fiducial plate, the distortion of each fiducial spot can be determined. The spatial correction for all pixels can be calculated and stored as a look-up table. Assuming that the detector behaves the same way in the real diffraction-data collection, the look-up table generated from the fiducial image can then be applied to the real diffraction frames.

The spatial calibration must be done at the same sample-to-detector distance as the diffraction-data collection.

2.5.3.3.3. *Frame integration*

2D frame integration is a data-reduction process which converts a two-dimensional frame into a one-dimensional intensity profile. Two forms of integration are generally of interest in the analysis of a 2D diffraction frame from polycrystalline materials: γ integration and 2θ integration. γ integration sums the counts in 2θ steps ($\Delta 2\theta$) along constant 2θ conic lines and between two constant γ values. γ integration produces a data set with intensity as a function of 2θ. 2θ integration sums the counts in γ steps ($\Delta\gamma$) along constant γ lines and between two constant 2θ conic lines. 2θ integration produces a data set with intensity as a function of γ. γ integration may also be carried out with the integration range in the vertical direction as a constant number of pixels. This type of γ integration may also be referred to as slice integration. A diffraction profile analogous to the conventional diffraction result can be obtained by either γ integration or slice integration over a selected 2θ range. Phase ID can then be done with conventional search/match methods. 2θ integration is of interest for evaluating the intensity variation along γ angles, such as for texture analysis, and is discussed in more depth in Chapter 5.3.

The γ integration can be expressed as

$$I(2\theta) = \int_{\gamma_1}^{\gamma_2} J(2\theta, \gamma)\, \mathrm{d}\gamma, \quad 2\theta_1 \leq 2\theta \leq 2\theta_2, \tag{2.5.23}$$

where $J(2\theta, \gamma)$ represents the two-dimensional intensity distribution in the 2D frame and $I(2\theta)$ is the integration result as a function of intensity *versus* 2θ. γ_1 and γ_2 are the lower limit and upper limit of integration, respectively, which are constants for γ integration. Fig. 2.5.13 shows a 2D diffraction frame collected from corundum (α-Al_2O_3) powder. The 2θ range is from 20 to 60° and the 2θ integration step size is 0.05°. The γ-integration range is from 60 to 120°. In order to reduce or eliminate the dependence of the integrated intensity on the integration interval, the integrated value at each 2θ step is normalized by the number of pixels, the arc length or the solid angle. γ integration with normalization by the solid angle can be expressed as

$$I(2\theta) = \frac{\int_{\gamma_1}^{\gamma_2} J(2\theta, \gamma)(\Delta 2\theta)\, \mathrm{d}\gamma}{\int_{\gamma_1}^{\gamma_2} (\Delta 2\theta)\, \mathrm{d}\gamma}, \quad 2\theta_1 \leq 2\theta \leq 2\theta_2. \tag{2.5.24}$$

Since the $\Delta 2\theta$ step is a constant, the above equation becomes

$$I(2\theta) = \frac{\int_{\gamma_1}^{\gamma_2} J(2\theta, \gamma)\, \mathrm{d}\gamma}{\gamma_2 - \gamma_1}, \quad 2\theta_1 \leq 2\theta \leq 2\theta_2. \tag{2.5.25}$$

There are many integration software packages and algorithms available for reducing 2D frames into 1D diffraction patterns for polycrystalline materials (Cervellino *et al.*, 2006; Rodriguez-Navarro, 2006; Boesecke, 2007). With the availability of tremendous computer power today, a relatively new method is the bin method, which treats pixels as having a continuous distribution in the detector. It demands more computer power than older methods, but delivers much more accurate and smoother results even with $\Delta 2\theta$ integration steps significantly smaller than the pixel size. Depending on the relative size of $\Delta 2\theta$ to the pixel size, each contributing pixel is divided into several 2θ 'bins'. The intensity counts of all pixels within the $\Delta 2\theta$ step are summarized. All the normalization methods in the above integration, either by pixel, arc or solid angle, result in an intensity

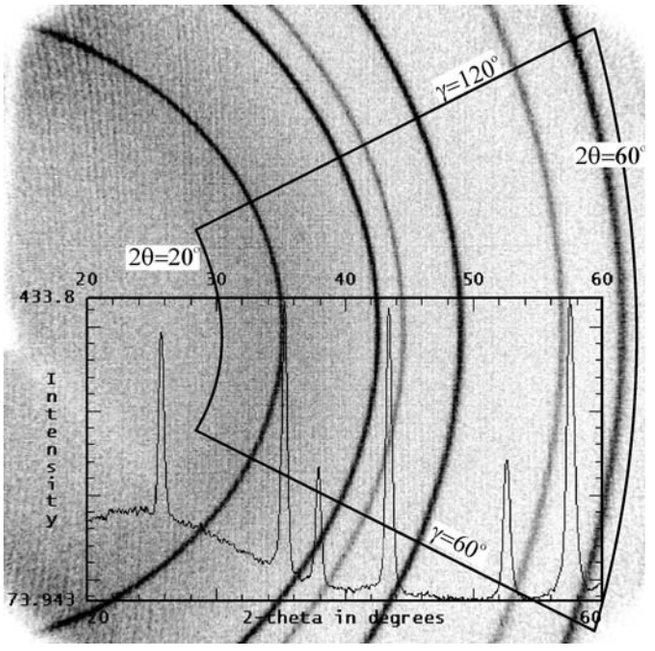

Figure 2.5.13
A 2D frame showing γ integration.

level of one pixel or unit solid angle. Since a pixel is much smaller than the active area of a typical point detector, the normalized integration tends to result in a diffraction pattern with fictitiously low intensity counts, even though the true counts in the corresponding $\Delta 2\theta$ range are significantly higher. In order to avoid this misleading outcome, it is reasonable to introduce a scaling factor. However, there is no accurate formula for making the integrated profile from a 2D frame comparable to that from a conventional point-detector scan. The best practice is to be aware of the differences and to try not to make direct comparisons purely based on misleading intensity levels. Generally speaking, for the same exposure time, the total counting statistics from a 2D detector are significantly better than from a 0D or 1D detector.

2.5.3.3.4. *Lorentz, polarization and absorption corrections*

Lorentz and polarization corrections may be applied to the diffraction frame to remove their effect on the relative intensities of Bragg peaks and background. The 2θ angular dependence of the relative intensity is commonly given as a Lorentz–polarization factor, which is a combination of Lorentz and polarization factors. In 2D diffraction, the polarization factor is a function of both 2θ and γ, therefore it should be treated in the 2D frames, while the Lorentz factor is a function of 2θ only. The Lorentz correction can be done either on the 2D frames or on the integrated profile. In order to obtain relative intensities equivalent to a conventional diffractometer with a point detector, reverse Lorentz and polarization corrections may be applied to the frame or integrated profile.

The Lorentz factor is the same as for a conventional diffractometer. For a sample with a completely random orientation distribution of crystallites, the Lorentz factor is given as

$$L = \frac{\cos\theta}{\sin^2 2\theta} = \frac{1}{4\sin^2\theta\cos\theta}. \tag{2.5.26}$$

The Lorentz factor may be given by a different equation for a different diffraction geometry (Klug & Alexander, 1974). The forward and reverse Lorentz corrections are exactly reciprocal

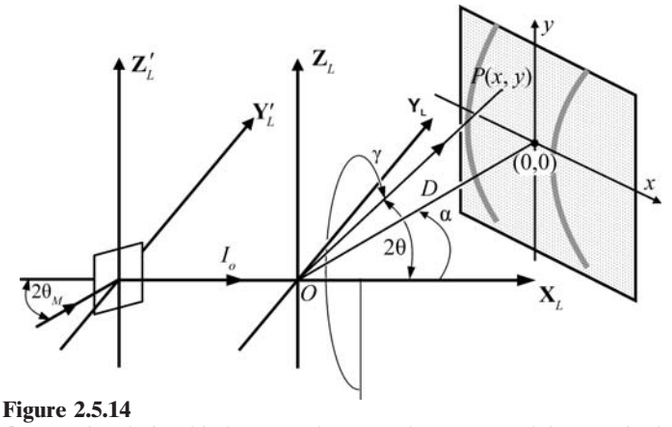

Figure 2.5.14
Geometric relationship between the monochromator and detector in the laboratory coordinates.

and effectively cancel each other. Therefore, it is not necessary to perform the Lorentz correction to the frame before integration if relative intensities equivalent to a conventional Bragg–Brentano diffractometer are expected. The Lorentz correction can be done on the integrated diffraction profiles in the same way as on the diffraction profiles collected with conventional diffractometers.

When a non-polarized X-ray beam is scattered by matter, the scattered X-rays are polarized. The intensity of the diffracted beam is affected by the polarization; this effect is expressed by the polarization factor. In two-dimensional X-ray diffraction the diffraction vectors of the monochromator diffraction and sample crystal diffraction are not necessarily in the same plane or perpendicular planes. Therefore, the overall polarization factor is a function of both 2θ and γ. Fig. 2.5.14 illustrates the geometric relationship between the monochromator and detector in the laboratory coordinates, X_L, Y_L, Z_L. The monochromator is located at the coordinates X_L, Y'_L, Z'_L, which is a translation of the laboratory coordinates along the X_L axis in the negative direction. The monochromator crystal is rotated about the Z'_L axis and $2\theta_M$ is the Bragg angle of the monochromator crystal. The diffracted beam from the monochromator propagates along the X_L direction. This is the incident beam to the sample located at the instrument centre O. The 2D detector location is given by the sample-to-detector distance D and swing angle α. The pixel $P(x, y)$ represents an arbitrary pixel on the detector. 2θ and γ are the corresponding diffraction-space parameters for the pixel. Since a monochromator or other beam-conditioning optics can only be used on the incident beam, the polarization factor for 2D-XRD can then be given as a function of both θ and γ:

$$P(\theta, \gamma) = \frac{(1 + \cos^2 2\theta_M \cos^2 2\theta)\sin^2\gamma + (\cos^2 2\theta_M + \cos^2 2\theta)\cos^2\gamma}{1 + \cos^2 2\theta_M}. \quad (2.5.27)$$

If the crystal monochromator rotates about the Y'_L axis, *i.e.* the incident plane is perpendicular to the diffractometer plane, the polarization factor for two-dimensional X-ray diffraction can be given as

$$P(\theta, \gamma) = \frac{(1 + \cos^2 2\theta_M \cos^2 2\theta)\cos^2\gamma + (\cos^2 2\theta_M + \cos^2 2\theta)\sin^2\gamma}{1 + \cos^2 2\theta_M}. \quad (2.5.28)$$

In the above equations, the term $\cos^2 2\theta_M$ can be replaced by $\left|\cos^n 2\theta_M\right|$ for different monochromator crystals. For a mosaic crystal, such as a graphite crystal, $n = 2$. For most real monochromator crystals, the exponent n takes a value between 1 and 2. For near perfect monochromator crystals, n approaches 1 (Kerr & Ashmore, 1974). All the above equations for polarization factors may apply to multilayer optics. However, since multilayer optics have very low Bragg angles, $\left|\cos^n 2\theta_M\right|$ approximates to unity. The γ dependence of the polarization factor diminishes in this case. The polarization factor approaches

$$P(\theta, \gamma) \simeq \frac{1 + \cos^2 2\theta}{2}. \quad (2.5.29)$$

2.5.3.3.5. *Air scatter*

X-rays are scattered by air molecules in the beam path between the X-ray source and detector. Air scatter results in two effects: one is the attenuation of the X-ray intensity, the other is added background in the diffraction pattern. Air scatter within the enclosed primary beam path – for instance, in the mirror, monochromator housing or collimator – results in attenuation of only the incident beam. The enclosed beam path can be purged by helium gas or kept in vacuum to reduce the attenuation so that no correction is necessary for this part of the air scatter. The open beam between the tip of the collimator and the sample generates an air-scatter background pattern, which is the major part of the air scatter. In the secondary beam path, the air scatter from the diffracted beam may generate background too, but the main effect of the air scatter is inhomogeneous attenuation of the diffraction pattern due to the different beam path lengths between the centre and the edge of the detector.

The background generated by air scattering from the open incident-beam path has a strong 2θ dependence. The specific scattering curve depends on the length of the open primary beam path, the beam size and the wavelength of the incident beam. There are two approaches to correct air scatter. One is to collect an air-scatter background frame under the same conditions as the diffraction frame except without a sample. The background frame is then subtracted from the diffraction frame. Another approach is to remove the background from the integrated profile, since the background is 2θ dependent.

The attenuation of the diffracted beam by air absorption depends on the distance between the sample and pixel. For a flat detector, air absorption can be corrected by

$$p_c(x, y) = p_o(x, y)\exp\left[\mu_{\text{air}}(D^2 + x^2 + y^2)^{1/2}\right], \quad (2.5.30)$$

where $p_o(x, y)$ is the original pixel intensity of the pixel $P(x, y)$ and $p_c(x, y)$ is the corrected intensity. The detector centre is given by (0, 0). μ_{air} is the linear absorption coefficient of air. The value of μ_{air} is determined by the radiation wavelength. By approximation, for air with 80% N_2 and 20% O_2 at sea level and at 293 K, $\mu_{\text{air}} = 0.01\ \text{cm}^{-1}$ for Cu $K\alpha$ radiation. Air scatter and absorption increases with increasing wavelength. For example, $\mu_{\text{air}} = 0.015\ \text{cm}^{-1}$ for Co $K\alpha$ radiation and $0.032\ \text{cm}^{-1}$ for Cr $K\alpha$ radiation. The absorption coefficient for Mo $K\alpha$ radiation, $\mu_{\text{air}} = 0.001\ \text{cm}^{-1}$, is only one-tenth of that for Cu $K\alpha$ radiation, so an air-absorption correction is not necessary. Alternatively, the absorption correction may be normalized to the absorption level in the beam centre as

$$p_c(x, y) = p_o(x, y)\exp\left\{\mu_{\text{air}}\left[(D^2 + x^2 + y^2)^{1/2} - D\right]\right\}. \quad (2.5.31)$$

In this normalized correction the attenuation by air scatter is not fully corrected for each pixel, but rather corrected to the same attenuation level as the pixel in the detector centre. This means that the effect of path-length differences between the detector centre pixel and other pixels are eliminated.

2.5.3.3.6. *Sample absorption*

The absorption of X-rays by the sample reduces the diffracted intensity. Many approaches are used to calculate and correct the absorption effect for various sample shapes and geometries [*International Tables for Crystallography* Volume C, Chapter 6.3 (Maslen, 1992); Ross, 1992; Pitschke *et al.*, 1996; Zuev, 2006]. The sample absorption can be measured by the transmission coefficient (also referred to as the absorption factor):

$$A = (1/V) \int_V \exp(-\mu\tau)\, \mathrm{d}V, \tag{2.5.32}$$

where A is the transmission coefficient, μ is the linear absorption coefficient and τ is the total beam path in the sample, which includes the incident-beam path and diffracted-beam path. Fig. 2.5.15(a) shows reflection-mode diffraction with a flat-plate sample. The thickness of the plate is t. z is the distance of the element dV from the sample surface. The normal to the reflection surface is **n**. The incident beam is represented by the unit vector $\mathbf{s}_o$ and the diffracted beam by the unit vector **s**. The transmission coefficient is given as (Maslen, 1992)

$$A = \frac{1 - \exp\{-\mu t[(1/\cos\eta) + (1/\cos\zeta)]\}}{\mu[(\cos\zeta/\cos\eta) + 1]}, \tag{2.5.33}$$

where η is the angle between the incident beam and the normal to the sample surface, and ζ is the angle between the diffracted beam and the sample normal. For two-dimensional X-ray diffraction, there is a single incident-beam direction at a time, but various diffracted-beam directions simultaneously, so

$$\cos\eta = \sin\omega\cos\psi \tag{2.5.34}$$

and

$$\cos\zeta = -\cos 2\theta \sin\omega\cos\psi - \sin 2\theta \sin\gamma\cos\omega\cos\psi - \sin 2\theta\cos\gamma\sin\psi. \tag{2.5.35}$$

The transmission coefficient from equation (2.5.33) contains a length unit, which creates ambiguity if such transmission coefficients are used to correct the intensity pixel-by-pixel. In order to make the relative intensity comparable to the results from Bragg–Brentano geometry, we introduce a new transmission coefficient, which is normalized by the transmission coefficient of the Bragg–Brentano geometry, $A_{\rm BB} = 1/(2\mu)$. This normalized transmission coefficient is also a numerical factor without units. The transmission coefficient with normalization will be denoted by T hereafter in this chapter. The transmission coefficient for reflection-mode diffraction with a flat sample of thickness t is then given as

$$T = A/A_{\rm BB} = \frac{2\cos\eta\big(1 - \exp\{-\mu t[(1/\cos\eta) + (1/\cos\zeta)]\}\big)}{\cos\eta + \cos\zeta}. \tag{2.5.36}$$

For a thick plate or material with a very high linear absorption coefficient, the transmission through the sample thickness is negligible and the above equation becomes

$$T = \frac{2\cos\eta}{\cos\eta + \cos\zeta}. \tag{2.5.37}$$

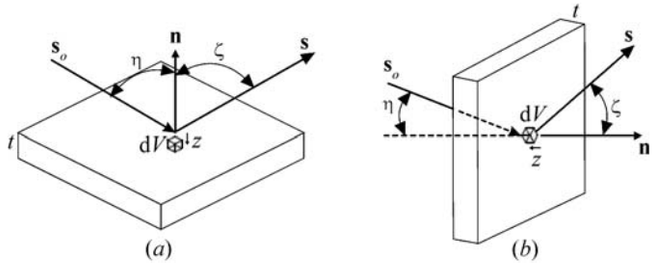

Figure 2.5.15
Absorption correction for a flat slab: (a) reflection; (b) transmission.

Fig. 2.5.15(b) shows transmission-mode diffraction with a flat-plate sample. The thickness of the plate is t. The normal to the reflection surface is represented by the unit vector **n**. The incident beam is represented by the unit vector $\mathbf{s}_o$ and the diffracted beam by the unit vector **s**. η is the angle between the incident beam and the normal of the sample surface, and ζ is the angle between the diffracted beam and the sample normal.

The transmission coefficient normalized by $A_{\rm BB} = 1/(2\mu)$ is given by (Maslen, 1992; Ross, 1992)

$$T = \frac{2\sec\eta[\exp(-\mu t\sec\eta) - \exp(-\mu t\sec\zeta)]}{\sec\zeta - \sec\eta} \quad \text{for } \sec\zeta \neq \sec\eta. \tag{2.5.38}$$

For two-dimensional X-ray diffraction in transmission mode

$$\cos\eta = \sin\omega\sin\psi\sin\varphi + \cos\omega\cos\varphi \tag{2.5.39}$$

and

$$\cos\zeta = (\sin\omega\sin\psi\sin\varphi + \cos\omega\cos\varphi)\cos 2\theta + (\cos\omega\sin\psi\sin\varphi - \sin\omega\cos\varphi)\sin 2\theta\sin\gamma - \cos\psi\sin\varphi\sin 2\theta\cos\gamma. \tag{2.5.40}$$

It is very common practice to set the incident angle perpendicular to the sample surface, *i.e.* $\eta = 0$. For most transmission-mode data collection, equation (2.5.40) becomes

$$T = \frac{2[\exp(-\mu t) - \exp(-\mu t\sec\zeta)]}{\sec\zeta - 1}. \tag{2.5.41}$$

When $\eta = \zeta$, both the numerator and denominator approach zero, and the transmission coefficient should be given by

$$T = 2\mu t\sec\zeta\exp(-\mu t\sec\zeta). \tag{2.5.42}$$

It is common practice to load the sample perpendicular to the incident X-ray beam at the goniometer angles $\omega = \psi = \varphi = 0$. Therefore, $\cos\eta = 1$ and $\cos\zeta = \cos 2\theta$, and the transmission coefficient becomes

$$T = \frac{2\cos 2\theta[\exp(-\mu t) - \exp(-\mu t/\cos 2\theta)]}{1 - \cos 2\theta}. \tag{2.5.43}$$

The maximum scattered intensity occurs when

$$t = \frac{\cos 2\theta\ln\cos 2\theta}{\mu(\cos 2\theta - 1)}. \tag{2.5.44}$$

This equation can be used to select the optimum sample thickness for transmission-mode diffraction. For example, if the measurement 2θ range is between 3 and 50°, the preferred sample thickness should be given by μt = 0.8–1.0.

2.5.4. Applications

2.5.4.1. *Phase identification*

In materials science, a phase is defined as a region that has uniform chemical composition and physical properties, including crystal structure. Therefore, every phase should give a unique diffraction pattern. A sample for X-ray diffraction may contain a single phase or multiple phases. Analysis of the diffraction pattern can accurately and precisely determine the contents of the sample. This qualitative analysis is called phase identification (phase ID). One of the most efficient methods of phase identification is to compare the diffraction pattern from an unknown material to those in a database of a large number of standard diffraction patterns. The most comprehensive database is the Powder Diffraction File (PDF), updated annually by the International Centre for Diffraction Data (ICDD).

Two-dimensional X-ray diffraction has enhanced phase identification in many respects (Rudolf & Landes, 1994; Sulyanov *et al.*, 1994; Hinrichsen, 2007). Because of its ability to collect diffracted X-rays in a large angular range in both the 2θ and γ directions, it can collect diffraction data with high speed and better sampling statistics than obtained by conventional diffraction. Owing to point-beam illumination on the sample, a relatively small sample size is required for phase identification. The large 2D detector allows for a large 2θ range to be analysed without any movement of the sample and detector. This makes it possible to perform *in situ* phase investigation on samples during phase transformations, chemical reactions and deformations. The diffraction information in the γ direction allows accurate phase identification of samples with large grains and preferred orientation.

In the Bragg–Brentano geometry, the 2θ resolution is controlled by the selection of the divergence slit and receiving slit in the diffractometer plane, and the axial divergence is controlled by Soller slits, while in a diffractometer with a 2D detector, the 2θ resolution is mainly determined by the spatial resolution of the detector and the sample-to-detector distance. The relative peak intensity in a diffraction pattern from a sample with texture measured with a 2D detector can be significantly different from the results measured with Bragg–Brentano geometry. It is imperative to study the nature of these discrepancies so that the diffraction patterns collected with 2D detectors can be used for phase ID with proper understanding and correction if necessary.

When two-dimensional diffraction is used for phase identification, the first step is to integrate the 2D diffraction frame into a diffraction profile resembling the diffraction pattern collected with a conventional diffractometer (Cervellino *et al.*, 2006; Rodriguez-Navarro, 2006; Boesecke, 2007; Fuentes-Montero *et al.*, 2011; Hammersley, 2016). The integrated diffraction profiles can be analysed with all existing algorithms and methods, including profile fitting with conventional peak shapes and fundamental parameters, quantification of phases, and lattice-parameter determination and refinement (Ning & Flemming, 2005; Flemming, 2007; Jabeen *et al.*, 2011). The results can be used to search a powder-diffraction database to find possible matches. Since there is a great deal of literature covering these topics (Cullity, 1978; Jenkins & Snyder, 1996; Pecharsky & Zavalij, 2003), this section will focus on the special characteristics of two-dimensional X-ray diffraction as well as system geometry, data-collection strategies and data analysis in dealing with relative peak intensities, 2θ resolution, grain size and distribution, and preferred orientation. Many factors and correction algorithms described here can help in understanding the characteristics of two-dimensional diffraction. In most applications, however, the γ-integrated profile can be used for phase identification without these corrections.

2.5.4.1.1. *Relative intensity*

The integrated intensity diffracted from polycrystalline materials with a random orientation distribution is given by

$$I_{hkl} = k_I \frac{p_{hkl}}{v^2}(\mathrm{LPA})\lambda^3 F_{hkl}^2 g_{hkl}(\alpha, \beta)\exp(-2M_t - 2M_s), \quad (2.5.45)$$

where k_I is an instrument constant that is a scaling factor between the experimental observed intensities and the calculated intensity, p_{hkl} is the multiplicity factor of the crystal plane (hkl), v is the volume of the unit cell, (LPA) is the Lorentz–polarization and absorption factors, λ is the X-ray wavelength, F_{hkl} is the structure factor for the crystal plane (hkl), $g_{hkl}(\alpha, \beta)$ is the normalized pole-density distribution function and $\exp(-2M_t - 2M_s)$ is the attenuation factor due to lattice thermal vibrations and weak static displacements (Warren, 1990; He *et al.*, 1994). Except for the texture effect, all the factors in the above equation are either discussed in the previous sections or have the same definitions and values as in conventional diffraction.

Phase-identification studies by XRD are preferably carried out on powders or polycrystalline samples with a random orientation distribution of crystallites. Preferred orientation causes relative intensities to deviate from theoretical calculations or those reported in reference databases. In practice, a sample with a perfectly random orientation distribution of crystallites is very hard to fabricate and most polycrystalline samples have a preferred orientation to a certain extent. Discrepancies in the relative peak intensities between conventional diffraction and 2D-XRD are largely due to texture effects. For B-B geometry, the diffraction vector is always perpendicular to the sample surface. With a strong texture, it is possible that the pole density of certain reflections in the sample normal direction is very low or even approaches zero. In this case, the peak does not appear in the diffraction pattern collected in B-B geometry. In 2D-XRD, several diffraction rings may be measured with a single incident beam; the corresponding diffraction vectors are not necessarily in the sample normal direction. The diffraction profiles from 2D frames are produced by γ integration, therefore the texture factor $g_{hkl}(\alpha, \beta)$ should be replaced by the average normalized pole-density function within the γ integration range $\langle g_{hkl}(\Delta\gamma)\rangle$. The relation between (α, β) and $(2\theta, \gamma)$ is given in Chapter 5.4. The chance of having zero pole density over the entire γ-integration range is extremely small. Therefore, phase identification with 2D-XRD is much more reliable than with conventional diffraction.

2.5.4.1.2. *Detector distance and resolution*

The 2θ resolution with B-B geometry is controlled by the size of the slits. Smaller apertures of the divergence slit are used for higher 2θ resolution and larger apertures for fast data collection. With a two-dimensional X-ray diffraction system, the 2θ resolution is achieved with different approaches. A flat 2D detector has the flexibility to be used at different sample-to-detector distances. The detector resolution is determined by the pixel size and point-spread function. For the same detector resolution and detector active area, a higher resolution can be achieved at larger distance, and higher angular coverage at shorter distance. The sample-to-detector distance should be optimized depending on the 2θ measurement range and required resolution. In situations where the 2θ range of one frame is not enough, several frames at

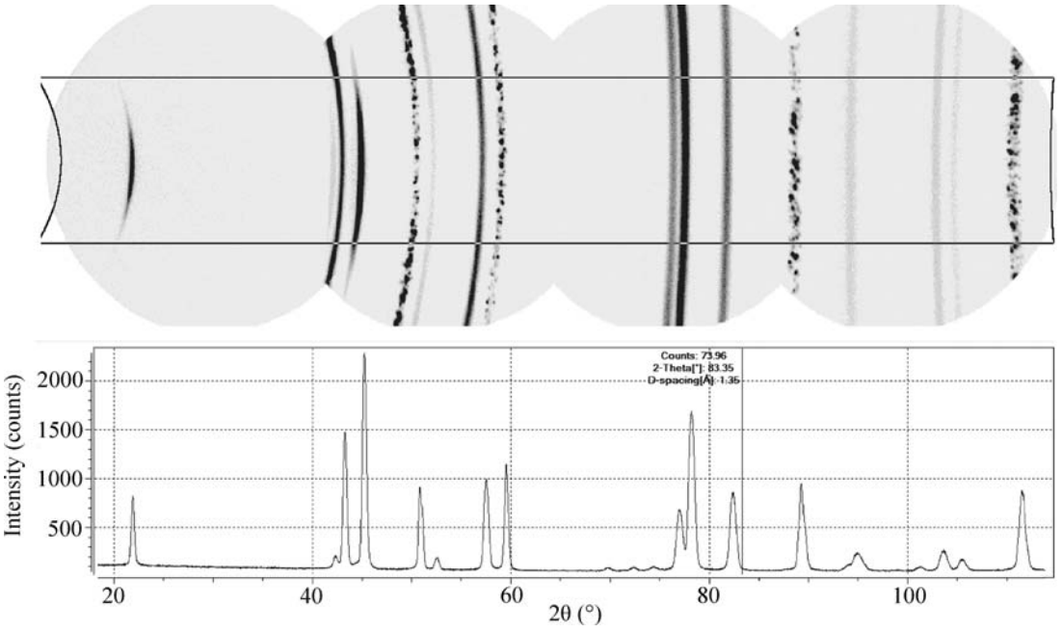

Figure 2.5.16
Diffraction pattern merged from four 2D frames collected from a battery material.

sequential 2θ ranges can be collected. The integrated profiles can then be merged to achieve a large 2θ range. Fig. 2.5.16 shows four 2D frames collected from a battery material with a microgap detector. The slice integration region is defined by two conic lines and two horizontal lines. The diffraction profile integrated from the merged frames is displayed below.

2.5.4.1.3. *Defocusing effect*

A 2D diffraction pattern over a range of 2θ is measured simultaneously with a single incident angle, so the incident angle has to be lower than the minimum 2θ angle. Since the reflected angle cannot always be the same as the incident angle, geometric aberrations are observed. The defocusing effect occurs when the incident angle is lower than the reflection angle. At low incident angles, the incident beam spreads over the sample surface into an area much larger than the size of the original X-ray beam. The observed diffracted beam size is magnified by the defocusing effect if the diffracted beam makes an angle larger than the incident angle. The defocusing effect for reflection-mode diffraction can be expressed as

$$\frac{B}{b} = \frac{\sin\theta_2}{\sin\theta_1} = \frac{\sin(2\theta - \omega)}{\sin\omega}, \qquad (2.5.46)$$

where θ_1 is the incident angle, b is the incident beam size and B is diffracted beam size. The ratio of B to b is a measurement of the geometric aberration and will be referred to as the defocusing factor. In principle, defocusing occurs only when B/b is larger than 1. The reflected beam is actually focused to the detector when $\theta_2 < \theta_1$. The defocusing effect occurs when $\theta_2 > \theta_1$ and the defocusing factor increases with increasing θ_2 or decreasing θ_1. The maximum defocusing appears at $\theta_2 = 90^\circ$. For the θ–2θ configuration, the incident angle $\omega\ (= \theta_1)$ is used in the equation.

For B-B geometry with a divergent slit and receiving slit of the same size the defocusing factor is always 1. With a 2D detector the defocusing factor varies with the 2θ angle. If a large 2θ range is measured on a flat sample in reflection mode, it is always desirable to collect several frames at different incident angles for each 2θ range so as to improve the 2θ resolution. A cylindrical detector may collect a diffraction pattern over a large 2θ range (Gelfi *et al.*, 2005). However, the defocusing effect prevents it from being used for a large 2θ range for a flat sample. Fig. 2.5.17 compares the effect for a flat detector and a cylindrical detector. Fig. 2.5.17(*a*) shows a cylindrical detector being used to collect a diffraction pattern from a flat sample for a 2θ range of 5 to 80°. The incident angle must be kept at 5° or lower. Fig. 2.5.17(*b*) shows a flat detector being used to collect the diffraction pattern over the same 2θ range. In order to minimize the defocusing effect, the data collection is done at four different incident angles (5, 15, 25 and 35°) with four corresponding detector swing angles (10, 30, 50 and 70°). Fig. 2.5.17(*c*) compares the defocusing factors of the two configurations. The horizontal dot-dashed line with defocusing factor $B/b = 1$ represents the situation with B-B geometry. The defocusing factor continues to increase with 2θ angle up to $B/b = 11$ for cylindrical detector. That means that the 2θ resolution would be 10 times worse than for the B-B geometry. For the diffraction pattern collected with a flat detector in four steps, the defocusing factor fluctuates above 1, with the worst value being less than 3. Another approach to avoiding defocusing is to collect the diffraction pattern in transmission mode. There is no defocusing effect in transmission when the incident beam is perpendicular to the sample surface. Therefore, the transmission pattern has significantly better 2θ resolution. Transmission-mode diffraction also has other advantages. For instance, the air scattering from the primary beam may be blocked by a flat sample, therefore lowering the background from air scattering. However, transmission-mode diffraction data can only be collected from samples with limited thickness, and the maximum scattering intensity is achieved at low 2θ angles with a sample thickness of $t = 1/\mu$, where μ is the linear absorption coefficient. The scattering intensity drops dramatically when the thickness increases.

2.5.4.1.4. *Sampling statistics*

In powder X-ray diffraction, the number of crystallites contributing to each reflection must be sufficiently large to generate reproducible integrated peak intensities (see Chapter 2.10). A larger number of contributing crystallites gives better precision or sampling statistics (also referred to as particle

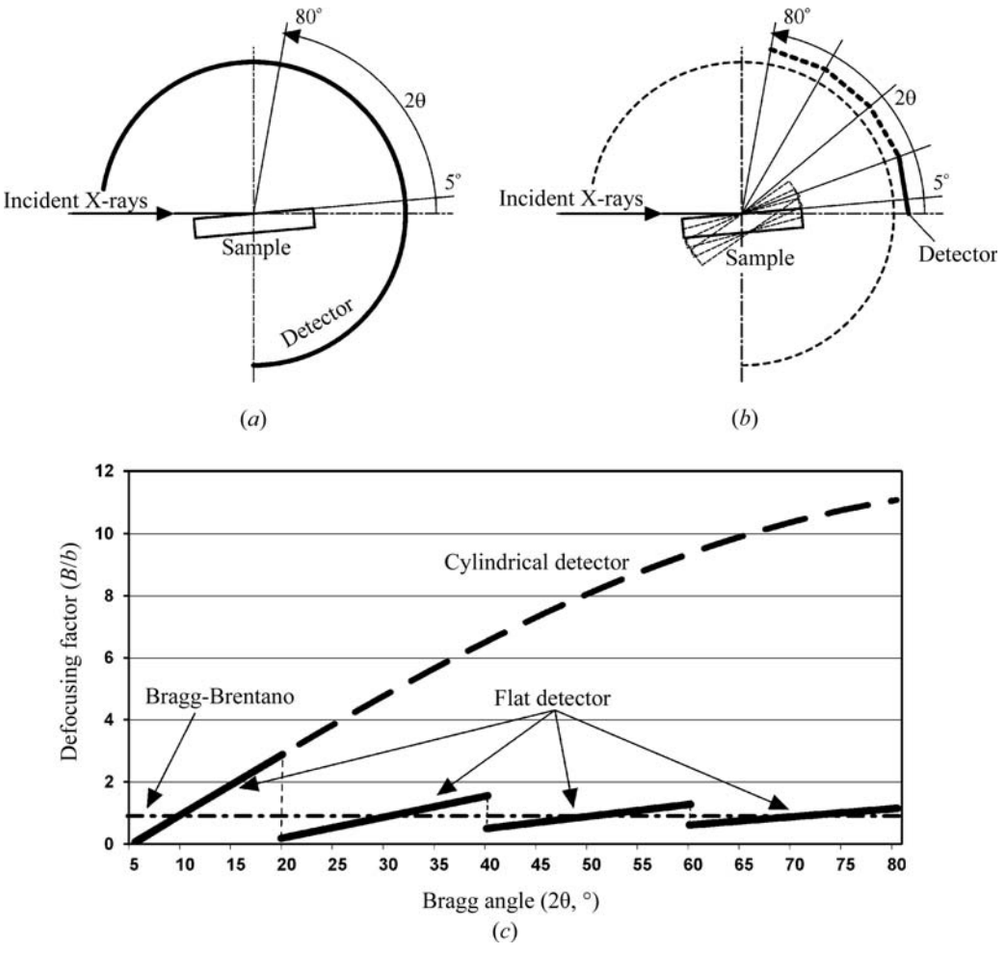

Figure 2.5.17
Defocusing effects: (*a*) cylindrical detector; (*b*) flat detector at various incident angles and detector swing angles; (*c*) comparison of defocusing factors.

statistics). Sampling statistics are determined by both the structure of the sample and the instrumentation. For a powder sample in which the crystallites are perfectly randomly oriented, the number of contributing crystallites for a diffraction peak can be given as

$$N_s = p_{hkl}\frac{Vf_i}{v_i}\frac{\Omega}{4\pi}, \tag{2.5.47}$$

where p_{hkl} is the multiplicity of the diffracting planes, V is the effective sampling volume, f_i is the volume fraction of the measuring crystallites (f_i = 1 for single-phase materials), v_i is the volume of individual crystallites and Ω is the angular window of the instrument (given as a solid angle). The multiplicity term, p_{hkl}, effectively increases the number of crystallites contributing to the integrated intensity from a particular set of (hkl) planes. The volume of individual crystallites, v_i, is an average of various crystallite sizes. The combination of the effective sampling volume and the angular window makes up the instrumental window, which determines the total volume of polycrystalline material making a contribution to a Bragg reflection. For 2D-XRD, the instrumental window is not only determined by the incident beam size and divergence, but also by the detective area and the sample-to-detector distance (γ angular coverage).

In B-B geometry, the effective irradiated volume is a constant,

$$V_{\rm BB} = A_o A_{\rm BB} = A_o/2\mu, \tag{2.5.48}$$

where A_o is the cross-section area of the incident beam measured on the sample surface, $A_{\rm BB} = 1/(2\mu)$ is the transmission coefficient for B-B geometry, and μ is the linear absorption coefficient. For 2D-XRD, the effective volume is given as

$$V = A_o A = A_o T/2\mu, \tag{2.5.49}$$

where A is the transmission coefficient and T is the transmission coefficient with B-B normalization for either transmission or reflection as given previously.

The angular window is given as a solid angle. The incident beam has a divergence angle of β_1 within the diffraction plane and β_2 in the perpendicular direction. The angular window corresponding to the incident-beam divergence is given by

$$\Omega = \beta_1\beta_2/\sin\theta \text{ or } \Omega = \beta^2/\sin\theta \text{ if } \beta = \beta_1 = \beta_2. \tag{2.5.50}$$

For 2D-XRD, the angular window is not only determined by the incident-beam divergence, but also significantly increased by γ integration. When γ integration is used to generate the diffraction profile, it actually integrates the data collected over a range of various diffraction vectors. Since the effect of γ integration on sampling statistics is equivalent to the angular oscillation on the ψ axis in a conventional diffractometer, the effect is referred to as virtual oscillation and $\Delta\psi$ is the virtual oscillation angle. In conventional oscillation, mechanical movement may result in some sample-position error. Since there is no actual physical movement of the sample stage during data collection, virtual oscillation can avoid this error. This is crucial for microdiffraction. The angular window with the contributions of both the incident-beam divergence and the virtual oscillation is

$$\Omega = \beta\Delta\psi = 2\beta\arcsin[\cos\theta\sin(\Delta\gamma/2)], \tag{2.5.51}$$

where β is the divergence of the incident beam. While increasing the divergence angle β may introduce instrumental broadening which deteriorates the 2θ resolution, virtual oscillation improves sampling statistics without introducing instrumental broadening.

In the cases of materials with a large grain size or preferred orientation, or of microdiffraction with a small X-ray beam size, it can be difficult to determine the 2θ position because of poor counting statistics. In these cases, some kind of sample oscillation, either by translation or rotation, can bring more crystallites into the diffraction condition. Angular oscillation is an enhancement to the angular window of the instrument. The effect is that the angular window scans over the oscillation angle. Any of the three rotation angles (ω, ψ, φ) or their combinations can be used as oscillation angles. Angular oscillation can effectively improve the sampling statistics for both large grain size and preferred orientation. As an extreme example, a powder-diffraction pattern can be generated from single-crystal sample if a sufficient angular window can be achieved by sample rotation in such as way as to simulate a Gandolfi camera (Guggenheim, 2005). Sample oscillation is not always necessary if virtual oscillation can achieve sufficient sampling statistics.

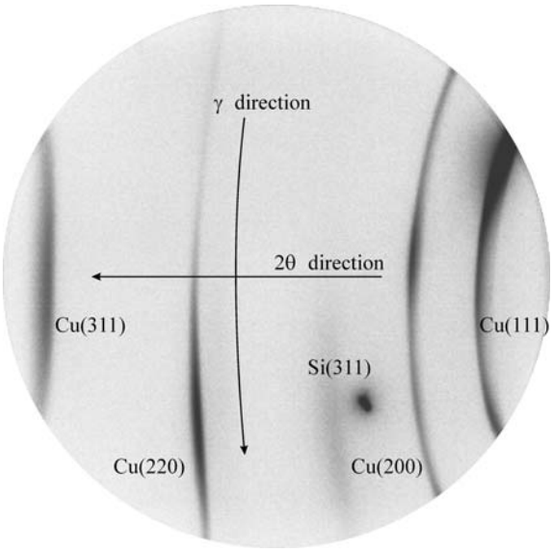

Figure 2.5.18
Diffraction frame collected from a Cu film on an Si substrate showing intensity variation along γ due to texture.

2.5.4.2. *Texture analysis*

Most natural or artificial solid materials are polycrystalline, consisting of many crystallites (also called grains) of various sizes, shapes and orientations. When the orientations of the crystallites in a material have a random distribution, it presents isotropic properties. The anisotropic orientation distribution of crystallites is referred to as preferred orientation or texture. Depending on the degree of the preferred orientation, a sample is referred to as having a weak, moderate or strong texture. Many electrical, optical or mechanical properties of materials are affected or determined by their texture. The determination and interpretation of textures are therefore of fundamental importance in materials science and technology (Bunge, 1983).

When a conventional X-ray diffractometer with a point detector is used for texture measurement, the crystallite orientation distribution in one direction is measured at a time, and full texture information is measured by rotating the sample to all the desired orientations. When a two-dimensional X-ray diffraction system is used for texture measurement, the orientation distributions of several crystallographic planes over a range of angles can be measured simultaneously so as to get better measurement results in a shorter data-collection time (Smith & Ortega, 1993; Blanton, 1994; Bunge & Klein, 1996; Helming *et al.*, 2003; Wenk & Grigull, 2003; He, 2009). The orientation relationships between different phases or between different layers of thin films and substrates can also be easily revealed. The texture effect may be observed and evaluated directly from the 2D diffraction frames without data processing.

2.5.4.2.1. *Pole density and pole figures*

XRD results from an 'ideal' powder in which the crystallites are randomly oriented normally serve as a basis for determining the relative intensity of each diffraction peak. The deviation of the grain orientation distribution of a polycrystalline material from that of an ideal powder is measured as texture. The pole figure for a particular crystallographic plane is normally used to represent the texture of a sample. Assuming that all grains have the same volume, each 'pole' represents a grain that satisfies the Bragg condition. The number of grains satisfying the Bragg condition at a particular sample orientation can be larger or smaller than the number of grains for an ideal sample, and likewise for the integrated intensity of that peak. The measured 2D diffraction pattern contains two very important parameters at each γ angle: the partially integrated intensity I and the Bragg angle 2θ. Fig. 2.5.18 shows a 2D frame for a Cu thin film on an Si wafer collected with a microgap 2D detector. It contains four Cu lines and one Si spot. The diffraction intensity varies along γ because of the anisotropic pole-density distribution. For each diffraction ring, the intensity is a function of γ and the sample orientation (ω, ψ, φ), *i.e.* $I = I(\gamma, \omega, \psi, \varphi)$.

Plotting the intensity of each (hkl) line with respect to the sample coordinates in a stereographic projection gives a qualitative view of the orientation of the crystallites with respect to a sample direction. These stereographic projection plots are called pole figures. As is shown in Fig. 2.5.19(a), the sample orientation is defined by the sample coordinates S_1, S_2 and S_3. For metals with rolling texture, the axes S_1, S_2 and S_3 correspond to the transverse direction (TD), rolling direction (RD) and normal direction (ND), respectively. Let us consider a sphere with unit radius and the origin at O. A unit vector representing an arbitrary pole direction starts from the origin O and ends at the point P on the sphere. The pole direction is defined by the radial angle α and azimuthal angle β. The pole density at the point P projects to the point P' on the equatorial plane through a straight line from P to the point S. The pole densities at all directions are mapped onto the equatorial plane by stereographic projection as shown in Fig. 2.5.19(b). This two-dimensional mapping of the pole density onto the equatorial plane is called a pole figure. The azimuthal angle β projects to the pole figure as a rotation angle about the centre of the pole figure from the sample direction S_1. When plotting the pole density into a pole figure of radius R, the location of the point P' in the pole figure should be given by β and

$$r = R\tan\left(\frac{\pi}{4} - \frac{\alpha}{2}\right) = R\tan\frac{\chi}{2}. \qquad (2.5.52)$$

For easy computer plotting and easy angular readout from the pole figure, the radial angle α may be plotted on an equally spaced angular scale, similar to a two-dimensional polar coordinate system. Other pole-figure mapping styles may be used, but must be properly noted to avoid confusion (Birkholz, 2006).

2.5.4.2.2. *Fundamental equations*

The α and β angles are functions of $\gamma, \omega, \psi, \varphi$ and 2θ. As shown in Fig. 2.5.19(*a*), a pole has three components h_1, h_2 and h_3, parallel to the three sample coordinates S_1, S_2 and S_3, respectively. The pole-figure angles (α, β) can be calculated from the unit-vector components by the following pole-mapping equations:

$$\alpha = \sin^{-1}|h_3| = \cos^{-1}(h_1^2 + h_2^2)^{1/2}, \tag{2.5.53}$$

$$\beta = \pm\cos^{-1}\frac{h_1}{(h_1^2 + h_2^2)^{1/2}} \qquad \begin{cases} \beta \geq 0^\circ \text{ if } h_2 \geq 0 \\ \beta < 0^\circ \text{ if } h_2 < 0 \end{cases}, \tag{2.5.54}$$

where α takes a value between 0 and 90° ($0^\circ \leq \alpha \leq 90^\circ$) and β takes values in two ranges ($0^\circ \leq \beta \leq 180^\circ$ when $h_2 > 0$ and $-180^\circ \leq \beta < 0^\circ$ when $h_2 < 0$). The condition for reflection-mode diffraction is $h_3 > 0$. For transmission diffraction it is possible that $h_3 < 0$. In this case, the pole with mirror symmetry about the S_1S_2 plane to the diffraction vector is used for the pole-figure mapping. The absolute value of h_3 is then used in the equation for the α angle. When $h_2 = 0$ in the above equation, β takes one of two values depending on the value of h_1 ($\beta = 0^\circ$ when $h_1 \geq 0$ and $\beta = 180^\circ$ when $h_1 < 0$). For Eulerian geometry, the unit-vector components $\{h_1, h_2, h_3\}$ are given by equation (2.5.11).

The 2θ integrated intensity along the diffraction ring is then converted to the pole-density distribution along a curve on the pole figure. The α and β angles at each point of this curve are calculated from ω, ψ, φ, γ and 2θ. The sample orientation (ω, ψ, φ) and 2θ for a particular diffraction ring are constants; only γ takes a range of values depending on the detector size and distance.

For a textured sample, the 2θ-integrated intensity of a diffraction ring from a family of (hkl) planes is a function of γ and the sample orientation (ω, ψ, φ), *i.e.* $I_{hkl} = I_{hkl}(\omega, \psi, \varphi, \gamma, \theta)$. From the pole-figure angle-mapping equations, we can obtain the integrated intensity in terms of pole-figure angles as

$$I_{hkl}(\alpha, \beta) = I_{hkl}(\omega, \psi, \varphi, \gamma, \theta). \tag{2.5.55}$$

The pole density at the pole-figure angles (α, β) is proportional to the integrated intensity at the same angles:

$$P_{hkl}(\alpha, \beta) = K_{hkl}(\alpha, \beta) I_{hkl}(\alpha, \beta), \tag{2.5.56}$$

where $I_{hkl}(\alpha, \beta)$ is the 2θ-integrated intensity of the (hkl) peak corresponding to the pole direction (α, β), $K_{hkl}(\alpha, \beta)$ is the scaling factor covering the absorption, polarization, background corrections and various instrument factors if these factors are included in the integrated intensities, and $P_{hkl}(\alpha, \beta)$ is the pole-density distribution function. Background correction can be done during the 2θ integration and will be discussed in Section 2.5.4.2.4. The pole figure is obtained by plotting the pole-density function based on the stereographic projection.

The pole-density function can be normalized such that it represents a fraction of the total diffracted intensity integrated over the pole sphere. The normalized pole-density distribution function is given by

$$g_{hkl}(\alpha, \beta) = \frac{2\pi P_{hkl}(\alpha, \beta)}{\int_0^{2\pi}\int_0^{\pi/2} P_{hkl}(\alpha, \beta)\cos\alpha \, \mathrm{d}\alpha \, \mathrm{d}\beta}. \tag{2.5.57}$$

The pole-density distribution function is a constant for a sample with a random orientation distribution. Assuming that the sample and instrument conditions are the same except for the pole-density distribution, we can obtain the normalized pole-density function by

$$g_{hkl}(\alpha, \beta) = \frac{I_{hkl}(\alpha, \beta)}{I_{hkl}^{\text{random}}(\alpha, \beta)}. \tag{2.5.58}$$

The integrated intensity from the textured sample without any correction can be plotted according to the stereographic projection as an 'uncorrected' pole figure. The same can be done for the sample with a random orientation distribution to form a 'correction' pole figure that contains only the factors to be corrected. The normalized pole figure is then obtained by dividing the 'uncorrected' pole figure by the 'correction' pole figure. This experimental approach is feasible only if a similar sample with a random orientation distribution is available.

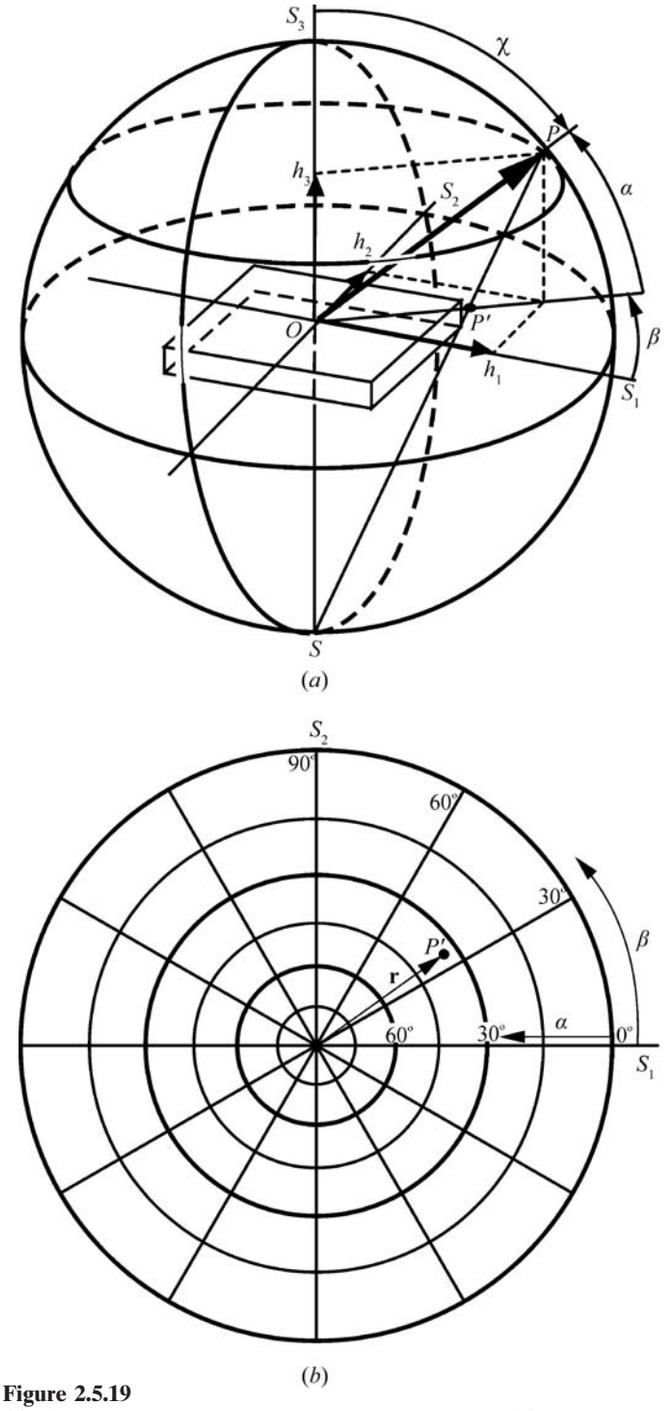

Figure 2.5.19
(*a*) Definition of pole direction angles α and β; (*b*) stereographic projection in a pole figure.

If the texture has a rotational symmetry with respect to an axis of the sample, the texture is referred to as a fibre texture and the axis is referred to as the fibre axis. The sample orientation containing the symmetry axis is referred to as the fibre axis. The fibre texture is mostly observed in two types of materials: metal wires or rods formed by drawing or extrusion, and thin films formed by physical or chemical deposition. The fibre axis is the wire axis for a wire and normal to the sample surface for thin films. Fibre texture can also be artificially formed by rotating a sample about its normal. If the fibre axis is aligned to the S_3 direction, the pole-density distribution function becomes independent of the azimuthal angle β. For samples with fibre texture, or artificially formed fibre texture by rotating, the pole-density function is conveniently expressed as a function of a single variable, $g_{hkl}(\chi)$. Here, χ is the angle between the sample normal and pole direction.

$$\chi = 90^\circ - \alpha \text{ or } \chi = \cos^{-1}|h_3|. \qquad (2.5.59)$$

The pole-density function for fibre texture can be expressed as a fibre plot. The fibre plot $g_{hkl}(\chi)$ can be calculated from the relative intensity of several peaks (He, 1992; He *et al.*, 1994) and artificial fibre texture can be achieved by sample spinning during data collection.

2.5.4.2.3. *Data-collection strategy*

Since a one-dimensional pole-density mapping is created from each 2D frame, it is important to lay out a data-collection strategy so as to have the optimum pole-figure coverage and minimum redundancy in data collection. The pole-figure coverage can be simulated from the diffraction 2θ angle, detector swing angle, detector distance, goniometer angles and scanning steps. When a large 2D detector is placed close to the sample, it is possible to collect a pole figure with a single φ scan. Fig. 2.5.20(a) shows an example of a scheme generated by a single φ scan of 5° steps with a detector 10.5 cm in diameter and D = 7 cm. The data collected with a single exposure at $\varphi = 0^\circ$ would generate a one-dimensional pole figure as shown in the curve marked by A and B. The pole figure can be generated by a full-circle rotation of 360°. The pole density at the centre represents the diffraction vector perpendicular to the sample surface. It is important to have the pole-density information in the centre region of the pole figure, especially for fibre texture. The pole-figure angle at the centre is $\alpha = 90^\circ$, and the best strategy is to put point A at the centre of pole figure. That is

$$h_3^A = \sin\theta\cos\psi\sin\omega - \cos\theta\sin\gamma_A\cos\psi\cos\omega - \cos\theta\cos\gamma_A\sin\psi = 1. \qquad (2.5.60)$$

In some cases, a single φ scan is not enough to cover sufficient pole-figure angles because of a large detector distance or limited detector area, so it is necessary to collect a set of data with φ scans at several different sample tilt angles. Fig. 2.5.20(b) illustrates the data-collection scheme with a detector that is 10.5 cm in diameter and D = 10 cm for the (111) plane of a Cu thin film. In this case, each pole figure requires two φ scans at different sample orientations. The data-collection strategy should also be optimized for several crystallographic planes if all can be covered in a frame. The step size of the data-collection scan depends highly on the strength of the texture and the purpose of the texture measurements. For a weak texture, or quality control for metal parts, φ (or ω, or ψ) scan steps of 5° may be sufficient. For strong textures, such as thin films with epitaxial structure, scan steps of 1° or smaller may be necessary.

The effectiveness of two-dimensional data collection for a texture can be compared with that using a point detector with the data-collection strategy of the Cu thin film as an example. Fig. 2.5.20(c) shows the pole-figure data-collection strategy with a point detector. For the same pole-figure resolution, significantly more exposures are required with a point detector. Considering that several diffraction rings are measured simultaneously with a 2D detector, the pole-figure measurement is typically 10 to 100 times faster than with a point detector. Therefore, quantitative high-resolution pole-figure measurements are only practical with a 2D-XRD system (Bunge & Klein, 1996).

2.5.4.2.4. *Texture-data processing*

For a specific diffraction ring, 2θ is a constant or at least assumed to be constant for texture analysis, and the sample-orientation angles (ω, ψ, φ) for a frame are also constants. Therefore, the pole-density information is given by the diffraction-intensity distribution as a function of γ only, or $I = I(\gamma)$. Integration of the diffraction intensities in the 2θ direction converts 2D information into the function $I(\gamma)$.

Fig. 2.5.21(a) shows a 2D diffraction ring for texture analysis. The low and high background and diffraction-ring 2θ–γ range are defined by three boxes, noted as B_L, B_H and $I(\gamma)$, respectively. All three boxes have the same γ range from γ_1 to γ_2. The 2θ ranges for the diffraction ring, low background and high background should be determined based on the width of the 2θ peak and available background between adjacent peaks. Assuming a normal distribution, a 2θ range of 2 times the FWHM covers 98% of the intensity peak, and 3 times the FWHM covers more than 99.9%. The 2θ range should also be broad enough to cover the possible 2θ shifts caused by residual stresses in the sample. Fig. 2.5.21(b) is the 2θ profile integrated over the section $\Delta\gamma$ in Fig. 2.5.21(a). The background ranges on the low and high 2θ sides are given by $2\theta_{L1}$–$2\theta_{L2}$ and $2\theta_{H1}$–$2\theta_{H2}$, respectively. The 2θ-integrated diffraction intensities as a function of γ are plotted in Fig. 2.5.21(c). The background can be calculated and removed from the intensity values of the low and high backgrounds or ignored if the contribution of the background is very small.

2θ integration without a background correction can be

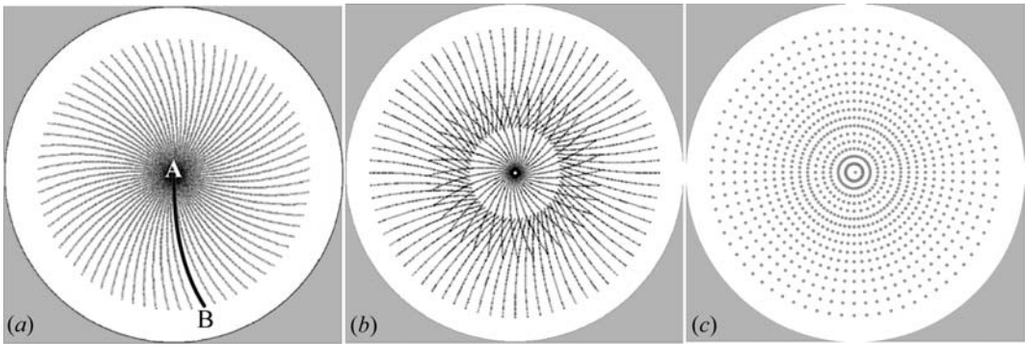

Figure 2.5.20
Data-collection strategy: (a) 2D detector with D = 7 cm; (b) 2D detector with D = 10 cm; (c) point detector.

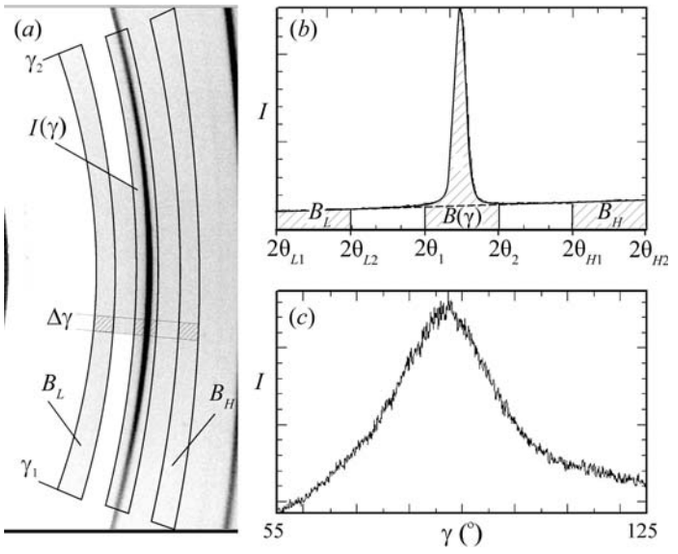

Figure 2.5.21
Pole-figure data processing: (*a*) a frame with the 2θ integration ranges for the (220) ring; (*b*) 2θ profile showing the background and peak; (*c*) integrated intensity distribution as a function of γ.

expressed as

$$I(\gamma) = \int_{2\theta_1}^{2\theta_2} J(2\theta, \gamma)\, \mathrm{d}(2\theta), \quad \gamma_1 \le \gamma \le \gamma_2. \tag{2.5.61}$$

A similar equation can be used for 2θ integration of the low and high backgrounds $B_L(\gamma)$ and $B_H(\gamma)$. Assuming a linear background change in the vicinity of the 2θ peak, the background under the peak, $B(\gamma)$, is then given by

$$B(\gamma) = B_L(\gamma)\frac{(2\theta_2 - 2\theta_1)(2\theta_{H2} + 2\theta_{H1} - 2\theta_2 - 2\theta_1)}{(2\theta_{L2} - 2\theta_{L1})(2\theta_{H2} + 2\theta_{H1} - 2\theta_{L2} - 2\theta_{L1})} + B_H(\gamma)\frac{(2\theta_2 - 2\theta_1)(2\theta_2 + 2\theta_1 - 2\theta_{L2} - 2\theta_{L1})}{(2\theta_{H2} - 2\theta_{H1})(2\theta_{H2} + 2\theta_{H1} - 2\theta_{L2} - 2\theta_{L1})}. \tag{2.5.62}$$

Then the background $B(\gamma)$ can be subtracted from the integrated intensity distribution $I(\gamma)$.

The algorithms of γ integration given in Section 2.5.4.2.3 can be easily modified for 2θ integration by exchanging γ and 2θ in the equations. Algorithms with solid-angle normalization should be used to get consistent integrated intensity over all areas of the detector. The 2θ-integrated intensity distribution can then be mapped onto a pole figure based on the fundamental equations (2.5.53) and (2.5.54). When a pole-figure pixel is overlapped by more than one data point from different scans, as shown in the region covered by two scans in Fig. 2.5.20(*b*), the average value should be mapped to that pole-figure pixel. Fig. 2.5.22(*a*) shows pole-density mappings on the pole figure. There are big gaps between the measured pole-density data points due to the large φ-scan steps of 5°.

All factors affecting relative intensities, such as Lorentz, polarization, air scattering, and Be-window and sample absorption, will have an effect on the measured pole densities for the pole figures. Some or all these corrections may be applied to the diffraction frames before 2θ integration if the texture study demands high accuracy in the relative pole densities. Among these factors, the most important factor is sample absorption, since data sets for pole figures are typically collected at several different incident angles. A ridge between the pole-density regions covered by two different incident angles may be observed if sample absorption is not properly corrected.

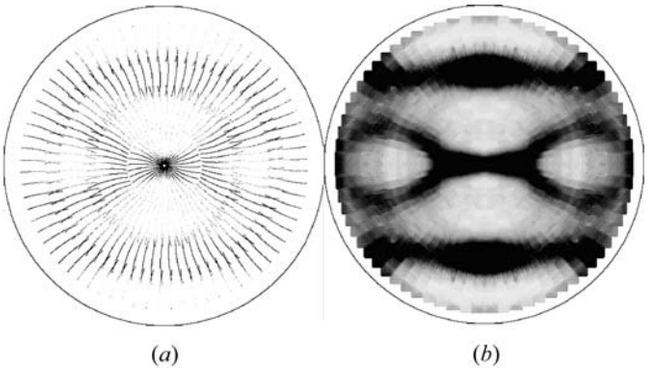

Figure 2.5.22
Pole-figure processing: (*a*) $I(\gamma)$ mapped to the pole figure; (*b*) Pole figure after interpolation and symmetry processing.

2.5.4.2.5. *Pole-figure interpolation and use of symmetry*

The pole figure is stored and displayed as a bitmap image. The pole-density data from the data set may not fill up all the pixels of the pole-figure image. In order to generate a smooth pole figure, the unmapped pixels are filled with values generated from the interpolation of the surrounding pixels. A linear interpolation within a defined box is sufficient to fill the unmapped pixels. The size of the box should be properly chosen. A box that is too small may not be able to fill all unmapped pixels and a box that is too big may have a smearing effect on the pole figure, especially if a sharp pole figure is processed. All the gaps between the measured pole-density points are filled after this interpolation. For a sample with sharp texture, smaller φ-scan steps should be used.

All pole figures possess symmetry as a consequence of the Laue symmetry of the crystallites in the sample. This symmetry can be used to fill in values for pixels in the pole figure for which data were not measured, or to smooth the pole figure. For example, orthorhombic materials exhibit *mmm* symmetry, thus one needs to collect only an octant or quadrant of the pole sphere to generate the entire pole figure. The pole figures of materials with higher symmetry may be treated by using lower symmetry in the processing. For instance, one can use 2/*m* or *mmm* symmetry for hexagonal materials and *mmm* for cubic materials. In symmetry processing, all the symmetry-equivalent pole-figure pixels are filled by the average value of the measured pixels. For the unmeasured pole-figure pixels, this symmetry processing fills in a value from the average of all the equivalent pixels. For the measured pixels, this average processing serves as a smoothing function. Fig. 2.5.22(*b*) shows the results after both interpolation and use of symmetry.

2.5.4.2.6. *Orientation relationship*

A 2D-XRD system can measure texture from a sample containing a single phase, multiple phases or single crystals. The orientation relationship between different phases, or thin films and substrates, can be revealed because data are collected from all phases of the sample simultaneously. One example is the measurement of pole figures for a magnetron sputter-deposited Cu film on an Si wafer (He *et al.*, 2005). Fig. 2.5.23 shows the overlapped pole figures of the Cu (111) film and Si (400) substrate in a 2D pole figure (*a*) and 3D surface plot (*b*). The three sharp spots from the (400) spots of the Si wafer show the wafer cut orientation of (111). The Cu (111) pole density maxi-

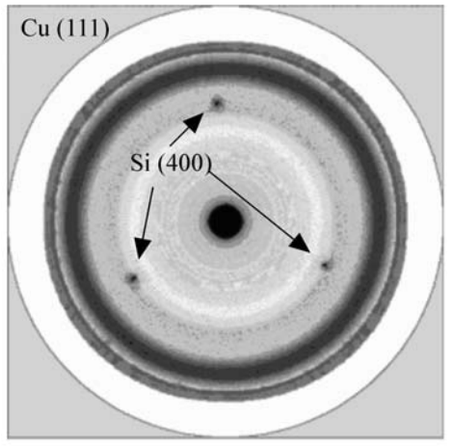

(*a*)

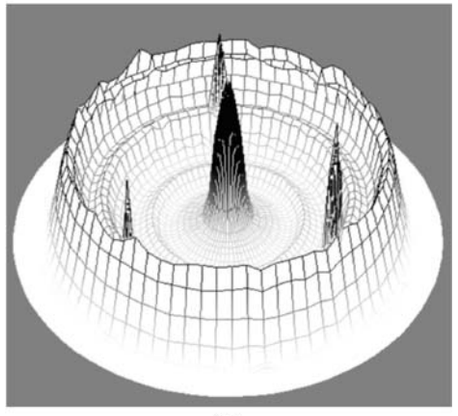

(*b*)

Figure 2.5.23
Combined pole figure of a Cu (111) film on an Si (400) substrate: (*a*) regular 2D projection; (*b*) 3D surface plot.

mized in the centre of the pole figure shows a strong (111) fibre texture. The orientation relationship between the film fibre axis and the substrate is clearly described by the combined pole figures. For samples containing multiple thin-film layers, the orientation relationships between the different layers of the films and substrate can be revealed by superimposing their pole figures.

2.5.4.3. *Stress measurement*

When a solid material is elastically deformed by a force, each crystallite in it changes shape or size. Assuming that the stresses in each crystallite represent the stresses in the solid, the stresses can be measured by measuring the lattice *d*-spacing changes in the crystallites. These *d*-spacing changes can be measured by the changes in diffraction-peak positions based on Bragg's law. In this case, the *d*-spacing serves as a gauge of the deformation. Stress measurement by X-ray diffraction is typically done using a point detector or line detector (Walter, 1971; James & Cohen, 1980; Noyan & Cohen, 1987; Lu, 1996); this will be referred to as the conventional method. The stress or stress tensor is calculated from many strain measurements from diffraction-peak 2θ shifts of a specific lattice-plane family. With a point or line detector, only a small cross section of the diffraction cone is measured at one sample orientation (ψ, φ). Compared to using a conventional detector, 2D detectors have many advantages in stress measurement (Borgonovi, 1984; Korhonen *et al.*, 1989; Yoshioka & Ohya, 1992; Fujii & Kozaki, 1993; He & Smith, 1997; Kämpfe *et al.*, 1999; Hanan *et al.*, 2004). Since a 2D diffraction pattern covers the whole or a large portion of the diffraction rings, it can be used to measure stress with higher accuracy and can be collected in a shorter time than a conventional diffraction pattern, especially when dealing with highly textured materials, large grain sizes, small sample areas, weak diffraction, stress mapping and stress-tensor measurement. The 2D method for stress measurement is based on the fundamental relationship between the stress tensor and the diffraction-cone distortion (He & Smith, 1997; He, 2000; European Standard, 2008).

There are two kinds of stresses, which depend on the source of the loading forces that produce them. One kind is applied stress, caused by external forces acting on the solid object. Applied stress changes when the loading forces change and it disappears once the forces are removed. The stresses measured by X-ray diffraction method are mostly residual stresses. Residual stress is caused by internal forces between different parts of a solid body. Residual stress exists without external forces or remains after the external forces have been removed. The net force and moment on a solid body in equilibrium must be zero, so the residual stresses in the body must be balanced within the body. This means that a compressive stress in one part of the body must come with a tensile stress in another part of the body. For example, the residual stress in a thin film is balanced by the stresses in the substrate. When residual stress in a solid body is mentioned it typically refers to a specific location.

Residual stresses are generally categorized as macroscopic or microscopic depending on the range over which the stresses are balanced. The macroscopic residual stress is the stress measured over a large number of grains. This kind of stress can be measured by X-ray diffraction through the shift of the Bragg peaks. The microscopic stress is the stress measured over one or a few grains, or as small a range as micro- or nanometres. This kind of stress alone will not cause a detectable shift of diffraction peaks, but is reflected in the peak profiles. In this chapter, we will focus on the X-ray diffraction method for stress measurement at the macroscopic level.

2.5.4.3.1. *Stress and strain relation*

Stress is a measure of the deforming force applied to a solid per unit area. The stress on an elemental volume in the sample coordinates S_1, S_2, S_3 contains nine components, given by

$$\sigma_{ij} = \begin{bmatrix} \sigma_{11} & \sigma_{12} & \sigma_{13} \\ \sigma_{21} & \sigma_{22} & \sigma_{23} \\ \sigma_{31} & \sigma_{32} & \sigma_{33} \end{bmatrix}. \tag{2.5.63}$$

A component is normal stress when the two indices are identical, or shear stress when the two indices differ. The group of the nine stress components is called the stress tensor. The stress tensor is a tensor of the second order. Under equilibrium conditions, the shear components must maintain the following relations:

$$\sigma_{12} = \sigma_{21},\ \sigma_{23} = \sigma_{32} \text{ and } \sigma_{31} = \sigma_{13}. \tag{2.5.64}$$

Therefore, only six independent components define the stress state in a solid. The following stress states are typically measured:

Uniaxial: all stress components are zero except one normal stress component.

Biaxial: all nonzero components are within the S_1S_2 plane.

Biaxial with shear: $\sigma_{33} = 0$, all other components are not necessarily zero.

Equibiaxial: a special case of biaxial stress where $\sigma_{11} = \sigma_{22} = \sigma$.

Triaxial: all components are not necessarily zero.

Equitriaxial: a special case of triaxial stress where $\sigma_{11} = \sigma_{22} = \sigma_{33} = \sigma$.

Strain is a measure of the resulting deformation of a solid body caused by stress. Strain is calculated from the change in the size and shape of the deformed solid due to stress. Analogous to normal stresses and shear stresses are normal strains and shear strains. The normal strain is calculated from the change in length of the solid body along the corresponding normal stress direction. Like the stress tensor, the strain tensor contains nine components:

$$\varepsilon_{ij} = \begin{bmatrix} \varepsilon_{11} & \varepsilon_{12} & \varepsilon_{13} \\ \varepsilon_{21} & \varepsilon_{22} & \varepsilon_{23} \\ \varepsilon_{31} & \varepsilon_{32} & \varepsilon_{33} \end{bmatrix}. \tag{2.5.65}$$

The directions of all strain components are defined in the same way as for the stress tensor. Similarly, there are six independent components in the strain tensor. Strictly speaking, X-ray diffraction does not measure stresses directly, but strains. The stresses are calculated from the measured strains based on the elasticity of the materials. The stress–strain relations are given by the generalized form of Hooke's law:

$$\sigma_{ij} = C_{ijkl}\varepsilon_{kl}, \tag{2.5.66}$$

where C_{ijkl} are elastic stiffness coefficients. The stress–strain relations can also be expressed as

$$\varepsilon_{ij} = S_{ijkl}\sigma_{kl}, \tag{2.5.67}$$

where S_{ijkl} are the elastic compliances. For most polycrystalline materials without texture or with weak texture, it is practical and reasonable to consider the elastic behaviour to be isotropic and the structure to be homogeneous on a macroscopic scale. In these cases, the stress–strain relationship takes a much simpler form. Therefore, the Young's modulus E and Poisson's ratio ν are sufficient to describe the stress and strain relations for homogeneous isotropic materials:

$$\begin{aligned} \varepsilon_{11} &= \frac{1}{E}[\sigma_{11} - \nu(\sigma_{22} + \sigma_{33})], \\ \varepsilon_{22} &= \frac{1}{E}[\sigma_{22} - \nu(\sigma_{33} + \sigma_{11})], \\ \varepsilon_{33} &= \frac{1}{E}[\sigma_{33} - \nu(\sigma_{11} + \sigma_{22})], \\ \varepsilon_{12} &= \frac{1+\nu}{E}\sigma_{12}, \quad \varepsilon_{23} = \frac{1+\nu}{E}\sigma_{23}, \quad \varepsilon_{31} = \frac{1+\nu}{E}\sigma_{31}. \end{aligned} \tag{2.5.68}$$

It is customary in the field of stress measurement by X-ray diffraction to use another set of macroscopic elastic constants, S_1 and $\frac{1}{2}S_2$, which are given by

$$\tfrac{1}{2}S_2 = (1+\nu)/E \ \text{ and } \ S_1 = -\nu/E. \tag{2.5.69}$$

Although polycrystalline materials on a macroscopic level can be considered isotropic, residual stress measurement by X-ray diffraction is done by measuring the strain in a specific crystal orientation of the crystallites that satisfies the Bragg condition. The stresses measured from diffracting crystallographic planes may have different values because of their elastic anisotropy. In such cases, the macroscopic elasticity constants should be replaced by a set of crystallographic plane-specific elasticity constants, $S_1^{\{hkl\}}$ and $\frac{1}{2}S_2^{\{hkl\}}$, called X-ray elastic constants (XECs). XECs for many materials can be found in the literature, measured or calculated from microscopic elasticity constants (Lu, 1996). In the case of materials with cubic crystal symmetry, the equations for calculating the XECs from the macroscopic elasticity constants $\frac{1}{2}S_2$ and S_1 are

$$\begin{aligned} \tfrac{1}{2}S_2^{\{hkl\}} &= \tfrac{1}{2}S_2[1 + 3(0.2 - \Gamma(hkl))\Delta] \\ S_1^{\{hkl\}} &= S_1 - \tfrac{1}{2}S_2[0.2 - \Gamma(hkl)]\Delta, \end{aligned} \tag{2.5.70}$$

where

$$\Gamma(hkl) = \frac{h^2k^2 + k^2l^2 + l^2h^2}{(h^2 + k^2 + l^2)^2} \ \text{ and } \ \Delta = \frac{5(A_{\rm RX} - 1)}{3 + 2A_{\rm RX}}.$$

In the equations for stress measurement hereafter, either the macroscopic elasticity constants $\frac{1}{2}S_2$ and S_1 or the XECs $S_1^{\{hkl\}}$ and $\frac{1}{2}S_2^{\{hkl\}}$ are used in the expression, but either set of elastic constants can be used depending on the requirements of the application. The factor of anisotropy ($A_{\rm RX}$) is a measure of the elastic anisotropy of a material (He, 2009).

2.5.4.3.2. *Fundamental equations*

Fig. 2.5.24 illustrates two diffraction cones for backward diffraction. The regular diffraction cone (dashed lines) is from the powder sample with no stress, so the 2θ angles are constant at all γ angles. The diffraction ring shown as a solid line is the cross section of a diffraction cone that is distorted as a result of stresses. For a stressed sample, 2θ becomes a function of γ and the sample orientation (ω, ψ, φ), *i.e.* $2\theta = 2\theta(\gamma, \omega, \psi, \varphi)$. This function is uniquely determined by the stress tensor. The strain measured by the 2θ shift at a point on the diffraction ring is $\varepsilon_{(\gamma,\omega,\psi,\varphi)}^{\{hkl\}}$, based on the true strain definition

$$\varepsilon_{(\gamma,\omega,\psi,\varphi)}^{\{hkl\}} = \ln\frac{d}{d_o} = \ln\frac{\sin\theta_o}{\sin\theta} = \ln\frac{\lambda}{2d_o\sin\theta}, \tag{2.5.71}$$

where d_o and θ_o are the stress-free values and d and θ are measured values from a point on the diffraction ring corresponding to (γ, ω, ψ, φ). The direction of $\varepsilon_{(\gamma,\omega,\psi,\varphi)}^{\{hkl\}}$ in the sample coordinates S_1, S_2, S_3 can be given by the unit-vector components h_1, h_2 and h_3. As a second-order tensor, the relationship between the measured strain and the strain-tensor components is then given by

$$\varepsilon_{(\gamma,\omega,\psi,\varphi)}^{\{hkl\}} = \varepsilon_{ij} \cdot h_i \cdot h_j. \tag{2.5.72}$$

The scalar product of the strain tensor with the unit vector in the above equation is the sum of all components in the tensor multiplied by the components in the unit vector corresponding to the first and the second indices. The expansion of this equation for i and j values of 1, 2 and 3 results in

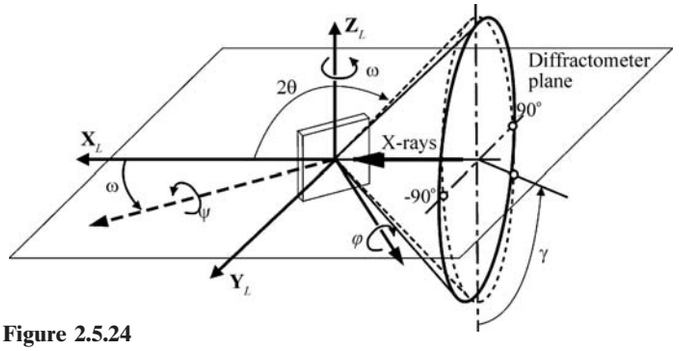

Figure 2.5.24
Diffraction-cone distortion due to stresses.

$$\varepsilon^{\{hkl\}}_{(\gamma,\omega,\psi,\varphi)} = h_1^2\varepsilon_{11} + 2h_1h_2\varepsilon_{12} + h_2^2\varepsilon_{22} + 2h_1h_3\varepsilon_{13} + 2h_2h_3\varepsilon_{23} + h_3^2\varepsilon_{33}. \tag{2.5.73}$$

Or, taking the true strain definition,

$$h_1^2\varepsilon_{11} + 2h_1h_2\varepsilon_{12} + h_2^2\varepsilon_{22} + 2h_1h_3\varepsilon_{13} + 2h_2h_3\varepsilon_{23} + h_3^2\varepsilon_{33} = \ln\left(\frac{\sin\theta_0}{\sin\theta}\right), \tag{2.5.74}$$

where θ_o corresponds to the stress-free d-spacing and θ are measured values from a point on the diffraction ring. Both θ and $\{h_1, h_2, h_3\}$ are functions of $(\gamma, \omega, \psi, \varphi)$. By taking γ values from 0 to 360°, equation (2.5.74) establishes the relationship between the diffraction-cone distortion and the strain tensor. Therefore, equation (2.5.74) is the fundamental equation for strain measurement with two-dimensional X-ray diffraction.

Introducing the elasticity of materials, one obtains

$$-\frac{\nu}{E}(\sigma_{11}+\sigma_{22}+\sigma_{33}) + \frac{1+\nu}{E}(\sigma_{11}h_1^2 + \sigma_{22}h_2^2 + \sigma_{33}h_3^2 + 2\sigma_{12}h_1h_2 + 2\sigma_{13}h_1h_3 + 2\sigma_{23}h_2h_3) = \ln\left(\frac{\sin\theta_0}{\sin\theta}\right) \tag{2.5.75}$$

or

$$S_1(\sigma_{11}+\sigma_{22}+\sigma_{33}) + \tfrac{1}{2}S_2(\sigma_{11}h_1^2 + \sigma_{22}h_2^2 + \sigma_{33}h_3^2 + 2\sigma_{12}h_1h_2 + 2\sigma_{13}h_1h_3 + 2\sigma_{23}h_2h_3) = \ln\left(\frac{\sin\theta_0}{\sin\theta}\right). \tag{2.5.76}$$

It is convenient to express the fundamental equation in a clear linear form:

$$p_{11}\sigma_{11} + p_{12}\sigma_{12} + p_{22}\sigma_{22} + p_{13}\sigma_{13} + p_{23}\sigma_{23} + p_{33}\sigma_{33} = \ln\left(\frac{\sin\theta_0}{\sin\theta}\right), \tag{2.5.77}$$

where p_{ij} are stress coefficients given by

$$p_{ij} = \begin{cases} (1/E)[(1+\nu)h_i^2 - \nu] = \tfrac{1}{2}S_2h_i^2 + S_1 & \text{if } i = j, \\ 2(1/E)(1+\nu)h_ih_j = 2\tfrac{1}{2}S_2h_ih_j & \text{if } i \neq j. \end{cases} \tag{2.5.78}$$

In the equations for the stress measurement above and hereafter, the macroscopic elastic constants $\frac{1}{2}S_2$ and S_1 are used for simplicity, but they can always be replaced by the XECs for the specific lattice plane $\{hkl\}$, $S_1^{\{hkl\}}$ and $\frac{1}{2}S_2^{\{hkl\}}$, if the anisotropic nature of the crystallites should be considered. For instance, equation (2.5.76) can be expressed with the XECs as

$$S_1^{\{hkl\}}(\sigma_{11}+\sigma_{22}+\sigma_{33}) + \tfrac{1}{2}S_2^{\{hkl\}}(\sigma_{11}h_1^2 + \sigma_{22}h_2^2 + \sigma_{33}h_3^2 + 2\sigma_{12}h_1h_2 + 2\sigma_{13}h_1h_3 + 2\sigma_{23}h_2h_3) = \ln\left(\frac{\sin\theta_0}{\sin\theta}\right). \tag{2.5.79}$$

The fundamental equation (2.5.74) may be used to derive many other equations based on the stress–strain relationship, stress state and special conditions. The fundamental equation and the derived equations are referred to as 2D equations hereafter to distinguish them from the conventional equations. These equations can be used in two ways. One is to calculate the stress or stress-tensor components from the measured strain (2θ-shift) values in various directions. The fundamental equation for stress measurement with 2D-XRD is a linear function of the stress-tensor components. The stress tensor can be obtained by solving the linear equations if six independent strains are measured or by linear least-squares regression if more than six independent measured strains are available. In order to get a reliable solution from the linear equations or least-squares analysis, the independent strain should be measured at significantly different orientations. Another function of the fundamental equation is to calculate the diffraction-ring distortion for a given stress tensor at a particular sample orientation (ω, ψ, φ) (He & Smith, 1998). The fundamental equation for stress measurement by the conventional X-ray diffraction method can also be derived from the 2D fundamental equation (He, 2009).

2.5.4.3.3. *Equations for various stress states*

The general triaxial stress state is not typically measured by X-ray diffraction because of low penetration. For most applications, the stresses in a very thin layer of material on the surface are measured by X-ray diffraction. It is reasonable to assume that the average normal stress in the surface-normal direction is zero within such a thin layer. Therefore, $\sigma_{33} = 0$, and the stress tensor has five nonzero components. In some of the literature this stress state is denoted as triaxial. In order to distinguish this from the general triaxial stress state, here we name this stress state as the 'biaxial stress state with shear'. In this case, we can obtain the linear equation for the biaxial stress state with shear:

$$p_{11}\sigma_{11} + p_{12}\sigma_{12} + p_{22}\sigma_{22} + p_{13}\sigma_{13} + p_{23}\sigma_{23} + p_{\rm ph}\sigma_{\rm ph} = \ln\left(\frac{\sin\theta_0}{\sin\theta}\right), \tag{2.5.80}$$

where the coefficient $p_{\rm ph} = \frac{1}{2}S_2 + 3S_1$ and $\sigma_{\rm ph}$ is the pseudo-hydrostatic stress component introduced by the error in the stress-free d-spacing. In this case, the stresses can be measured without the accurate stress-free d-spacing, since this error is included in $\sigma_{\rm ph}$. The value of $\sigma_{\rm ph}$ is considered as one of the unknowns to be determined by the linear system. With the measured stress-tensor components, the general normal stress (σ_φ) and shear stress (τ_φ) at any arbitrary angle φ can be given by

$$\sigma_\varphi = \sigma_{11}\cos^2\varphi + \sigma_{12}\sin 2\varphi + \sigma_{22}\sin^2\varphi, \tag{2.5.81}$$

$$\tau_\varphi = \sigma_{13}\cos\varphi + \sigma_{23}\sin\varphi. \tag{2.5.82}$$

Equation (2.5.81) can also be used for other stress states by removing the terms for stress components that are zero. For instance, in the biaxial stress state $\sigma_{33} = \sigma_{13} = \sigma_{23} = 0$, so we have

$$p_{11}\sigma_{11} + p_{12}\sigma_{12} + p_{22}\sigma_{22} + p_{\rm ph}\sigma_{\rm ph} = \ln\left(\frac{\sin\theta_0}{\sin\theta}\right). \tag{2.5.83}$$

In the 2D stress equations for any stress state with $\sigma_{33} = 0$, we can calculate stress with an approximation of d_o (or $2\theta_o$). Any error in d_o (or $2\theta_o$) will contribute only to a pseudo-hydrostatic term $\sigma_{\rm ph}$. The measured stresses are independent of the input d_o (or $2\theta_o$) values (He, 2003). If we use d_0' to represent the initial input, then the true d_o (or $2\theta_o$) can be calculated from $\sigma_{\rm ph}$ with

$$d_0 = d_0'\exp\left(\frac{1-2\nu}{E}\sigma_{\rm ph}\right), \tag{2.5.84}$$

$$\theta_0 = \arcsin\left[\sin\theta_0'\exp\left(\frac{1-2\nu}{E}\sigma_{\rm ph}\right)\right]. \tag{2.5.85}$$

Care must be taken that the $\sigma_{\rm ph}$ value also includes the measurement error. If the purpose of the experiment is to

determine the stress-free d-spacing d_o, the instrument should be first calibrated with a stress-free standard of a similar material.

2.5.4.3.4. *Data-collection strategy*

The practice of stress analysis with 2D-XRD involves the selection of the diffraction-system configuration and the data-collection strategy, frame correction and integration, and stress calculation from the processed data points. Most concepts and strategies developed for a conventional diffractometer are still valid for 2D-XRD. We will focus on the new concepts and practices due to the nature of the 2D detectors.

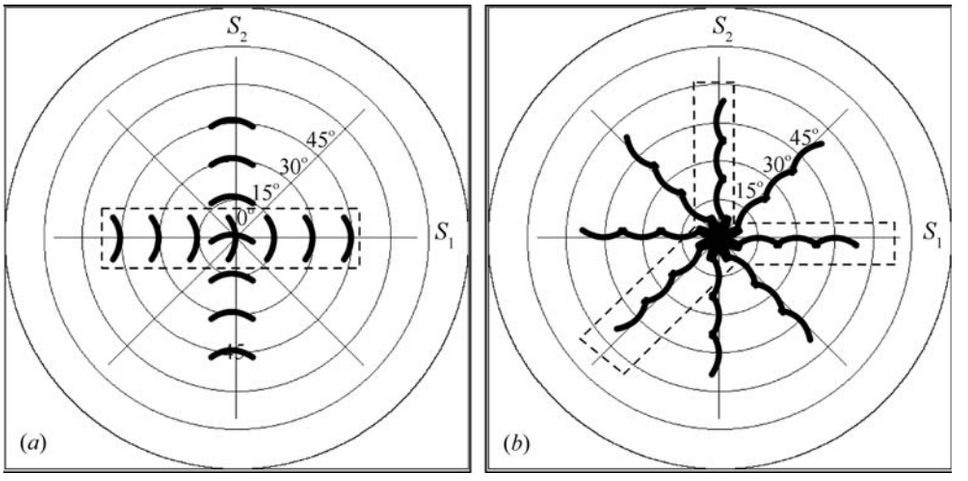

Figure 2.5.25
Data-collection strategy schemes: (*a*) $\omega + \varphi$ scan; (*b*) $\psi + \varphi$ scan.

The diffraction vector is in the normal direction to the measured crystalline planes. It is not always possible to have the diffraction vector in the desired measurement direction. In reflection mode, it is easy to have the diffraction vector normal to the sample surface, or tilted away from the normal, but impossible to have the vector on the surface plane. The stress on the surface plane, or biaxial stress, is calculated by elasticity theory from the measured strain in other directions. The final stress-measurement results can be considered as an extrapolation from the measured values. In the conventional $\sin^2\psi$ method, several ψ-tilt angles are required, typically at 15° steps from −45° to +45°. The same is true with a 2D-XRD system. The diffraction vectors corresponding to the data scan can be projected onto a 2D plot in the same way as the pole-density distribution in a pole figure. The 2D plot is called a data-collection strategy scheme.

By evaluating the scheme, one can generate a data-collection strategy suitable for the measurement of the intended stress components. Fig. 2.5.25 illustrates two schemes for data collection. In the bisecting condition ($\omega = \theta$ or $\theta_1 = \theta$ and $\psi = 0°$), the trace of the diffraction vector falls in the vicinity of the scheme centre. Either an ω tilt or a ψ tilt can move the vectors away from the centre. The circles on the scheme are labelled with the tilt angle of 15°, 30° and 45°. Scheme (*a*) is for an ω tilt of 0°, ±15°, ±30° and ±45° with the φ angle at 0° and 90°. It is obvious that this set of data would be suitable for calculating the biaxial-stress tensor. The data set with $\varphi = 0°$, as shown within the box enclosed by the dashed lines, would be sufficient on its own to calculate σ_{11}. Since the diffraction-ring distortion at $\varphi = 0°$ or $\varphi = 90°$ is not sensitive to the stress component σ_{12}, strategy (*a*) is suitable for the equibiaxial stress state, but is not able to determine σ_{12} accurately. In scheme (*b*), the ψ scan covers 0° to 45° with 15° steps at eight φ angles with 45° intervals. This scheme produces comprehensive coverage on the scheme chart in a symmetric distribution. The data set collected with this strategy can be used to calculate the complete biaxial-stress tensor components and shear stress (σ_{11}, σ_{12}, σ_{22}, σ_{13}, σ_{23}). The scheme indicated by the boxes enclosed by the dashed lines is a time-saving alternative to scheme (*b*). The rings on two φ angles are aligned to S_1 and S_2 and the rings on the third φ angle make 135° angles to the other two arrays of rings. This is analogous to the configuration of a stress-gauge rosette. The three φ angles can also be separated equally by 120° steps. Suitable schemes for a particular experiment should be determined by considering the stress components of interest, the goniometer, the sample size, the detector size and resolution, the desired measurement accuracy and the data-collection time.

2.5.4.3.5. *Data integration and peak evaluation*

The purpose of data integration and peak evaluation is to generate a set of data points along distorted diffraction rings. Data integration for stress analysis is γ integration over several defined segments so as to generate diffraction profiles representing the corresponding segments. The peak position can be determined by fitting the diffraction profile to a given analytic function. Fig. 2.5.26 illustrates data integration over a diffraction frame. The total integration region is defined by $2\theta_1$, $2\theta_2$, γ_1 and γ_2. The integration region is divided into segments given by $\Delta\gamma$. One data point on the distorted diffraction ring is generated from each segment. The γ value in the centre (denoted by the dot-dashed line) of each segment is taken as the γ value of the data point. γ integration of the segment produces a diffraction profile and the 2θ value is determined from the profile. The number of segments and the segment size ($\Delta\gamma$) are selected based on the quality of the data frame. The larger the segment size $\Delta\gamma$ is, the better the integrated diffraction profile as more counts are being integrated. γ integration also produces a smearing effect on the diffraction-ring distortion because the counts collected within the segment size $\Delta\gamma$ are considered as a single γ value at the segment

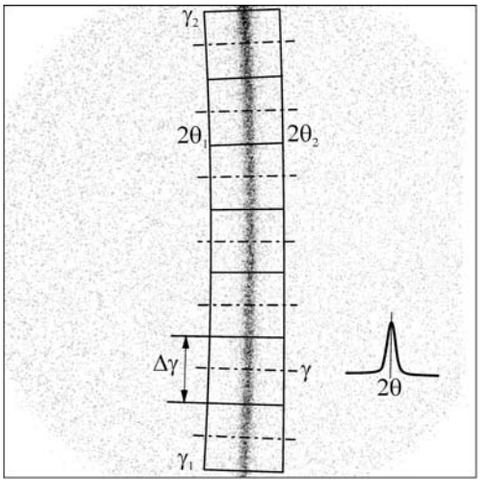

Figure 2.5.26
Data integration for stress measurement.

centre. The 2θ shift in the segment is averaged. The segment size $\Delta\gamma$ should be sufficient to produce a smooth diffraction profile, but not so large as to introduce too much smearing. For data frames containing high pixel counts, the integration segment can be small, *e.g.* $\Delta\gamma \leq 2^\circ$, and still have a smooth profile for each segment. For data frames having low pixel counts, for example the frames collected from a micron-sized area, from a sample with large grains or with a short data-collection time, it is critical to choose a sufficiently large segment size. The segment size can be determined by observing the smoothness of the integrated profile.

Peak evaluation in each segment can be done using the same algorithm used in the conventional method. The corrections to the integrated profiles are performed before or during the peak evaluation. Absorption correction eliminates the influence of the irradiated area and the diffraction geometry on the measured intensity distribution. The absorption for a given material and radiation level depends on the incident angle to the sample and the reflected angle from the sample. For 2D-XRD, the reflected angle is a function of γ for each frame. The polarization effect is also a function of γ. Therefore, the correction for polarization and absorption should be applied to the frame before integration. (Details of these corrections were discussed in Section 2.5.4.3.4.) The polarization and absorption correction is not always necessary if the error caused by absorption can be tolerated for the application, or if the data-collection strategy involves only ψ and φ scans.

In most cases, $K\alpha$ radiation is used for stress measurement, in which case the weighted average wavelength of $K\alpha_1$ and $K\alpha_2$ radiation is used in the calculations. For samples with a broad peak width, diffraction of $K\alpha_1$ and $K\alpha_2$ radiation is merged together as a single peak profile, and the profile can be evaluated as if there is a single $K\alpha$ line without introducing much error to the measured *d*-spacing. For samples with a relatively narrow peak width, the diffraction profile shows strong asymmetry or may even reveal two peaks corresponding to the $K\alpha_1$ and $K\alpha_2$ lines, especially at high 2θ angles. In this case the profile fitting should include contributions from both the $K\alpha_1$ and $K\alpha_2$ lines. It is common practice to use the peak position from the $K\alpha_1$ line and the $K\alpha_1$ wavelength to calculate the *d*-spacing after $K\alpha_2$ stripping.

Background correction is necessary if there is a strong background or the peak-evaluation algorithms are sensitive to the background, such as in $K\alpha_2$ stripping, peak fitting, and peak-intensity and integrated-intensity evaluations. Background correction is performed by subtracting a linear intensity distribution based on the background intensities at the lower 2θ side and the higher 2θ side of the diffraction peak. The background region should be sufficiently far from the 2θ peak so that the correction will not truncate the diffraction profile. The 2θ ranges of the low background and high background should be determined based on the width of the 2θ peak and available background in the profile. Based on a normal distribution, a 2θ range of 2 times the FWHM covers 98% of the peak intensity, and 3 times the FWHM covers more than 99.9%, so the background intensity should be determined at more than 1 to 1.5 times the FWHM away from the peak position. The background correction can be neglected for a profile with a low background or if the error caused by the background is tolerable for the application. The peak position can be evaluated by various methods, such as gravity, sliding gravity, and profile fitting by parabolic, pseudo-Voigt or Pearson-VII functions (Lu, 1996; Sprauel & Michaud, 2002).

2.5.4.3.6. *Stress calculation*

The final data set after integration and peak evaluation should contain many data points describing the diffraction-ring shape for all collected frames. Each measured data point contains three goniometer angles (ω, ψ, φ) and the diffraction-ring position (γ, 2θ). The peak intensity or integrated intensity of the diffraction profile is another value to be determined and may be used in the stress calculation. In most cases the number of data points is more than the number of unknown stress components, so a linear least-squares method can be used to calculate the stresses. In a general least-squares regression, the residual for the *i*th data point is defined as

$$r_i = y_i - \hat{y}_i, \tag{2.5.86}$$

where y_i is the observed response value, $\hat{y}_i$ is the fitted response value and r_i is the residual, which is defined as the difference between the observed value and the fitted value. The summed square of residuals is given by

$$S = \sum_{i=1}^{n} r_i^2 = \sum_{i=1}^{n} (y_i - \hat{y}_i)^2, \tag{2.5.87}$$

where n is the number of data points and S is the sum-of-squares error to be minimized in the least-squares regression. For stress calculation, the observed response value is the measured strain at each data point,

$$y_i = \ln\left(\frac{\sin\theta_0}{\sin\theta_i}\right), \tag{2.5.88}$$

and the fitted response value is given by the fundamental equation as

$$\hat{y}_i = p_{11}\sigma_{11} + p_{12}\sigma_{12} + p_{22}\sigma_{22} + p_{13}\sigma_{13} + p_{23}\sigma_{23} + p_{33}\sigma_{33} + p_{\rm ph}\sigma_{\rm ph}, \tag{2.5.89}$$

where all possible stress components and stress coefficients are listed as a generalized linear equation. Since the response-value function is a linear equation of unknown stress components, the least-squares problem can be solved by a linear least-squares regression. In order to reduce the impact of texture, large grains or weak diffraction on the results of the stress determination, the standard error of profile fitting and the integrated intensity of each profile may be introduced as a weight factor for the least-squares regression (He, 2009).

2.5.4.3.7. *Comparison between the 2D method and the conventional method*

Stress measurement on a polycrystalline material by X-ray diffraction is based on the strain measurements in a single or in several sample orientations. Each measured strain is calculated from the average *d*-spacing of specific lattice planes {*hkl*} over many crystallites (grains). A larger number of contributing crystallites gives better accuracy and sampling statistics (also referred to as particle statistics). The sampling statistics are determined by both the crystal structure and the instrumentation. The instrument window is mainly determined by the divergence of the incident X-ray beam. Lattice-plane families with high multiplicity will also effectively improve the sampling statistics. The number of contributing crystallites measured by a conventional diffractometer is limited by the sizes and divergences of the incident and diffracted beams to the point detector. In a two-

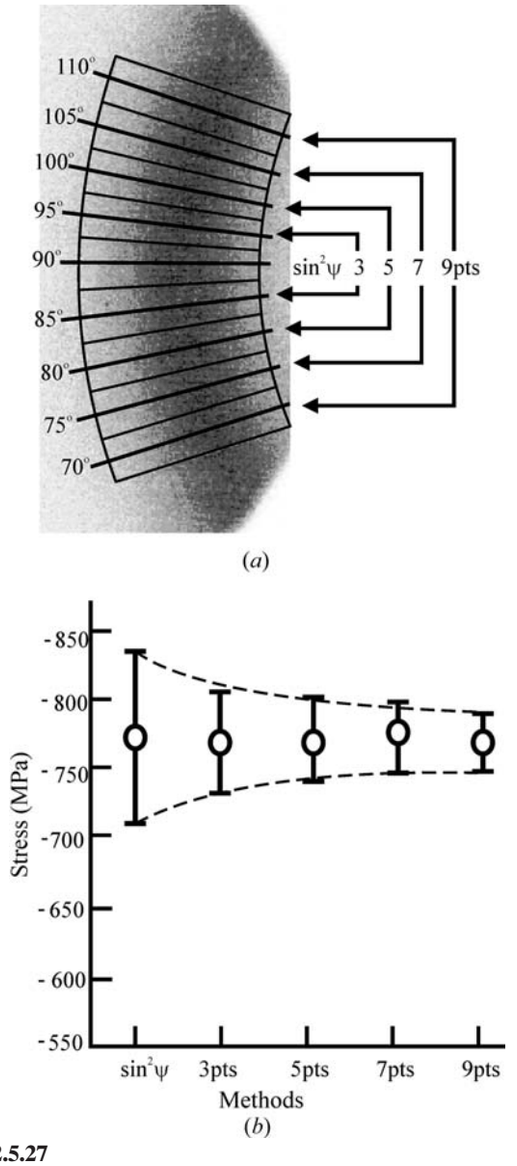

Figure 2.5.27
Stress calculation with the 2D method and the $\sin^2\psi$ method: (*a*) nine data points (abbreviated as pts) on the diffraction ring; (*b*) measured stress and standard deviation by different methods.

dimensional diffraction system, more crystallites can contribute to the diffraction because of the larger γ range.

An example of a stress calculation is provided by the measurement of the residual stress on the end surface of a carbon steel roller. One of the seven frames taken with an ω scan is shown in Fig. 2.5.27(*a*). The (211) ring covering the γ range 67.5 to 112.5° was used for stress analysis. First, the frame data were integrated along γ with an interval of $\Delta\gamma = 5°$. A total of nine diffraction profiles were obtained from γ integration. The peak position 2θ for each γ angle was then obtained by fitting the profile with a Pearson-VII function. A total of 63 data points can be obtained from the seven frames. The data points at $\gamma = 90°$ from seven frames, a typical data set for an ω diffractometer, were used to calculate the stress with the conventional $\sin^2\psi$ method. In order to compare the gain from having increased data points with the 2D method, the stress was calculated from 3, 5, 7 and 9 data points on each frame. The results from the conventional $\sin^2\psi$ method and the 2D method are compared in Fig. 2.5.27(*b*). The measured residual stress is compressive and the stress values from different methods agree very well. With the data taken from the same measurement (seven frames), the 2D method gives a lower standard error and the error decreases with increasing number of data points from the diffraction ring.

2.5.4.4. *Quantitative analysis*

2.5.4.4.1. *Crystallinity*

The crystallinity of a material influences many of its characteristics, including mechanical strength, opacity and thermal properties. Crystallinity measurement provides valuable information for both materials research and quality control in materials processing. The diffraction pattern from a material containing both amorphous and crystalline solids has a broad feature from the amorphous phase and sharp peaks from the crystalline phase. The weight percentage of the crystalline phases in a material containing both crystalline and amorphous phases can be determined by X-ray diffraction (Chung & Scott, 1973; Alexander, 1985; Murthy & Barton, 2000; Kasai & Kakudo, 2005). Assuming that the X-ray scattering intensity from each phase in such a material is proportional to its weight percentage, and that the scattering intensities from all phases can be measured within a given 2θ range, the per cent crystallinity is given by

$$x_{\rm pc} = 100\% \frac{I_{\rm crystal}}{I_{\rm crystal} + I_{\rm amorphous}}, \qquad (2.5.90)$$

where $x_{\rm pc}$ is the per cent crystallinity, $I_{\rm crystal}$ is the integrated intensity of all crystalline peaks and $I_{\rm amorphous}$ is the integrated intensity of the amorphous scattering. The accuracy of the measured per cent crystallinity depends on the integrated diffraction profile. Since most crystalline samples have a preferred orientation, it is very difficult to obtain a consistent measurement of crystallinity with a conventional diffractometer. Fig. 2.5.28 shows a 2D diffraction frame collected from an oriented polycrystalline sample. The diffraction is in transmission mode with the X-ray beam perpendicular to the plate sample surface. Fig. 2.5.28(*a*) shows a diffraction profile integrated from a horizontal region analogous to a profile collected with a conventional diffractometer. Only one peak from the crystalline phase can be observed in the profile. It is also possible that a different peak or no peak is measured if the sample is loaded in other orientations. Fig. 2.5.28(*b*) is the diffraction profile integrated from the region covering all peaks from the crystalline phase over almost all azimuthal angles. A total of four peaks from the crystalline phase are observed. This shows that a 2D-XRD system can measure per cent crystallinity more accurately and with more consistent results (Pople *et al.*, 1997; Bruker, 2000) than a conventional system.

2.5.4.4.2. *Crystallite size*

The size of the crystallites in a polycrystalline material has a significant effect on many of its properties, such as its thermal, mechanical, electrical, magnetic and chemical properties. X-ray diffraction has been used for crystallite-size measurement for many years. Most methods are based on diffraction-line broadening and line-profile analysis (Wilson, 1971; Klug & Alexander, 1974; Ungár, 2000). Another approach to crystallite-size measurement is based on the spotty diffraction rings collected with two-dimensional detectors when a small X-ray beam is used (Cullity, 1978; He, 2009). Line-profile analysis is based on the

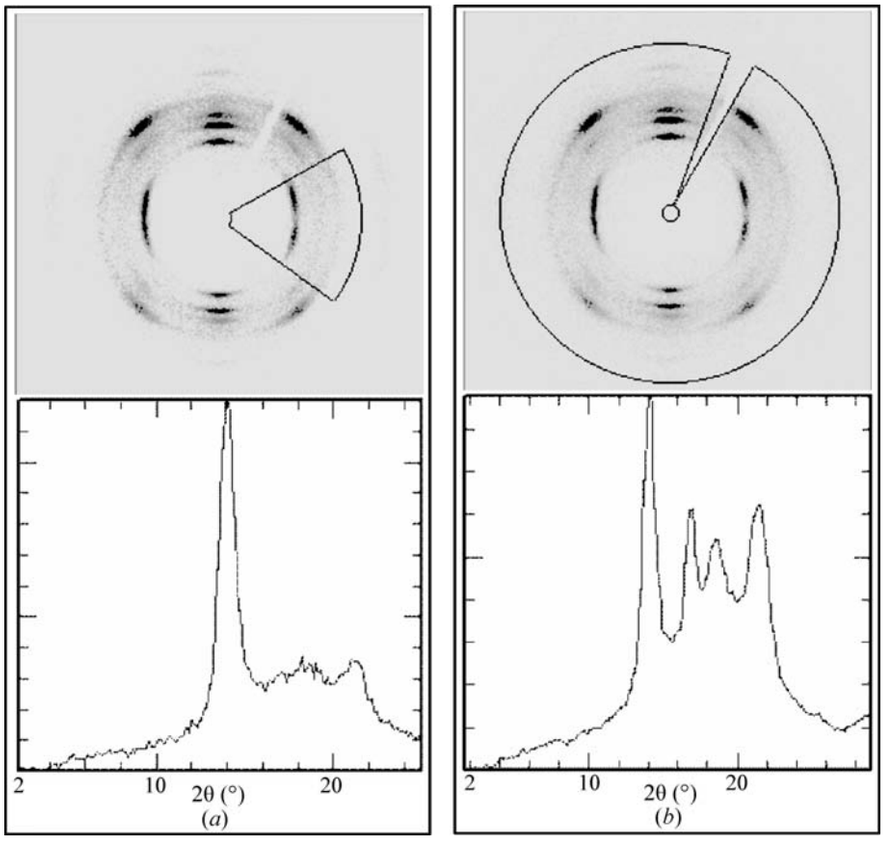

Figure 2.5.28
2D diffraction pattern from an oriented polycrystalline polymer sample. (*a*) Diffraction profile integrated from a horizontal region analogous to a profile collected with point detector. (*b*) Diffraction profile integrated from all parts of the 2D frame.

diffraction profile in the 2θ direction, while crystallite-size analysis with a spotty 2D diffraction pattern is based on the diffraction profile in the γ direction. The latter may be referred to as γ-profile analysis.

Fig. 2.5.29(*a*) shows a diffraction profile collected from gold nanoparticles and regular gold metal. The 2θ profile from the gold nanoparticles is significantly broader than the profile from regular gold metal. The crystallite size can be calculated by measuring the broadening and using the Scherrer equation:

$$B = \frac{C\lambda}{t\cos\theta}, \qquad (2.5.91)$$

where λ is the X-ray wavelength (in Å), B is the full width at half maximum (FWHM) of the peak (in radians) corrected for instrumental broadening and strain broadening, θ is the Bragg angle, C is a factor, typically from 0.9 to 1.0, depending on the crystallite shape (Klug & Alexander, 1974), and t is the crystallite size (also in Å). This equation shows an inverse relationship between crystallite size and peak-profile width. The wider the peak is, the smaller the crystallites. The 2θ diffraction profiles can be obtained either by using a conventional diffractometer with a point or line detector, or by γ integration from a diffraction pattern collected with 2D detector. When a 2D detector is used, a long sample-to-detector distance should be used to maximize the resolution. A small beam size and low convergence should also be used to reduce instrument broadening.

Fig. 2.5.29(*b*) shows a frame collected from an SRM660a (LaB_6) sample with a 2D-XRD system. The spotty diffraction rings are observed with average crystallite size of 3.5 μm. The number of spots in each diffraction ring is determined by the crystallite size and diffraction volume. Introducing a scaling factor covering all the numeric constants,

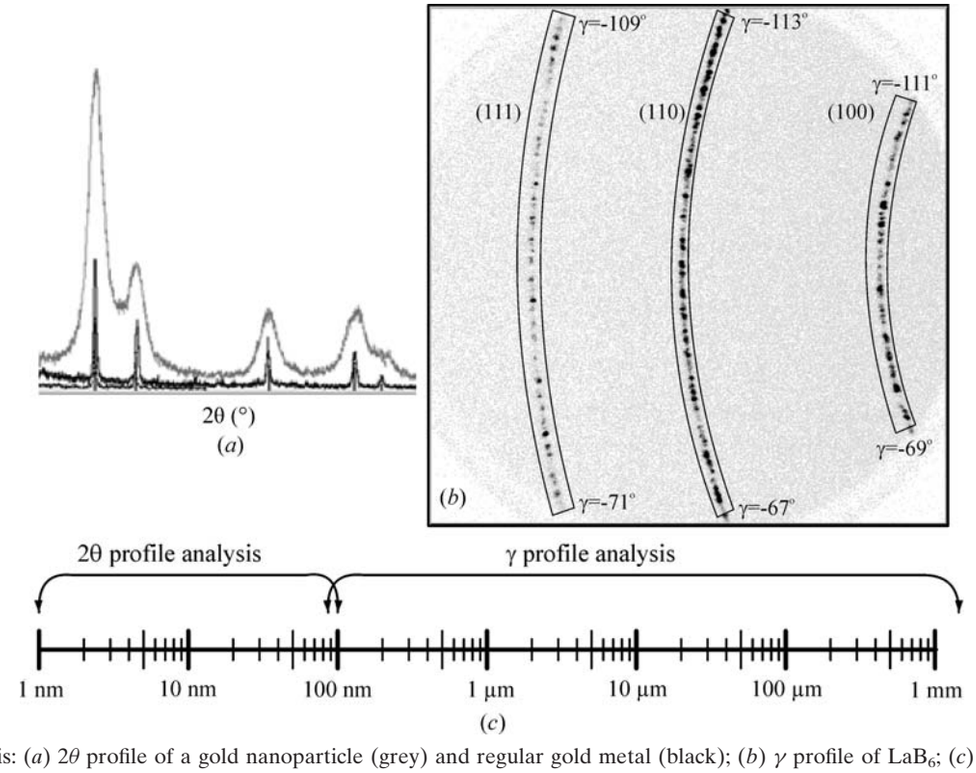

Figure 2.5.29
Crystallite-size analysis: (*a*) 2θ profile of a gold nanoparticle (grey) and regular gold metal (black); (*b*) γ profile of LaB_6; (*c*) measurement range.

the incident-beam divergence and the calibration factor for the instrument, we obtain an equation for the crystallite size as measured in reflection mode:

$$d = k\left\{\frac{p_{hkl} b^2 \arcsin[\cos\theta \sin(\Delta\gamma/2)]}{\mu N_s}\right\}^{1/3}, \qquad (2.5.92)$$

where d is the diameter of the crystallite particles, p_{hkl} is the multiplicity of the diffracting planes, b is the size of the incident beam (*i.e.* its diameter), $\Delta\gamma$ is the γ range of the diffraction ring, μ is the linear absorption coefficient and N_s is the number of spots within $\Delta\gamma$. For transmission mode, we have

$$d = k\left\{\frac{p_{hkl} b^2 t \arcsin[\cos\theta \sin(\Delta\gamma/2)]}{N_s}\right\}^{1/3}, \qquad (2.5.93)$$

where t is the sample thickness. In transmission mode with the incident beam perpendicular to the sample surface, the linear absorption coefficient affects the relative scattering intensity, but not the actual sampling volume. In other words, all the sample volume irradiated by the incident beam contributes to the diffraction. Therefore, it is reasonable to ignore the absorption effect $\exp(\mu t)$ for crystallite-size analysis as long as the sample is thin enough for transmission-mode diffraction. The effective sampling volume reaches a maximum for transmission-mode diffraction when $t = 1/\mu$.

For both reflection and transmission,

$$k = \left(\frac{3\beta}{8\pi}\right)^{1/3}, \qquad (2.5.94)$$

where β is the divergence of the incident beam. Without knowing the precise instrumental broadening, k can be treated as a calibration factor determined from the 2D diffraction pattern of a known standard. Since only a limited number of spots along the diffraction ring can be resolved, it can be seen from equation (2.5.94) that a smaller X-ray beam size and low-multiplicity peak should be used if a smaller crystallite size is to be determined.

Fig. 2.5.29(c) shows the measurement ranges of 2θ-profile and γ-profile analysis. The 2θ-profile analysis is suitable for crystallite sizes below 100 nm (1000 Å), while γ-profile analysis is suitable for crystallite sizes from as large as tens of μm down to 100 nm with a small X-ray beam size. By increasing the effective diffraction volume by translating the sample during data collection or multiple sample integration (or integrating data from multiple samples), the measurement range can be increased up to millimetres. Multiple sample integration can deal with large crystallite sizes without recalibration. The new calibration factor is given as

$$k_n = n^{1/3} k, \qquad (2.5.95)$$

where n is the number of targets that are integrated. The number of crystallites can be counted by the number of intersections of the γ profile with a threshold line. Every two intersections of the γ profile with this horizontal line represents a crystallite. In order to cancel out the effects of preferred orientation and other material and instrumental factors on the overall intensity fluctuation along the γ profile, one can use a trend line fitted to the γ profile by a second-order polynomial. It is always necessary to calibrate the system with a known standard, preferably with a comparable sample geometry and crystallite size. For reflection mode, it is critical to have a standard with a comparable linear absorption coefficient so as to have similar penetration.

References

Alexander, L. E. (1985). *X-ray Diffraction Methods in Polymer Science*. Malabar: Krieger Publishing Company.

Allahkarami, M. & Hanan, J. C. (2011). *X-ray diffraction mapping on a curved surface*. *J. Appl. Cryst.* **44**, 1211–1216.

Arndt, U. W. (1986). *X-ray position-sensitive detectors*. *J. Appl. Cryst.* **19**, 145–163.

Arndt, U. W. (1990). *Focusing optics for laboratory sources in X-ray crystallography*. *J. Appl. Cryst.* **23**, 161–168.

Bergese, P., Bontempi, E., Colombo, I. & Depero, L. E. (2001). *Micro X-ray diffraction on capillary powder samples: a novel and effective technique for overcoming preferred orientation*. *J. Appl. Cryst.* **34**, 663–665.

Bhuvanesh, N. S. P. & Reibenspies, J. H. (2003). *A novel approach to micro-sample X-ray powder diffraction using nylon loops*. *J. Appl. Cryst.* **36**, 1480–1481.

Birkholz, M. (2006). *Thin Film Analysis by X-ray Scattering*, pp. 191–195. Weinheim: Wiley-VCH.

Blanton, T. N. (1994). *X-ray diffraction orientation studies using two-dimensional detectors*. *Adv. X-ray Anal.* **37**, 367–373.

Blanton, T. N. (2003). *X-ray film as a two-dimensional detector for X-ray diffraction analysis*. *Powder Diffr.* **18**, 91–98.

Bloomer, A. C. & Arndt, U. W. (1999). *Experiences and expectations of a novel X-ray microsource with focusing mirror. I*. *Acta Cryst.* D**55**, 1672–1680.

Boesecke, P. (2007). *Reduction of two-dimensional small- and wide-angle X-ray scattering data*. *J. Appl. Cryst.* **40**, s423–s427.

Bontempi, E., Benedetti, D., Massardi, A., Zacco, A., Borgese, L. & Depero, L. E. (2008). *Laboratory two-dimensional X-ray microdiffraction technique: a support for authentication of an unknown Ghirlandaio painting*. *Appl. Phys. A*, **92**, 155–159.

Borgonovi, G. M. (1984). *Determination of residual stress from two-dimensional diffraction pattern*. *Nondestructive Methods for Material Property Determination*, edited by C. O. Ruud & R. E. Green Jr, pp. 47–57. New York: Plenum Publishing Corporation.

Bourgeois, D., Moy, J. P., Svensson, S. O. & Kvick, Å. (1994). *The point-spread function of X-ray image-intensifiers/CCD-camera and imaging-plate systems in crystallography: assessment and consequences for the dynamic range*. *J. Appl. Cryst.* **27**, 868–877.

Bruker (2000). *Percent crystallinity in polymer*. Bruker AXS Lab Report No. L86-E00005.

Bunge, H. J. (1983). *Texture Analysis in Materials Science*. London: Butterworth.

Bunge, H. J. & Klein, H. (1996). *Determination of quantitative, high-resolution pole-figures with the area detector*. *Z. Metallkd.* **87**(6), 465–475.

Campbell, J. W., Harding, M. M. & Kariuki, B. (1995). *Spatial-distortion corrections, for Laue diffraction patterns recorded on image plates, modelled using polynomial functions*. *J. Appl. Cryst.* **28**, 43–48.

Cervellino, A., Giannini, C., Guagliardi, A. & Ladisa, M. (2006). *Folding a two-dimensional powder diffraction image into a one-dimensional scan: a new procedure*. *J. Appl. Cryst.* **39**, 745–748.

Chung, F. H. & Scott, R. W. (1973). *A new approach to the determination of crystallinity of polymers by X-ray diffraction*. *J. Appl. Cryst.* **6**, 225–230.

Cullity, B. D. (1978). *Elements of X-ray Diffraction*, 2nd ed. Reading, MA: Addison-Wesley.

Derewenda, Z. & Helliwell, J. R. (1989). *Calibration tests and use of a Nicolet/Xentronics imaging proportional chamber mounted on a conventional source for protein crystallography*. *J. Appl. Cryst.* **22**, 123–137.

Dickerson, M. B., Pathak, K., Sandhage, K. H., Snyder, R. L., Balachandran, U., Ma, B., Blaugher, R. D. & Bhattacharya, R. N. (2002). *Applications of 2D detectors in x-ray analysis*. *Adv. X-ray Anal.* **45**, 338–344.

Durst, R. D., Carney, S. N., Diawara, Y. & Shuvalov, R. (2002). *Readout structure and technique for electron cloud avalanche detectors*. US Patent No. 6, 340, 819.

Eatough, M. O., Rodriguez, M. A., Blanton, T. N. & Tissot, R. G. (1997). *A comparison of detectors used for microdiffraction applications*. *Adv. X-ray Anal.* **41**, 319–326.

Ercan, A., Tate, M. W. & Gruner, S. M. (2006). *Analog pixel array detectors*. *J. Synchrotron Rad.* **13**, 110–119.

European Standard (2008). *Non-destructive Testing – Test Method for Residual Stress Analysis by X-ray Diffraction*. EN15305–2008.

Flemming, R. L. (2007). *Micro X-ray diffraction (μXRD): a versatile technique for characterization of Earth and planetary materials*. *Can. J. Earth Sci.* **44**, 1333–1346.

Fuentes-Montero, L., Montero-Cabrera, M. E. & Fuentes-Cobas, L. (2011). *The software package ANAELU for X-ray diffraction analysis using two-dimensional patterns*. *J. Appl. Cryst.* **44**, 241–246.

Fujii, N. & Kozaki, S. (1993). *Highly sensitive x-ray stress measurement in small area*. *Adv. X-ray Anal.* **36**, 505–513.

Fujita, H., Tsai, D.-Y., Itoh, T., Doi, K., Morishita, J., Ueda, K. & Ohtsuka, A. (1992). *A simple method for determining the modulation transfer function in digital radiography*. *IEEE Trans. Med. Imag.* **11**, 34–39.

Gelfi, M., La Vecchia, G. M., Lecis, N. & Troglio, S. (2005). *Relationship between through-thickness residual stress of CrN-PVD coatings and fatigue nucleation sites*. *Surf. Coat. Technol.* **192**, 263–268.

Giomatartis, Y. (1998). *Development and prospects of the new gaseous detector 'Micromegas'*. *Nucl. Instrum. Methods A*, **419**, 239.

Guggenheim, S. (2005). *Simulations of Debye–Scherrer and Gandolfi patterns using a Bruker Smart Apex diffractometer system*. Bruker AXS Application Note 373.

Hammersley, A. P. (2016). *FIT2D: a multi-purpose data reduction, analysis and visualization program*. *J. Appl. Cryst.* **49**, 646–652.

Hammersley, A. P., Svensson, S. O., Hanfland, M., Fitch, A. N. & Häusermann, D. (1996). *Two-dimensional detector software: From real detector to idealised image or two-theta scan*. *High Pressure Res.* **14**, 235–248.

Hanan, J., Űstündag, E. & Almer, J. D. (2004). *A new analysis method for two-dimensional X-ray data*. *Adv. X-ray Anal.* **47**, 174–180.

Hanna, S. & Windle, A. H. (1995). *A novel polymer fibre diffractometer, based on a scanning X-ray-sensitive charge-coupled device*. *J. Appl. Cryst.* **28**, 673–689.

He, B. (1992). *X-ray Diffraction from Point-Like Imperfection*. PhD dissertation, Virginia Tech, USA.

He, B. B. (2000). *Residual stress measurement with two-dimensional diffraction*. *The 20th ASM Heat Treating Society Conference Proceedings*, Vol. 1, pp. 408–417. St Louis, USA.

He, B. B. (2003). *Introduction to two-dimensional X-ray diffraction*. *Powder Diffr.* **18**, 71–85.

He, B. B. (2004). *Microdiffraction using two-dimensional detectors*. *Powder Diffr.* **19**, 110–118.

He, B. B. (2006). *Measurement of residual stresses in thin films by two-dimensional XRD*. *Mater. Sci. Forum*, **524–525**, 613–618.

He, B. B. (2009). *Two-dimensional X-ray Diffraction*. New York: John Wiley & Sons.

He, B. B., Anzelmo, J., LaPuma, P., Preckwinkel, U. & Smith, K. (2001). *XRD rapid screening system for combinatorial chemistry*. *Adv. X-ray Anal.* **44**, 1–5.

He, T., Durst, R. D., Becker, B. L., Kaercher, J. & Wachter, G. (2011). *A large area X-ray imager with online linearization and noise suppression*. *Proc. SPIE*, **8142**, 81421Q.

He, B. B. & Preckwinkel, U. (2002). *X-ray optics for two-dimensional x-ray diffraction*. *Adv. X-ray Anal.* **45**, 332–337.

He, B., Rao, S. & Houska, C. R. (1994). *A simplified procedure for obtaining relative x-ray intensities when a texture and atomic displacements are present*. *J. Appl. Phys.* **75**, 4456–4464.

He, B. B. & Smith, K. L. (1997). *Strain and stress measurement with two-dimensional detector*. *Adv. X-ray Anal.* **41**, 501–508.

He, B. B. & Smith, K. L. (1998). *Computer simulation of diffraction stress measurement with 2D detectors*. *Proceedings of 1998 SEM Spring Conference on Experimental and Applied Mechanics*, Houston, USA.

He, B. B., Xu, K., Wang, F. & Huang, P. (2005). *Two-dimensional X-ray diffraction for structure and stress analysis*. *Mater. Sci. Forum*, **490–491**, 1–6.

Helming, K., Lyubchenko, M., He, B. & Preckwinkel, U. (2003). *A new method for texture measurements using a general area detector diffraction system*. *Powder Diffr.* **18**, 99–102.

Hinrichsen, B. (2007). *Two-dimensional X-ray powder diffraction*. PhD dissertation, University of Stuttgart, Germany.

Jabeen, S., Raza, S. M., Ahmed, M. A., Zai, M. Y. & Erlacher, K. (2011). *Two dimensional X-ray diffraction (2D-XRD) studies on olivine of U. S. A*. *J. Chem. Soc. Pak.* **33**(5), 612–618.

James, M. R. & Cohen, J. B. (1980). *The measurement of residual stresses by x-ray diffraction techniques*. *Treatise on Materials Science and Technology*, **19A**, edited by H. Herman. New York: Academic Press.

Jenkins, R. & Snyder, R. L. (1996). *Introduction to X-ray Powder Diffractometry*. New York: John Wiley & Sons.

Kämpfe, A., Kämpfe, B., Goldenbogen, S., Eigenmann, B., Macherauch, E. & Löhe, D. (1999). *X-ray stress analysis on polycrystalline materials using two-dimensional detectors*. *Adv. X-ray Anal.* **43**, 54–65.

Kasai, N. & Kakudo, M. (2005). *X-ray Diffraction by Macromolecules*, pp. 393–417. Tokyo: Kodansha/Springer.

Kerr, K. A. & Ashmore, J. P. (1974). *Systematic errors in polarization corrections for crystal-monochromatized radiation*. *Acta Cryst.* A**30**, 176–179.

Khazins, D. M., Becker, B. L., Diawara, Y., Durst, R. D., He, B. B., Medved, S. A., Sedov, V. & Thorson, T. A. (2004). *A parallel-plate resistive-anode gaseous detector for X-ray imaging*. *IEEE Trans. Nucl. Sci.* **51**, 943–947.

Klein, J., Lehmann, C. W., Schmidt, H.-W. & Maier, W. F. (1998). *Combinatorial material libraries on the microgram scale with an example of hydrothermal synthesis*. *Angew. Chem. Int. Ed.* **37**, 3369–3372.

Klug, H. P. & Alexander, L. E. (1974). *X-ray Diffraction Procedures for Polycrystalline and Amorphous Materials*. New York: John Wiley & Sons.

Korhonen, M. A., Lindroos, V. K. & Suominen, L. S. (1989). *Application of a new solid state x-ray camera to stress measurement*. *Adv. X-ray Anal.* **32**, 407–413.

Krause, K. L. & Phillips, G. N. (1992). *Experience with commercial area detectors: a 'buyer's' perspective*. *J. Appl. Cryst.* **25**, 146–154.

Kugler, W. (2003). *X-ray diffraction analysis in the forensic science: the last resort in many criminal cases*. *Adv. X-ray Anal.* **46**, 1–16.

Lewis, R. (1994). *Multiwire gas proportional counters: decrepit antiques or classic performers? J. Synchrotron Rad.* **1**, 43–53.

Lu, J. (1996). *Handbook of Measurement of Residual Stress*. Society for Experimental Mechanics. Lilburn: The Fairmont Press.

Lutz, G. (2006). *Silicon drift and pixel devices for X-ray imaging and spectroscopy*. *J. Synchrotron Rad.* **13**, 99–109.

Maslen, E. N. (1992). *X-ray absorption*. *International Tables for Crystallography*, Vol. C, edited by A. J. C. Wilson, pp. 520–529. Dordrecht: Kluwer Academic Publishers.

Moy, J. P., Hammersley, A. P., Svensson, S. O., Thompson, A., Brown, K., Claustre, L., Gonzalez, A. & McSweeney, S. (1996). *A novel technique for accurate intensity calibration of area X-ray detectors at almost arbitrary energy*. *J. Synchrotron Rad.* **3**, 1–5.

Mudie, S. T., Pavlov, K. M., Morgan, M. J., Hester, J. R., Tabuchi, M. & Takeda, Y. (2004). *Collection of reciprocal space maps using imaging plates at the Australian National Beamline Facility at the Photon Factory*. *J. Synchrotron Rad.* **11**, 406–413.

Murthy, N. S. & Barton, R. Jr (2000). *Polymer industry*. *Industrial Applications of X-ray Diffraction*, edited by F. H. Chung & D. K. Smith, pp. 495–509. New York: Marcel Dekker.

Ning, G. & Flemming, R. L. (2005). *Rietveld refinement of LaB_6: data from μXRD*. *J. Appl. Cryst.* **38**, 757–759.

Noyan, I. C. & Cohen, J. B. (1987). *Residual Stress*. New York: Springer-Verlag.

Paciorek, W. A., Meyer, M. & Chapuis, G. (1999). *On the geometry of a modern imaging diffractometer*. *Acta Cryst.* A**55**, 543–557.

Pecharsky, V. K. & Zavalij, P. Y. (2003). *Fundamentals of Powder Diffraction and Structure Characterization of Materials*. Boston: Kluwer Academic Publishers.

Pitschke, W., Collazo, J. A. L., Hermann, H. & Hildenbrand, V. D. (1996). *Absorption corrections of powder diffraction intensities recorded in transmission geometry*. *J. Appl. Cryst.* **29**, 561–567.

Ponchut, C. (2006). *Characterization of X-ray area detectors for synchrotron beamlines*. *J. Synchrotron Rad.* **13**, 195–203.

Pople, J. A., Keates, P. A. & Mitchell, G. R. (1997). *A two-dimensional X-ray scattering system for in-situ time-resolving studies of polymer structures subjected to controlled deformations*. *J. Synchrotron Rad.* **4**, 267–278.

Rodriguez-Navarro, A. B. (2006). *XRD2DScan: new software for polycrystalline materials characterization using two-dimensional X-ray diffraction*. *J. Appl. Cryst.* **39**, 905–909.

Ross, C. R. (1992). *Measurement of powder diffraction sample absorption coefficients using monochromated radiation and transmission geometry*. *J. Appl. Cryst.* **25**, 628–631.
Rowe, R. (2009). *New statistical calibration approach for Bruker AXS D8 Discover microdiffractometer with Hi-Star detector using GADDS software*. *Powder Diffr.* **24**, 263–271.
Rudolf, P. R. & Landes, B. G. (1994). *Two-dimensional X-ray diffraction and scattering of microcrystalline and polymeric materials*. *Spectroscopy*, **9**(6), 22–33.
Scheidegger, S., Estermann, M. A. & Steurer, W. (2000). *Correction of specimen absorption in X-ray diffuse scattering experiments with area-detector systems*. *J. Appl. Cryst.* **33**, 35–48.
Schmidbauer, M., Schäfer, P., Besedin, S., Grigoriev, D., Köhler, R. & Hanke, M. (2008). *A novel multi-detection technique for three-dimensional reciprocal-space mapping in grazing-incidence X-ray diffraction*. *J. Synchrotron Rad.* **15**, 549–557.
Smilgies, D.-M. & Blasini, D. R. (2007). *Indexation scheme for oriented molecular thin films studied with grazing-incidence reciprocal-space mapping*. *J. Appl. Cryst.* **40**, 716–718.
Smith, K. L. & Ortega, R. B. (1993). *Use of a two-dimensional, position sensitive detector for collecting pole figures*. *Adv. X-ray Anal.* **36**, 641–647.
Sprauel, J. M. & Michaud, H. (2002). *Global X-ray method for the determination of stress profiles*. *Mater. Sci. Forum*, **404–407**, 19–24.
Stanton, M., Phillips, W. C., Li, Y. & Kalata, K. (1992). *Correcting spatial distortions and nonuniform response in area detectors*. *J. Appl. Cryst.* **25**, 549–558.
Sulyanov, S. N., Popov, A. N. & Kheiker, D. M. (1994). *Using a two-dimensional detector for X-ray powder diffractometry*. *J. Appl. Cryst.* **27**, 934–942.
Tate, M. W., Eikenberry, E. F., Barna, S. L., Wall, M. E., Lowrance, J. L. & Gruner, S. M. (1995). *A large-format high-resolution area X-ray detector based on a fiber-optically bonded charge-coupled device (CCD)*. *J. Appl. Cryst.* **28**, 196–205.
Tissot, R. G. (2003). *Microdiffraction applications utilizing a two-dimensional proportional detector*. *Powder Diffr.* **18**, 86–90.
Ungár, T. (2000). *Warren–Averbach applications*. *Industrial Applications of X-ray Diffraction*, edited by F. H. Chung & D. K. Smith, pp. 847–867. New York: Marcel Dekker.
Walter, N. M. (1971). *Residual Stress Measurement by X-ray Diffraction* – SAE J784a. Society of Automotive Engineering.
Warren, B. E. (1990). *X-ray Diffraction*. New York: Dover Publications.
Wenk, H.-R. & Grigull, S. (2003). *Synchrotron texture analysis with area detectors*. *J. Appl. Cryst.* **36**, 1040–1049.
Westbrook, E. M. (1999). *Performance characteristics needed for protein crystal diffraction X-ray detectors*. *Proc. SPIE*, **3774**, 2–16.
Wiesmann, J., Graf, J., Hoffmann, C. & Michaelsen, C. (2007). *New possibilities for x-ray diffractometry*. *Physics meets Industry*, edited by J. Gegner & F. Haider. Renningen: ExpertVerlag. ISBN 978–3-8169–2740-2.
Wilson, A. J. C. (1971). *Some further considerations in particle-size broadening*. *J. Appl. Cryst.* **4**, 440–443.
Winter, D. J. & Squires, B. A. (1995). *A new approach in performing microdiffraction analysis*. *Adv. X-ray Anal.* **38**, 551–556.
Yagi, N. & Inoue, K. (2007). *CMOS flatpanel detectors for SAXS/WAXS experiments*. *J. Appl. Cryst.* **40**, s439–s441.
Yoshioka, Y. & Ohya, S. (1992). *X-ray analysis of stress in a localized area by use of image plate*. *Adv. X-ray Anal.* **35**, 537–543.
Zuev, A. D. (2006). *Calculation of the instrumental function in X-ray powder diffraction*. *J. Appl. Cryst.* **39**, 304–314.

International Tables for Crystallography (2018). Vol. H, Chapter 2.6, pp. 150–155.

2.6. Non-ambient-temperature powder diffraction

C. A. Reiss

2.6.1. Introduction

X-ray powder diffraction (XRPD) is a powerful tool for the *in situ* investigation of the evolution of a specimen during a non-ambient experiment and for studying structural changes such as lattice expansions and contractions, phase transformations, phase composition, material stability, and alterations in crystallite size. X-rays (and neutrons) are more penetrating than other analytical probes and thus are ideally suited to carrying out *in situ* studies. Many (if not most) polycrystalline materials undergo transformations under non-ambient conditions. If the aim of an experiment is to discover structure–property correlations, it is crucial that the correct structure be used; thus *in situ* diffraction experiments are almost mandatory. This chapter highlights the best ways to perform non-ambient experiments, describing the different equipment for slightly and heavily absorbing materials and the corresponding optical pathways.

The focus is on commercially available equipment for laboratory diffractometers and not on special equipment built at synchrotrons and neutron facilities.

2.6.2. *In situ* powder diffraction

The Latin phrase '*in situ*' literally means 'in position', but it is used in many contexts. In the field of X-ray powder diffraction there is no strict definition of this phrase. If the phrase is taken literally, all non-ambient experiments are *in situ*; the material stays 'in position' during the non-ambient experiment. The environment changes while transforming the sample by outside influences (Norby & Schwarz, 2008). Temperature changes give rise to many processes that can be monitored with or without different gas environments. The main processes that are monitored are the formation of new compounds, phase transformations, and structural changes such as lattice expansions and contractions. Increasingly, surface-layer properties such as stress and texture are studied. The characterization of variations in the crystallite size of nanomaterials is a more recent application.

In situ X-ray diffraction is still a growing research field owing to the introduction of line detectors and area detectors (see Chapter 2.5). These make it possible to measure a large part of the diffraction pattern at once, making the scanning time much shorter compared with a point detector. This speed significantly improves the data quality and reduces the risk of collecting uninterpretable data because of changes in the material under study during the measurement. Another advantage of these detectors is that static detector measurements can be performed, making time-resolved and/or temperature-resolved studies possible.

2.6.3. Processes of interest

Many applications of XRPD contribute to industrial and environmental process development. Some typical application areas are heat treatment and annealing, which are frequently used in the production of alloys, ceramics and polymers; the annealing process affects the strength and/or hardness of materials through microstructural changes. Calcination and sintering are used in the fields of catalysts, building materials and zeolites. Dehydration processes in pharmaceuticals are studied to determine the influence of local environment on the microstructure of drugs and how time affects the availability or preservation of the active pharmaceutical ingredient. These very important topics can be investigated in the case of hydration or dehydration with a humidity chamber. Such chambers control the relative humidity at the same time as the temperature, and are commercially available. Another important topic for the pharmaceutical industry (see Chapter 7.5) is the polymorphic transformations that occur under near- and non-ambient conditions. In nearly all fields from alloys to drugs, from building materials to catalysts, and from nanomaterials to single-crystal materials, structure and phase changes are studied during the operation of processes. Increasingly, non-ambient studies also include other parameters besides temperature and gas environment, for example pressure and humidity. Processes such as the charging and discharging of batteries (see Chapter 7.3) can also be seen as a non-ambient or perhaps better as an '*in operando*' process.

2.6.4. General system setup of non-ambient chambers

2.6.4.1. *Sample stage*

The main requirement for a good non-ambient chamber is that the specimen is cooled/heated homogeneously at a controllable rate. The temperature of the goniometer and other parts of the diffractometer should not be affected while operating the temperature stage. Different sample-stage designs are possible: direct heating/cooling *via* a strip or plate, or surround heating/cooling with an oven or gas convection for a capillary. The advantage of an environmental heater/cooler is the good temperature homogeneity, as there is heat transfer from all sides by radiation and gas convection around the sample or capillary. In contrast, when using a direct heater such as a heating/cooling strip or plate only one-side heat transfer to the sample is possible through the contact surface. An advantage of direct heaters/coolers is the ability to achieve very high and low temperatures and rapid temperature changes. Other differences are the more accurate sample-temperature measurement in an oven compared with a strip heater, where temperature gradients can be present in the strip and the sample attached to the strip heater. For high-temperature measurements with capillaries, the best choice is fused silica ('quartz') glass with a melting point of ∼1973 K; for low-temperature measurements borosilicate glass capillaries are used. A typical hardware setup for a non-ambient X-ray diffraction experiment is shown in Fig. 2.6.1.

2.6.4.2. *Temperature-control unit, process controller*

To control the temperature, a temperature controller with an integrated process controller is needed. For controlled heating/cooling it is necessary to continuously measure the actual temperature and compare it with the set temperature. Often, a standard industrial process controller is used to convert the signal from the temperature sensor into a temperature value, to display

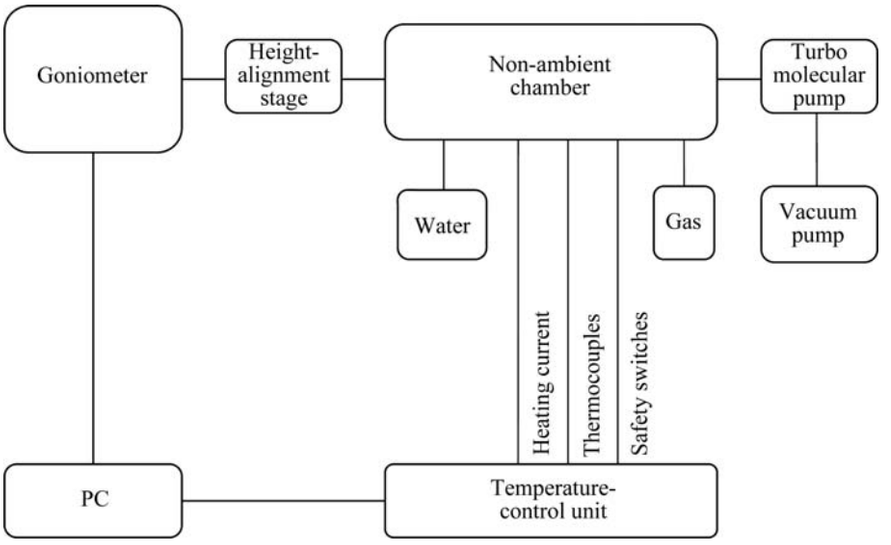

Figure 2.6.1
Typical hardware setup for a non-ambient X-ray diffraction experiment as described in Section 2.6.4; non-ambient chamber, temperature/process-control unit, vacuum/gas equipment, cooling water and goniometer with height-alignment stage connected to a PC.

the value, to send it to the control PC and to control the power for heating/cooling. In addition to controlling the sample conditions, the temperature-control unit (TCU) usually monitors other instrument components such as the cooling of the sample-stage housing and safety devices.

2.6.4.3. *Vacuum equipment, gas supply*

High-temperature X-ray diffraction measurements are often performed in vacuum or in an inert-gas atmosphere to avoid oxidation of the specimen or the sample support. Systems with a rotary pump typically achieve a vacuum of 10^{-2} mbar (where 1 mbar = 100 Pa); when adding a turbo molecular pump to the rotary pump, a vacuum of about 10^{-4} mbar can be reached. A low vacuum or a completely dry gas atmosphere, *e.g.* pure nitrogen (or helium, which has the advantage of a lower background in the diffraction patterns), is also needed for low-temperature experiments to avoid icing problems. Best practice is not to vent the flow of inert gas into the diffractometer enclosure or the laboratory atmosphere, but into the ventilation system (fume hood). Some local safety authorities may require such venting.

2.6.4.4. *Water cooling*

The housing of the sample stage must be kept close to room temperature to avoid heat transfer to the diffractometer and to ensure user safety. In most cases, water is used for this purpose, and the cooling water can be shared with the diffractometer.

2.6.4.5. *Diffractometer and height-compensation mechanism*

The non-ambient chamber has to be interfaced to the goniometer. Interfaces are available without and with a height-compensation mechanism; the latter can be manual or motorized.

When heating/cooling a specimen in an environmental heater, sample displacement is virtually unavoidable, mainly owing to the thermal expansion/contraction of the sample holder. It is possible to correct the temperature-dependent change of the sample position with a height-compensation mechanism (motorized z stage) or to model the displacement in the refinement software. When using a z stage that is controlled *via* software, the shifts in peak positions are only caused by the thermal lattice expansion/contraction of the sample under study. If no such mechanism is available, a parallel X-ray beam (which is not sensitive to sample displacement) can be used, but the resolution may be worse compared with measurements in para-focusing Bragg–Brentano geometry, and granularity may be significant. For strip heaters the displacement of the sample due to the strip is not so pronounced. If a peak of the material of the strip is visible in the diffractogram this can be used as a reference for height compensation if the thermal expansion of the strip material is also taken into account.

2.6.5. Specimen properties

In designing a non-ambient experiment the specimen properties must be taken into account; the holder material should not react with the sample. For flat sample geometry it is preferable that the specimen completely absorbs the X-ray beam. If the specimen is highly transparent, one can either use a thin specimen on a zero-background sample holder or use a capillary. For capillary measurements the X-ray beam must penetrate the capillary completely; if this is not the case, higher energy X-rays (such as Mo or Ag) can be used (Section 2.6.7.2). Every sample is unique, and a suitable solution must be devised.

2.6.6. High-temperature sample stages

A typical laboratory non-ambient setup consists of a non-ambient sample stage, often called a temperature chamber. The sample stage is mounted on a goniometer, preferably in a θ–θ configuration (Fig. 2.6.2). In this case the sample stays horizontal and there is no need to fear melting of the sample with the possibility of it dripping off/out of the sample holder.

A temperature-control unit, vacuum equipment, gas supply and water cooling have to be added to the system before it can be operational.

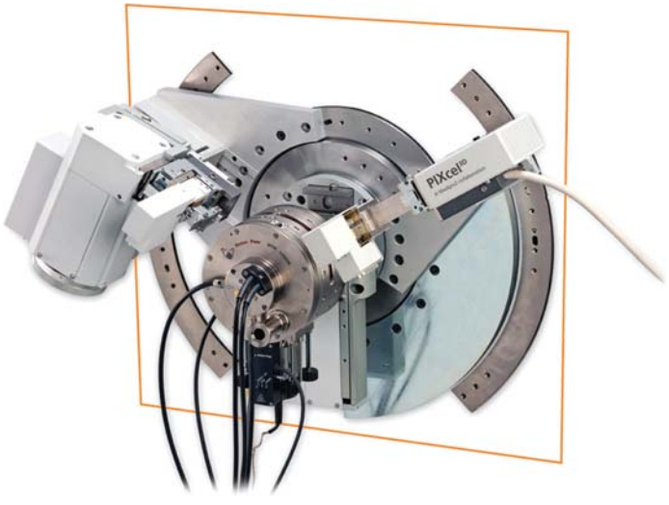

Figure 2.6.2
An Anton Paar HTK 1200N high-temperature oven chamber on a PANalytical Empyrean system equipped with a PIXcel3D detector.

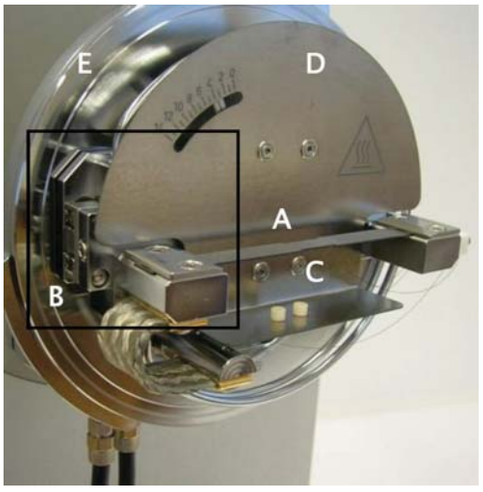

Figure 2.6.3
The interior of a typical strip-heater sample stage (Anton Paar HTK 2000N) with heating strip (A), mechanics to compensate strip expansion (B), thermocouple wires (C), heat shield (D) and water-cooled base plate (E).

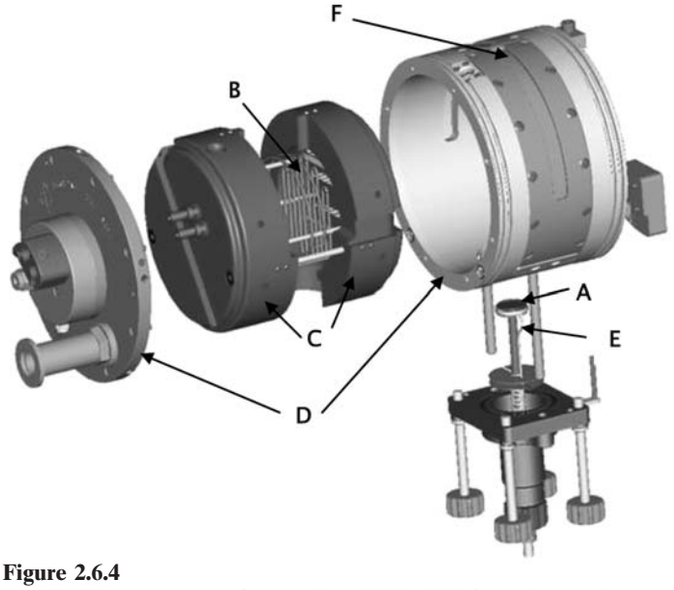

Figure 2.6.4
A typical furnace heater (Anton Paar HTK 1200N) consisting of sample holder (A), heater (B), thermal insulation (C), water-cooled housing (D), thermocouple (E) and X-ray window (F).

2.6.6.1. *Direct heating: strip heaters*

The highest temperatures can be reached with so-called strip heaters (Fig. 2.6.3). Commercial stages that can heat to up to 2573 K are available. Sample heating is performed with a high-current resistance heater. The specimen is placed directly on the strip or in a crucible on the strip. Typical strip materials are platinum (which can be heated in air to up to 1873 K) and tungsten (maximum temperature 2673 K), which requires a vacuum or an inert-gas atmosphere. Less common strip materials which have to be operated in vacuum or in an inert-gas atmosphere are graphite (maximum 1773 K), molybdenum (maximum 2173 K) and tantalum (maximum 2873 K). In addition to very high temperatures, these heaters offer very fast heating and cooling. The HTK 2000N from Anton Paar, for example, can reach up to 2573 K in 3 min. The temperature is measured with a thermocouple, which is usually welded to the heating strip. The main disadvantages of strip heaters are possible chemical reactions between the heating strip and sample, difficulties in measuring the sample temperature accurately and difficult sample preparation. Often, it is not the starting material that reacts but the products that form during heating. Another strip material can be chosen if reactions are known to occur. Inaccurate temperature measurements can be minimized by placing a second temperature sensor on top of the sample.

2.6.6.2. *Environmental heating: the oven*

The second common type of sample stage for high temperatures are oven heaters, also called environmental heaters (Fig. 2.6.4). An electrically heated wire is formed into a cage, which is surrounded with thermal insulation. The heater and insulation form a furnace which almost completely surrounds the sample, creating a very uniform temperature distribution on the inside and minimizing the heat transfer to the housing of the sample stage. Heat is transferred *via* radiation and convection to the sample. The sample is placed on a sample holder in the centre of the furnace, without direct contact with the heater. The sample temperature is measured with a thermocouple located close to the sample, providing accurate measurement of the sample temperature. In addition, it is possible to oscillate the sample to improve the data quality (by reducing granularity), and the user can measure (polycrystalline) solid samples as well as powder samples. In most cases, a long sample holder must be used to place the sample in the centre of the furnace. The thermal expansion of the sample holder while heating must be compensated for by z adjustment to avoid sample displacement (see Section 2.6.4.5). Windows for letting the X-rays enter and leave the chamber should preferably have no influence on the diffraction process. Different materials are available depending on the requirements of the non-ambient measurements. Kapton is the most commonly used window material, followed by graphite, aluminum and beryllium. Environmental heating is also one of two methods used to heat capillaries for X-ray diffraction with transmission geometry. The other option is heating the capillary with a gas flow.

Example: Cement. Cement consists of different calcium silicates (see Chapter 7.12). The exact phases that are present and their abundances determine important physical properties of a cement such as its strength. One of the phases in cement, belite (Ca_2SiO_4), exhibits rapid phase transitions. Fast transitions require good time resolution to detect short-lived intermediate phases and to follow the kinetics of fast phase transformations. An Anton Paar HTK 1200N oven was used for this experiment together with a PIXcel3D detector in static mode using a radius-reduction interface to allow snapshots to be taken over a 2θ range of 6° within a time frame of less than 1 min. Bragg–Brentano geometry was used to achieve a good resolution in 2θ and, to compensate for thermal expansion of the sample holder, an automatic height compensation was applied. On heating $CaCO_3$ with amorphous SiO_2 at 10 K min^{-1}, a solid-state reaction was seen at 853 K; α'_L-Ca_2SiO_4 is formed together with CO_2 (Fig. 2.6.5*a*). Dicalcium silicate exists in five polymorphic forms (Odler, 2000). During cooling, one of the other polymorphs of dicalcium silicate, β-Ca_2SiO_4, is formed, which has a different crystal structure and optical properties (Fig. 2.6.5*b*).

2.6.6.3. *Environmental heating: lamp furnace*

Another approach to designing an environmental chamber is the quadrupole lamp furnace developed by W. M. Kriven (Sarin

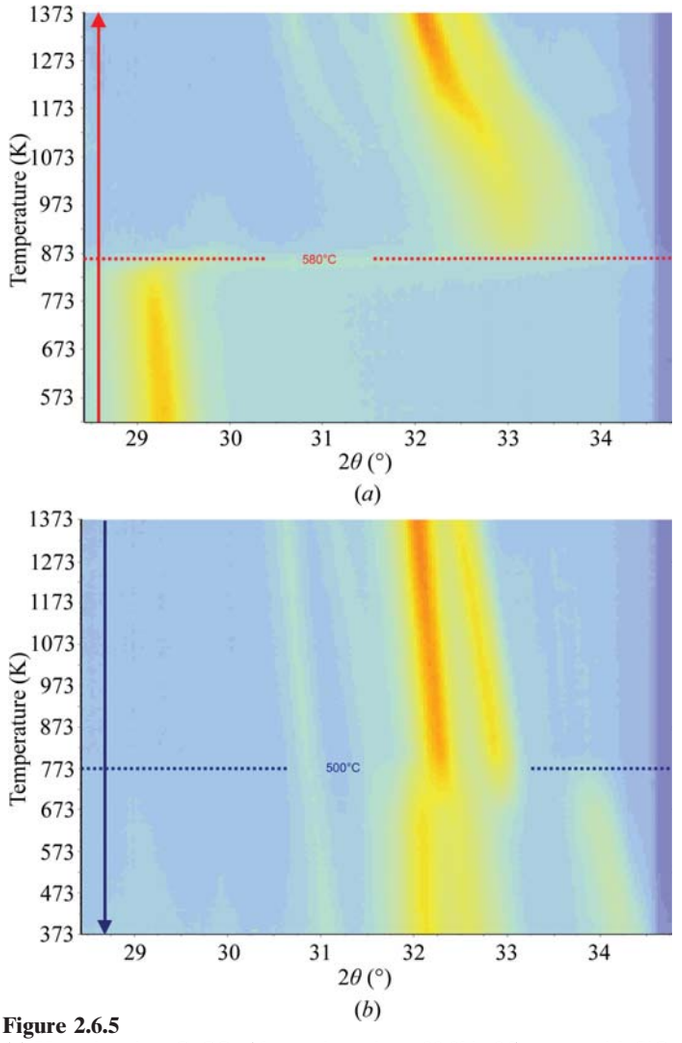

Figure 2.6.5
(*a*) Upon heating, $CaCO_3$ (the peak at about 29.3° in 2θ) reacts with SiO_2 (amorphous); at 853 K the new phase α'_L-Ca_2SiO_4 is formed (the peak between 33 and 32° in 2θ). (*b*) During cooling α'_L-Ca_2SiO_4 (the two peaks between 33 and 32° in 2θ), a different dicalcium silicate polymorph is formed at 773 K; this is β-Ca_2SiO_4.

et al., 2006). Such a furnace can heat a specimen to >2000 K in air. A recent application of this furnace is the characterization of high-temperature phase transitions in $Zr_2P_2O_9$ (Angelkort *et al.*, 2013).

2.6.6.4. *Domed hot stage*

Sample stages with an X-ray transparent dome, such as the DHS 1100 domed hot stage manufactured by Anton Paar (Fig. 2.6.6), give another dimension to polycrystalline diffraction. The dome is made of highly transparent graphite. The transmission of the primary and diffracted beams depends on the wavelength used, and for Cu $K\alpha$ radiation 65% is transmitted. The dome can be used on most of the commercially available modern multi-purpose X-ray diffractometers with linear or two-dimensional detectors. Mounted on an *XYZ* table or a cradle, these sample stages can be used to study texture, stress/strain and other phase-induced changes in (for example) thin-film layers under non-ambient conditions.

Example: thin films. A great deal of research has been devoted to the development of gallium nitride (GaN)-based high-electron-mobility transistor (HEMT) structures (Kelekci *et al.*, 2012; Butté *et al.*, 2007). The structural quality of the layers and their interfaces is critical for the performance of the device (Teke

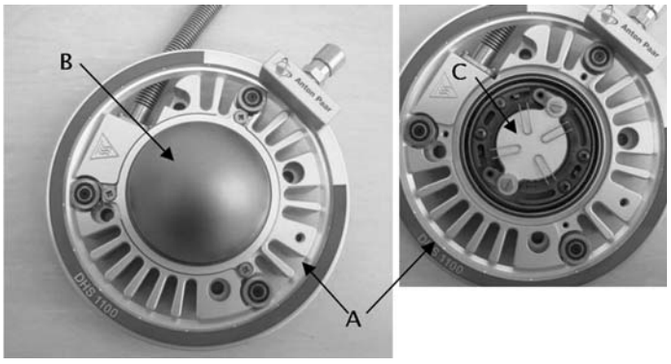

Figure 2.6.6
Sample-heating stage (Anton Paar DHS 1100) with lightweight, air-cooled housing (A), dome-shaped X-ray window (B) and heating plate with sample fixation (C).

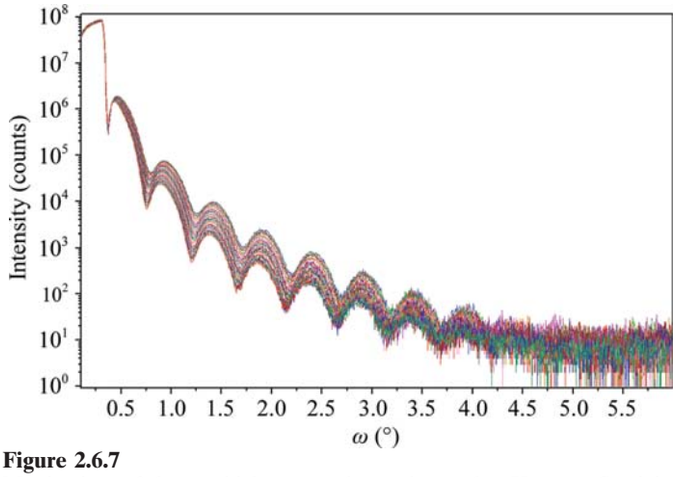

Figure 2.6.7
Monitoring of layer thickness and roughness by X-ray reflectivity measurements during annealing at 823 K.

et al., 2009). Detailed knowledge of the effects of further process steps, such as thermal annealing, on these parameters is crucial. X-ray reflectivity can be used for monitoring, among other things, the layer thickness and (interface) roughness (Daillant & Gibaud, 2009). To monitor the annealing process, a wurtzite-type AlInN/AlN/GaN/ heterostructure was mounted on a DHS 1100 domed hot stage; 26 scans were made, each of which lasted 1 h and 59 min at a temperature of 823 K (Fig. 2.6.7). From these reflectivity measurements the activation energy could be calculated and compared with the results from X-ray diffraction data from a nominally identical structure (Grieger *et al.*, 2013). The same value was found for both experiments within 5%, giving valuable information about heterostructure layer and interface stability.

2.6.7. Low-temperature sample stages

2.6.7.1. *Cryogenic cooling stages/cryostat*

For cryogenic experiments, liquid nitrogen (boiling point 77.4 K at 1 atm, where 1 atm = 101 325 Pa) or liquid helium (boiling point 4.3 K at 1 atm) is required (Weast, 1980). The most common types of chambers for medium-to-low temperatures are chambers with continuous-flow cooling. Here, a continuous flow of liquid nitrogen is provided from a Dewar storage vessel and the cooling process is controlled by a liquid-nitrogen controller. For lower temperatures helium is used. Helium is an expensive gas, and therefore a more economic method is to use a closed-

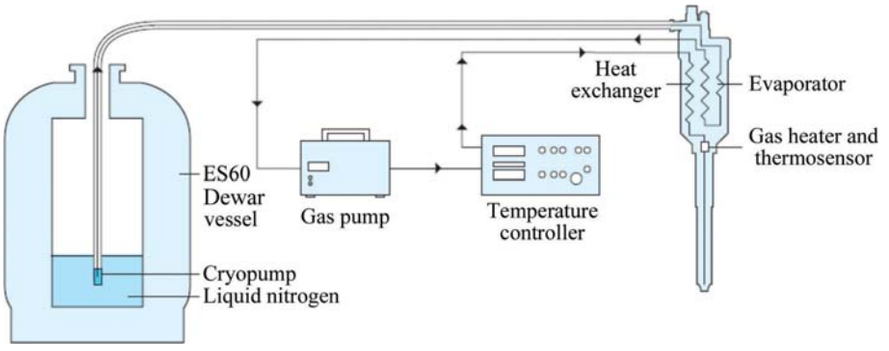

Figure 2.6.8
Schematic drawing of the Oxford Cryosystems cryostream setup.

cycle cryostat. This has the disadvantage that it consumes relatively large amounts of energy, but it does not need a continuous flow of helium and is also easy to use. The PheniX cryostat from Oxford Cryosystems is an example of such a chamber, which makes it possible to cool flat-plate powder samples to 20 K in just 35 min and to as low as about 12 K after a further 25 min. Recently, a group using beamline L11 at the Diamond Light Source synchrotron made some modifications to the PheniX cryostat to enable it to perform low-temperature Debye–Scherrer powder diffraction (Potter *et al.*, 2013). The original flat-plate sample holder in the cryostat was changed to a capillary sample holder.

2.6.7.2. *Cryogenic cooling stages/cryostream*

The cryostream from Oxford Cryosystems (Cosier & Glazer, 1986) cools the sample in a different way (Fig. 2.6.8). Originally developed for single-crystal X-ray diffraction experiments, it is currently also used to cool/heat capillaries in Debye–Scherrer experiments (Fig. 2.6.9). To prevent atmospheric moisture from freezing on the capillary, the cryogenic nitrogen-gas stream is shrouded in a second dry gas stream. When the two flows are balanced, the outer stream protects the inner nitrogen stream and temperatures as low as 80 K can be reached without ice formation on the capillary. The main advantage of measuring a powder sample in a capillary (transmission geometry) in contrast to flat-plate reflection geometry is minimization of preferred orientation of the sample. Attention must be paid, as in all non-ambient measurements, to temperature gradients in the sample. A short capillary is therefore advisable to minimize the occurrence of a gradient along the capillary.

For absorbing samples, hard radiation must be used to completely penetrate the capillary. Another possibility is to use capillaries with very small diameters, but this is not always very easy and filling them can be time consuming.

Example: buckminsterfullerene. An example that demonstrates the capability of the pair distribution function (PDF) method to independently probe the short-range and long-range atomic ordering in materials is C_{60}, also known as (C_{60}-I_h)[5,6]fullerene, fullerene or buckyball (Egami & Billinge, 2003). A buckyball molecule consists of 60 C atoms arranged on the vertices of a soccer-ball-like frame. At room temperature the C_{60} molecules are arranged in a face-centred cubic (f.c.c.) lattice and they assume completely random orientations as a result of thermal energy.

For long-range atomic order to be present, the atoms of the C_{60} molecules must remain in the same crystallographic position, which is not the case at room temperature. The time-averaged structure of the material can be represented as an f.c.c. structure, with space group $Fm\bar{3}m$, of uniform hollow balls with a diameter of about 7.1 Å. On cooling through 260 K a first-order structural phase transition occurs; the random rotation of each C_{60} molecule becomes slower and is now best described as a librational motion (Brown *et al.*, 2005). The phase transition is accompanied by a sudden contraction of the cubic lattice parameter and the long-range order can be described with a primitive cubic lattice (space group $Pa\bar{3}$).

Fig. 2.6.10 shows the atomic PDF at room and low temperature; only the short distances within the balls are clearly observed at room temperature (Reiss *et al.*, 2012). The correlation between atoms of neighbouring molecules cannot be seen, but ball–ball correlations are visible at larger distances. The low-temperature measurement shows similar peaks below 7.1 Å as the ambient measurement, but above 7.1 Å peaks are visible that result from distances from C atoms in one C_{60} molecule to C atoms in another C_{60} molecule.

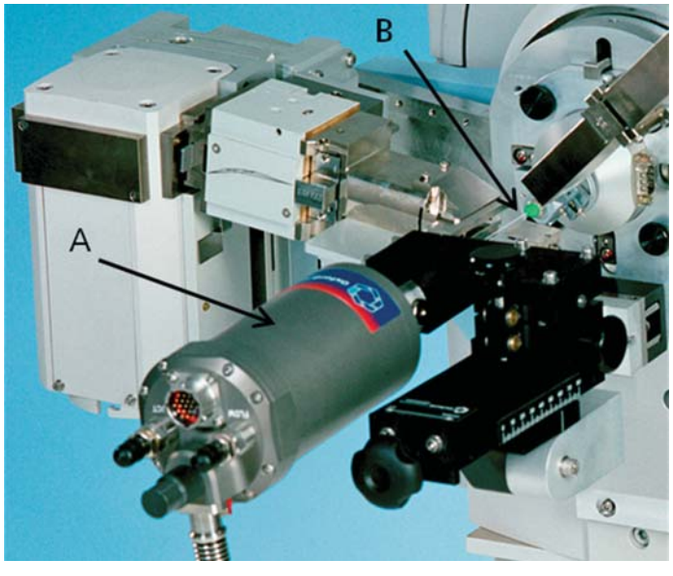

Figure 2.6.9
Oxford Cryostream (A) mounted on a PANalytical diffractometer for cooling a capillary (B).

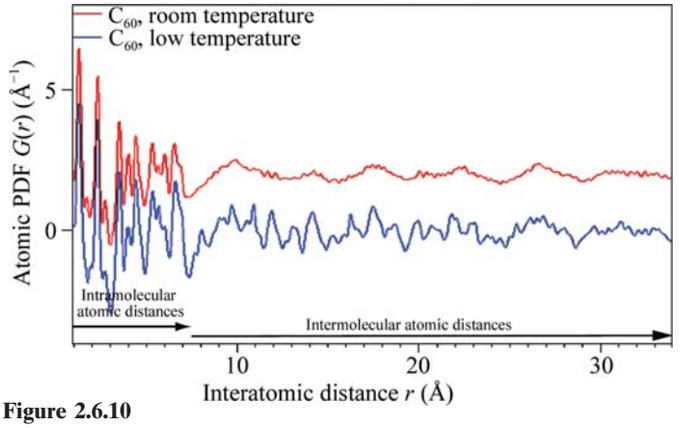

Figure 2.6.10
Atomic pair distribution function of C_{60} at room temperature (red) and at 100 K (blue).

2.6.8. Temperature accuracy

The accuracy of the temperature measurement of a non-ambient device has to be determined before starting a non-ambient experiment. At present no certified temperature standards for X-ray powder diffraction are available, only commonly used reference materials. A list of these materials can be found at https://www.xrayforum.co.uk/ and https://bl831.als.lbl.gov/~jamesh/pickup/Snell_SG_change_table.pdf.

A common method for validation of a non-ambient chamber is by determining the thermal expansion coefficient of a reference material as a function of temperature. Another is to determine the transition temperature of well known phase transformations. A third method is the so-called 'differential thermal expansion' method (Drews, 2001). This method utilizes the relative thermal expansion of two diffraction peaks. These peaks can be from the same or different reference material(s) but must be found in a narrow angular range and have different thermal expansion behaviour. Using only the relative separations of the peaks that are closely spaced eliminates the need for full pattern refinement to take into account geometrical aberrations and makes this method fast.

2.6.9. Future

A whole new field of non-ambient experiments has opened up with the study of new applications such as non-ambient PDF (see Section 2.6.7.2) and non-ambient SAXS measurements. And what happens in the nano world when large-scale models no longer hold at ambient and non-ambient temperatures? The future will tell; non-ambient diffraction/scattering experiments are more relevant now than ever before.

References

Angelkort, J., Apostolov, Z. D., Jones, Z. A., Letourneau, S. & Kriven, W. M. (2013). *Thermal properties and phase transition of $2ZrO_2{\cdot}P_2O_5$ studied by in situ synchrotron X-ray diffraction. J. Am. Ceram. Soc.* **96**, 1292–1299.

Brown, C., Copley, J. & Qiu, Y. (2005). *The orientational order/disorder transition in buckminsterfullerene (C_{60}): an experiment using the NCNR Disk Chopper Spectrometer*. Gaithersburg: NIST Center for Neutron Research. https://www.ncnr.nist.gov/summerschool/ss05/C60_EXPT_05.pdf.

Butté, R., *et al.* (2007). *Current status of AlInN layers lattice-matched to GaN for photonics and electronics. J. Phys. D Appl. Phys.* **40**, 6328–6344.

Cosier, J. & Glazer, A. M. (1986). *A nitrogen-gas-stream cryostat for general X-ray diffraction studies. J. Appl. Cryst.* **19**, 105–107.

Daillant, J. & Gibaud, A. (2009). Editors. *X-ray and Neutron Reflectivity: Principles and Applications.* Berlin, Heidelberg: Springer.

Drews, A. R. (2001). *Calibration of a high temperature X-ray diffraction stage by differential thermal expansion. Adv. X-ray Anal.* **44**, 44–49.

Egami, T. & Billinge, S. J. L. (2003). *Underneath the Bragg Peaks: Structural Analysis of Complex Materials.* Oxford: Pergamon.

Grieger, L., Kharchenko, L., Heuken, M. & Woitok, J. F. (2013). *15th European Workshop on Metalorganic Vapour Phase Epitaxy (EWMOVPE XV)*, Extended abstracts, pp. 51–54. Jülich: Forschungszentrum Jülich.

Kelekci, O., Tasli, P., Cetin, S. S., Kasap, M., Ozcelik, S. & Ozbay, E. (2012). *Investigation of AlInN HEMT structures with different AlGaN buffer layers grown on sapphire substrates by MOCVD. Curr. Appl. Phys.* **12**, 1600–1605.

Norby, P. & Schwarz, U. (2008). *Powder Diffraction: Theory and Practice*, edited by R. E. Dinnerbier & S. J. L. Billinge, pp. 439–463. Cambridge: Royal Society of Chemistry.

Odler, I. (2000). *Special Inorganic Cements*. London: CRC Press.

Potter, J., Parker, J. E., Lennie, A. R., Thompson, S. P. & Tang, C. C. (2013). *Low-temperature Debye–Scherrer powder diffraction on Beamline I11 at Diamond. J. Appl. Cryst.* **46**, 826–828.

Reiss, C. A., Kharchenko, A. & Gateshki, M. (2012). *On the use of laboratory X-ray diffraction equipment for pair distribution function (PDF) studies. Z. Kristallogr.* **227**, 256–261.

Sarin, P., Yoon, W., Jurkschat, K., Zschack, P. & Kriven, W. M. (2006). *Quadrupole lamp furnace for high temperature (up to 2050 K) synchrotron powder X-ray diffraction studies in air in reflection geometry. Rev. Sci. Instrum.* **77**, 092906.

Teke, A., Gökden, S., Tülek, R., Leach, J. H., Fan, Q., Xie, J., Özgür, Ü., Morkoç, H., Lisesivdin, S. B. & Özbay, E. (2009). *The effect of AlN interlayer thicknesses on scattering processes in lattice-matched AlInN/GaN two-dimensional electron gas heterostructures. New J. Phys.* **11**, 063031.

Weast, R. C. (1980). *CRC Handbook of Chemistry and Physics*, 61st ed. Boca Raton: CRC Press.

International Tables for Crystallography (2018). Vol. H, Chapter 2.7, pp. 156–173.

2.7. High-pressure devices

A. Katrusiak

2.7.1. Introduction

Although life in the biosphere of Earth exists within narrow limits of temperature and pressure, these thermodynamic conditions are unusual *on* Earth and in the Universe. Most of the matter in the Universe is contained in black holes, stars and planets, where it is exposed to extreme temperature and pressure. On the other hand, interstellar space constitutes most of the Universe's volume, where both pressure and temperature are close to their absolute-zero values. On Earth's surface at sea level, atmospheric pressure is about 1000 hPa [1 atm = kG cm^{-2} = 9.807 $\times$ 10^4 Pa $\simeq$ 0.1 MPa; currently, the pascal (abbreviated Pa) is the generally accepted pressure unit recommended by the International System of Units]. Under water on Earth, the pressure increases by 0.1 MPa for every 10 m depth, and rises to 120 MPa at the bottom of the Mariana Trench, 11 km below the sea's surface. A relatively low pressure change, to about 0.3 MPa at a depth of 20 m, affects the dissolution of nitrogen in human blood and can lead to decompression sickness (caisson disease); at 300 m in the oceans (3 MPa) and 288 K, methane forms stable hydrates, which constitute the most abundant deposits of carbon on Earth. All geological deposits are exposed to some pressure; at a depth of 1000 m this is about 300 MPa. Consequently, the structure and properties of very many minerals, formed and deposited in the crust, can transform considerably after their exposure to the surface. The syntheses of numerous minerals require high-pressure conditions. Thus, high-pressure experiments can provide indispensable information about the geological and stellar mechanisms, transformations and properties governing the matter forms, properties and distribution inside stars and planets.

Therefore, the pressure dependence of crystal structures is of primary interest to geologists, planetologists and astrophysicists (Hazen, 1999; Merlini *et al.*, 2012). The most cited examples of the effects of extreme conditions are thermonuclear synthesis, the formation of diamond (the dielectric carbon allotrope), the formation of stishovite (the dense form of SiO_2) and the propagation of seismic waves through the Earth's crust. The understanding of these and other phenomena requires that extreme conditions be reproduced and crystal structures investigated in laboratories. Most importantly, the conditions that are ubiquitous across the Universe are viewed as extreme only from our perspective of a narrow thermodynamic space, of a few tens of kelvin and a few megapascals around the triple point of water. From this narrow thermodynamic space, most of our knowledge of materials science has been developed. Extreme conditions allow theories to be verified and developed to a more general level. Moreover, extreme conditions can be utilized to produce new materials with desired properties (Hanfland *et al.*, 2011; Senyshyn *et al.*, 2009), including diamond or its other super-hard substitutes, or new forms of pharmaceutical drugs (Boldyreva, 2010; Boldyreva *et al.*, 2002, 2006; Fabbiani, 2010; Fabbiani & Pulham, 2006; Fabbiani *et al.*, 2004, 2005, 2009). The key element for such research is a sample-environment device for generating high pressure in the laboratory.

The pressure at the centre of Earth is about 364 GPa, one order of magnitude higher again inside the giant planets Jupiter and Saturn, and over 1 000 000 GPa (*i.e.* 1000 TPa) inside small stars like the Sun. Structural determinations under varied thermodynamic conditions are essential for the general understanding of physical and chemical phenomena, and to gain knowledge about the properties of materials and to describe the world around us. Indeed, the biosphere where we live is confined to a range from 0.33 atm (0.033 MPa) at the top of Chomolungma (Mt Everest), 8848 m above sea level, to about 1200 atm (120 MPa). The most commonly discussed and studied thermodynamic parameters are temperature (T), pressure (P) and composition (X). In principle, they affect the structure of matter differently. For example, the primary change induced by temperature is in the energy of atomic, molecular and lattice vibrations, whereas increasing pressure always reduces the volume. These changes are interdependent, and the compression of a structure can also reduce its thermal vibrations, change the types of cohesion forces and reverse the balance between competing compounds of different composition. This concerns all compounds, not only minerals deep under the Earth's surface. An exciting example of a molecular compound undergoing such transformations is water, transforming between at least ten polymorphic structures at high pressure, and also forming hydrates, depending on the thermodynamic conditions. Hence, pressure is now utilized to generate new polymorphs and solvates that cannot be obtained under normal conditions (Patyk *et al.*, 2012; Tomkowiak *et al.*, 2013; Fabbiani, 2010; Boldyreva, 2010).

For these reasons, high-pressure techniques have been developed dynamically, and the breakthrough invention of the diamond-anvil cell and its development in the second half of the 20th century greatly intensified high-pressure research. Today, the effects of high pressure on various materials and their reactions are studied both in small laboratories in universities and at large facilities, which provide powerful beams of X-rays from synchrotrons and beams of neutrons from reactors and spallation targets. The large facilities are either international initiatives, like the European Synchrotron Radiation Facility (ESRF) and Institute Laue–Langevin (ILL) in Grenoble, France, or national ones, like the Diamond Light Source and ISIS at the Rutherford Appleton Laboratory in Oxfordshire, UK, the Deutsches Elektronen Synchrotron (DESY) in Hamburg, Germany, the Photon Factory in Tsukuba, SPring-8 (Super Photon ring – 8 GeV) in Hyōgo Prefecture and the Japan Proton Accelerator Research Complex (J-PARC) in Tokal near Tokyo, Japan, the National Synchrotron Light Source (NSLS) at Brookhaven National Laboratory, USA, the Advanced Photon Source (APS) at Argonne National Laboratory and Los Alamos National Laboratory (LANL), New Mexico, USA, the Lawrence Livermore National Laboratory, California, USA, the Joint Institute for Nuclear Research (JINR) in Dubna, Russian Federation, the Spallation Neutron Source (SNS) at Oak Ridge National Laboratory, USA, and others. They provide access to the beams and high-pressure equipment to the general scientific community.

2.7.2. Historical perspective

The earliest concepts of pressure are often associated with Evangelista Torricelli's famous statement '*Noi viviamo sommersi nel fondo d'un pelago d'aria*' ('We live submerged at the bottom

of an ocean of air') in 1643, Otto von Guericke's experiment pitting the force of six horses against atmospheric pressure acting to squeeze together two hemispheres evacuated using the vacuum pump he had constructed in Magdeburg in 1654, and Blaise Pascal's measurements of pressure differences at different altitudes and his demonstrations of barrels being blown up by the force of water poured in through a tall pipe. The subsequently developed high-pressure devices were mainly of the piston-and-cylinder type.

At the beginning of the 19th century, pressures of about 400 MPa could be obtained, and at the beginning of the 20th century, often referred to as the end of the pre-Bridgman era, pressures up to about 2 GPa could be achieved. Then Percy W. Bridgman's remarkable inventions extended the pressure range greatly, to over 10 GPa (Bridgman, 1964). He devised new techniques for sealing pressure chambers, developed the opposed-anvils apparatus and introduced methods for the controlled measurement of various phenomena. Moreover, he used his new methods to describe a vast number of observations and properties of matter at high-pressure ranges hitherto unexplored. Bridgman's ingenious designs of high-pressure devices, such as the opposed-anvils apparatus, paved the path for future researchers. His scientific achievements won him the Nobel Prize in Physics in 1946.

The Bridgman era in high-pressure research ended in the late 1950s, when the diamond-anvil cell, often abbreviated to DAC, was invented (Weir *et al.*, 1959; Jamieson *et al.*, 1959; Piermarini, 2001). Soon after, the DAC became the main tool of high-pressure researchers; it gradually increased the range of attainable pressure by more than an order of magnitude, and under laboratory conditions it surpassed the pressure level at the centre of the Earth. Most importantly, the DAC allowed many new measuring techniques, particularly X-ray diffraction and optical spectroscopy, to be utilized. Before that, spectroscopic studies were limited to about 0.5 GPa. High-pressure X-ray diffraction, pioneered by Cohen (1933) in Berkeley for powders and by Vereshchagin *et al.* (1958) in Moscow for a single crystal of halite at 0.4 GPa in a beryllium high-pressure vessel, had been expensive, inefficient and inaccurate.

The DAC has become commonly available because of its low cost and easy operation. Today, the DAC continues to be the main and most versatile piece of laboratory pressure equipment and a record-breaking high-pressure apparatus. However, other sample environments provide complementary means of structural studies. For example, the large-volume press can be advantageous for neutron diffraction studies and in experiments where very stable high-pressure/high-temperature conditions are required. Naturally, the success of many high-pressure methods would not be possible without the development of other sciences and technologies, including computers, powerful sources of X-rays and neutrons and their detectors, and lasers.

2.7.3. Main types of high-pressure environments

High-pressure methods can be classified as dynamic or static. In the traditional dynamic methods, the pressure is generated for microseconds, usually at an explosion epicentre or at targets where ultra-fast bullets or gas guns are fired at the sample. The explosions are carried out either in special chambers or in bores underground (Batsanov, 2004; Ahrens, 1980, 1987; Keller *et al.*, 2012).

Even shorter, of a few nanoseconds' duration, the shock compression generated in targets using laser drivers coupled to the powerful X-ray pulses of a free-electron laser, or an otherwise generated X-ray beam, can further extend the attainable pressure limits. While this laser shock generates both high pressure and high temperature in the sample (the so-called Hugoniot compression path), in the ramp compression, also termed the off-Hugoniot path, the signal of the designed profile from an optical laser affords terapascal compression and approximates isothermal conditions (Wicks *et al.*, 2018; Smith *et al.*, 2014; Wang *et al.*, 2016).

The advantage of the gas and laser shock-wave and ramp-compression methods is that the attainable pressure is not limited by the tensile strength of the pressure chamber. Disadvantages include the inhomogeneous pressure, difficulties in controlling the temperature, the requirement for very fast analytical methods and the very high cost. The kinetic products generated during the explosion and in the shock waves can be different from the products recovered after the explosion, and different again from those formed under stable conditions. In most cases the laser-generated shock annihilates the sample.

Static methods are at present more suitable for crystallographic studies. The first variable-temperature sample-environment devices for structural studies of liquids and solids were designed soon after the inception of X-ray diffraction analysis. Structural investigations at high and low temperature at ambient pressure were mainly performed either by blowing a stream of heated or cooled gas onto a small sample (Abrahams *et al.*, 1950) or by placing the sample inside an oven or a cryostat. At present, a variety of attachments for temperature control are commercially available as standard equipment for X-ray and neutron diffractometers. Open-flow coolers using gaseous nitrogen and helium are capable of maintaining temperatures of about 90 K and a few kelvin, respectively, for days and weeks. They are easy to operate and pose no difficulties for centring the sample crystal, because the crystal is mounted, as in routine experiments, on a goniometer head with adjustable x–y–z translations and is visible at all positions through a microscope attached to the diffractometer. Cryostats and furnaces obscure the visibility of the sample and are usually heavy, and hence require strong goniometers; however, they often have the advantage of higher stability, a larger homogeneous area in the sample and a larger range of temperature (see Chapter 2.6).

Devices for static high-pressure generation are more difficult to construct because of the obvious requirement for strong walls capable of withstanding the high pressure applied to the sample. There are several types of high-pressure device and they can be classified in several ways. The piston-and-cylinder (PaC) press is the oldest type of pressure generator. However, the pressure range is limited in most advanced constructions (of multilayer negatively strained cylinders, like one shown in Fig. 2.7.1) to 3.0 GPa (Baranowski & Bujnowski, 1970; Besson, 1997; Dziubek & Katrusiak, 2014). PaC presses are ideal for volumetric measurements on a sample enclosed in the cylinder and for generating pressure in a hydrostatic medium transmitted through a capillary to other external high-pressure chambers containing the sample and optimized for a chosen measurement method, usually optical spectroscopy and diffraction. The external devices include chambers for loading the PaC with gas, which is either the hydrostatic medium or the sample itself (Tkacz, 1995; Rivers *et al.*, 2008; Couzinet *et al.*, 2003; Mills *et al.*, 1980; Yagi *et al.*, 1996; Kenichi *et al.*, 2001). In some pressure generators, a cascade of two or three PaC presses is applied for highly compressible pressure-transmitting media (gases) before the final setup stage.

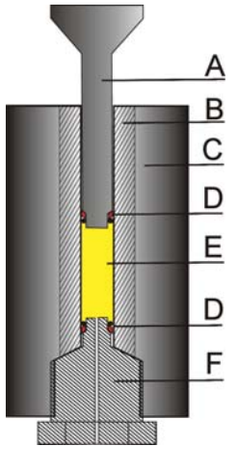

Figure 2.7.1
A cross section through a piston-and-cylinder device with a shrink-fitted double cylinder. In this design, the bottom piston (stopper F) is in the fixed position and only the top piston (A) is pushed into the cylinder by a hydraulic press. The main components of the device are: piston (A), inner cylinder (B), outer supporting shell (C), brass and rubber sealing rings (D), sample (E) and stopper (F).

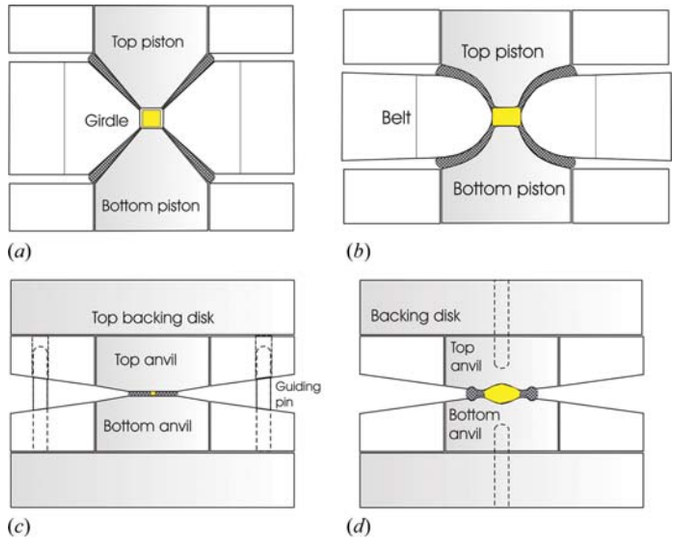

Figure 2.7.2
Cross sections of (*a*) the girdle anvil, (*b*) the belt anvil, (*c*) the Bridgman anvil and (*d*) the toroid anvil. The gaskets are dark grey, the tungsten carbide elements are pale grey and the sample chamber is yellow.

The PaC press can be considered as the prototype of other large-volume presses (LVPs). The PaC press consists of a cylinder closed at both ends with pistons, sealed with gaskets. The attainable pressure depends mainly on the tensile strength of the cylinder and of the gasket. The cylinder can be strengthened by the process of frettage, *i.e.* inducing tensile strain in the outer part and compressive strain inside (Onodera & Amita, 1991). This can be achieved by autofrettage, when a one-block cylinder is purposely overstrained to the point of plastic deformation and the deformation residues result in the required strain. Likewise, the cylinder can be built of shrink-fitted inner and outer tubes (the outer diameter of the inner tube is slightly larger than the inner diameter of the outer tube, which must be heated to assemble the cylinder) or of cone-shaped tubes (with a cone half-angle of *ca* 1°) pushed into one another to generate the frettaging strains. Alternatively, a coil of several layers of strained wire or tape can be wound around the cylinder, or the cylinder can be compressed externally to counteract its tensile strain simultaneously with the load being applied to the pistons (Baranowski & Bujnowski, 1970). The load against the cylinder walls can be reduced by containing the sample in a capsule of soft incompressible material, usually lead (Bridgman, 1964). Cylinder chambers with externally generated pressures up to 0.4 GPa (Blaschko & Ernst, 1974) and PaC cells capable of generating 2 GPa (Bloch *et al.*, 1976; McWhan *et al.*, 1974) have been used for neutron diffraction, and a beryllium cylinder has been used for X-ray diffraction on protein crystals to 100 MPa (Kundrot & Richards, 1986). The range of pressure up to a few hundred megapascals is often described as medium pressure. There are sample-environment chambers with externally generated medium pressure that are designed for in-house powder diffractometers operating in the Bragg–Brentano geometry (Koster van Groos *et al.*, 2003; Whitfield *et al.*, 2008).

If the cylinder length is reduced and the gasket reinforced by compression of the conical pistons, the girdle press is obtained (Fig. 2.7.2*a*). Its optimized modification is the belt apparatus (Fig. 2.7.2*b*). The girdle and belt presses generate pressures of about 10 GPa and can be internally heated to about 1500 K, and hence they have been used widely to synthesise materials. However, the opacity of the girdle/belt and anvils allows no access for X-ray or neutron beams between the anvils. This disadvantage is alleviated in the opposed-anvils press, operating on the massive-support principle, where the beams can pass through the gasket material. After the first record of a simple version of the opposed-anvils experiment in the mid 19th century performed in order to measure the effect of medium pressure on the electric conductibility of wires by Wartmann (1859), the opposed anvils were extensively developed and applied to much higher pressure by Bridgman (1935, 1941, 1952). He also equipped them with a pyrophyllite gasket separating the anvil faces (Bridgman, 1935), and in this form they are commonly known as Bridgman anvils (Fig. 2.7.2*c*). In the 1960s, the flat faces of the Bridgman anvils were modified to so-called toroidal anvils (Fig. 2.7.2*d*), where the sample space is considerably increased by hemispherical depressions at the anvil centre and surrounded by a groove supporting the gasket and preventing its extrusion (Khvostantsev, 1984; Khvostantsev *et al.*, 1977, 2004; Ivanov *et al.*, 1995). Anvils with a spherical sample cavity only, so-called Chechevitsa anvils, preceded the construction of toroidal anvils. Toroidal anvils were optimized for neutron diffraction by adding a small pneumatic press called the Paris–Edinburgh cell (Besson *et al.*, 1992). Toroidal anvils enabled neutron diffraction studies up to 50 GPa and 3000 K (Kunz, 2001; Zhao *et al.*, 1999, 2000; Redfern, 2002). Experiments on magnetic systems in a similar pressure range and at low temperature were performed in a very different design of opposed anvils, the sapphire Kurchatov–LBB cell, shown in Fig. 2.7.3 (Goncharenko & Mirebeau, 1998; Goncharenko, 2004).

More complex LVPs have been based on multi-anvil presses (Liebermann, 2011). These are usually very large devices capable of containing tens of cubic centimetres of sample. The sample is encapsulated and pressurized between anvils sealed with some kind of gasket. The attainable pressure depends on a number of factors, including the applied load and the strength of the anvils, which are made of steel, tungsten carbide, sapphire or sintered diamond; the maximum pressure depends inversely on the sample volume. Multi-anvil presses (Huppertz, 2004; Liebermann, 2011) – tetrahedral, trigonal–bipyramidal, cubic (Akimoto *et al.*, 1987) and octahedral (Onodera, 1987) – are optimized for larger sample volumes and for the high temperatures required for the synthesis of hard materials, especially diamond (Hazen, 1999). The multi-anvil presses are used for diffraction studies.

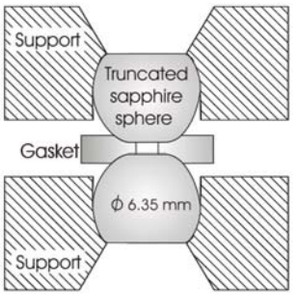

Figure 2.7.3
A schematic view of the opposed-sapphire anvil of the Kurchatov–LBB cell designed for neutron diffraction on magnetic materials (Goncharenko, 2004).

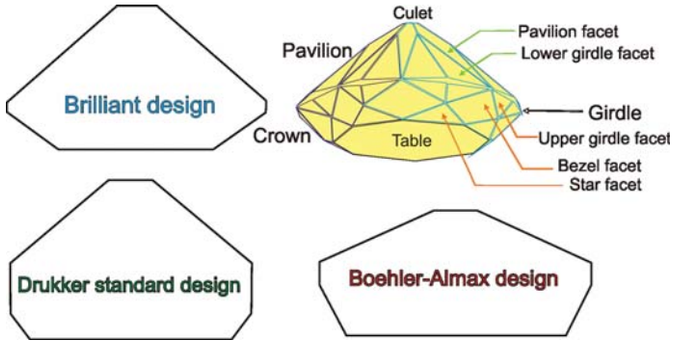

Figure 2.7.4
Cross sections of three types of diamond anvil used in high-pressure cells: the brilliant design (supported either on the table or on the crown rim), the Drukker design (supported on the table and crown) and the Boehler–Almax design (supported on the crown).

The sample can be either contained in a capsule or mixed with a pressure-transmitting pseudo-hydrostatic medium, which is inert and a weak absorber of X-rays. The sample is accessed by the X-ray beam between the anvils through a weakly absorbing sealing material, such as amorphous boron, magnesium oxide, corundum or pyrophyllite. Like the opposed-anvil presses, multi-anvil LVPs can be used effectively for X-ray diffraction at synchrotrons and neutron sources. However, these large installations also require (apart from intense primary beams) powerful translations for their precise centring relative to the primary beam and diffractometer axes. The main advantage of an LVP is stable and homogenous internal heating up to about 2000 K (Besson, 1997). Such stable conditions are particularly valuable for high-pressure synthesis and crystallization, for example of diamonds (Hazen, 1999).

2.7.4. The diamond-anvil cell (DAC)

The invention of the DAC revolutionized high-pressure studies, diversified their scope, greatly simplified the experimental procedures, increased the range of pressure and temperature, and initiated constant growth in the number of high-pressure structural studies, starting in the 1960s and continuing up to today. The DAC is built from a pair of opposing diamond anvils and a vice to generate their thrust. The sample is compressed between the culets of the anvils. Since its inception, the DAC has been modified and redesigned frequently, in order to adapt it to new experimental techniques or to take advantage of the parallel progress in scientific equipment. The original DAC built at the National Bureau of Standards (Maryland, USA) was used for infrared spectroscopy. Another DAC designed for powder diffraction experiments was made of beryllium, a relatively strong metal which weakly absorbs short-wavelength X-rays (Weir *et al.*, 1959; Bassett, 2009). The DAC, with steel frames and beryllium discs supporting the anvils, is still in use today.

The original and most efficient concept applied in the operation of the DAC was that the incident beam enters the pressure chamber through one diamond anvil and the reflections leave through the other anvil; this mode of operation is often referred to as transmission geometry. Together with the diamond anvils, Be discs constitute windows for the X-rays. However, beryllium has several disadvantages. It is the softest and weakest of the materials used in DAC construction, it softens at about 470 K, beryllium oxide is poisonous, and machining beryllium is difficult and expensive. Therefore, except for the pioneering DAC design by Weir *et al.* (1959), Be parts were initially limited to disc supports for the anvils. Moreover, polycrystalline Be discs produce broad reflection rings and a strong background, and the small central hole in the disc obscured optical observation of the sample. In many modern DACs the beryllium discs have been completely eliminated, and the diamond anvils are directly supported by steel or tungsten carbide platelets (Konno *et al.*, 1989; Ahsbahs, 2004; Boehler & De Hantsetters, 2004; Katrusiak, 2008). For this purpose new diamond anvils, exemplified in Fig. 2.7.4, were designed. Anvils of different sizes, culet dimensions, height-to-diameter ratios and other dimensions can be adjusted for the experimental requirements, such as the planned pressure range and the opening angles of the access windows.

Another DAC was independently designed for X-ray powder diffraction by Jamieson *et al.* (1959). In their DAC, the incident beam was perpendicular to the axis through the opposed anvils, and the primary beam passed along the sample contained and squeezed directly (no gasket was used) between the culets. The reflections were recorded on photographic film located on the other side of the DAC, perpendicular to the incident beam. This geometry was described as either panoramic, perpendicular or transverse. The transverse geometry is also used with beryllium or other weakly absorbing gaskets (Mao *et al.*, 1998). Other DACs, for example where both the incident beam and the reflections pass through one diamond anvil, were also designed (Denner *et al.*, 1978; Malinowski, 1987); however, the transmission geometry is most common owing to its advantages. In the transmission geometry the uniaxial support of the anvils leaves a window for optical observation of the sample, as well as for spectroscopic and diffractometric experiments along the cylindrical pressure chamber. Therefore, at present most DAC designs operate in transmission geometry.

The DAC construction can generally be described as a small vice generating thrust between opposed anvils. In the first DACs designed in the late 1950s, no gasket nor hydrostatic fluids were used and the sample was exposed to strong anisotropic stresses. Van Valkenburg (1962) enclosed the sample in a hole in a metal gasket, filled the hole with hydrostatic fluid and sealed it between the culets of the anvils. This most significant development of the miniature high-pressure chamber opened new possibilities for all sorts of studies under hydrostatic conditions, in particular powder and single-crystal diffraction studies. Since then, the gaskets have become an intrinsic part of the DAC. The hydrostatic conditions in the DAC have been used to grow *in situ* single crystals from the melts of neat compounds (Fourme, 1968; Piermarini *et al.*, 1969) and from solutions (Van Valkenburg *et al.*, 1971*a*,*b*). Now it is a common method for *in situ* crystallization under isothermal and isochoric conditions (Dziubek & Katrusiak, 2004; Bujak *et al.*,

2004; Fabbiani *et al.*, 2004; Fabbiani & Pulham, 2006; Budzianowski & Katrusiak, 2006*a*,*b*; Dziubek *et al.*, 2007; Paliwoda *et al.*, 2012; Sikora & Katrusiak, 2013).

The original designs of the DAC (Weir *et al.*, 1959; Jamieson *et al.*, 1959) were later adapted to various purposes. Significant modifications take advantage of new designs of diamond anvils and their supports. Initially, the brilliant-cut diamonds of traditional design, but with the culet ground off to form a flat thrust surface parallel to the table, were used (Fig. 2.7.4). Culets of 0.8 mm in size can be used to about 10 GPa, 0.4 mm culets to about 50 GPa, 0.1 mm culets to about 100 GPa and 0.02 mm (20 µm in diameter) or even smaller (Akahama *et al.*, 2014; Akahama & Kawamura, 2010; Dalladay-Simpson *et al.*, 2016) culets can be used for the megabar 200–400 GPa range. The megabar range requires bevels on the culets to protect their edges from very high strain and damage. The bevels are about 6–7° off the culet plane and the ratio of bevel-to-culet diameters is between 10 and 20. Also, the gasket material, the hole diameter and its height, being a fraction of the hole diameter, are of primary importance. Double bevels can be used to release the strain further, but it appears that a value of about 400 GPa is the maximum pressure attainable in the conventional DAC (c-DAC).

The pressure limits of the c-DAC are surpassed in a double-stage DAC (ds-DAC), in a toroidal DAC (t-DAC) or by shock compression. In the ds-DAC a pair of small anvils, constituting a microscopic DAC (m-DAC, also described as second-stage anvils), is contained inside the c-DAC. The micro-anvils are prepared from diamond or amorphous diamond using the focused ion-beam technique (Sakai *et al.*, 2015, 2018). For another type of ds-DAC, employing microscopic diamond hemispheres (Dubrovinsky *et al.*, 2012; Dubrovinskaia *et al.*, 2016), pressures exceeding 1 TPa have been reported. In the t-DAC, each diamond culet is modified in such a way that an ion-beam-eroded groove surrounds the central micro culet (Dewaele *et al.*, 2018; Jenei *et al.*, 2018; Mao *et al.*, 2018).

At present, the DAC most commonly applied in laboratories is a miniature Merrill–Bassett DAC, where the anvils are installed on two triangular frames driven by three screws along three sliding pins (Merrill & Bassett, 1974). Analogous designs with two or four thrust-generating screws are also in use. The original Merrill–Bassett DAC was equipped with a pair of brilliant-cut 0.2 carat diamonds with polished culets (Fig. 2.7.4) and the anvils were supported on Be discs. The Merrill–Bassett DAC is optimized for use with automatic diffractometers. It contains no rocking blocks but allows translation of one of the anvils. The light weight and small size allow the Merrill–Bassett cell to be routinely used on single-crystal diffractometers. This simple DAC design is suitable for experiments up to about 10 GPa. Dedicated DACs for higher pressure have rocking supports for the diamonds, in the form of either hemispheres or half-cylinders (Fig. 2.7.5).

A very fine adjustment of the anvils and fine and remote pressure control can be obtained in a membrane DAC, where the thrust is generated by a metal membrane operated with gaseous helium or nitrogen (Letoullec *et al.*, 1988; Chervin *et al.*, 1995). Owing to the ideally coaxial thrust generation by the membrane and the stable supports of the anvils, usually in the form of a piston and cylinder, the membrane DAC is suitable for generating pressures of hundreds of gigapascals. The membrane DAC can be operated remotely through a flexible metal capillary, which is advantageous for spectroscopy and both powder and single-crystal diffraction experiments at synchrotrons.

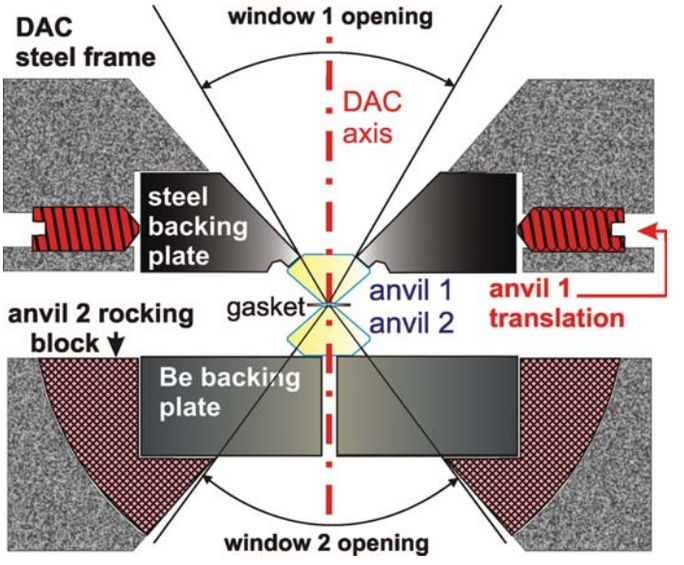

Figure 2.7.5
A cross section through the central part of a diamond-anvil cell, schematically showing the main elements applied in various designs. Usually, either beryllium backing plates or steel/tungsten carbide backing plates with conical windows are used. One of the plates can be translated and the other rocked in all directions (the hemispherical rocking mechanism). In other designs, one of the anvils can be rocked around and translated along one axis, and the other anvil rocked and translated in the perpendicular direction (two perpendicular hemicylindrical mechanisms). The usual thickness of the beryllium plate is 3 mm or more, and most constructions allow a window opening of about 40° to the DAC axis. The thickness of the diamond window (the table-to-culet distance) is usually about 1.5 mm.

2.7.5. Variable-temperature high-pressure devices

One of the most common interests in extreme conditions combines high pressure and high temperature. Several techniques for simultaneously controlling both pressure and temperature have been developed (Fei & Wang, 2000). The DAC can be heated externally (with respect to the sample chamber between the anvils' culets) when the entire DAC is placed in an oven or in a hot stream of air from an electrical heater (Fourme, 1968; Allan & Clark, 1999; Podsiadło & Katrusiak, 2008; Bujak *et al.*, 2008). External resistance-wire heaters placed immediately around the diamond anvils and the gasket are often used (Bassett & Takahashi, 1965; Takahashi *et al.*, 1982; Adams & Christy, 1992; Eremets, 1996; Moore *et al.*, 1970; Hazen & Finger, 1982; Besson, 1997; Dubrovinskaia & Dubrovinsky, 2003; Fei & Wang, 2000). External heating can routinely operate up to about 673 K. Its main advantages are stability, reliable measurement of temperature and high homogeneity of temperature in the chamber. The disadvantages include the relatively low temperature range and the large mass of the DAC mechanical parts that are heated. Their thermal expansion can cause loss of pressure. This does not apply to the membrane DAC, where a constant thrust from the membrane is transmitted to the anvils. A sophisticated externally heated DAC in an atmosphere of inert gases is capable of operating between 83 and 1473 K (Bassett *et al.*, 1993).

A very small turnbuckle DAC, about 6 mm in diameter, was originally constructed of plastic and hardened beryllium–copper alloy (BERYLCO 25) in order to perform magnetic measurements at low temperature in the small bore of a superconductive quantum interference device (SQUID) (Graf *et al.*, 2011; Giriat *et al.*, 2010). These are at present the smallest designs that can be

used for X-ray diffraction studies, with the whole DAC cooled by commercial low-temperature gas-stream attachments. Alireza & Lonzarich (2009) built another miniature DAC for high-pressure magnetic measurements in a SQUID.

Temperatures of several thousand kelvin can be achieved by internal heating, where the sample absorbs the focused light beam of a laser (Bassett, 2001; Ming & Bassett, 1974; Shen *et al.*, 1996) or is heated by a thin wire passing through the chamber or its immediate surroundings, either in the gasket walls (Boehler *et al.*, 1986; Mao *et al.*, 1987; Zha & Bassett, 2003; Dubrovinsky *et al.*, 1998) or in the culets of intelligent diamond anvils (Bureau *et al.*, 2006). Composite resistance gaskets, with a platinum chamber wall acting as a 35 W resistance heater, can increase the temperature to over 2273 K (Miletich *et al.*, 2000, 2009). Laser beam(s) focused through the DAC anvil(s) onto the sample (Boehler *et al.*, 2001) can heat it to over 3273 K. This requires that the laser beam, or several beams, or a fraction of their energy, be absorbed in the sample. In order to increase the absorption, the sample can be mixed with another compound, for example gold powder. The main disadvantage of laser heating is inhomogeneous distribution of the temperature within the sample.

Much smaller temperature gradients, of a few kelvin at 2773 K, can be obtained in large-volume presses (LVPs). The multi-anvil LVP has traditionally been applied for the synthesis of diamond, which requires stable conditions of both high pressure and high temperature (Hazen, 1999; Liebermann, 2011). In the LVP, a resistance heater installed inside the chamber can provide stable control of the temperature for days, while the pressure is controlled by a hydraulic press. Owing to the large sample volume, the diffraction pattern can be quickly recorded. Most often, energy-dispersive diffraction is applied for the beams entering and leaving the pressure chamber through the gasket material between the anvils. LVPs are generally very large and heavy, which contrasts with the compact construction of the Paris–Edinburgh and Kurchatov–LLB pressure cells (Besson *et al.*, 1992; Goncharenko, 2004, 2006). Both these opposed-anvil cells can be placed in cryostats, and they can be used for either energy- or angle-dispersive diffraction of neutrons or X-rays. The Kurchatov–LLB cell has been optimized for neutron diffraction studies of magnetic structures at high pressure and low temperature (Goncharenko & Mirebeau, 1998; Goncharenko *et al.*, 1995).

2.7.6. Soft and biomaterials under pressure

Interest in the effects of pressure on biological materials is connected to the processing of food and the search for methods of modifying the structure of living tissue and its functions. Soft biological compounds, including proteins, membranes, surfactants, lipids, polymer mesophases and other macromolecular assemblies present in living tissue, are susceptible to pressure, which can affect the molecular conformation and arrangement with relatively low energies of transformation (Royer, 2002). Medium pressure suffices for protein coagulation, as observed for egg white at 0.5 GPa by Bridgman (1914). However, single crystals of egg-white lysozyme survived a pressure of several gigapascals (Katrusiak & Dauter, 1996; Fourme *et al.*, 2004), which was connected to the concentration of the mother liquor used as the hydrostatic fluid. Cells with externally generated pressures up to about 200 MPa for diffraction measurements on single crystals in a beryllium capsule (Kundrot & Richards, 1986) and on powders contained between beryllium windows (So *et al.*, 1992) have been built. Powder diffraction studies have also been performed on samples frozen under high pressure and recovered to ambient pressure (Gruner, 2004). High-pressure studies can be conveniently performed in the DAC, but because of the usually weak scattering of macromolecular samples, synchrotron radiation is preferred for such experiments (Fourme *et al.*, 2004; Katrusiak & Dauter, 1996).

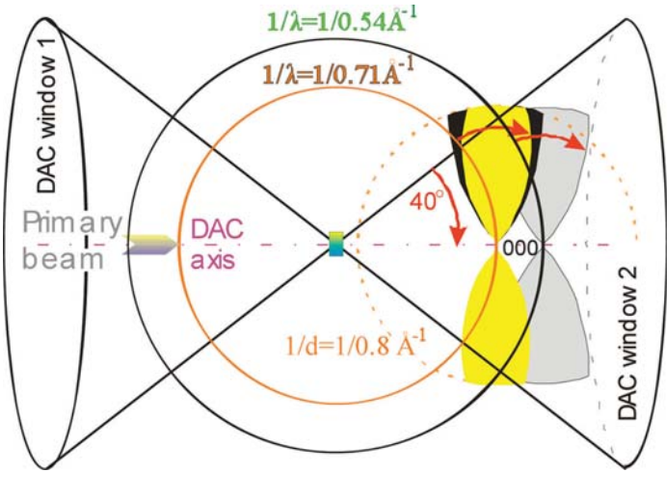

Figure 2.7.6
A diamond-anvil cell, showing the 40° half-angle opening of the conical windows and the reciprocal space accessed for a single-crystal sample and Mo $K\alpha$ or Ag $K\alpha$ radiation. In this schematic drawing, the window cones intersect at the disc-shaped sample (yellow–blue shaded rectangle) and around it the Ewald spheres of reciprocal radii corresponding to Mo $K\alpha$ and Ag $K\alpha$ wavelengths are drawn. The shape of the two yellow profiles meeting at the reciprocal 000 node is the cross section through the torus-like accessible volume of reciprocal space for Mo $K\alpha$ radiation; this torus is circularly symmetric about the DAC axis. The grey shape is likewise the accessible space for Ag $K\alpha$ radiation. Both are at the same resolution of $1/d_{hkl} = 1/0.8$ Å^{-1} (corresponding to θ angles of 26.4° for Mo $K\alpha$ radiation and 19.7° for Ag $K\alpha$). For a powdered sample, all reciprocal-space nodes contained within the resolution sphere (dotted circle) can be recorded. The DAC windows and the sample are shown at the initial 'zero' position, when the DAC axis coincides with the primary beam; the red arrows indicate the rotation of the DAC, sample and Ewald sphere to the limiting 40° angle.

2.7.7. Completeness of data

The steel parts of the DAC can restrict access of the incident beam to the sample and can obscure the exit of reflections. For a typical DAC working in transmission mode, the incident beam can be inclined to the DAC axis by up to about 25–40°, for the full opening of the window of 50–80°, respectively. In most DACs the collimator and detector sides are symmetric, so the opposing conical windows have the same opening angle. This limited access to the sample can affect the completeness of diffraction data for low-symmetry crystals, which can then pose considerable difficulties in solving and refining crystal structures from single-crystal measurements.

The restricted access of the primary and diffracted beams to the sample can conveniently be described by the concept of the reciprocal lattice (Fig. 2.7.6). The initial orientation of the crystal in the DAC defines the accessible region of the reciprocal lattice in such a way that the Ewald sphere can be inclined to the initial direction of the incident beam by up to the maximum window opening angle, denoted α_M. The sample can be accessed from both sides of the DAC (by rotating the DAC by 180°) and thus the accessible region of reciprocal space has the form of a round flat cushion, with surfaces touching at the cushion centre [described

as a donut cake by Merrill & Bassett (1974)], as shown in Fig. 2.7.6. In the directions perpendicular to the DAC axis, the maximum coordinate $d^*_{yz} = 2\lambda^{-1} \sin \alpha_M$ of reciprocal vectors is for many crystals larger than the resolution of the data (for a typical DAC, $\alpha_M = 40^\circ$, which for organic crystals or other weakly scattering substances is less than required, as the data measured with Mo $K\alpha$ radiation for molecular crystals often extend up to a maximum θ of only about 25°). However, access to the reciprocal lattice is significantly limited along the DAC axis (perpendicular to the flat cushion). In this direction, only those reflections can be accessed for which

$$d^*_x = 2\lambda^{-1} \sin^2(\alpha_M/2),$$

where d^*_x is the maximum coordinate of accessible reciprocal vectors along the x_L axis running from the sample to the radiation source in the laboratory reference system, λ is the wavelength, and α_M is the opening angle of the window measured from the DAC axis (or the maximum inclination of the DAC axis to the incident beam). For example, a DAC with a full window opening angle of $2\alpha_M = 60^\circ$ limits the laboratory reciprocal x coordinate to 0.1885 Å^{-1} when λ(Mo $K\alpha$) = 0.71073 Å is used; if the crystal x^* axis is aligned along the laboratory x_L axis, and if the crystal a^* = 0.10 Å^{-1}, then the maximum Bragg reflection index $|h|$ is 1. If the wavelength is decreased to λ(Ag $K\alpha$) = 0.56 Å, the maximum d_x increases to 0.2392 Å^{-1} and reflections with index h = 2 can be recorded.

Although the accessible region of the reciprocal lattice depends strongly on the DAC design, the final completeness of the data also depends on several other factors: (i) the symmetry of the sample crystal; (ii) the sample orientation; and (iii) the wavelength of the X-ray radiation. Therefore, the DAC is ideally suited to high-pressure studies of simple and high-symmetry crystals. The Laue-class symmetry of cubic crystals is either $m\bar{3}$ or $m\bar{3}m$, and in most cases the whole of the required resolution falls within the accessible flat-cushion reciprocal region. Thus, the completeness in high-pressure experiments on cubic samples mounted in the chamber at a random orientation is not limited. For hexagonal and tetragonal samples, the crystal orientation is very significant. The maximum completeness can be obtained when the hexagonal or tetragonal axis is perpendicular to the DAC axis. Then the sample reciprocal axis c^* is located along the flat-cushion plane. When two axes of a monoclinic or orthorhombic crystal are at 90° to the DAC axis, a considerable portion of the symmetry-independent part of the reciprocal lattice is not accessible. This reduces the completeness of the data, even though the redundancy of the data is increased. Optimum orientation of the sample can double the completeness compared with experiments measured for the same sample with its axes aligned along the DAC axis and plane.

The completeness of the data can be increased by collecting several data sets for samples oriented differently in the DAC and merging these data (Patyk *et al.*, 2012). This purpose can also be achieved by placing several crystal grains at different orientations in the high-pressure chamber, and then separating their reflections, indexing them and merging.

When the powder diffraction method is used, this problem of completeness is irrelevant. As shown in Fig. 2.7.7, for an ideal powder with randomly oriented grains all reciprocal-lattice nodes can be represented as spheres and they all satisfy the Bragg diffraction condition. The main problem occurring for samples with low symmetry and long lattice constants is overlapping reflections. The intensity of the powder reflection rings is low,

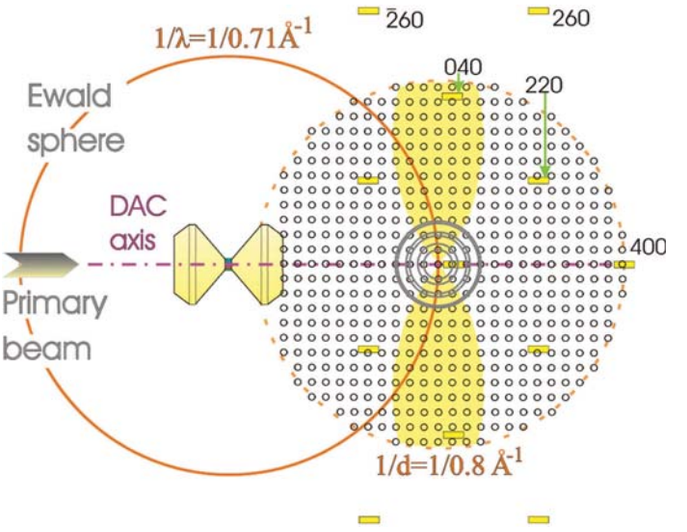

Figure 2.7.7
A schematic illustration of the reciprocal space associated with a sample enclosed in a diamond-anvil cell (DAC). For clarity, the sizes of the sample and diamond anvils have been increased. The Ewald sphere is drawn for the sample only and cubic symmetry with an a parameter of 10 Å has been assumed. Of the reciprocal lattice of the sample, only the layer of $hk0$ nodes is shown as small circles within the resolution limit of $1/d_{hkl}$ = 1/0.8 Å^{-1}. The Ewald spheres of the diamond anvils have been omitted, and only the layer of nodes $hk0$ of the detector anvil is shown as yellow rectangles. Owing to its short unit-cell parameter of 3.57 Å and $Fd\bar{3}m$ symmetry, there are few diamond reflections in the pattern. Note the displaced origins of the reciprocal lattices of the sample and of the detector anvil (the anvil on the detector side) as a result of the off-centre positions of the anvil. For a powdered sample, each node is distributed on a sphere. In this drawing, the spheres are represented by circles only for nodes 100, 110, 200, 210, 220 and 300. The other node spheres contained within the chosen resolution limit have been omitted for clarity; for a triclinic sample, the $hk0$ layer would include 266 powder reflections.

because only a small fraction of the sample volume, less than one part per million, contributes to the intensity at a specific point on the reflection ring. Furthermore, the sample volume in the DAC is very small. For these reasons, powder X-ray diffraction in the laboratory usually provides only qualitative information. After the introduction of synchrotron radiation and area detectors, powder diffraction became one of most efficient methods of high-pressure structural studies.

2.7.8. Single-crystal data collection

It is essential that a crystal sample is centred precisely on the diffractometer. Optical centring of a crystal is hampered by the limited view of the sample through the DAC windows in one direction only and by the strong refractive index of diamonds. Consequently, diffractometric methods of crystal centring are more precise for DAC centring. Hamilton's method comparing the diffractometer setting angles of reflections at equivalent positions (Hamilton, 1974) was modified for the purpose of the DAC by King & Finger (1979) and then generalized for any reflections, not necessarily at equivalent positions (Dera & Katrusiak, 1999). These methods are very precise, but they require the approximate orientation matrix (UB matrix) of the sample crystal (Busing & Levy, 1967) to be known and the reflections to be indexed. This information was determined at the beginning of an experiment when traditional diffractometers with a point detector were used. However, nowadays diffractometers with area detectors are used, and generally the crystal orientation

is not determined before collecting the diffraction data. To meet these requirements, a new efficient and semi-automatic method was devised, whereby the diffractometer measures a sequence of shadows of the gasket on the CCD detector and calculates the required corrections to the DAC position along the goniometer-head translations (Budzianowski & Katrusiak, 2004). Precise centring can only be achieved for very stable goniometer heads that do not yield under the weight of the DAC (Katrusiak, 1999).

The mode of data collection for a sample enclosed in a DAC can affect the data quality considerably. Data for a bare crystal on a four-circle diffractometer with a scintillation point detector were measured in the so-called bisecting mode, where the ω angle [diffractometer-axes positioning angles ω, χ, φ and θ of the Eulerian cradle will be used here (Busing & Levy, 1967), unless otherwise noted] was fixed to 0° and not used in the process of crystal positioning. In other words, the shaft φ and circle χ lie in the plane bisecting the angle formed by the incident beam and the reflection actually measured. The bisecting mode was optimal for avoiding collisions between the diffractometer shafts and detector, and also minimized absorption effects for most vertically mounted samples. However, these features are irrelevant for samples enclosed in a DAC. It was shown by Finger & King (1978) that the DAC absorption of the incident and reflected beams is a minimum when the Eulerian goniometer φ axis is not used and is always set to 0°. Hence, this is called the $\varphi = 0°$ mode. The $\varphi = 0°$ mode also minimizes the effect of the sample being shadowed by the gasket edges (Katrusiak, 2008). Moreover, in the $\varphi = 0°$ mode the DAC axis always lies in the diffraction plane of the diffractometer, which gives maximum access to the reciprocal-lattice nodes (Fig. 2.7.6).

The advent of area detectors facilitated high-pressure experiments considerably and extended the range of attainable conditions to simultaneous very high pressure and temperatures of several thousand kelvin. Single-crystal experiments are easier because the diffraction data can be recorded before the orientation matrix UB of the crystal is determined (Busing & Levy, 1967; Finger & King, 1978). The recorded data can thus be analysed after the experiment and all relevant structural models can be tested. The use of area detectors shortens the data-collection times for both single-crystal and powder diffraction measurements, and this is particularly efficient with the extremely intense X-ray beams provided by synchrotrons. In single-crystal experiments, several or even tens of reflections are partly scanned through or fully recorded in one image. Although these reflections are not each recorded at their optimum diffractometer settings, corresponding to the $\varphi = 0°$ mode setting described above, the redundancy of the data is increased and the intensities can be corrected for the absorption coefficients derived from differences between equivalent reflections. It is also advantageous that simultaneous diffraction events in the sample crystal and in one or both of the diamonds, which occur sporadically and weaken the recorded reflections, can be eliminated by comparing the intensities of the same reflection measured at several ψ angle positions as well as the equivalent reflections. Equivalent reflections measured at different positions are particularly useful for eliminating systematic errors in the data collection.

It is important that the so called 'run list', defining the diffractometer setting angles and scan directions for the detector exposures, takes into account the $\varphi = 0°$ mode of the DAC orientations, for which access to the DAC is still on average at its widest and the DAC absorption and gasket-shadowing effects are on average the smallest. Most importantly, such an optimum setting can be executed with a four-circle diffractometer, and cannot be done on simplified diffractometers with the φ shaft fixed at a χ angle of about 50°. Even fewer reflections can be accessed when the DAC is rotated about one axis only, which is still the case for some laboratory and synchrotron diffractometers.

2.7.9. Powder diffraction with the DAC

The DAC is often described as the workhorse of high-pressure research, owing to its versatile applications, low cost, easy operation and unrivalled attainable static pressure. However, the small size of the DAC chamber, containing sample volumes between 0.025 mm^3 for pressure to about 5 GPa, 0.005 mm^3 to about 10 GPa and less than 3×10^{-6} mm^3 for the megabar range, can be disadvantageous for powder diffraction studies. The disadvantages include the inhomogeneous distribution of temperature within the sample (particularly as it remains in contact with a diamond, which is the best known thermal conductor) and nonhydrostatic strain (often due to the technique of generating pressure by uniaxial compression of the chamber). In some samples close to the melting curve some grains increase in size at the expense of others, partly or fully dissolving, so the number of grains may be insufficient for obtaining good-quality powder diffraction patterns. This difficulty can be partly circumvented by rocking the DAC during the experiment about the ω axis. On the other hand, for a sample consisting of tens of grains it is possible to perform multi-grain analysis by merging the diffraction patterns to give the equivalent of single-crystal data. High-pressure powder diffraction patterns can also be affected by a low signal-to-noise ratio, too few crystal grains, and their preferential orientation in the DAC uniaxially compressed chamber. The preferential orientation is particularly significant when the grains are elongated and their compressibility is anisotropic; these effects can be further aggravated by the non-hydrostatic environment. Powder reflections are much weaker in intensity than the equivalent single-crystal reflections from the same sample volume. Small sample volumes are compensated for by the powerful beams available at synchrotrons. At present, high-pressure powder diffraction experiments are mainly carried out at synchrotrons by energy-dispersive (Buras *et al.*, 1997*a*,*b*; Baublitz *et al.*, 1981; Brister *et al.*, 1986; Xia *et al.*, 1990; Oehzelt *et al.*, 2002) and angle-dispersive methods (Jephcoat *et al.*, 1992; Nelmes & McMahon, 1994; Fiquet & Andrault, 1999; Crichton & Mezouar, 2005; Mezouar *et al.*, 2005; Hammersley *et al.*, 1996). Angle-dispersive methods are currently preferred to the energy-dispersive method owing to their higher resolution and simpler data processing. However, the energy-dispersive method requires less access for the X-ray beams probing the sample, and hence it is often preferred for studies in the megabar range (hundreds of gigapascals). For high-pressure powder diffraction studies in the laboratory, energy-dispersive methods are still preferred (Tkacz, 1998; Palasyuk & Tkacz, 2007; Palasyuk *et al.*, 2004). The main advantages of experiments at synchrotrons are:

(i) They have a very intense beam compared with traditional sealed X-ray tubes and modern micro-focus sources;
(ii) They offer the possibility of very narrow collimation of the beam, to a diameter of one or a few micrometres;
(iii) Very quick collection of high-quality diffraction data is possible, which is most useful for high-pressure and very high temperature data collections;
(iv) It is possible to measure diffraction data from very small samples, to reduce the dimensions of the DAC chamber and

hence to increase the attainable pressure, which is inversely proportional to the chamber diameter;

(v) The microbeam can illuminate a small selected portion of the sample chosen for the investigation, which can be used to perform single-crystal diffraction on a selected grain or for X-ray tomography of the sample and its inclusions;

(vi) The beam diameter is smaller than the diameter of the chamber, which minimizes or even eliminates the effects of beam shadowing;

(vii) The X-ray wavelength is tuneable down to about 0.3 Å. This considerably increases the data completeness and reduces absorption effects in the sample and DAC.

Owing to these features, synchrotron beams are ideally suited for high-pressure diffraction experiments and some researchers have completely stopped using in-house laboratory equipment with sealed X-ray tubes. Historically, the first use of synchrotron radiation for high-pressure studies was reported by Buras, Olsen & Gerward (1977) and Buras, Olsen, Gerward *et al.* (1977). Conventional diffractometers with sealed X-ray tubes can be effectively used for preliminary powder diffraction experiments. For example, a new high-pressure phase of (+)-sucrose was found in this way (Patyk *et al.*, 2012), although the data were insufficient for any structural refinements.

Diffraction data are collected in single and multiple exposures, and the pressure is controlled remotely by inflating a membrane through a gas system. Currently assembled high-pressure powder diffraction synchrotron beamlines incorporate on-line pressure calibration using ruby fluorescence and, often, Raman spectroscopy.

2.7.10. Sample preparation

Several basic techniques can be used to prepare a sample for a high-pressure experiment, for example:

(i) A solid sample can be mounted under ambient conditions in the high-pressure chamber together with the hydrostatic fluid, then sealed and pressurized;

(ii) A solid sample can be mounted under ambient conditions in the high-pressure chamber, condensed gas loaded at elevated pressure (Tkacz, 1995; Rivers *et al.*, 2008; Couzinet *et al.*, 2003; Mills *et al.*, 1980; Yagi *et al.*, 1996; Kenichi *et al.*, 2001) or under cryogenic conditions, and the sample sealed and further pressurized by gasket compression;

(iii) A liquid sample can fill the whole chamber volume under ambient conditions, or condensed gases or their mixtures can be loaded at elevated pressure, and after sealing the DAC the sample is frozen under isothermal conditions;

(iv) A crystal of the pure compound or of a solvate can precipitate from the mixture (solution) when compressed isothermally – the crystal can be in the form of a single crystal or a powder, fully or partly filling the DAC chamber;

(v) Samples completely filling the DAC chamber can be compressed isothermally or undergo isochoric treatment, but strains can be generated in a single crystal or in the grains of a compressed powder conglomerate by anisotropic thermal contraction/expansion; this strain can be avoided by having an excess of the hydrostatic component of the mixture;

(vi) A solid powdered sample can be mixed with a powder of another compound, which is much softer than the sample and is used as a pseudo-hydrostatic medium (halite and MgO are often used for this purpose) – this technique is mainly used for cubic or isotropic samples in large-volume presses, where (pseudo)isotropic strain and pseudo-spherical compression minimize the effect of preferential orientation in the sample.

Preferential orientation can significantly hamper the quality of powder diffraction data, and corrections for this effect should be applied in the Rietveld refinement. All Rietveld refinement programs include preferential orientation models, which fit the data with satisfactory results (McMahon, 2004, 2005; Filinchuk, 2010).

2.7.11. Hydrostatic conditions

Hydrostatic conditions in the sample chamber are essential for good-quality high-pressure diffraction data. They are equally important for single-crystal and powder diffraction experiments. To secure hydrostaticity, the sample is submerged in a hydrostatic medium. The pressure and temperature ranges of the planned experiment depend on the hydrostatic properties of the applied medium. Eventually all substances solidify because of crystallization or vitrification (Piermarini *et al.*, 1973; Eggert *et al.*, 1992; Grocholski & Jeanloz, 2005), which can lead to damage of single crystals, anisotropic strain in powder grains and inhomogeneity of pressure across the sample. It is also important to protect a solid sample from dissolution in the hydrostatic fluid. The dissolved sample can lose its required features (such as shape, polymorphic form or chemical composition) and recrystallize at higher pressure in an undesired form. For example, a fine powder may recrystallize into a few large and preferentially oriented grains. Another potential problem can arise from reactions between the sample and the hydrostatic medium. For example, a pure compound can form solvates incorporating molecules of the hydrostatic fluid (Olejniczak & Katrusiak, 2010, 2011; Andrzejewski *et al.*, 2011; Tomkowiak *et al.*, 2013; Boldyreva *et al.*, 2002; Fabbiani & Pulham, 2006). This has also been observed for helium and argon penetrating into the structures of the fullerenes C_{60} and C_{70} (Samara *et al.*, 1993) and into arsenolite As_4O_6 (Guńka *et al.*, 2015). High-pressure crystallization of water in the presence of helium leads to an inclusion compound interpreted as ice XII. Therefore, the hydrostatic medium should be carefully chosen for a specific experiment, depending on the sample solubility, the pressure range and the type of investigation, whether a mounted-sample study, or *in situ* crystallization or reaction (Sobczak *et al.*, 2018; Półrolniczak *et al.*, 2018).

Many minerals and inorganic samples hardly dissolve at all and a commonly applied pressure-transmitting medium is a mixture of methanol, ethanol and water (16:3:1 by volume), hydrostatic to over 10 GPa at 296 K (see Table 2.7.1); separately, pure methanol crystallizes at 3.5 GPa, ethanol at 1.8 GPa and water at 1.0 GPa. If a sample dissolves well in methanol, ethanol and water, other fluids can be selected (Piermarini *et al.*, 1973; Angel *et al.*, 2007). Liquids like glycerine (hydrostatic to 3 GPa) and special inert fluids, such as silicone oil (Shen *et al.*, 2004; Ragan *et al.*, 1996), Daphne oil (Yokogawa *et al.*, 2007; Murata *et al.*, 2008; Klotz *et al.*, 2009), or condensed gases, like helium, argon and hydrogen (Tkacz, 1995; Dewaele & Loubeyre, 2007), can be used. Alternatively, a saturated solution of the sample compound, for example in a methanol–enthanol–water mixture, can prevent sample dissolution, but on increasing the pressure the compound can precipitate in the form of a powder or single crystals. One can choose to load an excess of the sample into the chamber before filling it up with the hydrostatic fluid, which would dissolve only some of the sample.

Table 2.7.1
The (pseudo)hydrostatic limits of selected media at 296 K (Holzapfel, 1997; Miletich *et al.*, 2000)

Medium	Freezing point (GPa)	(Pseudo)hydrostatic limit (GPa)	Reference
4:1 Methanol:ethanol	–	9.8	Angel *et al.* (2007)
16:3:1 Methanol:ethanol:water	–	10.5	Angel *et al.* (2007)
Anhydrous propan-2-ol	–	4.2	Angel *et al.* (2007)
Neon	4.7	19	Klotz *et al.* (2009)
Argon	1.2	9/35	Bell & Mao (1981)/You *et al.* (2009)
Helium	11.8	70/150	Bell & Mao (1981)/Dewaele & Loubeyre (2007)
Hydrogen	5.7	177	Mao & Bell (1979)
Nitrogen	2.4	13	LeSar *et al.* (1979)
Glycerol	–	1.4	Angel *et al.* (2007)
Glycerin	–	3.0	Hazen & Finger (1982)
Glycerin		4.0	Tateiwa & Haga (2010)
Fluorinert FC84/87	–	7.0	Klotz *et al.* (2009)
Petroleum ether	–	6.0	Mao & Bell (1979)
Isopropyl alcohol		4.3	Piermarini *et al.* (1973)
1:1 Pentane:isopentane	–	7.4	Piermarini *et al.* (1973)
Silicone oil, viscosity 0.65 cSt	–	0.9	Angel *et al.* (2007)
Silicone oil	–	14	Klotz *et al.* (2009)
Daphne oil 7373		2.3	Murata *et al.* (2008)
Daphne oil 7474		3.7 at 296 K/6.7 at 273 K	Klotz *et al.* (2009)/Tateiwa & Haga (2010)
Vaseline	–	2.0	Tateiwa & Haga (2010)
NaCl	–	0.05/25	Tateiwa & Haga (2010)/You *et al.* (2009)

In situ crystallization at high pressure requires good, though not necessarily very good, solvents. Also, co-crystallizations can be performed in the DAC, and in this case the product that is obtained can depend on the solvents used and their concentration. Pressure effectively modifies intermolecular interactions, and new solvates can be obtained depending on the concentration of the substrates. It can be tricky to avoid co-crystallization of some compounds; in these cases a range of hydrostatic fluids has to be tried. A mixture of petroleum ethers, silicone or Daphne oils can be a good choice. Daphne oil, consisting mainly of alkylsilane (Murata *et al.*, 2008), has the rare feature of negligible thermal expansion, which is particularly useful for low-temperature high-pressure experiments: the DAC can be loaded under normal conditions and then pressurized and cooled to the required temperature, *e.g.* in a cryostat, without significant loss of pressure due to contraction of the medium.

The hydrostatic conditions can be checked by inspecting the width of reflections from the sample (full width at half-maximum, FWHM, is usually plotted), the width of the ruby fluorescence R_1 line and the R_1–R_2 line separation (You *et al.*, 2009). The pressure homogeneity can be checked by measurements for several ruby chips mounted across the DAC chamber. Nonhydrostatic conditions can cause inconsistent results and difficulties in their interpretation, which can prompt the researcher to consider changing the hydrostatic medium.

For hard samples, some departure from hydrostatic conditions is often acceptable. It is assumed that for a hard sample the nonhydrostatic compression component is small in a much softer medium, for example, hard corundum studied in soft NaCl. On the other hand, it may be easier to prepare a sample under normal conditions by uniformly mixing the powder of the specimen with a pseudo-hydrostatic medium, rather than using hydrostatic liquids or gases. The diffraction from the pseudo-hydrostatic medium powder can be used to monitor the pressure and measure non-hydrostaticity effects. Pseudo-hydrostatic solid media are often used for multi-anvil presses, where a solid sample facilitates loading and the uniaxial stress is not as drastic as in the opposed-anvil presses. Also, in high-temperature experiments the process of annealing reduces non-hydrostatic strain.

A relatively low nonhydrostatic effect was reported for argon frozen at 1.9 GPa: its pressure gradient up to 1% only is supported at 9 GPa (Bell & Mao, 1981) and up to 1.5% at 80 GPa (Liu *et al.*, 1990). This illustrates how the pseudo-hydrostaticity limit can be extended depending on the hardness of the specimen, the type of high-pressure device and the acceptance of deviatoric stress in the sample.

At very high pressure, exceeding 60 GPa, no compounds persisting as liquids are known (*cf.* Table 2.7.1). Diffraction data must then be corrected for a deviatoric stress component, causing the broadening of reflection rings and affecting their $2\theta_{\rm Bragg}$ positions, when the uniaxial stress is not collinear with the incident beam (Singh, 1993; Singh & Balasingh, 1994; Singh *et al.*, 1998; Mao *et al.*, 1998). The effect of uniaxial stress can be reduced or eliminated by sample annealing, which is often applied to improve the hydrostaticity of the sample.

2.7.12. High-pressure chamber and gasket in the DAC

A high-pressure device should be adjusted to the experiments planned, and in particular to the chemical activity of the sample. Gaseous hydrogen penetrates and dissolves in most metals, and therefore special alloys, such as beryllium bronze, have to be used for hydrogen setups. For some experiments non-metallic gaskets can be used, for example amorphous boron, corundum or diamond powders mixed with a resin. Owing to the insulating properties of such a gasket, the pressure dependence of the electric, dielectric and magnetic properties of the sample can be measured. Chemically aggressive samples can interact with the gasket material of the DAC chamber, and even with the diamond anvils, and this effect usually intensifies at high temperature and pressure. Consequently, both the sample and the high-pressure device can be affected. The erosion caused by an aggressive liquid can be considerably slowed down by its crystallization, which freezes the diffusion of molecules into the gasket. For example, *in situ* crystallization of halogen derivatives of acetic acid could only be performed in a DAC chamber with tungsten gaskets (Gajda & Katrusiak, 2009). In these experiments, the gasket was gradually eroded by the acid, but after its crystal-

lization the measurements could be performed over several days. In order fully to prevent erosion of the gasket, it can be coated with a layer of inert material, for example gold or platinum. Alternatively, a composite chamber can be prepared: after pre-indenting the gasket and drilling a hole at the centre of the indentation, a piece of gold wire can be fitted to the hole, and after pressing into a hole in the DAC again, a smaller hole can be drilled through this inset. A DAC chamber formed in this way has a gold lining and can be resistant to aggressive compounds.

2.7.13. High-pressure neutron diffraction

Neutron scattering is an indispensable and complementary technique in materials research (see Chapter 2.3), particularly for compounds containing heavy elements that strongly absorb X-rays, or light-atom weak X-ray scatterers (*e.g.* see Goncharenko & Loubeyre, 2005). However, the flux of neutron sources, both reactors and spallation targets, is several orders of magnitude lower than that of X-rays, even from traditional sealed X-ray tubes. Moreover, the scattering cross sections of neutrons are on average two orders of magnitude smaller than for X-rays (Bacon, 1975). These two considerations conflict with the requirement of small sample volume preferred for high-pressure devices. Consequently, a prohibitively long measurement time would be required to obtain meaningful neutron diffraction data from the DAC in its original form and size-optimized for X-ray studies. Therefore, initially, the designs of high-pressure devices for neutron scattering studies were based on typical large-volume presses: gas bombs with external multi-stage pressure generators, and piston-and-cylinder, multi-anvil and belt presses (Worlton & Decker, 1968; Bloch *et al.*, 1976; McWhan *et al.*, 1974; Srinivasa *et al.*, 1977; Besson, 1997; Klotz, 2012). The sample volume in the Bridgman-type opposed-anvil press, with flat anvils separated by a gasket of pipestone, was increased severalfold by making a recess at the centre of the pressure chamber of the so-called Chechevitsa anvils (Stishov & Popova, 1961*a*,*b*). The sample volume was further increased in toroid anvils by grooves supporting the gasket around the central recess (Khvostantsev *et al.*, 1977). This made them ideal for powder diffraction neutron measurements on samples of about 100 mm^3 to above 10 GPa in a Paris–Edinburgh hydraulic press (Besson *et al.*, 1992; Besson, 1997). The application of sintered diamond anvils increased this pressure range. High-pressure cells in a form optimized for neutron diffraction can contain between several cubic millimetres and a few cubic centimetres of sample volume. Such a large sample volume naturally limits the pressure range of cells used for neutron diffraction, compared with the DAC used for X-rays. However, the pressure range has increased considerably for neutron diffraction experiments during recent decades, to over 20 GPa in a moissanite anvil cell (Xu *et al.*, 2004; Dinga *et al.*, 2005), and to 40 GPa in a high-pressure cell capable of operating in helium cryostats at 0.1 K and in magnetic fields up to 7.5 T (Goncharenko, 2006; Goncharenko *et al.*, 1995). High-pressure high-temperature cells for neutron diffraction are usually equipped with internal heaters capable of exceeding 1500 K (Zhao *et al.*, 1999, 2000; Le Godec *et al.*, 2001, 2002).

It is particularly advantageous for the construction of large presses for neutron studies that most of the materials used have very low absorption of neutrons. There are also metals (vanadium, aluminium) with very low scattering lengths, and it is possible to obtain alloys ($Ti_{66}Zr_{34}$) with the scattering length scaled to zero. This allows access of the neutron beam to the sample and exit of reflections. In a Paris–Edinburgh cell operating in the time-of-flight mode, the incident beam enters the pressure chamber through the tungsten carbide anvil, along its axis, and the reflections leave the chamber through the gasket along the slit between the anvils with approximately ±6° opening (Besson *et al.*, 1992; Takahashi *et al.*, 1996). In this operation mode, highly neutron-absorbing anvils made of sintered cubic boron nitride (cBN) can also be used (Klotz, 2012). Alternatively, the monochromatic angle-dispersive mode of operation, with the incident and diffracted beams passing through the slit between the anvils, is possible but it is less efficient with regard to the use of the full spectrum of neutrons. The application of a focused neutron beam and the time-of-flight technique allow the use of small sample volumes of a fraction of a cubic millimetre in compact opposed-anvil high-pressure cells (Okuchi *et al.*, 2012). Two DACs were recently optimized for neutron diffraction on single crystals. Owing to the application of a white neutron beam, the structure of a crystal 0.005 mm^3 in volume was determined. All reflections could be recorded because of the smaller Merrill & Bassett (1974) design made of neutron-transparent beryllium–copper alloy (Binns *et al.*, 2016). Another design with a wide access to the sample for the primary and diffracted beams has been successfully used at a hot-neutron source (Grzechnik *et al.*, 2018).

2.7.14. Pressure determination

Pressure determination inside a high-pressure sample chamber is most straightforward in piston-and-cylinder devices, where the force applied to the piston and its surface area are known. Pressure is the force per unit area, with corrections for the friction between the cylinder wall and the piston (particularly significant above 1 GPa) and for the buoyancy of the piston, marginally important for all high pressures. Several types of mechanical pressure gauge are available. In the Bourdon gauge, a spiral metal tube that is pressurized inside unwinds and moves a pointer around a precise scale. Electrical resistance gauges are most often based on a manganin alloy sensor. The resistance of manganin changes at the rate of 2.4×10^{-5} GPa^{-1}, although precise calibration depends on the alloy composition and it changes with the age of the sensor. The resistance of manganin depends only very weakly on temperature.

The most common pressure calibration method used for the DAC is the fluorescence pressure scale of the ruby R_1 (λ_{R1} at 0.1 MPa is the reference; $\lambda_0 = 694.2$ nm) and R_2 (at 0.1 MPa, $\lambda_{R2} = 692.8$ nm) lines (Forman *et al.*, 1972; Barnett *et al.*, 1973; Syassen, 2008; Gao & Li, 2012). Synthetic ruby with a Cr^{3+} concentration of 3000–5500 p.p.m., illuminated with green laser light, is commonly used. Inclusions of spinels make natural ruby unsuitable as a pressure gauge. A piece of ruby is usually crushed into small pieces and one or several small chips are placed in the DAC chamber close to the sample (Hazen & Finger, 1982). Alternatively, small ruby spheres can be used for this purpose (Chervin *et al.*, 2001).

The linear pressure dependence of the ruby R_1 fluorescence line was established according to the equation of state (EOS) of NaCl to 19.5 GPa:

$$P\,(\mathrm{GPa}) = 2.74\Delta\lambda\,(\mathrm{nm}),$$

where $\Delta\lambda = \lambda_{R1} - \lambda_0$ (Piermarini *et al.*, 1975). The extension of the pressure range to 180 GPa, according to the equations of state of copper, gold and other metals, showed that $P(\Delta\lambda)$ is quasi-linear:

Table 2.7.2
Luminescence pressure sensors, their electronic transition types (s = singlet, d = doublet) and rates of spectral shifts (after Holzapfel, 1997)

Sensor	Transition	λ_0 (Å)	$d\lambda/dP$ (Å GPa^{-1})	$d\lambda/dT$ ($\times 10^{-2}$ Å K^{-1})	$(d\lambda/dP)/\Gamma$ (Å GPa^{-1})	$(d\lambda/dT)/(d\lambda/dP)$ ($\times 10^{-2}$ GPa K^{-1})
Cr^{3+}:Al_2O_3	$^2E\downarrow{}^4A_2$/d	6942	3.65 (9)	6.2 (3)	4.9	17.0
Sm^{2+}:SrB_4O_7	$^5D_0\downarrow{}^7F_0$/s	6854	2.55	−0.1	17.0	−0.4
Sm^{2+}:BaFCl	$^5D_0\downarrow{}^7F_0$/s	6876	11.0	−1.6	4.8	−1.5
Sm^{2+}:SrFCl	$^5D_0\downarrow{}^7F_0$/s	6903	11.2 (3)	−2.36 (3)	5.8	−2.1
Eu^{3+}:LaOCl	$^5D_0\downarrow{}^7F_0$/s	5787	2.5	−0.5	1.0	−2.0
Eu^{3+}:YAG	$^5D_0\downarrow{}^7F_1$/d	5906	1.97	−0.5	0.7	−2.5

Table 2.7.3
Parameters recommended for pressure determination by EOS measurements

Various face-centred cubic (f.c.c.) and body-centred cubic (b.c.c.) metals are used as calibrants, with the EOS given by equation (2.7.1) and the reference temperature T_R = 300 K (after Holzapfel, 1997).

Metal	a_{0R} (pm)	K_{0R} (GPa)	K'_{0R}	α_{0R} ($\times 10^6$ K)	$\delta_{\alpha R}$
Al	404.98 (1)	72.5 (4)	4.8 (2)	23.0 (4)	5.5 (11)
Cu	361.55 (1)	133.2 (2)	5.4 (2)	16.6 (3)	6.1 (6)
Ag	408.62 (1)	101.0 (2)	6.2 (2)	19.2 (4)	7.1 (6)
Au	407.84 (1)	166.7 (2)	6.3 (2)	14.2 (2)	7.2 (6)
Pd	388.99 (1)	189 (3)	5.3 (2)	11.6 (4)	6.0 (11)
Pt	392.32 (1)	277 (5)	5.2 (2)	8.9 (4)	5.9 (l1)
Mo	314.73 (1)	261 (5)	4.5 (5)	5.0 (4)	5.2 (14)
W	316.47 (1)	308 (2)	4.0 (2)	4.5 (4)	4.7 (11)

Table 2.7.4
Pressure fixed points at ambient temperature (after Holzapfel, 1997; Hall, 1980)

P (GPa)	Element transition
0.7569 (2)†	Hg freezing at 273 K
1.2 (1)†	Hg freezing at 298 K
2.55 (6)†	Bi I–II at 298 K
3.67 (3)†	Tl h.c.p.–f.c.c.
2.40 (10)†	Cs I–II
4.25 (1)†	Cs II–III
4.30 (1)†	Cs III–IV
5.5 (1)‡	Ba I–II
7.7 (2)‡	Bi III–IV
9.4 (3)†	Sn I–II
12.3 (5)†	Ba II–III
13.4 (6)†	Pb I–II

† Onset of forward transition. ‡ Centre of hysteresis.

$$P = 1904[(\lambda/\lambda_0)^B - 1]/B,$$

where B = 7.665 for quasi-hydrostatic and 5.0 for non-hydrostatic conditions (Mao *et al.*, 1986, 1978; Bell *et al.*, 1986).

The ruby fluorescence depends strongly on temperature (Barnett *et al.*, 1973; Vos & Schouten, 1991; Yamaoka *et al.*, 2012) and a temperature change of about 6 K causes R_1 line shifts equivalent to 0.1 GPa. The fluorescence-line dependence on temperature is much weaker for Sm^{2+}:SrB_4O_7 (Lacam & Chateau, 1989; Lacam, 1990; Datchi *et al.*, 1997) and the other rare-earth-doped sensors listed in Table 2.7.2. These sensors can be more sensitive to pressure than ruby, and together with ruby can be used simultaneously for both temperature and pressure calibration.

The calibration of most pressure gauges is based on comparisons of theoretical and shock-wave data (Holzapfel, 1997), so the derived equations of state are used with an accuracy of about 5% up to 1 TPa. The EOS recommended by Holzapfel (1997) is

$$P = [3K_0(1-x)/x^5]\exp[c_0(1-x)], \qquad (2.7.1)$$

where $x = a/a_0 = (V/V_0)^{1/3}$, $c_0 = 3(K_0' - 3)/2$, a is the unit-cell dimension, V is the unit-cell volume, a_{0R} and V_{0R} are the reference parameters under ambient conditions (Table 2.7.3), α_{0R} is the thermal expansion coefficient, K_{0R} is the bulk modulus, and $K_0' = dK_0/dP$. $dK_0/dT = -3\alpha_{0R}K_0\delta_{\alpha R}$, where $\delta_{\alpha R} = \partial(\ln\alpha)/\partial(\ln V)_{TR}$. Pressure can be computed by assuming constant K_0' and linear temperature relations for T close to or higher than T_R = 300 K:

$$a_0(T) = a_{0R}[1 + \alpha_{0R}(T - T_R)],$$
$$V_0(T) = V_{0R}[1 + 3\alpha_{0R}(T - T_R)],$$
$$K_0(T) = K_{0R}[1 - \alpha_{0R}\delta_{\alpha R}(T - T_R)].$$

The details of the parameterization are explained by Holzapfel (1991, 1994) and listed for the simple face-centred (f.c.c.) and body-centred (b.c.c.) cubic metals in Table 2.7.3 (Holzapfel, 1997). Powders of these metals can be mixed with the sample and its pressure can be calibrated according to the unit-cell dimension of the standard. The well known compressibilities of NaCl, CaF_2 and MgO, in the form of either powders or single crystals, are also often used as internal pressure standards (Dorfman *et al.*, 2010, 2012; Dorogokupets & Dewaele, 2007).

An independent pressure assessment can be obtained from standard materials undergoing pressure-induced phase transitions (Table 2.7.4). This method is limited to just a few pressure points (Holzapfel, 1997), but they can provide a useful verification of other pressure gauges.

Other methods of pressure calibration are still being developed. For example, it has been shown that very high pressure can be determined from the Raman shift of strained diamond-anvil culets (Akahama & Kawamura, 2004). The strong piezochromic effect of visible colour changes in soft coordination polymers allows pressure calibration without spectrometers. These changes can proceed gradually (Andrzejewski & Katrusiak, 2017*a*) and abruptly at phase transitions (Andrzejewski & Katrusiak, 2017*b*). Another method of pressure calibration is based on the luminescence lifetime of lanthanide nanocrystals (Runowski *et al.*, 2017).

2.7.15. High-pressure diffraction data corrections

Apart from the Lorentz and polarization (Lp) corrections routinely applied to reflection intensities measured for bare crystals (*i.e.* crystals not enclosed in environment devices), as well as other corrections like extinction and absorption in the sample, the effects of the high-pressure cell should additionally be accounted for. These effects mainly include absorption in the pressure-vessel walls, shadowing of the sample by the pressure-cell opaque elements and elimination of the reflections of the diamond anvils for measurements in a DAC. The set of corrections is usually described for the specific pressure vessel. For a

typical DAC with the anvils (about 1.7 mm high) supported directly on the edges of conical steel or tungsten carbide windows, and for Mo *K* radiation, the absorption is quite uniform and varies between about 0.50 and 0.60, for the beams passing close to the DAC axis and those close to the conical window edge, respectively. This absorption is even smaller at the shorter wavelengths used for high-pressure X-ray diffraction studies at synchrotrons. For this reason the absorption correction for the DAC is often neglected.

The sample-shadowing correction accounts for the loss of intensity due to the sample being partly shadowed by the gasket edges. This effect can be avoided by choosing a sufficiently small crystal or by applying a sufficiently narrow beam, which would illuminate only the central part of the sample. Such microbeams are now routinely used at synchrotrons. For these reasons, synchrotron data are often used straightforwardly after applying just the Lp corrections and incident-beam variation and eliminating the diamond reflections. In fact there are very few diamond reflections because of the small unit cell and many systematic absences, and the DAC can be treated as a low-background cuvette for powder diffraction.

The corrections for absorption and gasket shadowing are very important for high-pressure data collection in the laboratory, where a sealed X-ray tube is used. Its beam is relatively weak and for this reason the quality of the data (signal-to-background ratio) is low, but can be improved by increasing the sample volume. Ideally, a sample that completely fills the DAC chamber secures the highest intensity of reflections. However, for large samples the shadowing of the incident and diffracted beams by the gasket is very significant and should be corrected for (Katrusiak, 2004*a*,*b*).

The calculation of the so-called analytical corrections, obtained by dividing the high-pressure chamber into small pixels and calculating the beam's trajectory to and off each pixel, through all the DAC components (beryllium discs, if present, diamond anvils, hydrostatic fluid and sample) can precisely eliminate errors. Having the correct reflection intensities simplifies the structure solution of new phases and increases the accuracy of the refined structure. It has been shown that some incompleteness of accurate data does not cause systematic errors in the structural parameters (Dziubek & Katrusiak, 2002). In most calculations of reflection intensity corrections, the cylindrical symmetry of the DAC about its axis is assumed (Katrusiak, 2001, 2004*a*,*b*; Hazen & Finger, 1982; Angel, 2004; Kuhs *et al.*, 1996; Miletich *et al.*, 2000).

Diffraction measurements with area detectors have the advantage of collecting data with a considerable redundancy factor, which is often routinely used to calculate the so-called empirical absorption corrections, which are sometimes applied to a sample in a DAC. The intensities of powder diffraction reflections measured at synchrotrons with microbeams are often not corrected, particularly when the DAC axis is not significantly moved from the primary beam during data collection. The redundancy of the data also considerably reduces the effect of simultaneous diffraction events by the sample and one or two of the diamond anvils.

The most significant systematic errors in the diffraction of a sample in a DAC may be due to preferential orientation of the grains, which can occur for an anisotropic sample and non-hydrostatic conditions in the chamber. This effect can be accounted for in the process of Rietveld refinement (McMahon, 2004; Filinchuk, 2010), or may require repetition of the measurement after reloading a new sample into the DAC.

2.7.16. Final remarks

During the last 100 years, and particularly during the last few decades, high-pressure diffractometric techniques have been developed covering a broad range of research in different fields of science. It is simply impossible to present all aspects of high-pressure methodology in one chapter. Many books, book chapters and scientific papers have been written on high-pressure research and therefore I have chosen to present a 'flavour' of high-pressure crystallography, rather than concentrating on all its aspects. Readers interested in specific subjects can find the required information in a number of instructive books (Hazen & Finger, 1982; Eremets, 1996; Holzapfel, 1997; Katrusiak & McMillan, 2004; Boldyreva & Dera, 2010; McMahon, 2012) and in numerous articles in research journals. This chapter is only an introduction and gives some useful reference information for high-pressure crystallographers.

It should be stressed that the sample-preparation techniques for high-pressure studies are relatively demanding. Therefore, diffraction studies are often 'adjusted' to the form of the sample obtained in the high-pressure device. In particular, powder diffraction, single-crystal and spectroscopic measurements can be conducted on some synchrotron beamlines (see *e.g.* Dera *et al.*, 2013). Many experimental techniques complementary to high-pressure crystallographic studies have not been mentioned here.

It can be concluded that, over the years, high-pressure research has become quite popular in materials science and at present all over the world there are hundreds or even thousands of scientists capable of performing high-pressure experiments. Their scientific output is significant, and can be used as a guide for those interested in specific types of high-pressure research.

References

Abrahams, S. C., Collin, R. L., Lipscomb, W. N. & Reed, T. B. (1950). *Further techniques in single-crystal X-ray diffraction studies at low temperatures. Rev. Sci. Instrum.* **21**, 396–397.

Adams, D. M. & Christy, A. G. (1992). *Materials for high-temperature diamond-anvil cells. High Press. Res.* **8**, 685–689.

Ahrens, T. J. (1980). *Dynamic compression of Earth materials. Science*, **207**, 1035–1041.

Ahrens, T. J. (1987). *Shock wave techniques for geophysics and planetary physics.* In *Methods of Experimental Physics*, Vol. 24A, edited by C. G. Sammis & T. L. Henyey, pp. 185–235. New York: Academic Press.

Ahsbahs, H. (2004). *New pressure cell for single-crystal X-ray investigations on diffractometers with area detectors. Z. Kristallogr*. **219**, 305–308.

Akahama, Y., Hirao, N., Ohishi, Y. & Singh, A. K. (2014). *Equation of state of bcc-Mo by static volume compression to 410 GPa. J. Appl. Phys.* **116**, 223504.

Akahama, Y. & Kawamura, H. (2004). *High-pressure Raman spectroscopy of diamond anvils to 250 GPa: method for pressure determination in the multimegabar pressure range. J. Appl. Phys.* **96**, 3748–3751.

Akahama, Y. & Kawamura, H. (2010). *Pressure calibration of diamond anvil Raman gauge to 410 GPa. J. Phys. Conf. Ser.* **215**, 012195.

Akimoto, S., Suzuki, T., Yagi, T. & Shimomura, O. (1987). *Phase diagram of iron determined by high-pressure/temperature X-ray diffraction using synchrotron radiation*. In *High-Pressure Research in Mineral Physics*, Geophysics Monograph Series, Vol. 39, edited by M. H. Manghnani & Y. Syono, pp. 149–154. Washington, DC: AGU.

Alireza, P. L. & Lonzarich, G. G. (2009). *Miniature anvil cell for high-pressure measurements in a commercial superconducting quantum interference device magnetometer. Rev. Sci. Instrum.* **80**, 023906.

Allan, D. R. & Clark, S. J. (1999). *Impeded dimer formation in the high-pressure crystal structure of formic acid. Phys. Rev. Lett.* **82**, 3464–3467.

Andrzejewski, M. & Katrusiak, A. (2017*a*). *Piezochromic porous metal–organic framework. J. Phys. Chem. Lett.* **8**, 279–284.

Andrzejewski, M. &. Katrusiak, A. (2017*b*). *Piezochromic topology switch in a coordination polymer. J. Phys. Chem. Lett.* **8**, 929–935.

Andrzejewski, M., Olejniczak, A. & Katrusiak, A. (2011). *Humidity control of isostructural dehydration and pressure-induced polymorphism in 1,4-diazabicyclo[2.2.2]octane dihydrobromide monohydrate. Cryst. Growth Des.* **11**, 4892–4899.

Angel, R. J. (2004). *Absorption corrections for diamond-anvil pressure cells implemented in the software package Absorb6.0. J. Appl. Cryst.* **37**, 486–492.

Angel, R. J., Bujak, M., Zhao, J., Gatta, G. D. & Jacobsen, S. D. (2007). *Effective hydrostatic limits of pressure media for high-pressure crystallographic studies. J. Appl. Cryst.* **40**, 26–32.

Bacon, G. E. (1975). *Neutron Diffraction*. Oxford University Press.

Baranowski, B. & Bujnowski, W. (1970). *A device for generation of hydrogen pressure to 25000 at. Ann. Soc. Chim. Polonarum*, **44**, 2271–2273.

Barnett, J. D., Block, S. & Piermarini, G. J. (1973). *An optical fluorescence system for quantitative pressure measurement in the diamond-anvil cell. Rev. Sci. Instrum.* **44**, 1–9.

Bassett, W. A. (2001). *The birth and development of laser heating in diamond anvil cells. Rev. Sci. Instrum.* **72**, 1270–1272.

Bassett, W. A. (2009). *Diamond anvil cell, 50th birthday. High Press. Res*. **29**, 163–186.

Bassett, W. A., Shen, A. H., Bucknum, M. & Chou, I.-M. (1993). *A new diamond anvil cell for hydrothermal studies to 2.5 GPa and from −190 to 1200˚C. Rev. Sci. Instrum.* **64**, 2340–2345.

Bassett, W. A. & Takahashi, T. (1965). *Silver iodide polymorphs. Am. Mineral*. **50**, 1576–1594.

Batsanov, S. S. (2004). *Solid phase transformations under high dynamic pressure.* In *High-Pressure Crystallography*, edited by A. Katrusiak & P. F. McMillan, pp. 353–366. Dordrecht: Kluwer.

Baublitz, M. A., Arnold, V. & Ruoff, A. L. (1981). *Energy dispersive X-ray diffraction from high pressure polycrystalline specimens using synchrotron radiation. Rev. Sci. Instrum.* **52**, 1616–1624.

Bell, P. M. & Mao, H.-K. (1981). *Degree of hydrostaticity in He, Ne, and Ar pressure-transmitting media. Carnegie Inst. Washington Yearb.* **80**, 404–406.

Bell, P. M., Xu, J. A. & Mao, H.-K. (1986). *Static compression of gold and copper and calibration of the ruby pressure scale to pressures to 1.8 megabars.* In *Shock Waves in Condensed Matter*, edited by Y. M. Gupta, pp. 125–130. New York: Plenum Press.

Besson, J. M. (1997). *Pressure generation.* In *High-Pressure Techniques in Chemistry and Physics. A Practical Approach*, edited by W. B. Holzapfel & N. S. Isaacs, pp. 1–45. Oxford University Press.

Besson, J. M., Nelmes, R. J., Hamel, G., Loveday, J. S., Weill, G. & Hull, S. (1992). *Neutron powder diffraction above 10 GPa. Physica B*, **180–181**, 907–910.

Binns, J., Kamenev, K. V., McIntyre, G. J., Moggach, S. A. & Parsons, S. (2016). *Use of a miniature diamond-anvil cell in high-pressure single-crystal neutron Laue diffraction. IUCrJ*, **3**, 168–179.

Blaschko, O. & Ernst, G. (1974). *Autofrettaged high pressure chamber for use in inelastic neutron scattering. Rev. Sci. Instrum.* **45**, 526–528.

Bloch, D., Paureau, J., Voiron, J. & Parisot, G. (1976). *Neutron scattering at high pressure. Rev. Sci. Instrum.* **47**, 296–298.

Boehler, R. & De Hantsetters, K. (2004). *New anvil designs in diamond-cells. High Press. Res*. **24**, 391–396.

Boehler, R., Nicol, M., Zha, C. S. & Jonson, M. L. (1986). *Resistance heating of Fe and W in diamond anvil cells. Physica B*, **139–140**, 916–918.

Boehler, R., Ross, M. P. & Boercker, D. B. (2001). *High-pressure melting curves of argon, krypton, and xenon: deviation from corresponding states theory. Phys. Rev. Lett*. **86**, 5731–5734.

Boldyreva, E. V. (2010). *High-pressure studies of pharmaceuticals and biomimetics. Fundamentals and applications. A general introduction.* In *High-Pressure Crystallography. From Fundamental Phenomena to Technological Applications*, edited by E. Boldyreva & P. Dera, pp. 533–543. Dordrecht: Springer.

Boldyreva, E. V. & Dera, P. (2010). Editors. *High-Pressure Crystallography: From Fundamental Phenomena to Technological Applications*. Dordrecht: Springer.

Boldyreva, E. V., Dmitriev, V. P. & Hancock, B. C. (2006). *Effect of pressure up to 5.5 GPa on dry powder samples of chlorpropamide form-A. Int. J. Pharm.* **327**, 51–57.

Boldyreva, E. V., Shakhtshneider, T. P., Ahsbahs, H., Sowa, H. & Uchtmann, H. (2002). *Effect of high pressure on the polymorphs of paracetamol. J. Therm. Anal. Cal.* **68**, 437–452.

Bridgman, P. W. (1914). *The coagulation of albumen by pressure. J. Biol. Chem.* **19**, 511–512.

Bridgman, P. W. (1935). *Effects of high shearing stress combined with high hydrostatic pressure. Phys. Rev*. **48**, 825–847.

Bridgman, P. W. (1941). *Explorations toward the limit of utilizable pressures. J. Appl. Phys.* **12**, 461–469.

Bridgman, P. W. (1952). *The resistance of 72 elements, alloys and compounds to 100,000 kg/cm^2. Proc. Am. Acad. Arts Sci.* **81**, 167–251.

Bridgman, P. W. (1964). *Collected Experimental Papers*, Volumes I–VII. Cambridge, MA: Harvard University Press.

Brister, K. E., Vohra, Y. K. & Ruoff, A. L. (1986). *Microcollimated energy-dispersive X-ray diffraction apparatus for studies at megabar pressures with a synchrotron source. Rev. Sci. Instrum.* **57**, 2560–2563.

Budzianowski, A. & Katrusiak, A. (2004). *High-pressure crystallographic experiments with a CCD detector.* In *High-Pressure Crystallography*, edited by A. Katrusiak & P. F. McMillan, pp. 101–112. Dordrecht: Kluwer.

Budzianowski, A. & Katrusiak, A. (2006*a*). *Pressure tuning between NH···N hydrogen-bonded ice analogue and NH···Br polar dabcoHBr complexes. J. Phys. Chem. B*, **110**, 9755–9758.

Budzianowski, A. & Katrusiak, A. (2006*b*). *Pressure-frozen benzene I revisited. Acta Cryst.* B**62**, 94–101.

Bujak, M., Budzianowski, A. & Katrusiak, A. (2004). *High-pressure in-situ crystallization, structure and phase transitions in 1,2-dichloroethane. Z. Kristallogr.* **219**, 573–579.

Bujak, M., Podsiadło, M. & Katrusiak, A. (2008). *Energetics of conformational conversion between 1,1,2-trichloroethane polymorphs. Chem. Commun.* pp. 4439–4441.

Buras, B., Olsen, J. S. & Gerward, L. (1977). *White beam, X-ray, energy-dispersive diffractometry using synchrotron radiation. Nucl. Instrum. Methods*, **152**, 293–296.

Buras, B., Olsen, J. S., Gerward, L., Will, G. & Hinze, E. (1977). *X-ray energy-dispersive diffractometry using synchrotron radiation. J. Appl. Cryst.* **10**, 431–438.

Bureau, H., Burchard, M., Kubsky, S., Henry, S., Gonde, C., Zaitsev, A. & Meijer, J. (2006). *Intelligent anvils applied to experimental investigations: state of the art. High Press. Res*. **26**, 251–265.

Busing, W. R. & Levy, H. A. (1967). *Angle calculations for 3- and 4-circle X-ray and neutron diffractometers. Acta Cryst.* **22**, 457–464.

Chervin, J. C., Canny, B., Besson, J. M. & Pruzan, Ph. (1995). *A diamond anvil cell for IR microspectroscopy. Rev. Sci. Instrum.* **66**, 2595–2598.

Chervin, J. C., Canny, B. & Mancinelli, M. (2001). *Ruby-spheres as pressure gauge for optically transparent high pressure cells. High Press. Res*. **21**, 305–314.

Cohen, W. M. (1933). *X-ray investigations at high pressures. Phys. Rev*. **44**, 326–327.

Couzinet, B., Dahan, N., Hamel, G. & Chervin, J.-C. (2003). *Optically monitored high-pressure gas loading apparatus for diamond anvil cells. High Press. Res.* **23**, 409–415.

Crichton, W. A. & Mezouar, M. (2004). *Methods and application of the Paris–Edinburgh press to X-ray diffraction structure solution with large-volume samples at high pressures and temperatures.* In *Advances in High-Pressure Technology for Geophysical Applications*, edited by J. Chen, Y. Wang, T. S. Duffy, G. Shen & L. F. Dobrzhinetskaya, pp. 353–369. Amsterdam: Elsevier.

Dalladay-Simpson, P., Howie, R. T. & Gregoryanz, E. (2016). *Evidence for a new phase of dense hydrogen above 325 gigapascals. Nature*, **529**, 63–67.

Datchi, F., LeToullec, R. & Loubeyre, P. (1997). *Improved calibration of the SrB_4O_7:Sm^{2+} optical pressure gauge: advantages at very high pressures and high temperatures. J. Appl. Phys.* **81**, 3333–3339.

Denner, W., Schulz, H. & d'Amour, H. (1978). *A new measuring procedure for data collection with a high-pressure cell on an X-ray four-circle diffractometer. J. Appl. Cryst.* **11**, 260–264.

Dera, P. & Katrusiak, A. (1999). *Diffractometric crystal centering. J. Appl. Cryst.* **32**, 510–515.

Dera, P., Zhuravlev, K., Prakapenka, V., Rivers, M. L., Finkelstein, G. F., Grubor-Urosevic, O., Tschauner, O., Clark, S. M. & Downs, R. T. (2013). *High pressure single-crystal micro X-ray diffraction analysis with GSE_ADA/RSV software. High Press. Res*. **33**, 466–484.

Dewaele, A. & Loubeyre, P. (2007). *Pressurizing conditions in helium-pressure-transmitting medium. High. Press. Res.* **27**, 419–429.

Dewaele, A., Loubeyre, P., Florent Occelli, F., Marie O. & Mezouar, M. (2018). *Toroidal diamond anvil cell for detailed measurements under extreme static pressures. Nat. Commun.* **9**, 2913.

Dinga, Y., Xu, J., Prewitt, Ch. T., Hemley, R. J., Mao, H., Cowan, J. A., Zhang, J., Qian, J., Vogel, S. C., Lokshin, K. & Zhao, Y. (2005). *Variable pressure–temperature neutron diffraction of wüstite, $Fe_{1-x}O$: absence of long-range magnetic order to 20 GPa. Appl. Phys. Lett.* **86**, 052505.

Dorfman, S. M., Jiang, F., Mao, Z., Kubo, A., Meng, Y., Prakapenka, V. B. & Duffy, T. S. (2010). *Phase transitions and equations of state of alkaline earth fluorides CaF_2, SrF_2, and BaF_2 to Mbar pressures. Phys. Rev. B*, **81**, 174121.

Dorfman, S. M., Prakapenka, V. B., Meng, Y. & Duffy, T. S. (2012). *Intercomparison of pressure standards (Au, Pt, Mo, MgO, NaCl and Ne) to 2.5 Mbar. J. Geophys. Res.* **117**, B08210.

Dorogokupets, P. I. & Dewaele, A. (2007). *Equations of state of MgO, Au, Pt, NaCl-B1, and NaCl-B2: internally consistent high-temperature pressure scales. High Press. Res*. **27**, 431–446.

Dubrovinskaia, N. & Dubrovinsky, L. S. (2003). *Whole-cell heater for the diamond anvil cell. Rev. Sci. Instrum.* **74**, 3433–3437.

Dubrovinskaia, N., Dubrovinsky, L., Solopova, N. A., Abakumov, A., Turner, S., Hanfland, M., Bykova, E., Bykov, M., Prescher, C., Prakapenka, V. B., Petitgirard, S., Chuvashova, I., Gasharova, B., Mathis, Y.-L., Ershov, P., Snigireva, I. & Snigirev, A. (2016). *Terapascal static pressure generation with ultrahigh yield strength nanodiamond. Sci. Adv*. **2**, e1600341.

Dubrovinsky, L., Dubrovinskaia, N., Prakapenka, V. B. & Abakumov, A. M. (2012). *Implementation of micro-ball nanodiamond anvils for high-pressure studies above 6 Mbar. Nat. Commun.* **3**, 1163.

Dubrovinsky, L. S., Saxena, S. K. & Lazor, P. (1998). *High-pressure and high-temperature in situ X-ray diffraction study of iron and corundum to 68 GPa using an internally heated diamond anvil cell. Phys. Chem. Miner.* **25**, 434–441.

Dziubek, K. & Katrusiak, A. (2002). *Structural refinements on restricted intensity data collected in high-pressure diffraction experiments. Defect Diffus. Forum*, **208–209**, 319–322.

Dziubek, K. F. & Katrusiak, A. (2004). *Compression of intermolecular interactions in CS_2 crystal. J. Phys. Chem. B*, **108**, 19089–19092.

Dziubek, K. F. & Katrusiak, A. (2014). *Complementing diffraction data with volumetric measurements. Z. Kristallogr.* **229**, 129–134.

Dziubek, K., Podsiadło, M. & Katrusiak, A. (2007). *Nearly isostructural polymorphs of ethynylbenzene: resolution of $\equiv CH\cdots\pi$(arene) and cooperative $\equiv CH\cdots\pi(C\equiv C)$ interactions by pressure freezing. J. Am. Chem. Soc.* **129**, 12620–12621.

Eggert, J. H., Xu, L. W., Che, R. Z., Chen, L. C. & Wang, J. F. (1992). *High pressure refractive-index measurements of 4/1 methanol–ethanol. J. Appl. Phys.* **72**, 2453–2461.

Eremets, M. (1996). *High Pressure Experimental Methods*. New York: Oxford University Press.

Fabbiani, F. P. A. (2010). *New frontiers in physical form discovery: high-pressure recrystallization of pharmaceutical and other molecular compounds.* In *High-Pressure Crystallography. From Fundamental Phenomena to Technological Applications*, edited by E. Boldyreva & P. Dera, pp. 545–558. Dordrecht: Springer.

Fabbiani, F. P. A., Allan, D. R., David, W. I. F., Moggach, S. A., Parsons, S. & Pulham, C. R. (2004). *High-pressure recrystallization – a route to new polymorphs and solvates. CrystEngComm*, **6**, 504–511.

Fabbiani, F. P. A., Allan, D. R., Parsons, S. & Pulham, C. R. (2005). *An exploration of the polymorphism of piracetam using high pressure. CrystEngComm*, **7**, 179–186.

Fabbiani, F. P. A., Dittrich, B., Florence, A. J., Gelbrich, T., Hursthouse, M. B., Kuhs, W. F., Shankland, N. & Sowa, H. (2009). *Crystal structures with a challenge: high-pressure crystallisation of ciprofloxacin sodium salts and their recovery to ambient pressure. CrystEngComm*, **11**, 1396–1406.

Fabbiani, F. P. A. & Pulham, C. R. (2006). *High-pressure studies of pharmaceutical compounds and energetic materials. Chem. Soc. Rev.* **35**, 932–942.

Fei, Y. & Wang, Y. (2000). *High-pressure and high-temperature powder diffraction. Rev. Mineral. Geochem.* **41**, 521–557.

Filinchuk, Y. (2010). *Light metal hydrates under non-ambient conditions: probing chemistry by diffraction?* In *High-Pressure Crystallography. From Fundamental Phenomena to Technological Applications*, edited by E. Boldyreva & P. Dera, pp. 281–291. Dordrecht: Springer.

Finger, L. W. & King, H. E. (1978). *A revised method of operation of the single-crystal diamond cell and refinement of the structure of NaCl at 32 kbar. Am. Mineral*. **63**, 337–342.

Fiquet, G. & Andrault, D. (1999). *Powder X-ray diffraction under extreme conditions of pressure and temperature. J. Synchrotron Rad.* **6**, 81–86.

Forman, R. A., Piermarini, G. J., Barnett, J. D. & Block, S. (1972). *Pressure measurement made by the utilization of ruby sharp-line luminescence. Science*, **176**, 284–285.

Fourme, R. (1968). *Appareillage pour études radiocristallographiques sous pression et à température variable. J. Appl. Cryst.* **1**, 23–30.

Fourme, R. E., Girard, R., Kahn, I., Ascone, M., Mezouar, T., Lin, J. E. & Johnson (2004). *State of the art and prospects of macromolecular X-ray crystallography at high hydrostatic pressure.* In *High-Pressure Crystallography*, edited by A. Katrusiak & P. F. McMillan, pp. 527–542. Dordrecht: Kluwer.

Gajda, R. & Katrusiak, A. (2009). *Electrostatic matching versus close-packing molecular arrangement in compressed dimethyl sulfoxide (DMSO) polymorphs. J. Phys. Chem. B*, **113**, 2436–2442.

Gao, R. & Li, H. (2012). *Pressure measurement using the R fluorescence peaks and 417 cm^{-1} Raman peak of an anvil in a sapphire-anvil cell. High Press. Res*. **32**, 176–185.

Giriat, G., Wang, W., Attfield, J. P., Huxley, A. D. & Kamenev, K. V. (2010). *Turnbuckle diamond anvil cell for high-pressure measurements in a superconducting quantum interference device magnetometer. Rev. Sci. Instrum.* **81**, 073905.

Goncharenko, I. N. (2004). *Magnetic properties of crystals and their studies at high pressure conditions.* In *High-Pressure Crystallography*, edited by A. Katrusiak & P. F. McMillan, pp. 321–340. Dordrecht: Kluwer.

Goncharenko, I. N. (2006). *Magnetic and crystal structures probed by neutrons in 40 GPa pressure range. Acta Cryst.* A**62**, s95.

Goncharenko, I. & Loubeyre, P. (2005). *Neutron and X-ray diffraction study of the broken symmetry phase transition in solid deuterium. Nature*, **435**, 1206–1209.

Goncharenko, I. N., Mignot, J.-M., Andre, G., Lavrova, O. A., Mirebeau, I. & Somenkov, V. A. (1995). *Neutron diffraction studies of magnetic structure and phase transitions at very high pressures. High Press. Res*. **14**, 41–53.

Goncharenko, I. N. & Mirebeau, I. (1998). *Magnetic neutron diffraction under very high pressures. Study of europium monochalcogenides. Rev. High Press. Sci. Technol*. **7**, 475–480.

Graf, D. E., Stillwell, R. L., Purcell, K. M. & Tozer, S. W. (2011). *Nonmetallic gasket and miniature plastic turnbuckle diamond anvil cell for pulsed magnetic field studies at cryogenic temperatures. High Press. Res*. **31**, 533–543.

Grocholski, B. & Jeanloz, R. (2005). *High-pressure and -temperature viscosity measurements of methanol and 4:1 methanol:ethanol solution. J. Chem. Phys.* **123**, 204503.

Gruner, S. M. (2004). *Soft materials and biomaterials under pressure.* In *High-Pressure Crystallography*, edited by A. Katrusiak & P. F. McMillan, pp. 543–556. Dordrecht: Kluwer.

Grzechnik, A., Meven, M. & Friese, K. (2018). *Single-crystal neutron diffraction in diamond anvil cells with hot neutrons. J. Appl. Cryst.* **51**, 351–356.

Guńka, P. A., Dziubek, K. F., Gładysiak, A., Dranka, M., Piechota, J., Hanfland, M., Katrusiak, A. & Zachara, J. (2015). *Compressed arsenolite As_4O_6 and its helium clathrate $As_4O_{62}He$. Cryst. Growth Des.* **15**, 3740–3745.

Hall, H. T. (1980). *High pressure techniques*. In *Chemical Experimentation under Extreme Conditions, Techniques of Chemistry*, Vol. IX, ch. II, edited by A. Weissberger & B. Rossiter, pp. 9–72. Chichester: John Wiley & Sons.

Hamilton, W. C. (1974). *International Tables for X-ray Crystallography*, Vol. IV, pp. 273–284. Birmingham: Kynoch Press.

Hammersley, A. P., Svensson, S. O., Hanfland, M., Fitch, A. N. & Hauessermann, D. (1996). *Two-dimensional detector systems. From real detector to idealised image of two-theta scan. High Press. Res.* **14**, 235–248.

Hanfland, M., Proctor, J. E., Guillaume, Ch. L., Degtyareva, O. & Gregoryanz, E. (2011). *High-pressure synthesis, amorphization, and decomposition of silane. Phys. Rev. Lett.* **106**, 095503.

Hazen, R. M. (1999). *The Diamond Makers*. Cambridge Unversity Press.

Hazen, R. M. & Finger, L. (1982). *Comparative Crystal Chemistry*. New York: John Wiley & Sons.

Holzapfel, W. B. (1991). *Equations of state for strong compression. High. Press. Res.* **7**, 290–292.

Holzapfel, W. B. (1994). *Approximate equations of state for solids from limited data sets. J. Phys. Chem. Solids*, **55**, 711–719.
Holzapfel, W. B. (1997). *Pressure determination.* In *High-Pressure Techniques in Chemistry and Physics. A Practical Approach*, edited by W. B. Holzapfel & N. S. Isaacs, pp. 47–55. Oxford University Press.
Huppertz, H. (2004). *Multianvil high-pressure/high-temperature synthesis in solid state chemistry. Z. Kristallogr*. **219**, 330–338.
Ivanov, A. N., Nikolaev, N. A., Pashkin, N. V., Savenko, B. N., Smirnov, L. S. & Taran, Y. V. (1995). *Ceramic high pressure cell with profiled anvils for neutron diffraction investigations (up to 7 GPa). High-Press. Res.* **14**, 203–208.
Jamieson, J. C., Lawson, A. W. & Nachtrieb, N. D. (1959). *New device for obtaining X-ray diffraction patterns from substances exposed to high pressure. Rev. Sci. Instrum.* **30**, 1016–1019.
Jenei, Zs., O'Bannon, E. F., Weir, S. T., Cynn, H., Lipp, M. J. & Evans, W. J. (2018). *Single crystal toroidal diamond anvils for high pressure experiments beyond 5 megabar. Nat. Commun.* **9**, 3563.
Jephcoat, A. P., Finger, L. W. & Cox, D. E. (1992). *High pressure, high resolution synchrotron X-ray powder diffraction with a position-sensitive detector. High Press. Res*. **8**, 667–676.
Katrusiak, A. (1999). *A hinge goniometer head. J. Appl. Cryst.* **32**, 576–578.
Katrusiak, A. (2001). *Absorption correction for crystal-environment attachments from direction cosines. Z. Kristallogr.* **216**, 646–647.
Katrusiak, A. (2004*a*). *Shadowing and absorption corrections of single-crystal high-pressure data. Z. Kristallogr.* **219**, 461–467.
Katrusiak, A. (2004*b*). *Shadowing and absorption corrections of high-pressure powder diffraction data: toward accurate electron-density determinations. Acta Cryst.* A**60**, 409–417.
Katrusiak, A. (2008). *High-pressure crystallography. Acta Cryst.* A**64**, 135–148.
Katrusiak, A. & Dauter, Z. (1996). *Compressibility of lysozyme protein crystals by X-ray diffraction. Acta Cryst.* D**52**, 607–608.
Katrusiak, A. & McMillan, P. F. (2004). Editors. *High Pressure Crystallography*. Dordrecht: Kluwer Academic Press.
Keller, K., Schlothauer, T., Schwarz, M., Heide, G. & Kroke, E. (2012). *Shock wave synthesis of aluminium nitride with rocksalt structure. High Press. Res.* **32**, 23–29.
Kenichi, T., Sahu, P. Ch., Yoshiyasu, K. & Yasuo, T. (2001). *Versatile gas-loading system for diamond-anvil cells. Rev. Sci. Instrum.* **72**, 3873–3876.
Khvostantsev, L. G. (1984). *A verkh-niz (up-down) device of toroid type for generation of high pressure. High Temp. High Press.* **16**, 165–169.
Khvostantsev, L. G., Slesarev, V. N. & Brazhkin, V. V. (2004). *Toroid type high-pressure device: history and prospects. High Press. Res*. **24**, 371–383.
Khvostantsev, L. G., Vereshchagin, L. F. & Novikov, A. P. (1977). *Device of toroid type for high pressure generation. High Temp. High Press.* **9**, 637–639.
King, H. E. & Finger, L. W. (1979). *Diffracted beam crystal centering and its application to high-pressure crystallography. J. Appl. Cryst.* **12**, 374–378.
Klotz, S. (2012). *Techniques in High Pressure Neutron Scattering*. Boca Raton: CRC Press.
Klotz, S., Chervin, J.-C., Munsch, P. & Le Marchand, G. (2009). *Hydrostatic limits of 11 pressure transmitting media. J. Phys. D Appl. Phys.* **42**, 075413.
Konno, M., Okamoto, T. & Shirotani, I. (1989). *Structure changes and proton transfer between O···O in bis(dimethylglyoximato)platinum(II) at low temperature (150 K) and at high pressures (2.39 and 3.14 GPa). Acta Cryst.* B**45**, 142–147.
Koster van Groos, A. F., Guggenheim, S. & Cornell, C. (2003). *Environmental chamber for powder X-ray diffractometers for use at elevated pressures and low temperatures. Rev. Sci. Instrum.* **74**, 273–275.
Kuhs, W. F., Bauer, F. C., Hausmann, R., Ahsbahs, H., Dorwarth, R. & Hölzer, K. (1996). *Single crystal diffraction with X-rays and neutrons: high quality at high pressure? High Press. Res.* **14**, 341–352.
Kundrot, C. E. & Richards, F. M. (1986). *Collection and processing of X-ray diffraction data from protein crystals at high pressure. J. Appl. Cryst.* **19**, 208–213.
Kunz, M. (2001). *High pressure phase transformations.* In *Phase Transformations in Materials*, edited by G. Kostorz, pp. 655–695. Weinheim: Wiley-VCH Verlag.
Lacam, A. (1990). *The SrB_4O_7:Sm^{2+} optical sensor and the pressure homogenization through thermal cycles in diamond anvil cells. High Press. Res*. **5**, 782–784.
Lacam, A. & Chateau, C. (1989). *High-pressure measurements at moderate temperatures in a diamond anvil cell with a new optical sensor: SrB_4O_7:Sm^{2+}. J. Appl. Phys.* **66**, 366–372.
Le Godec, Y., Dove, M. T., Francis, D. J., Kohn, S. C., Marshall, W. G., Pawley, A. R., Price, G. D., Redfern, S. A. T., Rhodes, N., Ross, N. L., Schofield, P. F., Schooneveld, E., Syfosse, G., Tucker, M. G. & Welch, M. D. (2001). *Neutron diffraction at simultaneous high temperatures and pressures, with measurement of temperature by neutron radiography. Min. Mag*. **65**, 749–760.
Le Godec, Y., Dove, M. T., Redfern, S. A. T., Marshall, W. G., Tucker, M. G., Syfosse, G. & Besson, J. M. (2002). *A new high P–T cell for neutron diffraction up to 7 GPa and 2000 K with measurement of temperature by neutron radiography. High Press. Res.* **65**, 737–748.
LeSar, R., Ekberg, S. A., Jones, L. H., Mills, R. L., Schwalbe, L. A. & Schiferl, D. (1979). *Raman spectroscopy of solid nitrogen up to 374 kbar. Solid State Commun.* **32**, 131–134.
Letoullec, R., Pinceaux, J. P. & Loubeyre, P. (1988). *The membrane diamond anvil cell: a new device for generating continuous pressure and temperature variations. High Press. Res*. **1**, 77–90.
Liebermann, R. C. (2011). *Multi-anvil, high pressure apparatus: a half-century of development and progress. High Press. Res*. **31**, 493–532.
Liu, Z. X., Cui, Q. L. & Zou, G. T. (1990). *Disappearance of the ruby R-line fluorescence under quasihydrostatic pressure and valid pressure range of ruby gauge. Phys. Lett. A*, **143**, 79–82.
McMahon, M. I. (2004). *High pressure diffraction from good powders, poor powders and poor single crystals.* In *High-Pressure Crystallography*, edited by A. Katrusiak & P. F. McMillan, pp. 1–20. Dordrecht: Kluwer.
McMahon, M. I. (2005). *Structures from powders and poor-quality single crystals at high pressure. J. Synchrotron Rad.* **12**, 549–553.
McMahon, M. I. (2012). *High-pressure crystallography. Top. Curr. Chem.* **315**, 69–109.
McWhan, D. B., Bloch, D. & Parisot, G. (1974). *Apparatus for neutron diffraction at high pressure. Rev. Sci. Instrum.* **45**, 643–646.
Malinowski, M. (1987). *A diamond-anvil high-pressure cell for X-ray diffraction on a single crystal. J. Appl. Cryst.* **20**, 379–382.
Mao, H. K. & Bell, P. M. (1979). *Observations of hydrogen at room temperature (25°C) and high pressure (to 500 kilobars). Science*, **203**, 1004–1006.
Mao, H. K., Bell, P. & Hadidiacos, C. (1987). *Experimental phase relations in iron to 360 kbar, 1400°C, determined in an internally heated diamond-anvil apparatus.* In *High-Pressure Research in Mineral Physics*, edited by M. H. Manghnani & Y. Syono, pp. 135–138. San Francisco: Terrapub/AGU.
Mao, H.-K., Bell, B. M., Shaner, J. W. & Steinberg, D. J. (1978). *Specific volume measurements of Cu, Mo, Pd, and Ag and calibration of the ruby R_1 fluorescence pressure gauge from 0.06 to 1 mbar. J. Appl. Phys.* **49**, 3276–3283.
Mao, H.-K., Chen, X.-J., Ding, Y., Li, B. & Wang, L. (2018). *Solids, liquids and gases under high pressure. Rev. Mod. Phys.* **90**, 015007.
Mao, H. K., Shu, J., Shen, G. Y., Hemley, R. J., Li, B. S. & Singh, A. K. (1998). *Elasticity and rheology of iron above 220 GPa and the nature of the Earth's inner core. Nature*, **396**, 741–743.
Mao, H.-K., Xu, J. & Bell, P. M. (1986). *Calibration of the ruby pressure gauge to 800 kbar under quasi-hydrostatic conditions. J. Geophys. Res.* **91**, 4673–4676.
Merlini, M., Crichton, W. A., Hanfland, M., Gemmi, M., Müller, H., Kupenko, I. & Dubrovinsky, L. (2012). *Structures of dolomite at ultrahigh pressure and their influence on the deep carbon cycle. Proc. Natl Acad. Sci. USA*, **109**, 13509–13514.
Merrill, L. & Bassett, W. A. (1974). *Miniature diamond anvil pressure cell for single crystal X-ray diffraction studies. Rev. Sci. Instrum.* **45**, 290–294.
Mezouar, M., Crichton, W. A., Bauchau, S., Thurel, F., Witsch, H., Torrecillas, F., Blattmann, G., Marion, P., Dabin, Y., Chavanne, J., Hignette, O., Morawe, C. & Borel, C. (2005). *Development of a new state-of-the-art beamline optimized for monochromatic single-crystal and powder X-ray diffraction under extreme conditions at the ESRF. J. Synchrotron Rad.* **12**, 659–664.
Miletich, R., Allan, D. R. & Kuhs, W. F. (2000). *High-pressure single crystal techniques. Rev. Mineral. Geochem.* **41**, 445–519.

Miletich, R., Cinato, D. & Johänntgen, S. (2009). *An internally heated composite gasket for diamond-anvil cells using the pressure chamber wall as the heating element. High Press. Res.* **29**, 290–305.

Mills, R. L., Liebenberg, D. H., Bronson, J. C. & Schmidt, L. C. (1980). *Procedure for loading diamond cells with high-pressure gas. Rev. Sci. Instrum.* **51**, 891–895.

Ming, L. C. & Bassett, W. A. (1974). *Laser heating in the diamond anvil press up to 2000˚C sustained and 3000˚C pulsed at pressures up to 260 kilobars. Rev. Sci. Instrum.* **45**, 1115–1118.

Moore, M. J., Sorensen, D. B. & DeVries, R. C. (1970). *A simple heating device for diamond anvil high pressure cells. Rev. Sci. Instrum.* **41**, 1665–1666.

Murata, K., Yokogawa, K., Yoshino, H., Klotz, S., Munsch, P., Irizawa, A., Nishiyama, M., Iizuka, K., Nanba, T., Okada, T., Shiraga, Y. & Aoyama, S. (2008). *Pressure transmitting medium Daphne 7474 solidifying at 3.7 GPa at room temperature. Rev. Sci. Instrum.* **79**, 085101.

Nelmes, R. J. & McMahon, M. I. (1994). *High-pressure powder diffraction on synchrotron sources. J. Synchrotron Rad.* **1**, 69–73.

Oehzelt, M., Weinmeier, K., Heimel, G., Pusching, P., Resel, R., Ambrosch-Draxl, C., Porsch, F. & Nakayama, A. (2002). *Structural properties of anthracene under high pressure. High Press. Res*. **22**, 343–347.

Okuchi, T., Sasaki, S., Ohno, Y., Abe, J., Arima, H., Osakabe, T., Hattori, T., Sano-Furukawa, A., Komatsu, K., Kagi, H., Utsumi, W., Harjo, S., Ito, T. & Aizawa, K. (2012). *Neutron powder diffraction of small-volume samples at high pressure using compact opposed-anvil cells and focused beam. J. Phys. Conf. Ser.* **377**, 012013.

Olejniczak, A. & Katrusiak, A. (2010). *Pressure induced transformations of 1,4-diazabicyclo[2.2.2]octane (dabco) hydroiodide: diprotonation of dabco, its N-methylation and co-crystallization with methanol. CrystEngComm*, **12**, 2528–2532.

Olejniczak, A. & Katrusiak, A. (2011). *Pressure-induced hydration of 1,4-diazabicyclo[2.2.2]octane hydroiodide (dabcoHI). Cryst. Growth Des.* **11**, 2250–2256.

Onodera, A. (1987). *Octahedral-anvil high-pressure press. High Temp. High Press.* **19**, 579–609.

Onodera, A. & Amita, F. (1991). *Apparatus and operation.* In *Organic Synthesis at High Pressures*, edited by K. Matsumoto & R. M. Acheson. Chichester: John Wiley & Sons.

Palasyuk, T., Figiel, H. & Tkacz, M. (2004). *High pressure studies of $GdMn_2$ and its hydrides. J. Alloys Compd.* **375**, 62–66.

Palasyuk, T. & Tkacz, M. (2007). *Pressure-induced structural phase transition in rare earth trihydrides. Part II. SmH_3 and compressibility systematics. Solid State Commun*. **141**, 5, 302–305.

Paliwoda, D. K., Dziubek, K. F. & Katrusiak, A. (2012). *Imidazole hidden polar phase. Cryst. Growth Des.* **12**, 4302–4305.

Patyk, E., Skumiel, J., Podsiadło, M. & Katrusiak, A. (2012). *High-pressure (+)-sucrose polymorph. Angew. Chem. Int. Ed.* **51**, 2146–2150.

Piermarini, G. J. (2001). *High pressure X-ray crystallography with the diamond cell at NIST/NBS. J. Res. Natl Inst. Stand. Technol.* **106**, 889–920.

Piermarini, G. J., Block, S. & Barnett, J. D. (1973). *Hydrostatic limits in liquids and solids to 100 kbar. J. Appl. Phys.* **44**, 5377–5382.

Piermarini, G. J., Block, S., Barnett, J. D. & Forman, R. A. (1975). *Calibration of the pressure dependence of the R_1 ruby fluorescence line to 195 kbar. J. Appl. Phys.* **46**, 2774–2780.

Piermarini, G. J., Mighell, A. D., Weir, C. E. & Block, S. (1969). *Crystal structure of benzene II at 25 kilobars. Science*, **165**, 1250–1255.

Podsiadło, M. & Katrusiak, A. (2008). *Isostructural relations in dihalomethanes and disproportionation of bromoiodomethane. CrystEngComm*, **10**, 1436–1442.

Półrolniczak, A., Sobczak, S. & Katrusiak, A. (2018). *Solid-state associative reactions and the coordination compression mechanism. Inorg. Chem.* **57**, 8942–8950.

Ragan, D. D., Clarke, D. R. & Schiferl, D. (1996). *Silicone fluid as a high-pressure medium in diamond anvil cells. Rev. Sci. Instrum.* **67**, 494–496.

Redfern, S. A. T. (2002). *Neutron powder diffraction of minerals at high pressures and temperatures: some recent technical developments and scientific applications. Eur. J. Mineral*. **14**, 251–261.

Rivers, M., Prakapenka, V. B., Kubo, A., Pullins, C., Holl, Ch. M. & Jacobsen, S. D. (2008). *The COMPRES/GSECARS gas-loading system for diamond anvil cells at the Advanced Photon Source. High Press. Res.* **28**, 273–292.

Royer, C. A. (2002). *Revisiting volume changes in pressure-induced protein unfolding. Biochim. Biophys. Acta*, **1595**, 201–209.

Runowski, M., Marciniak, J., Grzyb. T., Przybylska, D., Shyichuk, A., Barszcz, B., Katrusiak, A. & Lis, S. (2017). *Lifetime nanomanometry – high-pressure luminescence of up-converting lathanide nanocrystals – $SrF_2:Yb^{3+},Er^{3+}$. Nanoscale*, **9**, 16030–16037.

Sakai, T., Yagi, T., Irifune, T., Kadobayashi, H., Hirao, N., Kunimoto, T., Ohfuji, H., Kawagushi-Imada, S., Ohishi, Y., Tateno, Sh. & Hirose, K. (2018). *High pressure generation using double-stage diamond anvil technique: problems and equations of state of rhenium. High Press. Res.* **38**, 107–119.

Sakai, T., Yagi, T., Ohfuji, H., Irifune, T., Ohishi, Y., Hirao, N., Suzuki, Y., Kuroda, Y., Asakawa, T. & Kanemura, T. (2015). *High-pressure generation using double stage micro-paired diamond anvils shaped by focused ion beam. Rev. Sci. Instrum.* **86**, 033905.

Samara, G. A., Hansen, L. V., Assink, R. A., Morosin, B., Schirber, J. E. & Loy, D. (1993). *Effects of pressure and ambient species on the orientational ordering in solid C_{60}. Phys. Rev. B*, **47**, 4756–4764.

Senyshyn, A., Engel, J. M., Oswald, I. D. H., Vasylechko, L. & Berkowski, M. (2009). *Powder diffraction studies of pressure-induced instabilities in orthorhombic $LnGaO_3$. Z. Kristallogr. Suppl.* **30**, 341–346.

Shen, G., Mao, H. K. & Hemley, R. J. (1996). *Laser-heated diamond anvil cell technique: double-sided heating with multimode Nd:YAG laser. Proceedings of the 3rd NIRIM International Symposium on Advanced Materials, ISAM'96*, 4–8 March 1996, Tsukuba, Japan, pp. 149–152. Tsukuba: National Institute for Research in Inorganic Materials.

Shen, Y., Kumar, R. S., Pravica, M. & Nicol, M. F. (2004). *Characteristics of silicone fluid as a pressure transmitting medium in diamond anvil cells. Rev. Sci. Instrum.* **75**, 4450–4454.

Sikora, M. & Katrusiak, A. (2013). *Pressure-controlled neutral–ionic transition and disordering of NH···N hydrogen bonds in pyrazole. J. Phys. Chem. C*, **117**, 10661–10668.

Singh, A. K. (1993). *The lattice strains in a specimen (cubic system) compressed nonhydrostatically in an opposed anvil device. J. Appl. Phys.* **73**, 4278–4286.

Singh, A. K. & Balasingh, C. (1994). *The lattice strains in a specimen (hexagonal system) compressed nonhydrostatically in an opposed anvil high pressure setup. J. Appl. Phys.* **75**, 4956–4962.

Singh, A. K., Balasingh, C., Mao, H. K., Hemley, R. J. & Shu, J. (1998). *Analysis of lattice strains measured under nonhydrostatic pressure. J. Appl. Phys.* **83**, 7567–7575.

Smith, R. F., Eggert, J. H., Jeanloz, R., Duffy, T. S., Braun, D. G., Patterson, J. R., Rudd, R. E., Biener, J., Lazicki, A. E., Hamza, A. V., Wang, J., Braun, T., Benedict, L. X., Celliers, P. M. & Collins G. W. (2014). *Ramp compression of diamond to five terapascals. Nature*, **511**, 330–333.

So, P. T. C., Gruner, S. M. & Shyamsunder, E. (1992). *Automated pressure and temperature control apparatus for X-ray powder diffraction studies. Rev. Sci. Instrum.* **63**, 1763–1770.

Sobczak, S., Drożdż, W., Lampronti, G. I., Belenguer, A. M., Katrusiak, A. & Stefankiewicz, A. R. (2018). *Dynamic covalent chemistry under high pressure: a new route to disulfide metathesis. Chem. Eur. J.* **24**, 8769–8773.

Srinivasa, S. R., Cartz, L., Jorgensen, J. D., Worlton, T. G., Beyerlein, R. A. & Billy, M. (1977). *High-pressure neutron diffraction study of Si_2N_2O. J. Appl. Cryst.* **10**, 167–171.

Stishov, S. M. & Popova, S. V. (1961*a*). *New dense polymorphic modification of silica. Geokhimiya*, **10**, 837–839.

Stishov, S. M. & Popova, S. V. (1961*b*). *New dense polymorphic modification of silica. Geochemistry*, **10**, 923–926.

Syassen, K. (2008). *Ruby under pressure. High Press. Res.* **28**, 75–126.

Takahashi, H., Mori, N., Matsumoto, T., Kamiyama, T. & Asano, H. (1996). *Neutron powder diffraction studies at high pressure using a pulsed neutron source. High Press. Res*. **14**, 295–302.

Takahashi, E., Yamada, H. & Ito, E. (1982). *An ultrahigh-pressure furnace assembly to 100 kbar and 1500˚C with minimum temperature uncertainty. Geophys. Res. Lett.* **9**, 805–807.

Tateiwa, N. & Haga, Y. (2010). *Appropriate pressure-transmitting media for cryogenic experiment in the diamond anvil cell up to 10 GPa. J. Phys. Conf. Ser.* **215**, 012178.

Tkacz, M. (1995). *Novel high-pressure technique for loading diamond anvil cell with hydrogen. Pol. J. Chem.* **69**, 1205.

Tkacz, M. (1998). *High pressure studies of the rhodium–hydrogen system in diamond anvil cell. J. Chem. Phys.* **108**, 2084–2087.

Tomkowiak, H., Olejniczak, A. & Katrusiak, A. (2013). *Pressure-dependent formation and decomposition of thiourea hydrates. Cryst. Growth Des.* **13**, 121–125.

Van Valkenburg, A. (1962). *Visual observations of high pressure transitions. Rev. Sci. Instrum.* **33**, 1462.

Van Valkenburg, A., Mao, H.-K. & Bell, P. M. (1971*a*). *Solubility of minerals at high water pressures. Carnegie Inst. Washington Yearb.* **70**, 233–237.

Van Valkenburg, A., Mao, H.-K. & Bell, P. M. (1971*b*). *Ikaite ($CaCO_3$·6H_2O), a phase more stable than calcite and aragonite ($CaCO_3$) at high water pressure. Carnegie Inst. Washington Yearb.* **70**, 237–238.

Vereshchagin, L. F., Kabalkina, S. S. & Evdokimova, V. V. (1958). *Kamera dlya rentgenostrukturnykh issledovanii monokristallov pod vysokim davleniem. (A camera for X-ray diffraction studies of single crystals at high pressure). Prib. Tekh. Eksp.* **3**, 90–92.

Vos, W. L. & Schouten, J. A. (1991). *On the temperature correction to the ruby pressure scale. J. Appl. Phys.* **69**, 6744–6746.

Wang, J., Coppari, F., Smith, R. F., Eggert, J. H., Lazicki, A. E., Fratanduono, D. E., Rygg, J. R., Boehly, T. R., Collins, G. W. & Duffy, T. S. (2016). *X-ray diffraction of molybdenum under ramp compression to 1 TPa. Phys. Rev. B*, **94**, 104102.

Wartmann, E. (1859). *On the effect of pressure on the electric conductibility of metallic wires. Philos. Mag.* **17**, 441–442.

Wicks, J. K., Smith, R. F., Fratanduono, D. E., Coppari, F., Kraus, R. G., Newman, M. G., Rygg, J. R., Eggert, J. H. & Duffy, T. S. (2018). *Crystal structure and equation of state of Fe–Si alloys at super-Earth core conditions. Sci. Adv.* **4**, eaao5864.

Weir, C. E., Lippincott, E. R., Van Valkenburg, A. & Bunting, N. E. (1959). *Infrared studies in the 1–15-micron region to 30,000 atmospheres. J. Res. Natl Bur. Stand. USA*, **63A**, 5–62.

Whitfield, P. S., Nawaby, A. V., Blak, B. & Ross, J. (2008). *Modified design and use of a high-pressure environmental stage for laboratory X-ray powder diffractometers. J. Appl. Cryst.* **41**, 350–355.

Worlton, T. G. & Decker, D. L. (1968). *Neutron diffraction study of the magnetic structure of hematite to 41 kbar. Phys. Rev.* **171**, 596–599.

Xia, H., Duclos, S. J., Ruoff, A. L. & Vohra, Y. K. (1990). *New high-pressure phase transition in zirconium metal. Phys. Rev. Lett.* **64**, 204–207.

Xu, J., Mao, H. K., Hemley, R. J. & Hines, E. (2004). *Large volume high-pressure cell with supported moissanite anvils. Rev. Sci. Instrum.* **75**, 1034–1038.

Yagi, T., Yusa, H. & Yamakata, M. (1996). *An apparatus to load gaseous materials to the diamond-anvil cell. Rev. Sci. Instrum.* **67**, 2981–2984.

Yamaoka, H., Zekko, Y., Jarrige, I., Lin, J.-F., Hiraoka N., Ishii, H., Tsuei, K. D. & Mizuki, J. (2012). *Ruby pressure scale in a low-temperature diamond anvil cell. J. Appl. Phys.* **112**, 124503.

Yokogawa, K., Murata, K., Yoshino, H. & Aoyama, Sh. (2007). *Solidification of high-pressure medium Daphne 7373. Jpn. J. Appl. Phys.* **46**, 3636–3639.

You, Sh.-J., Chen, L.-Ch. & Jin, Ch.-Q. (2009). *Hydrostaticity of pressure media in diamond anvil cells. Chin. Phys. Lett.* **26**, 096202.

Zha, C. S. & Bassett, W. A. (2003). *Internal resistive heating in diamond anvil cell for in situ X-ray diffraction and Raman scattering. Rev. Sci. Instrum.* **74**, 1255–1262.

Zhao, Y. S., Lawson, A. C., Zhang, J. Z., Bennett, B. I. & Von Dreele, R. B. (2000). *Thermoelastic equation of state of molybdenum. Phys. Rev. B*, **62**, 8766–8776.

Zhao, Y. S., Von Dreele, R. B. & Morgan, J. G. (1999). *A high P–T cell assembly for neutron diffraction up to 10 GPa and 1500 K. High Press. Res.* **16**, 161–177.

International Tables for Crystallography (2018). Vol. H, Chapter 2.8, pp. 174–188.

2.8. Powder diffraction in external electric and magnetic fields

H. Ehrenberg, M. Hinterstein, A. Senyshyn and H. Fuess

2.8.1. Introduction

The functionality of materials depends strongly on the crystalline structure and structural changes during operation. The term 'structure' usually refers to the ideal structure, which specifies the positions of the atoms in a lattice, and thus the distances and angles between them. This idealized model is, however, far too simple to describe the full functionality of a material in a device. Many types of defects, such as point defects, dislocations or grain boundaries, are essential to the functionality and have to be taken into account. As the length scales of defects range from atomic bond lengths *via* nanometres to micrometres, different methods have to be used for comprehensive structural characterization. High-resolution transmission electron microscopy (HRTEM) is the ideal tool for studying a material at the atomic scale, as it gives direct evidence of the arrangement of atoms. In addition, information on the chemical composition can be provided through X-ray or electron spectroscopies. However, in many cases electron microscopy requires a tremendous effort in sample preparation. Furthermore, the application of electric fields in a TEM column is a serious challenge with significant limitations. While electron microscopy will provide information on small sample volumes, diffraction methods probe larger quantities of samples, but give average information. In general, diffraction methods are based on electromagnetic or particle waves. X-ray photons with energies in the keV range have wavelengths similar to interatomic distances and, therefore, X-rays from laboratory sources or synchrotrons are the most widely used. Thermal neutrons with meV energies have complementary properties suited for other applications. While electrons are usually used for microscopy techniques, the field of electron crystallography has developed in recent years. However, given the very small size of an electron beam, its short wavelength (*circa* 0.03 Å) and high absorption, most particles studied by electron crystallography can be considered as single crystals. The combination of electron crystallography and powder diffraction is a powerful tool for tiny crystalline samples, especially inclusions (Weirich *et al.*, 2006).

In the field of *in situ* materials research, multiparametric measurements as functions of three or more external parameters, *e.g.* temperature–magnetic field–pressure or temperature–magnetic field–electric field, have been reported. However, the majority of so-called *in situ* studies are carried out as a function of temperature and sometimes of external pressure. Studies of structural changes under electric fields are relatively rare. Studies of changes due to magnetic fields almost entirely lie in the domain of neutron scattering, where single-crystal experiments usually give more details on the evolution of the magnetic structure. The challenges, necessary instrumentation and some examples of *in situ* diffraction measurements are described in Chapter 16 of the book *Modern Diffraction Methods* (Mittemeijer & Welzel, 2012).

2.8.2. Experimental conditions

Several challenges have to be overcome for experiments under external fields, so the exerimental conditions have to be adapted accordingly. As all these experiments are based on time-dependent conditions, the first requirement is a detecting system that allows fast data acquisition. Considerable progress in recent years has made time resolution of the order of nanoseconds possible (Schmitt *et al.*, 2007), thus enabling stroboscopic diffraction experiments. Higher time resolutions are possible with careful synchronization of the experiment with the time structure of a synchrotron X-ray beam. The electron bunches in a synchrotron are usually separated by several tens to hundreds of nanoseconds and have a width in the range of picoseconds. Once the gating window of an experiment is smaller than the time between successive bunches, the time resolution immediately reaches the width of a bunch. Structural responses to external stimuli are related to displacements of atoms and changes in unit-cell distortion (*i.e.* lattice parameters). The displacements are fairly small and thus very high sensitivity is a prerequisite. In order to study small unit-cell distortions, very good angular resolution is mandatory. The potential angular resolution that is possible in synchrotron experiments is very often not reached for powder samples, as the half-widths of the reflections are mainly determined by the microstructure.

In monochromatic neutron diffraction, the greater divergence of a neutron beam compared to a synchrotron beam and its spectral width ($\Delta\lambda/\lambda$) usually only allow a resolution in the range $\Delta d/d \simeq 10^{-2}$ to be achieved with medium-resolution (high-intensity) diffractometers; this can be tuned down to $\Delta d/d \simeq 10^{-3}$ by tightening the beam collimation at high-resolution monochromatic instruments. Significantly better resolution of $\Delta d/d \simeq 4 \times 10^{-4}$ can be achieved by combining the neutron time-of-flight technique with long neutron flight paths (*circa* 100 m) in back-scattering geometry. Even higher $\Delta d/d$ values (potentially down to 10^{-6}) can be obtained using the spin-echo-based neutron-scattering technique called Larmor diffraction (Repper *et al.*, 2009). The advantages of neutrons over X-rays are that they penetrate more deeply through materials, their scattering form factors are nearly independent of momentum transfer, and they are sensitive to the isotopic composition of a material, enabling accurate location of light elements in the presence of heavy ones, as well as the ability to distinguish between neighbouring elements in the periodic table. Whereas both synchrotron radiation and neutron scattering may be used to elucidate crystal structures under an electric field, neutrons can also be used to study magnetic order and its modification under a magnetic field. Therefore, the examples listed here for studies under electric fields use both kinds of radiation, whereas the examples of studies involving magnetic fields mainly use neutron scattering.

The properties of the materials discussed in this chapter are intimately related to their crystal structures; hence, any change in crystal structure is immediately reflected in the properties. The examples we have chosen are dominated by ferroelectric ceramics and lithium-ion battery materials on the one hand and multiferroic materials on the other.

Most reports in the literature on *in situ* or *in operando* studies deal either with the kinetics of chemical reactions (intercalation, crystallization, catalysis) or structural changes of materials under varying external conditions (temperature, pressure *etc.*). This

chapter is devoted to structural modifications under external fields, both electric and magnetic. The application of external fields requires dedicated sample environments; these often result in an increase in absorption and contribute to the scattering. Furthermore, some components of the devices used for these studies can cause inhomogeneity in the sample or texture. Challenges can be presented by, for example, the deposition of metallic contacts on ferroelectric ceramics, the pronounced materials interaction and mass transport accompanied by changes in electrode volumes in Li-ion batteries, and the housing of magnets.

2.8.2.1. *Detectors*

For an *in situ* or *in operando* study, the choice of detector depends on the specific demands of the study with respect to angular resolution and speed of data collection. High angular resolution is needed to investigate small changes in reflection profiles, resulting from tiny modifications in the microstructure. Fast data collection is generally desirable, but is particularly important when monitoring metastable states in fast and irreversible processes. For a general overview of commonly used X-ray detector systems see Chapter 2.1. The following is a detailed overview of detector systems with high angular or time resolution for X-ray as well as neutron powder diffraction.

For synchrotron X-ray diffraction, analyser crystals between the sample and detector allow angular resolutions to be achieved at the physical limit. Detection is performed point by point, or with a set of point detectors in a multi-analyser crystal detector (MAD) (Toraya *et al.*, 1996; Hodeau *et al.*, 1998; Lee *et al.*, 2008; Peral *et al.*, 2011). The angular resolution of these detectors is only limited by the Darwin width of the analyser crystals, the energy bandwidth of the monochromator and the divergence of the incoming beam.

Gas counters or neutron scintillators are usually used for the detection of thermal neutrons. Because of the shortage of ^{3}He for research applications, alternative technologies are undergoing rapid development, including ^{10}B-based detectors such as Cascade (Köhli *et al.*, 2016), Jalousie (Stefanescu *et al.*, 2017) and Multigrid (Anastasopoulos *et al.*, 2017). However, owing to their relatively low efficiency for thermal neutrons compared with ^{3}He gas counters, neutron detectors that involve $^{10}B(n,\alpha)^7Li$ conversion are mainly used for neutron non-diffraction applications. Even though an analyser setup would in theory be possible for neutron diffraction experiments, the drastically increased time that would be required for data acquisition means that it is not feasible. Alternative concepts have evolved for the use of monochromatic neutrons in powder diffraction with high angular resolution. Multidetectors consist of 80 (SPODI, Hoelzel *et al.*, 2007) or 128 (ECHIDNA, Liss *et al.*, 2006; D2B, Suard & Hewat, 2001) detection units [1/3, 1/2 or 1 inch (where 1 inch = 2.54 cm) diameter ^{3}He tubes, either position-sensitive or not] separated by a small angle and with Soller collimators installed in front. This requires a stepwise re-positioning of the detector bank in order to collect data for complete patterns. The angular resolution of these instruments is limited by the beam divergence, the energy bandwidth of the monochromator and grain-size effects (Liss *et al.*, 2006). A reduction in the divergence of a neutron beam is associated with a considerable loss of intensity. The prerequisites of low divergence and high take-off angle of the monochromator have to be optimized in combination with a two-dimensional detector system. The height of the detectors is limited, however, by the 'umbrella' effect, which produces a broadening of the Debye–Scherrer rings. This effect may be partially compensated for during the numerical data-reduction process (Hoelzel *et al.*, 2012). On the other hand, the detection of some extended sections of the Debye–Scherrer rings provides additional information on strain and texturing.

For a compromise of high angular resolution and fast data acquisition, one-dimensional strip detectors have become popular. These detectors allow data collection in one shot and thus no re-positioning is required. However, if more than one module is used, the gaps between the modules have to be filled by measuring two different positions. Silicon microstrip sensors are used for detecting X-rays (Bergamaschi *et al.*, 2009). The MYTHEN II detector system consists of a set of modules, each consisting of 1280 50 μm-pitch strips, which are wirebonded to the photon-counting readout (Bergamaschi *et al.*, 2009). In combination with a set of vertically focusing mirrors and a sagittally focusing second monochromator crystal, high angular resolution can be achieved together with short acquisition times (for example at the materials science beamline X04SA at the Swiss Light Source) (Patterson *et al.*, 2005). In order to cope with instantaneous many-photon deposition, which is typical of X-ray free-electron lasers (XFELs), a similar system based on the charge-integration principle has been developed (GOTTHARD, Cartier *et al.*, 2014).

For detecting neutrons, microstrip detectors are used, which consist of thin-film metallic strips of anodes and cathodes, deposited on electrically conducting Fe-containing 'black' glass in a ^{3}He gas chamber (*e.g.* D20, Hansen *et al.*, 2008). Similar specifications can be realized with a multiwire setup in ^{3}He gas chambers (WOMBAT, Studer *et al.*, 2006). The multiwire detector has the advantage of being fully two-dimensionally sensitive. This allows for a larger aperture along the wires. The angular resolution can be maintained in the data-reduction process through straightening of the Debye–Scherrer rings. As Soller collimators cannot be used in front of a multiwire or multistrip detector, the effects of sample environments are eliminated by radial oscillating collimators. Multiwire and multistrip detectors are usually installed at high-throughput instruments, whereas high-resolution powder diffractometers are equipped with multidetector systems.

In materials science the investigation of real structure effects can be important. These can include texturing, where the orientation of the sample with respect to the scattering vector is crucial, or diffuse scattering in crystalline materials, and where a large dynamic intensity range has to be covered. The most efficient way of detecting these effects is to use two-dimensional detectors. In most cases the detector is mounted on a set of translational stages, so that the setup can be optimized for either high angular resolution or a wide angular range (Herklotz *et al.*, 2013).

When high-energy X-rays are used, two-dimensional detectors based on digital flat-panel technology are the best choice. They combine an amorphous Si panel with a CsI:Tl or various Gd_2O_2S:Tb scintillators. Pixel sizes of 200 × 200 μm (Perkin Elmer 1621N ES, Herklotz *et al.*, 2013) or 154 × 154 μm (Pixium 4700, Daniels & Drakopoulos, 2009) together with frame rates of up to 60 frames per second overcome several drawbacks of the high-energy detectors that were previously available.

For soft X-rays a range of two-dimensional detectors has been developed. The PILATUS detector (Kraft *et al.*, 2009) is a silicon-based hybrid pixel detector system, similar to the MYTHEN strip detector. Instead of a one-dimensional strip setup, individual modules with 487 × 195 pixels of identical pitch (172 × 172 μm)

are combined into a detector array of up to 6 224 001 pixels. A further development of the PILATUS detector is the EIGER detector (Johnson *et al.*, 2014). The system consists of single-photon-counting modules of 256 × 256 pixels with a significantly reduced pitch of only 75 × 75 μm. Like GOTTHARD, the charge-integrating equivalent of MYTHEN, the JUNGFRAU detector (Mozzanica *et al.*, 2014) was developed as a charge-integrating equivalent to the PILATUS and EIGER detectors.

Even smaller pixel sizes of 55 × 55 μm have been achieved for the hybrid pixel detector Medipix3 (Ballabriga *et al.*, 2007). Modules of 256 × 256 pixels can be combined into large arrays. The electronics are highly configurable and allow charge summing, programmable binary counter and continuous count–read modes.

In principle, fast data collection seems to be desirable, but it has to be adjusted to the process that is being investigated. In most cases for a continuous frame rate the limiting factor is the data rate. The MYTHEN II detector (Schmitt *et al.*, 2003) installed at the Swiss Light Source allows a frame rate of 10–90 Hz, depending on the desired dynamic range (24–4 bits), and thus observations in the time range below 1 s to 10 ms. The two-dimensional detectors for high-energy X-rays can operate at a maximum of 30 Hz (Perkin Elmer) or 60 Hz (Pixium). In this context it is also worth mentioning the PILATUS detectors – a series of silicon pixel detectors also developed at the Swiss Light Source and further commercialized by Dectris. These detectors possess a high dynamic range over five orders of magnitude along with a rate capability of $>2 \times 10^6$ photons s^{-1} $pixel^{-1}$ and excellent detection efficiency of nearly single-photon counting (99% at 8 keV and 55% at 15 keV). The use of 1000 μm-thick CdTe instead of silicon enables >90% quantum efficiency at 20 keV, 81% at 40 keV, 90% at 60 keV, 77% at 80 keV and 56% at 100 keV. Complex detectors are often characterized by a long readout time of a large number of two-dimensional pixels, *e.g.* for PILATUS detectors the readout time per module is ∼2.7 ms.

Semiconductor-based detectors can operate at significantly higher frame rates. The EIGER detector can operate at a maximum frame rate of 24 kHz, while GOTTHARD can reach 40 kHz. In a special burst mode of 128 frames, a frame rate of 800 kHz is possible, reaching a single exposure time of 1.25 μs. The Timepix3 detector (Poikela *et al.*, 2014), which is a further development of the Medipix3 detector, can theoretically sustain continuous frame rates of up to 200 kHz, as long as the overall hit rate is less than 80 MHz.

In order to collect enough intensity for fast processes or to investigate even shorter timescales, stroboscopic measurements are useful. Thus, timescales in the range of milliseconds down to nanoseconds may be followed using a pump–probe setup. In this technique, the reaction is first triggered (pump) and after a specific time delay the diffraction pattern is collected (probed). The use of rapidly rotating choppers in the incoming beam is an attractive alternative to pump–probe experiments (Yoo *et al.*, 2011). Time resolution in the microsecond regime is routinely obtained in synchrotron experiments (Hinterstein, 2011; Hinterstein *et al.*, 2014) and in about the millisecond regime in neutron diffraction (Eckold *et al.*, 2010). When these experiments are conducted at a synchrotron and the periodic excitation of the sample is synchronized with the bunch clock of the synchrotron, the time resolution can be increased significantly. For a time resolution smaller than the temporal separation of the particle bunches (typically 8–200 ns), the time resolution suddenly drops to the bunch width, which is in the range of picoseconds. For neutron diffraction, the limiting factor for time resolution can be calculated from the energy bandwidth and the speed of the neutrons, which is dependent on the wavelength. The lower limit is typically in the range of 25 μs. These time ranges can be reached by multistrip or multiwire detectors in a stroboscopic setup.

In situ and *in operando* measurements require a specific sample environment, which is normally built using a different material to the sample and leads to additional contributions to the diffraction pattern. The use of strongly scattering materials such as thin metallic foils (Al foil in batteries, Ag or Au films as electrodes) or single crystals (sapphire capillaries for high-temperature experiments or diamonds in high-pressure experiments) may seriously bias data collection or damage the detector. If it is not possible to eliminate them by masking, they have to be taken into account by Rietveld analysis or profile matching. A correct treatment of the contributions from the sample environment has to take into consideration the fact that the additional scattering is normally off the diffractometer centre and this sample shift produces a non-linear shift in 2θ of the corresponding reflections in the pattern.

2.8.2.2. *Absorption*

Additional equipment is required for *in situ* experiments. The necessary parts are quite often constructed from metallic components. Light metals like aluminium are preferred for shielding parts within the beam for neutrons and X-rays. Vanadium is a suitable choice in neutron experiments, as it has a very small scattering cross section, so produces almost no coherent scattering. In most cases a suitable absorption correction is mandatory. For X-rays the energy dependence of the linear absorption coefficient $\mu(E)$ is very pronounced, especially close to X-ray absorption edges. Away from an absorption edge, higher energies lead to lower absorption. As an example, the linear absorption coefficient μ for steel (α-Fe) at 45 keV is 0.18 cm^{-1} and at 60 keV it is 0.076 cm^{-1}. The transmitted intensity after a beam has penetrated 1 mm steel with 100% packing density twice (once for the incoming and once for the outgoing beam) is therefore 2.7% for 45 keV but 22% for 60 keV. For one of the examples treated later, the piezoceramic $Pb(Zr_{0.5}Ti_{0.5})O_3$, the calculation for a sample diameter of 1 mm and a typical packing density of 60% in a powder leads to beam transmission of 3% (45 keV) and 21% (60 keV). Therefore, using high-energy X-rays enables transmission diffraction experiments that are not feasible with lower energies. The gain in measured intensities by decreasing absorption normally overcompensates for the decrease in scattering at shorter wavelengths, which is proportional to λ^3 within kinematical theory. The linear absorption coefficient of thermal neutrons (with wavelengths from 1 to about 3 Å) is small for most elements and scales in proportion to the wavelength, $\lambda = h/p = h/(2mE)^{1/2}$, *i.e.* λ (Å) = $9.045/E^{1/2}$ (meV) = $3956/v$ (m s^{-1}). However, the absorption cross sections for different isotopes of the same element may be very different. Numerical values are listed in Sears (1992) and *International Tables for Crystallography* Volume C, Table 4.4.4.1. For ferroelectric $Pb(Zr_{0.5}Ti_{0.5})O_3$, the linear neutron absorption coefficient at a wavelength λ = 1.5 Å and for a packing density of 60% is 0.026 cm^{-1}, significantly smaller than for X-rays; it is mainly determined by the Ti content.

As both the scattering and the absorption cross section for neutrons are in most cases much smaller than for X-rays, bigger samples are required. On the one hand, this leads to the advantage of better averaging over many particles. On the other hand,

the spatial resolution is significantly affected by the sample dimensions because of self-collimation. The appropriate choice of diffraction method is defined by the particular scientific challenge and has to take into consideration the different amount of sample that is needed for each experiment.

Very high absorption cross sections are desirable for shielding purposes. In X-ray diffraction, lead or tungsten are widely used. Only a few isotopes have a nuclear resonance in the thermal neutron range and thus a high absorption cross section. The most prominent are ^{10}B, ^{113}Cd and ^{157}Gd, which are used in neutron optics as collimators, attenuators and beam-shaping devices.

2.8.2.3. *Sample fluorescence and incoherent neutron scattering*

Sample fluorescence is a common problem for laboratory X-ray powder diffractometers, which are neither equipped with an analyser nor use detectors with a narrow energy resolution. In powder diffraction using synchrotron radiation, this problem is often solved either by adjusting the energy of the incident beam or by an adjustment of the dynamic range of the detector, or by a combination of both.

Like absorption cross sections, the incoherent neutron scattering lengths for different elements and isotopes do not vary in any obviously systematic way throughout the periodic table. Among the known stable isotopes, ^{1}H has the largest incoherent scattering length (25.274 fm) and has a small and negative coherent one (−3.7406 fm). The situation is very different for ^{2}H (deuterium), for which the incoherent and coherent scattering lengths are 4.04 and 6.671 fm, respectively. Differences between the coherent scattering lengths of hydrogen and deuterium form the basis of the isotopic labelling technique, called contrast matching; this is particularly important in applications of neutron scattering to hydrogen storage, structural biology and polymer science. Deuteration of samples is a challenging task, but obtaining high-quality powder diffraction data from hydrogenated samples is far more difficult. Use of neutron polarization analysis is a reliable way to subtract the incoherent scattering contribution from the diffraction data (Mikhailova *et al.*, 2012), but it is often accompanied by significant losses of incident neutron flux and, consequently, of data quality. Both sample fluorescence and incoherent neutron scattering are isotropic and, therefore, are often considered as a background in powder diffraction experiments.

2.8.3. Examples

2.8.3.1. *In situ studies of ferroelectrics in an external electric field*

The function of ferroelectrics as stress sensors, high-frequency microphones, medical injectors or large strain actuators is based on electric poling. A polycrystalline material exhibits a zero net polarization. When an electric field is applied to the sample, the spontaneous electric polarization of the ferroelectric material is reoriented along the electric field vector. This occurs by a reorientation of domains. Additional polarization is obtained by an increase of the spontaneous polarization induced by the applied electric field. With *in situ* experiments, the field-induced changes in the powder diffraction reflections are measured. Fig. 2.8.1 is a schematic representation of some *in situ* sample geometries. The electric field is applied *via* electrodes on the sample surface.

Many of these ferroelectric materials crystallize in a structure derived from the cubic perovskite type, but in a crystal system with lower symmetry and with a non-centrosymmetric space group. The most widely used material is lead zirconate-titanate ($PbZr_{1-x}Ti_xO_3$, PZT), which exhibits the highest strain response

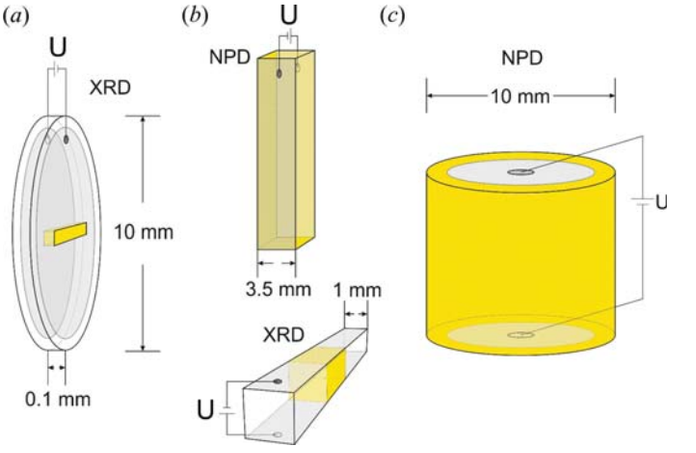

Figure 2.8.1
Sample geometries for *in situ* experiments with an applied electric field. Samples are poled *via* an applied voltage (U) at the sample electrodes (grey). Different sample geometries are necessary to account for different beam sizes, absorption and detector concepts. Yellow indicates the irradiated sample volume. (*a*) Flat-plate samples for X-ray experiments with strip detectors, limiting photon energies to around 30 keV. (*b*) Bar-shaped samples for high-intensity neutron powder diffraction (NPD) or high-energy X-ray diffraction (XRD). (*c*) Cylinder-shaped samples for high-resolution neutron diffraction with fixed detector collimators.

at the so-called morphotropic phase boundary with a composition of about 50% for Ti and Zr. It is generally accepted that the phase on the Ti-rich side of the PZT phase diagram has a tetragonal structure with space group *P*4*mm*. On the rhombohedral Zr-rich side, two ferroelectric phases can be identified, with space groups *R*3*m* for high and *R*3*c* for low temperatures. A considerable amount of work has been devoted to the elucidation of the crystal structure of the material close to the morphotropic phase boundary. Neutron and synchrotron diffraction detected monoclinic symmetry at low temperatures and nanometre-sized regions (the so-called polar nanoregions) were inferred from diffuse scattering (Noheda *et al.*, 2000; Hirota *et al.*, 2006). Alternative interpretations explained the new reflection found in the pattern between the 111_C and 200_C reflections (where the subscript 'C' corresponds to the cubic archetype structure) as diffuse scattering from diffuse incoherent scattering by small domains (Jin *et al.*, 2003).

Unique information on structural changes during poling is obtained from *in situ* studies in applied external electric fields (Hoffmann *et al.*, 2001). Fig. 2.8.2 displays two groups of powder reflections (Schönau, Schmitt *et al.*, 2007) observed by synchrotron X-ray diffraction. They are directly compared with the domain structure from TEM observations (Schmitt *et al.*, 2007) for a range of compositions near the morphotropic phase boundary. One group of reflections is derived from the cubic 111_C reflection, the other from the archetype 200_C reflection. The transition from the rhombohedral splitting to the tetragonal one with increasing Zr content is correlated with the forms of ferroelectric domains in TEM. Close to the morphotropic phase boundary, nanodomains (ranging in width from 20 to 200 nm) are observed in addition to the well known microdomains. The nanodomains react immediately under the influence of an electric field to become microdomains. Fig. 2.8.3 shows the intensity changes observed for the 110_C group of reflections. The changes under an electric field are pronounced and depend on the *c*/*a* ratio (Schönau, Knapp *et al.*, 2007), the formation and disappearance of nanodomains, and the local symmetry of these domains.

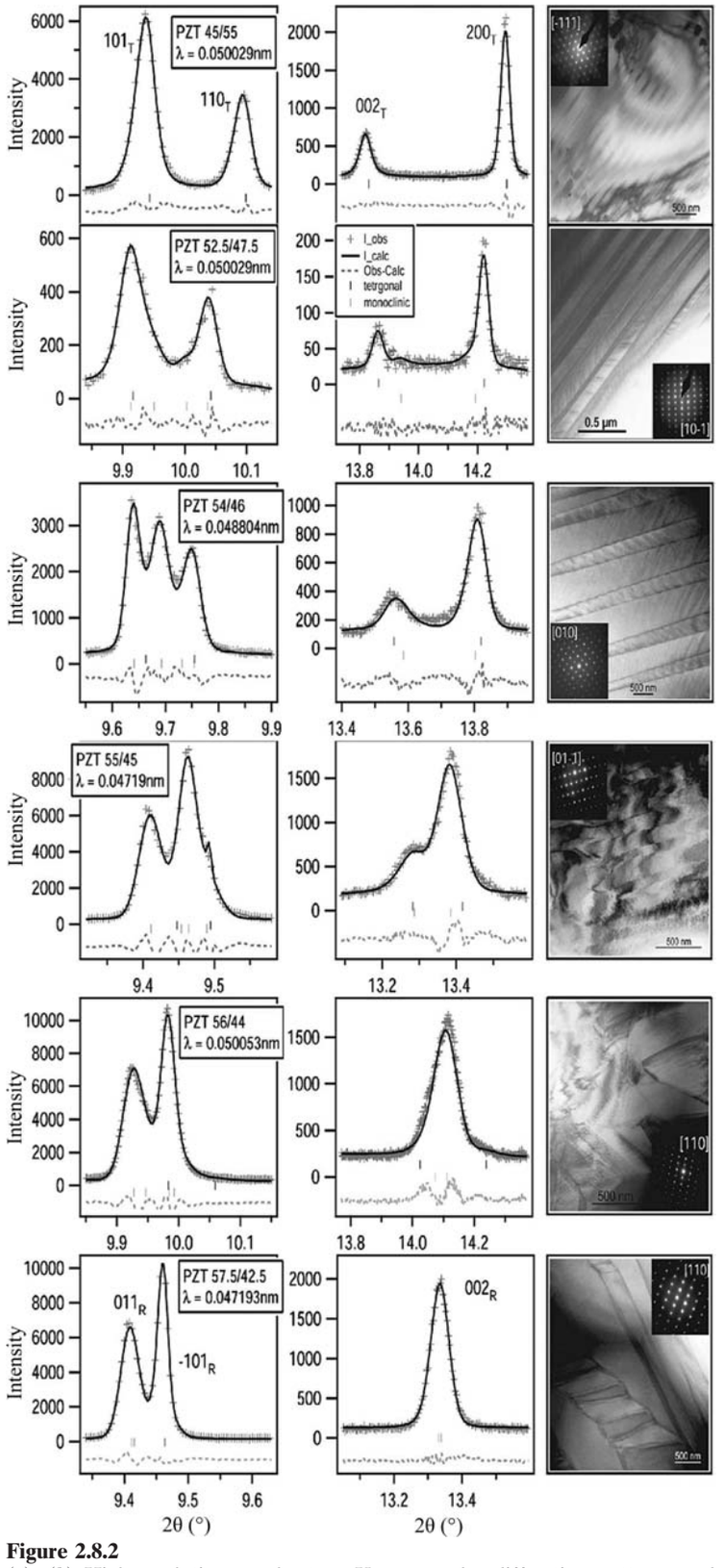

Figure 2.8.2
(*a*), (*b*) High-resolution synchrotron X-ray powder diffraction patterns and TEM imaging of PZT with a varying Zr/Ti ratio. An increase in broadening is seen in changes in shape and width of the 002_T reflection between the samples PZT 45/55, 52.5/47.5 and 54/46. The asymmetry and width of the tetragonal 101_T reflection not only change, but also evolve into a new peak between 101_T and 110_T in sample PZT 54/46, which gains in intensity towards PZT 57.5/42.5. This rise is accompanied by a decrease in intensity of the visible 110_T reflection, which then seems to be absent or overlapped in sample PZT 56/44. The domain structure changes from a lamellar tetragonal configuration *via* nanodomains to a rhombohedral herringbone structure. Reproduced with permission from Schönau, Schmitt *et al.* (2007). Copyright (2007) by the American Physical Society.

The different poling mechanisms can be studied in transmission geometry, which allows variation of the angle between the electric field vector **E** and the direction of the incident X-ray beam **k** from 0° to about 45° (Fig. 2.8.4) (Hinterstein *et al.*, 2011). Two sputtered electrodes (Ag, Pt) were used for polarization.

An extensive study under an electric field has been carried out on the commercially available sintered PZT material named PIC, in which Ti is partially replaced by Ni and Sb $[Pb_{0.99}Zr_{0.45}Ti_{0.47}(Ni_{0.33}Sb_{0.67})_{0.08}O_3]$, in transmission geometry. The angle between the electric field perpendicular to the flat sample surface and the incident beam was varied between 0 and 45°. The effect of domain switching in tetragonal symmetry mainly affects the $\{h00\}_C$ reflections, whereas the piezoelectric effect predominantly influences the $\{hhh\}_C$ reflections. Thus, the reflection pair 111_C and 200_C are the only reflections analysed in most studies. Fig. 2.8.5 displays just these reflections, with 200_C split into 002_T and 200_T, where the subscript 'T' refers to the tetragonal distorted cell, which is *translationengleich* to the cubic one (*i.e.* they have the same group of translations). The shift to higher angles of 111_C under an applied field indicates a decrease in volume. This is explained by the large angle between the electric field vector and the vector of spontaneous polarization for the unit cells contributing to 111_C. This induced compression remains in the remanent state.

While analysis of single reflections or orientations can yield valuable information on textured functional materials, a more sophisticated approach involves coupling the Eulerian angles to the diffraction patterns and modelling all observable mechanisms within a single refinement. By applying this method to a technically applied actuator material, Hinterstein, Hoelzel *et al.* (2015) could quantify all strain mechanisms and calculate the macroscopic response to an applied electric field with a structure model at the atomic scale.

The function of piezoceramics is related to periodic cycling of the polarization, accompanied by periodic changes of macroscopic strain. Fatigue in piezoceramic materials means that this strain is reduced as a result of the cycling; this has been studied with respect to the underlying structural changes (Hinterstein *et al.*, 2011, 2014).

Whereas strain is related to texturing, no preferred orientation is observed in fatigued samples. The orientation of nanodomains is demonstrated in different patterns: in Fig. 2.8.6 the two reflections are shown for the remanent state (0 kV mm^{-1}) at different diffraction angles and in Fig. 2.8.7 for values of the external field ranging from 0 to 2 kV mm^{-1}.

The diffuse scattering between the split 200_C reflections in the fatigued sample is reduced and the texturing increases after static poling for a few seconds. Thus, the fatigued samples show a more tetragonal appearance after cycling. The energy of the electric field induces a transition of well oriented nanodomains with preferred orientation along the field vector, leading to texturing for $\omega = 0°$. At a certain point the system will no longer respond to the electric field because of crack formation and a decrease in the volume of switchable nanodomains. From that point, the diffraction pattern recorded under a field is no different to the diffraction pattern recorded without a field.

Cyclic loading with high frequencies is required in real applications of ferroelectric ceramics. Exposure times

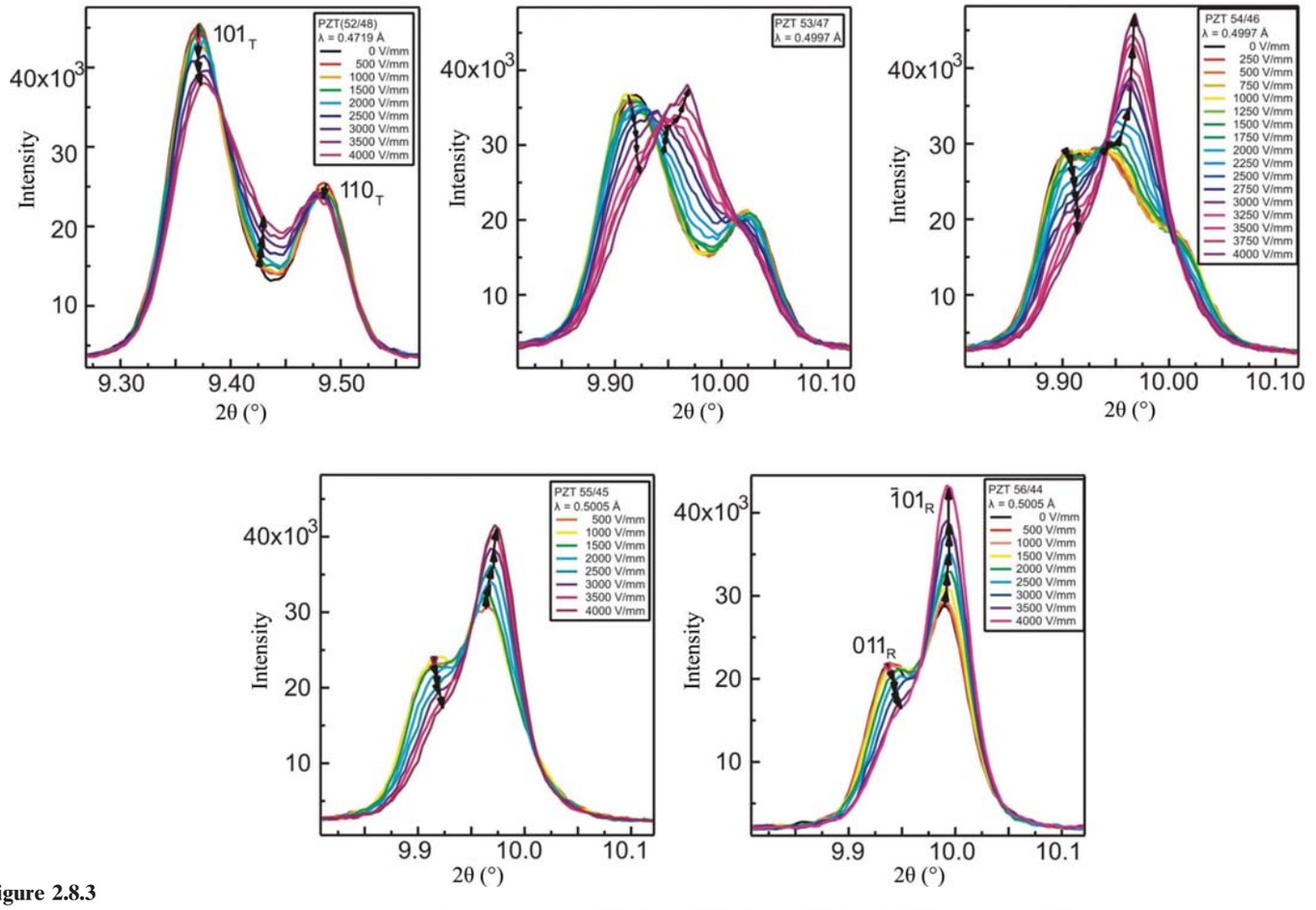

Figure 2.8.3
Diffraction patterns of the tetragonal 101_T /110_T reflection pairs of PZT 52/48, PZT 53/47, PZT 54/46, PZT 55/45 and PZT 56/44 recorded *in situ* under an electric field for the first poling cycle of up to 4 kV mm^{-1}. Reproduced with permission from Schönau, Knapp *et al.* (2007). Copyright (2007) by the American Physical Society.

in the range of seconds are necessary to ensure sufficient statistics for single diffraction experiments in the subsecond regime. Stroboscopic measurements can be used to achieve this.

Absolutely reversible processes are necessary for a successful stroboscopic analysis. The stability of the system is achieved by pre-cycling *circa* 10^5 times. Time resolutions in the range of several tens of milliseconds are possible with modern X-ray detectors. By repeating the excitation and summing the intensities, proper statistics can be achieved (Choe *et al.*, 2015; Hinterstein *et al.*, 2014).

The use of the stroboscopic data-collection technique and cyclic fields in neutron diffraction experiments enabled a direct measurement of non-180° domain wall motion during the application of subcoercive cyclic electric fields (Fig. 2.8.8) (Jones *et al.*, 2006, 2007; Jones, 2007; Daniels *et al.*, 2007). It was shown that the non-180° domain switching contributes 34% of the macroscopically measured strain during cycling with half of the coercive field.

The highest time resolutions are obtained in a pump–probe setup. Under the influence of an electric field of 2 kV mm^{-1}, the switching kinetics can be investigated directly. With a time

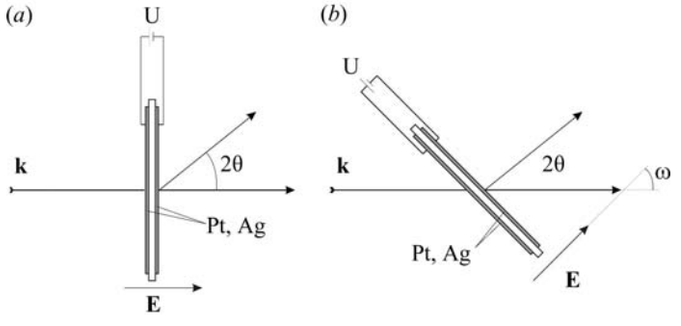

Figure 2.8.4
In situ transmission geometry developed by Schönau, Schmitt *et al.* (2007) with the electric field vector perpendicular to the flat-plate sample surface. The electric field results from an applied voltage U between two opposing sputtered electrodes (Ag, Pt) with a thickness of about 15 nm. (*a*) $\omega = 0°$ and (*b*) $\omega = 45°$.

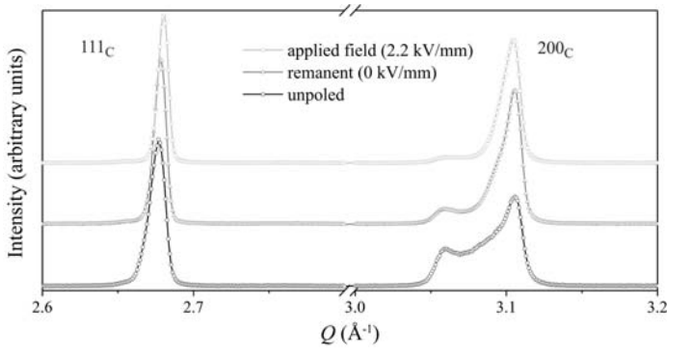

Figure 2.8.5
111_C and 200_C reflections of the unpoled, remanent and applied field state of PIC 151 at $\omega = 0°$. Owing to the piezoelectric effect, the 111_C reflection is shifted. The preferred orientation of the 200_C reflection indicates tetragonal 90° domain switching.

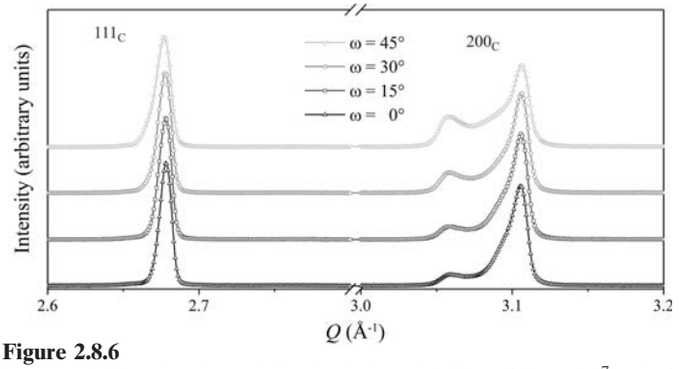

Figure 2.8.6
111_C and 200_C reflections of bipolar fatigued PIC 151 (50 Hz, 10^7 cycles) in the remanent state (0 kV mm^{-1} at $\omega = 0°$, 15°, 30° and 45°).

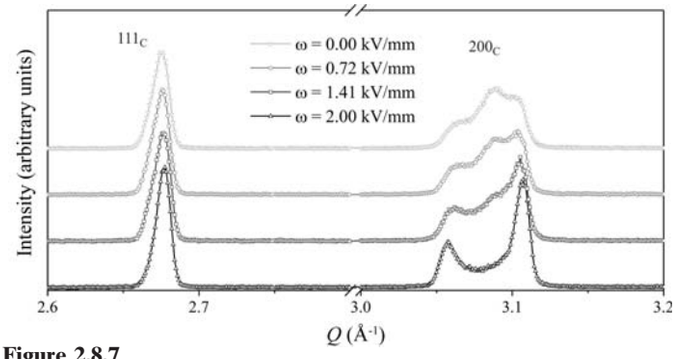

Figure 2.8.7
111_C and 200_C reflections of bipolar fatigued PIC 151 (50 Hz, 10^7 cycles) at $\omega = 45°$ with 0.0, 0.72, 1.41 and 2.0 kV mm^{-1}.

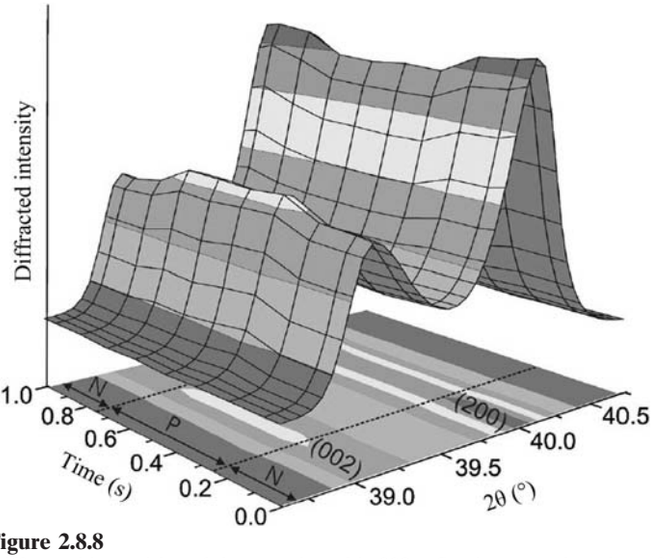

Figure 2.8.8
Diffracted intensities of the pseudo-cubic 002 reflections as a function of 2θ and time during application of a square, bipolar electric field waveform of frequency 1 Hz and amplitude of plus or minus half the coercive field. The timescale is described using eight steps. The positive (P) state of the electric field is applied between 0.25 and 0.75 s, which is bounded on either side by the negative (N) field state. The diffraction vectors 002 and 200 are parallel to the applied electric field. Reproduced with permission from Jones *et al.* (2006). Copyright (2006) AIP Publishing.

resolution of 1 ms only one intermediate step is observed (Fig. 2.8.9*a*). With a time resolution of 250 μs a significant number of intermediate steps can be studied (Fig. 2.8.9*b*). The commercially available soft-doped PZT material EC-65 has also been observed under the application of an electric field and mechanical stress. Lattice strains were measured under cyclic electric fields at times as short as 30 μs (Pramanick *et al.*, 2010).

The use of lead-containing materials may in the future be banned because of environmental concerns, hence considerable efforts are being made to find materials with properties similar to PZT. Only a few elements (Ba, Bi, Na, K, Nb, Ti) seem to be suitable. Nevertheless, a combination of the relevant oxides of these leads to a large variety of potential materials. $(Bi_{0.5}Na_{0.5})$-TiO_3–$BaTiO_3$ (BNT–BT) (Hinterstein, Schmitt *et al.*, 2015), $(Bi_{0.5}Na_{0.5})TiO_3$–$(Bi_{0.5}K_{0.5})TiO_3$ (BNT–BKT) (Levin *et al.*, 2013), BNT–BT–$K_{0.5}Na_{0.5}NbO_3$ (BNT–BT–KNN) (Schmitt *et al.*, 2010), BNT–BKT–KNN (Anton *et al.*, 2012) and BNT–KNN (Liu *et al.*, 2017) are the focus of most attention. The materials in the $(1 - x - y)$BNT–xBT–yKNN system exhibit remarkable piezoelectric properties over a narrow composition range $0.05 \leq x \leq 0.07$ and $0.01 \leq y \leq 0.03$ (Zhang *et al.*, 2007). Daniels *et al.* (2010) proposed a combinatorial approach to studying a range of compositions in a single sample, where different stoichiometries created a compositional gradient in the sample. A limited number of bulk homogeneous samples were prepared for comparison. Microfocus X-ray beams from a synchrotron allowed investigation of the gradient material under a field.

Fig. 2.8.10 displays the diffraction patterns under an external electric field up to 5.5 kV mm^{-1}. Data analysis was performed by fitting the data of the pseudo-cubic 002 reflection to distorted pseudo-cubic and tetragonal symmetry for each composition and electric field. Whereas in the 0.86BNT–0.14KNN composition only a distorted pseudo-cubic behaviour is observed

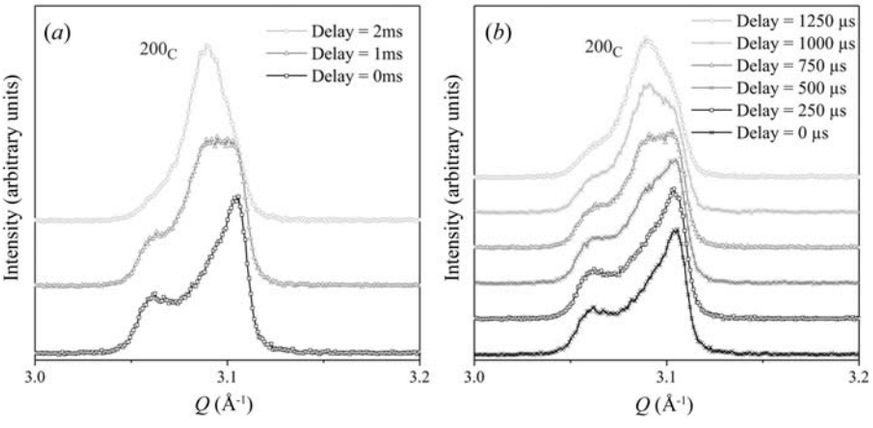

Figure 2.8.9
Pump–probe measurements of the 200_C reflection at $\omega = 45°$. Cycling switching between the remanent and the applied field state at 2 kV mm^{-1} with 50 Hz and a time resolution of (*a*) 1 ms and (*b*) 250 μs. Only a time resolution of 250 μs results in sufficient intermediate steps between the remanent and the poled state to study the processes during poling.

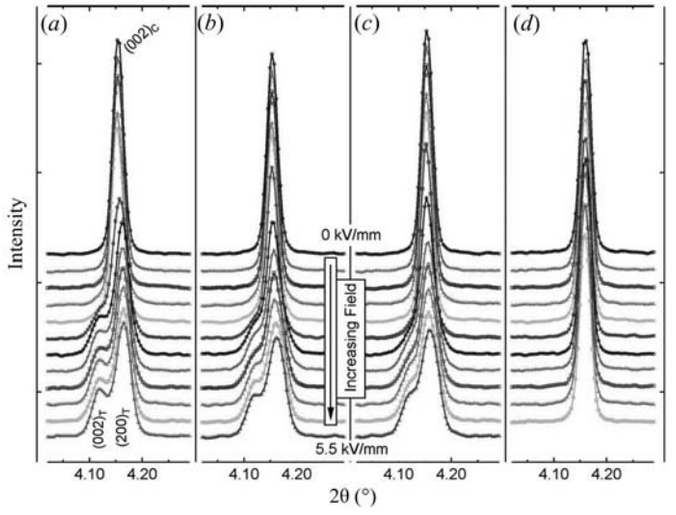

Figure 2.8.10
The pseudo-cubic 002 reflection of (*a*) 0.93BNT–0.07BT end member, (*b*) 0.938BNT–0.053BT–0.009KNN, (*c*) 0.932BNT–0.045BT–0.023KNN and (*d*) 0.86BNT–0.14KNN end member as a function of electric field from the initial zero-field state (top) to an applied field of 5.5 kV mm^{-1} (bottom). The sample orientation is such that the scattering vector is parallel to the electric field. Reproduced with permission from Daniels *et al.* (2010). Copyright (2010) Elsevier.

above a threshold of 0.5 kV mm^{-1}, a very pronounced distortion is observed for 0.93BNT–0.07BT, which eventually above 2 kV mm^{-1} develops into a tetragonal structure. In addition to the combination of various compositions, the authors simultaneously measured the X-ray fluorescence spectra, thus confirming the actual composition.

Fig. 2.8.11 depicts a Rietveld refinement of a lead-free ferroelectric material with the composition $0.92Ba_{0.5}Na_{0.5}TiO_3$–$0.06BaTiO_3$–$0.02K_{0.5}Na_{0.5}NbO_3$. New superstructure reflections (Fig. 2.8.11*b*, arrows) and a lattice distortion (Fig. 2.8.11*b*, circled) were observed due to a transition from space group *P*4*bm* to *R*3*c* (Hinterstein *et al.*, 2010).

In an overview, Jones summarized the use of diffraction techniques. Along with the importance of microdiffraction, diffuse scattering and texture effects, the importance of time-resolved studies including stroboscopy was acknowledged (Jones, 2007).

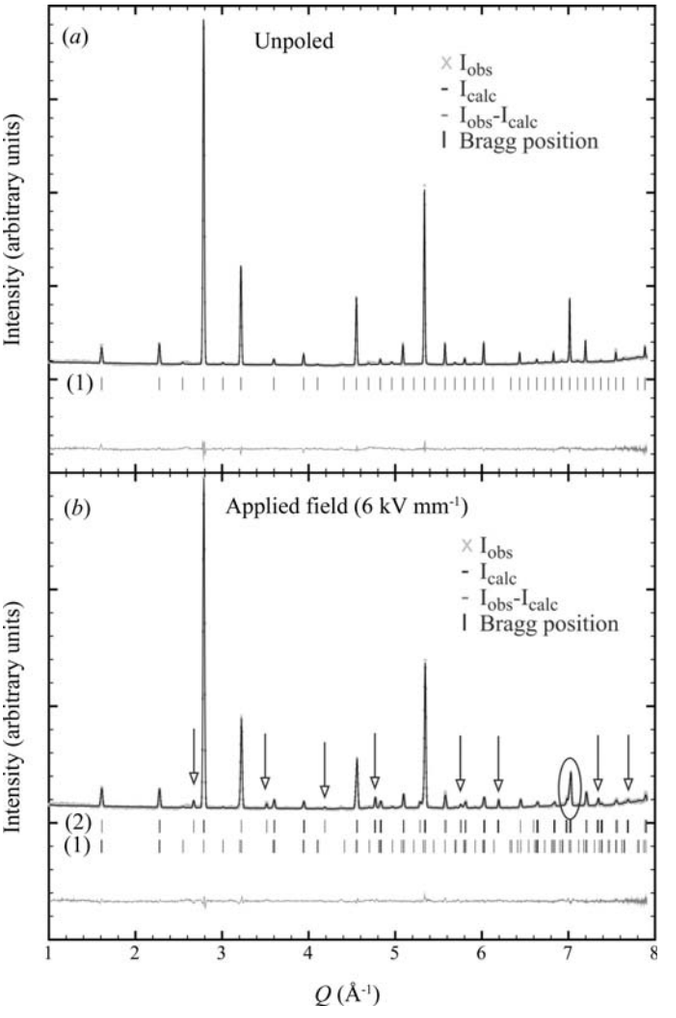

Figure 2.8.11
Rietveld refinement based on different patterns of $0.92Bi_{0.5}Na_{0.5}TiO_3$–$0.06BaTiO_3$–$0.02K_{0.5}NbO_3$ (*a*) in the unpoled and (*b*) in the applied field state at 6 kV mm^{-1}. Experimental data are shown by grey crosses, black lines denote calculated profiles, and the lower plot shows their difference. Calculated positions of Bragg reflections are shown by vertical tick marks, where the different rows correspond to the initial tetragonal phase with space group *P*4*bm* (1) and the field-induced rhombohedral phase with space group *R*3*c* (2). Arrows mark superlattice reflections of type $\frac{1}{2}\{ooe\}$ and the circle highlights the rhombohedral split 331_C reflection.

2.8.3.2. *In situ studies of electrode materials and in operando investigations of Li-ion batteries*

Rechargeable energy sources in mobile electronics are mainly based on lithium-ion batteries. Their application relies on the mobility of the small Li ions, which move from the cathode through an electrolyte to the anode during charge and back during discharge. Intensive research is underway to improve the performance of such energy-storage technology. High gravimetric and volumetric energy and power densities are required. Other additional challenges are safety, lifetime, the temperature range of stable operation and production costs per unit energy at the battery level. Knowledge of the correlation between the electrochemical functionality and the structure of the electrode materials during Li exchange is essential in order to interpret the underlying mechanisms and degradation processes and to find a promising approach to better materials. The high reactivity of the cell components and the very strong interactions between materials inside an electrochemical cell require studies on complete operational devices by non-invasive *in operando* methods. So-called electrochemical 'half cells' are often studied to follow structural changes in electrode materials. These are complete operational cells, but the electrode is cycled against an Li-metal counter electrode. Such half-cell studies are sometimes described as *in situ* studies. Limitations might occur with respect to fatigue studies and at very high charge and discharge rates, when the performance is determined by the Li-metal electrode. The classification of *in situ* and *in operando* methods is not unambiguous in structural studies on battery materials. Sometimes the term *quasi in situ* is used for studies where specific states of the materials are prepared electrochemically and handled in an Ar atmosphere with complete protection against humidity and air, but actually investigated *ex situ* (Oswald *et al.*, 2009).

Some early *in situ* setups have been described for neutron diffraction (Bergstöm, Andersson *et al.*, 1998) and transmission X-ray diffraction (Bergström, Gustafsson & Thomas, 1998), and also at elevated temperatures (Eriksson *et al.*, 2001). Today, for example, good-quality full diffraction patterns can be obtained

with exposure times well below 100 ms using synchrotron radiation (Herklotz *et al.*, 2013). Capillary-based micro-battery cells allow for *in situ* X-ray powder diffraction studies on one single electrode (Johnsen & Norby, 2013). Even spatially resolved neutron diffraction studies are possible on commercial cylindrical Li-ion batteries (Senyshyn *et al.*, 2015).

The mechanism of Li extraction and insertion differs for different types of electrodes. In intercalation-type electrodes the topology of the host structure remains mainly unchanged, and suitable sites in the structure are either occupied by Li or are vacant in the delithiated state. This use of intercalation chemistry for electrochemical energy storage was established for a battery based on Li metal as the negative electrode and TiS_2 as the positive electrode (Whittingham, 1976). In commercial cells today the negative electrode is also based on intercalation and consists of layered graphite, which hosts Li during the charge cycle up to the composition LiC_6. Another working mechanism for negative electrodes is electrochemical alloying with Li. The most promising examples involve Si, Al and Sn. These electrode concepts suffer from extreme volume changes: 100% for Al $\rightarrow$ LiAl or even 300% for Si $\rightarrow$ $Li_{21}Si_5$. In combination with the brittleness of these materials, the particles break down and become amorphous during successive charging and discharging, accompanied by contact losses and resulting pronounced fade in capacity. Two other mechanisms have also received considerable attention as they allow higher specific capacities. In a replacement reaction, one transition metal is replaced by Li while the topology of the structure is mainly preserved. During a conversion or displacement reaction the initial structures of transition-metal compounds, for example nanometre-sized oxides (Poizot *et al.*, 2000) or other binary compounds (Cabana *et al.*, 2010), are believed to be destroyed completely by either amorphization or phase transitions. The transition-metal ions are reduced to metallic nanoparticles, which are embedded in a complex network of Li_2O and reaction products from the electrolyte. In spite of the loss of long-range order, an important short-range structure remains. This has been shown in detail for ternary Cu–Fe oxides (Adam *et al.*, 2013). The reduction of Cu^{2+} from CuO takes place through the formation of a Cu_2O/Li_2O composite, in which Cu_2O reacts further to form Cu metal and Li_2O. Spinel-type $CuFe_2O_4$ and $CuFeO_2$ react to form α-$LiFeO_2$ with the extrusion of metallic Cu and Fe nanoparticles. At even lower potentials against Li^+/Li between 0.8 and 1.0 V, α-$LiFeO_2$ is further reduced into metallic Fe nanoparticles and Li_2O. While most of these displacement reactions suffer from very poor reversibility, good cycling stability was shown for $Cu_{2.33}V_4O_{11}$ (Morcrette *et al.*, 2003). During cell discharge Li penetrates into the well crystallized copper vanadate, forming a solid solution up to an Li content of $x = 0.6$, when Bragg peaks of metallic copper were observed. The end result was a composite electrode of an amorphous Li–V–O matrix with dispersed metallic copper. The essential point is the reversibility, with the disappearance of the metallic copper and the recrystallization of the initial $Cu_{2.33}V_4O_{11}$.

Two more examples belong to the class of intercalation materials: graphite as used for the negative electrode, and $LiNiO_2$ as a candidate for the positive electrode. 'Positive' and 'negative' electrodes are the preferred terms for secondary batteries instead of 'cathode' and 'anode', because anode and cathode reactions match only for discharge (interchange between the two electrodes occurs for the charge process). A comprehensive summary of structure reports on lithiated graphite can be found in Johnsen & Norby (2013). From the voltage plateau in cyclovoltammograms four distinct lithiated graphite phases have been postulated. However, only for two of them have complete structure models been reported and confirmed. The first is LiC_{12}, *P*6/*mmm* (space group No. 191), $a = 4.29$, $c = 7.03$ Å, with C on the 12*n* site with $x = 0.33$ and $z = 0.25$ and Li on the 1*a* site; the second is LiC_6, also *P*6/*mmm*, $a = 4.31$, $c = 3.70$ Å with C on the 6*k* site with $x = 0.33$ and Li again on the 1*a* site. According to the number of graphene layers that are needed for the smallest unit repeated by translational symmetry along the sixfold rotation axis, these structures are described as stage-II (LiC_{12}) and stage-I (LiC_6) compounds, like graphites intercalated with other alkaline elements. Note that in these phases the graphene layers are not shifted with respect to each other (*AA* sequence), in contrast to graphite (*AB* sequence). For a lower Li content, a much more complex structural behaviour was observed, including incommensurate Li distributions between the graphene layers, which were described as twisted bilayers (Senyshyn *et al.*, 2013). Higher-order reflections were observed for these phases and allowed indexing with a propagation vector (α, α, 0). Different structure models were discussed, but a complete description of the Li distribution is still lacking. Therefore, it is still an open question as to where the Li atoms in lithiated graphite are at low Li contents (below 1 Li per 12 C).

$LiNiO_2$ is considered to be a promising positive electrode material (Ohzuku *et al.*, 1993). However, it has some limitations, which are directly linked to the underlying structure. A high degree of cation disorder, *i.e.* Li on the Ni site and *vice versa*, hinders Li transport within the layers. Furthermore, Li and Ni exchange takes place rather easily, in contrast to $LiCoO_2$, because of a more favourable transport process through a tetrahedral interstitial site for Ni than for Co. In the cases of Li excess, $Li_{1+\delta}NiO_2$, or Ni excess, $(Li_{1-\delta}Ni_\delta)NiO_2$, some Ni^{2+} ions exist, which have a very similar ionic radius to that of Li^+. Therefore, it is nearly impossible to prepare stoichiometric $LiNiO_2$ with perfect separation of Li and Ni onto distinct layers. The best samples with respect to cation order are obtained from $NaNiO_2$ by successive Na $\rightarrow$ Li ion-exchange reactions. These drawbacks have prevented the commercial application of $LiNiO_2$, and more complex materials like $Li(Ni,Co,Al)O_2$ (NCA) and $Li(Ni,Co,Mn)O_2$ (NCM) are increasingly replacing $LiCoO_2$. Fig. 2.8.12 shows the structural changes in $LiNiO_2$ during the first charge and discharge. The detailed experimental conditions are the same as those described by Nikolowski *et al.* (2005) for $Li(Ni_{0.8}Co_{0.2})O_2$. One of the most characteristic features of the structural response to Li extraction and insertion is the pronounced change in the lattice parameters, shown by the changes in the *c*/*a* ratio for the rhombohedral structure. During Li extraction the *c* parameter increases, because there are fewer Li ions between (repulsive) O-atom layers. However, at lower Li contents, some of the O ions become oxidized, and the repulsion between the O-atom layers is weaker, resulting in shorter *c*-axis parameters. As a general rule, all layered oxides $LiMO_2$, with *M* = Mn, Co and/or Ni, become intrinsically unstable in the highly delithiated states beyond the maximum in the *c*/*a* ratio. Note that the as-prepared material has a very high degree of cation disorder (9.3% Ni on the Li site) and very poor capacity retention in the second cycle. The initial phase (*A*) gradually disappears and apparently transforms into a second phase (*B*) with a much lower degree of cation disorder (less than 3%). Note that this phase sequence does not necessarily reflect equilibrium conditions, but depends strongly on the chemical composition (Li or Ni excess), microstructure (size and strain) and the experimental conditions (charge rate, temperature, electrode formulation and more).

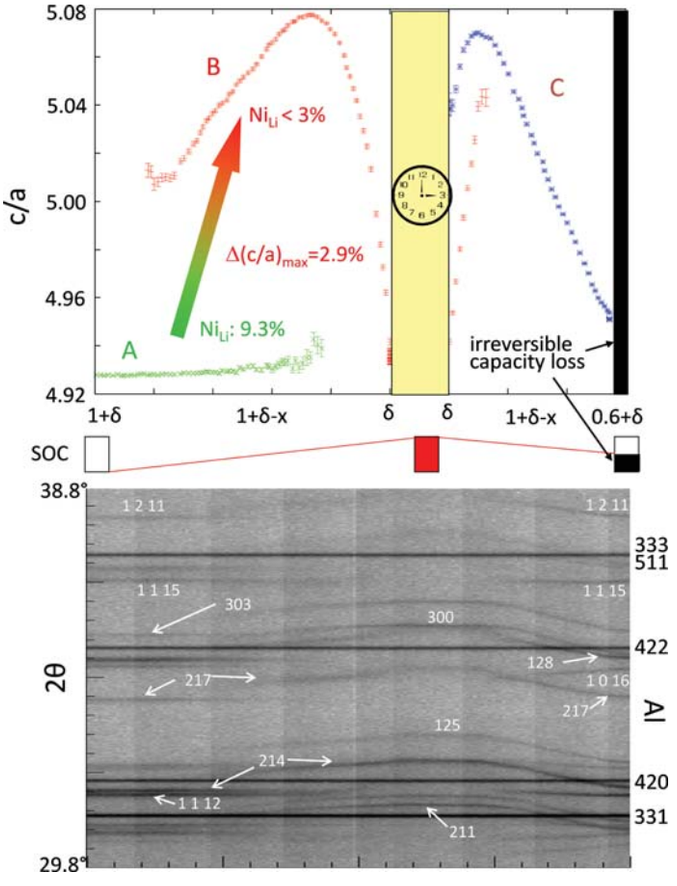

Figure 2.8.12
$Li_{1+\delta}NiO_2$ during charge and discharge. From about 210 complete diffraction patterns [a small section is shown below (λ = 0.499366 Å)], the structural response to Li extraction and insertion was monitored. In addition to changes in the unit-cell metric, the distribution of Li and Ni onto layers becomes more ordered during the first highly charged state. A pronounced capacity loss is observed during discharge after a holding time of 3 h in this overcharged state. A, B and C are three successively appearing phases. SOC = state of charge.

Such *in situ* studies are very important for elucidating the working mechanism and degradation processes for intercalation electrodes (Senyshyn *et al.*, 2012). Nevertheless, complementary methods are also essential for providing all the necessary information, especially about the surface near-interface region between the electrode and electrolyte, which has to be studied with surface-sensitive and local methods.

2.8.3.3. *Diffraction under a magnetic field*

2.8.3.3.1. *General remarks*

The majority of synchrotron and neutron experiments are currently limited to superconducting magnets with fields of 5–16 T. When higher fields are required there are essentially two possible solutions: pulsed resistive or steady-field resistive (or hybrid: resistive inner coil, superconducting outer coil) magnets. Pulsed fields are often used when signals are strong and the signal-to-noise ratio is good, whereas steady fields are primarily used for techniques with relatively long counting times and many data points. The relatively short pulse duration (from microseconds to milliseconds) along with the rather large sample volume required severely limit the use of pulsed magnetic fields in powder diffraction applications as well as more exotic methods of achieving high magnetic fields, *e.g.* magnetic flux compression or single-turn coils (Schneider-Muntau *et al.*, 2006). Furthermore,

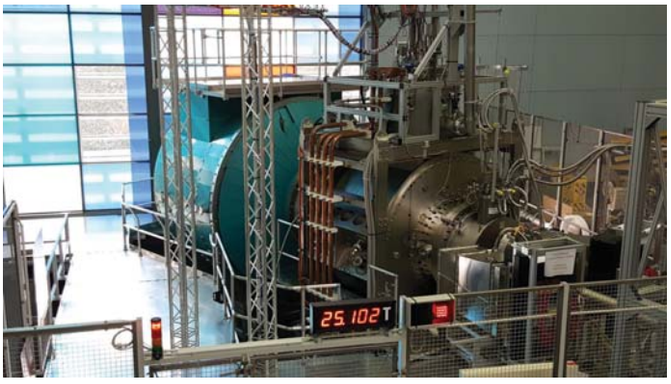

Figure 2.8.13
The High Magnetic Field Facility for Neutron Scattering at the Helmholtz-Zentrum Berlin has two main components: the High Field Magnet (HFM) and the Extreme Environment Diffractometer (EXED). Courtesy of Dr O. Prokhnenko.

because of the large stresses, the lifetime of a resistive/pulsed magnet is finite: pulsed magnets have typical lifetimes of 500 shots at 95% of the design field, and their lifetimes are virtually independent of pulse duration.

At present, the maximum field for technical superconductors is 23 T and modern developments in superconductor design along with robust magnet manufacturing techniques have made possible high-flux-density magnets for neutron scattering studies up to 16 T. For resistive magnets, there are in principle no limitations to the generation of the highest continuous fields apart from economics, as approximately 1 MW of electric power is consumed per 1 T field strength. Therefore, in order to reduce the running costs (*i.e.* the required power per unit magnetic field), hybrid magnets are becoming increasingly popular. In this context we mention the joint developments between the National High Magnetic Field Laboratory (Tallahassee, FL, USA), the Spallation Neutron Source (Oak Ridge, TN, USA) and Helmholtz-Zentrum Berlin (Germany) in the development of high-steady-field (25 T with a 4 MW resistive insert, 30 T with an 8 MW resistive insert) hybrid magnets for neutron scattering (Bird *et al.*, 2009). A high-field magnet has been installed and is in routine user operation (Fig. 2.8.13) at the Extreme Environment Diffractometer (HFM-EXED) of Helmholtz-Zentrum Berlin (Prokhnenko *et al.*, 2015).

On the other hand, it is quite simple to produce magnetic flux density uniformity or homogeneity over the required sample volume down to the p.p.m. level with a solenoid magnet. However, the majority take the form of split-pair solenoids. With this setup, the access to the sample environment (along the magnetic axis) can be orthogonal to the beam-access plane. The split-coil setup is the most popular in neutron scattering, but the geometry constraints imposed by the neutron aperture make the creation of very uniform flux density much more difficult. In general, for a typical neutron-scattering sample volume of 1 cm^3, the magnetic field homogeneity is normally limited to the range 0.1 to 5%. As the available current density for a given conductor decreases with increasing flux density, the flux density seen by the superconductor inside the magnet windings is greater than the 'nominal' central value. This is particularly the case for split-pair magnets, where the ratio of the two can be large, *e.g.* for a central value of 9 T, a ratio of 1.6 gives a maximum flux density of 14.3 T (Brown, 2010).

As already pointed out, diffraction studies under a magnetic field are almost always performed with neutrons. However,

Mitsui *et al.* (2009) have developed a device that includes a cryo-cooled split-pair NbTi superconducting magnet and a sample furnace, for high fields and temperatures above room temperature, respectively, which can be installed on a laboratory X-ray diffractometer. The magnetic field generated goes up to 5 T at the centre of a 50 mm vertical and 10 mm horizontal bore, with a field homogeneity of 0.1%. The first results of studies on the martensitic phase transition in the shape memory system $Ni_{40}Co_{10}Mn_{34}Al_{16}$ in a field of 5 T and at temperatures up to 473 K have been reported for powders (Mitsui *et al.*, 2009).

Synchrotron radiation can be used to study specific properties such as orbital contributions and their separation from the spin values. Diffraction studies with unpolarized neutrons are common at a constant field to elucidate simple magnetic structures: no confident conclusion about the spin direction can be obtained if the configurational symmetry is cubic, and in the case of uniaxial symmetry (either tetragonal, hexagonal or rhombohedral) only the angle with the unique axis of the magnetic structure can be defined (Shirane, 1959). The sensitivity of non-polarized neutron powder diffraction (the magnetic detection limit) is by a few orders of magnitude less than that of superconducting quantum interference device (SQUID) magnetometry, muon spin rotation or magnetic dichroism spectroscopy. In an antiferromagnetically ordered system the determination of magnetic moments below 0.1 μ_B per magnetic atom presents severe challenges, which become even more pronounced for the localization of weak ferromagnetic components. Less frequent are *in situ* investigations to determine magnetic phase diagrams. The use of powder samples at high magnetic fields is often limited by the redistribution of grains and texture effects.

Experiments with polarized neutrons are normally performed with single crystals. Out of the variety of compounds that have been studied, we have chosen materials with particular properties and report on *in situ* studies of them under magnetic fields.

2.8.3.3.2. *Frustrated magnetic systems*

Multiferroic systems (or more precisely magnetoelectric materials) have gained considerable attention because of their potential applications in devices. In fact, the efficient control of magnetism by an electric field allows magnetic information to be written electrically (with low energy consumption) and read magnetically. A real application, however, requires both phenomena to occur at room temperature. There are very few compounds that fulfil this requirement; examples include $BiFeO_3$ and β-$NaFeO_2$.

Magnetoelectric properties have been observed in many compounds with different structures and chemical compositions. However, they all have a geometrical magnetic frustration in common, which induces competition among multiple magnetic ground states. Furthermore, a magnetic phase transition is thought to be an essential ingredient for realizing a non-linear colossal response in the electric properties. In the colossal effect, the two properties not only coexist but couple strongly in their order parameter. Most novel multiferroic materials exhibit a cycloidal component to the magnetic structure; this has been considered as a guiding principle for tailoring new materials based on the non-collinearity of the spins. Many cycloidal compounds exhibit a small ferromagnetic component in their antiferromagnetic order, giving rise to the Dzyaloshinskii–Moriya interaction. We shall concentrate here on two systems linked by frustration in the magnetic ordering, namely orthovanadates and the manganites of the rare earths.

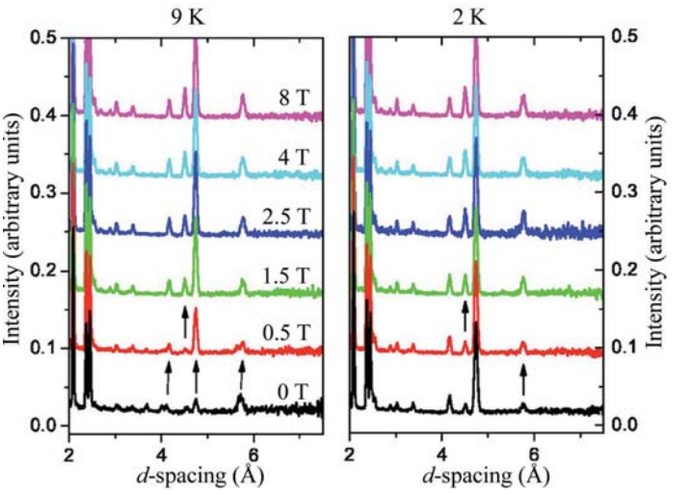

Figure 2.8.14
Neutron powder diffraction data for $Co_3V_2O_8$ at 9 K (left) and 2 K (right) under magnetic fields of 0, 0.5, 1.5, 2.5, 4.0 and 8.0 T. Data from a bank of detectors situated at the scattering angle 35° are shown. The arrows indicate the changes between the data at different fields. Individual curves are offset arbitrarily for display purposes. Reprinted with permission from Wilson *et al.* (2007). Copyright (2007) by the American Physical Society.

2.8.3.3.2.1. *Kagomé staircase systems*

Among the orthovanadates of 3*d* metals, $Co_3V_2O_8$ and $Ni_3V_2O_8$ have been identified as kagomé staircase magnetic structures, which exhibit a considerable number of phase transitions at low temperature. Their crystal structure was determined by Fuess *et al.* (1970) as orthorhombic (space group *Cmca*). Ferromagnetic order was found for the cobalt compound and an indication of antiferromagnetism for the nickel compound at 4.2 K. The crystal structure is characterized by edge-sharing CoO_6 octahedra forming buckled layers of corner-sharing triangles, called kagomé staircases, separated by VO_4 tetrahedra. The magnetic ions (Co or Ni) are situated at the corners of triangles, thus leading to spin frustration. Therefore, if a small amount of energy is supplied by an external magnetic field, a whole sequence of magnetic phase transitions can be introduced. The previously determined ferromagnetic order as the ground state for $Co_3V_2O_8$ was confirmed by Wilson *et al.* (2007). They also reported field-dependent neutron powder diffraction studies under a field of 8 T at 2 and 9 K (Fig. 2.8.14). At 9 K the system has an incommensurate magnetic structure. At a field as low as 0.5 T, new magnetic peaks indexed in a commensurate structure occur, accompanied by a shift in the position of others. The incommensurate ordering disappears completely at a higher field and a purely ferromagnetic behaviour is observed, similar to the low-temperature ground state at zero field. At 2 K and 8 T no additional magnetic reflections are observed but changes in the intensity of several existing ones are seen. The refinement of the magnetic structure based on these data indicated a change of the spin direction in the ferromagnetic arrangement as compared with the zero-field low-temperature structure. Furthermore, the magnetic moments on the two different Co sites in the structure are aligned under the field and reach the same value of 3.15 μ_B on both sites, which is similar to the spin-only moment of cobalt.

The reorientation of spins and the complete magnetic field *versus* temperature (*H*–*T*) phase diagram of the multiferroic $Ni_3V_2O_8$ has been reported (Kenzelmann *et al.*, 2006). The inversion symmetry of space group *Cmca* is broken at low temperature and a commensurate phase is observed. Thus, over a

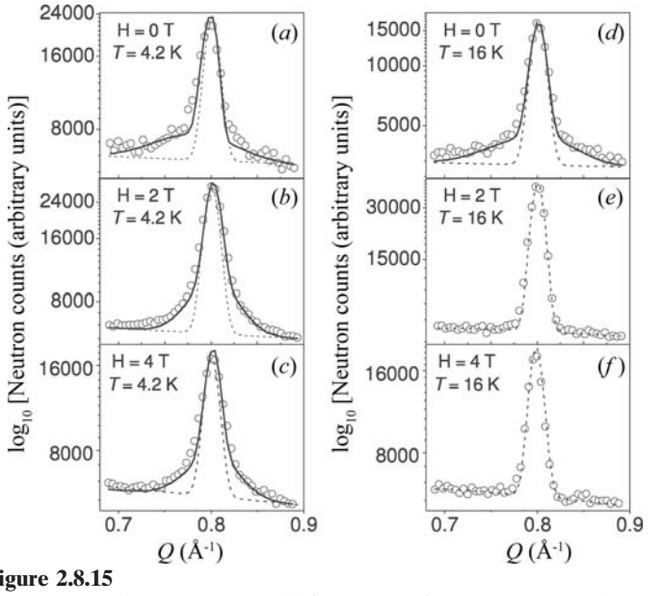

Figure 2.8.15
The observed Bragg reflection 100 (open circles) under an applied field of (*a*) 0 T, (*b*) 2 T and (*c*) 4 T at 4.2 K and (*d*) 0 T, (*e*) 2 T and (*f*) 4 T at 16 K (taken from Yusuf *et al.*, 2013). Copyright IOP Publishing. Reproduced with permission. All rights reserved.

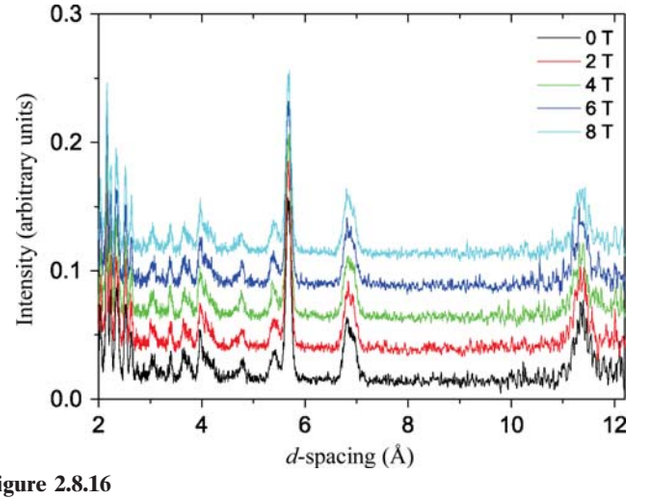

Figure 2.8.16
Time-of-flight diffraction patterns of YMn_2O_5 at 1.6 K under magnetic fields between 0 and 8 T (taken from Radaelli & Chapon, 2008). Copyright IOP Publishing. Reproduced with permission. All rights reserved.

narrow temperature range a macroscopic polar vector leads to a multiferroic behaviour. As this study was based on single-crystal neutron measurements, no further details are given here. Frustrated triangular-lattice Ising antiferromagnets have degenerate magnetic ground states, which give rise to very complex magnetic structures. As there are only small differences in the competing exchange interaction in such frustrated triangular-lattice compounds, a sequence of phase transitions is introduced by changes in temperature or magnetic field. The compound $Ca_3Co_2O_6$ is another example of a frustrated system. Field-dependent powder diffraction patterns were reported for the doped system $Ca_3Co_{1.8}Fe_{0.2}O_6$ by Yusuf *et al.* (2013). They distinguished the short-range magnetic order (SRO), reflected in the half-width of the Bragg reflections (Fig. 2.8.15), from the long-range order as given by the Bragg positions. They stated that even under magnetic fields up to 4 T the broadening of Bragg reflections indicates the persistence of SRO. In a field of 2 T, the observed change in the structure from incommensurate to commensurate indicates a reduction of spin frustration. In fields of 4 T, a ferrimagnetic system is introduced, followed by a ferromagnetic one above 5 T.

2.8.3.3.2.2. Manganite systems

Like the vanadates, in the class of rare-earth manganites of the type RMn_2O_5 successive magnetic phase transitions between commensurate (CO) and incommensurate phases (ICP) can occur. Intensive investigations have been undertaken to understand the relationship between their magnetic and dielectric properties. The spontaneous electric polarization is induced by a magnetic transition. Thus the primary order parameter is magnetic rather than structural. Among the rare-earth compounds, those containing Nd or an element lighter than Nd do not exhibit ferroelectricity. In all these materials a broken magnetic symmetry at lower temperatures leads to a polar symmetry group. In addition, a cycloidal component indicates a common underlying mechanism. The Mn^{3+} and Mn^{4+} ions are fully charge-ordered. Neutron diffraction studies of these phases have been performed by Radaelli & Chapon (2008), who also analysed the possible exchange pathways. In $TbMn_2O_5$ the *H–T* phase diagram of the commensurate–low-temperature–incommensurate (CO–LT–ICP) magnetic transitions shows an upward jump in the transition temperature from ∼25 K at zero field to 27 K at 9 T. The low-temperature ICP phase is stabilized under an external field for $TbMn_2O_5$ and the dielectric constant is enhanced. It was concluded that Tb and Mn order independently, implying the absence of coupling terms between them. Strong support for this suggestion was provided by an in-field neutron study on the analogue YMn_2O_5. Neither the positions nor the intensities of the magnetic Bragg reflections were affected by the magnetic field (Fig. 2.8.16). The magnetic low-temperature ICP phase in the Tb compound was stabilized under a magnetic field. This is in contrast to observations on $HoMn_2O_5$ by Kimura *et al.* (2007), using single crystals. In both cases, however, the neutron data correlate directly with the results obtained by dielectric measurements under a magnetic field. The difference in the behaviours is thus confirmed. The two studies also reveal different magnetic order at low temperatures. The same magnetic sequence at low temperatures as for Tb was observed in YMn_2O_5, which does not contain a magnetic rare-earth element. Under fields up to 8 T the positions and the intensities of the magnetic Bragg reflections remained unchanged, showing that the antiferromagnetic structure of the manganese sublattice is extremely stable. As in the vanadates, the main reason for the sequence of magnetic structures is frustration of the manganese spins. Without going too deeply into the details of the different exchange pathways and orbital occupancies, one factor behind this behaviour is the Jahn–Teller effect of the Mn^{3+} ion, which is also relevant in the multiferroic $TbMnO_3$ as part of the $RMnO_3$ family (Kimura *et al.*, 2003). Another feature often found in multiferroic systems is the small ferromagnetic component caused by small spin canting due to Dzyaloshinskii–Moriya interactions. This property strongly influences the low-temperature magnetism in RMn_2O_5 (Kimura *et al.*, 2009).

2.8.3.3.3. *Additional systems and scattering techniques*

Information about the anisotropy of the local magnetic susceptibility at different magnetic sites has been extracted from diffraction patterns for a $Tb_2Sn_2O_7$ powder measured using polarized neutrons under magnetic fields of 1 and 5 T (Gukasov

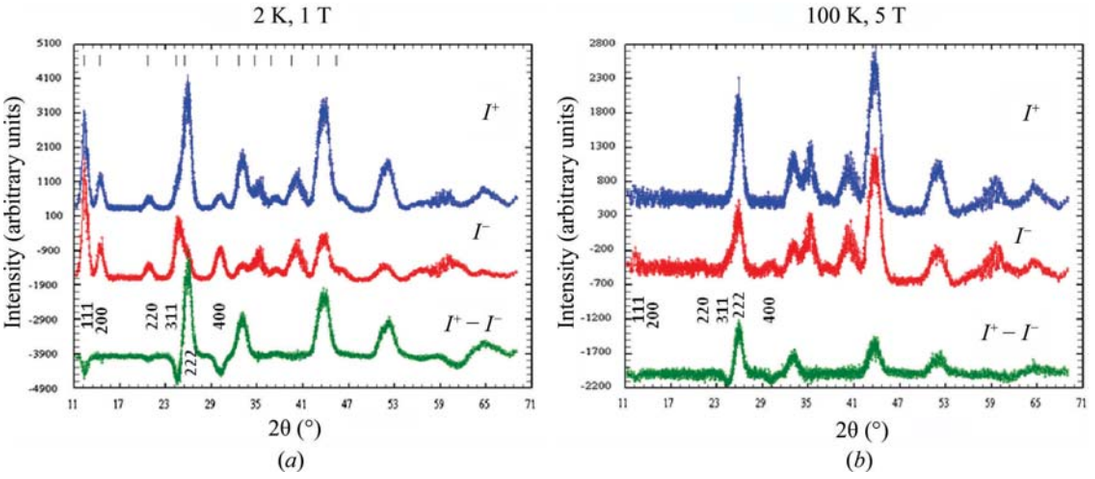

Figure 2.8.17
Polarized neutron diffraction patterns for $Tb_2Sn_2O_7$ at 2 K and 1 T (*a*) and 100 K and 5 T (*b*). I^+ and I^- are the intensities for spin-up and spin-down neutrons, respectively. Taken from Gukasov & Brown (2010). Copyright IOP Publishing. Reproduced with permission. All rights reserved.

& Brown, 2010). No magnetic contribution to the diffracted intensities was observed at 2 K in the absence of an external field. However, applying a field led to considerable changes in the diffraction pattern (Fig. 2.8.17). At 100 K and 5 T, the intensities of the reflections that are allowed for the cubic space group $Fd\bar{3}m$ increase considerably. Furthermore, they were found to depend strongly on the polarization of the incoming neutrons, as shown by the difference pattern in Fig. 2.8.17. At a field of 1 T, new reflections appear (Fig. 2.8.17*a*) that are forbidden for the occupied sites in $Fd\bar{3}m$ symmetry, such as 200, 222 and 240. The intensities of these new reflections do not change with the polarization of the neutrons, as demonstrated in the difference plot, hence they are purely magnetic. In conclusion, information on local anisotropic magnetic susceptibility at different sites can be obtained by using a combination of unpolarized and polarized neutron powder patterns. This demonstrates the usefulness of polarized neutron scattering, even for polycrystalline samples.

We now return to X-ray investigations of magnetic materials. A laboratory device for fields up to 5 T and temperatures above room temperature was mentioned in Section 2.8.3.3.1. The corresponding low-temperature apparatus (Koyama *et al.*, 2013) has produced results on magneto-caloric compounds of MnFeP-type materials. Substitution of P in $MnFeP_{1-x}Z_x$ with Z = As or Ge produces materials that exhibit a large magneto-caloric effect and thus allows control of the Curie temperature by chemical composition. Studies under magnetic fields are mandatory, as the refrigerants are working under a field. For two different compositions of the As compound the lattice parameters change drastically and the cell volume decreases with increasing magnetic field strength. In $MnFeP_{0.78}Ge_{0.22}$ a field-induced ferromagnetic phase was observed near the Curie temperature at 280 K. This phase is, however, not identical to the low-temperature ferromagnetic one (Koyama *et al.*, 2013).

2.8.3.3.4. *Concluding remarks*

Despite some shortcomings, powder diffraction studies as a function of magnetic fields are valuable for the qualitative and sometimes even quantitative interpretation of magnetic materials. Unpolarized neutrons are used in most experiments, but the additional information from polarized neutrons has also been exploited. X-rays do not interact directly with the magnetic moments, but structural changes as a consequence of magnetic phase transitions have been observed in several cases. *In situ* powder diffraction under magnetic fields reaching 4 T on an X-ray diffractometer with a rotating anode revealed details of lattice parameters and atomic positions in rare-earth alloys with a higher precision than that accessible by neutron diffraction (Pecharsky *et al.*, 2007). Furthermore, the two test-case compounds studied, Gd_5Ge_4 and $DyCo_2$, contain the rare-earth elements Gd and Dy with the highest absorption cross sections for neutrons in their natural isotope abundance. The data were used to refine the underlying structure models by Rietveld analysis. Advances in X-ray and neutron sources and optics delivered higher resolution and flux to the samples, which in combination with rapid computing made real-time experiments feasible.

2.8.4. Summary

We have shown here that *in situ* studies under electric and magnetic fields are in a well advanced state. Laboratory equipment can be used for diverse experiments where changes occur on a timescale that can be followed with an exposure time of minutes. Real progress is, however, achieved by using high-energy synchrotron radiation and by using neutrons, which can penetrate larger volumes. Thus *in operando* studies of real devices are feasible. In addition to such diffraction experiments, which provide average information on a macroscopic length scale, complementary experiments like electron microscopy are vital for revealing local structural information. Only the combination of several methods can give sufficient insight into structure–property relationships and the functionality of materials.

References

Adam, R., Wadewitz, D., Gruner, W., Klemm, V., Ehrenberg, H. & Rafaja, D. (2013). *Phase and microstructure development in the conversion type electrodes for Li-ion batteries based on the Cu-Fe-O system. J. Electrochem. Soc.* **160**, A1594–A1603.

Anastasopoulos, M., Bebb, R., Berry, K., Birch, J., Bryś, T., Buffet, J.-C., Clergeau, J.-F., Deen, P. P., Ehlers, G., van Esch, P., Everett, S. M., Guerard, B., Hall-Wilton, R., Herwig, K., Hultman, L., Höglund, C., Iruretagoiena, I., Issa, F., Jensen, J., Khaplanov, A., Kirstein, O., Higuera, I. L., Piscitelli, F., Robinson, L., Schmidt, S. & Stefanescu, I. (2017). *Multi-grid detector for neutron spectroscopy: results obtained on time-of-flight spectrometer CNCS. J. Instrum.* **12**, P04030.

Anton, E.-M., Schmitt, L. A., Hinterstein, M., Trodahl, J., Kowalski, B., Jo, W., Kleebe, H.-J., Rödel, J. & Jones, J. L. (2012). *Structure and temperature-dependent phase transitions of lead-free $Bi_{1/2}Na_{1/2}TiO_3$–$Bi_{1/2}K_{1/2}TiO_3$–$K_{0.5}Na_{0.5}NbO_3$ piezoceramics. J. Mater. Res.* **27**, 2466–2478.

Ballabriga, R., Campbell, M., Heijne, E. H. M., Llopart, X. & Tlustos, L. (2007). *The Medipix3 prototype, a pixel readout chip working in single photon counting mode with improved spectrometric performance. IEEE Trans. Nucl. Sci.* **54**, 1824–1829.

Bergamaschi, A., Cervellino, A., Dinapoli, R., Gozzo, F., Henrich, B., Johnson, I., Kraft, P., Mozzanica, A., Schmitt, B. & Shi, X. (2009). *Photon counting microstrip detector for time resolved powder diffraction experiments. Nucl. Instrum. Methods Phys. Res. A*, **604**, 136–139.

Bergström, Ö., Andersson, A. M., Edström, K. & Gustafsson, T. (1998). *A neutron diffraction cell for studying lithium-insertion processes in electrode materials. J. Appl. Cryst.* **31**, 823–825.

Bergström, O., Gustafsson, T. & Thomas, J. O. (1998). *An X-ray powder diffraction attachment for in situ studies of ion insertion processes in electrode materials. J. Appl. Cryst.* **31**, 103–105.

Bird, M. D., Hongyu Bai, Bole, S., Jingping Chen, Dixon, I. R., Ehmler, H., Gavrilin, A. V., Painter, T. A., Smeibidl, P., Toth, J., Weijers, H., Ting Xu & Zhai, Y. (2009). *The NHMFL hybrid magnet projects. IEEE Trans. Appl. Supercond.* **19**, 1612–1616.

Brown, F. J. (2010). *Aspects of superconducting magnet design for neutron scattering sample environments. J. Phys. Conf. Ser.* **251**, 012093.

Cabana, J., Monconduit, L., Larcher, D. & Palacín, M. (2010). *Beyond intercalation-based Li-ion batteries: the state of the art and challenges of electrode materials reacting through conversion reactions. Adv. Mater.* **22**, E170–E192.

Cartier, S., Bergamaschi, A., Dinapoli, R., Greiffenberg, D., Johnson, I., Jungmann, J. H., Mezza, D., Mozzanica, A., Schmitt, B., Shi, X., Stampanoni, M., Sun, J. & Tinti, G. (2014). *Micron resolution of MÖNCH and GOTTHARD, small pitch charge integrating detectors with single photon sensitivity. J. Instrum.* **9**, C05027.

Choe, H., Gorfman, S., Hinterstein, M., Ziolkowski, M., Knapp, M., Heidbrink, S., Vogt, M., Bednarcik, J., Berghäuser, A., Ehrenberg, H. & Pietsch, U. (2015). *Combining high time and angular resolutions: time-resolved X-ray powder diffraction using a multi-channel analyser detector. J. Appl. Cryst.* **48**, 970–974.

Daniels, J. E. & Drakopoulos, M. (2009). *High-energy X-ray diffraction using the Pixium 4700 flat-panel detector. J. Synchrotron Rad.* **16**, 463–468.

Daniels, J. E., Finlayson, T. R., Studer, A. J., Hoffman, M. & Jones, J. L. (2007). *Time-resolved diffraction measurements of electric-field-induced strain in tetragonal lead zirconate titanate. J. Appl. Phys.* **101**, 094104.

Daniels, J. E., Jo, W., Rödel, J., Honkimäki, V. & Jones, J. L. (2010). *Electric-field-induced phase-change behavior in $(Bi_{0.5}Na_{0.5})TiO_3$–$BaTiO_3$–$(K_{0.5}Na_{0.5})NbO_3$: a combinatorial investigation. Acta Mater.* **58**, 2103–2111.

Eckold, G., Schober, H. & Nagler, S. E. (2010). Editors. *Studying Kinetics with Neutrons. Springer Series in Solid State Sciences.* Berlin, Heidelberg: Springer.

Eriksson, T., Andersson, A. M., Bergström, Ö., Edström, K., Gustafsson, T. & Thomas, J. O. (2001). *A furnace for in situ X-ray diffraction studies of insertion processes in electrode materials at elevated temperatures. J. Appl. Cryst.* **34**, 654–657.

Fuess, H., Bertaut, E. F., Pauthenet, R. & Durif, A. (1970). *Structure aux rayons X, neutrons et propriétés magnétiques des orthovanadates de nickel et de cobalt. Acta Cryst.* B**26**, 2036–2046.

Gukasov, A. & Brown, P. J. (2010). *Determination of atomic site susceptibility tensors from neutron diffraction data on polycrystalline samples. J. Phys. Condens. Matter*, **22**, 502201.

Hansen, T. C., Henry, P. F., Fischer, H. E., Torregrossa, J. & Convert, P. (2008). *The D20 instrument at the ILL: a versatile high-intensity two-axis neutron diffractometer. Meas. Sci. Technol.* **19**, 034001.

Herklotz, M., Scheiba, F., Hinterstein, M., Nikolowski, K., Knapp, M., Dippel, A.-C., Giebeler, L., Eckert, J. & Ehrenberg, H. (2013). *Advances in in situ powder diffraction of battery materials: a case study of the new beamline P02.1 at DESY, Hamburg. J. Appl. Cryst.* **46**, 1117–1127.

Hinterstein, M. (2011). *Mikrostrukturanalyse von Piezokeramiken mit Hilfe von Synchrotron- und Neutronenstrahlung*. Goettingen: Sierke Verlag.

Hinterstein, M., Hoelzel, M., Rouquette, J., Haines, J., Glaum, J., Kungl, H. & Hoffman, M. (2015). *Interplay of strain mechanisms in morphotropic piezoceramics. Acta Mater.* **94**, 319–327.

Hinterstein, M., Knapp, M., Hölzel, M., Jo, W., Cervellino, A., Ehrenberg, H. & Fuess, H. (2010). *Field-induced phase transition in $Bi_{1/2}Na_{1/2}TiO_3$-based lead-free piezoelectric ceramics. J. Appl. Cryst.* **43**, 1314–1321.

Hinterstein, M., Rouquette, J., Haines, J., Papet, P., Glaum, J., Knapp, M., Eckert, J. & Hoffman, M. (2014). *Structural contribution to the ferroelectric fatigue in lead zirconate titanate ceramics. Phys. Rev. B*, **90**, 094113.

Hinterstein, M., Rouquette, J., Haines, J., Papet, Ph., Knapp, M., Glaum, J. & Fuess, H. (2011). *Structural description of the macroscopic piezo- and ferroelectric properties of lead zirconate titanate. Phys. Rev. Lett.* **107**, 077602.

Hinterstein, M., Schmitt, L. A., Hoelzel, M., Jo, W., Rödel, J., Kleebe, H.-J. & Hoffman, M. (2015). *Cyclic electric field response of morphotropic $Bi_{1/2}Na_{1/2}TiO_3$-$BaTiO_3$ piezoceramics. Appl. Phys. Lett.* **106**, 222904.

Hirota, K., Wakimoto, S. & Cox, D. E. (2006). *Neutron and X-ray scattering studies of relaxors. J. Phys. Soc. Jpn*, **75**, 111006.

Hodeau, J. L., Bordet, P., Anne, M., Prat, A., Fitch, A. N., Dooryheé, E., Vaughan, G. & Freund, A. (1998). *Nine-crystal multianalyzer stage for high-resolution powder diffraction between 6 keV and 40 keV. Proc. SPIE*, **3448**, 353–361.

Hoelzel, M., Senyshyn, A., Gilles, R., Boysen, H. & Fuess, H. (2007). *Scientific review: the structure powder diffractometer SPODI. Neutron News*, **18**, 23–26.

Hoelzel, M., Senyshyn, A., Juenke, N., Boysen, H., Schmahl, W. & Fuess, H. (2012). *High-resolution neutron powder diffractometer SPODI at research reactor FRM II. Nucl. Instrum. Methods Phys. Res. A*, **667**, 32–37.

Hoffmann, M. J., Hammer, M., Endriss, A. & Lupascu, D. C. (2001). *Correlation between microstructure, strain behavior, and acoustic emission of soft PZT ceramics. Acta Mater.* **49**, 1301–1310.

Jin, Y. M., Wang, Y. U., Khachaturyan, A. G., Li, J. E. & Viehland, D. (2003). *Conformal miniaturization of domains with low domain-wall energy: monoclinic ferroelectric states near the morphotropic phase boundaries. Phys. Rev. Lett.* **91**, 197601.

Johnsen, R. E. & Norby, P. (2013). *Capillary-based micro-battery cell for in situ X-ray powder diffraction studies of working batteries: a study of the initial intercalation and deintercalation of lithium into graphite. J. Appl. Cryst.* **46**, 1537–1543.

Johnson, I., Bergamaschi, A., Billich, H., Cartier, S., Dinapoli, R., Greiffenberg, D., Guizar-Sicairos, M., Henrich, B., Jungmann, J., Mezza, D., Mozzanica, A., Schmitt, B., Shi, X. & Tinti, G. (2014). *Eiger: a single-photon counting X-ray detector. J. Instrum.* **9**, C05032.

Jones, J. L. (2007). *The use of diffraction in the characterization of piezoelectric materials. J. Electroceram.* **19**, 69–81.

Jones, J., Hoffman, M., Daniels, J. E. & Studer, A. J. (2006). *Direct measurement of the domain switching contribution to the dynamic piezoelectric response in ferroelectric ceramics. Appl. Phys. Lett.* **89**, 092901.

Jones, J. L., Pramanick, A., Nino, J. C., Maziar Motahari, S., Üstündag, E., Daymond, M. R. & Oliver, E. C. (2007). *Time-resolved and orientation-dependent electric-field-induced strains in lead zirconate titanate ceramics. Appl. Phys. Lett.* **90**, 172909.

Kenzelmann, M., Harris, A. B., Aharony, A., Entin-Wohlman, O., Yildirim, T., Huang, Q., Park, S., Lawes, G., Broholm, C., Rogado, N., Cava, R. J., Kim, K. H., Jorge, G. & Ramirez, A. P. (2006). *Field dependence of magnetic ordering in kagomé-staircase compound. Phys. Rev. B*, **74**, 014429.

Kimura, H., Kamada, Y., Noda, Y., Wakimoto, S., Kaneko, K., Metoki, N., Kakurai, K. & Kohn, K. (2007). *Field-induced dielectric and magnetic phase transitions in multiferroic compounds of RMn_2O_5 (R = Er, Ho). J. Korean Phys. Soc.* **51**, 870–873.

Kimura, H., Noda, Y. & Kohn, K. (2009). *Spin-driven ferroelectricity in the multiferroic compounds of RMn_2O_5. J. Magn. Magn. Mater.* **321**, 854–857.

Kimura, T., Goto, T., Shintani, H., Ishizaka, K., Arima, T. & Tokura, Y. (2003). *Magnetic control of ferroelectric polarization. Nature*, **426**, 55–58.

Köhli, M., Allmendinger, F., Häussler, W., Schröder, T., Klein, M., Meven, M. & Schmidt, U. (2016). *Efficiency and spatial resolution of the CASCADE thermal neutron detector. Nucl. Instrum. Methods Phys. Res. A*, **828**, 242–249.

Koyama, K., Watanabe, K., Tegus, O., Brück, E., Buschow, K. H. J. & de Boer, F. R. (2013). *X-ray powder diffraction studies on $MnFeP_{0.78}Ge_{0.22}$ in high magnetic fields. J. Low Temp. Phys.* **170**, 279–284.

Kraft, P., Bergamaschi, A., Bronnimann, Ch., Dinapoli, R., Eikenberry, E. F., Graafsma, H., Henrich, B., Johnson, I., Kobas, M., Mozzanica, A., Schleputz, C. M. & Schmitt, B. (2009). *Characterization and calibration of PILATUS detectors. IEEE Trans. Nucl. Sci.* **56**, 758–764.

Lee, P. L., Shu, D., Ramanathan, M., Preissner, C., Wang, J., Beno, M. A., Von Dreele, R. B., Ribaud, L., Kurtz, C., Antao, S. M., Jiao, X. & Toby, B. H. (2008). *A twelve-analyzer detector system for high-resolution powder diffraction. J. Synchrotron Rad.* **15**, 427–432.

Levin, I., Reaney, I. M., Anton, E.-M., Jo, W., Rödel, J., Pokorny, J., Schmitt, L. A., Kleebe, H.-J., Hinterstein, M. & Jones, J. L. (2013). *Local structure, pseudosymmetry, and phase transitions in $Na_{1/2}Bi_{1/2}TiO_3$–$K_{1/2}Bi_{1/2}TiO_3$ ceramics. Phys. Rev. B*, **87**, 024113.

Liss, K. D., Hunter, B., Hagen, M., Noakes, T. & Kennedy, S. (2006). *Echidna – the new high-resolution powder diffractometer being built at OPAL. Physica B*, **385–386**, 1010–1012.

Liu, L., Knapp, M., Ehrenberg, H., Fang, L., Fan, H., Schmitt, L. A., Fuess, H., Hoelzel, M., Dammak, H., Thi, M. P. & Hinterstein, M. (2017). *Average vs. local structure and composition-property phase diagram of $K_{0.5}Na_{0.5}NbO_3$–$Bi_{1/2}Na_{1/2}TiO_3$ system. J. Eur. Ceram. Soc.* **37**, 1387–1399.

Mikhailova, D., Schwarz, B., Senyshyn, A., Bell, A. M. T., Skourski, Y., Ehrenberg, H., Tsirlin, A. A., Agrestini, S., Rotter, M., Reichel, P., Chen, J. M., Hu, Z., Li, Z. M., Li, Z. F. & Tjeng, L. H. (2012). *Magnetic properties and crystal structure of SrCoIrO and SrNiIrO. Phys. Rev. B*, **86**, 134409.

Mitsui, Y., Koyama, K. & Watanabe, K. (2009). *X-ray diffraction measurements in high magnetic fields and at high temperatures. Sci. Technol. Adv. Mater.* **10**, 014612.

Mittemeijer, E. J. & Welzel, U. (2012). Editors. *Modern Diffraction Methods*. Weinheim: Wiley-VCH.

Morcrette, M., Rozier, P., Dupont, L., Mugnier, E., Sannier, L., Galy, J. & Tarascon, J.-M. (2003). *A reversible copper extrusion–insertion electrode for rechargeable Li batteries. Nat. Mater.* **2**, 755–761.

Mozzanica, A., Bergamaschi, A., Cartier, S., Dinapoli, R., Greiffenberg, D., Johnson, I., Jungmann, J., Maliakal, D., Mezza, D., Ruder, C., Schaedler, L., Schmitt, B., Shi, X. & Tinti, G. (2014). *Prototype characterization of the JUNGFRAU pixel detector for SwissFEL. J. Instrum.* **9**, C05010.

Nikolowski, K., Baehtz, C., Bramnik, N. N. & Ehrenberg, H. (2005). *A Swagelok-type in situ cell for battery investigations using synchrotron radiation. J. Appl. Cryst.* **38**, 851–853.

Noheda, B., Gonzalo, J. A., Cross, L. E., Guo, R., Park, S. E., Cox, D. E. & Shirane, G. (2000). *Tetragonal-to-monoclinic phase transition in a ferroelectric perovskite: the structure of $PbZr_{0.52}Ti_{0.48}O_3$. Phys. Rev. B*, **61**, 8687–8695.

Ohzuku, T., Ueda, A. & Nagayama, M. (1993). *Electrochemistry and structural chemistry of $LiNiO_2$ (R3m) for 4 volt secondary lithium cells. J. Electrochem. Soc.* **140**, 1862–1870.

Oswald, S., Nikolowski, K. & Ehrenberg, H. (2009). *Quasi in situ XPS investigations on intercalation mechanisms in Li-ion battery materials. Anal. Bioanal. Chem.* **393**, 1871–1877.

Patterson, B. D., Brönnimann, C., Maden, D., Gozzo, F., Groso, A., Schmitt, B., Stampanoni, M. & Willmott, P. R. (2005). *The materials science beamline at the Swiss Light Source. Nucl. Instrum. Methods Phys. Res. B*, **238**, 224–228.

Pecharsky, V. K., Mudryk, Ya. & Gschneidner, K. A. Jr (2007). *In-situ powder diffraction in high magnetic fields. Z. Kristallogr. Suppl.* **26**, 139–145.

Peral, I., McKinlay, J., Knapp, M. & Ferrer, S. (2011). *Design and construction of multicrystal analyser detectors using Rowland circles: application to MAD26 at ALBA. J. Synchrotron Rad.* **18**, 842–850.

Poikela, T., Plosila, J., Westerlund, T., Campbell, M., Gaspari, M. D., Llopart, X., Gromov, V., Kluit, R., van Beuzekom, M., Zappon, F., Zivkovic, V., Brezina, C., Desch, K., Fu, Y. & Kruth, A. (2014). *Timepix3: a 65k channel hybrid pixel readout chip with simultaneous ToA/ToT and sparse readout. J. Instrum.* **9**, C05013.

Poizot, P., Laruelle, S., Grugeon, S., Dupont, L. & Tarascon, J.-M. (2000). *Nano-sized transition-metal oxides as negative-electrode materials for lithium-ion batteries. Nature*, **407**, 496–499.

Pramanick, A., Prewitt, A. D., Cottrell, M. A., Lee, W., Studer, A. J., An, K., Hubbard, C. R. & Jones, J. L. (2010). *In situ neutron diffraction studies of a commercial, soft lead zirconate titanate ceramic: response to electric fields and mechanical stress. Appl. Phys. A*, **99**, 557–564.

Prokhnenko, O., Stein, W.-D., Bleif, H.-J., Fromme, M., Bartkowiak, M. & Wilpert, T. (2015). *Time-of-flight extreme environment diffractometer at the Helmholtz-Zentrum Berlin. Rev. Sci. Instrum.* **86**, 033102.

Radaelli, P. G. & Chapon, L. C. (2008). *A neutron diffraction study of RMn_2O_5 multiferroics. J. Phys. Condens. Matter*, **20**, 434213.

Repper, J., Keller, T., Hofmann, M., Krempaszky, C., Werner, E. & Petry, W. (2009). *Neutron Larmor diffraction for the determination of absolute lattice spacing Adv. X-ray Anal.* **52**, 201–208.

Schmitt, B., Broennimann, C., Eikenberry, E. F., Gozzo, F., Hoermann, C., Horisberger, R. & Patterson, B. (2003). *Mythen detector system. Nucl. Instrum. Methods Phys. Res. A*, **501**, 267–272.

Schmitt, L. A., Hinterstein, M., Kleebe, H.-J. & Fuess, H. (2010). *Comparative study of two lead-free piezoceramics using diffraction techniques. J. Appl. Cryst.* **43**, 805–810.

Schmitt, L. A., Schönau, K. A., Theissmann, R., Fuess, H., Kungl, H. & Hoffmann, M. J. (2007). *Composition dependence of the domain configuration and size in $Pb[Zr_{1-x}Ti_x]O_3$ ceramics. J. Appl. Phys.* **101**, 074107.

Schneider-Muntau, H.-J., Gavrilin, A. V. & Swenson, C. A. (2006). *Magnet technology beyond 50 T. IEEE Trans. Appl. Supercond.* **16**, 926–933.

Schönau, K. A., Knapp, M., Kungl, H., Hoffmann, M. J. & Fuess, H. (2007). *In situ synchrotron diffraction investigation of morphotropic $Pb[Zr_{1-x}Ti_x]O_3$ under an applied electric field. Phys. Rev. B*, **76**, 144112.

Schönau, K. A., Schmitt, L. A., Knapp, M., Fuess, H., Eichel, R., Kungl, H. & Hoffmann, M. J. (2007). *Nanodomain structure of $Pb[Zr_{1-x}Ti_x]O_3$ at its morphotropic phase boundary: investigations from local to average structure. Phys. Rev. B*, **75**, 184117.

Sears, V. F. (1992). *Neutron scattering lengths and cross sections. Neutron News*, **3**, 26–37.

Senyshyn, A., Dolotko, O., Mühlbauer, M. J., Nikolowski, K., Fuess, H. & Ehrenberg, H. (2013). *Lithium intercalation into graphitic carbons revisited: experimental evidence for twisted bilayer behavior. J. Electrochem. Soc.* **160**, A3198–A3205.

Senyshyn, A., Mühlbauer, M. J., Dolotko, O., Hofmann, M. & Ehrenberg, H. (2015). *Homogeneity of lithium distribution in cylinder-type Li-ion batteries. Sci. Rep.* **5**, 18380.

Senyshyn, A., Mühlbauer, M. J., Nikolowski, K., Pirling, T. & Ehrenberg, H. (2012). *'In-operando' neutron scattering studies on Li-ion batteries. J. Power Sources*, **203**, 126–129.

Shirane, G. (1959). *A note on the magnetic intensities of powder neutron diffraction. Acta Cryst.* **12**, 282–285.

Stefanescu, I., Christensen, M., Fenske, J., Hall-Wilton, R., Henry, P. F., Kirstein, O., Müller, M., Nowak, G., Pooley, D., Raspino, D., Rhodes, N., Šaroun, J., Schefer, J., Schooneveld, E., Sykora, J. & Schweika, W. (2017). *Neutron detectors for the ESS diffractometers. J. Instrum.* **12**, P01019.

Studer, A. J., Hagen, M. E. & Noakes, T. J. (2006). *Wombat: the high-intensity powder diffractometer at the OPAL reactor. Physica B*, **385–386**, 1013–1015.

Suard, E. & Hewat, A. (2001). *The super-D2B project at the ILL. Neutron News*, **12**, 30–33.

Toraya, H., Hibino, H. & Ohsumi, K. (1996). *A new powder diffractometer for synchrotron radiation with a multiple-detector system. J. Synchrotron Rad.* **3**, 75–83.

Weirich, T. E., Lábár, J. L. & Zuo, X. (2006). Editors. *Electron Crystallography. Nato Science Series, Series II: Mathematics, Physics and Chemistry*, Vol. 211. Heidelberg: Springer-Verlag.

Whittingham, M. S. (1976). *Electrical energy storage and intercalation chemistry. Science*, **192**, 1126–1127.

Wilson, N. R., Petrenko, O. A. & Chapon, L. C. (2007). *Magnetic phases in the kagomé staircase compound studied using powder neutron diffraction. Phys. Rev. B*, **75**, 094432.

Yoo, C.-S., Wei, H., Chen, J.-Y., Shen, G., Chow, P. & Xiao, Y. (2011). *Time- and angle-resolved X-ray diffraction to probe structural and chemical evolution during Al-Ni intermetallic reactions. Rev. Sci. Instrum.* **82**, 113901.

Yusuf, S. M., Jain, A. & Keller, L. (2013). *Field induced incommensurate-to-commensurate magnetic phase transition in $Ca_3Co_{1.8}Fe_{0.2}O_6$: a neutron diffraction study. J. Phys. Condens. Matter*, **25**, 146001.

Zhang, S. T., Kounga, A. B., Aulbach, E., Ehrenberg, H. & Rödel, J. (2007). *Giant strain in lead-free piezoceramics $Bi_{0.5}Na_{0.5}TiO_3$–$BaTiO_3$–$K_{0.5}Na_{0.5}NbO_3$ system. Appl. Phys. Lett.* **91**, 112906.

International Tables for Crystallography (2018). Vol. H, Chapter 2.9, pp. 189–199.

2.9. Cells for *in situ* powder-diffraction investigation of chemical reactions

W. van Beek and P. Pattison

2.9.1. Introduction

In a time-resolved powder-diffraction experiment performed *in situ* (sometimes also called non-ambient diffraction), the aim is to follow the behaviour of a sample as a function of one or more external stimuli. The use of this technique can be roughly divided into two fields: academic research and industrial applications. In academic research, the goal is generally to understand the structure–property relationship of the studied material and then to use this understanding in order to improve the design of materials, pharmaceutical products, synthesis routes, reaction conditions *etc.* In the industrial world, one typically wants to learn whether a particular phase, phase mixture or polymorph arrives at a certain time in a production process. Reaction cells that are well suited to industrial applications may well be inadequate for academic research and *vice versa*. Owing to the huge variety of applications, it is impossible to come up with a generic cell design. In this chapter, we show what information content is accessible for a given combination of X-ray or neutron source and *in situ* cell through various case studies. The enabling technology that has driven these recent developments will be outlined in the next section, followed by an overview of the different types of reaction cells in use at home laboratories and at synchrotron and neutron facilities. Finally, we indicate some areas in which new developments can be expected.

2.9.2. Historical perspective

Within a decade of the discovery of the Bragg law, Westgren & Lindh (1921) had already observed several different polymorphs of iron as a function of temperature using powder diffraction. We have recently celebrated the centenary of the founding of X-ray crystallography, and during this time the use of *in situ* powder diffraction has become immensely popular. Although most of the pioneering powder-diffraction experiments were performed with X-ray tubes and scanning point detectors or with neutrons and an array of detectors, the real breakthrough came with the advent of synchrotron sources, providing high-energy penetrating X-rays, in combination with area detectors. This combination of source and detector type allowed diffraction experiments to be performed with both good angular and time resolution, thus opening up many new applications in chemical, physical, material and biological sciences. The topic of *in situ* cells for chemical reactions is therefore an enormous field and we cannot claim to provide an exhaustive list of instruments. We rather intend to point out the major cell designs, and to provide the reader with an overview to allow them to select the appropriate device for their application and available diffraction apparatus. We have tried to select where possible *in situ* case studies that use the full power of crystallography by solving structures and/or performing Rietveld refinements. A large number of review articles and book chapters written by some of the pioneers in this field have appeared during the last two decades with some overlap but slightly different emphasis. Walton & O'Hare (2000) describe many aspects of the crystallization of inorganic solids. Norby (2006) looks at zeolite synthesis, including an excellent commented reference list. Evans & Radosavljelić Evans (2004) focus on what can be performed with conventional equipment available in many university departments. Majuste *et al.* (2013) illustrate reactions relevant to hydrometallurgy studied with *in situ* synchrotron X-ray diffraction (XRD). Parise *et al.* (2000) also concentrate on synchrotron-based examples, and already foresee the abundance of data coming from modern third-generation powder-diffraction beamlines. Automated analysis tools are still underdeveloped, and we will comment on possible future developments in this area. Norby & Schwarz (2008) discuss powder diffraction under non-ambient conditions using X-ray sources, cells and diamond-anvil cell work. *In situ* gas–solid reactions are discussed by Møller *et al.* (2014), and Sharma *et al.* (2015) review the rapidly growing field of crystallographic–electrochemical investigations for both X-rays and neutrons. References to review articles for neutrons are given below (see Section 2.9.3.4).

2.9.3. Main types of reaction cells

2.9.3.1. *Introduction*

Powder-diffraction experiments can be performed either in transmission or reflection geometries. The diffraction signals can be collected in angular- or energy-dispersive mode with parallel or focused X-ray or neutron beams. Dedicated reaction cells have been developed for all possible permutations of the above variables. Each setup has its own trade-off in terms of time, angular and crystallographic resolution, and intrinsic limitations in data quality. In the last two decades, enormous progress has been made in instrumentation for diffraction experiments. A good example is the development of X-ray detectors where, as a direct consequence of the use of linear or area detectors, a time resolution of seconds or even shorter is now feasible in angular-dispersive mode. These and many other developments, such as more intense laboratory X-ray sources, have redefined the ways in which one can best perform *in situ* experiments. Energy-dispersive systems have lost some of their early advantages with respect to angular-dispersive geometries; nevertheless, there are still good grounds for selecting the energy-dispersive technique for some applications. Similarly, reflection-geometry flat-plate reactors have lost a lot of their early popularity because of well known problems with the diffraction geometry during heating. On the other hand, flat-plate strip heaters can reach thermal ramp rates that are hard to obtain otherwise. Flat-plate reflection-geometry reactors remain the main workhorses in academic and industrial home laboratories (mainly because of the good diffraction intensities which they provide) and several commercial vendors sell these units. Commercial and home-laboratory-developed cells, such as that from Moury *et al.* (2015) for high-pressure hydrogenation experiments, often provide the basis for further studies at central facilities. In this chapter, we intend rather to focus on new types of cells and their use with modern linear and area detectors, also indicating the level of information that can obtained. Microreactors in the form of capillary cells are popular for many different kinds of *in situ* diffraction experiments, and we therefore will review their use in some detail.

2.9.3.2. *Capillary cells*

Capillary cells, also called microreactors, exist in many variations. Depending on the application (temperature, pressure and chemical environment), capillaries may be made of polyimide, glass, quartz, single-crystal sapphire or steel. They are simple and extremely efficient devices which can accommodate a large number of different applications. The impetus for their development has mainly come from catalysis research, but they have also been successfully employed to perform *in situ* reactions on intercalation, ion exchange, gas sorption/desorption, cement hardening, hydration–dehydration, light-induced transitions, crystallization processes and polymorphism, to name a few. Capillary cells are almost always used together with temperature- and/or gas-handling (static pressure or flow) devices. In open geometry, or with simple heat shields, one can easily obtain temperatures ranging from 80 to 1000 K with cryogenic and hot-air blowers or resistive heaters close to the sample. Static gas pressures can be as high as 30 MPa and in flow cells 2 MPa is commonly reached, as well as vacuum conditions. Capillary cells were first applied by Clausen (1991) and have been adapted numerous times (Brunelli & Fitch, 2003; Chupas *et al.*, 2008; Jensen *et al.*, 2010; Madsen *et al.*, 2005; Norby *et al.*, 1998, 2000; Palancher *et al.*, 2005) together with gas-handling systems (Eu *et al.*, 2009; Hill, 2013; Krogh Andersen *et al.*, 1998; Llewellyn *et al.*, 2009), with large 6 mm-diameter samples (Andrieux *et al.*, 2014), with supercritical solvents up to 40 MPa with a swing-in blower for rapid heating (Becker *et al.*, 2010) or with pulsed supercritical flows (Mi *et al.*, 2014) for following synthesis reactions. A recent review of several capillary cells for high-pressure reactions (Hansen *et al.*, 2015) also contains useful information on how to calculate burst pressures.

One of the most critical issues is how to create a reliable leak-tight connection between the capillary and the metallic or polyether ether ketone (PEEK) gas/liquid supply line(s). For fragile capillaries there are basically two strategies: either to glue the capillary to a metal support with high-temperature epoxy (see Fig. 2.9.1), or to use ferules. When both ends of a capillary have to be tightened with thin-walled capillaries, the use of ferrules needs some skill (see Fig. 2.9.2).

If the working temperature permits, it is easy and reliable to use a stainless-steel bracket in which capillaries are glued such that all mechanical forces are transferred to the support instead of being taken up by the thin (glass) capillaries (van Beek *et al.*, 2011), as in Fig. 2.9.3. Gas systems are typically constructed from a combination of pressure reducers, mass-flow meters, valves and a manifold which supplies gases to the cell at controlled pressures and flow rates. It is worth pointing out the less-common back-pressure regulator used in Fig. 2.9.3. This unit allows 2 MPa of pressure to be maintained on the sample during flow experiments. Backpressure regulators for much higher pressures are commercially available, but these have so far not been used for *in situ* work. *In situ* diffraction has been coupled with stable-isotope analysis to correlate isotope fractionation with crystal structure. For this, a nonmetallic flowthrough capillary cell that avoids any contamination from the components of the cell itself was designed (Wall *et al.*, 2011). Many hundreds of studies have been performed over the last two decades with capillary devices in the above-mentioned fields.

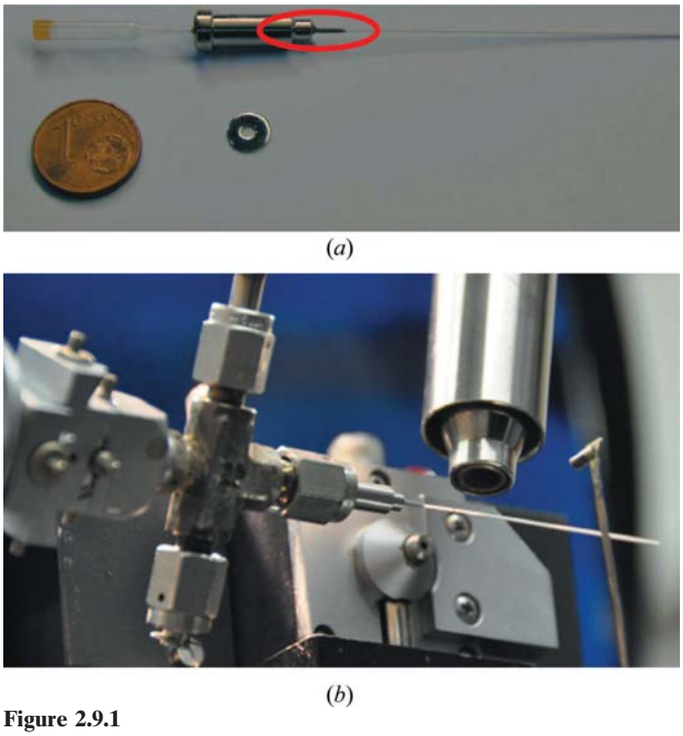

Figure 2.9.1
(*a*) Swagelock VCR gland with an epoxy-glued capillary (red ellipse). (*b*) VCR capillary cell on a beamline with a cryostream (adapted from Jensen *et al.*, 2010).

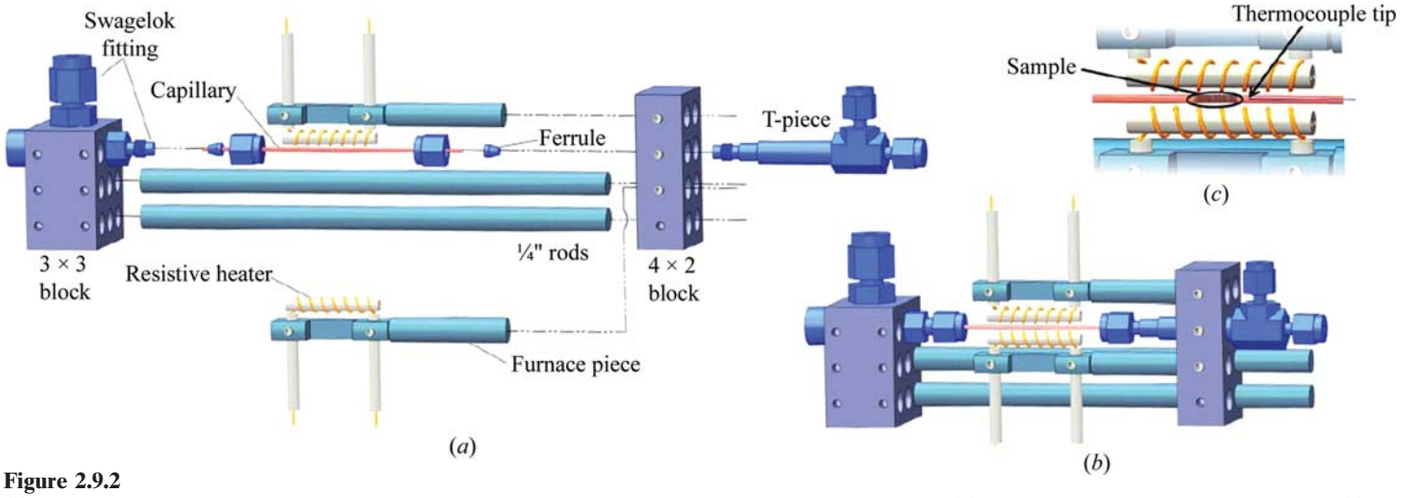

Figure 2.9.2
(*a*) An exploded representation of the flow-cell/furnace components, indicating how they fit together. (*b*) The fully assembled flow cell/furnace. (*c*) An expanded view of the sample region, indicating the relative position of the sample and thermocouple tip within the furnace hot zone (adapted from Chupas *et al.*, 2008).

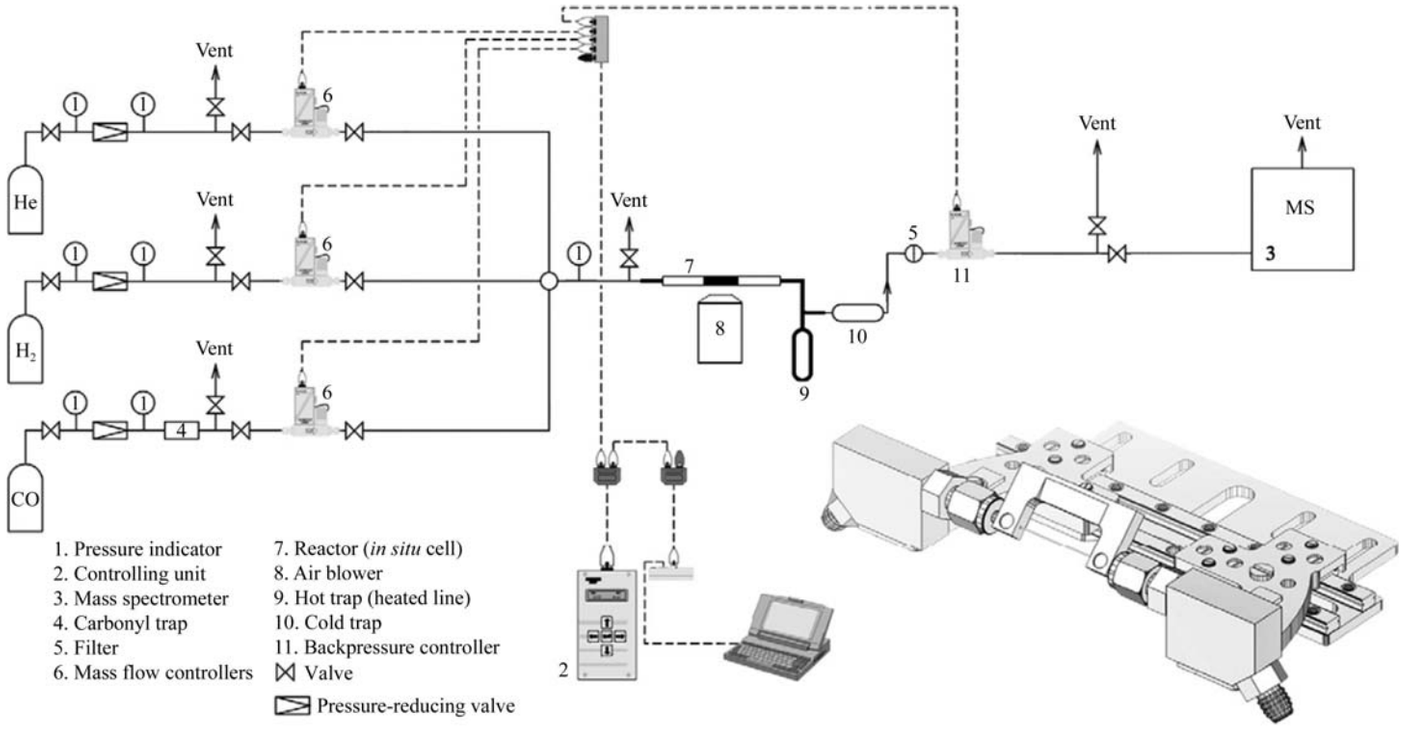

Figure 2.9.3
Sketch of a typical experimental setup and a three-dimensional drawing of the *in situ* flow cell. Note the strain-relief bracket over the capillary. Adapted from Tsakoumis *et al.* (2012), with permission from Elsevier.

Above 800 K, open capillary systems have severe heat loss and the use of insulation or reflectors around the sample or mirror furnaces is more appropriate. See Lorenz *et al.* (1993), Margulies *et al.* (1999), Proffen *et al.* (1995), Riello *et al.* (2013) and Yashima & Tanaka (2004) for special designs to minimize heat loss. Finally, it is worth mentioning the recent work of Figueroa *et al.* (2013), which combines the strong points of the various capillary designs, and also work by Johnsen & Norby (2013), who managed to create and study a working battery in a capillary.

In any powder-diffraction experiment (Warren, 1990), but particularly when using capillary cells, the experimentalist needs to take special care in order to obtain sufficient averaging in terms of grain statistics and to avoid preferred orientation. Typically *ex situ* capillaries are spun, but when gas lines are attached to the sample, spinning is not possible and only rocking or stationary geometry can be used. In addition, a fine (ground) polycrystalline powder giving perfect homogenous Debye–Scherrer rings, even without spinning, often results in an excessive pressure drop due to its high density and packing. In such cases, the sample may need to be pressed into a pellet and then crushed again to obtain larger agglomerates that allow sufficient gas flow through the sample (Jacques *et al.*, 2009). However, relatively large agglomerates, while reducing the packing density, might still give nonhomogeneous powder rings, which affects the intensities, especially on one-dimensional detector systems (strip detectors or crystal-analyser high-resolution systems). For all of these reasons it is not always straightforward to acquire reliable intensities under *in situ* conditions. If, however, proper care is taken, then precise structural parameters can indeed be refined from *in situ* data. For example, Milanesio *et al.* (2003) obtained a detailed view of the structural rearrangements induced by the template-burning process from 350 to 1000 K on a zeolitic MFI framework. Oxygen flowed through a rocking sample and diffraction data were collected on a translating two-dimensional image plate capable of verifying the reliability of the measured

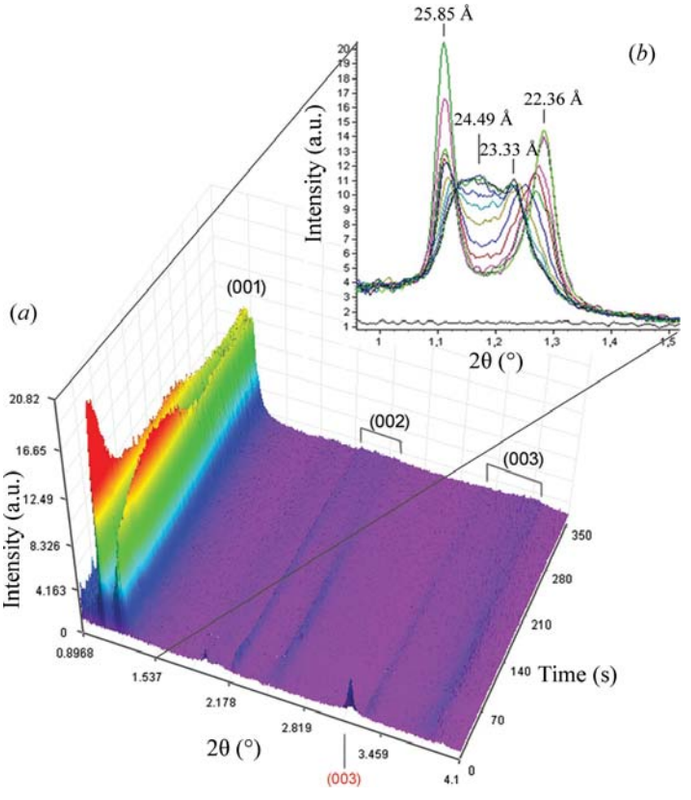

Figure 2.9.4
(*a*) *In situ* three-dimensional stacked plot of the intercalation of ibuprofen into an LDH. Miller indices are shown in black for the intercalation product peaks and in red for the LDH nitrate starting material peaks. (*b*) Two-dimensional patterns showing the low-angle peaks during the first instance of the reaction. Adapted with permission from Conterosito *et al.* (2013). Copyright (2013) American Chemical Society.

intensities with a time resolution of several minutes (Meneghini *et al.*, 2001). From the temperature-dependent *in situ* data, the authors were able to extract the overall template occupancy in the framework. This allowed a definition of the key steps in the template-removal process, namely the start of the template decomposition, the start of the template burning and the end of the template burning. These three steps were then used to explain the cell-parameter evolution and atomic displacement parameters of the Si-framework atoms. Kinetic analysis performed on the results from the Rietveld refinements suggested a diffusion-limited reaction of the volatile products of the template leaving the framework (Milanesio *et al.*, 2003).

Conterosito *et al.* (2013) reduced the time resolution to 100 ms per image using a Pilatus 300 K-W (Kraft *et al.*, 2009) pixel detector installed on an ESRF bending-magnet beamline in combination with a capillary reactor. In these experiments, a mechano-chemical method for fast and clean preparation of exchanged layered double hydroxides (LDHs) was investigated. The inorganic anion in the interlayer region (chloride or nitrate) was exchanged with a series of organic pharmaceutically important molecules. In Fig. 2.9.4, one can see the diffraction patterns of the intercalation process of ibuprofen into an LDH, which allowed the complex mechanism to be understood. Firstly, it is striking to note that the signal from the LDH starting material (the 003 reflection, in red) decreases, while the products and intermediates (001 reflections in black) grow already immediately after the first 100 ms image. Secondly, one can see that the low-angle peaks (<1.5°) show a different behaviour in time, suggesting a two-stage process with an intermediate phase and, thirdly, one sees that the intercalation process is over in ∼4 min. The reliability of the *in situ* procedure was confirmed by comparing the production yield of *ex situ* and *in situ* experiments. Owing to the complex two-stage process, kinetic analysis was not possible in the case of ibuprofen. In the same article, however, it was shown that it was possible to perform a full kinetic analysis on single-stage intercalation processes with different molecules reacting at comparable speeds. It is hard to imagine that so much detail on such timescales could be obtained using other techniques. For example, related intercalation experiments performed with energy-dispersive diffraction (Williams *et al.*, 2009) were, at that time, still limited to 10 s per pattern. Hence it was not possible to study the kinetics of such fast intercalation processes by other means.

Care must be taken to ensure that, when performing experiments at microgram or microlitre levels inside capillaries, the results are still representative of the bulk reaction. Therefore, when studying *in situ* catalytic reactions, it has become common practice to measure the activity or selectivity of the sample with gas chromotography or mass spectrometry (see Fig. 2.9.3) at the same time. It is also well known from reactor engineering that pressured drops, diffusion effects and flow disturbance are important parameters to take into account (Nauman, 2008). The term *operando* was introduced by Bañares (2005) during a discussion with colleagues (Weckhuysen, 2002) for these combined experiments coupling structure with the sample activity.

If the miniaturization turns out to be problematic, one could consider measuring bulky (∼1 cm or more) samples and/or using larger reaction vessels in combination with either energy-dispersive diffraction or extremely high X-ray energies (Tschentscher & Suortti, 1998). This gives the additional advantage that identical sample volumes to those for neutron studies can be used. Hence, one often needs to utilize reaction cells that are specifically designed for the application, as explained in the following section.

2.9.3.3. *Reactions requiring specialist cells*

2.9.3.3.1. *Cells for electrochemistry*

With ever-increasing standards of living, the world is becoming more and more dependent on energy. As natural resources (coal, gas and petrol) are limited, there has been a large impetus towards developing alternative ways of producing and storing energy, while also taking into account environmental issues. Despite many decades of research and tremendous progress in

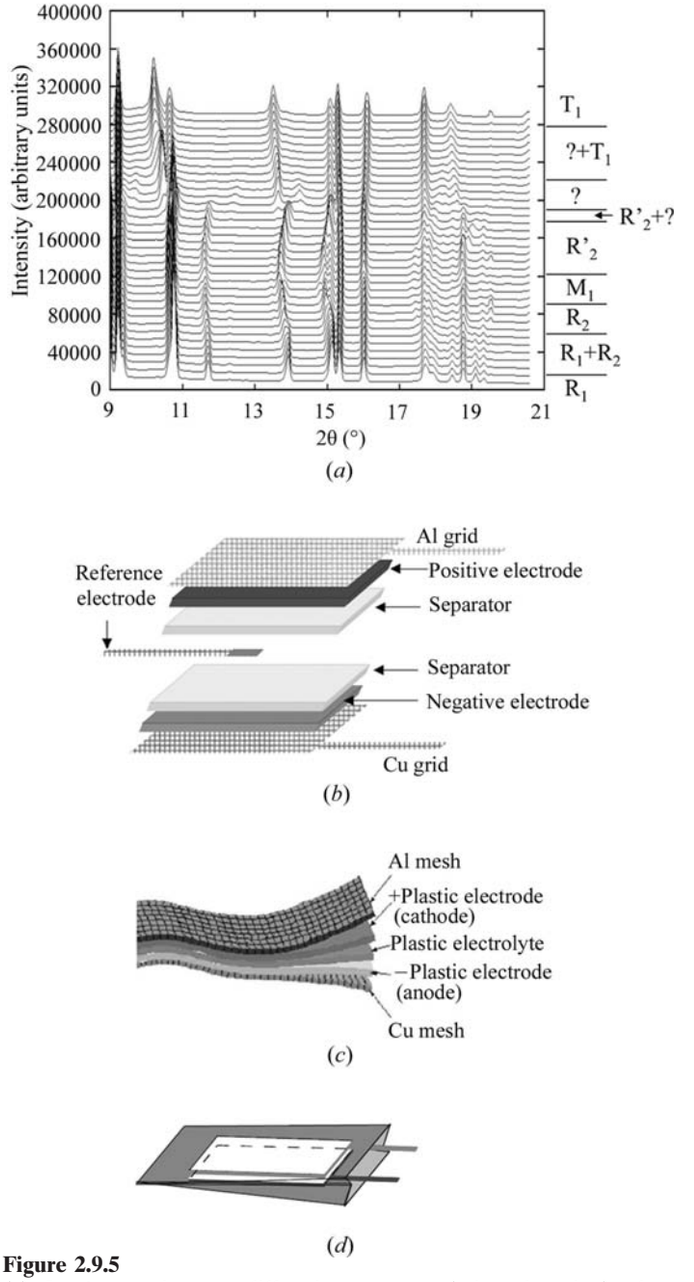

Figure 2.9.5
(*a*) *In situ* synchrotron diffraction patterns (selected region) of an $LiCoO_2$/Li cell collected during cell charging. Below: overview of a Bellcore flat three-electrode plastic Li-ion cell (*b*) with an enlargement (*c*) of the assembly steps during which all the separated laminates are brought together by a thermal fusion process *via* a laminator. The thicknesses of the plastic Li-ion cells assembled for *in situ* X-ray experiments were about 0.4/0.5 mm. A derived version of the Bellcore plastic Li-ion battery with a beryllium window thermally glued to the packing envelope on one side is shown in (*d*). Adapted from Morcrette *et al.* (2002) with permission from Elsevier.

this field, *in situ* diffraction was only adapted for electrochemical research in the 1990s. Nevertheless, this field now has the largest variety of cells. It is impossible to give a comprehensive overview of this complex subject here, and therefore the reader is referred to the articles by Brant *et al.* (2013), De Marco & Veder (2010) and Morcrette *et al.* (2002), which describe how to design and reference most existing miniaturized *in situ* cells. The recent work by Johnsen & Norby (2013), who have developed a capillary-based micro-battery cell, is not included in these reviews. The main advantage of this cell is that it allows diffraction data to be obtained from a single electrode. The recent work on electrochemical cells using conventional diffractometers (Shen *et al.*, 2014) and high-throughput cells for synchrotron applications (Herklotz *et al.*, 2013, 2016) is also relevant. When planning experiments on central facilities, not only appropriate cells but also dedicated ancillary equipment (*e.g.* a glove box) for cell loading owing to air sensitivity of the electrode material (*e.g.* lithium) are essential. In centralized facilities, this may lead to conflicts due to the incompatibility of liquid electrolytes with samples from other users, and dedicated electrochemistry glove boxes have started to appear. As an example of the use of an electrochemical cell, Morcrette *et al.* (2002) managed to perform structural Rietveld refinement during delithiation of an $LiCoO_2$ electrode. In order to obtain reliable intensities, five diffraction images at six different positions in the cell were averaged for each point in the charge cycle. Owing to the amount and quality of the data, six different structural phases could be determined, including lattice parameters, space group, atomic positions and *R* factors (see Fig. 2.9.5). As the potentiostat or galvanostat is driving and measuring the performance of the battery, the structure–activity relationship is obtained automatically. This is a similar concept to the *operando* methodology in catalysis research that uses a mass spectrometer to measure activity.

In analogy with microcapillary cells, miniaturized electrochemistry cells are extremely efficient for studying many aspects of an operational battery despite the fact that a fundamental understanding of electrochemical systems is inherently challenging. All the components of a cell influence each other at the interfaces during the cyclic charge-transfer process. It is also crucial to be able to establish the critical factors that determine the lifetime of the battery. To make efficient use of beamtime, it is common practice to construct many cells within one frame, all operating in parallel. The whole batch of cells is then mounted on translation stages on a diffractometer and measurements are taken periodically. However, miniature cells will never provide a complete picture, and there will always be a need to study large prototype or production cells (Rijssenbeek *et al.*, 2011) of the types discussed in Sections 2.9.3.3.3 and 2.9.3.4.3.

2.9.3.3.2. *Cells with humidity control*

Humidity is a relevant parameter in many areas of research. For instance, the interlayer spacing in clays, corrosion, pharmaceutical processes, cement hardening, phase transitions in minerals or proton conductors and crystal growth of salts are all dependent on relative humidity, often in combination with high temperatures.

Most work so far has been carried out in home laboratories with flat-plate commercial chambers connected to a manifold with a gas mass-flow controller and liquid mass-flow controllers, thus providing an air flow with controlled humidity (Chipera *et al.*, 1997; Kühnel & van der Gaast, 1993; Watanabe & Sato, 1988). In addition, capillary cells have also successfully been used

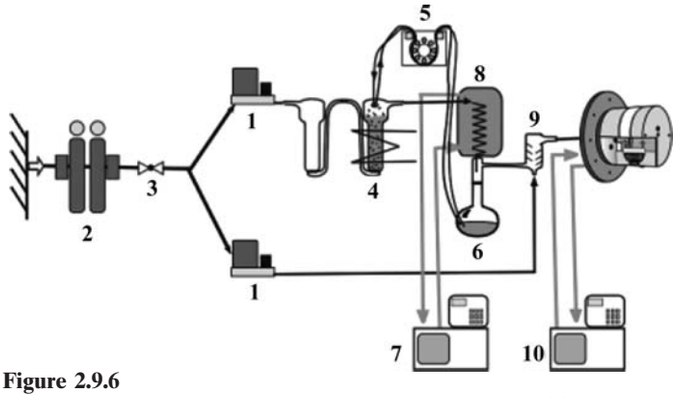

Figure 2.9.6
Schematic drawing of the humidity-control system: (1) mass-flow controller, (2) adsorption dryer, (3) pressure regulator, (4) heated bubbler, (5) peristaltic pump, (6) water reservoir, (7) thermostat, (8) condensation trap, (9) mixing chamber and (10) thermostat. Adapted with permission from Linnow *et al.* (2006). Copyright (2006) American Chemical Society.

(Walspurger *et al.*, 2010) on synchrotrons. It is imperative to have very good thermal stability and to avoid temperature gradients throughout the system. The dew point of water is strongly affected by temperature, and unwanted condensation of water can easily occur on colder parts of the system. Fig. 2.9.6 shows a schematic of a humidity-control system developed by Linnow *et al.* (2006). The thermal management in this design has been optimized to avoid condensation.

Linnow *et al.* (2006) and Steiger *et al.* (2008) have used the system in Fig. 2.9.6 to investigate the crystal growth of various salts, which is considered to be the cause of many failures in building materials (stone, brick, concrete). In order to do so, they scanned through the relative humidity (RH) *versus* temperature phase diagrams of these salts in various porous materials used in the building industry. Diffraction experiments revealed differences in reaction pathways and stress in both host and guest materials.

The NASA Phoenix Mars Lander has discovered perchlorate anions on Mars. This is important, since they could possibly be used as indicators for hydrological cycles. Robertson & Bish (2010) studied a magnesium perchlorate hydrate system, $Mg(ClO_4)_2{\cdot}nH_2O$, with the aim of solving the various unknown crystal structures as a function of water content *n*. Fig. 2.9.7 shows *in situ* diffraction data collected during dehydration in a

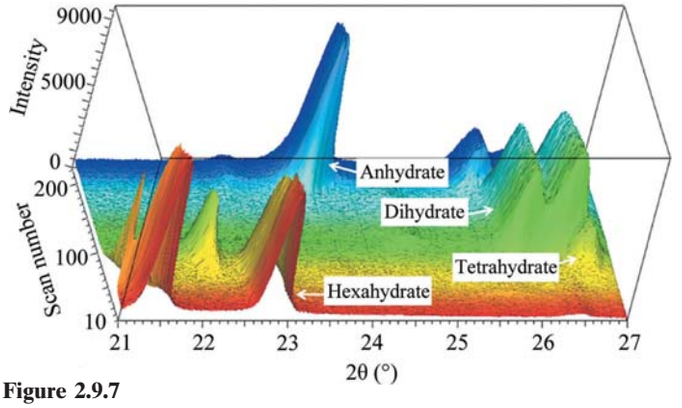

Figure 2.9.7
Sequence of XRD measurements between 21 and 27° 2θ. On heating at a rate of 2° min^{-1} at <1% RH, sequential dehydration was observed, with the anhydrate observed at the highest temperature. The vertical axis represents intensity. The 'time' (scan number) axis represents temperature from 298 to 498 K in 2° min^{-1} increments. Adapted from Robertson & Bish (2010).

commercial Anton Paar flat-plate heating stage connected to an automated RH control system similar to that shown in Fig. 2.9.6. The rapidly collected *in situ* data (30 s per scan, with a position-sensitive detector) were crucial to define at what temperatures longer data collections had to be taken in order to acquire single-phase, high-quality powder patterns suitable for crystal structure solution. Robertson & Bish (2010) managed to index and solve the dihydrate and tetrahydrate phases by charge flipping. Although the tetrahydrate structure was later revised by Solovyov (2012) using the exact same data, this example clearly indicates the level of complexity that can be studied in local laboratories under *in situ* conditions. In this case, this task included understanding the dehydration pathway, solving the structure of $Cl_2H_4MgO_{10}$ with two molecules in the unit cell and refining anisotropic displacement parameters using Rietveld refinement.

2.9.3.3.3. *Large-volume cells for energy-dispersive diffraction*

Large-volume cells have been used to date with great success almost exclusively with energy-dispersive diffraction (EDXRD). Early work on this was carried out by Munn *et al.* (1992) and He *et al.* (1992) using the synchrotron source at Daresbury Laboratory. Walton & O'Hare (2000), who continued the pioneering work, provide a good historical overview of the kinds of studies that can be performed. Norby (2006) also provides excellent references to and explanations of work in this field. In brief, the main advantages of EDXRD are that the X-ray high energies (*i.e.* 50–120 keV) present in the beam can penetrate and probe into large vessels. Furthermore, only minor modifications to create small entrance and exit windows on commercial autoclaves, which are standard equipment in many laboratories, are necessary in order to turn them into extreme-condition *in situ* reaction vessels. An additional advantage arises from the fact that there is no bias due to volume differences between the laboratory experiments and *in situ* reactions studied at the synchrotron (see Fig. 2.9.8).

The variety of scientific applications is huge: pressure-induced phase transitions of inorganic solids, hydrothermal synthesis of microporous solids, intercalation, growth of layered perovskites and breathing in metal-organic frameworks, to name a few examples (see Walton & O'Hare, 2000). Extreme conditions can be reached in terms of temperature (~1273 K) in an autoclave with subsecond XRD time resolution. EDXRD in combination with large-volume autoclaves has provided otherwise-inaccessible information on many processes: intermediates in crystallization routes, activation energies for reactions, and kinetic parameters crucial for their understanding and optimization. The major disadvantage of EDXRD is that the resolution in the diffraction pattern is limited, since it is defined by the energy resolution of the solid-state detector. This effectively excludes all access to precise structural information. However, recent efforts have allowed quantitative phase analysis (Rowles, 2011; Rowles *et al.*, 2012). With the advent of third-generation synchrotrons, which provide orders of magnitude more flux at high energies, and the availability of high-energy flat-panel detectors, angular-dispersive diffraction data can successfully be collected from samples in large-volume cells. Their use expands the available information dramatically. To date, however, there are very few high-energy angular-dispersive beamlines, and the use of the large-volume cells in combination with EDXRD remains an active field and has recently been developed further by, for example, Moorhouse *et al.* (2012) at the Diamond Light Source. The cell there can be equipped with various reaction vessels made of alumina, steel, PTFE-lined steel or glassy carbon tubes depending on the chemical reaction to be studied. It can achieve temperatures as high as 1473 K with infrared lamps and has a magnetic stirrer to avoid sedimentation of the reaction products. In addition, Styles *et al.* (2012) have developed a large furnace and *in situ* cell for salt electrolysis.

Rijssenbeek *et al.* (2011) have studied a full-size battery cell with EDXRD (see Fig. 2.9.9). Diffraction data were collected during charge/discharge at high temperature of the sodium metal halide (Na/MCl_2, M = Ni and/or Fe) cells. They were able to assess the charge-state variations as a function of space and time in the cell during many charge/discharge cycles, and identify local crystal structures and phase distributions. The data confirm the propagation of a known well-defined chemical reaction front beginning at the ceramic separator and proceeding inward.

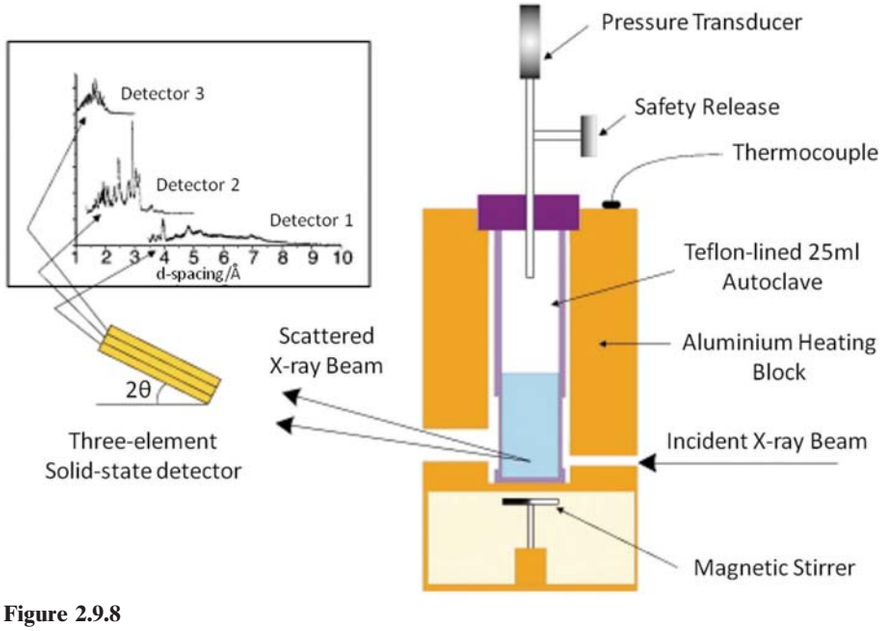

Figure 2.9.8
A schematic of the Oxford/Daresbury hydrothermal autoclave used for energy-dispersive X-ray diffraction studies. Adapted from Walton & O'Hare (2000) with permission of The Royal Society of Chemistry.

2.9.3.3.4. *Large-volume cells for angular-dispersive diffraction*

This application implies the use of monochromatic X-rays with extremely high energies (70 keV and above). Such energies can be easily reached on third-generation synchrotrons with in-vacuum undulators, thus providing sufficient flux for angular-dispersive diffraction experiments. The challenge with these experiments is to have a sufficiently high X-ray energy to penetrate large sample-cell vessels while maintaining reasonably good angular resolution in the diffraction pattern. When using large *in situ* cells with low-energy diffraction, there is a severe peak-broadening effect resulting in a deterioration of the data quality. At high energies, however, where the scattering angles are small, the sample thickness has little effect on the angular resolution provided that the area detector is positioned at a sufficient distance from the sample.

O'Brien *et al.* (2011) explain the trade-offs for such experiments in detail and have shown that it is possible to extract useful structural information. Large-volume cells that used to be exclusively the domain of neutron diffraction and EDXRD have now also been adapted for angular-dispersive powder diffraction with, in some cases, increased speed and information content. For instance, Wragg *et al.* (2012) studed an industrial methanol-to-olefin conversion process with *operando* time- and space-resolved diffraction. The sample is rapidly scanned up and down to provide one-dimensional spatial information. The results complement earlier experiments performed with a microreactor. Jacques *et al.* (2011) extracted three-dimensional information by using dynamic X-ray diffraction computed tomography (XRD-CT). They measured over 50 000 diffraction patterns on beamline ID15 at the ESRF with different sample orientations, positions and temperatures. From this huge amount of data, they reconstructed the catalyst body in three dimensions with a diffraction pattern assigned to each volume unit within the sample as a function of time. With this information, they were able to follow the evolution of the catalytically active phase throughout the sample. Wragg *et al.* (2015) have since performed Rietveld analysis on voxels from the XRD-CT data for a methanol-to-olefin reactor bed. It is also worth mentioning work by Jensen *et al.* (2007), performed on beamline 1-ID at APS Argonne National Laboratory, investigating the kinetics of nanoparticle formation involving a sol–gel reaction in supercritical CO_2 at 10 MPa. The reaction was studied with XRD and small-angle X-ray scattering (SAXS) in a large 30 ml vessel. In a different application, Friščić *et al.* (2013) mounted a laboratory-scale 10 ml ball mill on the ID15 beamline in order to study mechanochemical reactions, which are used in numerous industrial production processes. By averaging ten 400 ms frames, they obtained sufficiently good data to perform full-pattern refinements and kinetic analysis, providing information about otherwise completely inaccessible processes. We therefore foresee a bright future for such extreme high-energy applications together with large-volume studies, since they provide a useful bridge between the academic and industrial worlds.

2.9.3.4. *Cells specifically for neutrons*

2.9.3.4.1. *Introduction*

The special characteristics of neutrons imply both advantages and challenges for the design of *in situ* experiments and their associated equipment. The differences in penetration depths between X-rays and neutrons and the correspondingly smaller scattering cross sections for neutrons, together with the much lower flux densities, imply that cells for neutrons are quite different from the miniature capillary cells for X-rays described in the previous sections. Above all, the sample volume is by necessity often much larger than the equivalent volume required for a laboratory X-ray or synchrotron experiment. However, the ability of neutrons to penetrate deep into sample environments has been of great importance for studying samples at very low temperature, under high pressure or within strong magnetic fields. Similarly, reaction cells for *in situ* investigations profit from the ability of neutrons to penetrate through thick-walled vessels, for example for studying gas–solid reactions under high pressure. Only relatively recently, with the availability of high-energy synchrotron beamlines (>100 keV), can X-rays effectively compete with neutrons in this domain. Even in these cases, the very different scattering properties of neutrons (*e.g.* the strong variation of cross section with isotope) means that some measurements that are challenging, if not impossible, with X-rays can become quite feasible with neutrons. The solid–gas reaction of intermetallic phases with H_2 gas is a good example, where the positions of the interstitial H atoms can be located within a heavy-metal hydride (Kamazawa *et al.*, 2013). Similarly, the hydration of cement has been investigated many times, with improved time resolution resulting from developments in neutron optics and detector performance. *In situ* studies of oxidation reactions have also benefited from the better ability of

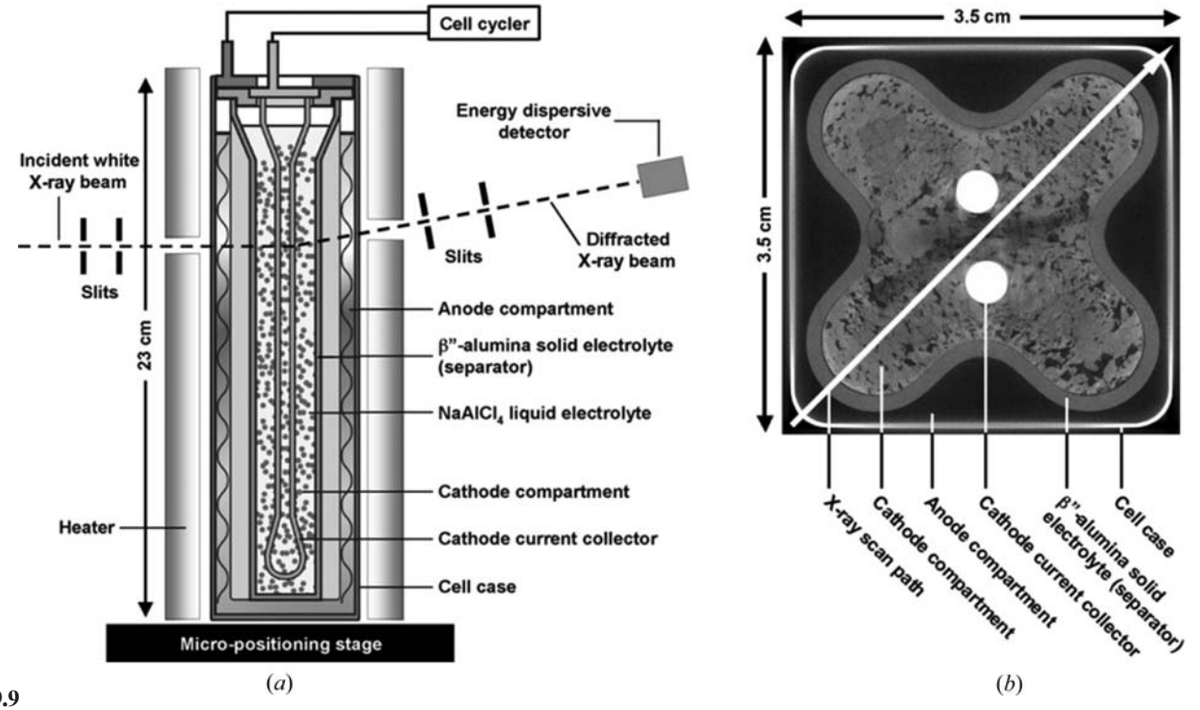

Figure 2.9.9
(*a*) Schematic of a sodium-halide cell in an *in situ* synchrotron EDXRD experimental setup. (*b*) Cross-sectional computed tomography image of a cell. The arrow along the cell diagonal denotes the path of the X-ray line scans used in this work. This corresponds to an X-ray penetration depth of up to 50 mm. Adapted from Rijssenbeek *et al.* (2011) with permission from Elsevier.

neutrons to determine the atomic positions of oxygen during synthesis (Bianchini *et al.*, 2013). The investigation of chemical processes in the electrodes of batteries has, for example, been particularly fruitful. Once again, specialist cells for electrochemistry have been developed that take advantage of the penetration power of the neutrons in order to reveal bulk behaviour within the electrode material. Examples of these and other applications are given in an extensive review of *in situ* and time-resolved neutron scattering (Isnard, 2007) and in the more recent articles by Hansen & Kohlmann (2014), Sharma *et al.* (2015) and Pang & Peterson (2015). It should also be noted that different geometrical arrangements are used in angular-dispersive monochromatic neutron diffraction or when using a fixed-angle detector bank for time-of-flight neutron diffraction, which can have important implications for the cell design. In the following sections, we will examine some of these specialist cells in more detail.

2.9.3.4.2. *Solid–gas reactions*

Suitable storage media for hydrogen and other small molecules include hydrides, hydrates, clathrates and other microporous materials [*e.g.* metal-organic frameworks (MOFs)]. *In situ* neutron powder diffraction has been the method of choice to investigate solid–gas reactions involving light molecules reacting with these types of framework structures, and a wide variety of *in situ* cells have been developed for this purpose. The design of the cell can be quite primitive, yet still be very successful for this kind of application. As a simple example, we consider the study of the reduction of a perovskite-related oxide under flowing hydrogen carried out at D20 at the Institut Laue–Langevin (ILL) in Grenoble (Tonus *et al.*, 2009). The powder sample was loaded into a quartz tube (12 mm diameter) and mounted in the standard D20 furnace. The tube was connected to a flow of reducing gas controlled by a needle valve. High-quality data could be collected in a short time (a few minutes) at high temperature under flowing H_2 gas, in this case up to a maximum temperature of 973 K. Occupancy factors for the different oxygen sites could be refined as a function of temperature under reducing and oxidizing conditions.

In another example, the goal was to investigate solid–gas reactions under pressures of 16 MPa and temperatures up to 673 K (Widenmeyer *et al.*, 2013). Since the use of thin-walled single-crystal sapphire capillaries has become routine in synchrotron powder X-ray diffraction, the authors decided to adopt a similar strategy for the neutron-diffraction experiment. In this case, they selected a 6 mm diameter sapphire tube with steel end caps and metal seals. Pressures of 16 MPa could be achieved over periods of days without measurable pressure loss, and the powder data were of high quality, allowing Rietveld refinement of crystal structures including light-atom positions, displacement parameters and site occupancies. In addition to providing good-quality data and a low background, the sapphire tube also has the advantage of being chemically very robust and hence avoiding, for example, the problem of hydrogen embrittlement.

2.9.3.4.3. *Electrochemistry using neutron diffraction*

The advantages of high penetration and sensitivity to light elements such as hydrogen, oxygen and lithium make neutron powder diffraction an interesting tool for investigating processes occurring within complex electrochemical systems. Lithium-ion batteries are one of the most widely used portable energy sources. These devices rely on the insertion of lithium ions into both positive and negative electrodes. A proper understanding of the structural processes that occur at the electrodes can only be obtained from *in situ* diffraction experiments performed during electrochemical charging and discharging. A suitable electrochemical cell for this type of measurement has been reported by Rosciano *et al.* (2008). The challenge for the design of this type of cell is to enable the neutron-diffraction data to be collected with the minimum of hindrance, while allowing electrochemical characterization to be performed at the same time. In addition, the fact that most separators and polycarbonate-based electrolyte solutions contain large amounts of hydrogen presents problems due to the large incoherent neutron-scattering cross section of hydrogen, which results in a deterioration in the signal-to-background ratio. However, as pointed out by Sharma *et al.* (2011), designs have been developed that minimize the amount of electrolyte required, and, where possible, deuterated solution can be used. Using a home-made design of a rollover, cylindrical cell that mimicked the geometry of commercial batteries, Sharma *et al.* (2011) were able to probe structural changes in real time (5 min per pattern) as a function of electrochemical cycling using the Wombat powder diffractometer (ANSTO). Sharma *et al.* (2015) have since reviewed both synchrotron and neutron electrochemistry cells. Pang & Peterson (2015) provide an overview of all lithium-ion and sodium-ion battery materials studied by neutron powder diffraction *in situ* since 1998.

Battery materials and fuel cells are extensively used in a vast variety of applications in energy conversion and storage, and there is no doubt that *in situ* neutron powder diffraction will continue to play an important role in the efforts to further improve the performance of these materials. In Japan, for example, a new neutron-diffraction instrument (SPICA at the J-PARC spallation source) will be used to analyse atomic structures and the behaviour of batteries during their charge cycle. Both at spallation and reactor-based neutron sources, improvements in neutron optics and detector performance have reduced both the volume of sample needed for *in situ* experiments and the time required to collect each powder pattern.

2.9.3.4.4. *Hydrothermal reaction cells*

Many materials with potential applications in technologically important fields can only be prepared by the supercritical hydrothermal synthesis method. A detailed knowledge of the reaction mechanisms is lacking, mainly because the processes take place within sealed and thick-walled reaction vessels. A technique is required that can penetrate the walls of the vessel during the reaction, and can reveal the kinetics and mechanism of bulk sample synthesis. Neutron diffraction is the ideal tool for this task. For example, Ok *et al.* (2010) constructed a relatively simple chemical-reaction cell for investigating syntheses, even under extreme supercritical conditions, using of time-of-flight techniques. The cell itself was machined from a single ingot of Inconel, and had a maximum wall thickness of 4.0 mm. Thinner sections of 2.7 mm thickness were used in parts of the cell to reduce attenuation of the incident and scattered neutron beams. The vessel had a normal working pressure and temperature of 40 MPa at 723 K. The experiments were carried out on the POLARIS diffractometer at the ISIS pulsed spallation neutron source.

Another example of a hydrothermal reaction cell of somewhat different design is that used by Xia *et al.* (2010). In this case, a large sample volume was chosen (320 ml internal volume) to

allow bulk properties to be investigated. The cell had a dumbbell configuration, assembled from commercial stainless-steel components, that held most of the hydrothermal liquid, and a zero-scattering Ti–Zr alloy sample compartment with a 0.4 mm wall thickness. This choice of material and wall thickness for the sample cell dramatically reduced the background scattering from the container, but limited the operational range to temperatures up to 573 K and pressures up to 9 MPa. The cell was commissioned at the Wombat neutron powder diffractometer at ANSTO, using the *in situ* kinetic study of the hydrothermal phase transformations from leucite ($KAlSi_2O_4$) to analcime ($NaAlSi_2O_6{\cdot}H_2O$) as a demonstration of the capabilities of the equipment.

2.9.4. Complementary methods and future developments

Standard crystallographic powder-diffraction methods can provide information about component phases and particle size, and can also be used to determine crystal structure, but the data quality required means that long-range crystalline order needs to be present. However, many real systems have amorphous components or demonstrate various degrees of disorder. In order to provide complementary information on the disordered components, alternative techniques are needed. In the early 1990s, Couves and co-workers started to combine XRD with XAFS in one setup in order to complement the XRD data (Couves *et al.*, 1991); they were quickly followed by Clausen and co-workers (Clausen *et al.*, 1993). Shortly afterwards, small-angle scattering (Dokter *et al.*, 1994) and vibrational spectroscopic techniques such as infrared and Raman were also added to complement the diffraction information (Newton & van Beek, 2010). More recently, a very old technique (Tarasov & Warren, 1936) based on the pair distribution function (PDF) has become immensely popular with the advent of high X-ray energies and efficient detectors (Chupas *et al.*, 2003). The PDF technique does not depend upon any assumptions about long-range crystalline order and can therefore be used to extract information on amorphous materials, defect structures and the structures of nanoparticles (see Chapter 5.7). It has the same huge variety of applications as traditional diffraction methods, and provides complementary information. Several of the *in situ* cells described above can also be used for combined techniques and PDF experiments at synchrotrons. One of the many reasons behind the rapid success of the PDF method is the availability of well developed software for data analysis (Juhás *et al.*, 2013) and modelling (Neder & Proffen, 2008).

We have seen in some of the examples above that acquisition times are reaching down into the millisecond range and the quantity of data being delivered by modern systems is becoming increasingly difficult to analyse. There is progress in automated sequential and parallel parametric refinements with traditional data-analysis software. However, we believe new strategies are necessary in order to make better, more efficient use of modern detectors. There are efforts in this direction in automated chemometric methods (Burley *et al.*, 2011) stemming from spectroscopy. However, these algorithms are not always well adapted to analyse data derived from powder-diffraction measurements. Chernyshov *et al.* (2011) have performed theoretical and experimental work taking the interference nature of diffraction into account in their method, which is based on modulation. Nevertheless, improvements in data analysis are still trailing far behind experimental progress and much effort will be necessary in this area. Choe *et al.* (2015) have even performed stroboscopic high-resolution powder diffraction on piezoelectric ceramics, detecting sub-millidegree shifts with microsecond time resolution.

In contrast to the pursuit of speed, the Diamond Light Source have decided to extend their powder-diffraction beamline and make it suitable for experiments lasting several months or even more, by moving slowly aging samples automatically into the measurement position at regular intervals (hours, days or even weeks) in a long-duration experiment (LDE) facility. Relevant applications are in batteries, fuel cells, crystallization, gas storage, mineral evolution, seasonal effects, thermal and electrical power cycling, and corrosion science.

In addition to the developments in instrumentation presented here, the availability of new radiation sources is opening up many interesting possibilities for studying chemical reactions. Not only are more, and better equipped, synchrotron beamlines becoming operational, but there are new facilities in planning or under construction that will dramatically change the way in which chemical processes can be investigated. New spallation sources and free-electron lasers (FELs) open up new possibilities in the time and space domains. In particular, FELs will facilitate the study of reactions on sub-picosecond timescales. Preliminary experiments using picosecond to nanosecond time resolution have already been carried out on synchrotron beamlines to investigate transient structural changes in organic powders (Techert *et al.*, 2001). It is evident that the huge increase in flux per pulse and the much shorter pulse length available from FELs will open up completely new dimensions in the field of *in situ* experiments.

References

Andrieux, J., Chabert, C., Mauro, A., Vitoux, H., Gorges, B., Buslaps, T. & Honkimäki, V. (2014). *A high-pressure and high-temperature gas-loading system for the study of conventional to real industrial sized samples in catalysed gas/solid and liquid/solid reactions. J. Appl. Cryst.* **47**, 245–255.

Bañares, M. A. (2005). *Operando methodology: combination of in situ spectroscopy and simultaneous activity measurements under catalytic reaction conditions. Catal. Today*, **100**, 71–77.

Becker, J., Bremholm, M., Tyrsted, C., Pauw, B., Jensen, K. M. Ø., Eltzholt, J., Christensen, M. & Iversen, B. B. (2010). *Experimental setup for in situ X-ray SAXS/WAXS/PDF studies of the formation and growth of nanoparticles in near- and supercritical fluids. J. Appl. Cryst.* **43**, 729–736.

Beek, W. van, Safonova, O. V., Wiker, G. & Emerich, H. (2011). *SNBL, a dedicated beamline for combined in situ X-ray diffraction, X-ray absorption and Raman scattering experiments. Phase Transit.* **84**, 726–732.

Bianchini, M., Leriche, J. B., Laborier, J.-L., Gendrin, L., Suard, E., Croguennec, L. & Masquelier, C. (2013). *A new null matrix electrochemical cell for Rietveld refinements of in-situ or operando neutron powder diffraction data. J. Electrochem. Soc.* **160**, A2176–A2183.

Brant, W. R., Schmid, S., Du, G., Gu, Q. & Sharma, N. (2013). *A simple electrochemical cell for in-situ fundamental structural analysis using synchrotron X-ray powder diffraction. J. Power Sources*, **244**, 109–114.

Brunelli, M. & Fitch, A. N. (2003). *A glass capillary cell for in situ powder X-ray diffraction of condensed volatile compounds. Solid HCFC-123a and HCFC-124. J. Synchrotron Rad.* **10**, 337–339.

Burley, J. C., O'Hare, D. & Williams, G. R. (2011). *The application of statistical methodology to the analysis of time-resolved X-ray diffraction data. Anal. Methods*, **3**, 814–821.

Chernyshov, D., van Beek, W., Emerich, H., Milanesio, M., Urakawa, A., Viterbo, D., Palin, L. & Caliandro, R. (2011). *Kinematic diffraction on a structure with periodically varying scattering function. Acta Cryst.* A**67**, 327–335.

Chipera, S. J., Carey, J. W. & Bish, D. L. (1997). *Controlled-humidity XRD analyses: application to the study of smectite expension/contraction. Adv. X-ray Anal.* **39**, 713–722.

Choe, H., Gorfman, S., Hinterstein, M., Ziolkowski, M., Knapp, M., Heidbrink, S., Vogt, M., Bednarcik, J., Berghäuser, A., Ehrenberg, H. & Pietsch, U. (2015). *Combining high time and angular resolutions: time-resolved X-ray powder diffraction using a multi-channel analyser detector. J. Appl. Cryst.* **48**, 970–974.

Chupas, P. J., Chapman, K. W., Kurtz, C., Hanson, J. C., Lee, P. L. & Grey, C. P. (2008). *A versatile sample-environment cell for non-ambient X-ray scattering experiments. J. Appl. Cryst.* **41**, 822–824.

Chupas, P. J., Qiu, X., Hanson, J. C., Lee, P. L., Grey, C. P. & Billinge, S. J. L. (2003). *Rapid-acquisition pair distribution function (RA-PDF) analysis. J. Appl. Cryst.* **36**, 1342–1347.

Clausen, B. S. (1991). *In situ cell for combined XRD and on-line catalysis tests: studies of Cu-based water gas shift and methanol catalysts. J. Catal.* **132**, 524–535.

Clausen, B. S., Gråbaek, L., Steffensen, G., Hansen, P. L. & Topsøe, H. (1993). *A combined QEXAFS/XRD method for on-line, in situ studies of catalysts: examples of dynamic measurements of Cu-based methanol catalysts. Catal. Lett.* **20**, 23–36.

Conterosito, E., Van Beek, W., Palin, L., Croce, G., Perioli, L., Viterbo, D., Gatti, G. & Milanesio, M. (2013). *Development of a fast and clean intercalation method for organic molecules into layered double hydroxides. Cryst. Growth Des.* **13**, 1162–1169.

Couves, J. W., Thomas, J. M., Waller, D., Jones, R. H., Dent, A. J., Derbyshire, G. E. & Greaves, A. N. (1991). *Nature (London)*, **354**, 465–468.

De Marco, R. & Veder, J.-P. (2010). *In situ structural characterization of electrochemical systems using synchrotron-radiation techniques. TrAC Trends Anal. Chem.* **29**, 528–537.

Dokter, W. H., Beelen, T. P. M., van Garderen, H. F., van Santen, R. A., Bras, W., Derbyshire, G. E. & Mant, G. R. (1994). *Simultaneous monitoring of amorphous and crystalline phases in silicalite precursor gels. An in situ hydrothermal and time-resolved small- and wide-angle X-ray scattering study. J. Appl. Cryst.* **27**, 901–906.

Eu, W. S., Cheung, W. H. & Valix, M. (2009). *Design and application of a high-temperature microfurnace for an in situ X-ray diffraction study of phase transformation. J. Synchrotron Rad.* **16**, 842–848.

Evans, J. S. O. & Radosavljević Evans, I. (2004). *Beyond classical applications of powder diffraction. Chem. Soc. Rev.* **33**, 539–547.

Figueroa, S. J. A., Gibson, D., Mairs, T., Pasternak, S., Newton, M. A., Di Michiel, M., Andrieux, J., Christoforidis, K. C., Iglesias-Juez, A., Fernandez-Garcia, M. & Prestipino, C. (2013). *Innovative insights in a plug flow microreactor for operando X-ray studies. J. Appl. Cryst.* **46**, 1523–1527.

Friščić, T., Halasz, I., Beldon, P. J., Belenguer, A. M., Adams, F., Kimber, S. A. J., Honkimäki, V. & Dinnebier, R. E. (2013). *Real-time and in situ monitoring of mechanochemical milling reactions. Nat. Chem.* **5**, 66–73.

Hansen, B. R. S., Møller, K. T., Paskevicius, M., Dippel, A.-C., Walter, P., Webb, C. J., Pistidda, C., Bergemann, N., Dornheim, M., Klassen, T., Jørgensen, J.-E. & Jensen, T. R. (2015). *In situ X-ray diffraction environments for high-pressure reactions. J. Appl. Cryst.* **48**, 1234–1241.

Hansen, T. C. & Kohlmann, H. (2014). *Chemical reactions followed by in situ neutron powder diffraction. Z. Anorg. Allg. Chem.* **640**, 3044–3063.

He, H., Barnes, P., Munn, J., Turrillas, X. & Klinowski, J. (1992). *Autoclave synthesis and thermal transformations of the alumino-phosphate molecular sieve VPI-5: an in situ X-ray diffraction study. Chem. Phys. Lett.* **196**, 267–273.

Herklotz, M., Scheiba, F., Hinterstein, M., Nikolowski, K., Knapp, M., Dippel, A.-C., Giebeler, L., Eckert, J. & Ehrenberg, H. (2013). *Advances in in situ powder diffraction of battery materials: a case study of the new beamline P02.1 at DESY, Hamburg. J. Appl. Cryst.* **46**, 1117–1127.

Herklotz, M., Weiss, J., Ahrens, E., Yavuz, M., Mereacre, L., Kiziltas-Yavuz, N., Dräger, C., Ehrenberg, H., Eckert, J., Fauth, F., Giebeler, L. & Knapp, M. (2016). *A novel high-throughput setup for in situ powder diffraction on coin cell batteries. J. Appl. Cryst.* **49**, 340–345.

Hill, A. H. (2013). *A new gas system for automated in situ powder diffraction studies at the European Synchrotron Radiation Facility. J. Appl. Cryst.* **46**, 570–572.

Isnard, O. (2007). *A review of in situ and/or time resolved neutron scattering. C. R. Phys.* **8**, 789–805.

Jacques, S. D. M., Di Michiel, M., Beale, A. M., Sochi, T., O'Brien, M. G., Espinosa-Alonso, L., Weckhuysen, B. M. & Barnes, P. (2011). *Dynamic X-ray diffraction computed tomography reveals real-time insight into catalyst active phase evolution. Angew. Chem. Int. Ed.* **50**, 10148–10152.

Jacques, S. D. M., Leynaud, O., Strusevich, D., Stukas, P., Barnes, P., Sankar, G., Sheehy, M., O'Brien, M. G., Iglesias-Juez, A. & Beale, A. M. (2009). *Recent progress in the use of in situ X-ray methods for the study of heterogeneous catalysts in packed-bed capillary reactors. Catal. Today*, **145**, 204–212.

Jensen, H., Bremholm, M., Nielsen, R. P., Joensen, K. D., Pedersen, J., Birkedal, H., Chen, Y.-S., Almer, J., Søgaard, E., Iversen, S. & Iversen, B. (2007). *In situ high-energy synchrotron radiation study of sol–gel nanoparticle formation in supercritical fluids. Angew. Chem. Int. Ed.* **46**, 1113–1116.

Jensen, T. R., Nielsen, T. K., Filinchuk, Y., Jørgensen, J.-E., Cerenius, Y., Gray, E. M. & Webb, C. J. (2010). *Versatile in situ powder X-ray diffraction cells for solid-gas investigations. J. Appl. Cryst.* **43**, 1456–1463.

Johnsen, R. E. & Norby, P. (2013). *Capillary-based micro-battery cell for in situ X-ray powder diffraction studies of working batteries: a study of the initial intercalation and deintercalation of lithium into graphite. J. Appl. Cryst.* **46**, 1537–1543.

Juhás, P., Davis, T., Farrow, C. L. & Billinge, S. J. L. (2013). *PDFgetX3: a rapid and highly automatable program for processing powder diffraction data into total scattering pair distribution functions. J. Appl. Cryst.* **46**, 560–566.

Kamazawa, K., Aoki, M., Noritake, T., Miwa, K., Sugiyama, J., Towata, S., Ishikiriyama, M., Callear, S. K., Jones, M. O. & David, W. I. F. (2013). *In-operando neutron diffraction studies of transition metal hydrogen storage materials. Adv. Energ. Mater.* **3**, 39–42.

Kraft, P., Bergamaschi, A., Broennimann, C., Dinapoli, R., Eikenberry, E. F., Henrich, B., Johnson, I., Mozzanica, A., Schlepütz, C. M., Willmott, P. R. & Schmitt, B. (2009). *Performance of single-photon-counting PILATUS detector modules. J. Synchrotron Rad.* **16**, 368–375.

Krogh Andersen, E., Krogh Andersen, I. G., Norby, P. & Hanson, J. C. (1998). *Kinetics of oxidation of fuel cell cathode materials lanthanum strontium manganates(III)(IV) at actual working conditions: in situ powder diffraction studies. J. Solid State Chem.* **141**, 235–240.

Kühnel, R. & van der Gaast, S. J. (1993). *Humidity controlled diffractometry and its application. Adv. X-ray Anal.* **36**, 439–449.

Linnow, K., Zeunert, A. & Steiger, M. (2006). *Investigation of sodium sulfate phase transitions in a porous material using humidity- and temperature-controlled X-ray diffraction. Anal. Chem.* **78**, 4683–4689.

Llewellyn, P. L., Horcajada, P., Maurin, G., Devic, T., Rosenbach, N., Bourrelly, S., Serre, C., Vincent, D., Loera-Serna, S., Filinchuk, Y. & Férey, G. (2009). *Complex adsorption of short linear alkanes in the flexible metal-organic-framework MIL-53(Fe). J. Am. Chem. Soc.* **131**, 13002–13008.

Lorenz, G., Neder, R. B., Marxreiter, J., Frey, F. & Schneider, J. (1993). *A mirror furnace for neutron diffraction up to 2300 K. J. Appl. Cryst.* **26**, 632–635.

Madsen, I. C., Scarlett, N. V. Y. & Whittington, B. I. (2005). *Pressure acid leaching of nickel laterite ores: an in situ diffraction study of the mechanism and rate of reaction. J. Appl. Cryst.* **38**, 927–933.

Majuste, D., Ciminelli, V. S. T., Eng, P. J. & Osseo-Asare, K. (2013). *Applications of in situ synchrotron XRD in hydrometallurgy: literature review and investigation of chalcopyrite dissolution. Hydrometallurgy*, **131–132**, 54–66.

Margulies, L., Kramer, M. J., McCallum, R. W., Kycia, S., Haeffner, D. R., Lang, J. C. & Goldman, A. I. (1999). *New high temperature furnace for structure refinement by powder diffraction in controlled atmospheres using synchrotron radiation. Rev. Sci. Instrum.* **70**, 3554–3561.

Meneghini, C., Artioli, G., Balerna, A., Gualtieri, A. F., Norby, P. & Mobilio, S. (2001). *Multipurpose imaging-plate camera for in situ powder XRD at the GILDA beamline. J. Synchrotron Rad.* **8**, 1162–1166.

Mi, J. L., Shen, Y., Becker, J., Bremholm, M. & Iversen, B. B. (2014). *Controlling allotropism in ruthenium nanoparticles: a pulsed-flow supercritical synthesis and in situ synchrotron X-ray diffraction study. J. Phys. Chem. C*, **118**, 11104–11110.

Milanesio, M., Artioli, G., Gualtieri, A. F., Palin, L. & Lamberti, C. (2003). *Template burning inside TS-1 and Fe-MFI molecular sieves: an in situ XRPD study. J. Am. Chem. Soc.* **125**, 14549–14558.

Møller, K. T., Hansen, B. R. S., Dippel, A.-C., Jørgensen, J.-E. & Jensen, T. R. (2014). *Characterization of gas-solid reactions using in situ powder X-ray diffraction. Z. Anorg. Allg. Chem.* **640**, 3029–3043.

Moorhouse, S. J., Vranješ, N., Jupe, A., Drakopoulos, M. & O'Hare, D. (2012). *The Oxford–Diamond in situ cell for studying chemical*

reactions using time-resolved X-ray diffraction. Rev. Sci. Instrum. **83**, 084101.
Morcrette, M., Chabre, Y., Vaughan, G., Amatucci, G., Leriche, J.-B., Patoux, S., Masquelier, C. & Tarascon, J.-M. (2002). *In situ X-ray diffraction techniques as a powerful tool to study battery electrode materials. Electrochim. Acta*, **47**, 3137–3149.
Moury, R., Hauschild, K., Kersten, W., Ternieden, J., Felderhoff, M. & Weidenthaler, C. (2015). *An in situ powder diffraction cell for high-pressure hydrogenation experiments using laboratory X-ray diffractometers. J. Appl. Cryst.* **48**, 79–84.
Munn, J., Barnes, P., Haüsermann, D., Axon, S. A. & Klinowski, J. (1992). *In-situ studies of the hydrothermal synthesis of zeolites using synchrotron energy-dispersive X-ray diffraction. J. Phase Transit.* **39**, 129–134.
Nauman, E. B. (2008). *Chemical Reactor Design, Optimization, and Scaleup.* Hoboken: John Wiley & Sons.
Neder, R. B. & Proffen, T. (2008). *Diffuse Scattering and Defect Structure Simulations.* Oxford University Press.
Newton, M. A. & van Beek, W. (2010). *Combining synchrotron-based X-ray techniques with vibrational spectroscopies for the in situ study of heterogeneous catalysts: a view from a bridge. Chem. Soc. Rev.* **39**, 4845–4863.
Norby, P. (2006). *In-situ XRD as a tool to understanding zeolite crystallization. Curr. Opin. Colloid Interf. Sci.* **11**, 118–125.
Norby, P., Cahill, C., Koleda, C. & Parise, J. B. (1998). *A reaction cell for in situ studies of hydrothermal titration. J. Appl. Cryst.* **31**, 481–483.
Norby, P., Hanson, J. C., Fitch, A. N., Vaughan, G., Flaks, L. & Gualtieri, A. (2000). *Formation of α-eucryptite, $LiAlSiO_4$: an in-situ synchrotron X-ray powder diffraction study of a high temperature hydrothermal synthesis. Chem. Mater.* **12**, 1473–1479.
Norby, P. & Schwarz, U. (2008). *Powder Diffraction, Theory and Practice*, edited by R. E. Dinnebier & S. J. L. Billinge, pp. 439–463. Cambridge: The Royal Society of Chemistry.
O'Brien, M. G., Beale, A. M., Jacques, S. D. M., Di Michiel, M. & Weckhuysen, M. (2011). *Closing the operando gap: the application of high energy photons for studying catalytic solids at work. Appl. Catal. A Gen.* **391**, 468–476.
Ok, K. M., O'Hare, D., Smith, R. I., Chowdhury, M. & Fikremariam, H. (2010). *New large volume hydrothermal reaction cell for studying chemical processes under supercritical hydrothermal conditions using time-resolved in situ neutron diffraction. Rev. Sci. Instrum.* **81**, 125107.
Palancher, H., Pichon, C., Rebours, B., Hodeau, J. L., Lynch, J., Berar, J. F., Prevot, S., Conan, G. & Bouchard, C. (2005). *A cell for in situ dynamic X-ray diffraction studies: application to the dehydration of zeolite SrX. J. Appl. Cryst.* **38**, 370–373.
Pang, W. K. & Peterson, V. K. (2015). *A custom battery for operando neutron powder diffraction studies of electrode structure. J. Appl. Cryst.* **48**, 280–290.
Parise, J. B., Cahill, C. L. & Lee, Y. (2000). *Dynamic powder crystallography with synchrotron X-ray sources. Can. Mineral.* **38**, 777–800.
Proffen, T., Frey, F., Plöckl, H. & Krane, H. G. (1995). *A mirror furnace for synchrotron diffraction experiments up to 1600 K. J. Synchrotron Rad.* **2**, 229–232.
Riello, P., Lausi, A., Macleod, J., Plaisier, J. R., Zerauschek, G. & Fornasiero, P. (2013). *In situ reaction furnace for real-time XRD studies. J. Synchrotron Rad.* **20**, 194–196.
Rijssenbeek, J., Gao, Y., Zhong, Z., Croft, M., Jisrawi, N., Ignatov, A. & Tsakalakos, T. (2011). *In situ X-ray diffraction of prototype sodium metal halide cells: time and space electrochemical profiling. J. Power Sources*, **196**, 2332–2339.
Robertson, K. & Bish, D. (2010). *Determination of the crystal structure of magnesium perchlorate hydrates by X-ray powder diffraction and the charge-flipping method. Acta Cryst.* B**66**, 579–584.
Rosciano, F., Holzapfel, M., Scheifele, W. & Novák, P. (2008). *A novel electrochemical cell for in situ neutron diffraction studies of electrode materials for lithium-ion batteries. J. Appl. Cryst.* **41**, 690–694.
Rowles, M. R. (2011). *On the calculation of the gauge volume size for energy-dispersive X-ray diffraction. J. Synchrotron Rad.* **18**, 938–941.
Rowles, M. R., Styles, M. J., Madsen, I. C., Scarlett, N. V. Y., McGregor, K., Riley, D. P., Snook, G. A., Urban, A. J., Connolley, T. & Reinhard, C. (2012). *Quantification of passivation layer growth in inert anodes for molten salt electrochemistry by in situ energy-dispersive diffraction. J. Appl. Cryst.* **45**, 28–37.
Sharma, N., Du, G., Studer, A. J., Guo, Z. & Peterson, V. K. (2011). *In-situ neutron diffraction study of the MoS_2 anode using a custom-built Li-ion battery. Solid State Ionics*, **199–200**, 37–43.
Sharma, N., Pang, W. K., Guo, Z. & Peterson, V. K. (2015). *In situ powder diffraction studies of electrode materials in rechargeable batteries. ChemSusChem*, **8**, 2826–2853.
Shen, Y., Pedersen, E. E., Christensen, M. & Iversen, B. B. (2014). *An electrochemical cell for in operando studies of lithium/sodium batteries using a conventional X-ray powder diffractometer. Rev. Sci. Instrum.* **85**, 084101.
Solovyov, L. A. (2012). *Revision of the $Mg(ClO_4)_2{\cdot}4H_2O$ crystal structure. Acta Cryst.* B**68**, 89–90.
Steiger, M., Linnow, K., Juling, H., Gülker, G., Jarad, A. E., Brüggerhoff, S. & Kirchner, D. (2008). *Hydration of $MgSO_4{\cdot}H_2O$ and generation of stress in porous materials. Cryst. Growth Des.* **8**, 336–343.
Styles, M. J., Rowles, M. R., Madsen, I. C., McGregor, K., Urban, A. J., Snook, G. A., Scarlett, N. V. Y. & Riley, D. P. (2012). *A furnace and environmental cell for the in situ investigation of molten salt electrolysis using high-energy X-ray diffraction. J. Synchrotron Rad.* **19**, 39–47.
Tarasov, L. P. & Warren, B. E. (1936). *X-ray diffraction study of liquid sodium. J. Chem. Phys.* **4**, 236–238.
Techert, S., Schotte, F. & Wulff, M. (2001). *Picosecond X-ray diffraction probed transient structural changes in organic solids. Phys. Rev. Lett.* **86**, 2030–2033.
Tonus, F., Bahout, M., Henry, P. F., Dutton, S. E., Roisnel, T. & Battle, P. D. (2009). *Use of in situ neutron diffraction to monitor high-temperature, solid/H_2-gas reactions. Chem. Commun.* pp. 2556–2558.
Tsakoumis, N. E., Voronov, A., Rønning, M., van Beek, W., Borg, Ø., Rytter, E. & Holmen, A. (2012). *Fischer–Tropsch synthesis: an XAS/XRPD combined in situ study from catalyst activation to deactivation. J. Catal.* **291**, 138–148.
Tschentscher, Th. & Suortti, P. (1998). *Experiments with very high energy synchrotron radiation. J. Synchrotron Rad.* **5**, 286–292.
Wall, A. J., Heaney, P. J., Mathur, R., Post, J. E., Hanson, J. C. & Eng, P. J. (2011). *J. Appl. Cryst.* **44**, 429–432.
Walspurger, S., Cobden, P. D., Haije, W. G., Westerwaal, R., Elzinga, G. D. & Safonova, O. V. (2010). *In situ XRD detection of reversible dawsonite formation on alkali promoted alumina: a cheap sorbent for CO_2 capture. Eur. J. Inorg. Chem.* **2010**, 2461–2464.
Walton, R. I. & O'Hare, D. (2000). *Watching solids crystallise using in situ powder diffraction. Chem. Commun.* pp. 2283–2291.
Warren, B. E. (1990). *X-ray Diffraction.* New York: Dover.
Watanabe, T. & Sato, T. (1988). *Expansion characteristics of montmorillonite and saponite under various relative humidity conditions. Clay Sci.* **7**, 129–138.
Weckhuysen, B. M. (2002). *Snapshots of a working catalyst: possibilities and limitations of in situ spectroscopy in the field of heterogeneous catalysis. Chem. Commun.* pp. 97–110.
Westgren, A. & Lindh, A. E. (1921). *Zur Kristallbau des Eisens und Stahl. I. Z. Phys. Chem.* **98**, 181.
Widenmeyer, M., Niewa, R., Hansen, T. C. & Kohlmann, H. (2013). *In situ neutron diffraction as a probe on formation and decomposition of nitrides and hydrides: a case study. Z. Anorg. Allg. Chem.* **639**, 285–295.
Williams, G. R., Khan, A. I. & O'Hare, D. (2009). *Mechanistic and kinetic studies of guest ion intercalation into layered double hydroxides using time-resolved, in-situ X-ray powder diffraction. Struct. Bond.* **119**, 161–192.
Wragg, D. S., O'Brien, M. G., Bleken, F. L., Di Michiel, M., Olsbye, U. & Fjellvåg, H. (2012). *Watching the methanol-to-olefin process with time- and space-resolved high-energy operando X-ray diffraction. Angew. Chem. Int. Ed.* **51**, 7956–7959.
Wragg, D. S., O'Brien, M. G., Di Michiel, M. & Lønstad-Bleken, F. (2015). *Rietveld analysis of computed tomography and its application to methanol to olefin reactor beds. J. Appl. Cryst.* **48**, 1719–1728.
Xia, F., Qian, G., Brugger, J., Studer, A., Olsen, S. & Pring, A. (2010). *A large volume cell for in situ neutron diffraction studies of hydrothermal crystallizations. Rev. Sci. Instrum.* **81**, 105107.
Yashima, M. & Tanaka, M. (2004). *Performance of a new furnace for high-resolution synchrotron powder diffraction up to 1900 K: application to determine electron density distribution of the cubic $CaTiO_3$ perovskite at 1674 K. J. Appl. Cryst.* **37**, 786–790.

International Tables for Crystallography (2019). Vol. H, Chapter 2.10, pp. 200–222.

2.10. Specimen preparation

P. S. Whitfield, A. Huq and J. A. Kaduk

Powder X-ray diffraction is a popular technique, as it is quick and easy to obtain a data set in a non-destructive manner. However, the old adage 'garbage in, garbage out' is as applicable to powder diffraction as to any other technique. Obtaining a high-quality data set is often not straightforward, and it can be impossible to distinguish visually a poor data set from a good one prior to attempting an analysis. This can be problematic if someone collects poor data and then spends days in a fruitless attempt to analyse it – or even worse unknowingly produces erroneous results. Specimen preparation is a key element in the quest to produce good data.

One of the tasks of the analyst is to determine what is required for a 'fit-for-purpose' data set. Practically, in the interests of time and instrument efficiency one might not need to aim for perfection in the preparation of every specimen. The majority of analyses carried out in most laboratories are for phase identification, whose minimum requirements for sample preparation are less stringent than for quantitative phase analysis or structure refinement. However, the need for more detailed analysis is never clear at the outset, and if the specimen has been altered or destroyed by other analyses, any economy in specimen preparation will turn out to have been false.

Although the laboratory instrument appears to be very different from synchrotron or neutron diffractometers at large central facilities, many of the concepts in the collection of powder diffraction data are common. Whether in the home institution with a basic laboratory system or in a huge instrument hall at a central facility, the basic concepts of specimen preparation are very similar (although neutrons have some unique issues). The imposing surroundings at large facilities may make specimen preparation seem like an unimportant distraction, but it is worth bearing in mind that repeating experiments if the data are poor may be impossible with limited beam time available. At the risk of overusing everyday sayings, 'if it's worth doing, it's worth doing right'. One common scenario is a user trying to replicate what has been seen in a literature paper without assessing critically whether the authors took the necessary care to collect accurate data.

Many of the problems that occur with powder diffraction specimens are related to size in some form – most often crystallite size, but sometimes particle size as well. Although the problems relating to size are described separately for the sake of clarity, where one of the issues exists the others are likely to follow. The first size-related problem to be described is particle statistics (granularity). Although theoretical models of varying success exist for the other issues of preferential orientation, microabsorption and extinction, no such model is possible when the data suffer from poor particle statistics. Consequently the message here is 'prevention through proper specimen preparation'; taking steps in specimen preparation to improve particle statistics will automatically reduce the effects of other potential problems.

The classic work on preparation of X-ray diffraction specimens is Buhrke *et al.* (1998). This book should be on the shelf of every powder diffractionist. It provides an excellent discussion on sampling, a discussion which is not necessary to repeat here. This chapter attempts to update and expand the advice given there on specimen preparation.

2.10.1. X-ray powder diffraction

Most people first encounter X-ray powder diffraction with laboratory instrumentation, but concepts applying to laboratory systems are also applicable to synchrotron and neutron beamlines. The scattering mechanisms of X-rays in the laboratory and at a synchrotron are the same, and apparent differences are usually due to specifics of the wavelength used or beamline/instrument geometry. Differences and similarities between synchrotron and laboratory experiments will be highlighted where they are significant. For example, differences in the polarization factor result in different intensities from the same specimen on laboratory and synchrotron instruments (Fig. 2.10.1). Issues specific to neutron powder diffraction will be covered in Section 2.10.2.

A typical laboratory instrument has the Bragg–Brentano reflection geometry, either with θ–θ (fixed specimen) or θ–2θ (fixed tube) setup. Other laboratory configurations are possible, such as transmission (capillary or flat plate) and spot focus with area detectors. Some of the concepts described affect both reflection and transmission, but some will be more important for one geometry over the other. Synchrotron beamlines can also be operated in reflection or transmission geometry, but capillary transmission geometry is much more common than in the laboratory. Some of the apparent differences are due to the

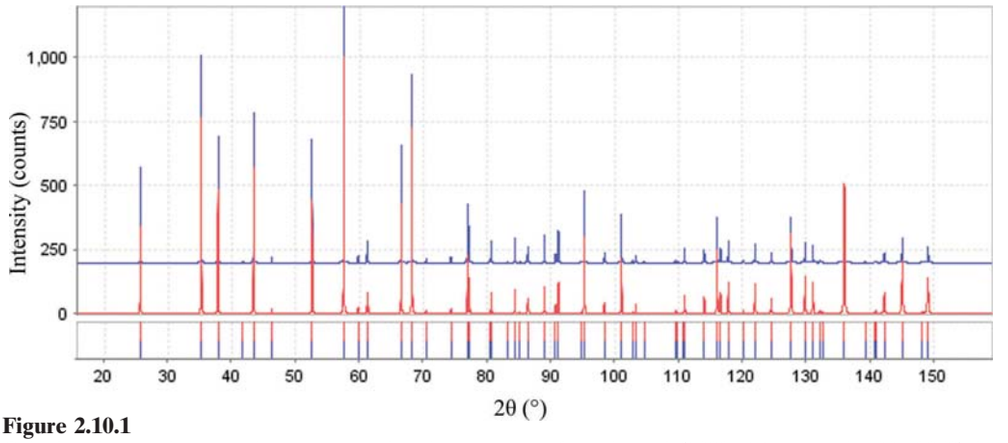

Figure 2.10.1
Calculated corundum powder patterns using the structure of Lewis *et al.* (1982; PDF entry 04–004-2852) for laboratory and synchrotron instruments, using the default profile settings from the Powder Diffraction File. The synchrotron pattern is displaced by 200 intensity units for clarity.

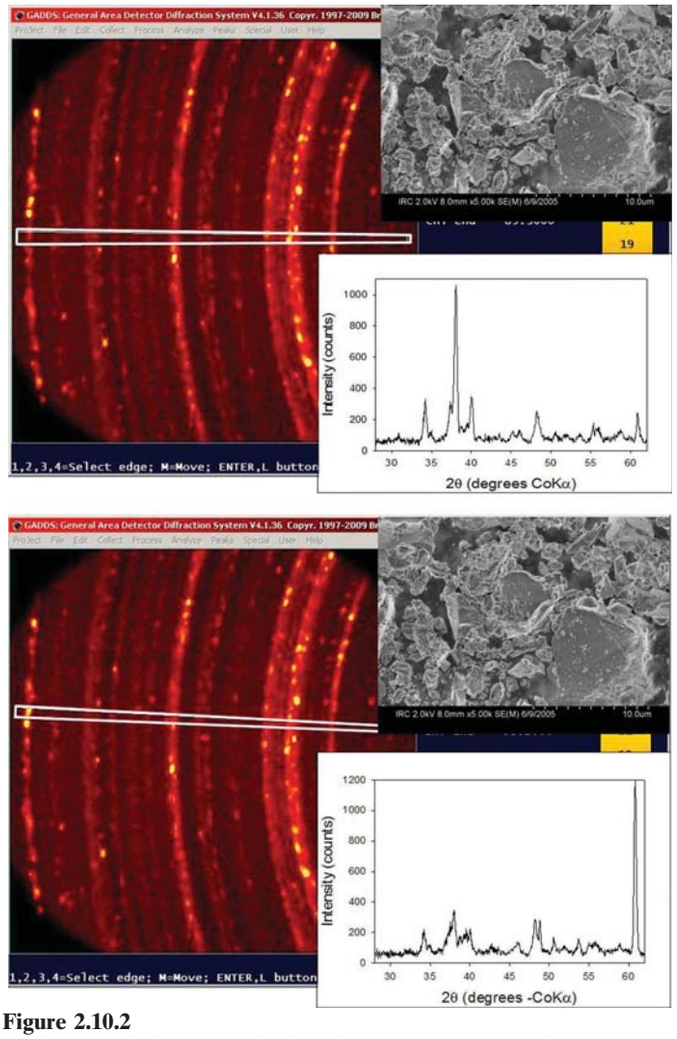

Figure 2.10.2
2D images of the spotty Debye rings of a coarse (~35 μm) cement powder using a Co *Kα* radiation 1 mm point source. Overlaid are SEMs of the sample material and integrated patterns from the thin slices indicated in the 2D patterns to illustrate what a point or 1D detector would see. Note: in these 2D data sets the low 2*θ* rings are on the right-hand side.

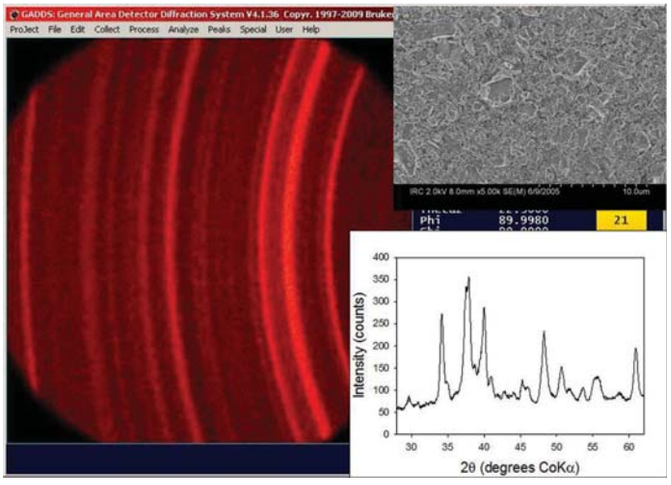

Figure 2.10.3
2D image from the same sample after reducing the crystallites down to a few μm, together with the properly averaged integrated data.

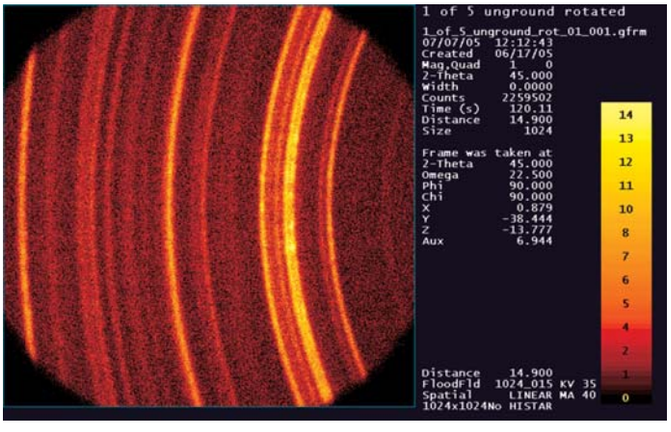

Figure 2.10.4
2D image showing the Debye rings when the unmilled sample from Fig. 2.10.2 is rotated. The slight spottiness shows that the quality is not as good as the milled sample, even when not rotated, as shown in Fig. 2.10.3.

typically very small beam divergence, and the tunable wavelength can be very helpful in circumventing some problems.

It will become apparent that many problems relating to specimen preparation and data quality are directly and indirectly the result of samples being too coarse to produce a random powder. The word 'powder' forms part of the name of the technique, but what makes a powder a powder?

2.10.1.1. *Powders and particle statistics (granularity)*

The question of when a powder is a 'true' powder is not new. It was dealt with in Klug & Alexander (1954) and Alexander & Klug (1948), and more recently by Smith (Smith, 2001; Buhrke *et al.*, 1998). The short answer is that at least 50 000 crystallites in the illuminated volume are necessary to obtain a random powder pattern.

The classic Debye rings of powder diffraction are formed by the random orientation of a large number of single crystallites, which are either physically separate or part of larger agglomerates. These rings used to be a common sight when film cameras were the norm, but can still be seen where two-dimensional (2D) or area detectors are used, most often on microdiffraction systems or synchrotron beamlines. Where there are sufficient crystallites diffracting, the spots from the crystallites merge into smooth rings. Problems with insufficient crystallites are often indicated by the presence of high-intensity spots in the Debye rings. When using 2D data sets, part or all of the intensity in the Debye rings may be integrated to produce an average 1D powder pattern.

More serious problems can arise in cases where 0D or 1D detectors are used. Most modern laboratory powder diffractometers use some form of 0D point detector (*e.g.* a scintillation counter) or 1D position-sensitive detector (PSD). When collecting data, these detectors pass through the Debye rings along a radius vector. Should the Debye ring be spotty, it is purely down to chance whether the detector will intersect with a spot of higher intensity or low intensity within the ring. An example of how spotty Debye rings can have an adverse effect on the integrated pattern can be seen in Fig. 2.10.2. Unfortunately there is usually no indication of the problem in the resulting integrated 1D pattern. The uncertainty with regard to the intensity of the Bragg reflections is something that must be minimized should accurate relative intensities be required for an analysis. This reproducibility is the concern when the term 'particle statistics' is used in relation to powder diffraction. The desirable smooth Debye rings shown in Fig. 2.10.3 were produced after reducing

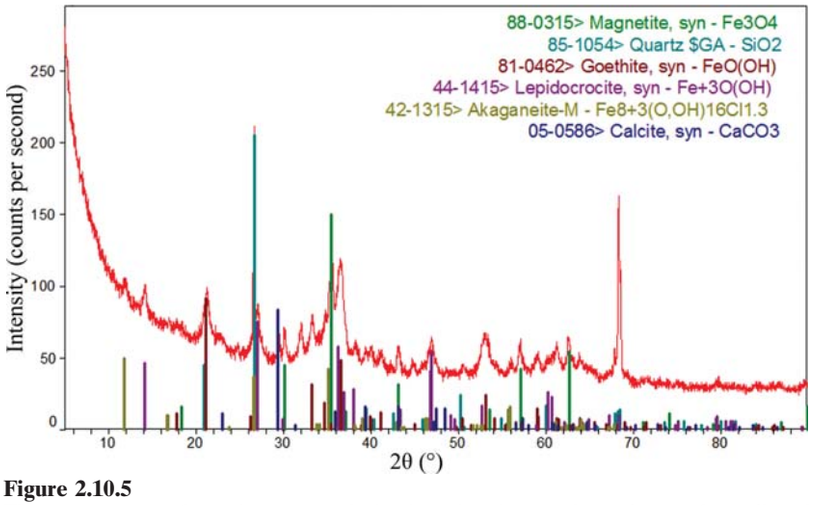

Figure 2.10.5
The appearance of specimen granularity in a hand-ground specimen of a railroad tank car corrosion deposit. The pattern was measured using a point detector. The intense sharp peak at ~68° 2θ turned out to come from a single crystal grain of sand at the surface of the specimen. The grain was detected by examination (after the measurement) in an optical microscope.

the crystallites to less than a few μm by milling. As shown in Fig. 2.10.4, rotating the coarse unmilled sample greatly improves the Debye rings compared with those seen in Fig. 2.10.2, but they are still not as uniform as those from the static milled sample in Fig. 2.10.3.

When using a point detector, granularity often manifests itself in the presence of a sharp (instrumental width) peak at relatively high diffraction angle. After a sharp peak at ~68° 2θ was observed in the pattern of a railroad tank car corrosion deposit (Fig. 2.10.5), examination of the specimen in an optical microscope indicated the presence of a single crystal grain of sand (quartz) on the surface. Re-grinding the specimen removed this artifact. Such sharp peaks tend to occur at relatively high diffraction angles, because at such angles the illuminated specimen area is smaller than at low angles, and the presence of a single crystal grain at the surface is relatively more important than when a larger area is illuminated.

An extreme example of granularity is provided by a hand-ground specimen of Scott's Moss Control Granules (Fig. 2.10.6). The even spacing of the strong peaks suggested severe preferred orientation, but examination of the specimen in an optical microscope (Fig. 2.10.7) revealed the presence of grains several tens of μm in size. Regrinding the sample in a McCrone micronizing mill reduced the crystallite size to a few μm (Fig. 2.10.7), and resulted in random powder data which could be used successfully in a Rietveld refinement (Fig. 2.10.8) and quantitative phase analysis.

An example of granularity at a synchrotron beamline is provided by $(Ba_{0.7}Sr_{1.3})TiO_4$ (Fig. 2.10.9). A Rietveld refinement using data collected from a static capillary specimen was unsuccessful. In an attempt to understand why, the diffractometer was driven to the 2θ angle of a strong peak, and a φ scan was carried out (rotating the capillary in steps). The intensity varied by a factor of five, as individual crystallites came into and out of diffracting position. Clearly, the intensities from such a measurement are not meaningful. When the capillary was rotated rapidly during a repeated φ scan, the intensity was constant and reliable.

Granularity can be encountered even in highly transparent organic specimens. A synchrotron pattern of 17α-estradiol showed that the sample was a mixture of the α-polymorph and an additional phase. Indexing the unknown peaks yielded the cell of the β-polymorph, the structure of which was unknown. The structure of the β-polymorph was solved using Monte Carlo simulated-annealing techniques, but the Rietveld refinement (Fig. 2.10.10) was not nearly as good as a Le Bail fit using the same cell and profile. The errors were then clearly in the structural model and/or the data. Examination of the specimen under an optical microscope revealed the presence of needles ~50 × 50 × 150–200 μm in size. Even the rapid rotation of the capillary specimen was not sufficient to obtain a powder average of such large crystallites.

Although granularity is normally considered to affect only the intensities of peaks, in extreme cases it can also affect the shapes. This is easily seen in a pattern from very coarse crystalline quartz in Fig. 2.10.11. The strange looking 101 reflection at 26.6° contains contributions from individual single crystals. When a wider view is taken, the relative intensities are distorted from those expected, similar to that seen in Fig. 2.10.2. Flat-plate data from highly-parallel-beam synchrotron beamlines are more (as opposed to less) susceptible, as shown by the comparison between flat-plate and capillary data of LaB_6 from the Australian Synchrotron in Fig. 2.10.12. Despite the use of ω-rocking and a Mythen position-sensitive detector, the flat-plate synchrotron data with 2–5 μm SRM660a LaB_6 crystallites show worse splitting of the Bragg peaks than lower-resolution laboratory data with 100 μm quartz crystallites.

The quantitative effect of particle statistics on diffraction results can be seen in Table 2.10.1. In the 15–50 μm sample the intensity varied from 4823 to 11 123 counts, which is a huge variation when trying to extract reliable intensities for analysis. Averaging over ten samples, the mean deviation was reduced from 18.2% to 1.2% when the smallest fraction of <5 μm was used. The absolute intensities of the largest fraction are significantly lower, which was attributed to extinction effects.

The source of this huge variation in errors can be understood more clearly when the theoretical treatment for quartz from

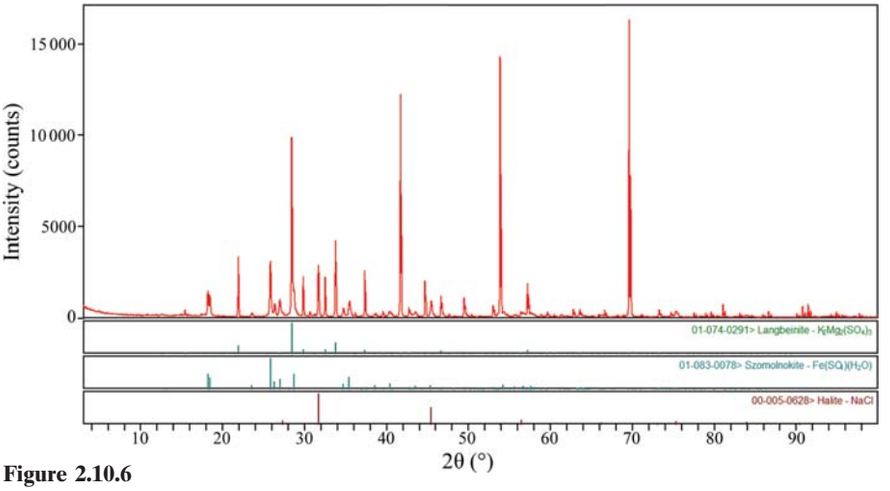

Figure 2.10.6
An extreme example of granularity. The pattern is of a hand-ground specimen of Scott's Moss Control Granules. No preferred orientation model could fit the langbeinite peaks.

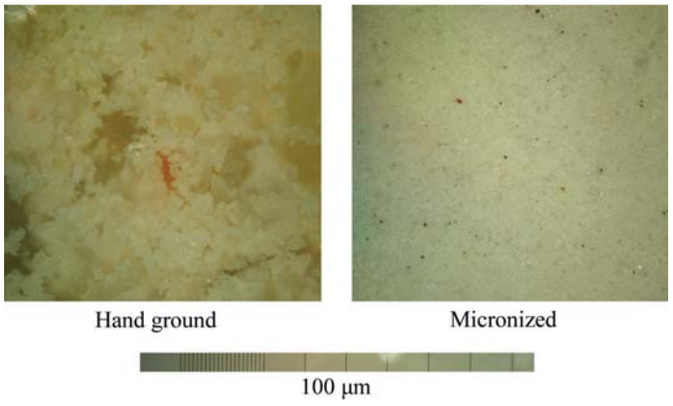

Figure 2.10.7
Optical microscope images of the surfaces of the hand-ground and micronized specimens of Scott's Moss Control Granules. The full length of the bar at the bottom is 100 µm. The hand-ground specimen contains grains much too large to yield a random powder pattern. Courtesy of B. J. Huggins, BP Analytical.

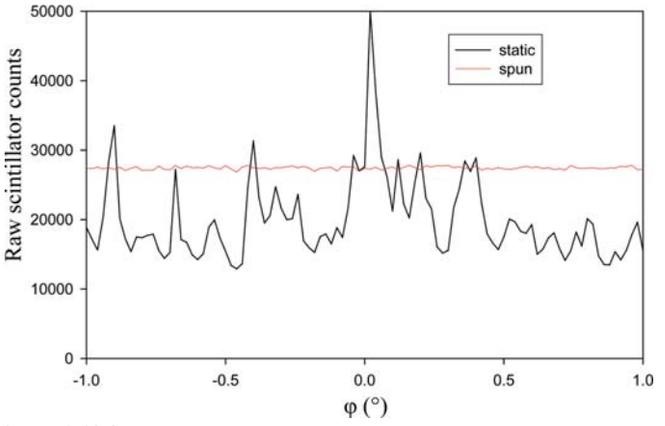

Figure 2.10.9
A rocking curve (φ scan) of $(Ba_{0.7}Sr_{1.3})TiO_4$, with the detector fixed at 9.647° 2θ, the top of a strong peak in the synchrotron pattern. The jagged plot is from a static specimen, and shows individual grains moving in and out of diffracting position. The flat curve is from a rotating specimen, and indicates that a powder average was obtained.

Smith (Smith, 2001; Buhrke *et al.*, 1998) is considered, which followed principles first described by de Wolff (1958). By considering the effects of crystallite size, illuminated volume and beam divergence, for a monodisperse 40 µm specimen Smith calculated that only 12 crystallites would be in the diffracting condition (assuming a point detector). Obviously this is nowhere near enough to create the desired smooth Debye rings. To obtain a standard error of less than 1% the number of diffracting crystallites should be over 52 900, which even the 1 µm sample fails to meet.

Why then does a powder diffraction experiment work? A number of factors may affect the effective number of crystallites, many of which will be mentioned in the following paragraphs. One that isn't is the multiplicity due to the crystal symmetry, meaning that there are always at least two equivalent orientations of each crystallite that would meet the diffraction condition, up to 48 for some cubic reflections. It is worth remembering that these figures relate to a single phase, so the impact on the errors in quantitative phase analysis can be considerable. For low-concentration phases, the number of crystallites is automatically smaller than those of the major phases, so the effects of granularity might be more pronounced.

When considering the granularity of a particular specimen there are a few things to consider. The number of diffracting crystallites depends on the illuminated volume (V), the size of the crystallites (s), the packing density (ρ) and the probability that a crystallite is in the correct orientation (P).

The illuminated volume V depends on a combination of instrument geometry, specimen geometry and the X-ray absorption of the sample. The footprint of the X-rays on a specimen in reflection depends on the beam width, beam length, the beam divergence (if any) and the diffraction angle. The effective beam width at the tube window with a typical long-fine-focus X-ray tube is 0.04 mm, with a length of 12 mm. The beam width may be increased up to 0.2 mm by using a broad-focus tube (Jenkins & Snyder, 1996), but these are rarely used in modern powder diffractometers. With Bragg–Brentano geometry the beam divergence may be increased to cover the available specimen, but large divergence angles degrade the peak resolution. A parallel-beam primary optic produces negligible beam divergence. The beam width may be reduced using an exit slit, but the largest beam width attainable is dependent on the characteristics of the mirror.

Additionally, V also depends on how deeply the X-rays can penetrate into the sample. This depends on the linear absorption coefficient of the specimen for the particular radiation being used, and is given (Klug & Alexander, 1954) by $t = (3.2\rho \sin\theta)/(\mu\rho')$, in which μ is the linear absorption coefficient, ρ is the crystal density and ρ' is the packing density. In the absence of other information, a reasonable assumption for the value of ρ'/ρ is 0.5. The penetration with Cu $K\alpha$ radiation can range from >1 mm for an organic material to a few µm for heavily absorbing specimens. With Bragg–Brentano geometry this leads to a potential trade-off between improving particle statistics and the peak shifts resulting from sample transparency. As a rule, doubling the diffracting volume will reduce the errors in intensity by about 1.5 times (Zevin &

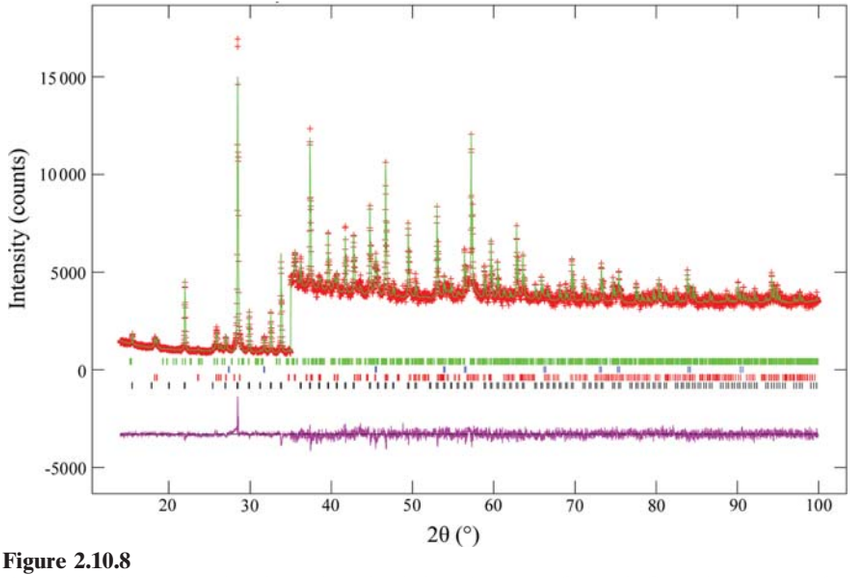

Figure 2.10.8
Rietveld refinement plot for micronized Scott's Moss Control Granules. No preferred orientation correction was necessary, and the specimen scattered as a random powder. For angles > 35° the vertical scale has been multipled by a factor of 5.

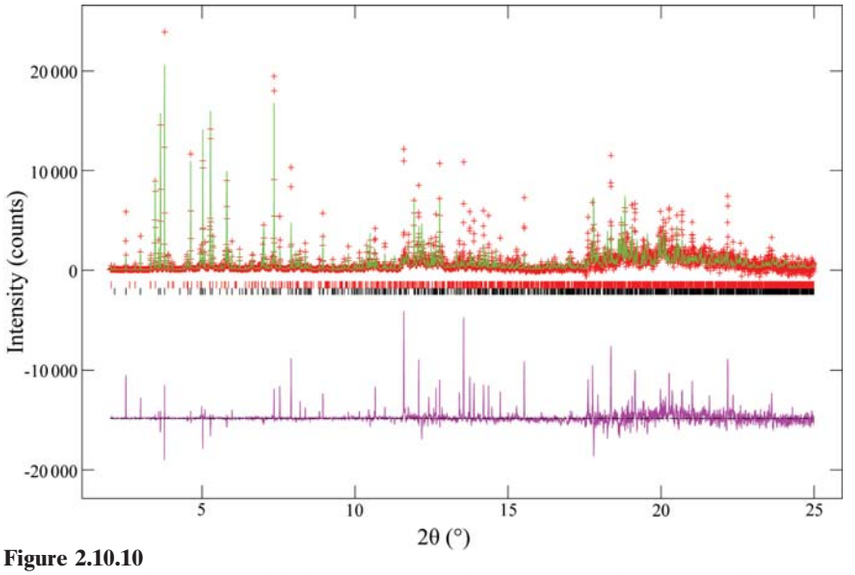

Figure 2.10.10
Rietveld plot of a mixture of β-17α-estradiol hemihydrate and α-17α-estradiol. The largest errors occur at the peaks of the β phase. Examination of the sample with an optical microscope revealed the presence of large single crystals. The rapid specimen rotation at the synchrotron beamline could not yield a powder average from such a coarse sample.

Kimmel, 1995), so is rarely sufficient on its own to solve problematic particle statistics.

Both the experimental data and theoretical treatment shown in Tables 2.10.1 and 2.10.2 show that with a typical laboratory setup, crystallites should ideally be in the range of a few μm in size to produce accurate intensity data. Reducing the crystallites to below 1 μm will improve the statistics further but may also induce crystallite-size and/or microstrain broadening depending on the instrument resolution. It is important to note that the crystallites must be uniformly small. Mineralogists often refer to 'rocks in dust', where there are a small number of very large crystallites scattered among the sample. Scattering of X-rays is sensitive to statistics by *volume*. A few very large crystallites will dominate (and probably distort) the resulting pattern, so the 'rocks in dust' scenario should be avoided whenever possible by correct specimen-preparation techniques.

As we have seen previously, the granularity can be seen visually in a 2D data set. If the researcher has access to a 2D detector this is the quickest way to assess a sample. However, where such a system is not available, an alternative is to use φ scans. In simple terms this involves taking data sets of a static specimen but rotating the specimen by a particular angle between data sets, for example at 0, 90, 180 and 270° in φ. Ideally the patterns should overlap exactly, although in practice one is looking for reproducible relative intensities, as the absolute intensities may change slightly. The examples used here are the so-called 'five fingers' of quartz. Although they are relatively weak reflections in the quartz pattern, three overlapping $K\alpha_{1,2}$ doublets provide a conveniently compact example. The three data sets shown in Fig. 2.10.13 are -400-mesh quartz (<38 μm), a commercial quartz with a size less than 15 μm and a sample milled to less than 5 μm. Optical micrographs of the -400 mesh and milled quartz samples are shown in Fig. 2.10.14.

The most obvious feature of the φ scans is that the reproducibility of the relative intensities is poor with the -400 mesh quartz sample. This has obvious consequences for any analytical technique relying on accurate peak intensities. All eight of the patterns from the micronized sample have practically identical relative peak intensities. It is worth comparing the similar results in the variability visible in Fig. 2.10.13 with the tabulated errors for the different methodology used for the data in Table 2.10.1.

The final approach to improving statistics is to increase the probability P that a crystallite is in the diffracting condition and visible to the detector. The latter is relevant today with 1D PSD detectors becoming more common, as the detector can simultaneously see multiple crystallite orientations at a particular incident beam angle, as shown in Fig. 2.10.15. P also increases with beam divergence; although there are many advantages of parallel-beam geometry, improving particle statistics is not one of them.

P is much higher with capillary transmission geometry than for reflection geometry. By rotating the specimen about an axis normal to the beam the effective number of orientations 'seen' by the detector increases greatly. This is the reason why a powder passing a 325-mesh sieve (<45 μm) almost always yields smooth

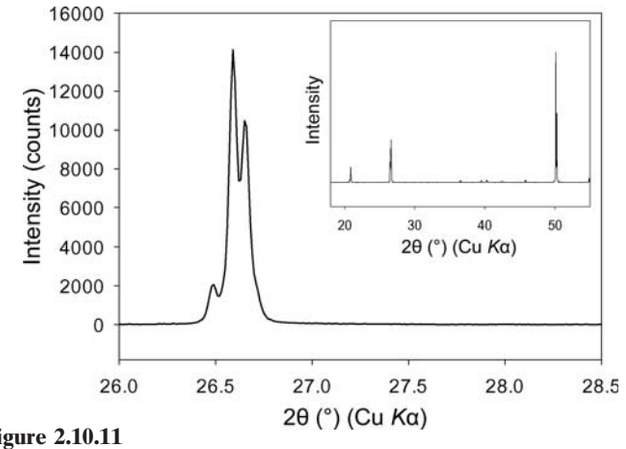

Figure 2.10.11
The main 101 reflection in data collected from a very coarse (~100 μm) highly crystalline quartz. The strange peak splitting is characteristic where there are very large crystallites present in the sample. The inset shows the diffraction pattern over a wider range and the strangely high intensity at 50° 2θ is caused by the detector intersecting a very intense diffraction spot similar to that seen in the lower part of Fig. 2.10.2.

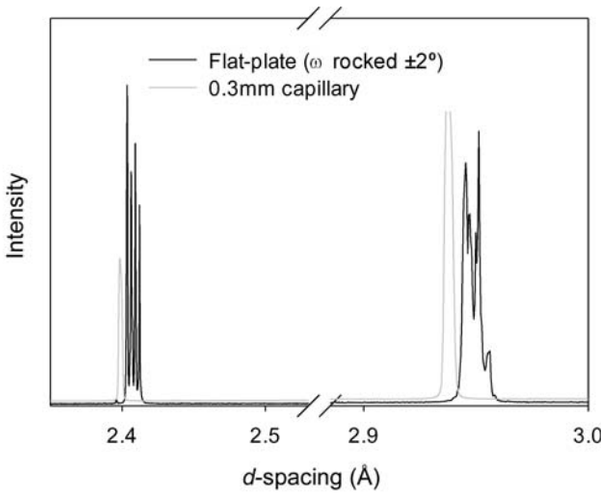

Figure 2.10.12
Comparison between capillary (0.3 mm, 0.8265 Å) and rocking flat-plate (strip heater, 1.2386 Å, ω ±2°) data from the Australian Synchrotron. Data courtesy of Ian Madsen, CSIRO.

Table 2.10.1
Intensity (counts) and mean deviation in intensity of the main quartz 101 reflection with a stationary sample of -325 mesh quartz powder

Data from Alexander *et al.* (1948) and Klug & Alexander (1954).

	Crystallite size			
Data set	15–50 μm	5–50 μm	5–15 μm	<5 μm
1	7612	8688	10841	11055
2	8373	9040	11336	11040
3	8255	10232	11046	11386
4	9333	9333	11597	11212
5	4823	8530	11541	11460
6	11123	8617	11336	11260
7	11051	11598	11686	11241
8	5773	7818	11288	11428
9	8527	8021	11126	11406
10	10255	10190	10878	11444
Mean % deviation	18.2	10.1	2.1	1.2

Table 2.10.2
Theoretical behaviour of different crystallite sizes of quartz in a volume of 20 mm^3

Data from Smith (2001).

Crystallite diameter (μm)	40	10	1
Crystallites per 20 mm^3	5.97×10^5	3.82×10^7	3.82×10^{10}
No. of diffracting crystallites	12	760	38 000

Debye rings in a capillary (Klug & Alexander, 1954), while the pattern would be granular in reflection. Specimen rotation has also been long employed in reflection geometry (de Wolff, 1958; de Wolff *et al.*, 1959), and a sample spinner is now a standard attachment for commercial diffractometers. When properly applied, the use of a spinner can reduce the standard deviation of the integrated intensity by a factor of approximately 4–5 (~7–8 for peak intensities) (de Wolff *et al.*, 1959), corresponding to a reduction in the effective crystallite size by a factor of 3 (Zevin & Kimmel, 1995). However, depending on the sample, as seen in Table 2.10.2 this can be insufficient on its own as it rotates the specimen only in a single plane. Where a spinner is used in conjunction with a point counter, it is important that the spinner must complete at least one rotation during each step to maximize its effectiveness. In order to further improve the particle statistics it is possible to construct spinners that tilt back and forth along an axis normal to the beam (similar to the capillary concept) in addition to the normal axis of rotation. This is effective in improving particle statistics but adversely affects the para-focusing condition in Bragg–Brentano geometry. It is important to note that specimen rotation improves grain-sampling statistics, but does nothing to alter preferred orientation.

The term 'micronized' is one that is frequently seen in papers on quantitative phase analysis. Potentially any kind of mill could be used to reduce the crystallites down to the desirable μm size range (such as shown in Fig. 2.10.14*a* and *b*). However, most mills use high-energy percussion-like impacts between the grinding media and the sample, which tend to damage the crystal structure in softer materials and induce microstrain into the material. In extreme cases the sample can become completely amorphous. There is also the potential problem of modifying the polymorph with samples susceptible to such changes. The mill produced by McCrone (http://www.mccrone.com) was designed specifically for the preparation of X-ray diffraction and X-ray fluorescence samples, and the shearing milling mechanism minimizes damage *versus* conventional impact milling. It is necessary to use wet milling to produce the best results, so it is up to the analyst to

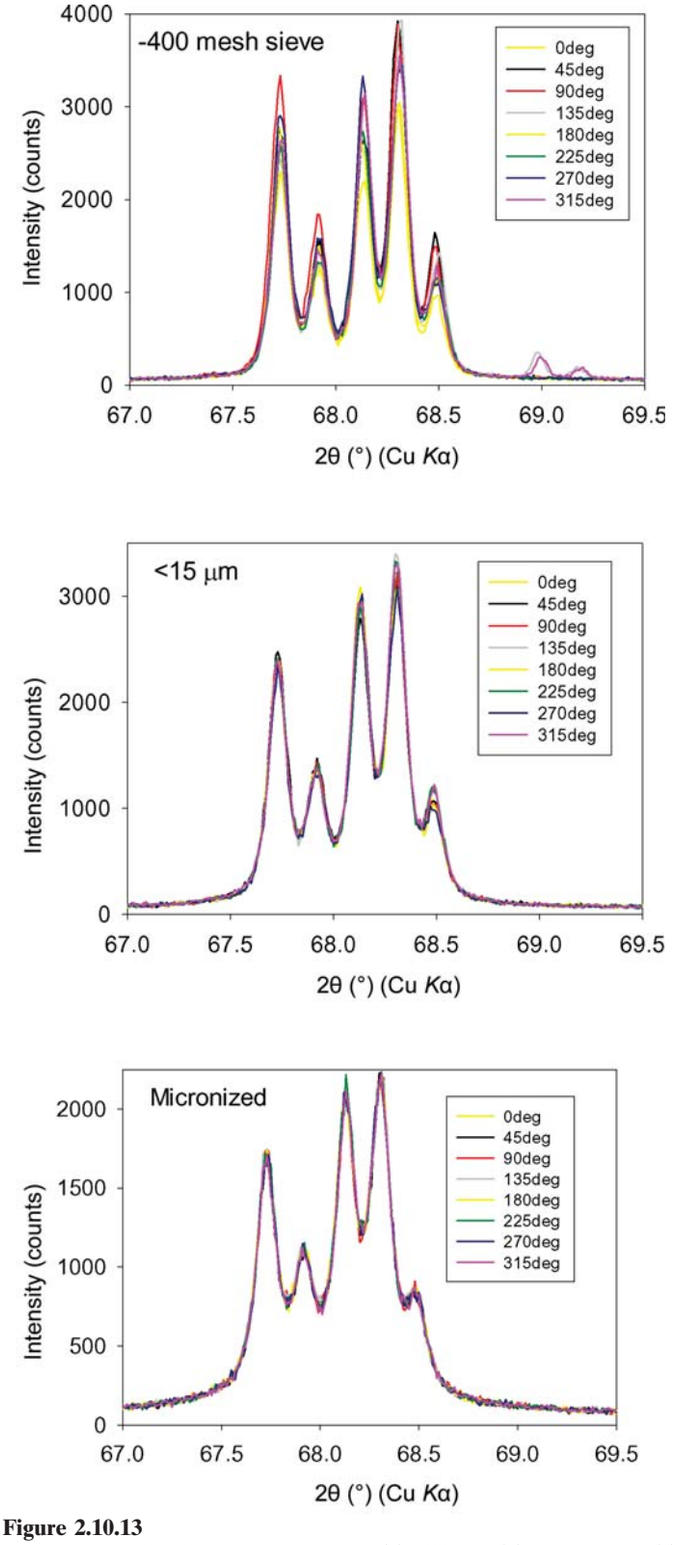

Figure 2.10.13
φ scans of the five fingers of quartz for (*a*) <38 μm, (*b*) <15 μm and (*c*) micronized samples.

choose the best media compatible with both the sample and the polymer micronizing vials. Commonly used are ethanol, isopropyl alcohol, *n*-hexane and water; it is not advisable to use acetone, as this solvent dissolves the polymer jars supplied with this mill. A limitation of most forms of milling is the requirement for a relatively large amount of sample. In the McCrone mill a volume of >1 ml is usually required, although desperate scientists have been known to dilute the specimen with amorphous material, such as silica gel. The analyst should also be aware of the possible contamination of samples by degrading and eroding grinding

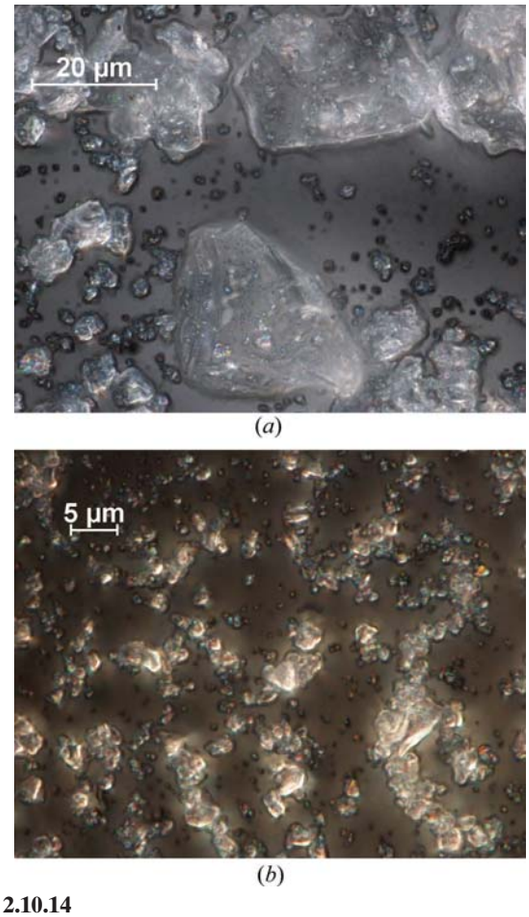

Figure 2.10.14
Optical micrographs of (*a*) -400 mesh quartz at 100× magnification and (*b*) quartz milled in a McCrone micronizer for 15 min in isopropyl alcohol at 150× magnification.

elements (corundum or agate in the micronizing mill; possibly iron, WC, SiC *etc*. in other types of mill).

Obviously, a reduction of the crystallite size to the μm-sized region will produce size broadening if the instrument has sufficient resolution to detect it. It is worth bearing in mind that micronizing does not guarantee a problem-free sample. Micronized specimens almost always exhibit some microstrain broadening. In principle, this could be decreased by an annealing treatment, but this step is rarely practiced. When a mixture contains both very hard and very soft phases, the hard phases may not mill properly. This has been observed in mixtures containing organics and a minor quartz fraction. Despite milling for 30 min or more, the classical split 101 quartz reflection (such as seen in Fig. 2.10.11) was still visible in some data sets, an indication of the 'rocks in dust' phenomenon. Although the McCrone mill is designed to minimize microstructural damage to samples, damage can still occur with very soft materials, and ductile materials may weld as opposed to mill. With very soft and pliable materials a possible alternative could be to cryo-mill the samples, taking advantage of the increased brittleness of materials at low temperature.

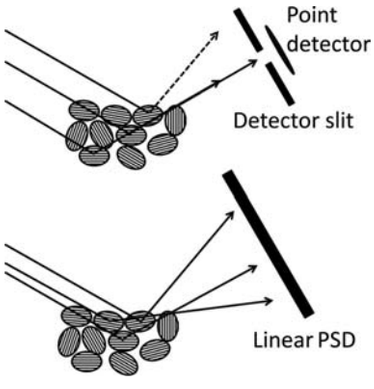

Figure 2.10.15
Diagram showing the source of improved particle statistics in reflection geometry using a 1D position sensitive detector (PSD) *versus* a point detector.

2.10.1.2. *Preferred orientation*

Preferred orientation is usually undesirable in a powder diffraction pattern, although sometimes it *is* the information required, as in texture studies. One of the exceptions is the analysis of clays, where orientation is deliberately induced to identify related reflections. Preferred orientation manifests itself as continuous but non-uniform intensity in the Debye rings, and so is easily characterized with 2D detectors. Preferred orientation does not change the total diffracted intensity, but renormalizes some classes of reflections with respect to others.

Reference is commonly made to a preferred-orientation 'correction'. Strictly speaking, what is done is 'modelling' of the preferred orientation. The proper way to correct preferred orientation is through better specimen preparation.

Models for preferred orientation exist in many analysis packages, specifically the March–Dollase (Dollase, 1986) and spherical-harmonics (Järvinen, 1993) formalisms. Apparent severe preferred orientation may be a sign of large crystallites, which may result in one or more of the other problems outlined in this section.

Additional care must be taken where software corrections are used during quantitative phase analysis, where overlapping reflections can cause serious correlations and erroneous results. The March–Dollase correction is less prone to this, as an orientation direction must be supplied by the analyst. The spherical-harmonics correction has no such constraint. It behaves properly where peak overlap is not extensive, but negative peak intensities are not uncommon (especially when too high an order is used) when applying it without thought in complex mixtures. Negative peak intensities are obviously impossible, so the results of such an analysis must be viewed with great suspicion.

The presence of preferred orientation can be most easily discerned by comparing the observed pattern to a calculated pattern (random) of the same phase from the Powder Diffraction File or other source. The likelihood of preferred orientation can be assessed by calculating the Bravais–Friedel–Donnay–Harker (Bravais, 1866; Friedel, 1907; Donnay & Harker, 1937) morphology from the crystal structure using *Mercury* (Sykes *et al.*, 2011) or other tools.

Orientation tends to occur in materials where the crystallites have either a needle or plate-like morphology. Plates are common in the analysis of mineral samples, such as the commercial phlogopite mica used here as an example. Conventional top-loading of such samples can result in very few reflections being visible because of almost perfect orientation of the plates during pressing, as seen in Fig. 2.10.16. Where the aspect ratio of the crystallites is large, micronizing the sample does not reduce the preferred orientation significantly (Fig. 2.10.17).

The most common approach to decrease preferred orientation of troublesome samples such as this mica is a technique known as back-loading. [Others are discussed in Buhrke *et al.* (1998).] The concept is that the surface of the sample is not subjected to

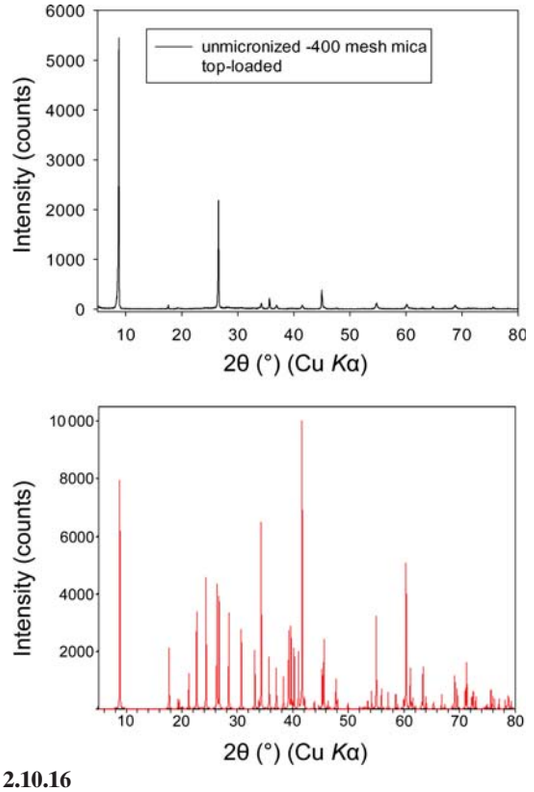

Figure 2.10.16
Top: diffraction pattern of top-loaded 400 mesh phlogopite mica. Bottom: calculated random pattern.

significant compression, yet remains flat. An example of a commercial back-loading holder is shown in Fig. 2.10.34. These holders are filled while upside down with the back removed. The cavity is filled with sample using minimal pressing, the back of the holder is replaced, and then the whole assembly including specimen is flipped the right way up. Generally, the deeper the holder the lower the compressive force on the analysed surface, but the trade-off is the requirement for large amounts of sample. Many of the samples exhibiting plate-like morphology possess low-angle reflections (such as mica and illite) so the sample area cannot be reduced too much to reduce sample volume, or beam overspill may occur.

A variation of the back-loading sample holder is the side-loading sample holder. These are less common, although the sample is still loaded against some surface in the same fashion as the back-loading variant. As the name implies, the difference is that the sample is introduced from a hole in the side as opposed to the back, and the hole is then plugged after filling.

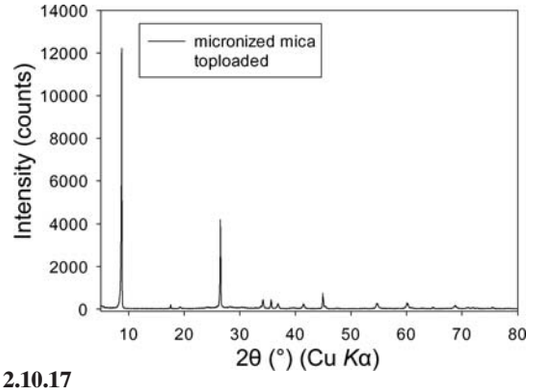

Figure 2.10.17
Diffraction pattern of top-loaded miconized phlogopite mica.

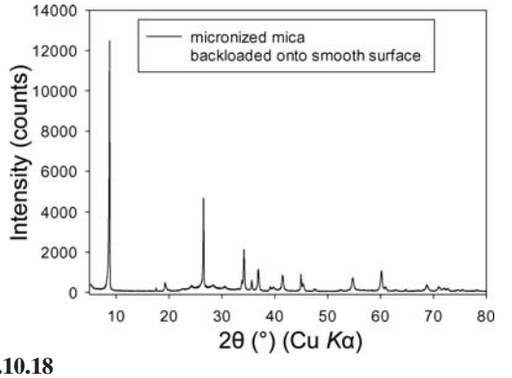

Figure 2.10.18
Diffraction pattern of miconized phlogopite mica when back-loaded onto a smooth surface.

Simple back-loading of samples in itself is not always sufficient for very platy samples such as the high-aspect-ratio mica used here. Fig. 2.10.18 shows the result from back-loading a micronized sample of the mica onto a smooth surface.

Although the result is improved, the specimen is still not a random powder. A useful approach in these circumstances is to make the surface of a back-loaded sample deliberately rough to break up the orientation of the plates. An easy way to achieve this is to load the sample onto the surface of sandpaper or a coarse ground glass slide. Sandpaper has the advantage of being disposable so avoiding cross-contamination among samples. Not all sandpaper has the desired jagged surface, so it may be necessary to experiment to find the best. The paper used for the data shown here was a 400-grit carborundum paper, the surface morphology of which is shown in Fig. 2.10.19. The rough surface will cause some slight defocusing in a parafocusing setup and reduce the count rates somewhat, but in many cases the advantages outweigh the disadvantages.

The result of back-loading the micronized mica onto the 400-grit carborundum paper is shown in Fig. 2.10.20. The dominance of the 00*l* reflections is reduced even further than when mounted onto a smooth surface. The approach is simple enough that it is used routinely in at least one laboratory dealing with large numbers of mining and mineral samples (Raudsepp, 2012). Back-loading samples is more time consuming than top-loading. Consequently, where high sample throughput is required, back-loading can be reserved for those samples where orientation is a problem.

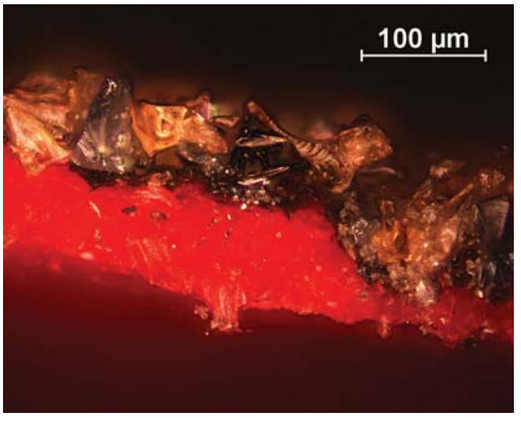

Figure 2.10.19
20× optical micrograph of a cross section of the 400-grit carborundum paper used for back-loaded mica.

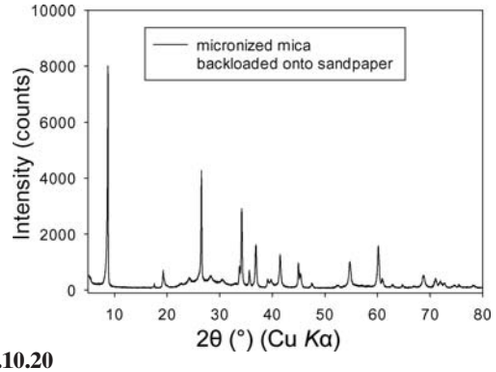

Figure 2.10.20
Diffraction pattern of micronized phlogopite mica when back-loaded onto 400-grit carborundum paper.

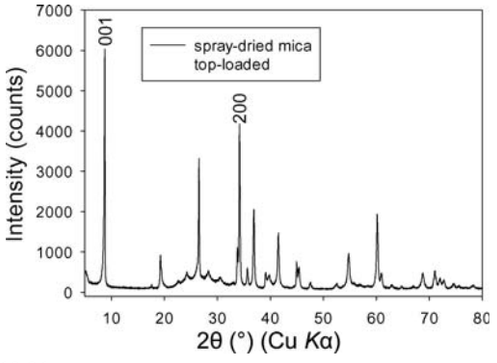

Figure 2.10.21
Diffraction pattern of top-loaded spray-dried phlogopite mica. The sample was not pressed; instead, a flat surface was produced by lightly scraping off excess material with a microspatula.

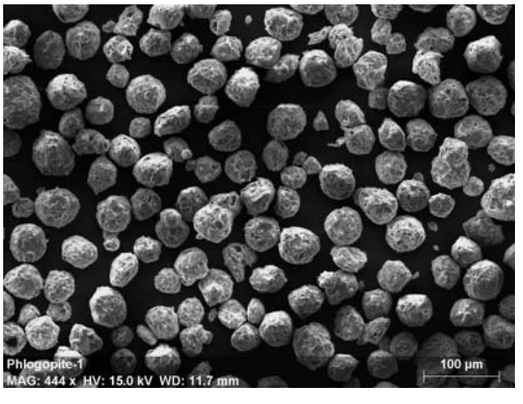

Figure 2.10.22
SEM micrograph of spray-dried micronized phlogopite mica (courtesy of M. Raudsepp, University of British Columbia).

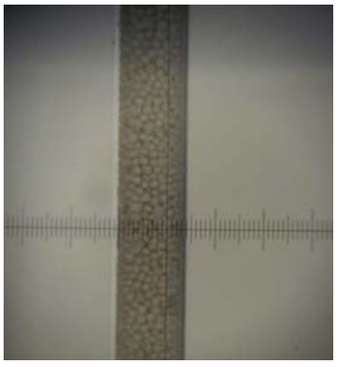

Figure 2.10.23
View through the alignment scope of the spherical spray-dried mica inside a 0.5 mm capillary.

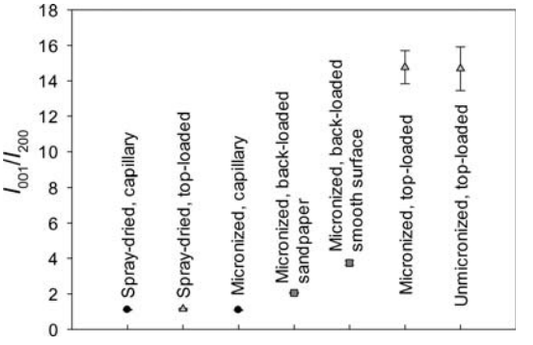

Figure 2.10.24
Plot of the ratio of the integrated intensities of the 001/200 reflections of the mica using different sample-preparation techniques.

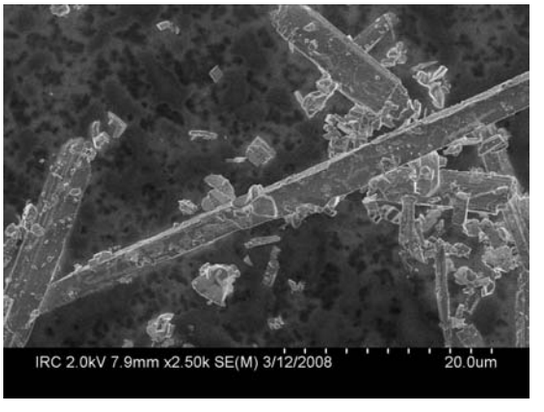

Figure 2.10.25
SEM micrograph of wollastonite needles.

Without resorting to transmission measurements, preferred orientation from platy samples may be almost, if not completely, eliminated by spray drying micronized samples (Hillier, 1999, 2002; see Fig. 2.10.21). This process produces spherical agglomerates (Fig. 2.10.22) that have no tendency to orient if handled gently. The disadvantage is that a relatively large amount of sample is often required because of inefficient sample recovery. Equipment optimized to reduce sample loss for spray-dried XRD samples may be bought in kit form (http://www.claysandminerals.com/spraydrykit), or constructed in house using a small air-brush and heated oven.

One potential practical problem when using spray-dried material with $\theta-2\theta$ geometry instruments is that the spherical particles can start to roll out of the specimen holder at higher 2θ angles (Raudsepp, 2012). The effectiveness of spray drying can be seen as the relative intensities from the top-loaded spray-dried material are almost identical to those in data obtained from the capillary experiments. The spray-dried spheres are very delicate and pressing of the sample must be avoided where possible.

It is worth noting that the platy nature of this mica was so extreme that the micronized mica tended to orient slightly inside the capillary if too much energy was applied during the filling process (*e.g.* using ultrasonics). Arguably, a capillary measurement using a spray-dried material is the ultimate precaution against preferred orientation effects, and the excellent flow characteristics of the spheres mean that the agglomerates remain

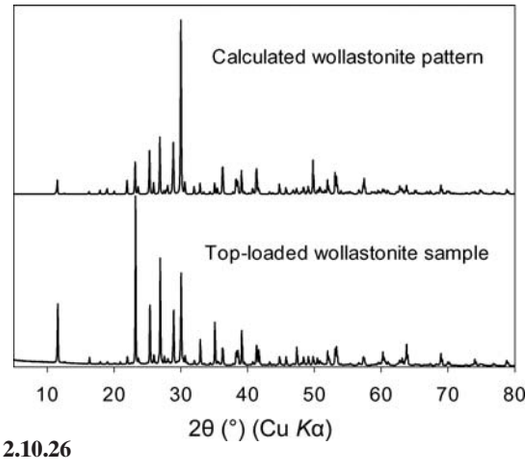

Figure 2.10.26
Effect of preferential orientation on data from top-loaded wollastonite compared with the calculated pattern from the literature wollastonite-1A structure (Ohashi, 1984).

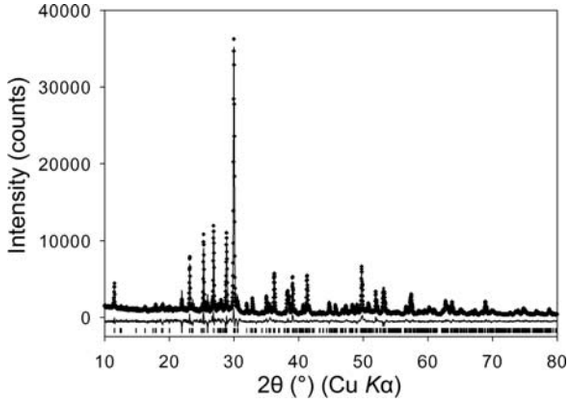

Figure 2.10.27
Rietveld refinement fit to the literature wollastonite-1A structure (Ohashi, 1984) with data from a 0.3 mm capillary with no orientation corrections.

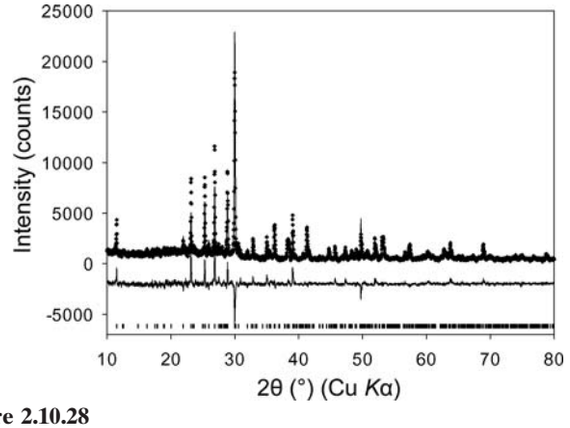

Figure 2.10.28
Rietveld refinement fit to the literature wollastonite-1A structure (Ohashi, 1984) with data from a 0.2 mm capillary with no orientation corrections.

intact while filling the capillary (Fig. 2.10.23). Fig. 2.10.24 gives a summary of the effectiveness of the different sample-preparation techniques for this particular mica sample in terms of the ratio of the integrated intensities of the 001 and 200 reflections. The spray-dried sample with careful top loading can produce a pattern practically equivalent to the capillary data set.

Plates are not the only problematic morphology. Needle-shaped crystallites such as those exhibited by wollastonite (Fig. 2.10.25) and some organic compounds can also show significant problems when top-loaded. In fact, lath-like crystallites such as wollastonite can orient in two directions at the same time, so the behaviour can be more complicated than that of materials with plate-like morphology (see Figs 2.10.26, 2.10.27 and 2.10.28).

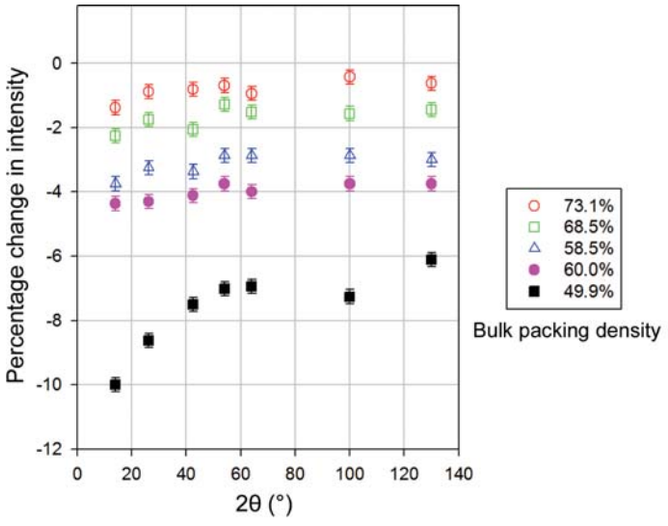

Figure 2.10.29
The effect of surface roughness on the intensity compared to that of a bulk copper specimen. Data from Suortti *et al.* (1972).

2.10.1.3. *Absorption (surface roughness), microabsorption and extinction*

Absorption, microabsorption and extinction effects all alter peak intensities, although particularly low absorption (*e.g.* from organics) can give rise to sample transparency in reflection geometry (as discussed in the section on the choice of sample mounting), where a peak shift and change in profiles can occur. Microabsorption and extinction solely affect the peak intensities.

Microabsorption (also known as absorption contrast) and extinction are effects that complicate quantitative phase analysis. They are both still related to size – particles in the case of microabsorption and crystallites in the case of extinction.

2.10.1.3.1. *Absorption (surface roughness)*

Absorption is an obvious issue when using capillaries in transmission (a convenient calculator is available on the 11-BM web site, http://11bm.xray.aps.anl.gov), but absorption can also affect data obtained in reflection using Bragg–Brentano geometry through the mechanism commonly described as 'surface roughness'. In essence, the increasing packing density with depth leads to lower intensities at low diffraction angles, leading to anomalously low or negative displacement parameters (much as absorption does in capillaries). There are two components to the effect (Fig. 2.10.29, Suortti, 1972). The constant decrease in intensity is generally incorporated into the refined scale factor. The angle-dependent portion becomes more significant as the packing density is reduced.

The effect is greatest with strongly absorbing materials analysed in reflection geometry, so care should be taken to produce a sample with a smooth surface and uniform density where possible. An example is provided by the patterns (Fig. 2.10.30) of a commercial cobalt silicate (which turned out to consist of a mixture of phases). A pattern from a slurry deposited on a zero-background cell – a technique useful for small samples, but which produces a rough surface – yielded significantly lower

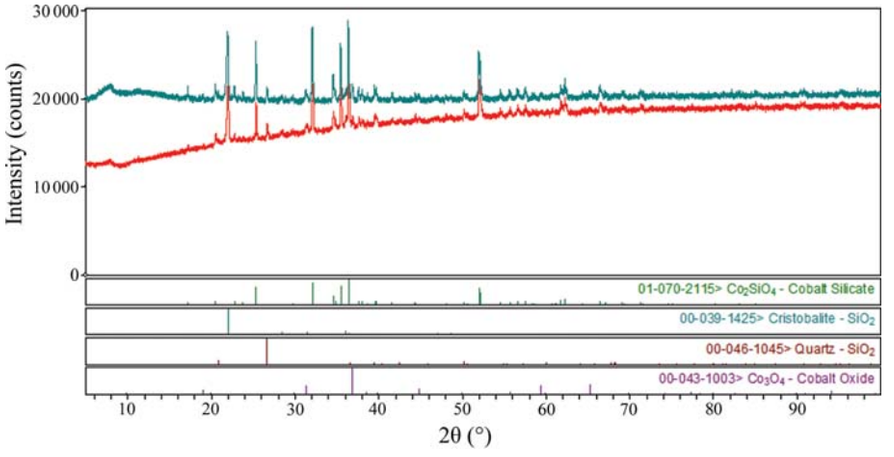

Figure 2.10.30
Powder patterns of a commercial cobalt silicate sample, measured from a (rough) slurry-mounted specimen (red) and from a (flat) conventional front-packed specimen (green). The surface roughness decreases the intensities of the low-angle peaks and background.

peak and background intensities at low angles than a conventionally front-packed specimen. Refinement using the 'rough' data yielded unreasonably negative displacement coefficients. Including a surface-roughness model in the refinement resulted in reasonable displacement coefficients, identical to those obtained using the 'flat' data.

Models by Suortti (1972) and Pitschke *et al.* (1993) exist in most analysis software. They both yield similar results, but the Suortti correction is generally regarded as slightly more stable at 2θ angles below 20°.

2.10.1.3.2. *Microabsorption*

Microabsorption is widely regarded as the greatest impediment to the application of quantitative phase analysis with powder X-ray diffraction data. Misapplication of a microabsorption correction can degrade accuracy (Scarlett *et al.*, 2002). The infamous sample 4 in the Commission for Powder Diffraction quantitative phase analysis round robin (Scarlett *et al.*, 2002) was deliberately designed to be difficult to analyse accurately using any wavelengths available to a laboratory X-ray diffractometer because of microabsorption effects.

Brindley (1945) published a theoretical correction (model) for microabsorption, but the range for an appropriate application can be easily exceeded. In the absence of such a correction, relative concentration errors can commonly be 20–30%. The extent of microabsorption for a phase was described by Brindley in terms of μD, where μ is the linear absorption coefficient and D is the particle (not crystallite) diameter. While a crystallite size can be estimated from the profile widths, determining the particle size requires additional information, such as laser light-scattering measurements. Where $\mu D > 0.1$ the Brindley correction may not be accurate, and ideally μD for every phase present should be less than 0.01, where microabsorption can safely be ignored. Brindley also suggested a rule-of-thumb for the maximum acceptable particle size for quantitative phase analysis, where $D_{max} = 1/(100\mu)$.

The terms μ and D show that microabsorption can be affected by X-ray wavelength and particle size. The easiest approach for the analyst with a troublesome sample is to reduce the particle size by micronizing the sample. Some in-house laboratories may have multiple systems or the flexibility to change wavelengths. As a rule the linear absorption coefficient decreases with increasing energy, but users should beware of absorption edges that can create a serious discontinuity in this trend. Synchrotron beamlines have more flexibility for avoiding absorption edges and can achieve higher energies that are not practical in laboratory systems. Even when using this high-energy 'sledgehammer' approach there is still a benefit to reducing the crystallite size to avoid some of the other effects mentioned in this chapter.

Microabsorption results from differences in linear absorption coefficients and particle sizes, and can sometimes arise in unexpected situations. Adding a NIST SRM 640b silicon internal standard to a micronized mullite sample (Kaduk, 2009) in order to quantify the amorphous content resulted in a significant microabsorption effect, the result of differences in both particle size and absorption coefficients. The microabsorption could be overcome by micronizing the mullite/Si blend.

Even in cases where the absorption contrast is small, large differences in particle size can result in significant microabsorption effects. For anatase/rutile mixtures (μ = 489.4 and 534.2 cm^{-1}, respectively) in which the anatase and rutile particle sizes were 3 and 150 μm, respectively, concentration errors of 20% relative were observed. The errors were corrected by micronizing the mixtures (Kaduk, 2013). Similarly, mixtures of large-particle (23 μm) MFI zeolite (μ = 65.66 cm^{-1}) and a quartz internal standard (μ = 96.39 cm^{-1}, 10 μm) resulted in relative concentration errors of 5%; these errors were corrected by micronizing the mixtures.

Neutrons are absorbed much less than X-rays, which means that microabsorption is practically nonexistent in neutron diffraction data. The lack of microabsorption is why neutron diffraction is often regarded as the 'gold standard' for quantitative phase analysis, although the beamline proposal process tends to make its application in conventional quantitative phase analysis uncommon. The application of quantitative phase analysis using neutron diffraction data is most often seen when studying phase evolution in an *in situ* experiment. Microabsorption is an issue specific to quantitative phase analysis and a more detailed discussion of the problem is given in Chapter 3.9.

2.10.1.3.3. *Extinction*

Extinction effects are not common in X-ray powder diffraction but may be significant when using neutrons. Extinction is dependent on the size/shape of the coherently diffracting domains, and is a multiple-scattering phenomenon. Primary extinction occurs when a second diffracting event occurs within a single crystallite. Secondary extinction occurs in mosaic crystals and is not seen in powders. When primary extinction occurs, the re-diffracted beam will continue in the same direction as the incident beam but interfere destructively with it. Re-diffraction within a crystallite is not likely to occur where imperfections disrupt the ordering of a crystallite. Consequently, primary extinction is usually only seen in powders of highly ordered and crystalline materials. A classic example is powdered single-crystal silicon as used in studies on extinction such as that by Cline & Snyder (1987). The most commonly encountered phase that can exhibit primary extinction is high-quality natural quartz.

Zachariasen (1945) described an extinction correction (model) including terms relating to crystallite size, wavelength, structure factor and scattering angle. Extinction effects will be apparent with large crystallites and long wavelengths. Extinction effects are also greater for the more intense (low-angle) reflections, so extinction mimics the effects of small displacement parameters. In a single-phase system, unexpectedly low or even negative displacement parameters may be the only sign that extinction effects are present. In a multiphase system the effects of extinction will reduce the apparent phase fraction of the affected phase with respect to the rest of the sample. In fact, studying extinction experimentally is often done by using its effects on quantitative phase analysis to untangle the different effects (Cline & Snyder, 1987). The frequently high quality of natural quartz makes the quantitative phase analysis of mineral samples the most likely scenario for the appearance of extinction in a practical laboratory setting.

The wide range of wavelengths and wide range of $(\sin\theta)/\lambda$ used in time-of-flight (TOF) neutron diffraction makes extinction effects particularly pronounced. Consequently TOF data often require the application of an extinction correction (Sabine *et al.*, 1988). Constant-wavelength neutron diffraction frequently uses longer wavelengths than normally used in the laboratory or synchrotron beamlines, so the user must be aware of possible problems.

Despite the danger of 'message fatigue', the dependence of primary extinction on crystallite size adds yet another reason to reduce the crystallite sizes to the order of 1 μm or so. Theoretically, single-crystal silicon will exhibit extinction with copper radiation with crystallite sizes of 5 μm.

2.10.1.4. *Holders*

2.10.1.4.1. *Reflection sample holders*

In a laboratory setting these are the most common type of holders – normally for use in a Bragg–Brentano instrument. A wide variety of sample holders for different applications are available. Several different holders and techniques will be described, but there are some issues common to all holders in reflection geometry, particularly with Bragg-–Brentano geometry.

In Bragg–Brentano parafocusing geometry care should be taken that the surface of the sample is flat. If the surface is not flat the parafocusing condition is violated and will degrade the peak resolution and positions; in addition, surface roughness can affect the intensities. Where there is a cavity it seems straightforward to make sure that the sample surface is level with the top surface of the holder. The peak positions obtained in Bragg–Brentano geometry are very sensitive to specimen displacement; a vertical displacement of 20 μm in a typical diffractometer will shift the peaks by approximately 0.01° 2θ. The derivation of the equation for the effect of displacement on peak position is given in Fig. 2.10.31. The minus sign in the equation reflects the convention that the displacement is positive if it increases the radius of the diffracting circle, *i.e.* the sample is too low. Front-packed specimens are almost always too high, so the analyst needs to refine his/her technique to minimize the displacement errors.

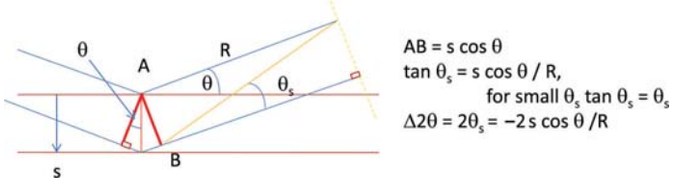

Figure 2.10.31
Derivation of the equation relating peak displacement to sample displacement (s) in parafocusing geometry. R is the goniometer radius.

Figure 2.10.32
A home-made top-loading zero-background silicon holder with a 0.5 mm deep cavity.

The sensitivity to specimen displacement is such that even dirt between the reference surface of the sample stage and the holder can produce a detectable peak shift. Dust accumulation inside a powder diffractometer is almost inevitable, so occasionally cleaning these surfaces is recommended.

Parallel-beam-geometry diffractometers have become popular in many laboratories because some of these problems are avoided. Although there are often some disadvantages in terms of peak resolution and grain sampling, they allow more flexibility in the mounting of specimens. For instance, rough sample surfaces and displacements do not cause the aberrations that are apparent in data from conventional parafocusing diffractometers when the same samples are analysed with a parallel-beam system.

Many different types of holders for reflection geometry are available commercially from the instrument vendors, but often home-made holders can be equally effective and customized for specific tasks. Most common are the different types of top-loading sample holders made from plastic or metal, often with a cavity to hold the sample. Commonly the cavities are larger or smaller than those offered by the vendors. The cavity may include some form of zero-background plate such as specially cut single-crystal silicon (Fig. 2.10.32) or quartz, although this does add a significant cost. Some quartz plates may exhibit forbidden reflections or contain inclusions, so they should be tested before use in a sample spinner.

In addition to the standard holders, more specialized holders may be bought or built, or indeed fabricated using a 3D printer. These include holders for air-sensitive samples (Fig. 2.10.33), back-loading (Fig. 2.10.34) and side-loading holders, holders for filter papers, clay samples *etc*. Any laboratory with a competent workshop can construct a wide variety of holders, including those for complex *in situ* work, which is discussed in Chapter 2.9. One common theme is that any material in the X-ray beam path must be kept to a minimum to reduce attenuation. Ideally any such material (such as the polymer dome of the air-sensitive holder shown in Fig. 2.10.33) should be as far away from the diffracting plane as possible. A secondary monochromator can be effective in stopping the parasitic scattering from reaching the detector, but with a PSD there is greater reliance on good design to reduce it as much as possible. A common approach with home-designed and -constructed sample holders for air- or moisture-sensitive samples is to cover the sample with a thin Kapton or Mylar film attached with a bead of silicone grease.

Figure 2.10.33
Commercial holder for air-sensitive samples. This particular holder for small samples has a flat silicon zero-background plate and a polymer dome which screws down against a rubber o-ring seal.

One of the most common questions asked by users of laboratory instructions is how to deal with small sample sizes. In an ideal world, a specialist microdiffraction system or capillary geometry could be used, but many laboratories do not have access to such equipment. How problematic such samples can be depends to some extent on the mass absorption coefficient of the sample. Conventional powder diffraction data relies on having a sample with an 'infinite sample depth'. However, that depth can be very small for samples with very high absorption coefficients. In those cases, spreading the sample in a very thin layer can still yield reasonable relative intensities across a large range of 2θ angles. With low-absorbing samples such as organics the relative intensities will drop off at higher angles as the sample is no longer

Figure 2.10.34
Filling a commercial back-loading sample holder. The holder is held against a base surface (sandpaper in this case) while filling, the back is replaced and then the holder is flipped over to reveal the sample surface once the clips are removed.

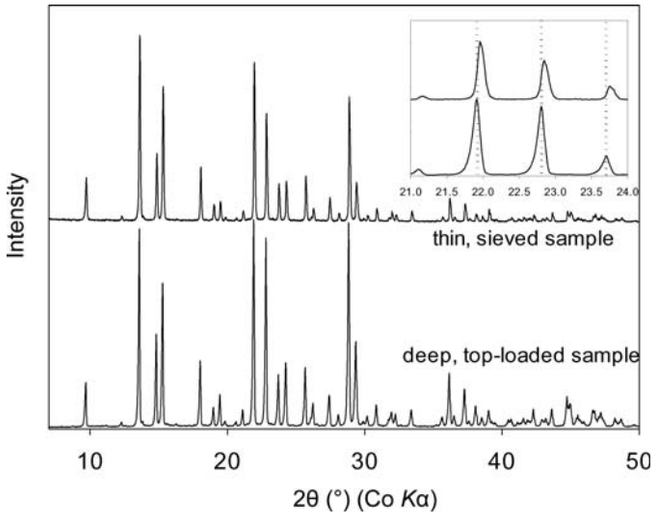

Figure 2.10.35
Data from powdered sucrose on a Bragg–Brentano instrument, with the peak intensities normalized to the first reflection. The thin sample was prepared by sieving onto a low-background silicon plate made slightly tacky using hairspray. The inset shows that there is a slight peak shift between the two data sets as well as the predicted decay in relative intensities with the thin sample with 2θ angle.

'infinitely thick', as shown in Fig. 2.10.35. However, the peak positions will be more accurate than with deeper samples because of the lack of transparency effects in thin samples. Consequently, it is not uncommon to obtain two data sets from such samples: from a thin sample to obtain good peak positions, and from a deep one to obtain better relative intensities. The details of sample penetration are given in Chapter 5.4.

Most modern holders are circular and the specimen is often loaded into a round cavity. As the beam 'footprint' is rectangular, this is not the most efficient use of the material, as a significant portion will always remain outside the beam. Prior to the introduction of sample spinners, square and rectangular cavities were quite common. It is good practice to know the footprint of the beam at various diffraction angles by observing the illuminated area of a fluorescent specimen. Should the material be in particularly short supply and sample spinning is not absolutely necessary, the powder may be mounted in the minimum rectangular shape to be illuminated by the incident beam. Such an approach may be combined with the use of motorized divergence slits to maintain a constant beam length on the sample. Although most analysis software assumes constant divergence slits, the correction is well known and implemented in most commercial software.

In order to avoid background from the sample holder, thin specimens are usually mounted on flat zero-background plates. It is useful to have the surface of the plate lower than the reference surface (50 μm is a common value) to minimize specimen displacement effects. In practical terms, thin samples are historically referred to as smear mounts. Slurry mounting using ethanol or acetone often yields a self-adhesive specimen, but it is tricky to obtain the correct slurry rheology to produce a non-lumpy, thin and even layer across the surface; surface roughness is often apparent in the pattern. Loose, friable samples may be problematic with spinning specimens or the tilting specimens in θ–2θ geometry. A number of materials have been used over the years to adhere thin powder samples to flat plates; common ones are thin smears of Vaseline or grease, but analysts often have their own favourites. The particular material used to stick the sample to the surface is often the result of testing a large number

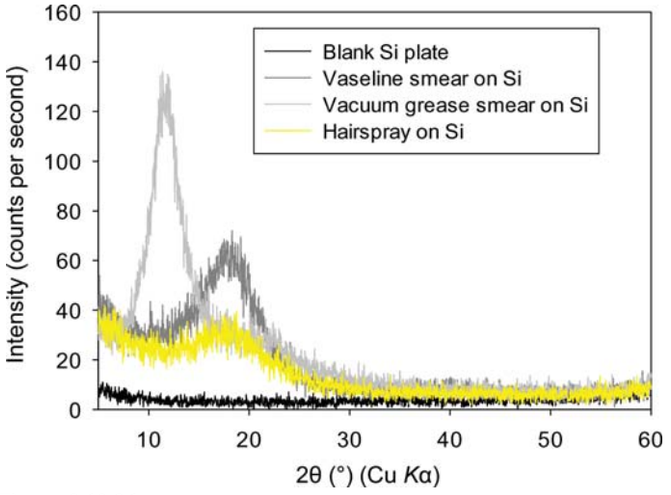

Figure 2.10.36
Diffraction pattern from a silicon-wafer zero-background holder, smears of Vaseline and Corning high-vacuum grease, and the surface treated with hairspray.

of options to find the one with the lowest background and fewest non-Bragg reflections. An unusual alternative is hairspray, which produces a tacky surface when applied correctly whilst having a minimal effect on the resulting diffraction pattern. The medium chosen may also depend on whether the sample must be recovered intact, as contamination with grease might not be acceptable. The effect on the background of different adhesion materials can be seen in Fig. 2.10.36. The Vaseline and vacuum grease smears add broad reflections at approx. 19 and 11° 2θ, respectively, with Cu $K\alpha$ radiation. Where data collection starts above the main portion of the peak the effect may be hardly noticeable, but could be problematic when starting at low 2θ angles. Such broad patterns are straightforward to model with a Debye (diffuse scattering) function, and it is not necessary to subtract them from the raw data.

Should the instrument have parallel-beam geometry, an alternative approach is to use a fixed incident-beam angle, more commonly known as grazing-incidence geometry. In this way the volume of sample illuminated is constant with angle, so in the absence of secondary diffractometer optics the relative intensities will match those expected with conventional geometry. An unfortunate effect of conventional grazing-incidence geometry with long slits is that the peak widths degrade significantly at lower incident angles (Toraya & Yoshino, 1994). It is possible to model the peak broadening in a Rietveld refinement (Rowles & Madsen, 2010) but it is not straightforward. Use of an appropriate secondary optic can avoid the peak-broadening problem but introduces a complex, geometry-dependent intensity correction (Toraya *et al.*, 1993).

2.10.1.4.2. *Transmission sample holders*

Transmission geometry of any type is best suited to samples with low absorption such as organics and polymers, and is preferred for such samples when available. Transmission geometry has advantages when data are required at low diffracting angles. While the beam often has to be stopped-down in reflection geometry to avoid overspilling the sample, this undesired attenuation of the beam is not required for transmission geometry. Another advantage common to both the foil and capillary transmission techniques is that a small quantity of a powdered sample is usually sufficient. Samples small enough to be problematic with reflection geometry will often be perfectly adequate for transmission.

Data collection in transmission geometry is best done with either a parallel-beam or focusing geometry; the focus should be at the detector. Data can be collected using a divergent-beam setup, but the intensities obtained are very low and the resolution is usually poor. Parallel-beam geometry has the advantage that it is able to perform reflection and transmission measurements equally well.

2.10.1.4.2.1. Flat foils

Although less commonly used with modern diffractometers, the foil-type transmission sample mounting was quite common in some older-style X-ray cameras. Sprinkling powders onto single-sided Scotch tape was sometimes used with instrumentation such as Hägg–Guinier cameras, but care should be taken as the quality of the tapes as diffraction substrates can vary wildly; the crystallinity of the polymer can be high or low, and the adhesive sometimes contains mineral inclusions, such as talc. In the modern diffractometer, foil-type transmission data can sometimes be collected using the same rotating sample stage as for reflection measurements. Simply turning the stage by 90° and using a different holder can be sufficient if the optical configuration is suitable for both reflection and transmission. For solid organic samples such as polymers this foil transmission geometry has significant advantages because of the lack of transparency effects. It is worth noting, however, that the processing of polymers can induce significant texture, such that the data collected from a film in reflection geometry will not necessarily be identical to those collected in transmission. Should a reproducible pattern independent of geometry be required, then steps should be taken to reduce the sample to a true random powder and/or a 2D detector should be used.

With powder samples the technique requires the use of a transparent substrate, usually in the form of a thin polymer film or foil. In an analytical laboratory the easiest place to find such a substrate is the X-ray fluorescence laboratory, where very thin X-ray transparent polymer films are used for both sample supports and covers for liquid cells. Some of the materials used in these applications are familiar in the diffraction community as windows, *i.e.* Mylar and Kapton, but others such as polypropylene are not. The substrate will obviously add to the background, but a good substrate from a diffraction standpoint combines transparency with a lack of sharp features in the diffraction pattern. This makes fitting the background much easier. Any holder must be capable of stretching or holding the film flat across an opening for the X-ray beam. A commercial version of a foil-type holder is shown prior to assembly in Fig. 2.10.37. Example data from three different XRF films are shown in Fig. 2.10.38, together with that from a thicker Kapton foil commonly used as window material. It is notable that, despite the two 7.6 µm Kapton films being almost twice as thick as the Mylar or polypropylene films, the scattering from them is almost identical. The lack of any distinctive, sharp features above 6° 2θ in the Kapton films makes them attractive in this region, but for low-angle data Mylar is probably the better choice. Although giving a generally higher background, the thicker 50 µm Kapton foils can be used very successfully (see Fig. 2.10.39). Despite the greater attenuation they are much easier to handle, as their greater stiffness and weight makes them less susceptible to static electricity.

One advantage of transmission foil mounts is the small amount of sample required. In a similar way to producing smear mounts

Figure 2.10.37
Parts prior to assembly of a transmission foil sample in the holder. In this instance, micronized quartz is held as a loose powder between two 50 μm Kapton foils while the upper foil is stretched into place by the black clip.

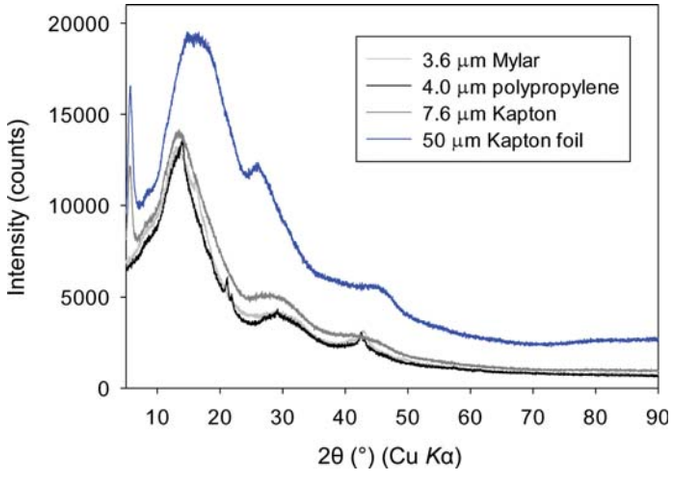

Figure 2.10.38
Transmission data from double layers (as used for powder samples) of different polymer substrate films. They include 3.6 μm Mylar, 4.0 μm polypropylene and 7.6 μm XRF films, and a thicker 50 μm Kapton foil.

for reflection geometry, there are a number of ways to prepare the thin layer required. Loose powders may be trapped between two foils as in Fig. 2.10.39, or alternatively a slurry or smear mount may be used in a similar way to reflection geometry. Although the sample may adhere sufficiently such that a single foil can be used, it may be necessary to use a sandwich in the same way as a loose powder. For instance, slurries do not usually adhere well to Kapton foils, so it is often better to sacrifice a little intensity from the additional Kapton attenuation and ensure the sample does not fall away during data collection. Lack of adhesion could be regarded as an advantage with regard to recovery of valuable samples. Where an adhesive is used, the same considerations as with a smear mount in reflection still apply with regard to background *etc*.

Ideally the sample thickness should be perfectly uniform, but in practice this will rarely be achieved. Commonly a specimen in visible light transmission will appear something like that seen in Fig. 2.10.40. Rotation is used to average out inhomogeneity in the specimen.

Sedimentation during slurry mounting and compression of powders between two foils can lead to preferential orientation

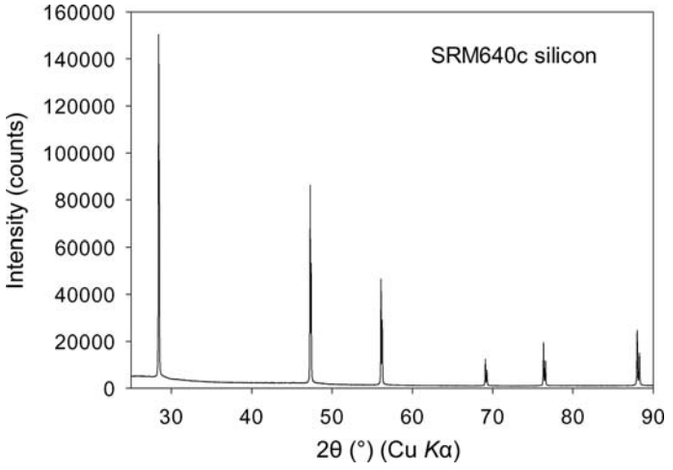

Figure 2.10.39
Diffraction pattern from loose SRM640c powder between two 50 μm Kapton foils.

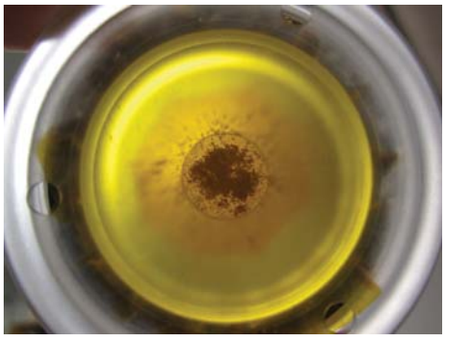

Figure 2.10.40
Transmitted light view of a micronized quartz sample through 50 μm Kapton foils.

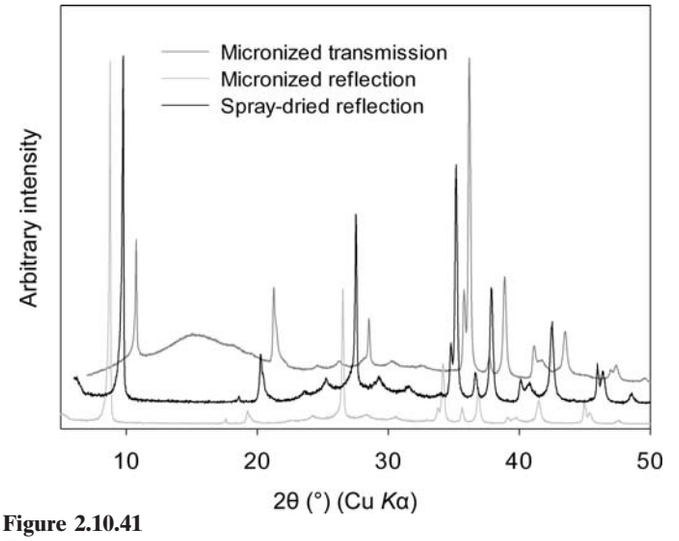

Figure 2.10.41
Comparison of data from micronized 40S mica taken in reflection and transmission geometry, and spray-dried material in reflection geometry. For improved clarity the spray-dried and transmission data sets are translated by +1° and +2° 2θ respectively.

in foil transmission samples just as with flat-plate reflection specimens. Although the physical effect is the same for plate-like crystallites, it should be remembered that the crystallite orientation with respect to the beam is rotated by 90°, so the

resulting diffraction patterns will not look the same. This becomes very apparent when comparing the foil transmission and reflection patterns from the micronized mica in Fig. 2.10.41.

Foil transmission specimens are usually rotated in a similar fashion to a reflection sample, but the improvement in statistics falls short of that found in the capillary geometry described in the next section.

One thing worth considering is that there is an inherent angular intensity aberration due to the plate transmission geometry. Owing to geometrical considerations, the path length through the specimen (and support) increases with angle with a resulting increase in absorption. For refinement work, a $1/\cos\theta$ correction can be applied.

2.10.1.4.2.2. Capillaries

Capillaries are particularly suitable for small samples, air- and moisture-sensitive samples and organics where the absorption is low enough to cause transparency effects in reflection data. They are also commonly used for materials with platy morphologies such as clays to eliminate or greatly reduce preferred-orientation effects. They are less effective at reducing preferred orientation in materials with needle-like morphologies but are still useful, a possible analogy being that the crystallites pack into the capillary like a handful of pencils in a glass. The extent of the problems with needles depends on the aspect ratio of the needles and the diameter of the capillary used – smaller diameter capillaries usually being more problematic. Figs. 2.10.27 and 2.10.28 show the example of wollastonite powder mounted in 0.3 and 0.2 mm capillaries, respectively, where orientation effects become pronounced in the 0.2 mm capillary. Fortunately, needle-like morphology is observed more often in organic crystallites, where larger-diameter capillaries can be tolerated.

Glass and fused silica ('quartz') capillaries can be bought commercially in a range of diameters between 0.1 and 2 mm. Different compositions of glass are available that have varying absorption characteristics (Table 2.10.3). The softer glass has a greater tendency to splinter but can be heat-sealed very easily by melting. Quartz tends to be stiffer and often breaks more cleanly when scored using a cutting stone, but requires a hydrogen flame for heat-sealing because of its high melting point. Alternative methods of sealing the open end of capillaries include using molten wax, epoxy and nail varnish. The choice may be restricted by the environment in which the capillary is being filled. In an argon-filled glove box the use of a flame or solvent-based method may not be feasible or desirable, whereas wax sealing with a heated filament is acceptable.

The small size and delicate nature of capillaries can make them extremely frustrating to fill, especially in environments such as glove boxes. Patience is an absolute must, especially with valuable or small samples where capillary breakage and sample loss are unacceptable. It is very important to make sure that the sample is fine enough to pass into the capillary without jamming. Even if it is fine enough, different powders can vary considerably in their tendency to aggregate. For example, NIST 640d silicon contains fine crystallites and flows extremely well, making it very easy to load into a capillary. However, some rutile powders can be very fine but don't flow well, making them difficult to load into smaller capillaries.

Once the small amount of material is in the capillary funnel (assuming it is a commercial capillary), it must be coaxed to drop to the bottom. This is usually done using some form of vibration. Anything from dedicated capillary-filling machines to ultrasonic baths, test-tube vibrators and nail files can be used. A common strategy is to drop the capillary down a vertical 50 cm glass tube, and allow the bouncing when the capillary hits the bottom to vibrate the sample. However, with very small and/or valuable samples the risk of the sample being vibrated out of the funnel may be too great to use automated techniques. In this case, very gently stroking the capillary using a fingernail to induce a low-frequency vibration may be the best option, changing the position at which the capillary is held to alter the vibration frequency as required. Agglomerates blocking a capillary can be very difficult to break up by vibrating the capillary manually, but an ultrasonic bath can often break up loosely bound agglomerates. Using a smaller-diameter quartz capillary or wire to tamp down a clog is possible, but riskier than using an ultrasonic bath.

Table 2.10.3
Absorption and physical characteristics of the capillaries whose data are shown in Fig. 2.10.46

Material	Linear absorption, Cu $K\alpha$ (cm^{-1})	Wall thickness (μm)	Outside diameter (mm)
Quartz (Hampton Research)	76	10	0.50
Soda lime glass (Hampton Research)	126	10	0.50
PET (Advanced Polymers)	10	19	0.58
Polyimide (Cole-Palmer)	9	25	0.55

The most commonly used capillaries range between 0.3 and 0.8 mm in diameter. Capillaries with a diameter less than 0.3 mm are extremely difficult to fill and very large ones can cause unwanted artifacts. For moisture-sensitive materials it is worth noting that significant moisture can adhere to the interior surface of commercial glass and quartz capillaries, so heating them in an oven prior to use is recommended.

The interplay between the sample absorption, radiation and optics can make the choice of capillary material and diameter a dynamic one. The capillary absorption is measured using the term μR, where μ is the effective linear absorption coefficient (taking account of the sample density) and R is the capillary radius. A convenient tool for estimating capillary absorption is available on the 11-BM web site (http://11bm.xray.aps.anl.gov). Ideally, the value of μR should be less than 3 for the absorption corrections in most software packages to adequately cope with the effect of absorption. A recent analytical correction has been shown to be effective to $\mu R = 10$ (Lobanov & Alte de Viega, 1998), but is not yet implemented in all current analysis software. A pre-analysis correction is always possible but not ideal. The effect of high capillary absorption can be seen visually by a reduction in peak intensity at lower angles, which correlates with the displacement parameters in a structure refinement. The easiest way to change μR is by changing the capillary diameter. More heavily absorbing samples usually require smaller capillaries, although using an alternative radiation such as Mo $K\alpha$ to change the linear absorption coefficient is a possible alternative. Determining an accurate sample packing density experimentally can be tricky. There can be significant variability between supposedly identical capillaries, so ideally the empty portion of the actual capillary being used should be measured. The packing density generally ranges from 20–50% depending on the morphology of the crystallites and the amount of energy applied in vibrating the sample into the capillary (*e.g.* sonicating the sample will increase the packing density).

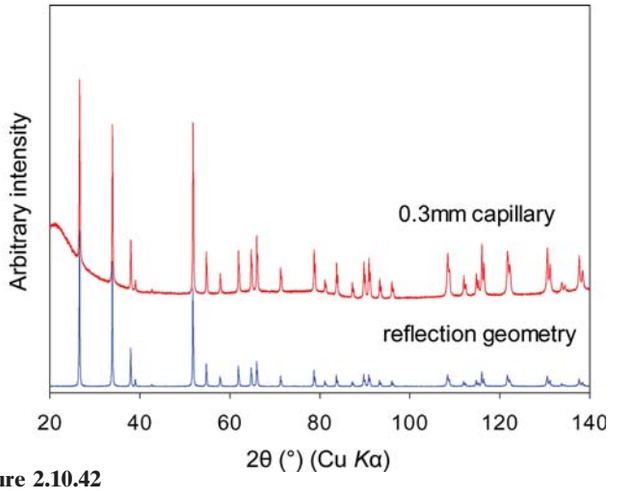

Figure 2.10.42
Comparison of the diffraction patterns of pure SnO_2 from a 0.3 mm quartz capillary in transmission and reflection geometries with Cu $K\alpha$ radiation. The very high absorption of SnO_2 leads to severe attenuation of the lower-angle reflections in the transmission data.

Where contaminating the sample is acceptable, another option is to dilute the sample with a material with very low absorption to reduce the overall sample absorption. There are two options here: either an amorphous material or a crystalline one. The addition of an amorphous material such as fumed silica (others could include amorphous boron, carbon black *etc.*) does not add any additional reflections to the pattern but will increase the background. Given that the backgrounds of capillaries using Cu $K\alpha$ radiation are often quite high already, this may not be desirable. Alternatively, a material such as diamond powder can be used, which will add a small number of lines at high angles but does not add to the background. The closely defined crystallite sizes of diamond polishing powder can also improve the flow characteristics of materials that tend to agglomerate. The phase purity of polishing media is not relevant to their intended use, and some diamond polishing powders can contain some SiC, corundum or quartz. Check the phase purity of any diluting phase before use.

Fig. 2.10.42 shows the pattern from a 0.3 mm capillary of pure SnO_2 (cassiterite) taken with Cu $K\alpha$ radiation compared with that from reflection geometry. The linear absorption coefficient of SnO_2 with Cu $K\alpha$ radiation is ~1400 cm^{-1}. Assuming a 50% packing density, μR with a 0.3 mm diameter capillary is 10.5, which is much higher than can be tolerated in any structural analysis. Absorption attenuates the lower-angle reflections as the X-rays cannot penetrate properly compared to the high angles. However, in addressing capillary absorption, less really can be more. Fig. 2.10.43 shows data sets from SnO_2 diluted with 8000 grit diamond powder and with amorphous carbon black. As expected, the background is higher with the amorphous carbon but without the additional reflections from the diamond powder. Despite there being only approximately 10 vol% SnO_2 in each of the sample mixtures, the raw low-angle intensities are much higher, and the relative intensities are comparable with those from the reflection data in Fig. 2.10.42. Assuming a 50% packing density for the mixture, the value of μR with a 0.3 mm capillary would be approximately 2.3, which is in the acceptable range for structural analysis.

The relative intensities are such that a good-quality Rietveld refinement of a heavily absorbing compound such as SnO_2 with Cu $K\alpha$ laboratory data can be easily carried out. Fig. 2.10.44 shows the fit of the diamond-diluted sample to the literature cassiterite SnO_2 structure. With very high dilution factors one should be careful not to compromise the particle statistics too much. Utilizing the full width of the detector with a full capillary will maximize the available statistics.

An alternative approach to dilution of heavily absorbing samples inside a capillary is to coat the outside (or inside) of a capillary. An appropriate absorption correction for annular samples does exist (Bowden & Ryan, 2010), so this is not an impediment. However, it is not available in common software packages so may have to be applied to the raw data prior to a structural analysis. One requirement is that a known thickness of sample needs to be applied to the surface of the capillary as uniformly as possible. This can be difficult to achieve and may require the use of an adhesive to bond the sample sufficiently to the capillary while spinning. The additional effect of an adhesive on the background should be considered in the same way as for a smear mount. Similar results to dilution may be achieved if done with care, as shown in Fig. 2.10.45.

Depending on the instrument geometry, a large diameter capillary can have an additional effect. Where an instrument does not have a focusing geometry (either primary or secondary), the peak resolution is degraded with increasing capillary diameter. With organic samples this can lead the analyst to use a smaller

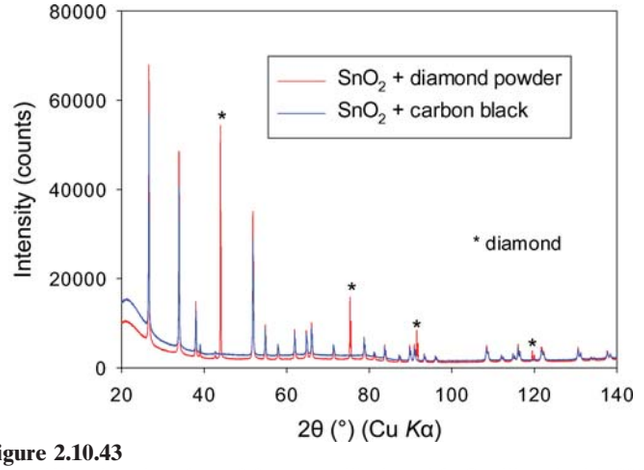

Figure 2.10.43
Raw diffraction data from 0.3 mm capillaries of SnO_2 diluted with 8000 grit diamond powder and carbon black. In each case the capillaries had approximately the same packing density of SnO_2, so yielded almost identical intensities.

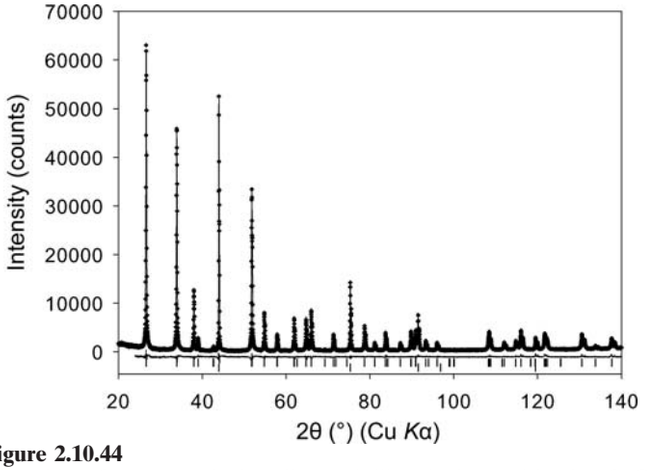

Figure 2.10.44
Rietveld refinement of the diamond-diluted data with the SnO_2 cassiterite structure. The capillary background was subtracted prior to the fitting whilst maintaining the correct counting statistics. The R_{wp} value for this fit was 8.4%.

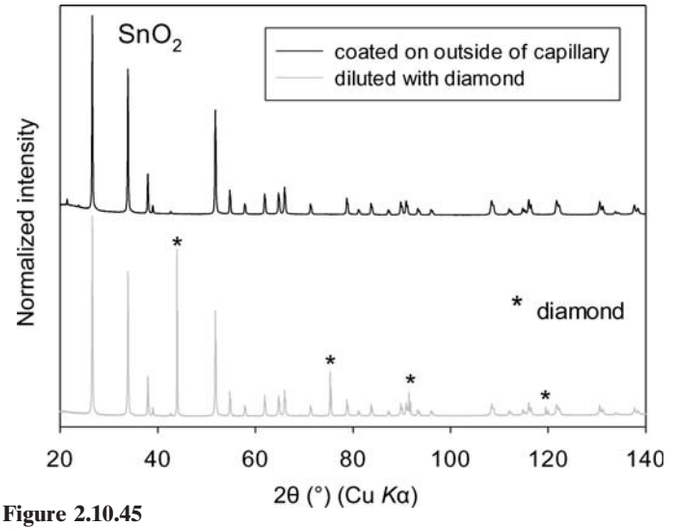

Figure 2.10.45
Comparison of data from SnO_2 when diluted with diamond inside a 0.3 mm capillary and pure SnO_2 coated on the outside of a 0.3 mm capillary.

Figure 2.10.47
Platform and pin mounts for capillary samples.

Figure 2.10.48
A 0.5mm capillary secured into a standard brass capillary pin using dental wax at both ends of the pin.

diameter capillary than optimal to retain reasonable resolution. Consequently, with organic samples where capillaries of 0.8 mm diameter are commonly used, it is highly recommended that an instrument with a primary focusing monochromator (or mirror) is used; the focus should be at the detector. Where the diffractometer is θ–θ geometry it is best to still collect capillary data as if it were a θ–2θ Debye–Scherrer instrument, simply by collecting 'detector scans' or the equivalent in the data-collection software. This has no effect on the data in a perfect situation, but it means that the sample illumination is constant over all diffracting angles even if there is a misalignment of the primary beam with respect to the capillary axis (caused either by misaligned optics, a misaligned capillary stage, or both). In addition, a correction for capillary displacement can be applied to data collected in conventional Debye–Scherrer geometry (Klug & Alexander, 1954) as the x and y displacements relative to the incident beam are constant over all 2θ angles.

Polymer capillaries are becoming increasingly common and are the standard at many synchrotron beamlines. They are easy to seal, but the lack of a funnel can make smaller sizes trickier to fill. A number of polymers can be used for capillaries, *e.g.* Mylar [poly(ethylene terephthalate) – PET] and Kapton [poly(oxydiphenylene pyromellitimide)]. The background from the capillary material itself is often more noticeable with a laboratory diffractometer than for higher-energy synchrotron instruments. A comparison of the background with a Cu $K\alpha$ focusing mirror laboratory diffractometer from 0.5 mm quartz, soda lime glass, PET and polyimide capillaries is shown in Fig. 2.10.46. A study of the different options for polymer capillaries in the laboratory environment was published by Reibenspies & Bhuvanesh (2006), which highlighted the awkward reflection with polyimide visible just above 5° 2θ in Fig. 2.10.46. It is also worth noting that the walls of polymer capillaries are not as stiff as those of quartz capillaries. If a low-temperature or other experiment might produce an internal vacuum (*i.e.* freezing a liquid sample), a polymer capillary can deform from a perfect cylinder, which may cause problems.

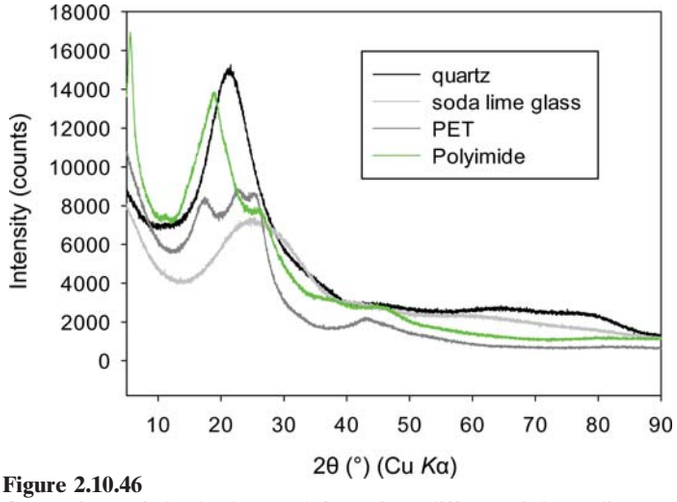

Figure 2.10.46
Comparison of the background from four different 0.5 mm-diameter capillaries. The quartz and glass capillaries are commercial capillaries for diffraction analysis. PET and Kapton capillary tubing are available from a number of different suppliers and are not made specifically for diffraction.

Mounting the filled capillary on the goniometer head can be achieved in different ways. Most commonly a hollow brass pin is used, but flat platforms are available (Fig. 2.10.47). The various pins/platforms are a standard size, so they should fit no matter where they are sourced from. The flat platforms have a hole in the middle, but it is only suitable for inserting small-diameter capillaries. Large-diameter capillaries must be affixed to the platform surface with wax and are vulnerable to sagging with horizontal goniometers because of the lack of support. The brass pins will accept larger capillaries and are to be preferred with respect to improved support for the capillary where the capillary is held at both ends of the brass pin (Fig. 2.10.48). Fixing the capillary onto the base is often done using wax or clay, although epoxy may be preferable if elevated temperatures are to be used. Coarse alignment is usually performed using a small desktop microscope before final alignment on the system. It is important to try to get the capillary rotating as straight as possible before mounting on the system, as removing tilt errors is much more difficult with the higher-magnification alignment scope mounted on the goniometer. Final alignment of a capillary is an exercise requiring patience. Never try to align out errors in two directions at once. Even if repeated attempts are necessary to stop the goniometer head in the correct position (Fig. 2.10.49), only correct errors perpendicular to the view in the scope. Ideally, the final alignment should only require correction of a side-to-side

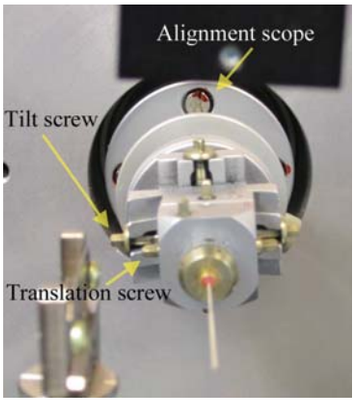

Figure 2.10.49
Goniometer head position in relation to the goniometer-mounted alignment scope.

movement rather than any wobble from tilt misalignment. However, it can still take some time. For systems where the goniometer spinning is controlled by computer software a wireless computer mouse is a very good investment, as it allows the person performing the alignment to stop the spinning capillary without taking their eyes off the sample.

2.10.2. Neutron powder diffraction

2.10.2.1. *Specimen form*

Large penetration depth and sensitivity to lighter elements (especially mobile species such as hydrogen, lithium and oxygen) in the presence of heavier elements make neutron diffraction a powerful and complementary technique to X-ray diffraction for structural studies. Because neutrons are highly penetrating and large sample volumes can be used, sometimes no specimen preparation is needed at all; sintered ceramic pellets, fish otoliths and renal calculi can be placed directly in the beam. However, the most traditional sample holder for standard neutron powder diffraction (Debye–Scherrer geometry) is cylindrical and is usually made of vanadium. If the diffraction instrument has reflection geometry, however, one has to use flat plates. Diffractometers built for the study of engineering materials can accommodate various shapes and forms because they can isolate small volumes within the sample.

2.10.2.2. *Sample size*

Traditionally, a large amount of sample was needed for neutron powder diffraction because of the limited flux available at various neutron sources. However, significant advances have been made in source power and detector technology, making it possible to do standard diffraction experiments with relatively small quantities of samples, both at reactor and spallation sources. There are multiple factors that have to be taken into account to determine how much sample is required. These include source power, detector coverage of the instrument, source-to-sample distance, the scattering power of the sample, beam size, available time and information sought from the measurement. Neutron powder diffraction instruments often have to trade intensity for resolution, and so often a larger quantity of sample is needed for high-resolution instruments. Sample mass can vary from milligrammes to several grammes, so it is always advisable to contact the scientists responsible for the particular instrument to determine the quantity needed for the proposed measurements.

(*a*)

(*b*)

Figure 2.10.50
Two examples of sample holders used in neutron powder diffraction. (*a*) A cell made of Inconel used for hydrogen absorption studies in Li_3N (Huq *et al.*, 2007). (*b*) Vanadium holders that were specially made for a sample changer built for the Powgen diffractometer located at Oak Ridge National Laboratory.

2.10.2.3. *Specimen containment*

The choice of materials for designing sample holders usually depends on the type of experiments, temperature or pressure conditions, the type of neutron source (constant-wavelength or time-of-flight), the presence or absence of fine radial collimators in the instrument and finally the sample. The scattering of vanadium (σ_{coh} = 0.0184 b) or a TiZr alloy (a null scatterer, because of exact matching of the negative scattering length of titanium and the positive scattering length of zirconium) is almost purely incoherent, making it ideal for sample containment for diffraction measurements. Although the coherent scattering of vanadium is small, in careful work it should not be a surprise to find weak peaks from V (space group $Im\bar{3}m$, a = 3.027 Å) in the powder pattern. Examples of vanadium sample cans are shown in Fig. 2.10.50(*b*). At a reactor source aluminium is even better if low-angle (large d-spacing) reflections are of interest, as in the case of many magnetic structural studies, because the aluminium incoherent scattering cross section is three orders of magnitude less than that of vanadium. At elevated temperatures, vanadium easily forms oxides or hydrides in the presence of air or hydrogen, making the cell brittle, so its use is limited to low-temperature studies or in vacuum furnaces. At temperatures higher than 1273 K one often has to use boron nitride caps and molybdenum screws for vanadium sample holders to avoid eutectic formation (an example is shown in Fig. 2.10.51*b*). For

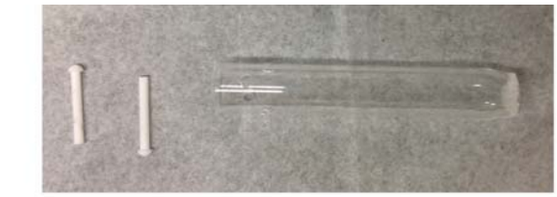

(*a*)

(*b*)

Figure 2.10.51
Two sample holders used for high-temperature studies. (*a*) A cell made of quartz with frits at the bottom to allow gas flow through the sample. (*b*) A holder on the right made of vanadium but using a boron nitride top with molybdenum bolt, nuts and washers to avoid melting due to eutectic formation. The fitting on the far left, which is made of stainless steel, is used to attach the boron nitride cap to the stick.

samples that react with vanadium, a thin layer of a noble metal such as gold can be vacuum deposited inside a vanadium can to stop it from reacting with the sample (Turner *et al.*, 1999). If this approach is used, it should be remembered that the melting point of gold is 1337 K, and when it is irradiated by neutrons it becomes activated with a half-life of 2.7 days. For experiments requiring hydrogen pressure at elevated temperature, Inconel (Fig. 2.10.50*a*) is often the material of choice (Bailey *et al.*, 2004). However, in this case for diffraction measurements one has to either exclude the Inconel peaks or make use of radial collimators to reduce the signal from the vessel itself. In spallation sources with large detector area coverage one can also do an experiment where only detectors at a scattering angle of 90° are used. For gas-absorption experiments at low temperatures, however, vanadium is still the material of choice. For pressure measurement in anvil-type cells, TiZr is used for the gasket.

For opposed-anvil pressure experiments the anvil materials can be either cubic tungsten carbide or boron nitride. The latter is preferred as boron is highly absorbing and does not contribute anvil reflections to the sample measurement, so therefore effectively works as an incident-beam collimator. The use of tungsten carbide is reserved for techniques where a 'through-gasket' approach is required, such as furnace measurements with a graphite heater where the use of a null scattering alloy as a gasket material is not possible. A recent development in high-pressure neutron scattering is the use of sintered diamond anvils, also called PCDs (from polycrystalline diamond). They allow the accessible pressure range to be doubled at the cost of adding very strong diamond reflections to the pattern.

However, for gas pressure cells aluminium is often used, as it can withstand higher pressure and Al absorbs neutrons only weakly as the absorption cross section of aluminium, σ_{abs} = 0.231 b for a wavelength of 1.8 Å, is small. For high-temperature gas-flow experiments fused silica ('quartz') glass is generally used for sample containment. These holders can also have glass frits attached at one or both ends for easy flow of gas through the sample, as shown in Fig. 2.10.51(*a*).

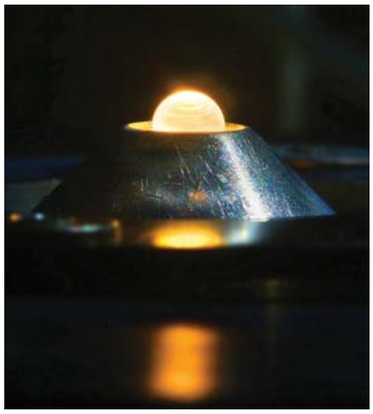

Figure 2.10.52
Aerodynamic levitation system to suspend melts at temperatures to 2773 K and beyond for neutron diffraction measurements.

A few very high intensity instruments are now able to carry out powder diffraction from milligramme quantities of sample. For these measurements vanadium cans produce too much background, as there is more vanadium in the beam than the sample. The use of thin-walled silica/glass or Kapton capillaries maybe more appropriate in those circumstances.

It is also important to remember that an exchange medium is used for low-temperature (heat transfer) and pressure (pressure transfer) measurements. Helium gas is generally used as a low-temperature exchange medium. Typically, cans are sealed with a flange and lid that supports an indium (or other soft metal) gasket. If the sample is air sensitive and has to be loaded in a glove box, one should try to use a helium-filled glove box. Argon- or nitrogen-filled glove boxes are more common but the freezing temperatures of argon and nitrogen are 84 K and 77 K, respectively. They will no longer work as exchange gases below these temperatures and, because of their rather large neutron-scattering lengths, new diffraction peaks will emerge at or below these temperatures. Similarly one should ensure that a pressure medium will remain hydrostatic for the pressure range for which it is being considered (Varga *et al.*, 2003).

It is also worth noting that cooling powder samples below 1 K relies entirely on thermal conduction through the walls of the sample holder and to the specimen itself. If great care is not taken, the specimen temperature may be far higher than that reported by a thermometer attached to the sample holder. At a minimum, the holder lid should be made from copper, as it is expected that the superconducting transitions in aluminium and vanadium would cause the walls of the sample holder to become thermally insulating and greatly reduce their ability to cool the sample. Of course, properly sealing the loose powder under an atmosphere of ^{4}He is equally important. It is essential that the indium seal be installed correctly, as ^{4}He undergoes a transition to a superfluid at 2.17 K and has effectively zero viscosity, and can easily escape from a poorly sealed can.

Levitation methods (*e.g.* gas flow, acoustic, electrostatic) as shown in Fig. 2.10.52 offer a containerless method, which eliminates altogether sample–container reaction problems and diffraction or additional background scattering from a sample container (Weber *et al.*, 2014). Levitated samples are typically used in conjunction with laser heating to achieve high temperatures, *in situ* melting of samples and prevention of heterogeneous nucleation.

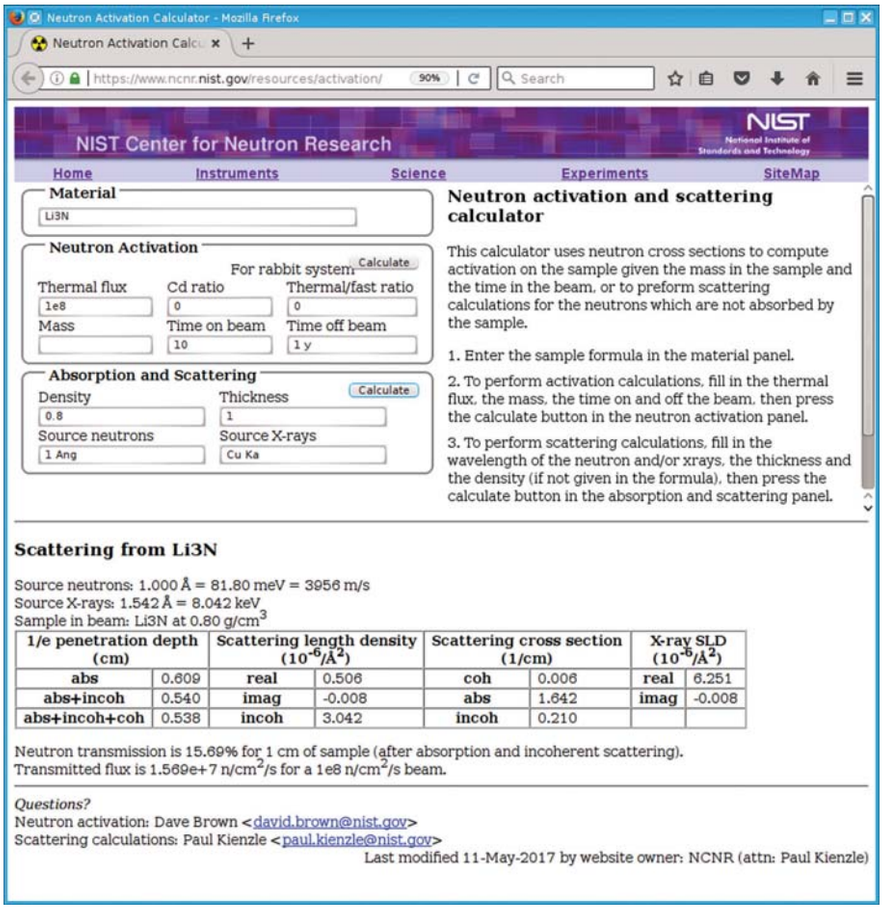

Figure 2.10.53
Calculation of the penetration of neutrons into Li_3N using the online tool at https://www.ncnr.nist.gov/resources/activation/.

2.10.2.4. *Isotopes, absorption and activation*

There are usually multiple sizes of vanadium cans available, the most common sizes being 6, 8 and 10 mm diameter. The choice of can depends on the quantity of sample available and the nature of the elements. Some elements such as cadmium, gadolinium and boron have extremely large absorption for neutrons and may not be feasible for measurements. Some elements have high absorption for the naturally occurring isotope mixes, but by choosing an alternative isotope one can often reduce or eliminate the absorption problem completely. For example, natural lithium is mostly ^{7}Li and has an absorption cross section of 70.5 b. However, pure ^{7}Li has an absorption cross section of 0.0454 b. The difference is due to the small amount of highly absorbing ^{6}Li (absorption cross section = 940 b) present in naturally occurring lithium. With commercially sourced lithium salts it is not always safe to assume a natural abundance of lithium isotopes. ^{6}Li is used in the production of tritium and, depending on their history, commercial lithium salts may be deficient in ^{6}Li. Given the significantly different scattering lengths of ^{6}Li and ^{7}Li, this can have serious consequences for a structure refinement, so it may be necessary to perform an isotopic analysis to verify the ^{6}Li:^{7}Li ratio. The various neutron scattering cross sections are available on the NIST website http://www.ncnr.nist.gov/resources/n-lengths/ and in Table 4.4.4.1 in *International Tables for Crystallography* Volume C (2006). If the sample contains any element with a large absorption and is not isotopically substituted, it is prudent to calculate by how much the neutrons will penetrate the sample. Tools are available at the NIST website http://www.ncnr.nist.gov/resources/activation/ to carry out this calculation. The input information is the composition of the compound, the density (generally a 50% packing fraction and hence $\frac{1}{2}$ of the calculated density is a good approximation for planning purposes) and the wavelength of the neutrons used. Fig. 2.10.53 shows a calculation for Li_3N. Natural lithium has a quite large absorption, but in this case 1 Å neutrons will penetrate through 5 mm and so the use of a 6-mm diameter can is appropriate.

However, if the penetration depth $1/e$ is 1–2 mm, one has to reconsider the choice of sample holder. For a high-intensity beamline capillaries can be considered. The other option is to use an annular holder made using co-axial, thin-walled vanadium or aluminium cylinders, or flat-plate mounts based on aluminium foils where the total depth of the sample is approximately the calculated $1/e$. Perhaps the best way to maximize the transmission and improve the signal-to-noise ratio is to use silicon flat-wafer sample holders. When loading a can it is also important to record the weight and height of the sample in the can so that the absorption correction for the sample can be calculated. Alternatively, the neutron transmission through the sample can be measured using a pinhole mask and a detector downstream from the sample.

One of the other factors to keep in mind for neutron sample preparation is that hydrogen is a very special element in terms of its interaction with neutrons. Hydrogen has a very large incoherent scattering cross section (σ_{inc}) of 80.26 b, while its coherent cross section (σ_{coh}) is 1.758 b. In comparison, for deuterium σ_{inc} = 2.05 b and σ_{coh} = 5.59 b. If the scattering nuclei contain a mixture of isotopes or have a non-zero nuclear spin, the neutron scat-

tering length consists of a coherent component, which is the average over all spins, and an incoherent part, which gives the deviation from this average value. In other words, coherent scattering describes interference between waves produced by the scattering of a single neutron from all the neutrons in the nuclei of the sample. On the other hand, incoherent scattering involves correlations between the position of an atom *j* at time zero and the position of the same atom at time *t*, and so the scattered waves from different nuclei no longer interfere. Thus incoherent scattering provides an excellent tool for studying processes involving atomic diffusion, but produces large backgrounds for diffraction experiments. Based on the available flux at the instrument of choice and the atom% hydrogen present in the sample, complete or partial deuteration of the sample may be necessary.

When illuminated by a neutron beam, some nuclei are converted into other radioactive nuclei (activated). Thus it may not be possible to return the specimen to the home laboratory, but it may have to be treated as radioactive waste. A sample-activation calculator is also available at http://www.ncnr.nist.gov/resources/activation/.

2.10.3. Conclusions

Powder diffraction as a technique encompasses a wide range of possible experimental setups. Diverse though they are, specimen-preparation methods are a key component in obtaining the best possible data for the best possible analysis. Many issues are common whether X-rays or neutrons are the probe of choice (*e.g.* particle statistics, preferred orientation), but neutrons do pose some unique issues such as sample activation and isotope-dependent scattering behaviour. Given that X-ray and neutron diffraction are frequently used in a joint analysis, some forethought may be required if the desired situation of the same sample being used for both is to be achieved.

For the common laboratory setups a recurring theme should be apparent through this overview – specimens should ideally have crystallite sizes of the order of a few μm. If this is the case, then many of the issues mentioned (particle statistics, preferred orientation, extinction) will either disappear or be significantly reduced. The same is true for microabsorption, except in this case it is particle as opposed to crystallite sizes that are the issue. Grinding or milling can easily reduce crystallite size to this range, but the milling action should be chosen so as to avoid damaging the crystal structure of the sample or possibly amorphizing it completely.

Ideally, the in-house laboratory should have the flexibility to tailor the experiment to the sample, using transmission or reflection geometry depending on the nature of the sample. Unfortunately, in many instances this is not possible. 'Coping strategies' for non-ideal samples such as diluting samples in capillaries or using very thin organic specimens on flat plates are available, but their limitations and compromises should be understood by the person receiving the data.

In many instances, the experimental configuration at a central facility, such as a synchrotron or neutron source, can be customized for a particular experiment. However, the need for high throughput for rapid-access mail-in services may dictate a more standardized setup.

In summary, specimen preparation is the foundation upon which powder diffraction measurements are built. Good specimen preparation will not guarantee excellent data, but poor preparation can pretty much guarantee poor data.

We would like to acknowledge the assistance of Mati Raudsepp of the Department of Earth and Ocean Sciences, University of British Columbia, for the production and SEM micrograph of the spray-dried mica sample. Ashfia Huq acknowledges support by the US Department of Energy (DE-AC05–00OR22725) with UT-Battelle, LLC. R.

References

Alexander, L. E. & Klug, H. P. (1948). *Basic aspects of X-ray absorption in quantitative diffraction analysis of powder mixture*. *Anal. Chem.* **20**, 886–894.

Alexander, L., Klug, H. P. & Kummer, E. (1948). *Statistical factors affecting the intensity of X-rays diffracted by crystalline powders*. *J. Appl. Phys.* **19**, 742–753.

Bailey, I. F., Done, R., Dreyer, J. W. & Gray, E. M. (2004). *A high-temperature high-pressure gas-handling cell for neutron scattering measurements*. *High Press. Res.* **24**, 309–315.

Bowden, M. & Ryan, M. (2010). *Absorption correction for cylindrical and annular specimens and their containers or supports*. *J. Appl. Cryst.* **43**, 693–698.

Bravais, A. (1866). *Etudes Cristallographiques*. Paris: Gauthier Villars.

Brindley, G. W. (1945). *The effect of grain or particle size on X-ray reflections from mixed powders and alloys, considered in relation to the quantitative determination of crystalline substances by X-ray methods*. *London Edinb. Dubl. Philos. Mag. J. Sci.* **36**, 347–369.

Buhrke, V. E., Jenkins, R. & Smith, D. K. (1998). *A Practical Guide for the Preparation of Specimens for X-ray Fluorescence and X-ray Diffraction Analysis*. New York: Wiley-VCH.

Cline, J. P. & Snyder, R. L. (1987). *The effects of extinction on X-ray powder diffraction intensities*. *Adv. X-ray Anal.* **30**, 447–456.

Dollase, W. A. (1986). *Correction of intensities for preferred orientation in powder diffractometry: application of the March model*. *J. Appl. Cryst.* **19**, 267–272.

Donnay, J. D. H. & Harker, D. (1937). *A new law of crystal morphology extending the law of Bravais*. *Am. Mineral.* **22**, 446–467.

Friedel, G. (1907). *Etudes sur la loi de Bravais*. *Bull. Soc. Fr. Mineral.* **30**, 326–455.

Hillier, S. (1999). *Use of an air brush to spray dry samples for X-ray powder diffraction*. *Clay Miner.* **34**, 127–135.

Hillier, S. (2002). *Spray drying for X-ray powder diffraction specimen preparation*. IUCr Commission on Powder Diffraction Newsletter, **27**, 7–9. http://www.iucr.org/__data/assets/pdf_file/0017/21626/cpd27.pdf.

Huq, A., Richardson, J. W., Maxey, E. R., Chandra, D. & Chien, W. (2007). *Structural studies of Li_3N using neutron powder diffraction*. *J. Alloys Compd.* **436**, 256–260.

International Tables for Crystallography (2006). Volume C, *Mathematical, Physical and Chemical Tables*, 1st online edition, edited by E. Prince. Chester: International Union of Crystalloagraphy. doi:10.1107/9780955360206000103.

Järvinen, M. (1993). *Application of symmetrized harmonics expansion to correction of the preferred orientation effect*. *J. Appl. Cryst.* **26**, 525–531.

Jenkins, R. & Snyder, R. (1996). *Introduction to X-ray Powder Diffractometry*. New York: Wiley-Interscience.

Kaduk, J. A. (2009). *A Rietveld tutorial – mullite*. *Powder Diffr.* **24**, 351–361.

Kaduk, J. A. (2013). Personal communication.

Klug, H. P. & Alexander, L. E. (1954). *X-ray Diffraction Procedures for Polycrystalline and Amorphous Materials*. New York: Wiley-Interscience.

Lewis, J., Schwarzenbach, D. & Flack, H. D. (1982). *Electric field gradients and charge density in corundum, α-Al_2O_3*. *Acta Cryst.* A**38**, 733–739.

Lobanov, N. N. & Alte de Viega, L. (1998). *Analytic absorption correction factors for cylinders to an accuracy of .5%*. Abstract P 2–16, 6th European Powder Diffraction Conference, Budapest, Hungary, 22–25 August. Zurich: Trans Tech Publications.

Ohashi, Y. (1984). *Polysynthetically-twinned structures of enstatite and wollastonite*. *Phys. Chem. Miner.* **10**, 217–229.

Pitschke, W., Hermann, H. & Mattern, N. (1993). *The influence of surface roughness on diffracted X-ray intensities in Bragg–Brentano geometry and its effect on the structure determination by means of Rietveld analysis*. *Powder Diffr.* **8**, 74–83.

Raudsepp, M. (2012). Personal communication.

Reibenspies, J. H. & Bhuvanesh, N. (2006). *Capillaries prepared from thin-walled heat-shrink poly(ethylene terephthalate) (PET) tubing for X-ray powder diffraction analysis*. *Powder Diffr.* **21**, 323–325.

Rowles, M. R. & Madsen, I. C. (2010). *Whole-pattern profile fitting of powder diffraction data collected in parallel-beam flat-plate asymmetric reflection geometry*. *J. Appl. Cryst.* **43**, 632–634.

Sabine, T. M., Von Dreele, R. B. & Jørgensen, J.-E. (1988). *Extinction in time-of-flight neutron powder diffractometry*. *Acta Cryst.* A**44**, 374–379.

Scarlett, N. V. Y., Madsen, I. C., Cranswick, L. M. D., Lwin, T., Groleau, E., Stephenson, G., Aylmore, M. & Agron-Olshina, N. (2002). *Outcomes of the International Union of Crystallography Commission on Powder Diffraction Round Robin on Quantitative Phase Analysis: samples 2, 3, 4, synthetic bauxite, natural granodiorite and pharmaceuticals*. *J. Appl. Cryst.* **35**, 383–400.

Smith, D. K. (2001). *Particle statistics and whole-pattern methods in quantitative X-ray powder diffraction analysis*. *Powder Diffr.* **16**, 186–191.

Suortti, P. (1972). *Effects of porosity and surface roughness on the X-ray intensity reflected from a powder specimen*. *J. Appl. Cryst.* **5**, 325–331.

Sykes, R. A., McCabe, P., Allen, F. H., Battle, G. M., Bruno, I. J. & Wood, P. A. (2011). *New software for statistical analysis of Cambridge Structural Database data*. *J. Appl. Cryst.* **44**, 882–886.

Toraya, H., Huang, T. C. & Wu, Y. (1993). *Intensity enhancement in asymmetric diffraction with parallel-beam synchrotron radiation*. *J. Appl. Cryst.* **26**, 774–777.

Toraya, H. & Yoshino, J. (1994). *Profiles in asymmetric diffraction with pseudo-parallel-beam geometry*. *J. Appl. Cryst.* **27**, 961–966.

Turner, J. F. C., Done, R., Dreyer, J., David, W. I. F. & Catlow, C. R. A. (1999). *On apparatus for studying catalysts and catalytic processes using neutron scattering*. *Rev. Sci. Instrum.* **70**, 2325–2330.

Varga, T., Wilkinson, A. P. & Angel, R. J. (2003). *Fluorinert as a pressure-transmitting medium for high-pressure diffraction studies*. *Rev. Sci. Instrum.* **74**, 4564–4566.

Weber, J. K. R., Benmore, C. J., Skinner, L. B., Neuefeind, J., Tumber, S. K., Jennings, G., Santodonato, L. J., Jin, D., Du, J. & Parise, J. B. (2014). *Measurements of liquid and glass structures using aerodynamic levitation and in-situ high energy X-ray and neutron scattering*. *J. Non-Cryst. Solids*, **383**, 49–51.

Wolff, P. M. de (1958). *Particle statistics in X-ray diffractometry*. *Appl. Sci. Res.* **7**, 102–112.

Wolff, P. M. de, Taylor, J. M. & Parrish, W. (1959). *Experimental study of effect of crystallite size statistics on X-ray diffractometer intensities*. *J. Appl. Phys.* **30**, 63–69.

Zachariasen, W. H. (1945). *Theory of X-ray Diffraction in Crystals*. New York: Dover Publications Inc.

Zevin, L. S. & Kimmel, G. (1995). *Quantitative X-ray Diffractometry*. New York: Springer-Verlag.

International Tables for Crystallography (2019). Vol. H, Chapter 3.1, pp. 224–251.

3.1. The optics and alignment of the divergent-beam laboratory X-ray powder diffractometer and its calibration using NIST standard reference materials

J. P. Cline, M. H. Mendenhall, D. Black, D. Windover and A. Henins

3.1.1. Introduction

The laboratory X-ray powder diffractometer has several virtues that have made it a principal characterization device for providing critical data for a range of technical disciplines involving crystalline materials. The specimen is typically composed of small crystallites (5–30 μm), which is a form that is suitable for a wide variety of materials. A continuous set of reflections can be collected with a single scan in θ–2θ angle space. Not only can timely qualitative analyses be carried out, but with the more advanced data-analysis methods a wealth of quantitative information may be extracted. Modern commercial instruments may include features that include focusing mirror optics and the ability to change quickly between various experimental configurations. In this chapter, we discuss results from a NIST-built diffractometer with features specific to the collection of data that complement the NIST effort in standard reference materials (SRMs) for powder diffraction. While this machine can be configured with focusing optics, here we consider only those configurations that use a divergent beam in Bragg–Brentano, para-focusing geometry.

A principal advantage of the divergent-beam X-ray powder diffractometer is that a relatively large number of crystallites are illuminated, providing a strong diffraction signal from a representative portion of the sample. However, the para-focusing optics of laboratory diffractometers produce patterns that display profiles of a very complex shape. The observed 2θ position of maximum diffraction intensity does not necessarily reflect the true spacing of the lattice planes (*hkl*). While advanced data-analysis methods can be used to model the various aberrations and account for the observed profile shape and position, there are a number of instrumental effects for which there is not enough information for reliable, *a priori* modelling of the performance of the instrument. The task may be further compounded when instruments are set up incorrectly, because the resultant additional errors are convoluted into the already complex set of aberrations. Therefore, the results are often confounding, as the origin of the difficulty is problematic to discern. The preferred method for avoiding these situations is the use of SRMs to calibrate the instrument performance. We will describe the various methods with which NIST SRMs may be used to determine sources of measurement error, as well as the procedures that can be used to properly calibrate the laboratory X-ray powder diffraction (XRPD) instrument.

The software discussed throughout this manuscript will include commercial as well as public-domain programs, some of which were used for the certification of NIST SRMs. In addition to the NIST disclaimer concerning the use of commercially available resources,[1] we emphasize that some of the software presented here was also developed to a certain extent through longstanding collaborative relationships between the first author and the respective developers of the codes. The codes that will be discussed include: *GSAS* (Larson & Von Dreele, 2004), the PANalytical software *HighScore Plus* (Degen *et al.*, 2014), the Bruker codes *TOPAS* (version 4.2) (Bruker AXS, 2014) and *DIFFRAC.EVA* (version 3), and the Rigaku code *PDXL 2* (version 2.2) (Rigaku, 2014). The fundamental-parameters approach (FPA; Cheary & Coelho, 1992) for modelling X-ray powder diffraction line profiles, as implemented in *TOPAS*, has been used since the late 1990s for the certification of NIST SRMs. To examine the efficacy of the FPA models, as well as their implementation in *TOPAS*, we have developed a Python-based code, the NIST Fundamental Parameters Approach Python Code (*FPAPC*), that replicates the FPA method in the computation of X-ray powder diffraction line profiles (Mendenhall *et al.*, 2015). This FPA capability is to be incorporated into *GSASII* (Toby & Von Dreele, 2013).

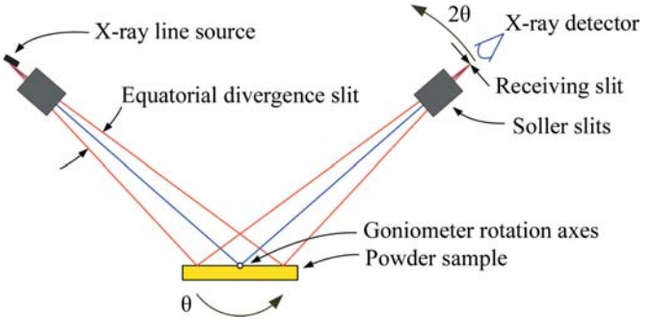

Figure 3.1.1
A schematic diagram illustrating the operation and optical components of a Bragg–Brentano X-ray powder diffractometer.

3.1.2. The instrument profile function

The instrument profile function (IPF) describes the profile shape and displacement as a function of 2θ that is the intrinsic instrumental response imparted to any data collected with that specific instrument. It is a function of the radiation used, the instrument geometry and configuration, slit sizes *etc*.[2] The basic optical layout of a divergent-beam X-ray powder diffractometer of Bragg–Brentano, para-focusing geometry using a tube anode in a line-source configuration is illustrated in Fig. 3.1.1. This figure shows the various optical components in the plane of diffraction, or equatorial plane. The dimensions of the optical components shown in Fig. 3.1.1 and the dimensions of the goniometer itself determine the resolution of the diffractometer. The divergent nature of the X-ray beam will increase the number of crystallites giving rise to the diffraction signal; the incident-beam slit defines an angular range within which crystallites will be oriented such that their diffraction is registered. One of the manifestations of this geometry is that knowledge of both the diffraction angle and

[1] Certain commercial equipment, instruments, or materials are identified in this in order to adequately specify the experimental procedure. Such identification does not imply recommendation or endorsement by the National Institute of Standards and Technology, nor does it imply that the materials or equipment identified are necessarily the best available for the purpose.

[2] See Chapters 3.6 and 5.1 for details of contributions to the profile shape from the sample.

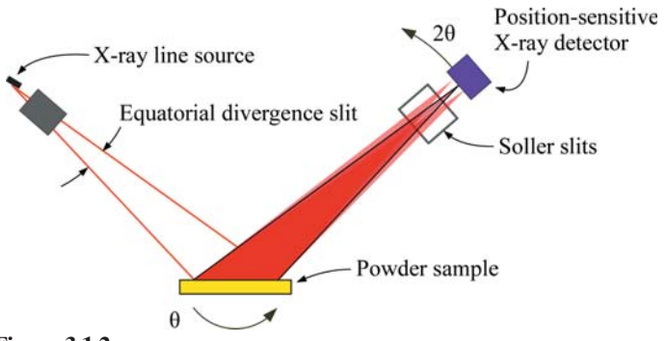

Figure 3.1.2
A schematic diagram illustrating the operation and optical components of a Bragg–Brentano X-ray diffractometer equipped with a position-sensitive detector. Only the rays striking the centre line of the PSD, outlined in black, are in accordance with Bragg–Brentano focusing.

specimen position are critical for the correct interpretation of the data. The goniometer radius is the distance between the rotation axes and the X-ray source (R_1), or the distance between the rotation axes and receiving slit (R_2), as shown in Fig. 3.1.1; these two distances must be equal. The specimen surface is presumed to be on the rotation axes; however, this condition is rarely realized and it is common to have to consider a specimen-displacement error.

Goniometer assemblies themselves can be set up in several configurations. Invariably, two rotation stages are utilized. Fig. 3.1.1 illustrates a machine of $\theta/2\theta$ geometry: the tube is stationary while one stage rotates the specimen through angle θ, sometimes referred to as the angle Ω, while a second stage rotates the detector through angle 2θ. Another popular configuration is θ/θ geometry, where the specimen remains stationary and both the tube and detector rotate through angle θ. However, the diffraction optics themselves do not vary with regard to how the goniometer is set up.

The detector illustrated in Fig. 3.1.1 simply reads any photons arriving at its entrance window as the diffracted signal is analysed by the receiving slit. Such detectors, which often use a scintillation crystal, are typically referred to as point detectors. A diffracted-beam post-sample monochromator is often added to the beam path after the receiving slit to filter out any fluorescence from the sample. The crystal optic of these monochromators typically consists of pyrolytic graphite with a high level of mosaicity that is bent to a radius in rough correspondence to that of the goniometer. This imposes a relatively broad energy bandpass of approximately 200 eV (with 8 keV Cu $K\alpha$ radiation) in width on the diffracted beam. This window is centred so as to straddle that of the energy of the source radiation being used, thereby filtering fluorescent and other spurious radiation from the detector while transmitting the primary features of the emission spectrum, presumably without distortion.

Within the last decade, however, the popularity of this geometry has fallen markedly, as the use of the post-sample monochromator/point-detector assembly has been largely displaced by the use of a position-sensitive detector (PSD). This geometry is illustrated in Fig. 3.1.2. A line detector replaces the point detector, and offers the ability to discriminate with respect to the position of arriving X-rays within the entrance window of the PSD. A multichannel analyser is typically used to map the arriving photons from the PSD window into 2θ space. Depending on the size of the PSD entrance window, increases in the counting rate by two orders of magnitude relative to a point detector can be easily achieved. Furthermore, this is accomplished by including the signal from additional crystallites, mitigating any problems with particle-counting statistics (Fig. 3.1.2). A drawback to the PSD is that the increased intensity is achieved with the inclusion of signals that are not within the Bragg–Brentano focusing regimen (compare Figs. 3.1.1 and 3.1.2), leading to a broadening of the line profiles. The level of broadening is proportional to the size of the PSD entrance window and inversely proportional to 2θ angle. The move to PSDs has been further augmented by the development of solid-state, silicon strip detectors that offer the advantages of a PSD without the maintenance issues of the early gas-flow proportional PSDs. Fluorescence can be problematic with a PSD; however, the problem can be countered with the use of filters. More recent developments in electronics have improved the ability of these PSDs to discriminate with respect to energy. We discuss only this newer class of solid-state linear PSDs in this chapter.

A monochromator can also be used to condition the incident beam so that it will consist exclusively of $K\alpha_1$ radiation. Monochromators of this nature are inserted into the beam path prior to the beam's arrival at the incident-beam slit shown in Fig. 3.1.1. These devices typically use a Ge(111) crystal as the optic; Ge monochromators have a much smaller energy bandpass than graphite monochromators. They are, therefore, much more complex and difficult to align. Here we discuss an incident-beam monochromator (IBM) using a Johansson focusing optic (Johansson, 1933), as shown in Fig. 3.1.3. When incorporating an IBM assembly into a powder diffractometer using reflection geometry, the focal line of the optic must be positioned on the goniometer radius as per the line source of the tube anode in a conventional setup, shown in the right-hand

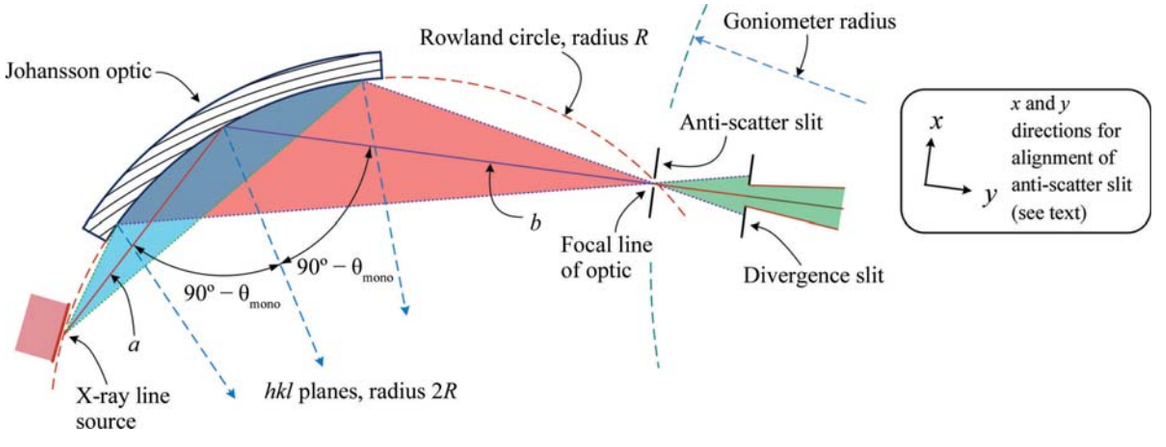

Figure 3.1.3
A schematic diagram illustrating the geometry of a Johansson incident-beam monochromator.

Table 3.1.1
Aberrations comprising the geometric component of the IPF

Aberration	Controlling parameters	Impact
X-ray source width (w_x)	Angle subtended by source: w_x/R	Symmetric broadening
Receiving-slit width or PSD strip width (w_r)	Angle subtended by slit/strip: w_r/R	Symmetric broadening
Flat specimen error/equatorial divergence	Angle of divergence slit: α	Asymmetric broadening to low 2θ, with decreasing 2θ
PSD defocusing	PSD window width, angle of divergence slit: α	Symmetric broadening with $1/(\tan\theta)$
Axial divergence Case 1: no Soller slits Case 2: Soller slits define divergence angle	 Axial lengths of the X-ray source (L_x), sample (L_s) and receiving slit (L_r) relative to goniometer radius (R) Acceptance angles Δ_I and Δ_D of the incident- and diffracted-beam Soller slits	Below $\sim 100°$: asymmetric broadening to low 2θ, with decreasing 2θ else to high 2θ, with increasing 2θ
Specimen transparency	Penetration factor relative to diffractometer radius $1/\mu R$	Asymmetric broadening to low 2θ, with $\sin(2\theta)$
Specimen displacement z height	Displacement of specimen surface from goniometer rotation axes	Displacement of profiles with $\cos\theta$

side of Fig. 3.1.3. In this way, a Johansson optic provides a monochromatic X-ray source, passing some portion of the $K\alpha_1$ emission spectrum, while preserving the divergent-beam Bragg–Brentano geometry as shown in Figs. 3.1.1 and 3.1.2. The use of an IBM reduces the number of spectral contributions to the observed line shape and results in an IPF that is more readily modelled with conventional profile fitting. Furthermore, equipping such a machine with a PSD affords all of its advantages, while the elimination of the *Bremsstrahlung* by the IBM reduces the impact of fluorescence that can otherwise be problematic with a PSD.

Throughout this manuscript we use the terms 'width' and 'length' when referring to the optics. Width expresses extent in the equatorial plane. Length is used to denote a physical dimension parallel to the rotation axes of the goniometer as defined in Fig. 3.1.1. The designation of the axial divergence angle, as well as the specifications concerning Soller slits, will be considered in terms of the double angle, both for incoming and outgoing X-rays. This is in contrast to the generally accepted single-angle definition shown in Klug & Alexander (1974); hence the axial-divergence angles reported throughout this chapter are twice those that are often encountered elsewhere.

The observed line shape in powder diffraction consists of a convolution of contributions from the instrument optics (referred to as the geometric profile), the emission spectrum and the specimen, as shown diagrammatically for divergent-beam XRPD in Fig. 3.1.4. The specimen contribution is often the dominant one in a given experiment; however, we do not consider it to any great extent in this discussion. The factors comprising the geometric profile are listed in Table 3.1.1. Technically, neither of the last two items (specimen transparency and displacement) are components of the geometric profile of the instrument. They are functions of the specimen and the manner in which it was mounted. However, it is not possible to use a whole-pattern data-analysis method without considering these two factors; as they play a critical role in the modelling of the observed profile positions and shapes they are included in this discussion. The convolution of the components of the geometric profile and emission spectrum forms the IPF. As will be discussed, both of these contributions are complex in nature, leading to the well known difficulty in modelling the IPF from Bragg–Brentano equipment. This complexity, and the relatively limited q-space (momentum space) range accessible with laboratory equipment, tends to drive the structure solution and refinement community, with their expertise in the development of data-analysis procedures, towards the use of synchrotron and neutron sources. A significant number of the models and analytical functions discussed here were developed for, and are better suited to, powder-diffraction equipment using such nonconventional sources.

We now consider the geometric profile with an examination of the aberrations listed in Table 3.1.1. Figs. 3.1.5–3.1.10 illustrate simulations of the aberration function associated with the factors listed in Table 3.1.1. The first two of these, the source and receiving-slit width or silicon strip width with a PSD, simply cause symmetric broadening, constant with 2θ angle, and are typically described with 'impulse' or 'top-hat' functions. The flat specimen error is due to defocusing in the equatorial plane. One can see from Fig. 3.1.1 that for any beam that is not on the centre line of the goniometer, R_1 is not equal to R_2. The magnitude of the effect is directly

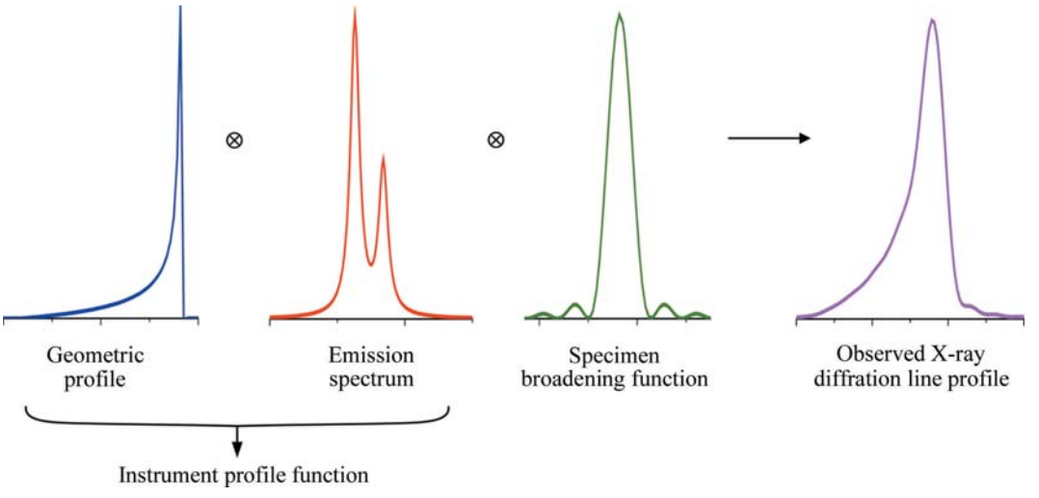

Figure 3.1.4
Diagrammatic representations of convolutions leading to the observed XRPD profile.

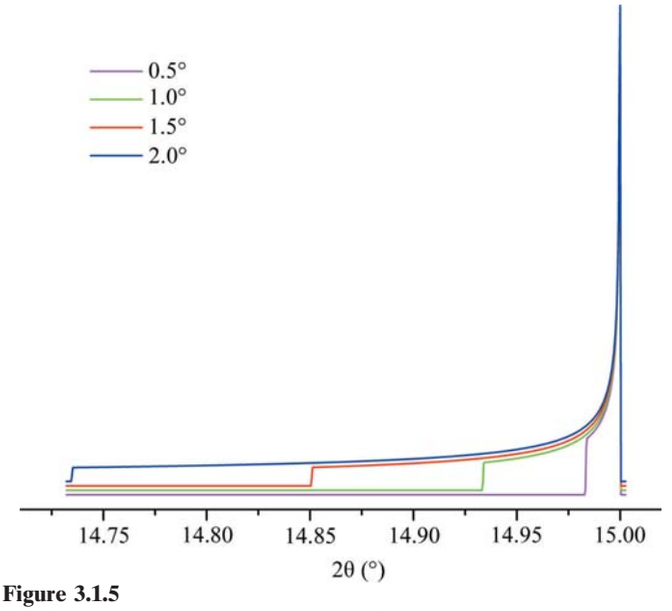

Figure 3.1.5
The flat specimen error aberration profile as a function of incident-slit size (R = 217.5 mm).

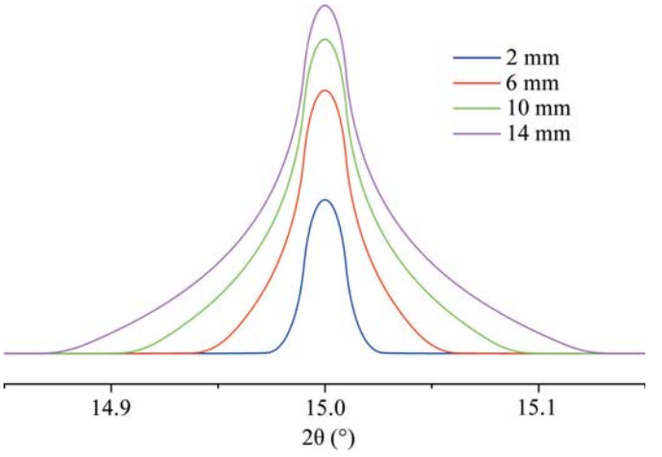

Figure 3.1.7
The PSD defocusing error aberration profiles for a silicon strip PSD as a function of window width (R = 217.5 mm, incident slit = 1° and strip width = 75 μm).

proportional to the divergent slit size as shown in Fig. 3.1.5. Its functional dependence on 2θ angle, *i.e.* 1/tan θ, is illustrated in Fig. 3.1.6. The flat specimen error leads to asymmetric profile broadening on the low-angle side, accentuated at decreasing values of 2θ. The functional dependence of this aberration on 2θ, shown in Fig. 3.1.6, is for a fixed slit; the use of a variable-divergence incident-beam slit to obtain a constant area of illumination reduces this dependence on the 2θ angle.

The broadening imparted to diffraction line profiles from the early gas-flow proportional PSDs was due to defocusing originating from both the equatorial width of the PSD window and parallax within the gas-filled counting chamber. Early models for these effects (Cheary & Coelho, 1994) included two parameters: one for the window width and a second for the parallax. The modern silicon strip PSDs do not need this second term as there is effectively no parallax effect. The aberration profile imparted to the data from a modern PSD (Mendenhall *et al.*, 2015) is illustrated in Fig. 3.1.7 as a function of window width. The profiles are symmetric about the centre line, exhibiting both increasing intensity and breadth as the window width is increased. The profile consists of two components: a central peak with a width independent of 2θ, which is due to the pixel strip width of the detector, and wings which are due to the defocusing. The breadths of the wings shown in Fig. 3.1.7 vary in proportion to the incident slit size and as 1/tan θ, and therefore are largely unobservable at high 2θ angles.

Cheary & Coelho (1998*a*,*b*) have modelled axial divergence effects in the context of two geometric cases. Case 1 is the situation in which the axial divergence is limited solely by the width of the beam path as determined by the length of the tube filament, the receiving slit and the size of the sample. The aberration function in which these parameters are 12 mm, 15 mm and 15 mm, respectively, is illustrated in Fig. 3.1.8; the extent of broadening is nearly 1° in 2θ at a 2θ angle of 15°. The other plots of Fig. 3.1.8 refer to a 'case 2' situation where axial divergence is limited by the inclusion of Soller slits in the incident- and diffracted-beam paths. One also has to consider the impact of a including a graphite post-monochromator. This would increase

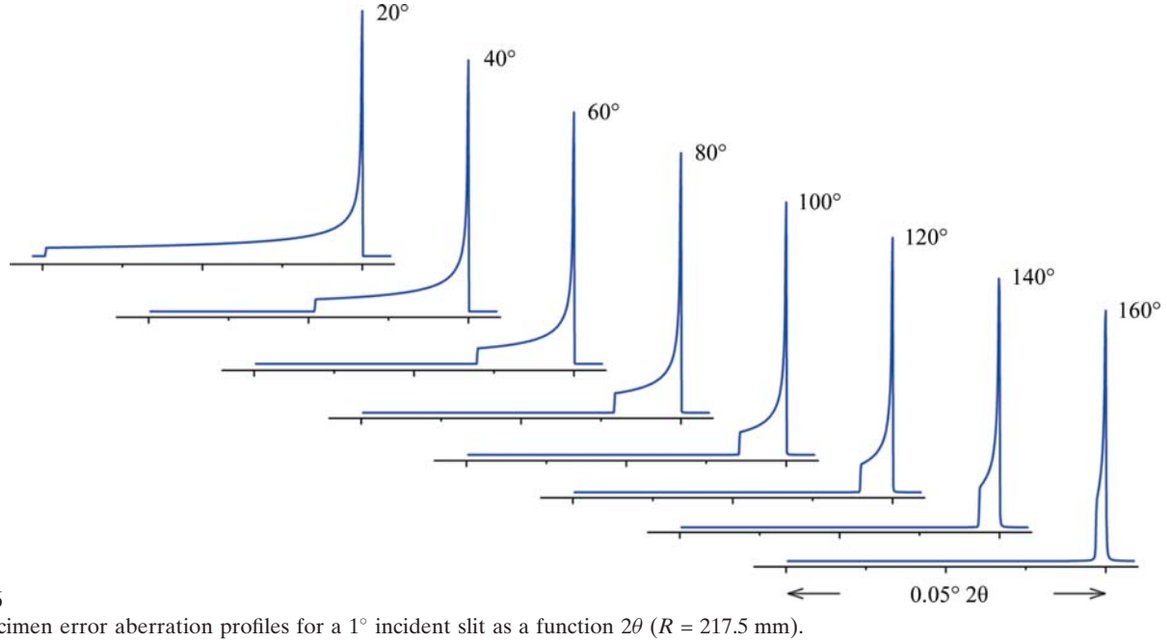

Figure 3.1.6
The flat specimen error aberration profiles for a 1° incident slit as a function 2θ (R = 217.5 mm).

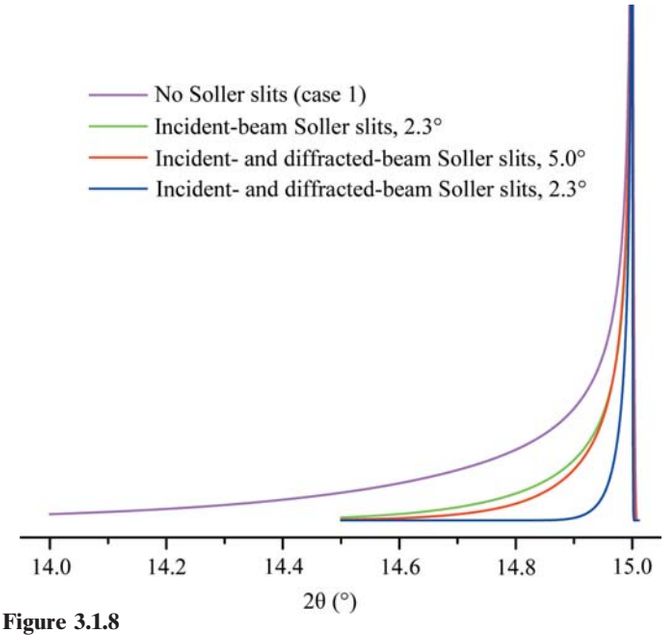

Figure 3.1.8
Axial divergence aberration profiles shown for several levels of axial divergence. Case 1 (of Table 3.1.1) is computed for a source length of 12 mm and a sample and receiving-slit length of 15 mm. The remaining three simulations include are of case 2, where Soller slits limit the axial divergence (R = 217.5 mm).

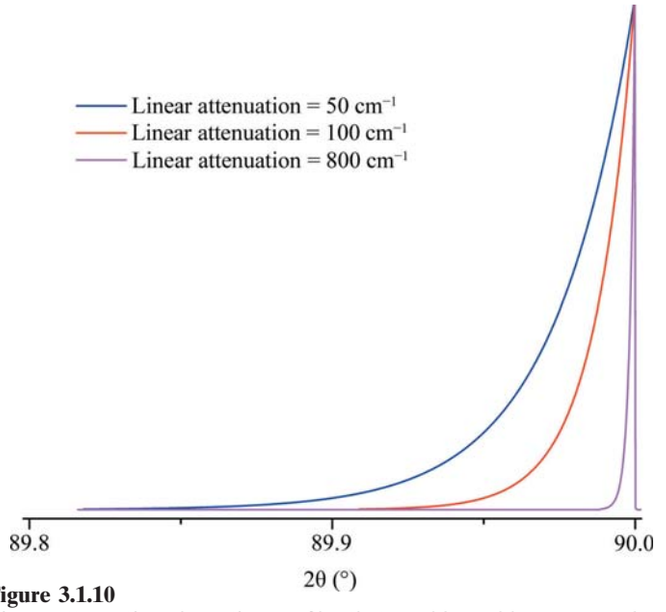

Figure 3.1.10
Linear attenuation aberration profiles that would roughly correspond to SRMs 676a (50 cm^{-1}), 640e and 1976b (100 cm^{-1}), and 660c (800 cm^{-1}) at 90° 2θ, where the transparency effect is at a maximum (R = 217.5 mm).

the path length of the diffracted beam by 10 to 15 cm, reducing axial divergence effects substantially and effectively functioning as a Soller slit. Cheary & Cline (1995) determined that the inclusion of a Soller slit with a post-monochromator did result in a slight improvement in resolution; however, this was at the cost of a threefold reduction in intensity. We do not use Soller slits in the diffracted beam when using a post-monochromator. The 5° primary and secondary Soller slit aberration profile of Fig. 3.1.8 corresponds to an instrument with a primary Soller slit and a graphite post-monochromator. The profiles shown for the two 2.3° Soller-slit configurations actually constitute a fairly high level of collimation given the double-angle definition of the specifications. Fig. 3.1.9 shows the functional dependence of the aberration profile for two 2.3° Soller slits on 2θ. Below approximately 100°, the effect increases with decreasing 2θ. Approximate symmetry is observed at 100°, while asymmetry to high angle increases thereafter. The aberration profile associated with specimen transparency to the X-ray beam is illustrated in Fig. 3.1.10. The figure shows the impact at 90° 2θ where the effect is at its maximum. The observed profile is broadened asymmetrically to low 2θ; the effect drops off in a largely symmetric manner with 2θ on either side of 90°.

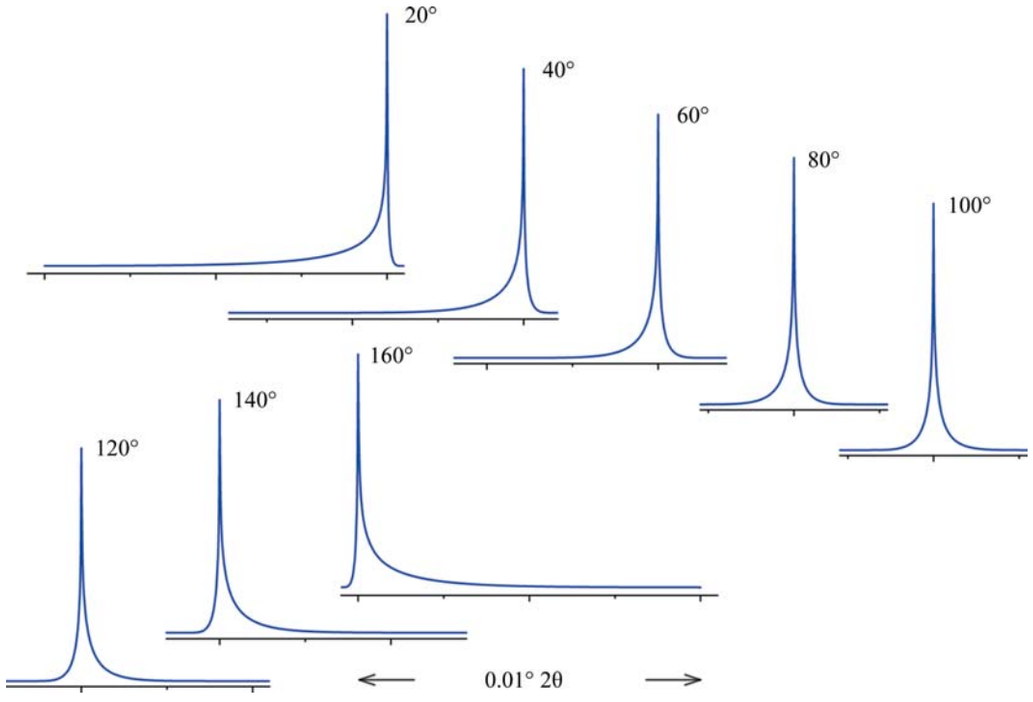

Figure 3.1.9
Axial divergence aberration profiles for primary and secondary Soller slits of 2.3° as a function of 2θ (R = 217.5 mm).

The wavelength profile or emission spectrum with its characterization on an absolute energy scale provides the traceability of the diffraction measurement to the International System of Units (SI) (BIPM, 2006). The currently accepted characterization of the emission spectrum of Cu $K\alpha$ radiation is provided by Hölzer *et al.* (1997) and is shown in Fig. 3.1.11. The spectrum is modelled with four Lorentzian profile shape functions (PSFs): two large ones for the primary $K\alpha_1$ and $K\alpha_2$ profiles, and two smaller ones displaced slightly to lower energy to account for the asymmetry in the observed line shape. The data shown in Fig. 3.1.11 are in energy space and are transformed into 2θ space with the dispersion relation. This is obtained by differentiating

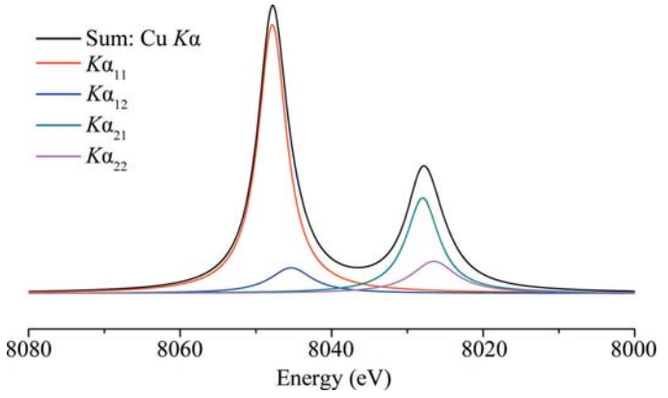

Figure 3.1.11
The emission spectrum of Cu $K\alpha$ radiation as provided by Hölzer *et al.* (1997), represented by four Lorentzian profiles: two primary ones and a pair of smaller ones to account for the observed asymmetry. The satellite lines, often referred to as the $K\alpha_3$ lines, are not displayed.

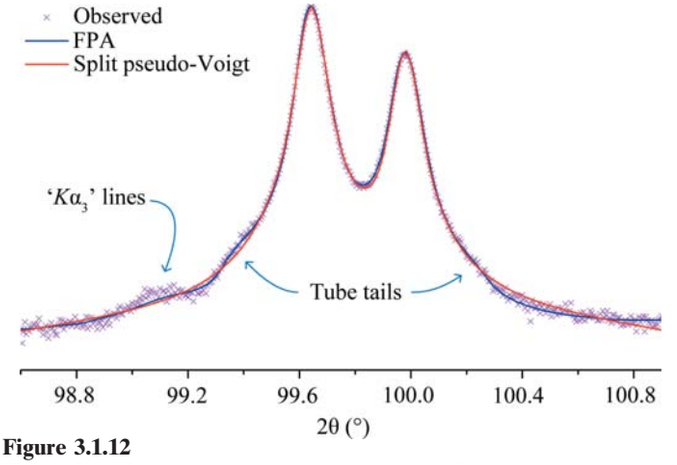

Figure 3.1.12
Illustration of the $K\alpha_3$ lines and tube-tails contributions to an observed profile on a log scale, shown with two fits: the fundamental-parameters approach, which includes these features, and the split pseudo-Voigt PSF, which does not.

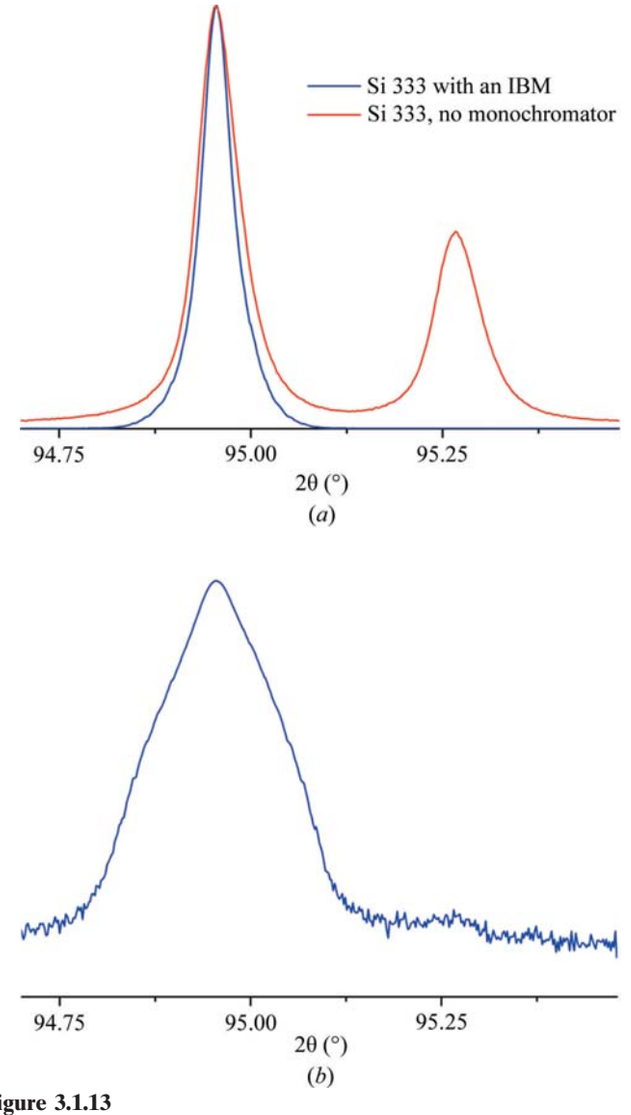

Figure 3.1.13
Illustration of the effect of the Johansson optic on the Cu $K\alpha$ emission spectrum. (*a*) Data collected for the Si 333 single-crystal reflection on a linear scale. (*b*) Analogous data from Johansson optic alone on a log scale. Both data sets were collected with 0.05 mm incident and receiving slits. The near absence of the $K\alpha_2$ scatter displayed in (*b*) can only be realized with the use of a properly aligned anti-scatter slit located at the focal line of the optic.

Bragg's law to obtain $d\theta/d\lambda$. The dominant term in the result is $\tan\theta$, which leads to the well known 'stretching' of the wavelength distribution with respect to 2θ. Maskil & Deutsch (1988) characterized a series of satellite lines in the Cu $K\alpha$ spectrum with an energy centred around 8080 eV and an intensity relative to the $K\alpha_1$ line of 6×10^{-3}. These are sometimes referred to as the $K\alpha_3$ lines, and are typically modelled with a single Lorentzian within the FPA. The 'tube tails' as reported by Bergmann *et al.* (2000) are a contribution that is strictly an artifact of how X-rays are produced in the vast majority of laboratory diffractometers. With the operation of an X-ray tube, off-axis electrons are also accelerated into the anode and produce X-rays that originate from positions other than the desired line source. They are not within the expected trajectory of para-focusing X-ray optics and produce tails on either side of a line profile as illustrated, along with the $K\alpha_3$ lines, in Fig. 3.1.12. Lastly, the energy bandpass of the pyrolytic graphite crystals used in post-monochromators is not a top-hat (or square-wave) function. Thus, the inclusion of a post-monochromator influences the observed emission spectrum.

A Johansson IBM dramatically reduces the complexity of the IPF by largely removing the $K\alpha_2$, $K\alpha_3$ and tube-tails contributions to the observed profile shape. The vast majority of the *Bremsstrahlung* is also removed. Furthermore, the inclusion of the IBM increases the path length of the incident beam by 25 to 30 cm. This substantially reduces the contribution of axial divergence to the observed profile shape. The crystals used are almost exclusively germanium (the 111 reflection), and are ground and bent to the Johansson focusing geometry, as shown in Fig. 3.1.3. They can be symmetric, with the source-to-crystal distance a and the crystal-to-focal point distance b being equal, in which case they will exhibit a bandpass of the order of 8 eV. They will slice a central portion out of the $K\alpha_1$ line, clipping the tails, to transmit perhaps 70% of the original width of the Cu $K\alpha_1$ emission spectrum. This yields a symmetric profile shape of relatively high resolution, or reduced profile breadth (other parameters being equal). The crystals can also be asymmetric, with the distance a being ~60% of the distance b. These optics will exhibit a bandpass of the order of 15 eV, in which case they transmit most of the $K\alpha_1$ line for a higher intensity, but with a lower resolution. The optic discussed here is of the latter geometry, as shown in Fig. 3.1.3.

A potential drawback to the use of an IBM concerns the nature of the $K\alpha_1$ emission spectrum it transmits, which may preclude the use of data-analysis methods that are based upon an accurate

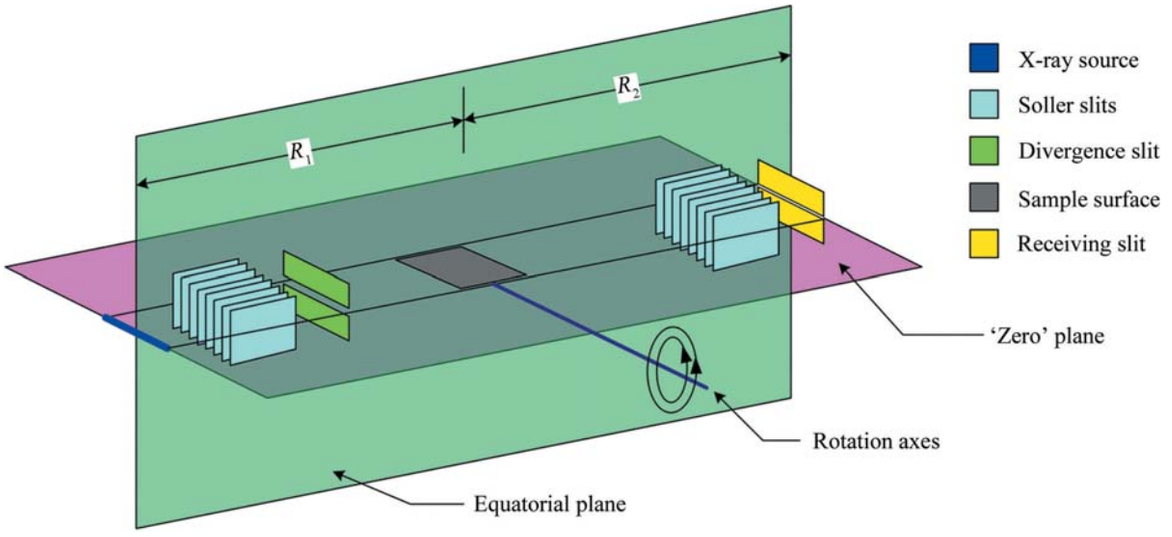

Figure 3.1.14
Diagrammatic explanation of the conditions necessary to realize a properly aligned X-ray powder diffractometer.

mathematical description of an incident spectrum. At best, a 'perfect' focusing crystal will impose an uncharacterized, though somewhat Gaussian, energy filter on the beam it diffracts. However, in certain optics the required bend radius of Johansson geometry is realized by clamping the crystal onto a curved form. The clamping restraint exists only at the edges of the optic, not in the central, active area where it is illuminated by the X-ray beam. The crystal itself however, can minimize internal stress by remaining flat; in this case an anticlastic curvature of the optic results. A 'saddle' distortion across the surface of the diffracting region of the crystal results in a complex asymmetric $K\alpha_1$ spectrum that defies accurate mathematical description. Johansson optics, however, can be bent by cementing the crystals into a preform, yielding an optic of superior perfection in curvature. Fig. 3.1.13 shows data collected from such an optic using an Si single crystal, 333 reflection, as an analyser. Parallel-beam conditions were approximated in this experiment with the use of very fine 0.05 mm incident and receiving slits. The observed symmetric emission profile of Fig. 3.1.13(a) can be modelled with a combination of several Gaussians. However, a Johansson optic will scatter 1–2% of high-energy radiation to a higher 2θ angle than the $K\alpha_1$ focal line of the optic. This unwanted scatter is dominated by, but not exclusive to, the $K\alpha_2$ spectrum. Louër (1992) indicated that it can be largely blocked with a knife edge aligned to just 'contact' the high-angle side of the optic's focal line. Alternatively, the NIST method is to use a slit aligned to straddle the focal line. Proper alignment of this anti-scatter slit is critical to achieving a good level of performance with the absence of '$K\alpha_2$' scatter, as illustrated in Fig. 3.1.13(b). As will be demonstrated, with use of any Johansson optic the elimination of the $K\alpha_2$ line is of substantial benefit in fitting the observed peaks with analytical profile-shape functions.

3.1.3. Instrument alignment

Modern instruments embody the drive towards interchangeable pre-aligned or self-aligning optics, which, in turn, has led to several approaches to obtaining proper alignment with minimum effort on the part of the user. We will not review these approaches, but instead we decribe here the methods used at NIST, which could be used to check the alignment of newer equipment. With the use of calibration methods that simply characterize the performance (which includes the errors) of the machine in an empirical manner and apply corrections, the quality of the instrument alignment may be surprisingly uncritical for a number of basic applications such as lattice-parameter refinement. However, with the use of the more advanced methods for characterization of the IPF that are based on the use of model functions, the proper alignment of the machine is critical. The models invariably include refineable parameter(s) that characterize the extent to which the given aberration affects the data; the correction is applied, and the results are therefore 'correct'. However, if the instrument is not aligned properly, the analysis attempts to model the errors due to misalignment as if they were an expected aberration. The corrections applied are therefore incorrect in degree and nature and an erroneous result is obtained.

The conditions for proper alignment of a Bragg–Brentano diffractometer (see Fig. 3.1.14) are:

(1) the goniometer radius, defined by the source-to-rotation-axes distance, R_1, equals that defined by the rotation-axes-to-receiving-slit distance, R_2 (to ± 0.25 mm);
(2) the X-ray line source, sample and receiving slit are centred in the equatorial plane of diffraction (to ± 0.25 mm);
(3) the goniometer rotation axes are co-axial and parallel (to ± 5 μm and <10 arc seconds);
(4) the X-ray line source, specimen surface, detector slit and goniometer rotation axes are co-planar, in the 'zero' plane, at the zero angle of θ and 2θ (to ± 5 μm and $\pm 0.001^\circ$); and
(5) the incident beam is centred on both the equatorial and 'zero' planes (to $\pm 0.05^\circ$).

The first three conditions are established with the X-rays off, while conditions (4) and (5) are achieved with the beam present, as it is actively used in the alignment procedure. Neither incident- nor diffracted-beam monochromators are considered; they are simply added on to the Bragg–Brentano arrangement and have no effect on the issues outlined here. Also, in order to execute this procedure, a sample stage that can be rotated by 180° in θ is required. However, this does not need to be the sample stage used for data collection. Before any concerted effort to achieve proper alignment, it is advisable to check the mechanical integrity of the equipment. Firmly but gently grasp a given component of the diffractometer, such as the tube shield, receiving-slit assembly or sample stage, and try to move it in a manner inconsistent with

its proper mounting and function. The number of defects, loose bolts *etc.*, that can be found this way, even with quite familiar equipment, can be surprising.

Let us briefly review the development of diffraction equipment and the subsequent impact on alignment procedures. The goniometer assemblies used for powder diffractometers utilize a worm/ring gear to achieve rotation of the θ and 2θ axes while allowing for the $\sim$0.002° resolution with the use of a stepper or servo motor actuating the worm gear. 'Home' switches, with a coarse one on the ring gear and a fine one on the worm shaft, allow the software to locate the reference angle(s) of the goniometer assembly to a repeatability of the stepper motor resolution. With the first generation of these automated goniometers, the zero angles were fixed relative to the home positions. With such a design the invariant reference was the receiving slit, and the operator adjusted the height of the tube shield and the angle of the θ stage to realize alignment condition (4). Second-generation machines offered the ability to set the zero angles relative to the home positions (or those of optical encoders) *via* software, in which case the exact angular position of either the X-ray tube focal line or of the receiving slit in θ–2θ space is arbitrary. The operator simply determines the positions where the θ and 2θ angles are zero, and then sets them there. There is no technical reason why the older designs cannot be aligned to the accuracy of newer ones. In practice, however, with older equipment the patience of the operator tends to become exhausted, and a less accurate alignment is accepted. An important consideration in evaluating modern equipment is that it is often the incident optic, not the X-ray source (focal line), that is used as the reference. Which situation is the case can be readily discerned with an inspection of the hardware: if the incident optic is anchored to the instrument chassis, then it is the reference. If it is attached to the tube shield, however, then the source establishes the reference. The NIST equipment has the latter design.

Condition (1) is that the goniometer radius, defined by the source-to-rotation-axis distance, R_1, equals that defined by the rotation-axis-to-receiving-slit distance, R_2. This condition is required for proper focusing and is generally realized with the use of rulers to achieve a maximum permissible error of $R \pm 0.25$ mm for a nominal $R = 200$ mm diffractometer. Condition (2) concerns the centring of the components in the plane of diffraction or equatorial plane. This condition is assured with the use of straightedges and rulers and, again for a line focus with an 8 to 12 mm source length, the maximum permissible error for deviations along the equatorial plane is $\pm$0.25 mm. One can also consider the takeoff angle at this time; this is the angle between the surface of the X-ray tube anode and the equatorial centre line of the diffractometer incident-beam path. As this angle decreases the resolution is improved at the expense of signal intensity, and *vice versa*, as a consequence of the variation in the size of the source that the specimen 'sees'. However, with modern fine-focus tubes, this is not a major effect. Qualitative experiments at NIST indicate that the exact angle is not critical; a 6° takeoff angle is reasonable.

The third issue concerns the concentricity of the θ and 2θ rotation axes of the goniometer assembly; this is a matter of underappreciated concern. It is not, however, one over which the end user has a great deal of control. Measurement of axes centricity requires the construction of some fairly complex and stiff structures capable of measuring displacements of the order of 1 to 2 μm and rotations of seconds of arc. The objective is to measure both the offset between the two axes and the angle between them. Concentricity errors affect XRPD data in a manner analogous to that of sample displacement; hence a 5 μm concentricity error is of concern. Worse yet is the possibility that some degree of precession occurs between the two axes with the operation of the goniometer. In this case, the performance of the machine will challenge description using established models.

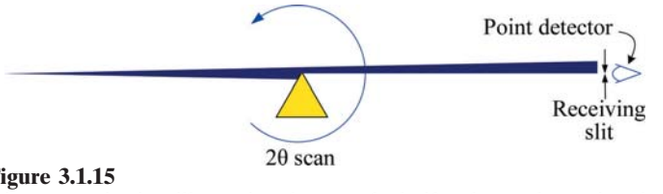

Figure 3.1.15
Diagrammatic view illustrating the use of a knife edge to determine the 2θ zero angle.

Subsequent experiments are performed with the X-rays present in order to achieve conditions (4) and (5). The criteria for proper alignment are universal, but there is a range of experimental approaches by which they can be realized. The specific approach may well be based on the age and make of the equipment as well as the inclinations of the operator. The essence of the experimental design remains constant, however: the operator uses optics mounted in the sample position that will either pass or block the X-ray beam in such a way as to tell the operator if and when the desired alignment condition has been realized. One approach is to use a knife edge mounted as shown in Fig. 3.1.15; a 2θ scan is performed using a point detector with a narrow receiving slit. When the intensity reaches 50% of the maximum, the X-ray source (focal line), the rotation axes of the goniometer and the 2θ (zero) angle are coplanar. However, the problematic presumption here is that the sample stage is aligned so exactly that the rotation axes of the goniometer assembly bisect the specimen surface, and therefore the knife edge, to within a few micrometres. This is equivalent to the z height being zero. The verification of this level of accuracy in stage alignment would be exceedingly difficult *via* direct measurements on the sample stage itself. While many would be inclined to trust the instrument manufacturer to have correctly aligned the stage, at NIST we use an alternative approach.

A straightforward means of addressing this problem is to use a stage that can be inverted, and perform the 2θ zero angle experiment in both orientations. 2θ scans of a knife edge in the normal and inverted positions can be compared to determine the true 2θ zero angle, independent of any z-height issue associated with the stage. It is often useful to draw a diagram of the results in order to avoid confusion; half the difference between the two measured zero angles yields the true one. With this information, the final alignment involves adjusting the specimen z height in the desired stage, which need not be invertible, until what is known to be the true 2θ zero angle is realized. The knife edge can also be used to centre the beam on the rotation axes, as per condition (5). Determination of the θ stage zero angle can be performed using a precision ground flat. An alternative optic to the knife edge is a rectangular 'tunnel' through which the X-ray beam passes. The entrance window of said tunnel may measure 20 to 40 μm in height and 10 mm in width, while the tunnel itself is 5 cm long. It is mounted in the beam path as illustrated in Fig. 3.1.16, with the 20 to 40 μm dimension defining the width of the beam and the 10 mm dimension describing the beam's length. Optics like this can be made of metal but are often made of glass. This optic will pass an X-ray beam only if it is parallel to the direction of the tunnel and can be used to determine both θ and 2θ zero angles. These are the optics used at NIST, *via* an experimental approach that will be discussed below.

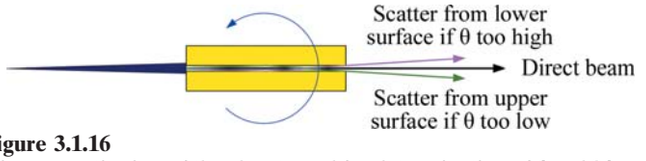

Figure 3.1.16
Diagrammatic view of the glass tunnel for determination of θ and 2θ zero angles.

If a diffractometer is being commissioned for the first time, or if major components have been replaced, it is appropriate to use fluorescent screens to achieve a rough alignment and to ensure that the incident beam does indeed cross the goniometer rotation axes and enter the detector; otherwise one may waste time looking for the beam. It is critical that these experiments are performed with the tube at operating power and that the equipment is at thermal equilibrium. Thermal effects will cause the anode to expand and contract, which will typically cause the position of the source to change. This is particularly critical when using optics to prepare the incident beam, as the performance of the optics can change markedly with movement of the source.

The objective of the first experiment using X-rays is to achieve parallelism between the line source of the tube anode, or focal line of the Johansson optic, and the receiving slit. A 5 µm platinum pinhole, which was originally manufactured as an aperture for transmission electron microscopy, is mounted in the sample position and used to image the focal line of the source onto the receiving slit (Fig. 3.1.17). This experiment is the one exception to the operating-power rule, as otherwise *Bremsstrahlung* will penetrate the platinum foil of the pinhole and produce confounding results. Success can be realized with settings of 20 kV and 10 mA; these reduced power settings are not thought to affect the angle between the tube anode and receiving slit (which is the issue addressed in this experiment). The incident slit is opened to the point at which the line source itself is imaged, not the incident slit. The Soller slits, and the post-monochromator if there is one, must also be removed to allow for the axial divergence that is needed for the success of this experiment. The pinhole images the line source onto the receiving slit; as the angle between the two decreases, progressively larger lengths of the receiving slit are illuminated during a 2θ scan. The tilt of the X-ray tube shield is varied and sequential 2θ scans are collected. As parallelism is approached, the profiles will exhibit a progressive increase in the maximum intensity value, with corresponding decreases in breadth. Conclusive results are shown in Fig. 3.1.18. It should be noted that this is a very difficult experiment to perform because the beam is essentially open and scatter is abundant. Shielding must be installed such that the detector can see only the signal that passes through the pinhole. The pinhole itself should also be shielded to minimize the area of (relatively transparent) platinum exposed to the direct beam.

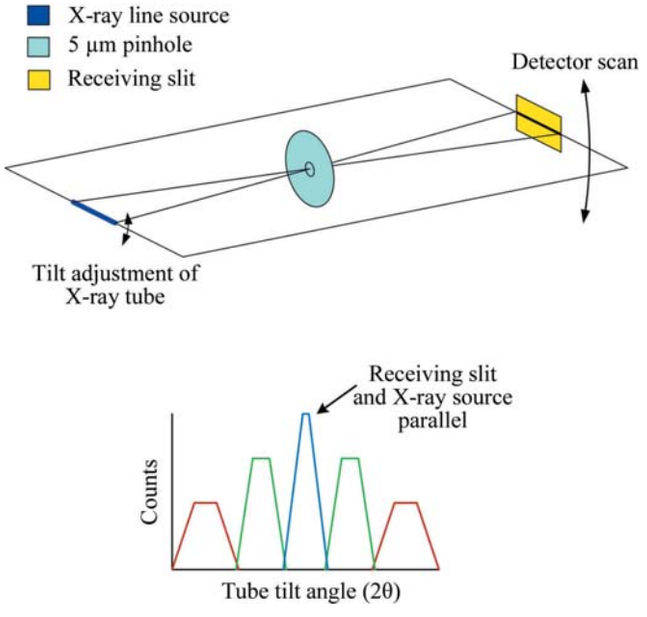

Figure 3.1.17
Design of experiments using a pinhole optic to align the X-ray source with the receiving slit.

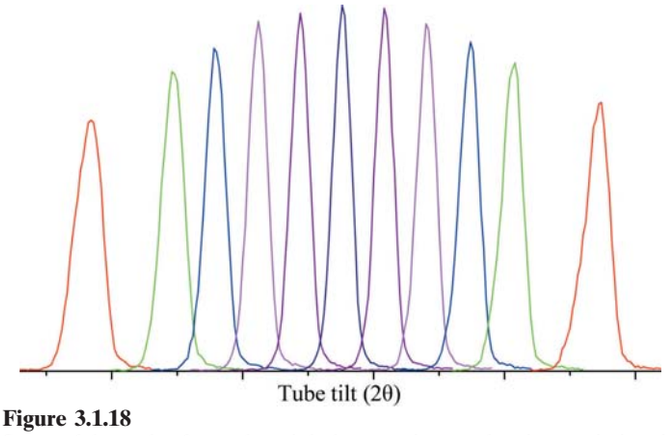

Figure 3.1.18
Successful results from the pinhole experiment showing variation in profile shape with successive adjustment of tube tilt; the central peak of highest intensity indicates the state of parallelism between the source and the receiving slit.

We now proceed to determine the θ and 2θ zero angles using the glass-tunnel optic. Initial experiments should be performed without a post-monochromator, as its presence tends to complicate finding the beam. However, it should be installed as experiments progress, as it will lead to an increase in resolution; it may alter the wavelength distribution slightly and its mass will change the torque moment on the 2θ axis. The latter two factors may alter the apparent 2θ zero by several hundredths of a degree. It is best to use a minimum slit size for the incident beam that will fully illuminate the entrance to the tunnel optic to avoid undue levels of scatter. The receiving slit should be the smallest size available, 0.05 mm in our case. The first experiment will determine a first approximation of the zero angle of θ. The tunnel optic is used, with a θ scan being performed with an open detector. Once an approximate zero angle of θ is determined, the receiving slit is installed and a 2θ scan is performed with θ at its zero point. Thus, we now have a qualitative idea of both zero angles. Then an experiment is performed as shown in Fig. 3.1.19; sequential 2θ scans are performed as θ is stepped through its zero point by very small steps (0.004° in the case of our experiment). The tunnel scatters radiation from its upper and lower surfaces when it is not parallel to the central portion of the beam, resulting in a lobe on each side of the direct beam in Fig. 3.1.19. When θ is at the desired zero angle, the direct beam is transmitted with minimum intensity in the lobes.

Once the zero positions of the θ and 2θ angles are determined, the stage is inverted and this set of experiments is repeated. It is desirable to drive the stage by 180°; however, remounting the stage in an inverted position is acceptable if the mounting structure centres the stage to within a few micrometres. Again, it is often useful to draw a diagram of the results from these two zero-angle determinations to ensure that the data are interpreted

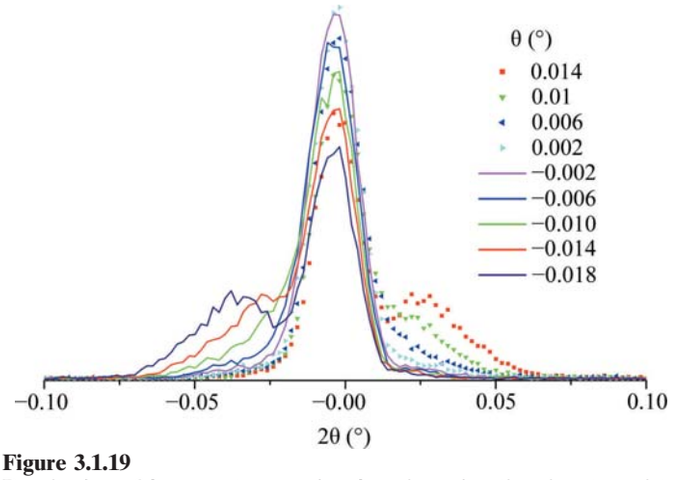

Figure 3.1.19
Results from 2θ scans at successive θ angles using the glass tunnel to determine the θ and 2θ zero angles.

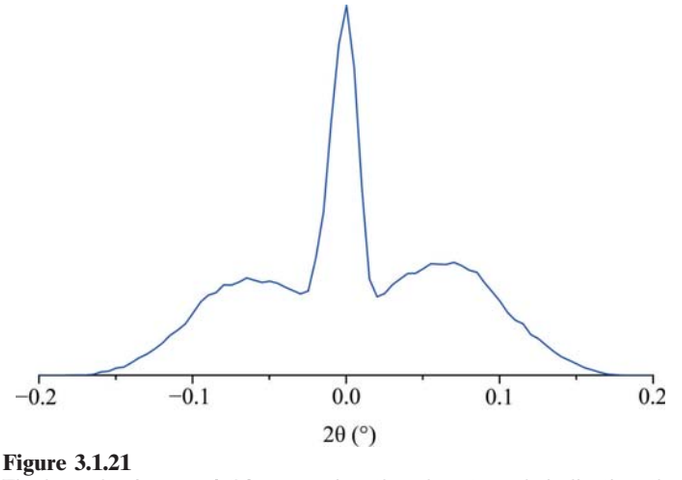

Figure 3.1.21
Final results from a θ–2θ scan using the glass tunnel, indicating the correct determination of θ and 2θ zero angles.

correctly, as shown in Fig. 3.1.20. In this example, the sample height is displaced in the positive z direction, otherwise the positions of orientation 1 and 180° from orientation 1 would be reversed. The operator should verify that fully self-consistent results are obtained with respect to the four zero angles shown in Fig. 3.1.20. Because the beam is divergent, the difference between the two θ zero angles will not be precisely 180°, as shown in Fig. 3.1.20. Again, half the difference between the two measured 2θ zero angles yields the true one, with respect only to the locations of the X-ray source and the goniometer rotation axes. Using the data of Fig. 3.1.20 and the goniometer radius, the z-height error on the stage in question could be computed and an adjustment made; this should be followed by repeating the two zero-angle measurements and checking for self-consistency to provide additional confidence in the alignment.

The final task is to mount the stage to be used in subsequent data collection and adjust its sample height until the known true 2θ zero angle is obtained. The final experiment is a θ–2θ scan of the tunnel optic to yield data of the kind shown in Fig. 3.1.21. The symmetry of the lobes on each side of the peak from the direct beam is indicative of the correct θ zero angle setting. This final high-resolution experiment is an excellent indicator of the state of the alignment of the instrument. These experiments, when used in conjunction with profile fitting, can yield measurements of the zero angles with an uncertainty for θ and 2θ of $\pm 0.001°$. Given the high certainty with which the zero angles are determined, they would then not be refined in subsequent data analyses. The alignment of the incident-beam slit, issue (5), is accomplished with a scan of the direct beam. If the machine is equipped with a variable-divergence incident-beam slit, it is important to evaluate it at several settings because changes in the centre line of the beam may occur as the divergence angle is altered. Use of an excessively narrow receiving slit should be avoided for scans of the direct beam, since the thickness of the metal blades used for the slit itself may be larger than the width of the slit, leading to a directional selectivity as the scan is performed.

The alignment presented here was carried out using a scintillation detector; however, much of it could be performed using a PSD in 'picture-taking' mode. In any case, the count rates have to be monitored to ensure that they are within the linear range of the detector (5000 to 10 000 counts per second), otherwise anomalous results are obtained. Attenuating foils that are flat and in good condition can be used to reduce the intensity. It should also be stressed that if the observations made during the experiments do not meet expectations, something is wrong and the desired outcome, *i.e.* the correct alignment, will not be realized. Drawing a diagram of the X-ray beam path can be very useful for discovering the cause of apparently unexplainable observations. Also, throughout these experiments it is appropriate for the operator to try various additional settings to ensure that the machine is operating as expected. Anomalous observations can almost always be explained in a quantitative manner with appropriate investigation. Patience is required.

In the past, achieving acceptable performance with a Johansson optic was considered so problematic that they were under-used, despite the improvements in the data quality they provided. Modern instrumentation can provide their advantages with dramatically reduced effort. The NIST Johansson IBM, however, was derived from an older design that was originally supplied with a Siemens D500, *circa* 1987. It uses a Huber 611 monochromator housing that provides 5 degrees of freedom in the positioning of the optic: the a distance, the takeoff angle, crystal 2θ, tilt and azimuth. For aforementioned reasons, we installed a modern Johansson optic manufactured by Crismatec (now part of Saint Gobain). There are two stages to the procedure for aligning the machine equipped with the IBM: first, the crystal optic itself is aligned

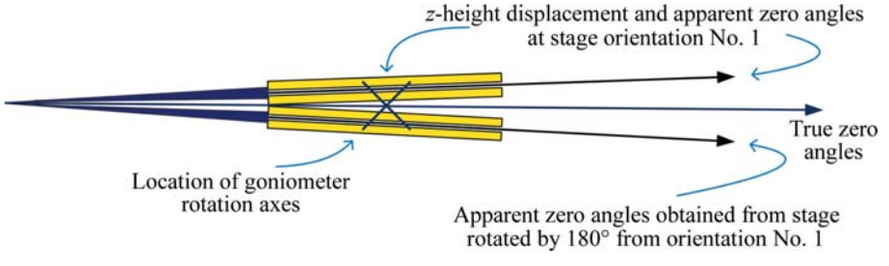

Figure 3.1.20
Diagram of hypothetical results from two zero-angle measurements (Fig. 3.1.19) with the sample stage in the normal and inverted positions to determine the true 2θ zero angle of the goniometer assembly in the absence of a z-height error from sample-stage misalignment.

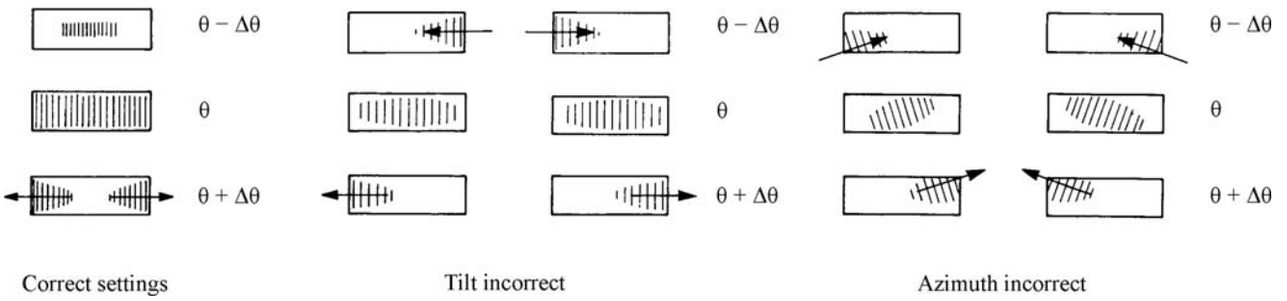

Figure 3.1.22
Figures found within the instructions for a Siemens D500 incident-beam monochromator in a Huber 611 monochromator housing, illustrating image formation and movement for correct and incorrect settings of tilt and azimuth angles (reproduced with verbal permission from Huber).

with the line source of the tube anode, and then the tube shield/IBM assembly is aligned with the goniometer. The second stage is analogous to the instrument alignment described above, so here we will discuss only the first stage (although not exhaustively).

The alignment of the Johansson optic to the X-ray source is done largely with the X-rays present. The crystal tilt and azimuth are set by using a fluorescent screen or camera to observe the diffraction images from the optic as it is rotated through its diffraction angle. Fig. 3.1.22, which is reproduced from the instructions supplied by Siemens, shows how the images form and move, informing the operator of necessary adjustments. Initially, a set of hex-drive extensions was used to drive the optic remotely through its 2θ angle. The source was operated at full power while the movement of the image was observed through a lead-impregnated window. Later, a motor drive was installed onto the 2θ actuator of the 611 housing. In the end, the incident-beam intensity realized from the optic is dependent upon the operator's ability to discern the subtleties in the image movement (Fig. 3.1.22). Blocking the axially divergent signals from the optic with a high-resolution 0.05° Soller slit dramatically improves the sensitivity of this observation to the setting of the tilt and azimuth angles. The inclusion of the Soller slit, however, will reduce the intensity markedly. A complete darkening of the room, including blocking of the shutter lights, as well as allowing time for pupil dilation, can be helpful. However, the use of an X-ray imager or a PSD in picture-taking mode improves the quality of the alignment by allowing for a more accurate interpretation of the observations.

The goal is the formation of an image in the centre of the beam path that splits symmetrically out to the edges with increasing crystal 2θ angle (Fig. 3.1.22). The directions supplied by Siemens and Huber allude to the fine adjustment [see Huber (2014) for movies] of the tilt and azimuth by examining the structure of the diffracted beam at the optic's focal point. A fluorescent screen located at the focal point and set at a 6° angle to the beam path is used to image the beam structure. With the use of the Soller slit for coarse alignment of tilt and azimuth, the desired final image for the fine-adjustment mode was, indeed, obtained. But it was not possible, even with a deliberate mis-setting of tilt and azimuth angles, to use the defective images at the focal point as a source of feedback for correcting the settings because they were too diffuse.

The Johansson optic is supplied with a and b distances that correspond to the angle of asymmetry in the diffraction planes and the bend radius. The instructions indicate that an incorrect setting in a will cause the optic's diffraction image to move up or down in the plane of diffraction with variation of the crystal 2θ angle. Again, a lack of sensitivity prevents the use of this effect as a feedback loop to set a. Alternative experiments for the optimization of the distance a of the optic were time consuming and not conclusive, so we decided to accept the supplied value for a. As before, we set the takeoff angle at 6°. A critical and quite difficult problem is the alignment of the slit located between the X-ray tube and the crystal optic (not shown in Fig. 3.1.3). This slit centres the beam onto the active area of the optic; misalignment leads to unwanted scatter from the optic's edges. It is aligned with the X-ray beam present, yielding an image of the shadow cast by the optic itself on one side, and one edge of the slit on the other. The optic is rotated in 2θ so that its surface is parallel to the X-ray beam, *i.e.* shadowing is minimized. The shadow from the second edge of the slit is obscured by the optic. Geometric considerations are used in conjunction with knowledge of the radius of curvature of the optic to obtain the correct location for the slit. A drawing is highly useful in this instance. After the installation of this slit, it is appropriate to re-check the tilt and azimuth settings, as the alignment of the optic is nearly complete.

The setting of the crystal 2θ is performed by evaluation of the direct beam, either with scans using a scintillation detector or by taking pictures with a PSD. With increasing crystal 2θ, the beam diffracted by the optic will build in the centre forming a broad profile; then the intensity on either side of the initial profile will rise, leading to the desired box form; and then intensity at the centre of the box will fall, followed lastly by the intensity at either side of the centre. This is consistent with Fig. 3.1.22. The process will repeat at half the $K\alpha_1$ intensity for the $K\alpha_2$ line. (Avoid tuning to the wrong line.) The crystal 2θ setting should be checked at regular intervals with a scan of the direct beam; this is the only setting on the IBM that has been observed to drift with time.

The final step in alignment of the IBM is the installation of the anti-scatter slit located at the focal line of the optic (Fig. 3.1.3). This is performed after the IBM assembly is aligned to the goniometer. Optimal performance of the anti-scatter slit can be expected only if it is located precisely at the focal line, which itself constitutes the smallest region within which a maximum of X-ray flux is transmitted. Therefore, the NIST alignment procedure includes an experiment using a narrow slit positioned by an x–y translator to evaluate the relative flux of the beam in the vicinity of the focal line. The y direction is parallel to the b direction (Fig. 3.1.3). A 0.05 mm slit is translated across the beam in the x direction, while intensity readings are recorded from an open detector. This process is repeated for a sequence of y distances. A plot of the recorded intensity *versus* x at a sequence of y settings will yield a set of profiles which broaden on either side of the true value of b; the narrowest, highest-intensity profile will indicate the location of the focal line. Thus, the experiment determines both the true b distance and the location in the x direction of the focal line. Once b is known, translational adjustment of the IBM

assembly may be required to locate the focal line precisely on the goniometer radius. The experiment also effectively measures the size of the focal line, in our case this was 0.15 mm. A slit of this dimension was fabricated, and the *x*–*y* translator was replaced with a standard slit retainer positioned at the desired location. The results are shown in Fig. 3.1.13.

3.1.4. SRMs, instrumentation and data-collection procedures

NIST maintains a suite of SRMs suitable for calibration of powder-diffraction equipment and measurements (NIST, 2015*a*,*b*,*c*,*d*). These SRMs can be divided into various categories based on the characteristic they are best at calibrating for: line position, line shape, instrument response or quantitative analysis, although some degree of overlap exists. The powder SRMs are certified in batches, typically consisting of several kilograms of feedstock, that are homogenized, riffled and bottled prior to the certification. A representative sample of the bottle population, typically consisting of ten bottles, undergoes certification measurements. The specific size of each lot is based on expected sales rates, mass of material per unit and an anticipated re-certification interval of 5 to 7 years. When the stocks of a given certification are exhausted, a new batch of the SRM is certified and a letter is appended to the code to indicate the new certification. Hence SRM 640e (2015) is the sixth certification of SRM 640, originally certified in 1973. The microstructural character of the SRM artifact and/or the certification procedure itself are expected to change (improve) with each renewal.

To understand the role of an SRM in the calibration of XRPD measurements and equipment, it is helpful to discuss briefly the documentation accompanying an SRM [see also Taylor & Kuyatt (1994), GUM (JCGM, 2008*a*) and VIM (JCGM, 2008*b*)]. NIST SRMs are known internationally as certified reference materials. Accompanying an SRM is a certificate of analysis (CoA), which contains both certified and non-certified quantity values and their stated uncertainties. Certified quantity values are determined by NIST to have metrological traceability to a measurement unit – often a direct linkage to the SI. Non-certified values (those lacking the word certified, as presented within a NIST CoA) are defined by NIST as best estimates of the true value provided by NIST where all known or suspected sources of bias have not been fully investigated. Both certified and non-certified quantity values are stated with an accompanying combined expanded (k = 2) uncertainty. Expanded uncertainty is defined as the combined standard uncertainty values for a given certified value multiplied by a coverage factor, k, of 2 and represents a 95% confidence interval for a given value. The combined standard uncertainties are determined by applying standard procedures for the propagation of uncertainty. The distinguishing characteristic of a NIST-certified quantity value is that all known instrumental measurement uncertainties have been considered, including the uncertainties from the metrological traceability chain. NIST defines uncertainties in two contexts: type A and type B. Type A are the random uncertainties determined by statistical methods, for example the standard deviation of a set of measurements. Type B uncertainties are systematic in nature and their extent is usually based on scientific judgment using all relevant information available on possible biases of the experiment. Assessing the technical origin and magnitude of these type-B uncertainties is a dominant part of the NIST X-ray metrology program.

XRPD SRM-certified quantity values are used primarily for calibration of XRPD measurement systems. The calibration data collected on test instruments also contain the two types of errors: random and systematic. It is the systematic measurement errors, or so-called instrument bias, that can be corrected with a calibration. Calibration is a multi-step process. First, certified quantity values are related to test instrument data. This is done by computing, from these values, what would constitute an 'ideal' data set from the 'measurement method' to be calibrated. The 'method' in this case would include the test instrument, its configuration settings and the data-analysis method to be used in subsequent measurements. Then a data set from the SRM is collected and analysed under the conditions of the method. Lastly, a calibration curve is generated by comparing the 'ideal' data set to the measured one. This would establish a correction to the instrument data and yield a calibrated measurement result. For XRPD, this correction has classically taken the form of a calibration function shifting the apparent 2θ indications. There is also the possibility that comparing the 'ideal' instrument response with the observed one indicates a mechanical, optical or electrical malfunction of the instrument. This, of course, requires further investigation and repair, rather than simply applying a calibration curve.

The generation of a calibration curve as just described can be thought of as a 'classical' calibration, and is applicable when the data-analysis procedure(s) use empirical methods to parameterize the observations. More recent, advanced methods such as the FPA use model functions that relate the form of the data directly to the characteristics of the diffraction experiment. The parameters of the model describing the experiment are refined in a least-squares context in order to minimize the difference between a computed pattern and the observed one. With the use of methods that use model functions, the calibration takes on a different form, as the collection and analysis of data can be thought of as replacing the aforementioned multi-step process. The calibration is completed by comparing the results of the refinement with certified quantity values from an appropriately chosen SRM and the known physical-parameter values that describe the optical configuration of the test instrument.

Random measurement error, describing the variation of data for a large set of measurements, can be estimated by repeating measurements over an extended period and computing the variance in the data. Furthermore, over time, one could recalibrate the system and look at the variance of the systematic bias for a given instrument, *i.e.* the rate of drift in the instrument. One would also have to investigate the sensitivity of both the random error and the variance in the systematic bias to environmental variables such as ambient temperature, power fluctuations *etc*. This systematic error variance, combined with the prior determined random error variance and the certified value and its uncertainty, provides an instrumental measurement uncertainty that can be applied to all measurements from a given instrument. Such an in-field study, however, would take years to complete. Instead, the instrumental measurement uncertainties for a given commercial XRPD measurement system are typically provided by the manufacturer, with the stated caveat that periodic calibrations should be performed *via* factory specifications. The instrumental measurement uncertainties determined through such a study are invariably much larger than those of the NIST-certified quantity values, as they contain both the instrument measurement errors (systematic and random) combined with certified quantity value uncertainties.

NIST maintains a suite of more than a dozen SRMs for powder diffraction. However, one often encounters discussions of non-institutionally-certified standards such as 'NAC' ($Na_2Ca_3Al_2F_{14}$), annealed yttrium oxide and silver behenate. Our discussions here

principally concern SRMs 640e (silicon), 660b (NIST, 2010) (lanthanum hexaboride), 1976b (2012) (a sintered alumina disc) and 676a (NIST, 2008) (alumina). SRM 660b has since been renewed as SRM 660c (2014). Most of the work presented here was performed using SRM 660b; however, SRM 660c could be used in any of these applications with identical results. SRMs certified to address the calibration of line position, such as SRMs 640e, 660c and 1976b, are certified in an SI-traceable manner with respect to lattice parameter. SRM 1976b is also certified with respect to 14 relative intensity values throughout the full 2θ range accessible with Cu $K\alpha$ radiation. As such, it is used to verify the correct operation of a diffractometer with respect to diffraction intensity as a function of 2θ angle, *i.e.* instrument sensitivity (Jenkins, 1992) or instrument response. SRM 676a is a quantitative-analysis SRM certified with respect to phase purity (Cline *et al.*, 2011). While SRM 676a is certified for use as a quantitative-analysis SRM, it is also certified with respect to lattice parameters.

Starting with the certification of SRM 640c in 2000, the 640*x* SRMs have been prepared in a way that minimizes sample-induced line broadening. These powders consist of single-crystal particles that were annealed after comminution in accordance to the method described by van Berkum *et al.* (1995). Their crystallite-size distributions (as determined by laser scattering) have a maximum probable size of approximately 4 μm with 10% of the population being above 8 μm and 10% of the population being below 2.5 μm (with trace quantities below 1 μm). With Cu $K\alpha$ radiation, silicon has a linear attenuation of 148 cm^{-1}, which is a relatively low value. SRMs 660*x* consist of lanthanum hexaboride, which was prepared to display a minimal level of both size and microstrain broadening. With the release of SRM 660a, high-resolution diffraction using synchrotron radiation must be used to detect microstructural broadening. However, the use of lanthanum hexaboride by the neutron-diffraction community is problematic, as the naturally abundant isotope ^{10}B has an extremely high neutron absorption cross section. Lanthanum hexaboride made from ^{10}B is essentially opaque to neutrons, rendering it unsuitable for neutron experiments. This problem was addressed with SRMs 660b and 660c by means of a dedicated processing run using a boron carbide precursor enriched with the ^{11}B isotope to a nominal 99% concentration. As such, SRMs 660b and 660c are suitable for neutron experiments; they display a miniscule reduction in microstrain broadening relative to 660a. SRMs 660b and 660c were prepared at the same time using identical procedures and equipment, but in different lots. Lanthanum hexaboride has a relatively high linear attenuation of 1125 cm^{-1} with Cu $K\alpha$ radiation. This linear attenuation virtually eliminates the contribution of specimen transparency to the observed data; as such it offers a more accurate assessment of the IPF for a machine of Bragg–Brentano geometry than is available from other SRMs in the suite. The powders of the SRM 660*x* series consist of aggregates, with the crystallite size being approximately 1 μm and the aggregate size distribution being centred at approximately 8 μm for SRM 660a and 10 μm for 660b and 660c. SRM 676a consists of a fine-grained, equi-axial, high-phase-purity α-alumina powder that does not display the effects of preferred orientation. It consists of approximately 1.5 μm-diameter aggregates with a broad crystallite-size distribution centred at 75 nm. Therefore, the diffraction lines from SRM 676a display a considerable degree of Lorentzian size broadening, with a $1/\cos\theta$ dependence.

SRM 1976b consists of a sintered alumina disc; this format eliminates the variable of sample-loading procedure from the diffraction data collected from this SRM. The alumina powder precursor for SRMs 1976, 1976a and 1976b consists of a 'tabular' alumina that has been calcined to a high temperature, approximately 1773 K. This calcination results in a phase-pure α-alumina powder with a plate-like crystal morphology, approximately 10 μm in diameter by 2 to 3 μm in thickness, leading to the texture displayed by these SRMs. The feedstock for SRMs 1976, 1976a and 1976b was manufactured with a common processing procedure: the compacts are liquid-phase sintered using a 3 to 5% anorthite glass matrix; hot forging was used to achieve a compact of approximately 97% of theoretical density. A unique outcome of the hot-forging operation used to manufacture these pieces was the axi-symmetric texture imparted to the microstructure. This axi-symmetric nature permits mounting of the sample in any orientation about the surface normal. Furthermore, as the sintered compacts cool, the viscosity of anorthite steadily increases, solidifying at approximately 1073 K. This permits intergranular movement during cooling, at least until 1073 K, and reduces the level of microstrain that would otherwise build between the grains due to the anisotropic thermal expansion behaviour of alumina. However, despite this relaxation mechanism, SRM 1976*x* still displays a discernable level of Gaussian microstrain broadening. SRMs 1976a and 1976b were manufactured in a single custom production run, and display a much more uniform level of texture than SRM 1976. This fact is reflected in the considerably smaller uncertainty bounds on the certified relative intensity values of SRMs 1976a and 1976b compared to the original SRM 1976.

Mounting of powder specimens for analysis using Bragg–Brentano geometry is a non-trivial process that typically requires 20 to 30 min. The objective is to achieve a maximum in packing density of the powder with a smooth, flat surface. A 5 μm displacement error in the position of the sample surface will have a noticeable impact on the data collected. Side-drifted mounts allow for realization of a flat surface with relative ease, though maximizing the density of the compact can be challenging. Top-mounted specimens can be compacted using a glass plate or bar that allows the operator to see the sample surface through the glass and, in real time, determine the success or failure in obtaining the desired outcome. Some powders, such as that of SRM 640e, 'flow' in the mount with the oscillation of the glass plate across the sample surface. Others, such as SRM 676a do not flow at all, but can be 'chopped' into the holder and compacted with a single compression. Several attempts may be necessary to realize a high-quality mount. A low-wetting-angle, low-viscosity silicone-based liquid resin, such as those marketed as vacuum-leak sealants for high-vacuum operations, can be used to infiltrate the compact once it is mounted; this results in a stable sample that will survive some degree of rough handling.

The diffractometer discussed in this work is a NIST-built instrument with a conventional optical layout, although it has several features that are atypical of equipment of this nature. It was designed and built to produce measurement data of the highest quality. This outcome is not only consistent with the certification of SRMs, but is also requisite to critical evaluation of modern data-analysis methods (another goal of this work), as discussed below. The essence of the instrument is a superior goniometer assembly that is both stiff and accurate in angle measurement, in conjunction with standard but thoroughly evaluated optics. The tube shield and incident-beam optics are mounted on a removable platform that is located *via* conical pins that constitute a semi-kinematic mount. This feature allows rapid interchange between various optical geometries. Fig. 3.1.23 shows

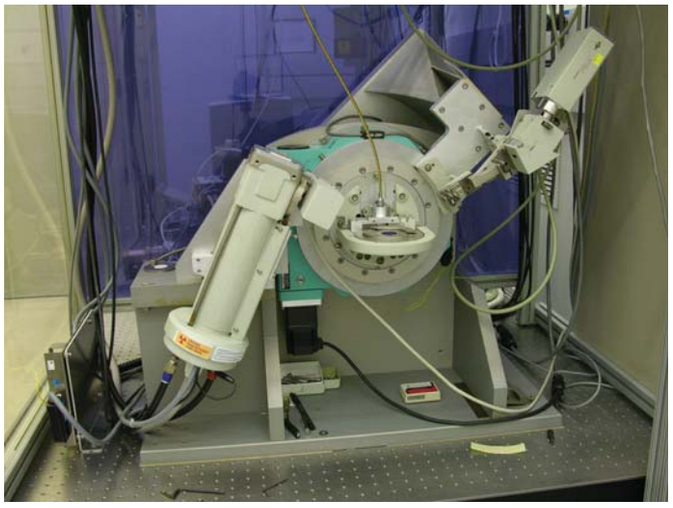

Figure 3.1.23
The X-ray powder diffractometer designed and fabricated at NIST, in conventional divergent-beam format.

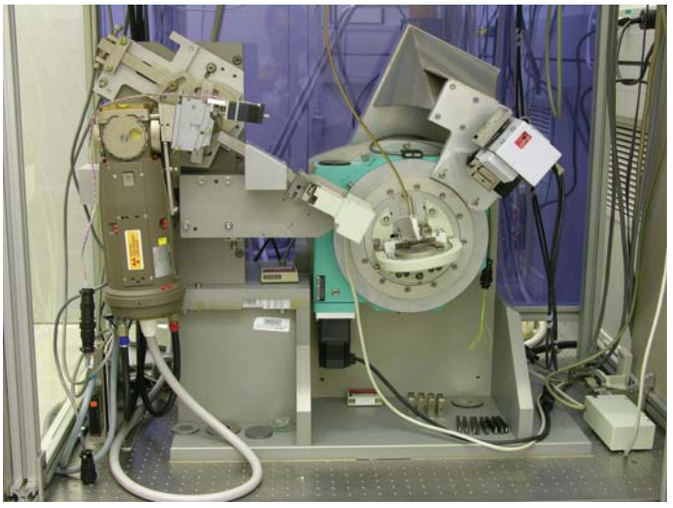

Figure 3.1.24
The NIST-built powder diffractometer configured with the Johansson incident-beam monochromator and a position-sensitive detector.

the instrument set up in conventional geometry with a post-monochromator and point detector, while Fig. 3.1.24 shows the setup with a Johansson IBM and a PSD. Data from these two configurations are discussed below.

The goniometer assembly, which is of θ–2θ geometry, uses a pair of Huber 420 rotation stages mounted concentrically with the rotation axes horizontal. The stage that provides the θ motion faces forward while the 2θ stage faces rearward; they are both mounted on a common aluminium monolith, visible in Figs. 3.1.23 and 3.1.24, which forms the basis of the chassis for the instrument. Both stages incorporate Heidenhain 800 series optical encoders mounted so as to measure the angle of the ring gear. With 4096-fold interpolation provided by IK220 electronics, an angle measurement to within $\pm 0.00028^\circ$ (1 arc second) was realized for both axes. The stages are driven by five-phase stepper motors that incorporate gear reducers of 10:1 for the θ stage and 5:1 for the 2θ stage, yielding step sizes of 0.0002° and 0.0004°, respectively. The manufacturer's specifications for the Huber 420 rotation stage claim an eccentricity of less than 3 μm and a wobble of less than 0.0008° (3 arc seconds). The construction of the goniometer assembly necessitated the development of a specialized jig to align the two 420 rotation stages with regard to both the concentricity (eccentricity) and parallelism (wobble) of their rotation axes. The result was that the overall eccentricity and wobble of the assembly met the specifications cited for the individual stages. The flexing of the detector arm, attached to the rearward-facing 2θ stage, was minimized by fabricating a honeycombed aluminium structure, 7.6 cm deep, which maximized stiffness while minimizing weight. Furthermore, the entire detector-arm assembly, including the various detectors, was balanced on three axes to minimize off-axis stress on the 2θ rotation stage (Black *et al.*, 2011). Thus, the goniometer assembly is exceedingly stiff and offers high-accuracy measurement and control of both the θ and 2θ angles.

The optics, graphite post-monochromator, sample spinner, X-ray generator and tube shield of the machine were originally components of a Siemens D5000 diffractometer, *circa* 1992. As previously discussed, the parts for the IBM configuration were obtained primarily from a Siemens D500, *circa* 1987. Both configurations include a variable-divergence incident-beam slit from a D5000. The PSD used in this work was a Bruker LynxEye XE. The cable attached to the sample spinner (as seen in Figs. 3.1.23 and 3.1.24) is a flexible drive for the spinner itself; the remote location of the drive motor (not shown) isolates the sample and machinery from the thermal influence of the motor. The machine was positioned on an optical table within a temperature-controlled (± 0.1 K) space. The temperature of the water used for cooling the X-ray tube and generator was regulated to within ± 0.01 K. Operation of the machine was provided through control software written in *LabVIEW*. Data were recorded in true x–y format using the angular measurement data from the optical encoders.

In conventional configuration, the 2.2 kW copper tube of long fine-focus geometry was operated at a power of 1.8 kW. This tube gives a source size of nominally 12×0.04 mm, while the goniometer radius is 217.5 mm. The variable-divergence slit was set to $\sim 0.9^\circ$ for the collection of the data discussed here. This results in a beam width, or footprint at the lowest θ angle, on the sample of about 20 mm, conservatively smaller than the sample size of 25 mm. A Soller slit with a divergence of 4.4° defined the axial divergence of the incident beam. A 2 mm anti-scatter slit was placed approximately 113 mm in front of the 0.2 mm (0.05°) receiving slit. The total path length of the scattered radiation (the goniometer radius plus the traverse through the post-monochromator) was approximately 330 mm. This setup reflects what is thought to be a medium-resolution diffractometer that would be suitable for a fairly broad range of applications and is therefore a reasonable starting point for a study of instrument calibration. With the IBM, the 1.5 kW copper tube of fine-focus geometry was operated at a power of 1.2 kW. This tube had a source size of nominally 8×0.04 mm. The variable-divergence incident slit was also set to 0.9° with a 0.2 mm (0.05°) receiving slit. The receiving optics were fitted with a 4.4° Soller slit. The total beam-path length was about 480 mm.

With the scintillation detector, data were collected using two methods, both of which encompassed the full 2θ range available with these instruments and for which the SRMs show Bragg reflections. The first involves data collection in peak regions only, as illustrated in Table 3.1.2 for SRM 660b. The run-time parameters listed in Table 3.1.2 reflect the fact that the data-collection efficiency can be optimized by collecting data in several regions, as both the intensity and breadth vary systematically with respect to 2θ. This was the manner in which data were collected for the certification measurements of SRMs 660c, 640e and 1976b. The

Table 3.1.2
Run-time parameters used for collection of the data used for certification of SRM 660b

The 'overhead time' associated with the operation of the goniometer is included.

hkl	Start angle (°)	End angle (°)	Step width (°)	Count time (s)	Total peak time (min)
100	20.3	22.2	0.01	2	6.3
110	29.1	31.4	0.01	1	3.8
111	36.4	38.4	0.01	3	10.0
200	42.7	44.4	0.01	5	14.2
210	48	50	0.008	2	8.3
211	53.2	54.896	0.008	5	17.7
110	62.5	64.204	0.008	11	39.0
300	66.7	68.596	0.008	4	15.8
310	70.9	72.7	0.008	6	22.5
311	75	76.904	0.008	9	35.7
222	79.3	80.804	0.008	47	147.3
320	83	84.904	0.008	15	59.5
321	86.9	88.9	0.008	8	33.3
400	95	96.704	0.008	42	149.1
410	98.6	100.8	0.008	9	41.3
330	102.7	104.9	0.008	12	55.0
331	106.9	108.9	0.01	27	90.0
420	111.1	113.1	0.01	20	66.7
421	115.3	117.6	0.01	10	38.3
332	119.9	122.1	0.01	19	69.7
422	129.6	131.796	0.012	32	97.6
500	134.9	137.396	0.012	27	93.6
510	140.5	144	0.014	7	29.2
511	147.5	150.908	0.016	15	53.2
					Total time = 20.0 hours

second involved a simple continuous scan of fixed step width and count time. It is generally accepted that a step width should be chosen so as to collect a minimum of five data points above the full-width-at-half-maximum (FWHM) to obtain data of sufficient quality for a Rietveld analysis (Rietveld, 1967, 1969; McCusker *et al.*, 1999). This does not, however, constitute any sort of threshold; collecting data of a finer step width can, with proper data analysis, result in a superior characterization of the IPF. However, one must consider the angular range of acceptance of the receiving slit that is chosen. For a slit of 0.05° a step width of 0.005° would add only 10% 'new' information, so selecting this step width would not be worth the extra data-collection time. We did, however, collect some data sets we refer to as 'ultra-high-quality' data; the step widths for these were half those shown in Table 3.1.2 and the count times were approximately three times higher than those in Table 3.1.2. For the reported instrument and configuration, the run-time parameters of Table 3.1.2 result in a minimum of 8 to 10 points above the FWHM. Count times were selected to obtain a uniform number of counts for each profile. It should be noted that it is probably not worth spending time collecting quality data from the 222 line of LaB_6, as it is of low intensity and relatively close to other lines of higher intensity; however, this is not the case with the 400 line. Selection of the run-time parameters can be an iterative process; the total width of each profile scan was set to include at least 0.3° 2θ of apparent background on either side of the profile. Except for the data for SRM 676a, the continuous scans discussed were collected with a step width of 0.008° 2θ and a count time of 4 s to result in a scan time of roughly 24 h. The scans of 676a were collected with 0.01° 2θ step width and 5 s count time.

The PSD used on the NIST diffractometer was a one-dimensional silicon strip detector operated in picture-taking mode for all data collection. It has an active window length of 14.4 mm that is divided into 192 strips for a resolution of 75 μm. With a goniometer radius of 217.5 mm this constitutes an active angular range of 3.80° with 0.020° per strip. Slits that would limit the angular range of the PSD window were not used; with each step the counts from all 192 channels were recorded. The PSD was stepped at 0.005° 2θ, for 25% new information per strip; however, to reduce the data-collection time a second coarse step was also included. Therefore, the data-collection algorithm includes the selection of three parameters: a fine step of 0.005°, the number of fine steps between coarse steps (4), and the size of a coarse step (typically 0.1° or 0.2° 2θ). This approach allows for the collection of high-resolution data without stepping through the entire pattern at the high-resolution setting. Data were collected with four fine steps per detector pixel and a coarse step of 0.1° 2θ. They were processed to generate x–y data for subsequent analysis. The operator can select the portion of the 192 channels, centred in the detector window, to be included in the generation of the x–y file. The PSD was fitted with a 1.5° Soller slit for collection of the data presented here.

3.1.5. Data-analysis methods

Data-analysis procedures can range from the entirely non-physical, using arbitrary analytical functions that have been observed to yield reasonable fits to the observation, to those that exclusively use model functions, derived to specifically represent the effect of some physical aspect of the experiment. The non-physical methods serve to parameterize the performance of the instrument in a descriptive manner. The origins of two of the most common measures of instrument performance are illustrated in Fig. 3.1.25. The first is the difference between the apparent position, in 2θ, of the profile maximum and the position of the Bragg reflection computed from the certified lattice parameter. These data are plotted *versus* 2θ to yield a $\Delta(2\theta)$ curve; a typical example is shown in Fig. 3.1.26. An illustration of the half-width-at-half-maximum (HWHM), which is defined as the width of either the right or left half of the profile at one half the value of maximum intensity after background subtraction, is also shown in Fig. 3.1.25. These values can be summed to yield the FWHM, and plotted *versus* 2θ to yield an indication of the profile breadth as it varies with 2θ (Fig. 3.1.27). In addition, the left and right HWHM values of Fig. 3.1.28 gauge the variation of profile asymmetry with 2θ; additional parameters of interest, such as the degree of Lorentzian and Gaussian contribution to profile shape,

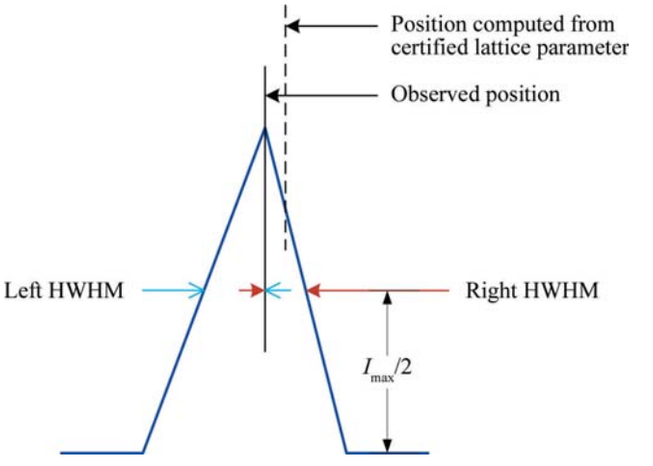

Figure 3.1.25
Diagrammatic representation of a powder-diffraction line profile, illustrating the metrics $\Delta(2\theta)$ and half-width-at-half-maximum (HWHM). The full-width-at-half-maximum (FWHM) = left HWHM + right HWHM.

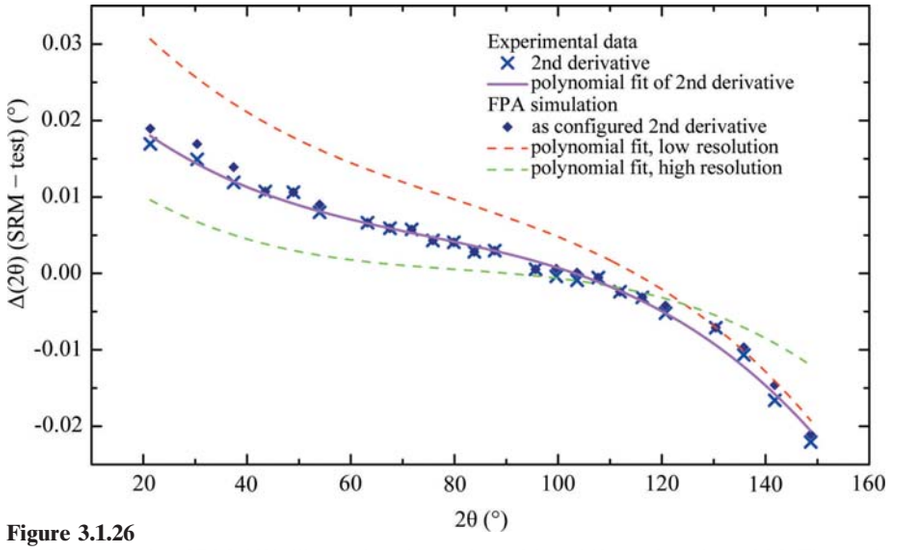

Figure 3.1.26
$\Delta(2\theta)$ curve using SRM 660b illustrating the peak-position shifts as function of 2θ. The peak positions were determined *via* a second-derivative algorithm, and $\Delta(2\theta)$ values (SRM − test) were fitted with a third-order polynomial. Simulated data are from *FPAPC* and were analysed *via* the second-derivative algorithm and polynomial fits as per the experimental data.

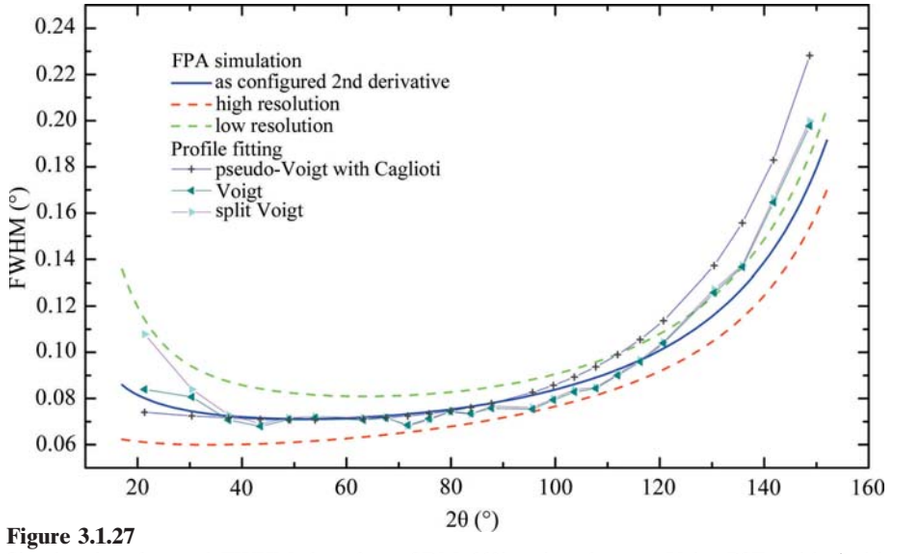

Figure 3.1.27
Simulated and actual FWHM data from SRM 660b using the two Voigt PSFs with ('with Caglioti') and without constraints.

can be plotted *versus* 2θ to describe the instrument and evaluate its performance.

The least computationally intensive methods for the analysis of XRPD data, which have been available since the onset of automated powder diffraction, are based on first- or second-derivative algorithms. These methods report peak positions as the 2θ value at which a local maximum in diffraction intensity is detected in the raw data. Typical software provides 'tuning' parameters so that the operation of these algorithms can be optimized for the noise level, step width and profile width of the raw data. These methods are highly mature and offer a quick and reliable means of analysing data in a manner suitable for qualitative analysis and lattice-parameter refinement. However, they only give information about the position of the top of the peak. Calibration of the diffractometer *via* this method is useful only for subsequent analyses that also use such peak-location methods.

Profile fitting with an analytical profile-shape function offers the potential for greater accuracy, because the entire profile is used in the analysis. As with the derivative-based methods, profile fitting also reports the observed 2θ position of maximum intensity, in addition to parameters describing profile shape and breadth. The discussion of the IPF in Section 3.1.1, as well as a quick look at Figs. 3.1.26–3.1.28, shows the complexity in the line profile shape from a Bragg–Brentano instrument. The profiles are symmetric only in a limited region of 2θ; in other regions, the degree and direction of profile asymmetry also vary as a function of 2θ. To a first approximation, the optics of an instrument contribute to the Gaussian nature of the profiles; this Gaussian nature will be constant with respect to 2θ. The Lorentzian contribution is primarily from the emission spectrum; given the dominance of angular-dispersion effects at high angle, one can expect to see an increase in the Lorentzian character of the profiles with increasing 2θ. While it can be argued that it is physically valid to model specific contributions to the IPF with Gaussian and Lorentzian PSFs, either of these two analytical functions alone cannot be expected to fit the complexities of the IPF and yield useful results. Combinations of these two functions, however, using shape parameters that vary as a function of 2θ, have given credible results for fitting of data from the Bragg–Brentano diffractometer and have been widely incorporated into Rietveld structure-refinement software. The Voigt function is a convolution of a Gaussian with a Lorentzian, while the pseudo-Voigt is the sum of the two. The parameters that are refined consist of an FWHM and shape parameter that indicates the ratio of the Gaussian to Lorentzian character. The Voigt, being a true convolution, is the more desirable PSF as it is more physically realistic; the pseudo-Voigt tends to be favoured as it is less computationally intensive and the differences between the two PSFs have been demonstrated to be minimal (Hastings *et al.*, 1984), although there is not universal agreement about this.

Refining the profile shapes independently invariably leads to errors when analysing patterns with peak overlap, as correlations

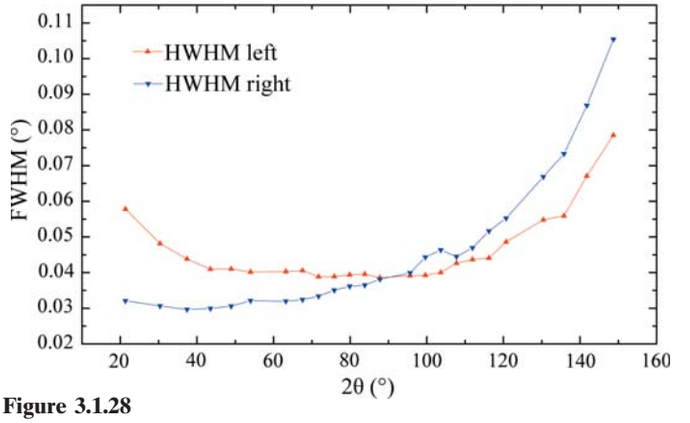

Figure 3.1.28
Left and right HWHM data from SRM 660b using the split pseudo-Voigt PSF fitted with uniform weighting.

occur between shape parameters of neighbouring profiles. This problem can be addressed by constraining the shape parameters to follow some functional form with respect to 2θ. Caglioti *et al.* (1958) developed such a function specifically for constant-wavelength neutron powder diffractometers; it has been incorporated in many Rietveld codes for use with XRPD data. It constrains the FWHM of the Gaussian contribution to the Voigt or pseudo-Voigt PSF:

$$\mathrm{FWHM}^2 = U\tan^2\theta + V\tan\theta + W, \qquad (3.1.1)$$

where the refineable parameters are U, V and W. The term U can be seen to correspond with microstrain broadening from the sample, and broadening due to the angular-dispersion component of the IPF. In *GSAS* an additional term, GP, in $1/\cos\theta$, is included to account for Gaussian size broadening. The Lorentzian FWHM in *GSAS* can vary as

$$\mathrm{FWHM} = \frac{LX}{\cos\theta} + LY\tan\theta, \qquad (3.1.2)$$

where LX and LY are the refineable parameters. Here LX varies with size broadening while LY is the Lorentzian microstrain and angular-dispersion term. Given that the emission spectrum is described with Lorentzian profiles, we would expect the LY term to model the effects of angular dispersion. Within the code *HighScore Plus*, the Lorentzian contribution is allowed to vary as

$$\mathrm{FWHM} = \gamma_1 + \gamma_2(2\theta) + \gamma_3(2\theta)^2, \qquad (3.1.3)$$

where γ_1, γ_2, and γ_3 are the refineable parameters. Alternatives to the Caglioti function have been proposed that are arguably more appropriate for describing the FWHM data from a Bragg–Brentano instrument (Louër & Langford, 1988; Cheary & Cline, 1995). However, they have not yet been incorporated into many computer codes.

The asymmetry in the observed profiles can be fitted with the use of a split profile, where the two sides of the PSF are refined with independent shape and HWHM parameters. This approach will improve the quality of the fit to the observations; however, it is empirical in nature. The more physically valid approach is the use of models to account for the origins of profile asymmetry. The Finger *et al.* (1994) model for axial divergence has been widely implemented in various Rietveld codes. It is formulated to model the axial-divergence effects of a synchrotron powder diffraction experiment where the incident beam is essentially parallel. The two refineable parameters, S/L and H/L, refer to the ratios of sample and receiving-slit length, relative to the goniometer radius; they define the level of axial divergence in the diffracted beam. This model is not in precise correspondence with the optics of a Bragg–Brentano diffractometer where both the incident and diffracted beams exhibit divergence in the axial direction. It does, however, give quality fits to such data. The use of such a model, as opposed to the sole use of a symmetric or split PSF, will yield peak positions and/or lattice parameters that are 'corrected' for the effects of the aberration in question. Therefore, results from the use of model(s) cannot be directly compared with empirical methods that simply characterize the form of the observation. In the case of the Bragg–Brentano experiment, the correction that the Finger model applies is not rigorously correct. However, the impact of axial divergence, regardless of the details of diffractometer optics, is universal; as such the use of the Finger model results in a more accurate assessment of 'true' peak position and, therefore, lattice parameters.

A third PSF that is in common use is the Pearson VII, or split Pearson VII, that was proposed by Hall *et al.* (1977) for fitting X-ray line profiles. No *a priori* physical justification exists for the use of this PSF. The refineable parameters are the FWHM, or HWHM, and an exponent, m. The exponent can range from 1, approximating a Lorentzian PSF, to infinity, where the function tends to a Gaussian. Owing to the lack of a clear physical justification for use of this PSF, it is not often used in Rietveld analysis software.

Convolution-based profile fitting, as shown in Fig. 3.1.4, was proposed by Klug and Alexander in 1954 (see Klug & Alexander, 1974) and much of the formalism of the aberration functions shown in Table 3.1.1 was developed by Wilson (1963). However, limitations in computing capability largely prevented the realization of the full fundamental-parameters approach method until 1992, with the work of Cheary & Coelho. This was made available to the community through the public-domain programs *Xfit*, and later *KoalaRiet* (Cheary & Coelho, 1996) and more recently *via TOPAS*. Other FPA programs are available, most notably *BGMN* (Bergman *et al.*, 1998); more recently, *PDXL 2* has had some FPA models incorporated. Within the FPA there are no PSFs other than the Lorentzians used to describe the emission spectrum, the shapes of which are not typically refined. All other aspects of the observation are characterized with the use of model functions that yield parameters descriptive of the experiment. Plausibility of the analysis is determined through evaluation of these parameters with respect to known or expected values. Direct comparison of the results from an FPA to those from methods using analytical PSFs is difficult because of the fundamental difference in the output from the techniques; for example, FWHM values are not obtained directly from the FPA method. However, the NIST program *FPAPC* can be used to determine FWHM values numerically.

The FPA models of *TOPAS*, *BGMN* and *PDXL 2* were developed specifically for the analysis of data from a laboratory diffractometer of Bragg–Brentano geometry. Analyses using this method would be expected to result in the lowest possible residual error terms that characterize the difference between calculation and observation. As has been discussed, the various aberrations affecting the diffraction line shape are such that the observed profile maxima do not necessarily correspond to the d-spacing of the diffracting plane (hkl), except perhaps in a limited region of 2θ, emphasizing the need for physically valid modelling of the observed line shape to realize a credible value for the lattice parameter. At NIST, we are particularly interested in the capabilities of the FPA method, as one of the primary interests of the NIST X-ray metrology program is obtaining the correct values for lattice parameters. Furthermore, experience has demonstrated that the refined parameters obtained through the use of FPA models can be used in a 'feedback loop' to isolate problems and anomalies with the equipment.

The instrument response, *i.e.* the diffracted intensity as a function of 2θ, is measured by Rietveld analysis using models for intensity-sensitive parameters such as crystal-structure parameters and Lorentz–polarization factors. The extraction of plausible crystal-structure parameters from standards *via* a Rietveld analysis serves as an effective and independently verifiable means of calibrating instrument performance. Considering these refined values provides an effective way to detect defects that vary smoothly over the full range of 2θ. However, errors that are only observable within limited regions of 2θ may be difficult to detect with a whole-pattern method; these should be investigated with second-derivative or profile-fitting methods. SRM

676a (alumina) is well suited to assessing instrument response because it is non-orienting and of high purity. Alumina is of lower symmetry than either silicon or lanthanum hexaboride; it has a considerable number of diffraction lines and has well established structure parameters. A Rietveld analysis of SRM 660c, however, yields the IPF in terms of code-specific profile shape terms and verifies that peak-position-specific aspects of the equipment and analysis are working correctly.

The instrument response may be evaluated with the more conventional data-analysis methods with use of SRM 1976b. Measurements of peak intensities are obtained from the test instrument, typically by profile fitting, and compared with the certified values. However, the use of SRM 1976b with diffraction equipment with different optical configurations may require the application of a bias to the certified values to render them appropriate for the machine to be qualified. This bias is needed to account for differences in the polarization effects from the presence, absence and character of crystal monochromators. The polarization factor for a diffractometer that is not equipped with a monochromator is (Guinier, 1994)

$$\frac{1+\cos^2 2\theta}{2}. \tag{3.1.4}$$

The polarization factor for a diffractometer equipped with only an incident-beam monochromator is (Azároff, 1955)

$$\frac{1+\cos^2 2\theta_m \cos^2 2\theta}{1+\cos^2 2\theta_m}, \tag{3.1.5}$$

where $2\theta_m$ is the 2θ angle of diffraction for the monochromator crystal. The polarization factor for a diffractometer equipped with only a diffracted-beam post-monochromator is (Yao & Jinno, 1982)

$$\frac{1+\cos^2 2\theta_m \cos^2 2\theta}{2}, \tag{3.1.6}$$

where $2\theta_m$ is the 2θ angle of the monochromator crystal. Equations (3.1.5) and (3.1.6) are appropriate when the crystal has an ideal mosaic structure, *i.e.* the diffracting domains are uniformly small and, therefore, the crystal is diffracting in the kinematic limit. This is in contrast to a 'perfect' crystal, which would diffract in accordance with dynamical scattering theory. Note that equations (3.1.5) and (3.1.6) both have the $\cos^2 2\theta_m$ multiplier operating on the $\cos^2 2\theta$ term. Since this multiplier is less than unity, the intensity change on machines equipped with a monochromator exhibits a weaker angular dependence.

The certification data for SRM 1976b were collected with the NIST machine equipped with the Johansson IBM and a scintillation detector. The simplified IPF of this machine is advantageous for the accurate fitting of the profiles and, therefore, intensity measurement. The validity of the 'ideal mosaic' assumption embodied in equation (3.1.5) was evaluated using this diffractometer; the validity of equation (3.1.6) was evaluated with data from the machine configured with the post-monochromator. With respect to equation (3.1.5), for a Ge crystal (111) reflection, $2\theta_m$ was set to 27.3°; with regard to equation (3.1.6), for a pyrolytic graphite crystal (0002) basal-plane reflection, $2\theta_m$ was set to 26.6°. Rietveld analyses of data from SRMs 660b, 1976b and 676a included a refinement of the polarization factor, modelled according to equations (3.1.5) and (3.1.6) in *TOPAS*, and yielded fits of high quality, indicating that these models were appropriate for these crystals and configurations. Equations (3.1.4), (3.1.5) and (3.1.6) were used to bias the certified values to correspond to those of alternative configurations. These values are included in the SRM 1976b CoA as ancillary data.

3.1.6. Instrument calibration

The calibration procedure has traditionally involved the comparison of measurements from a reference (an SRM) with those of the test instrument. However, the exact form of this comparison depends upon the data-analysis procedure to be used. A classical calibration, permitting qualitative analyses and lattice-parameter refinement, can be readily performed as per Fig. 3.1.26. These data are fitted with a polynomial that describes the 2θ error correction that is then applied to subsequent unknown samples. Furthermore, with this calibration method, the actual form of the curve of Fig. 3.1.26 is largely irrelevant. As the data-analysis methods become more advanced, physical models are chosen to replace analytical PSFs. The calibration is then based upon the observation that the machine performance does indeed correspond to the models used, and that acceptable values for refined parameters describing the experiment are obtained from an analysis of data from an SRM. A systematic approach to instrument calibration with a full evaluation of the data, including those obtained from the empirical methods shown in Figs. 3.1.26 and 3.1.27, results in the ability to use the advanced methods in a rational manner and obtain results in which one can have confidence. The advanced methods, while more complex to use and requiring a much more extensive instrument calibration process, reward the user with a sample characterization of greater breadth and reduced measurement uncertainty.

Consider the $\Delta(2\theta)$ curve illustrated in Fig. 3.1.26. The *y*-axis values are the differences between the peak positions computed from the certified lattice parameter of SRM 660b and those of each observed profile determined *via* a second-derivative-based peak-location algorithm. Therefore, each of the $\Delta(2\theta)$ data points plotted on Fig. 3.1.26 were determined independently. It is immediately apparent that the data follow a smooth, monotonic curve with no substantive outliers. Discontinuities or non-monotonicity would typically indicate mechanical difficulties with the equipment, such as loose components or problems with the goniometer assembly. Evaluation of independently determined data such as these is critical to verifying that there are no 'high-frequency' difficulties with the equipment that would otherwise be hidden or smoothed out with the use of methods that apply models or constraints across the entire 2θ range, such as a Rietveld analysis. The $\Delta(2\theta)$ values were fitted with a third-order polynomial that is also illustrated in Fig. 3.1.26. Consideration of the deviation values between the observations and the third-order fit indicates a random or 'top hat' distribution with a maximum excursion of $\pm 0.0025°$ 2θ; this provides further evidence that a machine is operating properly.

FPAPC was used to generate simulated data, which were then analysed using the same second-derivative algorithm as was applied to the raw data. The aforementioned optical setup of the NIST instrument was used in the as-configured simulation (see the caption for Fig. 3.1.26), while the high-resolution and low-resolution data were simulated with a 50% increase or decrease of the incident and Soller slit angles. For the 'high-resolution' and 'low-resolution' data, third-order polynomial fits to the $\Delta(2\theta)$ values are displayed in Fig. 3.1.26; for the 'as-configured' data, the Δ values themselves are indicated. The correspondence between the simulation and observation indicates that trends in the data can be readily explained in the context of the aberration functions discussed in Section 3.1.l and that such a machine can

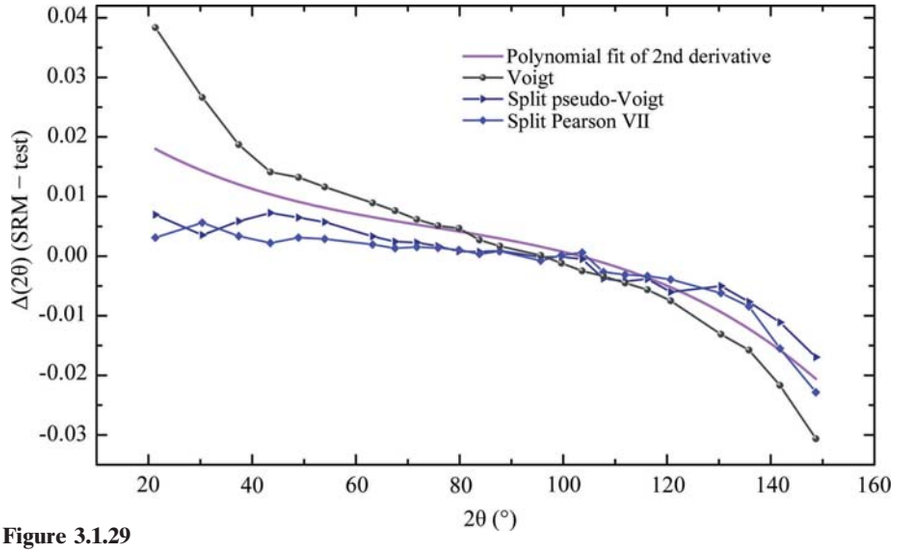

Figure 3.1.29
Comparison of $\Delta(2\theta)$ curves determined with profile fitting of SRM 660b data without the use of any constraints, as a function of 2θ.

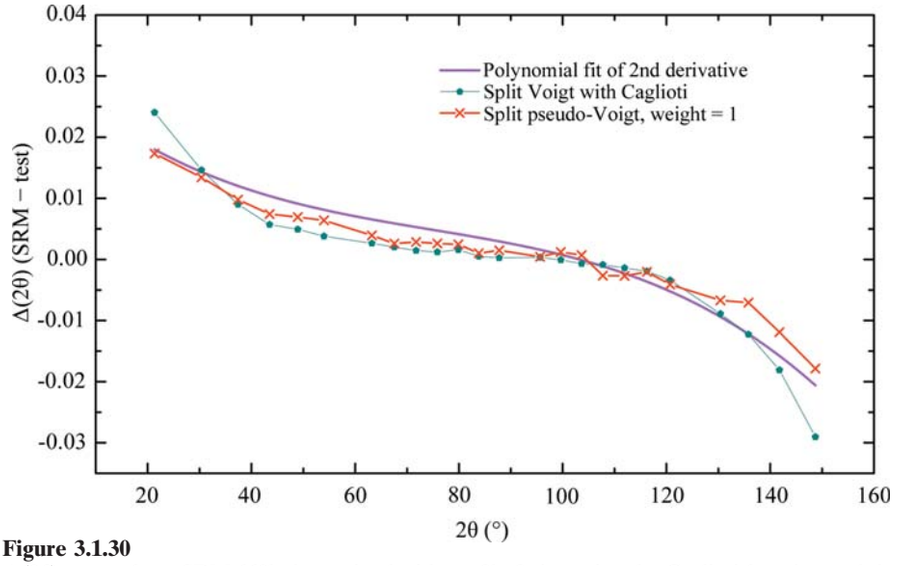

Figure 3.1.30
$\Delta(2\theta)$ curves from SRM 660b determined with profile fitting using the Caglioti function and the unconstrained split pseudo-Voigt PSF with uniform weighting.

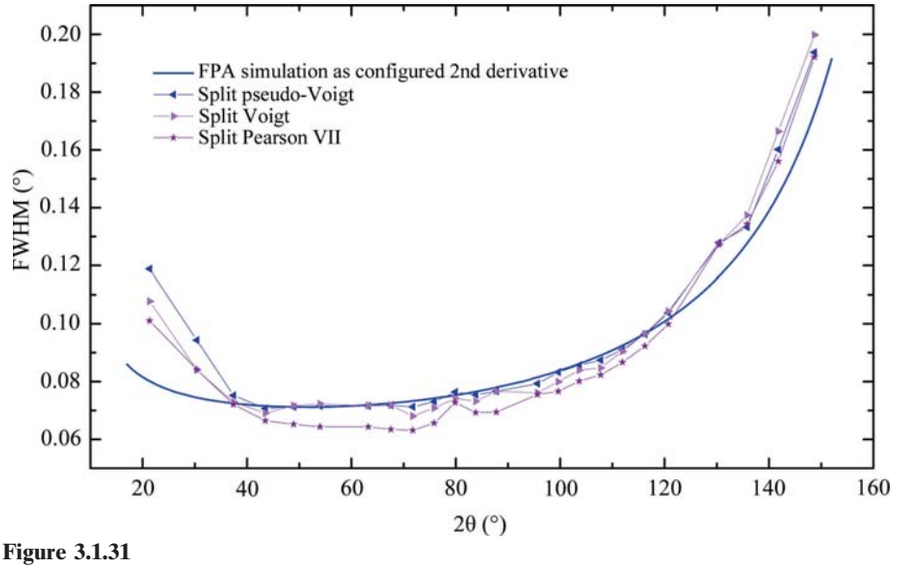

Figure 3.1.31
FWHM data from SRM 660b using various split PSFs fitted without constraints.

generate data for successful analysis with the FPA method, *i.e.* the metrological loop is closed. At low 2θ the profiles are displaced to low angle by the effects of the flat specimen error and axial divergence. The $\Delta(2\theta)$ curve crosses the zero point at approximately 100° 2θ where the profiles are largely symmetric; the slight asymmetry to low angle caused by the flat specimen error is somewhat offset by asymmetry of the emission spectrum at high angles. At higher 2θ the profiles are displaced to high angle by the combined effects of axial divergence and the asymmetry of the emission spectrum. As illustrated with the simulations at lower and higher resolution, the experimental curve of Fig. 3.1.26 would either flatten out or become steeper, respectively, with changes in instrument resolution. Given the uniformity of the data and overall plausibility of this $\Delta(2\theta)$ curve, the third-order polynomial fit is used as a reference against which the merits of other techniques can be judged.

It should also be noted that the data and method shown Fig. 3.1.26 constitute the 'low-hanging fruit' of powder diffraction. Data analogous to those of Fig. 3.1.26 can be used to correct peak positions of unknowns *via* either the internal- or external-standard method using a polynomial fit. The external-standard method, however, cannot account for specimen displacement or sample-transparency effects; these require use of the internal-standard method, which is the same procedure but applied to a standard admixed with the unknown. Either of these methods will correct for instrumental aberrations regardless of their form; the nature of the curve of Fig. 3.1.26 need only be continuous to permit modelling with a low-order polynomial. Studies performed in conjunction with the International Centre for Diffraction Data (ICDD) demonstrate that the use of the internal-standard method routinely yields results that are accurate to parts in 10^4 (Edmonds *et al.*, 1986). Fawcett *et al.* (2004) demonstrated the direct relationship between the use of standards, with the vast majority of analyses being performed *via* the internal- or external-standard methods, and the number of high-quality starred patterns in the ICDD database. Thus, the community's collective ability to perform the most routine of XRPD analyses, qualitative analysis, has been greatly enhanced over the past 30 or so years by these most basic methods and the use of SRMs.

The $\Delta(2\theta)$ and FWHM calibration curves shown in Figs. 3.1.27–3.1.31 were determined *via* profile fitting, using several PSFs,

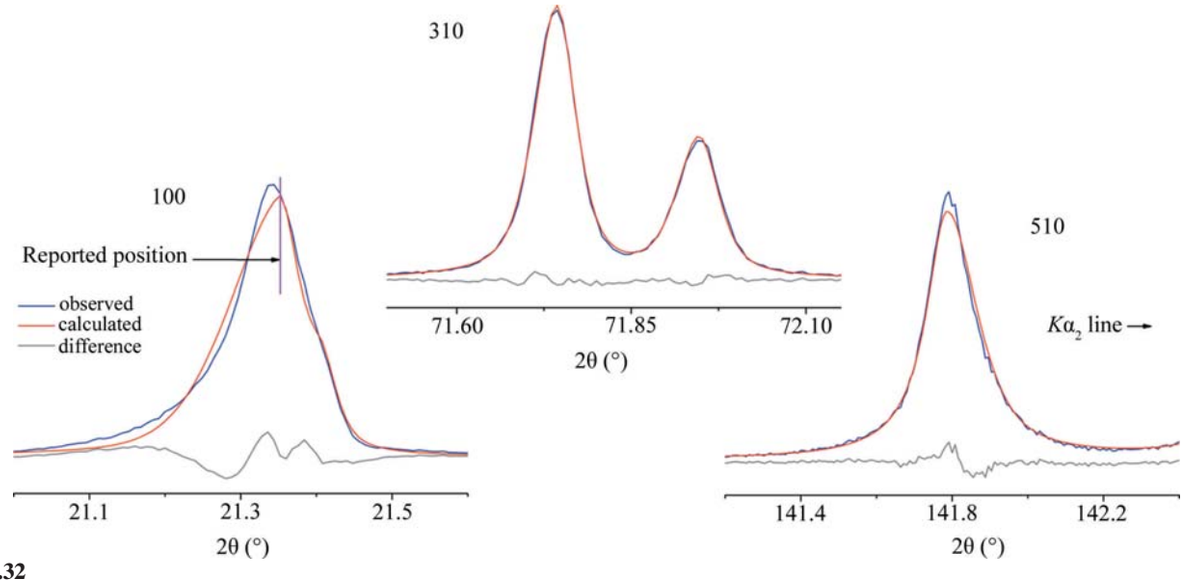

Figure 3.1.32
Fits of the split pseudo-Voigt PSF to the low-angle 100, mid-angle 310 and high-angle 510 lines from SRM 660b illustrating the erroneous peak position and FWHM value reported for the 100 and 510 lines, respectively.

of the same raw data from SRM 660b used to generate Fig. 3.1.26. In general, results from the three commercial codes were in close correspondence. When used on a split PSF, the Caglioti function was applied independently to the left and right FWHM values. A five- to seven-term Chebyshev polynomial was used for modelling the background in these refinements. The goodness of fit (GoF) (which is the square root of reduced χ^2) residual error term of the refinements ranged from 1.6 to 1.9, with the unconstrained refinements yielding the slightly improved fits to the data. Fig. 3.1.32 illustrates the fit quality of typical results using the split pseudo-Voigt PSF. However, as will be demonstrated, the more plausible parameters, particularly in the context of the FWHM values, were often obtained with the more constrained refinements.

The results from the fitting of the Voigt PSF provide a reference for consideration of the $\Delta(2\theta)$ data of Fig. 3.1.29. The use of any of the symmetric PSFs considered here, with or without the Caglioti constraint, resulted in curves virtually identical to the one displayed in Fig. 3.1.29 for the Voigt PSF. Not surprisingly, the symmetric PSF performs quite well in the mid-angle region where the profiles are symmetric but will report an erroneous position in the direction of the asymmetry, when it is present. However, the opposite effect was observed with the use of any of the split PSFs, as can be seen in Figs. 3.1.29 and 3.1.32. When two HWHM values are refined, the larger HWHM value will shift the reported peak position in the direction of the smaller one. This effect can be readily observed in the fit quality of the low-angle 100 reflection displayed in Fig. 3.1.32. The spilt PSFs yield results that reflect an overly asymmetric profile; thus the reported peak positions are displaced to high angle at 2θ angles below 100°, and to low angle at 2θ angles above 100°. Curiously this effect was markedly reduced in one of the commercial computer codes (not shown) and was the sole difference observed between them when the models were equivalent. It is apparent that subtleties in implementation of an ostensibly identical PSF and minimization algorithm (the Marquardt algorithm) can result in dramatic differences in results. Careful examination of the fit quality is required to assess the reliability of profile-fitting results. The data of Fig. 3.1.29 indicate that errors in peak position of up to 0.015° 2θ are plausible with profile fitting of these data with these PSFs. In contrast to its use with symmetric PSFs, the Caglioti function will improve results when using split PSFs (Fig. 3.1.30).

Consideration of the issues related to profile fitting shown in Fig. 3.1.32 led to the conjecture that fitting the data with a uniform weighting as opposed to Poisson statistical weighting might result in more accurate determination of the peak position and FWHM parameters. (In the vast majority of circumstances this approach would never be used, because the integrated intensity is a critical metric.) This was tried, and resulted in considerable success. Fig. 3.1.30 displays data from the use of split pseudo-Voigt that are in very good agreement with second-derivative values.

Experimental and simulated values of the FWHM are displayed in Figs. 3.1.27 and 3.1.31. Data from the profile refinements performed without the use of the Caglioti function, displayed in Figs. 3.1.27 and 3.1.31, yield independently determined measures of the FWHM. Again, the lack of scatter and the continuity of these FWHM values are consistent with proper operation of the instrument, *i.e.* an absence of 'high-frequency' problems. The basic trends are also consistent with the instrument optics: at low 2θ the observed increase in FWHM is due to both the flat specimen and axial divergence aberrations, while at high 2θ angular dispersion dominates and a substantial increase in FWHM with $\tan\theta$ is apparent. The FPA simulations were performed using the settings for high and low resolution. The FWHM values were determined numerically from the simulated patterns; no PSF was used. As shown with the simulated data, the degree of upturn at low 2θ increases with a decrease in instrument resolution and *vice versa*. Angular-dispersion effects, however, are less dependent on the instrument configuration; FWHM values tend towards convergence at high 2θ (Fig. 3.1.27).

As seen in Fig. 3.1.27, above 40° 2θ the Voigt and split-Voigt PSFs give similar values for the FWHM and a fairly accurate representation of instrument performance. It was observed that with regard to the correlation between FWHM values for split *versus* symmetric PSFs, the other PSFs behaved in an analogous manner to the Voigt (not shown): above 40° 2θ the values reported for the FWHM from split *versus* symmetric PSFs are nearly identical. From Fig. 3.1.31, the split Pearson VII PSF underestimates the FWHM throughout the mid-angle region; this error was duplicated with the use of the symmetric Pearson VII

PSF (not shown). When fitted with uniform weighting, however, these FWHM data from the Pearson VII PSF fell quite precisely (not shown) on the simulated curve. Below 40° 2θ, a split PSF will provide results that overestimate true FWHM values, as shown in Figs. 3.1.27 and 3.1.31. The cause for this is analogous to that discussed for the $\Delta(2\theta)$ values, and can be readily observed in the fit quality displayed in Fig. 3.1.32 for the low-angle 100 reflection. In accounting for the asymmetry to low angle, the FWHM of the observed profile is substantially overestimated by the calculated one. With all PSFs, the high-angle FWHM values are observed to be overestimated, as shown in Figs. 3.1.27 and 3.1.31; the problem is exacerbated with the use of the Caglioti function. Inspection of the fit quality of the high-angle 510 line shown in Fig. 3.1.32 indicates that there are two contributions to this effect: one is that the PSF cannot model the shape of the high side of the profile; the other is that the height of the profile is underestimated. These two effects, particularly the inability of the PSF to correctly model the height of the profile, were observed with all of the other PSFs considered here.

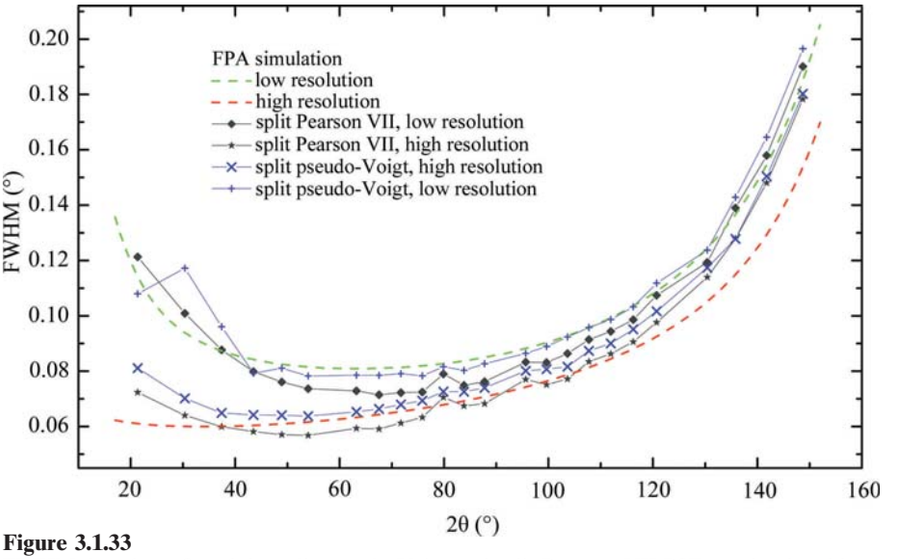

Figure 3.1.33
FWHM data from fits of the split pseudo-Voigt and split Pearson VII PSFs to simulated low- and high-resolution data.

The use of the pseudo-Voigt PSF with the Caglioti function results in a reasonable fit to the FWHM values of the observation; however, the breadth of the high-angle lines is overestimated. The *U*, *V* and *W* terms of the Caglioti function vary in a specific manner to account for various physical effects (*e.g.* see Fig. 3.1.27): the *U* term, in tan θ, accounts for angular dispersion; the *W* term describes the 'floor' and the *V* term accounts for the reduction of the FWHM values in the mid-2θ region. Therefore, the *U* and *W* terms should refine to positive values, while the *V* term should tend to a negative value; negative values for *V* were, indeed, obtained in these analyses. *V* should be constrained to negative values or set to zero, as positive values for *V* are non-physical. With an instrument configured for high resolution, however, values of $V = 0$ are entirely reasonable as the trend towards an upturn in FWHM at low 2θ angle will be suppressed.

To some extent, the difficulties in determining profile positions through the use of these PSFs can be ascribed to the Cu $K\alpha_1/K\alpha_2$ doublet as it is stretched by angular dispersion. The pattern can be thought of as divided into three regions, each of which will confound fitting procedures in a different manner: the low-2θ range, where profiles can be considered as a peak with a shoulder, the mid-2θ range (perhaps 40 to 110° 2θ), where the profiles can be considered as a doublet, and the high-angle region where they are two distinct peaks. This 'three-region' consideration is compounded by the direction and severity of the asymmetry in these profiles. The data shown in Fig. 3.1.27 largely correspond to the problematic effects of angular dispersion in the context of these three 2θ regions. These effects are particularly apparent, as shown in Fig. 3.1.31, with the use of the Pearson VII function: over-estimation of FWHM values occurs at low 2θ, underestimation occurs in the mid-2θ region, and credible values are obtained at high angle. The use of the Caglioti function is effective in addressing the more extreme excursions from plausible FWHM values. Fig. 3.1.28 shows the left and right HWHM values for SRM 660b using the split pseudo-Voigt PSF refined with uniform weighting. For reasons discussed in Section 3.1.2, the degree, direction and point of crossover in the profile asymmetry indicated in Fig. 3.1.28 are in correspondence with expectation and the previously discussed results from these data from SRM 660b.

To consider the impact of instrument resolution on the use of analytical PSFs for the determination of FWHM values, the simulated high-resolution and low-resolution data were analysed *via* profile fitting. Fig. 3.1.33 shows the results from the use of the split Pearson VII and spilt pseudo-Voigt PSFs. The data of Fig. 3.1.33 indicate an effect that is dependent on the PSF used. The performance of the split Pearson VII PSF is observed to improve with instrument resolution; FWHM values from the narrower profiles are observed to correspond with expectation in the low- and mid-angle regions, while substantial deviation is noted with the broader profiles. This is counter to expectation, as broader profiles are generally easier to fit than narrow ones. The performance of the split pseudo-Voigt PSF is observed to degrade marginally with either an increase or decrease in instrument resolution. Curiously, the breadths of the profiles in the high-resolution data are overestimated, while those in low-resolution data are largely underestimated. Both PSFs do quite poorly in fitting the high-angle data from the high-resolution setting. These observations emphasize the need to scrutinize the results with an examination of the fit quality, as per Fig. 3.1.32.

When the IPF is simplified with the use of a Johansson IBM, analytical PSFs can provide an excellent fit to the observations. Fig. 3.1.34 shows the fit quality of the split Pearson VII PSF to (high-quality) peak-scan data. The split Pearson VII PSF consistently provides a better fit to IBM data than either the split Voigt or split pseudo-Voigt PSFs. Note that the asymmetry exhibited by the profiles follows the same trends as were outlined previously, but to a much reduced extent because of the extended incident-beam path length and the resulting reduction in the effects of axial divergence. Fig. 3.1.35 shows the $\Delta(2\theta)$ calibration curves that were obtained as per the procedures outlined for Fig. 3.1.29. Indeed, the trends that are followed, and the reasons why, are largely analogous to those of Fig. 3.1.29, but to a much reduced extent because of the reduced profile asymmetry. Use of symmetric PSFs yields reported peak positions that are shifted in the direction of the asymmetry, while use of split PSFs yields positions shifted in the opposite direction owing to the fitted profiles displaying excessive levels of asymmetry. One notes the complete failure of the split pseudo-Voigt, split Voigt (not shown)

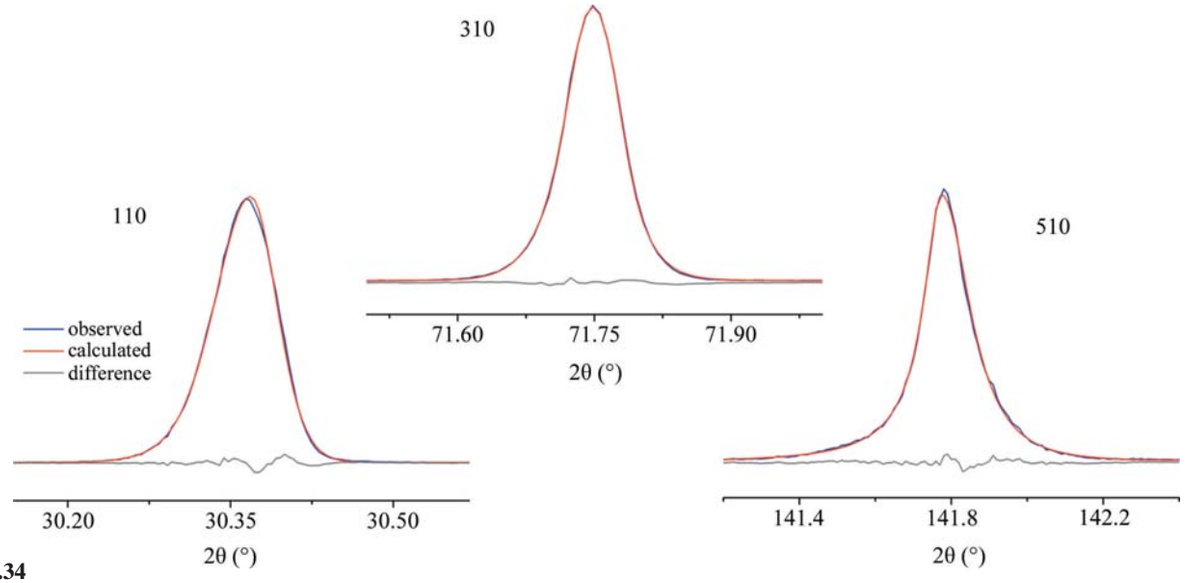

Figure 3.1.34
Fits of a split Pearson VII PSF to data from SRM 660b collected using a Johansson IBM.

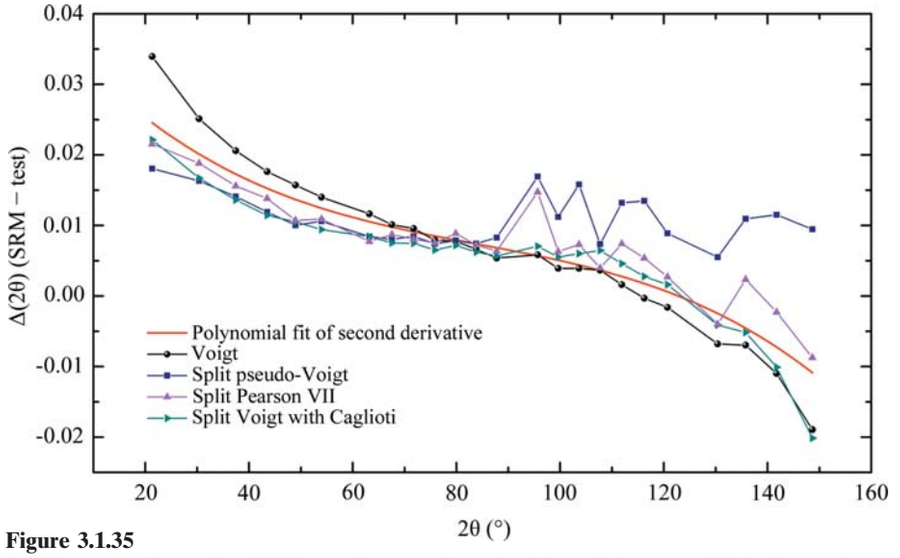

Figure 3.1.35
$\Delta(2\theta)$ curves from the NIST machine configured with a Johansson IBM, illustrating a comparison of results from second-derivative and various profile-fitting methods. Data are from SRM 660b.

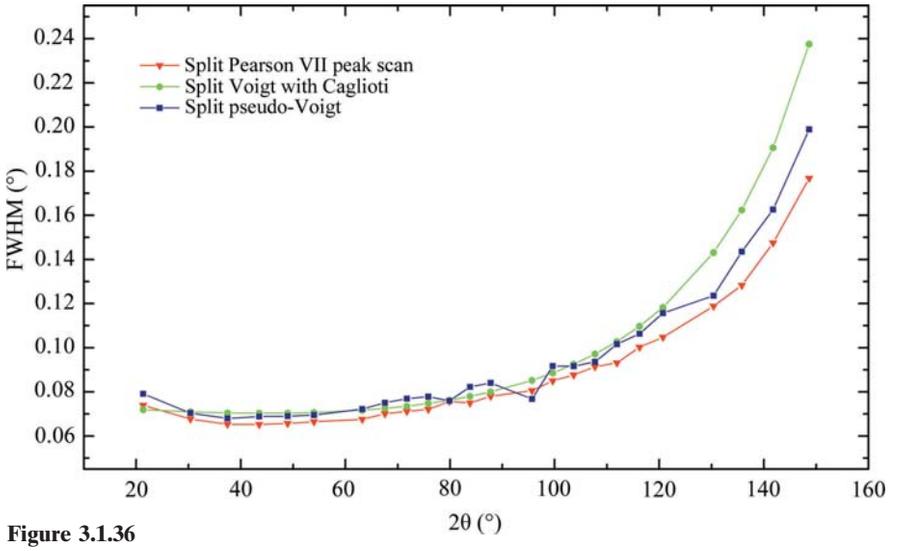

Figure 3.1.36
FWHM data from SRM 660b collected using the NIST machine configured with a Johansson IBM, illustrating a comparison of results from various profile-fitting and data-collection methods.

and, to a lesser extent, the split Pearson VII PSFs at high angle. However, the more accurate peak positions are obtained from the more intense reflections, indicating that higher-quality data may improve the results. Improvements in FWHM determination with the use of an IBM are illustrated in Fig. 3.1.36, where it can be seen that the pseudo-Voigt and Pearson VII yield values for the FWHM that differ in a systematic manner, but to a reduced extent than with the conventional data. The virtues of the peak-scan data are illustrated by the continuity of the FWHM values of Fig. 3.1.36 relative to the discontinuities observed in the corresponding data from the conventional scans that were fitted with the pseudo-Voigt PSF. The results from the use of the Caglioti function in Fig. 3.1.36 illustrate that otherwise noisy FWHM data are effectively smoothed out, but a significant bias at high angle is indicated.

FWHM values from the machine equipped with the IBM and PSD are shown Fig. 3.1.37, again with data from SRM 660b. These values were obtained from fits of the split Pearson VII PSF using uniform weighting. The resolution improvement from the use of the PSD is due to the 75 μm strip width, as opposed to the 200 μm receiving slit used with the scintillation detector. This is analogous to a reduction in the width of the top-hat function used to model the impact of the receiving slit or silicon strip width as discussed in Section 3.1.2. The impact is greatest at low 2θ angles where the other contributions to the overall breadth are small. With increasing 2θ angle, the contribution of a top-hat function to overall breadth is reduced because it is being convoluted with profiles influenced by ever-increasing spectral dispersion. The improve-

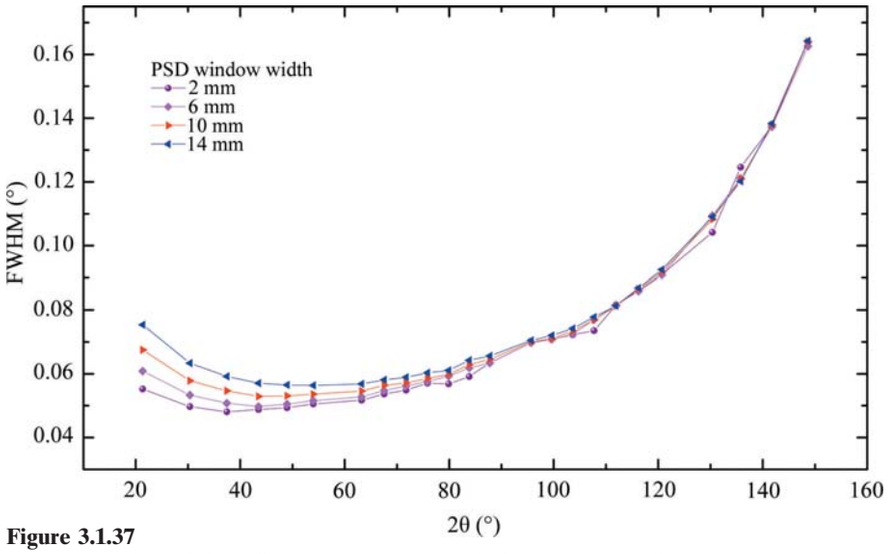

Figure 3.1.37
FWHM data from SRM 660b collected using the NIST machine configured with a Johansson IBM and PSD, illustrating the contribution to defocusing at low angles with increasing window width.

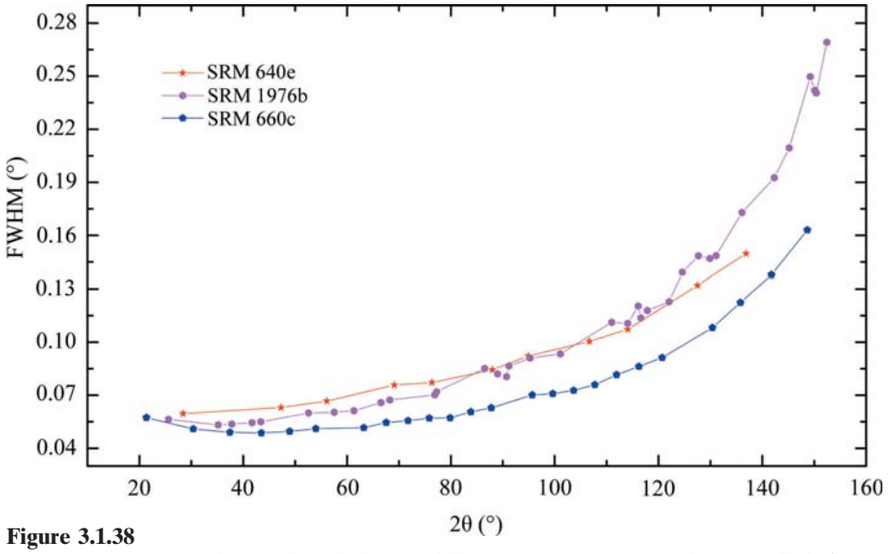

Figure 3.1.38
FWHM data from SRMs 640e, 1976b and 660c collected with the IBM and PSD (4 mm window) and fitted using the split Pearson VII PSF with uniform weighting.

ment in resolution with the reduction in the width of the PSD window is apparent, and is in accordance with expectations as per Fig. 3.1.7 of Section 3.1.2. Also, because of the $1/\tan\theta$ dependence of this broadening effect, the impact of the window size nearly vanishes above 100° 2θ.

Fig. 3.1.38 shows FWHM data obtained for SRMs 640e, 1976b and 660c using the split Pearson VII PSF, fitted using uniform weighting on data collected with the IBM and PSD with a 4 mm window. The 660c data set, which exhibits the lowest FWHM values, will be discussed first. The FPA analysis performed in the certifications of SRM 660b and 660c included a Lorentzian FWHM with a $1/\cos\theta$ dependence to account for size-induced broadening; a domain size of approximately 0.7 to 0.8 μm was indicated. There is a high level of uncertainty in these values, as they are reflective of an exceedingly small degree of broadening, the detection of which is near the resolution limit of the equipment. The term varying as $\tan\theta$, interpreted as microstrain, refined to zero. These values are found in the CoA for the SRMs. The linear attenuation coefficient for a compact of LaB_6, with an intrinsic linear attenuation of 1125 cm^{-1} and a particle-packing factor of 60 to 70%, would be approximately 800 cm^{-1}. Therefore, the contribution to the observed FWHM from specimen transparency with SRM 660c is negligible, as illustrated in Fig. 3.1.10. Likewise, the FPA analysis performed for the certification of SRM 640e included size and microstrain terms; a smaller crystallite size of 0.6 μm was obtained with a very slight amount of microstrain broadening. However, the linear attenuation coefficient for silicon is 148 cm^{-1}; for a powder compact it would be approximately 100 cm^{-1}. The transparency of this specimen would lead to significant broadening. (See Fig. 3.1.10 for the effect of an attenuation of 100 cm^{-1}.) Therefore, these three effects, in combination, would be expected to lead to a small degree of broadening throughout the 2θ range for SRM 640e, but with a substantial effect in the mid-angle region because of the $\sin 2\theta$ dependence of the transparency aberration. Lastly, SRM 1976b is a sintered compact of near theoretical density; therefore, considering the linear attenuation coefficient for alumina, 126 cm^{-1}, a value for the actual SRM 1976b specimen of somewhat less than this is expected. An FPA analysis of SRM 1976b indicates a domain size of 1 μm, but with a significant degree of Gaussian microstrain broadening; this is evident in the observed increase in FWHM with 2θ angle shown in Fig. 3.1.38. We conclude that the FWHM data from all three SRMs shown in Fig. 3.1.38 are in correspondence with expectations and can be used to select which SRM is best suited for a given application. We do not, however, recommend using an SRM other than SRM 660*x* for a microstructure analysis. It should be added that fitting the profiles of SRM 1976b is complicated by the fact that many of them overlap; this leads to the oscillations in the FWHM values shown in Fig. 3.1.38 for this SRM. The origins of this difficulty were discussed in Section 3.1.5 and can be addressed with the use of the Caglioti function.

With the use of model-based methods for calibration and subsequent data analysis, it is appropriate to consider a strategy for the refinement of the available parameters. The successful refinement will yield the right answer and, with the use of models that make sound physical sense with respect to the experimental design, a good fit to the observation. The refinement strategies for both FPA and Rietveld analyses can be based on a consideration of which terms are specific to the IPF and the manner in which they can be determined. Several parameters can be measured explicitly from experiments other than the diffraction experiment under examination. Examples of these 'well determined' parameters include the goniometer zero angles and the incident- and receiving-slit sizes. Conversely, indeterminate metrics that can only be determined through the diffraction experiment itself include the impact of the post-monochromator on the Cu $K\alpha_1/K\alpha_2$ ratio and the degree of axial divergence. Indeterminate parameters specific to the IPF are only refined using high-quality data from standards and are fixed for subse-

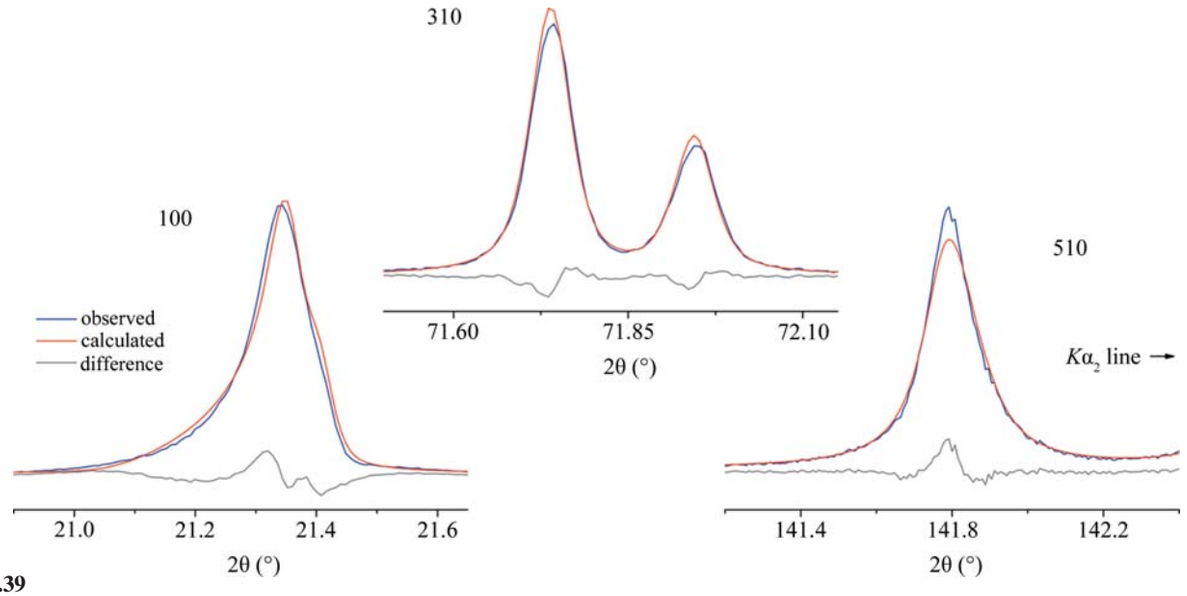

Figure 3.1.39
Fits of three SRM 660b lines obtained with a Rietveld analysis using the Thompson, Cox and Hastings formalism of the pseudo-Voigt PSF and the Finger model for asymmetry. *TOPAS* was used for the analysis.

quent analyses of unknowns. This approach tends to result in stable and robust refinements. Parameters can, therefore, be considered as falling into three groups: those that are specific to any given sample and are always refined, ones that are specific to the IPF and are refined using only high-quality data from standards, and lastly the highly determined parameters that are refined only as a basic test of the model.

To consider the Thompson, Cox & Hastings (1987) (TCH) formalism of the pseudo-Voigt PSF with the Finger model for asymmetry, which is common to many Rietveld codes, a Rietveld analysis of SRM 660b was performed using *GSAS* (using the type-3 PSF) and *TOPAS* (using the PV_TCHZ peak type). The TCH formalism allows for the direct refinement of the Gaussian and Lorentzian FWHM values. The Caglioti function was used; Lorentzian terms were constrained as per equation (3.1.2). The *S*/*L* and *H*/*L* terms are highly correlated; *S*/*L* was refined, while *H*/*L* was adjusted manually so that the two terms were nearly equal. Additional parameters that were refined included the lattice parameters, sample displacement and transparency terms, Chebyshev polynomial terms (typically 5 to 7) to represent the background, scale factors, the type-0 Lorentz–polarization term (*GSAS*), the Cu $K\alpha_1/K\alpha_2$ ratio, and structural parameters. With this strategy, the sample shift and transparency aberration functions, in conjunction with the Finger asymmetry model, were used to model the data of Fig. 3.1.26. Given that the Finger model is not entirely appropriate for divergent-beam laboratory data, the sample shift and transparency terms may refine to non-physical values. They will, however, correctly indicate relative values for sample *z* height and transparency. The model for specimen transparency in *TOPAS* is the asymmetric function illustrated in Fig. 3.1.10, while the model in *GSAS* consists of a profile displacement in $\sin 2\theta$. The TCH/Finger formalism of *TOPAS* reproduced the certified lattice parameter and resulted in a GoF of 1.5, whereas the GoF value realized with *GSAS* was 1.85. Fig. 3.1.39 displays the fit quality of the 100, 310 and 510 reflections obtained with *TOPAS*. The fit to the asymmetry of the 100 reflection is reasonable, with a 0.007° shift in position. The fit to the 510 reflection is not dissimilar to that shown in Fig. 3.1.32, indicating that the Caglioti function is working analogously to the manner previously discussed. The improvement in fit with the *TOPAS* implementation was most notable around the 70 to 90° 2θ region, where the transparency effects are at a maximum. These results validate the TCH/Finger formalism and constitute a valid calibration for this equipment and data-analysis method; the utility of the aberration function for specimen transparency as documented by Cheary & Coelho (1992) is demonstrated.

Differentiating between the profile-shape terms that are specific to the IPF and those refined to consider the microstructure of unknowns yields a stable refinement strategy when using the TCH/Finger formalism. The profile parameters *GU*, *GV*, *GW*, *LX*, *LY*, *S*/*L* and *H*/*L* as determined from SRM 660b constitute the IPF and are fixed, or used as floors, in subsequent refinements (Cline, 2000). The IPF for the NIST machine was described with only the *GW*, *LX* and *LY* parameters. In subsequent analyses only the *GP*, *GU*, *LX* and *LY* terms were refined to represent Gaussian size and microstrain and Lorentzian size and microstrain broadening, respectively, and thus yield microstructural information from the sample. Parameters that tend to values less than the IPF were fixed at IPF values. The Finger asymmetry parameters determined from the standard need not be refined with unknowns; it has, however, been observed that doing so will neither substantially improve the quality of the fit, nor will it result in instability. Additional parameters that are always refined with unknowns include: scale factors, lattice parameters, specimen displacement and transparency terms, background terms, and structural parameters.

While an analysis of SRM 660*x* permits the calibration of the instrument with respect to profile shape and position, it is also desirable to evaluate parameters related to the diffraction intensity. However, the analysis of data from high-symmetry materials such as silicon and lanthanum hexaboride may result in some degree of instability with the refinement of the intensity-specific parameters, perhaps because of the relatively small number of lines. Use of SRM 676a addresses this difficulty (Fig. 3.1.40). With this analysis, the Lorentz–polarization factor refined to a credible value and structure parameters were within the bounds of those obtained from the high-*q*-range experiments performed in the certification of SRM 676a (Cline *et al.*, 2011).

We start the discussion on the FPA method for instrument calibration by listing the parameters specific to the IPF that

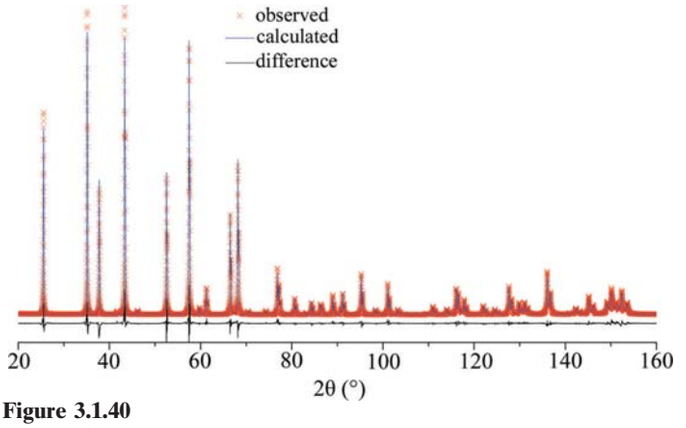

Figure 3.1.40
Fits of SRM 676a obtained from a Rietveld analysis using *GSAS* with the Thompson, Cox and Hastings formalism of the pseudo-Voigt PSF and the Finger model for asymmetry.

would have to be refined with a most basic calibration using an analysis of an SRM. The parameters to be refined for the emission spectrum include the positions and intensities of the $K\alpha_2$ profile, the satellite components and the tube tails. When addressing the $K\alpha_2$ profile, the relative positions and intensity ratios of the $K\alpha_{21}$ and $K\alpha_{22}$ Lorentzian profiles were constrained so as to preserve the overall shape as characterized by Hölzer *et al.* (1997). For the geometric profile, a single Soller-slit angle was refined, characterizing the degree of axial divergence and using the case-2 axial-divergence model applied to both the incident and diffracted beams. Other parameters of the geometric profile were fixed at known values. Additional parameters included a Lorentzian size-broadening term, background terms, and profile intensities and positions. A Gaussian microstrain term was included for analyses of SRM 1976b. Fig. 3.1.41 shows the quality of the fits obtained from an FPA analysis of SRM 660b. These fits present a substantial improvement over those using any of the analytical PSFs (Figs. 3.1.32 and 3.1.39). Furthermore, the GoF residual error term for an FPA profile analysis of a continuous scan of SRM 660b was 1.08, while the corresponding terms from analyses of the same data using the split pseudo-Voigt and split Pearson VII PSFs were 1.65 and 1.43, respectively (these three analyses were all from *TOPAS*). The FPA method can account for subtleties in the observed X-ray line profiles that analytical PSFs could never be expected to fit. In subsequent analyses of unknowns, it is not imprudent to fix parameters associated with the IPF; refining them, however, is typically not problematic with the FPA.

There were indications that the breadths of the profiles of the Cu $K\alpha$ emission spectrum as characterized by Hölzer *et al.* (1997) were in excess of those of our observations. This was investigated using the ultra-high-quality data. The FWHM ratios of the two pairs of Lorentzian profiles, the $K\alpha_{11}$ *versus* the $K\alpha_{12}$ and the $K\alpha_{21}$ *versus* the $K\alpha_{22}$, were constrained to those reported by Hölzer *et al.* (1997). The positions and intensities of the $K\alpha_2$ doublet were also refined, again with constraints applied to preserve the shape as per Hölzer *et al.* (1997). These refinements indicated that the breadths given by Hölzer *et al.* (1997) were significantly in excess of those that gave the best fit to the data. After an extensive investigation, this observation was confirmed to originate with the performance of the post-monochromator. Several graphite monochromator crystals were investigated using a beam diffracted from an Si single crystal (333 reflection) mounted in the specimen position. The graphite crystals that were manufactured within the last 15 years all gave identical results: after an alignment procedure to optimize the intensity of the $K\alpha_1$ line, they do clip the breadths of the profiles of the emission spectrum by approximately 20%. They also alter the position of diffraction lines by perhaps 0.01° in 2θ; therefore, the goniometer zero angles must be determined with the monochromator installed. We therefore used a reduced-breadth Hölzer emission spectrum in our FPA analysis. Note that these breadths vary with $\tan\theta$ because of angular dispersion, as does microstrain; therefore, only a microstrain-free specimen can be used for an analysis of the impact of a monochromator on the emission spectrum. We found that both SRMs 660c and 640e were suitable for this analysis.

The refinement strategy for the case-2 Soller-slit angle was also investigated with the ultra-high-quality data. Technically, the axial divergence of the incident beam, with the inclusion of the Soller slit, is less than that of the diffracted beam, which is limited by its extended beam-path length through the monochromator. Several strategies were investigated, some of which may have represented a more accurate physical model than that of a single divergence value applied to both beams, but none resulted in any improvement in the fit quality. Lastly, it was observed that the

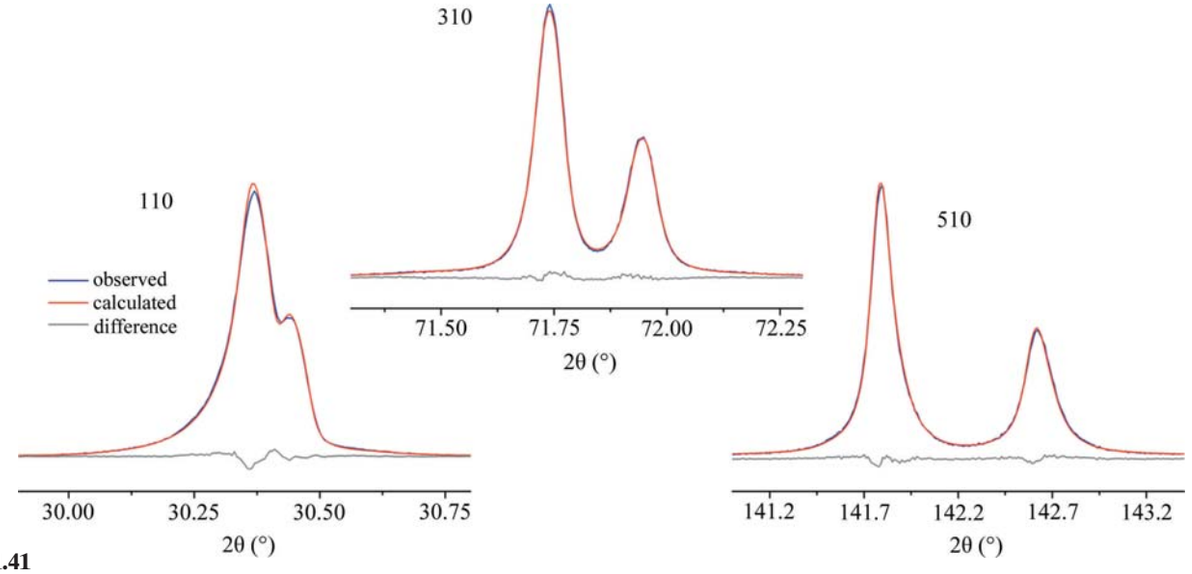

Figure 3.1.41
Fit quality realized with a fundamental-parameters-approach analysis of SRM 660b peak-scan data using *TOPAS*.

value for the width of the divergence slit, particularly with the use of the IBM, refined to values in excess of the known value. This observation will be discussed further.

With the certification of SRMs 640e, 660c and 1878b (respirable quartz, 2014), global refinements were set up allowing for the simultaneous analysis of the 20 high-quality data sets collected for the certification of each SRM. With this approach, the analyses could be carried out in the context of highly favourable Poisson counting statistics and permitted a robust analysis of FPA models that would otherwise be problematic because of parameter correlation. Data were collected from two samples from each bottle. With SRMs 640e and 660c, the machine was configured as per the work of this study with the post-monochromator; for 1878b, the machine was configured likewise with the IBM and scintillation detector. For SRM 660c the data were collected in accordance to the run-time parameters of Table 3.1.2, and in an analogous manner for SRM 640e. For SRM 1878b, the data were collected on mixtures of 50% SRM 1878b and 50% SRM 676a in continuous, 24 h scans. Concurrent with the effort to certify SRMs 640e and 660c, the agreement between the results from *FPAPC* and *TOPAS* was established, indicating that both codes operated in accordance with published FPA models (Mendenhall *et al.*, 2015). Initially with *FPAPC* and later with *TOPAS*, the data from these three SRMs were analysed using the global refinement strategy.

The global refinements were used to investigate possible difficulties with the FPA models. First, the global refinements were used to determine more robust values for the breadths of the emission spectrum as influenced by the post-monochromator. The issue concerning the refined value for the incident slit size was revisited with the global refinements. Values of 25% in excess of the known size were observed in refinements of IBM data from several materials using *TOPAS*. While these refinements were quite robust, corresponding analysis of ultra-high-quality post-monochromator data sets resulted in a slow increase in the slit value with little change in residual error terms, indicating a shallow χ^2 minimization surface. With the global analysis of the SRM 660c, 640e and 1878b data, however, the incident slit value refined to a value of 15 to 25% in excess of the known value in a robust manner. The reduced correlations between models with the global refinements led to this improved ability to reach the minimum in error space for both data types. An investigation into the sensitivity of the lattice-parameter value and GoF on the incident slit size was consistent with the shallow χ^2 minimization surface; changes in lattice parameters were less than 2 fm and only small changes in GoF were noted. The lowest-angle lines used in our analyses were at 18°; given the 1/tan θ dependence of the incident-slit correction, lower-angle lines are required for robust use of this model for refinement of incident-slit size. A second observation of concern was the low values for sample attenuation refined from data for SRM 660*x*. As previously stated, a reasonable value for a compact of LaB_6 would be 800 cm^{-1}, yet the fits were giving values in the 400 cm^{-1} range. Again, a sensitivity study indicated little dependence of either the lattice parameter or the GoF on the attenuation values when they are this large. In contrast, sensitivity studies on SRM 640*x* (silicon in the 80 to 100 cm^{-1} range) indicated a high level of response to changes in attenuation values. Again, in the range where the model is active, results are in correspondence with expectations; where there is little impact on the refinement, parameter values may differ from true values with little impact on the refinement as a whole. We are continuing to investigate the issue of the non-physical values obtained for the refined divergence-slit width.

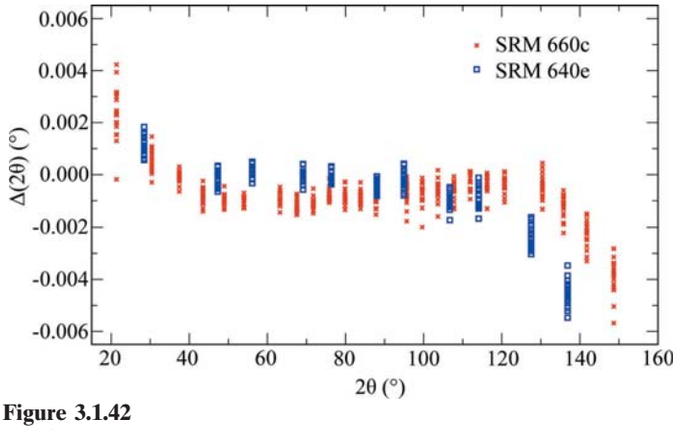

Figure 3.1.42
$\Delta(2\theta)$ data from the 20 data sets collected for the certification of SRMs 660c and 640e, determined *via* FPA analyses using *TOPAS*.

The $\Delta(2\theta)$ data shown in Fig. 3.1.42 illustrate results from an FPA analysis of the 20 data sets collected for the certification of SRMs 660c and 640e. The $\Delta(2\theta)$ values were generated using the certified lattice parameters of SRMs 660c and 640e to compute 'SRM' or reference peak positions, and the unconstrained profile positions from the FPA analysis were used as the 'test' data. The analyses were performed using *TOPAS* with the divergence-slit width fixed at the known value. The data in Fig. 3.1.42 clearly reflect the efficacy of the FPA method. The certification data for these SRMs were collected on the machine set up as for Fig. 3.1.26; the trends of the peak position for these data are identical to those of Fig. 3.1.26. Yet the FPA has corrected the profile positions to a degree indiscernible from the 'true' positions in the 40 to 120° 2θ region. The trends observed otherwise in these data are consistent with prior observations discussed at length above, albeit in 2θ regions limited to below 40° and above 120° and to a vastly reduced level. These deviations are consistent with shortcomings in the model, although the deviations are so small that it may be difficult to work out their origin. The unequivocal technical justification for use of the FPA in SRM certification is also apparent in Fig. 3.1.42; when properly used, the method is capable of reporting the 'true' *d*-spacing for profiles located in the 40 to 120° 2θ region.

Using SRM 1976b for calibration of the instrument response entails determining the integrated intensity of 14 profiles from the test instrument and comparing them with certified values. However, the test instrument in this case was the NIST instrument equipped with the graphite post-monochromator. Therefore, the relative intensity values used for comparison were the ones biased to account for the effects of polarization. They were obtained from Table 4 of the SRM 1976b CoA. Fig. 3.1.43 shows the results from various data-analysis techniques performed on a common raw data set from the test instrument. With the noteworthy exception of the split Pearson VII PSF, all methods gave an acceptable result. It can be seen that when intensity measurement is the issue, the use of unconstrained PSFs is more effective than the analyses described earlier, which were intended to determine the profile position or FWHM. With the use of *GSAS*, the pattern was fitted with a Rietveld analysis using a sixth-order spherical harmonic to model the texture. The reported relative intensity data are computed from the observed structure factors using the *GSAS* utility *REFLIST*. This approach is identical to that used for the certification of SRM 1976b, except the certification data were collected on the NIST instrument setup with the IBM.

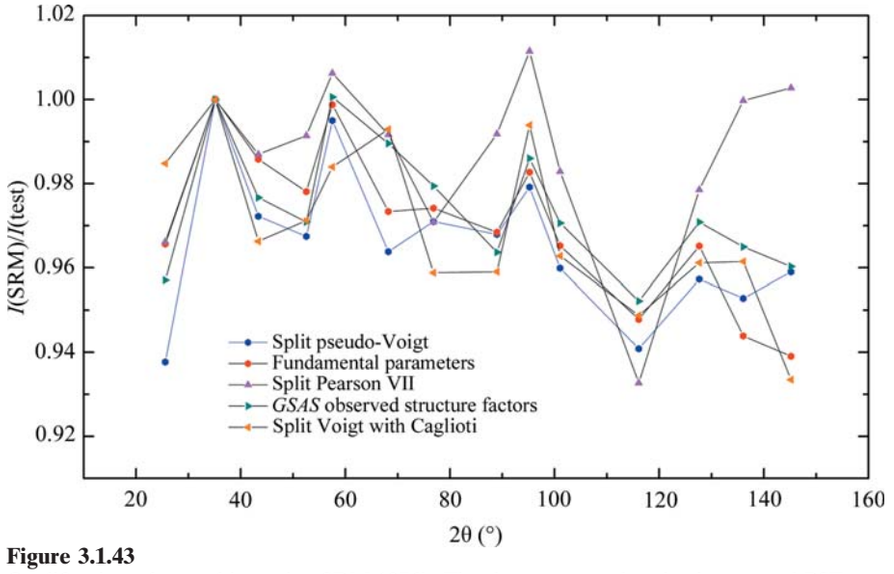

Figure 3.1.43
Qualification of a machine using SRM 1976b. The data were analysed using several PSFs.

The structure common to all the data sets of Fig. 3.1.43 is as yet unexplained. With any of these methods, modelling the background is of critical concern. The intensity scale of the fitted pattern must be expanded to allow for inspection of the background fit alone. The weak amorphous peak at approximately 25° 2θ, which is associated with the anorthite glass matrix phase, complicates the matter. Certain refinement programs allow for the insertion of a broad peak to account for this. Alternatively an 11- to 13-term Chebyshev polynomial could be used. Keeping the number of these terms to a minimum is consistent with preventing the background function from interfering with the modelling of the profiles. Lastly, the use of $K\beta$ filters in conjunction with a PSD can be problematic for the calibration of instrument response using SRM 1976b. Such filters typically impart an absorption edge in the background on the low-energy side of the profiles. With the use of a high-count-rate PSD, this effect can be quite pronounced and can cause difficulties in fitting the background and, therefore, erroneous determination of the profile intensity.

3.1.7. Conclusions

In this chapter, we reviewed the theoretical background behind the well known complexity of X-ray powder diffraction line profiles. A divergent-beam laboratory X-ray diffractometer with a conventional layout was used to rigorously examine the full range of procedures that have been developed for the analysis of the instrument profile function. The machine featured superlative accuracy in angle measurement, and attention was paid to the precision and stability of the optical components and sample positioning. The instrument was aligned in accordance with first-principles methods and was shown to exhibit an optical performance that conformed with the expectations of established theories for powder-diffraction optics.

Data-analysis methods can be divided into two categories that require fundamentally different approaches to instrument calibration. Empirical profile-analysis methods, either based on second-derivative algorithms or profile fitting using analytical profile-shape functions, seek to characterize the instrument performance in terms of shape and position parameters that are used in subsequent analysis for determining the character of the specimen. These methods, however, provide no information about the origins of the peak shift or profile shape that they describe. Model-based methods seek to link the observation directly to the character of the entire experiment. The calibration procedure for the first category can be regarded as a 'classical' calibration where a correction curve is developed through the use of an SRM and applied to subsequent unknowns. With model-based methods, it is the user's responsibility to calibrate the instrument in a manner that ensures that the models that are being used correctly correspond to the experiment. This is best accomplished through the analysis of results from empirical methods, particularly $\Delta(2\theta)$ curves, as well as the analysis of data from an SRM followed by a critical examination of the refined parameters.

Second-derivative-based algorithms for determining peak locations are able to provide the 2θ positions (the positions of the maxima in the observed profile intensity) to within $\pm 0.0025°$ 2θ. Profile fitting using analytical profile-shape functions to determine the peak position was shown to be problematic; errors of up to 0.015° 2θ were noted. The use of uniform weighting in the refinements resulted in improved accuracy in the reported peak positions and FWHM values. Using a Johansson incident-beam monochromator led to high-quality fits of diffraction data using analytical profile shape functions. The Caglioti function can be used to improve the reliability of FWHM values.

The fundamental-parameters approach was found to be effective in modelling the performance of the Bragg–Brentano divergent-beam X-ray diffractometer. The form of the $\Delta(2\theta)$ curve, determined *via* a second-derivative algorithm, can be explained quantitatively through an examination of FPA models. Furthermore, FPA simulations of diffraction data, computed from the instrument configuration using both commercial and NIST FPA codes, and analysed using the same second-derivative algorithm, reproduced the $\Delta(2\theta)$ results from the experimental data. This self-consistency verified the correct operation of both the instrument and the FPA models. Using the FPA for modelling the diffraction profiles provided the best fits to the observations and the most accurate results for the 'true' reported peak positions. The TCH/Finger models for profile shape yielded credible results for refinement of lattice parameters *via* the Rietveld method.

This chapter is based on an article published in the *Journal of Research of the National Institute of Standards and Technology* (Cline *et al.*, 2015).

References

Azároff, L. V. (1955). *Polarization correction for crystal-monochromatized X-radiation*. *Acta Cryst.* **8**, 701–704.
Bergmann, J., Friedel, P. & Kleeberg, R. (1998). *BGMN – a new fundamental parameters based Rietveld program for laboratory X-ray sources, it's use in quantitative analysis and structure investigations*. *IUCr Commission on Powder Diffraction Newsletter*, **20**, 5–8. http://www.iucr.org/resources/commissions/powder-diffraction/newsletter/.
Bergmann, J., Kleeberg, R., Haase, A. & Breidenstein, B. (2000). *Advanced fundamental parameters model for improved profile analysis*. In *Proceedings of the Fifth European Conference on Residual Stresses*, edited by A. J. Böttger, R. Delhez & E. J. Mittemeijer, *Mater.*

Sci. Forum, **347–349**, 303–308. Zürich Uetikon, Switzerland: Trans Tech. Publications.

Berkum, J. G. M. van, Sprong, G. J. M., de Keijser, T. H., Delhez, R. & Sonneveld, E. J. (1995). *The optimum standard specimen for X-ray diffraction line-profile analysis. Powder Diffr.* **10**, 129–139.

BIPM (2006). *The International System of Units (SI)*, 8th ed. Sèvres: Bureau International des Poids et Mesures. http://www.bipm.org/utils/common/pdf/si_brochure_8_en.pdf.

Black, D. R., Windover, D., Henins, A., Filliben, J. & Cline, J. P. (2011). *Certification of standard reference material 660b*. *Powder Diffr.* **26** (Special Issue 02), 155–158.

Bruker AXS (2014). *TOPAS Software*. https://www.bruker.com/products/x-ray-diffraction-and-elemental-analysis/x-ray-diffraction/xrd-software/topas.html.

Caglioti, G., Paoletti, A. & Ricci, F. (1958). *Choice of collimators for a crystal spectrometer for neutron diffraction*. *Nucl. Instrum.* **3**, 223–228.

Cheary, R. W. & Cline, J. P. (1995). *An analysis of the effect of different instrumental conditions on the shapes of X-ray line profiles*. *Adv. X-ray Anal.* **38**, 75–82.

Cheary, R. W. & Coelho, A. (1992). *A fundamental parameters approach to X-ray line-profile fitting*. *J. Appl. Cryst.* **25**, 109–121.

Cheary, R. W. & Coelho, A. (1994). *Synthesizing and fitting linear position-sensitive detector step-scanned line profiles*. *J. Appl. Cryst.* **27**, 673–681.

Cheary, R. W. & Coelho, A. A. (1996). Programs *XFIT* and *FOURYA*. CCP14 Powder Diffraction Library, Engineering and Physical Sciences Research Council, Daresbury Laboratory, UK. http://www.ccp14.ac.uk/.

Cheary, R. W. & Coelho, A. A. (1998*a*). *Axial divergence in a conventional X-ray powder diffractometer. I. Theoretical foundations*. *J. Appl. Cryst.* **31**, 851–861.

Cheary, R. W. & Coelho, A. A. (1998*b*). *Axial divergence in a conventional X-ray powder diffractometer. II. Realization and evaluation in a fundamental-parameter profile fitting procedure*. *J. Appl. Cryst.* **31**, 862–868.

Cline, J. P. (2000). *Use of NIST standard reference materials for characterization of instrument performance*. In *Industrial Applications of X-ray Diffraction*, edited by F. H. Chung & D. K. Smith, pp. 903–917. New York: Marcel Dekker, Inc.

Cline, J. P., Mendenhall, M. H., Black, D., Windover, D. & Henins, A. (2015). *The optics and alignment of the divergent beam laboratory X-ray powder diffractometer and its calibration using NIST standard reference materials*. *J. Res. NIST*, **120**, 173–222. http://nvlpubs.nist.gov/nistpubs/jres/120/jres.120.013.pdf.

Cline, J. P., Von Dreele, R. B., Winburn, R., Stephens, P. W. & Filliben, J. J. (2011). *Addressing the amorphous content issue in quantitative phase analysis: the certification of NIST standard reference material 676a*. *Acta Cryst.* A**67**, 357–367.

Degen, T., Sadki, M., Bron, E., König, U. & Nénert, G. (2014). *Powder Diffr.* **29**, S13–S18.

Edmonds, J., Brown, A., Fischer, G., Foris, C., Goehner, R., Hubbard, C., Evans, E., Jenkins, R., Schreiner, W. N. & Visser, J. (1986). *JCPDS – International Centre for Diffraction Data Task Group on Cell Parameter Refinement. Powder Diffr.* **1**, 66–76.

Fawcett, T. G., Kabbekodu, S. N., Faber, J., Needham, F. & McClune, F. (2004). *Evaluating experimental methods and techniques in X-ray diffraction using 280,000 data sets in the Powder Diffraction File*. *Powder Diffr.* **19**, 20–25.

Finger, L. W., Cox, D. E. & Jephcoat, A. P. (1994). *A correction for powder diffraction peak asymmetry due to axial divergence*. *J. Appl. Cryst.* **27**, 892–900.

Guinier, A. (1994). *X-ray Diffraction in Crystals, Imperfect Crystals, and Amorphous Bodies*. N. Chelmsford, USA: Courier Dover Publications.

Hall, M. M., Veeraraghavan, V. G., Rubin, H. & Winchell, P. G. (1977). *The approximation of symmetric X-ray peaks by Pearson type VII distributions*. *J. Appl. Cryst.* **10**, 66–68.

Hastings, J. B., Thomlinson, W. & Cox, D. E. (1984). *Synchrotron X-ray powder diffraction*. *J. Appl. Cryst.* **17**, 85–95.

Hölzer, G., Fritsch, M., Deutsch, M., Härtwig, J. & Förster, E. (1997). *$K\alpha_{1,2}$ and $K\beta_{1,3}$ X-ray emission lines of the 3d transition metals*. *Phys. Rev. A*, **56**, 4554–4568.

Huber (2014). Monochromator 611 manual. http://www.xhuber.de/fileadmin/user_upload/downloads/usermanuals/Guinier_Monochromator_611_online.pdf.

JCGM (2008*a*). *Uncertainty of Measurement – Part 3: Guide to the expression of uncertainty in measurement* (JCGM 100:2008, GUM: 1995). Tech. Rep. Joint Committee for Guides in Metrology. http://www.iso.org/sites/JCGM/GUM-introduction.htm.

JCGM (2008*b*). *International vocabulary of metrology – basic and general concepts and associated terms (VIM)*. Tech. Rep. Joint Committee for Guides in Metrology. http://www.bipm.org/en/publications/guides/vim.html.

Jenkins, R. (1992). *Round robin on powder diffractometer sensitivity*. ICDD Workshop at *Accuracy in Powder Diffraction II*, May 26–29, NIST, Gaithersburg, USA.

Johansson, T. (1933). *Über ein neuartiges, genau fokussierendes Röntgenspektrometer*. *Z. Phys.* **82**, 507–528.

Klug, H. P. & Alexander, L. E. (1974). *X-ray Diffraction Procedures*, 2nd ed. New York: John Wiley & Sons.

Larson, A. C. & Von Dreele, R. B. (2004). *General Structure Analysis System (GSAS)*. Tech. Rep. Los Alamos National Laboratory, New Mexico, USA.

Louër, D. (1992). Personal communication.

Louër, D. & Langford, J. I. (1988). *Peak shape and resolution in conventional diffractometry with monochromatic X-rays*. *J. Appl. Cryst.* **21**, 430–437.

McCusker, L. B., Von Dreele, R. B., Cox, D. E., Louër, D. & Scardi, P. (1999). *Rietveld refinement guidelines*. *J. Appl. Cryst.* **32**, 36–50.

Maskil, N. & Deutsch, M. (1988). *X-ray Kα satellites of copper*. *Phys. Rev. A*, **38**, 3467–3472.

Mendenhall, M. H., Mullen, K. & Cline, J. P. (2015). *An implementation of the fundamental parameters approach for analysis of X-ray powder diffraction line profiles*. *J. Res. NIST*, **120**, 223–251.

NIST (2008). *Standard Reference Material 676a: Alumina Internal Standard for Quantitative Analysis by X-ray Powder Diffraction*. SRM certificate. NIST, U. S. Department of Commerce, Gaithersburg, MD, USA. https://www-s.nist.gov/srmors/view_detail.cfm?srm=676a.

NIST (2010). *Standard Reference Material 660b: Lanthanum Hexaboride – Powder Line Position and Line Shape Standard for Powder Diffraction*. SRM certificate. NIST, U. S. Department of Commerce, Gaithersburg, MD, USA. https://www-s.nist.gov/srmors/view_detail.cfm?srm=660b.

NIST (2015*a*). *209.1 – X-ray Diffraction (powder and solid forms)*. SRM catalog. NIST, U. S. Department of Commerce, Gaithersburg, MD, USA. https://www-s.nist.gov/srmors/viewTableV.cfm?tableid=149.

NIST (2015*b*). *Standard Reference Material 1976b: Instrument Response Standard for X-ray Powder Diffraction*. SRM certificate. NIST, U. S. Department of Commerce, Gaithersburg, MD, USA. https://www-s.nist.gov/srmors/view_detail.cfm?srm=1976B.

NIST (2015*c*). *Standard Reference Material 640e: Line Position and Line Shape Standard for Powder Diffraction (Silicon Powder)*. SRM certificate. NIST, U. S. Department of Commerce, Gaithersburg, MD, USA. https://www-s.nist.gov/srmors/view_detail.cfm?srm=640E.

NIST (2015*d*). *Standard Reference Material 660c: Line Position and Line Shape Standard for Powder Diffraction (Lanthanum Hexaboride Powder)*. SRM certificate. NIST, U. S. Department of Commerce, Gaithersburg, MD, USA. https://www-s.nist.gov/srmors/view_detail.cfm?srm=660c.

Rietveld, H. M. (1967). *Line profiles of neutron powder-diffraction peaks for structure refinement*. *Acta Cryst.* **22**, 151–152.

Rietveld, H. M. (1969). *A profile refinement method for nuclear and magnetic structures*. *J. Appl. Cryst.* **2**, 65–71.

Rigaku (2014). *PDXL 2, Rigaku powder diffraction data analysis software version 2.2*. Rigaku Corporation, Tokyo, Japan.

Taylor, B. & Kuyatt, C. (1994). *TN1297: Guidelines for Evaluating and Expressing the Uncertainty of NIST Measurement Results*. Tech. Rep. NIST. Washington, DC: U. S. Government Printing Office. http://physics.nist.gov/cuu/Uncertainty/index.html.

Thompson, P., Cox, D. E. & Hastings, J. B. (1987). *Rietveld refinement of Debye–Scherrer synchrotron X-ray data from Al_2O_3*. *J. Appl. Cryst.* **20**, 79–83.

Toby, B. H. & Von Dreele, R. B. (2013). *GSAS-II: the genesis of a modern open-source all purpose crystallography software package*. *J. Appl. Cryst.* **46**, 544–549.

Wilson, A. J. C. (1963). *Mathematical Theory of X-ray Powder Diffractometry*. New York: Gordon & Breach.

Yao, T. & Jinno, H. (1982). *Polarization factor for the X-ray powder diffraction method with a single-crystal monochromator*. *Acta Cryst.* A**38**, 287–288.

International Tables for Crystallography (2019). Vol. H, Chapter 3.3, pp. 263–269.

3.3. Powder diffraction peak profiles

R. B. Von Dreele

3.3.1. Introduction

The analysis of a powder diffraction pattern usually involves the fitting of a model to the set of peaks that are found in that pattern. The desired result may be accurate peak positions to be used as input for an indexing procedure, or extraction of the suite of reflection intensities for crystal structure determination or a Rietveld refinement. In any case, a good description of the shape of the powder peak profile and how it varies across the entire pattern is of paramount importance for obtaining the highest-quality results, and this topic was briefly reviewed in Volume C of *International Tables for Crystallography* (Parrish, 1992).

The fitting is a least-squares procedure in which the model used to calculate the intensity of the profile is

$$Y(x) = \sum_j I_j P_j(\Delta) + B(x), \tag{3.3.1}$$

where I_j is the integrated intensity of the jth peak and P is the shape function for that peak, which depends on the offset ($\Delta = x - T_j$) of its position T_j from the observation point x. The sum is over all reflections that could contribute to the profile and $B(x)$ is a background intensity function. The observed shape of the peaks arises from a convolution of the intrinsic source profile (G_λ), the various instrumental profile contributions (G_I) (*e.g.* from slits and monochromators, discussed in Chapter 3.1) and the characteristics of the sample (G_S) that broaden the idealized reciprocal-space points (see Chapter 3.6):

$$P(\Delta) = G_\lambda * G_I * G_S. \tag{3.3.2}$$

In practice, the peak profile function is usually developed by either selecting a peak-shape function that has the required shape characteristics to fit the experimental peak profiles (the semi-empirical function approach, or SFA) or by selecting a number of contributing functions and doing the requisite convolutions (the fundamental parameters approach, or FPA) (Cheary & Coelho, 1998*b*).

Both approaches have been used for the analysis of constant-wavelength neutron and X-ray powder diffraction data and for neutron time-of-flight (energy-dispersive) powder data. In addition, the peaks can be seen to be displaced from their expected positions given by Bragg's law. As we will see, this displacement is partially a consequence of some geometric features of the experiment but is also dependent upon the particular description of the peak profile.

3.3.2. Peak profiles for constant-wavelength radiation (X-rays and neutrons)

3.3.2.1. *Introduction – symmetric peak profiles*

The realization that the neutron powder diffractometer at the Reactor Centrum Nederland, Petten, produced powder peak profiles that were Gaussian in shape led Rietveld (1967) to develop a full-pattern method for crystal structure refinement (Rietveld, 1967, 1969), now known as the Rietveld refinement method. The Gaussian is formulated as

$$P_G(\Delta, \Gamma_G \text{ or } \sigma^2) = \frac{(8\ln 2)^{1/2}}{\Gamma_G(2\pi)^{1/2}} \exp\left(\frac{-4\ln 2\Delta^2}{\Gamma_G^2}\right) = \frac{1}{(2\pi\sigma^2)^{1/2}} \exp\left(\frac{-\Delta^2}{2\sigma^2}\right), \tag{3.3.3}$$

where the width of the peak is expressed as either the full width at half-maximum (FWHM = Γ_G) or as the variance (σ^2). Rietveld also recognized the earlier analysis of the resolution of a neutron powder diffractometer by Caglioti *et al.* (1958), who showed that the contributions from the source size, collimators and monochromator crystal mosaic spread and scattering angle could be combined analytically to give

$$\Gamma_G^2 = U\tan^2\theta + V\tan\theta + W \tag{3.3.4}$$

with U, V and W adjustable during the Rietveld refinement. A modified form of this may have more stability in refinement (attributed to E. Prince by Young & Wiles, 1982):

$$\Gamma_G^2 = U'(\tan\theta - K_0)^2 + V'(\tan\theta - K_0) + W', \tag{3.3.5}$$

where K_0 is arbitrarily chosen as 0.6.

Improvements in the resolution of neutron powder diffractometers and (more importantly) attempts to apply the Rietveld method to X-ray powder diffraction data required the development of new powder profile functions (Malmros & Thomas, 1977; Young *et al.*, 1977; Young & Wiles, 1982); this is because the Gaussian function [equation (3.3.3)] gave poor fits to observed peak profiles, partially because of the Lorentzian emission line profile (G_λ) from laboratory X-ray tubes. Many functions were considered, including Lorentzian ('Cauchy'), various modified Lorentzians, Pearson VII and pseudo-Voigt. Of these the last two performed (on individual peak fits) about equally well; functional forms are:

Lorentzian 'Cauchy' function

$$P_L(\Delta, \Gamma_L) = \left(\frac{\Gamma_L}{2\pi}\right)\left\{\frac{4}{\left[\Gamma_L^2 + (2\Delta)^2\right]}\right\}, \tag{3.3.6}$$

Pearson VII function

$$P_{\rm P7}(\Delta, \xi, \mu) = \frac{\Gamma(\mu)}{\xi\Gamma\left(\mu - \frac{1}{2}\right)(\mu\pi)^{1/2}} \Big/ \left(1 + \frac{\Delta^2}{\mu\xi^2}\right)^{\mu}, \tag{3.3.7}$$

pseudo-Voigt function

$$P_{\rm PV}(\Delta, \Gamma, \eta) = \eta P_L(\Delta, \Gamma) + (1 - \eta)P_G(\Delta, \Gamma), \tag{3.3.8}$$

where Γ_L is the FWHM of the Lorentzian peak and $\Gamma(\mu)$ in the Pearson VII function is the Gamma function; μ may vary between 0 and ∞, and μ is the half width at $(1 + 1/\mu)^{-\mu}$ of the peak height (David, 1986); $P_{\rm P7}(\Delta, \Gamma, 1) \simeq P_L(\Delta, \Gamma)$ and $P_{\rm P7}(\Delta, \Gamma, \infty) \simeq P_G(\Delta, \Gamma)$. Although the Pearson VII function performs well in individual peak fits, it is of little use for Rietveld refinements because of the difficulty in relating its coefficients to physically meaningful characteristics of the sample and will not be considered further in this discussion.

The pseudo-Voigt function is an approximation to the Voigt function, which is the convolution of a Gaussian and a Lorentzian:

Voigt function

$$P_V(\Delta, \Gamma_L, \Gamma_G) = \int_{-\infty}^{\infty} P_L(\Delta, \Gamma_l) P_G(\Delta - \delta, \Gamma_G)\, \mathrm{d}\delta = \left(\frac{4 \ln 2}{\pi \Gamma_G^2}\right)^{1/2} \mathrm{Re}[\exp(-z^2)\mathrm{erfc}(-iz)], \quad (3.3.9)$$

where $z = \alpha + i\beta$, $\alpha = (4 \ln 2)^{1/2} \Delta / \Gamma_G$ and $\beta = (\ln 2)^{1/2} \Gamma_L / \Gamma_G$.

A number of formulations have been proposed for the pseudo-Voigt coefficients to make the best fit to the corresponding Voigt function (Hastings *et al.*, 1984; David, 1986; Thompson *et al.*, 1987). The latter is most commonly used and gives overall the FWHM, Γ and the mixing coefficient, η, to be used in equation (3.3.8) as functions of the individual FWHMs Γ_G and Γ_L:

$$\Gamma = [(\Gamma_G^5 + 2.69269\Gamma_G^4\Gamma_L + 2.42843\Gamma_G^3\Gamma_L^2 + 4.47163\Gamma_G^2\Gamma_L^3 + 0.07842\Gamma_G\Gamma_L^4 + \Gamma_L^5)]^{1/5}, \quad (3.3.10)$$

$$\eta = 1.36603(\Gamma_L/\Gamma) - 0.47719(\Gamma_L/\Gamma)^2 + 0.11116(\Gamma_L/\Gamma)^3. \quad (3.3.11)$$

The alternative given by David (1986) uses a more generalized version of the pseudo-Voigt function,

$$\begin{aligned} P_{\mathrm{PV}}(\Delta, W_G, W_L, \eta_G, \eta_L) &= \eta_L P_L(\Delta, W_L) + \eta_G P_G(\Delta, W_G), \\ \eta_G &= 0.00268\rho_1 + 0.75458\rho_1^2 + 2.88898\rho_1^3 - 3.85144\rho_1^4 \\ &\quad - 0.55765\rho_1^5 + 3.03824\rho_1^6 - 1.27539\rho_1^7, \\ \eta_L &= 1.35248\rho_2 + 0.41168\rho_2^2 - 2.18731\rho_2^3 + 6.42452\rho_2^4 \\ &\quad - 10.29036\rho_2^5 + 6.88093\rho_2^6 - 1.59194\rho_2^7, \\ W_G &= \Gamma(1 - 0.50734\rho_2 - 0.22744\rho_2^2 + 1.63804\rho_2^3 \\ &\quad - 2.28532\rho_2^4 + 1.31943\rho_2^5), \\ W_L &= \Gamma(1 - 0.99725\rho_1 + 1.14594\rho_1^2 + 2.56150\rho_1^3 \\ &\quad - 6.52088\rho_1^4 + 5.82647\rho_1^5 - 1.91086\rho_1^6), \end{aligned} \quad (3.3.12)$$

where $\Gamma = \Gamma_G + \Gamma_L$, $\rho_1 = \Gamma_G/\Gamma$ and $\rho_2 = \Gamma_L/\Gamma$; this is claimed to match the Voigt function to better than 0.3%.

3.3.2.2. *Constant-wavelength powder profile asymmetry*

Rietveld (1969) noted that at very low scattering angles the peaks displayed some asymmetry, which shifted the peak maximum to lower angles. He ascribed the effect to 'vertical divergence' and proposed a purely empirical correction for it. Subsequent authors (Cooper & Sayer, 1975; Howard, 1982; Hastings *et al.*, 1984) offered semi-empirical treatments of the profile shape that results from the intersection of a Debye–Scherrer cone with a finite receiving slit, which is described as 'axial divergence'. A more complete analysis of the problem in neutron powder diffraction was offered by van Laar & Yelon (1984), who considered the effect of a finite vertical slit ($2H$) intercepting a set of Bragg diffraction cones generated from a finite sample length ($2S$) within the incident beam for a goniometer radius (L). As seen in Fig. 3.3.1, this gives peak intensity beginning at $2\varphi_{\min} < 2\theta$ *via* scattering from only the ends of the sample; at $2\varphi_{\mathrm{infl}}$ the entire sample scatters into the detector. The resulting intensity profile is then convoluted with a Gaussian function to give the resulting asymmetric powder line profile (Fig. 3.3.2). This approach was then considered by Finger *et al.* (1994) for synchrotron powder diffraction and they created a Fortran code that was subsequently adopted *via* convolution with a pseudo-Voigt function [equation (3.3.12)] for use by many Rietveld refinement codes. Although originally formulated for parallel-beam neutron optics, it was shown by Finger *et al.* (1994) that it could be equally well applied to diverging X-ray and neutron optics by allowing the sample length to vary during the Rietveld refinement. They also showed that it could be applied to the asymmetry observed at low angles with Bragg–Brentano instrumentation. In that case the detector height is defined by the diffracted-beam Soller slits.

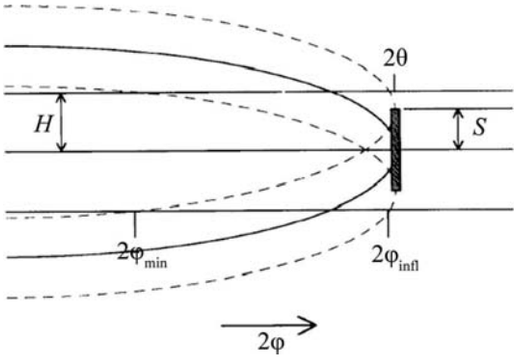

Figure 3.3.1
The band of intensity diffracted by a sample with height $2S$, as seen by a detector with opening $2H$ and a detector angle 2φ moving in the detector cylinder. For angles below $2\varphi_{\min}$ no intensity is seen. For angles between $2\varphi_{\mathrm{infl}}$ and 2θ, scattering from the entire sample can be seen by the detector. Figure and caption adapted from Finger *et al.* (1994).

Clearly, this asymmetric peak-shape function properly represents the offset of the peak top from the peak position, in contrast to functions such as the split Pearson VII function. Consequently, single peak fits using this function will give peak positions that are more readily indexed using methods such as those described in Chapter 3.4.

3.3.2.3. *Peak-displacement effects*

The position of the peak is also affected by various instrumental and geometric effects. For example, the sample position in a Bragg–Brentano experiment is ideally tangent to the focusing circle (Parrish, 1992). A radial displacement, s, of the sample will shift the Bragg peaks according to

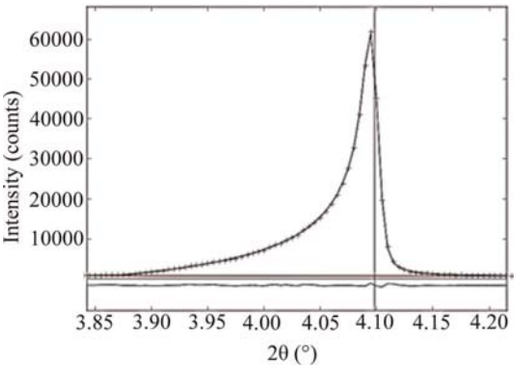

Figure 3.3.2
Low-angle synchrotron powder diffraction line ($2\theta \simeq 4.1^\circ$) fitted by the Finger *et al.* (1994) axial divergence powder line-shape function. The observed points (+), calculated curve, background and difference curves are shown. Note the offset of the peak top from the Bragg 2θ position (vertical line).

$$\Delta 2\theta = 360 s \cos\theta / \pi R, \tag{3.3.13}$$

where R is the goniometer radius. This is the major peak-displacement effect and can be detected for sample displacements as small as 10 μm.

A similar effect can be observed for Debye–Scherrer instrumentation when the goniometer axis is not coincident with the sample axis; this is a more common problem for neutron powder diffraction instruments where accurate placement of very massive goniometers can be difficult. In this case the peak displacement is

$$\Delta 2\theta = \frac{180}{\pi R}(s_x \cos 2\theta + s_y \sin 2\theta), \tag{3.3.14}$$

where s_x and s_y are displacements perpendicular and parallel to the incident beam, respectively, all in the diffraction plane.

In high-resolution instrumentation (even at a synchrotron) goniometer axis displacements less than 10 μm can be detected.

Specimen transparency in Bragg–Brentano diffraction can also cause peak displacements arising from the shift in effective sample position to below the surface at high scattering angles. This shift for a thick specimen is

$$\Delta 2\theta = 90 \sin 2\theta / \mu_{\rm eff} \pi R, \tag{3.3.15}$$

where $\mu_{\rm eff}$ is the effective sample absorption coefficient taking into account the packing density.

3.3.2.4. *Fundamental parameters profile modelling*

An alternative method for describing the source and instrumental part of the powder peak profile is to develop a set of individual functions that form the part of the profile arising from each of the instrumental components that shape the beam profile (Cheary & Coelho, 1992, 1998*a*,*b*). Ideally, each function is parameterized in terms of the physical parameters of the corresponding instrument component (*e.g.* slit width and height, sample dimensions and absorption, source size and emission characteristics, *etc.*), which are known from direct measurement. The set of functions are then convoluted *via* fast mathematical procedures to produce a line profile that matches the observed one. Any remaining profile-broadening parameters (*e.g.* for sample crystallite size and microstrain, see Section 3.3.5 for details) are then allowed to adjust during a Rietveld refinement. By employing this fundamental parameters (FP) approach, these parameters are unaffected by any instrumental parameterization.

The FP method offers two clear advantages over the more empirical approach outlined in Sections 3.3.2.1–3.3.2.3 above: (i) it can more closely describe the actual instrumental effects that contribute to the profile shape, thus improving the precision of the fit to the observed data and (ii) it can be used to describe a source characteristic or an instrumental arrangement that is outside the normally used configuration, yielding a result that would be difficult to obtain otherwise (Cheary *et al.*, 2004).

3.3.3. Peak profiles for neutron time-of-flight experiments

3.3.3.1. *The experiment*

The neutron source in a time-of-flight (TOF) powder diffraction experiment produces pulses of polychromatic neutrons; these travel over the distance from the source to the sample and then to the detectors which are placed at fixed scattering angles about the sample position; the travel times are of the order of 1–100 ms. This has been briefly described in Volume C of *International Tables for Crystallography* (Jorgensen *et al.*, 1992). Because neutrons of differing velocities (v) have differing wavelengths (λ) according to the de Broglie relationship ($\lambda = h/mv$) given Planck's constant (h) and the neutron mass (m), they will sort themselves out in their time of arrival at the detector. The powder pattern appears as a function of TOF *via* Bragg's law ($\lambda = 2d\sin\theta$) in which the wavelength is varied and θ is fixed. The approximate relationship between TOF, wavelength and d-spacing observed in a particular detector can be derived from the de Broglie relationship and Bragg's law to give

$$\mathrm{TOF} = 252.7784 L\lambda = 505.5568 L d \sin\theta. \tag{3.3.16}$$

The constants are such that given λ in ångströms and the total neutron flight path length L in metres, then the TOF will be in μs. An analysis of the possible variances in these components then gives an estimate of the powder diffraction peak widths:

$$\Delta d/d = [(\Delta t/t)^2 + (\Delta\theta \cot\theta)^2 + (\Delta L/L)^2]^{1/2}, \tag{3.3.17}$$

where Δd, Δt, $\Delta\theta$ and ΔL are, respectively, the uncertainties in d-spacing, TOF, scattering angle θ and total flight path L (Jorgensen & Rotella, 1982). Consequently, these three terms also determine the instrumental contribution to the neutron TOF powder peak profile.

3.3.3.2. *The neutron pulse shape*

The neutron pulse shape depends on the mode of production. Early studies (Buras & Holas, 1968; Turberfield, 1970) used one or more choppers to define a polychromatic pulse from a reactor source, resulting in essentially Gaussian powder peak profiles whose FWHM (Γ_G) is nearly constant ($B \simeq 0$):

$$\Gamma_G^2 = A + Bd^2, \tag{3.3.18}$$

so that the Rietveld technique can easily be used (*e.g.* Worlton *et al.*, 1976). Unfortunately, this approach gave very low intensities and relatively low resolution powder patterns.

A more useful approach uses a spallation source to produce the pulsed neutron beam. Neutrons are produced when a high-energy proton beam (>500 MeV) strikes a heavy metal target (usually W, U or liquid Hg) *via* a spallation process (Carpenter *et al.*, 1984). These very high energy neutrons strike small containers of moderating material (usually H_2O, liquid CH_4 or liquid H_2) which then comprise the neutron source seen by the powder diffraction instrument. The entire target/moderator system is encased in a neutron-reflective material (usually Be) to enhance the neutron flux and then further encased in a biological shield. Each moderator may be encased on the sides away from the instrument (*e.g.* powder diffractometer) in a thin neutron absorber (*e.g.* Cd or Gd) and may also contain an inner absorber layer ('poison') to sharpen the resulting pulse of thermal neutrons. These sources produce a polychromatic neutron beam that is rich in both thermal (<300 meV) and epithermal (>300 meV) neutrons. The proton pulses can have a very short duration (~200 ns) (from a 'short-pulse' source, *e.g.* ISIS, Rutherford Laboratory, UK or LANSCE, Los Alamos National Laboratory, USA) or a much longer duration (>500 ns) (a 'long-pulse' source, *e.g.* SNS, Oak Ridge National Laboratory, USA or ESS, European Spallation Source, Sweden); the pulse repetition rate at these sources is 10–60 Hz. These characteristics are largely dictated by the proton accelerator and neutron source design. The resulting neutron pulse results from complex down-scattering and thermalization processes in the whole target/moderator assembly; it may be further shaped by choppers,

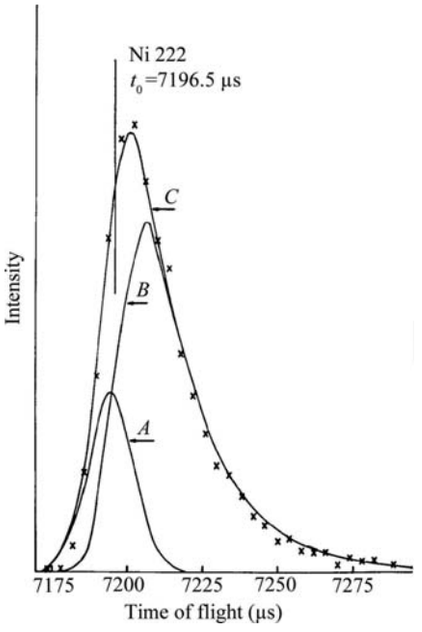

Figure 3.3.3
The observed and calculated Ni 222 diffraction line profile from the Back Scattering Spectrometer, Harwell Laboratory, Chilton, UK. The curves *A* and *B* are computed from the two terms in equation (3.3.19) and curve *C* is the sum (from Von Dreele *et al.*, 1982).

particularly for long-pulse sources, to give what is seen at the powder diffractometer.

Consequently, the neutron pulse structure from these sources has a complex and asymmetric shape, usually characterized by a very sharp rise and a slower decay, both of which are dependent on the neutron wavelength. The resulting powder diffraction peak profile (Fig. 3.3.3) is then the convolution [equation (3.3.2)] of this pulse shape (G_λ) with symmetric functions (G_I) arising from beamline components (*e.g.* slits and choppers) and the sample characteristics (G_S).

3.3.3.3. *The neutron TOF powder peak profile*

An early attempt at representing the TOF peak profile used a piecewise approach combining a leading-edge Gaussian, a peak-top Gaussian and an exponential decay for the tail (Cole & Windsor, 1980). Although single peaks could be fitted well with this function, the variation with TOF was complex and required many arbitrary coefficients.

A more successful approach empirically represented the pulse shape by a pair of back-to-back exponentials which were then convoluted with a Gaussian (Jorgensen *et al.*, 1978; Von Dreele *et al.*, 1982) to give

$$P(\Delta) = \frac{\alpha\beta}{\alpha+\beta}\left\{\exp\left[\frac{\alpha}{2}(\alpha\sigma^2+2\Delta)\right]\operatorname{erfc}\left[\frac{\alpha\sigma^2+\Delta}{\sigma(2^{1/2})}\right] + \exp\left[\frac{\beta}{2}(\beta\sigma^2-2\Delta)\right]\operatorname{erfc}\left[\frac{\beta\sigma^2-\Delta}{\sigma(2^{1/2})}\right]\right\}, \tag{3.3.19}$$

where α and β are, respectively, the coefficients for the exponential rise and decay functions; erfc is the complementary error function. Analysis of the data that were available then gave empirical relations for α, β and σ as

$$\alpha = \alpha_1/d; \quad \beta = \beta_0 + (\beta_1/d^4); \quad \sigma = \sigma_1 d. \tag{3.3.20}$$

The two terms in this function are shown in Fig. 3.3.3. The junction of the two exponentials defines the peak position (shown as a vertical line in Fig. 3.3.3); it is offset to the low side of the peak maximum. This arbitrary choice of peak position then affects the relationship between the TOF and reflection *d*-spacing; an empirical relationship (Von Dreele *et al.*, 1982) was found to suffice:

$$\mathrm{TOF} = Cd + Ad^2 + Z, \tag{3.3.21}$$

with three adjustable coefficients (C, A, Z) established *via* fitting to the pattern from a standard reference material.

Although this profile description was adequate for room-temperature moderators (H_2O or polyethylene) at low-power spallation sources, it does not describe well the wavelength dependence for cold moderators feeding neutron guides used at higher-power sources. An alternative description, employing a switch function to account for the fundamental change in the neutron leakage profile from the moderator between epithermal and thermal neutrons, was proposed (Ikeda & Carpenter, 1985; Robinson & Carpenter, 1990) to accommodate the profiles seen from liquid CH_4 or H_2 moderators. A drawback of this description is that the pulse profile is defined with the peak position at the low TOF edge; convolution with G_I and G_S results in a function where the peak position is far below the peak top. An empirical approach by Avdeev *et al.* (2007) simply requires tables to be established from individual peak fits to a standard material powder pattern for the values of α, β and TOF in place of the expressions given in equations (3.3.20) and (3.3.21); this establishes the G_λ and G_I contributions to the TOF line shape. More recently, some simple extensions (Toby & Von Dreele, 2013) to the empirical functions [equations (3.3.22) and (3.3.23)] appear to better cover the deviations arising from the enhanced epithermal contribution to the cold moderator spectrum:

$$\mathrm{TOF} = Cd + Ad^2 + B/d + Z, \tag{3.3.22}$$

$$\alpha = \frac{\alpha_1}{d}; \quad \beta = \beta_0 + \frac{\beta_1}{d^4} + \frac{\beta_2}{d^2}; \quad \sigma = \sigma_0 + \sigma_1 d^2 + \sigma_2 d^4 + \frac{\sigma_3}{d^2}. \tag{3.3.23}$$

3.3.4. Peak profiles for X-ray energy-dispersive experiments

In an X-ray dispersive powder diffraction experiment, a detector with good energy-discrimination capability is placed at a fixed scattering angle while the sample is illuminated by a 'white' beam of radiation. The detector response is binned into discrete energies by a multichannel analyser (MCA) (Glazer *et al.*, 1978). Typically these instruments display peaks that are purely Gaussian in shape with quite low resolution ($\Delta E/E \simeq 1\%$) and have widths that are proportional to the energy:

$$\Gamma_G = UE + W. \tag{3.3.24}$$

This is most useful for experiments with very limited angular access (*e.g.* high-pressure multi-anvil setups, as described in Chapter 2.7) using synchrotron radiation and can give very high data collection rates on very small samples. Glazer *et al.* (1978) showed that simple crystal structures can be modelled with the Rietveld technique after suitable corrections to account for the variation in source intensity, detector response and sample absorption effects. Otto (1997) expanded the peak-profile description to include possible sample-broadening effects *via* a Voigt profile; this extended the expression in equation (3.3.24) by adding a second-order term in energy and allowed extraction of

size and microstrain sample-broadening effects in cases where these were large.

A related alternative technique (Wang *et al.*, 2004) collects multiple energy-dispersive powder patterns over a narrow and coarse angular step scan; this is easily done in a typical multi-anvil high-pressure setup. The array of spectra are binned as multiple angle-dispersive patterns which are then combined into a single refinement; the complex corrections required for pure energy-dispersive patterns reduce to refinable scaling factors. Typically a scan over 10° 2θ with 0.1–0.2° steps suffices to give suitable data; binning into $\Delta E/E \simeq 20\%$ energy bands gives data that are used in a conventional multiple-data-set Rietveld refinement.

3.3.5. Sample broadening

Very often, particularly for synchrotron-radiation experiments, the powder diffraction peak profile is dominated by broadening effects from the sample, *e.g.*

$$P(\Delta) = G_\lambda * G_I * G_S \simeq G_S. \tag{3.3.25}$$

For the cases considered here, the focus will be on sample-broadening models that allow improved fits within the context of a Rietveld refinement; a more detailed treatment aimed at extracting sample characteristics (*e.g.* crystallite size distributions) is covered in Chapter 5.1.

Two mechanisms for sample broadening are considered here: crystallite size and 'microstrain' broadening; each will be discussed in turn.

3.3.5.1. *Crystallite size broadening*

The reciprocal space associated with an ideal large crystal will consist of a periodic array of infinitely sharp δ functions, one for each of the structure factors, as expected from the Fourier transform of the essentially infinite and periodic crystal lattice. For real crystals, this limit is reached for crystal dimensions exceeding *circa* 10 μm. The Fourier transform of a crystal lattice that is smaller than this will show a profile that follows the form described by the $\mathrm{sinc}(x) = \sin(\pi x)/\pi x$ function. Any dispersion in the crystal sizes in a powder sample will smear this into a form intermediate between a Gaussian and a Lorentzian, which is well described by either a Voigt [equation (3.3.9)], a pseudo-Voigt [equation (3.3.8)] or the less-useful Pearson VII [equation (3.3.7)] function. The physical process used to form the powder will influence the details of the size distribution; usually this will approximate a log-normal distribution and the resulting peak-shape contribution from crystallite size effects will be largely Lorentzian with a width Γ_{SL}. Predominantly Gaussian size broadening can only occur if the size distribution is very tightly monodisperse. Then, for isotropic crystal dimensions this broadening is uniformly the same everywhere in reciprocal space; *e.g.* Δd^* = constant $\simeq 1/p$, where p is the crystallite size. Transformation *via* Bragg's law to the typical measurement of a powder pattern as a function of 2θ gives this Lorentzian width as

$$\Gamma_{pL} = \frac{180}{\pi}\frac{K\lambda}{p\cos\theta} \tag{3.3.26}$$

expressed in degrees and the Scherrer constant, K, which depends on the shape of the crystallites; *e.g.* K = 1 for spheres, 0.89 for cubes *etc.* (see Table 5.1.1 in Chapter 5.1). A similar expression for the crystallite size from a neutron TOF experiment is

$$\Gamma_{pL} = \frac{CK}{p}, \tag{3.3.27}$$

where C is defined by equation (3.3.21). In some cases the crystallites have anisotropic shapes (*e.g.* plates or needles), in which case the peak broadening will be dependent on the respective direction in reciprocal space for each reflection. Many Rietveld refinement programs implement various models for this anisotropy.

3.3.5.2. *Microstrain broadening*

The existence of imperfections (*e.g.* deformation faults) within the crystal lattice produces local distortions of the lattice and thus a broadening of the points in reciprocal space. To a first approximation these points are broadened proportionally to their distance from the origin, *e.g.* $\Delta d^*/d^* = \Delta d/d \simeq$ constant.

As for crystallite size, there is normally dispersion in the density of defects and thus the peak shape will be intermediate between a Gaussian and a Lorentzian form, and it is well described by the Voigt, pseudo-Voigt or Pearson VII functions. Usually, the Lorentzian form dominates this type of broadening and it is the most common form of sample broadening in powder diffraction. It usually arises because of defects introduced during sample preparation (especially during grinding). The Lorentzian width contribution from microstrain broadening is

$$\Gamma_{sL} = \frac{180}{\pi} s \tan\theta, \tag{3.3.28}$$

where s is the dimensionless microstrain; it is frequently multiplied by 10^6. A similar expression for neutron TOF is

$$\Gamma_{sL} = Csd, \tag{3.3.29}$$

where C is defined by equation (3.3.21).

In many cases, the microstrain broadening is not isotropic; presumably this is a consequence of the interaction between the defects and the elastic properties of the crystals. A phenomenological description of these effects by Popa (1998) and Stephens (1999) is obtained by considering the variance of

$$\frac{1}{d^2} = M_{hkl} = \alpha_1 h^2 + \alpha_2 k^2 + \alpha_3 l^2 + \alpha_4 kl + \alpha_5 hl + \alpha_6 hk \tag{3.3.30}$$

with respect to each of the coefficients α_i.

$$\Gamma_{sL}^2 = \sum_{i,j} S_{ij} \frac{\partial M}{\partial \alpha_i}\frac{\partial M}{\partial \alpha_j} \tag{3.3.31}$$

where

$$\frac{\partial M}{\partial \alpha_i}\frac{\partial M}{\partial \alpha_j} = \begin{bmatrix} h^4 & h^2k^2 & h^2l^2 & h^2kl & h^3l & h^3k \\ h^2k^2 & k^4 & k^2l^2 & k^3l & hk^2l & hk^3 \\ h^2l^2 & k^2l^2 & l^4 & kl^3 & hl^3 & hkl^2 \\ h^2kl & k^3l & kl^3 & k^2l^2 & hkl^2 & hk^2l \\ h^3l & hk^2l & hl^3 & hkl^2 & h^2l^2 & h^2kl \\ h^3k & hk^3 & hkl^2 & hk^2l & h^2kl & h^2k^2 \end{bmatrix}. \tag{3.3.32}$$

Examination of this sum for the triclinic case collects terms to give

$$\begin{aligned}\Gamma_{sL}^2 = {} & S_{400}h^4 + S_{040}k^4 + S_{004}l^4 + 3(S_{220}h^2k^2 + S_{202}h^2l^2 + S_{022}k^2l^2) \\ & + 2(S_{310}h^3k + S_{103}hl^3 + S_{031}k^3l + S_{130}hk^3 + S_{301}h^3l + S_{013}kl^3) \\ & + 4(S_{211}h^2kl + S_{121}hk^2l + S_{112}hkl^2)\end{aligned} \tag{3.3.33}$$

with 15 coefficients S_{hkl}. The subscript hkl in S_{hkl} refers to the powers used for h, k, l in equations (3.3.33)–(3.3.44).

For Laue symmetries other than triclinic, there are restrictions on the allowed S_{hkl} terms and, as a practical matter, additional equivalences from symmetry-forced reflection overlaps for trigonal and tetragonal Laue symmetries.

Monoclinic (2/m, b axis unique; others similar, nine coefficients):

$$\Gamma_{sL}^2 = S_{400}h^4 + S_{040}k^4 + S_{004}l^4 + 3S_{202}h^2l^2 + 3(S_{220}h^2k^2 + S_{022}k^2l^2) + 2(S_{301}h^3l + S_{103}hl^3) + 4S_{121}hk^2l. \quad (3.3.34)$$

Orthorhombic (mmm, six coefficients):

$$\Gamma_{sL}^2 = S_{400}h^4 + S_{040}k^4 + S_{004}l^4 + 3(S_{220}h^2k^2 + S_{202}h^2l^2 + S_{022}k^2l^2). \quad (3.3.35)$$

Tetragonal (4/m, five coefficients):

$$\Gamma_{sL}^2 = S_{400}(h^4 + k^4) + S_{004}l^4 + 3S_{220}h^2k^2 + 3S_{202}(h^2l^2 + k^2l^2) + 2S_{310}(h^3k - hk^3). \quad (3.3.36)$$

The last coefficient (S_{310}) cannot normally be determined owing to exact reflection overlaps. Thus, equation (3.3.37) is normally used for both 4/m and 4/mmm Laue symmetries:

Tetragonal (4/mmm, four coefficients):

$$\Gamma_{sL}^2 = S_{400}(h^4 + k^4) + S_{004}l^4 + 3S_{220}h^2k^2 + 3S_{202}(h^2l^2 + k^2l^2). \quad (3.3.37)$$

Trigonal ($\bar{3}$, rhombohedral setting, five coefficients):

$$\Gamma_{sL}^2 = S_{400}(h^4 + k^4 + l^4) + 3S_{220}(h^2k^2 + h^2l^2 + k^2l^2) + 2S_{310}(h^3k + k^3l + hl^3) + 2S_{130}(h^3l + kl^3 + hl^3) + 4S_{211}(h^2kl + hk^2l + hkl^2). \quad (3.3.38)$$

The pair of coefficients S_{310} and S_{130} cannot normally be independently determined owing to exact reflection overlaps. Thus, equation (3.3.39) is normally used for both rhombohedral symmetries:

Trigonal ($\bar{3}m$, rhombohedral setting, four coefficients):

$$\Gamma_{sL}^2 = S_{400}(h^4 + k^4 + l^4) + 3S_{220}(h^2k^2 + h^2l^2 + k^2l^2) + 2S_{310}(h^3k + k^3l + hl^3 + h^3l + kl^3 + hl^3) + 4S_{211}(h^2kl + hk^2l + hkl^2). \quad (3.3.39)$$

Trigonal ($\bar{3}$, five coefficients):

$$\Gamma_{sL}^2 = S_{400}(h^4 + k^4 + 2h^3k + 2hk^3 + 3h^2k^2) + S_{004}l^4 + 3S_{202}(h^2l^2 + k^2l^2 + hkl^2) + S_{301}(2h^3l - 2k^3l - 6hk^2l) + 4S_{211}(h^2kl + hk^2l). \quad (3.3.40)$$

The coefficient S_{301} cannot normally be independently determined owing to exact reflection overlaps. Thus, equation (3.3.42) is normally used for $\bar{3}$ Laue symmetry.

Trigonal ($\bar{3}m1$, four coefficients):

$$\Gamma_{sL}^2 = S_{400}(h^4 + k^4 + 2h^3k + 2hk^3 + 3h^2k^2) + S_{004}l^4 + 3S_{202}(h^2l^2 + k^2l^2 + hkl^2) + S_{301}(3h^2kl - 3hk^2l + 2h^3l - 2k^3l). \quad (3.3.41)$$

The coefficient S_{301} cannot normally be independently determined due to exact reflection overlaps. Thus, equation (3.3.43) is normally used for $\bar{3}m1$ Laue symmetry.

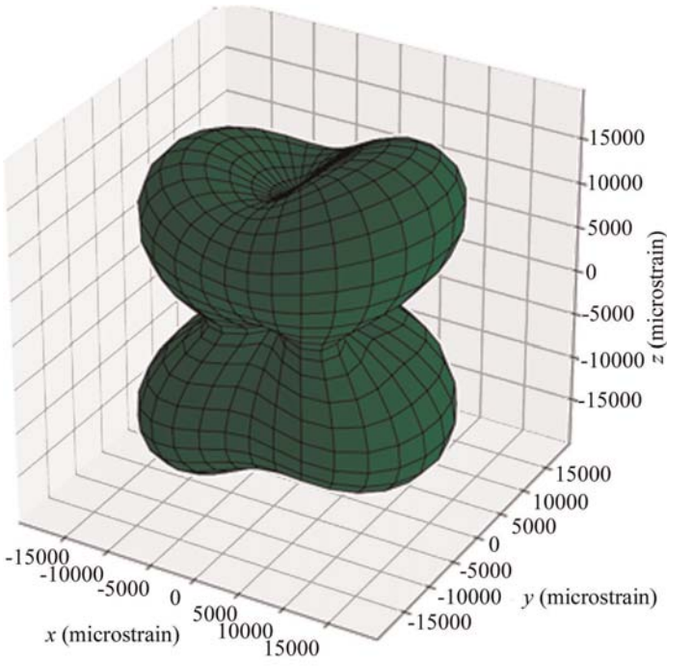

Figure 3.3.4
Microstrain surface for sodium parahydroxybenzoate multiplied by 10^6.

Trigonal ($\bar{3}1m$, four coefficients):

$$\Gamma_{sL}^2 = S_{400}(h^4 + k^4 + 2h^3k + 2hk^3 + 3h^2k^2) + S_{004}l^4 + 3S_{202}(h^2l^2 + k^2l^2 + hkl^2) + 4S_{211}(h^2kl + hk^2l). \quad (3.3.42)$$

Hexagonal (6/m and 6/mmm, three coefficients):

$$\Gamma_{sL}^2 = S_{400}(h^4 + k^4 + 2h^3k + 2hk^3 + 3h^2k^2) + S_{004}l^4 + 3S_{202}(h^2l^2 + k^2l^2 + hkl^2). \quad (3.3.43)$$

Cubic ($m\bar{3}$ and $m\bar{3}m$, two coefficients):

$$\Gamma_{sL}^2 = S_{400}(h^4 + k^4 + l^4) + 3S_{220}(h^2k^2 + h^2l^2 + k^2l^2). \quad (3.3.44)$$

These equations can be used with the refined values of the coefficients to produce a surface representing the extent of the microstrain in reciprocal space. The surface resulting from Stephens' (1999) analysis of powder diffraction data from sodium parahydroxybenzoate is shown Fig. 3.3.4. At the present time, the connection between the elastic properties and defects with these microstrain surface models is unclear. Some aspects of this for cubic and hexagonal systems are discussed in Chapter 5.1.

References

Avdeev, M., Jorgensen, J., Short, S. & Von Dreele, R. B. (2007). *On the numerical corrections of time-of-flight neutron powder diffraction data. J. Appl. Cryst.* **40**, 710–715.

Buras, B. & Holas, A. (1968). *Nukleonika*, **13**, 591–620.

Caglioti, G., Paoletti, A. & Ricci, F. P. (1958). *Choice of collimators for a crystal spectrometer for neutron diffraction. Nucl. Instrum.* **3**, 223–228.

Carpenter, J. M., Lander, G. H. & Windsor, C. G. (1984). *Instrumentation at pulsed neutron sources. Rev. Sci. Instrum.* **55**, 1019–1043.

Cheary, R. W. & Coelho, A. A. (1998*a*). *Axial divergence in a conventional X-ray powder diffractometer. I. Theoretical foundations. J. Appl. Cryst.* **31**, 851–861.

Cheary, R. W. & Coelho, A. A. (1998*b*). *Axial divergence in a conventional X-ray powder diffractometer. II. Realization and evalua-*

tion in a fundamental-parameter profile fitting procedure. J. Appl. Cryst. **31**, 862–868.
Cheary, R. W. & Coelho, A. (1992). *A fundamental parameters approach to X-ray line-profile fitting. J. Appl. Cryst.* **25**, 109–121.
Cheary, R. W., Coelho, A. A. & Cline, J. P. (2004). *Fundamental parameters line profile fitting in laboratory diffractometers. J. Res. Natl Inst. Stand. Technol.* **109**, 1–25.
Cole, I. & Windsor, C. G. (1980). *The lineshapes in pulsed neutron powder diffraction. Nucl. Instrum. Methods*, **171**, 107–113.
Cooper, M. J. & Sayer, J. P. (1975). *The asymmetry of neutron powder diffraction peaks. J. Appl. Cryst.* **8**, 615–618.
David, W. I. F. (1986). *Powder diffraction peak shapes. Parameterization of the pseudo-Voigt as a Voigt function. J. Appl. Cryst.* **19**, 63–64.
Finger, L. W., Cox, D. E. & Jephcoat, A. P. (1994). *A correction for powder diffraction peak asymmetry due to axial divergence. J. Appl. Cryst.* **27**, 892–900.
Glazer, A. M., Hidaka, M. & Bordas, J. (1978). *Energy-dispersive powder profile refinement using synchrotron radiation. J. Appl. Cryst.* **11**, 165–172.
Hastings, J. B., Thomlinson, W. & Cox, D. E. (1984). *Synchrotron X-ray powder diffraction. J. Appl. Cryst.* **17**, 85–95.
Howard, C. J. (1982). *The approximation of asymmetric neutron powder diffraction peaks by sums of Gaussians. J. Appl. Cryst.* **15**, 615–620.
Ikeda, S. & Carpenter, J. M. (1985). *Wide-energy-range, high-resolution measurements of neutron pulse shapes of polyethylene moderators. Nucl. Instrum. Methods Phys. Res. Sect. A*, **239**, 536–544.
Jorgensen, J. D., David, W. I. F. & Willis, B. T. M. (1992). *White-beam and time-of-flight neutron diffraction*. In *International Tables for Crystallography*, Vol. C, edited by A. J. C. Wilson. Dordrecht: Kluwer.
Jorgensen, J. D., Johnson, D. H., Mueller, M. H., Peterson, S. W., Worlton, J. G. & Von Dreele, R. B. (1978). *Profile analysis of pulsed-source neutron powder diffraction data*. Proceedings of the Conference on Diffraction Profile Analysis, Cracow 14–15 August 1978, pp. 20–22.
Jorgensen, J. D. & Rotella, F. J. (1982). *High-resolution time-of-flight powder diffractometer at the ZING-P″ pulsed neutron source. J. Appl. Cryst.* **15**, 27–34.
Laar, B. van & Yelon, W. B. (1984). *The peak in neutron powder diffraction. J. Appl. Cryst.* **17**, 47–54.
Malmros, G. & Thomas, J. O. (1977). *Least-squares structure refinement based on profile analysis of powder film intensity data measured on an automatic microdensitometer. J. Appl. Cryst.* **10**, 7–11.
Otto, J. W. (1997). *On the peak profiles in energy-dispersive powder X-ray diffraction with synchrotron radiation. J. Appl. Cryst.* **30**, 1008–1015.
Parrish, W. (1992). *Powder and related techniques: X-ray techniques*. In *International Tables for Crystallography*, Vol. C, edited by A. J. C. Wilson, ch. 2.3. Dordrecht: Kluwer.
Popa, N. C. (1998). *The (hkl) dependence of diffraction-line broadening caused by strain and size for all Laue groups in Rietveld refinement. J. Appl. Cryst.* **31**, 176–180.
Rietveld, H. M. (1967). *Line profiles of neutron powder-diffraction peaks for structure refinement. Acta Cryst.* **22**, 151–152.
Rietveld, H. M. (1969). *A profile refinement method for nuclear and magnetic structures. J. Appl. Cryst.* **2**, 65–71.
Robinson, R. A. & Carpenter, J. M. (1990). *On the use of switch functions in describing pulsed moderators*. Report LAUR 90-3125. Los Alamos National Laboratory, USA.
Stephens, P. W. (1999). *Phenomenological model of anisotropic peak broadening in powder diffraction. J. Appl. Cryst.* **32**, 281–289.
Thompson, P., Cox, D. E. & Hastings, J. B. (1987). *Rietveld refinement of Debye–Scherrer synchrotron X-ray data from Al_2O_3. J. Appl. Cryst.* **20**, 79–83.
Toby, B. H. & Von Dreele, R. B. (2013). *GSAS-II: the genesis of a modern open-source all-purpose crystallographic software package. J. Appl. Cryst.* **46**, 544–549.
Turberfield, K. C. (1970). *Time-of-flight neutron diffractometry*. In *Thermal Neutron Diffraction*, edited by B. T. M. Willis. Oxford University Press.
Von Dreele, R. B., Jorgensen, J. D. & Windsor, C. G. (1982). *Rietveld refinement with spallation neutron powder diffraction data. J. Appl. Cryst.* **15**, 581–589.
Wang, Y., Uchida, T., Von Dreele, R., Rivers, M. L., Nishiyama, N., Funakoshi, K., Nozawa, A. & Kaneko, H. (2004). *A new technique for angle-dispersive powder diffraction using an energy-dispersive setup and synchrotron radiation. J. Appl. Cryst.* **37**, 947–956.
Worlton, J. G., Jorgensen, J. D., Beyerlein, R. A. & Decker, D. L. (1976). *Multicomponent profile refinement of time-of-flight neutron diffraction data. Nucl. Instrum. Methods*, **137**, 331–337.
Young, R. A., Mackie, P. E. & von Dreele, R. B. (1977). *Application of the pattern-fitting structure-refinement method of X-ray powder diffractometer patterns. J. Appl. Cryst.* **10**, 262–269.
Young, R. A. & Wiles, D. B. (1982). *Profile shape functions in Rietveld refinements. J. Appl. Cryst.* **15**, 430–438.

International Tables for Crystallography (2019). Vol. H, Chapter 3.4, pp. 270–281.

3.4. Indexing a powder diffraction pattern

A. Altomare, C. Cuocci, A. Moliterni and R. Rizzi

3.4.1. Introduction

The crystal structure solution process presupposes that the crystal cell and the space group are known. In other words, the first step in the solution pathway is the identification of the unit-cell parameters. Knowledge of the crystal structure strongly depends on the determination of the cell: a cell incorrectly defined does not lead to the solution. The cell-determination process (which operates in a 6-dimensional continuous parameter space) is also called 'indexing' because it consists of assigning the appropriate triple (*hkl*) of Miller indices of the lattice plane to each of the N_l experimental diffraction lines (in a $3N_l$-dimensional integer-valued index space) (Shirley, 2003). (In this chapter, 'line' and 'peak' are used synonymously.) In the case of powder diffraction, the determination of the cell parameters is not a trivial task, and it is much more difficult than in the single-crystal case. This is because the information about the three-dimensional reciprocal space is compressed into the one-dimensional experimental powder pattern. Whatever the method used, working in the parameter or index space, powder pattern indexing aims to recover the three-dimensional information from the positions of the diffraction peaks in the observed profile. In particular, the experimental information used for carrying out the indexing process is the d_{hkl} interplanar spacings, which are related to the diffraction angles by the well known Bragg law:

$$2d_{hkl}\sin\theta_{hkl} = \lambda.$$

In theory, if we had available an experimental pattern at infinite resolution with well resolved peaks with no overlapping, the determination of the six cell parameters corresponding to a problem with six degrees of freedom would be easy (Shirley, 2003). In practice, only the first 20–30 observed lines are useful for two main reasons: (1) they are less sensitive to small changes in the cell parameters than the higher-angle lines; and (2) higher-angle lines (even if they seem to be single peaks) actually often consist of more than one overlapping peak and their positions cannot be accurately evaluated. Using higher-angle lines is therefore unwise. The successful outcome of powder pattern indexing is correlated to which and how many d_{hkl} values derived from the peaks in the diffraction pattern are selected and how reliable they are. Precision and accuracy in detecting peak positions are essential conditions for successful indexing (Altomare *et al.*, 2008). Unfortunately they can be degraded by different sources of errors: peak overlap, poor peak resolution, 2θ zero shift, errors in measurement, and a low peak-to-background ratio. Moreover, impurity lines (*i.e.* peaks from a different chemical phase in the sample to the compound being studied) can hinder the attainment of the correct result. The history of indexing, having its origin in the early 20th century (Runge, 1917), has produced several methods and software packages (Shirley, 2003; Werner, 2002) with surprising progress in strengthening and automating the cell-determination process. Innovative approaches that aim to reduce the dependence on the d_{hkl} values (by avoiding the peak-search step and considering the full information contained in the diffraction pattern) have also been developed. Despite great advances, powder pattern indexing is still a challenge in many cases. Factors that affect the success or failure of the process include: the presence of diffraction peaks from unexpected phases, the precision in the peak-position value, the size of the unit cell to be identified (indexing is easier if the unit cell is not too big) and the symmetry (indexing a pattern from a compound with high symmetry is generally more reliable than for a compound with lower symmetry). Before the zeroth step of the indexing process (the searching for peaks in the experimental pattern) it is always necessary to obtain good-quality diffraction data. Of course, the use of synchrotron radiation is preferable, but conventional laboratory X-ray data are usually suitable. Whether automated or manual, the peak search and each successive step of the indexing process must be carefully checked. For example, in a first attempt the positions that correspond to overlapping peaks could be set aside. If one attempt fails, the most useful tactic is to try another software package, since the programs available at present are based on different approaches.

The aim of this chapter is first to illustrate the background of the topic and the main theoretical approaches used to carry out the powder pattern indexing, and then to give some examples of applications. Section 3.4.2 is mainly devoted to the basic concepts of a crystalline lattice, the main indexing equations and figures of merits; Section 3.4.3 discusses the traditional and non-traditional methods developed for indexing a powder pattern, and Section 3.4.4 discusses some applications, referring to the most widely used indexing programs.

3.4.2. The basic concepts of indexing

We now describe some concepts that are fundamental in crystallography and useful for understanding the indexing process. The measured diffraction intensities correspond to the reciprocal-lattice points

$$\mathbf{r}^*_{hkl} = h\mathbf{a}^* + k\mathbf{b}^* + l\mathbf{c}^*.$$

The Miller indices (*hkl*) identify the plane of the direct lattice and $\mathbf{a}^*$, $\mathbf{b}^*$ and $\mathbf{c}^*$ are the three vectors of the reciprocal lattice, which are related to the direct lattice by

$$\mathbf{a} = \frac{\mathbf{b}^* \times \mathbf{c}^*}{V^*}, \quad \mathbf{b} = \frac{\mathbf{c}^* \times \mathbf{a}^*}{V^*}, \quad \mathbf{c} = \frac{\mathbf{a}^* \times \mathbf{b}^*}{V^*},$$

where

$$V^* = \mathbf{a}^* \cdot \mathbf{b}^* \times \mathbf{c}^*$$

is the reciprocal-cell volume (V^* is the inverse of the direct-unit-cell volume V).

In case of single-crystal data, the three-dimensional nature of the experimental diffraction data makes it easy to identify $\mathbf{a}^*$, $\mathbf{b}^*$, $\mathbf{c}^*$, from which the direct-space unit-cell vectors are derived (Giacovazzo, 2011).

In case of powder diffraction, the three-dimensional nature of the diffraction data is compressed into one dimension in the experimental pattern, and the accessible experimental information is the d_{hkl} values involved in the Bragg law and related to the

Table 3.4.1
Expressions for $Q(hkl)$ for different types of symmetry

Symmetry	$Q(hkl)$
Cubic	$(h^2 + k^2 + l^2)A_{11}$
Tetragonal	$(h^2 + k^2)A_{11} + l^2A_{33}$
Hexagonal	$(h^2 + hk + k^2)A_{11} + l^2A_{33}$
Orthorhombic	$h^2A_{11} + k^2A_{22} + l^2A_{33}$
Monoclinic	$h^2A_{11} + k^2A_{22} + l^2A_{33} + hlA_{13}$
Triclinic	$h^2A_{11} + k^2A_{22} + l^2A_{33} + hkA_{12} + hlA_{13} + klA_{23}$

diffraction angles by

$$d_{hkl} = \lambda/(2\sin\theta_{hkl}).$$

d_{hkl}, the spacing of the planes (hkl) in the direct lattice, is obtained by the dot products of the reciprocal-lattice vectors with themselves:

$$(\mathbf{r}^*_{hkl})^2 = \frac{1}{d^2_{hkl}} = h^2a^{*2} + k^2b^{*2} + l^2c^{*2} + 2hka^*b^*\cos\gamma^* + 2hla^*c^*\cos\beta^* + 2klb^*c^*\cos\alpha^*, \quad (3.4.1)$$

where α^* is the angle between $\mathbf{b}^*$ and $\mathbf{c}^*$, β^* is the angle between $\mathbf{c}^*$ and $\mathbf{a}^*$, and γ^* is the angle between $\mathbf{a}^*$ and $\mathbf{b}^*$. If we introduce

$$Q(hkl) = \frac{10^4}{d^2_{hkl}}$$

[where $Q(hkl)$ differs from $\sin^2\theta_{hkl}$ by a scale factor of $(200/\lambda)^2$], (3.4.1) becomes

$$Q(hkl) = h^2A_{11} + k^2A_{22} + l^2A_{33} + hkA_{12} + hlA_{13} + klA_{23}, \quad (3.4.2)$$

where

$$A_{11} = 10^4a^{*2},\ A_{22} = 10^4b^{*2},\ A_{33} = 10^4c^{*2},$$
$$A_{12} = 2\times10^4a^*b^*\cos\gamma^*,\ A_{13} = 2\times10^4a^*c^*\cos\beta^*,$$
$$A_{23} = 2\times10^4b^*c^*\cos\alpha^*.$$

The number of parameters A_{ij} in (3.4.2) depends on the type of symmetry: from 1 in the case of cubic symmetry to 6 for triclinic symmetry (see Table 3.4.1).

The quadratic form (3.4.2) relates the observed $Q(hkl)$ values to the reciprocal cell parameters and, consequently, to the direct cell. It is the basic equation used in powder-indexing procedures. Therefore the indexing problem (Werner, 2002) is to find A_{ij} and, for each observed $Q(hkl)$ value, three crystallographic indices (hkl) satisfying (3.4.2) within a suitable tolerance parameter Δ:

$$Q(hkl) - \Delta < h^2A_{11} + k^2A_{22} + l^2A_{33} + hkA_{12} + hlA_{13} + klA_{23} < Q(hkl) + \Delta. \quad (3.4.3)$$

The importance of using accurate $Q(hkl)$ values in (3.4.3) is obvious. Moreover, it is worth noticing that (3.4.3) must lead to physically reasonable indexing – low-angle peaks should correspond to small integer values for h, k and l and the values of the cell parameters and cell volume should be reasonable.

3.4.2.1. *Figures of merit*

An important task is the introduction of a figure of merit (FOM) that is able to (*a*) describe the physical plausibility of a trial cell and its agreement with the observed pattern, and (*b*) select the best cell among different possible ones. de Wolff (1968) made an important contribution in this direction. He developed the M_{20} figure of merit defined by

$$M_{20} = \frac{Q_{20}}{2\langle\varepsilon\rangle N_{20}}, \quad (3.4.4)$$

where Q_{20} is the Q value corresponding to the 20th observed and indexed peak, N_{20} is the number of different calculated Q values up to Q_{20}, and $\langle\varepsilon\rangle$ is the average absolute discrepancy between the observed and the calculated Q values for the 20 indexed peaks; the factor 2 is a result of statistics, explained by the larger chance for an observed line to sit in a large interval as compared with sitting in a small interval. The rationale behind M_{20} is as follows: the better the agreement between the calculated and the observed peak positions (the smaller the $\langle\varepsilon\rangle$ value) and the smaller the volume of the unit cell (the smaller the N_{20} value), the larger the M_{20} value and consequently the confidence in the proposed unit cell. A rule of thumb for M_{20} is that if the number of unindexed peaks whose Q values are less than Q_{20} is not larger than 2 and if $M_{20} > 10$, then the indexing process is physically reasonable (de Wolff, 1968; Werner, 2002). This rule is often valid, but exceptions occur. The use of the first 20 peaks is a compromise (coming from experience) between introducing a quite large number of observed peaks (depending on the number of parameters of the unit cell) and avoiding the use of high-angle peak positions, which are more affected by errors. M_{20} is statistically expected to be 1 in case of completely arbitrary indexing. It has no upper limit (it can be very large when $\langle\varepsilon\rangle$ is very small).

Smith & Snyder (1979) proposed the F_N criterion in order to overcome the limits of M_{20} with respect to its dependence on the 20 lines and on crystal class and space group. The F_N figure of merit is given by

$$F_N = \frac{1}{\langle|\Delta2\theta|\rangle}\frac{N}{N_{\rm poss}},$$

where $\langle|\Delta2\theta|\rangle$ is the average absolute discrepancy between the observed and calculated 2θ peak position values and $N_{\rm poss}$ is the number of possible diffraction lines up to the Nth observed line. The values of $\langle|\Delta2\theta|\rangle$ and $N_{\rm poss}$, $(\langle|\Delta2\theta|\rangle, N_{\rm poss})$, are usually given with F_N. With respect to M_{20}, F_N is more suitable for ranking the trial solutions and less for indicating their physical plausibility (Werner, 2002).

Both M_{20} and F_N, being based on the discrepancies between observed and calculated lines, are less reliable if there are impurity peaks; if the information about the unindexed lines is not taken into account, the risk of obtaining false solutions increases. Alternative FOMs based on joint probability have also been proposed (Ishida & Watanabe, 1967, 1971). Among the recently developed FOMs, we mention:

(1) $Q_{\rm partial}$ (Bergmann, 2007):

$$Q_{\rm partial} = \sum_i \min\left[w_i, \left(\frac{x_i - \hat{x}_i}{\delta_i}\right)^2\right],$$

where the summation is over the number of observed lines, w_i is the observed weight of line i, x and $\hat{x}_i$ are the observed and simulated line positions, respectively, and δ_i is the observed random error of line i. $Q_{\rm partial}$ is multiplied by a factor that depends on the symmetry of the simulated lattice (triclinic, ..., cubic), on the unit cell volume and on the number of ignored peaks.

(2) McM_{20} (Le Bail, 2008):

$$McM_{20} = [100/(R_pN_{20})]B_rS_y,$$

where N_{20} is the number of possible lines that might exist up to the 20th observed line (for a primitive P lattice). R_p is

the profile R factor (Young, 1993). B_r is a factor arbitrarily set to 6 for F and R Bravais lattices, 4 for I, 2 for A, B and C, and 1 for P. S_y is a factor equal to 6 for a cubic or a rhombohedral cell, 4 for a trigonal, hexagonal or tetragonal cell, 2 for an orthorhombic cell, and 1 for a monoclinic or triclinic cell.

(3) WRIP20 (Altomare *et al.*, 2009):

$$\mathrm{WRIP20} = \mathrm{RAT}_{Rp}^{2} \times \mathrm{RAT}_{\mathrm{Ind}} \times \mathrm{RAT}_{\mathrm{Pres}} \times w_u \times \mathrm{RAT}_{M20}^{1/2}. \quad (3.4.5)$$

Based on M_{20} (M_{20} and F_N remain the most widely used FOMs), WRIP20 has been developed for exploiting the full information contained in the diffraction profile. The factors that appear in (3.4.5) are

$$\mathrm{RAT}_{Rp} = \frac{1 - R_p}{1 - (R_p)_{\min}}, \quad \mathrm{RAT}_{\mathrm{Ind}} = \frac{\mathrm{PERC}_{\mathrm{Ind}}}{(\mathrm{PERC}_{\mathrm{Ind}})_{\max}},$$

$$\mathrm{RAT}_{\mathrm{Pres}} = \frac{(\mathrm{PERC}_{\mathrm{Pres}})_{\min}}{\mathrm{PERC}_{\mathrm{Pres}}}, \quad w_u = (N_{\mathrm{obs}} - N_u)/N_{\mathrm{obs}},$$

$$\mathrm{RAT}_{M20} = \frac{M_{20}}{(M_{20})_{\max}}, \quad \mathrm{PERC}_{\mathrm{Pres}} = \sum_{\mathrm{Pres}} \mathrm{mult} / \sum_{\mathrm{all}} \mathrm{mult}.$$

R_p is the profile-fitting agreement calculated after the Le Bail (Chapter 3.5) decomposition of the full pattern using the space group with the highest Laue symmetry compatible with the geometry of the current unit cell and no extinction conditions. $\mathrm{PERC}_{\mathrm{Ind}}$, the percentage of independent observations in the experimental profile, is estimated according to Altomare *et al.* (1995). For each extinction symbol compatible with the lattice geometry of the current unit cell, normalized intensities are calculated and subjected to statistical analysis in order to obtain a probability value associated with each extinction symbol in accordance with Altomare *et al.* (2004, 2005). For the extinction symbol with the highest probability value, the value of $\mathrm{PERC}_{\mathrm{Pres}}$ is calculated: $\sum_{\mathrm{all}} \mathrm{mult}$ is the total number of reflections (symmetry-equivalent included) for the space group having the highest Laue symmetry and no extinction conditions. (It varies with the volume of the unit cell and the data resolution.) $\sum_{\mathrm{Pres}} \mathrm{mult}$, which varies according to the extinction rules of the current extinction symbol, coincides with the number of non-systematically absent reflections (with the symmetry equivalents included). The subscripts min and max mark the minimum and the maximum values of each factor respectively, calculated for the possible unit cells that are to be ranked. N_{obs} and N_u are the number of observed and unindexed lines, respectively. All the terms in (3.4.5) are between 0 and 1, so ensuring that WRIP20 also lies between 0 and 1. In addition, WRIP20 has the following properties: (*a*) it is continuous, that is, definable in any interval of the experimental pattern; (*b*) it takes into account the peak intensities, the number of generated peaks and their overlap, and the systematically absent reflections (through the extinction-symbol test); and (*c*) it is not very sensitive to the presence of impurity lines (these usually have low intensities). WRIP20 is effective in finding the correct cell among a number of possible ones and selecting the corresponding most probable extinction symbol (see Example 3 in Section 3.4.4.6.2).

(4) Two new figures of merit based on de Wolff's method, the reversed figure of merit (M_n^{Rev}) and the symmetric figure of merit (M_n^{Sym}), have recently been proposed (Oishi-Tomiyasu, 2013). As observed by Oishi-Tomiyasu, the de Wolff figure of merit M_n does not use the observed and calculated lines in a symmetrical way, consequently it is (*a*) insensitive to computed but unobserved lines (*i.e.*, extinct peaks) and (*b*) sensitive to unindexed observed lines (*e.g.*, impurity peaks). M_n^{Rev} and M_n^{Sym} aim to compensate for the disadvantages of M_n. In particular, M_n^{Rev} has characteristics opposite to those of M_n with regard to sensitivity to extinct reflections and impurity peaks, and M_n^{Sym} has intermediate properties between M_n and M_n^{Rev}. They prove useful in selecting the correct solution, particularly in case of presence of impurity peaks. (See also Section 3.4.4.3.)

3.4.2.2. *Geometrical ambiguities*

Before discussing the concept of geometrical ambiguity in indexing, it is useful to introduce the definition of a reduced cell. While a unit cell defines the lattice, a lattice can be described by an unlimited number of cells. The Niggli reduced cell (Niggli, 1928) is a special cell able to uniquely define a lattice. Methods and algorithms have been derived for identifying the reduced cell starting from an arbitrary one (Buerger, 1957, 1960; Santoro & Mighell, 1970; Mighell, 1976, 2001). The reduced cell has the advantage of introducing a definitive classification, making a rigorous comparison of two lattices possible in order to establish whether they are identical or related (Santoro *et al.*, 1980). An algorithm based on the converse-transformation theory has been developed and implemented in the Fortran program *NIST*LATTICE* for checking relationships between any two cells (Karen & Mighell, 1991).

It is very important to recognize that two lattices are derivative of each other, because many crystallographic problems (twinning, indexing of powder patterns, single-crystal diffractometry) stem from the derivative properties of the lattices. Derivative lattices are classified as super-, sub- or composite according to the transformation matrices that relate them to the lattice from which they are derived (Santoro & Mighell, 1972).

A further obstacle to the correct indexing of a powder pattern is the problem of geometrical ambiguities. It may occur when '*two or more different lattices, characterized by different reduced forms, may give calculated powder patterns with the identical number of distinct lines in identical 2θ positions*' (Mighell & Santoro, 1975). The number of planes (*hkl*) contributing to each reflection may differ, however. Such ambiguity, due to the fact that the powder diffraction pattern only contains information about the length of the reciprocal-lattice vector and not the three-dimensional vector itself, is geometrical. It mainly occurs for high-symmetry cells (from orthorhombic up). The lattices having this property are related to each other by rotational transformation matrices. In Table 3.4.2 some examples of lattices giving geometrical ambiguities and the corresponding transformation matrices are given (Altomare *et al.*, 2008). Where there are geometrical ambiguities, additional prior information (*e.g.*, a single-crystal study) may be useful in order to choose one of the two possible lattices.

A recent procedure developed by Kroll *et al.* (2011) aims to reveal numerical and geometrical relationships between different reciprocal lattices and unit cells. The procedure is based on the assumption that distinct unit cells with lines in the same 2θ positions are derivatives of each other. However, two non-derivative lattices can have identical peak positions. Very recently, Oishi-Tomiyasu (2014*a*, 2016) has developed a new algorithm able to obtain all lattices with computed lines in the same positions as a given lattice. (See also Section 3.4.4.3.)

Table 3.4.2
Examples of lattices leading to geometrical ambiguities

$\boldsymbol{P} = \{P_{ij}\}$ is the transformation matrix from lattice I to lattice II, described by the vectors $\{\mathbf{a}_i\}$ and $\{\mathbf{b}_i\}$, respectively, with $\mathbf{b}_i = \sum_j P_{ij}\mathbf{a}_j$.

Lattice I	Lattice II	$\boldsymbol{P}$
Cubic *P*	Tetragonal *P*	$\begin{pmatrix} 0 & -1/2 & 1/2 \\ 0 & 1/2 & 1/2 \\ -1 & 0 & 0 \end{pmatrix}$
Cubic *I*	Tetragonal *P*	$\begin{pmatrix} 0 & -1/2 & 1/2 \\ 0 & -1/2 & -1/2 \\ 1/2 & 0 & 0 \end{pmatrix}$
	Orthorhombic *F*	$\begin{pmatrix} -1/3 & -1/3 & 0 \\ 0 & 0 & -1 \\ 1 & -1 & 0 \end{pmatrix}$
	Orthorhombic *P*	$\begin{pmatrix} 1/4 & -1/4 & 0 \\ 0 & 0 & 1/2 \\ -1/2 & -1/2 & 0 \end{pmatrix}$
Cubic *F*	Orthorhombic *C*	$\begin{pmatrix} -1/2 & 0 & 1/2 \\ 0 & 1 & 0 \\ -1/4 & 0 & -1/4 \end{pmatrix}$
	Orthorhombic *I*	$\begin{pmatrix} -1/6 & 0 & -1/6 \\ 1/2 & 0 & -1/2 \\ 0 & -1 & 0 \end{pmatrix}$
Hexagonal	Orthorhombic *P*	$\begin{pmatrix} 1/2 & 1/2 & 0 \\ 1/2 & -1/2 & 0 \\ 0 & 0 & -1 \end{pmatrix}$
Rhombohedral	Monoclinic *P*	$\begin{pmatrix} -1/2 & 0 & -1/2 \\ 1/2 & 0 & -1/2 \\ 0 & -1 & 0 \end{pmatrix}$

3.4.3. Indexing methods

Indexing methods aim to reconstruct the three-dimensional direct lattice from the one-dimensional distribution of d_{hkl} values. Systematic or accidental peak overlap, inaccuracy of peak positions, zero shift in the $2\theta_{hkl}$ Bragg angles and/or the presence of impurity peaks make the reconstruction difficult. Data accuracy is fundamental for increasing the probability of success; as emphasized by de Wolff: '*The 'indexing problem' is essentially a puzzle: it cannot be stated in rigorous terms (...). It would be quite an easy puzzle if errors of measurements did not exist*' (de Wolff, 1957).

Different approaches have been proposed for solving the indexing puzzle since the pioneering work of Runge (1917). As suggested by Shirley (2003), indexing procedures work in parameter space, or in index space, or in both spaces. As a general consideration, the parameter space allows the inclusion of the cell information and constraints, while the index space is more suitable in cases where there are accidental or systematic absences (Shirley, 1980). In this section an outline of the strategies and search methods adopted by the main traditional and non-traditional indexing approaches is given. For more details see the papers by Shirley (2003) and Bergmann *et al.* (2004).

Among the main indexing procedures, zone indexing (Section 3.4.3.1.1), SIW heuristic (Section 3.4.3.1.2), successive dichotomy (Section 3.4.3.1.5), the topographs method (Section 3.4.3.2.1) and global-optimization methods (Section 3.4.3.2.2) operate in the parameter space; index heuristics (Section 3.4.3.1.3) and index permutation (Section 3.4.3.1.4) work in the index space; and scan/covariance (Bergmann, 2007) operates both in index and parameter space. Each method can be classified as exhaustive or not. An exhaustive method systematically and rigorously searches in the solution space; a non-exhaustive method exploits coincidences and relations between the observed lines with the aim of finding the solution quickly. The classification is not rigorous: approaches that try to combine rigour and speed can be defined as semi-exhaustive (Table 3.4.3).

Indexing procedures can also be classified as traditional and non-traditional. Each indexing method generates a list of possible cells. Their reliability is assessed by FOMs with the aim of selecting the correct one (see Section 3.4.2.1).

3.4.3.1. *Traditional indexing methods*

The traditional indexing approaches adopted over the last century are based on the following strategies and search methods: (1) zone indexing, (2) SIW heuristic, (3) index heuristics, (4) index permutation and (5) successive dichotomy. All of them exploit information about a limited number of observed peak positions.

3.4.3.1.1. *Zone-indexing strategy*

The zone-indexing strategy was originally developed by Runge (1917), successively proposed by Ito (1949, 1950), generalized by de Wolff (1957, 1958) and enhanced by Visser (1969). This approach is based on the search for zones, *i.e.*, crystallographic planes, in the reciprocal lattice, defined by the origin O and two lattice points. If $\mathbf{r}^*_{hkl}$ and $\mathbf{r}^*_{h'k'l'}$ are two vectors in reciprocal space, *i.e.* the positional vectors of the lattice points A and A′, they describe a zone containing any lattice point B whose positional vector is of type $m\mathbf{r}^*_{hkl} \pm n\mathbf{r}^*_{h'k'l'}$, where m and n are positive integers. If ω is the angle between $\mathbf{r}^*_{hkl}$ and $\mathbf{r}^*_{h'k'l'}$, the squared distance of B from O (*i.e.*, $Q_{m,n}$) can be expressed by (de Wolff, 1958; Visser, 1969)

$$Q_{m,n} = m^2 Q_{\rm A} + n^2 Q_{\rm A'} \pm mnR, \qquad (3.4.6)$$

where $Q_{\rm A} = Q(hkl)$ and $Q_{\rm A'} = Q(h'k'l')$ are the squared distances of A and A′ from O, respectively, and $R = 2(Q_{\rm A}Q_{\rm A'})^{1/2}\cos\omega$. R can be derived as

$$R = |Q_{m,n} - m^2 Q_{\rm A} - n^2 Q_{\rm A'}|/mn. \qquad (3.4.7)$$

The method is applied as follows: $Q_{\rm A}$ and $Q_{\rm A'}$ are chosen among the first experimental Q_i values; the $\{Q_i\}$, up to a reasonable resolution, are introduced in (3.4.7) in place of $Q_{m,n}$; and a few positive integer values are assigned to m and n. Equation (3.4.7) provides a large number of R values; equal R values (within error limits) define a zone, for which the ω angle can easily be calculated. The search for zones is performed using different $(Q_{\rm A}, Q_{\rm A'})$ pairs. The R values that are obtained many times identify the most important crystallographic zones. The zones are sorted according to a quality figure, enabling selection of the best ones. In order to find the lattice, all possible combinations of the best zones are tried. For every pair of zones the intersection line is found, then the angle between them is determined and the lattice is obtained.

The method has the advantage of being very efficient for indexing low-symmetry patterns. The main disadvantage is its sensitivity to errors in the peak positions, particularly in the low 2θ region.

3.4.3.1.2. *Shirley–Ishida–Watanabe (SIW) heuristic strategy*

This needs only one single well-established zone, then it arbitrarily chooses the 001 line from the first-level lines. The indexing problem is thus lowered to two dimensions and an exhaustive search is carried out.

3.4.3.1.3. *Index-heuristics strategy*

The index-heuristics strategy searches for the correct cell *via* a trial-and-error approach, assigning tentative Miller indices to a few experimental peak positions (basis lines), usually belonging to the low 2θ region of the experimental pattern. It was first proposed by Werner (1964), then successively refined (Werner *et al.*, 1985) and made more robust and effective (Altomare *et al.*, 2000, 2008, 2009). This approach, which works in the index space, was defined by Shirley as semi-exhaustive (Shirley, 1980). The search starts from the highest-symmetry crystal system (cubic) and, if no plausible solution is found, it is extended to lower symmetry down to triclinic. The number of selected basis lines increases as the crystal symmetry lowers. A dominant zone occurs when one cell axis is significantly shorter than the other two; in this case most of the first observed lines (in terms of increasing $2\theta_{hkl}$ values) can be indexed with a common zero Miller index. Special short-axis tests, aimed at finding two-dimensional lattices, have been proposed for monoclinic symmetry in order to detect the presence of dominant zones (Werner *et al.*, 1985). The index-heuristics method is based on the main indexing equation [see equation (3.4.2)] that can be rewritten (Werner *et al.*, 1985) as

$$Q(hkl) = h^2x_1 + k^2x_2 + l^2x_3 + hkx_4 + hlx_5 + klx_6,$$

where $\{x_i\} = X$ is the vector of unknown parameters, which are derived by solving a system of linear equations

$$\mathbf{MX} = \mathbf{Q}, \tag{3.4.8}$$

where $\mathbf{M}$ is a matrix of Miller indices and $\mathbf{Q}$ is the vector of the selected $Q(hkl)$ values corresponding to the basis lines. The dimensions of $\mathbf{M}$, $\mathbf{X}$ and $\mathbf{Q}$ change according to the assumed symmetry. From the inverse matrix $\mathbf{M}^{-1}$ the corresponding $\mathbf{X}$ is obtained *via* $\mathbf{X} = \mathbf{M}^{-1}\mathbf{Q}$. In the case of monoclinic and higher symmetry, $\{x_i\}$ are calculated by Cramer's rule. Different $\mathbf{X}$ vectors are derived by using a different selection of basis lines. The possible solutions are checked by using the full list of peak positions (up to the first 25 experimental lines). The method is sensitive to errors on peak positions and to the presence of impurities (the presence of only one impurity peak is not critical). The correctness of the $\{x_i\}$ strongly depends on the accuracy of the observed Q values, especially for low-2θ region lines, which are the most dominant ones for this indexing procedure. The possibility of testing different combinations of basis-line sets enables the correct cell to be found by bypassing the cases for which errors in the basis lines occur.

The method has been recently enhanced (Altomare *et al.*, 2000, 2009) by introducing new procedures that are able to increase the probability of successful indexing (see Section 3.4.4.2.1); among them are: (1) a correction for systematic errors in the experimental 2θ values (positive and negative trial 2θ zero shifts are taken into account); this correction should, in principle, describe a real diffractometer error; in practice, it also approximates the specimen displacement error well (perhaps coupled with transparency for organic samples); (2) a more intensive search in solution space for orthorhombic and monoclinic systems; (3) an improvement of the triclinic search; (4) a new figure of merit, WRIP20, which is more powerful than M_{20} in identifying the correct solution among a set of possible ones (see Section 3.4.2.1); (5) a check for geometrical ambiguities; (6) an automatic refinement of the possible cells; and (7) a statistical study of the parity of the Miller indices, performed at the end of the cell refinement, aimed at detecting doubled axes or additional lattice points (for *A*-, *B*-, *C*-, *I*-, *R*- or *F*-centred cells) (such information is used in the successive steps).

3.4.3.1.4. *Index-permutation strategy*

This strategy was proposed by Taupin (1973), and is based on a systematic permutation of indices associated to observed lines for obtaining candidate cells. Because this trial-and-error strategy is similar to the index-heuristics approach, we do not describe it here.

3.4.3.1.5. *Successive-dichotomy search method*

The successive-dichotomy method, first developed by Louër & Louër (1972), is based on an exhaustive strategy working in direct space (except for triclinic systems, where it operates in reciprocal space) by varying the lengths of the cell axes and the interaxial angles within finite intervals. The search for the correct cell is performed in an n-dimensional domain D (where n is the number of cell parameters to be determined). If no solution belongs to D, the domain is discarded and the ranges for the allowed values of cell parameters are increased; on the contrary, if D contains a possible solution, it is explored further by dividing the domain into 2^n subdomains *via* a successive-dichotomy procedure. Each subdomain is analysed and discarded if it does not contain a solution. The method was originally applied to orthorhombic and higher-symmetry systems (Louër & Louër, 1972), but it has been successively extended to monoclinic (Louër & Vargas, 1982) and to triclinic systems (Boultif & Louër, 1991). The search can be performed starting from cubic then moving down to lower symmetries (except for triclinic) by partitioning the space into shells of volume $\Delta V = 400$ Å^3. For triclinic symmetry ΔV is related to the volume $V_{\rm est}$ suggested by the method proposed by Smith (1977), which is able to estimate the unit-cell volume from only one line in the pattern:

$$V_{\rm est} \simeq \frac{0.60 d_N^3}{\frac{1}{N} - 0.0052},$$

where d_N is the value for the Nth observed line; in the case $N = 20$ the triclinic cell volume is $V_{\rm est} \simeq 13.39 d_{20}^3$.

Let us consider, as an example, the monoclinic case; in terms of direct cell parameters, $Q(hkl)$ is given by (Boultif & Louër, 1991)

$$Q(hkl) = f(A, C, \beta) + g(B),$$

where $f(A, C, \beta) = h^2/A^2 + l^2/C^2 - 2hl\cos\beta/(AC)$, $A = a\sin\beta$, $C = c\sin\beta$, $g(B) = k^2/B^2$ and $B = b$. The search using the successive-dichotomy method is performed in a four-dimensional space that is covered by increasing the integer values i, l, m and n in the intervals $[A_-, A_+] = [A_- = A_0 + ip, A_+ = A_- + p]$, $[B_-, B_+] = [B_- = B_0 + lp, B_+ = B_- + p]$, $[C_-, C_+] = [C_- = C_0 + mp, C_+ = C_- + p]$ and $[\beta_-, \beta_+] = [\beta_- = 90 + n\theta, \beta_+ = \beta_- + \theta]$, where the step values of p and θ are 0.4 Å and 5°, respectively, and A_0, B_0 and C_0 are the lowest values of A, B and C (based on the positions of the lowest-angle peaks), respectively. Each quartet of intervals

defines a domain D and, by taking into account the current limits for the parameters A, B, C and β, a calculated pattern is generated, not in terms of discrete $Q(hkl)$ values but of allowed intervals $\left[Q_-(hkl), Q_+(hkl)\right]$. D is retained only if the observed Q_i values belong to the range $[Q_-(hkl) - \Delta Q_i, Q_+(hkl) + \Delta Q_i]$, where ΔQ_i is the absolute error of the observed lines (*i.e.*, impurity lines are not tolerated). If D has been accepted, it is divided into 2^4 subdomains by halving the original intervals $[A_-, A_+]$, $[B_-, B_+]$, $[C_-, C_+]$ and $[\beta_-, \beta_+]$ and new limits $\left[Q_-(hkl), Q_+(hkl)\right]$ are calculated; if a possible solution is found, the dichotomy method is applied iteratively. In case of triclinic symmetry the expression for $Q(hkl)$ in terms of direct cell parameters is too complicated to be treated *via* the successive-dichotomy method; therefore the basic indexing equation (3.4.2) is used. In this case, the $[Q_-(hkl), Q_+(hkl)]$ intervals are set in reciprocal space according to the A_{ij} parameters of (3.4.2). To reduce computing time the following restrictions are put on the (hkl) Miller indices associated with the observed lines: (1) maximum h, k, l values equal to 2 in case of the first five lines; (2) $h + k + l < 3$ for the first two lines.

The outcome of the successive-dichotomy method is not strongly influenced by the presence of a dominant zone. New approaches have been devoted to overcome the limitations of the method with a strict dependence on data accuracy and on impurities (Boultif & Louër, 2004; Louër & Boultif, 2006, 2007), see Section 3.4.4.2).

3.4.3.2. *Non-traditional indexing methods*

New indexing procedures that provide alternatives to the traditional approaches outlined in Section 3.4.3.1 have recently been proposed.

3.4.3.2.1. *The topographs method*

This method (Oishi *et al.*, 2009) is based on the Ito equation (de Wolff, 1957):

$$Q(\mathbf{h}_1 + \mathbf{h}_2) + Q(\mathbf{h}_1 - \mathbf{h}_2) = 2[Q(\mathbf{h}_1) + Q(\mathbf{h}_2)], \qquad (3.4.9)$$

where $Q(\mathbf{h})$ is the length of the reciprocal vector $\mathbf{r}^*_{hkl}$ corresponding to the Miller index vector $\mathbf{h} = (hkl)$. It uses Conway's topograph (Conway & Fung, 1997), a connected tree obtained by associating a graph to each equation of type (3.4.9) and consisting of infinite directed edges. According to Ito's method, if quadrupoles (Q_1, Q_2, Q_3, Q_4) detected among the observed Q_i values satisfy the condition $2(Q_1 + Q_2) = Q_3 + Q_4$, two Miller-index vectors $\mathbf{h}_1$ and $\mathbf{h}_2$ are expected to exist such that $Q_1 = Q(\mathbf{h}_1)$, $Q_2 = Q(\mathbf{h}_2)$, $Q_3 = Q(\mathbf{h}_1 - \mathbf{h}_2)$ and $Q_4 = Q(\mathbf{h}_1 + \mathbf{h}_2)$. If an additional value Q_5 satisfying the condition $2(Q_1 + Q_4) = Q_2 + Q_5$ is found, the graph of the quadrupole (Q_1, Q_2, Q_3, Q_4) grows *via* the addition of the Q_5 contribution; this procedure is iterated. If topographs share a Q value that corresponds to the same reciprocal-lattice vector, then a three-dimensional lattice is derived containing the two-dimensional lattices associated with the original topographs. Three-dimensional lattices are also obtained by combining topographs. The probability that topographs correspond to the correct cell increases with the number of edges of the graph structure. The method is claimed by the authors to be insensitive to the presence of impurity peaks.

3.4.3.2.2. *Global-optimization methods*

Global-optimization methods, widely adopted for solving crystal structures from powder data, have also been successfully applied to indexing. Among them, we provide brief descriptions of genetic algorithms, and Monte Carlo and grid-search methods.

3.4.3.2.2.1. Genetic-algorithm search method

The use of genetic algorithms (GAs) for solving the indexing problem was proposed by Tam & Compton (1995) and Paszkowicz (1996). Since then, Kariuki and co-workers (Kariuki *et al.*, 1999) have combined GAs with a whole-profile-fitting procedure for indexing powder diffraction patterns. This approach exploits the information of the full powder diffraction pattern. It is inspired by the Darwinian evolutionary principle based on mating, mutation and natural selection of the member of a population that survives and evolves to improve future generations. The initial population consists of a set of trial cell parameters, chosen randomly within a given volume range; a full pattern-decomposition process is performed using the Le Bail algorithm (Chapter 3.5) and the agreement between the calculated and observed profiles is derived and used for assessing the goodness of an individual member (*i.e.*, a set of unit-cell parameters). The most plausible cell is therefore found by exploring a six-dimensional hypersurface $R'_{wp}(a, b, c, \alpha, \beta, \gamma)$ and searching for the global minimum of R'_{wp} (see Section 3.4.4.3.2). In contrast to the main traditional methods, whose outcomes depend on the reliability of a set of peak positions, this procedure has the advantage of being insensitive to the presence of small impurity peaks that have a negligible influence on the agreement factor between the experimental and calculated profiles: the global minimum of R'_{wp} is reached if the majority phase is correctly indexed. The main disadvantage of the method is the computing time required, in particular in the case of low symmetry.

3.4.3.2.2.2. Monte Carlo search method

The Monte Carlo approach has also been applied to indexing powder diffraction patterns (Le Bail, 2004; Bergmann *et al.*, 2004; Le Bail, 2008). It exploits all the information contained in the full pattern, randomly generates and selects trial cell parameters, and calculates peak positions to which it assigns the corresponding Miller indices. An idealized powder pattern consisting of peak positions d and extracted intensities I is considered to test the trial cell. The cell reliability is assessed by suitable figures of merit (*e.g.* R_p and McM_{20}, see Section 3.4.2.1). The main drawback of this approach is the significant computing time required, in particular for triclinic systems.

3.4.3.2.2.3. Grid-search method

This performs an iterated 'step-and-repeat search' in the parameter space. It has the advantage of being flexible, exhaustive and not particularly sensitive to impurities or errors, and the disadvantage of being slow (Shirley, 2003).

3.4.4. Software packages for indexing and examples of their use

The different strategies and methods described in Section 3.4.3 have been implemented in a variety of automatic indexing programs (Bergman *et al.*, 2004). Almost all use one of the two different approaches working in parameter space (*i.e.*, unit-cell parameters) or index space (*i.e.*, reflection indices). Only the *EFLECH/INDEX* program (Bergman, 2007), applying the scan/covariance strategy, works in both spaces: in parameter space from cubic down to monoclinic, switching to index space for triclinic. The different indexing methods are classified according to Shirley (2003) in Table 3.4.3. Alternative classifications can be

Table 3.4.3
Classification of indexing methods

Method (strategy/search)	Space	Exhaustive
Zone indexing	Parameter	No
SIW heuristic	Parameter	Semi
Scan/covariance	Parameter (for cubic to monoclinic); index (for triclinic)	To monoclinic
Index heuristics	Index	Semi
Index permutation	Index	Yes
Successive dichotomy	Parameter	Yes
Grid search	Parameter	Yes
Genetic algorithms	Parameter	No
Monte Carlo	Parameter	No

made by considering whether a program works in direct or reciprocal space, or uses Bragg diffraction line positions or the whole experimental diffraction profile. Using the whole experimental diffraction profile requires a lot of computing time, but has become possible as a consequence of recent increases in the speed of computers. In the following, descriptions of the principal (default) steps of the most widely used indexing programs are given. Several non-default options are available for each program. The chances of success of the indexing step increase if more than one program is used.

3.4.4.1. *Traditional indexing programs*

3.4.4.1.1. *ITO (Visser, 1969)*

This program is based on the zone-indexing strategy and uses the Runge–Ito–de Wolff–Visser method of decomposition of the reciprocal space into zones, as described in Section 3.4.3.1.1.

The following steps are executed by the program:

(1) The potential zones are found always using the 20 lowest Bragg angle peaks. The program does not work with fewer peaks.
(2) All possible combinations of the six best zones (including the combination of each zone with itself) are found by searching for trial zones that share a row of common points. For every pair of such zones, the angle between them is found, thus giving a trial reciprocal lattice.
(3) The reduction of the resulting unit cells is carried out using the Delaunay–Ito method (Pecharsky & Zavalij, 2009).
(4) The program tries to index the first 20 lines and repeats this check after least-squares refinement of the unit-cell parameters.
(5) The figures of merit are calculated to assess the quality of each trial unit cell and the four best lattices are provided.

ITO is very efficient at indexing patterns with low symmetry and is only weakly sensitive to impurity peaks, if they occur at high angles. The most frequent causes of failure are inaccuracy or incompleteness of the input data.

3.4.4.1.2. *TREOR90 (Werner et al., 1985)*

Classified by Shirley (1980, 2003) as semi-exhaustive, *TREOR90* is based on the index-heuristics strategy (see Section 3.4.3.1.3) and uses a trial-and-error approach. It performs the following steps:

(1) Some basis lines are selected among the experimental d values, generally from the low-2θ region of the powder diffraction pattern. Five sets of basis lines are generally sufficient for orthorhombic tests, whereas more than seven sets may be necessary for the monoclinic system. At least 20–25 experimental d values are potentially required.
(2) The trial unit cells in the index space are searched by varying the Miller indices that are tentatively assigned to the basis lines.
(3) The analysis starts with cubic symmetry and, in a stepwise manner, tests for lower-symmetry crystal systems are performed. In the case of monoclinic symmetry, a special short-axis test is carried out.
(4) The solution of the linear system in equation (3.4.8) gives the possible cell parameters. Different combinations of the basis lines are tested.
(5) Each possible solution is checked by using the full list of experimental lines.
(6) The quality of the trial cell parameters is mainly assessed by using the M_{20} figure of merit [see equation (3.4.4)]. An effective rule for identifying a reliable solution is $M_{20} > 10$ and no more than one unindexed line.

The success of the program is related to the use of some suitable standard sets of parameter values (maximum unit-cell volume, maximum cell axis, tolerance of values *etc*.) arising from the accumulated experience of the authors; they can be easily changed by the user *via* suitable keywords in the input file.

3.4.4.1.3. *DICVOL91 (Boultif & Louër, 1991)*

This program works in direct space (down to the monoclinic system) by using the successive-dichotomy search method (see Section 3.4.3.1.5), which was introduced for the automatic indexing of powder diffraction patterns by Louër & Louër (1972). *DICVOL91* has been defined as exhaustive by Shirley (1980, 2003). Its main steps are:

(1) The unit-cell volume is partitioned by moving from high to low symmetry. Shells of 400 Å^3 of volume are scanned for all the symmetry systems except for triclinic; for the triclinic system the shells are based on the definition of volume proposed by Smith (1977) (see Section 3.4.3.1.5).
(2) A search using the successive-dichotomy method, based on suitable intervals (see Section 3.4.3.1.5), is carried out. In the case of the triclinic system the general expression for $Q(hkl)$ as function of the direct cell parameters is too complicated, and the reciprocal-space parameters in equation (3.4.2) are used for setting the intervals.
(3) The derived cell parameters are refined using the least-squares method.
(4) The quality of each trial unit cell is evaluated by using the M_N and F_N figures of merit (see Section 3.4.2.1).

The program is fast at performing exhaustive searches in parameter space (except for the triclinic case); on the other hand, its efficiency is strongly related to the quality of the data and to the presence of impurities (in fact, impurities are not permitted).

3.4.4.2. *Evolved indexing programs*

3.4.4.2.1. *N-TREOR09 (Altomare et al., 2009)*

Implemented in the *EXPO* program (Altomare *et al.*, 2013) to perform the powder pattern indexing step, *N-TREOR09* is an update of *N-TREOR* (Altomare *et al.*, 2000), which in turn is an evolution of *TREOR90*, and preserves the main strategies with some changes introduced to make the program more exhaustive and powerful. In particular:

(*a*) If the default indexing process fails, the unit-cell search is automatically repeated by changing some default choices, *e.g.*, increasing the tolerance value on the observed *d* values. If still no solution is obtained, the maximum (*hkl*) Miller indices assigned to the orthorhombic or monoclinic base lines are increased and the tolerance limits of the default values are halved in order to avoid the generation of wrong large unit cells.

(*b*) At the end of the first run, whatever the obtained results, a possible 2θ zero-position shift is taken into account: the indexing process starts again by applying positive and negative 2θ zero-position shifts to the original peak search result.

(*c*) An exhaustive triclinic search is performed. The dominant-zone tests that are usually carried out for the monoclinic system have been extended to include the triclinic case.

(*d*) A new figure of merit, WRIP20, more powerful than the classical M_{20}, is used. It is calculated when more than one possible cell is found and takes into account the M_{20} value, the full experimental pattern, the degree of reflection overlap, the systematically absent reflections and the number of unindexed lines (see Section 3.4.2.1).

This program is also able to index powder patterns from small proteins: see Example 4 in Section 3.4.4.6.2.

3.4.4.2.2. *DICVOL06 (Louër & Boultif, 2006, 2007) and DICVOL14 (Louër & Boultif, 2014)*

The most recent of a series of versions, *DICVOL14* is the successor of *DICVOL04* (Boultif & Louër, 2004) and *DICVOL06*. *DICVOL06* includes *DICVOL04* with its optimized search procedure and an extended search in shells of volumes. *DICVOL04* represented an improvement of *DICVOL91*. Among the features of *DICVOL06* are:

(*a*) A tolerance for unindexed lines that can result from the presence of unwanted additional phases or inaccurately measured peaks. The program can tolerate a user-defined number of unindexed lines. Care must be taken when using this option to avoid the possibility of generating erroneous cells. It is worth noting that the inclusion of the possibility of at least one unindexed peak has markedly increased the success rate of *DICVOL06*.

(*b*) A correction of the zero-point error in the measured data. *Via* an *a priori* zero-origin evaluation, two different approaches can be followed: (i) if there is a non-negligible zero shift (*i.e.*, ~0.1°), the reflection-pair method is adopted (Dong *et al.*, 1999); (ii) if the shift is small (<0.03°), a refinement of the experimental data zero point together with the cell parameters is carried out as soon as a solution is found. In the monoclinic and triclinic systems, a reduced-cell analysis is performed to choose among equivalent solutions.

(*c*) When a solution is found in a 400 Å^3 shell of volume, the exhaustive search is extended to the whole domain.

No formal limits on the number of input Bragg peaks have been established but, for reliable indexing, it is recommended that 20 or more peaks (in the low-2θ region) are used.

Compared to *DICVOL04*/*DICVOL06*, *DICVOL14* includes: an optimization of filters in the final stages of the convergence of the successive dichotomy process; an optimization and extension of scanning limits for the triclinic case; a new approach for zero-point offset evaluation; a detailed review of the input data from the resulting unit cells; and cell centring tests. *DICVOL14* has been improved particularly for triclinic cases, which are generally the most difficult to solve with the dichotomy algorithm.

3.4.4.3. *Non-traditional indexing programs*

The indexing programs described above are based on using, for a limited number of lines, the measured positions of peak maxima as directly obtained from the experimental powder diffraction pattern. *Conograph* (Oishi-Tomiyasu, 2014*b*), which has been more recently proposed, also belongs to that group of programs. A brief description of *Conograph* follows

3.4.4.3.1. *Conograph: indexing via the topographs method*

Conograph is based on the topographs method, and its main functions are the determination of the primitive unit cell and lattice symmetry, and refinement of lattice parameters. Among the main features we note:

(1) A new Bravais-lattice determination algorithm (Oishi-Tomiyasu, 2012), which has been proved to be stable with respect to peak-position errors under very general conditions. The algorithm applies the Minkowski reduction to primitive cells and the Delaunay reduction (Delaunay, 1933) to face-centred, body-centred, rhombohedral and base-centred cells in such a way that the computational efficiency of the process is better than the Andrews & Bernstein (1988) method.

(2) The two figures of merit $M_n^{\rm Rev}$ and $M_n^{\rm Sym}$ proposed by Oishi-Tomiyasu (2013) are used for for selecting the true unit cells. They are also used to estimate the zero-point shift.

(3) The use of many observed peaks in the default setting, which aims to make *Conograph* robust against dominant zones and missing or false peaks (Oishi-Tomiyasu, 2014*b*).

(4) The method for exhaustively searching unit cells that involve geometrical ambiguity (Oishi-Tomiyasu, 2014*a*, 2016). The geometrical ambiguities that are detected also include lattices with very similar calculated lines, because of the error tolerance in the *d* spacings.

Programs that use only the measured positions of peak maxima are particularly vulnerable to experimental errors in the measured peak positions and to the presence of impurity peaks. For these reasons, at the end of the 1990s new indexing strategies were developed that do not require the peak locations in the experimental pattern. These approaches are completely different from the methods described above because they use the whole diffraction profile. They try to explore the parameter space (direct space) exhaustively by applying different optimization techniques in order to find the cells in best agreement with the experimental powder diffraction pattern. Some of the most widely used indexing programs in direct space are described here.

3.4.4.3.2. *GAIN: indexing via a genetic-algorithm search method*

The use of genetic algorithms (GAs) for indexing powder diffraction data by exploiting the diffraction geometry (as in the traditional indexing methods) was firstly proposed by Tam & Compton (1995) and Paszkowicz (1996). Subsequently, Kariuki *et al.* (1999) applied GA techniques by using whole profile fitting with the aim of exploring the parameter space $\{a, b, c, \alpha, \beta, \gamma\}$ and finding the global minimum of the *R*-factor $\{a, b, c, \alpha, \beta, \gamma\}$ hypersurface, yielding the parameter set able to generate the best agreement between the observed and calculated powder diffraction patterns.

This new strategy has been implemented in the program *GAIN* (Harris *et al.*, 2000), whose main features are:

(1) Starting from a population of N_p sets of lattice parameters and using the evolutionary operations of mating, mutation and natural selection, the population is allowed to evolve

through several generations, with the aim of generating sets of possible trial cell parameters.
(2) The search procedure, using a GA, is performed in restricted, sensible cell-volume ranges consistent with the knowledge of the system under study.
(3) For each set of trial parameters a calculated powder diffraction pattern is constructed. The peak positions and parameters describing the shape and width of each peak are used in the Le Bail profile-fitting procedure (Chapter 3.5).
(4) The pattern is split into different regions (defined by the user), and the weighted profile R factor is calculated for each region; all the values are summed to obtain the overall $R'_{\rm wp}$:

$$R'_{\rm wp} = \sum_{\rm regions} \left[\frac{\sum_i w_i (y_i - y_{ci})^2}{\sum_i w_i y_i^2} \right]^{1/2},$$

where the summation is over the regions, i runs over the experimental points belonging to each region and y_i and y_{ci} are the observed and calculated profile at the ith experimental step, respectively. *Via* the $R'_{\rm wp}$ formula the residual for each region is scaled according to the total intensity in the region, so a region with only low-intensity peaks can make an important contribution to $R'_{\rm wp}$.

This approach is robust at handling the problems that may affect the experimental powder pattern: peak overlap, (*hkl*)-dependent effects and zero-point errors. It is time consuming (particularly in the case of low symmetry) but not very sensitive to the presence of minority impurity phases.

3.4.4.3.3. *McMaille: indexing via a Monte Carlo search method*

The information in the whole powder diffraction profile is exploited by the program *McMaille* (Le Bail, 2004), which is based on the random generation of cell parameters and uses the Monte Carlo optimization technique. Once the trial cell parameters have been generated and the Miller indices and the peak positions have been calculated, the quality of the cell is assessed by using, as figure of merit, the conventional Rietveld profile reliability factor R_p (Young, 1993) or McM_{20} (see Section 3.4.2.1). The program uses some tricks that can increase the success of the Monte Carlo algorithm:
(1) Only the trial cells corresponding to a value of R_p that is smaller than a user-defined value (∼50%) are retained for successive refinement.
(2) If all the observed peaks, except for a user-defined number of tolerated impurity peaks, are 'explained' whatever the R_p value, the cell is retained for successive examination.
(3) If either of the conditions (1) or (2) is fulfilled, the cell parameters are randomly changed in 200 to 5000 attempts (for cubic to triclinic cases, respectively) in which small random parameter variations *via* the Monte Carlo algorithm are carried out. The new parameters are preserved if an improvement of R_p is verified in 85% of the attempts.

This procedure is not sensitive to impurity lines, provided that the sum of their intensities is less than 10–15% of the total intensity. A zero-point error up to 0.05° is tolerated. To reduce the long computing time required to successfully complete the procedure, a significant increase in speed has been obtained by using idealized profiles generated by applying simplified line profiles to extracted line positions. A parallelized version of *McMaille* has also been developed. The indexing problem can usually be solved in few minutes if: (*a*) no triclinic symmetry is handled (because this requires more computing time); (*b*) the cell volume is less than 2000 Å^3; (*c*) no cell length is longer than 20 Å.

3.4.4.4. *Crysfire: a suite of indexing programs*

The *Crysfire* suite (Shirley, 2002) is a multi-program indexing facility. It can perform a self-calibration, which is aimed at detecting and correcting 2θ zero errors, and is able to strip out weak lines. Its single unified user interface and data-file format make a wide set of indexing packages accessible with minimal effort (especially to non-specialists). *Crysfire* provides a list of the possible cells suggested by each indexing program, suitably ranked. The *Crysfire* 2003 suite supports a total of 11 programs (Bergmann *et al.*, 2004), among which are *ITO*, *TREOR90*, *DICVOL91* and *McMaille*. The possibility of using different indexing programs, working in parameter space or index space and adopting different indexing approaches increases the probability of finding the correct cell.

3.4.4.5. *Two commercial programs*

3.4.4.5.1. *SVD-Index*

This commercial indexing program (Coelho, 2003*a*), which uses the Monte Carlo method, is part of the *TOPAS* (Coelho, 2003*b*) suite from Bruker AXS. The reciprocal-cell parameters in equation (3.4.2) are found by using, in an iterative way, the singular value decomposition (SVD) approach (Nash, 1990) to solve linear equations relating (*hkl*) values to d spacings. The method is particularly useful in cases for which there are more equations than variables. All the observed lines in the powder pattern are involved in the indexing procedure. It is claimed that the program is relatively insensitive to impurity peaks and missing high d spacings; it performs well on data with large diffractometer zero errors.

More recently, two indexing methods have been introduced in *TOPAS*: LSI (least-squares iteration), an iterative least-squares process which operates on the d-spacing values extracted from reasonable-quality powder diffraction data, and LP-Search (lattice parameter search), a Monte Carlo based whole-powder-pattern decomposition approach independent of the knowledge of the d-spacings (Coelho & Kern, 2005).

3.4.4.5.2. *X-CELL*

This commercial program is part of the *Materials Studio* suite from Accelrys (Neumann, 2003). To perform an exhaustive search, like *DICVOL*, the program uses the successive-dichotomy approach. Its principal features are:
(1) the user can define how many impurity lines can be tolerated;
(2) a search for the zero-point shift of the diffraction pattern; and
(3) systematic absences are taken into account.

The program is described as 'virtually exhaustive'; it is expected to work well when faced with missing lines, impurities and errors.

3.4.4.6. *Examples of applications of indexing programs*

3.4.4.6.1. *Indexing using DICVOL06*

The program *DICVOL06*, as implemented in the *WinPLOTR*/*FULLPROF* suite (Roisnel & Rodríquez-Carvajal, 2001) and recently introduced into *EXPO*, was applied to two experimental diffraction patterns.

Example 1

Norbornene (Brunelli *et al.*, 2001). Published information: C_7H_{10}, monoclinic, a = 7.6063 (9), b = 8.6220 (1), c = 8.749 (1) Å, β = 97.24 (1)°, $P2_1/c$, experimental range 5–60° 2θ, λ = 0.85041 Å, RES = 1.0 Å (where RES is the data resolution), synchrotron data, indexed by *Fzon* (Visser, 1969).

Figure 3.4.1
The list of possible cells for the decafluoroquarterphenyl structure automatically found using *N-TREOR09*.

The 2θ values of the first 25 peaks, in the range 5–25°, were determined by *WinPLOTR* and supplied to *DICVOL06*. The first 20 peaks were used for searching for the solution. No plausible cell was found when assuming that no impurity was present and exploring all the systems (from cubic to triclinic). *DICVOL06* was also unsuccessful when the non-default strategies of extended search and data correction for zero-point error were considered (by setting some flags to 1 in the input file). If it was supposed that two impurity lines might be present among the peaks (by setting the flag corresponding to the maximum number of accepted impurity/spurious lines to 2), *DICVOL06* was able to find the following monoclinic cell: a = 8.7480 (36), b = 8.6313 (32), c = 7.6077 (26) Å, β = 97.201 (33)°, with two unindexed lines, M_{18} = 41.5, F_{18} = 125(0.0041, 35). The refinement of the cell by considering all the 25 lines gave a = 7.6087 (26), b = 8.6295 (30), c = 8.7459 (34) Å, β = 97.201 (34)°, which is very similar to the published one; 23 indexed lines, M_{20} = 30.1, F_{20} = 102.6(0.0048, 41). The presence of the two impurity lines has been ascribed by the authors to a small amount of hexagonal plastic phase.

Example 2

Cu(II)–Schiff base complex (Banerjee *et al.*, 2002). Published information: $Cu(C_{15}H_{12}NO_2)_2$, triclinic, a = 11.928 (4), b = 12.210 (5), c = 9.330 (5) Å, α = 102.54 (4), β = 111.16 (5), γ = 86.16 (4)°, $P\bar{1}$, experimental range 6–100° 2θ, λ = 1.54056 Å, RES = 1.22 Å, high-quality X-ray laboratory data, indexed by *DICVOL91*. The 2θ values of the first 30 peaks, in the range 6–25°, were determined by *WinPLOTR* and supplied to *DICVOL06*. The first 20 peaks were used for searching for the solution. If it was assumed that no impurity was present, no plausible cell was found down to the monoclinic system. When the triclinic system was explored, *DICVOL06* suggested only one plausible solution: a = 12.2157 (73), b = 12.2031 (77), c = 9.3071 (41) Å, α = 65.798 (46), β = 102.572 (59), γ = 95.711 (61)°, with no unindexed lines, M_{20} = 27.0, F_{20} = 77.0(0.010, 26). The refinement of the cell considering all the 30 lines gave a = 12.2125 (65), b = 12.1989 (61), c = 9.3016 (32) Å, α = 65.826 (33), β = 102.569 (40), γ = 97.755 (44)°, no unindexed lines, M_{20} = 27.9, F_{20} = 72.8(0.0106, 26). For this, the corresponding conventional cell is a = 11.93313 (61), b = 12.2125 (65), c = 9.3016 (32) Å, α = 102.569 (40), β = 111.152 (33), γ = 86.151 (44)°, similar to the published one.

3.4.4.6.2. *Indexing using N-TREOR09*

Two examples of powder diffraction pattern indexing by using *N-TREOR09,* as implemented in the *EXPO* program, will be described. To activate the procedure some specific instructions must be given to *EXPO via* the input file or the graphical interface. As a first step, the peak-search procedure is automatically performed on the experimental powder pattern and the list of corresponding d values are supplied to *N-TREOR09*. During the indexing process a correction for zero-point error is automatically carried out (positive and negative shifts are taken into account). Both the examples below were successfully indexed by a default run of *EXPO*.

Example 3

Decafluoroquarterphenyl (Smrčok *et al.*, 2001). Published information: $C_{24}H_8F_{10}$, monoclinic, a = 24.0519 (9), b = 6.1529 (3), c = 12.4207 (5) Å, β = 102.755 (2)°, $I2/a$, experimental range 7–80° 2θ, λ = 1.79 Å, RES = 1.39 Å, medium-quality X-ray laboratory data. The first 43 peaks (in the range 7–67°) with intensities greater than a default threshold were selected (an intensity-based criterion is automatically adopted). The first 25 lines were used to find a possible cell that was then refined by considering all the 43 peaks. At the end of the automatic indexing procedure, *N-TREOR09* suggested two possible cells ranked according to WRIP20 [equation (3.4.5)], as shown in Fig. 3.4.1 (WRIP20 is denoted as

FOMnew in *N-TREOR09*). The first one in the list is the correct cell. It is worth mentioning that the classical M_{20} figure of merit was not able to pick up the solution. The best cell parameters, found according to FOMnew, were a = 24.0951 (50), b = 6.1697 (21), c = 12.4578 (37) Å, β = 102.724 (18)°, similar to those reported in the literature, with FOMnew = 0.61, M_{20} = 12; all the lines in the pattern were indexed. The program provided the solution thanks to its automatic check for a zero-point correction (2θ zero shift = 0.04°) and was able to correctly identify the extinction group (*I_a_*). For the second suggested cell (the wrong solution) FOMnew = 0.41, M_{20} = 15, and two lines were unindexed.

Example 4

Hexagonal turkey egg-white lysozyme (Margiolaki *et al.*, 2005). Published information: hexagonal, a = 71.0862 (3), c = 85.0276 (5) Å, $P6_122$, experimental range 0.4–12° 2θ, RES = 3.35 Å, synchrotron data. The first 94 peaks (in the range 0.4–6°, λ = 0.700667 Å) with intensities greater than a default threshold were selected. An intensity-based criterion was automatically adopted. The first 25 lines were used to find possible cells that were then refined by considering all 94 peaks. Five possible unit cells were automatically suggested by the program in the following systems: hexagonal (1), orthorhombic (1) and monoclinic (3). The highest value for WRIP20 was 0.99, and was for the correct hexagonal cell parameters: a = 71.0922 (4), c = 85.0269 (7) Å, which are similar to those reported in the literature; all the 94 selected lines in the pattern were indexed. For this cell, the program detected a geometrical ambiguity (see Section 3.4.2.2) between hexagonal and orthorhombic lattices and automatically selected the higher-symmetry one.

3.4.5. Conclusion

Indexing a powder diffraction pattern is sometimes described as a 'gateway technology', because the determination of the cell parameters is so fundamental: if no cell has been identified the execution of the subsequent steps of the structure solution process is impossible, and if a wrong cell has been used the correct solution is unreachable. Therefore extremely close attention must be paid to the indexing step of the process. From the early 1970s, the increasing interest in powder pattern indexing and the progress seen, in terms of both methods and algorithms, have strongly contributed to opening the door to modern applications of powder diffraction techniques. The availability of a quite large number of software packages, based on different indexing strategies, enables the scientist interested in solving crystal structures to switch from one program to another when the first fails, so increasing the possibility of success. In some cases indexing is still a challenging process. Good-quality data are necessary and careful inspection of each indexing step, in particular in the selection of the experimental peak positions to be used, is advisable.

References

Altomare, A., Caliandro, R., Camalli, M., Cuocci, C., da Silva, I., Giacovazzo, C., Moliterni, A. G. G. & Spagna, R. (2004). *Space-group determination from powder diffraction data: a probabilistic approach*. *J. Appl. Cryst.* **37**, 957–966.

Altomare, A., Camalli, M., Cuocci, C., da Silva, I., Giacovazzo, C., Moliterni, A. G. G. & Rizzi, R. (2005). *Space group determination: improvements in EXPO2004*. *J. Appl. Cryst.* **38**, 760–767.

Altomare, A., Campi, G., Cuocci, C., Eriksson, L., Giacovazzo, C., Moliterni, A., Rizzi, R. & Werner, P.-E. (2009). *Advances in powder diffraction pattern indexing: N-TREOR09*. *J. Appl. Cryst.* **42**, 768–775.

Altomare, A., Cascarano, G., Giacovazzo, C., Guagliardi, A., Moliterni, A. G. G., Burla, M. C. & Polidori, G. (1995). *On the number of statistically independent observations in a powder diffraction pattern*. *J. Appl. Cryst.* **28**, 738–744.

Altomare, A., Cuocci, C., Giacovazzo, C., Moliterni, A., Rizzi, R., Corriero, N. & Falcicchio, A. (2013). *EXPO2013: a kit of tools for phasing crystal structures from powder data*. *J. Appl. Cryst.* **46**, 1231–1235.

Altomare, A., Giacovazzo, C., Guagliardi, A., Moliterni, A. G. G., Rizzi, R. & Werner, P.-E. (2000). *New techniques for indexing: N-TREOR in EXPO*. *J. Appl. Cryst.* **33**, 1180–1186.

Altomare, A., Giacovazzo, C. & Moliterni, A. (2008). *Indexing and space group determination*. In *Powder Diffraction Theory and Practice*, edited by R. E. Dinnebier & S. J. L. Billinge, pp. 206–226. Cambridge: RSC Publishing.

Andrews, L. C. & Bernstein, H. J. (1988). *Lattices and reduced cells as points in 6-space and selection of Bravais lattice type by projections*. *Acta Cryst.* A**44**, 1009–1018.

Banerjee, S., Mukherjee, A., Neumann, M. A. & Louër, D. (2002). *Ab-initio structure determination of a Cu(II)-Schiff base complex from X-ray powder diffraction data*. *Acta Cryst.* A**58**, c264.

Bergmann, J. (2007). *EFLECH/INDEX – another try of whole pattern indexing*. *Z. Kristallogr. Suppl.* **26**, 197–202.

Bergmann, J., Le Bail, A., Shirley, R. & Zlokazov, V. (2004). *Renewed interest in powder diffraction data indexing*. *Z. Kristallogr.* **219**, 783–790.

Boultif, A. & Louër, D. (1991). *Indexing of powder diffraction patterns for low-symmetry lattices by the successive dichotomy method*. *J. Appl. Cryst.* **24**, 987–993.

Boultif, A. & Louër, D. (2004). *Powder pattern indexing with the dichotomy method*. *J. Appl. Cryst.* **37**, 724–731.

Brunelli, M., Fitch, A. N., Jouanneaux, A. & Mora, A. J. (2001). *Crystal and molecular structures of norbornene*. *Z. Kristallogr.* **216**, 51–55.

Buerger, M. J. (1957). *Reduced cells*. *Z. Kristallogr.* **109**, 42–60.

Buerger, M. J. (1960). *Note on reduced cells*. *Z. Kristallogr.* **113**, 52–56.

Coelho, A. A. (2003*a*). *Indexing of powder diffraction patterns by iterative use of singular value decomposition*. *J. Appl. Cryst.* **36**, 86–95.

Coelho, A. A. (2003*b*). *TOPAS*. *Version 3.1 User's Manual*. Bruker AXS GmbH, Karlsruhe, Germany.

Coelho, A. A. & Kern, A. (2005). *Discussion of the indexing algorithms within TOPAS*. *IUCr Commission on Powder Diffraction Newsletter*, **32**, 43–45.

Conway, J. H. & Fung, F. Y. C. (1997). *The Sensual (Quadratic) Form*. Washington, DC: The Mathematical Association of America.

Delaunay, B. (1933). *Neue Darstellung der geometrischen Kristallographie*. *Z. Kristallogr.* **84**, 109–149.

Dong, C., Wu, F. & Chen, H. (1999). *Correction of zero shift in powder diffraction patterns using the reflection-pair method*. *J. Appl. Cryst.* **32**, 850–853.

Giacovazzo, C. (2011). *Crystallographic computing.* In *Fundamentals of Crystallography*, 3rd ed., edited by C. Giacovazzo, pp. 66–156. Oxford: IUCr/Oxford University Press.

Harris, K. D. M., Johnston, R. L., Chao, M. H., Kariuki, B. M., Tedesco, E. & Turner, G. W. (2000). *Genetic algorithm for indexing powder diffraction data*. University of Birmingham, UK.

Ishida, T. & Watanabe, Y. (1967). *Probability computer method of determining the lattice parameters from powder diffraction data*. *J. Phys. Soc. Jpn*, **23**, 556–565.

Ishida, T. & Watanabe, Y. (1971). *Analysis of powder diffraction patterns of monoclinic and triclinic crystals*. *J. Appl. Cryst.* **4**, 311–316.

Ito, T. (1949). *A general powder X-ray photography*. *Nature*, **164**, 755–756.

Ito, T. (1950). *X-ray Studies on Polymorphism*. Tokyo: Maruzen Company.

Karen, V. L. & Mighell, A. D. (1991). *Converse-transformation analysis*. *J. Appl. Cryst.* **24**, 1076–1078.

Kariuki, B. M., Belmonte, S. A., McMahon, M. I., Johnston, R. L., Harris, K. D. M. & Nelmes, R. J. (1999). *A new approach for indexing powder*

diffraction data based on whole-profile fitting and global optimization using a genetic algorithm. *J. Synchrotron Rad.* **6**, 87–92.
Kroll, H., Stöckelmann, D. & Heinemann, R. (2011). *Analysis of multiple solutions in powder pattern indexing: the common reciprocal metric tensor approach*. *J. Appl. Cryst.* **44**, 812–819.
Le Bail, A. (2004). *Monte Carlo indexing with McMaille*. *Powder Diffr.* **19**, 249–254.
Le Bail, A. (2008). *Structure solution*. In *Principles and Applications of Powder Diffraction*, edited by A. Clearfield, J. H. Reibenspies & N. Bhuvanesh, pp. 261–309. Oxford: Wiley-Blackwell.
Louër, D. & Boultif, A. (2006). *Indexing with the successive dichotomy method, DICVOL04*. *Z. Kristallogr. Suppl.* **23**, 225–230.
Louër, D. & Boultif, A. (2007). *Powder pattern indexing and the dichotomy algorithm*. *Z. Kristallogr. Suppl.* **26**, 191–196.
Louër, D. & Boultif, A. (2014). *Some further considerations in powder diffraction pattern indexing with the dichotomy method. Powder Diffr.* **29**, S2, S7–S12.
Louër, D. & Louër, M. (1972). *Méthode d'essais et erreurs pour l'indexation automatique des diagrammes de poudre*. *J. Appl. Cryst.* **5**, 271–275.
Louër, D. & Vargas, R. (1982). *Indexation automatique des diagrammes de poudre par dichotomies successives*. *J. Appl. Cryst.* **15**, 542–545.
Margiolaki, I., Wright, J. P., Fitch, A. N., Fox, G. C. & Von Dreele, R. B. (2005). *Synchrotron X-ray powder diffraction study of hexagonal turkey egg-white lysozyme*. *Acta Cryst.* D**61**, 423–432.
Mighell, A. D. (1976). *The reduced cell: its use in the identification of crystalline materials*. *J. Appl. Cryst.* **9**, 491–498.
Mighell, A. D. (2001). *Lattice symmetry and identification – the fundamental role of reduced cells in materials characterization*. *J. Res. Natl Inst. Stand. Technol.* **106**, 983–995.
Mighell, A. D. & Santoro, A. (1975). *Geometrical ambiguities in the indexing of powder patterns*. *J. Appl. Cryst.* **8**, 372–374.
Nash, J. C. (1990). *Compact Numerical Methods for Computers: Linear Algebra and Function Minimisation*, 2nd ed. Bristol: Adam Hilger.
Neumann, M. A. (2003). *X-cell: a novel indexing algorithm for routine tasks and difficult cases*. *J. Appl. Cryst.* **36**, 356–365.
Niggli, P. (1928). *Handbuch der Experimentalphysik*, Vol. 7, Part 1. Leipzig: Akademische Verlagsgesellschaft.
Oishi, R., Yonemura, M., Hoshikawa, A., Ishigaki, T., Mori, K., Torii, S., Morishima, T. & Kamiyama, T. (2009). *New approach to the indexing of powder diffraction patterns using topographs*. *Z. Kristallogr. Suppl.* **30**, 15–20.
Oishi-Tomiyasu, R. (2012). *Rapid Bravais-lattice determination algorithm for lattice parameters containing large observation errors*. *Acta Cryst.* A**68**, 525–535.
Oishi-Tomiyasu, R. (2013). *Reversed de Wolff figure of merit and its application to powder indexing solutions*. *J. Appl. Cryst.* **46**, 1277–1282.
Oishi-Tomiyasu, R. (2014*a*). *Method to generate all the geometrical ambiguities of powder indexing solutions*. *J. Appl. Cryst.* **47**, 2055–2059.
Oishi-Tomiyasu, R. (2014*b*). *Robust powder auto-indexing using many peaks*. *J. Appl. Cryst.* **47**, 593–598.
Oishi-Tomiyasu, R. (2016). *A table of geometrical ambiguities in powder indexing obtained by exhaustive search*. *Acta Cryst.* A**72**, 73–80.
Paszkowicz, W. (1996). *Application of the smooth genetic algorithm for indexing powder patterns – tests for the orthorhombic system*. *Mater. Sci. Forum*, **228–231**, 19–24.
Pecharsky, V. K. & Zavalij, P. Y. (2009). *Determination and refinement of the unit cell*. In *Fundamentals of Powder Diffraction and Structural Characterization of Materials*, 2nd ed., pp. 407–495. New York: Springer.
Roisnel, T. & Rodríquez-Carvajal, J. (2001). *WinPLOTR: a windows tool for powder diffraction pattern analysis*. *Mater. Sci. Forum*, **378–381**, 118–123.
Runge, C. (1917). *Die Bestimmung eines Kristallsystems durch Rontgenstrahlen*. *Phys. Z.* **18**, 509–515.
Santoro, A. & Mighell, A. D. (1970). *Determination of reduced cells*. *Acta Cryst.* A**26**, 124–127.
Santoro, A. & Mighell, A. D. (1972). *Properties of crystal lattices: the derivative lattices and their determination*. *Acta Cryst.* A**28**, 284–287.
Santoro, A., Mighell, A. D. & Rodgers, J. R. (1980). *The determination of the relationship between derivative lattices*. *Acta Cryst.* A**36**, 796–800.
Shirley, R. (1980). *Data accuracy for powder indexing*. In *Accuracy in Powder Diffraction*, edited by S. Block & C. R. Hubbard, *NBS Spec. Publ.* **567**, 361–382.
Shirley, R. (2002). *User Manual, The Crysfire 2002 system for Automatic Powder Indexing*. Guildford: Lattice Press.
Shirley, R. (2003). *Overview of powder-indexing program algorithms (history and strengths and weaknesses)*. *IUCr Comput. Comm. Newsl.* **2**, 48–54. http://www.iucr.org/resources/commissions/crystallographic-computing/newsletters/2.
Smith, G. S. (1977). *Estimating the unit-cell volume from one line in a powder diffraction pattern: the triclinic case*. *J. Appl. Cryst.* **10**, 252–255.
Smith, G. S. & Snyder, R. L. (1979). *F_N: a criterion for rating powder diffraction patterns and evaluating the reliability of powder-pattern indexing*. *J. Appl. Cryst.* **12**, 60–65.
Smrčok, L., Koppelhuber-Bitschau, B., Shankland, K., David, W. I. F., Tunega, D. & Resel, R. (2001). *Decafluoroquarterphenyl – crystal and molecular structure solved from X-ray powder data*. *Z. Kristallogr.* **216**, 63–66.
Tam, K. Y. & Compton, R. G. (1995). *GAMATCH – a genetic algorithm-based program for indexing crystal faces*. *J. Appl. Cryst.* **28**, 640–645.
Taupin, D. (1973). *A powder-diagram automatic-indexing routine*. *J. Appl. Cryst.* **6**, 380–385.
Visser, J. W. (1969). *A fully automatic program for finding the unit cell from powder data*. *J. Appl. Cryst.* **2**, 89–95.
Werner, P.-E. (1964). *Trial-and-error computer methods for the indexing of unknown powder patterns*. *Z. Kristallogr.* **120**, 375–387.
Werner, P.-E. (2002). *Autoindexing*. In *Structure Determination from Powder Diffraction Data*, edited by W. I. F. David, K. Shankland, L. B. McCusker & Ch. Baerlocher, pp. 118–135. Oxford University Press.
Werner, P.-E., Eriksson, L. & Westdahl, M. (1985). *TREOR, a semi-exhaustive trial-and-error powder indexing program for all symmetries*. *J. Appl. Cryst.* **18**, 367–370.
Wolff, P. M. de (1957). *On the determination of unit-cell dimensions from powder diffraction patterns*. *Acta Cryst.* **10**, 590–595.
Wolff, P. M. de (1958). *Detection of simultaneous zone relations among powder diffraction lines*. *Acta Cryst.* **11**, 664–665.
Wolff, P. M. de (1968). *A simplified criterion for the reliability of a powder pattern indexing*. *J. Appl. Cryst.* **1**, 108–113.
Young, R. A. (1993). *Introduction to the Rietveld method*. In *The Rietveld Method*, edited by R. A. Young, pp. 1–38. Oxford: IUCr/Oxford University Press.

International Tables for Crystallography (2019). Vol. H, Chapter 3.5, pp. 282–287.

3.5. Data reduction to $|F_{hkl}|$ values

A. Le Bail

3.5.1. Introduction

Collecting the structure-factor amplitudes $|F_{hkl}|$ is the key step leading to structure solution from powder-diffraction data, just as from single-crystal data. However, there are specific difficulties and pitfalls associated with powder data, mainly because of diffraction-peak overlap. Once indexing is realized, data reduction to $|F_{hkl}|$ is a fast process, using whole-powder-pattern decomposition (WPPD) methods. This comfortable situation was not attained without past efforts, which are reviewed in this chapter. The introduction of modern WPPD methods occurred slowly and progressively over the past 30 years, thanks to increases in computer power, improvements in graphical user interfaces, diffractometer data digitalization, the availability of synchrotron and neutron radiation, and last but not least, the proposition of new algorithms. Innovations were not instantly accepted, this also being true for the Rietveld (1969) method, or could not be applied immediately to every type of powder data. Predecessors of the current WPPD methods extracted peak intensities without restraining the cell, so that each peak position was a parameter to be refined (as well as the peak intensity, and the peak shape and width). This is still useful if the aim is to obtain peak positions for indexing, although simple derivative methods can make searching for peak positions faster. Taking advantage of the indexing (Bergmann *et al.*, 2004), new WPPD methods that applied cell restraints to the peak positions opened the door to a long list of new possibilities and applications (including first indexing confirmation and manual or automatic space-group estimation) which are detailed in this chapter. A partial review of the applications realized in thousands of published papers is given, and the evolution of the methods will be discussed. Additional information on the topic of reduction to $|F_{hkl}|$ values can be found in the books by Young (1993), Giacovazzo (1998), David *et al.* (2002), Pecharsky & Zavalij (2003), Clearfield *et al.* (2008) and Dinnebier & Billinge (2008) or in selected reviews (Toraya, 1994; Langford & Louër, 1996; Le Bail, 2005).

3.5.2. Algorithms

Whole-powder-pattern fitting (WPPF) is a general definition including WPPD as well as the Rietveld method (Rietveld, 1969). In the latter method, the atomic coordinates are required for the intensity calculations, and the sum of all the peak contributions produces a calculated powder pattern which is compared to the observed one, allowing the least-squares refinement of profile and structural parameters. The Rietveld method historically preceded modern WPPD methods, though the latter are applicable without atomic coordinates. Of course, one may use WPPD methods if the structure is known, but in some cases one does not want to use that knowledge (not wanting to restrain the peak intensities by the structural model, for instance, nevertheless believing in the indexing or wanting to confirm it, using the restraint of the cell parameters). Any WPPF approach should be able to model the peak shape and width variations with diffraction angle (complications not considered here may occur in the case of anisotropic broadening intrinsic to the sample). This can be done by fitting some analytical profile shape and width parameters in a semi-empirical approach. The angular variation of these parameters is generally controlled by refining the U, V and W terms in the Caglioti *et al.* (1958) expression $[(\mathrm{FWHM})^2 = U\tan^2\theta + V\tan\theta + W]$ or a variation (where FWHM = full width at half maximum). The alternative is to use the fundamental parameter approach (FPA) (Cheary & Coelho, 1992). However, some of the original computer programs did not apply any cell restraint or even any restraint at all.

3.5.2.1. *Unrestrained cell*

Without a cell hypothesis, no $|F_{hkl}|$ values can be extracted; the intensity values collected will be noted by $I(i)$ until Miller indices are attributed, enabling the multiplicity correction. Obtaining all the peak positions, areas, breadths and shape parameters as independent values for a whole powder pattern is limited to simple cases where there is not too much peak overlap. With such an approach (both cell and space group unknown or unused) one has to estimate the number of peaks to be fitted, so that the fit of a complex group of peaks will lead to large uncertainties. However, knowing the cell and space group provides at least the correct number of peaks and an estimate of their starting positions. Such calculations were made as an alternative to the Rietveld method, during the first stage of the so-called two-stage method for refinement of crystal structures (Cooper *et al.*, 1981). In the case of X-ray data, the profile shapes applied in the Rietveld method (Gaussian at the beginning for neutron data) evolved a great deal (Wiles & Young, 1981), and on the WPPD side happened to be described in these two-stage approaches by a sum of Lorentzian curves, or double Gaussians (Will *et al.*, 1983, 1987). The computer program *PROFIT* (Scott, 1987), derived from software for individual profile fitting (Sonneveld & Visser, 1975) and extended to the whole pattern, was applied to the study of crystallite size and strain in zinc oxide (Langford *et al.*, 1986) and for the characterization of line broadening in copper oxide (Langford & Louër, 1991). Studying a whole pattern can also be done in simple cases by using software designed for the characterization of single or small groups of peaks; an example is a ZnO study (Langford *et al.*, 1993) using the computer program *FIT* (Socabim/Bruker). WPPD on complex cases is mostly realized today by using peak positions controlled by the cell parameters, with the benefit of stronger accuracy of the $|F_{hkl}|$ values, even if the lost degrees of freedom may lead to slightly worse fits, increasing the profile R factors. Before 1987, close to thirty structure determinations by powder diffractometry (SDPDs) were achieved using intensities extracted by using these old WPPD methods without cell constraints (see the SDPD database; Le Bail, 2007). It can be argued that freeing the peak positions allows one to take into account subtle effects in position displacement (in stressed samples, for example). But systematic discrepancy of observed peak positions with regard to the theoretical position, as expected from the cell parameters, can be modelled as well in modern WPPD methods or in the Rietveld method.

3.5.2.2. *Restrained cell*

WPPD methods that strictly applied the peak positions calculated from a cell (hypothesized from indexing results) marked a great step forward in the quest for improving the SDPD success rate. This is essentially because the quality of the estimated intensities increased, and even if the main handicap of powder diffraction (peak overlap) could not be completely circumvented, it was at least more clearly delimited. Today two generic names are retained for such cell-restrained WPPD methods that can produce a set of extracted $|F_{hkl}|$ values suitable for attempting a structure solution: the Pawley and Le Bail methods. Both were derived from the Rietveld (1969) method, so they share with it many equations which will not be restated here (see Chapter 4.7).

3.5.2.2.1. *Pawley method*

The idea of removing the crystal structure refinement part in a Rietveld program and adding the potential to refine an individual intensity for every expected Bragg peak produced a new software package (named *ALLHKL*) allowing refinement of the cell parameters very precisely and extraction of a set of structure-factor amplitudes (Pawley, 1981). The process was much later called the 'Pawley method'. Overcoming the least-squares ill conditioning due to peak overlap was achieved by using slack constraints (Waser, 1963). Pawley clearly insisted on the usefulness of the procedure for the confirmation of the indexing of a powder pattern of an unknown. Nevertheless, the structure of the C_6F_{10} (at 4.2 K) test case selected for demonstration purposes remained unsolved (but see Section 3.5.4.2 below). No SDPD of an unknown was realized using the Pawley method for several years (although successful tests were published corresponding to redeterminations of previously known structures). The first real SDPD of an unknown using the Pawley method seems to be that of I_2O_4 (Lehmann *et al.*, 1987); its powder pattern had been previously indexed, but the structure not determined because of the lack of a suitable single crystal. During these pioneering years, *ALLHKL* could not extract the intensities for more than 300 peaks, so that, in more complex cases, it was necessary to subdivide the pattern into several parts. Moreover, it was rather difficult to avoid completely the ill conditioning due to overlapping peaks. Successful fits yielded equipartitioned intensities (*i.e.*, equal structure factors for those Bragg peaks with exact overlap). Unsuccessful fits could easily produce negative intensities which, combined with positive ones for other peak(s) at the same angle, reproduced the global positive value. Moreover, the first version to apply Gaussian peak shapes could not easily produce any SDPD because of the relatively poor resolution of constant-wavelength neutron data, so that it needed to be adapted to X-ray data, with the implementation of more complex peak shapes. Several programs were subsequently developed, based on the same principles as the original Pawley method. The first of them, by Toraya (1986), extended the use to X-ray data with non-Gaussian profile shapes, and introduced two narrow band matrices instead of a large triangular matrix, saving both computation time and memory space in a program named *WPPF*. Some programs were used to produce intensities in order to apply the so-called two-stage method (Cooper *et al.*, 1981) for structure refinement, such as *PROFIT* (Scott, 1987) and *PROFIN* (Will, 1988) (no slack constraints, but equal division of the intensity between expected peaks when the overlap was severe). There was intense continuing activity on Pawley-like software with other programs such as *FULFIT* (Jansen *et al.*, 1988), *LSQPROF* (Jansen *et al.*, 1992) and *POLISH* (Byrom & Lucas, 1993). Estimation of intensities of overlapping reflections was improved in *LSQPROF* by applying relations between structure-factor amplitudes derived from direct methods, and the Patterson function was considered in the satellite program *DOREES* (Jansen *et al.*, 1992). The question of how to determine the intensities of completely (or largely) overlapping reflections (either systematic overlap due to symmetry or fortuitous overlap) from a single powder pattern cannot have a definite simple answer, but continues to be discussed, since it is essential for improving our ability to solve structures. An early view with a probabilistic approach was given by David (1987), later introducing Bayesian statistics (Sivia & David, 1994) into the Pawley method. Early detection of preferred orientation on the basis of analysis of the *E*-value distribution was another way (Peschar *et al.*, 1995) to improve the structure-factor-amplitude estimate. New computer programs based on the Pawley method continue to be written even today.

3.5.2.2.2. *Le Bail method*

In order to be able to estimate *R* factors related to integrated intensities, Rietveld (1969) stated [see also the book *The Rietveld Method* edited by Young (1993)]: 'a fair approximation to the observed integrated intensities can be made by separating the peaks according to the calculated values of the integrated intensities,' *i.e.*

$$I_{hkl}(\text{obs}) = \sum_j [w_{j,hkl} S^2_{hkl}(\text{calc}) y_j(\text{obs})/y_j(\text{calc})], \qquad (3.5.1)$$

where $w_{j,hkl}$ is a measure of the contribution of the Bragg peak at position $2\theta_{hkl}$ to the diffraction profile y_j at position $2\theta_j$ [corresponding to equation 7 in Rietveld (1969)]. S^2_{hkl} is the sum of the nuclear and magnetic contributions for neutron diffraction, or is more simply F^2_{hkl} for X-rays. The sum is over all y_j(obs) that can theoretically contribute to the integrated intensity I_{hkl}(obs). Bias is introduced here by apportioning the intensities according to the calculated intensities; this is why the observed intensities are said to be 'observed', in quotation marks, in the Rietveld method. These 'observed' intensities are used in the R_B and R_F calculations (residuals on intensities and structure-factor amplitudes, respectively). They are also required for Fourier-map estimations, which, as a consequence, are less reliable than those from single-crystal data.

A process using the Rietveld decomposition formula iteratively for WPPD purposes was first applied in 1988 (Le Bail *et al.*, 1988) and much later was called the 'Le Bail method' or 'Le Bail fit', or 'pattern matching' as well as 'profile matching' in the *FULLPROF* Rietveld program (Rodriguez-Carvajal, 1990). In the original computer program (named *ARITB*), arbitrarily all equal S^2_{hkl}(calc) values are first entered in the above equation, instead of using structure factors calculated from the atomic coordinates, resulting in 'I_{hkl}(obs)' which are then re-entered as new S^2_{hkl}(calc) values at the next iteration, while the usual profile and cell parameters (but not the scale) are refined by least squares (*ARITB* used profile shapes represented by Fourier series, either analytical or learned from experimental data, providing an easy way to realize convolution by broadening functions modelling size–strain sample effects, possibly anisotropic). Equipartition of exactly overlapping reflections comes from the strictly equal result from equation (3.5.1) for Bragg peaks at the same angles which would have equal starting calculated intensities. Not starting from a set of all equal S^2_{hkl}(calc) values avoids equipartition for the exactly overlapping reflections but produces I_{hkl}(obs) keeping the same original ratio

as the S^2_{hkl}(calc) ones. It is understandable that such an iterative process requires starting cell and profile parameters as good as the Rietveld method itself. The process is easier to incorporate within an existing Rietveld code than the Pawley method, so that most Rietveld codes now include structure-factor amplitudes extraction as an option (generally multiphase), with the possibility of combining Rietveld refinement(s) together with Le Bail fit(s).

A non-exhaustive list of programs applying this method (either exclusively or added within a Rietveld code) includes *MPROF* (Jouanneaux *et al.*, 1990), later renamed *WinMPROF*; *FULLPROF* (Rodriguez-Carvajal, 1990); *EXTRACT* (Baerlocher, 1990); *EXTRA* (Altomare *et al.*, 1995); *EXPO* (Altomare *et al.*, 1999), which is the integration of *EXTRA* and *SIRPOW.92* for solution and refinement of crystal structures; and *RIETAN* (Izumi & Ikeda, 2000). Then followed most well known Rietveld codes (*BGMN*, *GSAS*, *MAUD*, *TOPAS etc.*) or standalone programs (*AJUST* by Rius *et al.*, 1996). In the work of the Giacovazzo group, many modifications of the $|F_{hkl}|$ values for SDPD purposes were applied before or after the extraction and were integrated in *EXPO2011* (Altomare *et al.*, 2011): obtaining information about the possible presence of preferred orientation by statistical analysis of the normalized structure-factor moduli; using the positivity of the Patterson function in the decomposition process, this having been considered previously (David, 1987; Estermann & Gramlich, 1993); characterization of pseudotranslational symmetry used as prior information in the pattern-decomposition process; multiple Le Bail fits with random attribution of intensity to the overlapping reflections, instead of equipartition, followed by application of direct methods to large numbers of such data sets; use of a located structure fragment for improving the pattern-decomposition process; and use of probability (triplet-invariant distribution functions) integrated with the Le Bail algorithm. Another approach for solving the overlapping problem was proposed by using maximum-entropy coupled with likelihood evaluation (Dong & Gilmore, 1998). The list of structure solutions made from intensities extracted by using the Pawley and Le Bail methods is too long to be given here; a partial list (>1000 first cases, including those using $|F_{hkl}|$ values extracted by other methods) can be found on the web (Le Bail, 2007). The first application of the Le Bail method was to the structure solution of $LiSbWO_6$ (Le Bail *et al.*, 1988) using the *ARITB* software.

3.5.3. Pitfalls in the extraction of accurate $|F_{hkl}|$ values using the Pawley and Le Bail methods

In the Rietveld refinement guidelines published by the IUCr Commission on Powder Diffraction (McCusker *et al.*, 1999), it is said that the Rietveld R_{wp} value should approach the value obtained in a structure-free refinement (*i.e.* using WPPD methods). Such a refinement is recommended for the estimation of initial values of the Rietveld profile parameters. Consequently, $|F_{hkl}|$ values extracted by WPPD can be used to make a good reproduction of the experimental powder pattern if the cell is correct (which is ultimately only proven if the structure is solved and refined). Pitfalls can occur during post-treatment and application of the $|F_{hkl}|$ data if one neglects the possible errors that are inherently present due to exact or accidental overlap, preferred orientation effects or wrong background estimations, citing only three of the main possible causes of errors in these $|F_{hkl}|$ values.

3.5.3.1. *Consequences of (exact or accidental) overlap*

The uncertainties of the $|F_{hkl}|$ values of overlapped reflections cannot be overcome in a single powder-diffraction experiment. This problem has led to various approaches, all being more or less inefficient: equipartition, non-equipartition by random distribution *etc*. If direct methods are applied, the trend is to multiply the number of solution attempts, trying to identify the most convincing one by using structural arguments (such as atoms in chemically reasonable positions). When applying real-space methods (which require chemical knowledge, such as the three-dimensional molecular structure or the presence of definite polyhedra) one generally chooses to work either directly on the raw powder pattern or on a pseudo pattern built from the extracted $|F_{hkl}|$ values, so that wrong individual values are less of a problem, since only the sums of the contributions in overlapping regions are checked during the search for the molecule, polyhedra or atom positions. Indeed, working on the raw powder pattern does not need reduction to $|F_{hkl}|$ values in theory, but in practice either the Pawley or Le Bail methods are applied first in order to fix the zero point, background, cell and profile parameters which will then be applied during the structure model checking, and to speed the calculations. The extracted $|F_{hkl}|$ values can be used in mathematical expressions defining correlations induced by the overlap. These equations were developed by David *et al.* (1998) for the Pawley method in the real-space structure solution program *DASH* and by Pagola *et al.* (2000) for the Le Bail method in *PSSP*. Regenerating a powder pattern from the extracted $|F_{hkl}|$ values was carried out in the *ESPOIR* real-space computer program (Le Bail, 2001) using a simple Gaussian peak shape whose width follows the Caglioti relation established from the raw pattern. With such a pseudo powder pattern (without profile asymmetry, background *etc*.), the calculations are much faster than if the raw pattern is used. When using direct methods instead of real-space methods, the approaches are different, because direct methods require a more complete data set (up to d = 1 Å) of accurate $|F_{hkl}|$ values. However, removing up to half of them (those with too much overlap, *i.e.* where the overlap is greater than half the FWHM, for instance) can lead to success with direct methods. One can even remove up to 70–80% of the data if the Patterson method is applied and if only a small number of heavy atoms are to be located.

3.5.3.2. *Preferred-orientation effects*

One has to ensure that preferred orientation is minimized during the recording of the powder pattern if the extracted $|F_{hkl}|$ values are to be used for structure solution. In transmission geometry with a capillary specimen (provided that it is not composed of long needle-shaped particles that are all aligned), there is generally no problem. But in reflection geometry with samples pressed on the holder, preferred orientation is not rare, even if it is not obvious in the data. Collecting a second pattern from a sample dusted onto the holder through a fine sieve can be informative. However, some WPPD applications may not be sensitive to such a problem. If only the cell parameters have to be accurately estimated for thermal-expansion studies (Evans *et al.*, 1996), it can be much faster to use WPPD rather than the Rietveld method. However, it is not recommended to do this systematically, especially if the structure is complex and the resolution is low [see the warnings in Peterson (2005)].

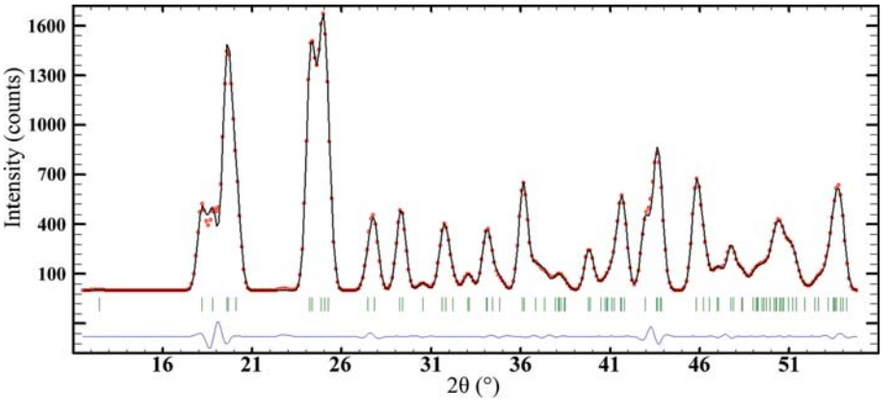

Figure 3.5.1
Data reduction to $|F_{hkl}|$ values for the C_6F_{10} Pawley (1981) test case by the Le Bail method using *FULLPROF*. The neutron powder pattern (4.2 K) was rebuilt (λ = 1.909 Å) from the intensities given in the original paper (*P*2/*m*). The extraction of $|F_{hkl}|$ values was carried out in the space group $P2_1/n$.

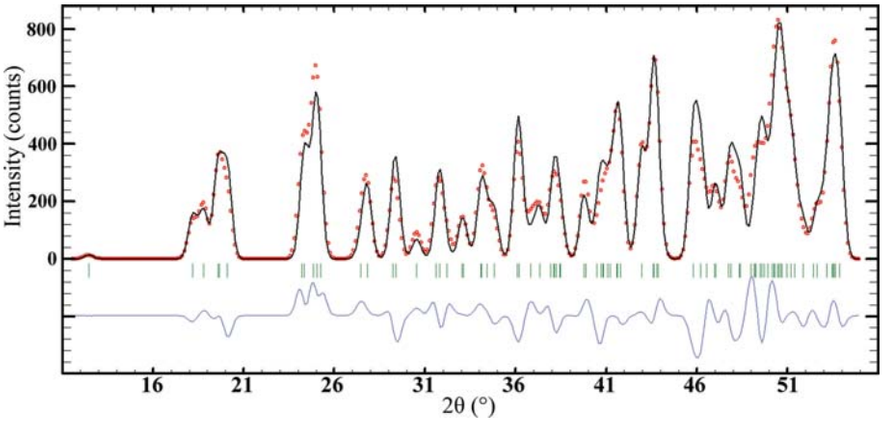

Figure 3.5.2
The C_6F_{10} Monte Carlo molecule positioning by the real-space *ESPOIR* program produces that best fit (R_p = 13.6%) of the pseudo powder pattern built from the previously extracted $|F_{hkl}|$ values (Fig. 3.5.1), overcoming the equipartition problem at the reduction stage. Compared to Fig. 3.5.1, which shows intensities, the multiplicity and geometrical factors are removed, leading to structure-factor amplitudes.

3.5.3.3. *Background-estimation effects*

Logically, a background value will never be higher than the observed intensity at the diffraction angle where it is visually estimated. In the first refinement cycles by the Pawley or Le Bail methods, it is preferable to keep the background fixed as well as the cell parameters, which assumes that the starting values have been carefully estimated or even (in the cell-parameter case) have already been refined from the peak positions that were used for indexing. This is because all refinement processes need to start from parameters close to the final values. Selecting background values leading to negative intensities after background removal could result in negative $|F_{hkl}|$ values if the software does not account for this.

3.5.4. Applications and by-products

The first modern WPPD method with cell restraints was developed for neutron data by Pawley (1981), 12 years after the publication of the paper that described the Rietveld (1969) method. In Le Bail *et al.* (1988) a new WPPD approach was used to extract intensities, making use of iterations of the Rietveld decomposition formula. It is clear that both these WPPD methods are children of the Rietveld method. Today most users of the Rietveld method do not cite the original Rietveld papers, but only refer to the computer program that they used. This is also now increasingly the case for the WPPD methods.

From the Thomson Reuters ISI citation index consulted in May 2015, the papers for the Pawley and Le Bail methods scored 892 and 1425 direct citations, respectively. There are several highly cited papers that then cite these two papers. The most highly cited paper (>5100 times) that cites both WPPD methods concerns use of the Le Bail intensity-extraction method by *FULLPROF* for solving magnetic structures (Rodriguez-Carvajal, 1993). This paper is also given as a reference for *FULLPROF* used in more standard Rietveld refinements. This suggests that the impact of WPPD methods is higher than commonly believed. The list of possible WPPD applications includes phase identification, quantitative phase analysis, measurement of crystallite sizes and strains, creation of Fourier maps for partially solved structures, structure refinement by the two-step method, studies of electron-density distribution, and characterization of pole figures, using either the Pawley or Le Bail methods. All routes to SDPD use at least one of them. WPPD has even entered into the indexing step, with Kariuki *et al.* (1999) using the Le Bail fit for testing cell hypotheses (for which it is faster than the Pawley method) in a new computer program that uses a genetic algorithm. But the main applications of the WPPD methods are to provide support for cell-parameter refinement and the determination of the space group, as a

prelude to the full use of the extracted $|F_{hkl}|$ values for *ab initio* structure solution.

3.5.4.1. *Supporting indexing and space-group determination*

As they yield the smallest possible profile R_p and R_{wp} factors (smaller than from the Rietveld method, which is limited by the crystal-structure refinement), the Pawley and Le Bail methods provide strong support for both the proposed indexing and the determination of the space group. Some computer programs provide an automated suggestion for the latter. This support is needed to show that it is worth attempting to solve the structure. Once the structure is solved, the structure constraint will remove the ambiguity between intensities of close Bragg peaks and necessarily improve the quality of the cell parameters. If the structure is already known, the best approach is the Rietveld method. There is a progression in the precision of the refined cell parameters from the lowest level (least squares from individually extracted peak positions) to a medium level (WPPD with cell restraint) to the highest possible level (Rietveld, adding the structure constraint). With both Pawley and Le Bail methods, the fit quality is checked using agreement factors which are the same as with the Rietveld method: R_p and R_{wp} (moreover, a careful visual check is recommended). The reliabilities relative to the structure (R_B and R_F), which can still be calculated, are meaningless (WPPD programs tending to obtain a value close to zero for both of them).

3.5.4.2. *Structure solution*

SDPD can be undertaken by various approaches, depending on the chemical knowledge of the sample (formula, molecular formula, presence of defined polyhedra . . .), either directly using the $|F_{hkl}|$ values for structure solution by direct or Patterson methods, or by rebuilding a pseudo powder pattern from them, or by applying fixed profile parameters from the Pawley or Le Bail fits during whole-powder-pattern fitting wherein the structure solution is attempted by real-space methods. In order to illustrate the power of WPPD methods and to show the progress realized over the last 30 years, the decafluorocyclohexene structure that was unsolved in the Pawley method paper of 1981 is reconsidered. As stated by Pawley, from plausible extinctions the space group of the C_6F_{10} crystal structure at 4.2 K could well be $P2_1/n$. The $|F_{hkl}|$ values were extracted from the rebuilt neutron powder pattern by applying the Le Bail method and used for attempting the structure solution by real-space methods. The neutron powder pattern was rebuilt from the 109 intensities extracted up to 54° 2θ, in space group $P2/m$, given in Table 2 of the original paper. The fit (using *FULLPROF*) in $P2_1/n$ of the data rebuilt in $P2/m$ is satisfactory (Fig. 3.5.1). The three-dimensional C_6F_{10} molecule was rotated and translated (six degrees of freedom) in the cell using the *ESPOIR* (Le Bail, 2001) Monte Carlo program, leading to a plausible starting model (R_p = 13.6%) ready for Rietveld refinement. This program builds a pseudo powder pattern from the extracted $|F_{hkl}|$ values, which is then compared to the data calculated from the model (Fig. 3.5.2). Unrefined atomic coordinates are available from the Crystallography Open Database (COD, CIF No. 3500009) (Grazulis *et al.*, 2009); a projection of the corresponding structure is shown in Fig. 3.5.3. The true crystal structure is apparently more complex (Solovyov *et al.*, 2014). Final resolution of the structure will require collection of a better experimental powder pattern. However, the coordinates have been refined by energy minimization in the solid state (Smrčok *et al.*, 2013).

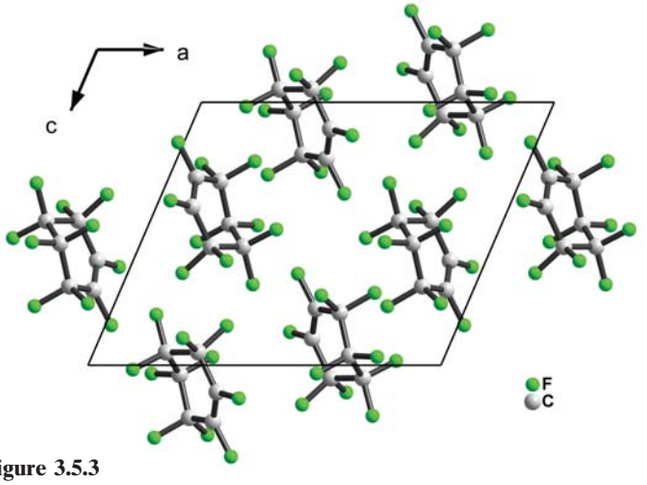

Figure 3.5.3
Projection along the *b* axis of the C_6F_{10} structure model in $P2_1/n$ before Rietveld refinement.

3.5.5. Conclusion

'Which is best: the Pawley or the Le Bail method?' is not a question with a simple conclusive answer. The fact is that both methods are able to estimate structure-factor amplitudes, which can lead to structure solution from powder-diffraction data in a more efficient way than was previously possible, even if the problem of peak overlap precludes attaining single-crystal quality data from only one powder pattern. The advantage of the Le Bail method over the Pawley method is its speed, which becomes apparent when several thousands of $|F_{hkl}|$ values have to be extracted, for instance from high-resolution synchrotron data of a complex compound, since no more than about ten parameters have to be refined instead of thousands. Chemical knowledge may reduce the number of $|F_{hkl}|$ values necessary for solving a structure to the first 100 Bragg peaks at low diffraction angles, as shown in the above example. Moreover, the small number of successful participants in the three SDPD round robins held in 1998, 2002 and 2008 (Le Bail *et al.*, 2009) did not allow us to conclude whether one approach is really better than the other, or even to be sure if all the further modifications of the extracted $|F_{hkl}|$ values in particular computer programs are really decisive improvements (the conclusion was that SDPD 'on demand' was still not an easy task). WPPD is not the only reef on the SDPD journey; indexing remains a considerable bottleneck for complex materials and low-resolution data.

References

Altomare, A., Burla, M. C., Camalli, M., Carrozzini, B., Cascarano, G. L., Giacovazzo, C., Guagliardi, A., Moliterni, A. G. G., Polidori, G. & Rizzi, R. (1999). *EXPO: a program for full powder pattern decomposition and crystal structure solution*. *J. Appl. Cryst.* **32**, 339–340.

Altomare, A., Burla, M. C., Cascarano, G., Giacovazzo, C., Guagliardi, A., Moliterni, A. G. G. & Polidori, G. (1995). *EXTRA: a program for extracting structure-factor amplitudes from powder diffraction data. J. Appl. Cryst.* **28**, 842–846.

Altomare, A., Cuocci, C., Giacovazzo, C., Moliterni, A. G. G. & Rizzi, R. (2011). *Obtaining models suitable for Rietveld refinement: the EXPO2011 techniques*. *Z. Kristallogr.* **226**, 869–881.

Baerlocher, Ch. (1990). *EXTRACT, a Fortran program for the extraction of integrated intensities from a powder pattern.* Institut für Kristallographie, ETH, Zürich, Switzerland.

Bergmann, J., Le Bail, A., Shirley, R. & Zlokazov, V. (2004). *Renewed interest in powder diffraction data indexing*. *Z. Kristallogr.* **219**, 783–790.

Byrom, P. G. & Lucas, B. W. (1993). *POLISH: computer program for improving the accuracy of structure-factor magnitudes obtained from powder data*. *J. Appl. Cryst.* **26**, 137–139.

Caglioti, G., Paoletti, A. & Ricci, F. P. (1958). *Choice of collimators for a crystal spectrometer for neutron diffraction*. *Nucl. Instrum.* **3**, 223–228.

Cheary, R. W. & Coelho, A. (1992). *A fundamental parameters approach to X-ray line-profile fitting*. *J. Appl. Cryst.* **25**, 109–121.

Clearfield, C., Reibenspies, J. & Bhuvanesh, N. (2008). *Principles and applications of powder diffraction*, pp. 261–309. Oxford: Wiley.

Cooper, M. J., Rouse, K. D. & Sakata, M. (1981). *An alternative to the Rietveld profile refinement method*. *Z. Kristallogr.*, **157**, 101–117.

David, W. I. F. (1987). *The probabilistic determination of intensities of completely overlapping reflections in powder diffraction patterns*. *J. Appl. Cryst.* **20**, 316–319.

David, W. I. F., Shankland, K., McCusker, L. B. & Baerlocher, Ch. (2002). *Structure Determination from Powder Diffraction Data*, IUCr Monographs on Crystallography, Vol 13. New York: Oxford University Press.

David, W. I. F., Shankland, K. & Shankland, N. (1998). *Routine determination of molecular crystal structures from powder diffraction data*. *Chem. Commun.* pp. 931–932.

Dinnebier, R. E. & Billinge, S. J. L. (2008). *Powder diffraction: theory and practice*, pp. 134–165. Cambridge: RSC Publishing.

Dong, W. & Gilmore, C. J. (1998). *The ab initio solution of structures from powder diffraction data: the use of maximum entropy and likelihood to determine the relative amplitudes of overlapped reflections using the pseudophase concept*. *Acta Cryst*. A**54**, 438–446.

Estermann, M. A. & Gramlich, V. (1993). *Improved treatment of severely or exactly overlapping Bragg reflections for the application of direct methods to powder data*. *J. Appl. Cryst.* **26**, 396–404.

Evans, J. S. O., Mary, T. A., Vogt, T., Subramanian, M. A. & Sleight, A. W. (1996). *Negative thermal expansion in ZrW_2O_8 and HfW_2O_8*. *Chem. Mater.* **8**, 2809–2823.

Giacovazzo, C. (1998). *Direct Phasing in Crystallography: Fundamentals and Applications*, IUCr Monographs on Crystallography, Vol. 8, pp. 410–444. New York: Oxford University Press.

Grazulis, S., Chateigner, D., Downs, R. T., Yokochi, A. F. T., Quirós, M., Lutterotti, L., Manakova, E., Butkus, J., Moeck, P. & Le Bail, A. (2009). *Crystallography Open Database - an open-access collection of crystal structures*. *J. Appl. Cryst.* **42**, 726–729.

Izumi, F. & Ikeda, T. (2000). *A Rietveld-analysis program RIETAN-98 and its applications to zeolites*. *Mater. Sci. Forum*, **321–324**, 198–205.

Jansen, E., Schäfer, W. & Will, G. (1988). *Profile fitting and the two-stage method in neutron powder diffractometry for structure and texture analysis*. *J. Appl. Cryst.* **21**, 228–239.

Jansen, J., Peschar, R. & Schenk, H. (1992). *On the determination of accurate intensities from powder diffraction data. I. Whole-pattern fitting with a least-squares procedure*. *J. Appl. Cryst.* **25**, 231–236.

Jouanneaux, A., Murray, A. D. & Fitch, A. N. (1990). *MPROF: a multipattern Rietveld refinement program for neutron, X-ray and synchrotron radiation*. SERC Daresbury Laboratory, Warrington, England.

Kariuki, B. M., Belmonte, S. A., McMahon, M. I., Johnston, R. L., Harris, K. D. M. & Nelmes, R. J. (1999). *A new approach for indexing powder diffraction data based on whole-profile fitting and global optimization using a genetic algorithm*. *J. Synchrotron Rad.* **6**, 87–92.

Langford, J. I., Boultif, A., Auffrédic, J. P. & Louër, D. (1993). *The use of pattern decomposition to study the combined X-ray diffraction effects of crystallite size and stacking faults in ex-oxalate zinc oxide*. *J. Appl. Cryst.* **26**, 22–33.

Langford, J. I. & Louër, D. (1991). *High-resolution powder diffraction studies of copper(II) oxide*. *J. Appl. Cryst.* **24**, 149–155.

Langford, J. I. & Louër, D. (1996). *Powder diffraction*. *Rep. Prog. Phys.* **59**, 131–234.

Langford, J. I., Louër, D., Sonneveld, E. J. & Visser, J. W. (1986). *Applications of total pattern fitting to a study of crystallite size and strain in zinc oxide powder*. *Powder Diffr.* **1**, 211–221.

Le Bail, A. (2001). *ESPOIR: A program for solving structures by Monte Carlo analysis of powder diffraction data*. *Mater. Sci. Forum*, **378**, 65–70.

Le Bail, A. (2005). *Whole powder pattern decomposition methods and applications: A retrospection*. *Powder Diffr.* **20**, 316–326.

Le Bail, A. (2007). *Structure Determination from Powder Diffraction Database – SDPD*. http://www.cristal.org/iniref.html.

Le Bail, A., Cranswick, L. M. D., Adil, K., Altomare, A., Avdeev, M., Cerny, R., Cuocci, C., Giacovazzo, C., Halasz, I., Lapidus, S. H., Louwen, J. N., Moliterni, A., Palatinus, L., Rizzi, R., Schilder, E. C., Stephens, P. W., Stone, K. H. & van Mechelen, J. (2009). *Third structure determination by powder diffractometry round robin (SDPDRR-3)*. *Powder Diffr.* **24**, 254–262.

Le Bail, A., Duroy, H. & Fourquet, J. L. (1988). *Ab-initio structure determination of $LiSbWO_6$ by X-ray powder diffraction*. *Mater. Res. Bull.* **23**, 447–452.

Lehmann, M. S., Christensen, A. N., Fjellvåg, H., Feidenhans'l, R. & Nielsen, M. (1987). *Structure determination by use of pattern decomposition and the Rietveld method on synchrotron X-ray and neutron powder data; the structures of $Al_2Y_4O_9$ and I_2O_4*. *J. Appl. Cryst.* **20**, 123–129.

McCusker, L. B., Von Dreele, R. B., Cox, D. E., Louër, D. & Scardi, P. (1999). *Rietveld refinement guidelines*. *J. Appl. Cryst.* **32**, 36–50.

Pagola, S., Stephens, P. W., Bohle, D. S., Kosar, A. D. & Madsen, S. K. (2000). *The structure of malaria pigment beta-haematin*. *Nature*, **404**, 307–310.

Pawley, G. S. (1981). *Unit-cell refinement from powder diffraction scans*. *J. Appl. Cryst.* **14**, 357–361.

Pecharsky, V. K. & Zavalij, P. Y. (2003). *Fundamentals of powder diffraction and structural characterization of materials*. New York: Springer.

Peschar, R., Schenk, H. & Capkova, P. (1995). *Preferred-orientation correction and normalization procedure for ab initio structure determination from powder data*. *J. Appl. Cryst.* **28**, 127–140.

Peterson, V. K. (2005). *Lattice parameter measurement using Le Bail versus structural (Rietveld) refinement: a caution for complex, low symmetry systems*. *Powder Diffr.* **20**, 14–17.

Rietveld, H. M. (1969). *A profile refinement method for nuclear and magnetic structures*. *J. Appl. Cryst.* **2**, 65–71.

Rius, J., Sane, J., Miravitlles, C., Amigo, J. M., Reventos, M. M. & Louër, D. (1996). *Determination of crystal structures from powder diffraction data by direct methods: extraction of integrated intensities from partially overlapping Bragg reflections*. *Anal. Quim.* **92**, 223–227.

Rodriguez-Carvajal, J. (1990). *FULLPROF: a program for Rietveld refinement and pattern-matching analysis*. Abstracts of the meeting Powder Diffraction, Toulouse, France, pp. 127–128.

Rodriguez-Carvajal, J. (1993). *Recent advances in magnetic structure detemination by neutron powder diffraction*. *Physica B*, **192**, 55–69.

Scott, H. G. (1987). *PROFIT – a peak-fitting program for powder diffraction profile*. IUCr Satellite Meeting on X-ray Powder Diffractometry, 20–23 August 1987, Fremantle, Western Australia. Abstract P28.

Sivia, D. S. & David, W. I. F. (1994). *A Bayesian approach to extracting structure-factor amplitudes from powder diffraction data*. *Acta Cryst.* A**50**, 703–714.

Smrčok, Ľ., Mach, P. & Le Bail, A. (2013). *Decafluorocyclohex-1-ene at 4.2 K – crystal structure and theoretical analysis of weak interactions*. *Acta Cryst.* B**69**, 395–404.

Solovyov, L. A., Fedorov, A. S. & Kuzubov, A. A. (2014). *Complete crystal structure of decafluorocyclohex-1-ene at 4.2 K from original neutron diffraction data*. *Acta Cryst.* B**70**, 395–397.

Sonneveld, E. J. & Visser, J. W. (1975). *Automatic collection of powder data from photographs*. *J. Appl. Cryst.* **8**, 1–7.

Toraya, H. (1986). *Whole-powder-pattern fitting without reference to a structural model: application to X-ray powder diffraction data*. *J. Appl. Cryst.* **19**, 440–447.

Toraya, H. (1994). *Applications of whole-powder-pattern fitting technique in materials characterization*. *Mater. Charact. Adv. X-ray Anal.* **37**, 37–47.

Waser, J. (1963). *Least-squares refinement with subsidiary conditions*. *Acta Cryst.* **16**, 1091–1094.

Wiles, D. B. & Young, R. A. (1981). *A new computer program for Rietveld analysis of X-ray powder diffraction patterns*. *J. Appl. Cryst.* **14**, 149–151.

Will, G. (1988). *Crystal structure analysis and refinement using integrated intensities from accurate profile fits*. *Aust. J. Phys.* **41**, 283–296.

Will, G., Masciocchi, N., Parrish, W. & Hart, M. (1987). *Refinement of simple crystal structures from synchrotron radiation powder diffraction data*. *J. Appl. Cryst.* **20**, 394–401.

Will, G., Parrish, W. & Huang, T. C. (1983). *Crystal-structure refinement by profile fitting and least-squares analysis of powder diffractometer data*. *J. Appl. Cryst.* **16**, 611–622.

Young, R. A. (1993). *The Rietveld Method*. IUCr Monographs on Crystallography, Vol. 5. New York: Oxford University Press.

International Tables for Crystallography (2019). Vol. H, Chapter 3.6, pp. 288–303.

3.6. Whole powder pattern modelling: microstructure determination from powder diffraction data

M. Leoni

3.6.1. Introduction

X-ray diffraction is a very simple technique, but is one of the most flexible and powerful tools for the analysis of materials. The diffraction pattern carries information about the atomic arrangement and motion at both the short and the long range; for nanostructured materials this means that a single technique can simultaneously provide structural and microstructural information.

Microstructure analysis *via* X-ray powder diffraction (XRD), often termed line-profile analysis (LPA), is mostly performed through the Scherrer (1918) formula. Just a few years after the discovery of X-ray diffraction, Scherrer derived a very simple relationship between the width of the diffraction peaks and the size of the so-called *Kristallchen* (translated as crystallites), the coherently scattering (nanocrystalline) domains composing the colloids that he was studying (the formula is rewritten here using an updated notation):

$$\langle D\rangle = \frac{K_w\lambda}{\mathrm{FWHM}_{hkl}\cos\theta_{hkl}}. \qquad (3.6.1)$$

The calculation of an 'average size' $\langle D\rangle$ is therefore immediate once the position and full-width at half-maximum of a peak ($2\theta_{hkl}$ and FWHM_{hkl}, respectively), measured with X-rays of wavelength λ, are available. The constant K_w (the Scherrer constant) carries information on the shape of the domains and has an order of magnitude of 1. Values of the Scherrer constant can be found in the literature for both isotropic and anisotropic shapes (in the latter case leading to different sizes for different reflections *hkl*): Table 3.6.1 contains the data of Langford & Wilson (1978) for common domain shapes. An elegant derivation of the Scherrer formula can be found in the work of Patterson (1939) and Warren (1990); a summary is also presented in Chapter 5.1.

Its simple mathematical nature is probably the main reason for the widespread (ab)use of equation (3.6.1). Simple, in fact, does not mean accurate.

The Scherrer formula and its variants are based on strong assumptions about the peak shape. In the original derivation [equation (3.6.1)] the peak was assumed to be Gaussian (see Appendix A3.6.1 for the definition of a unit-area Gaussian); in subsequent derivations, the peak-shape information is lost, as the peak is transformed into an equivalent rectangle *via* the use of the integral breadth (IB) $\beta = A/I$, where A and I are the area and the maximum intensity of the peak, respectively (see Table 3.6.1 for the corresponding Scherrer constant values). Together with this, we should consider that the size of the domains in a real specimen is always disperse; it can be easily proven that the quantity $\langle D\rangle$, which is called the 'average size' or 'mean size', is actually not the mean (first moment) of the size distribution, but is related to its third moment (*i.e.* it is volume-weighted). If we add that the finite size of the domains is not the only source of peak broadening, we immediately see where the abuse of the Scherrer formula can lie.

Table 3.6.1
Scherrer constants (K_w and K_β) for various domain shapes (Langford & Wilson, 1978)

Shape	K_w (FWHM)	K_β (integral breadth)
Sphere	0.89	1.07
Cube	0.83–0.91	1.00–1.16
Tetrahedron	0.73–1.03	0.94–1.39
Octahedron	0.82–0.94	1.04–1.14

To try to sort some of those issues out, Williamson & Hall (1953) proposed plotting the FWHM (or the IB) *versus* the reciprocal of the lattice spacing ($d^*_{hkl} = 1/d_{hkl} = 2\sin\theta_{hkl}/\lambda$). For spherical domains (*i.e.* size independent of the direction), a horizontal line is expected. An anisotropic shape would cause a scattering of the points, whereas other sources of broadening might also change the slope. Following the findings of Stokes & Wilson (1944), Williamson and Hall proposed writing the integral breadth in reciprocal space (reciprocal-space variable d^*) as a combination of the Scherrer formula with the differential of Bragg's law:

$$\beta(d^*) = \frac{K_\beta}{\langle D\rangle} + 2ed^*. \qquad (3.6.2)$$

Equation (3.6.2) describes a line for which the intercept (extrapolation of the integral breadth to the origin of the reciprocal space, *i.e.* to $d\rightarrow\infty$) is related to the reciprocal of the Scherrer size, and the slope parameter e accounts for the distribution of local strain inside the domains. For a Gaussian distribution of this local strain, the root-mean strain (also known as microstrain) $\langle\varepsilon^2\rangle^{1/2} = e\sqrt{2/\pi}$ can be obtained. The microstrain, which is mostly caused by the presence of imperfections, is often quoted together with the average size.

Even though the Williamson–Hall idea is straightforward, there is no physical reason why the two terms in equation (3.6.2) should be added: the only case where breadths are additive is when the peaks are Lorentzian (see Appendix A3.6.1 for the definition of a unit-area Lorentzian). The Williamson–Hall equation is therefore valid for Lorentzian peaks and under the condition that both the size and strain contributions are Lorentzian as well. We therefore immediately envisage a problem here, as the size contribution, described by the Scherrer equation, was derived in the Gaussian limit. This inconsistency is seldom reported or considered in the literature. The fact that, in the end, the profiles are often highly Lorentzian in character mathematically justifies the separation of a size and a strain term, but dilutes the quantitative meaning of the result.

Modification of the Williamson–Hall approach to remove the inconsistency of the size- and strain-broadening terms has been extensively discussed by Balzar & Popović (1996). Using Voigtians (*i.e.* the convolution of a Gaussian G and a Lorentzian L; see Appendix A3.6.1) to describe a profile, four combinations are possible for the size and strain terms: *L*–*L*, *L*–*G*, *G*–*L* and *G*–*G*. The Williamson–Hall method corresponds to the *L*–*L* case, whereas the combinations involving a Gaussian size term are more compatible with the Scherrer formula. Even in those cases, though, 'The pure-Gauss size-broadened profile is incompatible

with the definitions of surface-weighted domain size and column-length distribution function' (Balzar & Popović, 1996): integral breadth methods are therefore intrinsically limited for the microstructure analysis of real materials. This is in stark contrast to the fact that equation (3.6.2) is used, for example, by a large number of Rietveld refinement codes to describe the observed trend in line-profile broadening (and to perform a rough microstructure analysis). This situation can be improved a little by properly considering at least the anisotropic broadening component, as performed, for example, in the modified Williamson–Hall method (MWH; Ungár & Borbély, 1996; Ungár, 2001; Scardi *et al.*, 2004). The results are more accurate and related to some physical quantities (a dislocation density and a stacking fault probability), but they are still tightly bound to a Voigtian profile approximation.

An alternative to the integral breadth methods was developed by Warren & Averbach (1950, 1952) almost simultaneously with the idea of Williamson and Hall, but took longer to be fully employed owing to the lack of fast computing tools. It is based on the extensive use of Fourier transforms and represents the starting point of modern line-profile analysis techniques. The whole profile carries information on the microstructure, as each point in reciprocal space is related to the Fourier transform of real space (and thus to the size and shape of the domains and also the deviation from perfect three-dimensional periodicity). Each profile also contributes to a better picture of the microstructure, as it samples along a different direction in space.

For decades, these Fourier methods were only used in a very small number of scientific areas; the availability of fast computers and the fast Fourier transform has contributed greatly to their further diffusion. It is, however, only in recent years that the full power of the Fourier approach has been unveiled, with the development of whole-pattern methods and the extension of most models to a wider range of materials.

3.6.2. Fourier methods

3.6.2.1. *Definitions*

In the following, the diffraction peaks for a powder will be described in reciprocal space with reference to the Bragg position $d^*_{\{hkl\}}$ expected for the $\{hkl\}$ reflection family in the absence of any type of defect. The coordinate s, where

$$s = d^* - d^*_{\{hkl\}} = \frac{2}{\lambda}\left(\sin\theta - \sin\theta_{\{hkl\}}\right), \tag{3.6.3}$$

will be employed. Moving from reciprocal to diffraction space ('2θ space') involves a trivial but nonlinear change of variables: peaks that are symmetrical in reciprocal space will become asymmetrical in 2θ space and *vice versa*.

3.6.2.2. *Peak profile and the convolution theorem*

Each peak profile $h(s)$ in a powder diffraction pattern can be described as the convolution of an instrumental profile $g(s)$ with a function $f(s)$ accounting for sample-related effects (microstructure; see, for example, Jones, 1938; Alexander, 1954; Klug & Alexander, 1974; and references therein):

$$h(s) = \int_{-\infty}^{\infty} f(y)g(s-y)\,\mathrm{d}y = f \otimes g(s). \tag{3.6.4}$$

The calculation of the integral in equation (3.6.4) can be simplified through the use of a Fourier transform (FT). In fact, the convolution theorem states that the FT of a convolution is the product of the Fourier transforms of the functions to be folded:

$$\mathcal{C}(L) = \mathrm{FT}[h(s)] = \mathrm{FT}[f(s)] \times \mathrm{FT}[g(s)]. \tag{3.6.5}$$

In this equation, L is the (real) Fourier variable conjugate to s. The properties of the Fourier transform allow equation (3.6.4) to be rewritten as

$$h(s) = \mathrm{FT}^{-1}[\mathcal{C}(L)] = \mathrm{FT}^{-1}\big[\mathrm{FT}[h(s)]\big] = \mathrm{FT}^{-1}\big[\mathrm{FT}[f(s)]\mathrm{FT}[g(s)]\big]. \tag{3.6.6}$$

This equation is the basis of the Warren–Averbach approach and also of all modern LPA methods.

3.6.2.3. *The Warren–Averbach method and its variations*

The convolution theorem can be employed to disentangle the specimen-related broadening contributions described by $f(s)$. In fact, let us suppose, as in the Williamson–Hall method, that size and microstrain are the only two sources of specimen-related broadening. We call the Fourier transform of the profiles broadened by size and distortion effects only $A^S_{hkl}(L)$ and $A^D_{hkl}(L)$, respectively. As the size and distortion profiles are folded into $f(s)$, the following holds:

$$A(L) = \mathrm{FT}[f(s)] = \mathrm{FT}[h(s)]/\mathrm{FT}[g(s)] = A^S_{hkl}(L)A^D_{hkl}(L). \tag{3.6.7}$$

The separation of the size and distortion terms is straightforward for spherical domains: the size effects for a sphere are independent of the reflection order, whereas those related to distortions (causing the change in the slope of the Williamson–Hall plot) are order-dependent. To describe the distortion term it is convenient to follow the idea of Bertaut (1949*a*,*b*, 1950), considering the specimen as made of columns of cells along the **c** direction. The profile due to distortions is calculated by taking the average phase shift along the column due to the presence of defects. The analytical formula for the distortion term is thus of the type $A^D_{hkl}(L) = \langle\exp(2\pi i L n\varepsilon_L)\rangle$, where $\varepsilon_L = \Delta L/L$ is the average strain along **c** calculated for a correlation distance (*i.e.* Fourier length) L.

As a first-order approximation, the distortion terms give no profile asymmetry; $A^D_{hkl}(L)$ is just a cosine Fourier transform. We can thus expand it as (Warren, 1990)

$$A^D_{hkl}(L) = \langle\cos(2\pi L n\varepsilon_L)\rangle = 1 - 2\pi^2L^2n^2\langle\varepsilon_L^2\rangle. \tag{3.6.8}$$

If we now rewrite equation (3.6.7) on a log scale, taking equation (3.6.8) into account, we obtain

$$\begin{aligned}\ln[A_{hkl}(L)] &= \ln[A^S_{hkl}(L)] + \ln[A^D_{hkl}(L)] \\ &= \ln[A^S_{hkl}(L)] + \ln[1 - 2\pi2L^2n^2\langle\varepsilon_L^2\rangle] \\ &= \ln[A^S_{hkl}(L)] - 2\pi^2L^2n^2\langle\varepsilon_L^2\rangle.\end{aligned} \tag{3.6.9}$$

Equation (3.6.9) represents a line in the variable n^2: the intercepts at increasing L values provide the logarithm of the Fourier size term, whereas the slopes give the microstrain directly (Warren, 1990). From the size coefficients, we can obtain an average size, again following the idea of Bertaut (1949*a*, 1950), related to the properties of the Fourier transform:

$$\langle D\rangle = \left[-\frac{\partial A^S_{hkl}(L)}{\partial L}\bigg|_{L=0}\right]^{-1}. \tag{3.6.10}$$

This average size is thus related to the initial slope of the Fourier coefficients [assuming that they are well behaved, *i.e.* that the tangent is always below the $A^S_{hkl}(L)$ curve].

A long chain of operations is needed to obtain the size and the strain contributions; there is thus a risk that the final result will no longer be compatible with the experimental data. Only a few years after the introduction of this method, Garrod *et al.* (1954) wrote

> Hence, in any attempt to distinguish between particle size or strain broadening from a particular material, the use of the one or the other of these functions [Gaussian and Lorentzian] (together with the appropriate relationship between B, b, and β) involves an intrinsic initial assumption about the cause of the broadening, when the object of the investigation is to discover the cause. Such an assumption must inevitably weight the experimental results, partially at least, in favour of one or the other of the two effects. In this connexion it is therefore perhaps significant that in most previous work on the cause of line broadening from cold-worked metals, those investigators who have used the Warren relationship between B, b, and β have concluded that lattice distortion was the predominant factor, whilst those who have employed the Scherrer correction found that particle size was the main cause. The best procedure in such work therefore is to make no assumptions at all about the shape of the experimental line profiles . . .

This is owing to the fact that a direct connection between the experimental data and the final microstructural result does not really exist in those methods and that the whole information contained in the pattern is not exploited.

3.6.2.4. *Beyond the Warren–Averbach method*

The work of Alexander (see, for example, Alexander, 1954; Klug & Alexander, 1974; and references therein) was definitely pioneering here. Alexander proposed a set of formulae for the synthesis of the instrumental profile, with the aim of obtaining a correction curve to subtract the instrumental contribution to the measured breadth of the profiles (thus improving the accuracy of the size determination). The true power of this idea was not fully exploited, as the Scherrer formula was still used for microstructure analysis. A few decades later, Adler, Houska and Smith (Adler & Houska, 1979; Houska & Smith, 1981) proposed the use of simplified analytical functions to describe the instrument, size and strain broadening and to perform the convolution of the equation numerically *via* Gauss–Legendre quadrature. Rao & Houska (1986) improved the procedure by carrying out part of the integration analytically (for monodisperse spheres). The microstructure parameters are directly obtained from a fit of this numerical peak to the experimental data. The fit partly solves the problem of peak overlap: in traditional methods it is in fact impossible to establish the extent of overlap between the peaks and therefore to correctly extract the area or maximum intensity. The method is a major step forward, but is still related to the Warren–Averbach approach, as just two multiple-order peaks are considered.

Cheary & Coelho (1992, 1994, 1998*a*,*b*) pushed the idea forward with the fundamental parameters approach (FPA). The FPA is based on the intuition of Alexander (1954) and the general idea of the Rietveld (1969) method: the calculation speed is greatly improved to facilitate widespread use. The convolution is performed directly in 2θ space, where instrumental aberrations, which were extensively explored by these researchers, occur. Very simplistic models were employed to describe the broadening due to the specimen; the whole pattern (and therefore all of the measured information) is considered in place of one or more peaks and of the extracted information. For structural analysis and for the Rietveld method, the FPA is a huge step forward, as it allows a more accurate determination of lattice parameters and integrated intensities. Moreover, it enables some line-profile analysis on low-quality patterns or on data affected by strong peak asymmetry.

3.6.2.5. *Whole powder pattern modelling (WPPM)*

The techniques briefly illustrated in the previous section, as well as other alternatives appearing in the literature before the beginning of this century, lack full completeness for quantitative microstructure analysis. The whole powder pattern modelling method attempted to fill this gap. Starting with the same ideas as in Section 3.6.2.1 (*i.e.* peaks as convolution), it uses equations (3.6.5) and (3.6.6) to generate the peaks within a fully convolutional approach. The peak profiles are therefore generated from the Fourier transform of each broadening component; the resulting $h(x)$ function accounts just for the shape of the profile, which in turn can be represented as (Scardi & Leoni, 2002)

$$I_{\{hkl\}}(s) = k(d^*)h(s) = k(d^*) \int_{-\infty}^{\infty} \mathcal{C}(L) \exp(2\pi i L s)\, \mathrm{d}L, \quad (3.6.11)$$

where $k(d^*)$ includes all constant or known functions of d^* (*e.g.* structure factor, Lorentz–polarization factor *etc.*), whereas $\mathcal{C}(L)$ is the Fourier transform of the peak profile. The term k is a function of d^*; it is not necessarily a function of s, as the peak is actually centred in $d^*_{\{hkl\}}$.

Equation (3.6.11) assumes that the broadening sources act on the entire family of symmetry-equivalent reflections $\{hkl\}$ and therefore that a multiplicity term [included in $k(d^*)$] can be used: however, certain types of defects (*e.g.* faults) can act independently on each of the symmetry-equivalent reflections. Equation (3.6.11) then becomes more correctly

$$I_{\{hkl\}}(s) = k(d^*) \sum_{hkl} w_{hkl} I_{hkl}(s_{hkl}) = k(d^*) \sum_{hkl} w_{hkl} I_{hkl}(s - \delta_{hkl}), \quad (3.6.12)$$

where w_{hkl} is a weight function depending on the lattice symmetry and actual broadening source, $s_{hkl} = d^* - (d^*_{\{hkl\}} + \delta_{hkl}) = s - \delta_{hkl}$ is the distance, in reciprocal space, from the centroid of the peak hkl, and δ_{hkl} is the shift from $d^*_{\{hkl\}}$, the Bragg position in the absence of defects. The sum is over independent profile subcomponents selected on the basis of the specific defects (*e.g.* two for the {111} family in f.c.c. when faults are present; selection is based on the value of $|L_0| = |h + k + l|$, *i.e.* 3 or 1).

According to equation (3.6.5), the function $\mathcal{C}(L)$ is the product of the Fourier transforms of the broadening contributions. In a real material, broadening is mostly due to the specific nature of the instrument, to the finite size of the coherently diffracting domain (size effect) and to the presence of defects such as, for example, dislocations and faults (Cheary & Coelho, 1992; van Berkum, 1994; Scardi & Leoni, 2002). Taking these into account,

$$\mathcal{C}(L) = T^{\mathrm{IP}}(L) A^S_{hkl}(L) \langle \exp[2\pi i \psi_{hkl}(L)] \rangle \langle \exp[2\pi i \varphi_{hkl}(L)] \rangle \ldots, \quad (3.6.13)$$

where $T^{\mathrm{IP}}(L)$ and $A^S_{hkl}(L)$ are the FTs of the instrumental and domain-size components, respectively, whereas the terms in angle brackets $\langle\,\rangle$ are average phase factors related to lattice distortions (ψ_{hkl}) and faulting (φ_{hkl}).

Equation (3.6.13) is the core of the WPPM method: as indicated by the ellipsis, any other broadening source can easily be considered by including the corresponding (complex) Fourier transform (*i.e.* the corresponding average phase factor) in equation (3.6.13). Expressions are known for several cases of practical interest (see, for example, Scardi & Leoni, 2002, 2004,

2005; Leoni & Scardi, 2004; Leineweber & Mittemeijer, 2004; van Berkum, 1994; Cheary & Coelho, 1992).

The approach is strictly valid when the broadening sources can be considered as diluted and independent (*i.e.* uncorrelated defects). If this does not apply, then cross-terms should be considered and the whole approach revised. In fact, here we assume that the structure factor can be factored and the lattice is fully periodic in three dimensions: under these conditions, structure (peak intensity) and microstructure (peak shape) can be decoupled as the peak positions can be determined in a straightforward way. Extended defects (*e.g.* faults) cause the appearance of diffuse effects and the displacement of the Bragg peaks: in order to calculate the diffraction pattern, the structure and the microstructure must be simultaneously known (see, for example, Drits & Tchoubar, 1990).

3.6.2.6. *Broadening components*

A brief account is given of the main sources of broadening that can be encountered in practice. An accent will be placed on X-rays, but extension to electrons and neutrons is in most cases straightforward. Concerning electron diffraction, precession data can be used in a straightforward way, whereas for traditional data, containing dynamical effects, further calculations, for example of the intensity, are in principle needed.

3.6.2.6.1. *Instrument*

Each of the components of the diffraction instrument (*i.e.* source, optics, specimen stage, measurement geometry and detector) can have a dramatic impact both on the position and the broadening of the peaks. Axial divergence, for instance, introduces both an asymmetric broadening and an apparent shift of the low-angle peaks. When microstructure (*i.e.* specimen-related effects) is the focus of the analysis, the primary recommendation is to try to limit the instrumental influence. Alternatively, it is preferred to have an instrumental profile (no matter how complex) that can be well described and properly simulated: for instance the profile of an instrument with a $K\alpha_1$ primary monochromator (apparently advantageous) might be hard to model if the $K\alpha_2$ removal is not perfect. This becomes more and more important when the instrumental effects are of the same order of magnitude as the specimen-related broadening.

Two possible paths can be followed when dealing with the instrumental contribution: modelling using the fundamental parameters approach (see, for example, Cheary & Coelho, 1992; Kern & Coelho, 1998) or parameterization of the pattern of an ideal specimen. In the fundamental parameters approach, the geometry of the instrument and the effects of each optical component on the peak profile are described mathematically in 2θ. Most of the formulae for the various optical elements can be found, for example, in the work of Wilson (1963), Klug & Alexander (1974) and Cheary & Coelho (1992, 1994, 1998*a*,*b*). The aberration profiles are folded into the (X-ray) source emission profile (Hölzer *et al.*, 1997; Deutsch *et al.*, 2004) to generate a combined instrumental profile.

When no information on the instrument is available, it is possible to predict the instrumental profile just by using the nominal data for the optical components. It is however advised, whenever possible, to tune the instrumental parameters using the pattern of a line-profile standard [*e.g.* NIST LaB_6 SRM 660(x) series; Cline *et al.*, 2010] showing negligible specimen effects. These instrument-only parameters must then be kept fixed for any subsequent microstructure refinement. It is of paramount importance that all instrumental features are well reproduced when dealing with microstructure effects. Provided that this condition is met, we can therefore employ any arbitrary function to describe the instrumental profile. Thus, as an alternative to FPA, we can either 'learn' the instrumental profile from a standard (Bergmann & Kleeberg, 2001) or use a Voigtian to model it. The Voigtian is particularly convenient as it can be defined directly in L space and thus directly enter the Fourier product of equation (3.6.13).

3.6.2.6.2. *Source emission profile*

For X-rays, the source emission profile at an energy E_l can be well described by a Lorentzian of energy width Γ_l (Hölzer *et al.*, 1997; Deutsch *et al.*, 2004),

$$I_l(E) = \frac{2}{\Gamma_l \pi}\left[1 + 4\left(\frac{E - E_l}{\Gamma_l}\right)^2\right]^{-1}. \tag{3.6.14}$$

As $\mathrm{d}E/E = \mathrm{d}\lambda/\lambda = \mathrm{d}s/s$, the function can also be represented as a function of s:

$$I^{\mathrm{IP}}_{hkl,l}(s, d^*_{hkl}) = \frac{2}{\pi}\frac{E_l}{d^*_{hkl}\Gamma_l}\left[1 + 4\left(\frac{s_{hkl}}{d^*_{hkl}\Gamma_l/E_l}\right)^2\right]^{-1}. \tag{3.6.15}$$

For a laboratory tube emitting simultaneously a set of N_λ wavelengths, we have

$$I^{\mathrm{IP}}_{hkl}(s, d^*_{hkl}) = \sum_{l=1}^{N_\lambda} w_l I^{\mathrm{IP}}_{hkl,l}(s, d^*_{hkl}), \tag{3.6.16}$$

where w_l is the relative intensity of the lth wavelength component (referred, for example, to $w_1 = 1$). The corresponding Fourier transform entering (3.6.13) can be written as

$$\begin{aligned} T^{\mathrm{IP}}(L) &= \sum_{l=1}^{N_\lambda} \exp\left[2\pi i d^*_{hkl}\left(1 - \frac{\Gamma_l}{E_l}\right)L\right]\exp\left(-2\pi s_{hkl}\frac{\Gamma_l}{E_l}L\right) \\ &= \sum_{l=1}^{N_\lambda}\left\{\cos\left[2\pi d^*_{hkl}\left(1 - \frac{\Gamma_l}{E_l}\right)L\right] + i\sin\left[2\pi d^*_{hkl}\left(1 - \frac{\Gamma_l}{E_l}\right)L\right]\right\} \\ &\quad \times \exp\left(-2\pi s_{hkl}\frac{\Gamma_l}{E_l}L\right). \end{aligned} \tag{3.6.17}$$

The complex term in (3.6.17) accounts for the shift of each emission component with respect to the reference one. For more flexibility (for example to consider the non-ideal behaviour of the instrument), we can use a pseudo-Voigt (pV) in place of the Lorentzian in equation (3.6.14).

3.6.2.6.3. *Optical elements*

The equation of Caglioti *et al.* (1958), modified by Rietveld (1969) and originally developed for constant-wavelength neutron diffraction, is frequently employed for parameterization of the instrumental profile. The FWHM and the pV mixing parameter η (replacing the Lorentzian and Gaussian widths of the Voigt) are then parameterized according to functions in $\tan(\theta)$ and θ, respectively (Caglioti *et al.*, 1958; Leoni *et al.*, 1998; Scardi & Leoni, 1999),

$$\mathrm{FWHM}^2 = U\tan^2\theta + V\tan\theta + W, \tag{3.6.18}$$

$$\eta = a + b\theta + c\theta^2. \tag{3.6.19}$$

The parameters of the Fourier transform of a Voigt or pseudo-Voigt are then constrained to those of equations (3.6.18) and

(3.6.19). This is particularly convenient, as the Fourier transform of a Voigtian is analytical. In fact, for the pV case we have

$$T_{\rm pV}^{\rm IP}(L) = (1-k)\exp(-\pi^2\sigma^2L^2/\ln 2) + k\exp(-2\pi\sigma L), \tag{3.6.20}$$

where σ = FWHM/2 and where (Langford & Louër, 1982; Scardi & Leoni, 1999)

$$k = \left[1 + (1-\eta)/\left(\eta\sqrt{\pi\ln 2}\right)\right]^{-1}. \tag{3.6.21}$$

Equation (3.6.18) can be found in the literature in a different form and with additional terms accounting, for example, for size effects: besides forcing a symmetry of the profile in 2θ space, these extra terms are a contradiction as they have nothing to do with the instrument itself.

3.6.2.6.4. *Domain size and shape*

In nanostructured materials, the finite size of the scattering domains is usually the dominant source of line-profile broadening. Actually, when dealing with size, we should consider a size and a shape distribution of the domains. In most cases, one or more distributions of similar objects are considered. For an up-to-date description of issues related to size broadening, see Chapter 5.1. The domain shape is not a property of the material and therefore the use of symmetry constraints [*e.g.* spherical harmonics to describe the shape of the scattering object as in the model of Popa (1998) or as a size extension of Stephens' (1999) work] is not justified in the general case (Nye, 1987). Exceptions, however, exist.

The size-broadening contribution in WPPM follows the ideas of Bertaut (1949*a*,*b*, 1950) and of Stokes & Wilson (1942). Bertaut proposed the division of the domains into columns and the analysis of the independent scattering of these columns. The column-length distribution can always be extracted from the data: more complex models involving given shapes or distributions simply modify the way in which the columns are rearranged. Stokes and Wilson introduced the concept of a *ghost* to calculate the Fourier transform for a given shape: the volume common to a domain of shape c and its ghost, *i.e.* a copy of the same domain displaced by a quantity L along the scattering direction hkl, is proportional to the (size) Fourier transform $A^S_{c,hkl}(L, D)$ for the given domain. The calculation has been already carried out analytically for several simple shapes characterized by a single length parameter (Stokes & Wilson, 1942; Lele & Anantharaman, 1966; Wilson, 1969; Langford & Louër, 1982; Vargas *et al.*, 1983; Grebille & Bérar, 1985; Scardi & Leoni, 2001), and can be performed numerically in the general case (Leonardi *et al.*, 2012). It is possible to relate the Fourier coefficients to the size values obtained from traditional methods. In particular, the area-weighted average size $\langle L\rangle_S$ (Warren–Averbach method) and the volume-weighted average size $\langle L\rangle_V$ (Williamson–Hall method) are obtained as

$$\langle L\rangle_S = -\left[dA^S_c(L,D)/dL\big|_{L=0}\right]^{-1} = D/K_k = -D/H_1, \tag{3.6.22}$$

$$\langle L\rangle_V = [\beta(s)]^{-1} = 2\int_0^{D/K} A^S_c(L,D)\,{\rm d}L = D/K_\beta, \tag{3.6.23}$$

where $\beta(s)$ is the integral breadth and K_k and K_β are the initial slope and integral breadth Scherrer constants, respectively (Langford & Wilson, 1978; Scardi & Leoni, 2001).

The average size might have little physical significance in real cases: the size (and shape) distribution can in fact play a key role in determining both the properties and the diffraction line-profile shapes of the powder under analysis. Fortunately, the Fourier coefficients for the polydisperse case can be easily calculated for any given distribution: the log-normal and the gamma distributions are the most common (and the most flexible). The equations and the corresponding moments are

$$g_l(D) = \frac{1}{D\sigma_l\sqrt{2\pi}}\exp\left[-\frac{(\ln D-\mu_l)^2}{2\sigma_l^2}\right],$$
$$M_{l,n} = \exp\left(n\mu_l + \frac{n^2}{2}\sigma_l^2\right), \tag{3.6.24}$$

$$g_g(D) = \frac{\sigma_p}{\mu_g\Gamma(\sigma_g)}\left(\frac{\sigma_g D}{\mu_g}\right)^{\sigma_g-1}\exp\left(-\frac{\sigma_g D}{\mu_g}\right),$$
$$M_{g,n} = \left(\frac{\mu_g}{\sigma_g}\right)^n\frac{\Gamma(n+\sigma_g)}{\Gamma(\sigma_g)}. \tag{3.6.25}$$

The scattered intensity for the given distribution g_i, and the given shape c, is

$$\begin{aligned} I_{c,hkl}(s) &\propto \frac{\int_0^\infty\left[\int_{L=0}^{D/K_{hkl}} A^S_{c,hkl}(L,D)\exp(2\pi iLs)\,{\rm d}L\right]w(D)\,{\rm d}D}{\int_0^\infty w(D)\,{\rm d}D} \\ &\propto \int_{L=0}^\infty\left[\frac{\int_{D=LK_{hkl}}^\infty A^S_{c,hkl}(L,D)w(D)\,{\rm d}D}{\int_0^\infty w(D)\,{\rm d}D}\right]\exp(2\pi iLs)\,{\rm d}L \\ &\propto \int_{L=0}^\infty A^S_{hkl}(L)\exp(2\pi iLs)\,{\rm d}L, \end{aligned} \tag{3.6.26}$$

where $w(D) = g_i(D)V_c(D)$ and where

$$A^S_{hkl}(L) = \frac{\int_{D=LK_{hkl}}^\infty A^S_{c,hkl}(L,D)w(D)\,{\rm d}D}{\int_0^\infty w(D)\,{\rm d}D}. \tag{3.6.27}$$

With a suitable definition of the Fourier coefficients, the polydisperse case therefore becomes analogous to the monodisperse case. Analytic expressions can be obtained in particular cases. For instance, the Fourier coefficients for the log-normal and gamma distributions (Scardi & Leoni, 2001) are

$$A^S_l(L) = \sum_{n=0}^3 {\rm erfc}\left[\frac{\ln(LK_c)-\mu_l-(3-n)\sigma_l^2}{\sigma_l\sqrt{2}}\right]\frac{M_{l,3-n}}{2M_{l,3}}H_n^cL^n \tag{3.6.28}$$

and

$$A^S_g(L) = \sum_{n=0}^3\left(\frac{\sigma_g}{M_{g,1}}\right)^n\frac{\Gamma[\sigma_g+(3-n),K_cL\sigma_g/M_{g,1}]}{\Gamma(\sigma_g+3)}H_n^cL^n, \tag{3.6.29}$$

respectively, where

$$\Gamma(x,a) = \int_a^\infty y^{x-1}\exp(-y)\,{\rm d}y,$$
$$\Gamma(x) = \Gamma(x,0),$$
$${\rm erfc}(x) = 2\pi^{-1/2}\int_x^\infty\exp(-y^2)\,{\rm d}y,$$

with the definitions already given in equations (3.6.24) and (3.6.25).

The functional forms of equations (3.6.28) and (3.6.29) clearly suggest that the profile for a log-normal distribution of domains (which is frequently encountered in practice) is not Voigtian: all traditional line-profile analysis methods (based on Voigt or pseudo-Voigt functions) are therefore unable to correctly deal with a log-normally dispersed powder.

By analogy to the monodisperse case, it is possible to relate the parameters of the polydisperse system to the size obtained with traditional methods (Warren–Averbach and Williamson–Hall, respectively). The following holds (Krill & Birringer, 1998; Scardi & Leoni, 2001):

$$\langle L\rangle_S = \frac{1}{K_k}\frac{M_{i,3}}{M_{i,2}}, \quad \langle L\rangle_V = \frac{1}{K_\beta}\frac{M_{i,4}}{M_{i,3}}. \tag{3.6.30}$$

Here, it is clear that diffraction does not provide the first moment of the distribution directly: ratios between high-order moments are involved.

Using an analytical expression for the description of a size distribution can help in stabilizing the results (as the size distribution curve is forced to be zero at very small and very large size values). Some doubts can, however, arise as to the physical validity of this forcing. An example is the case of a multimodal system. The traditional LPA techniques are unable to directly deal with multimodal size distributions. In cases where the multimodal character is clear and the various distribution are well behaved (*i.e.* when they can be modelled with analytical functions), the pattern can be usually modelled by considering the material as made of different fractions, each of them characterized by a different size distribution.

A possible alternative has been proposed in the literature: replacing the analytical distribution with a histogram. The ability of this model to fit the experimental data has been demonstrated (Leoni & Scardi, 2004; Matěj *et al.*, 2011); a regularization might be necessary to stabilize the shape and/or smoothness of the size distribution. The quality of the measurement and the availability of models describing all contributions to the peak broadening are in most cases the limiting factors for extensive use of the histogram model: correlations of small sizes with the background and with features such as thermal diffuse scattering (Beyerlein *et al.*, 2012) can in fact occur. So far, this is the only available method for exploring cases where the analytical models are unable to correctly describe the observed broadening.

3.6.2.6.5. *Strain broadening (lattice distortions)*

A local variation of the lattice spacing (due, for example, to the presence of a defect) leads to an average phase term that, in general, is a complex quantity:

$$\begin{aligned}\langle\exp[2\pi i\psi_{hkl}(L)]\rangle &= \langle\cos[(2\pi L d^*_{\{hkl\}}\varepsilon_{\{hkl\}}(L)]\rangle \\ &\quad + i\langle\sin[2\pi L d^*_{\{hkl\}}\varepsilon_{\{hkl\}}(L)]\rangle \\ &= A^D_{\{hkl\}}(L) + iB^D_{\{hkl\}}(L).\end{aligned} \tag{3.6.31}$$

The strain $\varepsilon_{\{hkl\}}(L)$ represents the relative displacement of atoms at a (coherence) distance L along the scattering vector hkl. Knowledge of the actual source of distortion allows the explicit calculation of the various terms (van Berkum, 1994). It is quite customary to assume that the strain is the same for symmetry-equivalent reflections [$\varepsilon_{hkl}(L) = \varepsilon_{\{hkl\}}(L)$]: this is a reasonable hypothesis for a powder, where we assume that any configuration is equally probable.

Traditional LPA methods such as the Warren–Averbach method (Warren & Averbach, 1950, 1952; Warren, 1990) take a first-order MacLaurin expansion of equation (3.6.31) to extract the microstrain contribution from the measured data:

$$A^D_{\{hkl\}}(L) \cong 1 - 2\pi^2 L^2 d^{*2}_{\{hkl\}}\langle\varepsilon^2_{\{hkl\}}(L)\rangle, \tag{3.6.32}$$

$$B^D_{\{hkl\}}(L) \cong -\frac{4}{3}\pi^3 L^3 d^{*3}_{\{hkl\}}\langle\varepsilon^3_{\{hkl\}}(L)\rangle. \tag{3.6.33}$$

The term in equation (3.6.33) would cause peak asymmetry. However, we usually consider only the second-order moment of the strain distribution (*root-mean strain* or *microstrain*) and thus symmetric peaks. Owing to the anisotropy of the elastic properties, the broadening described by equation (3.6.32) is in general anisotropic: an extensive discussion of strain anisotropy and of the order dependence of strain broadening can be found, for example, in Leineweber & Mittemeijer (2010) and Leineweber (2011). It should be stressed that in their original form, traditional line-profile methods are unable to deal with this anisotropy (corrections have been proposed for particular cases, for example, in the so-called modified Williamson–Hall (MWH) and modified Warren–Averbach (MWA) analyses; Ungár & Borbély, 1996).

3.6.2.6.6. *Dislocations*

Dislocations are often the main source of strain broadening. The magnitude of this broadening depends not only on the elastic anisotropy of the material, but also on the relative orientation of the Burgers and diffraction vectors with respect to the dislocation line (Wilkens, 1970*a*,*b*). This problem was analysed in the 1960s by Krivoglaz and Ryaboshapka (Krivoglaz & Ryaboshapka, 1963; Krivoglaz, 1969) and then subsequently reprised and completed by Wilkens (1970*a*,*b*). Further elements have been added to put it into the present form (see, for example, Krivoglaz *et al.*, 1983; Groma *et al.*, 1988; Klimanek & Kuzel, 1988; van Berkum, 1994; Kamminga & Delhez, 2000). For the purpose of WPPM, the distortion Fourier coefficients caused by dislocations can be written as

$$A^D_{\{hkl\}}(L) = \exp[-\tfrac{1}{2}\pi b^2\overline{C}_{\{hkl\}}\rho d^{*^2}_{\{hkl\}}L^2 f(L/R'_e)], \tag{3.6.34}$$

where b is the modulus of the Burgers vector, $\overline{C}_{\{hkl\}}$ is the so-called average contrast factor of the dislocations, ρ is the density of the dislocations and R'_e is an effective outer cutoff radius. Only the low-L trend of equation (3.6.34) is well reproduced by Wilkens' theory: a decaying function $f(L/R'_e)$ has thus been introduced to guarantee a proper convergence to zero of the Fourier coefficients for increasing L. Actually, the function $f^*(\eta)$ is mostly quoted in place of (L/R'_e), where $\eta = (e^{-1/4}/2)L/R'_e$: the multiplicative term can however be dropped, considering that the cutoff radius is an effective value [some discussion of the meaning of the f and f^* functions and of the effective cutoff radius can be found in Scardi & Leoni (2004), Armstrong *et al.* (2006) and Kaganer & Sabelfeld, 2010)].

The most complete definition of $f^*(\eta)$ is from Wilkens (1970*a*,*b*):

$$f^*(\eta) = -\ln\eta + \frac{7}{4} - \ln 2 + \frac{256}{45\pi\eta} + \frac{2}{\pi}\left(1 - \frac{1}{4\eta^2}\right)\int_0^\eta \frac{\arcsin y}{y}\,\mathrm{d}y - \frac{1}{\pi}\left(\frac{769}{180\eta} + \frac{41}{90}\eta + \frac{\eta^3}{45}\right)(1-\eta^2)^{1/2} - \frac{1}{\pi}\left(\frac{11}{12\eta^2} + \frac{7}{2} + \frac{\eta^2}{3}\right)\arcsin\eta + \frac{\eta^2}{6}, \qquad \eta \le 1, \tag{3.6.35}$$

$$f^*(\eta) = \frac{256}{45\pi\eta} - \left(\frac{11}{24} + \frac{1}{4}\ln 2\eta\right)\frac{1}{\eta^2}, \qquad \eta \ge 1. \tag{3.6.36}$$

For $\eta < 1$, the integral in (3.6.35) can be calculated in terms of special functions as

$$\begin{aligned}\int_0^\eta \frac{\arcsin y}{y}\,\mathrm{d}y &= \frac{i}{12}\left\{\pi^2 - 6\arcsin^2\eta - 12i\ln\left[2\eta\left(\eta - i\sqrt{1-\eta^2}\right)\right]\arcsin\eta - 6\mathrm{Li}_2\left(1 - 2\eta^2 + 2i\eta\sqrt{1-\eta^2}\right)\right\}\\ &= \ln(2\eta)\arcsin\eta + \frac{1}{2}\mathrm{Im}\left[\mathrm{Li}_2\left(1 - 2\eta^2 + 2i\eta\sqrt{1-\eta^2}\right)\right]\\ &= \ln(2\eta)\arcsin\eta + \frac{1}{2}\mathrm{Cl}_2(2\arcsin\eta),\end{aligned} \tag{3.6.37}$$

where $\mathrm{Li}_2(z)$ and $\mathrm{Cl}_2(z)$ are the dilogarithm function (Spence's function) and the Clausen integral, respectively:

$$\mathrm{Li}_2(z) = \sum_{k=1}^{\infty} z^k/k^2, \tag{3.6.38}$$

$$\mathrm{Cl}_2(z) = \sum_{k=1}^{\infty} \sin(kz)/z^2 = -\int_0^x \ln[2\sin(t/2)]\,\mathrm{d}t. \tag{3.6.39}$$

The approximation proposed by van Berkum (1994) for (3.6.35) and (3.6.36),

$$f^*(\eta) = \begin{cases} -\ln\eta + \dfrac{7}{4} - \ln 2 + \dfrac{\eta^2}{6} - \dfrac{32\eta^3}{225\pi}, & \eta \le 1 \\ \dfrac{256}{45\pi\eta} - \left(\dfrac{11}{24} + \dfrac{1}{4}\ln 2\eta\right)\dfrac{1}{\eta^2}, & \eta \ge 1, \end{cases} \tag{3.6.40}$$

should not be employed, as the derivative is discontinuous at $\eta = 1$. A simpler approximation, valid over the whole η range, was provided by Kaganer & Sabelfeld (2010):

$$f^*(\eta) = -\ln\left(\frac{\eta}{\eta_0 + \eta}\right). \tag{3.6.41}$$

With $\eta_0 = 2.2$, the results of equation (3.6.41) are similar to those of (3.6.35) and (3.6.36).

Together with dislocation density and outer cutoff radius, a parameter traditionally quoted for the dislocations ensemble is Wilkens' dislocation arrangement parameter $M = R_e\sqrt{\rho}$ (Wilkens, 1970*a*). By combining the information on dislocation screening and dislocation distance, it gives an idea of the interaction of dislocations (strength of the dipole character; Ungár, 2001). A value close to or below unity indicates highly interacting dislocations (for example, dipole configurations or dislocation walls), whereas a large value is typical of a system with randomly dispersed dislocations (weak dipole character).

The anisotropic broadening caused by the presence of dislocations is mainly taken into account by the contrast (or orientation) factor C_{hkl}. The contrast factor depends on the strain field of the dislocation and therefore on the elastic anisotropy and orientation of the scattering vector with respect to the slip system considered. The average of the contrast factor over all equivalent slip systems, $\overline{C}_{hkl}$, is often used in the analysis of powders. The averaging is usually performed under the assumption that all equivalent slip systems are equally populated. The calculation of the contrast factor can be lengthy: full details can be found in the literature (Wilkens, 1970*a*,*b*, 1987; Krivoglaz *et al.*, 1983; Kamminga & Delhez, 2000; Groma *et al.*, 1988; Klimanek & Kuzel, 1988; Kuzel & Klimanek, 1989) for the cubic and hexagonal cases. For a generalization, the reader is referred to the recent work of Martinez-Garcia *et al.* (2007, 2008, 2009). It is possible to show that the contrast factor of a given material has the same functional form as the fourth-order invariant of the Laue class (Popa, 1998; Leoni *et al.*, 2007):

$$\begin{aligned}d^4_{\{hkl\}}C_{\{hkl\}} &= E_1h^4 + E_2k^4 + E_3l^4 + 2(E_4h^2k^2 + E_5k^2l^2 + E_6h^2l^2)\\ &\quad + 4(E_7h^3k + E_8h^3l + E_9k^3h + E_{10}k^3l + E_{11}l^3h + E_{12}l^3k)\\ &\quad + 4(E_{13}h^2kl + E_{14}k^2hl + E_{15}l^2hk).\end{aligned} \tag{3.6.42}$$

In the general case, 15 coefficients are thus needed to describe the strain anisotropy effects. Symmetry reduces the number of independent coefficients: for instance, two coefficients survive in the cubic case, and the average contrast factor is (Stokes & Wilson, 1944; Popa, 1998; Scardi & Leoni, 1999)

$$\overline{C}_{\{hkl\}} = (A + BH) = A + B\frac{h^2k^2 + h^2l^2 + k^2l^2}{(h^2 + k^2 + l^2)^2}. \tag{3.6.43}$$

The values of A and B can be calculated from the elastic constants and slip system according to the literature (Klimanek & Kuzel, 1988; Kuzel & Klimanek, 1989; Martinez-Garcia *et al.*, 2007, 2008, 2009). Excluding the case of $\overline{C}_{\{h00\}} = 0$, the parameterization $\overline{C}_{\{hkl\}} = \overline{C}_{\{h00\}}(1 + qH)$ proposed by Ungár & Tichy (1999) can also be used. Some calculated values for cubic and hexagonal materials can be found in Ungár *et al.* (1999) and Dragomir & Ungár (2002), respectively.

As the calculation of the contrast factor for a dislocation of general character is not trivial, it is customary to evaluate it for the screw and edge case and to refine an effective dislocation character φ (Ungár *et al.*, 1999),

$$\begin{aligned}\overline{C}_{\{hkl\}} &= [\varphi\overline{C}_{E,\{hkl\}} + (1-\varphi)\overline{C}_{S,\{hkl\}}]\\ &= [\varphi A_E + (1-\varphi)A_S] + [\varphi B_E + (1-\varphi)B_S]H,\end{aligned} \tag{3.6.44}$$

where the geometric term H is the same as in equation (3.6.43). Although not completely correct, the approach proposed in equation (3.6.44) allows the case where a mixture of dislocations of varying character are acting on equivalent slip systems to be dealt with. For a proper refinement, however, the active slip systems as well as the contrast factors of the edge and screw dislocations should be known.

It is worth mentioning that the invariant form proposed by Popa (1998) has been reprised by Stephens (1999) to describe the strain-broadening anisotropy, for example, within the Rietveld method: the formula correctly accounts for the relative broadening (*i.e.* for the anisotropy), but it does not give any information on the actual shape of the profiles. This is the major reason

why the Stephens model can be considered as only phenomenological (it captures the trend but not the details): when the source of microstrain broadening is known, we can obtain the functional form of the profile (as proposed, for example, here for dislocations) and the model can become exact.

3.6.2.6.7. *Twin and deformation faults*

Planar defects, *i.e.* a mismatch in the regular stacking of crystallographic planes, are quite frequent in a vast family of technologically important materials and, in some cases, are responsible for their macroscopic properties. In the general case, the analysis of faulting using a Bragg-type method is troublesome. The local change in the structure causes the appearance of diffuse scattering (*i.e.* extra intensity) between the Bragg spots. This can be handled in the single-crystal case (Welberry, 2004), but can be challenging in a powder, where the reciprocal space is rotationally averaged and the (weak) diffuse scattering is lost in the background. The handling of diffuse phenomena is the main difference between the Rietveld (1969) and the pair distribution function (PDF) (Billinge, 2008) methods.

A simple description of the broadening effects of faulting, useful for WPPM, is available only for a restricted class of systems, namely face-centred cubic (f.c.c.) ($Fm\bar{3}m$), body-centred cubic (b.c.c.) ($Im\bar{3}m$) and hexagonal close packed (h.c.p.) ($P6_3/mmc$) lattices. Monatomic metals with f.c.c. (*e.g.* Cu, Ni and Au), h.c.p. (*e.g.* Ti, Co and Zr) and b.c.c. (*e.g.* W and Mo) structures fall into this list. Faulting in the wurtzite structure ($P6_3mc$) leading to a local transformation into sphalerite ($F\bar{4}3m$) can be handled with rules completely analogous to those for the h.c.p./f.c.c. case. The main types of faults in all of these systems are the so-called deformation and twin faults: looking at the planes on the two sides of the faulting, a deformation fault appears as a shear, whereas twinning causes a mirroring of the atomic positions. The effect of these defects can be modelled using recurrence equations for the stacking. Initially proposed for the h.c.p. case by Wilson (Edwards & Lipson, 1942; Wilson, 1942), this idea was then extended to the f.c.c. case (Paterson, 1952; Gevers, 1954*a*,*b*; Warren, 1959, 1963). More recently, Estevez-Rams *et al.* (2003, 2008) improved the accuracy and extended the validity range by including all terms in the stacking probability formulae, whereas Velterop *et al.* (2000) corrected the formalism to properly take the various *hkl* components of a peak into account.

In an f.c.c. system, reliable information can be obtained up to a few per cent of faults on the {111} plane. The trick is to describe the lattice with hexagonal axes, effectively transforming the problem into that of ⟨001⟩ stacking on the {111} plane. Under these hypotheses, the average phase term due to faulting can be written as

$$\left\langle \exp\left[2\pi i\varphi(L; d^*_{\{hkl\}}, L_0/h_0^2)\right]\right\rangle = A^F_{hkl}(L) + iB^F_{hkl}(L), \qquad (3.6.45)$$

where $L_0 = h + k + l$ and $h_0^2 = h^2 + k^2 + l^2$. The lattice symmetry influences the definitions of these two parameters. Faulting is one of the typical cases where a complex (sine) term is present, as peak shift and asymmetry in the profiles is expected (unless twin faults are absent). Following the treatment of Warren (see, for example, Warren, 1963), a set of recurrence equations can be written for the probability of the occurrence of faulting. The solution of the recurrence equations is used to generate the Fourier coefficients for faulting. In particular, if the probabilities of deformation and twin fault are α and β, respectively, then

$$S^2 = 3 - 12\alpha - 6\beta + 12\alpha^2 - \beta^2 + 24\alpha\beta(1-\alpha),$$
$$Z = \sqrt{(1-\beta^2) + S^2}/2 \qquad (3.6.46)$$

and, introducing the sign function,

$$\sigma_{L_0} = \begin{cases} +1 & \text{for } L_0 = 3N+1 \\ 0 & \text{for } L_0 = 3N \\ -1 & \text{for } L_0 = 3N-1 \end{cases} \qquad N = 0, \pm1, \pm2, \ldots, \qquad (3.6.47)$$

the Fourier coefficients can be obtained as

$$A^F_{hkl}(L) = \exp\left[\tfrac{1}{2}\ln(Z)|Ld^*_{\{hkl\}}\sigma_{L_0}L_0/h_0^2|\right], \qquad (3.6.48)$$

$$B^F_{hkl}(L) = -\sigma_{L_0}\frac{L}{|L|}\frac{L_0}{|L_0|}\frac{\beta}{S}A^F_{hkl}(L). \qquad (3.6.49)$$

Besides being asymmetric, each profile subcomponent can also be shifted with respect to the average Bragg position. For the subcomponent *hkl* the shift is

$$\delta_{hkl} = -\left[\frac{1}{2\pi}\arctan\left(\frac{s}{1-\beta}\right) - \frac{1}{6}\right]d^*_{\{hkl\}}\frac{L_0}{h_0^2}\sigma_{L_0}. \qquad (3.6.50)$$

In a given reflection family {*hkl*}, reflections affected and unaffected by faulting coexist, leading to peculiar shapes of the corresponding peak profiles.

Analogous formulae can be obtained for the b.c.c. and h.c.p. cases. In the former, the selection rule becomes $L_0 = -h - k + 2l$, whereas for the latter $L_0 = l$ and the condition for faulting is based on $h - k = 3N \pm 1$. Implementation requires the application of the proper formula to the particular reflection *hkl* considered in the analysis.

Analysing faults by observing just the peak shift, as in the original treatment of Warren (1959, 1963) or within the Warren–Averbach method (Warren & Averbach, 1950, 1952), would be erroneous, as it does not take the fine details of the broadening into account.

An alternative to the adoption of Warren's formalism was proposed by Balogh *et al.* (2006). Instead of performing the calculation explicitly, the authors parameterized the profiles obtained from the *DIFFaX* software (Treacy *et al.*, 1991) calculated for increasing quantities of faulting. The *DIFFaX* software is based on a recursive description of the stacking: the intensity is calculated along rods in reciprocal space using the tangent cylinder approximation. The parameterization, which is performed in terms of a sum of Lorentzian curves, is then employed for the evaluation of the fault-broadening profile at any angle. The modelling should be performed on a profile that contains a faulting-only contribution: note that for high faulting probabilities, it becomes arbitrary whether to assign the diffuse scattering part to one or another Bragg reflection. This introduces some arbitrariness in the subsequent (directional) convolution of the faulting profile with the other broadening effects. When applicable, however, this parameterization has several advantages: it takes the actual shape of the reciprocal-space rods into account (in an effective way), it does not necessitate any *hkl* selection rule and an analytical treatment can be employed, as the Lorentzian has an analytical transform. With the above caveats, it is in principle not even necessary to decompose the *DIFFaX*-generated profile if a numerical convolution is employed. This would also correspond to an extension of WPPM to the *DIFFaX*+ idea (Leoni, Gualtieri & Roveri, 2004; Leoni, 2008), or *vice versa*, where *DIFFaX*+ uses a corrected and improved version of the recursive approach of *DIFFaX* to

generate the profiles, but allows the refinement of all model parameters. [*DIFFaX+* is available from the author (matteo.leoni@unitn.it) on request.]

3.6.2.6.8. *Antiphase domain boundaries*

In the diffraction pattern of an ordered alloy, a dissimilar broadening can often be observed for structure and superstructure peaks (with the former being present in both the ordered and disordered states). The superstructure peaks, in fact, bear microstructural information on the interface between the ordered regions in the material: broadening occurs when domains meet out of phase, creating an antiphase domain boundary (APB or APDB). A general formula for APDB-related broadening does not exist: for a given ordered structure, the Fourier coefficients correspond to the normalized value of $A_{\mathrm{APDB},hkl}(L) = \overline{F(0)F^*(L)}$, where $F(0)$ is the structure factor of a cell positioned at $L = 0$ and $F^*(L)$ is the complex conjugate of the structure factor of a cell at a distance L along the direction $[hkl]$. Being the result of a combination of probabilities, the peak is always expected to be Lorentzian.

Explicit formulae have been derived for the Cu_3Au ordered alloy ($L1_2$ phase; Wilson, 1943; Wilson & Zsoldos, 1966; Scardi & Leoni, 2005). Several types of boundaries can form, depending on the way that the domains meet: the broadening depends both on the boundary plane and on the local arrangement of Au atoms leading to conservative (no Au atoms in contact) or nonconservative (Au atoms in contact) boundaries. By arranging the indices in such a way that $h \geq k \geq l$ and that l is always the unpaired index, the broadening of the superstructure reflections can be described as (Scardi & Leoni, 2005)

$$A^{\mathrm{APDB}}(L) = \exp[-2L\delta f(h, k, l)]. \tag{3.6.51}$$

In this formula, $\delta = \gamma_{\mathrm{APDB}}/a_0$ is the probability of occurrence of an APDB, a_0 is the unit-cell parameter and $f(h, k, l)$ is a function of hkl defined in Table 3.6.2, obtained from the results of Wilson (1943) and Wilson & Zsoldos (1966).

The average distance between two APDBs is given by $1/\delta$. For a random distribution of faults, the broadening is Lorentzian and $A^{\mathrm{APDB}} = \exp(-4L\delta/3)$.

3.6.2.7. *Assembling the equations into a peak and modelling the data*

As previously mentioned, the broadening contributions briefly illustrated in the previous sections are employed to generate the powder peak profile for reflections from the set of planes $\{hkl\}$ using equations (3.6.11) and (3.6.12) and where

$$\begin{aligned} I_{hkl}(s) &= k(d^*) \int_{-\infty}^{\infty} C(L)\exp(2\pi iLs)\,\mathrm{d}L \\ &= k(s) \int_{-\infty}^{\infty} T_{\mathrm{pV}}^{\mathrm{IP}}(L)A_{hkl}^{S}(L)[A_{hkl}^{D}(L)\cos(2\pi Ls) + iB_{hkl}^{D}(L)\sin(2\pi Ls)] \\ &\quad \times \ldots \times [A_{hkl}^{F}(L)\cos(2\pi Ls) + iB_{hkl}^{F}(L)\sin(2\pi Ls)]\,\mathrm{d}L. \end{aligned} \tag{3.6.52}$$

Table 3.6.2
Models for antiphase domain boundaries for the Cu_3Au case
$N = h^2 + k^2 + l^2$.

ID	Model	$f(h, k, l)$
1	Random	2/3
2	{100} planes	$\frac{2}{3}\frac{h+k+l}{\sqrt{N}}$
2.I	{100} planes, no Au–Au contacts	$(k+l)/\sqrt{N}$ if h is the unpaired index $(h+l)/\sqrt{N}$ if k is the unpaired index $(h+k)/\sqrt{N}$ if l is the unpaired index
2.II	{100} planes, only Au–Au contacts	$\frac{2h+k+l}{2\sqrt{N}}$ if h is the unpaired index $\frac{h+2k+l}{2\sqrt{N}}$ if k is the unpaired index $\frac{h+k+2l}{2\sqrt{N}}$ if l is the unpaired index
3	{110} planes	$\frac{2}{3}\frac{4h+2k}{\sqrt{2N}}$
3.I	{110} planes, Au displacement parallel or perpendicular to plane normal	$\frac{4h}{\sqrt{2N}}$ if h is the unpaired index $\frac{2h+2k}{\sqrt{2N}}$ otherwise
3.II	{110} planes, Au displacement at 60° to plane normal	$\frac{2h+2k}{\sqrt{2N}}$ if h is the unpaired index $\frac{3h+k}{\sqrt{2N}}$ otherwise
4	{111} planes	$\frac{8h}{3\sqrt{3N}}$ if $h \geq (k+l)$ $\frac{4(h+k+l)}{3\sqrt{3N}}$ otherwise

Equation (3.6.52) represents an asymmetrical peak profile (the asymmetry is given by the sine terms). Fast Fourier transform and space remapping (usually s to 2θ) are then employed to generate the peaks in the measurement space; intensities are multiplied by the Lorentz and, if needed, polarization terms, and a background is added to the whole pattern. Other aberrations (affecting the position, the intensity or the shape of the peak) can be included as needed.

The various reflections are then positioned on the basis of the (reference) Bragg angle $2\theta_B$ calculated from the unit-cell parameters, and a background (for example, a Chebychev polynomial) is suitably added. For completeness, thermal diffuse scattering should be included, as it can contribute to the broadening near the peak tails (see, for example, Beyerlein *et al.*, 2012). In addition, small-angle scattering can be considered to improve the WPPM result and to account for the observed increase in the background at low angle (Scardi *et al.*, 2011). The final equation is thus similar to that of the Rietveld (1969) or the Pawley (1981) methods,

$$I(2\theta) = \text{SAXS} + \text{TDS} + \text{bkg} + k(2\theta)LP\sum_{hkl} I_{\{hkl\}}(x), \quad (3.6.53)$$

the main difference being in the focus of the analysis and in the way that the profiles are generated.

The model parameters are then refined using a nonlinear least-squares routine (*e.g.* based on the Marquardt algorithm or suitable modifications, as proposed, for example, by Coelho, 2005) to directly match the synthesized pattern to the experimental data. The usual weight, related to Poisson counting statistics, is employed.

As the shape of each peak is bound to the underlying physical models, the number of parameters to be refined is usually quite limited. Compared with the four parameters per peak (intensity, width, shape and position) necessary for a Scherrer-type analysis, in WPPM we refine, for example, two parameters for a domain-size distribution, three parameters for dislocations (ρ, R_e' and φ), two parameters for faulting (α and β), at most six lattice parameters, a few background parameters (*e.g.* four parameters) and one parameter (intensity) per peak. In addition, we can also refine some further specimen-related parameters such as a misalignment error. No atomic coordinates are involved.

A flexible software package implementing WPPM (*PM2K*: Leoni *et al.*, 2006) is available from the author on request (matteo.leoni@unitn.it): the software includes all of the broadening models illustrated here. The user can work with any type and any simultaneous set of diffraction data (X-ray, neutrons or electrons) and build their own model with no *a priori* restriction on the quantity and type of parameters, the number of phases, the models or the relationships between the parameters. The WPPM method has also been implemented in the *TOPAS* refinement software [version 5 (Coelho, 2009; Bruker, 2009)] using the flexible macro language provided.[1]

3.6.2.7.1. *Alternative approaches*

Convolutional multiple whole profile fitting (CMWP; Ribárik *et al.*, 2004) and extended convolutional multiple whole profile fitting (eCMWP; Balogh *et al.*, 2006) have been developed to solve the same problem.

CMWP, introduced as a convolutive version of multiple whole profile fitting (MWP; Ungár *et al.*, 2001; Ribárik, 2008), is very similar to the WPPM. The notable differences are:

(i) The instrumental profile is employed directly without interpolation and the profile of the instrumental peak closest to the peak under analysis is used. The instrumental profile imposes conditions on the range of L used in profile modelling.

(ii) In CMWP a subset of data points is used for speed.

(iii) The background is given by the user (as a spline or Legendre polynomial).

(iv) All points of a given (generated) peak are weighted by the same value related to the maximum intensity. However, the correct weighting scheme with individual weights for data points is available as an option.

The authors also suggest using the MWP procedure in other cases, for example separately measured profiles or single crystals. The MWP procedure works in Fourier space so there is no direct possibility of checking the agreement between the model and data.

In the extended version (Balogh *et al.*, 2006), (e)CMWP introduces an interesting model for faults based on a parameterization of the profiles simulated with the *DIFFaX* software (Treacy *et al.*, 1991). This simulates the diffraction pattern of a faulted structure within the tangent cylinder approximation. The proposed parameterization allows more complex faulting models, at the expense of the calculation and parameterization of the profiles for any new, intermediate or mixed case or for any peak lying outside the parameterized range. The application of (e)CMWP is limited to cubic, hexagonal and orthorhombic powders with spherical or ellipsoidal domain shapes and assumes the presence of dislocations and faults.

It is worth mentioning two more alternative approaches: the Debye scattering equation (Debye, 1915; for some applications, see, for example, Cervellino *et al.*, 2003; Cozzoli *et al.*, 2006) and the total scattering (TS) approach [also known as pair distribution function (PDF) analysis; Egami & Billinge, 2003; Billinge, 2008; see also Chapter 5.7]. Both techniques work in real space: the first creates the pattern directly from atomic positions and the other extracts the real-space information (the PDF) from the diffraction data. As the information content does not change on moving from reciprocal (measured) to direct space, provided that similar hypotheses are employed (similar microstructure and, if necessary, structure), real-space and reciprocal-space methods should give similar results. Of course there are differences, related to the way that the data are handled. For instance, it is easier to visualize the anisotropic effects in reciprocal space, as the information is contained in the peak broadening (different peaks show different breadths): in the PDF this information is sparser as it should be reflected in a variation in the correlation lengths, but also (highly integrated) in a variation of the decay of the curve. Conversely, information on the atomic arrangement (*i.e.* on possible defects) appears more clearly in the PDF, where variations in the distances and in coordination are well localized, contrary to the diffraction pattern, where the information is contained in the (weak) diffuse signal, in the broadening and in the peak position.

Direct-space and reciprocal-space methods thus each have their own advantages and disadvantages. Combined or comparative modelling, whenever possible, is therefore always the best solution: we can match the flexibility and immediacy

[1] Some small errors are present in some versions of the WPPM macros implemented in *TOPAS*. An example of a corrected macro for a lognormal distribution of spheres is given in the supporting information. The implementation using the mean and variance of the distribution *versus* the lognormal mean and variance is straightforward. Please refer to Chapter 5.1 for corrected versions of the Fourier coefficients and ancillary equations that should be present in the macros.

of a real-space approach with the possibility of working directly with the measured data as typical in reciprocal-space methods.

3.6.3. Examples of WPPM analysis

To illustrate the power of the WPPM approach, a few examples are provided based both on simulated and on real data. The analyses were performed using the *PM2K* software (Leoni *et al.*, 2006). Similar results are obtained using the WPPM implementation in the commercial program *TOPAS*.

3.6.3.1. *Nanocrystalline ceria*

The first example concerns a nanocrystalline ceria powder obtained by the calcination of a cerium isopropoxide gel (Leoni, Di Maggio *et al.*, 2004; Leoni & Scardi, 2004; Scardi *et al.*, 2004). A large amount of XRD and transmisson electron microscopy (TEM) data have been collected on the same system (and specimen), starting from the xerogel and following calcination (Scardi *et al.*, 2010). Fig. 3.6.1(*a*) shows the X-ray powder diffraction pattern of the gel calcined for 1 h at 673 K measured with Cu radiation (40 kV, 45 mA) on a Rigaku PMG/VH diffractometer.

The data were collected over the 2θ range 18–154° (with a step of 0.05°) with a counting time of 60 s per step: a wide angular range and a high signal-to-noise ratio (SNR) are prerequisites for a proper line-profile analysis. The large span in reciprocal space is important for the complete characterization of any anisotropy in the broadening (a large set of independent directions in reciprocal space needs to be sampled), whereas the high SNR guarantees the collection of data at peak tails where the differences between similar microstructure models manifest themselves. The log scale employed in Fig. 3.6.1(*a*) highlights the low level of noise present in the pattern.

The diffractometer had 0.5° divergence and 2° Soller slits mounted on the primary arm and 0.15 mm antiscatter, 0.5° receiving and 2° Soller slits and a curved graphite analyser crystal mounted on the secondary arm. This setup provided a narrow and symmetrical instrumental profile that could be described by a pseudo-Voigt curve and was thus ideal for line-profile analysis studies. The Caglioti *et al.* (1958) parameterization of the instrumental profile [*cf.* equations (3.6.18) and (3.6.19)] performed on the profiles of the NIST SRM 660a standard (LaB_6) is shown in Fig. 3.6.2.

Analysis of the pattern using traditional methods (see Scardi *et al.*, 2004) required 59 parameters, 53 of which were actually refined:

(i) one unit-cell parameter (a_0),
(ii) six (fixed) parameters defining the instrumental contribution [five parameters for the Caglioti parameterization (U, V, W, a and b) and one for the $K\alpha_2$ intensity ratio],
(iii) three parameters for the background,
(iv) one parameter for the specimen displacement,
(v) 48 parameters for the peaks (intensity, FWHM and shape for 16 peaks).

An analysis using traditional analysis methods resulted in an 'average domain size' of 3.65 (10) nm using the (modified) Warren–Averbach method and in the range from 4.95 (10) to 5.3 (1) nm using a (modified) Williamson–Hall approach. A discussion of the meaning and accuracy of the results can be found in Scardi *et al.* (2004).

The WPPM result, shown in Fig. 3.6.1(*b*), matches the experiment quite well: this is remarkable considering that the whole pattern (1800 data points) is modelled using just 32 parameters (26 free parameters):

(i) one unit-cell parameter (a_0),
(ii) six (fixed) parameters defining the instrumental contribution [five parameters for the Caglioti parameterization (U, V, W, a and b) and one for the $K\alpha_2$ intensity ratio],

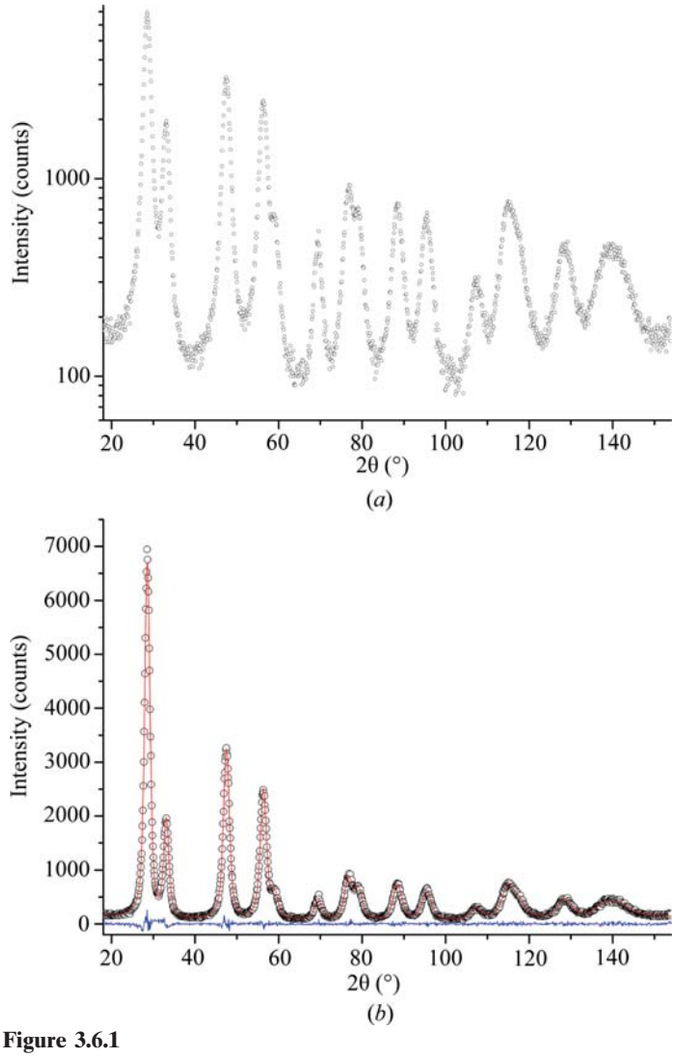

Figure 3.6.1
X-ray powder diffraction pattern of nanocrystalline ceria calcined at 673 K. In (*a*) the pattern is shown on a log scale to highlight the weak features in the data. In (*b*) the results of WPPM are shown: raw data (dots), model (line) and difference (lower line).

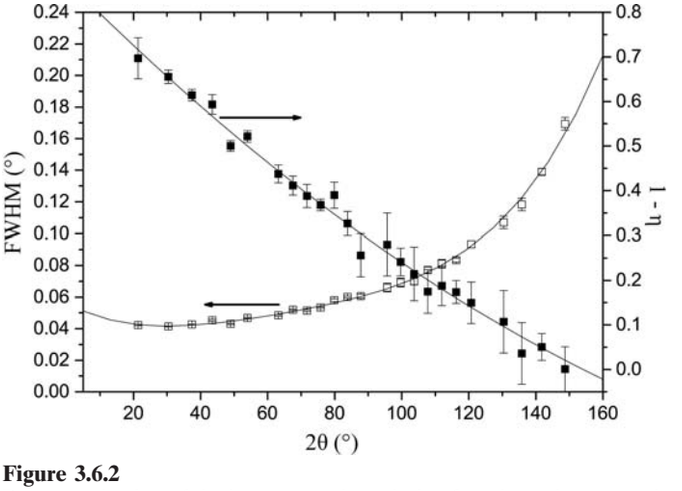

Figure 3.6.2
Parameterization of the instrumental resolution function using a pseudo-Voigt and the relationship of Caglioti *et al.* (1958).

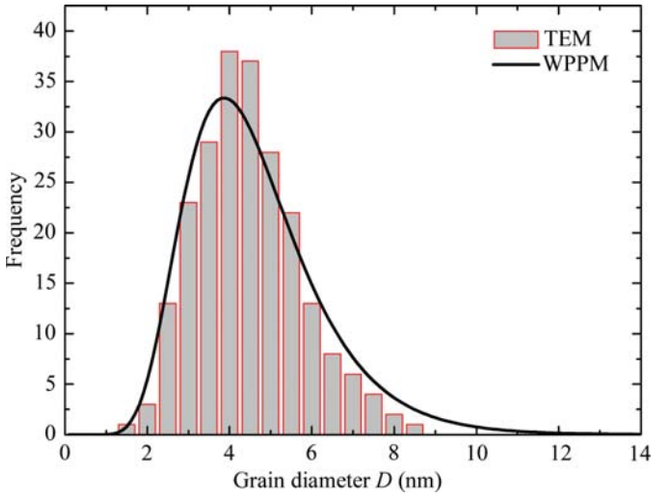

Figure 3.6.3
Size distribution of the ceria powder: WPPM (line) and TEM (histogram).

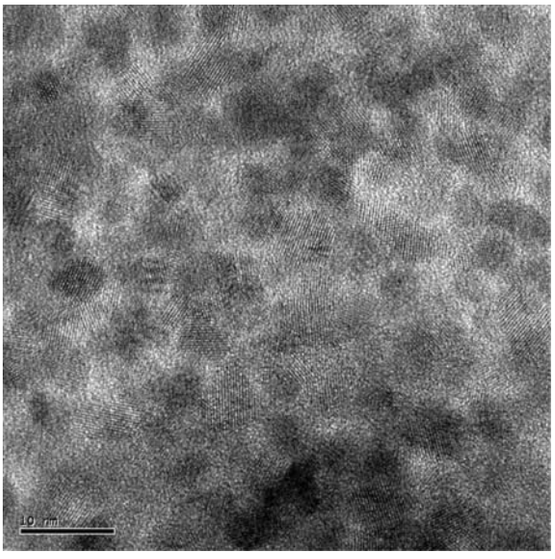

Figure 3.6.4
TEM micrograph of the calcined ceria powder. The scale bar represents 10 nm.

(iii) two parameters for the log-normal size distribution (μ and σ),
(iv) three parameters for the dislocation contributions (ρ, R_e and the mixing parameter f_e),
(v) three parameters for the background,
(vi) one parameter for the specimen displacement,
(vii) 16 parameters for the intensity of the peaks.

It is therefore possible to obtain more complete results with a number of parameters that is dramatically lower than that needed for the traditional analysis: the shapes of the peaks are interlinked *via* the microstructure models. It is suggested that the parameters are initialized with values providing a minimal but measurable effect (*i.e.*, for instance, $\mu = 2$, $\sigma = 0.4$, $\rho = 10^{15}$ m^{-2}, $f_e = 0.5$) to favour a rapid convergence.

By way of a check, Fig. 3.6.3 shows the good agreement between the size distribution obtained by WPPM and that obtained on the same specimen from the analysis of a large set of TEM micrographs (800 grains surveyed; Fig. 3.6.4). The data were collected on a 300 kV JEOL 3010 microscope (0.17 nm point-to-point resolution) equipped with a Gatan slow-scan 974 CCD camera (Leoni, Di Maggio *et al.*, 2004). Even if the particles are well separated, the analysis is quite tedious and prone to bias from the operator. The large and small particles are in fact easily missed, and overlapping particles are hard to separate and are usually not considered. Moreover, only the cross section is measured, as the transverse direction is difficult to access.

The statistical validity of the WPPM result is quite clear: a few million grains are probed by the X-rays *versus* the few hundred actually considered in microscopy. The WPPM result allows not only the mean (first moment) and variance to be obtained from the refined size distribution, but also the recovery of the most probable values for the traditional results (we know the shape and we can weight the column-length distribution by the surface or by the volume). In this case the numerical mean is ~4.3 nm: we can immediately understand the risk of placing faith in the results of a traditional analysis. The agreement between TEM and XRD is in any case excellent. The residual differences may be due both to the issues related to sizing under the microscope and to the simplified treatment employed in the WPPM (perfectly spherical domains, monodisperse shape, absence of surface relaxation *etc.*). A more complex model (accounting, for example, for surface relaxation effects) can be considered (see Scardi & Leoni, 2002; Leoni & Scardi, 2004), but the effects on the distribution are minimal.

The possibility of extracting information on the type of defects (*e.g.* dislocations, faults and APDBs) and on their amount is definitely a major advantage of WPPM over traditional methods and over TEM. For the determination of the dislocation density, the average contrast factor is needed; the actual expressions can be readily obtained from the single-crystal elastic constants (c_{11} = 403, c_{12} = 105 and c_{44} = 60 GPa; Nakajima *et al.*, 1994) as

$$\overline{C}_{\mathrm{CeO_2},e} = 0.122945 + 0.358092\frac{h^2k^2 + k^2l^2 + h^2l^2}{(h^2 + k^2 + l^2)^2}, \qquad (3.6.54)$$

$$\overline{C}_{\mathrm{CeO_2},s} = 0.105762 + 0.207999\frac{h^2k^2 + k^2l^2 + h^2l^2}{(h^2 + k^2 + l^2)^2} \qquad (3.6.55)$$

for edge and screw dislocations, respectively.

A dislocation density of 1.4×10^{16} m^{-2} was obtained for the specimen analysed here. This dislocation density immediately appears to be quite high when compared with the number of dislocations that can be identified in high-resolution TEM micrographs, as it corresponds to approximately one dislocation every couple of grains (Leoni & Scardi, 2004). However, the dislocations visible in the micrographs are just a small fraction of the total: if a dislocation is not properly aligned with the zone axis, it is in fact invisible (its presence can only be inferred from the effects of the distortion field). It is true that a sufficiently large number of dislocations must be present in order to give appreciable effects on the diffraction pattern, and TEM is still the better technique if the density of dislocations is below, for example, 10^{14} m^{-2}.

3.6.3.2. *Copper oxide*

The true power of WPPM, and of diffraction in general, can be appreciated in multi-phase systems. The unequivocal assignment of a structure to each grain is definitely impossible using TEM, unless each grain is individually sampled and carefully analysed. It is therefore quite hard to identify the phases present in the specimen and to characterize their microstructure independently from a micrograph alone. Conversely, information on the various phases is well separated in a diffraction pattern. The various (known) phases in a specimen can easily be identified (for

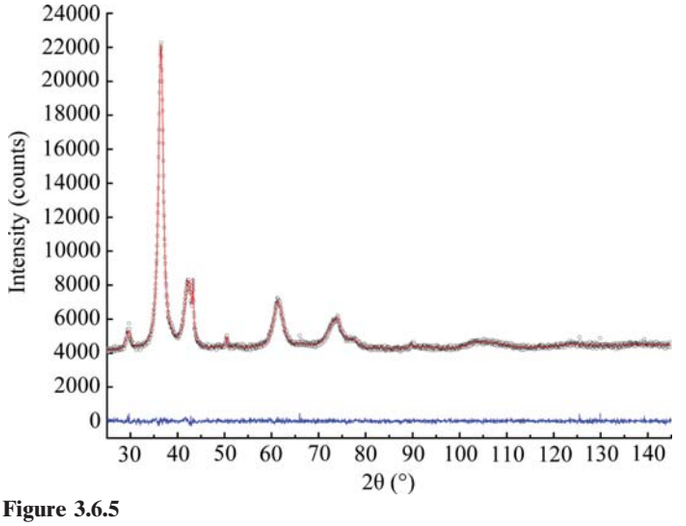

Figure 3.6.5
Result of WPPM of ball-milled Cu_2O: raw data (dots), model (line) and difference (lower line).

example by search/match in a large database such as the ICDD Powder Diffraction File): each diffraction peak belongs to a well defined phase and bears information on the microstructure of that phase.

As an example, Fig. 3.6.5 shows the diffraction pattern of a Cu_2O powder specimen obtained by grinding commercial Cu_2O powder (Carlo Erba) in a high-energy shatter mill (Fritsch Pulverisette 9). To limit the heating of the cup that would lead to dynamic recrystallization, milling was performed in 30 steps consisting of 10 s milling followed by 120 s room-temperature cooling (Martinez-Garcia *et al.*, 2007). The powder diffraction pattern was collected on the same diffractometer that was used for the analysis of the ceria powder. To obtain a sufficient SNR, the data were collected in the 18–154° 2θ range with a step size of 0.1° and a fixed acquisition time of 150 s per point. The fluorescence of the Cu present in the specimen is responsible for the large background that was not eliminated by the crystal analyser. From a quick comparison of Figs. 3.6.5 and 3.6.1, we notice a large difference at high angle: high strain effects (due to dislocations) are expected in this specimen as an effect of the extensive cold-work deformation introduced by the milling process.

A search match signals the presence of not just Cu_2O (cuprite, $Pn\bar{3}m$) but also metallic Cu (f.c.c. copper, $Fm\bar{3}m$) and CuO (tenorite, Cc) as minor phases, presumably due to reduction of the higher oxide. WPPM of the diffraction pattern, performed by considering all three observed phases, shows a flat residual (see Fig. 3.6.5). The severe peak overlap and the large broadening at high angle do not help in the analysis: the intensities of tenorite peaks (minor and broadened phase) were then constrained by a structural model (only a scale parameter was refined). Atomic coordinates and Debye–Waller factors for CuO were taken from the ICSD file (FIZ#69094; Brese *et al.*, 1990) and were considered to be constant.

Spherical domains were chosen for all phases. A log-normal distribution was used to model the minor phases. A histogram distribution was chosen for cuprite instead: the peaks clearly have a peculiar shape with a rather sharp tip, possibly indicating a wide, bimodal or odd size distribution (Leoni & Scardi, 2004). The size distribution resulting from the WPPM analysis is shown in Fig. 3.6.6(a): in this case it would be impossible for a traditional method to provide a physically sound result. The breadth of the profile is not fully informative: as the diffraction signal is proportional to the volume of matter, the actual distribution

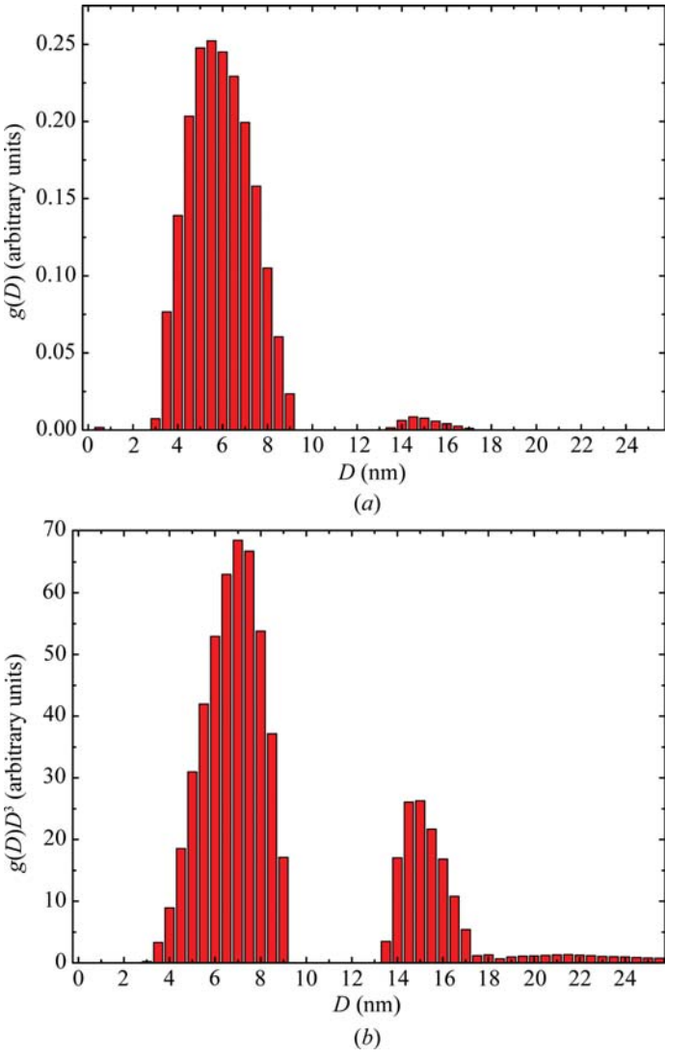

Figure 3.6.6
Domain-size distribution of cuprite: (a) WPPM result and (b) distribution multiplied by D^3.

'seen' in the experiment is that of Fig. 3.6.6(b), obtained by multiplying the result of Fig. 3.6.5(a) by D^3.

The larger size fraction therefore makes a non-negligible contribution to the pattern: as a rule of thumb, the smaller the domains and the wider the distribution, the stronger the contribution of the large domains. This problem of 'visibility' of small domains is attenuated when an analytical distribution (*e.g.* a log normal) can be used as the function goes smoothly to zero at zero size.

Dislocations can also be observed in these specimens: their quantification by TEM is nearly impossible due to the high defect density. The anisotropy term, *i.e.* the average contrast factor, has to be calculated for each of the three phases (Scardi *et al.*, 2007).

The slip system for Cu (c_{11} = 169, c_{12} =122, c_{44} = 75.3 GPa; Every & McCurdy, 1992a) is $\frac{1}{2}\langle 1\bar{1}0\rangle\{111\}$ and the corresponding average contrast factor (for edge and screw dislocations, respectively), is

$$\overline{C}_{\mathrm{Cu},e} = 0.304062 - 0.500211\,\frac{h^2k^2 + k^2l^2 + h^2l^2}{(h^2 + k^2 + l^2)^2}, \qquad (3.6.56)$$

$$\overline{C}_{\mathrm{Cu},s} = 0.298340 - 0.708805\,\frac{h^2k^2 + k^2l^2 + h^2l^2}{(h^2 + k^2 + l^2)^2}. \qquad (3.6.57)$$

For cuprite, the literature (Tromans & Meech, 2001) suggests that the main slip system is ⟨001⟩{100}. The contrast factor can be calculated analytically from the single-crystal elastic constants of cuprite (c_{11} = 121, c_{12} = 105 and c_{44} = 12.1 GPa; Every & McCurdy, 1992*b*) following Martinez-Garcia *et al.* (2007):

$$\overline{C}_{\mathrm{Cu_2O},e} = 0.355963 - 0.609491\,\frac{h^2k^2 + k^2l^2 + h^2l^2}{(h^2 + k^2 + l^2)^2}, \quad (3.6.58)$$

$$\overline{C}_{\mathrm{Cu_2O},s} = \frac{2}{3}\frac{h^2k^2 + k^2l^2 + h^2l^2}{(h^2 + k^2 + l^2)^2}. \quad (3.6.59)$$

For tenorite, a different approach was followed. The phase is minor and the single-crystal elastic constants are not readily available: we can therefore use the contrast factor in an effective way by refining the coefficients of the corresponding invariant [see equation (3.6.42)]. This preserves the profile shape determined by Wilkens' theory and just dilutes the meaning of the dislocation density. The average contrast factor is

$$\begin{aligned}\overline{C}_{\mathrm{CuO},\{hkl\}} &= \Big\{4\big[E_1h^4 + E_2k^4 + E_3l^4 + 2(E_4h^2k^2 + E_5k^2l^2 + E_6h^2l^2) \\ &\quad + 4(E_7h^3k + E_8h^3l + E_9k^3h)\big]Y^4Z^4\sin^4\beta\Big\} \\ &\quad \times \Big(\big\{k^2Z^2 + 2Y^2(l^2 + h^2Z^2) - Z[4hlY^2\cos(\beta) + k^2Z\cos(2\beta)]\big\}^2\Big)^{-1}, \end{aligned} \quad (3.6.60)$$

where a, b, c and β are the unit-cell parameters of tenorite, $Y = b/a$ and $Z = c/a$.

The dislocation density in Cu_2O is quite high [ρ = 2.8 (5) × 10^{16} m^{-2}]: dislocations are more of the edge character [f_E = 0.85 (3)] and the outer cutoff radius R_e = 9 (3) nm leads to a Wilkens' parameter of approximately 1.5, suggesting a strong dislocation interaction. The high dislocation density in this material is justified by the very low shear modulus (G = 10.3 GPa; Every & McCurdy, 1992*b*), whereas the high dislocation interaction is the result of the severe deformation induced by the milling.

APPENDIX A3.6.1
Functions for profile shapes

The unit-area Gaussian $G(x, \omega)$ and Lorentzian $L(x, \omega)$ functions are defined as

$$G(x, \omega) = \frac{2\sqrt{\ln 2/\pi}}{\omega}\exp\left(-\frac{4x^2\ln 2}{\omega^2}\right), \quad (3.6.61)$$

$$L(x, \omega) = \frac{2}{\pi\omega}\left(\frac{1}{1 + 4x^2/\omega^2}\right), \quad (3.6.62)$$

where x is the running variable and ω is the full-width at half-maximum. Based on these definitions, the Voigt and pseudo-Voigt are

$$V(x, \omega_L, \omega_G) = L(x, \omega_L) \otimes G(x, \omega_G) \quad (3.6.63)$$

and

$$\mathrm{pV}(x, \omega_L, \omega_G) = \eta L(x, \omega_L) + (1 - \eta)G(x, \omega_G), \quad (3.6.64)$$

respectively, where η is the mixing parameter (ranging between 0 and 1) and w_L and w_G are the width of the Lorentzian and Gaussian components, respectively.

References

Adler, T. & Houska, C. R. (1979). *Simplifications in the X-ray line-shape analysis. J. Appl. Phys.* **50**, 3282–3287.

Alexander, L. (1954). *The synthesis of X-ray spectrometer line profiles with application to crystallite size measurements. J. Appl. Phys.* **25**, 155–161.

Armstrong, N., Leoni, M. & Scardi, P. (2006). *Considerations concerning Wilkens' theory of dislocation line-broadening. Z. Kristallogr. Suppl.* **23**, 81–86.

Balogh, L., Ribárik, G. & Ungár, T. (2006). *Stacking faults and twin boundaries in fcc crystals determined by X-ray diffraction profile analysis. J. Appl. Phys.* **100**, 023512.

Balzar, D. & Popović, S. (1996). *Reliability of the simplified integral-breadth methods in diffraction line-broadening analysis. J. Appl. Cryst.* **29**, 16–23.

Bergmann, J. & Kleeberg, R. (2001). *Fundamental parameters versus learnt profiles using the Rietveld program BGMN. Mater. Sci. Forum*, **378–381**, 30–37.

Berkum, J. G. M. van (1994). *Strain Fields in Crystalline Materials*. PhD thesis, Technische Universiteit Delft, Delft, The Netherlands.

Bertaut, E. F. (1949*a*). *Etude aux rayons X de la répartition des dimensions des cristallites dans une poudre cristalline. C. R. Acad. Sci.* **228**, 492–494.

Bertaut, E. F. (1949*b*). *Signification de la dimension cristalline mesurée d'apres la largeur de raie Debye-Scherrer. C. R. Acad. Sci.* **228**, 187–189.

Bertaut, E. F. (1950). *Raies de Debye–Scherrer et repartition des dimensions des domaines de Bragg dans les poudres polycristallines. Acta Cryst.* **3**, 14–18.

Beyerlein, K. R., Leoni, M. & Scardi, P. (2012). *Temperature diffuse scattering of nanocrystals. Acta Cryst.* A**68**, 382–392.

Billinge, S. J. L. (2008). *Local structure from total scattering and atomic pair distribution function (PDF) analysis.* In *Powder Diffraction: Theory and Practice*, edited by R. E. Dinnebier & S. J. L. Billinge. London: Royal Society of Chemistry.

Brese, N. E., O'Keeffe, M., Ramakrishna, B. L. & Von Dreele, R. B. (1990). *Low-temperature structures of CuO and AgO and their relationships to those of MgO and PdO. J. Solid State Chem.* **89**, 184–190.

Bruker (2009). *DIFFRAC.SUITE TOPAS*, *Total Pattern Analysis Solution.* Version 5. Bruker AXS, Karlsruhe, Germany.

Caglioti, G., Paoletti, A. & Ricci, F. P. (1958). *Choice of collimator for a crystal spectrometer for neutron diffraction. Nucl. Instrum.* **3**, 223–228.

Cervellino, A., Giannini, C. & Guagliardi, A. (2003). *Determination of nanoparticle structure type, size and strain distribution from X-ray data for monatomic f.c.c.-derived non-crystallographic nanoclusters. J. Appl. Cryst.* **36**, 1148–1158.

Cheary, R. W. & Coelho, A. (1992). *A fundamental parameters approach to X-ray line-profile fitting. J. Appl. Cryst.* **25**, 109–121.

Cheary, R. W. & Coelho, A. (1994). *Synthesizing and fitting linear position-sensitive detector step-scanned line profiles. J. Appl. Cryst.* **27**, 673–681.

Cheary, R. W. & Coelho, A. A. (1998*a*). *Axial divergence in a conventional X-ray powder diffractometer. I. Theoretical foundations. J. Appl. Cryst.* **31**, 851–861.

Cheary, R. W. & Coelho, A. A. (1998*b*). *Axial divergence in a conventional X-ray powder diffractometer. II. Realization and evaluation in a fundamental-parameter profile fitting procedure. J. Appl. Cryst.* **31**, 862–868.

Cline, J. P., Black, D., Windover, D. & Henins, A. (2010). *SRM 660b – Line Position and Line Shape Standard for Powder Diffraction.* https://www-s.nist.gov/srmors/view_detail.cfm?srm=660b.

Coelho, A. A. (2005). *A bound constrained conjugate gradient solution method as applied to crystallographic refinement problems. J. Appl. Cryst.* **38**, 455–461.

Coelho, A. A. (2009). *TOPAS Academic.* Version 5. http://www.topas-academic.net/.

Cozzoli, P. D., Snoeck, E., Garcia, M. A., Giannini, C., Guagliardi, A., Cervellino, A., Gozzo, F., Hernando, A., Achterhold, K., Ciobanu, N., Parak, F. G., Cingolani, R. & Manna, L. (2006). *Colloidal synthesis and characterization of tetrapod-shaped magnetic nanocrystals. Nano Lett.* **6**, 1966–1972.

Debye, P. (1915). *Zerstreuung von Röntgenstrahlen. Ann. Phys.* **351**, 809–823.

Deutsch, M., Forster, E., Holzer, G., Hartwig, J., Hämäläinen, K., Kao, C.-C., Huotari, S. & Diamant, R. (2004). *X-ray spectrometry of copper: new results on an old subject. J. Res. Natl Inst. Stand. Technol.* **109**, 75–98.

Dragomir, I. C. & Ungár, T. (2002). *Contrast factors of dislocations in the hexagonal crystal system. J. Appl. Cryst.* **35**, 556–564.

Drits, V. A. & Tchoubar, C. (1990). *X-ray Diffraction by Disordered Lamellar Structures: Theory and Applications to Microdivided Silicates and Carbons.* Berlin: Springer-Verlag.

Edwards, O. S. & Lipson, H. (1942). *Imperfections in the structure of cobalt. I. Experimental work and proposed structure. Proc. R. Soc. Lond. Ser. A*, **180**, 268–277.

Egami, T. & Billinge, S. J. L. (2003). *Underneath the Bragg Peaks. Structural Analysis of Complex Materials.* Oxford: Elsevier.

Estevez-Rams, E., Leoni, M., Scardi, P., Aragon-Fernandez, B. & Fuess, H. (2003). *On the powder diffraction pattern of crystals with stacking faults. Philos. Mag.* **83**, 4045–4057.

Estevez-Rams, E., Welzel, U., Pentón Madrigal, A. & Mittemeijer, E. J. (2008). *Stacking and twin faults in close-packed crystal structures: exact description of random faulting statistics for the full range of faulting probabilities. Acta Cryst.* A**64**, 537–548.

Every, A. G. & McCurdy, A. K. (1992*a*). *Landolt–Börnstein: Crystal and Solid State Physics New Series*, Group III, Vol. 29, edited by D. F. Nelson, p. 12. Berlin: Springer.

Every, A. G. & McCurdy, A. K. (1992*b*). *Landolt–Börnstein: Crystal and Solid State Physics New Series*, Group III, Vol. 29, edited by D. F. Nelson, p. 68. Berlin: Springer.

Garrod, R. I., Brett, J. F. & MacDonald, J. A. (1954). *X-ray line broadening and pure diffraction contours. Aust. J. Phys.* **7**, 77–95.

Gevers, R. (1954*a*). *X-ray diffraction by close-packed crystals with 'growth stacking faults' assuming an 'N-layer influence'. Acta Cryst.* **7**, 492–494.

Gevers, R. (1954*b*). *X-ray diffraction by close-packed crystals with 'growth-' and 'deformation or transformation stacking faults' assuming an 'N-layer influence'. Acta Cryst.* **7**, 740–744.

Grebille, D. & Bérar, J.-F. (1985). *Calculation of diffraction line profiles in the case of a major size effect: application to boehmite AlOOH. J. Appl. Cryst.* **18**, 301–307.

Groma, I., Ungár, T. & Wilkens, M. (1988). *Asymmetric X-ray line broadening of plastically deformed crystals. I. Theory. J. Appl. Cryst.* **21**, 47–54.

Hölzer, G., Fritsch, M., Deutsch, M., Härtwig, J. & Förster, E. (1997). *$K\alpha_{1,2}$ and $K\beta_{1,3}$ X-ray emission lines of the 3d transition metals. Phys. Rev. A*, **56**, 4554–4568.

Houska, C. R. & Smith, T. M. (1981). *Least-squares analysis of X-ray diffraction line shapes with analytic functions. J. Appl. Phys.* **52**, 748.

Jones, F. W. (1938). *The measurement of particle size by the X-ray method. Proc. R. Soc. Lond. Ser. A*, **166**, 16–43.

Kaganer, V. M. & Sabelfeld, K. K. (2010). *X-ray diffraction peaks from correlated dislocations: Monte Carlo study of dislocation screening. Acta Cryst.* A**66**, 703–716.

Kamminga, J.-D. & Delhez, R. (2000). *Calculation of diffraction line profiles from specimens with dislocations. A comparison of analytical models with computer simulations. J. Appl. Cryst.* **33**, 1122–1127.

Kern, A. A. & Coelho, A. A. (1998). *A new fundamental parameters approach in profile analysis of powder data.* New Delhi: Allied Publishers.

Klimanek, P. & Kuzel, R. (1988). *X-ray diffraction line broadening due to dislocations in non-cubic materials. I. General considerations and the case of elastic isotropy applied to hexagonal crystals. J. Appl. Cryst.* **21**, 59–66.

Klug, H. P. & Alexander, L. E. (1974). *X-ray Diffraction Procedures for Polycrystalline and Amorphous Materials*, 2nd ed. New York: Wiley.

Krill, C. E. & Birringer, R. (1998). *Estimating grain-size distributions in nanocrystalline materials from X-ray diffraction profile analysis. Philos. Mag. A*, **77**, 621–640.

Krivoglaz, M. A. (1969). *Theory of X-ray and Thermal Neutron Scattering by Real Crystals.* New York: Plenum Press.

Krivoglaz, M. A., Martynenko, O. V. & Ryaboshapka, K. P. (1983). *Influence of correlation in position of dislocations on X-ray diffraction by deformed crystals. Phys. Met. Metall.* **55**, 1–12.

Krivoglaz, M. A. & Ryaboshapka, K. P. (1963). *Theory of X-ray scattering by crystals containing dislocations. Screw and edge dislocations randomly distributed throughout the crystal. Phys. Met. Metall.* **15**, 14–26.

Kuzel, R. & Klimanek, P. (1989). *X-ray diffraction line broadening due to dislocations in non-cubic crystalline materials. III. Experimental results for plastically deformed zirconium. J. Appl. Cryst.* **22**, 299–307.

Langford, J. I. & Louër, D. (1982). *Diffraction line profiles and Scherrer constants for materials with cylindrical crystallites. J. Appl. Cryst.* **15**, 20–26.

Langford, J. I. & Wilson, A. J. C. (1978). *Scherrer after sixty years: a survey and some new results in the determination of crystallite size. J. Appl. Cryst.* **11**, 102–113.

Leineweber, A. (2011). *Understanding anisotropic microstrain broadening in Rietveld refinement. Z. Kristallogr.* **226**, 905–923.

Leineweber, A. & Mittemeijer, E. J. (2004). *Diffraction line broadening due to lattice-parameter variations caused by a spatially varying scalar variable: its orientation dependence caused by locally varying nitrogen content in ε-$FeN_{0.433}$. J. Appl. Cryst.* **37**, 123–135.

Leineweber, A. & Mittemeijer, E. J. (2010). *Notes on the order-of-reflection dependence of microstrain broadening. J. Appl. Cryst.* **43**, 981–989.

Lele, S. & Anantharaman, T. R. (1966). *Influence of crystallite shape on particle size broadening of Debye–Scherrer reflections. Proc. Indian Acad. Sci. A*, **64**, 261–274.

Leonardi, A., Leoni, M., Siboni, S. & Scardi, P. (2012). *Common volume functions and diffraction line profiles of polyhedral domains. J. Appl. Cryst.* **45**, 1162–1172.

Leoni, M. (2008). *Diffraction analysis of layer disorder. Z. Kristallogr.* **223**, 561–568.

Leoni, M., Confente, T. & Scardi, P. (2006). *PM2K: a flexible program implementing whole powder pattern modelling. Z. Kristallogr. Suppl.* **23**, 249–254.

Leoni, M., Di Maggio, R., Polizzi, S. & Scardi, P. (2004). *X-ray diffraction methodology for the microstructural analysis of nanocrystalline powders: application to cerium oxide. J. Am. Ceram. Soc.* **87**, 1133–1140.

Leoni, M., Gualtieri, A. F. & Roveri, N. (2004). *Simultaneous refinement of structure and microstructure of layered materials. J. Appl. Cryst.* **37**, 166–173.

Leoni, M., Martinez-Garcia, J. & Scardi, P. (2007). *Dislocation effects in powder diffraction. J. Appl. Cryst.* **40**, 719–724.

Leoni, M. & Scardi, P. (2004). *Nanocrystalline domain size distributions from powder diffraction data. J. Appl. Cryst.* **37**, 629–634.

Leoni, M., Scardi, P. & Langford, J. I. (1998). *Characterization of standard reference materials for obtaining instrumental line profiles. Powder Diffr.* **13**, 210–215.

Martinez-Garcia, J., Leoni, M. & Scardi, P. (2007). *Analytical expression for the dislocation contrast factor of the ⟨001⟩{100} cubic slip-system: Application to Cu_2O. Phys. Rev. B*, **76**, 174117.

Martinez-Garcia, J., Leoni, M. & Scardi, P. (2008). *Analytical contrast factor of dislocations along orthogonal diad axes. Philos. Mag. Lett.* **88**, 443–451.

Martinez-Garcia, J., Leoni, M. & Scardi, P. (2009). *A general approach for determining the diffraction contrast factor of straight-line dislocations. Acta Cryst.* A**65**, 109–119.

Matěj, Z., Matějová, L., Novotný, F., Drahokoupil, J. & Kuzel, R. (2011). *Determination of crystallite size distribution histogram in nanocrystalline anatase powders by XRD. Z. Kristallogr. Proc.* **1**, 87–92.

Nakajima, A., Yoshihara, A. & Ishigame, M. (1994). *Defect-induced Raman spectra in doped CeO_2. Phys. Rev. B*, **50**, 13297–13307.

Nye, J. F. (1987). *Physical Properties of Crystals: Their Representation by Tensors and Matrices*, reprint edition. Oxford University Press.

Paterson, M. S. (1952). *X-ray diffraction by face-centered cubic crystals with deformation faults. J. Appl. Phys.* **23**, 805–811.

Patterson, A. L. (1939). *The Scherrer formula for X-ray particle size determination. Phys. Rev.* **56**, 978–982.

Pawley, G. S. (1981). *Unit-cell refinement from powder diffraction scans. J. Appl. Cryst.* **14**, 357–361.

Popa, N. C. (1998). *The (hkl) dependence of diffraction-line broadening caused by strain and size for all Laue groups in Rietveld refinement. J. Appl. Cryst.* **31**, 176–180.

Rao, S. & Houska, C. R. (1986). *X-ray diffraction profiles described by refined analytical functions. Acta Cryst.* A**42**, 14–19.

Ribárik, G. (2008). *Modeling of Diffraction Patterns Properties.* PhD thesis, Eötvös University, Budapest.

Ribárik, G., Gubicza, J. & Ungár, T. (2004). *Correlation between strength and microstructure of ball-milled Al–Mg alloys determined by X-ray diffraction. Mater. Sci. Eng. A Struct. Mater.* **387–389**, 343–347.

Rietveld, H. M. (1969). *A profile refinement method for nuclear and magnetic structures. J. Appl. Cryst.* **2**, 65–71.

Scardi, P. & Leoni, M. (1999). *Fourier modelling of the anisotropic line broadening of X-ray diffraction profiles due to line and plane lattice defects. J. Appl. Cryst.* **32**, 671–682.

Scardi, P. & Leoni, M. (2001). *Diffraction line profiles from polydisperse crystalline systems. Acta Cryst.* A**57**, 604–613.

Scardi, P. & Leoni, M. (2002). *Whole powder pattern modelling. Acta Cryst.* A**58**, 190–200.

Scardi, P. & Leoni, M. (2004). *Whole powder pattern modelling: theory and application.* In *Diffraction Analysis of the Microstructure of Materials*, edited by E. J. Mittemeijer & P. Scardi, pp. 51–91. Berlin: Springer-Verlag.

Scardi, P. & Leoni, M. (2005). *Diffraction whole-pattern modelling study of anti-phase domains in Cu_3Au. Acta Mater.* **53**, 5229–5239.

Scardi, P., Leoni, M. & Beyerlein, K. R. (2011). *On the modelling of the powder pattern from a nanocrystalline material. Z. Kristallogr.* **226**, 924–933.

Scardi, P., Leoni, M. & Delhez, R. (2004). *Line broadening analysis using integral breadth methods: a critical review. J. Appl. Cryst.* **37**, 381–390.

Scardi, P., Leoni, M., Müller, M. & Di Maggio, R. (2010). *In situ size-strain analysis of nanocrystalline ceria growth. Mater. Sci. Eng. A Struct. Mater.* **528**, 77–82.

Scardi, P., Leoni, M., Straffelini, G. & Giudici, G. D. (2007). *Microstructure of Cu–Be alloy triboxidative wear debris. Acta Mater.* **55**, 2531–2538.

Scherrer, P. (1918). *Bestimmung der Grösse und der inneren Struktur von Kolloidteilchen mittels Röntgenstrahlen. Nachr. Ges. Wiss. Göttingen*, pp. 98–100.

Stephens, P. W. (1999). *Phenomenological model of anisotropic peak broadening in powder diffraction. J. Appl. Cryst.* **32**, 281–289.

Stokes, A. R. & Wilson, A. J. C. (1942). *A method of calculating the integral breadths of Debye–Scherrer lines. Math. Proc. Cambridge Philos. Soc.* **38**, 313–322.

Stokes, A. R. & Wilson, A. J. C. (1944). *The diffraction of X-rays by distorted crystal aggregates – I. Proc. Phys. Soc.* **56**, 174–181.

Treacy, M. M. J., Newsam, J. M. & Deem, M. W. (1991). *A general recursion method for calculating diffracted intensities from crystals containing planar faults. Proc. R. Soc. Lond. Ser. A*, **433**, 499–520.

Tromans, D. & Meech, J. A. (2001). *Enhanced dissolution of minerals: stored energy, amorphism and mechanical activation. Miner. Eng.* **14**, 1359–1377.

Ungár, T. (2001). *Dislocation densities, arrangements and character from X-ray diffraction experiments. Mater. Sci. Eng. A Struct. Mater.* **309–310**, 14–22.

Ungár, T. & Borbély, A. (1996). *The effect of dislocation contrast on X-ray line broadening: a new approach to line profile analysis. Appl. Phys. Lett.* **69**, 3173.

Ungár, T., Dragomir, I., Révész, Á. & Borbély, A. (1999). *The contrast factors of dislocations in cubic crystals: the dislocation model of strain anisotropy in practice. J. Appl. Cryst.* **32**, 992–1002.

Ungár, T., Gubicza, J., Ribárik, G. & Borbély, A. (2001). *Crystallite size distribution and dislocation structure determined by diffraction profile analysis: principles and practical application to cubic and hexagonal crystals. J. Appl. Cryst.* **34**, 298–310.

Ungár, T. & Tichy, G. (1999). *The effect of dislocation contrast on X-ray line profiles in untextured polycrystals. Phys. Stat. Solidi A Appl. Res.* **171**, 425–434.

Vargas, R., Louër, D. & Langford, J. I. (1983). *Diffraction line profiles and Scherrer constants for materials with hexagonal crystallites. J. Appl. Cryst.* **16**, 512–518.

Velterop, L., Delhez, R., de Keijser, Th. H., Mittemeijer, E. J. & Reefman, D. (2000). *X-ray diffraction analysis of stacking and twin faults in f.c.c. metals: a revision and allowance for texture and non-uniform fault probabilities. J. Appl. Cryst.* **33**, 296–306.

Warren, B. E. (1959). *X-ray studies of deformed metals. Progr. Met. Phys.* **8**, 147–202.

Warren, B. E. (1963). *Single- and double-deformation faults in face-centered cubic crystals. J. Appl. Phys.* **34**, 1973–1975.

Warren, B. E. (1990). *X-ray Diffraction.* New York: Dover Publications. (Unabridged reprint of the original 1969 book.)

Warren, B. E. & Averbach, B. L. (1950). *The effect of cold-work distortion on X-ray patterns. J. Appl. Phys.* **21**, 595–599.

Warren, B. E. & Averbach, B. L. (1952). *The separation of cold-work distortion and particle size broadening in X-ray patterns. J. Appl. Phys.* **23**, 492.

Welberry, T.R. (2004). *Diffuse X-ray Scattering and Models of Disorder.* Oxford University Press.

Wilkens, M. (1970*a*). *The determination of density and distribution of dislocations in deformed single crystals from broadened X-ray diffraction profiles. Phys. Stat. Solidi A Appl. Res.* **2**, 359–370.

Wilkens, M. (1970*b*). *Fundamental Aspects of Dislocation Theory*, edited by J. A. Simmons, R. de Wit & R. Bullough, Vol. II, pp. 1195–1221. Washington DC: National Institute of Standards and Technology.

Wilkens, M. (1987). *X-ray line broadening and mean square strains of straight dislocations in elastically anisotropic crystals of cubic symmetry. Phys. Stat. Solidi A Appl. Res.* **104**, K1–K6.

Williamson, G. K. & Hall, W. H. (1953). *X-ray line broadening from filed aluminium and wolfram. Acta Metall.* **1**, 22–31.

Wilson, A. J. C. (1942). *Imperfections in the structure of cobalt. II. Mathematical treatment of proposed structures. Proc. R. Soc. Lond. Ser. A*, **180**, 277–285.

Wilson, A. J. C. (1943). *The reflexion of X-rays from the 'anti-phase nuclei' of $AuCu_3$. Proc. R. Soc. Lond. Ser. A*, **181**, 360–368.

Wilson, A. J. C. (1963). *Mathematical Theory of X-ray Powder Diffractometry.* New York: Gordon & Breach.

Wilson, A. J. C. (1969). *Variance apparent particle sizes for cylinders, prisms and hemispheres. J. Appl. Cryst.* **2**, 181–183.

Wilson, A. J. C. & Zsoldos, L. (1966). *The reflexion of X-rays from the 'anti-phase nuclei' of $AuCu_3$. II. Proc. R. Soc. Lond. Ser. A*, **290**, 508–514.

International Tables for Crystallography (2019). Vol. H, Chapter 3.7, pp. 304–324.

3.7. Crystallographic databases and powder diffraction

J. A. Kaduk

3.7.1. Introduction

Identifying compounds using powder-diffraction data requires a comparison of the current experimental pattern with essentially all previous crystallographic information. This information is incorporated into the Powder Diffraction File (Fawcett *et al.*, 2017), which is traditionally the primary tool for phase identification, but other databases are important to the process, as well as being the repositories of the atom coordinates necessary for Rietveld refinements. This chapter summarizes the characteristics of the various databases that the author has found useful in the practice of powder diffraction. It also provides several examples of the thought processes and capabilities which can be used to identify phases.

3.7.1.1. *History of the PDF/ICDD*

Although powder-diffraction experiments date from the beginning of the 20th century (Debye & Scherrer, 1916, 1917; Hull, 1919), what we now know as the Powder Diffraction File and the International Centre for Diffraction Data date from two papers from the Dow Chemical Company (Hanawalt & Rinn, 1936; Hanawalt *et al.*, 1938). The importance of these papers lies not only in the compilation of a database but also in a method for the identification of materials, and how the database was organized to work with the method. Discussion among industrial and academic scientists made the need for a central collection of powder-diffraction patterns apparent. The Joint Committee for Chemical Analysis by Powder Diffraction Methods was founded in 1941. It produced a primary reference of X-ray powder diffraction data, which became known as the Powder Diffraction File (PDF). This effort was supported initially by Committee E-4 of the American Society for Testing and Materials (ASTM). Over the next two decades, other professional bodies added their support, culminating in 1969 with the establishment of the Joint Committee on Powder Diffraction Standards (JCPDS). The JCPDS was incorporated as a separate nonprofit corporation to continue the mission of maintaining the PDF. In 1978 the name was changed to the International Centre for Diffraction Data to highlight the global nature of this scientific endeavour. Additional information on the history of the powder method is given in Parrish (1983) and on the early history of the Powder Diffraction File in Hanawalt (1983).

3.7.1.2. *Search/match*

What is now known as the Hanawalt search method (Hanawalt & Rinn, 1936; Hanawalt *et al.*, 1938) is an empirical scheme which was based on earlier ideas (Hull, 1919; Davey, 1922, 1934; Winchell, 1927; Waldo, 1935; Boldyrev *et al.*, 1938). The basic ideas behind the scheme have been summarized in more modern language by Hanawalt (1986). Other discussions of the method can be found in Jenkins & Rose (1990) and Hull (1983).

The patterns in the PDF are divided into 40 groups according to the *d*-spacing of the strongest peak and including error limits on the *d*-spacing. The entries within each group are sorted by the position of the second strongest peak. Because the peak intensities can be more difficult to measure than the positions and may vary from sample to sample, PDF entries appear in the index multiple times ('rotations' in the current nomenclature). All patterns appear at least once. Patterns appear twice when $I_2/I_1 > 0.75$ and $I_3/I_1 \leq 0.75$, three times when $I_3/I_1 > 0.75$ and $I_4/I_1 \leq 0.75$, and four times when $I_4/I_1 > 0.75$ (where I_1 is the strongest peak, I_2 is the second strongest and so on). There are four more rules, dealing with things such as low-angle peaks, rounding of *d*-spacings and closely spaced peaks.

The phase-identification process actually involves several steps. This was realized by Hanawalt, Rinn and Frevel even in 1938. The first step is to *search* the experimental data against an index (a structured subset of a database) to identify potential compounds. The printed *Hanawalt Search Manual* was such an index, and contemporary search/match programs all generate indices to enhance the speed of the phase-identification process. The second step is the *match* of the full PDF entry against the full experimental pattern to use all peaks in the identification process. Typically, the quality of the match is evaluated at this point to rank the potential candidate match among the others in the list; the hit list is sorted on goodness of match, similarity index, figure of merit or some similar quantity generated by the program. The third step is to *identify* the phase (generally by computer, but best with some human judgement). The pattern of the identified phase is then subtracted from the experimental pattern and the process is repeated to identify additional phases. The final step in the process is often quantification of the concentrations. Ultimately, the errors introduced during the subtractions limit the number of phases which can be identified in a mixture, and additional techniques are required to identify minor or trace phases. As specimen-preparation methods and equipment and standardized reference data have improved with time (over decades), the residual errors in the subtraction process have diminished, generally increasing the number of phases that can be identified when appropriate techniques are applied.

An early computer version of the Hanawalt search algorithm was implemented by Frevel (Frevel, 1965; Frevel *et al.*, 1976). This program used a 300-phase microfile database of common phases resulting from empirical work performed over decades at the Dow Chemical Company. Another early computer implementation of the Hanawalt search algorithm was developed by Snyder (1981). The index file stored the *d*/*I* pairs in the PDF as 16-bit integers: 11 bits for 1/*d* and five bits for *I*. The index file was an indexed sequential file with the PDF entries sorted on d_1 (the *d*-spacing of the strongest peak). Each PDF set was indexed separately, and smaller MICRO (300 phases) and MINI (2500 common phases) index files were also generated to permit faster searches on the slow computers of the day. After input of the *d*/*I* list for the experimental pattern, the program located PDF entries whose d_1 values lay within $\pm 0.1^\circ$ 2θ (copper radiation) of the observed d_1. If the reference pattern passed three tests – it was a member of a user-specified subfile, all PDF entry peaks with $I \geq 50$ were present in the unknown pattern and user-specified chemical constraints were satisfied – a figure of merit (FOM) was calculated. The pattern with the highest FOM was saved for the match step, and the process was repeated for d_2 and d_3. If no hits were obtained, larger error windows and then weaker peaks were used.

The FOM was calculated as

$$\text{FOM} = d_R I_R^2 d_U, \tag{3.7.1}$$

where d_R is the percentage of the reference peaks which match the unknown (within the error window) and have I greater than that of the lowest-intensity matched peak, I_R is the percentage of the reference intensity ($I_{\rm ref}$) matched and d_U is the percentage of the unknown peaks (with intensities $I_{\rm unk}$) matched.

PDF hits were considered for the match step if the FOM was >10. For the hit with the highest FOM, an I-weighted linear regression between $I_{\rm ref}$ and $I_{\rm unk}$ was carried out. Peaks with $I_{\rm calc} < I_{\rm obs} - 5$ were assigned as overlapped, and the least-squares scale factor was recalculated using only the non-overlapped peaks. The scaled PDF entry was subtracted from the unknown pattern and the residual was sent back to the search step.

Several commercial search/match programs have been developed, not from Snyder's implementation of the Hanawalt algorithm, but from the Johnson–Vand algorithm (Johnson & Vand, 1967, 1968; Cherukuri *et al.*, 1983). This algorithm used constant error windows in $1/d$ and $\log(I)$ and used integer arithmetic. The d/I pairs were packed into characteristic integers PSI = $(1000/d) \times 10 + 5 \log_{10} I_3$. An inverted PDF was created, an index which contained the characteristic integers of the strongest lines of the reference patterns (PSI, PDF No. pairs) sorted by decreasing PSI. The input d/I list was compared with the index. All patterns that contained the characteristic integers within the bandpass were considered as potential hits. The full PDF was used to compare observed and reference patterns. A Davey minimum concentration (DMC) was calculated; this was the largest value in the range $0 \le \text{DMC} \le 1$ for which $I_{\rm PDF}\text{DMC} \le I_{\rm unk}$ for all peaks. The PDF entry was then subtracted from the unknown pattern and the process was repeated. Initially, there were no chemistry or user filters; these appeared in later versions.

The Johnson–Vand figure of merit,

$$\text{FOM} = A\left[1 - \frac{\sum_N |\Delta D|}{(IW)N}\right]\left[1 - \frac{\sum_N |\Delta I| - K}{\sum_N I}\right], \tag{3.7.2}$$

was calculated, in which A is the percentage of peak match in the d-space range considered (above the background), $\Delta D = d_{\rm unk} - d_{\rm ref}$ (integer), N is the number of peaks under consideration, $\Delta I = I_{\rm unk} - I_{\rm ref}$, K is a scale factor and $IW = d$ is the error window (integer).

A derivative of the Johnson–Vand program was *μPDSM* (Marquart *et al.*, 1979; Marquart, 1986). This program also used the integer $1000/d$ internally, and considered the probability of the occurrence of a d-spacing in calculating its figure of merit. It used the 15 strongest peaks of the reference patterns in the search step and was the first to make extensive use of pre-screens (especially chemistry) to speed up the search. In addition to the similarity index, other measures of the quality of a match were the numbers of matched and missing lines.

Sometimes, references to 'generations' of search/match programs will be encountered. The first-generation programs include those of Johnson & Vand (1967, 1968), Nichols (1966), Frevel *et al.* (1976), Marquart *et al.* (1979) and O'Connor & Bagliani (1976). The distinction between first- and second-generation programs (Snyder, 1981; Jobst & Goebel, 1982; Huang & Parrish, 1982; Schreiner *et al.*, 1982; Goehner & Garbauskas, 1984; Toby *et al.*, 1990; Caussin *et al.*, 1988) is fuzzy, and is partially a matter of timing and features. Contemporary third-generation programs such as *Jade* (Materials Data, 2016), *EVA* (Caussin *et al.*, 1989; Nusinovici & Bertelmann, 1993; Nusinovici & Winter, 1994), *HighScore* (Degen *et al.*, 2014), *Match!* (Crystal Impact, 2012), *Crystallographica Search-Match* (Oxford Cryosystems, 2012) and *Siroquant* (Sietronics, 2012) are distinguished mainly by the ability to use raw data in addition to peak lists. The presence and absence of peaks in particular regions are both considered in the calculation of the figure of merit. The width of the peak profiles serves as an error window. After the mid-1990s, there is virtually nothing in the open literature about search/match programs, and we are forced to rely on the help documentation of the commercial programs. Occasionally, one will encounter references to a fourth-generation program such as *SNAP* (Barr *et al.*, 2004; Gilmore *et al.*, 2004), *PolySNAP* (Barr *et al.*, 2009) or *FULLPAT* (Chipera & Bish, 2002). There is current development in using similarity indices as a complementary method for the analysis of noncrystalline materials, as these methods depend on whole-pattern fitting instead of peak location and intensity. These methods also cluster isotypical and isostructural crystalline materials, and can be applied to nanomaterial analyses, where there is frequently severe peak overlap.

Originally developed for use with both electron and/or X-ray diffraction data, the Fink search (Bigelow & Smith, 1964) uses the d-spacings of the eight strongest peaks in the pattern, but does not otherwise use the intensities. The justification for not using the intensities was that electron-diffraction intensities were not very reliable, often as a result of poor counting statistics in the small areas analysed in a typical electron-diffraction attachment to a scanning or transmission electron microscope coupled with the effects of dynamical scattering and sample decomposition in the electron beam. The search was named in honour of William H. Fink, a long-time chairman of the JCPDS/ICDD. In the current *SIeve+* module of the PDF, all eight rotations (considering each of the eight peaks as the strongest in turn) are commonly used. *SIeve+* also incorporates a 'Long 8' search, which uses the eight lowest-angle peaks. Fundamentally, searches using electron-diffraction data have deviated from traditional powder-diffraction searches because of the unreliability of both the intensities and the peak locations often brought about by the limited space within an electron microscope. Most modern electron-diffraction searches incorporate elemental data as an integral part of the method. As for X-ray diffraction, there are various generations that integrate elemental composition data, d-spacings or crystallographic data into a search/match process. The *SIeve+* program can also incorporate composition data into the search process.

3.7.2. Powder Diffraction File (PDF)

The PDF is a collection of single-phase X-ray powder patterns in the form of tables of characteristic interplanar spacings and corresponding relative intensities, along with other pertinent physical, chemical and crystallographic properties. The PDF contains various subfiles, which include alkaloids, amino acids, peptides and complexes, battery materials, bioactive compounds, carbohydrates, cement materials, ceramics (bioceramics, ferroelectrics, microwave materials, perovskites and semiconductors), common phases, education, explosives, forensic, hydrogen-storage materials, inorganics, intercalates, ionic conductors, Merck Index compounds, metals and alloys, meso- and microporous (clathrates, metal–organic frameworks and zeolites), mineral-related (minerals, gems, natural and synthetic), modulated structures, nucleosides and nucleotides, organics, pharmaceuticals, pigments and dyes, polymers, porphyrins, corrins and complexes, steroids, superconducting

materials (conventional superconductors, superconductor reaction products, superconductor-related and high-T_c superconductors), terpenes and thermoelectric materials. There is an educational package for classroom use, and the complete PDF is available for educational use on a time-limited basis. A primary purpose of the subfile system is to limit the size of the search universe by applying prior knowledge of the system being studied. This greatly reduces the number of false positives in a database that contains hundreds of thousands of materials. Field experts are consulted to guide the criteria for subfile selection, allowing novices to use the subfiles without being a subject expert.

3.7.2.1. *Sources and formats of the PDF*

The data incorporated into the Powder Diffraction File are acquired through contributions from individual scientists, corporate laboratories, literature surveys and a Grant-in-Aid programme. Approximately 200 leading scientific journals are searched manually for powder-diffraction data. Additional literature surveys covering patents, dissertations and the remaining open literature are performed using various online resources and search techniques.

Release 2019 (the current release as of this writing) contains more than 893 400 unique material data sets. The large size and comprehensive coverage of the PDF is achieved through the ICDD's historical sources of powder data (searches of the original literature, contributions and the Grant-in-Aid programme) as well as current and historic collaborations with crystallographic database organizations. Each PDF entry is assigned a unique identifying number of the format *ss-mmmnnnn*. The integer *ss* indicates the source of the data: 00, ICDD location/generation of powder data; 01, Inorganic Crystal Structure Database; 02, Cambridge Structural Database; 03, NIST (a short-term collaboration focused on metals and alloys); 04, Pearson's Crystal Data; 05, ICDD extraction of atomic coordinates from published sources (including incommensurate/modulated structures). Powder-diffraction data for sources 01 through 05 are computed from the crystal structures provided by these sources.

The Powder Diffraction File is designed and produced in several different formats in order to serve different groups of users. The PDF-2 database is designed for phase identification of inorganic materials; many common organic materials have also been added to this database. The PDF-4+ database is the most advanced database and is designed for both phase identification and quantitative analysis. This database has comprehensive coverage of inorganic materials and contains numerous additional features such as digitized (raw) patterns, molecular graphics and atomic coordinates to facilitate Rietveld refinements. The PDF-4+ database is also available as a portable full-function WEBPDF-4+ version. The PDF-4/Minerals database is a subset of the PDF-4+ database, and is the most comprehensive collection of mineral diffraction data. The PDF-4/Organics database is designed for phase identification of organic and coordination compounds. It contains data from ICDD sources (both experimental powder patterns and extraction of coordinates) as well as patterns calculated from CSD entries.

Advances in hardware, software and computing power have led to the collection of higher-quality powder data, and thus have necessitated higher-quality reference data to perform more complex multiphase analyses and total-pattern analyses. The PDF now includes tools that permit users to evaluate different types of data collected using different types of detectors and different sources, including X-rays, neutrons and electrons. The goal is to include ideal specimen patterns in the PDF, patterns that can be modified by the user to correspond to the current experiment. The user can select the wavelength type and various instrumental parameters to simulate the whole diffraction pattern. A crystallite size calculation was added in 2007 and an orientation function in 2011.

Since 2006, the ICDD has begun to include several types of less-crystalline materials in the database, materials for which too much information is lost when reducing the raw data to a list of *d*-spacings and intensities. These materials include clays and other layered materials, mixed-crystallinity polymers, amorphous materials and nanomaterials.

Nanomaterials often contain crystalline and amorphous fractions, and their powder patterns are difficult to generate from an ideal crystal structure. The ICDD has developed quality-evaluation methods for noncrystalline materials, and has established two additional quality marks: 'good' (G) and 'minimal acceptable' (M). These marks reflect the quality of the supporting data used to characterize the material. An amorphous material with a G quality mark has been characterized by independent analyses verifying the stated composition or thermogravimetric/differential scanning calorimetry analyses confirming the physical stability or the presence of a glass transition. A G quality mark indicates that the editors are satisfied that the pattern is representative of both the diffraction conditions and the stated chemistry and have confidence that the user can reproduce the pattern using similar conditions. The quality mark M indicates that the ICDD received some supporting documentation but it was insufficient for structural interpretation and classification of the material.

Great care needs to be taken in interpreting the patterns of mixtures of crystalline and amorphous phases, particularly in the definition and subtraction of the background. Significant work is under way to develop and adapt numerical techniques for processing full patterns of low-crystallinity materials.

3.7.2.2. *Quality marks in the PDF*

All data are critically reviewed and evaluated by the PDF editorial staff. Each pattern must pass through a four-tiered editorial review process before it can be included in the PDF. As technology evolves, the quality requirements for reference data also evolve. As a result, the information in the PDF is continuously reviewed and upgraded for accuracy and quality.

For many years, a quality mark has been assigned to each experimental PDF entry. A Star (*/S) pattern represents high-quality diffractometer or Guinier data. Several criteria must be satisfied for a pattern to be assigned a Star quality mark:

(i) The chemical composition must be well characterized.
(ii) The intensities must have been measured objectively; no visual estimation is allowed.
(iii) The pattern has a good range and an even spread of intensities.
(iv) The completeness of the pattern is sensible.
(v) The *d*-spacing of each reflection with $d \leq 2.500$ Å is given to at least three decimal places. The *d*-spacings of reflections with $d \leq 1.2000$ Å are given to at least four decimal places.
(vi) No serious systematic errors exist.
(vii) The $|\Delta 2\theta|$ value (*i.e.* the difference between the observed peak position and the position calculated from the unit

cell) of a qualifying reflection is $\leq 0.05^\circ$. In the case of multiply-indexed reflections, only the minimum absolute $\Delta 2\theta$ is considered.

(viii) The average $|\Delta 2\theta| \leq 0.03^\circ$ for qualifying reflections.

(ix) No unindexed, space-group-extinct or impurity reflections are present.

An Indexed (I) quality mark indicates that the pattern has been indexed; therefore, the material is almost certainly single-phase. There is a reasonable range and spread of intensities, and the completeness of the pattern is sensible. The d-spacings of reflections with $d \leq 2.000$ Å have at least three significant figures after the decimal point. No serious systematic errors exist. No qualifying reflection has $|\Delta 2\theta| \geq 0.20^\circ$ and the average $|\Delta 2\theta|$ is $\leq 0.06^\circ$. The maximum number of unindexed, space-group-extinct or impurity reflections is two, but none of these reflections are among the eight strongest lines.

A Blank (B) quality mark represents a mid-range quality. An O quality mark means that the data have been obtained from a poorly characterized material or that the data are known (or are suspected) to be of low precision and accuracy. Such patterns include those from multiphase mixtures or from a phase that is poorly characterized chemically. The O mark is commonly assigned to patterns for which no unit cell is reported, unless qualifying information indicates a single-phase material. Usually, the editor will have inserted a comment to explain why the O mark was assigned. For patterns with a unit cell, the following criteria are used to suggest the presence of two or more phases: the number of unindexed, space-group-extinct or impurity reflections is ≥ 3, or one of the three strongest peaks is unindexed.

Beginning with Release 2006, the quality-mark system was extended to patterns calculated from structural data supplied by ICDD partners. The focus of the quality mark is to determine the confidence level of the structural model used and its impact on the calculated pattern (especially for the purpose of phase identification). The major step involves several crystallographic and editorial checks by the ICDD, followed by extraction and flagging of the warnings/comments in the structural databases. The resulting calculated patterns are classified based on the significance and nature of the warnings. Any possible corrections that can be applied to resolve the errors are performed before publishing the calculated pattern.

The crystallographic checking rules are designed based on the expected quality of a contemporary crystal structure. An estimate of the missing electron density is made based on the difference between the reported composition and the structural composition. Transformations of nonstandard space groups are checked; the reported site multiplicities must match those generated by the symmetry operators. All of the eigenvalues of the anisotropic tensor matrix for each atomic displacement must be positive. All anisotropic tensor coefficients must be permitted by the site symmetry. Displacement coefficients should fall in the range $0.001 < U < 0.1$ Å^2. Isotropic displacement coefficients must be positive. Mixed displacement coefficients are converted to a standard type. The reported value of Z must be consistent with the sum of the site multiplicities. Lattice parameters are checked for missing decimal points, missing standard uncertainties and the magnitudes of the uncertainties. R factors close to the theoretical limits (0.83 for centrosymmetric structures and 0.59 for non-centrosymmetric structures) are signs of potential errors in the conversion to/from absolute/percentage values. Site occupancies cannot be greater than 1. Refining part of the structure as a group without locating the positions of the constituent atoms (for example, in C_{60}) will generate a warning. Possible typographical errors in element symbols are checked by comparing the chemical formula, atomic coordinate list and chemical name. When a measured density is available, the percentage difference between the measured and calculated density is determined.

Many warnings/comments from the collaborating databases are used in assignment of the quality mark. Editorial comments on unusually short or long bond lengths or questionable bond angles are considered; the comment needs to be very specific for structures exhibiting disorder or partial/mixed occupancies. A listing of other types of comments considered is contained in the PDF-4+ database help documentation. Entries are assigned a quality mark of * (no warning found during data evaluation), I (minor warning), B (significant warning found), O (major warning), P (the structure was assigned by the editor based on a prototype) or H (hypothetical) according to the criteria in Table 3.7.1.

3.7.2.3. *Features of the PDF*

Most users access the PDF through the software provided by their instrument manufacturer, but it is a powerful standalone database. The PDF is a large relational database consisting of many linked tables. The complete set of features can be accessed through the PDF front end supplied by the ICDD. It is possible to directly access a PDF entry by entering its PDF number. However, one can search for an entry or a class of entries through a series of search tabs. Queries from multiple tabs can be combined in a single search, or individual searches can be saved in a history and combined using Boolean operations. The results of such searches can be analysed as a group or can be used as subfiles for *SIeve*, the search/index phase-identification add-on for the PDF.

Selections on the main search screen permit selection by the source of data, quality mark, primary/alternate, ambient/non-ambient and subfile or subclass. The comprehensive nature of the PDF means that there are often many entries for an individual material. The ICDD editorial staff and volunteer task groups assign one experimental and one calculated entry (if present) as primary entries for each phase so that the user can avoid the duplication if desired. The other entries are designated as alternates. The subfiles and subclasses provide a convenient means for the user to limit the size of the search universe based on prior knowledge and result in faster searches and fewer false-positive matches.

Perhaps the most commonly used screen is the Periodic Table tab for chemistry searches. Individual elements, groups, periods and pre-defined selections (nonmetals, semimetals *etc.*) can be selected and combined in various ways. The 'and' operation requires that all selected elements be present in the entries in the selection set, but other elements can also be present. The 'or' operation requires at least one of the selected elements to be present. The 'only' operation requires that all of the selected elements, and only those elements, be present in the hit. The 'just' operation results in a hit list of entries that contain the selected elements in all combinations: elements, binaries, ternaries *etc.* The results of these four types of element searches can also be combined using Boolean operations. An alternative way of using periodic-table screening is through the labelling of each element with 'yes', 'no' or 'maybe' to indicate elements that are known to be present, absent or unsure in the specimen.

The Formula/Name tab facilitates searches on formula, empirical formula, structural formula and formula type ANX [as in the Inorganic Crystal Structure Database (ICSD)]. The formulae may be exact or contain individual elements or strings.

Table 3.7.1
Criteria for the assignment of quality marks to calculated patterns in the Powder Diffraction File

A Star (*/S) pattern has no warnings.

Minor warning (I)	Significant warning (B)	Major warning (O)
Density calculated from reported and calculated compositions differ ($1\% < x < 3\%$)	Density calculated from reported and calculated compositions differ ($1\% < x < 15\%$)	Density calculated from reported and calculated compositions differ ($15\% < x$)
No e.s.d. reported/abstracted on cell dimensions	Lattice parameters taken from figure (approximated)	Incorrect lattice parameters
Magnitude of e.s.d.s on lattice parameters > 1000 p.p.m.	Missing decimal point in lattice parameter	Incorrect space group
$0.07 < R < 0.12$ (single crystal), $0.10 < R < 0.15$ (powder)	$0.12 < R$ (single crystal), $0.15 < R$ (powder)	Incommensurate/modulated structure. Only average structure of the subcell is given.
No R reported/abstracted	Anisotropic displacement tensor is non-positive definite	Published atomic coordinates are wrong
Reported Z is inconsistent with the sum of the site multiplicities	Anisotropic tensor coefficient not permitted by site symmetry	Structural database removed the entry corresponding to a published calculated pattern
Type of experiment (single crystal/powder) is not mentioned	Magnitude of displacement coefficients outside the range $0.001 < U < 0.1$ Å^2	
Structure corrected by the editor	$U_{iso} < 0.0$	
Difference between measured and calculated density > 2%	Source-database warning on bond length/angle	
Misprint in original paper corrected in database	Average structure of a modulated structure	
Site occupation factor > 1.0	Probable site-occupation factor deduced from the nominal composition	
	Part of the structure was refined as a group without locating the constituent atoms	
	Comments containing a reference to a contradicting structure exist	
	Structure determined from projections	
	Structure determined using electron diffraction	

Searches on the number of elements present in the compound, as well as composition searches (by weight or atom per cent, *i.e.* wt% or at.%), are also possible.

The Formula/Name tab also permits searches on compound name, common name, mineral name and all names. It is also the screen from which searches on zeolite structure-type code (the International Zeolite Association codes are used) and mineral classification (according to the International Mineralogical Association) are performed.

Under the Reference tab, searches on author, journal name, CODEN, year, volume and title of the paper are possible. The titles were not originally included in PDF entries, but have been added to all entries in recent years. Also possible from this tab are searches on the Chemical Abstracts Service Registry Number (CASRN). Such searches are very powerful for organic compounds, with their complicated nomenclature. CASRNs are present for many, but not all, PDF entries.

The Classification and Crystallography tabs contain searches on Pearson symbol code, space group and space-group number, prototype structure, centrosymmetric/noncentrosymmetric and whether the entry contains atomic coordinates. Searches on the authors' cell, the Pearson's Crystal Data cell or the reduced cell are also possible. I find it useful to use fairly large tolerances (say 0.3–0.5 Å on edges) in such searches. I prefer to examine a longer list of potential matches which contains the correct phase, rather than risk missing an identification.

The Diffraction tab includes searches on the longest (lowest-angle or highest d-spacing) and strongest lines in the pattern. A line can be specified to be one of the three longest/strongest, or the first, second or third. This screen also includes searches on density, I/I_c (which is $I/I_{corundum}$, a measure of the inherent scattering power of a phase and useful in quantitative phase analysis), melting point, R value, colour and Smith–Snyder figure of merit. There are check boxes to select whether the entries in the hit list include 'PD3' patterns (raw data) and property sheets. These property sheets are PDF documents embedded in an entry. These sheets are starting to be included for materials in subfiles that are defined by a particular property, such as superconductivity or thermoelectricity. These sheets are generated by groups of ICDD consulting editors.

Once a hit list has been generated, an individual entry can be selected (double clicked) to bring up the complete PDF entry. The results display can be customized using the Preferences menu (or by right clicking in the entry). The powder pattern can be plotted and additional PDF entries and/or raw data can be overlaid and scaled. In the Plot window, a PDF entry can be exported to several formats. The most useful is a CIF; the crystal

structure described by the CIF can then be imported into to the user's graphics or Rietveld package.

Free-text searches of the comments are also included on this screen. These are particularly useful, as ICSD collection codes and CSD refcodes are included in the comments. If the user has the CSD installed on the same machine as the PDF, the PDF entry links live to the coordinates in the CSD entry.

By using the Results menu option when a hit list is displayed, ranges of cells in the spreadsheet can be selected and simple descriptive statistics (mean, median and estimated standard deviation) can be generated. Also under Results is a Graph Fields option. The variables used for the *x* and *y* axes of the plot can be selected and both scatter plots and histograms can be generated. Each of the points in such a plot is 'live' and can be clicked to display the full PDF entry. Fig. 3.7.1 shows a plot of the cubic lattice parameter with respect to at.% Fe in FeO (Fe and O only, space group No. 225) under ambient conditions. From such data it is easy to generate a correlation between the Fe stoichiometry and the lattice parameter.

An optional add-on module to the PDF is *SIeve* (Search Index). This is a peak-based search/match program which enables the use of a manually entered (or imported) peak list or derives a peak list from imported ASCII raw powder-diffraction data in several formats. It also has a flexible ASCII data-import module. Hanawalt, Fink, Long8 (the eight lowest-angle peaks in the pattern) or electron-diffraction searches can be carried out. Again, there is a Preferences option to customize the searches. A particularly useful (and easy-to-use) feature is the ability to apply a filter to the search/match. This filter can be selected from several pre-defined filters and/or any previous search in the session (stored in a history list). The combination of conventional search/match and Boolean searches can be very powerful, as illustrated in the next section.

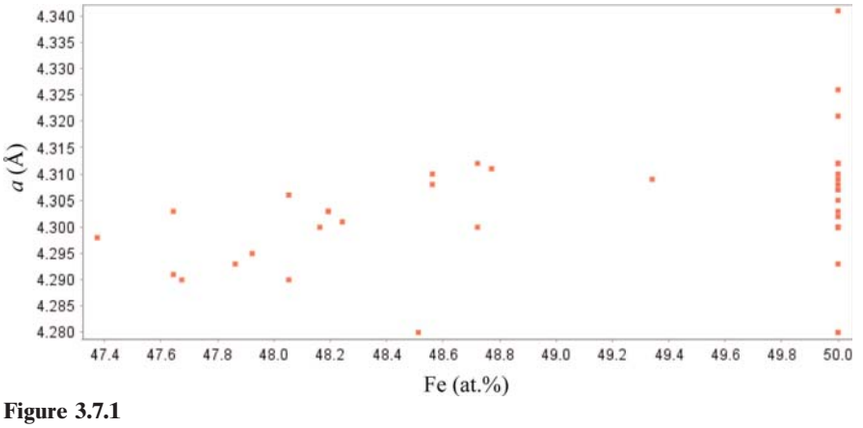

Figure 3.7.1
A plot generated by the Results/Graph Fields function in the Powder Diffraction File. The search was for entries containing only Fe and O and with space group No. 225 (resulting in FeO entries) measured under ambient conditions. One outlier was removed from the hit list manually. The trend in the cubic *a* lattice parameter with Fe content is apparent, as well as the large number of apparently stoichiometric FeO entries, some of which may not be correctly characterized.

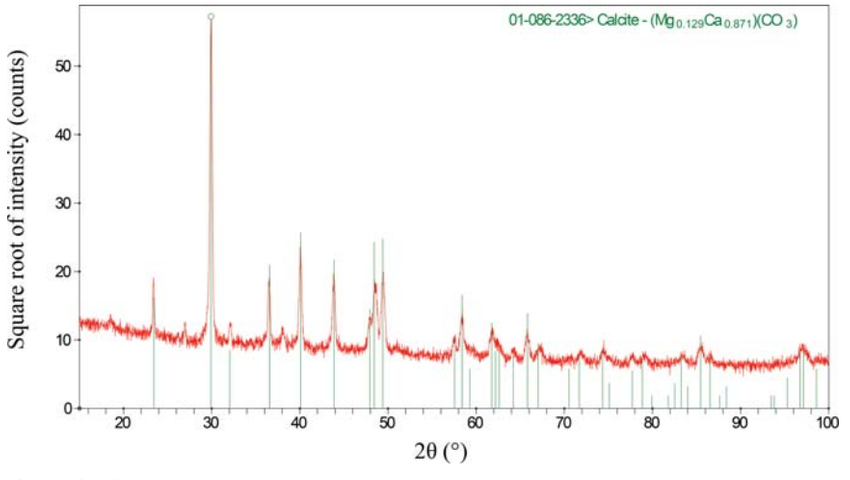

Figure 3.7.2
The result of applying a commercial search/match program (*Jade* 9.5; Materials Data, 2012) to the powder pattern of a water-still scale. Weak peaks not accounted for by the major magnesian calcite phase are apparent and additional tools in the Powder Diffraction File were needed to identify the additional phases.

3.7.2.4. *Boolean logic in phase identification*

Most phase identifications are carried out using the peak-based or full-pattern algorithms supplied by the instrument vendor. These often work well for major phases and can be customized to improve their success in identifying minor/trace phases. The native capabilities of the PDF (not all of which are accessible through some vendors' software) can be very powerful in identifying those extra peaks that result from a Rietveld difference plot (or any difference plot from pattern-fitting software) using the major phases. Below we use examples to illustrate several strategies.

3.7.2.4.1. *Water-still deposit*

A water still in my home eventually generates scale, much of which flakes off the walls, permitting easy analysis in the powder diffractometer. Any commercial search/match program will easily identify magnesian calcite (Fig. 3.7.2; files kadu1389.gsas, kadu1389.raw and iitd26_0510.prm, available in the supporting information). There are, however, three additional weak peaks at d/I = 4.788/38, 3.3089/51 and 2.3697/56. In Naperville, Illinois, the tap water comes from Lake Michigan. The bedrock underlying the Chicago region is the Racine Dolomite. Given the identity of the major phase in the scale and the source of the water, it seems likely that any minor phases will be mineral-related and contain some combination of the elements Ca, Mg, C, O and H (to include the possibility of hydrates and hydroxides). Accordingly, a search of mineral-related entries containing 'just' the elements Ca, Mg, C, O and H was performed and used as a filter in a Hanawalt search using these three peaks. This limits the search universe to 692 of the 328 660 entries in the PDF-4+ in 2012. The seven highest goodness-of-match entries in the hit list were brucite, $Mg(OH)_2$. This phase was added to the Rietveld refinement. Analysis of the difference plot indicated an unaccounted-for peak at a *d*-spacing of 3.3089 Å. A search for mineral-related entries with the same chemistry and having one of their three strongest peaks in the range 3.309 (30) Å yielded the vaterite polymorph of $CaCO_3$ as the hit with the highest goodness of match. This phase was added to the Rietveld refinement. The final quantitative phase analysis was: 94.7 (1) wt% $Ca_{0.84}Mg_{0.16}(CO_3)$, 5.2 (4) wt% $Mg(OH)_2$ and 0.2 (1) wt% vaterite.

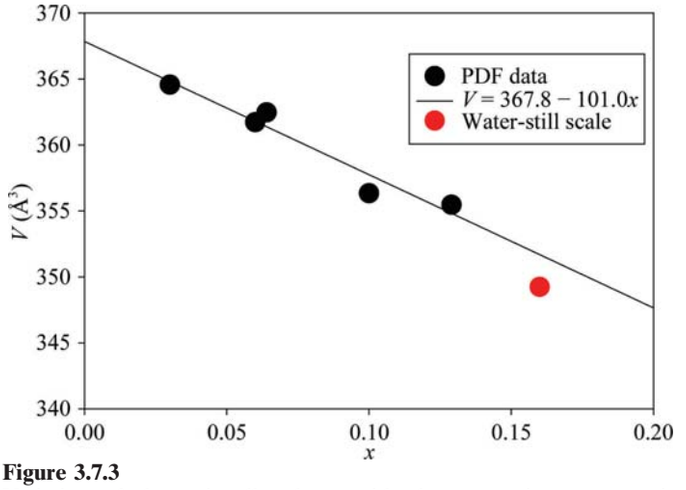

Figure 3.7.3
Variation of the unit-cell volume with the magnesium content in magnesian calcites in the Powder Diffraction File.

The composition of the major phase was refined, constraining the sum of the Ca and Mg site occupancies to equal 1.0. To understand how this fitted with previous magnesian calcites, a search for compounds containing only Ca, Mg, C and O, ambient conditions and space group No. 167 was carried out. Some manual editing of the hit list was required. Adjusting the preferences to include the display of composition in at.% and the unit-cell volume made it convenient to plot the variation in unit-cell volume as a function of Mg content x in $Ca_{1-x}Mg_x(CO_3)$ (Fig. 3.7.3). This magnesian calcite in the water-still scale has a higher Mg concentration than most, but falls close to the trend line. The flexibility and content of the Powder Diffraction File makes such data mining relatively straightforward.

3.7.2.4.2. *Vanadium phosphate butane-oxidation catalyst*

Vanadyl pyrophosphate [$(VO)_2P_2O_7$] catalysts are used commercially for the selective oxidation of butane to maleic anhydride. Modern third-generation search/match programs [using the background-subtracted, $K\alpha_2$-stripped data (files goed80.gsas, GOED80.raw and d8v3.prm); Fig. 3.7.4] had no trouble in identifying the desired major phase $(VO)_2P_2O_7$, but had difficulty with the minor phases that were clearly present. Unless the display of duplicate entries is turned off, most programs will yield several duplicate hits at the top of the list. Both 00-050-0380 and 04-009-2740 are Star quality, but only the Linus Pauling File (LPF) entry 04-009-2740 contains atom coordinates for a Rietveld refinement. Entry 01-070-8726 has the lower-quality B mark.

The native capabilities of the PDF proved helpful in identifying the minor phases. The lowest-angle peak not accounted for by the major phase is at a d-spacing of 7.2107 Å. A search for phases containing just the elements V, P, O and H (known from the synthesis procedure) and having one of their three strongest peaks in the range 7.21 ± 0.05 Å (an estimated range) yielded only the single hit 00-047-0967: $H_4V_3P_3O_{16.5}(H_2O)_2$. This is a low-precision (O quality mark) pattern from a US Patent (Harju & Pasek, 1983), and the pattern contains only four lines. The comments in the PDF entry indicate that this hydrated phase was formed by exposing a catalyst to ambient conditions, so it seems chemically reasonable but poorly defined.

To see whether this phase had been better characterized by a crystal structure, the four peaks were entered into *SIeve+* and a Hanawalt search using a wider than default tolerance of 0.3° on the peak positions and the 'just' chemistry filter V, P, O and H was carried out. As expected, PDF entry 00-047-0967 was at the top of the hit list, but close to the top was entry 04-017-1008 (Shpeizer *et al.*, 2001): $[H_{0.6}(VO)_3(PO_4)_3(H_2O)_3](H_2O)_4$. The article by Shpeizer *et al.* (2001) indicates that this phase was formed from an anhydrous precursor by exposing it to ambient conditions. The single-crystal structure was obtained at 173 K. The similarity of the two PDF entries (Fig. 3.7.5) and the difference in data-collection temperatures makes it clear that these correspond to the same phase, and that the structure of $[H_{0.6}(VO)_3(PO_4)_3(H_2O)_3](H_2O)_4$ could be used in a Rietveld refinement.

There were still unaccounted-for peaks at 3.5823 and 3.0760 Å. Under the assumption that these came from a single phase, two separate searches for phases containing just V, P, O and H and with one of their three strongest lines in the ranges 3.58 ± 0.03 and 3.08 ± 0.03 Å were carried out and then combined (using the History option) with a Boolean 'and' operation. All five of the entries on the hit list corresponded to α-$VOPO_4$. This yellow V^{5+} compound was consistent with the altered colour of the V^{4+}-based catalyst, and is a common impurity.

Close examination of the Rietveld difference plot from a refinement including these three phases indicated that there was a weak shoulder at a d-spacing of 3.985 Å. A search for phases containing just V, P, O and H and having a strong peak near this d-spacing yielded β-$(VO)(PO_3)_2$, another common catalyst impurity (Fig. 3.7.6). Including this compound as a fourth phase yielded a satisfactory Rietveld refinement and a quantitative analysis of 84.8 (1) wt% $(VO)_2P_2O_7$, 5.9 (1) wt% $[H_{0.6}(VO)_3(PO_4)_3(H_2O)_3](H_2O)_4$, 5.6 (1) wt% α-$VOPO_4$ and 3.7 (1) wt% β-$VO(PO_3)_2$.

3.7.2.4.3. *Valve deposit from a piston aviation engine*

Applying a commercial search/match program to the diffraction pattern of a deposit from a valve in a gasoline-powered aircraft engine easily identified quartz and corundum. The specimen was scraped from the valve seat and micronized. The corundum represents abrasion from the elements of the micronizing mill, as it was not present in the pattern of the as-scraped sample. Metal particles were visibly present in the deposit, so one could reasonably guess the presence of both ferrite and austenite (Fig. 3.7.7; files maso04.gsas, maso04.rd and padv.prm). A Rietveld refinement using these four phases was carried out.

Six peaks picked from the difference plot were entered into *SIeve+* and a Hanawalt search was carried out. No chemically reasonable simple compounds were near the top of the hit list, so extra information was sought. An XPS analysis indicated the presence of Pb, Br, Fe, P, O and C (and H assumed). Aviation gasoline is still leaded, and ethylene dibromide is sometimes added as a lead scavenger. The result of a 'just' chemistry search using these seven elements (6543/328 660 entries) was applied as a filter to the Hanawalt search. Near the top of the hit list was $PbBr_2$. Although apparently surprising, this phase is reasonable given our chemical knowledge. Lead bromide was added to the Rietveld refinement. Further analysis of the difference pattern using the same techniques indicated the presence of cohenite, Fe_3C, from the steel, and $Fe_3Fe_4(PO_4)_6$, the reaction product of the steel with a phosphate fuel additive. The final Rietveld refinement yielded a quantitative analysis of 26.5 (4) wt% austenite (γ-Fe, stainless steel), 47.9 (4) wt% ferrite (α-Fe, carbon steel), 17.7 (4) wt% quartz (sand/dirt), 2.9 (2) wt% $PbBr_2$, 2.6 (2) wt% $Fe_3Fe_4(PO_4)_6$ and 2.2 (2) wt% cohenite (Fig. 3.7.8).

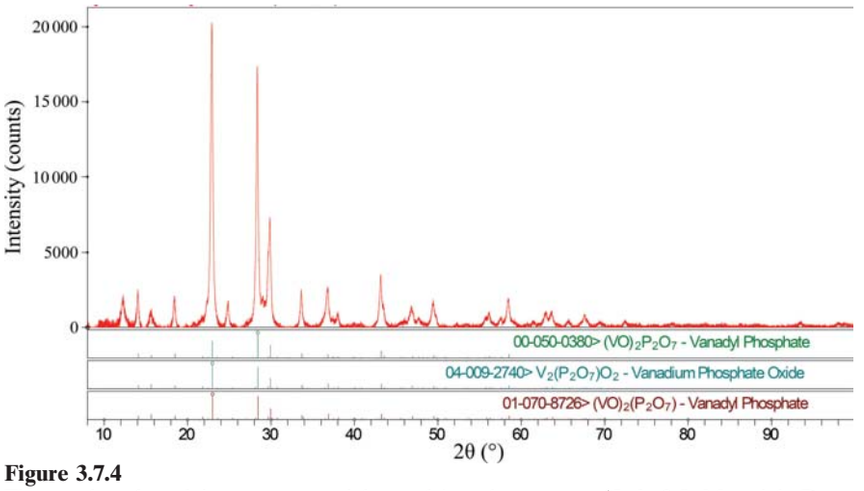

Figure 3.7.4
The results of applying a commercial search/match program (*Jade* 9.5; Materials Data, 2012) to the (background-subtracted, $K\alpha_2$-stripped) powder pattern of a butane-oxidation catalyst. The first three patterns in the hit list had equivalent figures of merit. The PDF entries 00-050-0380 and 04-009-2740 had Star quality marks and 04-009-2740 contained the atomic coordinates necessary for a Rietveld refinement. Additional peaks are apparent. The phases that give rise to them were identified using the native capabilities of the Powder Diffraction File.

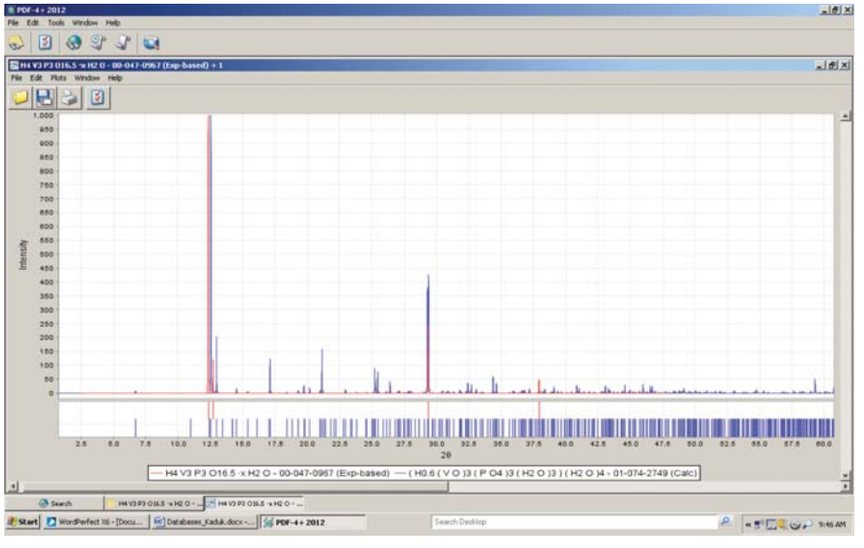

Figure 3.7.5
Comparison of the low-quality experimental PDF entry 00-047-0967 with the high-quality calculated pattern 01-074-2749 located by searching the experimental pattern against the rest of the PDF. The similarity in patterns and chemistry demonstrated that the two phases were the same and that the coordinates used to calculate entry 01-074-2749 could be used in a Rietveld refinement of a butane-oxidation catalyst.

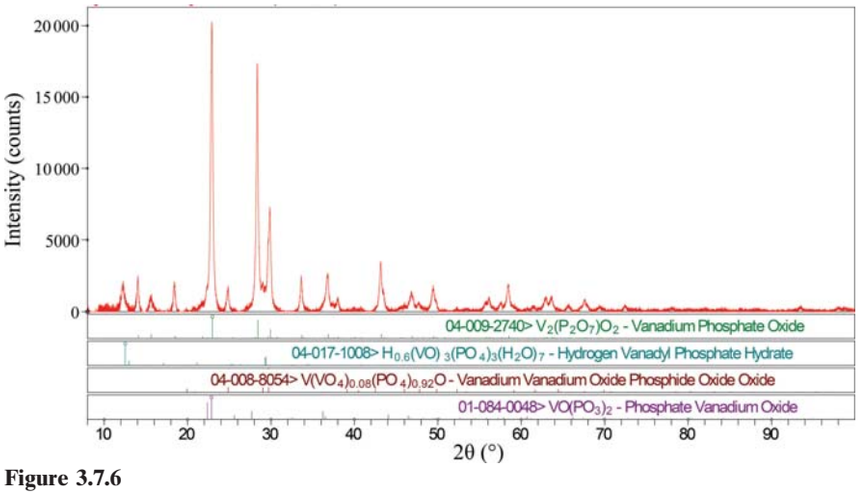

Figure 3.7.6
The four crystalline phases identified in a butane-oxidation catalyst.

3.7.2.4.4. *Isocracker sludge*

An isocracker is a refinery unit which simultaneously carries out cracking and isomerization reactions to produce more high-octane gasoline. A black deposit isolated from such a unit was surprisingly crystalline (Fig. 3.7.9; files NALK157.gsas, NALK157.raw and padv.prm). It was easy to identify small concentrations of elemental sulfur, pyrrhotite-4M (now called pyrrhotite-4C), haematite, lepidocrocite and dolomite, but the major peaks did not match well those of any entry in the PDF.

It seemed likely that a mineral-related phase would serve as a structural prototype for an apparently new phase, so two separate searches for mineral-related phases with one of their three strongest peaks in the *d*-spacing ranges 7.09 ± 0.03 and 5.57 ± 0.03 Å were combined. The two hits in the search list were both uranium minerals. These seemed unlikely in a refinery deposit(!). Widening the search ranges to 7.09 ± 0.10 and 5.57 ± 0.07 Å yielded rasvumite, KFe_2S_3 (PDF entry 00-033-1018), as the second entry in the hit list.

The fit to the major peaks in the deposit was reasonable, but there should not be any potassium in a refinery deposit and none was detected in a bulk chemical analysis. When the jar containing the deposit was opened, it smelled strongly of ammonia. Ammonium and potassium ions are about the same size and often form isostructural compounds. The infrared spectrum of the deposit was dominated by bands of ammonium ions.

The potassium in the structure of rasvumite (PDF entry 01-083-1322, used as a reference) was replaced by nitrogen. Analysis of potential hydrogen-bonding interactions yielded approximate hydrogen positions in the ammonium ion. These positions were refined using a density-functional geometry optimization. This model yielded a satisfactory Rietveld refinement (Fig. 3.7.10) and the quantitative analysis 45.7 (2) wt% $(NH_4)Fe_2S_3$, 12.8 (4) wt% S_8, 22.0 (6) wt% lepidocrocite (γ-FeOOH), 5.5 (5) wt% haematite (α-Fe_2O_3), 6.6 (3) wt% pyrrhotite-4C (Fe_7S_8) and 6.6 (3) wt% dolomite [$CaMg(CO_3)_2$; limestone environmental dust]. The powder pattern and crystal structure of $(NH_4)Fe_2S_3$ are now included in the PDF as entry 00-055-0533.

3.7.2.4.5. *Amoxicillin*

The amoxicillin powder from a commercial antibiotic capsule was highly crystalline. Its powder pattern (files kadu918.gsas, KADU918.raw, d8v3.prm and KADU921.rd) was matched well by the PDF entries 00-039-1832 and 00-033-1528 for amoxicillin trihydrate, but there was an additional peak at a *d*-spacing of 16.47 Å (5.37° 2θ). With such a low-angle peak, it seemed prudent to measure the pattern again

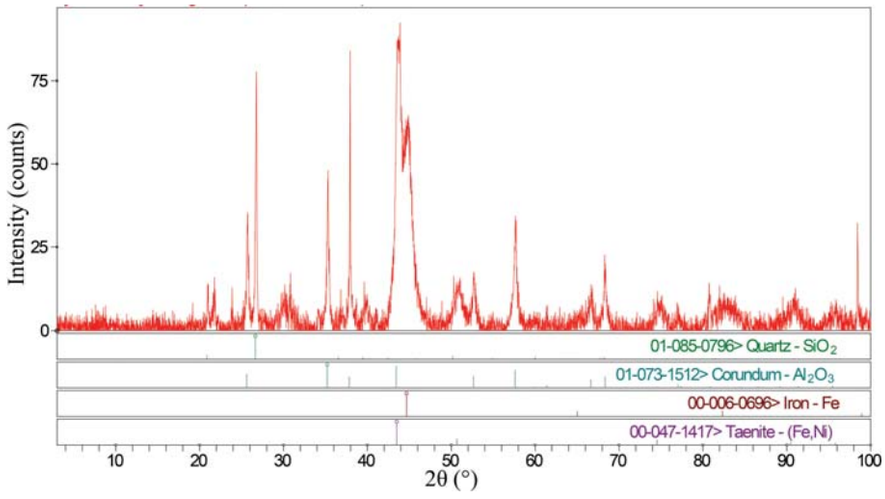

Figure 3.7.7
The four phases identified in a valve deposit from an aircraft engine by automated search/match methods and guessing based on the appearance of the sample. The pattern has had the background and $K\alpha_2$ peaks removed.

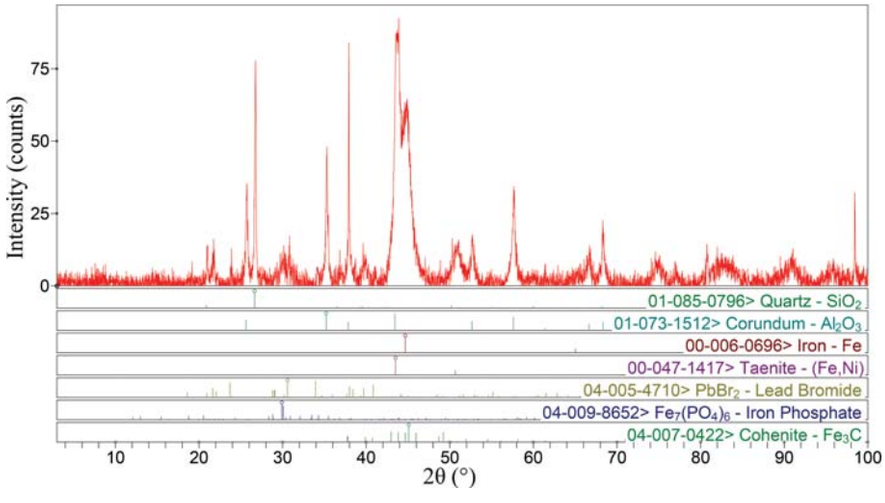

Figure 3.7.8
The seven phases identified in the valve deposit from an aircraft engine.

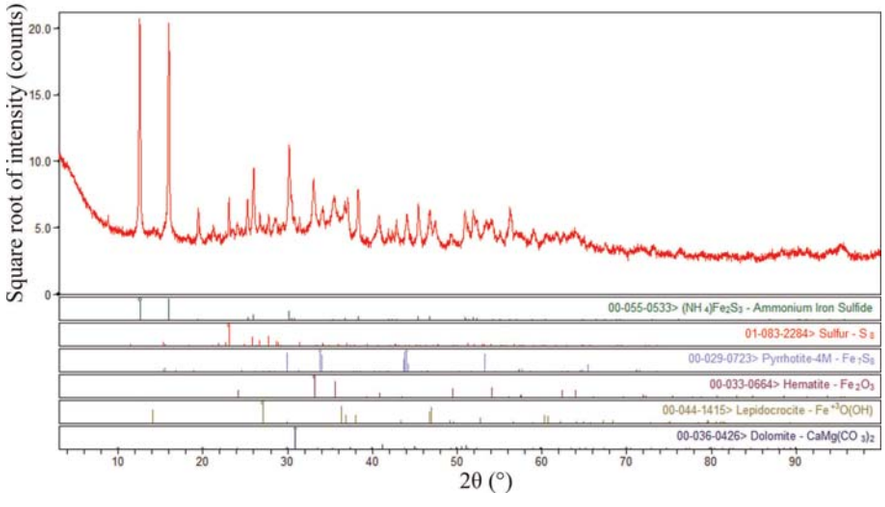

Figure 3.7.9
The phases identified in a deposit from a refinery isocracker. At the time, the $(NH_4)Fe_2S_3$ was a new phase, identified by analogy to KFe_2S_3, rasvumite.

starting at 3°, and another peak was observed at d = 24.80 Å (3.56° 2θ).

A search of the PDF-4/Organics 2013 for phases having two such peaks among their longest (lowest-angle) peaks yielded entry 00-005-0010 for calcium stearate at the top of the hit list, as well as two lead stearates. We can safely assume that lead stearate is not present in a pharmaceutical. Calcium stearate, however, has its strongest peak at 1.76°, so another pattern was measured starting at 1.5° 2θ. This peak is indeed present (Fig. 3.7.11).

The primary literature suggests that the compound in PDF entry 00-005-0010 is really calcium stearate monohydrate, and that its structure (like those of many other stearate salts) has not yet been determined. The CSD entry for amoxicillin trihydrate (AMOXCT10; Boles *et al.*, 1978) contained some incorrect H-atom positions and was missing an H atom, so these were corrected before a Rietveld refinement was carried out.

3.7.2.4.6. *Pseudoephedrine*

As P. W. Stephens was measuring the powder pattern of a commercial pseudoephedrine-based decongestant on beamline X16C at the National Synchrotron Light Source at Brookhaven National Laboratory, he noted that extra peaks were present. The lowest-angle peak was at a d-spacing of 12.73 Å, and other peaks occurred at 5.74, 4.62 (strongest) and 4.407 Å. A search in the PDF-4/Organics for compounds having the string 'ephed' in the name, a long line at 12.73 ± 0.05 Å and a strong line at 4.62 ± 0.02 Å yielded the single hit 00-041-1946, pseudoephedrine hydrochloride, a reasonable impurity in pseudoephedrine.

3.7.2.4.7. *Commercial multivitamin: Centrum A to Zn*

Commercial multivitamins are challenging phase-identification problems because they contain small concentrations of many different components. The application of a commercial search/match program to a pattern of Centrum A to Zn collected on beamline ID-32 at the Advanced Photon Source at Argonne National Laboratory using a wavelength of 0.495850 Å (files centrum.gsas and id320304.prm) easily identified brushite, $CaHPO_4(H_2O)_2$, and sylvite, KCl (Fig. 3.7.12).

To identify additional phases, 64 peaks with d > 1.91 Å were picked from the plot and entered into *SIeve+* in the PDF-4/Organics 2013 database. The PDF-4/Organics database was used to enhance the success in identifying organic compounds, and the relatively short d-spacing limit was used to ease the identifi-

cation of the simple inorganic compounds which are often present in commercial vitamins.

A Hanawalt search using these peaks easily identified iron fumarate (00-062-1294), szmikite [$MnSO_4(H_2O)$; 00-033-0906], L-ascorbic acid (02-063-2295), monetite ($CaHPO_4$; 01-070-0359) and calcite ($CaCO_3$; 00-005-0586). Note that these hits come from four different data sources; searches based on just one source would not have identified all of these compounds.

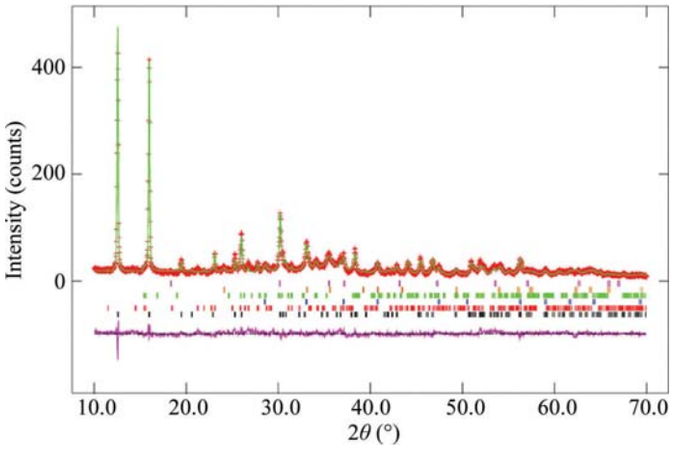

Figure 3.7.10
The final Rietveld plot from refinement of the isocracker deposit.

There were strong high-angle peaks that had not yet been accounted for at *d*-spacings of 2.4762, 2.1068, 1.4900 and 1.4783 Å. These four peaks were entered into a new Hanawalt search, which identified periclase (MgO; 01-071-3631) and zincite (ZnO; 01-075-9742).

Superimposing the peaks for all of these compounds onto the raw data made it clear that there were broad peaks in the pattern at *d*-spacings of approximately 5.8750, 5.3273, 4.3277 and 3.9217 Å. Since the lowest and highest angles of these four were the best defined, separate searches for compounds having each of these peaks as one of their three strongest lines were combined using a Boolean 'and'. Among the hit list was cellulose I_β (00-060-1502), which is a common constituent of pharmaceuticals. The structure model from PDF entry 00-056-1718 was added to the Rietveld refinement as a ninth phase.

One last peak at 5.9915 Å was unaccounted for. A search for pharmaceutical-related compounds with this peak as one of the three strongest included nicotinamide (02-063-5340; niacin or vitamin B_3). Ten phases were thus identified and these account for all of the peaks in the pattern.

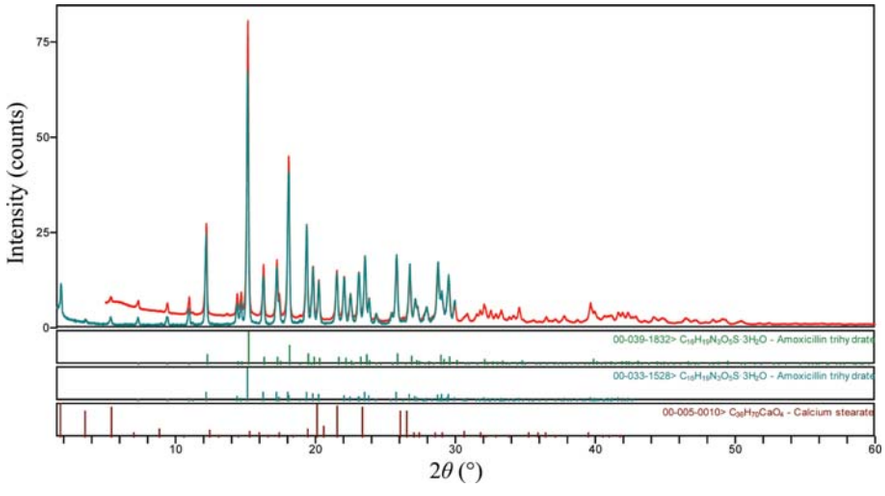

Figure 3.7.11
Phases identified in amoxicillin powder from a commercial capsule.

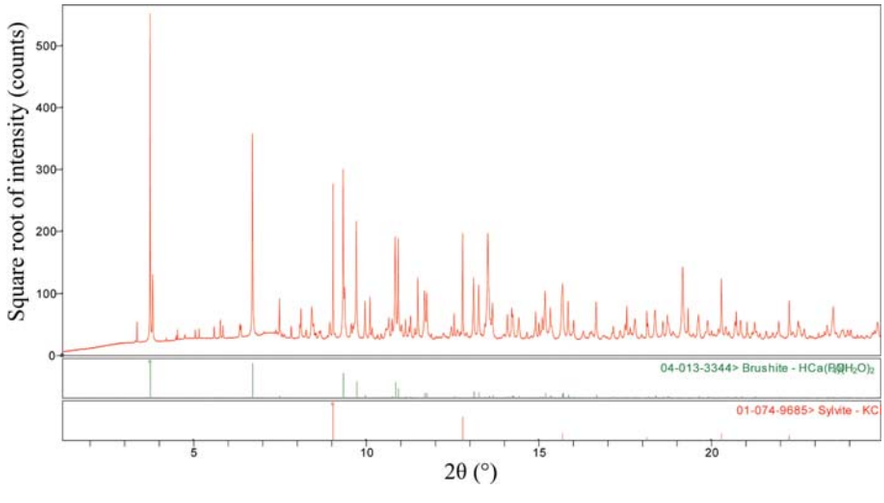

Figure 3.7.12
Phases identified by automated search/match in a Centrum A to Zn multivitamin tablet. Additional phases were identified using the native capabilities of the Powder Diffraction File.

3.7.3. Cambridge Structural Database (CSD)

Some features of the Cambridge Structural Database system (CSD; https://www.ccdc.cam.ac.uk; Groom *et al.*, 2016) are described in Chapter 22.5 of *International Tables for Crystallography* Volume F (Allen *et al.*, 2011). The CSD contains X-ray and neutron diffraction analyses of carbon-containing molecules with up to 1000 atoms (including hydrogens), including organic compounds, compounds of the main-group elements, organometallic compounds and metal complexes. The CSD covers peptides of up to 24 residues; higher polymers are covered by the Protein Data Bank. The CSD also covers mononucleotides, dinucleotides and trinucleotides; higher oligomers are covered by the Nucleic Acid Database (http://ndbserver.rutgers.edu). There is a small overlap between the CSD and the Inorganic Crystal Structure Database in the area of molecular inorganics.

Capabilities particularly useful for structure validation are covered in Chapter 4.9 of this volume. This discussion will not attempt a comprehensive description of the capabilities of the CSD, but will concentrate on features that are particularly relevant to powder diffraction.

The principal interface to the CSD is the program *ConQuest* (Bruno *et al.*, 2002). Its most distinctive feature is the ability to draw molecular structures and fragments and carry out substructure searches. Such searches eliminate the ambiguities that can arise when searching by compound name or other text-based properties. These chemical-connectivity

searches can include the number of H atoms bonded to a particular atom, the charge, the number of bonded atoms and whether the atom is part of a ring. In addition, three-dimensional quantities can be defined, tabulated and analysed. These quantities can be analysed in *Mercury* (Macrae *et al.*, 2008) and *Mogul* (Bruno *et al.*, 2004). Such analyses are useful for defining geometrical restraints in a Rietveld refinement. A general practice is to use the mean and standard deviations directly output by *Mogul* for the restraints. It is important to understand the CSD conventions for defining bond types to obtain successful results.

In *ConQuest*, searches can be carried out on author and/or journal name, as well as the normal bibliographic characteristics. Compounds can be located by chemical and/or common names, but such searches should be complemented by chemical-connectivity searches. It is possible to limit the search universe by chemical class, including carbohydrates, nucleosides and nucleotides, amino acids, peptides and complexes, porphyrins, corrins and complexes, steroids, terpenes, alkaloids and organic polymers. Searches on elements and formulae are possible, as well as searches on space groups and crystal systems. Particularly useful in searching for structure analogues are reduced-cell searches. Queries on Z, Z' and density are useful in data mining. A wide variety of searches on experimental parameters are possible; there is an option to exclude powder structures. Searches on both pre-defined terms and general text searches are possible. Particularly convenient for users of the PDF-4/Organics database is the retrieval of individual refcodes; the refcode from the PDF entry can be input directly into *ConQuest*. Starting with the 2013 release of the PDF-4/Organics database this link is live; the display of a PDF entry will result in import of the coordinates from the CSD entry. Boolean operations can be used to combine search queries in many flexible ways.

In recent years, many (if not most) single-crystal structures have been determined at low temperatures, while most powder-diffraction measurements are made under ambient conditions. Thermal expansion (often anisotropic) can result in differences between the observed peak positions and those in a PDF-4/Organics entry calculated from a CSD entry. For successful phase identification, larger than default tolerances must often be used in the search/match process. Transparency effects in pure organic compounds can also lead to significant peak shifts to lower angles, as well as significant asymmetry, so wider search windows may be necessary for phase identification.

3.7.3.1. *Mercury*

The structure-visualization program *Mercury* (Macrae *et al.*, 2008) is available as a free version and as a version with the CSD which has additional capabilities that are useful for powder diffraction. *Mercury* reads and writes a variety of molecular and crystal structure file formats, but is most commonly used with CIFs. Structures can be edited, and among the edit options is Normalize Hydrogens. This is particularly useful to improve the approximate H-atom positions that are often used in the early and intermediate stages of a Rietveld refinement. It is always worth including the H atoms in the structure model (in at least approximate positions) because better residuals and improved molecular geometry are obtained.

The Display Symmetry Elements tool is particularly useful for teaching symmetry. The Display Voids tool is useful in validating structures after solution. For most materials (zeolites and metal–organic frameworks are notable exceptions) we do not expect empty spaces in the crystal structure, so the presence of voids suggests the presence of an incomplete structure model and/or errors.

Among the options in the Calculate menu is Powder Pattern. The calculation can be customized by the user to match the desired instrumental configuration. The calculated pattern can be saved in several formats for comparison in the user's instrument software. *Mercury* expects the displacement coefficients to be given as U values. CIFs can come from many sources and can use different conventions for the displacement coefficients or may be missing them entirely. Manual editing of the input CIF is often required, otherwise strange powder patterns can be calculated.

Among the CSD-Materials/Calculations options is BFDH morphology (Bravais, 1866; Friedel, 1907; Donnay & Harker, 1937). Although a simple calculation, it is often realistic enough to suggest the likelihood of profile anisotropy and preferred orientation, along with expected directions. The calculation can thus save guessing about preferred directions.

The Structure Overlay and Molecule Overlay options are very useful for comparing structures quantitatively. There is also an interface to the semi-empirical code *MOPAC*, which can also be a useful tool for assessing structural reasonableness. The H-Bonds and Short Contacts options are useful in completing a structure solved using powder data, as often the 'interesting' H-atom positions have to be deduced. There is a relatively new Solid Form menu, which contains several tools for analysing crystal structures.

3.7.4. Inorganic Crystal Structure Database (ICSD)

The Inorganic Crystal Structure Database (ICSD; https://icsd.fiz-karlsruhe.de; Bergerhoff & Brown, 1987; Belsky *et al.*, 2002; Hellenbrandt, 2004) strives to contain an exhaustive collection of inorganic crystal structures published since 1913, including their atomic coordinates. It is a joint project between FIZ Karlsruhe and NIST. The database is accessed through the online WebICSD or the locally-installed program *FINDIT*. Typical interatomic distances in inorganic compounds derived from the ICSD have been collected in Chapter 9.4 of *International Tables for Crystallography* Volume C (Bergerhoff & Brandenburg, 1999). Applications of the ICSD have been discussed by Kaduk (2002), Behrens & Luksch (2006) and Allmann & Hinek (2007).

The ICSD began as an inorganic crystal structure database of published structures with atomic coordinates. The scope was gradually extended to include intermetallic compounds. Since 2003, FIZ Karlsruhe has started to fill in the gaps, and the aim is for the ICSD to include all published intermetallic compounds. Originally the ICSD did not contain structures with C—H or C—C bonds. After 2003, this rule was modified so that new entries should not contain both C—H and C—C bonds; compounds containing tetramethylammmonium and oxalate ions are now included.

The ICSD contains fully determined structures with atomic coordinates. Coordinates of light atoms (such as H atoms) or extra-framework species (such as in zeolites) may be missing. Structures described as isotypic to other structures, but without determination of the atomic coordinates, are included using the coordinates from the corresponding structure-type prototype. Such entries get a special remark/comment: 'Cell and Type only determined by the author(s). Coordinates estimated by the editor in analogy to isotypic compounds.' Currently there are more than

26 000 entries with derived coordinates. At present, the ICSD contains more than 187 000 entries, including 2033 crystal structures of elements, 34 785 records for binary compounds, 68 730 records for ternary compounds and 68 083 records for quaternary and quintenary compounds. About 149 000 entries have been assigned a structure type; there are currently 9093 structure prototypes.

Most of the structures contained in the ICSD are from published journal articles, although private communications are also accepted. The entries are tested for formal errors, plausibility and logical consistency. The data are stored as published; the authors' settings of space groups are considered to be valuable information which should not be changed. Only some 'exotic' space groups are transformed. In addition, for each entry in the ICSD the structure is standardized using the program *STRUCTURE TIDY* by Gelato & Parthé (1987). The published cell, standardized cell and reduced cell are all searchable. Since 2003, FIZ Kalrsruhe has been assigning structure-type classifications (Allmann & Hinek, 2007). In the future, this feature will enable easier searches for compounds that are closely related in structure.

3.7.4.1. *General features of the ICSD*

The chemical name is given in English following IUPAC rules, with the oxidation state in roman numerals. The formula upon which the name is based is calculated from all atoms with defined coordinates. Phase (polymorph) designations are given after a hyphen. Mineral names and group names are given for all entries that correspond to minerals. Details of the origin are given after a hyphen. The formula is coded as a structural formula, which provides the opportunity to search for typical structure units (such as SiO_4). Such searches can be useful, but can easily miss structurally similar compounds, and should be used with caution.

The title of the publication is given in English, French or German. There can be several citations, but an author list is only given for the first reference. I have encountered truncated author lists. Authors' surnames can vary when the original publication uses a non-roman alphabet. In some cases, the first and last names of Chinese authors may be interchanged.

The Hermann–Mauguin space-group symbol is given according to the conventions of *International Tables for Crystallography* Volume A. If different origin choices are available, those space groups with the origin at a centre of symmetry (origin choice 2) are characterized by an additional '*z*', while an additional '*s*' is used for special origins (origin choice 1). Thus, the space group for magnetite may be reported as *Fd*-3*mz* or *Fd*-3*ms*, depending on which origin the authors used. Since all contemporary Rietveld programs use origin choice 2, care must be taken when importing coordinates.

Along with the fractional coordinates, atom identifiers are reported. These are principally running numbers and may differ from those reported by the authors. The oxidation state is given with a sign. When importing coordinates into a Rietveld program these oxidation states can influence which scattering factors are used, and so should be examined by the user. Both site multiplicities and Wyckoff positions are generated for all atoms.

The ICSD archives displacement coefficients (both isotropic and aniostropic) according to what the authors reported. Isotropic displacement coefficients can be given as either *B* or *U* values and anisotropic coefficients can be given as β, *B* or *U* values (or, in rare cases, using other conventions). Displacement coefficients imported into a Rietveld program should always be checked, as it is common for the program to interpret *B* as *U* and *vice versa*. Such wrong displacement coefficients can make Rietveld refinements hard to perform. There are a number of standard remarks and standard test codes; these text fields can be useful for limiting the universe of the search (such as for neutron-diffraction structures).

3.7.4.2. *Features particularly useful for powder crystallography*

A field which is particularly useful for identifying structural analogues is the ANX formula. This formula is generated according to the following rules:

(i) H^+ is not taken into account, even if coordinates are available.

(ii) The coordinates of all sites of all other atoms must be determined.

(iii) Different atom types on the same positions (for example, in solid solutions) are treated as a single atom type.

(iv) An exception: if cations and anions occupy the same site they will not be treated as one atom type.

(v) All sites occupied by the same atom type are combined, unless the oxidation state is different. Thus, $Fe^{2+}(Fe^{3+})_2O_4$ yields AB2X4, while $(Fe^{2.667+})_3O_4$ yields A3X4.

(vi) For each atom type, the multiplicities are multiplied by the site-occupancy factors and the products are added. The sums are rounded and divided by the greatest common divisor.

(vii) If the rounded sum equals zero, all sums are multiplied by a common factor so that the smallest sum equals unity, so no element will be omitted.

(viii) Cations are assigned the symbols A–M, neutral atoms are assigned N–R and anions are assigned X, Y, Z and S–W.

(ix) The symbols are sorted alphabetically and the characters are assigned according to ascending indices: AB2X4, not A2BX4.

(x) All ANX symbols with more than four cation symbols, three neutral atom symbols or three anion symbols are deleted.

The utility of these symbols is illustrated by the fact that the three garnets $Mg_3Al_2(SiO_4)_3$, $Ca_3(Al_{1.34}Fe_{0.66})Si_3O_{12}$ and $(Mg_{2.7}Fe_{0.3})(Al_{1.7}Cr_{0.3})Si_3O_{12}$ all yield ANX = A2B3C3X12.

Reduced-cell searches [see *International Tables for Crystallography* Volume A, Section 3.1.3 (de Wolff, 2016)] are particularly easy to carry out in the 'Cell' section of Advanced Searches. Once a unit cell has been determined by indexing the powder pattern, it is always worth carrying out a reduced-cell search to identify potential isostructural compounds using lattice-matching techniques. It is often wise to first carry out such a search using relatively narrow tolerances (say, 1% on the lattice parameters) and then carry out additional searches using larger tolerances. Systematic searches of the subcells and supercells of a given unit cell, as could be carried out using the *NBS*LATTICE* program with the NIST Crystal Data Identification File (Mighell & Himes, 1986; Mighell, 2003), are not yet implemented.

Under the 'Crystal Chemistry' section it is possible to search for crystal structures that contain bonds between particular atom types in a distance range. Such searches are particularly valuable in assessing the chemical reasonableness of crystal structures, such as the study by Sidey (2013) on the shortest B^{III}—O bonds.

Because the ICDD Powder Diffraction File '01' entries contain the ICSD collection code in the comments, searching for the collection code of a hit in a search/match is particularly easy in the 'DB Information' section. In this way, the relevant ICSD

entry can be located without any ambiguity and the best structure for the problem at hand can be used to start the Rietveld refinement.

3.7.5. Pearson's Crystal Data (PCD/LPF) (with Pierre Villars and Karen Cenzual)

3.7.5.1. *General information*

The Pearson's Crystal Data database (PCD; Villars & Cenzual, 2013) is an outgrowth of the (Linus) Pauling File (LPF; Villars *et al.*, 1998; http://www.paulingfile.com), which was designed to combine crystal structures, phase diagrams and physical properties under the same computer framework to form a tool useful for materials design. PCD is the result of a collaboration between Material Phases Data Systems (Vitznau, Switzerland) and ASM International (Materials Park, Ohio, USA). The retrieval software was developed by Crystal Impact (Bonn, Germany). As suggested by the name, Pearson's Crystal Data is a follow-up product to *Pearson's Handbook: Crystallographic Data for Intermetallic Phases* (Villars & Calvert, 1985, 1991; Villars, 1997). However, in contrast to the latter, it also covers oxides and halides, which represent about 80% of the compounds with more than four chemical elements.

The 2016/2017 release of Pearson's Crystal Data contains more than 288 000 data sets for more than 165 300 different chemical formulae, representing over 53 000 distinct chemical systems. To achieve this, the editors have processed over 93 500 original publications; recent literature is surveyed in a cover-to-cover approach, including about 250 journal titles. Over 153 000 database entries contain refined atom coordinates, as well as isotropic and/or anisotropic displacement parameters when published, whereas more than 72 000 data sets contain atom coordinates corresponding to the structure prototype assigned by the authors of the original publication or by the database editors. Approximately 15 000 data sets contain only crystallographic data such as the lattice parameters and possibly a space group.

When available in the original publications, each data set contains comprehensive information on the sample-preparation and experimental procedure, as well as on the stability of the phase with respect to temperature, pressure and composition. The presence of plots (cell parameters or diffraction patterns) in the original paper is indicated, and over 30 000 descriptions of the variation of the cell parameters as a function of temperature, pressure or composition are proposed. Roughly 18 300 experimental diffraction patterns are reported.

The Linus Pauling File was designed as a phase-oriented, fully relational database system. This required the creation of a 'distinct phases' table, with internal links between the three parts of the database. In practice, this means that the senior editors have evaluated the distinct phases existing in the system for every chemical system using all information available in the LPF. Each structure entry in Pearson's Crystal Data has been linked to such a distinct phase, which allows a rapid overview of a particular chemical system.

3.7.5.2. *Evaluation procedure*

Extensive efforts have been made to ensure the quality and reliability of the crystallographic data. Pearson's Crystal Data is checked for consistency by professional crystallographers, assisted by an original software package, *ESDD* (*Evaluation, Standardization and Derived Data*), containing more than 60 different modules (Cenzual *et al.*, 2000). The checking is carried out progressively, level by level. The following checks are made.

Individual database fields:

(i) order of magnitude of numerical values;
(ii) Hermann–Mauguin symbols, Pearson symbols;
(iii) consistency of journal CODEN, year, volume, first page, last page;
(iv) formatting of chemical formulae;
(v) neutrality of oxides and halides;
(vi) spelling.

Consistency within individual data sets:

(i) atom coordinates, Wyckoff letters, site multiplicities;
(ii) chemical elements in different database fields;
(iii) computed, published values (cell volume, density, absorption coefficient, *d*-spacings);
(iv) Pearson symbol, space group, cell parameters;
(v) Bravais lattice, Miller indices;
(vi) site symmetry, anisotropic displacement parameters.

Particular crystal-structure checks:

(i) interatomic distances, sum of atomic radii;
(ii) geometry of functional groups;
(iii) search for overlooked symmetry elements;
(iv) composition from refinement, chemical formula.

Consistency within the database:

(i) comparison of cell-parameter ratios for isotypic entries;
(ii) comparison of atom coordinates for isotypic entries with refined coordinates;
(iii) comparison of densities;
(iv) thorough search for duplicates, also considering translated references.

Wherever possible, misprints have been corrected based on arguments explained in remarks; as a result, more than 13 000 crystallographic data sets are accompanied by at least one erratum. In other cases remarks drawing the attention to discrepancies or unexpected features have been added.

The *ESDD* software package also produces derived data such as the Niggli reduced cell, equivalent isotropic displacement parameters, density and formula weight.

3.7.5.3. *Standardized crystallographic data*

The crystallographic data in Pearson's Crystal Data are presented as published, respecting the original site labels, but are also standardized following the method proposed by Parthé and Gelato (Parthé & Gelato, 1984, 1985; Parthé *et al.*, 1993). This second presentation of the same data has been further adjusted so that compounds crystallizing with the same prototype structure (isotypic compounds) can be easily compared. It is prepared in a three-step procedure as follows.

(i) The crystallographic data are checked for the presence of overlooked symmetry elements. Whenever it is possible to describe the structure in a higher-symmetry space group, or with a smaller unit cell, without any approximations, this is performed.
(ii) In the next step, the crystallographic data are standardized using the program *STRUCTURE TIDY* (Gelato & Parthé, 1987).
(iii) The resulting data are compared with the standardized data of the type-defining data set and, if relevant, adjusted using an *ESDD* module based on the program *COMPARE* (Berndt, 1994).

For data sets with no published coordinates, the cell parameters are standardized following the criteria defined for the unit-cell

and space-group setting. For data sets with unknown space group, the cell parameters have been standardized assuming the space group of lowest symmetry in agreement with the Pearson symbol, *e.g. P*222 for *oP** or *o***.

Standardized data are described with respect to the standard settings described in *International Tables for Crystallography* Volume A, with the following additional restraints: inversion centre at the origin, unique *b* axis and 'best' cell for monoclinic structures (Parthé & Gelato, 1985), triple-hexagonal cell for rhombohedral structures or Niggli reduced cell for triclinic structures. As a consequence, they can easily be incorporated into any program handling crystallographic data. The systematic standardization of the crystallographic data also greatly simplifies the classification of crystal structures into different prototypes.

A conversion tool to standardize cell parameters and/or compute the Niggli reduced cell is included in the software of Pearson's Crystal Data.

3.7.5.4. *Consequent prototype assignment*

The prototype is a well known concept in inorganic chemistry, where a large number of compounds often crystallize with very similar atom arrangements. The compilation *Strukturbericht* started to catalogue crystal structures into types named by codes such as A1, B1 or A15. These notations are still in use; however, today prototypes are generally referred to by the name of the compound for which this particular kind of atom arrangement was first identified, *i.e.* Cu, NaCl and Cr_3Si for the types enumerated above. Pearson's Crystal Data uses a longer notation which also includes the Pearson symbol and the space-group number: Cu,cF4,225, NaCl,cF8,225 and Cr_3Si,cP8,223. In a few cases several prototypes correspond to the same code, for example several polytypes of CdI_2 have the same notation. A similar situation occurs for the wrong and the correct structure proposals for FeB, which have the same Pearson code and space group. In these cases a letter is added after the type-defining compound, for example the correct FeB type will be referred to as FeB-b,oP8,62.

Each prototype is defined on a particular PCD database entry. In principle, this data set represents a recent refinement of the structure of the type-defining compound, but no effort has been made to find or use the most recent determination.

All of the data sets with published coordinates in Pearson's Crystal Data have been classified into prototypes following the criteria defined in *TYPIX* (Parthé *et al.*, 1993, 1994). According to this definition, isotypic compounds must crystallize in the same space group and have similar cell-parameter ratios; the atoms should occupy the same Wyckoff positions in the standardized description and have similar positional coordinates. If all of these criteria are fulfilled, the atomic environments should be similar. Note that H^+ (protonic hydrogen) is ignored in the assignment of the prototype as well as in the Wyckoff sequence, Pearson symbol/code and atomic environments. Isopointal substitution variants are usually distinguished; however, no distinction is made between structures with fully and partly occupied atom sites. At present, 29 470 prototypes are represented.

When possible, a prototype has also been assigned to data sets without published atom coordinates. The prototype is often stated in the publication; in other cases the editors have assigned it. The editor will have added the exact space-group setting to which the cell parameters refer when this was not published. It is important to note that a prototype has been assigned at two different levels. The first is intimately related to the published data (entry level), whereas the second is assigned at the phase level and may, in some cases, be inconsistent with the crystallographic data listed below.

For partly investigated structures, the available structural information is given using a similar way, for example the complete Pearson symbol may be replaced by *t*** (tetragonal) or *cI** (cubic body-centred) and the place of the type-defining compound is occupied by an asterisk.

3.7.5.5. *Assigned atom coordinates*

In order to give an approximate idea of the actual structure, a complete set of positional coordinates and site occupancies is proposed for data sets where a prototype could be assigned but the atom coordinates were not determined. The coordinates of the type-defining entry are proposed as a first approximation. The atom distribution is inserted by an *ESDD* module that compares the chemical formula of the type-defining entry with the chemical formula of the isotypic compound where the chemical elements have been reordered by the editor so that the first element is expected to occupy the same atom sites as the first element in the type-defining formula, and so on. Depending on the character of the prototype, substitutions and/or vacancies are either distributed over all atom sites occupied by the corresponding element or are expected to occur selectively on particular atom sites.

For this category of database entries, structure drawings, diffraction patterns and interatomic distances have also been computed. The structural portion of the database is thus more extensive than the primary literature.

3.7.5.6. *External links*

When relevant, the database entries contain links to external data sources, including ASM International Alloys Phase Diagrams Centre Online, SpringerMaterials (The Landolt–Börnstein Database incorporating Inorganic Solid Phases PAULING FILE Multinaries Edition – 2010 in SpringerMaterials) and the original publication (through https://www.crossref.org/). A (static) reference to the Powder Diffraction File entry number is provided for database entries that are included in the PDF4+ product.

3.7.5.7. *Retrievable database fields*

In addition to bibliographic (*e.g.* a particular institute) and chemical (*e.g.* sulfates) searches, many characteristics of the experiment and data processing (*e.g.* single crystal, neutron diffraction, range of temperature or reliability factors) or additional studies (*e.g.* pressure-dependence studies, magnetic structure) can be used as search criteria. Published crystal data, standardized crystal data and the Niggli reduced cells can be searched, as well as crystallographic classifications such as crystal class, Pearson symbol, Pearson code, Wyckoff sequence, structure prototype or structure class. Such searches can be very valuable in identifying a structural model for a new composition and saving the work of an *ab initio* structure determination.

The Quick Search pane includes commonly used searches on chemical elements (including cations in a particular oxidation state for oxides and halides), the number of elements and functional groups. The chemical selection (and/or/not) can be combined with selection on structure prototypes, space-group numbers and symbols or the crystal system. Retrieval on cell parameters (with ranges) and bibliographic information is also

possible and the desired level of structural studies (*e.g.* complete) may be specified.

Many more searches can be carried out in the complete Search Dialog. Particularly useful are searches on atomic environments and interatomic distances. The atomic environment is defined by the coordination number, the geometry of the coordination polyhedron and the identities of the central and peripheral atoms. Searches on the number of different atomic environment types in the same structure can also be carried out. Specifying a pair of elements makes it possible to select a range of interatomic distances to be included in the search. These histograms are also useful in assessing the reasonableness of a particular distance in a Rietveld refinement.

3.7.5.8. *Particular software features*

All searches use the 'Perpetual Restraining' feature, which updates the selection set in real time as a new query is introduced, so that the progress of the search scheme can easily be monitored. The complete Search Dialog offers a large variety of features that make the retrieval and presentation of information extremely flexible.

The Chemical System Matrix View makes it easy to locate phases in binary, ternary, quaternary and pseudo-quaternary systems. The Phases List View collects a selection set into its 'distinct' phases. From the individual database entry it is particularly easy to find all database entries with the same prototype structure and plot the unit-cell volume as a function of selected atomic radii. The standard display of an entry includes a short summary about the phase, structural, bibliographic, experimental and editorial data, as well as a structure drawing, a powder pattern and a table of interatomic distances.

The software for producing structure drawings offers the visualization of atomic environments (coordination polyhedra), the statistics of interatomic distances and the calculation of selected distances and angles. Four different models are available (ball and stick, wires, sticks and space-filling), with on-the-fly rotation controlled by the mouse. The nearest-neighbour histogram of a selected atom is compared with a statistical plot containing all distances in the database involving the same chemical elements, and the atomic environments can be instantaneously modified by clicking on the nearest-neighbour histogram.

Powder-diffraction patterns can be computed for any user-defined wavelength and the visualization includes a tool for zoom-in/out tracking. Patterns based on published lists of interplanar spacings can also be visualized. It is further possible to export database entries as CIF files, tables (*e.g.* powder-diffraction pattern, distances and angles) or graphics (*e.g.* structure drawings; BMP, GIF, JPG, PNG, TIFF or Diamond documents), and individually tailored dossiers can be designed and printed.

3.7.6. Metals data file (CRYSTMET)

CRYSTMET (White *et al.*, 2002) began as a database of critically evaluated crystallographic data for metals, including alloys, intermetallics and minerals, and has grown to include inorganic compounds in general. It was started in 1960 by Cromer and Larson at Los Alamos National Laboratory, and its development was continued by the National Research Council of Canada. In 1996, the production and dissemination was transferred to Toth Information Systems.

CRYSTMET contains chemical, crystallographic and bibliographic data, together with comments regarding experimental details for each study. Using these data, a number of associated data files are generated, with the major one being a file of calculated powder patterns. Entry into CRYSTMET is *via* a number of search screens, including chemistry, bibliographic information, unit cell and reduced cell, powder patterns (using the positions of the strongest peaks as input), formula, structure type, Pearson symbol and space group. The results of queries reside in sets, which can be further manipulated using logical operations.

The results are displayed as a series of screens, which include crystallographic data, distances and angles, and the powder pattern. There is some ability to customize the calculation of the powder pattern of an entry; the calculation is performed for Debye–Scherrer geometry. Included on the Results tabs is a direct interface to the *MISSYM* program (Le Page, 1987, 1988), which searches the reported structure for additional symmetry elements. This is a very useful tool for detecting missed symmetry.

3.7.7. Protein Data Bank (PDB)

The Protein Data Bank is described in Chapter 24.1 of *International Tables for Crystallography* Volume F (Berman *et al.*, 2011). Current information is available on the web at https://www.wwpdb.org/.

3.7.7.1. *Powder diffraction by proteins*

Although powder-diffraction techniques had been applied to proteins as long ago as 1936 (Wyckoff & Corey, 1936; Corey & Wyckoff, 1936), and proof-of-principle experiments had been carried out (Rotella *et al.*, 1998, 2000), real progress in protein powder crystallography began with the work of Von Dreele (Von Dreele, 1998, 1999, 2003; Von Dreele *et al.*, 2000).

Progress in powder crystallography on macromolecules has been reviewed by Margiolaki & Wright (2008) and is also discussed in Chapter 7.1 of this volume. Notable studies include the characterization of the binding of *N*-acetylglucosamine oligosaccharides to hen egg-white lysozyme (Von Dreele, 2007*a*) and determination of the second SH3 domain of ponsin (Margiolaki *et al.*, 2007).

As with all powder diffraction, peak overlap ultimately limits the information available. Multi-pattern strategies to overcome the overlap problem have been investigated by Von Dreele (2007*b*). Multiple-pattern resonant-diffraction experiments have enabled study of the binding of $PtBr_6^{2-}$ ions to lysozyme (Helliwell *et al.*, 2010). A bootstrap approach has been used to determine the structure of bacteriorhodopsin to 7 Å resolution (Dilanian *et al.*, 2011). Parametric resonant-scattering experiments have been used to determine the secondary structures of lysozyme derivatives (Basso *et al.*, 2010). Powder-diffraction experiments have also been used to gain insight into the general features of a nonstructural protein 3 (nsp3) macro domain (Papageorgiou *et al.*, 2010).

The structure of a five-residue peptide has been determined *ab initio* using laboratory powder data (Fujii *et al.*, 2011). We can expect further useful results at this interface between small-molecule and protein powder crystallography.

As is typical in other areas of science, powder diffraction has proven to be useful in more practical features of protein processing. It has been used to identify insulin (Norrman *et al.*, 2006) and GB1 (Frericks Schmidt *et al.*, 2007) polymorphs and

lot-to-lot variations in lyophilized protein formulations (Hirakura *et al.*, 2007), and has been explored for use in structure-based generic assays (Allaire *et al.*, 2009).

3.7.7.2. *Calculation of protein powder patterns (with Kenny Ståhl)*

The Powder Diffraction File contains a few experimental powder patterns of proteins. These include silk fibroin protein (00-054-1394), tubulin (00-036-1547 and 00-036-1548), insulin (00-060-1360 through 00-060-1368), tomato bushy stunt virus (00-003-0001) and tobacco mosaic virus (00-003-0003 and 00-003-0004). Patterns have not yet been calculated from the structures in the Protein Data Bank because the calculated intensities generally fit poorly to those in experimental patterns.

Protein structures in the PDB do not generally contain H-atom positions, and the contributions from the disordered solvent in the solvent channels (which is the major source of the discrepancy) is not described (Hartmann *et al.*, 2010). The conventional Lorentz factor tends to infinity when approaching $2\theta = 0^\circ$. Differences in data-collection temperatures and solvent content between powder and single-crystal specimens often mean that the lattice parameters differ. The relatively poor scattering from the protein and the large scattering from the mother liquor and sample holder result in significant background contributions to experimental powder patterns.

Optimization of the lattice parameters is generally straightforward and is important because most protein crystal structures are determined at low temperatures, while powder data are collected under ambient conditions. Protein crystals contain 30–80% disordered solvent. The solvent contribution to the diffraction pattern is most important for the low-angle powder data. In conventional protein crystallography several correction models have been developed (Moews & Kretsinger, 1975; Phillips, 1980; Jiang & Brünger, 1994), but the flat bulk-solvent model is the simplest one which yields a realistic correction (Jiang & Brünger, 1994; Hartmann *et al.*, 2010). This model includes two parameters: $k_{\rm sol}$, which defines the level of electron density in the solvent region, and $B_{\rm sol}$, which defines the steepness of the border between the solvent and macromolecular regions. These parameters are typically refined in contemporary software and cluster around $k_{\rm sol} = 0.35$ e Å^{-3} and $B_{\rm sol} = 46$ Å^2 (Fokine & Urzhumtsev, 2002).

The flat bulk-solvent correction can be applied using *phenix.pdbtools* (Adams *et al.*, 2010), which requires a PDB coordinate file and values of $k_{\rm sol}$ and $B_{\rm sol}$ as input. Average values can be used, but refined values or values from the Electron Density Server (EDS; Kleywegt *et al.*, 2004) can improve the results. The bulk-solvent correction is highly anisotropic, and both parameters affect the anisotropy.

The ideal H-atom positions can be calculated using *phenix.pdbtools*. The solvent and hydrogen contributions to the pattern can be significant (Fig. 3.7.13).

The Lorentz factor L describes the fraction of a reflection that is in the diffracting condition. For Bragg–Brentano and Debye–Scherrer geometries it is given by

$$L = \frac{1}{\sin 2\theta}\frac{1}{\sin\theta}. \tag{3.7.3}$$

This equation assumes ideal crystals, resulting in infinitesimally small reciprocal-lattice points. The true size of the lattice points depends on the crystallite size and imperfections (strain). This smearing needs to be included in the Lorentz factor at low angles. A revised Lorentz factor for protein powder diffraction has been derived (Hartmann *et al.*, 2010),

$$L_{\rm rev} = \frac{1}{\sin 2\theta}\frac{1}{\sin\theta}\frac{\sin^2\theta}{(\sin^2\theta + \lambda^2\eta^2/12)}, \tag{3.7.4}$$

in which η reflects the distribution of scattering-vector amplitudes. For Guinier geometry these equations become more complex (Hartmann *et al.*, 2010). Fig. 3.7.14 shows that the Lorentz factor has a smaller effect than the solvent and H atoms, but that it is still significant. By applying these corrections it should be possible for the ICDD editorial staff to calculate useful powder patterns from PDB entries that could be included in the Powder Diffraction File.

Separating the background from the diffraction pattern is not straightforward (Frankaer *et al.*, 2011). Estimation of the background is greatly assisted by a correct calculated pattern. The calculated pattern can be scaled to the experimental data using *PROTPOW* (http://www.kemi.dtu.dk/english/Research/PhysicalChemistry/Protein_og_roentgenkrystallografi/Protpow).

Ståhl *et al.* (2013) have demonstrated that existing search/match procedures can be used to identify proteins using their powder patterns, and that powder patterns calculated from Protein Data Bank coordinates with proper care can be added to a database and included in the search/match procedure. Several problems can be foreseen when including large amounts of protein data into the Powder Diffraction File. It may be worthwhile including powder patterns with several levels of solvent correction, rather than just an average value. Asymmetry from instrumental effects and specimen transparency, which can affect the peak positions, needs to be taken into account. The use of an average thermal expansion coefficient may be sufficient to account for the differences in lattice parameters between low-temperature single-crystal structures and powder patterns measured under ambient conditions.

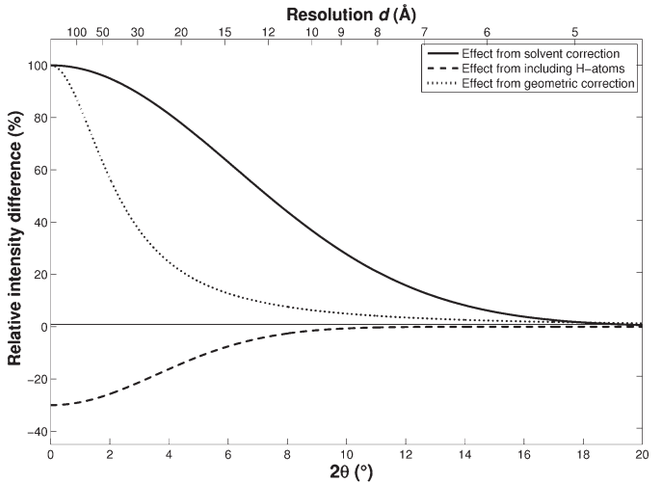

Figure 3.7.13
Overview of the trends from the different corrections. The effects are shown as the relative intensity difference $(I_{\rm non\text{-}corr} - I_{\rm corr})/I_{\rm non\text{-}corr}$ plotted as functions of the scattering angle 2θ (using Cu $K\alpha_1$) and resolution $d = \lambda/(2\sin\theta)$. The curves are based on average corrections of lysozyme and insulin data. $I_{\rm non\text{-}corr}$ is the raw intensity from a calculated pattern which has only been Lorentz corrected. The geometric correction curve was calculated using $\eta = 0.045$ Å^{-1}. From Hartmann *et al.* (2010).

3.7.8. Crystallography Open Database (COD) (with Saulius Gražulis)

The Crystallography Open Database (COD) project (http://www.crystallography.net/cod/; Gražulis *et al.*, 2009, 2012) aims at collecting in a single open-access database all organic, inorganic and organometallic structures, except for the structures of biological macromolecules, which are available in the Protein Data Bank (Berman *et al.*, 2003, 2011). The database was founded by Armel Le Bail, Lachlan Cranswick, Michael Berndt, Luca Lutterotti and Robert M. Downs in February 2003 as a response to Michael Berndt's letter published on the Structure Determination by Powder Diffractometry (SDPD) mailing list (Berndt, 2003). Since December 2007, the main database server has been maintained and new software has been developed by Saulius Gražulis and Andrius Merkys at the Institute of Biotechnology of Vilnius University (VU). Currently, the database includes more than 376 000 entries describing structures of small molecules and small-to-medium-sized unit-cell materials as published in IUCr journals and other major crystallographic and peer-reviewed journals, as well as contributions by crystallographers from major laboratories. Most of the mineral data are obtained from the American Mineralogist Structure Database (Rajan *et al.*, 2006) and are donated by its maintainer and COD co-founder Robert M. Downs.

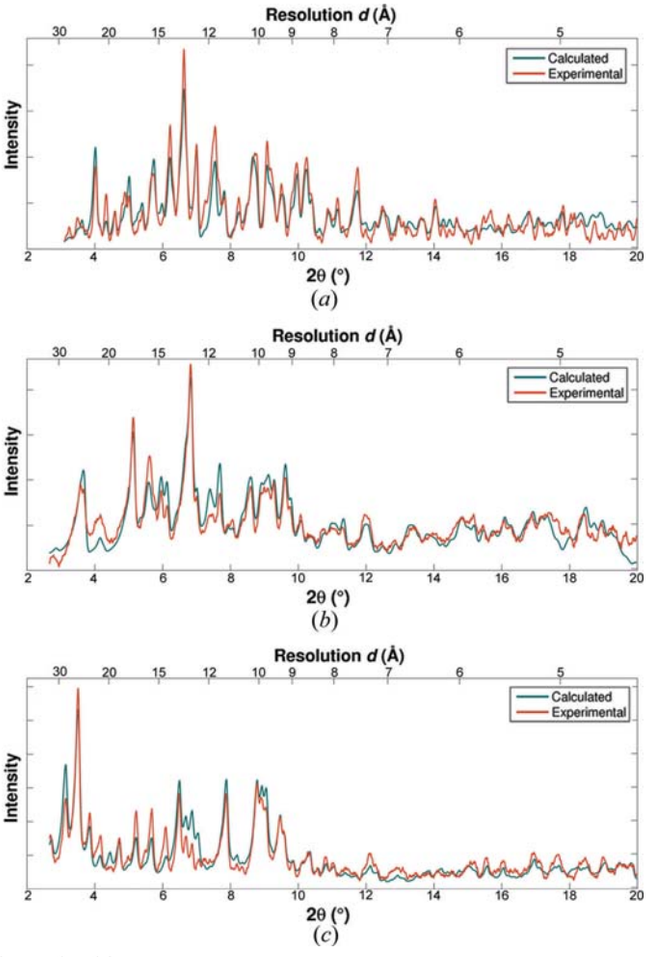

Figure 3.7.14
Calculated and experimental powder patterns for (*a*) lysozyme, (*b*) trigonal insulin and (*c*) cubic insulin. The calculated patterns (blue) are corrected for bulk-solvent and geometrical effects using the revised Lorentz factor. From Hartmann *et al.* (2010).

The database is an internet resource (Fig. 3.7.15) with data-search and download capabilities designed by Armel Le Bail and Michael Berndt. In addition, registered users may deposit new data, whether from previous publications or as personal communications, using the deposition web site designed at VU by

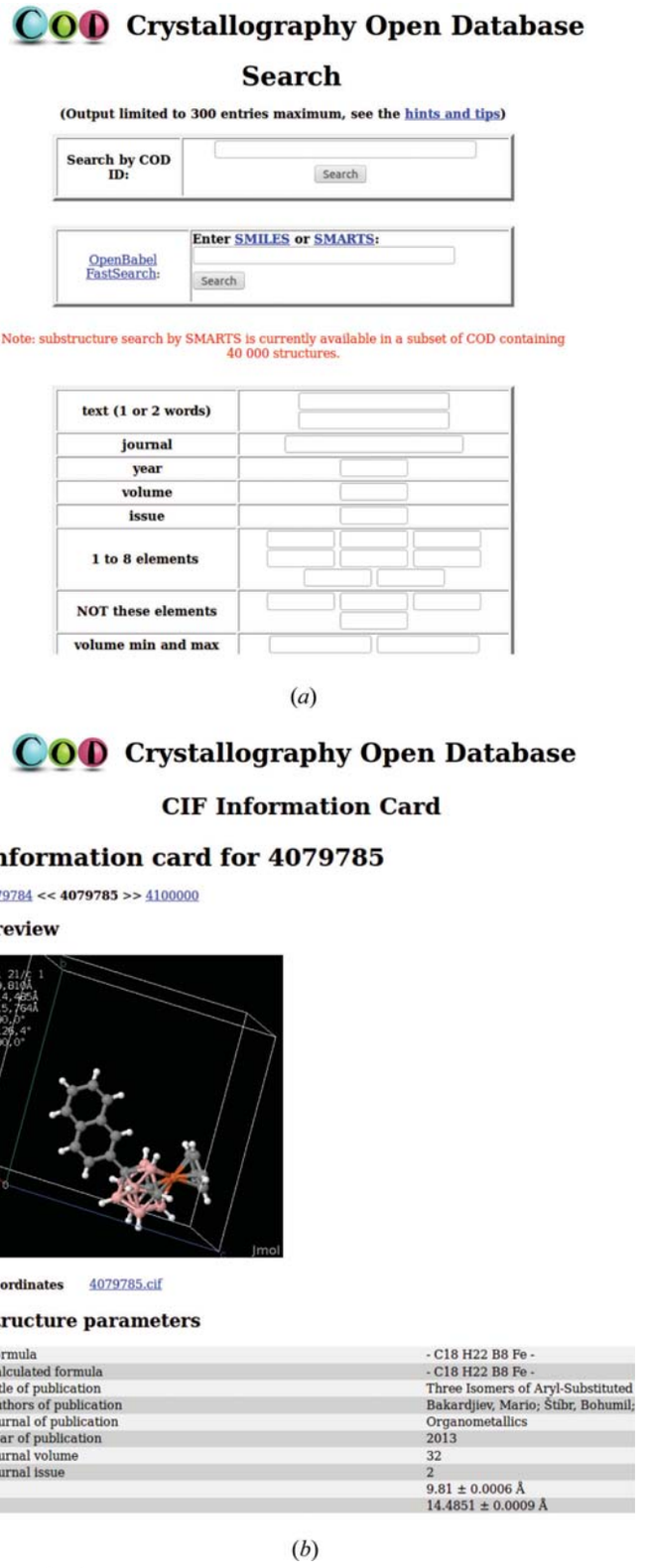

Figure 3.7.15
(*a*) The website and search interface of the Crystallography Open Database (COD) permits searches of crystallographic data by a range of parameters and unrestricted retrieval of the found data. (*b*) Data can be viewed online in the interactive *Jmol* applet (Hanson, 2010, 2013) or downloaded for further processing either one record at a time or in bulk.

Saulius Gražulis, Justas Butkus and Andrius Merkys. The deposition software performs rigorous checks of syntax and semantics.

The COD website allows searching on COD numerical identifier, unit-cell parameters, chemical composition and bibliographic data. Substructure searches using SMILES and SMARTS strings have been implemented. The free software package *OpenBabel* (O'Boyle *et al.*, 2011; Hutchison, 2007) is used for both the CIF-to-SMILES transformation and the actual search.

The retrieved records can be viewed online or downloaded for further processing. For massive data mining, COD permits downloads and updates of the whole database using Subversion, Rsync or http protocols. The ease of access to the COD data and its open nature has spurred the use of this resource for software testing (Grosse-Kunstleve & Gildea, 2011), teaching (Moeck, 2004) and research (First & Floudas, 2013). Multiple mirrors around the globe (Quirós-Olozábal, 2006; Gražulis, 2007; Moeck, 2007*a*; Chateigner, 2010) ensure data preservation, provide off-site backups, offer improved search interfaces (Moeck, 2007*b*) and increase reliability.

For the powder-diffraction community, the COD is interesting not only as an archive of structures solved by powder-diffraction methods, but also as a possibility for use in search/match procedures to identify crystalline compounds. Recently, the development of an open full-pattern search/match internet tool was launched by the COD developers. It allows phase quantifications from X-ray, neutron and electron powder patterns (with high- or medium-resolution instruments) provided that the structures are already in the COD. This tool is particularly suited to nanocrystalline powders, in which severe line broadening appears, precluding phase identification from only peak positions (Lutterotti *et al.*, 2012). COD-derived databases are also offered for software produced by several diffractometer vendors (Rigaku, 2011; PANalytical, 2012*a*,*b*; Bruker, 2013). In addition to the COD, searches and matches can be performed against its sister database, the PCOD, which contains structures predicted by the *GRINSP* program (Le Bail, 2005) and hypothetical zeolites (Pophale *et al.*, 2013). The power of such an approach is demonstrated by PCOD entry 3102887 (formulated as SiO_2). It was recently identified as corresponding structurally to a new phosphorus(V) oxonitride polymorph δ-PON (Baumann *et al.*, 2012).

3.7.9. Other internet databases

Other useful databases include the following:

(i) The American Mineralogist Crystal Structure Database (http://rruff.geo.arizona.edu/AMSamcsd.php).
(ii) The Mineralogy Database (http://webmineral.com).
(iii) MinCryst (http://database.iem.ac.ru/mincryst/index.php).
(iv) The International Zeolite Association Database of Zeolite Structures (http://www.iza-structure.org/databases).
(v) The Incommensurate Structures Database (http://webbdcrista1.ehu.es/incstrdb/).
(vi) The Nucleic Acid Database (http://ndbserver.rutgers.edu).

I thank Timothy G. Fawcett and Cyrus Crowder of the International Centre for Diffraction Data, Colin Groom of CCDC, Stephan Ruehl of FIZ Karlsruhe, Pierre Villars and Karen Cenzual of Material Phases Data Systems, and Saulius Gražulis of Vilnius University Institute of Biotechnology for their valuable comments and additions.

References

Adams, P. D., Afonine, P. V., Bunkóczi, G., Chen, V. B., Davis, I. W., Echols, N., Headd, J. J., Hung, L.-W., Kapral, G. J., Grosse-Kunstleve, R. W., McCoy, A. J., Moriarty, N. W., Oeffner, R., Read, R. J., Richardson, D. C., Richardson, J. S., Terwilliger, T. C. & Zwart, P. H. (2010). *PHENIX: a comprehensive Python-based system for macromolecular structure solution. Acta Cryst.* D**66**, 213–221.

Allaire, M., Moiseeva, N., Botez, C. E., Engel, M. A. & Stephens, P. W. (2009). *On the possibility of using polycrystalline material in the development of structure-based generic assays. Acta Cryst.* D**65**, 379–382.

Allen, F. H., Cole, J. C. & Verdonk, M. L. (2011). *The relevance of the Cambridge Structural Database in protein crystallography. International Tables for Crystallography*, Vol. F, 2nd ed., edited by E. Arnold, D. M. Himmel & M. G. Rossmann, pp. 736–748. Chichester: Wiley.

Allmann, R. & Hinek, R. (2007). *The introduction of structure types into the Inorganic Crystal Structure Database ICSD. Acta Cryst.* A**63**, 412–417.

Barr, G., Dong, W. & Gilmore, C. J. (2009). *PolySNAP3: a computer program for analysing and visualizing high-throughput data from diffraction and spectroscopic sources. J. Appl. Cryst.* **42**, 965–974.

Barr, G., Gilmore, C. J. & Paisley, J. (2004). *SNAP-1D: a computer program for qualitative and quantitative powder diffraction pattern analysis using the full pattern profile. J. Appl. Cryst.* **37**, 665–668.

Basso, S., Besnard, C., Wright, J. P., Margiolaki, I., Fitch, A., Pattison, P. & Schiltz, M. (2010). *Features of the secondary structure of a protein molecule from powder diffraction data. Acta Cryst.* D**66**, 756–761.

Baumann, D., Sedlmaier, S. J. & Schnick, W. (2012). *An unprecedented AB_2 tetrahedra network structure type in a high-pressure phase of phosphorus oxonitride (PON). Angew. Chem. Int. Ed.* **51**, 4707–4709.

Behrens, H. & Luksch, P. (2006). *A bibliometric study in crystallography. Acta Cryst.* B**62**, 993–1001.

Belsky, A., Hellenbrandt, M., Karen, V. L. & Luksch, P. (2002). *New developments in the Inorganic Crystal Structure Database (ICSD): accessibility in support of materials research and design. Acta Cryst.* B**58**, 364–369.

Bergerhoff, G. & Brandenburg, K. (1999). *Typical interatomic distances: inorganic compounds. International Tables for Crystallography*, Vol. C, edited by E. Prince, pp. 770–781. Dordrecht: Kluwer Academic Publishers.

Bergerhoff, G. & Brown, I. D. (1987). *Crystallographic Databases*, edited by F. H. Allen, G. Bergerhoff & R. Sievers. Chester: International Union of Crystallography.

Berman, H. M., Henrick, K., Kleywegt, G., Nakamura, H. & Markley, J. (2011). *The Worldwide Protein Data Bank. International Tables for Crystallography*, Vol. F, 2nd ed., edited by E. Arnold, D. M. Himmel & M. G. Rossmann, pp. 827–832. Chichester: Wiley.

Berman, H., Henrick, K. & Nakamura, H. (2003). *Announcing the Worldwide Protein Data Bank. Nature Struct. Mol. Biol.* **10**, 980.

Berndt, M. (1994). Thesis, University of Bonn, Germany. Updates by O. Shcherban, SCC Structure-Properties Ltd, Lviv, Ukraine.

Berndt, M. (2003). *Open crystallographic database – a role for whom?* http://www.cristal.org/SDPD-list/2003/msg00025.html.

Bigelow, W. C. & Smith, J. V. (1964). *Two new indexes to the Powder Diffraction File. ASTM Spec. Tech. Publ.* STP372, 54. https://doi.org/10.1520/STP48334S.

Boldyrev, A. K., Mikheev, V. I., Dubinina, V. N. & Dovalev, G. A. (1938). *X-ray determination tables for minerals, Ft. I. Ann. Inst. Mines Leningrad*, **11**, 1–157.

Boles, M. O., Girven, R. J. & Gane, P. A. C. (1978). *The structure of amoxycillin trihydrate and a comparison with the structures of ampicillin. Acta Cryst.* B**34**, 461–466.

Bravais, A. (1866). *Etudes Cristallographiques*. Paris: Gathier Villars.

Bruker-AXS (2013). Crystallography Open Database for DIFFRAC.EVA. https://www.bruker.com/products/x-ray-diffraction-and-elemental-analysis/x-ray-diffraction/xrd-software/eva/cod.html.

Bruno, I. J., Cole, J. C., Edgington, P. R., Kessler, M., Macrae, C. F., McCabe, P., Pearson, J. & Taylor, R. (2002). *New software for searching the Cambridge Structural Database and visualizing crystal structures. Acta Cryst.* B**58**, 389–397.

Bruno, I. J., Cole, J. C., Kessler, M., Luo, J., Motherwell, W. D. S., Purkis, L. H., Smith, B. R., Taylor, R., Cooper, R. I., Harris, S. E. & Orpen, A. G. (2004). *J. Chem. Inf. Comput. Sci.* **44**, 2133–2144.

Caussin, P., Nusinovici, J. & Beard, D. W. (1988). *Using digitized X-ray powder diffraction scans as input for a new PC-At search/match program. Adv. X-ray Anal.* **31**, 423–430.

Caussin, P., Nusinovici, J. & Beard, D. W. (1989). *Specific data handling techniques and new enhancements in a search-match program. Adv. X-ray Anal.* **32**, 531–538.

Cenzual, K., Berndt, M., Brandenburg, K., Luong, V., Flack, E. & Villars, P. (2000). *ESDD* software package. Updates by O. Shcherban, SCC Structure-Properties Ltd, Lviv, Ukraine.

Chateigner, D. (2010). *Crystallography Open Database Mirror at ENSICAEN*. http://cod.ensicaen.fr.

Cherukuri, S. C., Snyder, R. L. & Beard, D. W. (1983). *Comparison of the Hanawalt and Johnson–Vand computer search/match strategies. Adv. X-ray Anal.* **26**, 99–104.

Chipera, S. J. & Bish, D. L. (2002). *FULLPAT: a full-pattern quantitative analysis program for X-ray powder diffraction using measured and calculated patterns. J. Appl. Cryst.* **35**, 744–749.

Corey, R. B. & Wyckoff, R. W. G. (1936). *Long spacings in macromolecular solids. J. Biol. Chem*. **114**, 407–414.

Crystal Impact (2012). *Match!* v.2. Crystal Impact, Bonn, Germany.

Davey, W. P. (1922). *A new X-ray diffraction apparatus. Gen. Elec. Rev.* **25**, 565.

Davey, W. P. (1934). *Study of Crystal Structure and Its Applications*. New York: McGraw-Hill.

Debye, P. & Scherrer, P. (1916). *Interference on inordinate orientated particles in Roentgen light. Phys. Z.* **17**, 277–283.

Debye, P. & Scherrer, P. (1917). *Interference on inordinate orientated particles in X-ray light. III. Phys. Z.* **18**, 291–301.

Degen, T., Sadki, M., Bron, E., König, U. & Nénert, G. (2014). *The HighScore suite. Powder Diffr.* **29**, S13–S18.

Dilanian, R. A., Darmanin, C., Varghese, J. N., Wilkins, S. W., Oka, T., Yagi, N., Quiney, H. M. & Nugent, K. A. (2011). *A new approach for structure analysis of two-dimensional membrane protein crystals using X-ray powder diffraction data. Protein Sci.* **20**, 457–464.

Donnay, J. D. H. & Harker, D. (1937). *A new law of crystal morphology extending the law of Bravais. Am. Mineral.* **22**, 463–467.

Fawcett, T. G., Kabekkodu, S. N., Blanton, J. R. & Blanton, T. N. (2017). *Chemical analysis by diffraction: the Powder Diffraction File. Powder Diffr.* **32**, 63–71.

First, E. L. & Floudas, C. A. (2013). *MOFomics: computational pore characterization of metal–organic frameworks. Microporous Mesoporous Mater.* **165**, 32–39.

Fokine, A. & Urzhumtsev, A. (2002). *Flat bulk-solvent model: obtaining optimal parameters. Acta Cryst.* D**58**, 1387–1392.

Frankaer, C. G., Harris, P. & Ståhl, K. (2011). *A sample holder for in-house X-ray powder diffraction studies of protein powders. J. Appl. Cryst.* **44**, 1288–1290.

Frericks Schmidt, H. L., Sperling, L. J., Gao, Y. G., Wylie, B. J., Boettcher, J. M., Wilson, S. R. & Rienstra, C. M. (2007). *Crystal polymorphism of protein GB1 examined by solid-state NMR spectroscopy and X-ray diffraction. J. Phys. Chem. B*, **111**, 14362–14369.

Frevel, L. K. (1965). *Computational aids for identifying crystalline phases by powder diffraction. Anal. Chem.* **37**, 471–482.

Frevel, L. K., Adams, C. E. & Ruhberg, L. R. (1976). *A fast search-match program for powder diffraction analysis. J. Appl. Cryst.* **9**, 199–204.

Friedel, G. (1907). *Etudes sur la loi de Bravais. Bull. Soc. Fr. Miner.* **30**, 326–455.

Fujii, K., Young, M. T. & Harris, K. D. M. (2011). *Exploiting powder X-ray diffraction for direct structure determination in structural biology: the P2X4 receptor trafficking motif YEQGL. J. Struct. Biol.* **174**, 461–467.

Gelato, L. M. & Parthé, E. (1987). *STRUCTURE TIDY – a computer program to standardize crystal structure data. J. Appl. Cryst.* **20**, 139–143.

Gilmore, C. J., Barr, G. & Paisley, J. (2004). *High-throughput powder diffraction. I. A new approach to qualitative and quantitative powder diffraction pattern analysis using full pattern profiles. J. Appl. Cryst.* **37**, 231–242.

Goehner, R. P. & Garbauskas, M. F. (1984). *PDIDENT – a set of programs for powder diffraction phase identification. X-ray Spectrom.* **13**, 172–179.

Gražulis, S. (2007). *COD Mirror in Vilnius*. http://cod.ibt.lt/cod/.

Gražulis, S., Chateigner, D., Downs, R. T., Yokochi, A. F. T., Quirós, M., Lutterotti, L., Manakova, E., Butkus, J., Moeck, P. & Le Bail, A. (2009). *Crystallography Open Database – an open-access collection of crystal structures. J. Appl. Cryst.* **42**, 726–729.

Gražulis, S., Daškevič, A., Merkys, A., Chateigner, D., Lutterotti, L., Quirós, M., Serebryanaya, N. R., Moeck, P., Downs, R. T. & Le Bail, A. (2012). *Crystallography Open Database (COD): an open-access collection of crystal structures and platform for world-wide collaboration. Nucleic Acids Res.* **40**, D420–D427.

Groom, C. R., Bruno, I. J., Lightfoot, M. P. & Ward, S. C. (2016). *The Cambridge Structural Database. Acta Cryst.* B**72**, 171–179.

Grosse-Kunstleve, R. & Gildea, R. (2011). *Computational Crystallography Initiative: COD stats.* http://cci.lbl.gov/cod_stats.

Hanawalt, J. D. (1983). *History of the Powder Diffraction File (PDF). Crystallography in North America*, edited by D. McLachlan & J. P. Glusker, pp. 215–219. Buffalo: American Crystallographic Association.

Hanawalt, J. D. (1986). *Manual search/match methods for powder diffraction in 1986. Powder Diffr.* **1**, 7–13.

Hanawalt, J. D. & Rinn, H. W. (1936). *Identification of crystalline materials. Ind. Eng. Chem. Anal. Ed.* **8**, 244–247.

Hanawalt, J. D., Rinn, H. W. & Frevel, L. K. (1938). *Chemical analysis by X-ray diffraction. Ind. Eng. Chem. Anal. Ed.* **10**, 457–512.

Hanson, R. M. (2010). *Jmol – a paradigm shift in crystallographic visualization. J. Appl. Cryst.* **43**, 1250–1260.

Hanson, R. M. (2013). *Jmol: an open-source Java viewer for chemical structures in 3D*. http://www.jmol.org.

Harju, P. & Pasek, P. (1983). *Vanadium–hydrogen–phosphorus–oxygen catalytic material.* US Patent 4374756; PDF entry 00-047-0967.

Hartmann, C. G., Nielsen, O. F., Ståhl, K. & Harris, P. (2010). *In-house characterization of protein powder. J. Appl. Cryst.* **43**, 876–882.

Hellenbrandt, M. (2004). *The Inorganic Crystal Structure Database (ICSD) – present and future. Crystallogr. Rev.* **10**, 17–22.

Helliwell, J. R., Bell, A. M. T., Pryant, P., Fisher, S. J., Habash, G., Helliwell, M., Margiolaki, I., Kaenket, S., Watier, Y., Wright, J. P. & Yalamanchilli, S. (2010). *Time-dependent analysis of K_2PtBr_6 binding to lysozyme studied by protein powder and single crystal X-ray analysis. Z. Kristallogr.* **225**, 570–575.

Hirakura, Y., Yamaguchi, H., Mizuno, M., Miyanishi, H., Ueda, S. & Kitamura, S. (2007). *Detection of lot-to-lot variations in the amorphous microstructure of lyophilized protein formulations. Int. J. Pharm.* **340**, 34–41.

Huang, T. C. & Parrish, W. (1982). *A new computer algorithm for qualitative X-ray powder diffraction analysis. Adv. X-ray Anal.* **25**, 213–219.

Hull, A. W. (1919). *A new method of chemical analysis. J. Am. Chem. Soc.* **41**, 1168–1175.

Hull, A. W. (1983). *An account of early studies at Schenectady. Crystallography in North America*, edited by D. McLachlan & J. P. Glusker, p. 32. Buffalo: American Crystallographic Association.

Hutchison, G. R. (2007). *OpenBabel: The Open Source Chemistry Toolbox*. http://openbabel.org.

ICDD (2016). *PDF-4+ 2016 (Database)*. Newtown Square: International Centre for Diffraction Data. http://www.icdd.com.

Jenkins, R. & Rose, R. N. (1990). *Don Hanawalt – early days and his contribution to qualitative powder diffractometry. Powder Diffr.* **5**, 70–75.

Jiang, J.-S. & Brünger, A. T. (1994). *Protein hydration observed by X-ray diffraction. Solvation properties of penicillopepsin and neuraminidase crystal structures. J. Mol. Biol.* **243**, 100–115.

Jobst, B. A. & Goebel, H. E. (1982). *IDENT – a versatile microfile-based system for fast interactive XRPD phase analysis. Adv. X-ray Anal.* **25**, 273–282.

Johnson, G. G. Jr & Vand, V. (1967). *A computerized powder diffraction identification system. Ind. Eng. Chem.* **59**, 19–31.

Johnson, G. G. Jr & Vand, V. (1968). *Computerized multiphase X-ray powder diffraction identification system. Adv. X-ray Anal.* **11**, 376–384.

Kaduk, J. A. (2002). *Use of the Inorganic Crystal Structure Database as a problem solving tool. Acta Cryst.* B**58**, 370–379.

Kleywegt, G. J., Harris, M. R., Zou, J., Taylor, T. C., Wählby, A. & Jones, T. A. (2004). *The Uppsala Electron-Density Server. Acta Cryst.* D**60**, 2240–2249.

Le Bail, A. (2005). *Inorganic structure prediction with GRINSP. J. Appl. Cryst.* **38**, 389–395.

Le Page, Y. (1987). *Computer derivation of the symmetry elements implied in a structure description. J. Appl. Cryst.* **20**, 264–269.

Le Page, Y. (1988). *MISSYM1.1 – a flexible new release. J. Appl. Cryst.* **21**, 983–984.

Lutterotti, L. (2012). *Qualitative Phase Analysis: Method Developments.* In *Uniting Electron Crystallography and Powder Diffraction*, pp. 233–242. Dordrecht: Springer.

Macrae, C. F., Bruno, I. J., Chisholm, J. A., Edgington, P. R., McCabe, P., Pidcock, E., Rodriguez-Monge, L., Taylor, R., van de Streek, J. & Wood, P. A. (2008). *Mercury CSD 2.0 – new features for the visualization and investigation of crystal structures. J. Appl. Cryst.* **41**, 466–470.

Margiolaki, I. & Wright, J. P. (2008). *Powder crystallography on macromolecules. Acta Cryst.* A**64**, 169–180.

Margiolaki, I., Wright, J. P., Wilmanns, M., Fitch, A. N. & Pinotsis, N. (2007). *Second SH3 domain of ponsin solved from powder diffraction. J. Am. Chem. Soc.* **129**, 11865–11871.

Marquart, R. G. (1986). *μPDSM: mainframe search/match on an IBM PC. Powder Diffr.* **1**, 34–39.

Marquart, R. G., Katsnelson, I., Milne, G. W. A., Heller, S. R., Johnson, G. G. & Jenkins, R. (1979). *A search-match system for X-ray powder diffraction data. J. Appl. Cryst.* **12**, 629–634.

Materials Data (2016). *Jade* 9.6. Livermore: Materials Data Inc. https://materialsdata.com/.

Mighell, A. D. (2003). *The normalized reduced form and cell mathematical tools for lattice analysis – symmetry and similarity. J. Res. Natl Inst. Stand. Technol.* **108**, 447–452.

Mighell, A. D. & Himes, V. L. (1986). *Compound identification and characterization using lattice-formula matching techniques. Acta Cryst.* A**42**, 101–105.

Moeck, P. (2004). *EDU-COD: Educational Subset of COD.* http://nanocrystallography.research.pdx.edu/search/edu.

Moeck, P. (2007*a*). *Crystallography Open Database Mirror in North America.* http://nanocrystallography.org.

Moeck, P. (2007*b*). *Alternative COD search interface at Portland State University.* http://nanocrystallography.research.pdx.edu/search/codmirror.

Moews, P. C. & Kretsinger, R. H. (1975). *Refinement of the structure of carp muscle calcium-binding parvalbumin by model building and difference Fourier analysis. J. Mol. Biol.* **91**, 201–225.

Nichols, M. (1966). *A Fortran Program for the Identification of X-ray Powder Diffraction Patterns*. Report UCRL-70078, Lawrence Livermore National Laboratory, USA.

Norrman, M., Ståhl, K., Schluckebier, G. & Al-Karadaghi, S. (2006). *Characterization of insulin microcrystals using powder diffraction and multivariate data analysis. J. Appl. Cryst.* **39**, 391–400.

Nusinovici, J. & Bertelmann, D. (1993). *Practical determination of the acceptable 2θ error for non-ambiguous identification of pure phases with DIFFRAC-AT. Adv. X-ray Anal.* **36**, 327–332.

Nusinovici, J. & Winter, M. J. (1994). *Diffrac-At search: search/match using full traces as input. Adv. X-ray Anal.* **37**, 59–66.

O'Boyle, N. M., Banck, M., James, C. A., Morley, C., Vandermeersch, T. & Hutchison, G. R. (2011). *Open Babel: an open chemical toolbox. J. Cheminf.* **3**, 33.

O'Connor, B. H. & Bagliani, F. (1976). *A semi-automated system for identifying crystalline materials with powder diffraction data. J. Appl. Cryst.* **9**, 419–423.

Oxford Cryosystems (2012). *Crystallographica Search-Match (CSM)*. Oxford: Oxford Cryosystems Ltd. http://www.oxcryo.com/software/.

PANalytical (2012*a*). *HighScore Plus*. Almelo: PANalytical B.V.

PANalytical (2012*b*). *The COD database files for the PANalytical HighScore or HighScore Plus software packages*. http://www.crystallography.net/archives/2012/PANalytical.

Papageorgiou, N., Watier, Y., Saunders, L., Coutard, B., Lantez, V., Gould, E. A., Fitch, A. N., Wright, J. P., Canard, B. & Margiolaki, I. (2010). *Preliminary insights into the non structural protein 3 macro domain of the Mayaro virus by powder diffraction. Z. Kristallogr.* **225**, 576–580.

Parrish, W. (1983). *History of the X-ray powder method in the USA*. *Crystallography in North America*, edited by D. McLachlan & J. P. Glusker, pp. 201–214. Buffalo: American Crystallographic Association.

Parthé, E., Cenzual, K. & Gladyshevskii, R. (1993). *Standardization of crystal structure data as an aid to the classification of crystal structure types. J. Alloys Compd*, **197**, 291–301.

Parthé, E. & Gelato, L. M. (1984). *The standardization of inorganic crystal-structure data. Acta Cryst.* A**40**, 169–183.

Parthé, E. & Gelato, L. M. (1985). *The 'best' unit cell for monoclinic structures consistent with b axis unique and cell choice 1 of International Tables for Crystallography (1983). Acta Cryst.* A**41**, 142–151.

Parthé, E., Gelato, L., Chabot, B., Penzo, M., Cenzual K. & Gladyshevskii, R. (1993, 1994). *TYPIX – Standardized Data and Crystal Chemical Characterization of Inorganic Structure Types.* Heidelberg: Springer. https://doi.org/10.1007/978-3-662-10641-9.

Phillips, S. E. V. (1980). *Structure and refinement of oxymyoglobin at 1.6 Å resolution. J. Mol. Biol.* **142**, 531–554.

Pophale, R., Daeyaert, F. & Deem, M. W. (2013). *Computational prediction of chemically-synthesizable organic structure directing agents for zeolites. J. Mater. Chem. A*, **1**, 6750–6760.

Quirós-Olozábal, M. (2006). *COD Mirror of Granada University.* http://qiserver.ugr.es/cod.

Rajan, H., Uchida, H., Bryan, D., Swaminathan, R., Downs, R. M. & Hall-Wallace, M. (2006). *Building the American Mineralogist Crystal Structure Database: A recipe for construction of a small internet database. Geoinformatics: Data to Knowledge*, edited by A. Sinha. McLean: Geological Society of America. https://doi.org/10.1130/2006.2397(06).

Rigaku (2011). *COD for PDXL: Integrated Powder X-ray Diffraction Software.* http://www.crystallography.net/archives/2011/Rigaku.

Rotella, F. J., Duke, N. & Kaduk, J. A. (1998). *X-ray powder diffraction from biological macromolecules. What do we see? What can we tell? American Crystallographic Association Meeting Abstracts, Washington DC, 18–23 July*. Buffalo: American Crystallographic Association.

Rotella, F. J., Duke, N. & Kaduk, J. A. (2000). *Powder diffraction from biological macromolecules using synchrotron X-rays. American Crystallographic Association Meeting Abstracts, St Paul MN, 22–27 July*. Buffalo: American Crystallographic Association.

Schreiner, W. N., Surdukowski, C. & Jenkins, R. (1982). *A new minicomputer search/match/identify program for qualitative phase analysis with the powder diffractometer. J. Appl. Cryst.* **15**, 513–523.

Shpeizer, B., Ouyang, X., Heising, J. M. & Clearfield, A. (2001). *Synthesis and crystal structure of a new vanadyl phosphate* $[H_{0.6}(VO)_3(PO_4)_3(H_2O)_3].4H_2O$ *and its conversion to porous products. Chem. Mater.* **13**, 2288–2296.

Sidey, V. (2013). *On the shortest* $B^{III}—O$ *bonds. Acta Cryst.* B**69**, 86–89.

Sietronics (2012). *Siroquant* v.4. Canberra: Sietronics. http://www.siroquant.com.

Snyder, R. L. (1981). *A Hanawalt type phase identification procedure for a minicomputer. Adv. X-ray Anal.* **24**, 83–90.

Ståhl, K., Frankaer, C. G., Petersen, J. & Harris, P. (2013). *Monitoring protein precipitates by in-house X-ray powder diffraction. Powder Diffr.* **28**, S448–S457.

Toby, B. H., Harlow, R. L. & Holomany, M. A. (1990). *The POWDER SUITE: computer programs for searching and accessing the JCPDS-ICDD powder diffraction database. Powder Diffr.* **5**, 2–7.

Villars, P. (1997). *Pearson's Desk Edition*, Vols. 1–2. Materials Park: ASM International.

Villars, P. & Calvert, L. D. (1985). *Pearson's Handbook of Crystallographic Data for Intermetallic Phases*, 1st Ed., Vols. 1–3. Materials Park: ASM International.

Villars, P. & Calvert, L. D. (1991). *Pearson's Handbook of Crystallographic Data for Intermetallic Phases*, 2nd Ed., Vols. 1–4. Materials Park: ASM International.

Villars, P. & Cenzual, K. (2013). *Pearson's Crystal Data: Crystal Structure Database for Inorganic Compounds* (CD-ROM). Materials Park: ASM International.

Villars, P., Onodera, N. & Iwata, S. (1998). *The Linus Pauling File (LPF) and its application to materials design. J. Alloys Compd*, **279**, 1–7.

Von Dreele, R. B. (1998). *Protein structures by powder diffraction? Abstr. Pap. Am. Chem. Soc.* **215**, U759.

Von Dreele, R. B. (1999). *Combined Rietveld and stereochemical restraint refinement of a protein crystal structure. J. Appl. Cryst.* **32**, 1084–1089.

Von Dreele, R. B. (2003). *Protein crystal structure analysis from high-resolution X-ray powder-diffraction data. Methods Enzymol.* **368**, 254–267.

Von Dreele, R. B. (2007*a*). *Binding of N-acetylglucosamine oligosaccharides to hen egg-white lysozyme: a powder diffraction study. Acta Cryst.* D**61**, 22–32.

Von Dreele, R. B. (2007*b*). *Multipattern Rietveld refinement of protein powder data: an approach to higher resolution. J. Appl. Cryst.* **40**, 133–143.

Von Dreele, R. B., Stephens, P. W., Smith, G. D. & Blessing, R. H. (2000). *The first protein crystal structure determined from high-resolution X-ray powder diffraction data: a variant of T_3R_3 human insulin–zinc complex produced by grinding. Acta Cryst.* D**56**, 1549–1553.

Waldo, A. W. (1935). *Identification of the copper ore minerals by means of X-ray powder diffraction patterns. Am. Mineral.* **20**, 575–597.

White, P. S., Rodgers, J. R. & Le Page, Y. (2002). *CRYSTMET: a database of the structures and powder patterns of metals and intermetallics. Acta Cryst.* B**58**, 343–348.

Winchell, A. N. (1927). *Further studies in the mica group. Am. Mineral.* **12**, 267–279.

Wolff, P. M. de (2016). *International Tables for Crystallography*, Vol. A, 6th ed., edited by M. I. Aroyo, pp. 709–714. Chichester: Wiley.

Wyckoff, R. W. G. & Corey, R. B. (1936). *X-ray diffraction patterns of crystalline tobacco mosaic proteins. J. Biol. Chem.* **116**, 51–55.

International Tables for Crystallography (2019). Vol. H, Chapter 3.8, pp. 325–343.

3.8. Clustering and visualization of powder-diffraction data

C. J. Gilmore, G. Barr and W. Dong

3.8.1. Introduction

In high-throughput crystallography, crystallization experiments using robotics coupled with automatic sample changers and two-dimensional (2D) detectors can generate and measure over 1000 powder-diffraction patterns on a series of related compounds, often polymorphs or salts, in a day (Storey *et al.*, 2004). It is also possible to simultaneously measure spectroscopic data, especially Raman (Alvarez *et al.*, 2009). The analysis of these patterns poses a difficult statistical problem: a need to classify the data by putting the samples into clusters based on diffraction-pattern similarity so that unusual samples can be readily identified. At the same time, suitable visualization tools to help in the data-classification process are required; the techniques of classification and visualization go hand-in-hand. Interestingly, the techniques developed for large data sets with poor-quality data also have great value when looking at smaller data sets, and the visualization tools developed for high-throughput studies are especially useful when looking at phase transitions, mixtures *etc.*

In this chapter the methods for comparing whole patterns will be described. The mathematics of cluster analysis will then be explained, followed by a discussion of the associated visualization tools. Examples using small data sets from pharmaceuticals, inorganics and phase transitions will be given; the techniques used can be readily scaled up for handling large, high-throughput data sets. The same methods also work for spectroscopic data and the use of such information with and without powder X-ray diffraction (PXRD) data will be discussed. Finally, the use of visualization tools in quality control is demonstrated.

3.8.2. Comparing 1D diffraction patterns

Comparing 1D diffraction patterns or spectra cannot be done by simply using the peaks and their relative intensities for a number of reasons:

(1) The accurate determinations of the peak positions may be difficult, especially in cases where peak overlap occurs or there is significant peak asymmetry.
(2) The hardware and the way in which the sample is prepared can also affect the d-spacing (or 2θ value) that is recorded for the peak. Shoulders to main peaks and broad peaks can also be problematic.
(3) There is a subjective element to deciding how many peaks there are in the pattern, especially for weak peaks and noisy data.
(4) Weak peaks may be discarded. This can affect the quantitative analysis of mixtures if one component diffracts weakly or is present only in small amounts.
(5) Differences in sample preparation and instrumentation can lead to significant differences in the powder-diffraction patterns of near-identical samples.
(6) Preferred orientation may be present: this is a very difficult and common problem.
(7) The reduction of the pattern to point functions can also make it difficult to design effective algorithms.

In order to use the information contained within the full profile, algorithms are required that utilize each measured data point in the analysis. We use two correlation coefficients for the purpose of comparing PXRD patterns: the Pearson and the Spearman coefficients.

3.8.2.1. *Spearman's rank order coefficient*

Consider two diffraction patterns, i and j, each with n measured points $n((x_1, y_1), \ldots, (x_n, y_n))$. These are transformed to ranks $R(x_k)$ and $R(y_k)$. The Spearman test (Spearman, 1904) then gives a correlation coefficient (Press *et al.*, 2007),

$$R_{ij} = \frac{\sum_{k=1}^{n} R(x_k)R(y_k) - n\left(\frac{n+1}{2}\right)^2}{\left(\sum_{k=1}^{n} R(x_k)^2 - n\left(\frac{n+1}{2}\right)^2\right)^{1/2}\left(\sum_{k=1}^{n} R(y_k)^2 - n\left(\frac{n+1}{2}\right)^2\right)^{1/2}}, \tag{3.8.1}$$

where $-1 \leq R_{ij} \leq 1$.

3.8.2.2. *Pearson's r coefficient*

Pearson's r is a parametric linear correlation coefficient widely used in crystallography. It has a similar form to Spearman's test, except that the data values themselves, and not their ranks, are used:

$$r_{ij} = \frac{\sum_{k=1}^{n} (x_k - \overline{x})(y_k - \overline{y})}{\left[\sum_{k=1}^{n} (x_k - \overline{x})^2 \sum_{k=1}^{n} (y_k - \overline{y})^2\right]^{1/2}}, \tag{3.8.2}$$

where $\overline{x}$ and $\overline{y}$ are the means of intensities taken over the full diffraction pattern. Again, r can lie between -1.0 and $+1.0$.

Fig. 3.8.1 shows the use of the Pearson and Spearman correlation coefficients (Barr *et al.*, 2004*a*). In Fig. 3.8.1(*a*) $r = 0.93$ and $R = 0.68$. The high parametric coefficient arises from the perfect match of the two biggest peaks, but the much lower Spearman coefficient acts as a warning that there are unmatched regions in the two patterns. In Fig. 3.8.1(*b*) the situation is reversed: $r = 0.79$, whereas $R = 0.90$, and it can be seen that there is a strong measure of association with the two patterns, although there are some discrepancies in the region 15–35°. In Fig. 3.8.1(*c*) $r = 0.66$ and $R = 0.22$; in this case the Spearman test is again warning of missing match regions. Thus, the use of the two coefficients acts as a valuable balance of their respective properties when processing complete patterns. The Spearman coefficient is also robust in the statistical sense and useful in the case of preferred orientation.

3.8.2.3. *Combining the correlation coefficients*

Correlation coefficients are not additive, so it is invalid to average them directly; they need to be transformed into the Fisher Z value to give

$$\rho_{ij} = \tanh\left[\left(\tanh^{-1}R_{ij} + \tanh^{-1}r_{ij}\right)/2\right]. \quad (3.8.3)$$

3.8.2.4. *Full-profile qualitative pattern matching*

Before performing pattern matching, some data pre-processing may be necessary. In order not to produce artefacts, this should be minimized. Typical pre-processing activities are:

(1) The data are normalized such that the maximum peak intensity is 1.0.
(2) The patterns need to be interpolated if necessary to have common increments in 2θ. High-order polynomials using Neville's algorithm can be used for this (Press *et al.*, 2007).
(3) If backgrounds are large they should be removed. High-throughput data are often very noisy because of low counting times and the sample itself. If this is the case, smoothing of the data can be carried out. The SURE (Stein's Unbiased Risk Estimate) thresholding procedure (Donoho & Johnstone, 1995; Ogden, 1997) employing wavelets is ideal for this task since it does not introduce potentially damaging artefacts, for example ringing around peaks (Barr *et al.,* 2004*a*; Smrčok *et al.*, 1999).

After pre-processing, which needs to be carried out in an identical way for each sample, the following steps are carried out:

(1) The intersecting 2θ range of the two data sets is calculated, and each of the pattern correlation coefficients is calculated using only this region.
(2) A minimum intensity is set, below which profile data are set to zero. This reduces the contribution of background noise to the matching process without reducing the discriminating power of the method. We usually set this to $0.1I_{\max}$ as a default, where $I_{\max}$ is the maximum measured intensity.
(3) The Pearson correlation coefficient is calculated.
(4) The Spearman R is computed in the same way.
(5) An overall ρ value is calculated using (3.8.3).
(6) A shift in 2θ values between patterns is often observed, arising from equipment settings and data-collection protocols. Three possible simple corrections are

$$\Delta(2\theta) = a_0 + a_1\cos\theta, \quad (3.8.4)$$

which corrects for the zero-point error *via* the a_0 term and, *via* the $a_1\cos\theta$ term, for varying sample heights in reflection mode, or

$$\Delta(2\theta) = a_0 + a_1\sin\theta, \quad (3.8.5)$$

which corrects for transparency errors, for example, and

$$\Delta(2\theta) = a_0 + a_1\sin 2\theta, \quad (3.8.6)$$

which provides transparency coupled with thick specimen error corrections, where a_0 and a_1 are constants that can be determined by shifting patterns to maximize their overlap as measured by ρ. It is difficult to obtain suitable expressions for the derivatives $\partial a_0/\partial\rho_{ij}$ and $\partial a_1/\partial\rho_{ij}$ for use in the optimization, so we use the downhill simplex method (Nelder & Mead, 1965), which does not require their calculation.

3.8.2.5. *Generation of the correlation and distance matrices*

Using equation (3.8.3), a correlation matrix is generated in which a set of n patterns is matched with every other to give a symmetric $(n \times n)$ correlation matrix $\boldsymbol{\rho}$ with unit diagonal. The matrix $\boldsymbol{\rho}$ can be converted to a Euclidean distance matrix, **d**, of the same dimensions *via*

$$\mathbf{d} = 0.5(1.0 - \boldsymbol{\rho}) \quad (3.8.7)$$

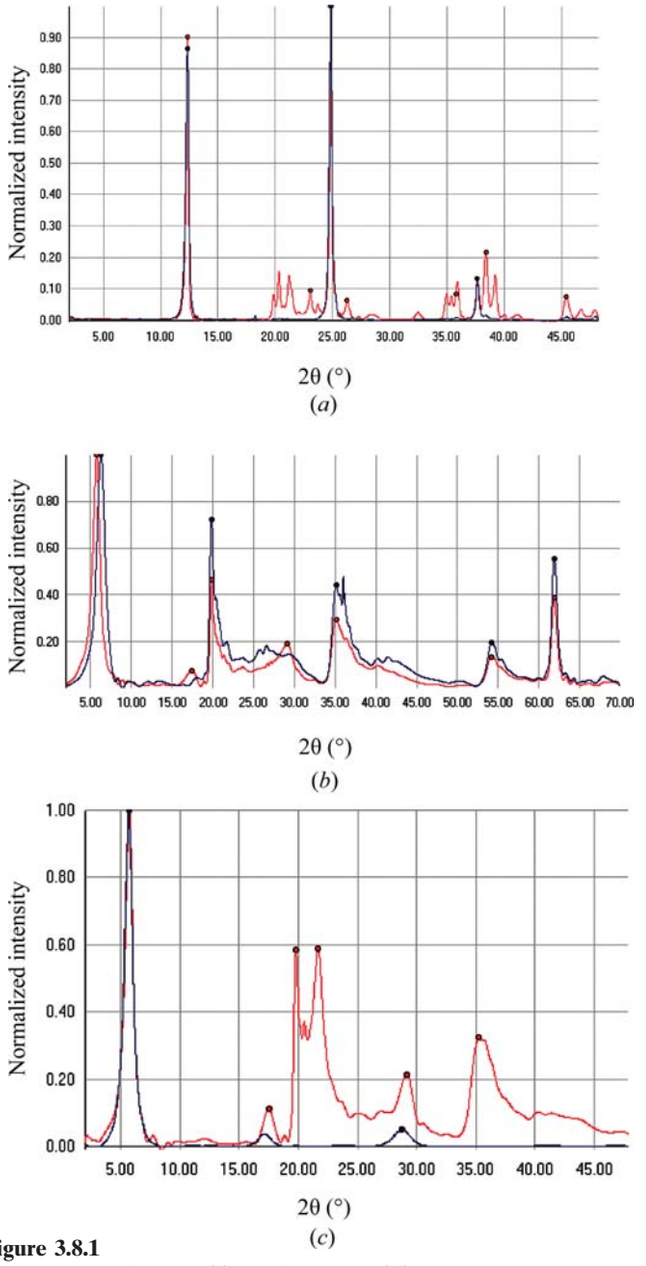

Figure 3.8.1
The use of the Pearson (r) and Spearman (R) correlation coefficients to quantitatively match powder patterns: (*a*) $r = 0.93$, $R = 0.68$; (*b*) $r = 0.79$, $R = 0.90$; (*c*) $r = 0.66$, $R = 0.22$.

or a distance-squared matrix,

$$\mathbf{D} = 0.25(1 - \boldsymbol{\rho})^2 \quad (3.8.8)$$

for each entry i, j in **d**, $0.0 \leq d_{ij} \leq 1.0$. A correlation coefficient of 1.0 translates to a distance of 0.0, a coefficient of -1.0 to 1.0, and zero to 0.5. There are other methods of generating a distance matrix from $\boldsymbol{\rho}$ (see, for example, Gordon, 1981, 1999), but we have found this to be both simple and as effective as any other.

For other purposes a dissimilarity matrix **s** is also needed, whose elements are defined *via*

$$s_{ij} = 1 - d_{ij}/d^{\max}, \quad (3.8.9)$$

where $d^{\max}$ is the maximum distance in matrix **d**. A dissimilarity matrix, $\boldsymbol{\delta}$, is also generated with elements

$$\delta_{ij} = d_{ij}/d_{ij}^{\max}. \quad (3.8.10)$$

Table 3.8.1
Six commonly used clustering methods

For each method, the coefficients α_i, β and γ in equation (3.8.11) are given.

Method	α_i	β	γ
Single link	$\frac{1}{2}$	0	$-\frac{1}{2}$
Complete link	$\frac{1}{2}$	0	$\frac{1}{2}$
Average link	$n_i/(n_i + n_j)$	0	0
Weighted-average link	$\frac{1}{2}$	0	0
Centroid	$n_i/(n_i + n_j)$	$-n_i n_j/(n_i + n_j)^2$	0
Sum of squares	$(n_i + n_k)/(n_i + n_j + n_k)$	$-n_k/(n_i + n_j + n_k)$	0

In some cases it can be advantageous to use $I^{1/2}$ in the distance-matrix generation; this can enhance the sensitivity of the clustering to weak peaks (Butler *et al.*, 2019).

3.8.3. Cluster analysis

Cluster analysis uses **d** (or **s**, or $\boldsymbol{\delta}$) to partition the patterns into groups based on the similarity of their diffraction profiles. Associated with cluster are a number of important ancillary techniques all of which will be discussed here. A flowchart of these methods is shown in Fig. 3.8.4.

3.8.3.1. *Dendrograms*

Using **d** and **s**, agglomerative, hierarchical cluster analysis is now carried out, in which the patterns are put into clusters as defined by their distances from each other. [Gordon (1981, 1999) and Everitt *et al.* (2001) provide excellent and detailed introductions to the subject. Note that the two editions of Gordon's monograph are quite distinct and complementary.] The method begins with a situation in which each pattern is considered to be in a separate cluster. It then searches for the two patterns with the shortest distance between then, and joins them into a single cluster. This continues in a stepwise fashion until all the patterns form a single cluster. When two clusters (C_i and C_j) are merged, there is the problem of defining the distance between the newly formed cluster $C_i \cup C_j$ and any other cluster C_k. There are a number of different ways of doing this, and each one gives rise to a different clustering of the patterns, although often the difference can be quite small. A general algorithm has been proposed by Lance & Williams (1967), and is summarized in a simplified form by Gordon (1981). The distance from the new cluster formed by merging C_i and C_j to any other cluster C_k is given by

$$d(C_i \cup C_j,\ C_k) = \alpha_i d(C_i, C_k) + \alpha_j d(C_j, C_k) + \beta d(C_i, C_j) + \gamma \left| d(C_i, C_k) - d(C_j, C_k) \right|. \quad (3.8.11)$$

There are many possible clustering methods. Table 3.8.1 defines six commonly used clustering methods, defined in terms of the parameters α, β and γ. All these methods can be used with powder data; in general, the group-average-link or single-link formalism is the most effective, although differences between the methods are often slight.

The results of cluster analysis are usually displayed as a dendrogram, a typical example of which is shown in Fig. 3.8.6(*a*), where a set of 13 powder patterns is analysed using the centroid method. Each pattern begins at the bottom of the plot as a separate cluster, and these amalgamate in stepwise fashion linked by horizontal tie bars. The height of the tie bar represents a similarity measure as measured by the relevant distance. As an indication of the differences that can be expected in the various algorithms used for dendrogram generation, Fig. 3.8.6(*e*) shows the same data analysed using the single-link method: the resulting clustering is slightly different: the similarity measures are larger, and, in consequence, the tie bars are higher on the graph. [For further examples see Barr *et al.* (2004*b*,*c*) and Barr, Dong, Gilmore & Faber (2004).]

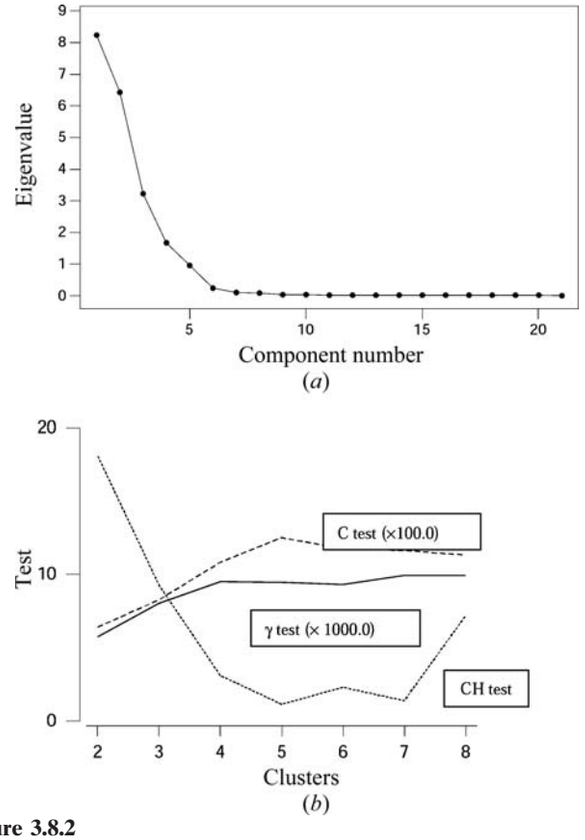

Figure 3.8.2
Four different methods of estimating the number of clusters present in a set of 23 powder patterns for the drug doxazosin. A total of five polymorphs are present, as well as two mixtures of these polymorphs. (*a*) A scree plot from the eigenvalue analysis of the correlation matrix; (*b*) the use of the C test (the coefficients have been multiplied by 100.0), which gives an estimate of five clusters using its local maximum. The γ test estimates that there are seven clusters and the CH test has a local maximum at seven clusters. Numerical details are given in Table 3.8.2.

3.8.3.2. *Estimating the number of clusters*

An estimate of the number of clusters present in the data set is needed. In terms of the dendrogram, this is equivalent to 'cutting the dendrogram' *i.e.* the placement of a horizontal line across it such that all the clusters as defined by tie lines above this line remain independent and unlinked. The estimation of the number of clusters is an unsolved problem in classification methods. It is easy to see why: the problem depends on how similar the patterns need to be in order to be classed as the same, and how much variability is allowed within a cluster. We use two approaches: (*a*) eigenvalue analysis of matrices $\boldsymbol{\rho}$ and **A**, and (*b*) those based on cluster analysis.

Eigenvalue analysis is a well used technique: the eigenvalues of the relevant matrix are sorted in descending order and when a fixed percentage (typically 95%) of the data variability has been accounted for, the number of eigenvalues is selected. This is shown graphically *via* a scree plot, an example of which is shown in Fig. 3.8.2.

We carry out eigenvalue analysis on the following:

(1) Matrix $\boldsymbol{\rho}$.
(2) Matrix **A**, as described in Section 3.8.3.3.
(3) A transformed form of $\boldsymbol{\rho}$ in which $\boldsymbol{\rho}$ is standardized to give $\boldsymbol{\rho}_s$ in which the rows and columns have zero mean and unit variance. The matrix $\boldsymbol{\rho}_s\boldsymbol{\rho}_s^T$ is then computed and subjected to eigenanalysis. It tends to give a lower estimate of cluster numbers than (1).

The most detailed study on cluster counting is that of Milligan & Cooper (1985), and is summarized by Gordon (1999). From this we have selected three tests that seem to operate effectively with powder data:

(4) The Calinński & Harabasz (1974) (CH) test:

$$\mathrm{CH}(c) = \big[B/(c-1)\big]/\big[W/(n-c)\big]. \qquad (3.8.12)$$

A centroid is defined for each cluster. W denotes the total within-cluster sum of squared distances about the cluster centroids, and B is the total between-cluster sum of squared distances. Parameter c is the number of clusters chosen to maximize CH.

(5) A variant of Goodman & Kruskal's (1954) γ test, as described by Gordon (1999). The dissimilarity matrix is used. A comparison is made between all the within-cluster dissimilarities and all the between-cluster dissimilarities. Such a comparison is marked as concordant if the within-cluster dissimilarity is less than the between-cluster dissimilarity, and discrepant otherwise. Equalities, which are unusual, are disregarded. If S_+ is the number of concordant and S_- the number of discrepant comparisons, then

$$\gamma(c) = \big(S_+ - S_-\big)/\big(S_+ + S_-\big). \qquad (3.8.13)$$

A maximum in γ is sought by an appropriate choice of cluster numbers.

(6) The C test (Milligan & Cooper, 1985). This chooses the value of c that minimizes

$$\mathrm{C}(c) = \big[W(c) - W_{\min}\big]/(W_{\max} - W_{\min}). \qquad (3.8.14)$$

$W(c)$ is the sum of all the within-cluster dissimilarities. If the partition has a total of r such dissimilarities, then $W_{\min}$ is the sum of the r smallest dissimilarities and $W_{\max}$ is the sum of the r largest.

The results of tests (4)–(6) depend on the clustering method being used. To reduce the bias towards a given dendrogram method, these tests are carried out on four different clustering methods: the single-link, the group-average, the sum-of-squares and the complete-link methods. Thus there are 12 semi-independent estimates of the number of clusters from clustering methods, and three from eigenanalysis, making 15 in all.

A composite algorithm is used to combine these estimates. The maximum and minimum values of the number of clusters ($c_{\max}$ and $c_{\min}$, respectively) given by the eigenanalysis results [(1)–(3) above] define the primary search range; tests (4)–(6) are then used in the range $\min(c_{\max}+3, n) \le c \le \max(c_{\min}-3, 0)$ to find local maxima or minima as appropriate. The results are averaged, any outliers are removed, and a weighted mean value is taken of the remaining indicators, then this is used as the final estimate of the number of clusters. Confidence levels for c are also defined by the estimates of the maximum and minimum cluster numbers after any outliers have been removed.

A typical set of results for the PXRD data from 23 powder patterns for doxazosin (an anti-hypertension drug) in which five polymorphs are present, as well as two mixtures of polymorphs, is shown in Fig. 3.8.2(*a*) and (*b*) (see also Table 3.8.2). The scree plot arising from the eigenanalysis of the correlation matrix indicates that 95% of the variability can be accounted for by five components, and this is shown in Fig. 3.8.2(*a*). Eigenvalues from other matrices indicate that four clusters are appropriate. A search for local optima in the CH, γ and C tests is then initiated in the range 2–8 possible clusters. Four different clustering methods are tried, and the results indicate a range of 4–7 clusters. There are no outliers, and the final weighted mean value of 5 is calculated. As Fig. 3.8.2(*b*) shows, the optimum points for the C and γ tests are often quite weakly defined (Barr *et al.*, 2004*b*).

Table 3.8.2
Estimate of the number of clusters for the 23 sample data set for doxazosin

There are five polymorphs present, plus two mixtures of these polymorphs. The maximum estimate is 7; the minimum estimate is 4; the combined weighted estimate of the number of clusters is 6, and the median value is 5. The dendrogram cut level is set to give 5 clusters, and the lower and upper confidence limits are 4 and 7, respectively.

Method	No. of clusters
Principal-component analysis (non-transformed matrix)	5
Principal-component analysis (transformed matrix)	4
Multidimensional metric scaling	4
γ statistic using single linkage	7
CH statistic using single linkage	7
C statistic using single linkage	—
γ statistic using group averages	7
CH statistic using group averages	5
C statistic using group averages	—
γ statistic using sum of squares	—
CH statistic using sum of squares	5
C statistic using sum of squares	—
γ statistic using complete linkage	—
CH statistic using complete linkage	5
C statistic using complete linkage	—

3.8.3.3. *Metric multidimensional scaling*

This is, in its essentials, the particle-in-a-box problem. Each powder pattern is represented as a single sphere, and these spheres are placed in a cubic box of unit dimensions such that the positions of the spheres reproduce as closely as possible the distance matrix, **d**, generated from correlating the patterns. The spheres have an arbitrary orientation in the box.

To do this, the $(n \times n)$ distance matrix **d** is used in conjunction with metric multidimensional scaling (MMDS) to define a set of p underlying dimensions that yield a Euclidean distance matrix, $\mathbf{d}^{\mathrm{calc}}$, whose elements are equivalent to or closely approximate the elements of **d**.

The method works as follows (Cox & Cox, 2000; Gower, 1966; Gower & Dijksterhuis, 2004).

The matrix **d** has zero diagonal elements, and so is not positive semidefinite. A positive definite matrix, $\mathbf{A}(n \times n)$ can be constructed, however, by computing

$$\mathbf{A} = -\frac{1}{2}\left[\mathbf{I}_n - \frac{1}{n}\mathbf{i}_n\mathbf{i}_n'\right]\mathbf{D}\left[\mathbf{I}_n - \frac{1}{n}\mathbf{i}_n\mathbf{i}_n'\right], \qquad (3.8.15)$$

where $\mathbf{I}_n$ is an $(n \times n)$ identity matrix, $\mathbf{i}_n$ is an $(n \times 1)$ vector of unities and **D** is defined in equation (3.8.8). The matrix $[\mathbf{I}_n - (1/n)\mathbf{i}_n\mathbf{i}_n']$ is called a centring matrix, since **A** has been derived from **D** by centring the rows and columns.

The eigenvectors $\mathbf{v}_1, \mathbf{v}_2, \ldots, \mathbf{v}_n$ and the corresponding eigenvalues $\lambda_1, \lambda_2, \ldots, \lambda_n$ are then obtained. A total of p eigenvalues of **A** are positive and the remaining $(n-p)$ will be zero. For the p

non-zero eigenvalues a set of coordinates can be defined *via* the matrix $\mathbf{X}(n \times p)$,

$$\mathbf{X} = \mathbf{V}\Lambda^{1/2}, \tag{3.8.16}$$

where $\mathbf{\Lambda}$ is the vector of eigenvalues.

If $p = 3$, then we are working in three dimensions, and the $\mathbf{X}(n \times 3)$ matrix can be used to plot each pattern as a single point in a 3D graph. This assumes that the dimensionality of the problem can be reduced in this way while still retaining the essential features of the data. As a check, a distance matrix $\mathbf{d}^{\rm calc}$ can be calculated from $\mathbf{X}(n \times 3)$ and correlated with the observed matrix $\mathbf{d}$ using both the Pearson and Spearman correlation coefficients. In general the MMDS method works well, and correlation coefficients greater than 0.95 are common. For large data sets this can reduce to ~0.7, which is still sufficiently high to suggest the viability of the procedure. Parallel coordinates based on the MMDS analysis can also be used, and this is discussed in Sections 3.8.4.2.1 and 3.8.4.2.2.

There are occasions in which the underlying dimensionality of the data is 1 or 2, and in these circumstances the data project onto a plane or a line in an obvious way without any problems.

An example of an MMDS plot is shown in Fig. 3.8.6(*b*), which is linked to the dendrogram in Fig. 3.8.6(*a*).

3.8.3.4. *Principal-component analysis*

It is also possible to carry out principal-component analysis (PCA) on the correlation matrix. The eigenvalues of the correlation matrix can be used to estimate the number of clusters present *via* a scree plot, as shown in Fig. 3.8.2(*a*), and the eigenvectors can be used to generate a score plot, which is an $\mathbf{X}(n \times 3)$ matrix and can be used as a visualization tool in exactly the same way as the MMDS method to indicate which patterns belong to which class. Score plots traditionally use two components with the data thus projected on to a plane; we use 3D plots in which three components are represented. In general, we find that the MMDS representation of the data is nearly always superior to the PCA analysis for powder and spectroscopic data.

3.8.3.5. *Choice of clustering method*

It is possible to use the MMDS plot (or, alternatively, PCA score plots) to assist in the choice of clustering method, since the two methods operate semi-independently. The philosophy here is to choose a technique that results in the tightest, most isolated clusters as follows:

(1) The MMDS formalism is used to derive a set of three-dimensional coordinates stored in matrix $\mathbf{X}(n \times 3)$.
(2) The number of clusters, c, is estimated as described in Section 3.8.3.2.
(3) Each of six dendrogram methods (see Table 3.8.1) is employed in turn, stopping when c clusters have been generated. Each entry in $\mathbf{X}$ can now be assigned to a cluster.
(4) A sphere is drawn around each point in $\mathbf{X}$ and the average between-cluster overlap of the spheres is calculated for each of the N clusters C_1 to C_N. If the total number of overlaps is m, this can be written as

$$S = \sum_{i=1}^{n} \sum_{\substack{j=1,n \\ j \neq i}}^{n} \left(\int_V s_{i \in C_i} s_{j \in C_j} \, {\rm d}s \right) \Big/ m. \tag{3.8.17}$$

If the clusters are well defined then S should be a minimum. Conversely, poorly defined clusters will tend to have large values of S. In the algorithm used in *PolySNAP* (Barr, Dong & Gilmore, 2009) and *DIFFRAC.EVA* (Bruker, 2018), the sphere size depends on the number of diffraction patterns.
(5) The tightness of each cluster is also estimated by computing the mean within-cluster distance. This should also be a minimum for well defined, tight clusters.
(6) The mean within-cluster distance from the centroid of the cluster can also be computed, which should also be a minimum.
(7) Steps (4)–(6) are repeated using coordinates derived from PCA 3D score plots.
(8) Tests (4)–(7) are combined in a weighted, suitably scaled mean to give an overall figure of merit (FOM); the minimum is used to select which dendrogram method to use (Barr *et al.*, 2004*b*).

3.8.3.6. *The most representative sample*

Similar techniques can be used to identify the most representative sample in a cluster. This is defined as the sample that has the minimum mean distance from every other sample in the clusters, *i.e.* for cluster J containing m patterns, the most representative sample, i, is defined as that which gives

$$\min \left(\sum_{\substack{j=1 \\ i,j \in J}}^{m} d(i,j)/m \right). \tag{3.8.18}$$

The most representative sample is useful in visualization and can, with care, be used to create a database of known phases (Barr *et al.*, 2004*b*).

3.8.3.7. *Amorphous samples*

Amorphous samples are an inevitable consequence of high-throughput experiments, and need to be handled correctly if they are not to lead to erroneous indications of clustering. To identify amorphous samples the total background for each pattern is estimated and its intensity integrated; the integrated intensity of the non-background signal is then calculated. If the ratio falls below a preset limit (usually 5%, but this may vary with the type of samples under study) the sample is treated as amorphous. The distance matrix is then modified so that each amorphous sample is given a distance and dissimilarity of 1.0 from every other sample, and a correlation coefficient of zero. This automatically excludes the samples from the clustering until the last amalgamation steps, and also limits their effect on the estimation of the number of clusters (Barr *et al.*, 2004*b*). Of course, the question of amorphous samples is not a binary (yes/no) one: there are usually varying degrees of amorphous content, which further complicates matters.

3.8.4. Data visualization

3.8.4.1. *Primary data visualization*

It is important when dealing with large data sets to have suitable visualization tools. These tools are also a valuable resource for exploring smaller data sets. This methodology provides four primary aids:

(1) A pie chart is produced for each sample, corresponding to the sample wells used in the data-collection process, in which each well is given a colour as defined by the dendrogram. If mixtures of known phases are detected, the pie charts give the relative proportions of the pure samples as estimated by quantitative analysis (see Section 3.8.7).

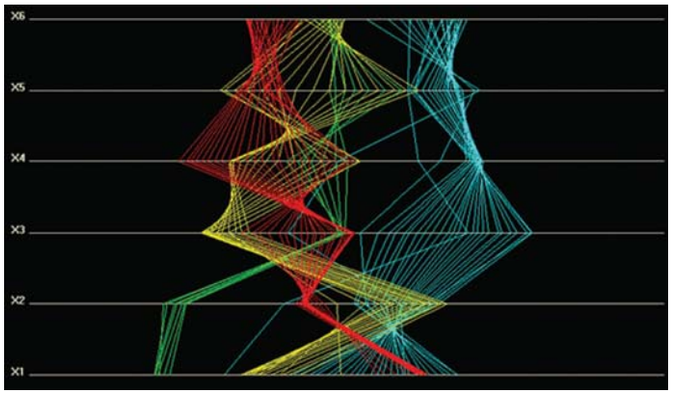

Figure 3.8.3
Example of a parallel-coordinates plot in six dimensions, with axes labeled X1, X2, ..., X6, for a set of 80 organic PXRD samples partitioned into four clusters. The plot shows that the clustering looks realistic and that it is maintained when the data are examined in six dimensions.

(2) The dendrogram gives the clusters, the degree of association within the clusters and the differential between a given cluster and its neighbours. Different colours are used to distinguish each cluster. The cut line is also drawn along with the associated confidence levels. The dendrogram is the primary visualization tool.
(3) The MMDS method reproduces the data as a 3D plot in which each point represents a single powder pattern. The colour for each point is taken from the dendrogram. The most representative sample for each cluster is marked with a cross.
(4) Similarly, the eigenvalues from principal-component analysis can be used to generate a 3D score plot in which each point also represents a powder pattern. Just as in the MMDS formalism, the colour for each point is taken from the dendrogram, and the most representative sample is marked with a cross.

These aids give graphical views of the data that are semi-independent and thus can be used to check for consistency and discrepancies in the clustering. They are also interactive. No one method is optimal, and a combination of mathematical and visualization techniques is required, techniques that often need tuning for each individual application (Barr, Cunningham *et al.*, 2009; Barr, Dong & Gilmore, 2009).

3.8.4.2. *Secondary visualization using parallel coordinates, the grand tour and minimum spanning trees*

In the MMDS and PCA methods $p = 3$ [equation (3.8.16)] to work in three dimensions; the **X** matrix can then be used to plot each pattern as a single point in a 3D graph. However, this has reduced the dimensionality of the data to three, and the question arises as to the validity of this: are three dimensions sufficient? The use of parallel-coordinates plots coupled with the grand tour can assist here as well as giving us an alternative view of the data.

3.8.4.2.1. *Parallel-coordinates plots*

A parallel-coordinates plot is a graphical data-analysis technique for plotting multivariate data. Usually orthogonal axes are used when doing this, but in parallel-coordinates plots orthogonality is abandoned and replaced with a set of N equidistant parallel axes, one for each variable and labelled X1, X2, X3, ..., XN (Inselberg, 1985, 2009; Wegman, 1990). Each data point is plotted on each axis and the points are joined *via* a line connecting each data point. The data now become a set of lines. The lines are given the colours of the cluster to which they belong as defined by the current dendrogram. A parallel-coordinates display can be interpreted as a generalization of a two-dimensional scatterplot, and it allows the display of an arbitrary number of dimensions. The method can also be used to validate the clustering itself without using dendrograms. Using this technique it is possible to determine whether the clustering shown by the MMDS (or PCA) plot in three dimensions continues in higher dimensions.

Fig. 3.8.3 shows a typical example for a set of 80 organic samples partitioned into four clusters (Barr, Dong & Gilmore, 2009). The plot shows that the clustering looks realistic when

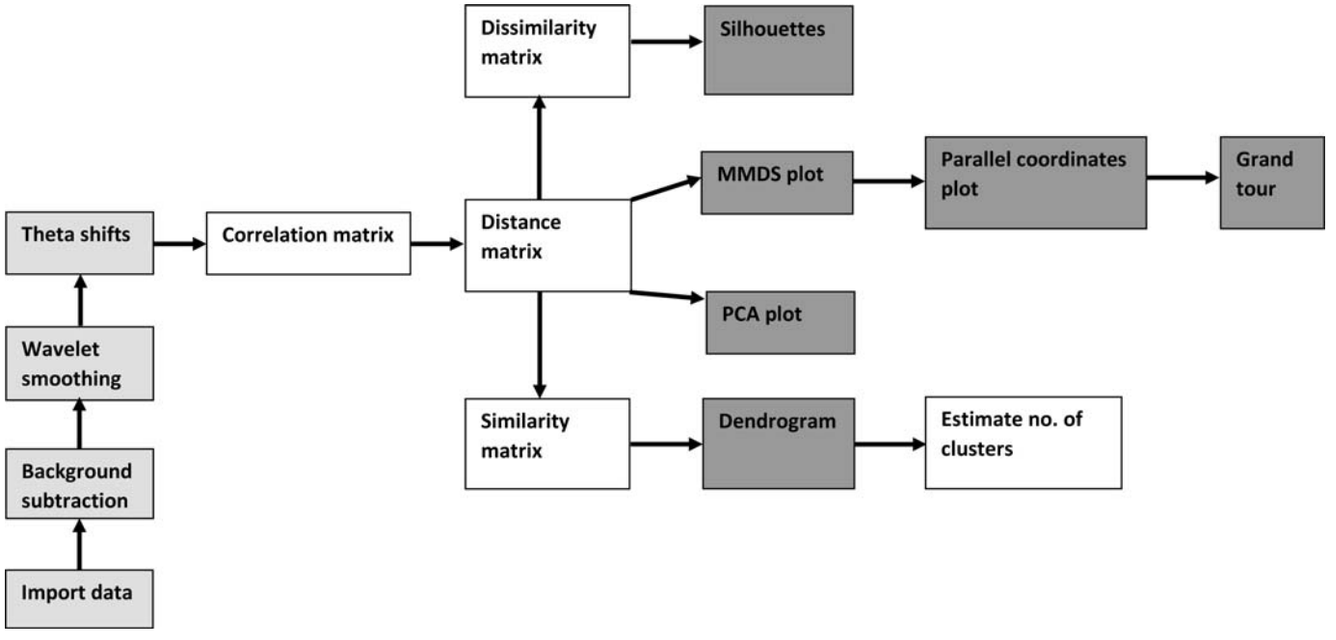

Figure 3.8.4
Flowchart for the cluster-analysis and data-visualization procedure described in this chapter. The light grey boxes denote data-visualization elements and the dark grey objects are optional data pre-processing operations.

viewed in this way and that it is maintained when the data are examined in six dimensions.

3.8.4.2.2. *The grand tour*

The grand tour is a method of animating the parallel-coordinates plot to examine it from all possible viewpoints. Consider a 3D data plot using orthogonal axes: a grand tour takes 2D sections through these data and displays them in parallel-coordinates plots in a way that explores the entire space in a continuous way. The former is important, because the data can be seen from all points of view, and the latter allows the user the follow the data without abrupt discontinuities. This concept was devised by Asimov (1985) and further developed by Wegman (1990). In more than three dimensions it becomes a generalized rotation of all the coordinate axes. A d-dimensional tour is a continuous geometric transformation of a d-dimensional coordinate system such that all possible orientations of the coordinate axes are eventually achieved. The algorithm for generating a smooth and complete view of the data is described by Asimov (1985).

To do this, the restriction of $p = 3$ in the MMDS calculation is relaxed to 6, so that there is now a 6D data set with six orthogonal axes. The choice of six is somewhat arbitrary – more can be used, but six is sufficient to see whether the clustering is maintained without generating unduly complex plots and requiring extensive computing resources. The data are plotted as a parallel-coordinates plot. The grand-tour method is then applied by a continuous geometric transformation of the 6D coordinate system such that all possible orientations of the axes are achieved. Each orientation is reproduced as a parallel-coordinates plot using six axes.

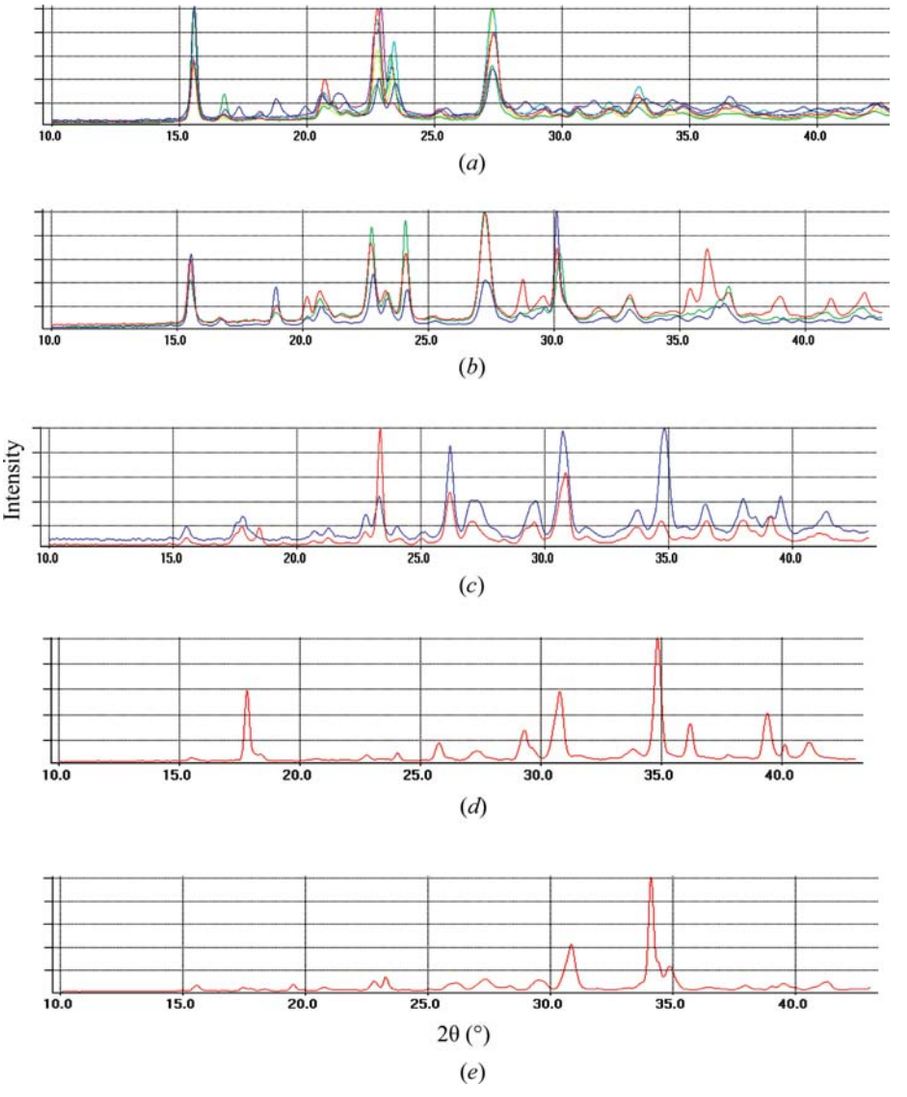

Figure 3.8.5
Powder patterns for 13 commercial aspirin samples partitioned into five sets. The patterns are in highly correlated sets: (*a*) comprises patterns 1, 3, 5, 6, 9 and 12; (*b*) comprises patterns 10, 11 and 13; (*c*) contains patterns 2 and 4; (*d*) contains pattern 7 and (*e*) contains pattern 8.

Figs. 3.8.9(*j*) and (*k*) show an example from the clustering of the 13 aspirin samples using PXRD data. Fig. 3.8.9(*j*) shows the default parallel-coordinates plot. Fig. 3.8.9(*k*) shows alternative views of the data taken from the grand tour. In Fig. 3.8.9(*j*) there appears to be considerable overlap between clusters in the 4th, 5th and 6th dimensions (X4, X5 and X6), but the alternative view given in Fig. 3.8.9(*k*) show that the clustering is actually well defined in all six dimensions (Barr, Dong & Gilmore, 2009).

3.8.4.2.3. *Powder data as a tree: the minimum spanning trees*

The minimum spanning tree (MST) displays the MMDS plot as a tree whose points are the data from the MMDS calculation (in three dimensions) and whose weights are the distances between these points. The minimum-spanning-tree problem is that of joining the points with a minimum total edge weight. (As an example, airlines use minimum spanning trees to work out their basic route systems: the best set of routes taking into account airport hubs, passenger numbers, fuel costs *etc.* is the minimum spanning tree.) Because a tree is used, each point is only allowed a maximum of three connections to other points.

To do this Kruskal's (1956) algorithm can be used, in which the lowest weight edge is always added to see if it builds a spanning tree; if so, it is added or otherwise discarded. This process continues until the tree is constructed. An example is shown in Figs. 3.8.7 for the 13-sample aspirin data. A complete tree for this data set using three dimensions and the MMDS-derived coordinates is shown in Fig. 3.8.7(*a*). This has 12 links between the 13 data points. Reducing the number of links to 10 gives Fig. 3.8.7(*b*).

3.8.5. Further validating and visualizing clusters: silhouettes and fuzzy clustering

Other techniques exist to validate the clusters, and these are discussed here.

3.8.5.1. *Silhouettes*

Silhouettes (Rousseeuw, 1987; Kaufman & Rousseeuw, 1990) are a property of every member of a cluster and define a coef-

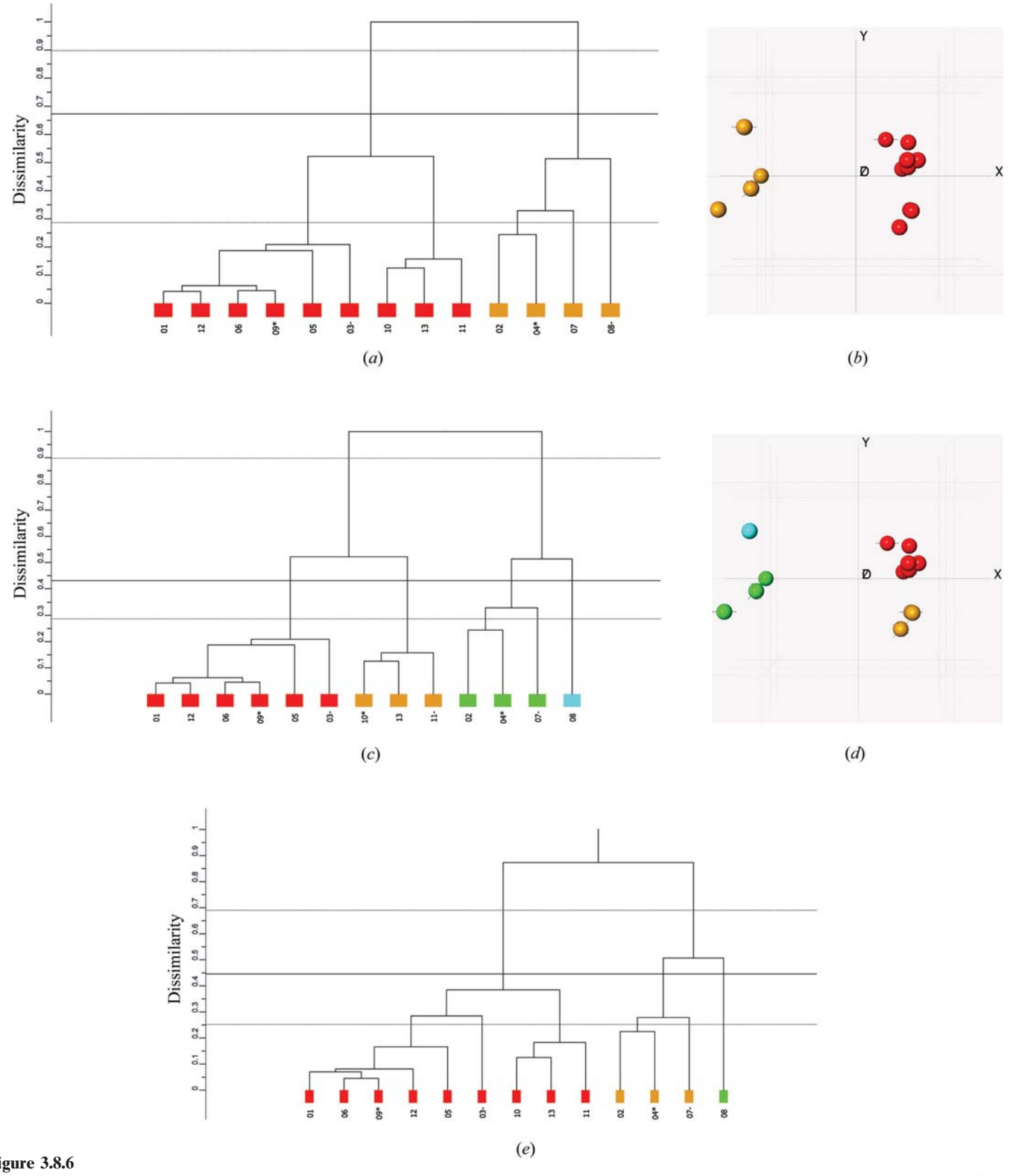

Figure 3.8.6
(*a*) The initial default dendrogram using the centroid clustering method on 13 PXRD patterns from 13 commercial aspirin samples. (*b*) The corresponding MMDS plot. It can be seen that both clusters have a natural break in them and should be partitioned into two clusters. (*c*) The dendrogram cut line is reduced. (*d*) The corresponding MMDS plot. The red cluster is now partitioned into two; the remaining patterns are a light-blue singleton and a green triplet cluster. (*e*) The default dendrogram using the single-link method.

ficient of cluster membership. To compute them, the dissimilarity matrix, $\boldsymbol{\delta}$, is used. If the pattern i belongs to cluster C_r which contains n_r patterns, we define

$$a_i = \sum_{\substack{j \in C_r \\ j \neq i}} \delta_{ij}/(n_r - 1). \tag{3.8.19}$$

This defines the average dissimilarity of pattern i to all the other patterns in cluster C_r. Further define

$$b_i = \min_{s \neq r} \left\{ \sum_{j \in C_s} \delta_{ij}/n_s \right\}. \tag{3.8.20}$$

The silhouette for pattern i is then

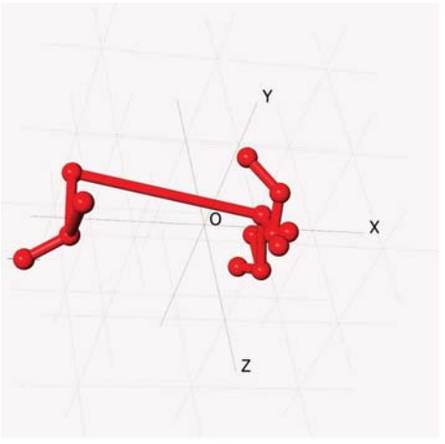

(*a*)

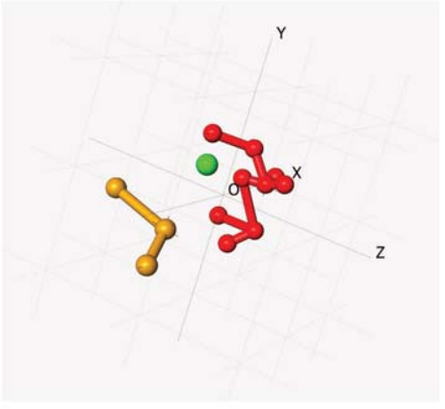

(*b*)

Figure 3.8.7
The use of minimum spanning trees (MSTs). (*a*) The MST with 12 links. (*b*) The MST with 10 links; three clusters are now present.

$$h_i = \frac{b_i - a_i}{\max(a_i,\ b_i)}. \tag{3.8.21}$$

Clearly $-1 \leq h_i \leq 1.0$. It is not possible to define silhouettes for clusters with only one member (singleton clusters). Silhouettes are displayed such that each cluster is represented as a histogram of frequency plotted against silhouette values so that one can look for outliers or poorly connected plots.

From our experience with powder data collected in reflection mode on both organic and inorganic samples (Barr *et al.*, 2004*b*), we conclude that for any given pattern

(1) $h_i > 0.5$ implies that pattern i is probably correctly classified;
(2) $0.2 < h_i < 0.5$ implies that pattern i should be inspected, since it may belong to a different or new cluster;
(3) $h_i < 0.2$ implies that pattern i belongs to a different or new cluster.

The use of silhouettes in defining the details of the clustering is shown for the aspirin data in Fig. 3.8.8. The silhouettes for the red cluster corresponding to the dendrogram in Fig. 3.8.6(*a*) are shown in Fig. 3.8.8(*a*) and those for the corresponding orange cluster are shown in Fig. 3.8.8(*b*). Both sets of silhouettes have values < 0.5, which indicates that the clustering is not optimally defined. When the cut line is moved to give the dendrogram in Fig. 3.8.6(*c*), the silhouettes for the red cluster are shown in Fig. 3.8.8(*c*). The entry centred on a silhouette value of 0.15 is pattern 3. This implies that pattern 3 is only loosely connected to the cluster and this is demonstrated in Fig. 3.8.8(*d*) where pattern 3 and the most representative pattern for the cluster (No. 9) are superimposed. Although there is a general sense of similarity there are significant differences and the combined correlation coefficient is only 0.62. In Fig. 3.8.8(*e*), the silhouettes for the orange cluster are shown. They imply that this is a single cluster without outliers. The silhouettes for the green cluster corresponding to the dendrogram in Fig. 3.8.6(*c*) are shown in Fig. 3.8.8(*f*). The clustering is poorly defined here.

3.8.5.2. *Fuzzy clustering*

In standard clustering methods a set of n diffraction patterns are partitioned into c disjoint clusters. Cluster membership is defined *via* a membership matrix $\mathbf{U}(n \times c)$, where individual coefficients, u_{ik}, represent the membership of pattern i of cluster k. The coefficients are equal to unity if i belongs to c and zero otherwise, *i.e.*

$$u_{ik} \in [0, 1] \quad (i = 1, \ldots, n; k = 1, \ldots, c). \tag{3.8.22}$$

If these constraints are relaxed, such that

$$0 \leq u_{ik} \leq 1 \quad (i = 1, \ldots, n; k = 1, \ldots, c), \tag{3.8.23}$$

$$0 < \sum_{i=1}^{n} u_{ik} < n \quad (k = 1, \ldots, c) \tag{3.8.24}$$

and

$$\sum_{k=1}^{c} u_{ik} = 1, \tag{3.8.25}$$

then fuzzy clusters are generated, in which there is the possibility that a pattern can belong to more than one cluster (see, for example, Everitt *et al.*, 2001; Sato *et al.*, 1966). Such a situation is quite feasible in the case of powder diffraction, for example, when mixtures can be involved. It is described in detail by Barr *et al.* (2004*b*).

3.8.5.3. *The PolySNAP program and DIFFRAC.EVA*

All these techniques have been incorporated into the *PolySNAP* computer program (Barr *et al.*, 2004*a*,*b*,*c*; Barr, Dong, Gilmore & Faber, 2004; Barr, Dong & Gilmore, 2009), which was developed from the *SNAP-D* software (Barr, Gilmore & Paisley, 2004). *PolySNAP* has subsequently been incorporated into the Bruker *DIFFRAC.EVA* program (Bruker, 2018), and the following sections are based on its use.

3.8.6. Examples

All the elements for clustering and visualization are now in place. Fig. 3.8.4 shows this as a flowchart. Hitherto we have looked at elements of the aspirin data to demonstrate how methods work; we now examine the aspirin data in detail as a single analysis.

3.8.6.1. *Aspirin data*

In this example we use 13 powder patterns from commercial aspirin samples collected in reflection mode on a Bruker D8 diffractometer. Since these samples include fillers, the active pharmaceutical ingredient (API) and other formulations, it is not surprising that peak widths are high: ∼0.5° full width at half maximum (FWHM). The data-collection range was 10–43° in 2θ using Cu $K\alpha$ radiation. The 13 powder data sets are shown in Fig. 3.8.5 arranged into groups based on similarity. We have already described the methods of analysis and have shown typical results in Figs. 3.8.6 to 3.8.8, and now present detailed examples. The correlation matrix derived from equation (3.8.3) is shown in Fig.

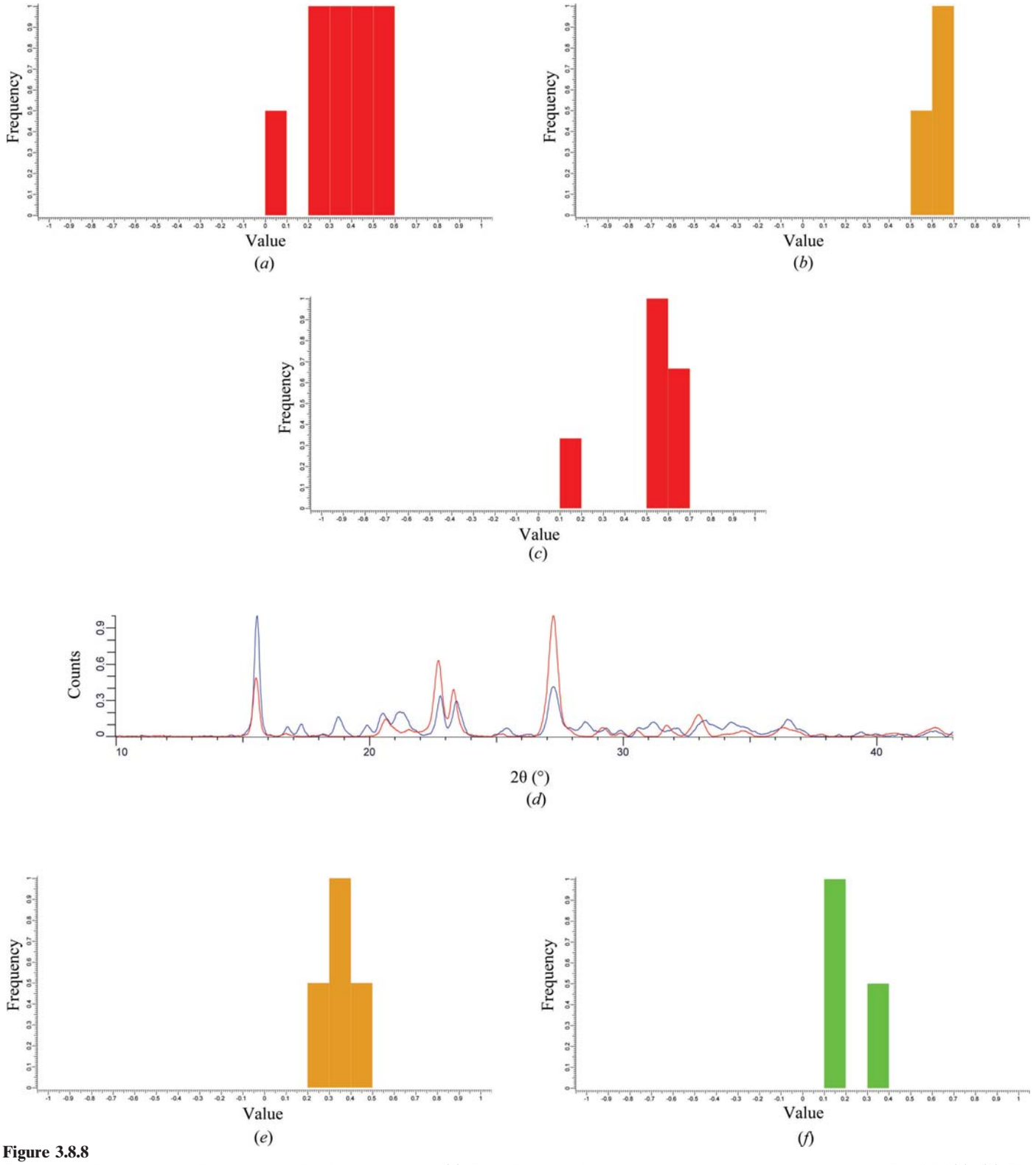

Figure 3.8.8
The use of silhouettes in defining the details of the clustering. (*a*) The silhouettes for the red cluster in the dendrogram from Fig. 3.8.6(*a*). (*b*) The corresponding orange cluster. Both sets of silhouettes have values that are less than 0.5, which indicates that the clustering is not well defined. (*c*) The silhouettes for the red cluster corresponding to the dendrogram in Fig. 3.8.6(*c*). The entry centred on a silhouette value of 0.15 is pattern 3. This implies that pattern 3 is only loosely connected to the cluster and this is demonstrated in part (*d*), where pattern 3 and the most representative pattern for the cluster (No. 9) are superimposed. Although there is a general sense of similarity there are significant differences and the combined correlation coefficient is only 0.62. (*e*) The silhouettes for the orange cluster corresponding to the dendrogram in Fig. 3.8.6(*c*). The silhouettes imply that this is a single cluster without outliers. (*f*) The silhouettes for the green cluster corresponding to the dendrogram in Fig. 3.8.6(*c*). The clustering is poorly defined here.

3.8.9(*a*), colour coded to reflect the values of the coefficients; the darker the shade, the higher the correlation. The resulting dendrogram and MMDS plot are shown in Figs. 3.8.9(*b*) and (*c*), respectively. Four clusters are identified in the dendrogram and these have been appropriately coloured. Other visualization tools are now shown. In Fig. 3.8.9(*d*) the pie chart is displayed; the number of rows can be adjusted to reflect the arrangement of the samples in a multiple sample holder. Fig. 3.8.9(*e*)

shows the default minimum spanning tree with 12 links. In Fig. 3.8.9(*f*) the scree plot indicates that three clusters will account for more than 95% of the data variability. The steep initial slope is a clear indication of good cluster estimation. The silhouettes are shown in Fig. 3.8.9(*g*–*i*). These were discussed in Section 3.8.5.1. In Fig. 3.8.9(*j*) the default parallel-coordinates plot for the same data is shown, and in Fig. 3.8.9(*k*) there is another view taken from the grand tour. These two plots validate the clustering and also indicate that there is no significant error introduced into the MMDS plot by truncating it into three dimensions.

3.8.6.1.1. *Aspirin data with amorphous samples included*

As a demonstration of the handling of data from amorphous samples, five patterns for amorphous samples were included in the aspirin data and the clustering calculation was repeated. The results are shown in Fig. 3.8.10. Fig. 3.8.10(*a*) shows the dendrogram. It can be seen that the amorphous samples are positioned as isolated clusters on the right-hand end. They also appear as an isolated cluster in the MMDS plot and the parallel-coordinates plots, as shown in Figs. 3.8.10(*b*) and (*c*). It could be argued that these samples should be treated as a single, five-membered cluster rather than five individuals, but we have found that this confuses the clustering algorithms, and it is clearer to the user if the data from amorphous samples are presented as separate classes.

3.8.6.2. *Phase transitions in ammonium nitrate*

Ammonium nitrate exhibits temperature-induced phase transformations. Between 256 and 305 K it crystallizes in the orthorhombic space group *Pmmm* with a = 5.745, b = 5.438, c = 4.942 Å and Z = 2; from 305 to 357 K it crystallizes in *Pbnm* with

(*a*)

Rank:	01 #1	02 #2	03 #3	04 #4	05 #5	06 #6	07 #7	08 #8	09 #9	10 #10	11 #11
01 #1	1	0.2148	0.6625	0.2903	0.8183	0.9189	0.1231	0.2363	0.93	0.6693	0.6275
02 #2	0.2148	1	0.2527	0.8174	0.267	0.3246	0.5152	0.5315	0.2628	0.253	0.2168
03 #3	0.6625	0.2527	1	0.2578	0.7207	0.6678	0.1319	0.2566	0.6362	0.5434	0.6153
04 #4	0.2903	0.8174	0.2578	1	0.2404	0.3076	0.7214	0.6004	0.2899	0.2712	0.2111
05 #5	0.8183	0.267	0.7207	0.2404	1	0.8379	0.0725	0.2015	0.8577	0.5756	0.6262
06 #6	0.9189	0.3246	0.6678	0.3076	0.8379	1	0.1093	0.2047	0.9551	0.7228	0.6686
07 #7	0.1231	0.5152	0.1319	0.7214	0.0725	0.1093	1	0.4933	0.0936	0.121	0.0772
08 #8	0.2363	0.5315	0.2566	0.6004	0.2015	0.2047	0.4933	1	0.186	0.1148	0.1221
09 #9	0.93	0.2628	0.6362	0.2899	0.8577	0.9551	0.0936	0.186	1	0.7054	0.6424
10 #10	0.6693	0.253	0.5434	0.2712	0.5756	0.7228	0.121	0.1148	0.7054	1	0.8061
11 #11	0.6275	0.2168	0.6153	0.2111	0.6262	0.6686	0.0772	0.1221	0.6424	0.8061	1
12 #12	0.9146	0.2163	0.6435	0.2422	0.8341	0.8967	0.0374	0.1693	0.9189	0.6574	0.6453
13 #13	0.7674	0.229	0.5318	0.2629	0.6623	0.8141	0.0829	0.1239	0.8072	0.875	0.817

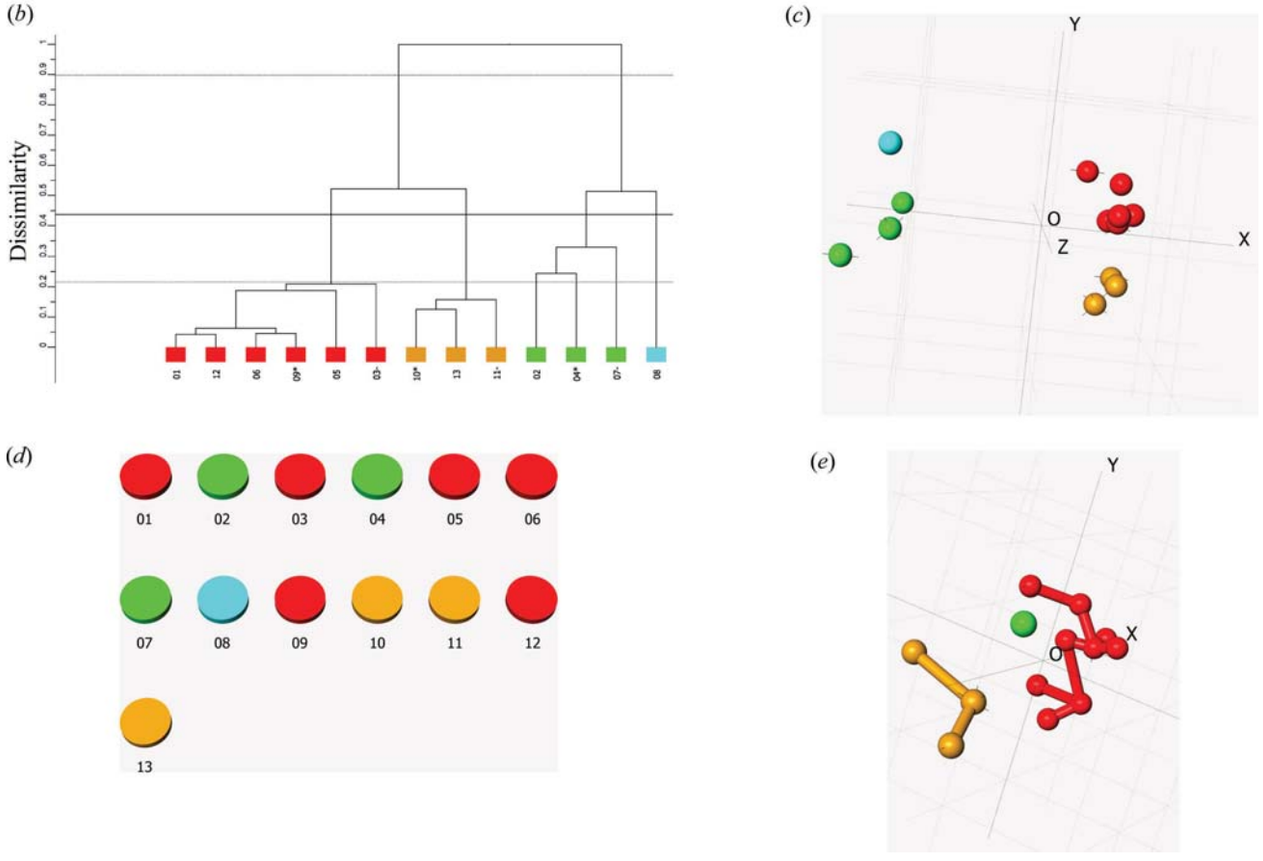

Figure 3.8.9
The complete cluster analysis for the aspirin samples. (*a*) The correlation matrix, which is the source of all the clustering results. The entries are colour coded: the darker the shade, the higher the correlation. (*b*) The dendrogram. The colours assigned to the samples are used in all the visualization tools. (*c*) The corresponding MMDS plot. The clustering defined by the dendrogram is well defined. (*d*) The pie-chart view. (*e*) The minimum spanning tree.

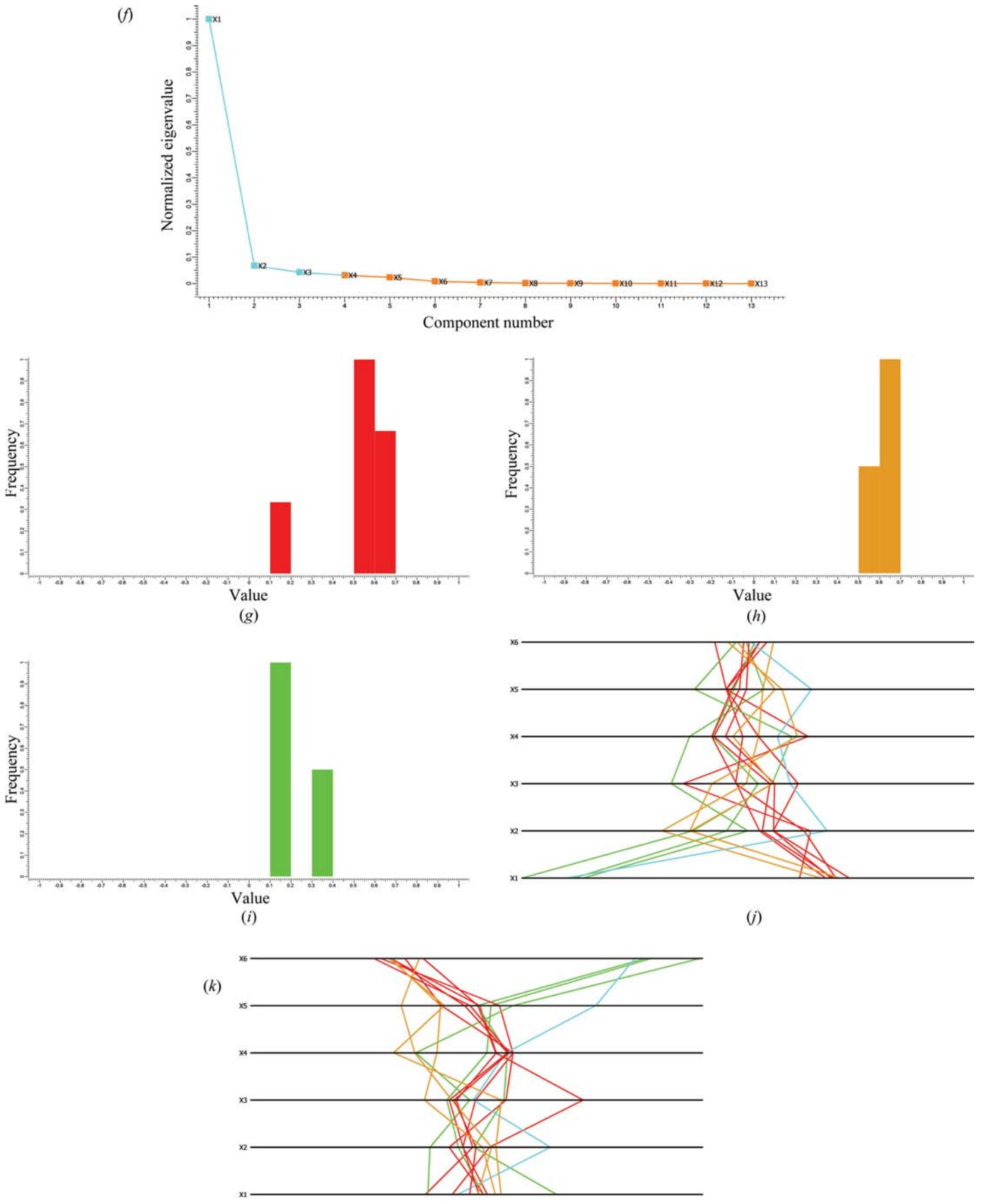

Figure 3.8.9 (continued)
The complete cluster analysis for the aspirin samples (continued). (*f*) The scree plot. It indicates that three clusters explain 95% of the variance of the distance matrix derived from (*a*). (*g–i*) The silhouettes for the red, the orange and the green clusters, respectively. These are discussed in detail in the caption to Fig. 3.8.8. (*j*) The default parallel-coordinates plot. The clusters are well maintained into the 4th, 5th and 6th dimensions. (*k*) Another view of the parallel coordinates using the grand tour. The clustering remains well maintained in higher dimensions.

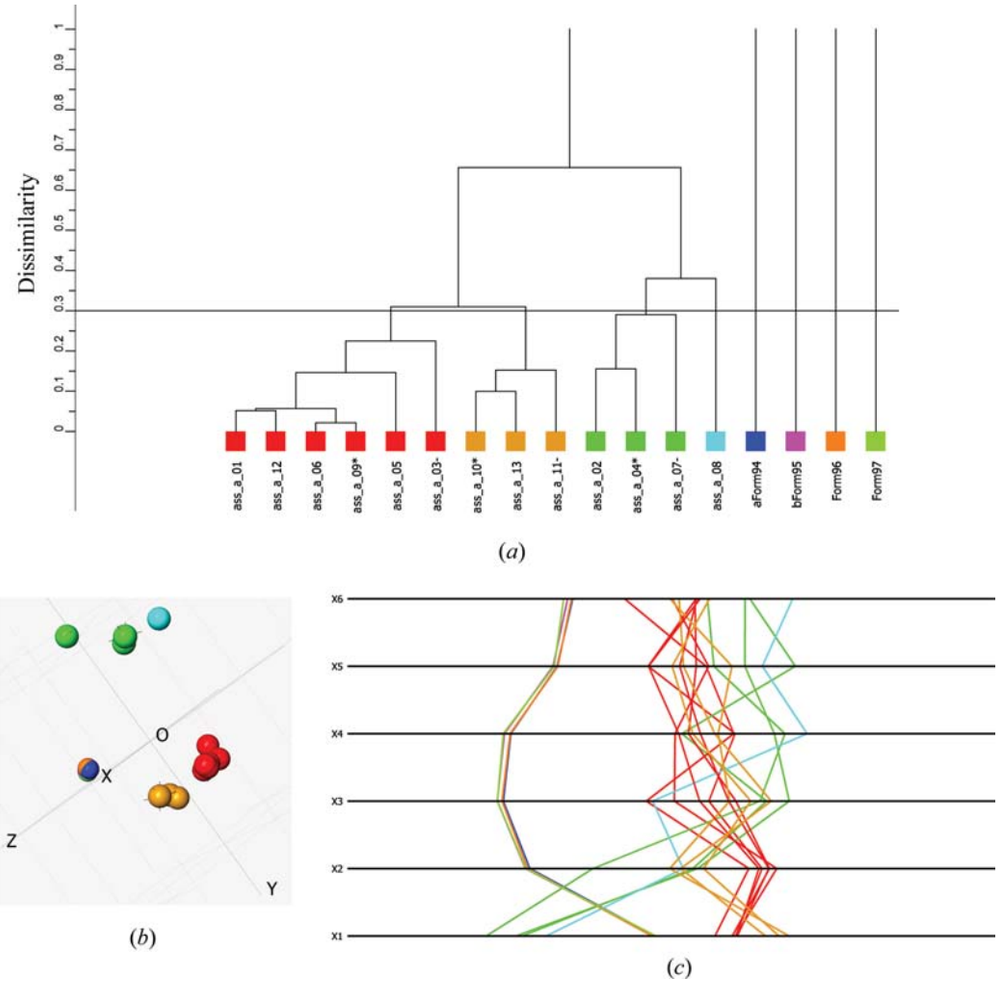

Figure 3.8.10
The aspirin data including data from five amorphous samples. (*a*) The resulting dendrogram and (*b*) the corresponding MMDS plot. (*c*) The parallel-coordinates plot.

$a = 7.14$, $b = 7.65$, $c = 5.83$ Å with $Z = 4$; between 357 and 398 K it crystallizes in the tetragonal space group $P\bar{4}2_1m$ with $a = 5.719$, $c = 4.932$ Å, $Z = 2$, and above 398 K it transforms to the cubic space group $Pm\bar{3}m$ with $a = 4.40$ Å and $Z = 1$. PXRD data containing 75 powder patterns taken at intervals of 3 K starting at 203 K using a D5000 Siemens diffractometer and Cu $K\alpha$ radiation with a 2θ range of 10–100° were used (Herrmann & Engel, 1997). Fig. 3.8.11(*a*) shows the data in the 2θ range 17–45°.

The visualization of these data following cluster analysis is shown in Fig. 3.8.11(*b*) using an MMDS plot on which has been superimposed a line showing the route followed by the temperature increments. The purple line follows the transition from a mixture of forms IV and V at low temperature (red) through form IV (yellow), form II (blue) and finally form I at high temperature (green). This is an elegant and concise representation of the data in a single diagram.

3.8.7. Quantitative analysis with high-throughput PXRD data without Rietveld refinement

Since mixtures are so common in high-throughput experiments, and indeed in many situations with multiple data sets, it is useful to have a method of automatic quantitative analysis. The quality of data that results from high-throughput crystallography makes it unlikely that an accuracy better than 5–10% can be achieved but, nonetheless, the identification of mixtures can be carried out by whole-profile matching. First a database of N pure phases is created, or, if that is not possible, then the most representative patterns with appropriate safeguards can be used. Assume that there is a sample pattern, S, which is considered to be a mixture of up to N components. S comprises m data points, $S_1, S_2, \ldots, S_m$. The N patterns can be considered to make up fractions $p_1, p_2, p_3, \ldots, p_N$ of the sample pattern. The best possible combination of the database patterns to fit the sample pattern is required. A system of linear equations can be constructed in which x_{11} is measurement point 1 of pattern 1 *etc.*:

$$\begin{aligned} x_{11}p_1 + x_{12}p_2 + x_{13}p_3 + \ldots + x_{1N}p_N &= S_1, \\ x_{21}p_1 + x_{22}p_2 + x_{23}p_3 + \ldots + x_{2N}p_N &= S_2, \\ &\vdots \\ x_{m1}p_1 + x_{m2}p_2 + x_{m3}p_3 + \ldots + x_{mN}p_N &= S_m. \end{aligned} \tag{3.8.26}$$

Writing these in matrix form, we get

$$\begin{bmatrix} x_{11} & x_{12} & x_{13} & \cdots & x_{1N} \\ x_{21} & x_{22} & x_{23} & \cdots & x_{2N} \\ \vdots & \vdots & \vdots & \ddots & \vdots \\ x_{m1} & x_{m2} & x_{m3} & \cdots & x_{mN} \end{bmatrix} \begin{bmatrix} p_1 \\ p_2 \\ \vdots \\ p_N \end{bmatrix} = \begin{bmatrix} S_1 \\ S_2 \\ \vdots \\ S_N \end{bmatrix} \tag{3.8.27}$$

or

$$\mathbf{xp} = \mathbf{S}. \tag{3.8.28}$$

A solution for S that minimizes

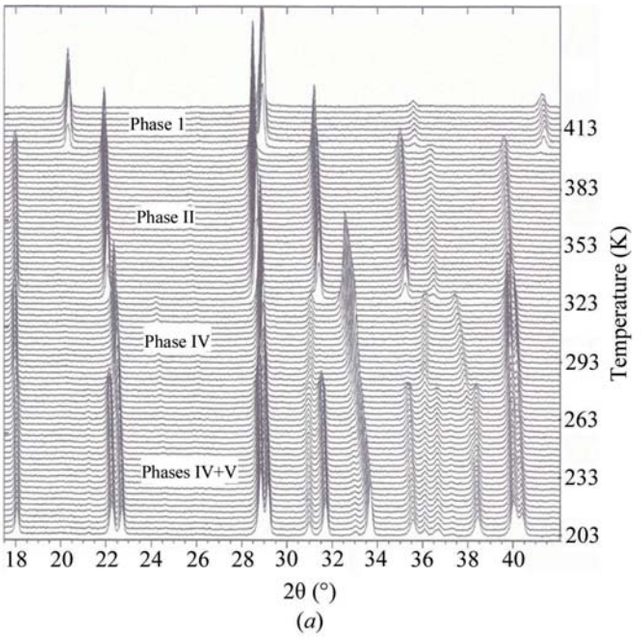

(*a*)

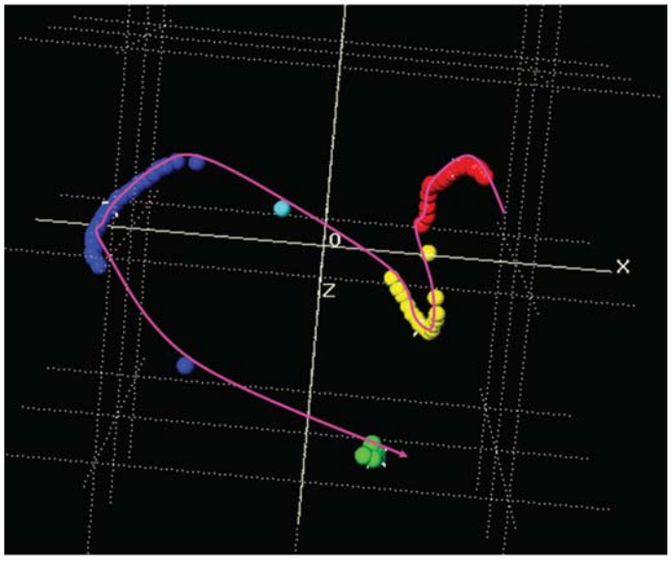

(*b*)

Figure 3.8.11
Ammonium nitrate phase transitions. (*a*) The raw powder data measured between 203 and 425 K. Reproduced with permission from Herrmann & Engel (1997). Copyright (1997) John Wiley and Sons. (*b*) The MMDS plot. The purple line follows the temperature change from 203 to 425 K.

$$\chi^2 = \left|\mathbf{xp} - \mathbf{S}\right|^2. \tag{3.8.29}$$

is required. Since $N \ll m$, the system is heavily overdetermined, and least-squares or singular value decomposition can be used to solve (3.8.29) for the fractional percentages arising from the scattering power of the component mixtures, $s_1, s_2, \ldots, s_N$. The values of s can be used to calculate a weight fraction for that particular phase provided that the atomic absorption coefficients are known, and this in turn requires the unit-cell dimensions and cell contents, but not the atomic coordinates (Smith *et al.*, 1988; Cressey & Schofield, 1996). The general formula for the weight fraction of component n in a mixture comprising N components is (Leroux *et al.*, 1953)

$$c_n = p_n \frac{\mu^*}{\mu_n^*}, \tag{3.8.30}$$

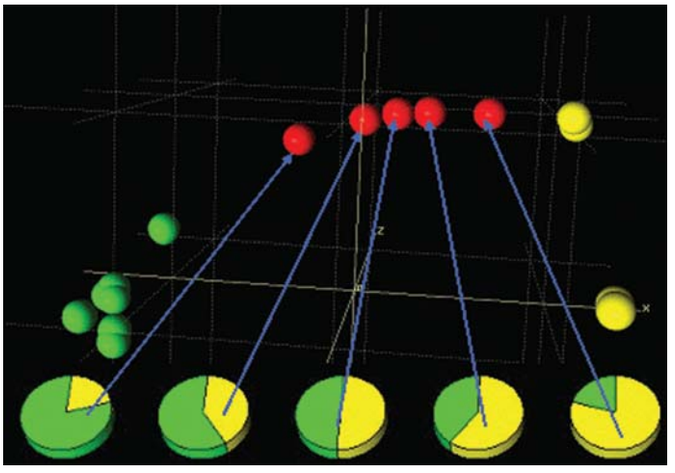

Figure 3.8.12
Identifying mixtures using lanthanum strontium copper oxide and caesium thiocyanate diffraction data taken from the ICDD Clay Minerals database. The green spheres represent pure phases of lanthanum strontium copper oxide and the yellow pure caesium thiocyanate. The red spheres represent mixtures of the two in the relative proportions of lanthanum strontium copper oxide/caesium thiocyanate 80/20, 60/40, 50/50, 40/60 and 20/80 in an arc commencing on the left-hand side of the diagram. The pie charts give the results of an independent quantitative calculation in which lanthanum strontium copper oxide and caesium thiocyanate have been included as pure phases in a reference database.

where

$$\mu^* = \sum_{j=1}^{N} c_j \mu_j^* \tag{3.8.31}$$

and

$$\mu_j^* = \mu_j / \rho_j, \tag{3.8.32}$$

where μ_j is the atomic X-ray absorption coefficient and ρ_j is the density of component j. For polymorphs, the absorption coefficients are sufficiently close and the method sufficiently approximate that the effects of absorption can be ignored.

3.8.7.1. *Example: inorganic mixtures*

As an example, a set of 19 patterns from set 78 of the ICDD database for inorganic compounds (ICDD, 2018) was imported into *DIFFRAC.EVA*. To this was added some simulated mixture data generated by adding the patterns for lanthanum strontium copper oxide and caesium thiocyanate in the proportions 80/20, 60/40, 50/50, 40/60 and 20/80. Two calculations were performed: an analysis without the pure-phase database and a second where the pure phases of lanthanum strontium copper oxide and caesium thiocyanate were present.

The results are shown in Fig. 3.8.12. In the MMDS plot the green spheres represent pure lanthanum strontium copper oxide while the yellow are pure caesium thiocyanate. The red spheres represent mixtures of the two. The latter form an arc between the green and yellow clusters. The distance of the spheres representing mixtures from the lanthanum strontium copper oxide and caesium thiocyanate spheres gives a semi-quantitative representation of the mixture contents. Running the analysis in quantitative mode gives the pie charts also shown in Fig. 3.8.12; they reproduce exactly the relative proportions of the three components.

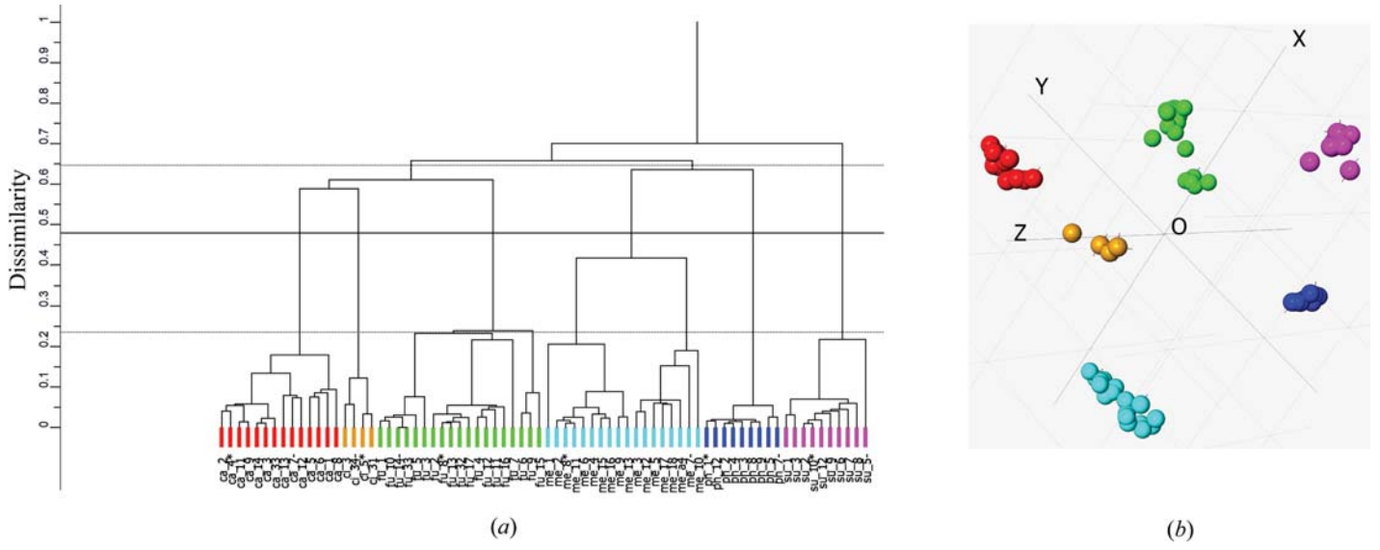

Figure 3.8.13
(*a*) The dendrogram generated from 74 Raman spectra without background corrections applied. Labelling from the left-hand side, the red samples are carbamazepine, the orange are cimetidene, the green are two forms of furosemide, the light blue is mefenamic acid, the dark blue is phenilbutazone and the purple at the right-hand side is sulfamerazine. (*b*) The MMDS plot. The sphere colours are taken from the dendrogram. This representation shows clearly discrete clusters in correspondence with those generated by the dendrogram.

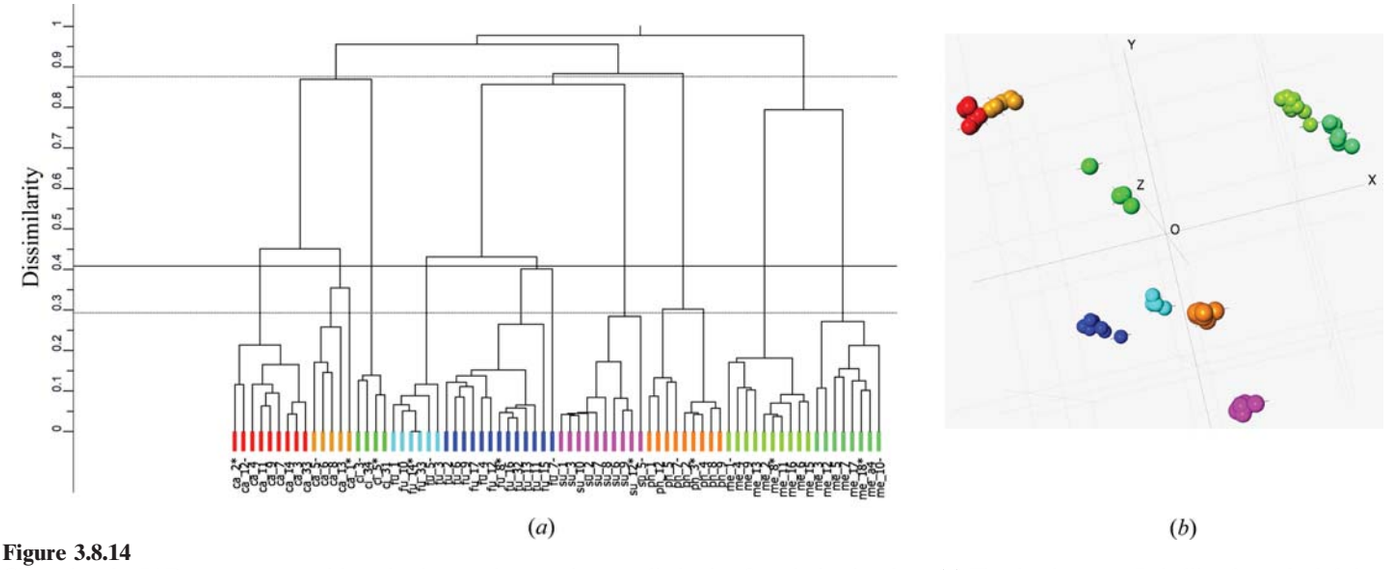

Figure 3.8.14
Clustering the 74 Raman spectra without background corrections applied using first-derivative data. (*a*) The dendrogram. Labelling from the left-hand side, the red and orange entries are carbamazepine; the green are cimetidene; the light blue and dark blue are two forms of furosemide; the purple are sulfamerazine; the brown are phenilbutazone and the right-hand light and dark green are two forms of mefenamic acid. (*b*) The MMDS plot. The clusters are well defined but the orange and red (both carbamazepine) are very close to each other.

For further details of this method with organic samples, see Dong *et al.* (2008).

3.8.8. Using spectroscopic data

There is no reason why the methodology described in this chapter cannot be used for other 1D data sets, *e.g.* Raman, IR, NMR and near-IR spectroscopies, although different data pre-processing is usually required. Raman spectroscopy is well suited to high-throughput screening: good-quality spectra can be collected in a few minutes, and sample preparation is straightforward and flexible, although the resulting spectra are not always as distinct as the PXRD equivalents (Mehrens *et al.*, 2005; Boccaleri *et al.*, 2007).

As an example we show the results of cluster analysis carried out on samples of carbamazepine, cimetidene, furosemide, mefenamic acid, phenilbutazone and sulfamerazine using Raman spectroscopy. A total of 74 samples were measured on a LabRam HR-800/HTS-Multiwell spectrometer at room temperature, equipped with a backscattering light path system of a light-emitting diode laser (785 nm, 300 mW) as an excitation source and an air-cooled charge-coupled device detector. A 20-fold superlong working distance objective lens was used to collect the backscattered light. The spectra were acquired with 5.84 cm^{-1} spectral width and at least 30 s exposure (Kojima *et al.*, 2006). The spectra had backgrounds subtracted but no other corrections were carried out.

The initial clustering is shown in Fig. 3.8.13(*a*) with the default cut level in the dendrogram. There are six clusters: labelling from the left-hand side, the red are three polymorphs of carbamazepine; the orange are cimetidene; the green cluster contains three polymorphs of furosemide; the light blue contains three poly-

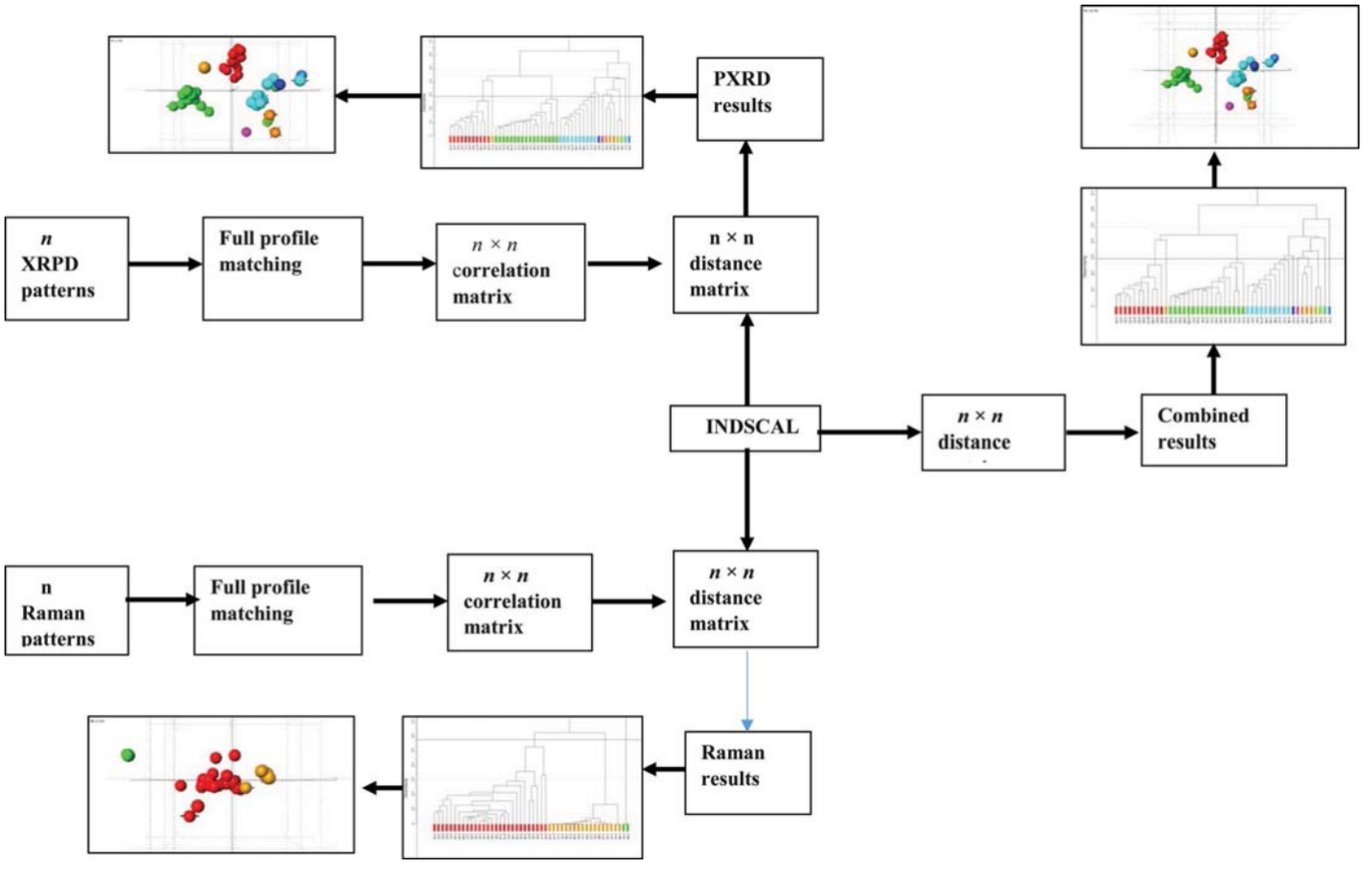

Figure 3.8.15
A flowchart for the INDSCAL method using Raman and PXRD data. Note that any combination of any 1D data can be used here.

morphs of mefenamic acid; the dark blue contains phenilbutazone; and finally the purple cluster contains sulfamerazine. The MMDS plot gives a complementary visualization of the data that supports the clustering.

It is also possible to use derivative data in place of the original spectra for clustering. The results of this for the 74 Raman spectra without initial background subtraction followed by the generation of first-derivative data are shown in Fig. 3.8.14. The clusters are well defined but now the carbamazepine data have split into two clusters. These correspond to forms I and III of carbamazepine, although the differences in the Raman spectra for these three species are small (O'Brien *et al.*, 2004). At the same time, both furosemide and mefenamic acid are each split into two groups. This is probably the best description of the data in terms of clustering and cluster membership corresponding to the chemical differences in the samples. The dendrogram also has the feature that the tie bars between samples are higher, *i.e.* the similarities are lower, reflecting the fact that the use of first derivatives accentuates small differences in the data.

It is interesting to note that, in general, PXRD works less well with derivative data. The reason for this is not clear, but possibly the presence of partial overlapping peaks and the associated issues of peak shape are partly responsible.

3.8.9. Combining data types: the INDSCAL method

It is now common to collect more than one data type, and some instruments now exist for collecting spectroscopic and PXRD data on the same samples, for example the Bruker D8 Screenlab, which combines PXRD and Raman measurement for high-throughput screening (Boccaleri *et al.*, 2007).

A technique for combining the results of more than one data type is needed. One method would be to take individual distance matrices from each data type and generate an average distance matrix using equation (3.8.3), but this leaves open the question of how best to define the associated weights in an optimal, objective way. Should, for example, PXRD be given a higher weight than Raman data? The individual differences scaling method (INDSCAL) of Carroll & Chang (1970) provides an unbiased solution to this problem by, as the name suggests, scaling the differences between individual distance matrices.

In this method, let $\mathbf{D}_k$ be the squared distance matrix of dimension $(n \times n)$ for data type k with a total of K data types. For example, if we have PXRD, Raman and differential scanning calorimetry (DSC) data for each of n samples, then $K = 3$. A group-average matrix $\mathbf{G}$ (which we will specify in two dimensions) is required that best represents the combination of the K data types. To do this, the $\mathbf{D}$ matrices are first put into inner-product form by the double-centring operation to give

$$\mathbf{B}_k = -\tfrac{1}{2}(\mathbf{I} - \mathbf{N})\mathbf{D}_k(\mathbf{I} - \mathbf{N}), \tag{3.8.33}$$

where $\mathbf{I}$ is the identity matrix and $\mathbf{N}$ is the centring matrix $I - \mathbf{1}\mathbf{1}'/N$; $\mathbf{1}$ is a column vector of ones. The inner-product matrices thus generated are matched to the weighted form of the group average, $\mathbf{G}$, which is unknown. To do this the function

$$S = \sum_{1}^{K} \left\| \mathbf{B}_k - \mathbf{G}\mathbf{W}_k^2\mathbf{G}' \right\| \tag{3.8.34}$$

is minimized. The weight matrices, $\mathbf{W}_k$, are scaled such that

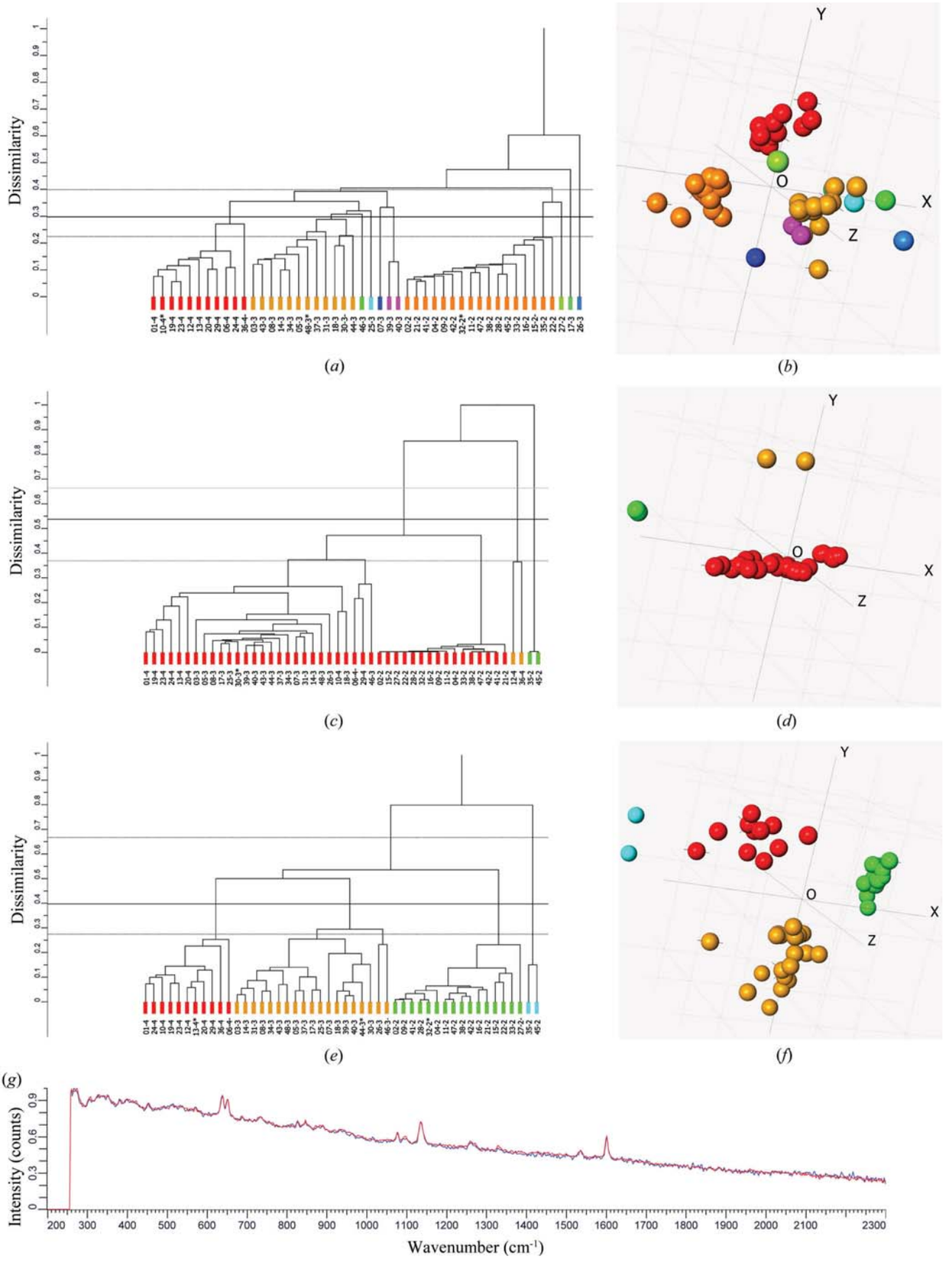

Figure 3.8.16
Clustering 48 PXRD spectra with background corrections applied for three polymorphs of sulfathiazole. (*a*) The dendrogram. Each sample is identified by a four-digit code. The first two digits are the well number, and the last digit defines whether the sample is form 2, 3 or 4 of sulfathiazole. (*b*) The MMDS plot: the red cluster is well defined but the rest of the spheres are diffuse and intermingled. (*c*) The dendrogram derived from clustering 48 Raman spectra of sulfathiazole with background corrections applied. (*d*) The corresponding MMDS plot. The clusters are poorly defined. (*e*) The results of the INDSCAL method. The dendrogram is shown with the default cut level. The clustering is correct; all the samples are placed in the correct group except for patterns 35-2 and 45-2. (*f*) The MMDS plot validates the dendrogram. (*g*) The Raman patterns for 35-2 and 45-2 superimposed. They are primarily background noise.

$$\sum_{k=1}^{K} \mathbf{W}_k^2 = K\mathbf{I}. \qquad (3.8.35)$$

The INDSCAL method employs an iterative technique to solve equation (3.8.7) in which one parameter is kept fixed whilst the other is determined by least-squares refinement. An initial estimate for **G** is taken either from the average of the **D** matrices for each sample or as a random matrix. This is then used to estimate the weight matrices, and the whole process repeated until a minimum value of S is obtained. The algorithm derived by Carroll and Chang was used in the example below. When random matrices are used to generate the initial **G** matrix, the INDSCAL procedure is repeated 100 times and the solution with the minimum value of S is kept. In practice, there is very little difference in the results of these two procedures. The resulting **G** matrix is used as a standard-distance matrix, and used in the standard way to generate dendrograms, MMDS plots *etc*. The method has the property that where data types show samples to be very similar this is reinforced, whereas where there are considerable variations the differences are accentuated in the final **G** matrix. For a fuller description of the INDSCAL method with examples see Gower & Dijksterhuis (2004), Section 13.2, and for a useful geometric interpretation see Husson & Pagès (2006).

3.8.9.1. *An example combining PXRD and Raman data*

We now present an example of the INDSCAL method applied to data collected on sulfathiazole using PXRD and Raman spectroscopy (Barr, Cunningham *et al.*, 2009). A flowchart is shown in Fig. 3.8.15. Three polymorphs of sulfathiazole were prepared and PXRD data were collected on a Bruker C2 GADDS system. Each sample was run for 2 min over a 3–30° range in 2θ using Cu $K\alpha$ radiation. Raman data were collected on a Bruker SENTINEL. The Raman probe was integrated into the PXRD instrument.

The only data pre-processing performed was background removal. Fig. 3.8.16(*a*) shows the resulting dendrogram (with the default cut level) and Fig. 3.8.16(*b*) shows the corresponding MMDS plot. To identify each sample they are numbered *via* a four-digit code: the first two digits are the well number, and the last digit defines whether the sample is form 2, 3 or 4 of sulfathiazole. It can be seen that the clustering is only partly successful: form 4 (red) is correctly clustered; form 3 (orange) gives five clusters and form 2 gives three clusters.

Fig. 3.8.16(*c*) shows the clustering from the Raman spectra. The results are poor: most of form 2 is correctly clustered, but forms 4 and 3 are intermixed, and the MMDS plot in Fig. 3.8.16(*d*) is diffuse with little structure.

The INDSCAL method is now applied starting from random **G** matrices and the results are shown in Fig. 3.8.16(*e*) and (*f*) with the dendrogram cut level at its default value. The clustering is almost correct; all the samples are placed in the correct groups except that there are two outliers coloured in blue. Fig. 3.8.16(*g*) shows the Raman patterns for these samples: they are primarily background with very little usable signal.

3.8.10. Quality control

Quality control (Gilmore, Barr & Paisley, 2009) is designed for situations where the stability of a material is being monitored over time, for example as part of a production-line system, or for periodic equipment alignment. A set of reference patterns is collected that represents acceptable measurements – any measurement sufficiently close to these references represents a good measurement. Various sample patterns are then imported and compared with those reference patterns, and any that vary significantly from the ideal are noted and highlighted.

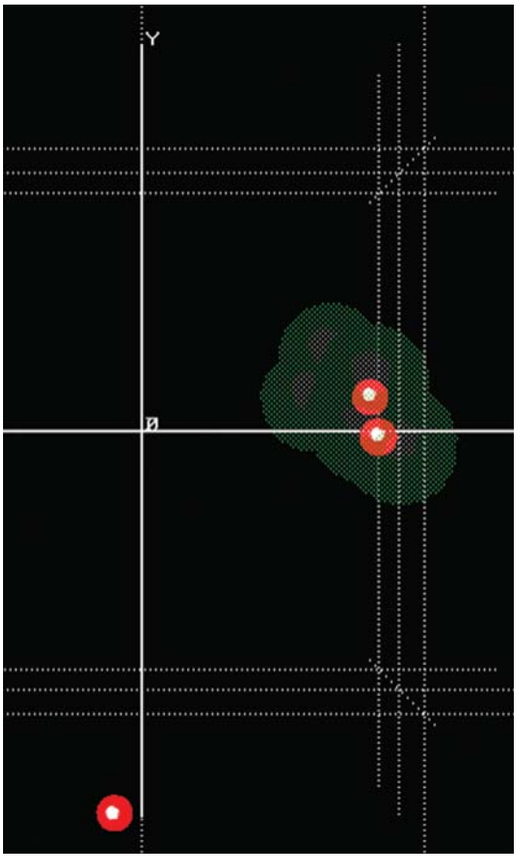

Figure 3.8.17
Visualization tools for quality-control procedures using a modified MMDS plot. The red outlier is a sample unacceptably far from the cluster of reference measurements.

The results are best displayed graphically using a variant of the MMDS method, of which an example is shown in Fig. 3.8.17. The reference patterns define a green shaded surface with acceptable sample patterns, coloured red, shown within it, and potentially problematic sample patterns appearing outside it. The volume of the green shape is defined by intersecting spheres around each reference sample and these can be altered to allow more- or less-stringent quality control.

3.8.11. Computer software

These calculations can be carried out using MATLAB (http://www.mathworks.co.uk/products/matlab/) or the open-source R software (http://www.r-project.org/; Crawley, 2007) with graphics using the *GGobi* software (Cook & Swayne, 2007). There are four commercial packages for handling powder data: *DIFFRAC.EVA* and *PolySNAP 3*, both from Bruker (http://www.bruker.com/; Gilmore, Barr & Paisley, 2004; Barr, Dong & Gilmore, 2009), *Jade* from Materials Data Inc. (http://www.materialsdata.com) and *HighScore* from Malvern PANalytical (http://www.panalytical.com/).

Data were kindly provided by Gordon Cunningham at Glasgow University, Arnt Kern of Bruker AXS in Karlsruhe and Michael Herrman at the Fraunhofer Institute, Germany.

References

Alvarez, A. J., Singh, A. & Myerson, A. S. (2009). *Polymorph screening: comparing a semi-automated approach with a high throughput method. Cryst. Growth Des.* **9**, 4181–4188.

Asimov, D. (1985). *The grand tour: a tool for viewing multidimensional data. SIAM J. Sci. Stat. Comput.* **6**, 128–143.

Barr, G., Cunningham, G., Dong, W., Gilmore, C. J. & Kojima, T. (2009). *High-throughput powder diffraction V: the use of Raman spectroscopy with and without X-ray powder diffraction data. J. Appl. Cryst.* **42**, 706–714.

Barr, G., Dong, W. & Gilmore, C. J. (2004*a*). *High-throughput powder diffraction. II. Applications of clustering methods and multivariate data analysis. J. Appl. Cryst.* **37**, 243–252.

Barr, G., Dong, W. & Gilmore, C. J. (2004*b*). *High-throughput powder diffraction. IV. Cluster validation using silhouettes and fuzzy clustering. J. Appl. Cryst.* **37**, 874–882.

Barr, G., Dong, W. & Gilmore, C. J. (2004*c*). *PolySNAP: a computer program for analysing high-throughput powder diffraction data. J. Appl. Cryst.* **37**, 658–664.

Barr, G., Dong, W. & Gilmore, C. J. (2009). *PolySNAP3: a computer program for analysing and visualizing high-throughput data from diffraction and spectroscopic sources. J. Appl. Cryst.* **42**, 965–974.

Barr, G., Dong, W., Gilmore, C. & Faber, J. (2004). *High-throughput powder diffraction. III. The application of full-profile pattern matching and multivariate statistical analysis to round-robin-type data sets. J. Appl. Cryst.* **37**, 635–642.

Barr, G., Gilmore, C. J. & Paisley, J. (2004). *SNAP-1D: a computer program for qualitative and quantitative powder diffraction pattern analysis using the full pattern profile. J. Appl. Cryst.* **37**, 665–668.

Boccaleri, E., Carniato, F., Croce, G., Viterbo, D., van Beek, W., Emerich, H. & Milanesio, M. (2007). *In situ simultaneous Raman/high-resolution X-ray powder diffraction study of transformations occurring in materials at non-ambient conditions. J. Appl. Cryst.* **40**, 684–693.

Bruker (2018). *DIFFRAC.EVA: software to evaluate X-ray diffraction data*. Version 4.3. https://www.bruker.com/eva.

Butler, B. M., Sila, A., Nyambura, K. D., Gilmore, C. J., Kourkoumelis, N. & Hillier, S. (2019). *Pre-treatment of soil X-ray powder diffraction data for cluster analysis. Geoderma*, **337**, 413–424.

Calinński, T. & Harabasz, J. (1974). *A dendritic method for cluster analysis. Commun. Stat.* **3**, 1–27.

Carroll, J. D. & Chang, J. J. (1970). *Analysis of individual differences in multidimensional scaling via n-way generalization of 'Eckhart–Young' decomposition. Psychometria*, **35**, 283–319.

Cook, D. & Swayne, D. F. (2007). *Interactive and Dynamic Graphics for Data Analysis with R and GGobi*. New York: Springer.

Cox, T. F. & Cox, M. A. A. (2000). *Multidimensional Scaling*, 2nd ed. Boca Raton: Chapman & Hall/CRC.

Crawley, M. J. (2007). *The R Book*. Chichester: Wiley.

Cressey, G. & Schofield, P. F. (1996). *Rapid whole-pattern profile-stripping method for the quantification of multiphase samples. Powder Diffr.* **11**, 35–39.

Dong, W., Gilmore, C., Barr, G., Dallman, C., Feeder, N. & Terry, S. (2008). *A quick method for the quantitative analysis of mixtures. 1. Powder X-ray diffraction. J. Pharm. Sci.* **97**, 2260–2276.

Donoho, D. L. & Johnstone, I. M. (1995). *Adapting to unknown smoothness via wavelet shrinkage. J. Am. Stat. Assoc.* **90**, 1200–1224.

Everitt, B. S., Landau, S. & Leese, M. (2001). *Cluster Analysis*, 4th ed. London: Arnold.

Gilmore, C. J., Barr, G. & Paisley, W. (2004). *High-throughput powder diffraction. I. A new approach to qualitative and quantitative powder diffraction pattern analysis using full pattern profiles. J. Appl. Cryst.* **37**, 231–242.

Goodman, L. A. & Kruskal, W. H. (1954). *Measures of association for cross-classifications. J. Am. Stat. Assoc.* **49**, 732–764.

Gordon, A. D. (1981). *Classification*, 1st ed., pp. 46–49. London: Chapman and Hall.

Gordon, A. D. (1999). *Classification*, 2nd ed. Boca Raton: Chapman and Hall/CRC.

Gower, J. C. (1966). *Some distance properties of latent root and vector methods used in multivariate analysis. Biometrika*, **53**, 325–328.

Gower, J. C. & Dijksterhuis, G. B. (2004). *Procrustes Problems*. Oxford University Press.

Herrmann, M. J. & Engel, W. (1997). *Phase transitions and lattice dynamics of ammonium nitrate. Propellants Explos. Pyrotech.* **22**, 143–147.

Husson, F. & Pagès, J. (2006). *INDSCAL model: geometrical interpretation and methodology. Comput. Stat. Data Anal.* **50**, 358–378.

ICDD (2018). *The Powder Diffraction File*. International Centre for Diffraction Data, 12 Campus Boulevard, Newton Square, Pennsylvania 19073-3273, USA.

Inselberg, A. (1985). *The plane with parallel coordinates. Vis. Comput.* **1**, 69–91.

Inselberg, A. (2009). *Parallel Coordinates. Visual multidimensional geometry and its applications.* New York: Springer.

Kaufman, L. & Rousseeuw, P. J. (1990). *Finding Groups in Data*. New York: Wiley.

Kojima, T., Onoue, S., Murase, N., Katoh, F., Mano, T. & Matsuda, Y. (2006). *Crystalline form information from multiwell plate salt screening by use of Raman microscopy. Pharm. Res.* **23**, 806–812.

Kruskal, J. B. (1956). *On the shortest spanning subtree of a graph and the traveling salesman problem. Proc. Am. Math. Soc.* **7**, 48–50.

Lance, G. N. & Williams, W. T. (1967). *A general theory of classificatory sorting strategies: 1. Hierarchical systems. Comput. J.* **9**, 373–380.

Leroux, J., Lennox, D. H. & Kay, K. (1953). *Direct quantitative X-ray analysis by diffraction absorption technique. Anal. Chem.* **25**, 740–743.

Mehrens, S. M., Kale, U. J. & Qu, X. (2005). *Statistical analysis of differences in the Raman spectra of polymorphs. J. Pharm. Sci.* **94**, 1354–1367.

Milligan, G. W. & Cooper, M. C. (1985). *An examination of procedures for determining the number of clusters in a data set. Psychometrika*, **50**, 159–179.

Nelder, J. A. & Mead, R. (1965). *A simplex method for function minimization. Comput. J.* **7**, 308–313.

O'Brien, L. E., Timmins, P., Williams, A. C. & York, P. (2004). *Use of in situ FT-Raman spectroscopy to study the kinetics of the transformation of carbamazepine polymorphs. J. Pharm. Biomed. Anal.* **36**, 335–340.

Ogden, R. T. (1997). *Essential Wavelets for Statistical Applications and Data Analysis*, pp. 144–148. Boston: Birkhäuser.

Press, W. H., Teukolsky, S. A., Vetterling, W. T. & Flannery, B. P. (2007). *Numerical Recipes*. 3rd ed. Cambridge University Press..

Rousseeuw, P. J. (1987). *Silhouettes: a graphical aid to the interpretation and validation of cluster analysis. J. Comput. Appl. Math.* **20**, 53–65.

Sato, M., Sato, Y. & Jain, L. C. (1966). *Fuzzy Clustering Models and Applications*. New York: Physica-Verlag.

Smith, D. K., Johnson, G. G. & Wims, A. M. (1988). *Use of full diffraction spectra, both experimental and calculated, in quantitative powder diffraction analysis. Aust. J. Phys.* **41**, 311–321.

Smrčok, Ľ., Ďurík, M. & Jorík, V. (1999). *Wavelet denoising of powder diffraction patterns. Powder Diffr.* **14**, 300–304.

Spearman, C. (1904). *The proof and measurement of association between two things. Am. J. Psychol.* **15**, 72–101.

Storey, R., Docherty, R., Higginson, P., Dallman, C., Gilmore, C., Barr, G. & Dong, W. (2004). *Automation of solid form screening procedures in the pharmaceutical industry–how to avoid the bottlenecks. Crystallogr. Rev.* **10**, 45–56.

Wegman, E. J. (1990). *Hyperdimensional data analysis using parallel coordinates. J. Am. Stat. Assoc.* **85**, 664–675.

International Tables for Crystallography (2018). Vol. H, Chapter 3.9, pp. 344–373.

3.9. Quantitative phase analysis

I. C. Madsen, N. V. Y. Scarlett, R. Kleeberg and K. Knorr

3.9.1. Introduction

The field of quantitative phase analysis (QPA) from powder diffraction data is almost as old powder diffraction itself. Debye and Scherrer first developed the method around 1916 (Debye & Scherrer, 1916, 1917) and between 1917 and 1925 Hull (1917, 1919) and Navias (1925) were reporting studies of QPA related to the new technique. However, further developments in QPA were relatively slow, as much of the activity in X-ray diffraction (XRD) at the time was dedicated to the solution of crystal structures rather than the extraction of other information present in a powder diffraction pattern. While a small number of QPA applications continued to be published in the intervening years, it was not until the advent of scanning diffractometers around 1947 (Langford, 2004, Parrish, 1965) and the work of Alexander and Klug in 1948 (Alexander & Klug, 1948), which provided the formal methodology and a practical approach, that the field began to expand.

Since those original developments, which utilized the intensity of individual peaks or a small group of peaks in the diffraction pattern, there have been extensions to the methodology that use whole-pattern approaches. These methods operate *via* the summation of either (i) patterns collected from pure components or (ii) component contributions calculated from their crystal structures. There are a number of benefits accruing from the whole-pattern approaches since all reflections in the pattern, which may number in the hundreds or thousands, now contribute to the final analysis.

The mathematical basis of QPA is well established and, ideally, QPA should be a relatively straightforward science. However, there are a significant number of factors, many of them experimental, that serve to decrease the accuracy that can be obtained (Chung & Smith, 2000). Some of these, such as accuracy and precision in measurement of peak position and intensity, resolution of overlapping peaks and counting statistics, relate to instrument geometry and data-collection conditions. Other sources of error derive from sample-related issues and include effects such as (i) preferred orientation (which distorts the observed relative intensities from those expected for a randomly oriented powder); (ii) crystallite size and strain broadening (leading to increased peak width and hence overlap); (iii) the grain-size effect (where there may be too few crystallites contributing to the diffraction process to ensure that a representative powder pattern can be measured);[1] and (iv) microabsorption (where phases that strongly absorb the incident and diffracted beams are underestimated with respect to weakly absorbing phases). Of these, microabsorption remains the largest impediment to accurate QPA and is more pronounced in X-ray diffraction than in neutron-based studies.

While there is a very broad scope for the application of diffraction-based estimation of phase abundance, the perceived difficulty involved in developing and using these methods often deters non-specialist users. Consequently, they may resort to other, non-diffraction, material characterization techniques that are more readily implemented.

Analytical techniques for most of the 92 naturally occurring elements are generally well established and, in many cases, the subject of internationally accepted standards. However, the physical properties of minerals and materials formed by these elements, and the manner in which they react, is not solely dependent on their chemical composition but also on how the constituent elements are arranged; that is, their crystal structures. This finite number of known elements combines in an almost infinite array within the 230 crystallographic space groups. Further variability is induced by factors such as solid solution, degree of crystallinity and morphology, thus making QPA by diffraction methods considerably more difficult to implement.

In industry, many manufacturing or processing lines are controlled by measurement of elemental composition alone, simply because these values can be readily obtained to a high degree of accuracy and precision. For example, a plant extracting Cu from an ore body might measure the Cu content of the feed ore and the concentrate, and the plant conditions are optimized based on efficiency of extraction. However, if the mineralogical form of the Cu changes in the feed, then it may not behave in the same manner during grinding, flotation and density separation, and this will affect the recovery. Frequently, where knowledge of the mineralogy or phase abundance is actually used in plant optimization and control, it is derived from bulk or microcompositional analysis rather than being measured directly. This is often achieved by normative calculation, where the results of element composition analysis are assigned to specific phases based on an assumed knowledge of individual phase composition. Further details of this approach can be found in Chapter 7.7.

In materials science, new compounds are being synthesized at a rapidly increasing rate with techniques such as high-throughput synthesis capable of generating hundreds of new variants in a single experiment. Such techniques are being used in fields ranging from drug discovery, catalyst synthesis and new metal alloy design. The properties of these materials, and their suitability for their designed purpose, are not only dependent on their structural form but, for multiphase materials, on the amount of each component present. In this case, accurate, or at the very least reproducible, QPA is crucial to the screening process.

This chapter focuses on the application of QPA techniques for the extraction of phase abundance from diffraction data. While there is extensive coverage of the QPA methodology in other texts (Klug & Alexander, 1974; Smith *et al.*, 1987; Snyder & Bish, 1989; Zevin & Kimmel, 1995), some of the more commonly used approaches will be described here along with examples of their use in practical applications.

3.9.2. Phase analysis

There are a number of traditional methods for the estimation of phase abundance in multiphase materials (Zevin & Kimmel, 1995). In summary, these can be divided into two groups:

[1] It is worth noting that the grain-size effect becomes even more of an issue as the divergence of the instrument is decreased with, for example, high-resolution laboratory or synchrotron-based instruments, since fewer crystallites are likely to meet the diffraction condition.

(1) *Indirect methods* – these are usually based on the measurement of total chemical composition, which is then apportioned according to an assumed composition for each phase. A very widely used form of this normative calculation approach is the Bogue method (Bogue, 1929) for the quantitative estimation of Portland cement phases. The limitations in this approach arise when the actual compositions of individual phases vary from those assumed in the calculation. This frequently occurs in the cement industry, where variance in local materials and production conditions can affect detailed phase compositions. Normative calculation has the potential to be unstable when a number of phases in the mixture have similar chemical composition and it cannot be used at all for the limiting case of polymorphs that have identical chemical composition.

(2) *Direct methods* – these are based on a property that is specific to phases of interest in the sample. These methods are often not generally applicable to the entire sample, but are useful in estimating abundances of selected components. Examples include:

   (*a*) Magnetic susceptibility – this is applicable to samples in which component phases have different magnetic properties. The magnetic component can be separated and weighed to determine its weight fraction in the starting material. This approach assumes that the magnetic phase is well separated from non-magnetic phases and accuracy will be reduced when there is a fine inseparable intergrowth of magnetic and non-magnetic components.

   (*b*) Selective dissolution – where the rate and extent of dissolution can be phase dependent, and the weight fraction of the residue is used to determine the fractions of soluble and insoluble components.

   (*c*) Density – involves the physical separation of phases with different densities. As with magnetic separation, this approach assumes that the phase of interest is well separated from other phases.

   (*d*) Image analysis – optical microscopy using thin sections is still frequently used for the analysis of mineralogical samples. Thin sections can be time consuming to prepare and analyse, and the observations can be highly subjective depending on the analyst's experience. While automated image analysis of optical and electron-beam images brings more consistency to the estimation of phase abundance, issues in stereology may still affect the determined phase abundances.

   (*e*) Thermal analysis – where the magnitude of endo- and exothermic features during phase transitions are proportional to the amount of the phases present. This can be effective for well known and characterized phases, but is less useful for new phases or complex multiphase samples where there may be significant overlap in the features in the observed patterns. There may also be difficulty in distinguishing features related to individual minerals, for example H_2O evolution from co-existing hydrated minerals.

   (*f*) Infrared (IR) techniques – these are gaining in popularity, especially in mineral exploration environments because of their portability, speed and ability to measure directly from a cleaned drill core or section. However, because the IR beam only penetrates 1–2 μm into the sample, it is a surface-analysis technique providing a semi-quantitative analysis at best. To work effectively, the method needs to be calibrated using other techniques such as diffraction-based phase analysis.

   (*g*) Powder diffraction may be included in the direct-methods category, as it distinguishes and quantifies phases on the basis of their unique crystal structures, giving the technique broad applicability for crystalline materials.

Quantification from powder diffraction data is reliant on determination of the contribution to the final pattern of each component phase in a mixture. Commonly used methods can be divided into two distinct groups:

(1) The traditional 'single-peak' methods, which rely on the measurement of the intensity of a peak, or group of peaks, for each phase of interest and assumes that the intensity of these peaks is representative of the abundance of the individual phases. This is often not the case because of peak overlap and phase-dependent factors, such as preferred orientation and microabsorption, which affect the relative observed intensities.

(2) Whole-pattern methods, which rely on the comparison of observed diffraction data over a wide range of 2θ with a calculated pattern formed from the summation of individual phase components which have either been (i) measured from pure phase samples, or (ii) calculated from crystal-structure information.

3.9.3. QPA methodology

The integrated intensity $I_{(hkl)\alpha}$ of reflection *hkl* for phase α in a multiphase mixture, measured on a flat-plate sample of infinite thickness using a diffractometer with Bragg–Brentano geometry, is given by (Snyder & Bish, 1989; Zevin & Kimmel, 1995; Madsen *et al.*, 2013)

$$I_{(hkl)\alpha} = \left[\frac{I_0\lambda^3}{32\pi r}\frac{e^4}{m_e^2c^4}\right] \times \left[\frac{M_{hkl}}{2V_\alpha^2}\left|F_{(hkl)\alpha}\right|^2\left(\frac{1+\cos^2 2\theta\cos^2 2\theta_m}{\sin^2\theta\cos\theta}\right)\exp\left(-2B(\sin\theta/\lambda)^2\right)\right] \times \left[\frac{W_\alpha}{\rho_\alpha\mu_m^*}\right], \quad (3.9.1)$$

where I_0 is the incident-beam intensity, λ is the wavelength, e is the charge on an electron, m_e is the mass of an electron, r is the distance from the scattering electron to the detector and c is the speed of light. M_{hkl} and F_{hkl} are the multiplicity and structure factor of the *hkl* reflection, respectively, V_α is the unit-cell volume of phase α, and θ and θ_m are the diffraction angles for the *hkl* reflection and the monochromator (if present), respectively. B is the mean atomic displacement parameter (ADP). W_α and ρ_α are the weight fraction and density of phase α respectively, while μ_m^* is the mass absorption coefficient of the entire sample.

3.9.3.1. *Absorption–diffraction method*

The various terms in equation (3.9.1) are related to the (i) instrument configuration (first set of square brackets), (ii) crystal-structure-related parameters for reflection *hkl* of phase α (second set of square brackets), and (iii) phase-specific and whole-sample parameters including the weight fraction W_α for phase α (last set of square brackets).

The instrument-related and phase-dependent parameters, including phase density, can be grouped together and defined as a constant $C_{i\alpha}$ for the ith reflection of phase α for a specific set of

measurement conditions. This greatly simplifies the relationship between reflection intensity and weight fraction to

$$I_{i\alpha} = C_{i\alpha}\frac{W_\alpha}{\mu_m^*}. \quad (3.9.2)$$

On rearrangement, the weight fraction can be derived from

$$W_\alpha = \frac{I_{i\alpha}\mu_m^*}{C_{i\alpha}}. \quad (3.9.3)$$

Application of equation (3.9.3) (Klug & Alexander, 1974), referred to as the absorption–diffraction method, requires:

(1) the determination of $C_{i\alpha}$ using a rearranged equation (3.9.3) by (i) the preparation of standards with known additions W of phase α_α, (ii) measurement of peak intensity $I_{i\alpha}$ for the standards, and (iii) estimation of the standard sample mass absorption coefficient μ_m^*;
(2) measurement of $I_{i\alpha}$ and estimation of μ_m^* for the unknown samples; and
(3) calculation of W_α *via* equation (3.9.3).

The value of μ_m^* can be estimated by direct measurement of the beam intensity through a sample of known thickness t in a beam of the same wavelength as that used in the XRD data collection. Following measurement of the beam intensity with the sample in (I) and removed from (I_0) the beam, μ_m^* can be calculated using

$$\frac{I}{I_0} = \exp(-\mu_m^*\rho_m t). \quad (3.9.4)$$

However, this usually involves (i) the preparation of an additional, thinner, sample for presentation to the X-ray beam, (ii) in some cases, the addition of a diluent with a low mass absorption coefficient to produce I/I_0 ratios in a range where reasonable accuracy can be achieved, and (iii) knowledge of the 'mass thickness' $\rho_m t$. It should also be noted that there are few commercially available instruments that would be suitable for such measurements due to safety-related issues in accessing the X-ray beam path.

An alternative approach is to calculate μ_m^* from the sum of the products of the theoretical mass absorption coefficient (μ_j^*) of each element (or phase) and the weight fractions (W_j) of all n elements (or phases) in the sample. The elemental composition may be determined, for example, by X-ray fluorescence (XRF) measurement and its use is more accurate than the use of phase composition as it takes into account any amorphous material not represented by peaks in the diffraction pattern but which still contributes to μ_m^*,

$$\mu_m^* = \sum_{j=1}^{n}\mu_j^* W_j. \quad (3.9.5)$$

3.9.3.2. *Internal standard method*

A more general, and experimentally simpler, approach is to eliminate μ_m^* from the analysis altogether *via* the inclusion of an internal standard s in known weight fraction W_s. Substitution of the measured intensity of the jth peak (or group of peaks) of the standard phase, I_{js}, into equation (3.9.2) yields

$$I_{js} = C_{js}\frac{W_s}{\mu_m^*}. \quad (3.9.6)$$

The ratio of equations (3.9.2) and (3.9.6) gives

$$\frac{I_{i\alpha}}{I_{js}} = \frac{C_{i\alpha}}{C_{js}}\frac{W_\alpha}{W_s}. \quad (3.9.7)$$

Since μ_m^* now appears both in the numerator and denominator, its effect on the analysis, and hence the need to measure or calculate it, is removed from the calculation. Rearrangement of equation (3.9.7) yields

$$\frac{I_{i\alpha}}{I_{js}}\frac{W_s}{W_\alpha} = \frac{C_{i\alpha}}{C_{js}} = C_{js}^{i\alpha}, \quad (3.9.8)$$

where $C_{js}^{i\alpha}$ is a calibration constant specific to the phase and internal standard used. Once $C_{js}^{i\alpha}$ has been determined, the weight fraction of the unknown, W_α, can then be determined from

$$W_\alpha = \frac{W_s}{C_{\alpha s}^{ij}}\frac{I_{i\alpha}}{I_{js}}. \quad (3.9.9)$$

This approach, referred to as the *internal standard method*, relies on the determination of $C_{\alpha s}^{ij}$ using known mixtures of standard and analyte phases. The value of $C_{\alpha s}^{ij}$ will be specific to the diffraction peaks used in its determination; if other lines are used in subsequent analysis, then an appropriate value of C will have to be redetermined.

It should be noted that the presence of systematic errors (such as preferred orientation and microabsorption) that influence the measurement of intensity and vary as a function of W_α will not be detected through application of equation (3.9.9). The use of consistent sample-preparation and presentation techniques is required to minimize the effect of these aberrations on the analysis (Zevin & Kimmel, 1995).

3.9.3.2.1. *Selection of an internal standard*

The selection of an appropriate material for use as an internal standard for QPA is not always straightforward. Ideally, the material selected should:

(1) Have a simple diffraction pattern resulting in minimal overlap with peaks of interest in the sample.
(2) Have a mass absorption coefficient similar to that of the sample to avoid introducing microabsorption effects and thus reducing accuracy.
(3) Have minimal sample-related aberrations that may affect observed intensities. For example, it should be fine-grained to ensure minimal grain-size effects on the observed intensities and not be subject to preferred orientation. Importantly, it should have 100% (or known) crystallinity.
(4) Be stable over an extended time and be unreactive, especially for *in situ* studies where it may be subjected to extreme conditions.

Some possibilities for use as internal standard include α-Al_2O_3 (corundum), TiO_2 (rutile), ZnO (zincite), Cr_2O_3 (eskolaite), α-Fe_2O_3 (haematite), CeO_2 (cerianite), CaF_2 (fluorite) and C (diamond). Cline *et al.* (2011) have described the certification of the standard reference material SRM 676a with accurately known amorphous content for use as an internal standard for QPA (see Chapter 3.1). Alternatively, it is possible to use an independent measure (*e.g.* chemical analysis) to derive the concentration of a phase already present in the sample and then to designate it as the internal standard.

Selection of the amount of internal standard to add is often based on folklore or local practices with reported additions ranging from 5 to 50 wt%. Westphal *et al.* (2009) have described the mathematical basis for selecting the optimal internal standard addition in the context of amorphous phase determination. The

amount of internal standard added has a strong influence on the precision of the determination of amorphous content and 'a poor choice can make determination impossible, while a clever choice can enhance the precision'.

With the exception of diamond, all of the phases listed above tend to have absorption coefficients that are too high for use with organic materials. The development and verification of a suitable low-absorption-coefficient standard material that meets the criteria given above remains an important area of research.

3.9.3.3. *Reference intensity ratio methods*

The reference intensity ratio (RIR) (Hubbard *et al.*, 1976; Hubbard & Snyder, 1988) is an instrument-independent phase constant developed specifically for use in quantitative phase analysis and is defined as the ratio of strongest peak of phase α to the strongest peak of standard s. The RIR can be derived directly from equation (3.9.8):

$$\mathrm{RIR}_{\alpha s} = C_{js}^{i\alpha} = \frac{I_{i\alpha}}{I_{js}} \frac{W_s}{W_\alpha}. \tag{3.9.10}$$

In some cases, the strongest lines of either the standard or phase of interest may not be accessible for measurement if, for example, they strongly overlap with peaks from another phase or if they are out of the 2θ range considered. Equation (3.9.10) can be generalized (Hubbard & Snyder, 1988) to use less intense peaks while keeping the same value of RIR:

$$\frac{I_{i\alpha}}{I_{js}} \frac{I_{js}^{\mathrm{rel}}}{I_{i\alpha}^{\mathrm{rel}}} \frac{W_s}{W_\alpha} = \mathrm{RIR}_{\alpha s}, \tag{3.9.11}$$

where I^{rel} is the ratio of the intensity of the peak used for analysis to the most intense peak for the phase. $\mathrm{RIR}_{\alpha,s}$ is now the generalized reference intensity ratio for phase α with respect to standard s.

Quantification of the unknown phase in the presence of a known standard addition can be achieved by the rearrangement of equation (3.9.11):

$$W_\alpha = \frac{I_{i\alpha}}{I_{js}} \frac{I_{js}^{\mathrm{rel}}}{I_{i\alpha}^{\mathrm{rel}}} \frac{W_s}{\mathrm{RIR}_{\alpha s}}. \tag{3.9.12}$$

The generally accepted reference material for QPA *via* the RIR method is corundum because of its relatively simple diffraction pattern, stability and availability as a highly crystalline and pure single phase. If corundum is used, the RIR equates to I/I_c (or 'I over I corundum') for the phase; these are the most commonly reported values in the literature.

RIRs can be determined either by (i) calculation using published crystal-structure information with Rietveld analysis software set to pattern-calculation mode, or (ii) direct measurement by taking the ratio of the strongest peak of the pattern to the intensity of the strongest peak of corundum in a 50/50 weight mixture [or through use of equation (3.9.11) for non-equal proportions]. However, for some phases, there can be ambiguity about which peak is the most intense. For example, the 104 (2.551 Å) and 113 (2.085 Å) peaks of corundum have very similar observed intensities, as do the 111 (3.154 Å) and 022 (1.932 Å) peaks of fluorite. This may lead the analyst to select a peak different from that chosen for reported RIR values.

Collated lists of RIR values for frequently encountered phases can be found in the ICDD database (Fawcett *et al.*, 2017) and Smith *et al.* (1987). It is important to note, however, that the user must be very careful when selecting an appropriate RIR value for their particular experiment. The values of RIR will depend upon the data-collection and measurement strategy employed (for example, peak height, integrated peak area, whole pattern, X-ray wavelength employed and so on) in their derivation. This must match the conditions used in the experiment to which the value is to be applied. In general, RIR values should be determined for the material currently being studied using the methodologies employed rather than relying on published values. Greater accuracy will be achieved if the relative intensities are determined as part of the calibration process using pure samples of the phase and standard or, preferably, samples in which the phases of interest have high and known concentration. If published values of RIR are used, then the determined phase abundances must be referred to as being only semi-quantitative.

3.9.3.4. *Matrix-flushing method*

An important feature of RIR-based techniques is that, once the RIRs are determined for the analyte phases of interest, the standard phase does not need to be present in the sample. The effect of the sample mass absorption coefficient is also removed by taking the ratio of the intensity of phase α to another unknown phase β. Hence the ratio of the weight fractions of the two phases can be derived from

$$\frac{W_\alpha}{W_\beta} = \frac{I_{i\alpha}}{I_{j\beta}} \frac{I_{j\beta}^{\mathrm{rel}}}{I_{i\alpha}^{\mathrm{rel}}} \frac{\mathrm{RIR}_{\beta s}}{\mathrm{RIR}_{\alpha s}}. \tag{3.9.13}$$

For a system comprising n phases, equation (3.9.13) allows the derivation of $n - 1$ weight fraction ratios. Chung (1974*a*,*b*) has demonstrated that, if all components are crystalline and included in the analysis, an additional constraint of the following form can be included:

$$\sum_{k=1}^{n} W_k = 1.0. \tag{3.9.14}$$

This forms a system of n linear equations which can be solved to give the weight fractions of all components in the analysis according to (Chung, 1974*a*,*b*; Snyder & Bish, 1989)

$$W_\alpha = \frac{I_\alpha}{\mathrm{RIR}_{\alpha s} I_\alpha^{\mathrm{rel}}} \left(\sum_{k=1}^{n} \frac{I_k}{\mathrm{RIR}_{ks} I_k^{\mathrm{rel}}} \right)^{-1}. \tag{3.9.15}$$

The weight fractions analysed *via* this method are correct relative to each other but may not be correct in an absolute sense if unidentified or amorphous materials are present in the sample. In this case, the reported phase abundances will be overestimated. The addition of an internal standard to the system, or knowledge of the amount of a component phase determined by another technique, allows calculation of the absolute amount $W_{\alpha(\mathrm{abs})}$ of each phase [equation (3.9.16)] and thus the derivation of the amount W_{unk} of unknown (amorphous and/or unidentified) components [equation (3.9.17)].

$$W_{\alpha(\mathrm{abs})} = W_\alpha \times \frac{W_{\mathrm{std(known)}}}{W_{\mathrm{std(meas)}}}, \tag{3.9.16}$$

$$W_{\mathrm{unk}} = 1.0 - \sum_{k=1}^{n} W_{k(\mathrm{abs})}, \tag{3.9.17}$$

where $W_{\alpha(\mathrm{abs})}$ is the absolute weight fraction of phase α, $W_{\mathrm{std(known)}}$ is the known weight fraction of the standard added to the sample, $W_{\mathrm{std(meas)}}$ is the weight fraction of the standard

reported by equation (3.9.15) and W_{unk} is the weight fraction of the unidentified and/or amorphous component in the mixture.

If an internal standard has been used, then initial calculation of its concentration *via* equation (3.9.15) may be:

(i) the same as the weighed amount, indicating that there are unlikely to be amorphous or unidentified phases present;
(ii) greater than the weighed amount, indicating that amorphous or unidentified phases may be present; or
(iii) less than the weighed amount, indicating operator error or the use of invalid RIR or I^{rel} values.

3.9.3.5. *Full-pattern fitting methods*

The quantitative XRD techniques described above have traditionally been applied using phase intensity estimates derived from either single peaks or a small group of peaks. This approach can be effective when there is minimal peak overlap but becomes less useful in complex phase systems where it may be difficult to identify freestanding peaks in the pattern. In addition, the presence of sample-related effects such as preferred orientation skew the measured intensities from what would be expected from an ideal powder diffraction pattern, thus reducing the expected accuracy.

Some of these effects can be partially overcome by using full-pattern fitting methods (Smith *et al.*, 1987; Batchelder & Cressey, 1998; Chipera & Bish, 2002, 2013; Eberl, 2003; Toraya & Tsusaka, 1995; Cressey & Schofield, 1996), where wide-range diffraction patterns of phases of interest are scaled, summed and compared with the observed diffraction data in a least-squares minimization process. The method relies on the generation of a library of standard patterns for each phase expected in the analysis collected under the same instrumental conditions as those used in subsequent analyses. The selection of standards that are a good match for the phases in the unknown sample is a critically important step. While the library will normally contain patterns of well ordered phases, it can also include patterns for less well ordered material such as glasses, polymers, clay minerals and gels, thus allowing their direct quantification. Where it is not possible to obtain a measured pattern, calculated patterns may also be included in the library.

Weight fractions are obtained by the solution of simultaneous equations that take into account the scale factors of the individual components and the mass absorption coefficients derived from knowledge of the elemental composition of each phase.

Alternatively, the contribution of library patterns to observed data can be normalized by scaling phases to an internal standard, typically corundum, using an RIR approach. Given the compositional and structural variability of some phases, especially in mineralogical applications, RIRs measured using the same minerals as those to be analysed are preferred to reported RIRs. Toraya (Toraya 2016*a*,*b*) has devised a QPA method which uses observed integrated peaks intensities measured of a wide 2θ range. Phase calibration constants are calculated using only their chemical formula weight and the sum of the square of the number of electrons in the formula unit. While the method is effective for wide-range data, it cannot be applied to single-peak data or data that cover only a limited 2θ range.

The full-pattern fitting method is relatively easy to use and can be applied to difficult samples containing highly disordered materials. For some disordered phases where no crystal structure is available and where peak overlap means that individual peak intensities cannot be measured, full-pattern fitting may be the most appropriate approach to QPA. The major limitations of the method include the need (i) to define and subtract the pattern background, with a subsequent impact on QPA, and (ii) to obtain or generate a library of standard patterns of the phases of interest. The use of an internal standard is recommended and the method is best applied when all standard patterns have first been normalized to an internal standard intensity (Chipera & Bish, 2002, 2013).

3.9.3.6. *Rietveld-based QPA*

The advent of the Rietveld method (Rietveld, 1969) and its extension into the field of QPA (Bish & Howard, 1988; Hill, 1983; Hill & Howard, 1987; O'Connor & Raven, 1988; Taylor, 1991) has brought some significant benefits when compared with the conventional single-peak and pattern-addition methods. Recent surveys (Madsen *et al.*, 2001; Scarlett *et al.*, 2002) show that the majority of participants, greater than 75%, use a Rietveld-based approach for QPA. The benefits derive from (Hill, 1991; Kaduk, 2000):

(i) The use of the entire diffraction pattern. Depending on the 2θ range of the data and the crystallography of the component phases, this may involve hundreds or thousands of reflections rather than the few peaks in conventional methods. This helps to minimize the impact of some systematic sample-related effects such as preferred orientation and extinction.
(ii) The ability to accurately deconvolute overlapping peaks to extract the component intensities, thus allowing more complex patterns to be analysed. The development of fundamental-parameters models (Bergmann *et al.*, 1998, 2000; Cheary & Coelho, 1992; Cheary *et al.*, 2004), which aim to distinguish instrument from sample contributions to the diffraction pattern, minimizes the number of profile parameters that need to be refined, further enhancing this profile-fitting step.
(iii) Refinement of the crystal structure, when supported by the data, to minimize differences between the intensities in the calculated and observed patterns. This brings additional information such as systematic changes in structure parameters from published data.
(iv) The ability to model some remaining systematic effects such as preferred orientation or anisotropic crystallite size/strain peak broadening.

The Rietveld method uses a least-squares procedure to minimize the difference between a calculated pattern and the measured data. The calculated pattern is derived from a model containing crystal-structure information for each phase included in the analysis, convoluted with expressions describing peak shape and width, along with functions to correct systematic variances such as preferred orientation. The calculated pattern is multiplied by an overall scaling factor which may be equated to the peak intensities ($I_{i\alpha}$) considered by the single-peak methods. The Rietveld scale factor for phase α, S_α, can be defined as (Bish & Howard, 1988; Hill, 1991; Hill & Howard, 1987; O'Connor & Raven, 1988)

$$S_\alpha = \left[\frac{K}{V_\alpha^2}\right]\left[\frac{W_\alpha}{\rho_\alpha}\right]\frac{1}{2\mu_m^*}, \qquad (3.9.18)$$

where K is an 'experiment constant' used to put W_α on an absolute basis, and V_α, W_α and ρ_α are the volume of the unit cell, the weight fraction and the density for phase α, respectively.

Since equation (3.9.18) inherently contains the weight-fraction information, it can be rearranged to derive W_α:

$$W_\alpha = \frac{S_\alpha \rho_\alpha V_\alpha^2 \mu_m^*}{K}. \quad (3.9.19)$$

O'Connor & Raven (1988) and Bish & Howard (1988) have shown that K is dependent only on the instrumental conditions and is independent of individual phase and overall sample-related parameters. Therefore a single measurement is sufficient to determine K for a given instrument configuration and set of data-collection conditions. Determination of K may be carried out by (i) a measurement of either a pure phase, or a phase of known proportion in a mixture, separately from the measurement of the actual unknown mixture, or (ii) using a phase that is present in the sample in a known amount. The value of K calculated in this way will be appropriate for the calibration of subsequent measurements as long as all instrumental and data-collection conditions remain the same as those used in its determination.

For each phase, the density ρ_α can be calculated from the published (or refined) crystal-structure information using

$$\rho_\alpha = \frac{ZM_\alpha}{V_\alpha}, \quad (3.9.20)$$

where ZM is the mass of the unit-cell contents (Z is the number of formula units in the unit cell and M is the molecular mass of the formula unit) and V is the unit-cell volume.[2]

Substitution of equation (3.9.20) in equation (3.9.19) shows that

$$W_\alpha = \frac{S_\alpha (ZMV)_\alpha \mu_m^*}{K}. \quad (3.9.21)$$

In this context, $(ZMV)_\alpha$ is the 'phase constant' and can be calculated from published or refined crystal-structure information alone. It is worth noting that, if the crystal structure is refined as part of the analysis, ZMV is updated and hence becomes a dynamic phase constant.

The methodology embodied in equation (3.9.21) is important in many applications in that it produces, within the limits of experimental error, *absolute phase abundances* and is referred to hereafter as the *external standard* approach. While the use of a phase that already exists within the sample to determine K may be considered as an internal standard approach, in some applications, including *in situ* studies, that phase may be removed from the system through, for example, decomposition or dissolution. However, the value of K remains valid for subsequent determination of phase abundances provided that the instrumental and data-collection conditions do not change.

Equation (3.9.21) is directly applicable to the analysis of those phases for which detailed crystal-structure information is available. For phases where only a partial structure (for example, an indexed unit cell but no atom coordinates or site-occupation factors) is available, an empirical ZMV can be derived using mixtures of the phase of interest with known amounts of a well characterized standard (Scarlett & Madsen, 2006). QPA of phases with partial structure is also possible through the use of equation (3.9.19), but an estimate of the phase density, obtained through direct measurement, is required.

The limitations of the approach embodied in equations (3.9.19) and (3.9.21) derive from the need to (i) conduct a measurement of K and (ii) estimate the value of the mass absorption coefficient μ_m^* for the sample(s) used to determine K, as well as for each sample of interest. However, similar to the earlier discussion about the single-peak methods, μ_m^* can be determined by direct measurement or calculation using equations (3.9.4) or (3.9.5), respectively. The benefits that can be derived from the extraction of the absolute, rather than relative, phase abundances, make it worth pursuing in many analytical situations. For example, in time-resolved studies where phases transform and material is lost in the course of reaction, the calculation of relative abundances summed to 100% may give a misleading impression of increased amounts of the remaining phases.

In some diffraction instruments, there may be decay in the incident-beam intensity during the course of measurement. This may happen on the timescale of months for a laboratory-based instrument owing to X-ray tube ageing, or on the scale of minutes at a synchrotron instrument where the storage-ring current is only refreshed once or twice per day. In this case, the change in incident intensity can be taken into account by incorporating an additional term into equation (3.9.21):

$$W_{\alpha i} = \frac{S_{\alpha i} (ZMV)_\alpha \mu_m^*}{K} \frac{I_0}{I_i}, \quad (3.9.22)$$

where I_0 and I_i are the incident beam intensities present during the determination of K and the collection of data set i, respectively.

The need to measure K, and measure or calculate μ_m^*, serves to increase the overall experimental difficulty and can be eliminated in ways analogous to those used in the single-peak methodology described earlier. For a simple two-phase mixture where both phases, α and β, are 100% crystalline, the sum of their weight fractions W_α and W_β equals unity and can be expressed as (Bish & Howard, 1988)

$$W_\alpha = \frac{W_\alpha}{W_\alpha + W_\beta}. \quad (3.9.23)$$

Substitution of equation (3.9.21) for phases α and β in equation (3.9.23) results in

$$W_\alpha = \frac{S_\alpha (ZMV)_\alpha}{S_\alpha (ZMV)_\alpha + S_\beta (ZMV)_\beta}. \quad (3.9.24)$$

Alternatively, in a multiphase sample, the addition of an internal standard s in known amount W_s and taking the ratio of equation (3.9.21) for analyte and standard phases provides the relationship

$$W_\alpha = W_s \frac{S_\alpha (ZMV)_\alpha}{S_s (ZMV)_s}. \quad (3.9.25)$$

The method embodied in equation (3.9.25) is analogous to the *internal standard* approach in equation (3.9.9) and also serves to produce *absolute phase abundances* $W_{\alpha(\mathrm{abs})}$. Once again, the benefit accruing from the use of absolute phase abundances is the ability to estimate the presence and amount of any amorphous and/or unidentified phases $W_{(\mathrm{unk})}$ through application of equations (3.9.16) and (3.9.17).

Hill & Howard (1987) and Bish & Howard (1988) have adapted the matrix-flushing method of Chung (1974*a*,*b*) to the Rietveld analysis context. By constraining the sum of the analysed weight fractions to the assumed concentration of the crystalline components (usually unity), the weight fraction of phase α in an n-phase mixture is given by the relationship[3]

[2] When calculating phase density from crystallographic parameters, a factor of $1.6604 = 10^{24}/6.022 \times 10^{23}$ is needed to convert ρ in a.m.u. Å^{-3} to g cm^{-3}.

[3] It should be noted that the implementation of the matrix-flushing method by Bish and Howard retains the use of phase density, but their approach is essentially the same as that of Hill and Howard.

$$W_\alpha = \frac{S_\alpha (ZMV)_\alpha}{\sum_{k=1}^{n} S_k (ZMV)_k}. \qquad (3.9.26)$$

The use of equation (3.9.26) in QPA again eliminates the need to measure the instrument calibration constant and estimate the sample mass absorption coefficient. However, the necessity of normalizing the sum of the analysed weight fractions to unity only produces the correct *relative phase abundances*. This approach is the most widely used in Rietveld-based QPA and is almost universally coded into Rietveld analysis programs. If the sample contains amorphous phases and/or minor amounts of unidentified crystalline phases, the analysed weight fractions will be overestimated. Where absolute phase abundances are required in, for example, the derivation of reaction mechanisms in *in situ* studies, then one of the methods that produces absolute phase abundances must be used.

3.9.4. Demonstration of methods

The sample 1 suite from the IUCr Commission on Powder Diffraction (CPD) round robin on QPA (Madsen *et al.*, 2001) provides a useful basis for demonstrating the applicability some of the methods described above. Sample 1 was designed to provide a relatively simple analytical system in order to determine the levels of accuracy and precision that could be expected under ideal conditions. The key design criteria required that the phases exhibit little peak overlap in the low-angle region of the diffraction pattern and the samples have at least one freestanding peak for each phase in the *d*-spacing range 3.7 to 1.9 Å.

The three components (corundum, α-Al_2O_3; fluorite, CaF_2; and zincite, ZnO) were prepared in a ternary design to provide a total of eight different mixtures in order to cover as wide a range of composition as possible for each phase. The result is that each phase is present in the suite with concentrations of approximately 1, 4, 15, 33, 55 and 95 wt%. The exact compositions (Madsen *et al.*, 2001) can be found in Table 3.9.1. The unique chemical composition of the component phases also allowed the weighed compositions to be confirmed by measurement of total elemental composition using X-ray fluorescence (XRF) methods.

Data sets were collected from three replicates of the eight mixtures using a Philips X'Pert diffractometer equipped with a Cu long fine focus tube operated at 40 kV and 40 mA. The beam path was defined with 1° divergence, 0.3 mm receiving and 1° scatter slits. A curved graphite post-diffraction monochromator was fitted to eliminate $K\beta$ radiation. Data were collected from 15 to 145° 2θ in increments of 0.02° using a counting time of 1.5 s per step. These data sets are available as supporting information from http://it.iucr.org/ for any reader wishing to develop and test their skills in various methods.

For the single-peak methods, the net intensity for all peaks in the range 22 to 65° 2θ was extracted using a fundamental-parameters approach to peak fitting coded in the *TOPAS* software package (Bruker AXS, 2013). The choice of peak profile type is important, since any misfit will be reflected in the estimation of peak area and hence in the QPA. Unless otherwise stated, QPA was undertaken using the strongest peak in the pattern for each phase (corundum 113, d = 2.085 Å; fluorite 022, d = 1.932 Å; zincite 011, d = 2.476 Å). The average values for these peaks can be found in Table 3.9.2. For those methods requiring knowledge of the mass absorption coefficient, μ_m^* for each sample was calculated from the XRF chemical analysis results.

Table 3.9.1
Weighed composition (weight fraction) of the eight mixtures comprising sample 1 in the IUCr CPD round robin on QPA (Madsen *et al.*, 2001)

Sample	Corundum	Fluorite	Zincite
1A	0.0115	0.9481	0.0404
1B	0.9431	0.0433	0.0136
1C	0.0504	0.0136	0.9359
1D	0.1353	0.5358	0.3289
1E	0.5512	0.2962	0.1525
1F	0.2706	0.1772	0.5522
1G	0.3137	0.3442	0.3421
1H	0.3512	0.3469	0.3019

Table 3.9.2
Average values (n = 3) of net peak intensity derived using profile fitting for the strongest peaks of corundum (113), fluorite (022) and zincite (011)

The figures in parentheses are the standard deviations of the means. The sample mass absorption coefficient μ_m^* was calculated from the XRF-L determined composition.

Sample	Corundum	Fluorite	Zincite	μ_m^* ($cm^2\ g^{-1}$)
1A	34.8 (0.6)	8958.7 (33.0)	509.9 (6.0)	93.02
1B	6561.3 (28.6)	1095.5 (7.1)	474.3 (3.8)	34.45
1C	244.4 (0.9)	250.9 (10.1)	22898.0 (37.0)	49.03
1D	474.5 (3.5)	6559.6 (2.8)	5468.5 (9.5)	71.71
1E	2525.3 (27.9)	4835.5 (27.0)	3370.7 (16.3)	53.17
1F	1251.3 (7.8)	2935.8 (9.0)	12494.9 (22.4)	52.67
1G	1295.0 (8.7)	5041.7 (17.0)	6787.9 (26.6)	59.64
1H	1436.5 (7.3)	5132.0 (13.6)	5996.8 (59.5)	59.10

3.9.4.1. *Absorption–diffraction method*

In this method, the QPA of each phase is conducted independently of the others. For each phase, the determination of a specific calibration constant, C, was achieved using a rearranged equation (3.9.3). The sample where the relevant phase was present at about 55 wt% (sample 1E for corundum, 1D for fluorite and 1F for zincite) was taken to be the calibration sample.

For fluorite the determination of C proceeded using

$$C_{i,\alpha} = I_{i,\alpha} \frac{\mu_m^*}{W_\alpha} = 6559.6 \times \frac{71.71}{0.5358} = 877\,919. \qquad (3.9.27)$$

All data sets were then analysed using equation (3.9.3), as demonstrated here using sample 1H.

$$W_\alpha = I_{i,\alpha} \frac{\mu_m^*}{C_{i,\alpha}} = 5132.0 \times \frac{59.1}{877919} = 0.3455, \qquad (3.9.28)$$

compared with a value of 0.3469 added to the sample by weight. Fig. 3.9.1 shows the analysed concentration for all 24 fluorite measurements along with the bias from the known values. The bias (analysed − known) all fall within the range −0.3 to 0.5 wt% with no systematic bias as a function of concentration. The similar results achieved for corundum and zincite demonstrate the validity of the approach where there is minimal peak overlap.

3.9.4.2. *Internal standard method*

Application of the internal standard method normally requires the addition of an appropriate phase in known amount to each sample to be analysed. In order to use this data for demonstration of the internal standard method, it is necessary to designate one of the existing phases as the internal standard. Sample 1H has been used to derive the calibration constant, with fluorite considered to be the phase of interest while zincite is designated

as the internal standard. The intensities (Table 3.9.2) and known concentrations (Table 3.9.1) of these phases can then be used to derive $C_{\alpha s}^{ij}$ from equation (3.9.8) to eliminate the need to know or measure μ_m^* for the sample.

$$\frac{I_{\text{fluorite}}}{I_{\text{zincite}}}\frac{W_{\text{zincite}}}{W_{\text{fluorite}}} = C_{\alpha s}^{ij} = \frac{5132.0}{5996.8} \times \frac{0.3019}{0.3469} = 0.7448. \qquad (3.9.29)$$

Analysis of the unknowns (Fig. 3.9.2) then proceeds *via* equation (3.9.9) and is demonstrated here using sample 1D:

$$W_{\text{fluorite}} = \frac{W_{\text{zincite}}}{C_{\alpha s}^{ij}}\frac{I_{\text{fluorite}}}{I_{\text{zincite}}} = \frac{0.3289}{0.7448}\frac{6559.6}{5468.5} = 0.5297, \qquad (3.9.30)$$

compared with a value of 0.5358 added to the sample by weight.

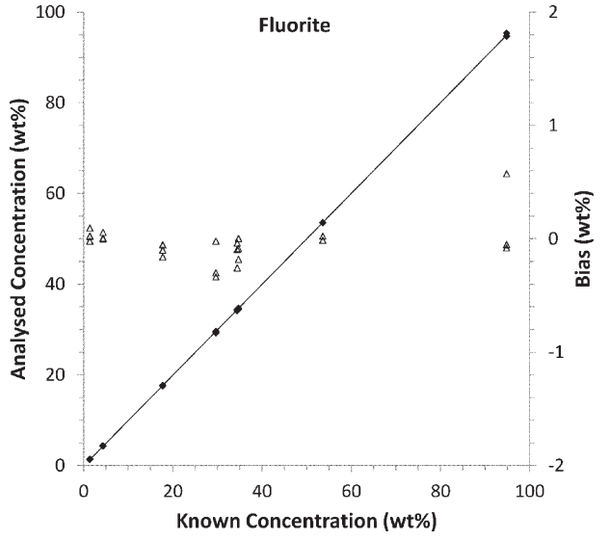

Figure 3.9.1
Plot of the analysed concentration (black diamonds – left axis) and the bias (open triangles – right axis) expressed as wt% for fluorite using the absorption–diffraction method. The analysis was calibrated using sample 1D, which has a fluorite concentration of 53.58 wt%.

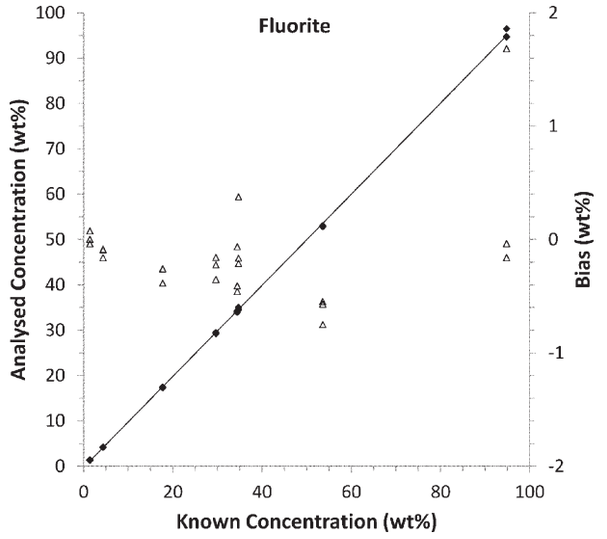

Figure 3.9.2
Plot of the analysed concentration (black diamonds – left axis) and the bias (open triangles – right axis) expressed as wt% for fluorite using the internal standard method with zincite designated as the internal standard. The analysis was calibrated using sample 1H where the fluorite and zincite concentrations are 34.69 and 30.19 wt%, respectively.

3.9.4.3. *Reference intensity ratio*

For this exercise, the peak intensities and phase concentrations in Tables 3.9.1 and 3.9.2 for sample 1H can be used to determine the RIRs for fluorite and zincite.

$$\text{RIR}_{\text{fluorite}} = \frac{5132.0}{1436.5} \times \frac{0.3512}{0.3469} = 3.617, \qquad (3.9.31)$$

$$\text{RIR}_{\text{zincite}} = \frac{5996.8}{1436.5} \times \frac{0.3512}{0.3019} = 4.856. \qquad (3.9.32)$$

These RIRs should be compared with reported values for fluorite in the ICDD database (ICDD, 2015) which have an average of 3.83 (n = 33) but range from 2.40 to 4.21. For zincite the reported RIR values have an average of 5.24 (n = 50) and range from 4.50 to 5.87. The discrepancies in the various reported values of the RIRs highlight the need to determine them under the same conditions as the samples being analysed if the highest accuracy is to be achieved.

Fig. 3.9.3 shows the RIR values calculated from all 24 (eight samples, three replicates each) measurements for fluorite and zincite plotted as a function of corundum concentration. At intermediate concentrations there is quite good agreement between the determined values. However, there are significant deviations at low corundum concentration, resulting in insufficient measured intensity in the corundum peak to ensure sufficient accuracy in the RIR. Hence, care should be taken to ensure that there are sufficient counts in the peaks used to determine the RIR. In addition, a low concentration automatically means that there are fewer grains contributing to the diffraction process; hence particle statistics may also present a significant problem.

The presence of other sample-related aberrations that affect the measured intensities also needs to be considered. For example, microabsorption may affect measured RIR values differently in different concentration ranges. The impact of such effects on the analysis is reduced by their inclusion in the measured RIR provided that variation induced by, for example, sample preparation can be kept to a minimum.

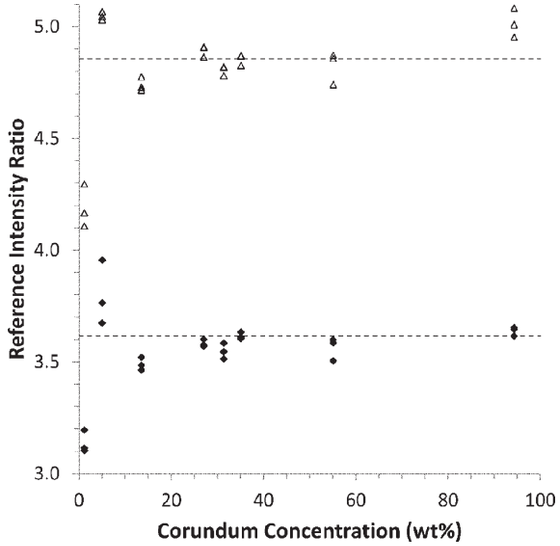

Figure 3.9.3
Plot of the 24 determined RIR values for fluorite (black diamonds) and zincite (open triangles) as a function of corundum concentration. The dashed lines represent the average RIR values for fluorite (lower) and zincite (upper) determined from the three replicates of sample 1H where all phases have approximately equal concentration.

3.9.4.4. *Matrix flushing*

Once the correct value of RIR is determined for each phase, the matrix-flushing method can be applied using equation (3.9.15). For fluorite in sample 1D, the calculation proceeds as follows:

$$W_{\text{fluorite}} = \frac{I_{\text{fluorite}}/\text{RIR}_{\text{fluorite}}}{\sum_{k=1}^{n} I_k/\text{RIR}_{ks}} = \frac{6559.6/3.617}{474.5/1.0 + 6559.6/3.617 + 5468.5/4.856} = 0.5312, \quad (3.9.33)$$

compared with a value of 0.5358 added to the sample by weight. Fig. 3.9.4 shows the bias for fluorite in all samples analysed by the matrix-flushing method. Once again, there is good agreement between the weighed and analysed amounts. However, it is worth reiterating that this method normalizes the sum of all analysed weight fractions to unity. If amorphous or non-analysed phases are present in the sample, then the weight fractions will be overestimated relative to their absolute abundances.

3.9.4.5. *Rietveld-based methods*

The strengths and weaknesses of some of the methods described in Section 3.9.3 are highlighted through a study of the mechanism and kinetics of nucleation and crystal growth in the context of the Bayer process for the extraction of aluminium from bauxite ores (Webster *et al.*, 2010). Specifically, the experiments utilize synthetic Bayer liquors, consisting of Al-loaded caustic solutions to which a variety of seed material is added. Several polymorphs of $Al(OH)_3$ (gibbsite, bayerite and nordstrandite) crystallize from solution onto the seed material. The rate of crystallization and the ratio of the phases formed depend on the sample conditions used, including the Al and caustic concentrations in solution, as well as sample temperature.

The mechanism and rate of crystallization were followed by collecting XRD data at the powder-diffraction beamline of the Australian Synchrotron[4] over a period of about 3 h. The diffractometer incorporates a Mythen detector (Schmitt *et al.*, 2003) which allows for the simultaneous collection of 80° 2θ of the diffraction pattern. A wavelength of 0.826 Å was used to ensure adequate penetration of the beam in the sample. The sample environment (Madsen *et al.*, 2005; Norby *et al.*, 1998) consisted of a 1-mm quartz glass capillary containing a slurry of the seed and Bayer liquor heated to temperatures between 333 and 348 K using a hot-air blower.

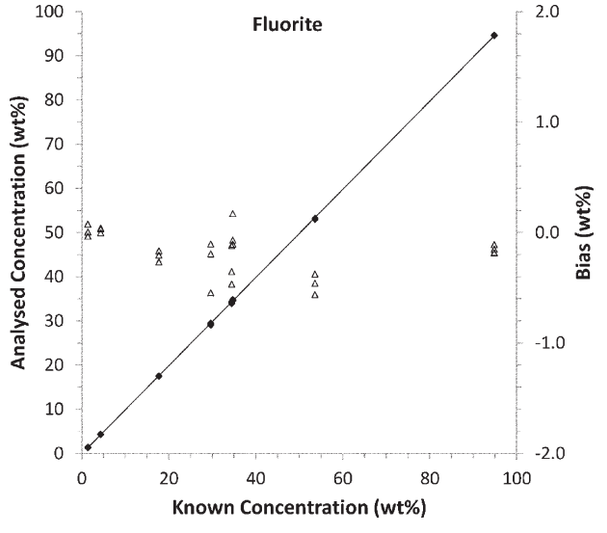

Figure 3.9.4
Plot of the analysed concentration (black diamonds – left axis) and the bias (open triangles – right axis) expressed as wt% for fluorite using the matrix-flushing method with RIRs of 1.0, 3.617 and 4.856 for corundum, fluorite and zincite, respectively. The RIRs were determined using sample 1H where the corundum, fluorite and zincite concentrations are 35.12, 34.69 and 30.19 wt%, respectively.

The data were analysed using *TOPAS* (Bruker AXS, 2013), where a learned-profile approach to peak modelling was used with an empirical instrument width and shape contribution determined using the NIST SRM660 LaB_6 profile standard. For the samples in the study, refined parameters included 2θ zero offset, a Chebychev polynomial pattern background and, for each phase, the Rietveld scale factor, crystallite size and strain, and unit-cell dimensions.

A number of different approaches were used to extract the phase abundances at each stage of the reaction. Initially, QPA was derived using equation (3.9.26); the value that many Rietveld analysis programs output as their first estimate of phase abundance. Fig. 3.9.5 shows the QPA output from an *in situ* experiment in which goethite (FeOOH) was added as the seed.

At the start of the experiment, prior to the crystallization of any of the $Al(OH)_3$ polymorphs, Fig. 3.9.5 shows that the reported concentration of the goethite seed is 100 wt% since it is the only phase represented in the analysis at that time. On formation of gibbsite, bayerite and nordstrandite, the goethite concentration appears to decrease progressively to about 65 wt% while the total $Al(OH)_3$ concentration reaches about 35 wt% at the end of the experiment. However, these figures are in disagreement with (i) the fact that goethite is unlikely to dissolve or otherwise be consumed in this system (Murray *et al.*, 2009), (ii) the known addition of goethite to the sample (14.13 wt%) and (iii) the total amount of $Al(OH)_3$ available from solution (15.92 wt%). The problem with the QPA in this case arises from the fact that only the crystalline components are considered in the analysis and that equation (3.9.26) normalizes the sum of their analysed weight fractions to unity. However, aluminium, which is in solution at the start of the run, forms crystalline phases continuously throughout the reaction after an initial induction period. In order to overcome the anomalies in the QPA results, it is necessary to consider the sample as a whole; that is, the concentration of both the solid and liquid components in the X-ray beam for the duration of the experiment.

In this sample, the concentration of the goethite seed was 14.13 wt% in the slurry injected into the sample capillary. If the assumption is made that, in this environment, goethite is unreactive and its concentration will not change during the reaction, it can be used as an internal standard to put the $Al(OH)_3$ concentrations on an absolute basis. The QPA results derived using the internal standard or 'spiked' approach in equation (3.9.25) are shown in Fig. 3.9.6.

The goethite concentration is fixed at the known addition (14.13 wt%) at the start of the experiment. However, the concentrations of the $Al(OH)_3$ polymorphs are now put on an absolute scale, thus allowing derivation of more meaningful reaction mechanisms.

If, however, there is residual doubt about the reactivity of the goethite, it may be necessary to use the external standard approach embodied in equation (3.9.21). In this case, the value for the instrument constant, K, can be derived using the Rietveld scale factor, ZMV and the known addition of goethite in a

[4] Australian Synchrotron beamtime award number AS091/PD1035.

rearranged equation (3.9.21). For this determination, the goethite scale factor from the first few data sets, prior to the start of the reaction, was averaged to minimize any errors that may be introduced by counting statistics. The value of the sample mass absorption coefficient μ_m^* was set to an arbitrary value of unity for both the determination of K and all subsequent analyses, since the overall chemical content of the capillary, and hence the attenuation of the X-ray beam, does not change during the reaction.

This experimental work was conducted at the Australian Synchrotron where the storage-ring current was boosted every 12 h. Between these times the current, and hence the incident-beam intensity, decays, resulting in what amounts to a change in the 'instrument configuration'. This requires a modification of the K value and subsequent calculation of concentration to compensate for the changing incident intensity using equation (3.9.22).

Fig. 3.9.7 now shows the results of QPA derived from equation (3.9.22). In this case the concentrations of the $Al(OH)_3$ polymorphs are similar to those in Fig. 3.9.6. However, since the phase abundances are derived using an external standard approach, any changes in the apparent goethite concentration can now be monitored. Fig. 3.9.7 shows that the goethite concentration did not change significantly in the early stages of the experiment ($t < 10$ min) before $Al(OH)_3$ crystallization was observed but there is a small, systematic decrease in the apparent goethite concentration as the experiment progresses. At the end of the experiment, the goethite concentration appears to be lower by about 1% relative to the concentration at the start.

This apparent decrease could be due to a number of causes including (i) poor correction for beam-intensity changes or (ii) solid material moving about in the capillary with some movement out of the X-ray beam. Alternatively, the decrease could be attributed to the 'shielding' of the goethite from the X-ray beam by the $Al(OH)_3$ phases as they form and coat the goethite particles. This decrease could then be used to obtain an average thickness of the $Al(OH)_3$ phases on the seed particles. This layer was calculated to be about 5.5 μm (assuming a linear absorption coefficient of 9.5 cm^{-1} for gibbsite at 0.826 Å) resulting in an overall particle size of about 11 μm at the end of the run (the goethite particles are about 0.2 × 2 μm and hence do not contribute significantly to the overall particle size). These values are in good agreement with independent studies (Webster *et al.*, 2010) where the gibbsite was examined using scanning electron microscopy (SEM) techniques (Fig. 3.9.8) following crystallization under similar conditions to those used here.

3.9.5. Alternative methods for determination of calibration constants

3.9.5.1. *Standardless determination of the phase constant C*

In order to determine the phase calibration constant C, it is common to obtain (i) a pure sample of the phase of interest that accurately reflects the form of the phase in the samples to be analysed, or (ii) a multiphase sample in which the phase concentration is known by other means (for example, chemical analysis or point counting). In some systems, there may be insufficient sample available to risk 'contaminating' it with an internal standard, especially if the material needs to be analysed using other techniques. The addition of an internal standard may also introduce microabsorption problems or increase the complexity of patterns that are already highly overlapped. For other situations, the time frame demanded for the analysis may prohibit the time-consuming procedures of standard addition, data collection and separate determination of the phase calibration constant.

Zevin & Kimmel (1995) have described an approach to the derivation of phase constants which relies on having a suite of samples to be analysed that (i) have the same phases present in all samples and (ii) exhibit a wide range of composition of these phases in various samples in order to stabilize the analysis. If we reconsider the relationship between the weight fraction W_α and the observed intensity [equation (3.9.3)],

$$W_\alpha = \frac{I_\alpha \mu_m^*}{C_\alpha}, \tag{3.9.34}$$

and assume that all phases in the system are known and included in the analysis, we can introduce the additional constraint that the sum of all W_α's is unity (or at least a known value):

$$\sum_{j=1}^{n} W_j = 1.0. \tag{3.9.35}$$

In a system of n samples containing m phases, we can explicitly write the relationships expressed in equations (3.9.34) and (3.9.35) as a set of simultaneous equations:

$$\begin{aligned}
1.0 &= \frac{1}{C_1} I_{11}\mu_1^* + \frac{1}{C_2} I_{12}\mu_1^* + \ldots + \frac{1}{C_m} I_{1m}\mu_1^*, \\
1.0 &= \frac{1}{C_1} I_{21}\mu_2^* + \frac{1}{C_2} I_{22}\mu_2^* + \ldots + \frac{1}{C_m} I_{2m}\mu_2^*, \\
1.0 &= \frac{1}{C_1} I_{n1}\mu_n^* + \frac{1}{C_2} I_{n2}\mu_n^* + \ldots + \frac{1}{C_m} I_{nm}\mu_n^*,
\end{aligned} \tag{3.9.36}$$

where μ_n^* is the mass absorption coefficient for the nth sample.

Knudsen (1981) has described a modification to this approach by including an internal standard in each of the samples to be analysed and using the ratio of intensities of the analyte and internal standard phases in place of the I_{nm} in equation (3.9.36). While this eliminates the need to determine and use the mass absorption coefficient, the tedious procedure of adding and mixing an internal standard is required for each sample and for reasons described above may not be appropriate.

The relationships embodied in equations (3.9.36) can be expressed more simply in matrix notation as

$$\mathbf{L}' = \mathbf{I}'\mathbf{C}', \tag{3.9.37}$$

where $\mathbf{L}'$ is a column vector (dimensions $1 \times n$) containing the known (or assumed) sum of weight fractions for each sample (unity in this case), $\mathbf{C}'$ is a column vector (dimensions $1 \times m$) containing the calibration constants for each phase and $\mathbf{I}'$ is a rectangular matrix (dimensions n rows × m columns) containing the measured peak intensities (or scale factors) for each phase multiplied by the sample mass absorption coefficient.

A least-squares solution of equation (3.9.37) to derive the value for C for each phase can be calculated using matrix-manipulation methods (Knudsen, 1981):

$$\mathbf{C}' = \left(\mathbf{I}'^T\mathbf{I}'\right)^{-1}\mathbf{I}'^T\mathbf{L}', \tag{3.9.38}$$

where the superscripts T and -1 represent the transpose and inverse matrix functions, respectively.

Accuracy in the calculation of the individual values of C is improved by having (i) phases of the same or similar composition in all samples and (ii) a wide range of concentrations of each phase across the sample suite. These conditions may be met in,

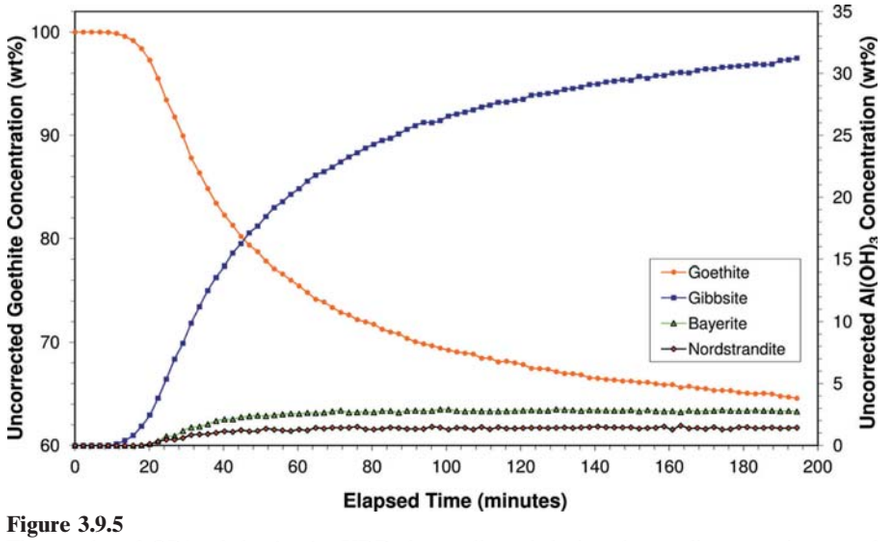

Figure 3.9.5
The results of QPA of the *in situ* XRD data collected during the seeding experiments of Webster *et al.* (2010). The values were derived using the Hill/Howard (Hill & Howard, 1987) relationship in equation (3.9.26). Note the decrease in apparent goethite concentration (left axis) as the polymorphs of $Al(OH)_3$ (right axis) crystallize from solution.

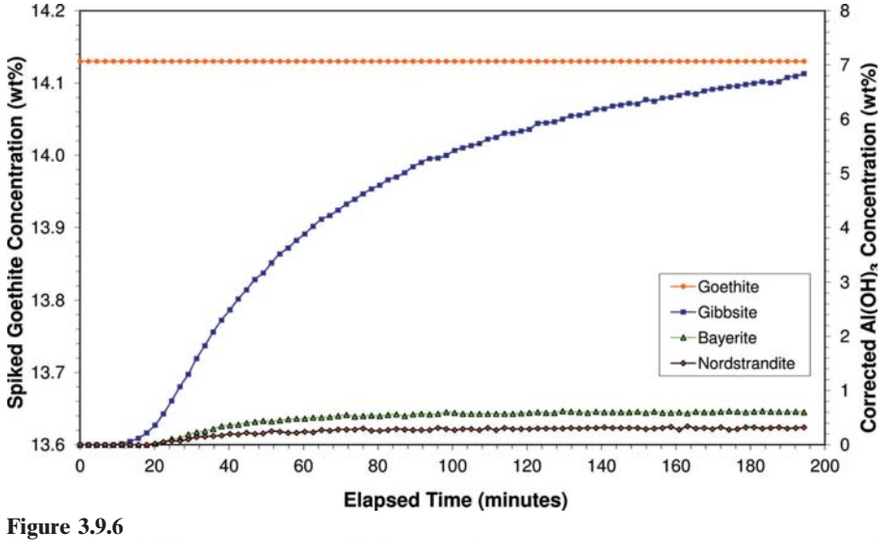

Figure 3.9.6
The results of QPA of the *in situ* XRD data collected during the seeding experiments of Webster *et al.* (2010).The values are absolute phase abundances derived using the internal standard relationship in equation (3.9.25).

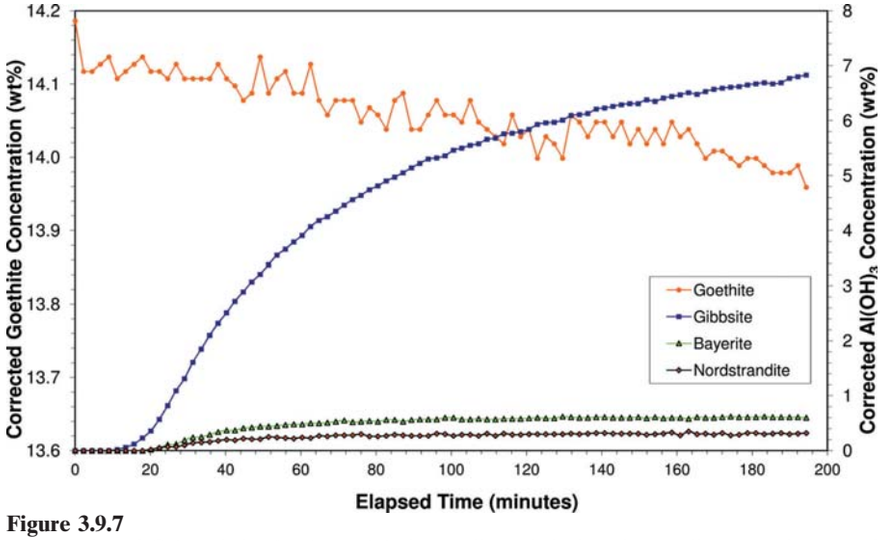

Figure 3.9.7
The results of QPA of the *in situ* XRD data collected during the seeding experiments of Webster *et al.* (2010). The values are absolute phase abundances derived using the external standard relationship in equation (3.9.22). Note the slight decrease in the goethite concentration (left axis) during the run.

for example, mineral exploration samples where a limited number of phases are present in a drill core but their abundance varies as a function of depth. In mineral processing or industrially based material manufacture, the goal is usually to control the system to minimize compositional variation in the product. The side effect of this is that the values of intensity in matrix **I** have too little variation, resulting in large errors in the derived values for *C*. In the limiting case, the system may become indeterminate with no unique solution available. To overcome this, forced or accidental changes to processing conditions may introduce sufficient compositional variation to stabilize the determination of the *C* values through equation (3.9.38). Alternatively, physical or chemical separation of selected components may be sufficient to provide the required compositional variation. Knudsen (1981) provides a detailed statistical analysis used in the determination of the errors in the phase constants.

While Zevin (Zevin & Kimmel, 1995) and Knudsen (1981) have demonstrated the application of this approach for single-peak methods, it is equally applicable if scale factors derived from whole-pattern fitting or Rietveld-based methods are used.

3.9.5.2. *Demonstration of the Zevin approach*

The sample 1 suite from the IUCr CPD round robin on QPA again provides an ideal platform for demonstrating the applicability of this method due to the wide variation of concentration of the constituent phases. A measure of intensity was derived using an hkl_phase (see Section 3.9.6) in which the peak positions were constrained to the space group and unit-cell parameters but the individual peak intensities were refined to empirical values using a pure sub-sample of each of the three phases. For the analysis of the samples, the relative peak intensities were fixed and an overall scale factor *S* for each phase in each sample (eight samples, three replicates, three phases), multiplied by the mass absorption coefficient calculated from the XRF-determined composition, was used as the measure of intensity. These $S\mu_m^*$ values then formed the intensity matrix **I** in equations (3.9.37) and (3.9.38) while all values in the vector **L** were assumed to be 1.0 (*i.e.* all samples were assumed to be fully crystalline). Microsoft Excel provides a useful platform for these calculations since it contains all of the matrix-manipulation functions required by equation (3.9.38). The determined values for *C* for the three phases are given in Table 3.9.3. The values in the C/C_{corundum} column should be compared with the values derived in Section 3.9.4.3 above.

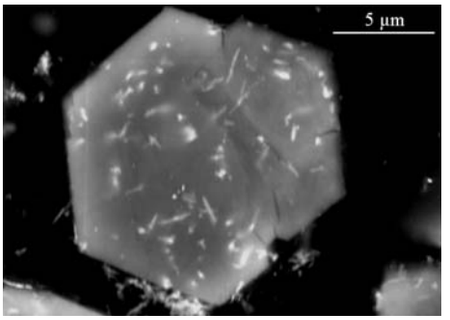

Figure 3.9.8
SEM image of $Al(OH)_3$ (grey hexagon) which has crystallized on goethite seed (light grey needles) (Webster *et al.*, 2010).

Application of these C values to the analysis of all samples *via* equation (3.9.34) yields the results given in Fig. 3.9.9. The results, displayed as bias from the known values, show that at all concentration ranges the analyses are within about ±1% of the weighed values. The important point to note here is that there has been *no prior calibration* conducted to obtain this result; the system is self-calibrating and has only relied on having a wide range of concentrations of the three phases in the sample suite. The only prior knowledge used in the analysis is (i) a measure of peak intensity embodied in the empirical phase scale factor and (ii) an estimate of μ_m^* for each sample calculated from the elemental composition.

3.9.5.3. *Experiment constant – a whole-sample approach*

Earlier discussion has noted that the experiment constant K used in equation (3.9.21) can be determined using (i) a standard pure phase or mixture measured separately from the measurement of the actual unknown mixture being analysed, or (ii) using a phase that is present in the sample in a known amount. However, in some cases, these approaches are not always effective in producing reliable values of K because the methodology assumes that the mass of sample contributing to the diffraction process is constant. While this condition is true for infinitely thick samples in Bragg–Brentano geometry, it is unlikely to be true for capillary or flat-plate samples in transmission geometry. In these cases, the sample thickness and packing density will have a significant influence on the amount of sample contributing to the diffraction process and hence on the observed intensity and the derived values of K. Therefore, a K value determined from one capillary sample is unlikely to be applicable to another capillary even though all other instrumental conditions remain the same. However, for *in situ* studies, a K value determined at the start of an experiment should remain valid as the analysis proceeds.

K can also be determined using the whole sample, rather than an individual phase. Since the determined value of K then applies equally to all phases in the sample, equation (3.9.21) can be summed over all analysed components thus:

$$\sum_{i=1}^{n} W_i = (\mu_m^*/K) \sum_{i=1}^{n} S_i(ZMV)_i. \qquad (3.9.39)$$

If the crystallinity of the sample is known (or can safely be assumed), then individual phase abundances are not required and K can be calculated from

$$K = \frac{\mu_m^* \sum_{i=1}^{n} S_i(ZMV)_i}{\sum_{i=1}^{n} W_i}, \qquad (3.9.40)$$

where $\sum W_i$ is the assumed crystallinity of the entire sample.

Table 3.9.3
Phase calibration constants for corundum, fluorite and zincite determined using the Zevin (Zevin & Kimmel, 1995) and Knudsen (Knudsen, 1981) method

The RIR values were derived earlier in this chapter.

Phase	C	C/C_{corundum}	RIR
Corundum	240.91	1.0	1.0
Fluorite	874.27	3.629	3.617
Zincite	1190.81	4.943	4.856

For a sample that is 100% crystalline and all components included in the analysis, then the denominator is unity and K is simply the sum of the product of the scale factors and their respective ZMV's multiplied by the mass absorption coefficient of the entire sample.

For *in situ* studies where a reaction or process is examined dynamically, sealed capillary sample geometry is frequently used. In this environment, the *chemical* composition of the capillary contents will not change during the course of the reaction even though individual phases may be undergoing transformation. Equation (3.9.40) can be further simplified since the overall sample mass absorption coefficient remains constant throughout the reaction and can therefore be deleted and its effect incorporated into K.

This whole-sample approach to the determination of K is also useful in systems where there are residual errors that may not be evident when equation (3.9.21) is used with the concentration of a single phase. By way of demonstration, the sample 1 suite from the IUCr CPD round robin on QPA has been used to calculate K in two distinct ways:

(1) *Phase specific*: Three replicate measurements of the eight mixtures were analysed using a Rietveld-based surface-analysis approach (Stinton & Evans, 2007). This approach refines a single model to all data sets in the suite simultaneously allowing parameters that are common to all samples to be determined with a greater degree of certainty. Since the sample suite contains corundum, fluorite and zincite in a wide range of concentrations, application of a rearranged equation (3.9.21) using the refined scale factors results in 72 separate determinations of K. The value of μ_m^* for each sample was derived from XRF-determined compositions using equation (3.9.5), while the values for W_i were taken from the known weight additions.

(2) *Whole sample*: Equation (3.9.40) was applied to each of the 24 data sets (*i.e.* three replicates each of the eight samples) assuming (i) that all phases were known and fully crystalline, *i.e.* $\sum W_i = 1$; and (ii) μ_m^* for each sample was derived in the manner described above.

Fig. 3.9.10 shows the 72 individual determinations of K from the phase-specific method as a function of known phase concentration. At high concentrations, the values for K derived from each of the three phases are similar indicating that, for effectively pure phase samples, the approach embodied in equation (3.9.21) is valid. However, if K is determined using the known concentration of a single phase at a lower concentration in a multiphase sample, then residual errors in the measurement of pattern intensity serve to reduce its accuracy. At lower concentrations of corundum, there is a systematic increase in the determined value of K resulting from a small microabsorption effect present in these samples. Since corundum has the lowest mass absorption coefficient of the three phases in this system its intensity, and hence Rietveld scale factor, is slightly

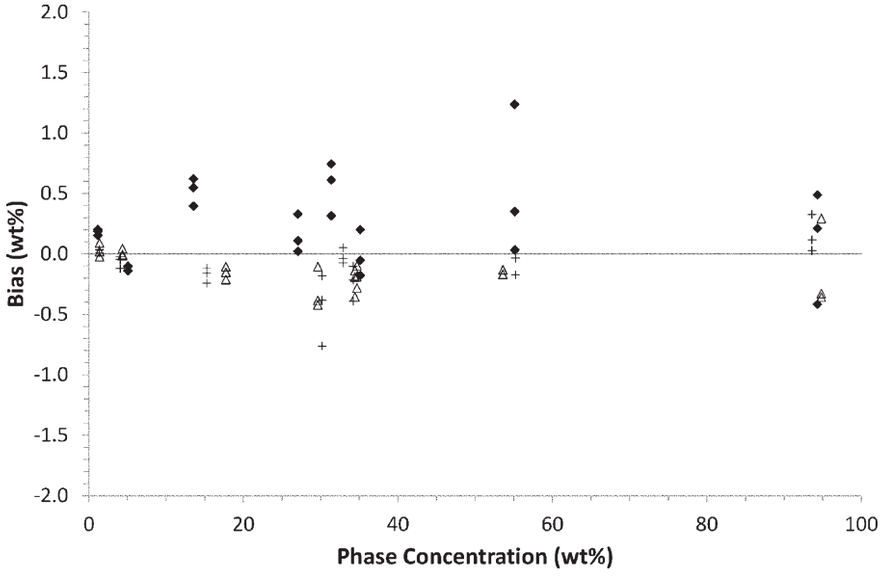

Figure 3.9.9
Plot of the bias (known − determined) in the analysed phase abundances using the Zevin & Kimmel (1995) approach for corundum (black diamonds), fluorite (open triangles) and zincite (crosses). The 72 determinations derive from three replicates of eight mixtures containing three phases each.

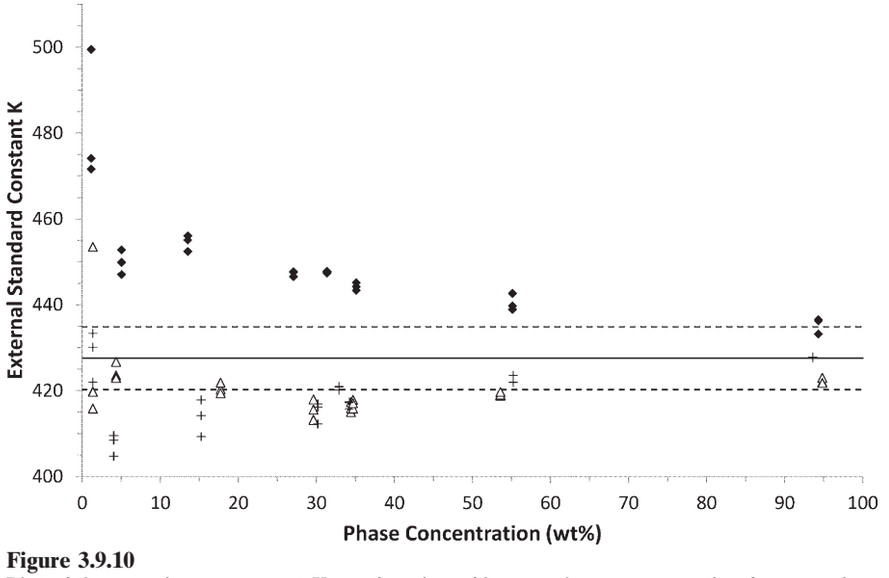

Figure 3.9.10
Plot of the experiment constant K as a function of known phase concentration for corundum (closed diamonds), fluorite (open triangles) and zincite (crosses) using the phase-specific method. The 72 determinations derive from three replicates of eight mixtures containing each of the three phases. The solid line is the mean of 24 values determined using the whole-sample approach. The dashed lines represent ±2 standard deviations about this mean.

overestimated relative to the fluorite and zincite. This results in an overestimation of the value of K relative to an ideal sample; the magnitude of this difference is about 5% relative. Use of these values for subsequent analysis will result in an underestimation of phase concentrations using equation (3.9.21). The converse is true if fluorite or zincite is used to determine K.

However, if the whole-sample approach embodied in equation (3.9.40) is used for the determination of K, these residual sample-related aberrations can be eliminated; the results of the determination of 24 values of K using this approach are also included in Fig. 3.9.10. The mean of all 24 determinations is 427.6 (3.7) representing a relative error of <0.8%. The important point to note here is that knowledge of the individual phase concentrations is not needed; the only assumption needed relates to the total crystallinity of each sample.

For *in situ* studies, using equation (3.9.40) to calculate K at each step i in the reaction (defined as K_i) can be useful in deriving details of the reaction mechanism. If K_i increases as the reaction progresses, this may be indicative of increasing crystallinity in the sample. Reductions in K_i during the reaction may point to the formation of intermediate amorphous material or unidentified crystalline components, the total concentration of which can be readily calculated using

$$\mathrm{wt\%}_{\mathrm{amorphous}} = 100\left(1 - \frac{K_i}{K}\right). \qquad (3.9.41)$$

Application of this can be demonstrated using sample 3 from the QPA round robin (Scarlett *et al.*, 2002), as it contains the same three crystalline phases as the sample 1 suite with the addition of 29.47 wt% amorphous silica flour. Calculation of K_i for sample 3, based only on the three crystalline phases, results in a value of 301.8. Substituting this into equation (3.9.41) along with the previously determined value of K (427.6) gives a measured amorphous content of 29.42 wt% – this is in good agreement with the known weighed amount. The important point to note here is that the data for sample 3 were collected at the same time, and under the same instrumental conditions, as for sample 1, which ensured that the true value of K was the same for all data.

3.9.6. Quantification of phases with partial or no known crystal structures

While the Rietveld-based methods described in Section 3.9.3.6 work for well ordered phases with known crystal structures, they are limited when published structure data do not accurately represent the phase actually present in the sample, are incomplete or do not exist. Poor agreement with published structure data is a common occurrence in mineralogical research where disorder exists and observed diffraction data deviate significantly from the ideal; this situation occurs with many of the clay minerals. The issue of incomplete or non-existent structure data can occur in almost any area where new materials are either synthesized or discovered. The growing demand for the analysis of materials from the nanotechnology community, where phases are at the boundary of what can be considered crystalline, serves to further highlight these limitations. Recent developments in diffraction methods have sought to address these issues and have used approaches that include the development of calibrated models or, where appropriate, the extension of existing structure data to incorporate systematic disorder such as stacking faults in clay minerals.

3.9.6.1. *Use of calibrated models*

Calibrated models are generally developed in one of two ways. The first (which uses what is referred to hereafter as an

hkl_phase) is obtained *via* the use of partial structure information. Here the peak positions are constrained by a unit cell and space group but the relative intensities, in the absence of atom types and locations in the unit cell, are determined empirically from a pure sample or one where the phase is present in a mixture at a known concentration. The second method involves the use of a discrete set of peaks whose positions, intensities, width and shape are all determined empirically. Once determined using a standard sample, this group of peaks may then be scaled as a single unit and is referred to hereafter as a peaks_phase.

The software *SIROQUANT* (Taylor & Rui, 1992) employs the simultaneous use of observed and calculated standard profiles within the framework of the Rietveld method. It draws on a library of structures that are stored as lists of reflections and intensities (hkl files). These are calculated on a cycle-by-cycle basis for well described crystalline materials but are read directly from the hkl files for poorly defined materials such as clay minerals. This method still requires some knowledge of the crystal chemistry of all phases involved and that they be included within the programme's database. By the inclusion of reflection information in this way some aberrations such as preferred orientation may be allowed for. This approach to clay mineralogy also provides for the refinement of two sets of halfwidth parameters in order to model the co-existing sharp and broad reflections generated by such minerals.

A subsequent development of the whole-pattern approach is the 'partial or no known crystal structure' (PONKCS) method (Scarlett & Madsen, 2006). This method operates within the framework of the Rietveld method but replaces the traditional crystal structure of the phases in question with an empirical set of peaks (either as an hkl_phase or a peaks_phase). These can then be scaled as a single unit in the course of refinement in similar fashion to the set of structure factors derived from a crystal structure. Since the full structure information is not available, it is not possible to calculate the *ZMV* phase constant normally required for quantification *via* equation (3.9.26) (Hill & Howard, 1987); hence, an empirical value must be derived through calibration.

3.9.6.1.1. *Generation of calibrated PONKCS models*

The generation of a suitable PONKCS model requires that:

(1) The unknown phase is available as either a pure specimen or as a component of a mixture where its abundance is known (in some instances, this may be achieved by other means, such as the measurement of bulk and/or microchemical composition.)

(2) The unknown phase does not vary considerably from the material used to derive the relative intensities of the model. Preferred orientation and other sample-related effects may be compensated for based upon an indexed diffraction pattern.

The initial step in the generation of a PONKCS model is to describe the contribution to the diffraction pattern of the phase with a series of peaks. If the phase of interest has been indexed, the Le Bail or Pawley methods (see Chapter 3.5) can be used to constrain peak positions to the space group and unit-cell parameters while the individual reflection intensities are allowed to vary to best match the observed peaks (*i.e.* an hkl_phase). If the phase has not been indexed, a series of unrelated peaks can be refined using a standard material and scaled as a group during analysis (*i.e.* a peaks_phase). While this approach is effective in most cases, it restricts the refinable parameters that may be used in the treatment of systematic errors such as preferred orientation.

The next step is to calibrate the hkl_phase or peaks_phase and derive a 'phase constant' that is equivalent to the *ZMV* value in crystal-structure-based quantification. This is achieved by the preparation of a mixture in which there are known amounts W_α and W_s of the unknown and standard, respectively. Recalling equation (3.9.25), the ratio of the weight fractions is then given by

$$\frac{W_\alpha}{W_s} = \frac{S_\alpha (ZMV)_\alpha}{S_s (ZMV)_s}, \tag{3.9.42}$$

where S_α and S_s are the refined scale factors for the unknown and standard, respectively.

Rearrangement of equation (3.9.42) then provides the means for determining an empirical value of $(ZMV)_\alpha$, which is required for the calibration of a peaks_phase:

$$(ZMV)_\alpha = \frac{W_\alpha}{W_s}\frac{S_s}{S_\alpha}(ZMV)_s. \tag{3.9.43}$$

For an hkl_phase the value of V can be determined from the refined unit-cell parameters and hence can be removed from the phase constant resulting in

$$(ZM)_\alpha = \frac{W_\alpha}{W_s}\frac{S_s}{S_\alpha}\frac{(ZMV)_s}{V_\alpha}. \tag{3.9.44}$$

Unlike the *ZMV* value derived from the unit-cell contents of a crystal structure, the phase constants derived using equations (3.9.43) and (3.9.44) have no physical meaning, since they have been derived by empirical measurement. For an hkl_phase, a more physically meaningful value of *ZM* can be obtained by deriving the true unit-cell mass from the measured phase density according to

$$(ZM)_{\alpha(\text{true})} = \frac{\rho_\alpha V_\alpha}{1.6604}. \tag{3.9.45}$$

The empirical 'structure factor' values in the hkl_phase could then be scaled according to the relation $ZM_{\alpha(\text{true})}/ZM_\alpha$, making them approximate 'real' structure factors for the material. Note that this final step is not necessary for quantification, but may make the method more generally applicable.

3.9.6.1.2. *Application of the model*

The PONKCS method is applicable to any mixture in which there are one or more phases that are not fully characterized crystallographically, including essentially amorphous material, provided appropriate calibration samples can be obtained. In the mineralogical context, it may not be possible to obtain pure phase specimens typical of those found in the bulk mixtures, but it may be possible to concentrate them to a point where they can be used. Methods of achieving this may include gravity or magnetic separation, or selective chemical dissolution.

The original paper describing this method (Scarlett & Madsen, 2006) gives a detailed example based upon sample 1 from the IUCr CPD round robin on QPA (Madsen *et al.*, 2001; Scarlett *et al.*, 2002). There, corundum was regarded as the unknown phase, fluorite as an impurity of known crystal structure and zincite a standard material added at known weight fraction. In the same paper, there is a more realistic example regarding the poorly ordered clay mineral nontronite, which is of commercial significance but difficult to quantify *via* traditional structure-based Rietveld methodology. Further details regarding quantification of this mineral *via* the PONKCS method is given in articles detailing

its importance in low-grade nickel laterite ores (Scarlett *et al.*, 2008; Wang *et al.*, 2011).

A calibration-based method such as PONKCS may also find increasing application with phases that have a known crystal structure. It has the greatest potential for accuracy, as the calibration process may obviate residual aberrations in the data such as microabsorption. Assuming that the sample suite has the same absorption characteristics as that used for calibration, such aberrations will be included in the calibration function and require no further correction during the sample analysis. This is a realistic scenario for routine analyses in industries as diverse as mineral processing, cement production and pharmaceutical production.

3.9.6.2. *Modelling of structural disorder*

One major challenge for QPA is the treatment of stacking disorder. An alternative to the use of calibrated models is to develop extended structure models that more effectively represent the phases present in the sample than the simple structure models. Stacking disorder occurs in layered structures where long-range order is present within the layers but there is only partial or even no relationship from one layer to another. It is a commonly occurring type of microstructure and is of great interest in various fields including mineralogy and material science.

The most common types of stacking faults in lamellar structures are:

(i) translational stacking faults, characterized by well defined translation vectors between successive layers;
(ii) rotational stacking faults, characterized by irregular but well defined rotation of adjacent layers in a stack; and
(iii) random stacking faults (turbostratic stacking), where there is no registry from one layer to another. This can be readily visualized as a stack of playing cards lying flat on top of each other but with no alignment between the edges (Fig. 3.9.11).

Mixed-layer (interstratified) systems contain different types of layers in a single stack, hence it is necessary to distinguish these from the types above. In this case, the layer types have different basal spacings and atomic coordinates (for example, illite–smectite interstratifications; Reynolds & Hower, 1970). Combinations of several of these types of disorder frequently occur in natural clay minerals. Intricate structural analysis using modelling techniques can give a reliable picture of the disorder of selected pure clay minerals, but such information is difficult to obtain from multiphase samples. Therefore, the type and degree of disorder of the components in natural rocks is one of the major unknowns when starting a quantitative analysis of such samples. The field of clay mineralogy represents a discipline where QPA has a long tradition, but has struggled with issues arising from a wide variety of disorder types. This complexity has led practitioners away from the use of crystallographic models and encouraged modification of the classical methods of quantitative analysis to incorporate empirical, calibration-based techniques such as those described earlier in this section.

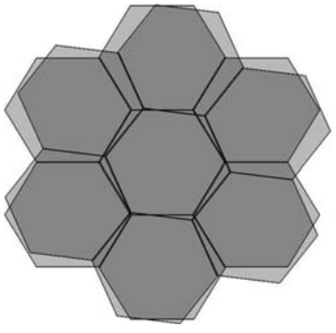

Figure 3.9.11
Turbostratic disorder, illustrated by the stacking of two hexagonal layers rotated by 7°.

An alternative approach is the application of a robust mathematical description of the observed features in the diffraction pattern, thus minimizing their impact on the QPA. In QPA, the existence of disorder contributes to inaccuracy through line broadening and shifting, which results in difficulties in the extraction of integral intensities or scale factors. A range of tools for the modelling of diffraction patterns of disordered layer structures has existed since the middle of the last century (Hendricks & Teller, 1942; Warren, 1941); these have been summarized by Drits & Tchoubar (1990).

In clay mineralogy, highly oriented samples are used for phase identification and characterization. One-dimensional diffraction patterns are collected initially from these, commonly air-dried, oriented samples and contain the information along **c*** that is characteristic of the type, composition and sequence of the layers comprising the clay. Based on this information, the clay minerals are classified into layer types, a classification which is a precursor to more precise identification of mineral species. Diffraction patterns are often collected again following various treatments of the oriented samples (*e.g.* solvation with ethylene glycol, heating to predetermined temperatures for specified times, wetting and drying cycles). Changes in peak positions, shapes and intensities between treatments are also diagnostic for identification of the clay mineral type present.

From a mathematical point of view, the one-dimensional calculation of intensities is much less laborious than a three-dimensional one, because only z coordinates are used and a–b translations and rotations are not considered. In 1985 Reynolds introduced the software package *NEWMOD* for the simulation of one-dimensional diffraction patterns for the study of interstratified systems of two clay minerals (Reynolds, 1985). This simulation was based upon a suite of parameters including instrumental, chemical and structural factors, and has been widely applied to the QPA of interstratified clays *via* the 'pattern-mixing' approach. An updated version (*NEWMOD+*; Yuan & Bish, 2010) has since been developed that incorporates improvements in clay-structure modelling, an improved GUI and the calculation of various fitting parameters that improve the operator's ability to estimate the quality of the profile fit.

The principal drawback of one-dimensional pattern approaches to QPA is that they are limited to the quantification of the ratio of layered structures only. Other minerals within the sample cannot be quantified at the same time. The degree of preferred orientation achieved in the oriented specimens may also differ between the mineral species present depending upon the method of sample preparation (Lippmann, 1970; Taylor & Norrish, 1966; Zevin & Viaene, 1990). This will affect the intensities of the observed peaks, which in turn affects the modelling of the relative proportions of the constituent minerals (Dohrmann *et al.*, 2009; Reynolds, 1989). Therefore, the quantification of minerals from severely oriented samples such as these is frequently inaccurate, as existing correction models are unable to describe the intensity aberrations adequately (Reynolds, 1989).

Quantification of clay minerals within multiphase specimens requires the modelling of the three-dimensional pattern of the randomly ordered clay. There are a number of approaches

incorporated in various software packages for the calculation of these three-dimensional diffraction patterns of disordered structures. *WILDFIRE* (Reynolds, 1994) calculates three-dimensional diffraction patterns of randomly oriented illite and illite–smectite powders with various types and quantities of rotational disorder. This is limited, however, to specific mineral types (the procedure has provided much information about the structural disorder of illite, for example) and is computationally demanding. Another approach is the general recursive method of Treacy *et al.* (1991), which simulates diffraction effects from any crystal with stacking disorder. This uses the intensity calculations of Hendricks & Teller (1942) and Cowley (1976) along with Michalski's recurrence relations describing disorder (Michalski, 1988; Michalski *et al.*, 1988). The calculation process for this method is less time consuming than that of *WILDFIRE*, but has the drawback of requiring the user to define the complete stacking sequence including stacking-transition probabilities and interlayer vectors. The original software for this method, *DIFFAX* (Treacy *et al.*, 1991), was extended by a refinement algorithm to *DIFFAX+* (Leoni *et al.*, 2004) and *FAULTS* (Casas-Cabanas *et al.*, 2006), but multiphase analysis is not possible within either package.

The application of Rietveld-based methods is widespread with many industrial applications, but their application to samples containing disordered materials is not yet routine. As the classical Rietveld method is based on the calculation of intensity for discrete reflections, the question of how the diffraction patterns of disordered phases may be modelled arises.

In principle, every atomic arrangement can be described in the space group *P*1 if the cell parameters are sufficiently large and a reflection-intensity calculation using the Rietveld method could then be performed. But the absence of symmetry in such 'large cell' models makes them inflexible, and parameters describing probabilities of translational and rotational stacking faults and layer-type stacking may not be directly included and refined. Nevertheless, some applications of such externally generated, large-cell structures in Rietveld phase analysis have been published; for example the phase analysis of montmorillonite (Gualtieri *et al.*, 2001).

The use of small, ideal cells in a traditional Rietveld approach for the calculation of diffraction patterns is hampered by the fact that the number of reflections generated by such models is insufficient to fit the asymmetric peak shapes of disordered layer structures. Standard anisotropic line-broadening models exist, such as ellipsoids (Le Bail & Jouanneaux, 1997), spherical harmonics (Popa, 1998) or the distribution of lattice metric parameters (Stephens, 1999), but these are typically unable to fit the patterns of disordered layered structures. They may also become unstable when physically unrealistic parameters are introduced, such as higher-order spherical harmonics. The application of such standard broadening models to clay minerals has therefore not proved successful.

Other Rietveld-based methods attempt to approximate the diffraction features of disordered layered materials by empirical enhancement of the number of reflections. The simplest method is the splitting of the reflections of a traditional cell into two or three separate reflections that can be separately broadened and shifted, following prescribed rules (Bergmann & Kleeberg, 1998). In this way, the broadening of special classes of peaks, for example reflections with $k \neq 3n$, can be modelled. This method is particularly suitable for structures showing well defined stacking faults, such as **b**/3 translations or multiples of 120° rotations. However, when structures show more complex disorder, such as turbostratic stacking, simple geometric dependencies of broadening and shifting are not sufficient to approximate their diffraction patterns.

Turbostratically disordered structures can be depicted in reciprocal space as infinite rods perpendicular to the *ab* plane and parallel to $\mathbf{c}^*$; see Fig. 3.9.12 (Ufer *et al.*, 2004). The diffraction features from such disordered materials consist of two-dimensional asymmetric bands, as can be observed typically for smectites and some other clay minerals (Brindley, 1980). One method for approximating the diffraction effects along the reciprocal-lattice rods within the Rietveld method is *via* the 'single-layer' approach (Ufer *et al.*, 2004). Here, a single layer is placed in a cell elongated along $\mathbf{c}^*$, which is effectively a 'supercell'. In doing this, an enhanced number of discrete lattice points are generated along the rods, according to the factor of elongation of the cell. This elongation generates a continuous distribution of additional *hkl* positions on the reciprocal rods. The inclusion of only a single layer in the supercell destroys periodicity, which is lacking in turbostratically disordered structures. By treating the pseudo-peaks of the supercell in the same manner as other structures within the Rietveld method (*i.e.*, introducing additional broadening, scaling the intensity) and separately calculating the peaks of the 00*l* series, the patterns of turbostratic structures like smectites can be reliably fitted. The model generated in this fashion can be used directly in phase quantification (Ufer, Kleeberg *et al.*, 2008; Ufer, Stanjek *et al.*, 2008).

However, this approach is limited to the turbostratic case. Moreover, the basal 00*l* series points are conventionally calculated, assuming rational diffraction from constant basal spacings in the stack. So the method cannot be applied to mixed-layered structures.

In order to overcome this limitation, Ufer *et al.* (Ufer, Kleeberg *et al.*, 2008; Ufer *et al.*, 2012) combined the recursive calculation method of Treacy *et al.* (1991) and the supercell approach in the structure-description code of the Rietveld software *BGMN* (Bergmann *et al.*, 1998). In this method a supercell is used to generate numerous discrete *hkl* spots along $\mathbf{c}^*$, but the partial structure factors are calculated by the recursive algorithm. This allows the refinement of structural parameters of mixed-layered structures and simultaneous Rietveld QPA to be performed (Ufer *et al.*, 2012). A broader introduction of such models in Rietveld phase analysis can be expected with the

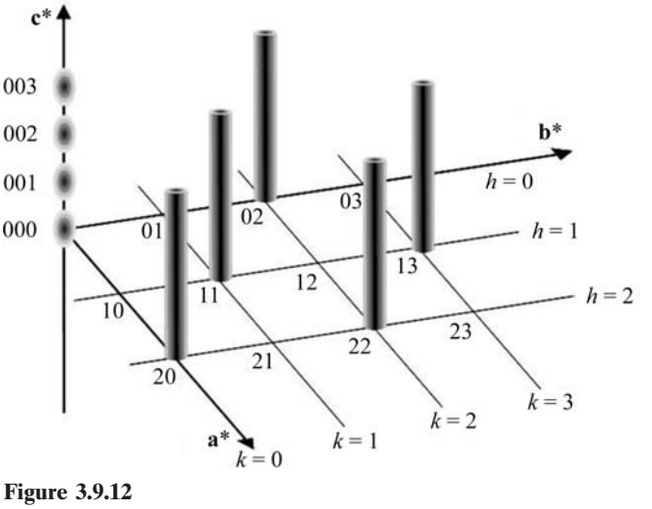

Figure 3.9.12
Section of the reciprocal lattice of a turbostratically disordered pseudo-hexagonal *C*-centred structure.

development of reliable structure models and enhanced computational power (Coelho *et al.*, 2016, 2015; Bette *et al.*, 2015).

3.9.6.3. *Quantitative determination of amorphous material*

Traditionally, most activity in diffraction-based QPA has been concerned with the assessment of the crystalline components. However, all materials possess a non-diffracting surface layer with some degree of disorder or contain some surface reaction products and adsorbed species. While such a layer can easily account for ∼1 wt% of the entire sample in a finely divided solid, the fraction of this surface layer will increase as the particle size decreases (Cline *et al.*, 2011). In addition, some materials can contain separate phases that may be amorphous or at least poorly crystalline. The advent of nanotechnology has served to further blur the boundaries between what is defined by powder XRD as crystalline or amorphous.

During *in situ* studies, some phases undergo transformations *via* amorphous intermediate components; the presence of these phases has the potential to influence our understanding of reaction mechanisms. Given the potential for these amorphous components to influence bulk-material properties, the need to quantify them is an increasingly important issue for analysts using diffraction-based methods. Many of the traditional phase-quantification techniques described in this chapter fail to take into account the occurrence of amorphous material in the sample and, without careful attention by the analyst, its presence may remain undetected.

Madsen *et al.* (2011) recently reviewed a range of techniques for the determination of amorphous content and assessed their applicability for various analytical situations. The study used both single-peak and whole-pattern methodology and applied it in two distinct ways.

(1) The first method used an indirect approach; the crystalline components were quantified and put onto an absolute scale using either an internal- or external-standard method. The amorphous content was then determined by subtracting the sum of the absolute weight fractions of the crystalline components from unity.
(2) The second method used a direct approach; it relied on being able to 'see' the amorphous contribution in the diffraction and being able to obtain an estimate of its intensity during analysis (Fig. 3.9.13). Intensity contributions of amorphous phases are not always evident in the diffraction pattern, especially at low concentrations. Even when their presence is apparent, it can be difficult to resolve their contribution from other components of the diffraction pattern such as pattern background. However, once an intensity estimate is obtained, and an appropriate calibration constant derived, the amorphous phase can be included in the analysis along with the crystalline components.

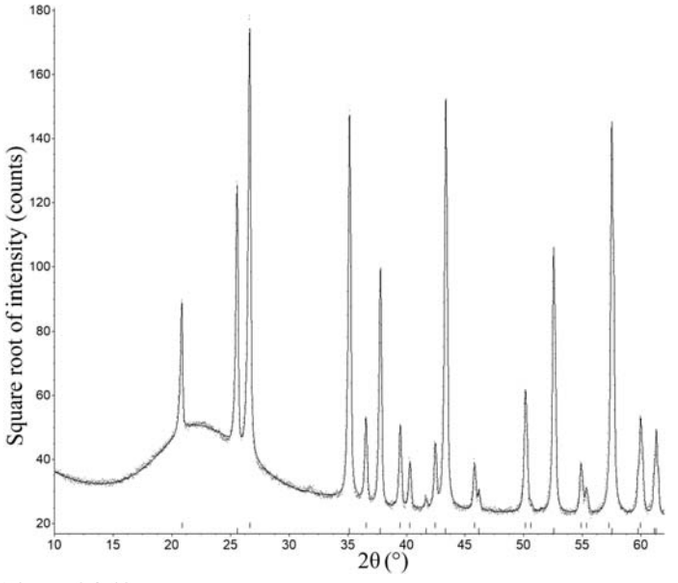

Figure 3.9.13
Output of Rietveld refinement of XRD data (Cu $K\alpha$ radiation) for a synthetic sample containing a mixture crystalline and amorphous phases. The observed data are represented as grey dots and the calculated pattern as the solid black line overlaying them. The broad peak centred at ∼22° 2θ is due to amorphous silica flour. The rows of tick marks at the bottom represent the positions of the Bragg reflections for quartz (upper) and corundum (lower).

In general, for the determination of amorphous material the problem will dictate the method(s) used. All methods discussed in the study of Madsen *et al.* (2011) are, in principle, capable of determining the concentration of amorphous material in mixtures with similar levels of accuracy and precision as is possible for crystalline phases (down to ∼1% absolute or better). The limitations are similar to those for the QPA of crystalline phases, and are dictated by sample properties and the analytical techniques used.

A summary of the recommendations resulting from the study include:

(1) Where the intensity contribution of the amorphous content to the diffraction pattern is not evident, one of the indirect methods (internal or external standard) should be used. For indirect methods, any errors in the analysis of the crystalline phases will decrease the overall accuracy attainable since the amorphous phase abundance is determined by difference.
(2) Where intensity contributions of amorphous phases are evident in the diffraction pattern, any method based on the direct modelling of the amorphous component provides improved accuracy relative to the indirect methods.
(3) Calibration-based methods usually have the potential to achieve the highest accuracy, as residual aberrations in the data, such as microabsorption, are included in the calibration function. Caution is advised here as the magnitudes of these residual errors may change with different sample suites, and so a calibration function derived for one sample suite may not be generally applicable.
(4) A sample of pure amorphous material, or a sample where the amorphous content is high and its concentration known, is normally required to establish an accurate model for the direct methods.

Some materials contain more than one amorphous phase and there may be a desire to quantify these separately rather than as a group. This provides a significant challenge since their broad diffraction patterns will be highly overlapped, thus leading to a high degree of correlation during analysis. However, Williams *et al.* (2011) have demonstrated that, with careful experimentation and data analysis, it is possible to provide QPA for two poorly crystalline components in geopolymers.

Phase abundances reported in the literature are often provided in a manner that suggests they are absolute values. Where no specific allowance for amorphous content has been made and reported, it is better to assume that the reported phase abundances are correct relative to one another, but may be overestimated in an absolute sense. Therefore, standard practice in QPA should be to use methodology which produces *absolute* rather than *relative* phase abundances. Any positive difference between unity and the sum of the absolute weight fractions will

alert the analyst to the presence of non-analysed material in the sample.

3.9.7. QPA from *in situ* experimentation

In situ analysis is a growth area in the field of powder diffraction (Ehrenberg *et al.*, 2013) and is dealt with in depth elsewhere in this volume (see Chapter 2.9). The technique is unparalleled in providing information about reaction mechanisms and kinetics under simulated operational conditions and without the artefacts potentially associated with post-mortem sampling or *ex situ* methods.

An *in situ* experiment collects dynamic, time-resolved data, which present unique challenges for QPA. The phase assemblages formed in such experiments may be quite complex and change dramatically over the course of the experiment. In addition, the data are generally of lower quality than those collected for *ex situ* samples at ambient conditions. This may be due to poor counting statistics resulting from the rapid counting times needed to follow various phase transitions. Data for *in situ* studies are often collected using area detectors, some of which are not photon-counting devices. Care should be taken in the error propagation and hence the weighting used during data analysis.

The data quality may also be affected by components in the sample chamber that are required in order to achieve the environmental conditions (temperature, pressure, solution or gaseous atmosphere, and so on) necessary for the experiment: these components may either attenuate the incident and diffracted beams or contribute features to the pattern resulting from scattering of the beam.

One very important issue that arises from *in situ* studies is the large number of data sets generated. The rapid counting times available at modern synchrotron and neutron facilities mean that hundreds or thousands of diffraction patterns can be collected over the duration of the *in situ* experiment.

3.9.7.1. *Data analysis*

There are usually a series of steps involved in the analysis of *in situ* diffraction data. Given the large number of data sets collected, it is generally not practicable to undertake detailed analysis of every pattern individually. Since any changes to the component phases are transitions generally observed in a sequence of patterns, data analysis focused on extracting QPA could be undertaken using the following steps:

(1) Cluster the data into a number of groups necessary to describe the major phase regions present during the reaction. This can be achieved (i) visually, using software that allows the plotting of three-dimensional data sets of the type shown in Fig. 3.9.14, or (ii) through the use of automatic clustering algorithms using, for example, principal-component analysis.

(2) Select the 'most typical' pattern of each cluster as well as the two 'least typical' patterns at the extreme ends of the cluster. These patterns are often identified by clustering software based on the statistical similarity between patterns in the cluster.

(3) Identify the phases present in each cluster using the most typical pattern. This is not always a trivial task since (i) new phases that are not currently present in databases may have been generated; (ii) effects such as thermal expansion or variation of chemical composition may have changed the peak positions so that search/match procedures are no longer successful; or (iii) impurity elements may have stabilized phases that are not expected from related phase-diagram studies.

(4) For the discussion here, it will be assumed that the quantification process will be *via* a whole-pattern method.
   (*a*) Develop appropriate (crystal structure or PONKCS) models for every phase observed within the data suite.
   (*b*) Optimize the pattern and phase-analysis parameters using the most typical pattern selected from each cluster.
   (*c*) Set the relevant parameter refinement limits using the least typical patterns. It is necessary to limit the range over which refined parameters can vary to avoid the return of physically unrealistic values.

(5) Owing to the large number of data sets, analysis for QPA will generally be approached as a batch process with limited refinement of structural parameters. This limitation on the total number of refinable parameters is necessary during batch processing in order to avoid instability in the refined values as the phases progress from major to minor concentration.

(6) Batch processing of data suites may be conducted in a variety of ways including:
   (*a*) Sequential refinement, beginning with either the first or final pattern of the suite and including all phases present in the entire suite. This methodology must be tempered by a means to either remove or severely restrict refinement of any phases that are not present in all patterns of the suite in order to avoid the reporting of 'false positives' where absent phases have been included. Some software packages allow phases to be removed from the analysis if their abundance is below a selected level or has an error that exceeds some predefined criteria (Bruker AXS, 2013).
   (*b*) Parametric Rietveld refinement (Stinton & Evans, 2007), where the entire suite of diffraction data is analysed simultaneously. Selected parameters are constrained to the applied external variable (*e.g.* temperature) with a function describing their evolution throughout the data sequence. For example, the unit-cell parameters for a phase can be constrained to vary according to their thermal coefficients of expansion. This method can bring stability to refined parameters and allows the refinement of noncrystallographic parameters such as temperature and reaction rate constants directly from the diffraction data. This methodology is particularly suited to relatively simple phase systems, but is difficult to develop for complex multiphase mineralogical systems.

(7) In selecting a model for use in QPA, it is highly recommended that one of the approaches that generate absolute phase abundances is used. Many reactions generate intermediate amorphous phases that convert to crystalline components later in the reaction. If relative phase abundances [such as those produced by the *ZMV* approach embodied in equation (3.9.26)] are used, the amounts of the crystalline phases will be overestimated and this will give misleading indications about the reaction mechanism and kinetics.

Whichever method is employed, it is always necessary to examine a sample of individual results as a test of veracity rather than just accepting the suite of numbers for parameter values and QPA resulting from batch processing.

The study of Webster *et al.* (2013) demonstrates many of these points by following the formation mechanisms of the iron-ore

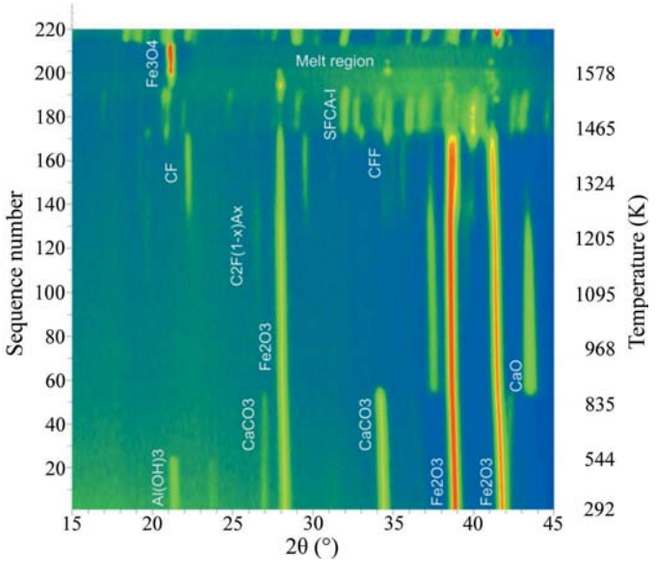

Figure 3.9.14
Raw *in situ* XRD data (Co $K\alpha$ radiation) collected during the synthesis of the iron-ore sinter bonding phase SFCA-I (Webster *et al.*, 2013). The data, collected as a function of heating temperature, are viewed down the intensity axis with red representing the highest intensity and blue the lowest intensity. The identified phases include gibbsite $Al(OH)_3$, calcite $CaCO_3$, haematite Fe_2O_3, lime CaO, calcium ferrites CF and CFF, calcium alumina-ferrite $C_2F_{1-x}A_x$, magnetite Fe_3O_4, and SFCA-I.

sinter bonding phase, SFCA-I, where SFCA = silico-ferrite of calcium and aluminium (Scarlett, Madsen *et al.*, 2004; Scarlett, Pownceby *et al.*, 2004; Webster *et al.*, 2013). The starting material, comprising a synthetic mixture of gibbsite, $Al(OH)_3$, haematite, Fe_2O_3, and calcite, $CaCO_3$, was heated to about 1573 K using an Anton Paar heating stage. The laboratory-based XRD data, collected using an Inel CPS120 diffractometer, are shown in Fig. 3.9.14, while the QPA results are shown in Fig. 3.9.15. Both figures show that there are several phase changes, including the formation of transient intermediate phases before the final production of SFCA.

In Fig. 3.9.15(*a*) the QPA results are derived using the Hill/Howard algorithm (Hill & Howard, 1987) in equation (3.9.26): this is the 'default' value reported by most Rietveld analysis software and normalizes the sum of the analysed components to 100 wt%. The apparent increase in haematite concentration at about 533 and 868 K results from the decomposition of gibbsite and calcite, respectively. There are no possible mechanisms in this system that could lead to an increase in haematite concentration at these temperatures; the reported increases are an artefact derived from normalizing the sum of all analysed phases to 100 wt%. Fig. 3.9.15(*b*) shows the correct result derived using the external-standard approach (O'Connor & Raven, 1988) embodied in equation (3.9.21), which has placed the values on an absolute scale. Fig. 3.9.15 demonstrates the importance of putting the derived phase abundances on an absolute scale for a realistic derivation of reaction mechanism and kinetics.

3.9.8. QPA using neutron diffraction data

One of the early papers detailing the application of the Rietveld method to quantitative phase analysis used neutron diffraction (ND) data (Hill & Howard, 1987). The reasons stated within this work define many of the advantages of neutrons over X-rays for diffraction in general and QPA in particular. One of the most significant advantages for QPA derives from the fact that neutrons interact weakly with matter, hence there is very little microabsorption with ND even in samples comprising a mixture of high- and low-atomic-number materials.

The high penetration capability of neutrons also enables the use of larger sample environments in *in situ* studies, thus enabling studies to be undertaken at, for example, higher pressures than would be possible with many X-ray sources. In addition, larger sample volumes can be investigated, which in turn produces better particle statistics and makes the technique less sensitive to grain size. It also makes ND a bulk technique in comparison with XRD, which is effectively surface-specific with a penetration depth of the order of microns or tens of microns.

The different strengths of ND and XRD mean that they can be exploited in combination to provide complementary information. For example, XRD generally has higher angular resolution and is therefore better at resolving small lattice distortions and heavily overlapped phases. However, the observed intensities in ND do not decrease as strongly with decreasing *d*-spacing. This results in ND providing more accurate determination of atomic displacement parameters and therefore the Rietveld scale factors; this then improves the accuracy of QPA derived from these scale factors (Madsen *et al.*, 2011).

Hill *et al.* (1991) have investigated the phase composition of Mg-PSZ (partially stabilized zirconia) using both ND and XRD. The surfaces of these materials were subjected to various treatments, which meant that they were no longer representative of the bulk. From the more highly penetrating ND data they obtained bulk properties including crystal structure and size and strain parameters of the components along with QPA. From XRD they were able to examine the surface of the samples to investigate the effects of surface grinding and polishing.

The majority of Rietveld-based QPA still relies on the use of accurate crystal structure models; consequently, it is of increasing importance that powder diffraction methods used for structure solution be robust and reliable. Combining laboratory or synchrotron XRD and ND has been shown to be of considerable benefit in the solution of complex structures *via* powder diffraction (Morris *et al.*, 1992). This joint-refinement approach has been used to determine the crystal structure of a component phase of Portland cement (De La Torre *et al.*, 2002) for subsequent use in Rietveld-based QPA.

One of the disadvantages of neutron sources is that they are much less accessible than laboratory X-ray sources and of much lower flux than either laboratory or synchrotron X-rays sources. In addition, larger samples are generally required; this is not always practical in the investigation of many materials.

In many phase systems, the presence of severe microabsorption in XRD data serves to limit the accuracy that can be obtained. The collection of ND data, where microabsorption is virtually absent, from selected samples provides more accurate QPA; selected ND-based values can therefore act as a benchmark for the more routine XRD-based studies.

3.9.9. QPA using energy-dispersive diffraction data

Energy-dispersive diffraction (EDD) involves the use of high-energy white-beam radiation, often from a synchrotron source. This provides very high penetration and is, therefore, ideal as a probe to examine the internal features of relatively large objects (Barnes *et al.*, 2000; Cernik *et al.*, 2011; Hall *et al.*, 1998, 2000). In an experimental arrangement such as that in Fig. 3.9.16, diffraction data can be measured by energy-dispersive detec-

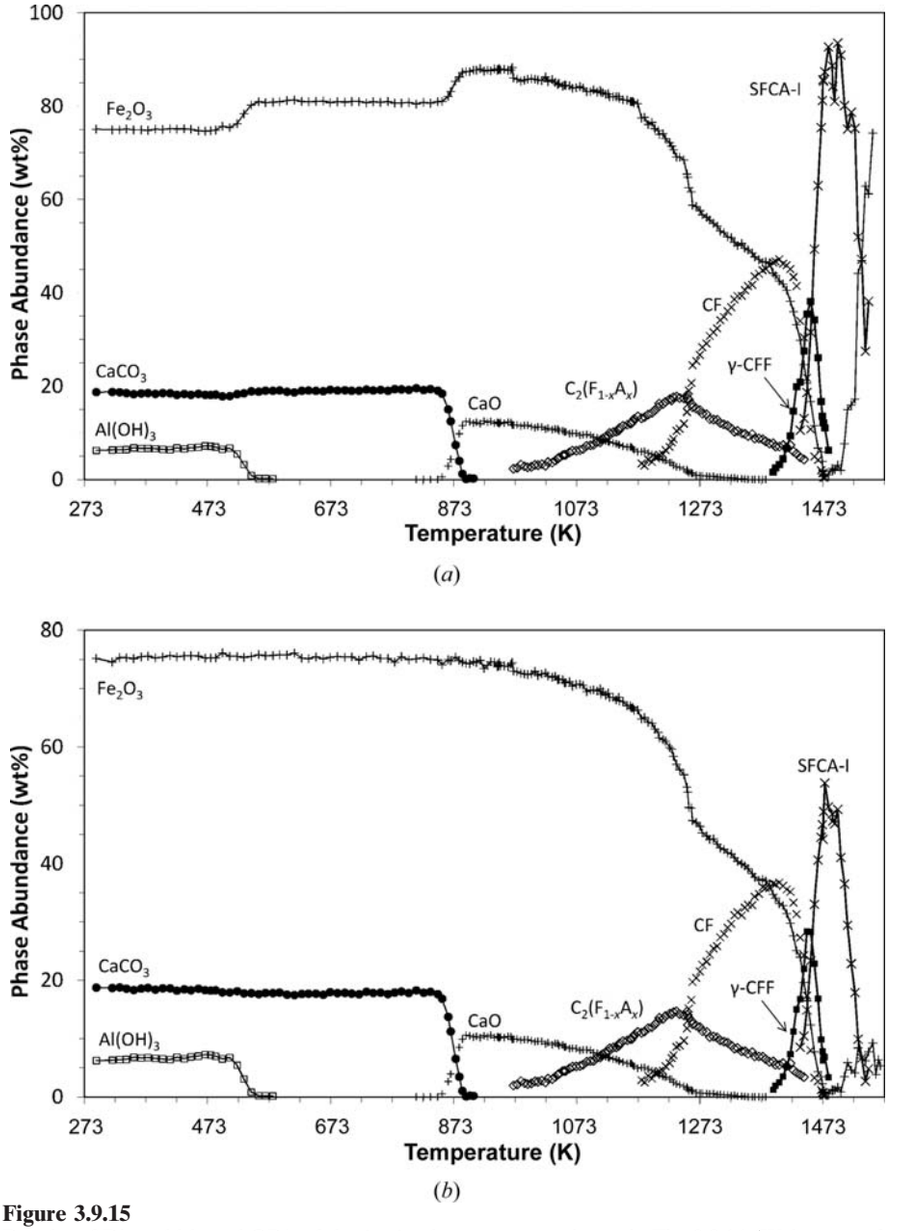

Figure 3.9.15
Results of Rietveld-based QPA of the *in situ* data sequence shown in Fig. 3.9.14 (Webster *et al.*, 2013). The relative phase abundances (upper) are derived using the Hill/Howard algorithm (Hill & Howard, 1987) in equation (3.9.26), while the absolute phase abundances (lower) have been derived from the external-standard approach (O'Connor & Raven, 1988) embodied in equation (3.9.21).

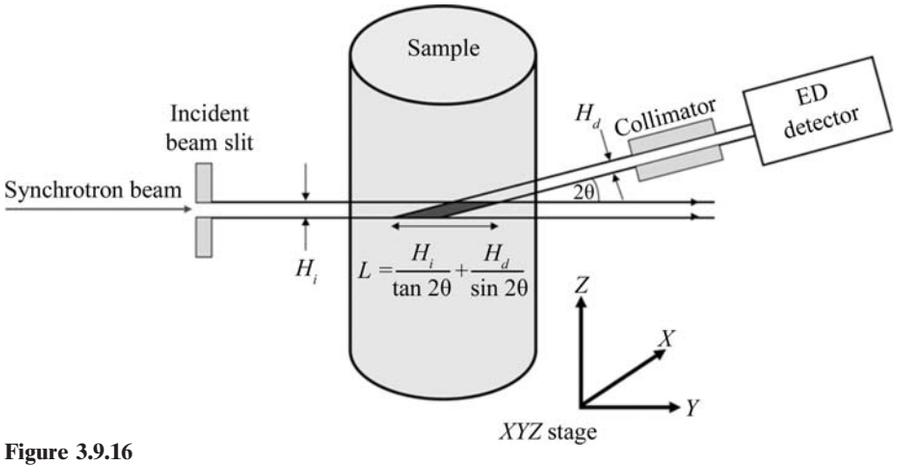

Figure 3.9.16
Basic experimental arrangement for energy-dispersive diffraction. The length of the active area or lozenge (dark grey region), L, is given by the function relating the incident- and diffracted-beam heights (H_i and H_d, respectively) and the angle of diffraction (2θ).

tors producing a spectrum of diffracted intensity as a function of energy.

Traditional angle-dispersive diffraction (ADD) satisfies Bragg's law by using a fixed wavelength and varying 2θ to map the d-spacings. In contrast, EDD data are collected directly on an energy scale at a constant 2θ and the energy is measured to map the d-spacings. This impinges upon the use of Rietveld methodology for QPA since, in contrast to ADD, the structure factors now vary as a function of energy. Energy is related to wavelength *via*

$$E\ (\text{keV}) = \frac{hc}{\lambda} \simeq \frac{12.395}{\lambda}, \qquad (3.9.46)$$

where E is the energy of the incident radiation in keV, h is Planck's constant, c is the speed of light and λ is the wavelength associated with that energy in ångstroms. Rearrangement of equation (3.9.46) and substitution for λ in Bragg's law enables the mapping of the measured energy scale to d-spacings:

$$E\ (\text{keV}) = \frac{6.197}{d \sin\theta}, \qquad (3.9.47)$$

where 2θ is the angle between the incident beam and the detector slit.

EDD data can be analysed using structureless profile-fitting methods such as those of Le Bail *et al.* (see Chapter 3.5) once the energy scale has been converted to a d-spacing scale (Frost & Fei, 1999; Larson & Von Dreele, 2004; Zhao *et al.*, 1997). If the distribution of intensities in the incident spectrum can be measured, it is possible to normalize the EDD data, correct for absorption and convert the pattern to an ADD form using a 'dummy' wavelength (Ballirano & Caminiti, 2001). Access to the incident spectrum, however, is not always possible, especially at synchrotron-radiation sources where the highly intense incident beam could damage the detector.

An alternative approach is to model the pattern directly on the energy scale *via* equation (3.9.47) (Rowles *et al.*, 2012; Scarlett *et al.*, 2009) and extract phase abundances using the methodologies described earlier in this chapter.

However, the major impediment to achieving this is the nonlinearity of the intensity distribution in the incident spectrum. This is due to (i) the nonlinear distribution of intensity as a function of energy in the incident beam, (ii) nonlinear detector responses (Bordas *et al.*, 1977) and (iii) absorption along the beam path (by the sample and air), which skews the energy distribution to the higher energies. This overall nonlinearity can be modelled empirically by functions such a lognormal

curve (Bordas *et al.*, 1977; Buras *et al.*, 1979) or by an expansion of a power function (Glazer *et al.*, 1978). Alternatively, it may be determined experimentally by the use of standards measured under the same conditions as the experiment (Scarlett *et al.*, 2009). This latter approach allows some separation of the contributions from the instrument and the sample, and allows some degrees of freedom in the refinement of sample-related parameters that may be of benefit in dynamic experiments. Other contributions to the diffraction pattern that must also be accounted for include any fluorescence peaks arising from the sample or shielding or collimators, and any detector escape peaks from both diffracted and fluorescence peaks. Fluorescence peak positions and relative intensities should be constant throughout the measurement and may therefore be modelled using a fixed 'peak group' whose overall intensity can be refined during analysis. Escape peaks can be accounted for by the inclusion of a second phase identical to the parent phase but with an independent scale factor and a constant energy offset determined by the nature of the detector (Rowles *et al.*, 2012).

Currently, few Rietveld software packages are capable of dealing directly with the differences between EDD and ADD, specifically (i) the variance of structure factors as a function of energy, (ii) the nonlinear distribution of intensity in the incident beam as a function of energy further modified by a nonlinear detector response, and (iii) the preferential absorption of lower-energy X-rays by the sample/air. *TOPAS* (Bruker AXS, 2013) embodies algorithms that allow the pattern to be modelled directly on the energy scale and also the inclusion of equations to account for intensity variations arising from the experimental conditions. This allows quantification from such data to be achieved directly using Rietveld-based crystal-structure modelling incorporating the Hill and Howard algorithm in equation (3.9.26) (Hill & Howard, 1987). The application of *TOPAS* to a complex EDD experiment investigating the changes to the anode during molten-salt electrochemistry conducted in molten $CaCl_2$ at about 1223 K has been described by Rowles *et al.* (2012) and Styles *et al.* (2012).

3.9.10. Improving accuracy

There are many factors that influence the accuracy and precision of QPA results where (i) accuracy is defined as the agreement between the analytical result and the true value, and (ii) precision is the agreement between results if the analysis is repeated under the same conditions. Precision may further be split into (i) repeatability, which is the agreement between repeated measurement and analysis of the same specimen, and (ii) reproducibility, which additionally includes re-preparation, measurement and analysis of the sample.

3.9.10.1. *Standard deviations and error estimates*

Determination of the actual accuracy of an analysis is not a trivial task in a standardless method. In fact, it cannot be achieved without recourse to another measure of the sample that does incorporate standards. Too often, analysts will report Rietveld errors calculated in the course of refinement as the errors in the final quantification. However, these numbers relate purely to the mathematical fit of the model and have no bearing on the accuracy of the quantification itself.

Consider, for example, a three-phase mixture of corundum, magnetite and zircon. Such a sample was presented as sample 4 in the IUCr CPD round robin on QPA (Scarlett *et al.*, 2002). Its components were chosen with the deliberate aim of creating a sample in which severe sample-related aberrations occur. Table 3.9.4 shows the weighed amounts of each component and the results of replicate analyses of three different sub-samples of this material.

Table 3.9.4
Comparison of errors generated during the analysis of XRD data (Cu $K\alpha$ radiation) from three sub-samples of sample 4 from the IUCr CPD round robin on QPA (Scarlett *et al.*, 2002)

The bias values are (measured − weighed) while the values denoted XRF are the phase abundances generated from elemental concentrations measured by X-ray fluorescence methods.

	Phase		
n = 3	Corundum	Magnetite	Zircon
Weighed	50.46	19.46	29.90
Mean XRD measured wt%	56.52	17.06	26.42
Mean of Rietveld errors	0.15	0.11	0.11
Standard deviation of measured wt%	0.63	0.41	0.35
Mean of bias	6.06	−2.58	−3.48
XRF	50.4(2)	19.6(1)	29.5(1)

It is apparent that the standard deviation of the mean abundances of the three replicates, which represents the expected precision in the analysis, is 3 to 4 times greater than the errors reported by the Rietveld software. The good level of fit achieved in conducting these analyses (evidenced by low R factors) could lead the analyst to conclude that the mean value ± the standard deviation of the mean is an adequate measure of the phase abundances and their errors.

However, both the Rietveld errors and the precision are at least an order of magnitude smaller than the bias. The large bias, in this case due to the presence of severe microabsorption, represents the true accuracy that can be achieved in this example. Unfortunately, there is nothing in the XRD data and Rietveld analysis process that indicates that there may be a problem. It is only when the QPA is compared with other estimates, in this case derived from XRF chemical-analysis results, that the problem becomes apparent. The analyst must take further steps to identify sample-preparation and/or data-collection protocols that may improve accuracy and, importantly, seek ways to verify the results.

3.9.10.2. *Minimizing systematic errors*

The fundamental measured quantities in a diffraction pattern are the integrated intensities of the observed peaks. The precision of these measurements can be improved by: (i) increasing the primary intensity of the diffractometer using optics or higher-power X-ray sources; (ii) using scanning linear detectors (see Chapter 2.1), which have multiple detector elements to collect individual intensities many times; these are then summed to achieve higher accumulated counts; (iii) increasing the number of counts accumulated at each step, that is increasing the step counting time T; and (iv) increasing the number of points, N, measured across the peak.

Often, the temptation is to collect data with large values of N and T to maximize counting statistics. However, the resulting increased precision is only useful up to the point where counting variance becomes negligible in relation to other sources of error; thereafter data-collection time is wasted. For example, if the sample is affected by the presence of severe sample-related

aberrations, the collection of highly precise data will not improve the accuracy of the resulting analysis significantly.

Therefore, the most important approach to improving the accuracy of an analysis is to eliminate the systematic errors. Given that the largest sources of error in QPA are experimental (Chung & Smith, 2000) and relate to sampling and specimen preparation, then this is the area on which the most careful attention needs to be focused. A detailed discussion of sample preparation and data-collection procedures is beyond the scope of this chapter but further details can be found in Chapter 2.10, and in Hill & Madsen (2002) and Buhrke *et al.* (1998).

3.9.10.3. *Minimizing sample-related errors*

3.9.10.3.1. *Crystallite-size issues*

Crystallite size is considered here as the length of a coherent scattering domain and should not be confused with the terms grain or particle size used frequently in powder diffraction to describe the macroscopic size of the components in the sample. The macroscopic size of the particle is somewhat irrelevant (as in ceramics or other solid pieces of samples) as long as the crystallites (or domains) that comprise the particle are (i) sufficiently small to ensure that there are enough crystallites contributing to the diffraction process (Smith, 1992) and (ii) randomly oriented, thus ensuring a true powder-average representation of intensities. However, for large domains or crystallites this assumption is usually not fulfilled and therefore it is necessary to reduce the crystallite size by reducing the size of the particles or grains that constitute the macroscopic objects of a powder.

Most issues in sample preparation are related to crystallite size and preferred orientation of the particles in the sample holder. For QPA a representative sampling of all possible orientations of crystallites with respect to the diffraction geometry is required. Rotation of the sample improves the particle statistics, since more crystallites can satisfy the diffraction condition (Elton & Salt, 1996).

Large-crystallite issues are easily detected using two-dimensional (2D) detectors, where the Debye rings show a 'spotty' intensity distribution. However, most QPA measurements are performed using 0D (point) or 1D (strip) detectors. The effect of large crystallites in a 1D pattern is that a few crystallites may contribute to irregularly high intensities for selected reflections. In the diffraction pattern, this situation is usually identified by intense reflections having a sharp peak profile compared with the surrounding peaks in the pattern. Furthermore, in a Rietveld refinement this situation is manifested by large intensity differences between the observed and calculated pattern that may not be associated with a particular crystallographic direction and hence to preferred orientation. Another way of detecting inhomogeneous crystallite distributions is to measure a series of scans from the same specimen at various rotation angles and comparing the relative peak intensities. It is worth noting that the push towards ever higher resolution in both laboratory and synchrotron instruments serves to further exacerbate the crystallite-size issue. This arises from the use of beams with decreased divergence, resulting in fewer crystallites likely to satisfy the diffraction condition.

There is no simple mathematical correction for large-crystallite issues and the effect is often misinterpreted in Rietveld refinement as preferred orientation. In this case, the correction would typically involve use of several directions for March–Dollase-type functions (Dollase, 1986) or an increasing order of spherical-harmonics coefficients (Ahtee *et al.*, 1989). In any case, this is an improper use of these corrections and the necessity to do so clearly points to deficiencies in the sample preparation and data-collection regime.

The best way to minimize the large-crystallite issue is to reduce the crystallite size through grinding of the sample. However, size-reduction methods need to be carefully assessed, since over-grinding can cause peak broadening due to (i) a decrease of long-range order and hence crystallite size and (ii) the introduction of microstrain (Hill & Madsen, 2002). The practical effect of peak broadening is increasing peak overlap, which may complicate the phase identification. For whole-pattern-based QPA, overgrinding is not as serious as long as it does not yield nanometre-sized particles or amorphous materials. This is because the integral intensity of the peaks is preserved. It should be noted that some phases can undergo transformation to other polymorphs or decompose to other phases during grinding (Hill & Madsen, 2002).

In practice, there is no generally applicable comminution strategy. For each material, a suitable milling device and grinding strategy needs to be identified. Inhomogeneous materials such as ores, concentrates and other mineralogical materials may have very different comminution properties for their constituents, leading to size fractionation during grinding. Large-crystallite issues are frequently observed for hard minerals (*e.g.* quartz, feldspar) while the grain size of soft minerals (*e.g.* talc) is reduced more rapidly.

A practical way of finding a best compromise for the milling conditions of a mixture may be the analysis of a series of samples of the same material where, for example, the grinding time is successively increased and the quantification results are compared. Fig. 3.9.17 shows the variation of analysed wt% with grinding time for two minerals: a stable result is eventually obtained.

There is a more extensive discussion of the impact of large-crystallite size on observed diffraction data (Smith, 1992) and ways to minimize its effect (Elton & Salt, 1996) in the published literature.

3.9.10.3.2. *Preferred orientation*

In order to generate peak intensities that accurately represent the intensity-weighted reciprocal lattice, the crystallites in the powder must not only be sufficient in number, but they must also be randomly oriented. In other words, each crystal orientation should have the same probability of diffracting. Preferred orientation can arise when particles align in the sample holder according to their morphology. This is most common with platy or

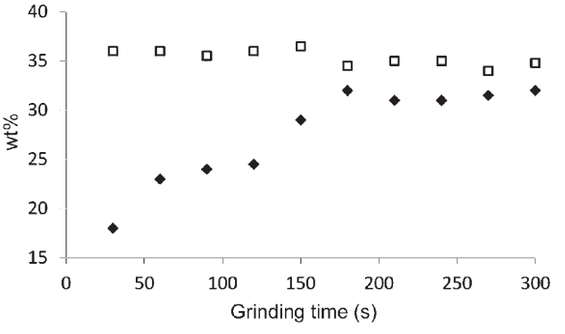

Figure 3.9.17
Variation of the magnetite (filled diamonds) and quartz (open squares) concentration of an iron-ore sample with grinding time. Stable conditions are obtained after about 180 s. Data courtesy ThyssenKrupp – Resource Technologies (Knorr & Bornefeld, 2013).

needle-like materials and the effect on the diffraction pattern is the observation of enhanced intensity along specific crystallographic directions with a subsequent decrease of intensity along other directions.

A number of sample-presentation methods can be used to minimize preferred orientation. For flat specimens, back pressing and side drifting into the sample holder can be effective. These methods tend to produce much less preferred orientation than front-mounted samples, but tend not to be very effective for chronic preferred orientation such as that exhibited by phases like clays, feldspars and chlorite. Reducing the size of the crystallites improves the probability of achieving random alignment of the crystallites in the sample holder. Gradually milling a sample and monitoring the preferred-orientation coefficients as a function of grinding time may again help to find the correct, or at least reproducible, grinding conditions (Fig. 3.9.18).

A major advantage of whole-pattern-based QPA over single-peak methods is that all classes of reflections are considered in the calculation. In this sense, the method is less prone to preferred orientation of a particular class of peaks. Furthermore, orientation effects may be corrected by applying March–Dollase (Dollase, 1986) or spherical-harmonics (Ahtee *et al.*, 1989) corrections. A properly applied correction may be of high importance for QPA in cases where a phase is present at low concentration and only a few peaks can clearly be identified in the pattern. If those peak(s) are affected by preferred orientation, the March–Dollase coefficient correlates strongly with scale factors and leads to biased QPA results. Examples of this effect occur with layered materials that have sheet-like morphology perpendicular to the *c* axis, including mica and clay minerals, which typically show stronger than expected intensity for the 00*l* reflections.

The crucial factor seems to be to what extent the orientation parameters correlate with the Rietveld scale factor. An example where the correlation is only minor is sample 2 from the IUCr CPD round robin on QPA (Scarlett *et al.*, 2002). In that example, brucite [$Mg(OH)_2$] shows strong preferred orientation along the 00*l* direction. This may be corrected by the March–Dollase model, which returns a refined value of 0.66. However, the introduction of this preferred-orientation correction only changes the brucite concentration from 35 to 36 wt% (weighed = 36.36 wt%); this is surprising because the orientation is strong and the weighted residual R_{wp} changes from 30 to 15%. Close examination of the correlations reveals a strong correlation between the brucite scale factor and preferred-orientation factor.

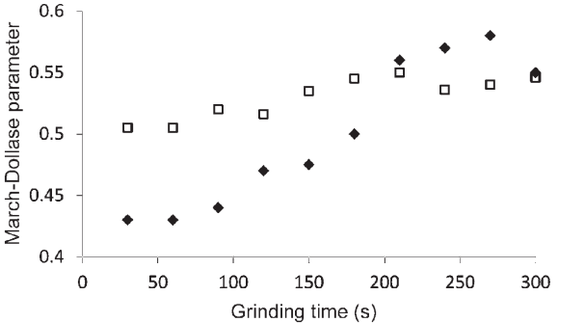

Figure 3.9.18
Increase of the March–Dollase (Dollase, 1986) parameter and related decrease of the degree of preferred orientation with grinding time for the two amphibole species actinolite (filled diamonds) and grunerite (open squares) in an iron ore. Data courtesy ThyssenKrupp – Resource Technologies (Knorr & Bornefeld, 2013).

However, the correlation of the brucite preferred-orientation parameter to the other scale factors (zincite, corundum and fluorite) is close to zero; this explains why in this example the QPA is not highly dependent on preferred orientation. In cases of strong correlation between the orientation parameter of one phase and the scale factors of other phases, preferred orientation should probably not be refined, or at least it should be verified carefully. It is worth noting that, in all Rietveld-based analyses, users should examine the correlation matrix as a matter of general practice to establish which parameters might be affecting parameters of interest.

It should be noted that sample rotation around the scattering vector (typically employed in flat-plate Bragg–Brentano geometry) during the scan does not reduce preferred orientation, since there is no change between the preferred-orientation direction and the diffraction vector. Using capillaries in transmission geometry assists in the reduction of preferred orientation, but the time-consuming nature of packing capillaries makes this technique infeasible in industrial applications where diffraction-based QPA is used for routine quality control.

3.9.10.3.3. *Microabsorption*

The strongest on-going impediment to accuracy in QPA using XRD data is microabsorption. The microabsorption effect occurs when a multiphase sample contains both low- and highly absorbing phases. For the highly absorbing phases, the X-ray beam is more likely to be absorbed in the surface layers of the grain; thus, the fraction of the grain contributing to the diffraction pattern will decrease as the size of the grain increases above the beam-penetration depth. For the low-absorbing phases, the beam penetrates further into the particle resulting in a greater likelihood of the desired 'volume diffraction' occurring (Brindley, 1945). The overall effect is the observation of a disproportionate amount of observed intensity from individual grains relative to what would be expected for the average absorption of the sample; the highly absorbing phases are under-represented relative to the low-absorbing phases. There is extensive discussion of the microabsorption issue in Zevin & Kimmel (1995).

Brindley (1945) has described the particle absorption contrast factor τ_α as

$$\tau_\alpha = (1/V)\int_0^V \exp\left(-(\mu_\alpha - \bar{\mu})\right) \mathrm{d}v, \qquad (3.9.48)$$

where V is the particle volume, and μ_α and $\bar{\mu}$ are the linear absorption coefficients of phase α and the entire sample, respectively. While it is relatively easy to calculate the absorption coefficients, equation (3.9.48) implies knowledge of the *particle* size of each component; this information is only available through independent microscope or light-scattering characterization.

This correction term is commonly incorporated into QPA through a modification to equation (3.9.26) of the form

$$W_\alpha = \frac{S_\alpha (ZMV)_\alpha / \tau_\alpha}{\sum_{k=1}^{n} S_k (ZMV)_k / \tau_k}. \qquad (3.9.49)$$

Brindley has also devised criteria by which to assess whether a microabsorption problem is likely to be present or not. Calculation of μD (where μ is the linear absorption coefficient and D is the particle diameter) yields the following criteria:

(i) $\mu D < 0.01$ – fine powder. There is negligible microabsorption and hence no correction is necessary.

Table 3.9.5
Calculated values of μD (where μ is the linear absorption coefficient and D is the particle diameter) for Cu $K\alpha$ X-rays for corundum, magnetite and zircon with a range of particle sizes

	μD		
Diameter (μm)	Corundum, Al_2O_3 (μ = 125 cm^{-1})	Magnetite, Fe_3O_4 (μ = 1167 cm^{-1})	Zircon, $ZrSiO_4$ (μ = 380 cm^{-1})
0.1	0.001	0.012	0.004
0.2	0.003	0.023	0.008
0.5	0.006	0.058	0.019
1	0.013	0.117	0.038
2	0.025	0.233	0.076
5	0.063	0.584	0.190
10	0.125	1.167	0.380
20	0.251	2.334	0.759

(ii) $0.01 < \mu D < 0.1$ – medium powder. Microabsorption is likely to be present and the normal Brindley correction model can be applied.

(iii) $0.1 < \mu D < 1.0$ – coarse powder. A large microabsorption effect is present. The Brindley model can only be used to provide an approximate correction provided that μD is closer to the lower limit of the range.

(iv) $\mu D > 1.0$ – very coarse powder. This indicates that severe microabsorption is likely to be present and that any correction is well beyond the limits of the model.

It is difficult for the analyst encountering a new sample to determine whether a correction for microabsorption is required without first obtaining additional information. A minimum requirement should be to calculate μD for each phase present. However, this requires knowledge of the particle size which, in a multiphase sample, can be very difficult to obtain unambiguously. Even when the particle size is measured by, for example, dynamic light scattering or optical or SEM image analysis, the applicability of the correction can still be unclear. In addition, the correction factor embodied in equations (3.9.48) and (3.9.49) makes the assumption that the particles of the phase of interest are spherical and of uniform size. This assumption is unrealistic in almost all samples; in reality, each phase is likely to be present at a wide range of particle sizes and the particles are highly unlikely to be spherical.

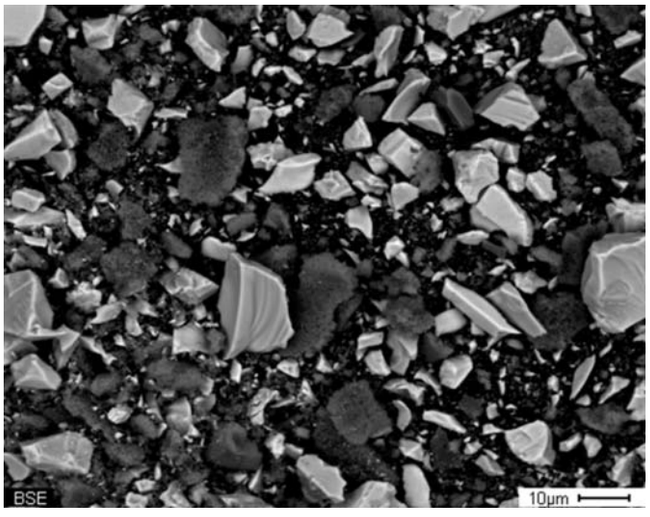

Figure 3.9.19
Backscattered-electron SEM image of a mixture of approximately equal amounts of corundum (dark grey), magnetite and zircon (lighter grey). Note the wide range of particle sizes present for each of the three phases.

Table 3.9.5 shows the calculated values of μD for Cu $K\alpha$ radiation for some commonly encountered phases in mineralogical analysis. For the least absorbing phase (corundum), the upper range of applicability of the Brindley model (medium powder) is reached at about 5 μm; by 8 μm, the coarse powder criterion has been reached and the correction model is no longer applicable. For magnetite, these limits are reached an order of magnitude earlier at about 0.5 and 0.9 μm, respectively.

Fig. 3.9.19 shows an SEM image of a mixture of approximately equal amounts of corundum, magnetite and zircon. The individual components of the sample were weighed and the mixture ground in ethanol in a McCrone micronizing mill (McCrone Research Associates, London) for 10 min g^{-1}. This approach to sample preparation is generally accepted as best practice for powder XRD because it minimizes structural damage during grinding (Hill & Madsen, 2002). After decanting and drying, the sample was back-packed into a cavity sample holder for XRD data collection; the same sample was then used to obtain the SEM image in Fig. 3.9.19. Visual observation shows a wide range of particle sizes (from submicron to greater than 10 μm) and shapes that do not even approximate spheres. Even if this information is obtained, selection of a particle size that best represents each individual phase is a difficult task. In addition, in many sample suites, the component phases exhibit a range of hardness resulting in different rates of grinding and hence difference size ranges. Regrettably, what happens too often in practice is that analysts will micronize the sample and then select an arbitrary particle size in order to derive a 'preferred' value for the final analysis. Therefore, caution is advised in the application of these correction models. The IUCr CPD round robin on QPA (Madsen *et al.*, 2001; Scarlett *et al.*, 2002) showed that many participants severely degraded their results by applying a correction when none was necessary.

Equation (3.9.48) shows that there two ways to minimize microabsorption. The first is to reduce the absorption contrast by, for example, changing the X-ray wavelength. While corundum and magnetite have very different linear absorption coefficients for Cu $K\alpha$ radiation (126 and 1123 cm^{-1}, respectively), the difference is reduced to 196 and 231 cm^{-1}, respectively, for Co $K\alpha$ radiation. The second approach is to reduce the particle size in order to meet Brindley's fine- or medium-powder criteria.

However, even these steps may not be sufficient to eliminate the microabsorption effect. Slightly different absorption coefficients, or different particle sizes for phases with the same absorption coefficients, may still introduce a bias between expected and analysed concentrations. In this situation, it may be better to use a calibrated hkl_phase or peaks_phase (Section 3.9.6) instead of a Rietveld, structure-based phase. The calibration step involved in the generation of such a phase incorporates the microabsorption problem into the calibration constant.

Fig. 3.9.20 shows the bias between known concentrations (derived from chemical analysis) and QPA-determined concentrations for a series of salt samples. The samples contain halite (NaCl), sylvite (KCl) and kieserite ($MgSO_4{\cdot}H_2O$) as major phases and small amounts of anhydrite ($CaSO_4$), langbeinite [$K_2Mg_2(SO_4)_3$] and carnallite [$KMgCl_3{\cdot}6(H_2O)$]. The linear absorption coefficient of sylvite (254 cm^{-1}) is much higher than halite (165 cm^{-1}). Using crystal-structure-based analysis, there is a systematic deviation of up to 3% with an overestimation of the low absorber (halite) and an underestimation of the high absorber (sylvite). After replacing sylvite by a calibrated

hkl_phase, the bias is reduced to about 1% and does not show systematic deviations.

It should be noted, however, that the phase constants developed using such a calibration approach will only be applicable to the sample suite and preparation conditions for which it was developed. The calibration process will need to be repeated if there are significant changes to the sample suite or sample-preparation conditions.

3.9.10.3.4. *Whole-pattern-refinement effects*

One of the distinct advantages of structure-based whole-pattern fitting for QPA is that no standards need to be prepared because the structure for each phase provides the phase constant *ZMV*; the unit-cell dimensions allow the calculation of the cell volume *V* and the unit-cell contents provide the mass *ZM* (Bish & Howard, 1988; Hill & Howard, 1987). These values are used, along with the Rietveld scale factor *S*, in equation (3.9.26) to derive the phase abundance. This is especially useful for complex systems where the preparation of multiple standards would add considerably to the analytical complexity.

An additional advantage is the ability to refine the crystal structure (unit-cell dimensions and site-occupation factors, for example), when the data are of sufficiently high quality, in order to obtain the best fit between observed and calculated patterns. In addition to updating the *ZMV* value, the site occupancies are contained in the structure-factor calculation and, therefore, will change the relative reflection intensities and have an impact on the scale factor and QPA. Other structural parameters that have a strong effect on the scale factor and QPA are the atomic displacement parameters (ADPs). Strong correlation between the ADPs and amorphous material concentration has been shown by Gualtieri (2000) and Madsen *et al.* (2011).

This leads to the question: which crystal structure should be selected for QPA? Databases contain multiple entries for the same phase with the structures determined using different methods. While ADPs and site-occupation factors determined using neutron diffraction and single-crystal analysis should be favoured over those determined using X-ray powder data, many database entries do not have refined ADPs for all (and in some cases, any) atoms. Often, arbitrarily chosen default values of 0.5 or 1.0 $Å^2$ for B_{eq} are entered for all atoms, but this should be viewed or used with great caution. There is clearly a need to carefully evaluate the crystal-structure data used for QPA. This is particularly worth mentioning in view of the advent of new 'user-friendly' software that automatically assigns crystal structures after having performed the phase identification.

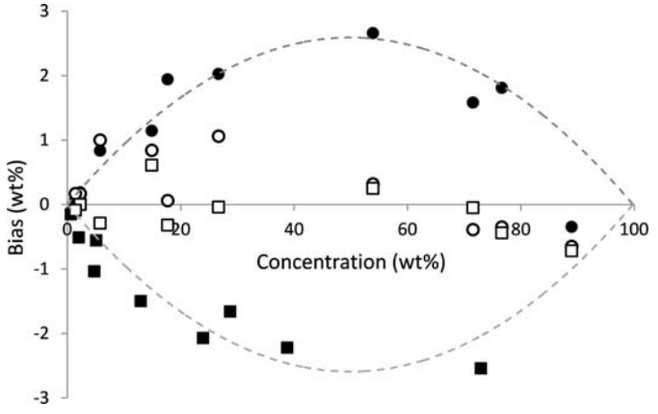

Figure 3.9.20
Bias as a function of phase concentration for industrial salt samples for (i) structure-based QPA (filled symbols) and (ii) calibrated hkl_phase (open symbols) for halite (circles) and sylvite (squares). The broken lines indicate the trend of the bias for structure-based QPA. Data are courtesy of K+S AG, Germany.

Empirical profile-shape models contribute significantly to the complexity (and correlations) of whole-powder-pattern fitting for QPA because of the large number of phases and multiple parameters required to model the profile shape of each phase. The use of convolution-based profile fitting [in, for example, *BGMN* (Bergmann *et al.*, 1998, 2000) and *TOPAS* (Bruker AXS, 2013)] greatly reduces the number of parameters, because the instrument-resolution function (which is constant for a given setup) can be separated from sample-related peak broadening. The instrument component can be refined using a standard and then fixed for subsequent analysis. The sample contribution to peak width and shape can then be related directly to crystallite size and microstrain using a minimal number of parameters. The reduction of the total number of parameters reduces the refinement complexity and the chance of parameter correlation.

The choice of the function used to model the pattern background may also have a strong influence on amorphous content (Gualtieri, 2000; Madsen *et al.*, 2011). Given that the intensities of both the background and the amorphous contribution vary slowly as a function of 2θ, it is inevitable that there will be a high degree of correlation between them. Hence, any errors in determining the true background will result in errors in amorphous phase determination. A simple approach is to use a background function with a minimal number of parameters. A more exact approach requires the separation of the amorphous contribution from background components such as Compton scattering and parasitic scattering by the sample environment and air in the beam path. This is routinely done in pair distribution function (PDF) analysis; details can be found in Chapter 5.7 in this volume and in Egami & Billinge (2003).

Another parameter that correlates with the pattern background is the width of broad peaks for phases of low concentration. If allowed to refine to very large width values, the peaks are 'smeared' over a broad range of the pattern with no clear distinction between peaks and background. The same issue applies when there is a high degree of peak overlap, particularly at high angles, leading to severe under- or over-estimation of the phase. The careful use of limits for either crystallite size or corresponding parameters in empirical peak-shape modelling assists in minimizing this effect.

There can be a subtle interplay between the profile-shape function and the pattern background that has an impact on whole-pattern fitting (Hill, 1992). The data in Fig. 3.9.21, collected using a Cu tube and an Ni $K\beta$ filter, exhibit low-angle truncation of the peak tails at the β-filter absorption edge. On the high-angle side, the anatase peak displays a wide tail which extends to the position of the strongest rutile peak at about 27.5° 2θ. In this case, rutile is present as a minor phase and the error in the background determination using conventional peak-profile modelling (Fig. 3.9.21*a*) introduces about 0.5% bias in the rutile QPA. The use of a more accurate profile model that incorporates the effect of the β-filter absorption edge (Fig. 3.9.21*b*) serves to improve the accuracy (Bruker AXS, 2013).

3.9.10.3.5. *Element analytical standards*

XRD-based derivation of elemental abundances relies on (i) the QPA abundances, and (ii) the assumed or measured stoichiometry of the crystalline phases. The accuracy of the QPA

Table 3.9.6
Compositional analysis of the Dillinger Hütte iron-ore certified reference material SX 11-14, (i) derived from QPA results, taking into account the nominal stoichiometry of the phases (XRD) and (ii) the certified analyses (Cert) (Knorr & Bornefeld, 2013)

Phase	wt%		Fe	FeO	SiO_2	Al_2O_3	MgO	CaO	K_2O	Na_2O	C
Haematite	0.37		0.26	—	—	—	—	—	—	—	—
Goethite	3.86		2.43	—	—	—	—	—	—	—	—
Magnetite	85.97		62.21	26.68	—	—	—	—	—	—	—
Quartz	5.73		—	—	5.73	—	—	—	—	—	—
Gibbsite	0.71		—	—	—	0.46	—	—	—	—	—
Talc	1.79		—	—	1.13	—	0.57	—	—	—	—
Orthoclase	0.30		—	—	0.19	0.05	—	—	0.05	—	—
Albite	0.89		—	—	0.60	0.18	—	—	—	0.10	—
Calcite	0.40		—	—	—	—	—	0.22	—	—	0.19
			Fe	FeO	SiO_2	Al_2O_3	MgO	CaO	K_2O	Na_2O	C
		XRD	64.89	26.68	7.66	0.70	0.57	0.22	0.05	0.10	0.19
		Cert	65.55	27.20	7.47	0.27	0.56	0.42	0.06	0.08	0.12
		Bias	−0.66	−0.52	0.19	0.43	0.01	−0.20	−0.01	0.02	0.07

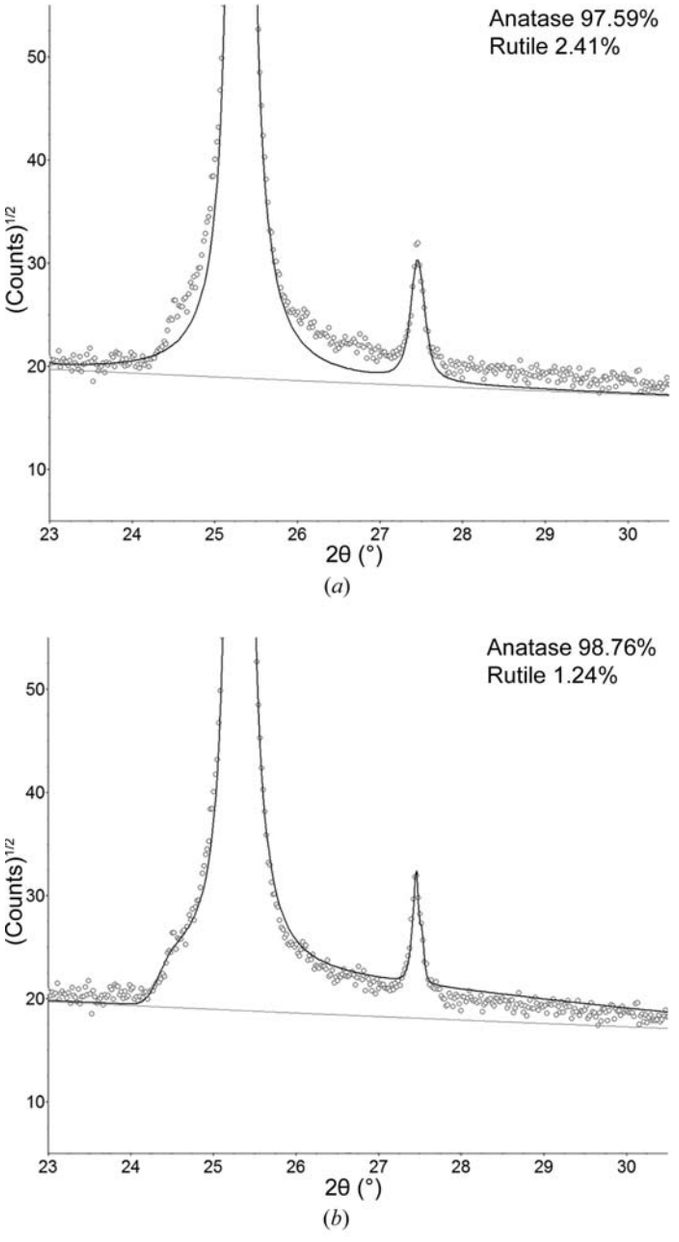

Figure 3.9.21
Profile fit of anatase and rutile (*a*) without and (*b*) with a $K\beta$ filter absorption-edge correction.

result may then be evaluated by comparing the calculated elemental abundances with those determined by traditional chemical-analysis techniques. However, for the best level of agreement, this method requires that the composition of the crystalline phases be well defined. A complication, in particular for minerals, is that idealized compositions may be reported but do not necessarily match the actual composition of the species present in the sample. Where possible, detailed phase analysis using microbeam techniques should be undertaken to establish the true composition for each phase. A complication that serves to decrease the agreement is that chemically based compositional analysis does not distinguish between crystalline and amorphous phase content, while the diffraction-based QPA usually measures only the crystalline phases. Generally, the composition of amorphous phases may not be known accurately and even highly crystalline material can contain amorphous components because of non-diffracting surface layers of the grains (Cline *et al.*, 2011).

An example demonstrating the level of agreement that can be achieved is that of the iron-ore certified reference material SX 11-14 from Dillinger Hütte (Fig. 3.9.22). The material is moderately complex and consists of nine distinct mineral species. The data were measured with Co $K\alpha$ radiation and analysed using Rietveld-based QPA in *TOPAS* (Bruker AXS, 2013). The phase abundances are converted to elemental and oxide compositions for comparison with the certified elemental analyses (Table 3.9.6). There is excellent agreement between the XRD results and the chemical analysis with bias values better than ±1 wt%.

3.9.10.3.6. *Phase-specific methods: diffraction SRMs, round-robin samples and synthetic mixtures*

In contrast to elemental compositional analysis, where standard reference materials (SRMs) are widespread, there are only a very limited number of SRMs available for diffraction-based QPA. Prominent examples are SRMs for the cement industry [NIST reference material clinker 8486 (Stutzman & Leigh, 2000) and ordinary Portland cement NIST SRM 2686] or ceramics materials (silicon nitride CRM BAM-S001) (Peplinski *et al.*, 2004). Similar to elemental standards, the certified values do not necessarily represent the true composition. Rather, they are published values that are typically averaged over the results from different independent methods, instruments and laboratories. Therefore, confidence limits of concentrations are provided that may be much larger than estimated standard deviations of concentrations within a single laboratory.

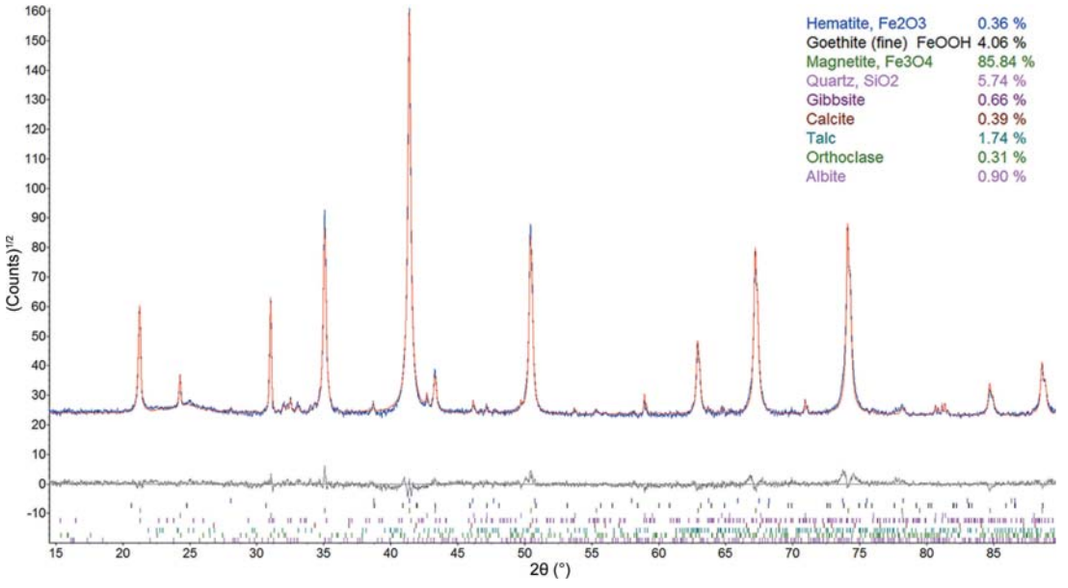

Figure 3.9.22
Output of Rietveld refinement and results of QPA for the iron-ore certified reference material SX 11-14 from Dillinger Hütte. The data were measured with Co *Kα* radiation.

Finally, a number of inter-laboratory tests, or round robins, have been conducted on synthetic mixtures in order to set benchmarks for particular materials and/or the application of methods. Examples range from well ordered, high-symmetry phases discussed in earlier sections of this chapter (Madsen *et al.*, 2001; Scarlett *et al.*, 2002) to standard mixtures of geological material, granite and bauxites (Bish & Post, 1993), and technical products like artificial Portland cements (De la Torre & Aranda, 2003) where relative biases of 2–3% for the main phases and 5–10% for minor phases were found.

Very recently, the precision and accuracy of QPA for the analysis of Portland clinker and cement were determined for synthetic mixtures and commercial samples. The scatter of the results from the inter-laboratory comparison, and the fact that individual errors are much smaller than the standard deviations of all submitted results, points to the widespread presence of user-dependent systematic errors (Léon-Reina *et al.*, 2009).

One of the most challenging round robins is the Reynolds Cup (Ottner *et al.*, 2000; McCarty, 2002; Kleeberg, 2005; Omotoso *et al.*, 2006; Raven & Self, 2017), organized biannually since the year 2000 by the Clay Minerals Society. Synthetic mixtures representing typical sedimentary rock types are analysed and require a very high level of sample preparation and analytical skills because of the presence of a variety of clay minerals.

While most round robins have dealt with inorganic materials, one for pharmaceutical materials was organised by the International Centre for Diffraction Data (ICDD) together with the Pharmaceutical Powder XRD symposium series (PPXRD) (Fawcett *et al.*, 2010). A major outcome was the identification of operator errors in all steps of the analysis to be the largest source of error. This highlights the importance of reducing systematic errors for improving accuracy in QPA.

As a concluding remark, a variety of factors may influence the precision and accuracy of QPA. Nonetheless, better than 1 wt% agreement may be achieved for simple systems of well crystallized material. Moderately complex mixtures such as those routinely observed in cement plants and in the mining industry can be typically analysed at a 1 wt% level of accuracy provided that the analyst chooses the most appropriate sample-preparation, data-collection and analysis methodologies for the samples in question.

3.9.11. Summary

The value in using diffraction-based methods for the determination of phase abundance arises from the fact that the observed data are derived directly from the crystal structure of each phase. Knowledge of phase abundance is valuable in many fields including (i) mineral exploration, where the type and amount of major minerals serve as indicators for valuable minor minerals, (ii) mineral extraction, where the performance of the process line is governed by the mineralogy, not the commonly used elemental compositions, (iii) *in situ* studies, where the mechanism and kinetics of phase evolution resulting from the application of an external variable can be examined and (iv) the optimization of production conditions for advanced materials.

The methodology of QPA is fraught with difficulties, many of which are experimental or derive from sample-related issues. Hence, it is necessary to verify diffraction-based phase abundances against independent methods. This should include calculation of the expected sample element composition (using the QPA and an assumed or measured composition of each phase) and comparing these values with the measured element composition. In those circumstances where this is not possible, the QPA values should be regarded only as semi-quantitative. While such values may be useful for deriving trends within a particular system, they cannot be regarded as an absolute measure.

References

Ahtee, M., Nurmela, M., Suortti, P. & Järvinen, M. (1989). *Correction for preferred orientation in Rietveld refinement. J. Appl. Cryst.* **22**, 261–268.

Alexander, L. E. & Klug, H. P. (1948). *Basic aspects of X-ray absorption in quantitative diffraction analysis of powder mixtures. Anal. Chem.* **20**, 886–889.

Ballirano, P. & Caminiti, R. (2001). *Rietveld refinements on laboratory energy dispersive X-ray diffraction (EDXD) data. J. Appl. Cryst.* **34**, 757–762.

Barnes, P., Colston, S., Craster, B., Hall, C., Jupe, A., Jacques, S., Cockcroft, J., Morgan, S., Johnson, M., O'Connor, D. & Bellotto, M.

(2000). *Time- and space-resolved dynamic studies on ceramic and cementitious materials. J. Synchrotron Rad.* **7**, 167–177.
Batchelder, M. & Cressey, G. (1998). *Rapid, accurate phase quantification of clay-bearing samples using a position-sensitive X-ray detector*. *Clays Clay Miner.* **46**, 183–194.
Bergmann, J., Friedel, P. & Kleeberg, R. (1998). *Bgmn – a new fundamental parameters based Rietveld program for laboratory X-ray sources; its use in quantitative analysis and structure investigations*. *IUCr Commission on Powder Diffraction Newsletter*, **20**, 5–8.
Bergmann, J. & Kleeberg, R. (1998). *Rietveld analysis of disordered layer silicates. Mater. Sci. Forum*, **278–281**, 300–305.
Bergmann, J., Kleeberg, R., Haase, A. & Breidenstein, B. (2000). *Advanced fundamental parameters model for improved profile analysis. Mater. Sci. Forum*, **347–349**, 303–308.
Bette, S., Dinnebier, R. E. & Freyer, D. (2015). *Structure solution and refinement of stacking-faulted NiCl(OH). J. Appl. Cryst.* **48**, 1706–1718.
Bish, D. L. & Howard, S. A. (1988). *Quantitative phase analysis using the Rietveld method. J. Appl. Cryst.* **21**, 86–91.
Bish, D. L. & Post, J. E. (1993). *Quantitative mineralogical analysis using the Rietveld full-pattern fitting method. Am. Mineral.* **78**, 932–940.
Bogue, R. H. (1929). *Calculation of the compounds in Portland cement. Ind. Eng. Chem. Anal. Ed.* **1**, 192–197.
Bordas, J., Glazer, A. M., Howard, C. J. & Bourdillon, A. J. (1977). *Energy-dispersive diffraction from polycrystalline materials using synchrotron radiation. Philos. Mag.* **35**, 311–323.
Brindley, G. W. (1945). *The effect of grain or particle size on X-ray reflections from mixed powders and alloys, considered in relation to the quantitative determination of crystalline substances by X-ray methods. London Edinb. Dubl. Philos. Mag. J. Sci.* **36**, 347–369.
Brindley, G. W. (1980). *Crystal structures of clay minerals and their X-ray identification*. Mineralogical Society Monograph No. 5, edited by G. W. Brindley & G. Brown, pp. 125–195. London: Mineralogical Society.
Bruker AXS (2013). *Topas v5: General profile and structure analysis software for powder diffraction data*. Version 5. https://www.bruker.com/topas.
Buhrke, V. E., Jenkins, R. & Smith, D. K. (1998). *A Practical Guide for the Preparation of Specimens for X-Ray Fluorescence and X-ray Diffraction Analysis*. New York: Wiley-VCH.
Buras, B., Gerward, L., Glazer, A. M., Hidaka, M. & Staun Olsen, J. (1979). *Quantitative structural studies by means of the energy-dispersive method with X-rays from a storage ring. J. Appl. Cryst.* **12**, 531–536.
Casas-Cabanas, M., Rodríguez-Carvajal, J. & Palacín, M. R. (2006). *FAULTS, a new program for refinement of powder diffraction patterns from layered structures. Z. Kristallogr. Suppl.* **23**, 243–248.
Cernik, R. J., Hansson, C. C. T., Martin, C. M., Preuss, M., Attallah, M., Korsunsky, A. M., Belnoue, J. P., Jun, T. S., Barnes, P., Jacques, S., Sochi, T. & Lazzari, O. (2011). *A synchrotron tomographic energy-dispersive diffraction imaging study of the aerospace alloy Ti 6246. J. Appl. Cryst.* **44**, 150–157.
Cheary, R. W. & Coelho, A. (1992). *A fundamental parameters approach to X-ray line-profile fitting. J. Appl. Cryst.* **25**, 109–121.
Cheary, R. W., Coelho, A. A. & Cline, J. P. (2004). *Fundamental parameters line profile fitting in laboratory diffractometers. J. Res. Natl Inst. Stand. Technol.* **109**, 1–25.
Chipera, S. J. & Bish, D. L. (2002). *FULLPAT: a full-pattern quantitative analysis program for X-ray powder diffraction using measured and calculated patterns. J. Appl. Cryst.* **35**, 744–749.
Chipera, S. J. & Bish, D. L. (2013). *Fitting full X-ray diffraction patterns for quantitative analysis: a method for readily quantifying crystalline and disordered phases. Adv. Mater. Phys. Chem.* **3**, 47–53.
Chung, F. H. (1974*a*). *Quantitative interpretation of X-ray diffraction patterns of mixtures. I. Matrix-flushing method for quantitative multicomponent analysis. J. Appl. Cryst.* **7**, 519–525.
Chung, F. H. (1974*b*). *Quantitative interpretation of X-ray diffraction patterns of mixtures. II. Adiabatic principle of X-ray diffraction analysis of mixtures. J. Appl. Cryst.* **7**, 526–531.
Chung, F. H. & Smith, D. K. (2000). *Industrial Applications of X-ray Diffraction*, edited by F. H. Chung & D. K. Smith, ch. 1, pp. 3–10, and ch. 2, pp. 13–32. New York: Marcel Dekker.
Cline, J. P., Von Dreele, R. B., Winburn, R., Stephens, P. W. & Filliben, J. J. (2011). *Addressing the amorphous content issue in quantitative phase analysis: the certification of NIST standard reference material 676a. Acta Cryst.* A**67**, 357–367.
Coelho, A. A., Evans, J. S. O. & Lewis, J. W. (2016). *Averaging the intensity of many-layered structures for accurate stacking-fault analysis using Rietveld refinement. J. Appl. Cryst.* **49**, 1740–1749.
Coelho, A. A., Chater, P. A. and Kern, A. (2015). *Fast synthesis and refinement of the atomic pair distribution function. J. Appl. Cryst.* **48**, 869–875
Cowley, J. M. (1976). *Diffraction by crystals with planar faults. I. General theory. Acta Cryst.* A**32**, 83–87.
Cressey, G. & Schofield, P. F. (1996). *Rapid whole-pattern profile-stripping method for the quantification of multiphase samples. Powder Diffr.* **11**, 35–39.
De La Torre, A. G., Ángeles, G., Bruque, S., Campo, J. & Aranda, M. A. G. (2002). *The superstructure of C3S from synchrotron and neutron powder diffraction and its role in quantitative phase analyses. Cem. Concr. Res.* **32**, 1347–1356.
De la Torre, A. G. & Aranda, M. A. G. (2003). *Accuracy in Rietveld quantitative phase analysis of Portland cements. J. Appl. Cryst.* **36**, 1169–1176.
Debye, P. & Scherrer, P. (1916). *Interferenzen an regellos orientierten Teilchen im Röntgenlicht Phys. Z.* **17**, 277–283.
Debye, P. & Scherrer, P. (1917). *X-ray interference produced by irregularly oriented particles: Constitution of graphite and amorphous C. Phys. Z.* **18**, 291–301.
Dohrmann, R., Rüping, K. B., Kleber, M., Ufer, K. & Jahn, R. (2009). *Variation of preferred orientation in oriented clay mounts as a result of sample preparation and composition. Clays Clay Miner.* **57**, 686–694.
Dollase, W. A. (1986). *Correction of intensities for preferred orientation in powder diffractometry: application of the March model. J. Appl. Cryst.* **19**, 267–272.
Drits, V. A. & Tchoubar, C. (1990). *X-ray diffraction by disordered lamellar structures: Theory and application to microdivided silicates and carbons*. Heidelberg: Springer Verlag.
Eberl, D. D. (2003). *User's guide to rockjock - a program for determining quantitative mineralogy from powder x-ray diffraction data.* U.S. Geological Survey Open-File Report 2003-78. http://pubs.er.usgs.gov/publication/ofr200378.
Egami, T. & Billinge, S. J. L. (2003). *Underneath the Bragg Peaks: Structural Analysis of Complex Materials*. Oxford: Elsevier.
Ehrenberg, H., Senyshyn, A., Hinterstein, M. & Fuess, H. (2013). *Modern Diffraction Methods*, edited by E. J. Mittemeijer & U. Welzel, pp. 491–517. Weinheim: Wiley-VCH Verlag GMBH & Co.
Elton, N. J. & Salt, P. D. (1996). *Particle statistics in quantitative X-ray diffractometry. Powder Diffr.* **11**, 218–229.
Fawcett, T. G., Kabekkodu, S. N., Blanton, J. R. & Blanton, T. N. (2017). *Chemical analysis by diffraction: the Powder Diffraction File. Powder Diffr.* 32, 63–71.
Fawcett, T. G., Needham, F., Faber, J. & Crowder, C. E. (2010). *International Centre for Diffraction Data round robin on quantitative Rietveld phase analysis of pharmaceuticals. Powder Diffr.* **25**, 60–67.
Frost, D. J. & Fei, Y. (1999). *Static compression of the hydrous magnesium silicate phase d to 30 GPa at room temperature. Phys. Chem. Miner.* **26**, 415–418.
Glazer, A. M., Hidaka, M. & Bordas, J. (1978). *Energy-dispersive powder profile refinement using synchrotron radiation. J. Appl. Cryst.* **11**, 165–172.
Gualtieri, A. F. (2000). *Accuracy of XRPD QPA using the combined Rietveld–RIR method. J. Appl. Cryst.* **33**, 267–278.
Gualtieri, A. F., Viani, A., Banchio, G. & Artioli, G. (2001). *Quantitative phase analysis of natural raw materials containing montmorillonite. Mater. Sci. Forum*, **378–381**, 702–709.
Hall, C., Barnes, P., Cockcroft, J. K., Colston, S. L., Häusermann, D., Jacques, S. D. M., Jupe, A. C. & Kunz, M. (1998). *Synchrotron energy-dispersive X-ray diffraction tomography. Nucl. Instrum. Methods Phys. Res. B*, **140**, 253–257.
Hall, C., Colston, S. L., Jupe, A. C., Jacques, S. D. M., Livingston, R., Ramadan, A. O. A., Amde, A. W. & Barnes, P. (2000). *Non-destructive tomographic energy-dispersive diffraction imaging of the interior of bulk concrete. Cem. Concr. Res.* **30**, 491–495.
Hendricks, S. & Teller, E. (1942). *X-ray interference in partially ordered layer lattices. J. Chem. Phys.* **10**, 147–167.
Hill, R. J. (1983). *Calculated X-ray powder diffraction data for phases encountered in lead/acid battery plates. J. Power Sources*, **9**, 55–71.
Hill, R. J. (1991). *Expanded use of the Rietveld method in studies of phase abundance in multiphase mixtures. Powder Diffr.* **6**, 74–77.

Hill, R. J. (1992). *The background in X-ray powder diffractograms: a case study of Rietveld analysis of minor phases using Ni-filtered and graphite-monochromated radiation. Powder Diffr.* **7**, 63–70.

Hill, R. J. & Howard, C. J. (1987). *Quantitative phase analysis from neutron powder diffraction data using the Rietveld method. J. Appl. Cryst.* **20**, 467–474.

Hill, R. J., Howard, C. J. & Reichert, B. E. (1991). *Quantitative phase abundance in Mg-PSZ by Rietveld analysis of neutron and X-ray diffraction data. Mater. Sci. Forum*, **34–36**, 159–163.

Hill, R. J. & Madsen, I. C. (2002). *Structure Determination from Powder Diffraction Data*, edited by W. David, K. Shankland, L. McCusker & C. Baerlocher, ch. 6, pp. 98–116. Oxford University Press.

Hubbard, C. R., Evans, E. H. & Smith, D. K. (1976). *The reference intensity ratio, I/Ic, for computer simulated powder patterns. J. Appl. Cryst.* **9**, 169–174.

Hubbard, C. R. & Snyder, R. L. (1988). *RIR – measurement and use in quantitative XRD. Powder Diffr.* **3**, 74–77.

Hull, A. W. (1917). *A new method of X-ray crystal analysis. Phys. Rev*. **10**, 661–696.

Hull, A. W. (1919). *A new method of chemical analysis. J. Am. Chem. Soc.* **41**, 1168–1175.

ICDD (2015). The Powder Diffraction File, database of the International Centre for Diffraction Data, release PDF4+, 2015. ICDD, 12 Campus Boulevard, Newton Square, Pennsylvania 19073–3273, USA.

Kaduk, J. A. (2000). In *Industrial Applications of X-ray Diffraction*, edited by F. H. Chung & D. K. Smith, pp. 207–253. New York: Marcel Dekker.

Kleeberg, R. (2005). *Results of the second Reynolds Cup contest in quantitative mineral analysis*. IUCr Commission on Powder Diffraction Newsletter, **30**, 22–26.

Klug, H. P. & Alexander, L. E. (1974). *X-ray Diffraction Procedures: For Polycrystalline and Amorphous Materials*. New York: Wiley.

Knorr, K. & Bornefeld, M. (2013). Proceedings of Process Mineralogy ’12, 7–9 November 2012. Cape Town, South Africa, pp. 651–652. http://www.proceedings.com/16755.html.

Knudsen, T. (1981). *Quantitative X-ray diffraction analysis with qualitative control of calibration samples. X-ray Spectrom.* **10**, 54–56.

Langford, J. I. (2004). In *Diffraction Analysis of the Microstructure of Materials*, edited by E. J. Mittemeijer & P. Scardi, pp. 3–11. Berlin: Springer-Verlag.

Larson, A. C. & Von Dreele, R. B. (2004). *General Structure Analysis System (GSAS)*. Report LAUR 86-748, Los Alamos National Laboratory, New Mexico, USA.

Le Bail, A., Duroy, H. & Fourquet, J. L. (1988). *Ab-initio structure determination of $LiSbWO_6$ by X-ray powder diffraction. Mater. Res. Bull.* **23**, 447–452.

Le Bail, A. & Jouanneaux, A. (1997). *A qualitative account for anisotropic broadening in whole-powder-diffraction-pattern fitting by second-rank tensors. J. Appl. Cryst.* **30**, 265–271.

León-Reina, L., De la Torre, A. G., Porras-Vázquez, J. M., Cruz, M., Ordonez, L. M., Alcobé, X., Gispert-Guirado, F., Larrañaga-Varga, A., Paul, M., Fuellmann, T., Schmidt, R. & Aranda, M. A. G. (2009). *Round robin on Rietveld quantitative phase analysis of Portland cements. J. Appl. Cryst.* **42**, 906–916.

Leoni, M., Gualtieri, A. F. & Roveri, N. (2004). *Simultaneous refinement of structure and microstructure of layered materials. J. Appl. Cryst.* **37**, 166–173.

Lippmann, F. (1970). *Functions describing preferred orientation in flat aggregates of flake-like clay minerals and in other axially symmetric fabrics. Contr. Miner. Petrol.* **25**, 77–94.

McCarty, D. K. (2002). *Quantitative mineral analysis of clay-bearing mixtures: The ‘Reynolds Cup’ contest*. IUCr Commission on Powder Diffraction Newsletter, **27** 12–16.

Madsen, I. C., Scarlett, N. V. Y., Cranswick, L. M. D. & Lwin, T. (2001). *Outcomes of the International Union of Crystallography Commission on Powder Diffraction Round Robin on Quantitative Phase Analysis: samples 1a to 1h. J. Appl. Cryst.* **34**, 409–426.

Madsen, I. C., Scarlett, N. V. Y. & Kern, A. (2011). *Description and survey of methodologies for the determination of amorphous content via x-ray powder diffraction. Z. Kristallogr.* **226**, 944–955.

Madsen, I. C., Scarlett, N. V. Y., Riley, D. P. & Raven, M. D. (2013). *Modern Powder Diffraction*, edited by E. J. Mittemeijer & U. Welzel, pp. 283–320. Weinheim: Wiley-VCH.

Madsen, I. C., Scarlett, N. V. Y. & Whittington, B. I. (2005). *Pressure acid leaching of nickel laterite ores: an in situ diffraction study of the mechanism and rate of reaction. J. Appl. Cryst.* **38**, 927–933.

Michalski, E. (1988). *The diffraction of X-rays by close-packed polytypic crystals containing single stacking faults. I. General theory. Acta Cryst.* A**44**, 640–649.

Michalski, E., Kaczmarek, S. M. & Demianiuk, M. (1988). *The diffraction of X-rays by close-packed polytypic crystals containing single stacking faults. II. Theory for hexagonal and rhombohedral structures. Acta Cryst.* A**44**, 650–657.

Morris, R. E., Harrison, W. T. A., Nicol, J. M., Wilkinson, A. P. & Cheetham, A. K. (1992). *Determination of complex structures by combined neutron and synchrotron X-ray powder diffraction. Nature*, **359**, 519–522.

Murray, J., Kirwan, L., Loan, M. & Hodnett, B. K. (2009). *In-situ synchrotron diffraction study of the hydrothermal transformation of goethite to hematite in sodium aluminate solutions. Hydrometallurgy*, **95**, 239–246.

Navias, L. (1925). *Quantitative determination of the development of mullite in fired clays by an X-ray method. J. Am. Ceram. Soc.* **8**, 296–302.

Norby, P., Cahill, C., Koleda, C. & Parise, J. B. (1998). *A reaction cell for in situ studies of hydrothermal titration. J. Appl. Cryst.* **31**, 481–483.

O’Connor, B. H. & Raven, M. D. (1988). *Application of the Rietveld refinement procedure in assaying powdered mixtures. Powder Diffr.* **3**, 2–6.

Omotoso, O., McCarty, D. K., Hillier, S. & Kleeberg, R. (2006). *Some successful approaches to quantitative mineral analysis as revealed by the 3rd Reynolds Cup contest. Clays Clay Miner.* **54**, 748–760.

Ottner, F., Gier, S., Kuderna, M. & Schwaighofer, B. (2000). *Results of an inter-laboratory comparison of methods for quantitative clay analysis. Appl. Clay Sci.* **17**, 223–243.

Parrish, W. (1965). Editor. *X-ray Analysis Papers*, 2nd ed. Eindhoven: Centrex Publishing Company.

Pawley, G. S. (1980). *EDINP, the Edinburgh powder profile refinement program. J. Appl. Cryst.* **13**, 630–633.

Pawley, G. S. (1981). *Unit-cell refinement from powder diffraction scans. J. Appl. Cryst.* **14**, 357–361.

Peplinski, B., Kleeberg, R., Bergmann, J. & Wenzel, J. (2004). *Quantitative phase analysis using the Rietveld method – estimates of possible problems based on two interlaboratory comparisons. Mater. Sci. Forum*, **443-444**, 45–50.

Popa, N. C. (1998). *The (hkl) dependence of diffraction-line broadening caused by strain and size for all Laue groups in Rietveld refinement. J. Appl. Cryst.* **31**, 176–180.

Raven, M. D. & Self, P. G. (2017). *Outcomes of 12 years of the Reynolds Cup quantitative mineral analysis round robin. Clays Clay Miner.* **65**, 122–134.

Reynolds, R. C. (1985). *Newmod, a computer program for the calculation of one-dimensional diffraction patterns of mixed-layered clays.* Hanover, USA.

Reynolds, R. (1989). *Quantitative mineral analysis of clays*. In *CMS Workshop Lectures 1*, edited by D. R. Pevear & F. A. Mumpton, pp. 4–37. Boulder: The Clay Minerals Society.

Reynolds, R. C. (1994). *Wildfire, a computer program for the calculation of threee-dimensional powder X-ray diffraction patterns for mica polytypes and their disordered variations.* Hanover, USA.

Reynolds, R. C. & Hower, J. (1970). *The nature of interlayering in mixed-layer illite-montmorillonites. Clays Clay Miner.* **18**, 25–36.

Rietveld, H. M. (1969). *A profile refinement method for nuclear and magnetic structures. J. Appl. Cryst.* **2**, 65–71.

Rowles, M. R., Styles, M. J., Madsen, I. C., Scarlett, N. V. Y., McGregor, K., Riley, D. P., Snook, G. A., Urban, A. J., Connolley, T. & Reinhard, C. (2012). *Quantification of passivation layer growth in inert anodes for molten salt electrochemistry by in situ energy-dispersive diffraction. J. Appl. Cryst.* **45**, 28–37.

Scarlett, N. V. Y. & Madsen, I. C. (2006). *Quantification of phases with partial or no known crystal structures. Powder Diffr.* **21**, 278–284.

Scarlett, N. V. Y., Madsen, I. C., Cranswick, L. M. D., Lwin, T., Groleau, E., Stephenson, G., Aylmore, M. & Agron-Olshina, N. (2002). *Outcomes of the International Union of Crystallography Commission on Powder Diffraction Round Robin on Quantitative Phase Analysis: samples 2, 3, 4, synthetic bauxite, natural granodiorite and pharmaceuticals. J. Appl. Cryst.* **35**, 383–400.

Scarlett, N. V. Y., Madsen, I. C., Evans, J. S. O., Coelho, A. A., McGregor, K., Rowles, M., Lanyon, M. R. & Urban, A. J. (2009). *Energy-*

dispersive diffraction studies of inert anodes. *J. Appl. Cryst.* **42**, 502–512.

Scarlett, N. V. Y., Madsen, I. C., Pownceby, M. I. & Christensen, A. N. (2004). *In situ X-ray diffraction analysis of iron ore sinter phases*. *J. Appl. Cryst.* **37**, 362–368.

Scarlett, N. V. Y., Madsen, I. C. & Whittington, B. I. (2008). *Time-resolved diffraction studies into the pressure acid leaching of nickel laterite ores: a comparison of laboratory and synchrotron X-ray experiments*. *J. Appl. Cryst.* **41**, 572–583.

Scarlett, N. V. Y., Pownceby, M. I., Madsen, I. C. & Christensen, A. N. (2004). *Reaction sequences in the formation of silico-ferrites of calcium and aluminum in iron ore sinter*. *Metall. Mater. Trans. B*, **35**, 929–936.

Schmitt, B., Brönnimann, C., Eikenberry, E. F., Gozzo, F., Hörmann, C., Horisberger, R. & Patterson, B. (2003). *Mythen detector system*. *Nucl. Instrum. Methods Phys. Res. A*, **501**, 267–272.

Smith, D. K. (1992). *Particle statistics and whole pattern methods in quantitative x-ray powder diffraction analysis. Adv. X-ray Anal.* **35**, 1–15.

Smith, D. K., Johnson, G. G., Scheible, A., Wims, A. M., Johnson, J. L. & Ullmann, G. (1987). *Quantitative X-ray powder diffraction method using the full diffraction pattern*. *Powder Diffr.* **2**, 73–77.

Snyder, R. L. & Bish, D. L. (1989). In *Modern Powder Diffraction*, edited by D. L. Bish & J. E. Post, pp. 101–142. Washington DC: Mineralogical Society of America.

Stephens, P. W. (1999). *Phenomenological model of anisotropic peak broadening in powder diffraction*. *J. Appl. Cryst.* **32**, 281–289.

Stinton, G. W. & Evans, J. S. O. (2007). *Parametric Rietveld refinement*. *J. Appl. Cryst.* **40**, 87–95.

Stutzman, P. E. & Leigh, S. (2000). Proceedings of the Twenty-Second International Conference on Cement Microscopy, 11–13 September 2000, Quebec City, Canada. https://cemmicro.org/publications/.

Styles, M. J., Rowles, M. R., Madsen, I. C., McGregor, K., Urban, A. J., Snook, G. A., Scarlett, N. V. Y. & Riley, D. P. (2012). *A furnace and environmental cell for the in situ investigation of molten salt electrolysis using high-energy X-ray diffraction*. *J. Synchrotron Rad.* **19**, 39–47.

Taylor, J. C. (1991). *Computer programs for standardless quantitative analysis of minerals using the full powder diffraction profile*. *Powder Diffr.* **6**, 2–9.

Taylor, J. C. & Rui, Z. (1992). *Simultaneous use of observed and calculated standard profiles in quantitative XRD analysis of minerals by the multiphase Rietveld method: the determination of pseudorutile in mineral sands products*. *Powder Diffr.* **7**, 152–161.

Taylor, R. M. & Norrish, K. (1966). *The measurement of orientation distribution and its application to quantitative X-ray diffraction analysis*. *Clay Miner.* **6**, 127–142.

Toraya (2016*a*). *A new method for quantitative phase analysis using X-ray powder diffraction: direct derivation of weight fractions from observed integrated intensities and chemical compositions of individual phases. J. Appl. Cryst.* **49**, 1508–1516

Toraya (2016*b*). *A new method for quantitative phase analysis using X-ray powder diffraction: direct derivation of weight fractions from observed integrated intensities and chemical compositions of individual phases. Corrigendum. J. Appl. Cryst.* **50**, 665.

Toraya, H. & Tsusaka, S. (1995). *Quantitative phase analysis using the whole-powder-pattern decomposition method. I. Solution from knowledge of chemical compositions*. *J. Appl. Cryst.* **28**, 392–399.

Treacy, M. M. J., Newsam, J. M. & Deem, M. W. (1991). *A general recursion method for calculating diffracted intensities from crystals containing planar faults*. *Proc. R. Soc. London Ser. A*, **433**, 499–520.

Ufer, K., Kleeberg, R., Bergmann, J., Curtius, H. & Dohrmann, R. (2008). *Refining real structure parameters of disordered layer structures within the Rietveld method*. *Z. Kristallogr.* Suppl. **27**, 151–158.

Ufer, K., Kleeberg, R., Bergmann, J. & Dohrmann, R. (2012). *Rietveld refinement of disordered illite-smectite mixed-layer structures by a recursive algorithm. II: powder-pattern refinement and quantitative phase analysis*. *Clays Clay Miner.* **60**, 535–552.

Ufer, K., Roth, G., Kleeberg, R., Stanjek, H. & Dohrmann, R. (2004). *Description of x-ray powder pattern of turbostratically disordered layer structures with a Rietveld compatible approach*. *Z. Kristallogr.* **219**, 519–527.

Ufer, K., Stanjek, H., Roth, G., Dohrmann, R., Kleeberg, R. & Kaufhold, S. (2008). *Quantitative phase analysis of bentonites by the Rietveld method*. *Clays Clay Miner.* **56**, 272–282.

Wang, X., Li, J., Hart, R. D., van Riessen, A. & McDonald, R. (2011). *Quantitative X-ray diffraction phase analysis of poorly ordered nontronite clay in nickel laterites*. *J. Appl. Cryst.* **44**, 902–910.

Warren, B. E. (1941). *X-ray diffraction in random layer lattices*. *Phys. Rev.* **59**, 693–698.

Webster, N. A. S., Madsen, I. C., Loan, M. J., Knott, R. B., Naim, F., Wallwork, K. S. & Kimpton, J. A. (2010). *An investigation of goethite-seeded $Al(OH)_3$ precipitation using in situ X-ray diffraction and Rietveld-based quantitative phase analysis. J. Appl. Cryst.* **43**, 466–472.

Webster, N. A. S., Pownceby, M. I. & Madsen, I. C. (2013). *In situ X-ray diffraction investigation of the formation mechanisms of silico-ferrite of calcium and aluminium-I-type (SFCA-I-type) complex calcium ferrites*. *ISIJ Int.* **53**, 1334–1340.

Westphal, T., Füllmann, T. & Pöllmann, H. (2009). *Rietveld quantification of amorphous portions with an internal standard – mathematical consequences of the experimental approach*. *Powder Diffr.* **24**, 239–243.

Williams, R. P., Hart, R. D. & van Riessen, A. (2011). *Quantification of the extent of reaction of metakaolin-based geopolymers using X-ray diffraction, scanning electron microscopy, and energy-dispersive spectroscopy*. *J. Am. Ceram. Soc.* **94**, 2663–2670.

Yuan, H. & Bish, D. (2010). *NEWMOD+, a new version of the NEWMOD program for interpreting X-ray powder diffraction patterns from interstratified clay minerals*. *Clays Clay Miner.* **58**, 318–326.

Zevin, L. & Viaene, W. (1990). *Impact of clay particle orientation on quantitative clay diffractometry*. *Clay Miner.* **25**, 401–418.

Zevin, L. S. & Kimmel, G. (1995). *Quantitative X-ray Diffractometry*. Springer-Verlag New York, Inc.

Zhao, Y., Von Dreele, R. B., Shankland, T. J., Weidner, D. J., Zhang, J., Wang, Y. & Gasparik, T. (1997). *Thermoelastic equation of state of jadeite $NaAlSi_2O_6$: an energy-dispersive Rietveld refinement study of low symmetry and multiple phases diffraction*. *Geophys. Res. Lett.* **24**, 5–8.

3.10. Accuracy in Rietveld quantitative phase analysis with strictly monochromatic Mo and Cu radiations

L. León-Reina, A. Cuesta, M. García-Maté, G. Álvarez-Pinazo, I. Santacruz, O. Vallcorba, A. G. De la Torre and M. A. G. Aranda

3.10.1. Introduction

Most industrial materials are multiphase systems and the accurate determination of their phase assemblage is key to understanding their performances. There are different approaches to carrying out quantitative phase analysis (QPA; see Chapter 3.9); however, nowadays, the Rietveld method is the most widely employed methodology for QPA of crystalline materials (Madsen *et al.*, 2001; Scarlett *et al.*, 2002), including cements (Stutzman, 2005; León-Reina *et al.*, 2009; Chapter 7.12).

The factors affecting the accuracy and precision of Rietveld quantitative phase analysis (RQPA) results can be gathered into three main groups: (i) instrument related, (ii) sample-preparation related and (iii) data-analysis protocol(s). The Rietveld method is a standardless methodology which uses the crystal-structure descriptions of each crystalline component to calculate its powder pattern. For this reason, the correct choice of crystal-structure description for each phase in multiphase materials is key (Zevin & Kimmel, 1995; Madsen *et al.*, 2001, 2011). The influence of the instrument type on RQPA has previously been evaluated (Madsen *et al.*, 2001) and the main conclusion was that neutron and synchrotron powder diffraction yielded the best results owing to larger irradiated volumes and also to the minimization of microabsorption effects.

High-energy (short-wavelength) X-rays contribute (i) to minimize absorption and microabsorption effects, (ii) to the measurement of a higher number of Bragg peaks and (iii) to increase the irradiated volume of the specimen. Figs. 3.10.1(*a*) and 3.10.1(*b*) show the irradiated volumes bathed by X-rays when using flat samples for Mo and Cu radiations in transmission geometry, and Fig. 3.10.1(*c*) shows the irradiated volume for Cu in reflection mode (Cuesta *et al.*, 2015). Mo radiation combined with a flat sample in transmission geometry allows an irradiated volume of close to 100 mm^3; meanwhile, for Cu radiation (flat samples in reflection and transmission geometries) the irradiated volumes are close to 5 mm^3 (Cuesta *et al.*, 2015). In this context, it is worth mentioning that the absorption correction for flat-

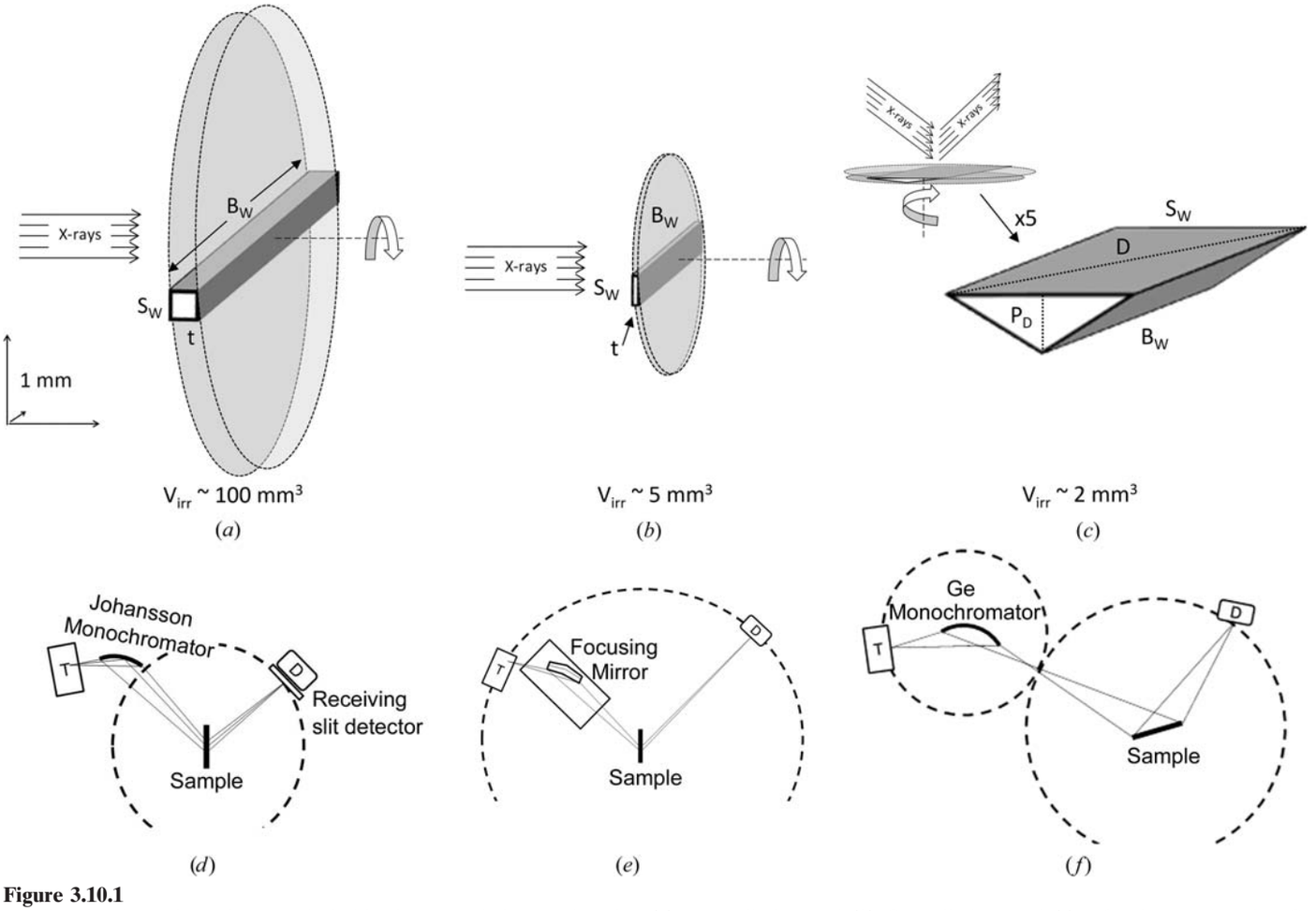

Figure 3.10.1
Irradiated volume for a flat sample holder in transmission mode using (*a*) Mo radiation and (*b*) Cu radiation, and (*c*) reflection mode using Cu radiation. Diffraction-geometry sketches: (*d*) transmission geometry with primary monochromator, (*e*) transmission geometry with focusing mirror and (*f*) reflection geometry with primary monochromator. [Reprinted from Cuesta *et al.* (2015) with permission from Cambridge University Press.]

Table 3.10.1
Cambridge Structural Database (CSD)/Inorganic Crystal Structure Database (ICSD) reference codes for all phases used for Rietveld refinements in this work and the linear absorption coefficients for the wavelengths used

Phase	Chemical formula	CSD/ICSD refcode	μ (cm^{-1}), Cu $K\alpha_1$, λ = 1.5406 Å	μ (cm^{-1}), Mo $K\alpha_1$, λ = 0.7093 Å	μ (cm^{-1}), λ = 0.7744/0.4959 Å	Reference
Glucose	$C_6H_{12}O_6$	Glucsa10	12	1	1.3/—	Brown & Levy (1979)
Fructose	$C_6H_{12}O_6$	Fructo11	12	1	1.3/—	Kanters *et al.* (1977)
α-Lactose monohydrate	$C_{12}H_{22}O_{11}{\cdot}H_2O$	Lactos10	12	1	1.3/—	Fries *et al.* (1971)
Xylose	$C_5H_{10}O_5$	Xylose	12	1	1.2/—	Hordvik (1971)
Gypsum	$CaSO_4{\cdot}(H_2O)_2$	151692	141	16	22/—	De la Torre *et al.* (2004)
Quartz	SiO_2	41414	92	10	11/2.9	Will *et al.* (1988)
s-Anhydrite	$CaSO_4$	16382	219	24	31/—	Kirfel & Will (1980)
i-Anhydrite	$CaSO_4$	79527	219	24	31/—	Bezou *et al.* (1995)
Zincite	ZnO	65120	285	244	—/89.1	Albertsson *et al.* (1989)
Calcite	$CaCO_3$	80869	194	22	27/7.3	Maslen *et al.* (1995)
$SrSO_4$	$SrSO_4$	22322	299	187	40/—	Garske & Peacor (1965)

sample transmission geometry is conceptually similar to that for flat-plate reflection geometry, but the length of the scattered beam path has to be properly defined. The corresponding equation is given in section A5.2.5 of Egami & Billinge (2003).

It must also be noted that Mo radiation has a major drawback when compared with Cu radiation. The λ^3 dependence of diffraction intensity favours the use of Cu radiation by a factor of 10.2. Thus, a detector receives approximately ten times as many diffracted X-ray photons with Cu than with Mo (this calculation neglects the different fractions of photons lost in the diffractometer optical paths). This fact can be partially overcome in modern X-ray detectors by increasing the counting time for patterns collected with Mo radiation without reaching prohibitively long times.

As discussed in Chapter 3.9, there are many factors that affect the accuracy and precision of QPA results. It must be recalled that accuracy is the agreement between the analytical result and the true value, and precision is the agreement between results for analyses repeated under the same conditions. Precision may be further divided into repeatability, the agreement between analyses derived from several measurements on the same specimen, and reproducibility, the agreement including re-preparation, re-measurement and data re-analysis of the same sample. Since the largest sources of errors in RQPA are experimental, sample preparation is key, as the reproducibility of peak-intensity measurements is mainly governed by particle statistics (Elton & Salt, 1996). It is generally accepted that the diffraction intensities have to be collected with an accuracy close to $\pm 1\%$ to obtain patterns that are suitable for good RQPA procedures (Von Dreele & Rodriguez-Carvajal, 2008). Milling the sample to reduce the particle size is an approach that should be exercised with care to avoid peak broadening or amorphization (Buhrke *et al.*, 1998). In order to improve particle statistics, a very common practice is to continuously spin the sample during data collection. A much less developed approach is to use high-energy, highly penetrating laboratory X-rays.

Another important issue in the QPA of mixtures is the limit of detection (LoD) and the limit of quantification (LoQ). In this context, the LoD can be defined as the minimal concentration of analyte that can be detected with acceptable reliability (Zevin & Kimmel, 1995), *i.e.* for which its strongest (not overlapped) diffraction peak in the powder pattern has a signal-to-noise ratio larger than 3.0. The 'reliability' criterion is flexible and may be defined by regulatory agencies, as is mainly the case for active pharmaceutical ingredients. Evidently, the LoD can be reduced (improved) by increasing the intensity of the X-ray source, for example using synchrotron radiation. In this context, the LoQ can be defined as the minimum content of an analyte that can be determined with a value at least three times larger than its standard deviation and determined to an acceptable reliability level. For RQPA, this type of approach can be straightforward, although the accuracy for minor phases may be quite poor.

The main aim of the study described here was to test whether the use of high-energy Mo radiation, combined with high-resolution X-ray optics, could yield more accurate RQPA than well established procedures using Cu radiation. In order to do so, three sets of mixtures with increasing amounts of a given phase (the spiking method) were prepared and the corresponding RQPA results were evaluated with calibration curves (least-squares fits) and quantitatively by statistical analysis based on the Kullback–Leibler distance (KLD; Kullback, 1968). The three series were (i) crystalline inorganic phase mixtures with increasing amounts of an inorganic phase, (ii) crystalline organic phase mixtures with increasing amounts of an organic compound and (iii) a series with an increasing content of amorphous ground glass. This last series is the most challenging case because the amorphous content is derived from a small overestimation of the internal standard employed. Amorphous content determination is important for many industries, including cements, glasses, pharmaceuticals and alloys.

3.10.2. Compounds and series

3.10.2.1. *Single phases*

Table 3.10.1 provides information about the phases used in this work. Further details can be found in the original publication (León-Reina *et al.*, 2016). All of the mixtures were prepared by grinding the weighed phases by hand in an agate pestle and mortar for 20 min to ensure homogeneity.

3.10.2.2. *Crystalline inorganic series*

A constant matrix of calcite (C), gypsum (Gp) and quartz (Q) was prepared. Six samples with known increasing amounts of insoluble anhydrite (i-A) were then produced and were labelled CGpQ_*x*A, where *x* repesents the target i-A content: 0.00, 0.125, 0.25, 0.50, 1.0, 2.0 or 4.0 wt%.

3.10.2.3. *Crystalline organic series*

A constant matrix of glucose (G), fructose (F) and lactose (L) was prepared. Six samples with known increasing amounts of xylose (X) were then produced and labelled GFL_*x*X, where *x* represents the target X content: 0.00, 0.125, 0.25, 0.50, 1.0, 2.0 or 4.0 wt%.

3.10.2.4. *Variable amorphous content series*

A constant matrix of calcite (C) and zincite (Z) was prepared. Five samples with increasing contents of amorphous ground glass (Gl) were then prepared. The elemental composition of the ground glass is given in García-Maté *et al.* (2014). The mixtures were labelled CZQ_*x*Gl, where *x* indicates 0, 2, 4, 8, 16 or 32 wt% Gl. The amorphous content was determined by adding ∼20 wt% quartz (Q) as an internal standard.

3.10.3. Analytical techniques

All phases and mixtures were studied with Mo $K\alpha_1$ (transmission geometry) and Cu $K\alpha_1$ (reflection geometry) monochromatic radiation. Table 3.10.1 shows the X-ray linear absorption coefficients for all of the phases, as microabsorption is always a concern in RQPA. A microabsorption correction was not applied in this work, but readers must be aware that this effect, if relevant, is one of the greatest source of inaccuracy in RQPA (Madsen *et al.*, 2001; Scarlett *et al.*, 2002). All of the phases were also characterized by scanning electron microscopy (see Fig. 3.10.2).

3.10.3.1. *Mo $K\alpha_1$ laboratory X-ray powder diffraction (LXRPD)*

Mo $K\alpha_1$ powder patterns were collected in transmission geometry in constant irradiated volume mode, in order to avoid any correction of the measured intensities, on a D8 ADVANCE (Bruker AXS) diffractometer (188.5 mm radius) equipped with a Ge(111) primary monochromator, which gives monochromatic Mo radiation (λ = 0.7093 Å). The X-ray tube operated at 50 kV and 50 mA. The optics configuration was a fixed divergence slit (2°) and a fixed diffracted anti-scatter slit (9°). A LYNXEYE XE 500 µm energy-dispersive linear detector, optimized for high-energy radiation, was used with the maximum opening angle. Using these conditions, the samples were measured between 3 and 35° 2θ with a step size of 0.006° and with a total measurement time of 3 h 5 min. The flat samples were placed into cylindrical holders between two Kapton foils (Cuesta *et al.*, 2015) and rotated at a rate of 10 revolutions per minute during data collection. Moreover, the absorption factor of each sample was experimentally measured by comparing the direct beam with and without the sample (Cuesta *et al.*, 2015). The amount of sample loaded (which determines the height of the cylinder) in the holders was adjusted to obtain a total absorption (μt) of ∼1, which corresponds to an absorption factor of ∼2.7 or 63% of direct-beam attenuation. For the organic samples this criterion was not followed as it would lead to very thick specimens. In this case, the maximum holder thickness was used (1.7 mm).

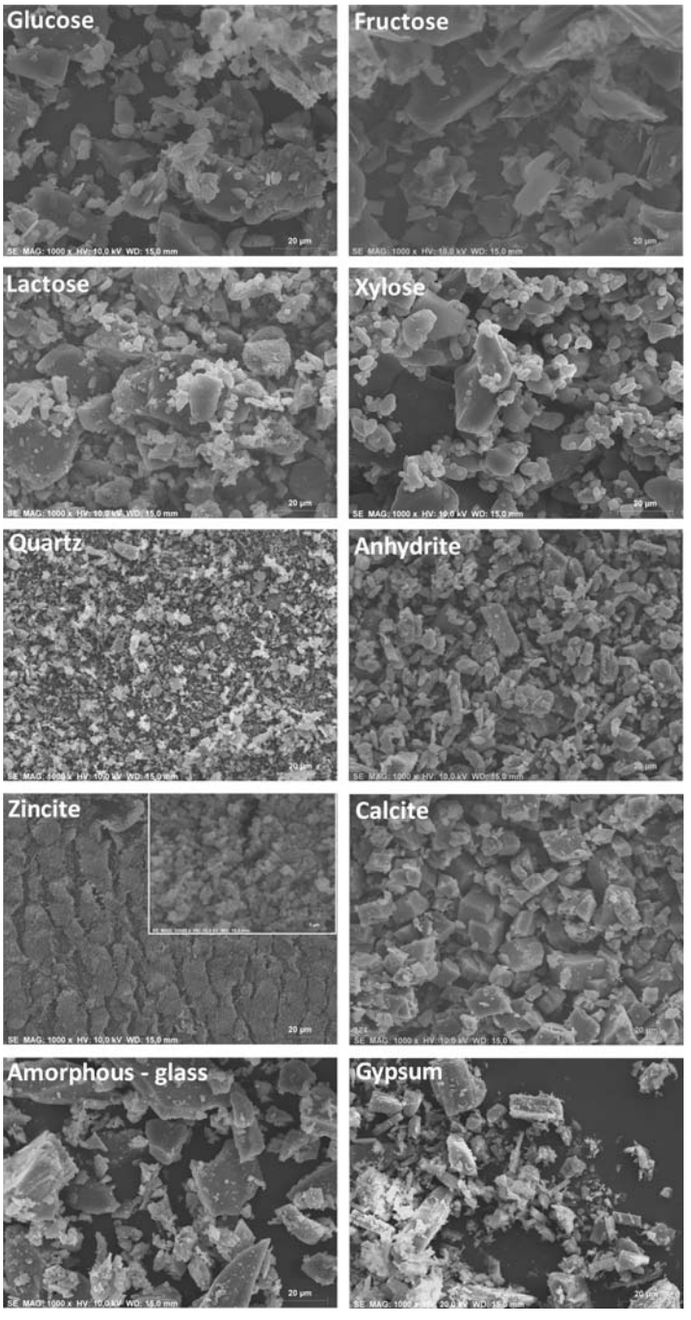

Figure 3.10.2
Scanning electron microscopy micrographs for the studied phases (×1000). The inset in the zincite micrograph shows the powder at higher magnification (×20 000).

3.10.3.2. *Cu $K\alpha_1$ laboratory X-ray powder diffraction (LXRPD)*

Cu $K\alpha_1$ powder patterns for exactly the same samples were recorded in reflection geometry ($\theta/2\theta$) on a X′Pert MPD PRO (PANalytical B.V.) diffractometer (240 mm radius) equipped with a Ge(111) primary monochromator, which gives monochromatic Cu radiation (λ = 1.54059 Å). The X-ray tube was operated at 45 kV and 40 mA. The optics configuration was a fixed divergence slit (0.5°), a fixed incident anti-scatter slit (1°), a fixed diffracted anti-scatter slit (0.5°) and an X′Celerator RTMS (real-time multiple strip) detector operating in scanning mode with the maximum active length. Using these conditions, the samples were measured between 6.5 and 81.5° 2θ with a step size of 0.0167° and a total measurement time of 2 h 36 min. The flat samples were prepared by rear charge of a flat sample holder in order to minimize preferred orientation and were rotated at a rate of 10 revolutions per minute.

The lowest analyte content samples, CGpQ_0.12A and GFL_0.12X, were measured three times using both radiations, Mo $K\alpha_1$ and Cu $K\alpha_1$, for a precision (reproducibility) assessment. Therefore, regrinding and reloading of the mixtures in the sample holder was carried out prior to every measurement.

3.10.3.3. *Transmission synchrotron X-ray powder diffraction (SXRPD)*

Powder patterns for the lowest analyte content samples, CGpQ_0.12A and GFL_0.12X, were also measured using synchrotron radiation. SXRPD data were collected in Debye–Scherrer (transmission) mode using the powder diffractometer at

the ALBA Light Source (Fauth *et al.*, 2013). The wavelength, λ = 0.77439 (2) Å, was selected with a double-crystal Si(111) monochromator and was determined using the NIST SRM640d Si standard (a = 5.43123 Å). The diffractometer is equipped with a MYTHEN-II detector system. The samples were loaded into glass capillaries 0.7 mm in diameter and were rapidly rotated during data collection to improve the diffracting-particle statistics. The data-acquisition time was 20 min per pattern to attain a very good signal-to-noise (S/N) ratio over the angular range 1–35° 2θ. Three patterns, taken at different positions along the capillaries, were collected for each sample.

SXRPD data for the amorphous content series, CZQ_xGl, were also measured at the ALBA Light Source. The experimental setup was the same as described above but the working wavelength was λ = 0.49591 (2) Å.

3.10.4. Powder-diffraction data analysis

All powder patterns were analysed by the Rietveld method using the *GSAS* software package (Larson & Von Dreele, 2000) with the pseudo-Voigt peak-shape function (Thompson *et al.*, 1987) for RQPA. The refined overall parameters were phase scale factors, background coefficients (linear interpolation function), unit-cell parameters, zero-shift error, peak-shape parameters and preferred-orientation coefficient, when needed. The March–Dollase preferred-orientation adjustment algorithm was employed (Dollase, 1986). The modelling direction must be given as input for the calculations. In this case, the directions for the different phases were taken from previous studies. Alternatively, this direction can be extracted from the pattern from an analysis of the differences between observed and calculated intensities for non-overlapped diffraction peaks. The crystal structures used are reported in Table 3.10.1.

In order to provide a single numerical assessment of the performance of each analysis, a statistic based on the KLD distance was used (Kullback, 1968). This approach was previously used to evaluate the accuracy of RQPA applied to standard mixtures (Madsen *et al.*, 2001; Scarlett *et al.*, 2002; León-Reina *et al.*, 2009). Both phase-related KLD distances and absolute values of the Kullback–Leibler distance (AKLD) were calculated. Accurate analyses are mirrored by low values of AKLD.

The overall amorphous content was determined from the internal standard methodology approach (De la Torre *et al.*, 2001; Aranda *et al.*, 2012) with quartz as an internal standard [using isotropic atomic displacement parameters (ADPs) of 0.045 and 0.0087 Å^2 for Si and O, respectively]. If the original sample contains an amorphous phase, the amount of standard will be overestimated in RQPA. From the (slight) overestimation of the standard, the amorphous content of the investigated sample can be derived (De la Torre *et al.*, 2001). The important role of the values of the ADPs in the results of RQPA mainly in amorphous content determinations using the internal-standard method has been discussed previously (Madsen *et al.*, 2011).

3.10.5. Crystalline single phases

All of the single phases were selected according to several parameters, such as relevance to selected applications, purity, particle size of the powder and preferred orientation. In order to check the suitability of the crystal structures used, all of the phases were first studied using powder diffraction with Mo $K\alpha_1$ radiation. These preliminary studies were of special interest for organic phases, as the CIF files obtained from the Cambridge

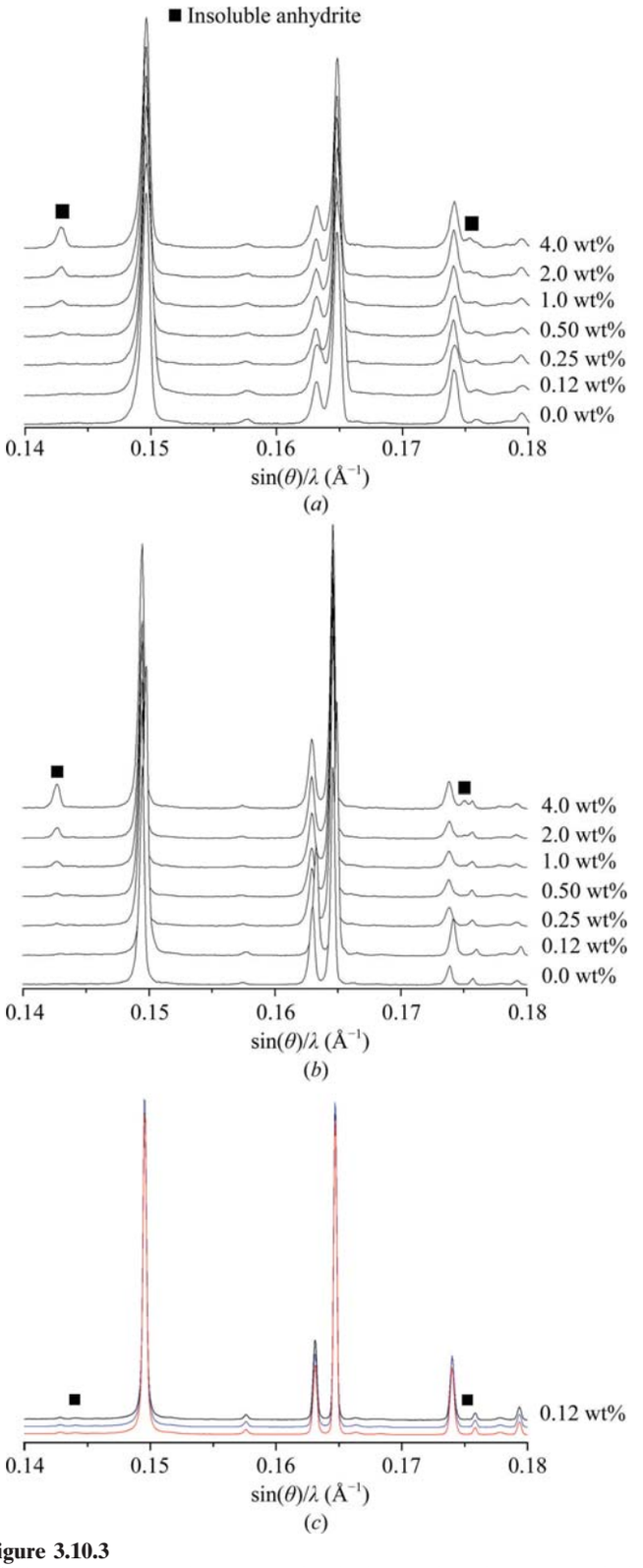

Figure 3.10.3
(*a*) Raw Mo $K\alpha_1$ powder patterns for the inorganic series composed of a constant matrix of calcite, gypsum and quartz, and increasing amounts of insoluble anhydrite (peaks highlighted with a solid square). (*b*) Raw Cu $K\alpha_1$ powder patterns for the same inorganic series. (*c*) Raw SXRPD patterns for CGpQ_0.12A collected at three different positions of the capillary (red, black and blue traces). The intensity values in (*c*) have been artificially offset to show the three different patterns.

Structural Database (CSD) did not contain the atomic displacement parameters (ADPs). For lactose and fructose, the ADPs were obtained from the original publications and were introduced manually into the *GSAS* control file. For glucose and

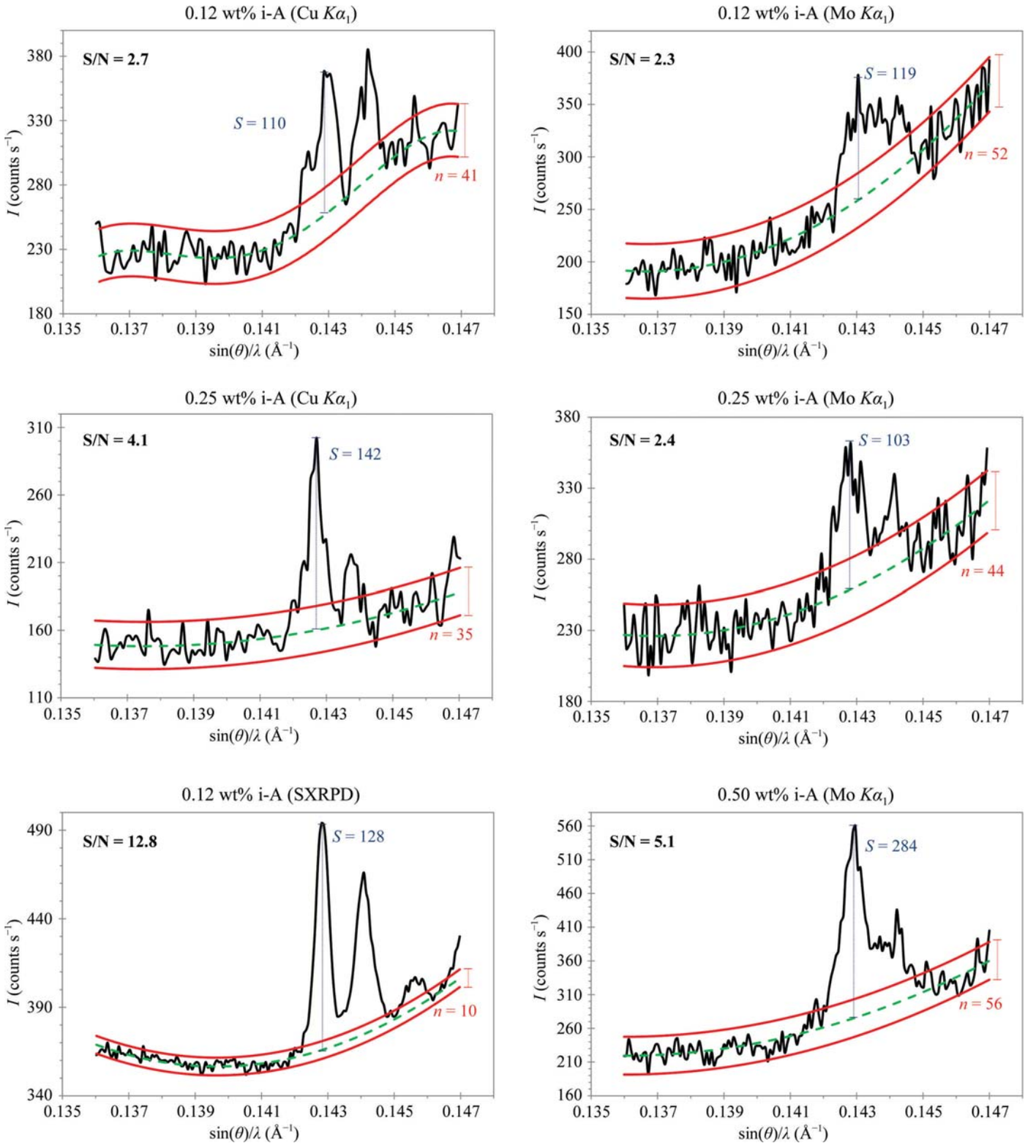

Figure 3.10.4
Selected region of the powder patterns showing the main diffraction peak of insoluble anhydrite for the low-content samples to investigate the limit of detection. Top left: Cu $K\alpha_1$ pattern for CGpQ_0.12A. Middle left, Cu $K\alpha_1$ pattern for CGpQ_0.25A. Bottom left, SXRPD pattern for CGpQ_0.12A. Top right, Mo $K\alpha_1$ pattern for CGpQ_0.12A. Middle right, Mo $K\alpha_1$ pattern for CGpQ_0.25A. Bottom right, Mo $K\alpha_1$ pattern for CGpQ_0.50A. The main peak of anhydrite, $(\theta)/\lambda = 0.143$ Å^{-1}, is located at 25.4, 11.6 and 12.7° 2θ for Cu $K\alpha_1$, Mo $K\alpha_1$ and synchrotron radiations, respectively. The peak at $\sin(\theta)/\lambda = 0.1445$ Å^{-1} is due to the soluble anhydrite from gypsum (constant content in all the samples). The very tiny peak at $\sin(\theta)/\lambda = 0.1457$ Å^{-1}, which is slightly visible only in the SXRPD pattern, arises from $SrSO_4$ (0.39 wt%) from gypsum.

xylose, the ADP values were not reported in the original publications. Hence, they were obtained from the fits to the Mo $K\alpha_1$ patterns for the single phases. Three groups of isotropic ADPs were refined: those for O, C and H atoms. The final ADP values are given in León-Reina *et al.* (2016) as well as the R_F values before and after optimization, showing the improvements in the fits. For RQPA of all of the mixtures the ADPs were kept fixed.

Preferred orientation was modelled by the March–Dollase algorithm along the [001] axis for both glucose and lactose. Since microparticle sizes and distributions for different phases may

result in some sample-related effects, such as preferred orientation, microabsorption and 'rock-in-the-dust/graininess' effects, all powders were characterized by scanning electron microscopy (SEM). Fig. 3.10.2 shows SEM micrographs for all of the phases. All inorganic samples were single phases except for gypsum and insoluble anhydrite. The impurity-phase contents for these two samples were reported in León-Reina *et al.* (2016).

Both organic and inorganic phases were also measured using Cu $K\alpha_1$ radiation in reflection mode. As expected, a transparency effect was observed in the Cu $K\alpha_1$ patterns for organic samples (Buhrke *et al.*, 1998).

3.10.6. Limits of detection and quantification

LoD and LoQ are two important quantities in the validation of any analytical method. LoD/LoQ are terms that are used to describe the smallest concentration of an analyte that can be reliably detected/assessed by an analytical procedure, as discussed in Section 3.10.1. In techniques such as Rietveld analysis, the approach of having a powder pattern with its strongest (not overlapped) diffraction peak with an S/N ratio of larger than 3.0 is not straightforward because the full powder pattern is evaluated.

Fig. 3.10.3 shows Mo $K\alpha_1$ and Cu $K\alpha_1$ raw patterns for the inorganic series with increasing amounts of insoluble anhydrite (labelled with solid squares) and Fig. 3.10.4 shows the strongest diffraction peak for i-A in the mixtures containing 0.123 wt% anhydrite (CGpQ_0.12A) and 0.25 wt% anhydrite (CGpQ_0.25A) to evaluate the limits of detection in the conditions reported in Section 3.10.5. For CGpQ_0.12A, both laboratory powder patterns yielded peaks with S/N ratios lower than 3.0 (top panels in Fig. 3.10.4). For CGpQ_0.25A, the Cu $K\alpha_1$ pattern yielded a clear peak with S/N = 4.1; therefore, it can be concluded that the LoD for insoluble anhydrite with this radiation in this mixture is slightly lower than 0.2 wt%. For Mo $K\alpha_1$ radiation, the CGpQ_0.25A and CGpQ_0.50A samples yielded patterns with peaks with S/N ratios of 2.4 and 5.1, respectively. Hence, it can be concluded that the LoD for i-A with this radiation in this mixture is quite close to 0.3 wt%.

The LoQ for i-A in this matrix was also studied. Three Mo $K\alpha_1$ and Cu $K\alpha_1$ patterns were collected for CGpQ_0.12A. For the three Mo $K\alpha_1$ patterns, the average analysis result for i-A was 0.28 (2) wt%, but the accuracy of the obtained value is poor, as the expected value was 0.12 wt%. Similarly, the average value for the analyses of three Cu $K\alpha_1$ patterns was 0.24 (2) wt%. The RQPA results are given as supporting information in León-Reina *et al.* (2016). It was concluded that i-A can be quantified in this mixture at the level of 0.12 wt%, but with a relative error close to 100%. If the 'acceptable reliability' criterion in the analysis is taken into consideration, the LoQ value would be close to 1.0 wt% in order to have a relative associated error lower than 20%.

CGpQ_0.12A was also studied by SXRPD. Fig. 3.10.3(*c*) shows the SXRPD patterns collected at three different positions of the capillary, which were almost identical, and Fig. 3.10.4 (bottom left) shows the main diffraction peak of anhydrite. The S/N ratio for the strongest diffraction peak of anhydrite was 12.8 and hence the limit of detection for i-A with synchrotron radiation in this matrix is below 0.10 wt%.

To quantify the accuracy of the analyses, the KLD methodology was used. The AKLD values for each analysis as well as the KLD values for i-A are reported in León-Reina *et al.* (2016). The synchrotron analyses clearly had better accuracy than those using laboratory radiation. Moreover, the Mo $K\alpha_1$ radiation analyses were slightly better than those obtained using Cu $K\alpha_1$ radiation.

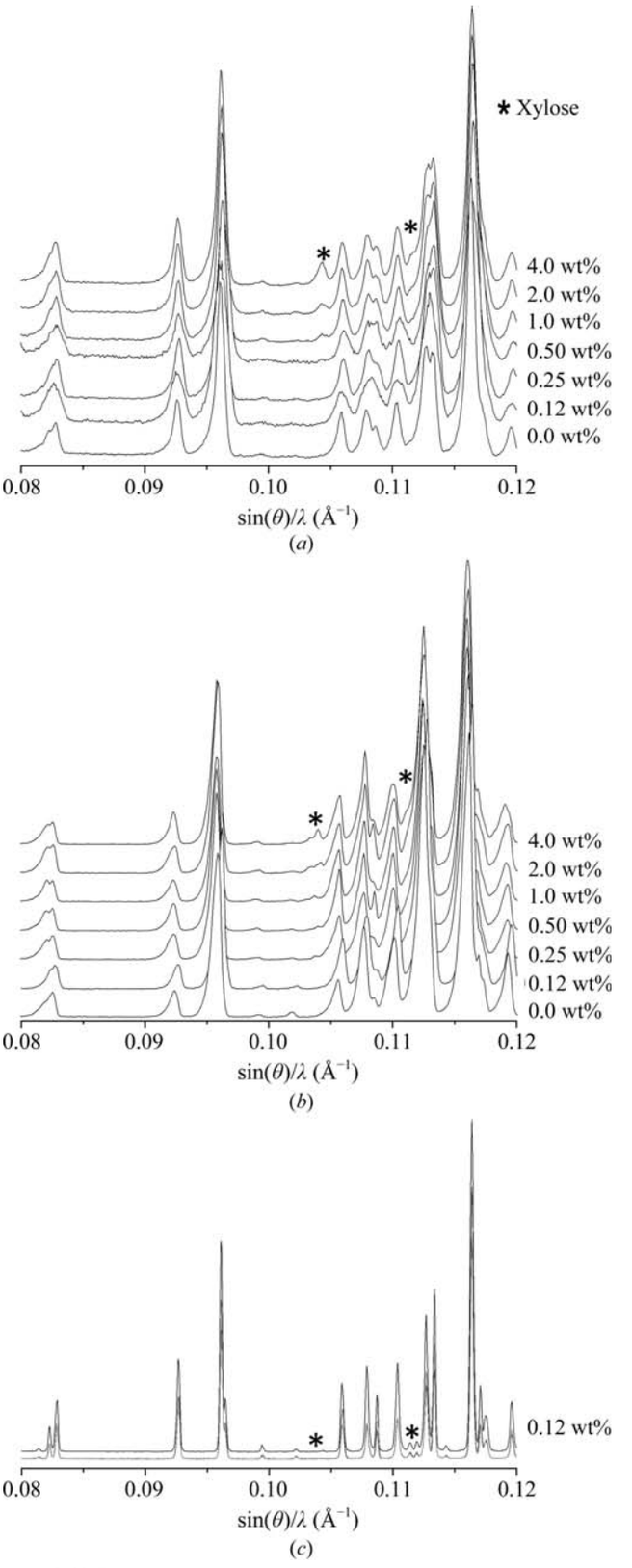

Figure 3.10.5
(*a*) Raw Mo $K\alpha_1$ powder patterns for the organic series composed of a constant matrix of glucose, fructose and lactose, and increasing amounts of xylose (peaks highlighted with an asterisk). (*b*) Raw Cu $K\alpha_1$ powder patterns for the same organic series. (*c*) Raw SXRPD patterns for GFL_0.12X collected at three different positions of the capillary (as collected).

Table 3.10.2
Rietveld quantitative phase analyses for the crystalline inorganic mixtures measured with Cu $K\alpha_1$ and Mo $K\alpha_1$ radiations

Weighed amounts (wt%) are also shown for comparison. Absolute values of the Kullback–Liebler distance (AKLD) for each mixture and the KLD value for i-anhydrite are also included. Trm, transmission; rfl, reflection.

	CGpQ_0.0A			CGpQ_0.25A			CGpQ_0.50A		
Phases	wt%	Mo trm	Cu rfl	wt%	Mo trm	Cu rfl	wt%	Mo trm	Cu rfl
C	32.9	32.6 (1)	30.4 (2)	32.8	32.0 (1)	33.6 (1)	32.7	33.2 (1)	32.8 (1)
Gp	31.7	31.7 (1)	34.5 (1)	31.7	32.5 (1)	31.6 (1)	31.6	30.1 (1)	30.7 (1)
Q	34.2	34.6 (1)	33.7 (1)	34.1	33.9 (1)	33.0 (1)	34.0	34.6 (1)	34.2 (1)
s-A	0.8	0.66 (3)	0.76 (5)	0.8	0.77 (4)	0.78 (5)	0.8	0.97 (3)	1.15 (5)
$SrSO_4$	0.4	0.44 (4)	0.70 (6)	0.4	0.44 (4)	0.67 (5)	0.4	0.39 (4)	0.56 (5)
i-A	—	—	—	0.28	0.42 (3)	0.42 (4)	0.52	0.71 (3)	0.71 (4)
AKLD sum		0.0089	0.0605		0.0198	0.0235		0.0295	0.0180
(i-A) KLD					−0.001	−0.001		−0.002	−0.002

	CGpQ_1.0A			CGpQ_2.0A			CGpQ_4.0A		
Phases	wt%	Mo trm	Cu rfl	wt%	Mo trm	Cu rfl	wt%	Mo trm	Cu rfl
C	32.5	32.8 (1)	32.6 (2)	32.2	31.3 (1)	31.4 (1)	31.6	31.2 (1)	31.8 (1)
Gp	31.5	30.4 (1)	30.7 (1)	31.1	32.1 (1)	32.3 (1)	30.5	30.7 (1)	30.5 (1)
Q	33.8	34.1 (1)	33.8 (1)	33.5	33.5 (1)	32.6 (1)	32.8	32.8 (1)	32.0 (1)
s-A	0.8	1.03 (4)	1.11 (5)	0.7	0.54 (3)	0.58 (5)	0.7	0.67 (3)	0.77 (4)
$SrSO_4$	0.4	0.43 (4)	0.68 (5)	0.4	0.48 (4)	0.68 (6)	0.4	0.45 (4)	0.63 (5)
i-A	1.02	1.23 (3)	1.17 (5)	2.02	2.05 (4)	2.38 (9)	4.02	4.30 (8)	4.33 (9)
AKLD sum		0.0214	0.0152		0.0218	0.0358		0.0095	0.0156
(i-A) KLD		−0.002	−0.001		0.000	−0.003		−0.004	−0.003

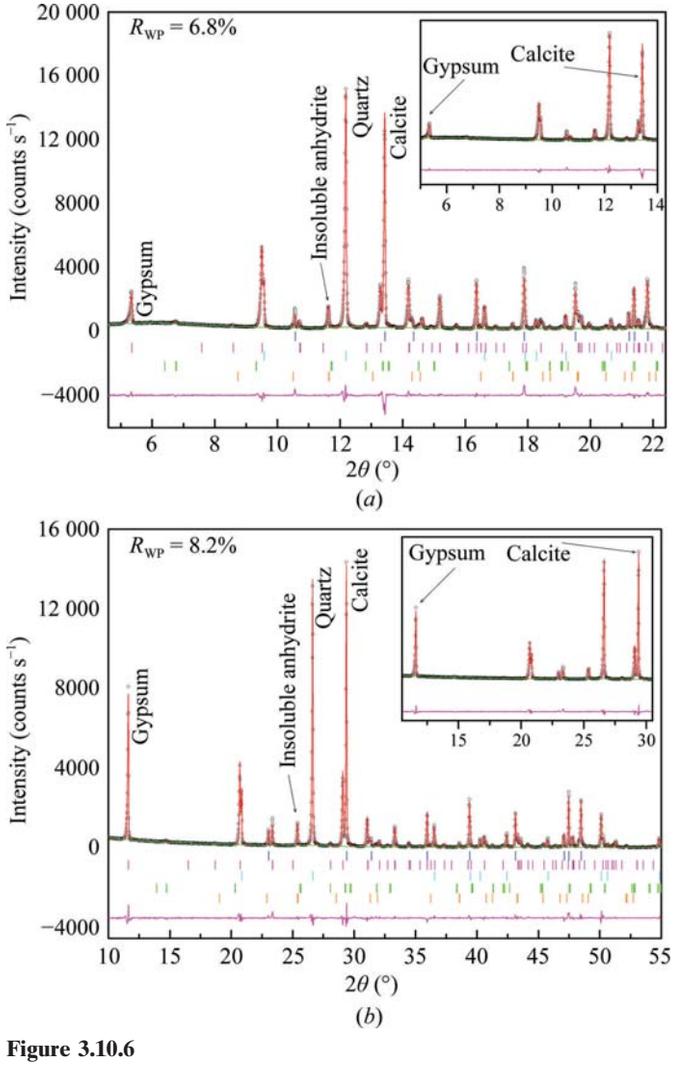

Figure 3.10.6
Selected range of the Rietveld plots for CGpQ_4.0A: (*a*) Mo $K\alpha_1$ and (*b*) Cu $K\alpha_1$ patterns. The inset highlights the effect of preferred orientation for gypsum and calcite.

Fig. 3.10.5 shows Mo $K\alpha_1$ and Cu $K\alpha_1$ raw patterns of the organic mixtures with increasing amounts of xylose. The strongest powder-diffraction peak for xylose in the GFL_0.12X patterns (with both Mo and Cu radiations) was not observed. The corresponding peak was observed in the GFL_0.25X patterns. Therefore, the LoD can be established as close to 0.25 wt%. The analysis results for xylose in GFL_0.25X were reported in León-Reina *et al.* (2016). These values showed that the results from Mo $K\alpha_1$ powder diffraction were slightly more accurate.

The LoQ for xylose was also studied. Once again, three Mo $K\alpha_1$ and Cu $K\alpha_1$ patterns were collected for GFL_0.12X. The average value for the analysis of the three Mo patterns was 0.18 (8) wt%. Similarly, the average result for the analyses of three Cu patterns was 0.34 (6) wt%. Full RQPA results are reported in the supporting information of León-Reina *et al.* (2016). The LoQ for xylose in this mixture for the two radiations can be established as close to 0.12 wt%. Indeed, if one applies an 'acceptable reliability' criterion, the LoQ would be much higher at above 1 wt%. The output of this study was that Cu $K\alpha_1$ radiation yielded a slightly less accurate result than that obtained from the Mo $K\alpha_1$ data.

GFL_0.12X was also studied by SXRPD in a rotating glass capillary in transmission mode. Fig. 3.10.5(*c*) shows SXRPD patterns for GFL_0.12X collected at three different positions of the same capillary. The powder patterns showed quite different peak ratios. It is important to bear in mind that filling a glass capillary with organic compounds is sometimes not easy due to electrostatic charge effects. For this reason, the phase ratio within the part of capillary bathed by the X-rays might not be the same as that of the sample under study. The behaviour observed in Fig. 3.10.5(*c*) could be explained by inhomogeneous capillary filling. Hence, in this case, the RQPA results are unreliable. Even in 'well behaved' samples, inhomogeneous filling of small capillaries could result in problems. Readers should be aware of this, and the authors strongly recommend that at least three patterns should be collected along the capillary and superimposed. If there is inhomogeneous filling the patterns will differ, and extreme care

has to be exercised when filling capillaries in order to minimize this problem.

3.10.7. Increasing inorganic crystalline phase content series

Table 3.10.2 reports the RQPA results for six inorganic mixtures with increasing amounts of i-A measured with Mo $K\alpha_1$ (transmission) and Cu $K\alpha_1$ (reflection). The Rietveld plots of the mixture with 4 wt% i-A are shown in Fig. 3.10.6. For most of the samples, the AKLD values (see Table 3.10.2) for Mo $K\alpha_1$ radiation are slightly smaller than the corresponding values obtained for Cu $K\alpha_1$ radiation. For this reason, we can conclude that the Mo $K\alpha_1$ analyses are slightly better than those derived using Cu $K\alpha_1$ radiation.

On the other hand, calcite and gypsum presented preferred orientations, with the axes being [104] and [010], respectively. This effect was modelled using the March–Dollase algorithm. Preferred orientation makes the $0l0$ reflections for gypsum have higher intensities in the Cu $K\alpha_1$ patterns, and smaller intensities in the Mo $K\alpha_1$ patterns, than those calculated from the crystal structure (see insets in Fig. 3.10.6). As a consequence, the refined values for flat samples in reflection and transmission geometries were smaller and larger than 1.0, respectively (Cuesta *et al.*, 2015). Although preferred orientation is present in all patterns, the Cu $K\alpha_1$ patterns were recorded in reflection geometry (flat samples), while the Mo $K\alpha_1$ measurements were collected in transmission (also flat samples). This results in opposite diffraction intensity changes and points towards another (possible) fruitful use: joint refinement of these two types of patterns to counterbalance the effects of preferred orientation in RQPA.

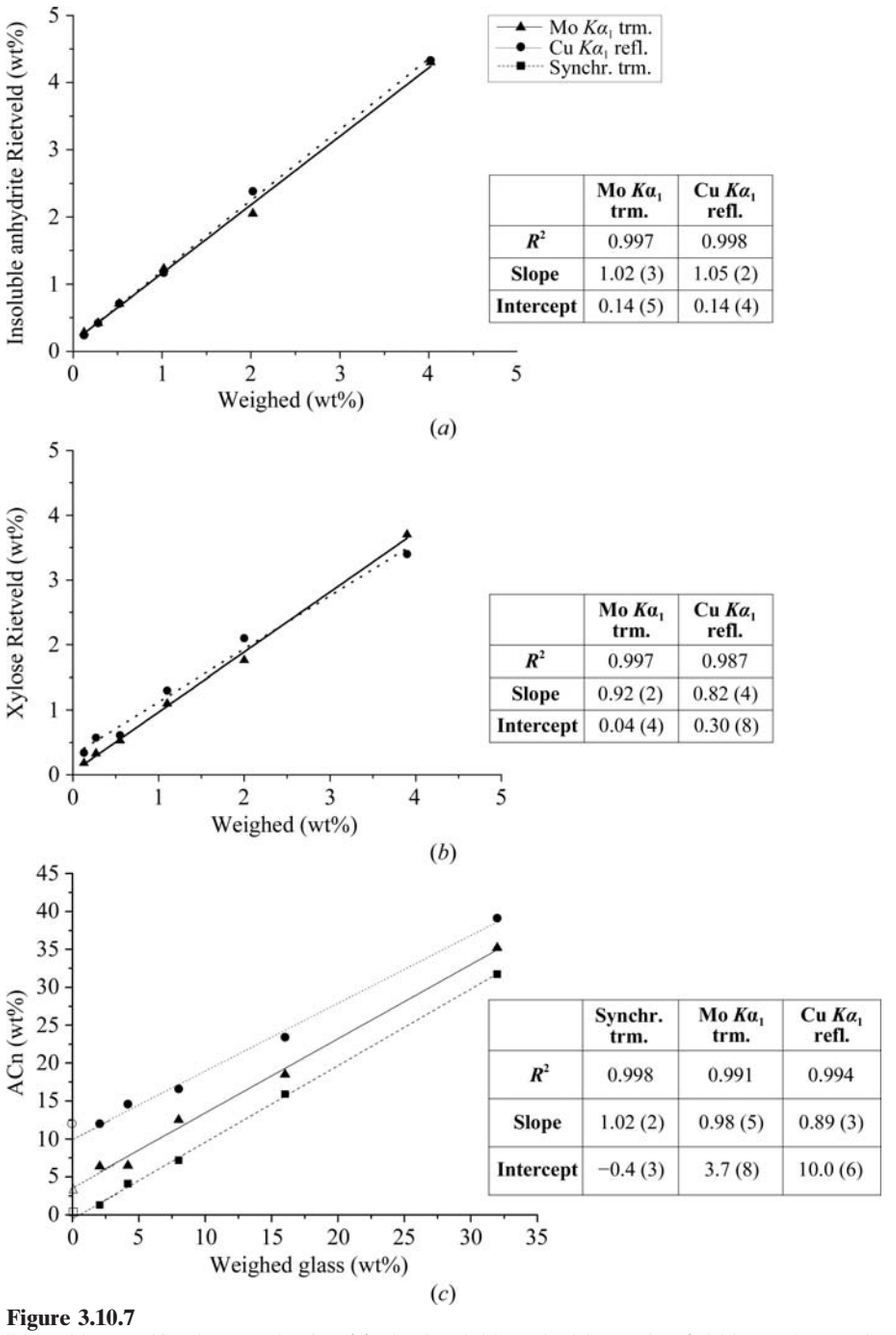

	Mo $K\alpha_1$ trm.	Cu $K\alpha_1$ refl.
R^2	0.997	0.998
Slope	1.02 (3)	1.05 (2)
Intercept	0.14 (5)	0.14 (4)

	Mo $K\alpha_1$ trm.	Cu $K\alpha_1$ refl.
R^2	0.997	0.987
Slope	0.92 (2)	0.82 (4)
Intercept	0.04 (4)	0.30 (8)

	Synchr. trm.	Mo $K\alpha_1$ trm.	Cu $K\alpha_1$ refl.
R^2	0.998	0.991	0.994
Slope	1.02 (2)	0.98 (5)	0.89 (3)
Intercept	−0.4 (3)	3.7 (8)	10.0 (6)

Figure 3.10.7
Rietveld quantification results for (*a*) the insoluble anhydrite series (within an inorganic crystalline matrix), (*b*) the xylose series (within an organic crystalline matrix) and (*c*) the ground-glass series (within an inorganic crystalline matrix) as a function of the weighed amount of each phase. Open symbols represent the derived amorphous contents in the mixtures without any added glass. The results of the least-squares fits are also shown.

Fig. 3.10.7(*a*) shows the quantified i-A contents (wt%), as determined by the Rietveld methodology, as a function of the weighed i-A amount. The two R^2 values for the fits are very close to 1.00, and the intercept values are very close to zero, showing the appropriateness of the Rietveld methodology for quantifying crystalline materials. Furthermore, the slopes of the calibration curves are also 1.00 in both cases. Consequently, this study allows it to be concluded that RQPA for crystalline inorganic phases using powder-diffraction patterns collected using Mo $K\alpha_1$ radiation yields results that are as accurate as those obtained from the well established method using Cu $K\alpha_1$.

3.10.8. Increasing crystalline organic phase content series

Table 3.10.3 shows RQPA results for six mixtures prepared with G, F, L and an increasing amount of X measured with Mo $K\alpha_1$ (transmission) and Cu $K\alpha_1$ (reflection). In general, the values obtained using both radiations are quite similar to the weighed values. The AKLD values and the KLD values for the xylose phase are also reported in Table 3.10.3. The AKLD values from Mo $K\alpha_1$ and Cu $K\alpha_1$ radiations are relatively similar. The main problem for RQPA of organic mixtures measured in reflection geometry is related to the low X-ray absorption of the samples and the transparency effects that lead to poor peak shapes and even some split peaks in the powder patterns, as discussed previously (León-Reina *et al.*, 2016).

Fig. 3.10.7(*b*) shows the quantified xylose contents (wt%) as determined by the Rietveld methodology as a function of the weighed amount of xylose added to the mixtures. The results were plotted to obtain the calibration lines with increasing content of the analyte. Both plots gave R^2 values close to 1.0. However, the slope values were 0.92 and 0.82 for Mo $K\alpha_1$ and Cu $K\alpha_1$ radiations, respec-

Table 3.10.3
RQPA for the crystalline organic mixtures measured with Cu $K\alpha_1$ and Mo $K\alpha_1$ radiations

Weighed amounts (wt%) are also shown for the sake of comparison. Absolute values of the Kullback–Liebler distance (AKLD) for each mixture and the KLD value for xylose are also included. Trm, transmission; rfl, reflection.

	GFL_0.0X			GFL_0.25X			GFL_0.50X		
Phases	wt%	Mo trm	Cu rfl	wt%	Mo trm	Cu rfl	wt%	Mo trm	Cu rfl
G	33.4	33.8 (1)	33.5 (3)	33.3	33.6 (1)	33.1 (2)	33.2	32.3 (2)	33.5 (2)
F	33.5	31.7 (1)	32.7 (3)	33.4	32.3 (1)	34.3 (2)	33.3	32.1 (2)	33.4 (2)
L	33.1	34.5 (1)	33.7 (3)	33.0	33.7 (1)	32.0 (2)	33.0	35.0 (3)	32.5 (2)
X	—	—		0.27	0.33 (4)	0.57 (9)	0.55	0.53 (8)	0.61 (9)
AKLD sum		0.0362	0.0150		0.0216	0.0231		0.0410	0.0096
(X) KLD		—	—		−0.001	−0.002		0.000	−0.001

	GFL_1.0X			GFL_2.0X			GFL_4.0X		
Phases	wt%	Mo trm	Cu rfl	wt%	Mo trm	Cu rfl	wt%	Mo trm	Cu rfl
G	33.0	34.7 (1)	33.6 (2)	32.7	32.2 (1)	31.5 (2)	32.0	32.8 (1)	33.6 (2)
F	33.1	32.6 (1)	33.7 (2)	32.8	31.7 (1)	34.4 (2)	32.2	30.7 (1)	32.5 (2)
L	32.8	31.6 (2)	31.4 (2)	32.5	34.3 (1)	32.0 (2)	31.8	32.9 (1)	30.5 (2)
X	1.1	1.10 (5)	1.3 (1)	2.0	1.76 (5)	2.1 (1)	3.9	3.70 (5)	3.4 (2)
AKLD sum		0.0338	0.0280		0.0363	0.0339		0.0361	0.0372
(X) KLD		0.000	−0.002		0.003	−0.001		0.002	0.005

Table 3.10.4
Rietveld quantitative phase analyses of the CQZ_*x*Gl mixture, where quartz (Q) is the internal standard, to derive amorphous content (am), obtained from SXRPD, Mo $K\alpha_1$ and Cu $K\alpha_1$ patterns

Absolute values of the Kullback–Liebler distance (AKLD) for each mixture and the KLD value for the amorphous content are also included. Trm, transmission; rfl, reflection.

	Weighed			Synchrotron trm				
Mixture	C wt%	Z wt%	Gl wt%	C wt%	Z wt%	Am wt%	AKLD sum	Am KLD
CZQ_0Gl	50.01	49.99	0.00	49.9 (1)	49.6 (1)	0.4 (1)	0.0050	—
CZQ_2Gl	48.98	48.96	2.05	49.7 (1)	49.0 (1)	1.3 (1)	0.0169	0.009
CZQ_4Gl	47.93	47.91	4.17	47.9 (1)	47.6 (1)	4.5 (1)	0.0066	−0.003
CZQ_8Gl	46.00	46.00	7.99	46.6 (1)	45.9 (1)	7.5 (1)	0.0120	0.005
CZQ_16Gl	41.99	41.99	16.01	42.0 (1)	41.6 (1)	16.4 (1)	0.0079	−0.004
CZQ_32Gl	34.00	34.00	31.99	34.0(1)	33.7 (1)	32.3 (1)	0.0061	−0.003

	Mo $K\alpha_1$ trm					Cu $K\alpha_1$ rfl				
Mixture	C wt%	Z wt%	Am wt%	AKLD sum	Am KLD	C wt%	Z wt%	Am wt%	AKLD sum	Am KLD
CZQ_0Gl	47.5 (1)	49.0 (1)	3.5 (1)	0.0358	—	47.2 (1)	40.8 (1)	12.0 (1)	0.1305	—
CZQ_2Gl	45.9 (1)	47.7 (1)	6.4 (1)	0.0679	−0.023	47.4 (1)	40.6 (1)	12.0 (1)	0.1440	−0.036
CZQ_4Gl	46.5 (1)	47.0 (1)	6.5 (1)	0.0422	−0.019	45.8 (1)	39.7 (1)	14.6 (1)	0.1641	−0.052
CZQ_8Gl	42.6 (1)	44.8 (1)	12.5 (1)	0.0832	−0.036	45.3 (1)	38.1 (1)	16.6 (1)	0.1522	−0.058
CZQ_16Gl	39.9 (1)	41.7 (1)	18.5 (1)	0.0475	−0.023	40.9 (1)	35.8 (1)	23.4 (1)	0.1388	−0.061
CZQ_32Gl	31.7 (1)	33.1 (1)	35.2 (1)	0.0635	−0.031	32.2 (1)	28.7 (1)	39.1 (1)	0.1403	−0.064

tively. Slope values close to 1.0 mirror accurate analyses. Furthermore, the *y*-intercept values were 0.04 and 0.30 for Mo $K\alpha_1$ and Cu $K\alpha_1$ radiations, respectively. A *y*-intercept value close to 0.0 mirrors accurate analyses. Hence, it can be concluded that slightly more accurate analyses are obtained for Mo $K\alpha_1$ powder diffraction in transmission when compared with Cu $K\alpha_1$ powder diffraction in reflection for organic crystalline samples.

3.10.9. Increasing amorphous content series within an inorganic crystalline phase matrix

Fig. 3.10.8 shows Mo $K\alpha_1$ (transmission), Cu $K\alpha_1$ (reflection) and SXRPD (transmission) raw patterns for the mixtures with increasing amounts of glass. It is important to highlight that the increase in the background due to the glass is very modest even for ∼32 wt% of glass. Table 3.10.4 shows the RQPA of these mixtures, prepared with C, Z and an increasing amount of Gl, for the three radiations. The glass-free sample may contain amorphous material from the employed phases. Hence, we used the SXRPD data to calculate a correction factor for quartz to yield zero amorphous content for the glass-free sample (León-Reina *et al.*, 2016).

The linear fit to the amorphous content values obtained using SXRPD was very good, R^2 = 0.998, with the slope being 1.00 within the errors (see Fig. 3.10.7*c*). This plot also shows the quantified amorphous contents, in weight percentage, as a function of the amount of added ground glass, measured with Mo $K\alpha_1$ and Cu $K\alpha_1$ radiations. Open symbols indicate the derived amorphous contents obtained with the internal-standard method in the mixture without any added glass, CZQ_0Gl. Both R^2 values are quite close to 1.00, showing the consistency of the internal-standard methodology. However, the slope values were 0.98 and 0.89 for Mo $K\alpha_1$ and Cu $K\alpha_1$ radiations, respectively. Furthermore, the *y*-intercept values were 3.7 and 10.0 for Mo $K\alpha_1$ and Cu $K\alpha_1$ radiations, respectively. Again, slope values close to 1.0 and *y* intercepts close to 0.0 mirror accurate analyses. It must also

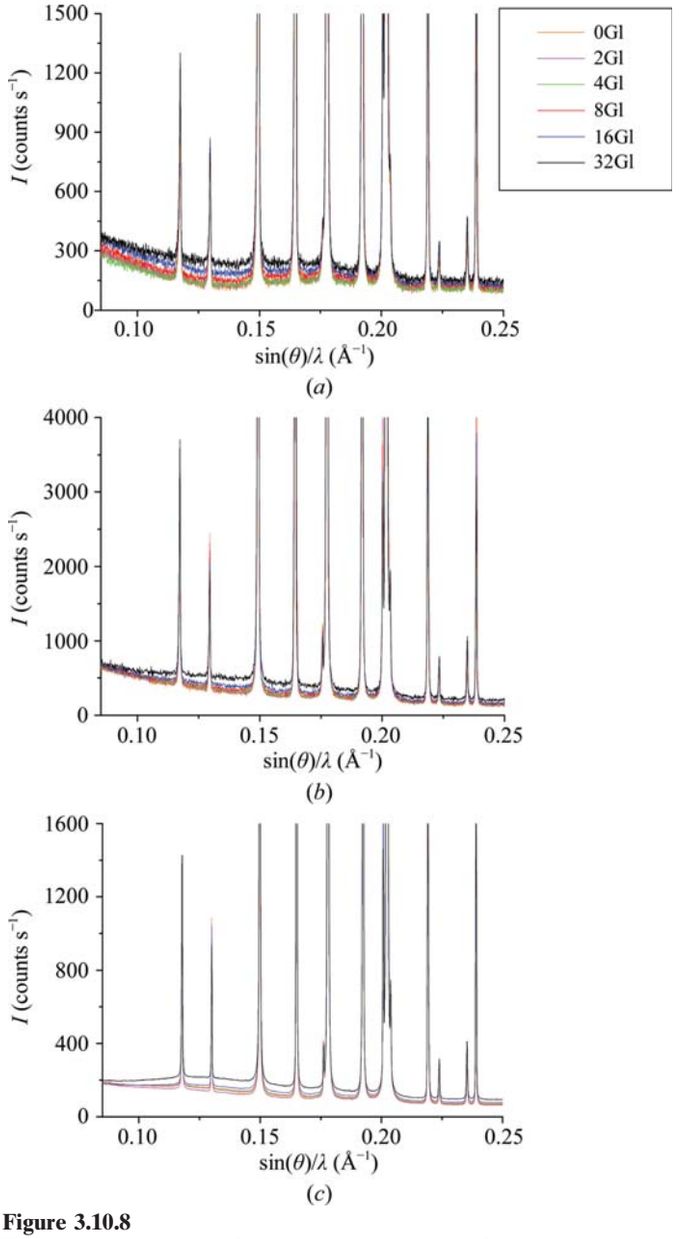

Figure 3.10.8
Raw powder patterns for the amorphous-material-containing series composed of a constant matrix of calcite and zincite, and increasing amounts of ground glass. Quartz was added as internal standard. (*a*) Mo $K\alpha_1$, (*b*) Cu $K\alpha_1$ and (*c*) SXRPD radiations. The intensities of the patterns have been rescaled to highlight the contributions of the glass to the background.

be pointed out that for the Mo $K\alpha_1$ analyses the value from the measurement of the Gl-free sample, 3.5 wt%, matches the value from the *y* intercept of the plot, 3.7 wt%, very well. Meanwhile, there is a much larger discrepancy for the similar Cu-based analyses, 12.0 and 10.0 wt%, respectively, which is quite far from zero. Hence, it is concluded that the amorphous contents derived from Mo $K\alpha_1$ data are more accurate than those derived from Cu $K\alpha_1$ data. However, it is not possible to reliably quantify amorphous contents below ~8–10 wt% from Mo $K\alpha_1$ and Cu $K\alpha_1$ diffraction data (see Table 3.10.4) with the internal-standard method.

On the contrary, SXRPD reliably allows quantification of amorphous contents down to ~2 wt% for this relatively simple mixture. In addition, the AKLD and the KLD values reported in Table 3.10.4 demonstrate that the synchrotron analyses are indeed much better than the laboratory analyses.

3.10.10. Conclusions

(i) We have thoroughly studied the limit of detection for a well crystallized inorganic phase in an inorganic compound matrix. We have determined the following LoDs for insoluble anhydrite: ~0.2 wt%, ~0.3 wt% and lower than 0.1 wt% for Cu $K\alpha_1$, Mo $K\alpha_1$ and synchrotron radiations, respectively. We conclude that the LoD is slightly better for Cu $K\alpha_1$ than for Mo $K\alpha_1$ because the λ^3 dependence of the diffraction intensity, with similar acquisition times, yielded slightly better signal-to-noise ratios in the Cu patterns. Of course, detector efficiencies also play a role in the measured signal-to-noise ratios.

(ii) We have also studied the limit of quantification for a well crystallized inorganic phase using laboratory X-ray powder diffraction. This phase could be quantified at the level of 0.12 wt% in stable fits with repeatable outputs and good precision. However, the accuracy of these analyses was quite poor, with relative errors close to 100%. Only contents higher than 1.0 wt% yielded analyses with relative errors lower than 20%.

(iii) The Rietveld quantitative phase analysis results from high-resolution Mo $K\alpha_1$ powder diffraction (transmission geometry) and high-resolution Cu $K\alpha_1$ powder diffraction (reflection geometry) were quite similar for a series of crystalline inorganic phase samples. We inferred the validation of the Mo-based analyses procedure from this initial study, as it yielded results very close to well established high-resolution Cu radiation analyses (see Fig. 3.10.7*a*). From the comparison of the AKLD values for the two types of analyses, it was demonstrated that the Mo $K\alpha_1$ analyses were slightly better than those using Cu $K\alpha_1$.

(iv) Comparison of the results obtained from Mo-based and Cu-based patterns for a series of crystalline organic phase mixtures showed that the Mo $K\alpha_1$ analyses gave slightly more accurate values. This conclusion was drawn because the calibration curve obtained from Mo patterns with increasing content of xylose gave an R^2 value closer to 1.0, a slope closer to 1.0 and an intercept value close to 0.0 (see Fig. 3.10.7*b*). The slightly poorer results from Cu $K\alpha_1$ analyses are very likely to be due to the transparency effects in reflection geometry.

(v) Comparison of the results obtained from Mo $K\alpha_1$ and Cu $K\alpha_1$ patterns for a series containing increasing amounts of amorphous glass also indicated that the Mo-based analyses were slightly more accurate than the corresponding Cu $K\alpha_1$ analyses. This conclusion was drawn because the obtained calibration curve from the Mo data has (1) a slope closer to 1.0, (2) a smaller amorphous value for the glass-free sample and (3) a closer agreement between the intercept from the least-squares fit and the determined amorphous value for the glass-free sample (see Fig. 3.10.7*c*). The AKLD analysis confirmed this outcome. Furthermore, the results from synchrotron data have the best accuracy, as shown by the calibration plot and the AKLD analysis.

Finally, we conclude that for the challenging quantification analyses studied here, the results derived from high-energy Mo $K\alpha_1$ patterns were slightly more accurate than those obtained from Cu $K\alpha_1$ patterns. We justify this conclusion based on the larger tested volume for Mo $K\alpha_1$ analyses, which led to better statistics/accuracy in the recorded powder-pattern intensities. The minimization of microabsorption in the Mo $K\alpha_1$ transmission

data is very likely to be an additional factor in the improved accuracy.

This chapter is based on an article *Accuracy in Rietveld quantitative phase analysis: a comparative study of strictly monochromatic Mo and Cu radiations* by León-Reina *et al.* [(2016), *J. Appl. Cryst.* **49**, 722–735]. The work was supported by Spanish MINECO through BIA2014-57658-C2-2-R, which is co-funded by FEDER, and BIA2014-57658-C2-1-R research grants. Funding from Junta de Andalucía (grant P11-FQM-07517) is also acknowledged. We thank CELLS-ALBA (Barcelona, Spain) for providing synchrotron beam time on the BL04-MSPD beamline. All raw powder-diffraction data files underlying this work can be accessed at Zenodo at https://doi.org/10.5281/zenodo.1291900 and used under the Creative Commons Attribution license.

References

Albertsson, J., Abrahams, S. C. & Kvick, Å. (1989). *Atomic displacement, anharmonic thermal vibration, expansivity and pyroelectric coefficient thermal dependences in ZnO. Acta Cryst.* B**45**, 34–40.

Aranda, M. A. G., De la Torre, Á. G. & León-Reina, L. (2012). *Rietveld quantitative phase analysis of OPC clinkers, cements and hydration products. Rev. Mineral. Geochem.* **74**, 169–209.

Bezou, C., Nonat, A., Mutin, J.-C., Christensen, A. N. & Lehmann, M. S. (1995). *Investigation of the crystal structure of γ-$CaSO_4$, $CaSO_4$·0.5H_2O, and $CaSO_4$·0.6H_2O by powder diffraction methods. J. Solid State Chem.* **117**, 165–176.

Brown, G. M. & Levy, H. A. (1979). *α-D-Glucose: further refinement based on neutron-diffraction data. Acta Cryst.* B**35**, 656–659.

Buhrke, V. E., Jenkins, R. & Smith, D. K. (1998). *A Practical Guide for the Preparation of Specimens for X-ray Fluorescence and X-ray Diffraction Analysis.* New York: Wiley.

Cuesta, A., Álvarez-Pinazo, G., García-Maté, M., Santacruz, I., Aranda, M. A. G., De la Torre, Á. G. & León-Reina, L. (2015). *Rietveld quantitative phase analysis with molybdenum radiation. Powder Diffr.* **30**, 25–35.

De La Torre, A. G., Bruque, S. & Aranda, M. A. G. (2001). *Rietveld quantitative amorphous content analysis. J. Appl. Cryst.* **34**, 196–202.

De la Torre, Á. G., López-Olmo, M., Álvarez-Rua, C., García-Granda, S. & Aranda, M. A. G. (2004). *Structure and microstructure of gypsum and its relevance to Rietveld quantitative phase analyses. Powder Diffr.* **19**, 240–246.

Dollase, W. A. (1986). *Correction of intensities for preferred orientation in powder diffractometry: application of the March model. J. Appl. Cryst.* **19**, 267–272.

Egami, T. & Billinge, S. J. L. (2003). *Underneath the Bragg Peaks. Structural Analysis of Complex Materials.* Amsterdam: Pergamon.

Elton, N. J. & Salt, P. D. (1996). *Particle statistics in quantitative X-ray diffractometry. Powder Diffr.* **11**, 218–229.

Fauth, F., Peral, I., Popescu, C. & Knapp, M. (2013). *The new material science powder diffraction beamline at ALBA synchrotron. Powder Diffr.* **28**, S360–S370.

Fries, D. C., Rao, S. T. & Sundaralingam, M. (1971). *Structural chemistry of carbohydrates. III. Crystal and molecular structure of 4-O-β-D-galactopyranosyl-α-D-glucopyranose monohydrate (α-lactose monohydrate). Acta Cryst.* B**27**, 994–1005.

García-Maté, M., Santacruz, I., Cuesta, A., León-Reina, L., Aranda, M. A. G., Baco, I., Morin, V., Walenta, G., Gartner, E. & De la Torre, A. G. (2014). *Amorphous content determination in calcium sulfoaluminate related materials by external and internal standard methodologies. Adv. Cem. Res.* **27**, 417–423.

Garske, D. & Peacor, D. R. (1965). *Refinement of the structure of celestite $SrSO_4$. Z. Kristallogr.* **121**, 204–210.

Hordvik, A. (1971). *The crystal and molecular structure of α-xylose. Acta Chem. Scand.* **25**, 2175–2182.

Kanters, J. A., Roelofsen, G., Alblas, B. P. & Meinders, I. (1977). *The crystal and molecular structure of β-D-fructose, with emphasis on anomeric effect and hydrogen-bond interactions. Acta Cryst.* B**33**, 665–672.

Kirfel, A. & Will, G. (1980). *Charge density in anhydrite, $CaSO_4$, from X-ray and neutron diffraction measurements. Acta Cryst.* B**36**, 2881–2890.

Kullback, S. (1968). *Information Theory and Statistics*, pp. 1–11. New York: Dover.

Larson, A. C. & Von Dreele, R. B. (2000). *General Structure Analysis System (GSAS)*. Los Alamos National Laboratory Report LAUR 86-748.

León-Reina, L., De la Torre, A. G., Porras-Vázquez, J. M., Cruz, M., Ordonez, L. M., Alcobé, X., Gispert-Guirado, F., Larrañaga-Varga, A., Paul, M., Fuellmann, T., Schmidt, R. & Aranda, M. A. G. (2009). *Round robin on Rietveld quantitative phase analysis of Portland cements. J. Appl. Cryst.* **42**, 906–916.

León-Reina, L., García-Maté, M., Álvarez-Pinazo, G., Santacruz, I., Vallcorba, O., De la Torre, A. G. & Aranda, M. A. G. (2016). *Accuracy in Rietveld quantitative phase analysis: a comparative study of strictly monochromatic Mo and Cu radiations. J. Appl. Cryst.* **49**, 722–735.

Madsen, I. C., Scarlett, N. V. Y., Cranswick, L. M. D. & Lwin, T. (2001). *Outcomes of the International Union of Crystallography Commission on Powder Diffraction Round Robin on Quantitative Phase Analysis: samples 1a to 1h. J. Appl. Cryst.* **34**, 409–426.

Madsen, I. C., Scarlett, N. V. Y. & Kern, A. (2011). *Description and survey of methodologies for the determination of amorphous content via X-ray powder diffraction. Z. Kristallogr.* **226**, 944–955.

Maslen, E. N., Streltsov, V. A., Streltsova, N. R. & Ishizawa, N. (1995). *Electron density and optical anisotropy in rhombohedral carbonates. III. Synchrotron X-ray studies of $CaCO_3$, $MgCO_3$ and $MnCO_3$. Acta Cryst.* B**51**, 929–939.

Scarlett, N. V. Y., Madsen, I. C., Cranswick, L. M. D., Lwin, T., Groleau, E., Stephenson, G., Aylmore, M. & Agron-Olshina, N. (2002). *Outcomes of the International Union of Crystallography Commission on Powder Diffraction Round Robin on Quantitative Phase Analysis: samples 2, 3, 4, synthetic bauxite, natural granodiorite and pharmaceuticals. J. Appl. Cryst.* **35**, 383–400.

Stutzman, P. (2005). *Powder diffraction analysis of hydraulic cements: ASTM Rietveld round-robin results on precision. Powder Diffr.* **20**, 97–100.

Thompson, P., Cox, D. E. & Hastings, J. B. (1987). *Rietveld refinement of Debye–Scherrer synchrotron X-ray data from Al_2O_3. J. Appl. Cryst.* **20**, 79–83.

Von Dreele, R. B. & Rodriguez-Carvajal, J. (2008). *Powder Diffraction: Theory and Practice*, edited by R. E. Dinnebier & S. J. L. Billinge, pp. 58–88. Cambridge: Royal Society of Chemistry. https://doi.org/10.1039/9781847558237-00058.

Will, G., Bellotto, M., Parrish, W. & Hart, M. (1988). *Crystal structures of quartz and magnesium germanate by profile analysis of synchrotron-radiation high-resolution powder data. J. Appl. Cryst.* **21**, 182–191.

Zevin, L. S. & Kimmel, G. (1995). *Quantitative X-ray Diffractometry*. New York: Springer-Verlag.